Talanta

The International Journal of Pure and Applied Analytical Chemistry

Aims & Scope

Talanta provides a forum for the publication of original research papers, preliminary communications, and critical reviews in all branches of pure and applied analytical chemistry. Papers are evaluated based on established guidelines, including the fundamental nature of the study, scientific novelty, substantial improvement or advantage over existing technology or methods, and demonstrated analytical applicability. Original research papers on fundamental studies, and novel sensor and instrumentation development, are especially encouraged. Novel or improved applications in areas such as clinical and biological chemistry, environmental analysis, geochemistry, and materials science and engineering are welcome.

Analytical performance of methods should be determined, including interference and matrix effects, and methods should be validated by comparison with a standard method, or analysis of a certified reference material. The developed method should especially comprise information on selectivity, sensitivity, detection limits, accuracy, and reliability. However, applying official validation or robustness studies to a routine method or technique does not necessarily constitute novelty. Proper statistical treatment of the data should be provided. Relevant literature should be cited, including related publications by the authors, and authors should discuss how their proposed methodology compares with previously reported methods.

Since classical spectrophotometric measurements and applications (including derivative spectrophometry), fluorimetry, solvent extraction, titrimetry, chemometrics, etc. are well established and are considered routine analytical methods, studies in such areas should demonstrate a unique and substantial advantage over presently known systems. New reagents or systems should demonstrate clear advantage, and their presentation should be comprehensive rather than generating a series of similar papers for several analytes or similar reagents. Modifications of reagents should demonstrate significant improvements. Obvious application of known chemistries or methods to established instrumental techniques are discouraged.

Application of established analytical approaches to relatively simple matrices having no major interferences, such as pharmaceutical preparations, are discouraged unless considerable improvements over other methods in the literature are demonstrated. Papers dealing with analytical data such as stability constants, pK_a values, etc. should be submitted to more specific journals, unless novel analytical methodology is demonstrated, or important analytical data are provided which could be useful in the development of analytical procedures.

Talanta 79 (2009) 900–904

Contents lists available at ScienceDirect

Talanta

journal homepage: www.elsevier.com/locate/talanta

Determination of low level nitrite and nitrate in biological, food and environmental samples by gas chromatography–mass spectrometry and liquid chromatography with fluorescence detection

Mehmet Akyüz*, Şevket Ata

Zonguldak Karaelmas University, Faculty of Arts and Sciences, Department of Chemistry, 67100 Zonguldak, Turkey

ARTICLE INFO

Article history:
Received 18 November 2008
Received in revised form 30 April 2009
Accepted 13 May 2009
Available online 22 May 2009

Keywords:
Nitrite and nitrate
NAT
GC–MS and LC-FL
Biological
Food and environmental samples

ABSTRACT

Gas chromatography–mass spectrometry (GC–MS) and liquid chromatography with fluorescence detection (LC-FL) methods have been proposed for the determination of low level nitrite and nitrate in biological, food and environmental samples. The methods include derivatization of aqueous nitrite with 2,3-diaminonaphthalene (DAN), enzymatic reduction of nitrate to nitrite, extraction with toluene and chromatographic analyses of highly fluorescent 2,3-naphthotriazole (NAT) derivative of nitrite by using GC–MS in selected-ion-monitoring (SIM) mode and LC-FL. Nitrite and nitrate ions in solid samples were extracted with 0.5 M aqueous NaOH by sonication. The recoveries of nitrite and nitrate ions based on GC–MS and LC-FL results were 98.40% and 98.10% and the precision of these methods, as indicated by the relative standard deviations (RSDs) were 1.00% for nitrite and 1.20% for nitrate, respectively. The limits of detection of the GC–MS in SIM mode and LC-FL methods based on S/N = 3 were 0.02 and 0.29 pg/ml for nitrite and 0.03 and 0.30 pg/ml for nitrate, respectively.

1. Introduction

Nitrite (NO_2^-) and nitrate (NO_3^-), the major stable oxidation products of nitric oxide (NO) [1–3], are ubiquitous within biological, food and environmental samples [4] and their biological levels are proposed as indices of cellular NO production [5–7]. Nitric oxide, biosynthesized from the amino acid L-arginine by a specific neuronal NO synthase [3,5], is an important neurotransmitter in various regions of the central nervous system that plays a significant and mysterious role in many biological and physiological functions such as inhibition of platelet aggregation, atherosclerosis, myorelaxant activity, inflammation, blood pressure, immune response and cardiovascular regulation. NO, well known for its cytoprotective and cytotoxic effects [8,9], has a very short half-life ($t_{1/2} < 5$ s) in biological fluids and reacts with oxygen species and biological molecules such as dioxygen, superoxide and oxyhemoglobin to form a variety of products, mainly including nitrite and nitrate [1–3]. Therefore, the determination of nitrite and nitrate are often performed to estimate NO level in biological fluids and cell culture medium [2–6,10].

Nitrite and/or nitrate are usually added to processed meat products as their sodium or potassium salts to retain the red colour and flavour of fresh meat and provide protection against microorganisms, such as *Clostridium botulinum* that can cause food poisoning [11–13]. Nitrite, causes the condition known as methemoglobinemia, also called "blue baby syndrome", can be reacted with especially secondary amines and amides to form carcinogenic nitrosamines and nitrosamides in food products and within the human digestive systems [14,15]. Nitrate is also a concern because it can readily be converted to nitrite by microbial reduction in food products and saliva, although it is more stable and less toxic than nitrite [14,16,17].

Nitrogen oxides (NO_x), destroy the lining of the respiratory surface, thereby reducing the intake of oxygen for the body leading to respiratory allergies like asthma [18,19], are primary air pollutants and they form NO_3^- and its conjugated acid (HNO_3) as a major components of atmospheric aerosols [20]. The HNO_3/NO_3^- not only represents a significant flux from the atmosphere to surface water, but also contributes substantially to the acidity of precipitation. Nitrite and its conjugated nitrous acid (HONO) are involved in the formation of nitrosamines in condensed phases and the photolysis of these N(III) species are considered as a predominant source of OH radicals in the low atmosphere, particularly, in the early morning when the concentrations of other hydroxyl radical sources such as formaldehyde and ozone, are low [21].

Nitrite and nitrate are widespread contaminants of both ground and surface waters and the levels of these compounds are increased as a result of excrements of livestock and human and organic wastes from chemical industries, domestic wastes, septic tank effluents and the use of nitrogenous fertilizers and herbicides in agriculture [20,22]. Therefore, determination of low level nitrite and nitrate

* Corresponding author. Tel.: +90 372 257 40 10x1371; fax: +90 372 257 41 81.
E-mail address: makyuz2004@yahoo.co.uk (M. Akyüz).

0039-9140/$ – see front matter © 2009 Elsevier B.V. All rights reserved.
doi:10.1016/j.talanta.2009.05.016

in biological, food and environmental samples are important to protect human health and the environment.

The liquid chromatography (LC) coupled with different detectors is the most widely used technique to determine nitrite and nitrate in biological [6,10,20,23–31], food [11] and environmental samples [20,22,32]. The other analytical techniques described in the literature are spectrophotometry [19,33–38] and gas chromatography–mass spectrometry (GC–MS) [39–42].

The objective of this study was to develop sensitive, specific and reliable analytical techniques that could be applied to a variety of samples to determine nitrite and nitrate. This paper presents GC–MS and LC-FL methods, proposed to enable the precise determination of trace level nitrite and nitrate in biological, food and environmental samples. The procedures offer several significant advantages over the other techniques available, such as higher sensitivity, reliability and selectivity in isolation. In the proposed method, aqueous nitrite was reacted with DAN under acidic conditions to form NAT and extracted with toluene. For analysis of nitrate, it was converted to nitrite enzymatically by nitrate reductase in the presence of enzyme and NADPH, derivatized with DAN and then extracted with toluene. The toluene layers were then analyzed for NAT by GC–MS and LC-FL. Nitrite and nitrate ions in solid samples were extracted with 0.5 M aqueous NaOH by sonication. The aqueous phase containing nitrite and nitrate ions was then analyzed in the same way as the aqueous samples.

2. Experimental

2.1. Chemicals and reagents

All the reagents were of analytical grade and double distilled–deionized water was used in all experiments. Sodium nitrite, sodium nitrate, methanol and toluene were purchased from Merck. 2,3-Diaminonaphthalene, nitrate reductase (NAD(P)H) from aspergi (N7265) and beta-NADP reduced form were supplied by SIGMA. Flavin adenine dinucleotide disodium was purchased from Fluka.

Standard nitrite solution (20 ppm) was prepared by dissolving dried sodium nitrite (at 110 °C for 4 h) in water and then 20 drops of chloroform and a pellet of sodium hydroxide were added to make the solution stable by preventing the liberation of nitrous acid and inhibition of bacterial growth.

DAN reagent was prepared daily by dissolving 10 mg of DAN in 100 ml of 0.25 M aqueous HCl solution and stored in the darkness at −18 °C.

2.2. Samples extraction and derivatization

The aqueous samples (5–25 ml) were extracted with toluene at pH of 8.20 and removed. The DAN reagent (250–500 μl) was added to aqueous phase to react nitrite with DAN under acidic conditions to yield the highly fluorescent 2,3-naphthotriazole (NAT). The pH of the aqueous phase was again adjusted to 8.20, as it has been found to be the optimum pH, by drop-wise addition of 1 M Na_2HPO_4 and then the NAT was extracted twice with toluene (2 × 1 ml). For analysis of nitrate in the remaining aqueous phase, it was converted to nitrite enzymatically by addition of 50 μl of nitrate reductase (6.6 U/l) and 20 μl mixture of 1 μM NADPH and 0.03 μM FAD (1:1) solutions [10], derivatized with 250–500 μl of DAN reagent and then the formed NAT was extracted twice with toluene (2 × 2 ml). The toluene layers obtained before and after enzymatic reduction were first shaken twice with 1–1.5 ml of slightly acidic 85% methanol–water solution (pH 5.5) and then dried over anhydrous sodium sulphate. The toluene layers containing the NAT were separated by centrifuging at 4000 × *g* for 2–3 min and dried under a gentle stream of nitrogen then reconstituted to a certain volume of toluene (100–250 μl depending on the sample type). The final solutions were injected into LC-FL and GC–MS in splitless mode (5 min purge off) and nitrite ions were then analyzed as their NAT derivatives by GC–MS in SIM mode and LC-FL. Although the NAT derivatives of nitrite ions in toluene were stable at least for a week when stored in the darkness under −10 °C, they were analyzed as soon as they were prepared.

The solid samples (0.1–0.5 g) were extracted with 10–25 ml of 0.5 M aqueous NaOH by sonication at 40–45 °C for 20 min and filtered. The aqueous phase was deproteinized by drop-wise addition of 0.5 M $ZnSO_4$ solution until white precipitate of $Zn(OH)_2$ did not appear. The aqueous phase containing nitrite and nitrate ions was filtered and then analyzed in the same way as the aqueous samples.

2.3. Instrumental analysis of the NAT

2.3.1. LC-FL analysis

The LC analyses were performed by Thermo Finnigan LC system (San Jose, USA) consisting of a P1000 pump equipped with a Rheodyne injection valve (20 μl injection loop), a SCM 1000 degasser and a FL3000 fluorescence detector. The system was controlled by a Specta System Controller SN 4000 and a software package Chromquest 4.0. Separation was performed by means of a Phenomenex Synergi POLAR-RP column (250 mm × 4.6 mm, 4 μm) protected by a C_{18} guard column (4 mm × 3 mm, Phenomenex). Fluorescence excitation and emission wavelengths were 364 and 416 nm, respectively.

A gradient elution program was optimized by using the mobile phases of acetonitrile and double distilled–deionized water consisted of 0.1% TFA. The separation was performed at room temperature with a constant flow-rate of 1.0 ml/min by employing the elution program as follows; 0–5 min acetonitrile–water 40:60 (v/v), a linear gradient elution from 40% acetonitrile at 5 min to 60% acetonitrile at 12 min and then elution from 60% acetonitrile at 12 min to 100% acetonitrile at 20 min, followed by isocratic elution with acetonitrile for 5 min. Finally, 5 min were necessary to re-establishing the initial conditions.

2.3.2. GC–MS analysis

A Thermo-Finnigan MAT 4500 GC–MS/MS instrument operating in the electron impact (EI) ionization and selected-ion-monitoring (SIM) mode observed at *m*/*z* 114, 141 and 169 was used. The specifications of the apparatus are as follows: Column identification, ZB-5 ms; column length, 30 m; I.D., 0.25 mm; film thickness, 0.25 μm. Temperature program: initial temperature, 140 °C 1 min hold and 9 °C/min to 290 °C 3 min hold. Scan range, 50–250 *m*/*z*; electron energy, 70 eV for EI.

3. Results and discussion

3.1. Recovery of nitrite from aqueous samples

Firstly, nitrite standard was derivatized with DAN and its NAT derivative was analyzed by GC–MS in SIM mode and LC-FL. The LC-FL and GC–MS-SIM chromatograms of NAT are shown in Fig. 1.

The derivatized nitrite was then diluted in toluene to give a final concentration of 100 μg/ml. Seven calibration standards with the concentrations in the range from 2.5 to 100 pg/ml were prepared by diluting the derivatized standard solution (100 μg/ml) and used for the calibration. Calibration standards of nitrite were analyzed as their NAT derivatives by GC–MS in SIM mode and LC-FL in triplicate and calibrations were performed by calculating the peak areas. The calibration curves of nitrite were performed for seven replicate runs in the investigated concentration range using standard solutions at different concentrations and the calibration graphs were linear for the concentration ranges stated. The linearities of the

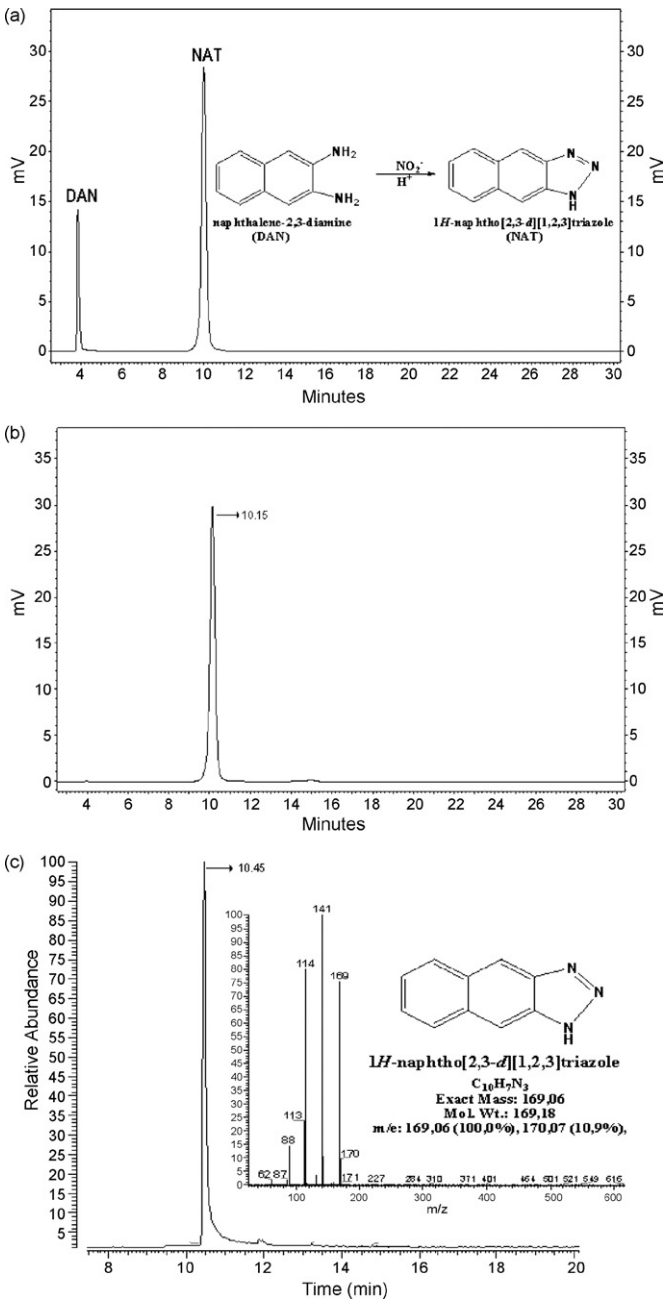

Fig. 1. The LC-FL chromatogram of (a) DAN and NAT (unwashed), (b) NAT (washed) and (c) GC–MS-SIM chromatogram of NAT together with its EI mass spectrum.

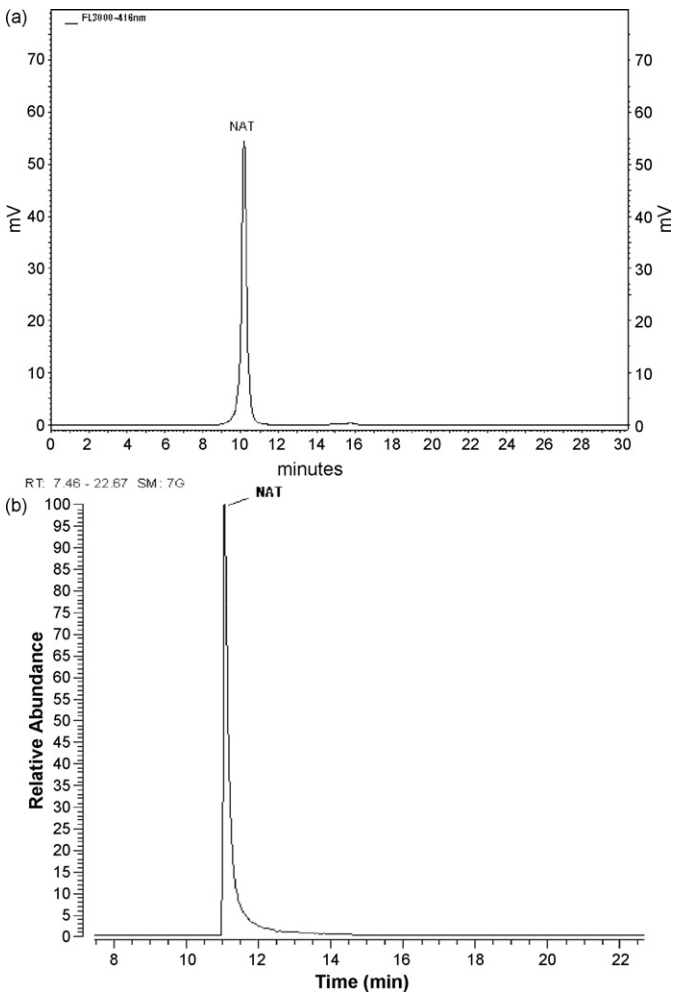

Fig. 2. The LC-FL (a) and GC–MS-SIM (b) chromatogram of NAT isolated from one of the serum samples.

proposed methods for the analysis of the compounds of interest in aqueous samples were calculated in the investigated concentration range, as the determination coefficients (R^2) and calibration curves ($y = ax + b$), shown in Table 1. The limit of detections (LOD) and limits of quantification (LOQ) of nitrite and nitrate ions by GC–MS in SIM mode and LC-FL were estimated for seven replicate runs by comparing the signal-to-noise ratio (S/N) of the lowest detectable concentration to S/N of 3 and 10, respectively.

In order to evaluate recovery of nitrite from aqueous solution, a solution of a known concentration of nitrite (100 μg/ml) was prepared by diluting the standard solution and known volumes of this solution were spiked into the double distilled–deionized water that had previously been analyzed, to give final concentrations in the range from 2.5 to 100 pg/ml of nitrite. Spiking the known volumes (5, 10, 25, 50 and 100 μl) of nitrite and nitrate solutions (10 ng/ml) with water samples (5, 10 and 25 ml) which were analyzed for the nitrite was also performed to evaluate absolute recoveries from aqueous samples (plus the blank value). Quantitative analyses of nitrite ions in known amounts of these samples were performed in seven replicates using GC–MS in SIM mode and LC-FL. The concentrations of nitrite ions as their NAT derivatives were calculated by peak areas and these areas were compared with the calibration graphs of the standards. Spiking the known volumes (5, 10, 25, 50

Table 1
The absolute recoveries of nitrite and nitrate ions for overall procedure with RSDs at optimum extraction pH, calibration curves, R^2, LOD and LOQ.

	Recoveries (%) with RSD	GC–MS-SIM				LC-FL			
		R^2	$y = ax + b$	LOD (pg/ml)	LOQ (pg/ml)	R^2	$y = ax + b$	LOD	LOQ
Nitrite	98.40 (1.00)	0.9997	$y = 97353x + 3103$	0.02	0.09	0.9999	$y = 14208x + 1278$	0.29	0.98
Nitrate	98.10 (1.20)	0.9997	$y = 96234x + 2419$	0.03	0.11	0.9999	$y = 16631x + 1413$	0.30	0.99

and 100 μl) of nitrite solution (10 ng/ml) with biological samples including blood serum, gastric juice and urine which were analyzed for the nitrite was also performed and the spiked samples were then analyzed by the same method in seven replicate for NAT derivatives of nitrite to evaluate absolute efficiency of enzymatic reduction (plus the blank value).

To evaluate recovery of nitrite solution from solid samples, air-dried sediment or food samples (0.1–0.5 g) which have been analyzed by the proposed method were spiked with 5, 10, 25, 50 and 100 μl of nitrite solutions (100 ng/ml) and the solid samples were then analyzed by the same method in seven replicate for NAT derivatives of nitrite (plus the blank value).

To investigate optimum extraction pHs of nitrite ions as their NAT derivatives, standard solutions at different concentrations in the range from 2.5 to 100 pg/ml were analyzed for the compounds of interest by the proposed method in triplicate at different pHs within the range from 5.0 to 11.0 and the optimum extraction pH of the method was found to be 8.2. The absolute recoveries of nitrite ions were evaluated in the investigated concentration range at pH of 8.2.

Toluene layers containing both DAN and NAT were washed with 85% methanol–water solution at different pHs within the range of 3.5–7.0 to remove unreacted DAN. The obtained results indicated that washing of toluene layer with methanol at a pH higher than 6.0 was not satisfactory to remove DAN completely, while methanol solution gradually degrade the NAT at a pH lower than 4.0. The optimum pH of the methanol–water solution was therefore selected to be 5.5 to completely remove DAN without degradation of NAT.

In order to investigate efficiency of enzymatic reduction, nitrate solutions at different concentrations within the range of 0.01 and 100 ng/ml were analyzed for nitrite by the proposed method in triplicate after enzymatic conversion of nitrate to nitrite by addition of 50 μl of nitrate reductase (6.6 U/l) and 20 μl mixture of 1 μM NADPH and 0.03 μM FAD (1:1) solutions. Spiking the known volumes (5, 10, 25, 50 and 100 μl) of nitrite solution (1 ng/ml) with biological, food and environmental samples which were analyzed for the nitrite was also performed and the spiked samples were then analyzed by the same method in seven replicate for NAT derivatives of nitrite to evaluate absolute efficiency of enzymatic reduction (plus the blank value). The absolute efficiency of enzymatic reduction was evaluated to be 99.50 with RSD of 0.20.

The absolute recovery of nitrite for overall procedure described in this work was estimated considering recovery of the compound of interest from aqueous solution with RSD at optimum extraction pH and the recovery of nitrite from solid samples. The absolute recoveries of nitrate were estimated in the same way as that of nitrite after enzymatic reduction to nitrite considering the reduction efficiency and recoveries from standard solution, spiked aqueous and solid samples.

The lower detection limits were obtained by GC–MS in SIM mode, while better correlation coefficients were obtained by LC-FL. The absolute recoveries of nitrite and nitrate ions for overall procedure with RSDs, calibration curves ($y = ax + b$), correlation coefficients (R^2), limits of detection (LOD) and limits of quantification (LOQ) are shown in Table 1.

3.2. Determination of nitrite/nitrate ions as their NAT derivatives in biological, food and environmental samples

In order to confirm the viability, the proposed methods were applied to biological, food and environmental samples to determine nitrite and nitrate ions. The biological samples including blood serum (1–4 ml), gastric juice (3–10 ml) and urine (10–25 ml) were provided by University Research Hospital were analyzed for the contents of nitrite and nitrate by both methods in triplicate as their NAT derivatives and the compounds of interest were determined in the all of samples. Quantitative analyses of nitrite and nitrate ions were performed using their peak areas and these areas were compared with the calibration graphs. The results obtained by both methods were found to be very close to each other and they were within the range of standard deviation of the methods. The LC-FL (a) and GC–MS-SIM (b) chromatograms of NAT isolated from one of the serum samples are shown in Fig. 2. The nitrite and nitrate levels were generally found lower in serum samples collected from hypertensive patients in comparison with those of healthy persons and the results are in good agreement with the literature [43,44]. Nitrate was found at the highest concentrations to be up to 143.50 ppm in urine samples, whereas nitrite was found at highest concentrations up to be 5.80 ppm in gastric juice samples. Diverging values of nitrite and nitrate which can only in part be explained by differences in dietary intake of these salts [1] were observed especially in biological samples and the concentration levels of these compounds

Table 2
The ranges and mean concentrations with RSD of nitrite and nitrate in biological, food and environmental samples.

Samples		Nitrite Concentration range	Mean concentration with RSD	Nitrate Concentration range	Mean concentration with RSD
Biological		ng/ml			
Serum	Hypertensive patients ($n = 21$)	0.01–2.84	0.55 (0.96)	8.40–100	18.67 (26.39)
	Healthy persons ($n = 15$)	11–223	60.7 (55.13)	96–1084	664.7 (270)
		μg/ml			
Gastric Juice ($n = 10$)		0.8–5.8	2.65 (1.66)	1.12–23.94	8.87 (8.3)
Urine ($n = 15$)		0.002–3.04	0.22 (0.78)	3.35–143.5	41.81 (38.10)
Food		μg/g			
Cheese ($n = 15$)		0.01–2.16	0.76 (0.63)	0.12–10.64	3.73 (3.13)
Salami ($n = 19$)		0.5–17.8	3.81 (4.3)	6.8–647	123.35 (149.35)
Sausage ($n = 15$)		3.2–14.8	7.66 (2.97)	169–634	296.4 (141.98)
Environmental		ng/ml			
Snow ($n = 11$)		0.4–7.9	2.25 (2.21)	132–380	202.7 (68.81)
Rain water ($n = 10$)		0.1–12.4	4.07 (4.48)	781–2450	1608.6 (533.66)
Drinking water ($n = 15$)		0.01–1.52	0.33 (0.43)	180–2780	1620 (898)
Tap water ($n = 15$)		0.17–38.5	6.28 (10.29)	960–3800	2002 (860)
		μg/ml			
Lake water ($n = 7$)		3.9–19.7	10.2 (5.38)	10.9–236.8	161.1 (74.4)
Seawater ($n = 7$)		11.6–86.3	54.2 (22.61)	189.7–498.6	332.7 (97.81)
		μg/g			
Sediment ($n = 7$)		8.4–21.4	9.14 (6.10)	71.4–142.5	115.2 (24.81)

n, number of experiments.

are shown in Table 2. The results obtained from analyses on the biological samples revealed that the proposed methods can reliably be employed for the monitoring of trace levels of these compounds for clinical studies.

A number of homogenized food samples (0.1–0.5 g) including cheese, salami and sausage supplied from food markets in Turkey were analyzed for nitrite and nitrate ions. The highest concentrations of both nitrite and nitrate were found in sausage samples to be up to 17.80 and 647.00 ppm, respectively. The mean concentration of nitrate was determined in sausages to be 296.40 ppm which is higher than that of its restricted value of 250 ppm according to Turkish Food Regulations [17].

A variety of environmental water (5–25 ml) and air-dried sediment (0.1–0.5 g) samples collected from Zonguldak province in Turkey were also analyzed for the contents of nitrite and nitrate by both methods in triplicate. The highest concentrations of both nitrite and nitrate were found in seawater samples to be up to 54.20 and 332.70 ppm, whereas the lowest concentrations of nitrite in drinking water and nitrate in snow samples were found to be 0.01 and 132.00 ppb, respectively. The ranges and mean concentrations together with RSD of nitrite and nitrate ions determined in biological, food and environmental samples are shown in Table 2.

4. Conclusion

The GC–MS and LC-FL methods proposed have been successfully applied to biological, food and environmental samples to determine nitrite and nitrate ions and good agreement was obtained between GC–MS and LC-FL techniques for the analysis of samples. The recoveries of nitrite and nitrate ions based on GC–MS and LC-FL results were 98.40% and 98.10% and the precision of these methods, as indicated by the relative standard deviations (RSDs) were 1.00% for nitrite and 1.20% for nitrate, respectively. The limits of detection of the GC–MS in SIM mode and LC-FL methods based on S/N = 3 were 0.02 and 0.29 pg/ml for nitrite and 0.03 and 0.30 pg/ml for nitrate, respectively. Excellent linearities were obtained for both GC–MS and LC-FL techniques in the concentration range of 2.5–100 pg/ml. The methods described in this study have been shown to be suitable with satisfactory accuracy and good reproducibility for the qualitative and quantitative determination of nitrite and nitrate ions in the same sample.

The isolation procedure, consisting of derivatization with 2,3-diaminonaphthalene (DAN) and extraction of 2,3-naphthotriazole (NAT) derivatives with toluene which provides better stability and higher sensitivity is well suited for both GC–MS and LC-FL determination of nitrite and nitrate in a variety of aqueous and solid samples.

Through the obtained results, it may be concluded that the isolation procedure combined with GC–MS and LC-FL techniques can be proposed as more sensitive, reliable and selective methods compared with the other methods available for the precise determination of trace levels of nitrite and nitrate in biological, food and environmental samples.

Acknowledgement

The authors wish to thank the Zonguldak Karaelmas University (2007-13-02-02) for the opportunity and support to carry out this research.

References

[1] D. Tsikas, F.M. Gutzki, D.O. Stichtenoth, Eur. J. Clin. Pharmacol. 62 (2006) 51.
[2] D. Tsikas, Free Radical Res. 39 (2005) 797.
[3] N.S. Bryan, M.B. Grisham, Free Radical Biol. Med. 43 (2007) 645.
[4] M.J. Moorcroft, J. Davis, R.G. Compton, Talanta 54 (2001) 785.
[5] M. Grau, U.B. Hendgen-Cotta, P. Brouzos, C. Drexhage, T. Rassaf, T. Lauer, A. Dejam, M. Kelm, P. Kleinbongard, J. Chromatogr. B 851 (2007) 106.
[6] D. Tsikas, J. Chromatogr. B 851 (2007) 51.
[7] L. Peri, D. Pietraforte, G. Scorza, A. Napolitano, V. Fogliano, M. Minetti, Free Radical Biol. Med. 39 (2005) 668.
[8] P.C.A.G. Pinto, J.L.F.C. Lima, M.L.M. de, S. Saraiva, Clin. Chim. Acta 337 (2003) 69.
[9] A. Moriyama, A. Tabaru, H. Unoki, S. Abe, A. Masumoto, M. Otsuki, Clin. Chim. Acta 296 (2000) 181.
[10] F. Romitelli, S.A. Santini, E. Chierici, D. Pitocco, B. Tavazzi, A.M. Amorini, G. Lazzorino, E. Di Stasio, J. Chromatogr. B 851 (2007) 257.
[11] I.M.P.L.V.O. Ferreira, S. Silva, Talanta 74 (2008) 1598.
[12] T.R.L.C. Paixão, J.L. Cardoso, M. Bertotti, Talanta 71 (2007) 186.
[13] K.O. Honikel, Meat Sci. 78 (2008) 68.
[14] A.S. Pannala, A.R. Mani, J.P.E. Spencer, V. Skinner, K.R. Bruckdorfer, K.P. Moore, C.A. Rice-Evans, Free Radical Biol. Med. 34 (2003) 576.
[15] Y. Kono, H. Shibata, Y. Kodama, Y. Sawa, Biochem. J. 312 (1995) 947.
[16] D.C. Siu, A. Henshall, J. Chromatogr. A 804 (1998) 157.
[17] B. Sırıken, M. Özdemir, H. Yavuz, S. Pamuk, Food Control 17 (2006) 923.
[18] V.J. Erpenbeck, R.A. Jörres, M. Discher, H. Krentel, D. Tsikas, B. Luettig, N. Krug, J.M. Hohfeld, Nitric Oxide 13 (2005) 125.
[19] S. Biswas, B. Chowdhury, B.C. Ray, Talanta 64 (2004) 308.
[20] Y. Zuo, C. Wang, T. Van, Talanta 70 (2006) 281.
[21] Y. Zuo, Y. Deng, Chemosphere 36 (1998) 181.
[22] M. Cemek, L. Akaya, Y.O. Birdane, K. Seyrek, S. Bulut, M. Konuk, J. Food Comp. Anal. 20 (2007) 236.
[23] W.S. Jobgen, S.C. Jobgen, H. Li, C.J. Meininger, G. Wu, J. Chromatogr. B 851 (2007) 71.
[24] N. Gharavi, A.O.S. El-Kadi, J. Pharm. Pharmaceut. Sci. 6 (2003) 302.
[25] C.C.T. Smith, L. Stanyer, D.J. Betteridge, J. Chromatogr. B 779 (2002) 201.
[26] V. Jedličkova, Z. Paluch, Š. Alušik, J. Chromatogr. B 780 (2002) 193.
[27] J. Woitzik, N. Abromeit, F. Schaefer, Anal. Biochem. 289 (2001) 10.
[28] H. Li, C.J. Meininger, G. Wu, J. Chromatogr. B 746 (2000) 199.
[29] M. Wada, C. Morinaka, T. Ikenaga, N. Kuroda, K. Nakashima, Anal. Sci. 18 (2002) 631.
[30] A. Daiber, M. Bachschmid, C. Kavakli, D. Frein, M. Wendt, V. Ulrich, T. Munzel, Nitric Oxide 9 (2003) 44.
[31] M.R.L. Stratford, M.F. Dennis, R. Cochrane, C.S. Parkins, S.A. Everett, J. Chromatogr. A 770 (1997) 151.
[32] Y. Zuo, H. Chen, Talanta 59 (2003) 875.
[33] R. Esquembre, I. Pastor, R. Mallavia, C.R.R. Mateo, J. Photochem. Photobiol. A: Chem. 173 (2005) 384.
[34] X.F. Yue, Z.Q. Zhang, H.T. Yan, Talanta 62 (2004) 97.
[35] J.S. Li, H. Wang, X. Zhang, H.S. Zhang, Talanta 61 (2003) 797.
[36] M.F. Cancio, E.M.F. Vitos, J.J. Centelles, S. Imperial, Clin. Chem. Acta 312 (2001) 205.
[37] A.M. Rao, A. Doğan, J.F. Hatcher, R.J. Dempsey, Brain Res. 793 (1998) 265.
[38] F. Guozhen, X. Qing, F. Mei, Microchem. J. 60 (1998) 258.
[39] A. Mitschke, F.M. Gutzki, D. Tsikas, J. Chromatogr. B 851 (2007) 287.
[40] S.M. Helmke, M.W. Duncan, J. Chromatogr. B 851 (2006) 83.
[41] D. Tsikas, Anal. Chem. 72 (2000) 4064.
[42] S. Kage, K. Kudo, N. Ikeda, J. Chromatogr. B 742 (2000) 363.
[43] D.C. Paik, T.D. Wendel, H.P. Freeman, Nutr. Res. 25 (2005) 1049.
[44] B. Sözmen, C. Kazaz, D. Taşkıran, L. Aslan, A. Akyol, E.Y. Sözmen, Tr. J. Med. Sci. 28 (1998) 525.

Talanta 79 (2009) 603–612

Contents lists available at ScienceDirect

Talanta

journal homepage: www.elsevier.com/locate/talanta

Usage of Empore™ membrane in alcoholic media for copper(II) distribution studies

Giancarla Alberti*, Maria Giovanna Guiso, Raffaela Biesuz

Dipartimento di Chimica Generale, Università di Pavia, via Taramelli 12, 27100 Pavia, Italy

ARTICLE INFO

Article history:
Received 19 January 2009
Received in revised form 7 April 2009
Accepted 16 April 2009
Available online 3 May 2009

Keywords:
Copper(II) species
Empore™ chelating membrane
Alcoholic media
Grappa
Flemma

ABSTRACT

The sorption of copper(II) on a solid, iminodiacetic based, chelating material, the Empore™ membrane, in alcoholic solutions is considered. Determination of the acid–base properties, kinetic of metal sorption and complexing properties, in solutions with different percentages of ethanol, ranging from 0 to 40% is undertaken. The results are compared with those obtained using the classical iminodiacetic resin Chelex 100 in beads. No significant differences are found in the thermodynamic properties, but the kinetics of the metal sorption on the membrane is slower and a dependence of the process rate with the alcoholic content is observed. In the present investigation, the detection of copper(II) species both in alcoholic Italian distillate "grappa" and in its intermediate product ("flemma"), is carried out by the Resin Titration (RT) method using, as competitive reagent, the Empore™ membrane. To validate the procedure, synthetic solutions containing different percentages of ethanol are analysed.

1. Introduction

Grappa is the Italian version of the distilled spirit obtained through the distillation of grape marc, a by-product of the wine-making process. Wine lees can also be added to grape marc before the distillation process. European Union regulations (EU Regulation 1576/89, 1989) require that the spirit called "grappa" is made only in Italy [1].

Two distinct distillation systems can be used for grappa production: the batch system for the production of highly flavoured spirit, and the continuous still to produce lighter flavoured spirits. Continuous distillation is generally spread over two steps. First, marc is introduced into an evaporator in which ethanol is steam-stripped to give a so-called "low-wine" or "flemma" at about 15–20% (v/v) of ethanol. Secondly, this flemma feeds the column in order to get an alcohol recovery greater than 70% [2]. If the grappa obtained is not going to be aged, or if it is not going to be consumed with that content, an alcoholic content reduction is performed through water blending. The law enforces the utilization of distilled water. For most commercially available products, the alcoholic content may range from about 38 to 40% (v/v) of ethanol.

On the other hand, craft grappa products are normally obtained through the traditional discontinuous distillation apparatuses, which still use alembics made completely of copper, and therefore the distillate may have a quite high copper content. It is known, for instance, that during the distillation process some quantities of *verdigris*, i.e. the compound $CuCO_3Cu(OH)_2$, is formed on the container wall; this substance can be dissolved by acidic alcoholic vapours, so contaminating the spirits [3].

Since a high copper content in alcoholic distillates can be harmful to consumer's health, the control of this metal ion concentration is fundamental both from a toxicological point of view and with regard to the overall quality control of the product. The EC and Italian legislations do not establish a maximum permissible copper level for these matrices. However, in other Countries, as for instance in Brazil, the legislation sets the maximum limit of 5 mg l^{-1} for Cu concentration in alcoholic distillates [4].

Since long time ago, an important part of our research has been devoted to characterize solid sorbents of different nature and to apply them to study the metals distribution in natural waters [5,6]. According to the proposed Resin Titration (RT) method, a strong chelating resin, with well defined sorbing properties, sets up a competition with the natural ligand for metal complexation. The strength of the competition could be quantified and information about the original distribution of species can be achieved.

For this kind of application, the Empore™ membranes seemed very promising to overcome several practical troubles concerning the usage of beads in particular in on-field applications, which are mainly related to the strongly controlled cleaning procedures needed for metal investigation in non-contaminated waters.

The solid chelating membrane Empore™, commercialized by 3M [7] is constituted of a styrene divinylbenzene resin with iminodiacetic moieties as active groups, blocked in a network of polytetrafluoroethylene (PTFE) fibrils. According to the manufac-

* Corresponding author. Tel.: +39 0382 987347; fax: +39 0382 528544.
E-mail address: galberti@unipv.it (G. Alberti).

0039-9140/$ – see front matter © 2009 Elsevier B.V. All rights reserved.
doi:10.1016/j.talanta.2009.04.034

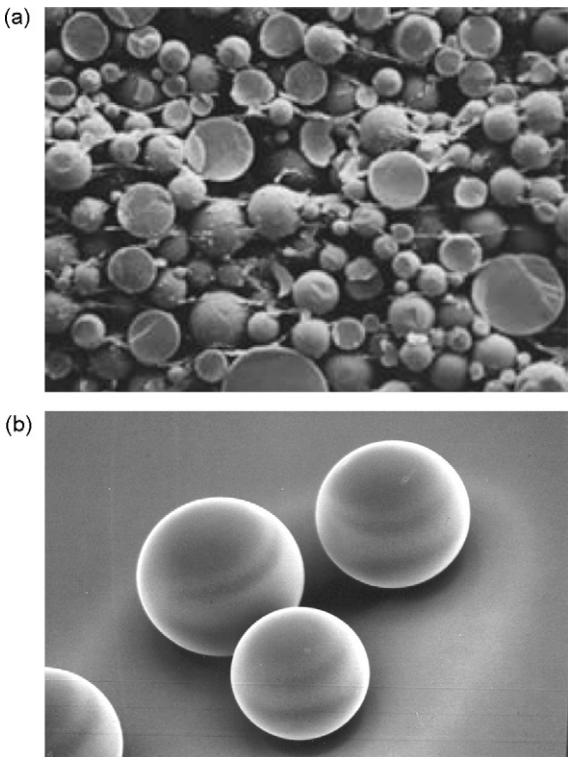

Fig. 1. In (a) picture of Empore™ membrane [7] compared with that of the iminodiacetic resin of BioRad, Chelex 100 (obtained with a scanning electronic microscope, Cambrige steroscan, Au 100 Å sputtering), in (b).

turer not only "the particles are tightly held together within an inert matrix of polytetrafluoroethylene (90% sorbent:10% PTFE, by weight)" but "The PTFE fibrils do not interfere with the activity of the particles in any way." Indeed the picture they proposed for the membrane (Fig. 1a) [7] compared with that of the imodiacetic resin of BioRad, Chelex 100 (obtained with a scanning electronic microscope, Cambrige steroscan, Au 100 Å sputtering) (Fig. 1b) confirms the description.

"The Empore™ membrane fabrication process results in a denser, more uniform extraction medium than can be achieved in a traditional Solid Phase Extraction (SPE) column or cartridge prepared with the same size particles" [7]. Accordingly, the chelating membranes are proposed as extraction disks to be used with typical devices for any liquid–liquid extraction (as for the mobile-phase cleanup in liquid chromatography) "with faster flow rates and higher throughput compared to traditional packed column technology" [7].

Our way of using the Empore™ membrane is completely different from that proposed by the manufacturer because, for our applications, we cannot connect the disk to a filtering device. However, we have chosen this product for a number of advantages, i.e. easy handling of the sorbent, cleaning with reduced volumes of ultrapure acid, separation from the original solution avoiding filtration and trouble-free elution of metals. Thanks to these potentialities, we have decided to characterize and apply the Empore™ membrane in metals distribution studies.

In the present investigation, a wide study on the sorbing properties of the membrane is undertaken, to determine acid–base properties, kinetic of copper(II) sorption and complexation reactions, in alcoholic media. The results are compared with the proprieties of a classical iminodiacetic resin in beads, Chelex 100.

The characterization is a fundamental task to employ the sorbent in metal distribution studies using the Resin Titration (RT) method. Examples of applications of Empore™ membrane to detect copper(II) species both in alcoholic Italian distillate "grappa" and in its intermediate product ("flemma"), are reported. All our measurements are performed at 25 °C and in alcoholic solutions from 0 to 40% of ethanol, since most of the commercial grappa contains 40 ± 5% of ethanol, and the intermediate flemma is an alcoholic solution with 15–20% of ethanol. When it comes to the electrolyte employed as background medium, the literature on alcoholic beverages suggests the use of KCl solutions, between 0.001 and 0.1 M, to reproduce the natural condition of salinity [8]. We employ 0.1 M, being in any case close to the natural salt composition and, since this is an usual media used for studying the resin in water solution [9], to possibly evaluate how alcoholic media affect exchange equilibria.

1.1. Characterization of the Empore™ membrane properties in hydro-alcoholic solutions

1.1.1. Thermodynamic model of the metal sorption

The model is based on the Gibbs–Donnan description of ion-exchangers [10–12]. The sorbent is represented as a solution phase, usually concentrated, separated from the external solution by an interface through which water, neutral molecules and ions can diffuse, but the active groups, permanently linked to the solid matrix, cannot. Due to the different mobilities of ions, a potential difference is set up at the interface [13], referred to as the Donnan potential.

At equilibrium, the chemical potential of each of the mobile components is the same in both phases and, for each couple of ions that can diffuse through the interface, the Donnan equilibrium is given by:

$$a_A a_C = \overline{a_A a_C} \quad a_A/a_B = \overline{a_A}/\overline{a_B} \tag{1}$$

For simplicity the charges are omitted and are considered to be monovalent. The overbar represents species in the solid phase. The activity of an ion inside the sorbent cannot ever be measured, but it can be evaluated from Eq. (1) which is of basic importance for the proposed model.

In practise when solid sorbents are employed, the active sites is always in excess with respect to the metal ion, which is often at trace or sub-trace levels. Under this condition, it can be assumed that mechanisms, other than formation of complexes, are negligible [12,14] and that the concentration of active sites does not depend on complex formation.

The general exchange equilibrium is:

$$\mathrm{M} + n\,\overline{\mathrm{H}_r\mathrm{L}} \leftrightarrows \overline{\mathrm{MH}_p\mathrm{L}_n} + q\mathrm{H} \tag{2}$$

where M is the metal ion, H_rL the r-protonated form of the active site of the chelating sorbent, H the proton.

The exchange coefficient, β_{1npex}, is given by:

$$\beta_{1npex} = \frac{\left[\overline{\mathrm{MH}_p\mathrm{L}_n}\right] \cdot [\mathrm{H}]^q}{[\mathrm{M}] \cdot \left[\overline{\mathrm{H}_r\mathrm{L}}\right]^n} \tag{3}$$

The exchange coefficients depend on the concentration of the counter ion in the solution and in the solid phase, while the intrinsic complexation constants (β_{1npi}) are independent of the composition of the solution, so they characterized the sorption equilibria. The relationship between the exchange coefficient and the intrinsic complexation constant is demonstrated to be [12,14]:

$$\beta_{1npi} = \beta_{1npex} \frac{\gamma_{\mathrm{H}}^q \cdot \gamma_{\mathrm{C}}^{(m-q)}}{\gamma_{\mathrm{M}}} \frac{[\mathrm{C}]^{(m-q)}}{[\overline{\mathrm{C}}]^{(m-q)}} \tag{4}$$

where m is the charge of the metal e γ_X indicates the activity coefficients of the species X.

Similar relations hold for the protonation equilibria of the chelating sorbent.

The exchange coefficients are evaluated from the expression for the fraction of metal ion sorbed on the solid phase, f. It is given by the following relationship:

$$f = \frac{c}{c_{tot}} = \frac{[\overline{MH_pL_n}] \cdot w}{[\overline{MH_pL_n}] \cdot w + \alpha_{M(I)} \cdot [M] \cdot V} = \frac{1}{1 + (\alpha_{M(I)} \cdot [H]^q \cdot V/\beta_{1npex} \cdot [\overline{H_rL}]^n \cdot w)} = \frac{1}{1 + (\alpha_{M(I)} \cdot V/K^* \cdot w)} \quad (5)$$

where w is the mass of dry sorbent, V is the volume of the solution, c_{tot} is the total concentration of the metal in the sample, c is the concentration of the metal ion sorbed on the solid phase, $\alpha_{M(I)}$ represents the reaction coefficient [15] of the free metal ion in the solution phase following equilibration with the sorbent. It is the ratio of the total metal concentration in solution (free and complexed with a ligand I present in solution), and the concentration of the free metal ion: $\alpha_{M(I)} = \sum[MI]/[M]$, $\alpha_{M(I)}$ is equal to one when the metal is only present as a free hydrated ion in the aqueous solution. $[\overline{H_rL}]$ is evaluated from the total concentration of the free active groups inside the sorbent (c_L) and its concentration is in analytical excess with respect to the total metal ion concentration (see below).

Eq. (5), defined for the formation of one complex, can be extended by considering the formation of other complexes, as accounted for in the last term on the r.h.s. of Eq. (5).

K^* represents the ratio of total metal ion in the solid phase to the free metal ion in solution. It is the partition coefficient and is given by the following relation:

$$K^* = \frac{c\,V}{[M]w} = \frac{\sum \beta_{1npex}[\overline{H_rL}]^n}{[H]^q} \quad (6)$$

The summation is extended to all the complexes formed by the considered metal ion with the active groups of the sorbent [5,16].

Since f is experimentally determined, the pH of the solution, the concentration of the active sites in the solid phase and the value of $\alpha_{M(I)}$ are known, the value of β_{1npex} can be calculated from Eq. (5). The number of protons released during the complexation can be estimated through a logarithmic form of Eq. (5), as previously suggested [12].

From the set of β_{1npex} values in function of pH, β_{1npi} can be calculated if also the concentration of the counter ion in the solid phase ($[\overline{C}]$) is known (see Eq. (4)).

Conversely, the intrinsic complexation constant can be used to calculate the exchange coefficients and the expected values of f_{calc}, at any particular condition. The calculated curves of f_{calc} as a function of pH show graphically the ability of the model to describe the experimental sorption data.

The correlation coefficient (c.c.) and the relative error, R.E. $= \sqrt{(f_{cal} - f_{exp})^2/f_{cal}^2}$, are used to compare the experimental and the calculated values of f.

The strategy for selecting the sorption reactions is to first consider the simplest stoichiometries and reactions equal to those of the monomeric units in solution.

To select the proper set, the effect of the stoichiometry on the ionic media contribution to the exchange coefficients (see Eq. (4)) is considered, and consequently similar experiments are run at different ionic strength concentrations. Further indications are obtained from the evolution of profiles observed after adding a competitive ligand to the solution (see Eq. (5)). In this way, it is usually possible to define the intrinsic complexation constants that will describe the sorption under any experimental conditions.

1.1.2. Determination of $\overline{H_rL}$ concentration

As for the classical resin in beads, protonation coefficients and the capacity of the membrane can be calculated from the acid–base titration of the sorbent. The method was extensively described elsewhere [17] and here briefly reported.

$[\overline{H_rL}]$ is evaluated from the total concentration of the free active groups inside the sorbent (c_L) according to the following relationship: $[\overline{H_rL}] = c_L/\alpha_{\overline{H_rL}}$. The reaction coefficient of the active groups, $\alpha_{\overline{H_rL}}$ is determined from the protonation coefficients.

The protonation coefficient (K^H):

$$K^H = \frac{[\overline{H_{r-1}L}]\,[H]}{[\overline{H_rL}]} \quad (7)$$

is defined in analogy with the exchange coefficient, so its value depends on the counter ion concentration and on the pH. For the same reason mentioned above, it is related to the intrinsic protonation constant, K_{ri}^H [12]:

$$K_{ri}^H = K_{rex}^H \frac{\gamma_H \gamma_C\,[C]}{[\overline{C}]} \quad (8)$$

It is assumed that sorbed alkali metal ions are not associated with functional groups, whereas all hydrogen ions (and metal ions) are. The association of hydrogen/metal ions and functional groups does not contribute to the internal ionic strength value. The counter ion in the solid phase depends on the amount of salt transferred. This quantity can be determined experimentally. It requires a large amount of experimental work, but it can be calculated through an iterative procedure that has been previously proposed [18].[1] It produces an estimate of $[\overline{H_rL}]$ and $[\overline{C}]$ as a function of pH for a given counter ion concentration in solution, for the sorbent.

1.1.3. Sorption kinetic

The models selected to describe our data, from the kinetic point of view, are the following two, widely used in literature: the Homogeneous Particle Diffusion Model [19] and the Shell Progressive (Shrinking Core) Model [20].

1.1.3.1. Homogeneous particle diffusion model (HPDM). In this model, the extraction mechanism involves counter diffusion of Cu^{2+} ions from the solution and Na^+ ions from the solid phase through a number of possible resistances.

The exchange of Cu^{2+}/Na^+ can be rigorously described by the Nernst Plank equation. This applies to counter diffusion of two species in a quasi-homogeneous media.

The species originally in the solution phase must diffuse across the liquid film surrounding the resin particle. If this liquid film diffusion controls the rate of the process, the following equation can be used:

$$-\ln(1-f) = kt \quad \text{where } k = \frac{3DC}{r_o \delta \overline{C}} \quad (9)$$

f is the fraction of metal sorbed, i.e. the ratio of sorbed to total metal ion $f = c/c_{tot}$, k the rate constant (s^{-1}), r_o the radius of the ion exchanger (m), D the diffusion coefficient in the film ($m^2\,s^{-1}$), δ the film thickness and C the total metal concentration ($mol\,l^{-1}$); overbar refers to solid phase.

After that, there is a transfer of the species across the solution/particle interface and then the species diffuse into the bulk of the solid phase. If this is the limiting step, the following equation

[1] An algorithm incorporated in a MS-Excel spreadsheet can be acquired to the authors.

is applied:

$$-\ln(1-f^2) = 2kt \quad \text{where } k = \frac{3\bar{D}\pi^2}{r_0^2} \tag{10}$$

The third, generally fast, not limiting step is the chemical reaction between Cu^{2+} and the active sites (iminodiacetic groups) of the membrane.

1.1.3.2. Shell progressive model (SPM). When the porosity of the polymer is small and thus practically impervious to the fluid reactant, the reaction may be explained by the "Shell Progressive" or "Shrinking core" approach. The kinetic concept of a "Shell Progressive" mechanism can be described in terms of the concentration profile of a liquid reactant containing the analyte advancing into a spherical bead of a partially substituted ion exchanger. In this case, the relationship between time and f is given by the following expressions:

(a) Fluid film controls:

$$f = \frac{3C_{Ao}K_{mA}}{ar_oC_{so}}t \tag{11}$$

(b) Diffusion through the reacted layer controls:

$$[3-3(1-f)^{2/3}-2f] = \frac{6\bar{D}C_{Ao}}{ar_o^2C_{so}}t \tag{12}$$

(c) Chemical reaction controls:

$$\left[1-(1-f)^{1/3}\right] = \frac{k_sC_{Ao}}{r_o}t \tag{13}$$

The description of the rate of sorption according to a shell–core mechanism might be valid for species with a high affinity for the solid sorbent resulting in quasi-irreversible sorption.

In Eqs. (11)–(13), a is the stoichiometric coefficient of the metal in the exchange reaction, C_{Ao} the concentration of the analyte in the bulk solution (mol l^{-1}), C_{so} the concentration of the solid reactant at the unreacted core (mol l^{-1}) and K_{mA} is the mass transfer coefficient of species A through the liquid film (m s^{-1}).

The aim of this kinetic study is to find a mathematical model that describes the experimental data, to determine the rate controlling steps and to evaluate the time required to reach equilibrium.

1.2. Resin Titration (RT)

The Resin Titration (RT) largely employed in metal distribution studies using different kinds of resin in beads, is here applied for the first time to alcoholic beverages, using as sorbent the Empore™ chelating membrane.

The method consists in measuring the metal ion sorbed on the solid phase (c) when different ratios V/w are employed; from this quantity information about the distribution in species of the metal is obtained.

The parameter used to describe the metal complexation in the solution is the side reaction coefficient, $\alpha_{M(I)}$ [15] (see definition in Section 1.1.1). $\alpha_{M(I)}$ is equal to one when the metal is present only as free hydrated ions; in this case the quantity sorbed by the membrane is independent of V/w. When $\alpha_{M(I)}$ is high enough, a competition sets up between the ligand I and the active groups of the membrane, and the metal is only partially sorbed on the solid phase.

The concentration of metal ion sorbed at each point of the titration (V/w) is modelled by the following relationship:

$$c = \frac{c_{tot}}{1+(\alpha_{M(I)}\cdot V/K^*\cdot w)} \tag{14}$$

c_{tot} is the total concentration of the metal ion in the solid phase when V/w tends to 0. The parameters c_{tot} and $\alpha_{M(I)}$ are evaluated by non-linear square fitting.

From Eq. (14) it can be seen that the active group of the sorbent is able to compete with the ligand I for metal complexation only in case the side reaction coefficient is in between two limiting values. The detection window of the specific titration is [5]:

$$\frac{0.1K^*\cdot w}{V} < \alpha_{M(I)} < \frac{10K^*\cdot w}{V} \tag{15}$$

It is important to highlight that Eq. (14) holds only if the natural ligand I is in excess with respect to the metal ion. It is a borderline case of a more general relationship, still obtained considering the formation of 1:1 metal to ligand ratio. Indeed, in view of the mass balance of the ligand I, $c_I = [I] + [MI]$, the expression for the reaction coefficient, $\alpha_{M(I)} = ([M]+[MI])/[M] = 1 + K_I[I]$ (K_I is the conditional complexation constant of the complex MI), and the mass balance of the metal, $c_{tot} = c + [M]\cdot\alpha_{M(I)}$, the following quadratic equation is obtained:

$$c^2\cdot\left(K_I + \frac{K_I\cdot V}{K^*\cdot w}\right) + c\cdot\left(1 + K_I\cdot c_I - K_I\cdot c_{tot} + \frac{K^*\cdot w}{V}\right) - \frac{c_{tot}\cdot K^*\cdot w}{V} = 0 \tag{16}$$

The parameters c_{tot}, K_I and c_I are evaluated by non-linear square fitting of Eq. (16).

Eq. (14) derives from Eq. (16) when the ligand I is in excess with respect to the metal, so the product $K_I\cdot c_I \approx \alpha_{M(I)}$ and $c_{tot} \ll c_I$.

The shape of the titration curve can give a first indication about the presence of a ligand in excess or in deficit with respect to the metal, and about the degree of complexation. In Fig. 2 a simulation of three different cases is reported as example. The curve (a) represents the titration of a ligand in excess with respect to the metal: a very steep curve soon decreasing to 0 by increasing V/w ratio is expected. In this case Eq. (14) can be appropriate to fit the experimental data. Conversely, when a constant sorption, $c \neq 0$, is found for higher V/w values, it means that there is a deficit of ligand I and a fraction of the total metal is free or linked to another ligand with $\alpha_{M(I)} < (0.1\cdot K^*\cdot w/V)$. It is the case of the titration reported as curve (b) in Fig. 2; from the difference between the total metal and the concentration at the plateau of the curve (free or weakly

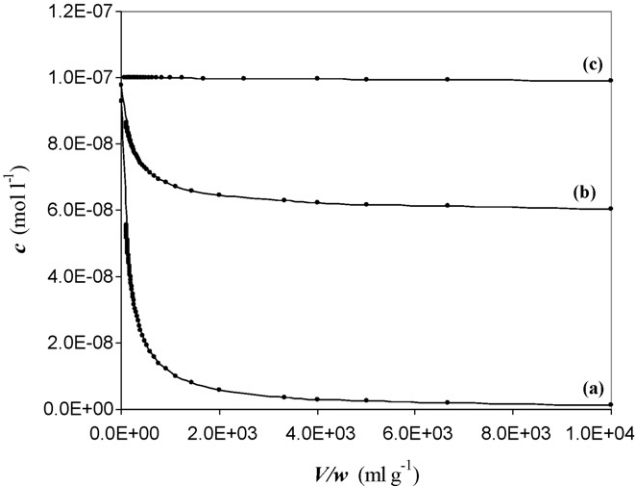

Fig. 2. Simulation of Resin Titration curves. Curve (a) represents the titration of a ligand in excess with respect to the metal; curve (b) represents the titration of a ligand I in deficit with respect to the metal and curve (c) represents a limit situation when the total metal in solution is free or linked to a weak ligand, not able to compete with the active sites of the sorbent for the metal complexation.

bound metal) an estimation of the ligand concentration is obtained. For this kind of titration, the fitting has to be done applying Eq. (16).

When the RT curve is a straight line parallel to the abscissa, as curve (c) in Fig. 2, it means that the total metal in solution is free or linked to a weak ligand, not able to compete with the active sites of the sorbent for the metal complexation.

In principle a very wide range of V/w could be explored for intermediate situation, but being always limited by the lowest reproducible amount of membrane (never less than 10 mg) and the maximum volume of the solution (here always 100 ml).

2. Experimental section

2.1. Membrane, reagents and solutions

Empore™ Extraction Disks with Chelating Resin (Iminodiacetate Functionalized Poly[styrenedivinylbenzene] – 3M, United States), was delivered in sodium form. Each disk was washed and converted in H^+ form with 20 ml of 3 mol l^{-1} HCl allowing it to soak for 10 min. The acidic solution was removed and the disk was washed at least three times with 50 ml of Milli-Q water to eliminate any residual acid. The capacity of the membrane, i.e. mmol of active groups per g of dry Empore™ membrane in H^+ form, was determined by acid–base titration, as described elsewhere [9].

A Cu(II) stock solution of 1000 mg l^{-1} for spectroscopy and copper sulphate ≥99.0% Fluka [CAS 7758-98-7] were used to obtain the proper Cu(II) concentration in the solution phase.

KCl ≥ 99.0% Sigma–Aldrich [CAS 7447-40-7] was used to prepare electrolyte solutions employed as background medium.

Solutions were prepared with ultrapure water (Milli-Q) with the required % of ethanol (99.5%, ACS [CAS 64-17-5] (Sigma–Aldrich). The solutions prepared by mixing water and ethanol in percentage less then 20%, show a slight contraction in volume (below 0.3%) that was considered negligible. For higher percentages of ethanol, a large contraction of volume was observed (for example a 3% contraction of volume in 40% ethanolic solution), but metals and ligands concentrations were computed rigorously with the final total volume.

The grappa and flemma samples were delivered from the Distillery Francoli (Ghemme, Italy). Samples indicated with capital letter "B" were grappa and flemma of the kind "Bracchetto" and those indicated with "P" were of the kind "Piemonte".

2.2. Apparatus

A PHM 84 Research pH meter, Radiometer Copenaghen, with ABU 80 autoburette and a combined Orion glass electrode were used for studying the proton and copper exchange on Empore™ membrane. A small over pressure of nitrogen was applied in the vessel that had been thermostated at 25 ± 0.1 °C by means of a liquid circulation in the outer chamber of the titration cell. The potentiometric cell was standardised in the H^+ concentration employing alkalinimetric titrations of hydrochloric acid with a standard carbonate free potassium hydroxide, as previously reported [9].

The calibration constants show that the glass electrode has given a Nernstian response, with a slope of (59.2 ± 0.1) mV. The autoprotolysis constants (K_w) for each medium were determined by using the same acid–base titration data and are compatible with those mentioned in scientific journals [21].

An ICP-AES PerkinElmer Optima 3300 DV (dual view) was used to determine Cu(II) at relatively high concentrations, the linearity being up to 5 mg l^{-1} and the LOD 0.007 mg l^{-1}.

An AA-6601G/GFA Shimadzu graphite furnace atomic absorption spectrophotometer with 6100 Shimadzu autosampler was employed for determining the concentrations of Cu(II) < 0.03 mg l^{-1}. In this case the linearity was up to 5 μg l^{-1} and the LOD 0.1 μg l^{-1}.

2.3. Determination of the protonation profiles and of the water in the membrane

Acid–base titrations of Empore™ membrane in ethanolic solutions were performed in KCl 0.1 M, according to the usual experimental procedure reported elsewhere. A fixed volume of solution (30 ml) was equilibrated with a portion of Empore™ membrane in a thermostated vessel. The membrane was suspended into the vessel by a nylon wire and the solution, gently stirred, was under a low N_2 overpressure to avoid any contact of solution with atmospheric CO_2. A minimum of 0.5 h was found to be the time needed for the equilibrium to be reached. The equilibrium condition was considered to be obtained when the drift of the glass electrode was no greater than 0.1 mV/min. The maximum time between two additions of base was fixed at 4 h. Each titration lasted approximately 48 h [17].

A batch technique was used to evaluate the amount of water associated with the solid phase at each point of its neutralization. The amount of water sorbed (gram of water per gram of dry membrane) was calculated for each titration point from the experimental values by an interpolation procedure [17].

2.4. Determination of the sorption profiles

The experimental sorption profiles represent the ratio of sorbed to total metal ion $f = c/c_{tot}$ reported vs. pH at the given conditions; the procedure used is the same applied for the resin in beads, described in detail elsewhere [16], and it is here briefly reported.

A fixed volume of solution (30 ml) with a known composition and concentration of metal ion was equilibrated with a portion of Empore™ membrane suspended into the solution. The amount of membrane was selected to have a large excess of active groups compared to the mmol of metal ion. The pH was measured potentiometrically and adjusted with small amounts of acid or base. The equilibration time adopted for the copper(II) sorption on the solid phase was around 5 h as checked in preliminary experiments. After the equilibration, the pH was measured and recorded; a small amount of solution (0.1 ml) was collected, diluted to 10 ml with HNO_3 0.1 M and analysed, as previously described. The amount of the sorbed copper(II) was calculated by difference from the total.

2.5. Procedure for the kinetic experiments

To determine the kinetic profile (sorption as a function of time), the same experimental setup used in the previous thermodynamic studies, is applied. A fixed volume of solution (30 ml) with a known composition and concentration of metal ion was contacted with a portion of Empore™ membrane suspended into the solution. At each selected time period and without interruption of the stirrer, a small amount of solution (0.1 ml) was collected, diluted to 10 ml with HNO_3 0.1 M, and then analysed as previously described. The amount of the sorbed copper(II) was calculated by difference from the total.

2.6. Procedure of the Resin Titration (RT)

The RTs were carried out on equal volumes of solution contacted with different portions of membrane in at least six bottles. The subsamples were equilibrated over 3 nights with the membrane, on a shaking plate. Species that do not dissociate within 72 h are considered inert. The acidity of each aliquot was measured following equilibration. The solution was removed, the membrane was washed with a small portion of Milli-Q water to remove any trace of the sample solution, and then 5 ml of 1 M HNO_3 were introduced into the bottle to desorb the metal ion from the membrane. The concentrations of copper(II) were determined in the stripping solutions

Table 1
Intrinsic protonation constants for Empore™ membrane and for Chelex 100 in 0.1 M KCl hydro-alcoholic solutions at different percentages of ethanol (numbers in parentheses are the 95% confidence intervals, expressed as variation of the last significant digit).

EtOH (%)	Empore™			Chelex 100		
	Capacity (mmol g^{-1})	$\log K^{H}_{2i}$	$\log K^{H}_{1i}$	Capacity (mmol g^{-1})	$\log K^{H}_{2i}$	$\log K^{H}_{1i}$
0	1.5	3.1(1)	8.6(3)	1.8	3.2(2)	8.9(3)
12				1.6	3.2(2)	8.6(1)
20	1.0	3.3(1)	n.d.	1.7	3.2(1)	8.8(1)
30				1.9	3.1(1)	8.9(1)
40	1.2	3.1(1)	n.d.	2.0	3.0(1)	8.9(1)

n.d.: not determined.

by ICP-AES or AAS-GF, in function of the metal content. Concentrations were referred to the original volumes. Each titration was repeated twice, and the concentrations are referred to the mean values. CV was around 3%.

3. Results

3.1. Acid–base equilibria of Empore™ membrane in hydro-alcoholic solutions

The acid–base equilibria of Empore™ membrane in 0.1 M KCl solutions, containing different percentages of ethanol are studied, according to a procedure reported in the experimental section. Within the experimental domain, in the iminodiacetic moiety, only the amine and one carboxylate are titrated, while the second carboxylic group protonates at a too acid pH to be detected. The titrations curves allow determining the capacity of the ion exchanger that was found a little less compared to the resin in beads. The values are reported in Table 1, together with the intrinsic protonation constants, evaluated from the protonation coefficients for each titration curve. To make a comparison with the resin in beads, the intrinsic protonation constants of Chelex 100 obtained in hydro-alcoholic solutions are also reported.

About the first protonation constant, K^{H}_{2i}, the values obtained in solutions at the same ionic strength (0.1 M KCl) but with different percentages of ethanol, are not significantly different at 95% of confidence. They are also not significantly different from values found for the Chelex 100, as expected since the presence of the same active groups on the two sorbents.

Some problems have been found to determine the second protonation constant for the Empore™ membrane, in solutions with the high alcoholic content; indeed the data obtained are not reproducible. Probably this is due to the long time needed to reach the equilibrium, especially at high pH, so the maximum time of 4 h between two additions of base applied in these titrations could be inadequate. Other experiments have to be done to clarify this aspect. However in the present study, given the good agreement between the values of the first protonation constant for both sorbents, we have considered for the Empore™ membrane the K^{H}_{1i}, values obtained for Chelex 100.

It is reported that the $\log K^{H}$ of carboxylate groups tends to increase from water to alcoholic solution as the dielectric constant decreases [22]. For the results here obtained, the difference is within the experimental error, probably because the values found for ion exchangers are affected by a higher uncertainty, in comparison with those determined for soluble ligands.

3.2. Sorption equilibria of copper(II) on Empore™ membrane in hydro-alcoholic solutions

The exchange properties of Empore™ membrane with copper(II) are studied in 0.1 M KCl hydro-alcoholic solutions with different percentages of ethanol. The sorption profiles are obtained with the active groups of the membrane in excess with respect to the total metal ion in the solution, so that important simplifications in equations hold.

Sorption is quantitative at pH higher than 2, and it is described by only one sorption reaction. As expected, it does not depend on the metal concentration. The values of the intrinsic complexation constants are reported in Table 2.

Sorption was also studied in the presence of different ligands in solution, as for instance, nitrilotriethanoic acid (NTA) and 2,6-pyridine dicarboxylic acid (PDCA). They compete with the active groups of the sorbent, shifting the sorption at higher pH, making it possible to identify other complexes of the metal ion in the solid phase. The SC_Query database by IUPAC (SC_Query Vn 5.18) was

Table 2
Intrinsic complexation constants for Empore™ membrane and for Chelex 100, in 0.1 M KCl hydro-alcoholic solutions, at different percentages of ethanol (numbers in parentheses are the 95% confidence intervals, and refer to the last significant digit).

EtOH (%)	Added ligand (mol l^{-1})	Cu (mol l^{-1})	$\log \beta_{110i}$	$\log \beta_{120i}$	Fitting parameters	
					c.c.	R.E.
Empore™						
0	None	7.9×10^{-6}	−0.7(1)		0.958	0.09
0	NTA, 1×10^{-3}	6.9×10^{-6}	−0.5(2)	−6.2(4)	0.970	0.16
0	PDCA, 1×10^{-3}	9.6×10^{-6}		−6.4(3)	0.996	0.12
20	None	7.1×10^{-5}	−0.8(1)		0.957	0.06
40	None	8.2×10^{-6}	−0.7(1)		0.956	0.05
Chelex 100						
0	IDA, 5.1×10^{-2}	1.1×10^{-3}	−0.75[a]	−6.70[a]		
12	None	9.7×10^{-6}	−0.3(1)		0.986	0.09
12	NTA, 1×10^{-3}	9.6×10^{-6}	−0.4(1)	−7.0(1)	0.982	0.09
12	PDCA, 1.1×10^{-3}	1.0×10^{-5}		−6.9(6)	0.986	0.16
40	None	8.2×10^{-6}	−0.4(2)		0.894	0.20
40	NTA, 1×10^{-3}	8.9×10^{-6}	−0.3(1)	−6.3(5)	0.962	0.13

c.c.: the correlation coefficient of the calculated and experimental values of f; R.E.: the relative error.
[a] Ref. [24].

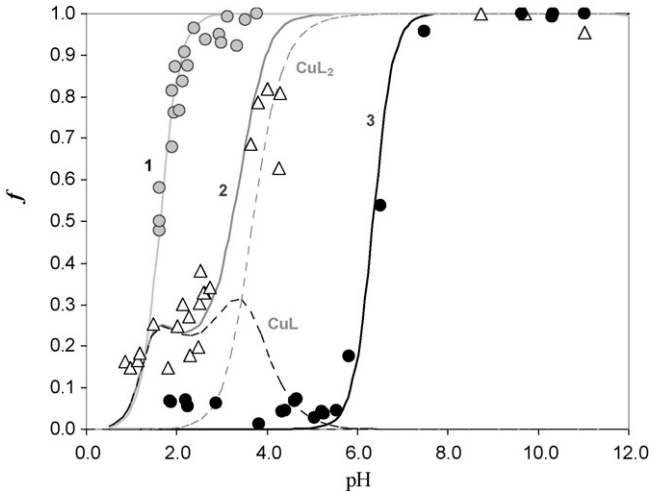

Fig. 3. Sorption profile of copper(II) on Empore™ membrane in 0.1 M KCl, in absence and in the presence of ligands. V = 50 ml, w = 0.132 g dry membrane, Cu(II) = 63 nM. (◯) Without competing ligand; (△) with NTA 1 mM; (●) with PDCA 1 mM. Continuous lines are calculated sorption curves based on the intrinsic complexation constant of the complexes CuL and CuL_2 in the solid phase. *Line 1*, considering only hydrolysis competition; *line 2*, considering hydrolysis and NTA complexation competition; *line 3*, considering hydrolysis and PDCA complexation competition. The dashed lines are calculated with the same condition considered for *line 2* but taking into account only for one complex in the solid phase: (-·-·-) only CuL; (···) only CuL_2.

used to collect the protonation and the complexation constants for the considered systems [23].

For example, sorption profiles obtained in absence and in the presence of ligands for 0.1 M KCl solution are reported in Fig. 3. Besides the 1:1 complex, the 1:2 complex is identified and it is predominant at pH higher than 4.

The values of the intrinsic complexation constants obtained from the different experimental profiles are reported in Table 2, together with those found for the resin in beads Chelex 100. As for the protonation, the results obtained in solutions at the same ionic strength (0.1 M KCl) but with different percentages of ethanol, are not significantly different at 95% of confidence (Fig. 4) and they are also not significantly different from the values obtained for Chelex 100. Once more, they could not be considered different from those previously determined in water solutions, whose values were $\log \beta_{110i} = -0.75$ and $\log \beta_{120i} = -6.7$ [24].

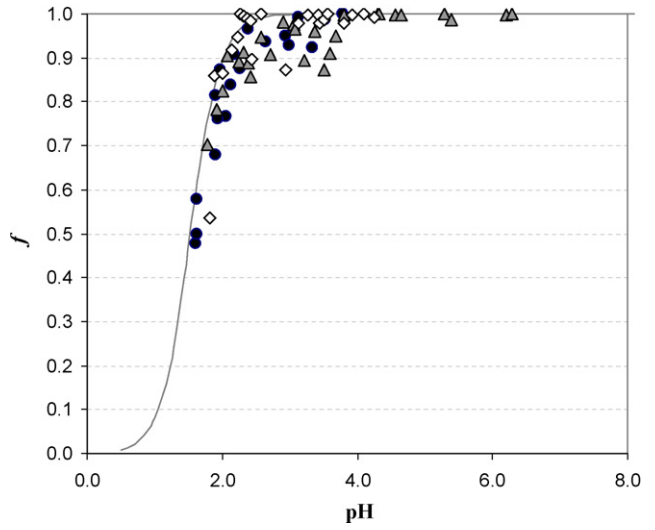

Fig. 4. Sorption profile of copper(II) on Empore™ membrane in 0.1 M KCl hydro-alcoholic solutions at different percentages of ethanol. (●) 0% of ethanol; (▲) 20% of ethanol; (◊) 40% of ethanol.

On the basis of these results, it is possible to calculate the K^* values at the desired pH. This is a parameter of outmost importance since it defines the performance of the chelating sorbent for determining the metal distribution in an unknown solution. For instance, on the basis of K^* values, it is possible to establish which complexes could be detected through RT in relation with the considered metal ion. In the present case we are interested in applying the membranes to determine copper(II) species distribution in "flemma" and "grappa" samples. Consequently the detection window of Empore™ is calculated at ionic strength 0.1 M, pH around 3 and alcoholic content ranging from 20 to 40%, employing a volume of 100 ml and a mass of dry membrane from 0.020 to 1.000 g (in these conditions the centre value of the detection window with $K^* = 6 \times 10^5$, is 1.2×10^3 considering an average value of 0.2 g of dry membrane). However it should be highlighted that the detection window can be calculated for any other experimental condition.

3.3. Sorption kinetic of copper(II) on Empore™ membrane in hydro-alcoholic solutions

Our way of using the Empore™ membrane, not connected to a filtering device as proposed from the manufacturer, is to stir with a magnetic stirrer the solution into which the membrane is suspended. Its behaviour possibly differs also from that of Chelex 100, which offers the higher surface of the discrete beads to the water phase: indeed we always found that the sorption kinetic for Empore™ membrane is slower.

Fig. 5 shows the results of the copper(II) sorption kinetic, from 0.1 M KCl solutions at pH 3, on Chelex 100 (black diamonds: Cu(II) 0.01 mM) and on Empore™ at two different metal concentrations (white circles: Cu(II) 2.5 μM; grey circles: Cu(II) 0.9 mM); it is immediately evident the faster kinetics on the resin than on the beads: copper is quantitatively sorbed in around 15 min. For

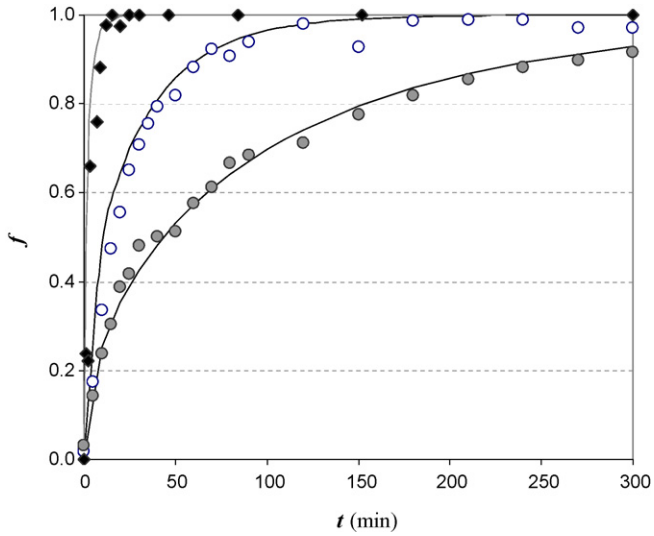

Fig. 5. Kinetic profiles of copper(II) on Empore™ and on Chelex 100, in 0.1 M KCl solution at pH 3. (♦) Chelex 100, Cu(II) 0.01 mM; continuous curve is calculated considering the fitting parameter obtained by the application of the homogeneous diffusion model (film diffusion Eq. (9)): slope = 0.29(3) min^{-1} (R^2 = 0.954, E = 0.198). (◯) Empore™, Cu(II) 2.5 mM; continuous curve is calculated considering the fitting parameter obtained by the application of the shrinking core model (diffusion through the reacted layer controls Eq. (12)): slope = $1.05(3) \times 10^{-2}$ min^{-1} (R^2 = 0.996, E = 0.008). (◍) Empore™, Cu(II) 0.9 μM; continuous curve is calculated considering the fitting parameter obtained by the application of the shrinking core model (diffusion through the reacted layer controls Eq. (12)): slope = $2.6(1) \times 10^{-3}$ min^{-1} (R^2 = 0.974, E = 0.010).

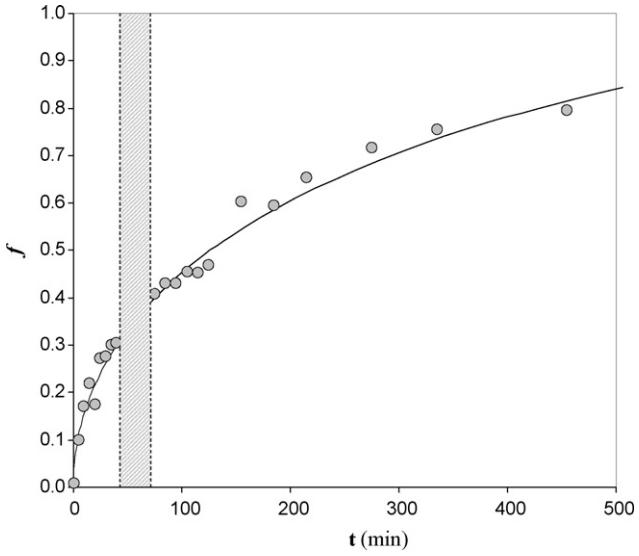

Fig. 6. Interruption test for copper sorption on Empore™, in 0.1 M KCl, Cu(II) 7.2 μM, 20% EtOH solution at pH 3. Continuous curve is calculated considering the fitting parameter obtained by the application of the shrinking core model (diffusion through the reacted layer controls Eq. (12)): slope = $8.7(2) \times 10^{-4}$ min^{-1}; $R^2 = 0.990$.

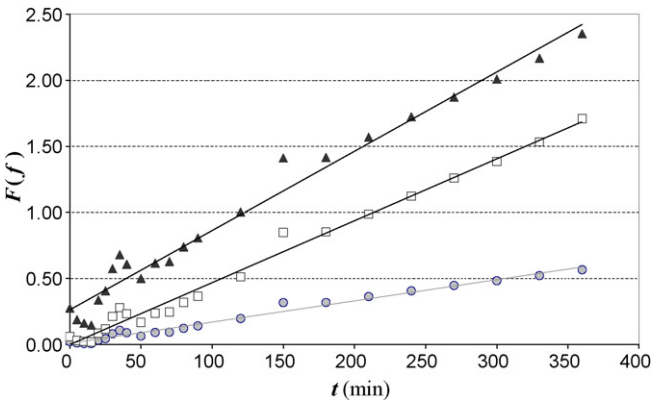

Fig. 7. Test of the kinetic model equations $F(f)$ vs. t defined by Eqs. (9)–(12). Rate of copper sorption on Empore™ in 0.1 M KCl, Cu(II) 0.01 mM solution at pH 3 and 40% of ethanol. Linear regression parameters are reported in Table 3. (▲) HPDM, film diffusion; (□) HPDM, particle diffusion; (◯) SPM, diffusion through the reacted layer controls.

Empore™ the sorption rate is lower and it decreases by increasing the metal concentration. Moving on the kinetic models, while for Chelex 100 the limiting kinetic step is the film diffusion, in the case of membrane both the particle diffusion and shell progressive model, in particular "the diffusion though the reacted layer controls", seem to fit the data satisfactorily. To better discriminate between the two models, some theoretic considerations and experiments are performed. Firstly the shell progressive model is considered because the kinetic profile depends on the concentration of the metal ion in solution (see Eq. (12)), but to further investigate the best fit model, interruption tests [25,26] are set up. The membrane is removed from the solution for a brief period of time and is then re-immersed. If the interruption affects the process and the rate immediately after the re-immersion of the sorbent into the solution is greater than prior to the interruption, the process is controlled by the particle diffusion. As an example in Fig. 6, the results of an interruption test obtained from a 0.1 M KCl, 7.2 μM Cu(II) and 20% EtOH solution at pH 3, is shown and no differences between the rate before and after interruption is found. So also these experiments are supporting the hypothesis of the shell progressive model to describe the data.

The effect of the alcoholic content to the sorption kinetic of copper(II) on the Empore™ membrane is also considered. As an example, Fig. 7 shows the results of the sorption kinetics from copper(II) 0.01 mM solution, at pH 3 and 40% of ethanol, in the form of different kinetic models defined by Eqs. (9), (10) and (12). It could be observed that the film diffusion control could be discarded since the poor fit and, for the reasons just above reported, the shell progressive model is used to describe all the kinetic profiles.

In Table 3 results of three experiments considering solutions with the same content of copper(II) in 0.1 M KCl but different percentages of ethanol, are shown. It is evident a decrease of the sorption rate by increasing the alcoholic content, so the ethanol seems to hinder the access of copper(II) in the solid phase. It can be due to the less swelling of the sorbent in solutions at high alcoholic content [27] or to the decrease of the diffusion coefficient of the metal ion in solutions with increasing alcoholic content [28].

A more accurate kinetic treatment is outside of the aim of this study.

3.4. The species distributions

The previous thermodynamic and kinetic characterizations of the copper(II) sorption on Empore™ are fundamental tasks needed to apply the chelating membranes in metal distributions studies. In the present investigation, the detection of copper(II) species both in alcoholic Italian distillate "grappa" and in its intermediate product ("flemma"), is carried out by the Resin Titration (RT) method using, as competitive reagent, the Empore™ membrane (Table 4).

Prior synthetic solutions containing different percentage of ethanol are analysed to validate the procedure and to verify that no artefacts are introduced during the experiments. As expected, in hydro-alcoholic solutions of copper(II) in absence of ligands a quantitative sorption was obtained and it is independent of the V/w ratio. Just because not any strong ligand for copper(II) was found in these solutions does not mean that not any organic matter is released by labware or by Empore™, but that these substances, if present, are not able to compete with the active groups of the membrane for the complexation with copper(II). In Fig. 8 an example of RT is reported and it refers to a synthetic hydro-alcoholic solu-

Table 3
Kinetic of Cu(II) on Empore™ in 0.1 M KCl, Cu(II) 0.01 mM solution at pH 3. Test of the kinetic model equations $F(f)$ vs. t defined by Eqs. (9)–(13): linear regression analysis (numbers in parentheses are the 95% confidence intervals, and refer to the last significant digit).

EtOH (%)	HPDM FD – Eq. (9)		HPDM PD – Eq. (10)		SPM DRLC – Eq. (12)	
	Slope, k (min^{-1})	Fitting parameters	Slope, k (min^{-1})	Fitting parameters	Slope, k (min^{-1})	Fitting parameters
0	$3.5(2) \times 10^{-2}$	R^2: 0.982; E: 0.077	$1.42(4) \times 10^{-2}$	R^2: 0.994; E: 0.027	$1.05(3) \times 10^{-2}$	R^2: 0.996; E: 0.008
20	$1.5(9) \times 10^{-2}$	R^2: 0.936; E: 0.236	$7.9(2) \times 10^{-3}$	R^2: 0.991; E: 0.042	$5.5(2) \times 10^{-3}$	R^2: 0.990; E: 0.001
40	$6.6(4) \times 10^{-3}$	R^2: 0.953; E: 0.108	$2.33(6) \times 10^{-3}$	R^2: 0.985; E: 0.060	$1.63(5) \times 10^{-3}$	R^2: 0.981; E: 0.009

HPDM: homogeneous particle diffusion model; SPM: shell progressive model; FD: film diffusion; PD: particle diffusion; DRLC: diffusion through the reacted layer controls.
E = root mean error = $\sqrt{(\sum (F(f)_{calc} - F(f)_{sper})^2)/d}$; d = degrees of freedom.

Table 4
Results of RTs of copper(II) in flemma and grappa samples (numbers in parentheses are the 95% confidence intervals, and refer to the last significant digit).

	Flemma B	Grappa B	Flemma P	Grappa P
pH[a]	2.82	2.97	2.45	2.71
K^{*}[b]	1.91×10^{5}	3.85×10^{5}	3.51×10^{4}	1.16×10^{5}
c_{tot} (mol l^{-1})	$1.04(5) \times 10^{-4}$	$1.9(4) \times 10^{-6}$	$3.0(1) \times 10^{-5}$	$1.55(7) \times 10^{-6}$
$c_{tot,RT}$ (mol l^{-1})	$1.07(4) \times 10^{-4}$	$2.2(1) \times 10^{-6}$	$3.3(2) \times 10^{-5}$	$1.6(2) \times 10^{-6}$
$\log \alpha_{M(I)}$	1.53(5)	1.93(7)	0.73(3)	1.87(9)

c_{tot} = direct measure of the total metal contents by analysis on an acidified portion of the original sample; $c_{tot,RT}$ = total metal concentration obtained by RT; B = flemma and grappa "Bracchetto"; P = flemma and grappa "Piemonte".

[a] After equilibration with the membrane.

[b] Evaluated at the pH of the RT, and for the ionic composition of the sample. Values obtained from the intrinsic complexation constants of copper(II) in the solid phase.

tion containing KCl 0.1 M, Cu(II) 7.6 μM and 40% of ethanol (white circles).

The RT procedure is then applied to the flemma and grappa distillates. For each sample two titrations were performed on different aliquots of the solution. The results are summarized in Table 4 and the RT of "grappa Bracchetto" is reported in Fig. 8 (grey diamonds) as an example.

For all samples, the total copper content directly measured on an acidified portion of the solution (c_{tot}) agrees with the value obtained from the elaboration of RT data by non-linear square fitting ($c_{tot,RT}$). It means that copper(II) complexes with $\alpha_{M(I)} > 10K^{*}w/V$ are not present, and all metal in the sample could be free or bound to ligands with a strength less or similar to that of the iminodiacetic group of the membrane. This behaviour has been already observed in previous investigations for several metals and using the resin in beads Chelex 100 on certified seawater [29] and different natural waters [30,31]. It is an important result because by the RT method using an enough strong sorbent, the quantification of the total metal content can be achieved also when the direct analysis on the sample is not possible (i.e. for very complex matrices at high salinity or at high organic content).

As expected, the concentration of copper(II) in the row distillates "flemma" is higher than in the grappa samples. As discussed before, to produce the grappa distillate, grape marcs are loaded into special copper baskets. Usually, heating of each copper boiler is indirectly by steam injection. Steam passes through the marcs and produces the "flemma" at around 20% ethanol content, and then the "flemma" feeds the distillation column which generates several fractions: the heads, the heart or spirit cut and the tails. The heads contain the most volatile elements (e.g. acetaldehyde, methyl acetate, ethyl acetate, etc.) which are often detrimental to the quality of the spirit. The heart contains the noblest constituents of the aroma in their ideal proportions. The tails pass over after the spirit cut, these are still rich in alcohols, but contain less volatile components which need to be eliminated in order not to spoil the fineness of the spirit [32]. So, moving from "flemma" to the final distillate "grappa", most copper is left over in the tails fraction of the distillation column.

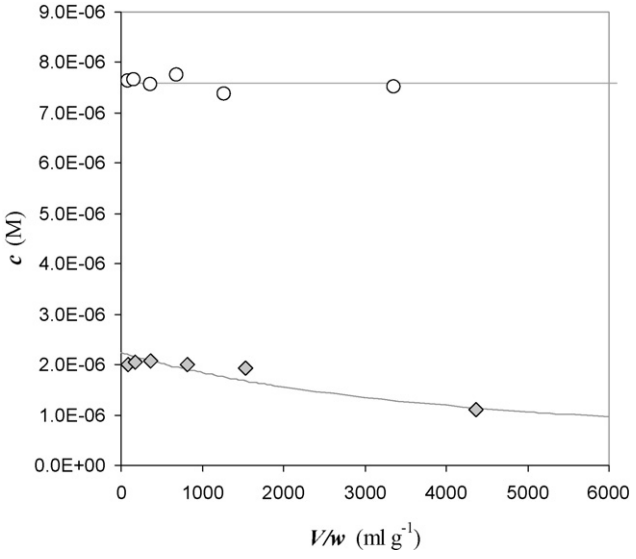

Fig. 8. Examples of Resin Titration curves using Empore™. V = 50 ml; w = 0.02–1 g of dry membrane. (○) Synthetic solution: KCl 0.1 M, Cu(II) 7.6 μM and 40% of ethanol at pH 3; (◇) grappa "Bracchetto" sample.

For all samples, the RT data can be satisfactorily fitted by Eq. (14); this means that the natural ligands in these samples are in excess with respect to the copper, so all metal is complexed in species with $\alpha_{M(I)}$ that falls in the detection window of the titration (see Eq. (15)).

The values of $\alpha_{M(I)}$ obtained for the "flemma" samples are just lower than those found for the "grappa" distillates, and these small discrepancies could be due to the different pH and to the different kind of grape marc. It could be deduced that similar substances, but at different concentration, would be responsible for the copper complexation in the flemma and grappa samples here examined. They could be natural organics since these samples contain, among others, higher alcohols, esters, fatty acids and other organic substances and these may bind, in various extents, with the copper(II).

4. Conclusion

In the present investigation, the detection of copper(II) species both in alcoholic Italian distillate "grappa" and in its intermediate product ("flemma"), is carried out by the Resin Titration (RT) method using, as competitive reagent, the Empore™ membrane.

An accurate characterization of the sorption properties is performed to apply the chelating membrane in metal distribution studies.

About the protonation mechanism and the equilibria reactions of copper(II) in the solid phase, no differences between the Empore™ membrane and the resin in beads Chelex 100 is found, as expected because the same iminodiacetic active groups on the two chelating sorbents. A good agreement between intrinsic constants, evaluated in different hydro-alcoholic media, is obtained.

On the contrary, the sorption kinetic on the membrane is completely different with respect to that on the resin in beads; in particular a very low sorption rate is observed: if copper(II) is quantitatively sorbed on Chelex 100 in 15 min, the time required to the Empore™ to obtain the same sorption is around 5 h, and it increases when the alcoholic content increases.

These characterizations are needed to effectively apply Empore™ in metal distribution studies using the Resin Titration (RT) method; in particular in the present investigation, the detection of copper(II) species both in alcoholic Italian distillate "grappa" and in its intermediate product ("flemma"), is carried out. In all samples, copper is bound to ligands in excess with respect to the metal and able to compete with the iminodiacetic groups of the membrane for copper complexation. Although by the RT method it is not possible to understand the nature of the ligands, because the very complex matrices with several different organic substances, the quantification of the metal fraction linked to these ligands is fundamental both from a toxicological point of view and with regard to the overall quality control of the product.

The usage of the Empore™ in metal distribution studies certainly makes easier the manipulation of the samples even if a longer equilibration is needed with respect to the resin in beads. It has been proposed by the manufacture to be used in a filtering device. For our application, we recommend to gently stir the solution containing

the membrane, due to its limited mechanic stability. Indeed with a vigorous vibration on a shaking plate, the micro beads of resin appear in solution. The main drawback is represented by the cost: we estimate a final cost 3€/g for Chelex 100 in comparison with 27€/g for the Empore™ (prizes in autumn 2008). So as perspectives we would like to use these membranes for *in situ* speciation and we are also looking for other similar but possibly more economic materials.

Acknowledgments

We wish to thank Dr Alessandro Francoli for providing the materials of this study. We also greatly appreciate the contribution of him and of the people of the distillery laboratory for the useful suggestions and the fundamental information.

We wish to thank Dr. Jennifer J. Heitkamp (M.S. Bioanalytical Technologies - Empore Dyneon LLC, 3M Center) for her important tips.

This work is partially supported by Distillery Francoli - C.so Romagnano, 20, 28074 Ghemme (Italy) and by FAR, Fondo Ateneo per la Ricerca, Università di Pavia, Italy.

References

[1] European Council, General Rules on Definition, Description and Presentation of Spirituous Beverages, 1989.
[2] C.Da. Porto, Int. J. Food Sci. Technol. 37 (2002) 395.
[3] M.A. Baldo, S. Daniele, Electroanalysis 18 (2006) 633.
[4] Brasilian Ministry of Agriculture, Complementation on Identification and Quality Standards for Alcoholic Distillates, 1974.
[5] R. Biesuz, G. Alberti, G. D'Agostino, E. Magi, M. Pesavento, Mar. Chem. 101 (2006) 180.
[6] R. Biesuz, G. Alberti, M. Pesavento, J. Solution Chem. 37 (2008) 527.
[7] http://solutions.3m.com/wps/portal/3M/en_US/Empore/, 2008.
[8] M.A. Baldo, S. Daniele, C. Bragato, G.A. Mazzocchin, Electroanalysis 13 (2001) 737.
[9] M. Pesavento, R. Biesuz, M. Gallorini, A. Profumo, Anal. Chem. 65 (1993) 2522.
[10] Y. Merle, J. Marinsky, Talanta 31 (1984) 199.
[11] Ö. Szabadka, E. Varga, L. Nagy, Talanta 59 (2003) 1081.
[12] M. Pesavento, R. Biesuz, React. Funct. Polym. 36 (1998) 135.
[13] F. Helfferich, Ion Exchange, McGraw-Hill, New York, 1962, p. 72.
[14] R. Biesuz, M. Pesavento, G. Alberti, F. Dalla Riva, Talanta 55 (2001) 541.
[15] A. Ringbom, E. Still, Anal. Chim. Acta 59 (1972) 143.
[16] M. Pesavento, R. Biesuz, G. Alberti, M. Sturini, Anal. Bioanal. Chem. 376 (2003) 1023.
[17] R. Biesuz, A.A. Zagorodni, M. Muhammed, J. Phys. Chem. B 105 (2001) 4721.
[18] M. Pesavento, R. Biesuz, G. Alberti, F. Dalla Riva, React. Funct. Polym. 46 (3) (2001) 233.
[19] J.L. Cortina, A. Warshawsky, N. Kahana, V. Kampel, C.H. Sampaio, R.M. Kautzmann, React. Funct. Polym. 54 (2003) 25.
[20] S. Gonzalez-Luque, M. Streat, Hydrometallurgy 11 (1983) 207.
[21] E. Kilic, N. Aslan, Microchim. Acta 151 (2005) 89.
[22] P.G. Daniele, P. Amico, G. Ostacoli, J. Inorg. Nucl. Chem. 43 (1981) 2183.
[23] L.D. Pettit, K.J. Powell, Stability Constants Database. SolEq Solution Equilibria: Principles and Applications [Computer Program], Academic Software, Otley, Yorks, UK, 2001.
[24] M. Pesavento, R. Biesuz, Anal. Chem. 67 (1995) 3558.
[25] F. Helfferich, Ion Exchange, McGraw-Hill, New York, 1962, p. 256.
[26] A.A. Zagorodni, Ion Exchange Materials, Elsevier, Oxford, 2007, p. 229.
[27] A.A. Zagorodni, Ion Exchange Materials, Elsevier, Oxford, 2007, p. 140.
[28] E. Companys, M. Naval-Sánchez, N. Martínez-Micaelo, J. Puy, J. Galceran, J. Agric. Food Chem. 56 (2008) 8296.
[29] M. Pesavento, R. Biesuz, F. Baffi, C. Gnecco, Anal. Chim. Acta 401 (1999) 265.
[30] G. Alberti, R. Biesuz, M. Pesavento, Microchem. J. 86 (2007) 166.
[31] M. Pesavento, R. Biesuz, G. Alberti, A. Profumo, G. D'Agostino, Chem. Spec. Bioavailab. 16 (2004) 35.
[32] C. Da Porto, D. Decorti, Int. J. Food Sci. Technol. 43 (2008) 638.

Talanta 79 (2009) 687–694

Contents lists available at ScienceDirect

Talanta

journal homepage: www.elsevier.com/locate/talanta

Electrochemical study and analytical applications for new biologically active 2-nitrophenylbenzimidazole derivatives

A. Álvarez-Lueje*, C. Zapata-Urzúa, S. Brain-Isasi, M. Pérez-Ortiz, L. Barros, H. Pessoa-Mahana, M.J. Kogan

Bioelectrochemistry Laboratory, Chemical and Pharmaceutical Sciences Faculty, University of Chile, P.O. Box 233, Santiago 1, Chile

ARTICLE INFO

Article history:
Received 5 February 2009
Received in revised form 23 April 2009
Accepted 25 April 2009
Available online 3 May 2009

Keywords:
2-Nitrophenylbenzimidazole
Differential pulse polarography
Tast polarography
Cyclic voltammetry

ABSTRACT

The present study addresses the electrochemical behavior and the analytical applications of six 2-nitrophenylbenzimidazole derivatives with activity against *Trypanosoma cruzi*. When studied in a wide range of pH, by differential pulse polarography, tast polarography and cyclic voltammetry, these compounds exhibited two irreversible cathodic responses. With analytical purposes, the differential pulse polarography mode was selected, which exhibited adequate analytical parameters of repeatability, reproducibility and selectivity. The percentage of recovery was in all cases over 99%, and the detection and quantitation limits were at the level of 1×10^{-7} mol L^{-1} and 1×10^{-6} mol L^{-1}, respectively. In addition, the differential pulse polarography method was successfully applied to study the hydrolytic degradation kinetic of one of the tested compounds. Activation energy, kinetic rate constants at different temperatures and half-life values of such application are reported.

1. Introduction

Parasitic diseases are a public health problem in many countries of the world. It is reported that approximately 18 million of people are infected with *Trypanosoma cruzi*, the protozoa responsible of Chagas' disease, especially in rural and poor areas in South and Latin America [1]. At present, there are two available drugs for the treatment of Chagas' disease: nifurtimox and benznidazole, which have significant activity in the acute phase of the disease, although limited efficacy in the chronic stages, carrying severe side effects [2].

Compounds with benzimidazolic nucleus present a wide spectrum of biological activities such as antiparasitic, antibacterial, antiviral and antitumoral, amongst others [3,4].

On the other hand, nitroaromatic compounds have proven antiparasitic, antibacterial, antimycotic and antitumoral activities, which are related to their electrochemical properties. The nitro group is very reactive in the presence of oxygen, and its complete reduction involves the addition of 6 electrons to form the amine, *via* nitro radical anion ($1e^-$), nitroso ($2e^-$) and hydroxylamine ($4e^-$) intermediates [5–8].

There is evidence that free-radical metabolites from nitroaromatics compounds can cause deleterious effects in bacteria, parasitic and mammalian cells, which can be correlated with the pharmacological activity of these compounds. According to the $E_{1/2}$ values determined in aqueous solutions by cyclic voltammetry or polarography, the reduction of the nitro group is not reversible and may involve the addition of up to 4 electrons, being the first one usually the most difficult to add [9].

According to the above, combining a benzimidazole nucleus with a nitroaromatic ring could result in compounds with relevant biological activity against parasites. In a previous report [10], using HPLC and UV-spectrophotometric techniques we characterized a new series of 2-nitrophenylbenzimidazole derivatives which exhibited growth and oxygen uptake inhibitory effects in *T. cruzi* epimastigotes. Aiming to further studying these compounds and taking into account the relevance of the electrochemical properties on their biological activity, in this work we have addressed the electrochemical behavior and the development of electroanalytical methods for the following six nitrophenylbenzimidazole derivatives: 2-(2-nitrophenyl)-1H-benzimidazole (NB), 1-benzoyl-2-(2-nitrophenyl)-benzimidazole (BNB), 1-(4-methoxybenzoyl)-2-(2-nitrophenyl)-benzimidazole (PMNB), 1-(4-chlorobenzoyl)-2-(2-nitrophenyl)-benzimidazole (PCNB), 1-(4-fluorobenzoyl)-2-(2-nitrophenyl)-benzimidazole (PFNB) and 1-(4-nitrobenzoyl)-2-(2-nitrophenyl)-benzimidazole (PNB) (Fig. 1).

2. Experimental

2.1. Reagents and drugs

2-(2-Nitrophenyl)-1H-benzimidazole ($C_{13}H_9N_3O_2$, MW: 239.06 g mol^{-1}, MP: 277–278.5 °C); 1-benzoyl-2-(2-nitrophenyl)-

* Corresponding author. Fax: +56 7378920.
E-mail address: aalvarez@ciq.uchile.cl (A. Álvarez-Lueje).

0039-9140/$ – see front matter © 2009 Elsevier B.V. All rights reserved.
doi:10.1016/j.talanta.2009.04.054

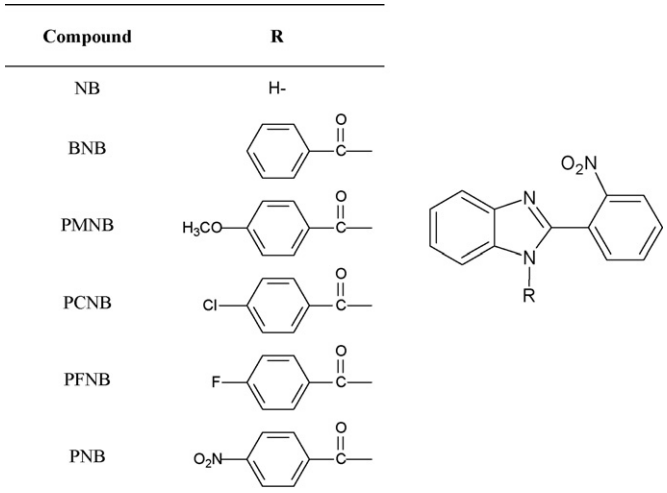

Fig. 1. Chemical structures of 2-(2-nitrophenyl)-1H-benzimidazole (NB), 1-benzoyl-2-(2-nitrophenyl)-1H-benzimidazole (BNB), 1-(4-methoxybenzoyl)-2-(2-nitrophenyl)-1H-benzimidazole (PMNB), 1-(4-chlorobenzoyl)-2-(2-nitrophenyl)-1H-benzimidazole (PCNB), 1-(4-fluorobenzoyl)-2-(2-nitrophenyl)-benzimidazole (PFNB) and 1-(4-nitrobenzoyl)-2-(2-nitrophenyl)-1H-benzimidazole (PNB).

benzimidazole ($C_{20}H_{13}N_3O_3$, MW: 343.33 g mol^{-1}, MP: 161 °C); 1-(4-methoxybenzoyl)-2-(2-nitrophenyl)-benzimidazole ($C_{21}H_{15}N_3O_4$, MW: 373.36 g mol^{-1}, MP: 124–126 °C); 1-(4-chlorobenzoyl)-2-(2-nitrophenyl)-benzimidazole ($C_{20}H_{12}N_3O_3Cl$, MW: 377.78 g mol^{-1}, MP: 127–129 °C); 1-(4-fluorobenzoyl)-2-(2-nitrophenyl)-benzimidazole ($C_{20}H_{12}N_3O_3F$, MW: 361.33 g mol^{-1}, MP: 165–166 °C) and 1-(4-nitrobenzoyl)-2-(2-nitrophenyl)-benzimidazole ($C_{20}H_{12}N_4O_5$, MW: 388.33 g mol^{-1}, MP: 174–176.9 °C) were obtained in our laboratory according to a procedure previously described [11,12]. The purity of these compounds was assessed by ^{1}H NMR, ^{13}C NMR, IR and melting point. All reagents were of analytical grade, unless indicated otherwise. Methanol and acetonitrile, HPLC grade, were used. Deionized water was obtained in the laboratory, using ionic exchange columns (Milli-Q).

2.2. Solutions preparation

2.2.1. Buffer solutions

0.1 mol L^{-1} Britton–Robinson buffer (acetic acid/boric acid/phosphoric acid) [13] was used for polarographic experiments, and desired pH adjusted with NaOH or HCl concentrated solutions.

2.2.2. Stock drug solutions

NB and BNB were dissolved in ethanol. PMNB, PCNB, PFNB and PNB were dissolved in acetonitrile. All solutions were prepared to a final concentration of 1×10^{-3} mol L^{-1}, and protected from light using amber glass material.

2.2.3. Work solutions

For differential pulse polarographic (DPP) and tast polarographic (TP) experiments in protic medium, 2.5 mL aliquots of the NB and BNB stock solutions were taken and then diluted to 25 mL with ethanol/0.1 mol L^{-1} Britton–Robinson buffer solution (final ratio of 30/70 v/v). For the other compounds 2.5 mL aliquots were taken and diluted to 25 mL with acetonitrile/0.1 mol L^{-1} Britton–Robinson buffer solution (final ratio of 30/70 v/v for PFNB and 50/50 v/v for PMNB and PCNB) or acetonitrile/0.2 mol L^{-1} phosphate buffer solution for PNB (final ratio of 50/50 v/v).

For cyclic voltammetric (CV) experiments in protic medium, working solutions were employed as previously described. In non-aqueous medium, the studies were carried out in dimethylformamide containing as supporting electrolyte tetrabutylammonium perchlorate (0.1 mol L^{-1}). All the compounds were employed at 1×10^{-3} mol L^{-1} concentration.

2.3. Apparatus

2.3.1. Voltammetric analyzer

DPP and TP experiments were performed with a Metrohm Model 693 VA-Processor, equipped with a model 694 VA-stand. A 25-mL thermostated Metrohm measuring cell, equipped with either a dropping or a hanging mercury electrode (Metrohm) as the working electrode, a platinum wire counter electrode and a calomel reference electrode, was employed. The operating conditions were: sensitivity 2.5–10 μA; drop time 0.6 s; potential range 0 to −1800 mV; ΔE_p −6 mV; pulse retard 40 ms; pulse height −50 mV. CV experiments were performed in a Bioanalytical System (BAS), CV-50W, couple to Pentium computer with CV-50W acquisition and treatment program.

2.4. Molecular modeling

All calculations were run on a SGI workstation and the protocol for the iterative simulated annealing (ISA) calculations was similar to one previously described [14]. This protocol was run five times, employing fully extended starting structures of NB, BNB, PMNB, PCNB, PFNB and PNB, obtaining the same global minimums each time for each compound.

2.5. Analytical procedure

2.5.1. Calibration curve preparation

Working solutions, ranging between 1×10^{-6} mol L^{-1} and 1×10^{-4} mol L^{-1}, were prepared by diluting each stock solution with ethanol/0.1 mol L^{-1} Britton–Robinson buffer pH 4.0 for NB, pH 5.0 for BNB (final ratio of 30/70 v/v) or acetonitrile/0.1 mol L^{-1} Britton–Robinson buffer pH 6 for PMNB and PCNB (final ratio of 50/50 v/v), pH 7 for PFNB (final ratio of 30/70 v/v) or acetonitrile/0.2 mol L^{-1} phosphate buffer pH 7 for PNB (final ratio of 50/50 v/v).

2.5.2. Selectivity studies [15]

2.5.2.1. Degradation trials. Hydrolysis: 1 mL of each compound stock solution was placed in a 10 mL-distillation flask and (a) 5 mL 0.1 mol L^{-1} HCl for acid hydrolysis or (b) 5 mL 0.1 mol L^{-1} NaOH for basic hydrolysis, was added. Then each solution was boiled for 3 h at reflux.

Photolysis: Separately, 3 mL of each compound stock solution were placed in UV-cells and disposed on a black box and then irradiated with UV light (UV black-ray long wave UV lamp, UVP model B 100 AP, 50 Hz, 2.0 A, with a 100 W Par 38 Mercury lamp equipped with a 366 nm filter) at a distance of 15 cm for 8 h (1.2×10^{19} quanta s^{-1}, determined by using potassium ferrioxalate chemical actinometer [16]).

Samples of each of the solutions obtained through the degradation trials were diluted, as previously described in Section 2.2.3, with ethanol/0.1 mol L^{-1} Britton–Robinson buffer, acetonitrile/0.1 mol L^{-1} Britton–Robinson buffer or with acetonitrile/0.2 mol L^{-1} phosphate buffer, to obtain a theoretical concentration of 5×10^{-5} mol L^{-1}. Each sample was analyzed in duplicate.

2.5.2.2. Pharmaceutical interferents. Typical pharmaceutical excipients: cornstarch, magnesium stearate, lactose, sodium lauryl sulfate, titanium dioxide, sodium carbonate, polyethylenglycol 400 and 4000, hydroxypropylcellulose, hydroxypropylmethylcelullose, sorbitol, talc, sodium starch glycolate/sodium carboxymethyl starch (Explotab®) and microcristalline cellulose (Avicel® pH 101), were tested.

2.5.2.3. Stability studies. A stock solution of BNB was diluted to obtain an initial concentration ranging between 1.0×10^{-4} mol L^{-1} and 1.0×10^{-5} mol L^{-1} in a final ratio of 30/70 (v/v) ethanol/0.1 mol L^{-1} Britton–Robinson buffer solution, at selected pH (3, 4, 5, 6, 7.4, 8, 9 and 10), and its degradation was studied at 25 °C. The solution prepared at pH 7.4 was further studied by placing in an oven at 25 °C, 40 °C and 60 °C (±0.2 °C) samples contained in 2 mL amber vials (at least two for each point of the degradation curve). According to the temperature of exposure, vials were removed from the oven at selected time intervals (at 30 min, 20 min and 10 min for 25 °C, 40 °C and 60 °C, respectively), placed on ice immediately after to quench the reaction, and assayed by DPP. Degradation experiments were carried out in duplicate and monitored, at least, over three half-lives.

2.5.2.4. Activation energy (E_a). Each E_a value was obtained from Arrhenius model, by plotting $\ln k$ *vs.* $1/T$ for each concentration tested. The final E_a value represents the average of the E_a calculated for a concentration of 1×10^{-4} mol L^{-1} at pH 7.4. In all cases, regression coefficient values higher than 0.993 were obtained.

3. Results and discussion

3.1. Electrochemical studies

NB, BNB, PMNB, PCNB and PFNB in protic media were reduced on a mercury electrode surface. The polarograms obtained by DPP or TP exhibit, in a broad range of pH, two peaks or two waves, respectively. In all cases, the main signal obtained (I) is a well-resolved peak. The second signal appears at more negative potentials and lower peak

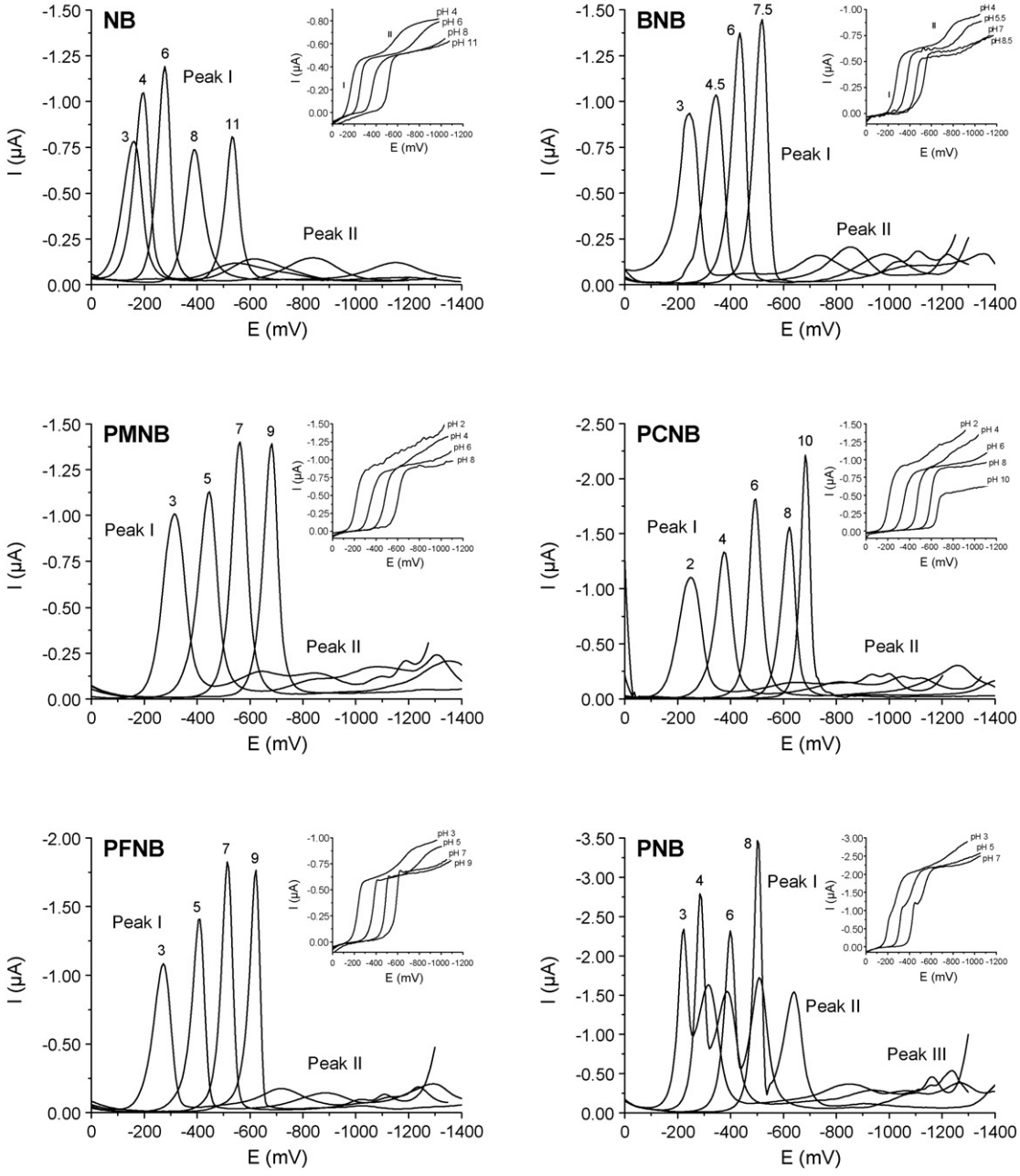

Fig. 2. DPP evolution with pH of 2-nitrophenylbenzimidazole derivatives. Insert: TP dependence with pH.

currents (II). Fig. 2 depicts the polarographic evolution of the compounds as a function of the pH. At low potentials, the first signal (I) for these compounds would correspond to the reduction of the nitro group, generating the hydroxylamine derivative, which involves 4-electrons, according to [17]: $R\text{-}NO_2 + 4e^- + 4H^+ \rightarrow R\text{-}NHOH + H_2O$. On the other hand, signal II is likely to correspond to the azomethine reduction [18–20].

Unlike the above, PNB exhibits a more complex polarogram with two overlapped signals, due to the presence of two nitro groups in its structure. Regardless of the organic solvent/buffer solution used (acetonitrile/Britton–Robinson, methanol/phosphate, dimethylformamide/phosphate, acetonitrile/phosphate); these signals could not be well resolved. By comparing the polarographic responses of the other N-substituted derivatives studied with PNB, signal I would correspond to the p-nitro reduction, signal II to the o-nitro reduction and signal III to the azomethine reduction.

Peak potential evolution with pH is shown in Fig. 3. As can be seen, peaks potential I and II shift towards more cathodic potential as the pH increases, exhibiting a linear dependence with pH, reaching a pH-independent behavior from pH 9–12 (peak II) for NB. Also, for the main peak (I), breaks in the linear response are clearly observed for NB, BNB and PFNB, between pH 4 and 5; probably due to the pK_a values of these derivatives. In the TP mode, all studied compounds presented dependence between $E_{1/2}$ and the pH, showing breaks at around pH 5. Table 1 summarizes the slopes of the linear segments and the corresponding breaks for each of the studied compound. As can be seen, the amphoteric compound NB exhibits a lower dependence with the pH for the first signal ($\delta E_{1/2}/\delta pH \sim 30\,mV\,pH^{-1}$). Such behavior differs from that of the other N-substituted derivatives, which are weak bases and exhibit slopes around twice greater ($\delta E_{1/2}/\delta pH$ between $65\,mV\,pH^{-1}$ and $71\,mV\,pH^{-1}$); these structural and acid–base differences between NB and the others compounds would produce changes in the electrodic mechanism, affecting the α_n term (where α is the transfer coefficient) that translates into a significant change in the slope of the potential *vs.* pH plot [21]. In a previous report, we calculated the

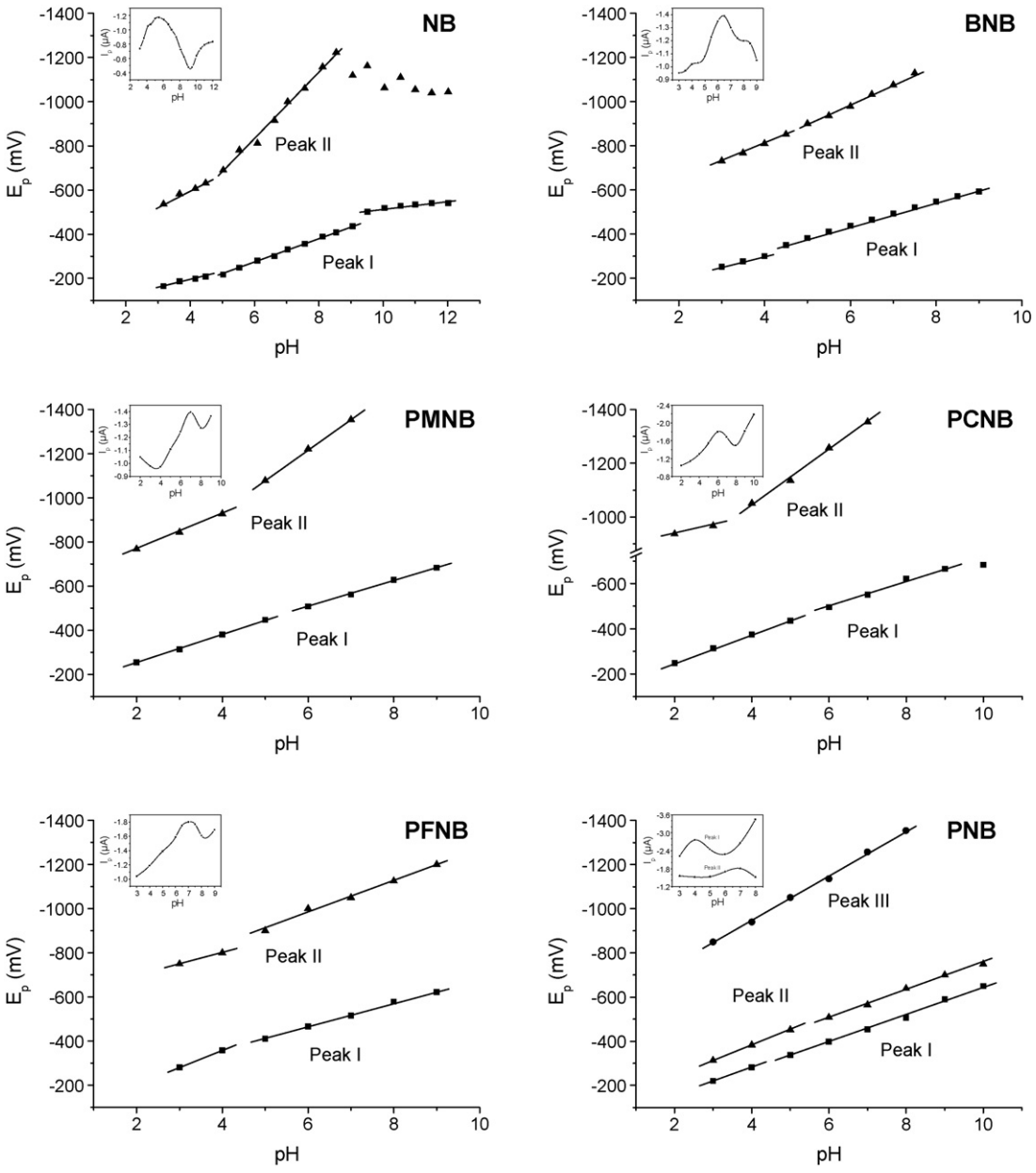

Fig. 3. Peak potential evolution with pH of 2-nitrophenylbenzimidazole derivatives. Insert: peak current dependence with pH.

Table 1
$\delta E_{1/2}/\delta$pH values for the linear segments for the 2-nitrophenylbenzimidazole derivatives in protic media (signal I, TP).

Compound	1st segment, mV pH^{-1} (pH range)	2nd segment, mV pH^{-1} (pH range)
NB	29.6 (2–4.5)	52.6 (4.5–9.5)
BNB	69.7 (2–5.5)	55.3 (5.5–9)
PMNB	65.7 (2–6)	59.1 (6–9)
PCNB	65.6 (2–6)	55.7 (6–9)
PFNB	71 (2–5.5)	51.1 (5.5–9)
PNB	58.5 (2–5)[a]; 69.6 (2–5)[b]	55.6 (5–8)[a]; 61.9 (5–8)[b]

[a] Signal I.
[b] Signal II.

pK_a value of each compound by means of UV-spectrophotometry [10]; NB exhibits two pK_a values, 5.69 and 11.38 for the N=C and NH, respectively, unlike other benzimidazole derivatives that present only one pK_a value, corresponding to their weak base imidazole nitrogen ($pK_{a\ BNB} = 4.90$; $pK_{a\ PMNB} = 4.71$; $pK_{a\ PCNB} = 4.69$; $pK_{a\ PFNB} = 4.86$ and $pK_{a\ PNB} = 4.79$). These values are in agreement with the breaks observed above in the electrochemical studies. On the other hand, it can be seen that the peak current reaches its maximum value near pH 6 and its behavior is consistent with peak potential evolution seen for peak I (insert in Fig. 3).

The differences in the reduction potentials seen between the various 2-nitrophenylbenzimidazole derivatives could be explained by either, the loss of coplanarity of the nitro group from the plane with respect to the phenyl ring, as a consequence of a steric effect of the 2-benzimidazole substituent [22], or the staking of the phenyl ring of the 2-nitrophenylbenzimidazole nucleus with that of the N-benzoyl substituent. In either case, a reduction of the nitro group at the electrode would become more difficult to occur [23]. Thus, the distortion of the coplanar arrangement diminishes the resonance between the nitro group and the aromatic system, producing shifts towards more negative potentials. These effects can be clearly appreciated when the peak potentials of NB (without N-substitution) and BNB (N-benzoyl substituted) are compared with that of the others N-p-benzoyl substituted derivatives; while the former exhibit values of −360 mV and −490 mV, the latter present peak potentials higher than −500 mV (values obtained in acetonitrile/0.1 mol L^{-1} Britton–Robinson buffer, 30/70 v/v, pH 7). In order to support the above assumptions, a conformational search to find the global minimum conformers for each compound was carried out using an ISA calculation [14]. Unlike the other compounds, NB shows no coplanarity or staking phenomena (due to the absence of a N-benzoyl substituent) (Fig. 4A). In the case of BNB, the staking was partial (Fig. 4B) while for the other compounds such effect was complete, shifting the potential to more negative values (Fig. 4C depicts the case of PFNB).

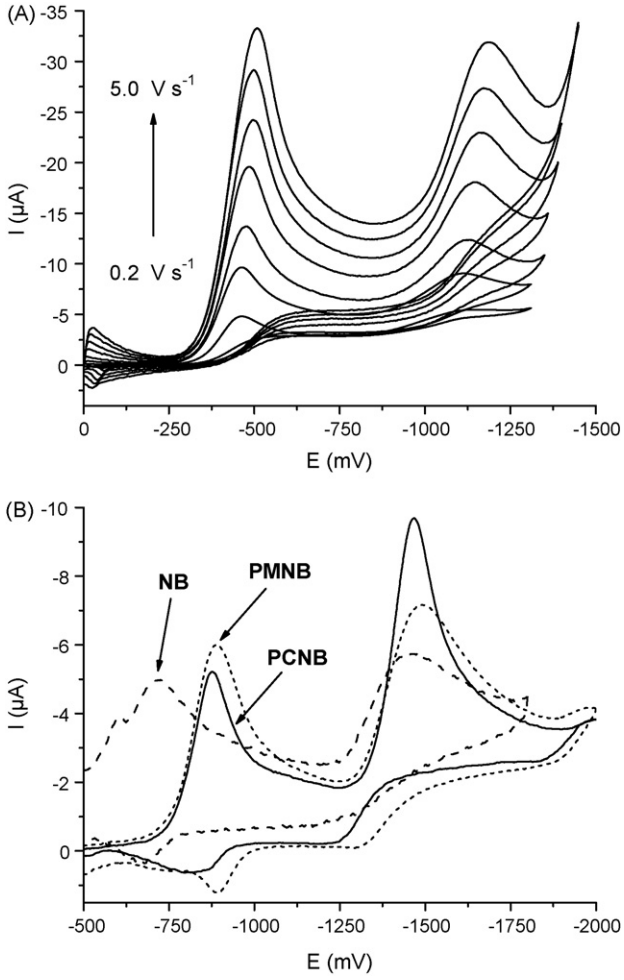

Fig. 5. Cyclic voltammograms of (A) 1×10^{-3} mol L^{-1} PCNB in acetonitrile/0.1 mol L^{-1} Britton–Robinson buffer (50/50 v/v) at different sweep rates; (B) 1×10^{-3} mol L^{-1} solutions of NB, PMNB and PCNB in non-aqueous medium at 1 V s^{-1}.

Additionally, CV studies were conducted at different pH and sweep rates (Fig. 5A). In protic media, the 2-nitrophenylbenzimidazole derivatives displayed, at all pH (3, 7 and 10) and scan rate (0.1–10 V s^{-1}) studied, an irreversible signal, being observed that each signal moves towards more negative potentials as the pH was increased (data not shown).

Upon analyzing the relationship between peak current and sweep rate ($\log I_p$ *vs.* log sweep rate plot), slope values near to

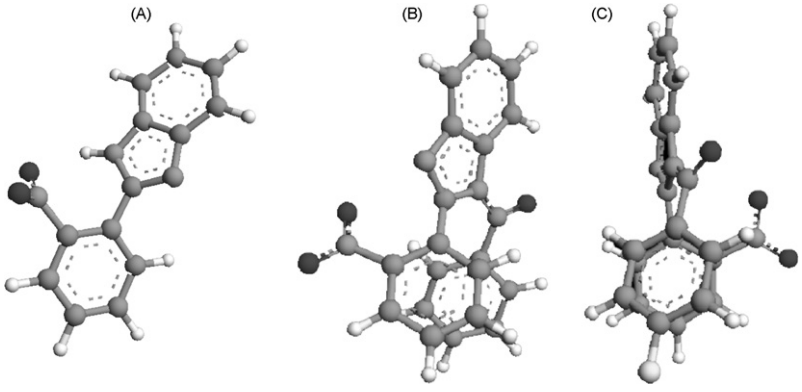

Fig. 4. Ball and Stick conformational representation of global minimum energy conformer of NB (A), BNB (B) and PFNB (C).

Table 2
Analytical parameters of 2-nitrophenylbenzimidazole derivatives by DPP.

	NB[a]	BNB[b]	PMNB[c]	PCNB[c]	PFNB[d]	PNB[e]
Potential detection (mV)	−119	−373	−500	−494	−519	−652
Repeatability, CV (%) 3×10^{-6} mol L^{-1}; 1×10^{-5} mol L^{-1}; 7×10^{-5} mol L^{-1}	1.0; 0.4; 1.7	2.4; 2.2; 0.6	1.2; 1.3; 1.4	1.0; 1.8; 1.6	1.7; 0.9; 0.4	0.59; 0.59; 1.3
Reproducibility, CV (%) 3×10^{-6} mol L^{-1}; 1×10^{-5} mol L^{-1}; 7×10^{-5} mol L^{-1}	1.5; 2.6; 2.3	1.4; 1.5; 1.4	1.8; 1.4; 1.4	1.36; 1.74; 1.77	1.4; 1.2; 1.1	0.49; 0.67; 1.8
Recovery (%) ±s.d.	99.0 ± 0.6	99.1 ± 0.8	102.6 ± 1.4	102.5 ± 2.7	99.3 ± 0.5	99.1 ± 0.8
Concentration range (mol L^{-1})	1×10^{-6}–7×10^{-5}	1×10^{-6}–7×10^{-5}	4×10^{-6}–3×10^{-5}	4×10^{-6}–1×10^{-5}	4×10^{-6}–2×10^{-5}	4×10^{-6}–5×10^{-5}
Calibration curve (I_p, nA; [c], mol L^{-1})	$I_p = 1.28\times10^{7}$ [c] + 4.29 (r = 0.9977, n = 8)	$I_p = 1.0\times10^{7}$ [c] + 4.39 (r = 0.9999, n = 7)	$I_p = 1.5\times10^{7}$ [c] − 1.9 (r = 0.9999, n = 7)	$I_p = 1.8\times10^{7}$ [c] + 4.9 (r = 0.9995, n = 7)	$I_p = 1.58\times10^{7}$ [c] + 14.1 (r = 0.9998, n = 6)	$I_p = 1.63\times10^{7}$ [c] + 5.1 (r = 0.9998, n = 6)
Detection limit (mol L^{-1})	4.5×10^{-7}	7.8×10^{-7}	7.5×10^{-7}	5.9×10^{-7}	2.8×10^{-6}	5.4×10^{-6}
Quantitation limit (mol L^{-1})	1.2×10^{-6}	2.5×10^{-6}	1.6×10^{-7}	1.4×10^{-6}	6.5×10^{-6}	1.7×10^{-5}

[a] Ethanol/0.1 mol L^{-1} Britton–Robinson buffer (30/70 v/v) pH 4.
[b] Ethanol/0.1 mol L^{-1} Britton–Robinson buffer (30/70 v/v) pH 5.
[c] Acetonitrile/0.1 mol L^{-1} Britton–Robinson buffer (50/50 v/v) pH 6.
[d] Acetonitrile/0.1 mol L^{-1} Britton–Robinson buffer (30/70 v/v) pH 7.
[e] Acetonitrile/0.2 mol L^{-1} phosphate buffer (50/50 v/v) pH 7.

0.5 were obtained, which reveals that that the electrodic process is diffusion-controlled [24]. On the other hand, when the experiments were carried out in non-aqueous medium it became possible to distinguish the typical reversible monoelectronic couple corresponding to nitro radical generation ($\Delta E_p \approx 60$ mV at 10 V s^{-1}) [25].

The experimental cathodic potentials in non-aqueous medium at 1 V s^{-1} were, for NB, BNB, PMNB, PCNB, PFNB, −715, −899, −890, −870 and −850 mV, respectively, and for PNB, −936 and −1110 mV (Fig. 5B shows typical CVs for NB, PMNB and PCNB derivatives). These peak potential reduction values are in agreement with those previously described for other nitroaromatic compounds with recognized biological activity [26–31]; particularly relevant is the similarity that arises from comparing the reduction potential of the compounds tested in the present study and that of nifurtimox (−876 mV) [10,32]. Considering that the easiness of reduction of nitroaromatic compounds tends to correlate with their pharmacological activity [22,32], it seems reasonable to state that the growth and oxygen uptake inhibitory effects seen in *T. cruzi* observed previously for these 2-nitrophenylbenzimidazole [10] be attributed to their easiness to undergo nitroreduction.

3.2. Analytical applications

With analytical purposes, DPP mode was selected. In Table 2, both the optimal experimental conditions and the analytical parameters are summarized [33]. Repeatability and reproducibility at different concentration levels were adequate with RSD lower than 3%. In addition, the developed method was checked for selectivity by testing hydrolysis, photolysis, oxidation, synthesis precursor interferences and typical excipients commonly found in pharmaceutical formulations. In these experiments, no new signal or decrease of peak current in the polarograms were observed, with the exception of the hydrolysis test in which a new signal appears at more anodic potentials for BNB, PMNB, PCNB, PFNB and PNB (data not shown).

The developed polarographic methodology was applied to follow the hydrolytic degradation kinetic of BNB. Fig. 6 depicts the polarograms obtained from hydrolysis trials carried out at pH 7.4 and 25 °C. As can be seen, the polarographic peak of BNB (−485 mV) diminishes along the time of hydrolysis and a new signal appears at −333 mV, which corresponds to that of NB, the electroactive decomposition product of BNB. To test the kinetic order of the hydrolytic degradation, experiments at different initial concentrations of BNB and pH were conducted. Changes in the initial BNB concentration did not affect the slopes of the decay

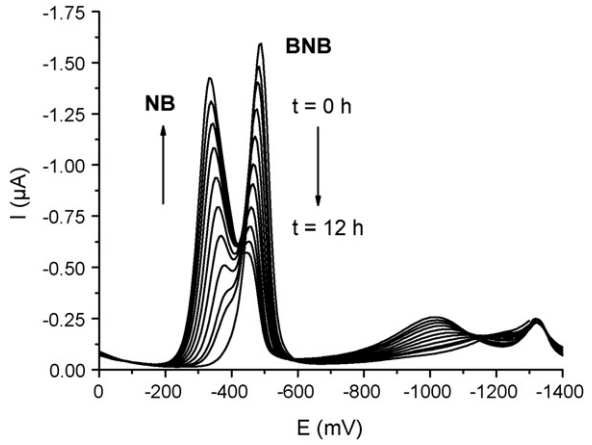

Fig. 6. DP polarograms of 1×10^{-4} mol L^{-1} BNB in ethanol/0.1 mol L^{-1} Britton–Robinson buffer (30/70 v/v) submitted to hydrolysis at pH 7.4 and 25 °C at different times.

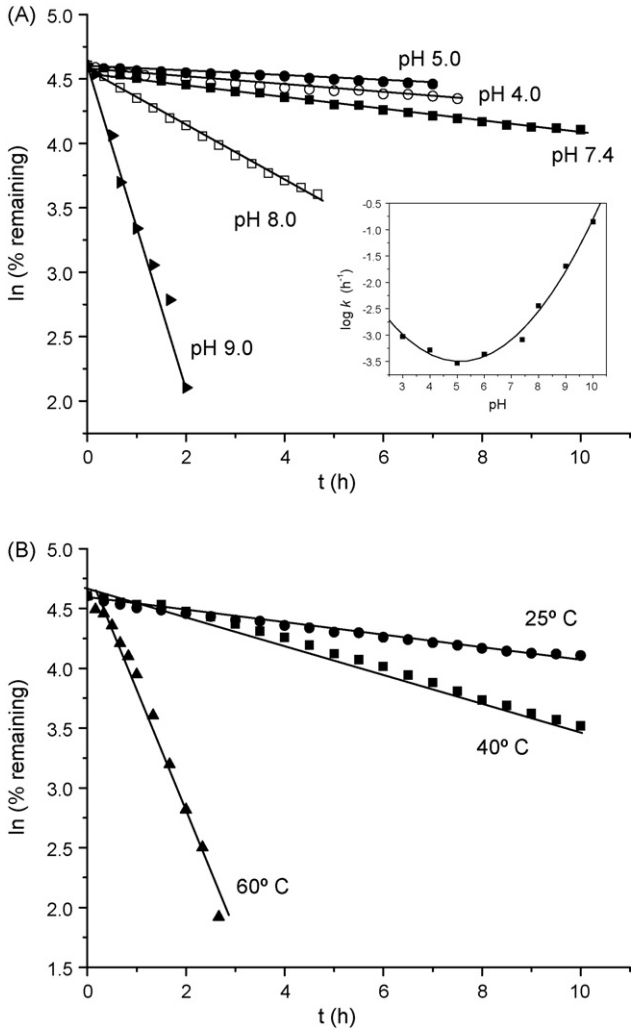

Fig. 7. (A) Effect of pH on degradation of 1.2×10^{-4} mol L^{-1} BNB solution at 25 °C, insert: pH rate profile of the hydrolysis process of BNB at 25 °C. (B) Effect of temperature on degradation of 1.2×10^{-4} mol L^{-1} BNB solution at pH 7.4.

curves, and plots of ln concentration *vs.* hydrolysis time were found to be linear (data not shown). Consequently, from these experiments we conclude that the hydrolytic degradation of BNB follows a first order kinetic [34,35].

Regarding the influence of the pH, BNB exhibited a pH-dependent degradation (Fig. 7A) and the rate constants (k) increase concomitantly with the pH. Table 3 summarizes the k values and the half-lives ($t_{1/2}$) obtained at 25 °C and different pHs. On the other hand, the hydrolysis was found to also depend on the temperature; increasing the latter, from 25 °C to 40 °C and from 40 °C to 60 °C, dramatically changed the k values by 2.3- and 20.5-fold, respectively (Fig. 7B). From Arrhenius plot, an activation energy value of 14.9 kcal/mol was calculated. This value is in agreement with that of reported for other drug undergoing hydrolytic decomposition [34]. In addition, the pH-rate profile corresponding to the hydrolysis process of BNB at 25 °C is shown in Fig. 7A (insert). As can be seen, BNB exhibits it maximum stability near its pK_a value ($pK_{a\ BNB} = 4.90$) and also presents base catalysis hydrolysis from pH 7.5 [35].

Table 3
Rate constant (k) and half-life ($t_{1/2}$) values for BNB degradation at different pHs (25 °C).

pH	k (h^{-1})	$t_{1/2}$ (h)
3.0	9.36×10^{-4}	12.3
4.0	5.17×10^{-4}	22.3
5.0	2.94×10^{-4}	39.2
6.0	4.33×10^{-4}	26.7
7.4	8.12×10^{-4}	14.2
8.0	3.58×10^{-3}	3.2
9.0	2.03×10^{-2}	0.6
10.0	1.40×10^{-1}	0.08

4. Concluding remarks

The six 2-nitrophenylbenzimidazole compounds studied in protic media by DPP, TP and CV, present two irreversible cathodic responses in a wide range of pH; a main signal was found to be due to a nitro group reduction and a second one, probably to due to the reduction of azomethine. In DPP and TP experiments, the peak potential of the main signal exhibited, for each of the tested compounds, a linear dependence with the pH, showing breaks that are in agreement with the pK_a values of each one. The differences in the reduction potentials seen amongst the derivatives were explained by both the loss of coplanarity of the nitro group from the plane to the phenyl ring and the staking between the phenyl ring of the 2-nitrophenylbenzimidazole nucleus and the N-benzoyl substituent. On the other hand, in CV experiments in non-aqueous medium was possible to distinguish the typical reversible monoelectronic couple corresponding to the nitro radical generation, and peak potential reduction values were in agreement with those previously described for other nitroaromatic compounds with recognized biological activity.

Finally, on the basis of the electrochemical response of the six new 2-nitrobenzimidazole derivatives, DPP methods were developed, exhibiting adequate accuracy, reproducibility and selectivity. These methods could be applied for the determination of these compounds in pharmaceutical forms and in further stability studies. Application of the here developed DPP methods requires no treatment of the samples, is less time-consuming and less expensive than other ones, such as HPLC or UV–vis spectrophotometry [10].

Acknowledgement

Authors are grateful for the support of FONDECYT Grant No. 1061144.

References

[1] J.D. Maya, B.K. Cassels, P. Iturriaga-Vásquez, J. Ferreira, M. Faúndez, N. Galanti, A. Ferreira, A. Morello, Comp. Biochem. Phys. A 146 (2007) 601.
[2] S.L. Croft, M.P. Barrett, J.A. Urbina, Trends Parasitol. 21 (2005) 508.
[3] Z.H. Zhang, L. Yin, Y.M. Wang, Catal. Commun. 8 (2007) 1126.
[4] J. Valdez, R. Cedillo, A. Hernández-Campos, L. Yépez, F. Hernández-Luis, G. Navarrete-Vázquez, A. Tapia, R. Cortes, M. Hernández, R. Castillo, Bioorg. Med. Chem. Lett. 12 (2002) 2221.
[5] J.H. Tocher, R.C. Knight, D.I. Edwards, Free Radic. Res. Commun. 5 (1989) 319.
[6] J.H. Tocher, Gen. Pharmacol. 28 (1997) 485.
[7] P. Kovacic, J.R. Ames, M.D. Ryan, J. Electroanal. Chem. 275 (1989) 269.
[8] J.E. Biaglow, M.E. Varnes, L. Roizen-Towle, E.P. Clark, E.R. Epp, M.B. Astor, E.J. Hall, Biochem. Pharmacol. 35 (1986) 77.
[9] B.D. Palmer, W.R. Wilson, S. Cliffe, W.A. Denny, J. Med. Chem. 35 (1992) 3214.
[10] S. Brain-Isasi, C. Quezada, H. Pessoa, A. Morello, M.J. Kogan, A. Álvarez-Lueje, Bioorg. Med. Chem. 16 (2008) 7622.
[11] J.A. Valderrama, H. Pessoa-Mahana, G. Sarrás, R. Tapia, Heterocycles 51 (1999) 2193.
[12] H. Pessoa-Mahana, C.D. Pessoa-Mahana, R. Salazar, J.A. Valderrama, E. Saez, R. Araya-Maturana, Synthesis 3 (2004) 436.
[13] H.T.S. Britton, Hydrogen Ions, 4th Ed., Chapman & Hall, London, 1952, p. 113.
[14] S. Izquierdo, M.J. Kogan, T. Parella, A.G. Moglioni, V. Branchadell, E. Giralt, R.M. Ortuño, J. Org. Chem. 69 (2004) 5093.
[15] O.A. Quattrochi, S.A. De Andrizzi, R.F. Laba, Introducción a la HPLC, Aplicación y Práctica, Artes Gráficas Farro SA, Argentina, 1992.
[16] K. Akimoto, H. Kurosaka, I. Nakagawa, K. Sugimoto, Chem. Pharm. Bull. 36 (1988) 1483.

[17] H. Lund, in: H. Lund, O. Hammerich (Eds.), Organic Electrochemistry, 4th Ed., Marcel Dekker, New York, 2001, p. 390.
[18] E. Hammam, A. Tawfik, M.M. Ghoneim, J. Pharm. Biomed. Anal. 36 (2004) 149.
[19] S.F. De Betona, J.M. Moreda, A. Arranz, J.F. Arranz, Anal. Chim. Acta 329 (1996) 25.
[20] M.M. Ghoneim, M.M. Mabrouk, A.M. Hassanein, A. Tawfik, J. Pharm. Biomed. Anal. 25 (2001) 933.
[21] A.J. Bard, L.R. Faulkner, Electrochemical Methods: Fundamentals and Applications, 2nd Ed., John Wiley & Sons, Inc., New York, 2001.
[22] L.J. Núñez-Vergara, P. Santander, P.A. Navarrete-Encina, J.A. Squella, J. Electroanal. Chem. 580 (2005) 135.
[23] A. Agostiano, P. Cosma, M. Trotta, L. Mons-Scolaro, N. Micali, J. Phys. Chem. B 106 (2002) 12820.
[24] P. Kissinger, W. Heineman, Laboratory Techniques in Electroanalytical Chemistry, 10th Ed., Marcel Dekker, New York, NY, 1984.
[25] A. Álvarez-Lueje, H. Pessoa, L.J. Núñez-Vergara, J.A. Squella, Bioelectrochem. Bioener. 46 (1998) 21.
[26] P. Kovacic, M.A. Kassel, B.A. Feinberg, M.D. Corbett, R.A. McClelland, Bioorg. Chem. 18 (1990) 265.
[27] P. Wardman, Environ. Health Persp. 64 (1985) 309.
[28] C. Viodé, N. Bettache, N. Cenas, R.L. Krauth-Siegel, G. Chauvière, N. Bakalara, J. Périé, Biochem. Pharmacol. 57 (1999) 549.
[29] J. Argüello Da Silva, L.J. Núñez Vergara, S. Bollo, J.A. Squella, J. Electroanal. Chem. 591 (2006) 99.
[30] F.C. de Abreu, P.A.L. Ferraz, M.O.F. Goulart, J. Braz. Chem. Soc. 13 (2002) 19.
[31] F. Santos de Paula, E.M. Sales, M. Vallaro, R. Fruttero, M.O.F. Goulart, J. Electroanal. Chem. 579 (2005) 33.
[32] S. Bollo, L.J. Núñez-Vergara, M. Bonta, G. Chauviere, J. Perie, J.A. Squella, J. Electroanal. Chem. 511 (2001) 46.
[33] J. Ermer, J.H.McB. Miller (Eds.), Method Validation in Pharmaceutical Analysis. A Guide to Best Practice, Wiley-VCH Verlag GmbH & Co., KGaA, Weinheim, 2005.
[34] K.A. Connors, C.L. Amidon, V.J. Stella, Chemical Stability of Pharmaceuticals: A Handbook for Pharmacist, J. Willey, New York, 1986.
[35] S. Yoshioka, V.J. Stella, Stability of Drugs and Dosage Forms, Kluwer Academic Publishers, New York, 2002.

Talanta 79 (2009) 621–626

Contents lists available at ScienceDirect

Talanta

journal homepage: www.elsevier.com/locate/talanta

Liquid-waveguide spectrophotometric measurement of low silicate in natural waters

Natchanon Amornthammarong[a,b], Jia-Zhong Zhang[a,*]

[a] Ocean Chemistry Division, Atlantic Oceanographic & Meteorological Laboratory, National Oceanic & Atmospheric Administration (NOAA), 4301 Rickenbacker Causeway, Miami, FL, 33149, USA

[b] Cooperative Institute for Marine and Atmospheric Studies (CIMAS), Rosenstiel School of Marine and Atmospheric Science, University of Miami, 4600 Rickenbacker Causeway, Miami, FL, 33149, USA

ARTICLE INFO

Article history:
Received 29 January 2009
Received in revised form 17 April 2009
Accepted 20 April 2009
Available online 3 May 2009

Keywords:
Silicate
Silicic acid
Seawater
Silicomolybdenum blue
Molybdate

ABSTRACT

This paper describes a robust, sensitive method for measurement of low silicate in natural water. The method is based on the reaction of silicate with ammonium molybdate to form a yellow silicomolybdate complex, which is then reduced to silicomolybdenum blue by ascorbic acid. This method shows no refractive index effect and a small salinity effect that can be corrected for seawater samples. It was found that the use of poly-vinyl alcohol can prevent the precipitation formation in the ammonium molybdate solution and improve the stability of the silicomolybdenum blue complex. The sensitivity of this method is substantially enhanced by using a liquid-waveguide capillary cell. The detection limit is 0.1 μM, and working range is 0.1–10 μM for using 2-m liquid-waveguide capillary cell (LWCC). The method can be used for both freshwater and seawater samples and has been used to study the distribution of silicate in surface seawater of Gulf Stream in Florida straight.

Published by Elsevier B.V.

1. Introduction

Silicon is an essential nutrient required for the growth of some aquatic organisms in both freshwater and marine environment. Such aquatic organisms, most notably diatoms and radiolaria, use silicon as building blocks for their skeletons. In oceanic subtropical gyres, it has been observed that the silicate concentration in surface seawaters is seasonally or chronically depleted to 0.1–0.6 μM, particularly after spring blooms [1,2]. The low concentration of silicate in ocean surface waters can limit the productivity of diatoms, which can affect the carbon export in these waters [3–6]. To study the nutrient dynamics, including silicon, in these waters, development of a sensitive spectrophotometric method that can perform on-site measurements of low silicate in surface seawaters is urgently needed.

Quantitative analysis of silicate in seawater is mostly based on its reaction with molybdate in acidic media to form a yellow complex, β-silicomolybdate. The yellow complex is then reduced by a reductant to silicomolybdenum blue. The reaction allows determination of silicic acid concentration in natural waters; however, the sensitivity is inadequate for the determination of low silicon concentrations (below 3 μM) [7]. Lower detection limit can be obtained by prolonged reaction time but this approach is not practical [8]. The method detection limit was improved 10 times by a preconcentration method [9] with a magnesium induced co-precipitation (MAGIC) method. Alternatively, the sensitivity of this reaction was increased 30 times by a solvent extraction method [10], which is based on the formation of silicomolybdic acid by reaction of silicic and molybdic acids at low pH, extraction of the silicomolybdic acid into *n*-butanol and reduction with *p*-methylaminophenol sulfate and sulfite mixture. Although improving the sensitivity of the detection, the preconcentration and the solvent extraction method were cumbersome for applying to field operation. Recently, an electrochemical method for silicate determination in seawater has been proposed [11] in order to develop a reagentless sensor, which is suitable for long-term *in situ* deployments. However, the detection limit of 1 μM for this electrochemical method is still not suitable for low silicate seawater. Furthermore, several methods have been developed to measure nanomolar silicate in ultrapurified water [12–15]. Alternate methods based on the electrochemical determination of the silicomolybdic complex in freshwater have also been proposed [16–19].

According to the Lambert–Beer's law, the magnitude of absorbance signals is proportional to the optical pathlength, the molar absorptivity of chromophore, and the concentration of the analyte. Because the molar absorptivities of the chromophoric organic compounds used in the colorimetric analysis fall in a small range ($\sim 10^3$ to 5×10^4 L mol^{-1} cm^{-1}), increasing the optical pathlength of the detection cells has been considered as the most feasible approach to increase method sensitivity. In early long

* Corresponding author. Tel.: +1 305 361 4512; fax: +1 305 361 4447.
E-mail address: jia-zhong.zhang@noaa.gov (J.-Z. Zhang).

0039-9140/$ – see front matter. Published by Elsevier B.V.
doi:10.1016/j.talanta.2009.04.050

capillary cell construction, metal coatings were used to refract light which resulted in severe light loss and non-linearity response and limit their applications to gaseous sample measurements [20,21]. In 1990s amorphous fluoropolymers (Teflon AF family) manufactured by Dupont provided material with refractive index (1.29–1.31) lower than that of water. Total internal reflection of light can be achieved with a liquid-waveguide capillary flow cell constructed with Teflon AF [22,23]. The liquid-core waveguides cells have been used in UV–vis spectrophotometry, fluorescence and Raman spectroscopy [24–26]. The porous structure of amorphous fluoropolymers also provides high gas permeability for constructing gas sensors [27–33]. However, its porous structure is prone to trap air bubbles and adsorb surface-reactive species from aqueous samples losing its waveguide performance [34]. Improved design of capillary cell with cladding Teflon AF on the outer surface of capillary quartz tubing has been found to reduce the chance of contamination and bubble trapping. The application of such liquid-waveguide capillary flow cells has enhanced the sensitivity of spectrophotometric analysis of various species, including nitrite [34,35], molybdate and chromate [36], iron [37], phosphate [38,39], ammonium [40], nitrate [41–43], as well as colored dissolved organic matter in waters [44,45].

In this study, we describe sensitive spectrophotometric measurement of silicate in seawater using a liquid-waveguide long-path capillary cell. By using a syringe pump and an injection valve, we achieved a robust fluidic system that required little maintenance. The performance of liquid-waveguide capillary cells was studied in comparison with a typical short flow cell (1-cm path length). We also tested the effect of poly-vinyl alcohol (PVA) on the stability of the silicomolybdenum blue reaction. In addition, the salinity effect was investigated for seawater application. The method has been used to examine the distribution of low silicate in surface seawater of Gulf Stream in Florida straight.

2. Experimental

2.1. Reagents

2.1.1. Reagent 1 (R1)

Ammonium molybdate solution (10 g/L) was made by dissolving 5 g of ammonium molybdate (VI) tetrahydrate (12054-85-2, ACROS) in approximately 400 mL of 0.05 M sulfuric acid solution and then adding 0.005 g PVA (poly-vinyl alcohol, P-8136, Sigma) and finally making up to 500 mL with 0.05 M sulfuric acid solution. The solution was stored in an amber plastic bottle. This solution needs to be re-prepared every two days.

2.1.2. Reagent 2 (R2)

Oxalic acid solution (50 g/L) was made by dissolving 50 g of oxalic acid dehydrate (6153-56-6, J.T. Baker) in deionized water (DIW) and diluting to 1 L with deionized water. The solution was stored in an amber plastic bottle. This solution can be used for one month.

2.1.3. Reagent 3 (R3)

Ascorbic acid solution was made by dissolving 8.8 g of ascorbic acid (50-81-7, Sigma–Aldrich) in 400 mL of deionized water and 25 mL of acetone, then making up to 500 mL with deionized water. The solution is stored in an amber plastic bottle and kept in refrigerator at 4 °C. The fresh solution should be replaced at the same time as Reagent 1.

2.1.4. Reagent 4 (R4)

10% HCl (v/v) was made by transferring 100 mL concentrated HCl to 800 mL deionized water and then making up to 1000 mL by deionized water.

2.1.5. Stock silicate solution (100 mg Si/L)

This was made by quantitatively transferring 0.6696 g of sodium hexafluorosilicate (Na_2SiF_6) to 800 mL deionized water in a plastic beaker. The solution was stirred using a Teflon-coated stirring bar on a magnetic stir plate for 24 h. The final solution was diluted to 1000 mL in a plastic volumetric flask with deionized water. The stock solution was stored in a plastic bottle.

2.1.6. Low nutrient sea water (LNSW)

It was obtained from surface seawater in the Gulf Stream or Sargasso Sea (salinity 36, silicate < 0.03 mg Si/L) and filtered through 0.45 μm pore size non-glass membrane filters.

2.2. Analytical system

The fluidic system is shown in Fig. 1. It consists of one syringe pump (P/N 54022, Kloehn, Las Vegas, NV) equipped with an eight-way distribution valve SV (P/N 17620) and one injection valve (6-port medium pressure, Upchurch Scientific, WA). The syringe pump SP is equipped with a 5-mL capacity zero dead volume syringe (P/N 24691). The injection valve IV is equipped with a Teflon injection coil IC (0.78 mL, 1 mm i.d., 100 cm). Table 1 summarizes one analytical cycle. Initially, IV is set to position 'Load' and SV equipped at the head of the syringe pump is set to port B. Then, SP aspirates 2 mL sample solution to fill the injection coil. After that, in step 2, SP pushes the excess solution out to port G, which is equipped with a mixing coil MC (6.3 mL, 1 mm i.d., 8 m). Steps 3–6 are used to clean the syringe and MC with 10% HCl and DIW. In step 7, IV is set to 'Inject' and SV is set to port C. Then, SP aspirates both R1 and sample solution (in IC) together into the 5-mL syringe chamber. In Steps 8 and 9, SP aspirates 0.78 mL of R2 and R3 to mix with R1 and sample in the syringe chamber. In Step 10–12, SP alternately dispenses and withdraws 3.12 mL of solution into the open-ended coil MC for 20 times to mix all reagents with sample completely. If a higher sensitivity is needed, these mixing cycles can be set more than 20 times to increase the reaction time for a higher absorbance. The step 13 is to dispense entire mixed solution to LWCC (liquid-waveguide capillary cell) for absorbance measurement by the detector. Steps 14 and 15 are used to clean LWCC with DIW. All steps have been fully controlled by in-house software developed with LabVIEW (National Instruments, Texas).

The absorption spectra of silicomolybdenum blue complex show two peaks at 660 and 820 nm with a greatest absorbance at 820 nm.

Table 1
One-cycle operation of silicate determination.

Step	IV	SV	Syringe pump
1	Load	B	Aspirate 2 mL at 9.4 mL/min (fill injection valve by sample).
2	Load	G	Dispense 2 mL at 31.2 mL/min.
3	Load	E	Aspirate 3 mL at 12.5 mL/min.
4	Load	G	Dispense 3 mL at 31.2 mL/min (clean MC by 10%HCl).
5	Load	A	Aspirate 5 mL at 12.5 mL/min.
6	Load	G	Dispense 5 mL at 31.2 mL/min (clean MC by DIW).
7	Inject	C	Aspirate 1.56 mL at 3.1 mL/min.
8	Inject	D	Aspirate 0.78 mL at 3.1 mL/min.
9	Inject	F	Aspirate 0.78 mL at 3.1 mL/min.
10	Inject	G	Dispense 3.12 mL at 31.2 mL/min.
11	Inject	G	Aspirate 3.12 mL at 7.5 mL/min.
12	Inject	G	Repeat steps 10 and 11, 20 times (mix contents together in MC).
13	Inject	H	Dispense 3.12 mL at 2.8 mL/min (pump contents to LWCC)
14	Inject	A	Aspirate 5 mL at 31.2 mL/min
15	Inject	H	Dispense 5 mL at 6.2 mL/min (clean flow cell by DIW)

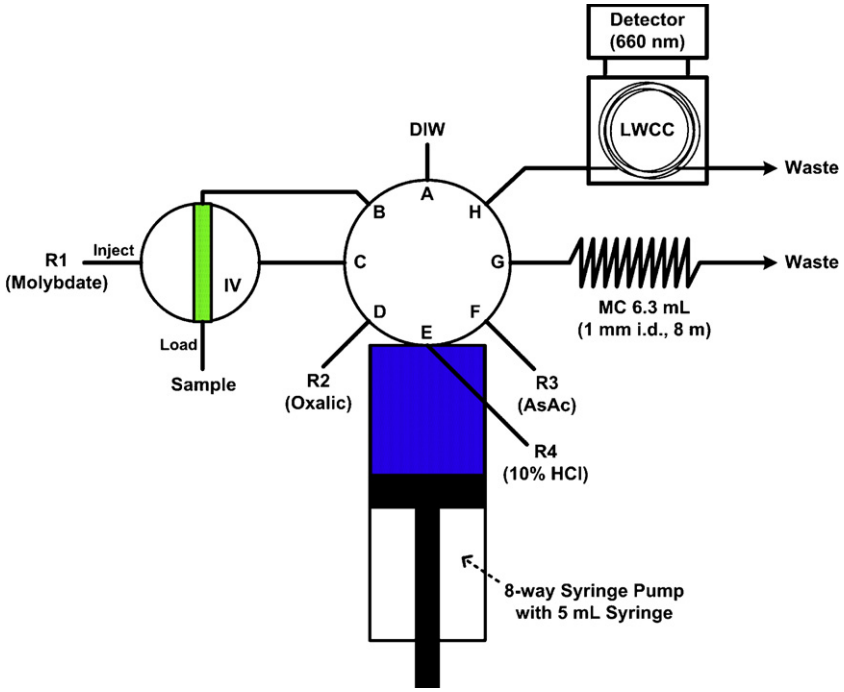

Fig. 1. Liquid-waveguide analyzer for silicate determination: LWCC, liquid-waveguide capillary cell; MC, mixing coil; AsAc, ascorbic acid; IV, injection valve; DIW, deionized water; R1, molybdate solution; R2, oxalic acid solution; R3, ascorbic acid solution; R4, 10%HCl (v/v).

However, the working wavelength of the detector is from 190 to 800 nm. In this method, the spectrophotometer was set at a wavelength of 660 nm. The sensitivity at wavelength 660 nm is satisfactory for this work and the measured absorbance at this wavelength is dominated by the reduced α-silicomolybdic acid (stable form) and is less influenced by the unstable β-silicomolybdic acid [46].

3. Results and discussion

3.1. Comparison of performance of different flow cells

Three flow cells (1 cm, 2-m LWCC, and 4-m LWCC) were compared in terms of sensitivity, linearity, noise and detection limit. The liquid-waveguide capillary cells (World Precision Instruments, Sarasota, FL) are optical sample cells that increase optical pathlength with small sample volumes. They were in-house modified to be connected via optical fibers to a spectrophotometer (UV1000, Thermo Separation Products) [47]. As shown in Table 2, the 2-m LWCC enhanced the sensitivity by two orders of magnitude as compared to 1-cm cell. The 4-m cell further enhanced the sensitivity of method. The detection limit increased from 30 to 0.1 μM when cell length increased from 1 to 200 cm. The 4-m LWCC provided almost two times higher sensitivity than 2-m LWCC with a lower detection limit (0.07 μM). This is in agreement with previous observation of enhancement of sensitivity with increasing the length of the capillary flow cells in flow injection analysis of nitrite [34]. In application to natural waters, the 2-m liquid-waveguide capillary cell provides a sufficient sensitivity within a useful working range of 0.1–10 μM with a much lower back pressure.

3.2. Reagent composition and long-term reproducibility

The effect of molybdate, oxalic acid, and ascorbic acid was studied by analysis of silicate samples in freshwater. Fig. 2 shows the effect of molybdate concentration. In the absence of PVA, the response signals increase with increasing concentration of molybdate. At a concentration higher than 40 g/L, the standard deviation of signals is unacceptable because the solution is rapidly precipitated. The concentration at 10 g/L was chosen because of no visible precipitation within one day. The system with no PVA added can operate properly less than 20 h with %RSD = 2.8 (n = 52). However, the molybdate solution starts to precipitate after two days. In the standard method of EPA (U.S. Environmental Protection Agency, method 366.0), a couple drop of surfactant (Dowfax 2A1, Dow Chemical Company) is added to the molybdate solution for lubricating the gas segmented continuous flow system. Although Dowfax can smooth the flow system, it causes high reagent blank (about 0.3 absorbance unit) and does not prevent the precipitation. Therefore, poly-vinyl alcohol (PVA) was tested to replace Dowfax. Fig. 3 shows the long-term reproducibility of the system with different PVA concentrations. Apparently, addition of 1 mg PVA in 100 mL molybdate solution can stabilize the reagent baseline (with %RSD = 2.0, n = 125) for 50 h. However, adding excessive PVA (5 mg/100 mL) can cause higher baseline noise (%RSD = 5.6 from 0 to 46 h, n = 114) in the system.

In the previous study, silicate was found to cause interference in phosphate determination by molybdate reduction method [49]. Addition of oxalic acid is needed to avoid reduction of the excess molybdate and to suppress the interference of phosphate present in the sample. As shown in Fig. 4, the response signals are constant

Table 2
Performance comparison of 1-cm flow cell, 2-m LWCC, and 4-m LWCC.

Flow-cell length	Calibration curve	Linear regression (r^2)	Noise (Abs)	SD (Abs)	DL (3× noise) (μM)	DL (3× SD) (μM)
1 cm	$y = (0.0004 \pm 0.0000)x + (0.0153 \pm 0.0103)$	0.9933	0.005	0.004	33.5	26.1
2 m	$y = (0.1298 \pm 0.0037)x + (0.0075 \pm 0.0223)$	0.9968	0.005	0.004	0.12	0.09
4 m	$y = (0.2165 \pm 0.0045)x + (0.0878 \pm 0.0137)$	0.9983	0.005	0.005	0.07	0.07

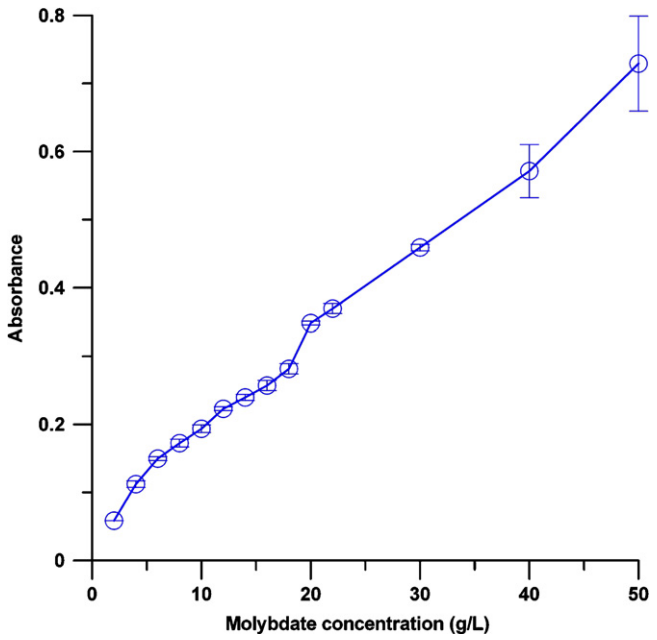

Fig. 2. Effect of ammonium molybdate concentration on absorption intensity. The reagents used are oxalic acid 50 g/L, ascorbic acid 4.4 g/250 mL.

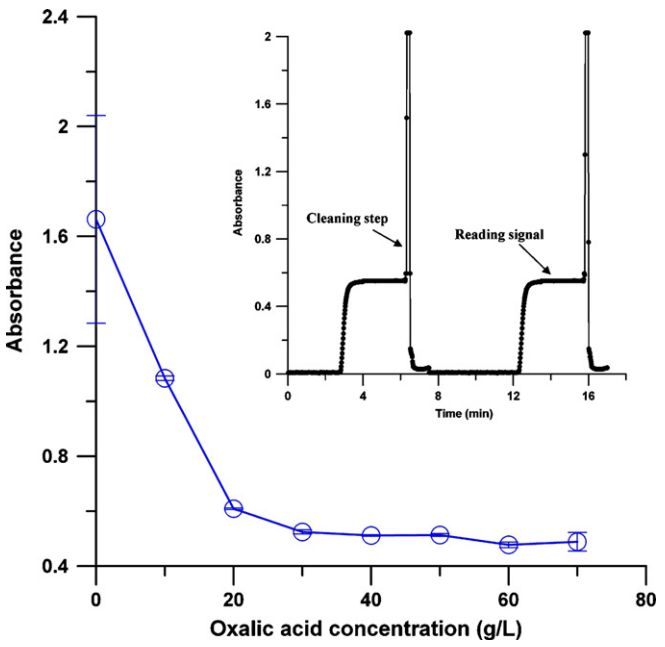

Fig. 4. Effect of oxalic acid concentration on absorption intensity. The reagents used are ammonium molybdate 10 g/L, ascorbic acid 4.4 g/250 mL. The inset shows typical system outputs of 4 μM silicate sample.

at >40 g/L of oxalic acid concentration. The concentration 50 g/L of oxalic acid was chosen for this method. Under the optimal reagent recipe, the potential interference of phosphate was evaluated with a sample of 5 μM of phosphate, a concentration much higher than those typically observed in natural waters. We found that the interference from 5 μM of phosphate under our reaction condition was negligible. The inset of Fig. 4 shows two typical system outputs of 4 μM silicate sample. Because the silicon complex is unstable in the presence of oxalic acid, the reductant (ascorbic acid) is added immediately after the oxalic acid to form the blue silicomolybdic complex. The effect of ascorbic acid concentration on the method sensitivity is shown in Fig. 5. We found that increasing the concentration of ascorbic acid increases the response signals; however, it also increases the noise level of the signals. The concentration at 4 g/250 mL of ascorbic acid provides a sufficient response signals with an acceptable standard deviation.

3.3. Salinity effect in seawater analysis

It has been reported that the response signals are affected by change in salinity of the sample solution due to the β- and α-isomer transformation [46,48]. The effect of salinity was tested by different

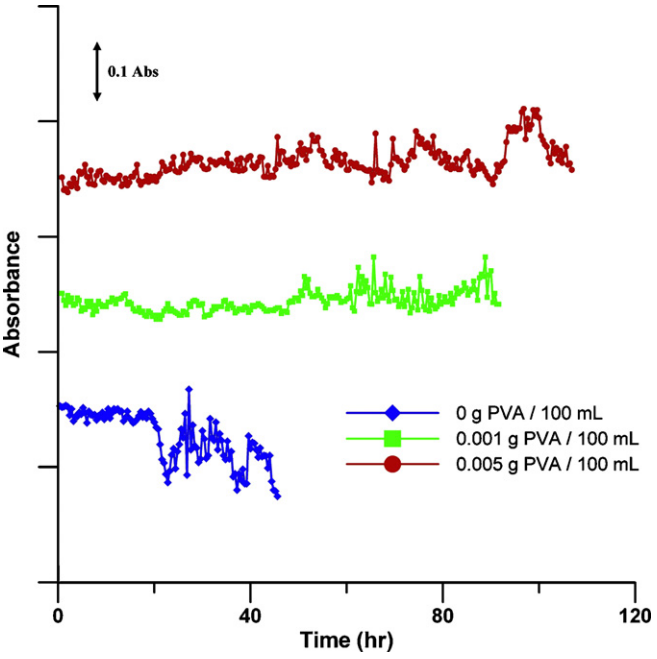

Fig. 3. Effect of poly-vinyl alcohol (PVA) on precision and stability of system. The reagents used are ammonium molybdate 10 g/L, oxalic acid 50 g/L, ascorbic acid 4.4 g/250 mL.

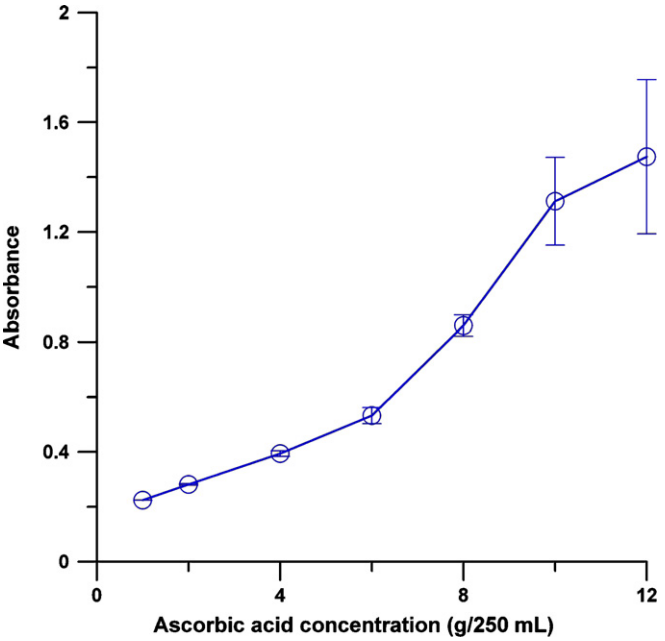

Fig. 5. Effect of ascorbic acid concentration on absorption intensity. The reagents used are ammonium molybdate 10 g/L, oxalic acid 50 g/L.

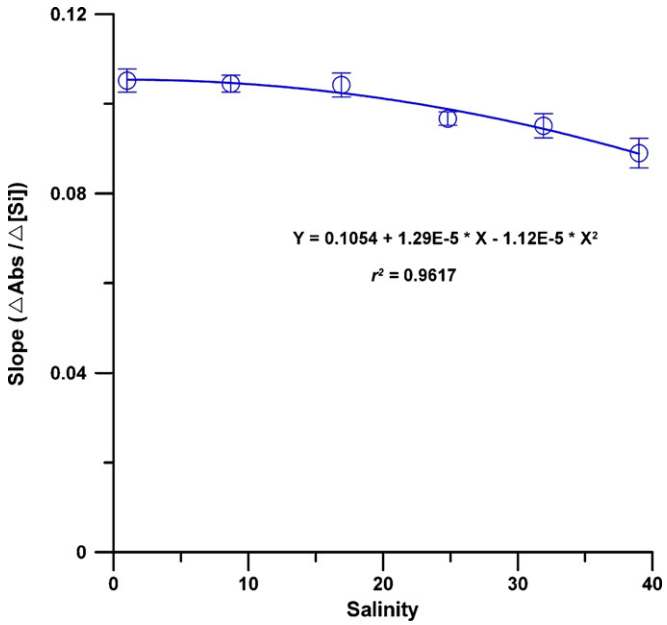

Fig. 6. Salinity effect of sample solution upon the sensitivity of system. The reagents used are ammonium molybdate 10 g/L, oxalic acid 50 g/L, ascorbic acid 4.4 g/250 mL, standard Si solution 0–8 μM.

salinity samples that were made by mixing of LNSW with DIW in different ratios. Samples of each salinity were tested by measuring five different concentrations (0–8 μM) of silicate to construct a calibration curve for a given salinity sample. The slopes of the calibration curve for different salinity samples are plotted versus salinity as shown in Fig. 6. The result obviously shows decreasing of sensitivity with increasing salinity of the sample solution. The slopes of the calibration curve cab be fitted as a function of salinity as follows:

$$S_X = S_{DIW} + (1.29 \times 10^{-5})X - (1.12 \times 10^{-5})X^2 \quad (1)$$

S_X, slope at salinity of X; S_{DIW}, slope value from a calibration curve made in DIW; X, salinity value of sample;

This Eq. (1) is necessary because the calibration standard solutions must be prepared in DIW and samples may vary in salinity. The LNSW cannot be used as a matrix to prepare standards because of unknown amount of silicate in LNSW.

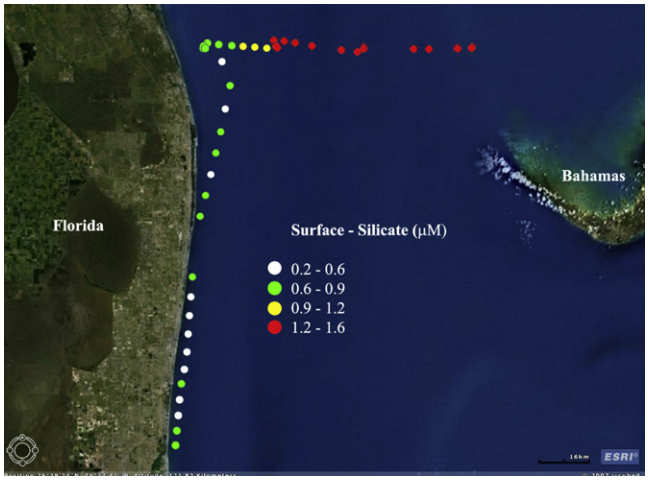

Fig. 7. Shipboard measurements of silicate concentrations in surface waters during a cruise from Miami, Florida to the Bahamas in July 2008.

3.4. Field application

The method was tested aboard the research vessel *F.G. Walton Smith* (RSMAS, University of Miami, Florida, USA) on a cruise from Miami, Florida to the Bahamas coast during July 2008. Surface waters were sampled for shipboard analysis. Fig. 7 shows the results of the silicate measurement from surface water samples. The results indicate that the silicate concentrations in the surface water range from 0.2 to 1.6 μM. The concentration of silicate seems lower in the Gulf Stream, which flows northward along the east coast of Florida peninsula, in comparison with the open ocean surface waters near Bahamas.

Acknowledgments

We would like to thank Ryan H. Smith (PhOD/AOML/NOAA) for his kind supports during the field operations. Financial support for this study was provided by NOAA's Coastal Ocean Program and Climate and Global Change Program. This research was carried out, in part, under the auspices of the Cooperative Institute for Marine and Atmospheric Studies (CIMAS), a joint institute of the University of Miami and the National Oceanic and Atmospheric Administration, cooperative agreement #NA67RJ0149. The statements, findings, conclusions, and recommendations are those of the authors and do not necessarily reflect the views of NOAA or the U.S. Department of Commerce.

References

[1] M.A. Brzezinski, D.M. Nelson, Deep-Sea Res. I 42 (1995) 1215–1237.
[2] J.-C. Marty, J. Chiaverini, M.-D. Pizay, B. Avril, Deep-Sea Res. II 49 (2002) 1965–1985.
[3] M.A. Brzezinski, M.-L. Dickson, D.M. Nelson, R. Sambrotto, Deep-Sea Res. II 50 (2003) 619–633.
[4] D.M. Nelson, R.F. Anderson, R.T. Barber, M.A. Brzezinski, K.O. Buesseler, Z. Chase, R.W. Collier, M.-L. Dickson, R. Francois, M.R. Hiscock, S. Honjo, J. Marra, W.R. Martin, R.N. Sambrotto, F.L. Sayles, D.E. Sigmon, Deep-Sea Res. II 49 (2002) 1645–1674.
[5] D.E. Sigmon, D.M. Nelson, M.A. Brzezinski, Deep-Sea Res. II 49 (2002) 1747–1763.
[6] C.L. De La Rocha, M.A. Brzezinski, M.J. DeNiro, Geochim. Cosmochim. Acta 64 (2000) 2467–2477.
[7] J.B. Mullin, J.P. Riley, Anal. Chim. Acta 12 (1955) 162–176.
[8] J. Thomsen, K.S. Johnson, R.L. Petty, Anal. Chem. 55 (1983) 2378–2382.
[9] P. Rimmelin-Maury, T. Moutin, B. Queguiner, Anal. Chim. Acta 587 (2007) 281–286.
[10] M.A. Brzezinski, D.M. Nelson, Mar. Chem. 19 (1986) 139–151.
[11] M. Lacombe, V. Garcon, M. Comtat, L. Oriol, J. Sudre, D. Thouron, N.L. Bris, C. Provost, Mar. Chem. 106 (2007) 489–497.
[12] J. Isoe, K. Morita, E. Kaneko, Analyst 130 (2005) 872–877.
[13] A. Sabarudin, M. Oshima, N. Ishii, S. Motomizu, Talanta 60 (2003) 1277–1285.
[14] A. Sabarudin, M. Oshima, S. Motomizu, Anal. Chim. Acta 532 (2005) 27–35.
[15] M. Yaqoob, A. Nabi, P.J. Worsfold, Anal. Chim. Acta 519 (2004) 137–142.
[16] N.G. Carpenter, A.W.E. Hodgson, D. Pletcher, Electroanalysis 9 (1997) 1311–1317.
[17] A.W.E. Hodgson, D. Pletcher, Electroanalysis 10 (1998) 321–325.
[18] W. Er-Kang, W. Meng-Xia, Anal. Chim. Acta 144 (1982) 147–153.
[19] A.G. Fogg, N.K. Bsebsu, Talanta 28 (1983) 473–476.
[20] W. Lei, K. Fujiwara, K. Fuwa, Anal. Chem. 55 (1983) 951–955.
[21] F.I. Ormaza-Gonzalez, P.J. Statham, Anal. Chim. Acta 244 (1991) 63–70.
[22] T. Dallas, P.K. Dasgupta, Trends Anal. Chem. 23 (2004) 385–392.
[23] L.J. Gimbert, P.J. Worsfold, Trends Anal. Chem. 26 (2007) 914–930.
[24] Q.Y. Li, K.J. Morris, P.K. Dasgupta, I.M. Raimundo, H. Temkin, Anal. Chim. Acta 479 (2003) 151–165.
[25] L. Song, S.Y. Liu, V. Zhelyaskov, M.A. El-Sayed, Appl. Spectrosc. 52 (1998) 1364–1367.
[26] K. Fujiwara, T. Kagoshima, T. Uchida, T. Miyakawa, Spectrosc. Lett. 36 (2003) 551–560.
[27] J. Li, P.K. Dasgupta, Anal. Chem. 72 (2000) 5338–5347.
[28] J. Li, P.K. Dasgupta, Anal. Chim. Acta 442 (2001) 63–70.
[29] P.K. Dasgupta, Z. Genfa, S.K. Poruthoor, S. Caldwell, S. Dong, Anal. Chem. 70 (1998) 4661–4669.
[30] P.K. Dasgupta, Z. Genfa, J. Li, B. Boring, S. Jambunathan, R. Al-Horr, Anal. Chem. 71 (1999) 1400–1407.
[31] H. Larsson, P.K. Dasgupta, Anal. Chim. Acta 485 (2003) 155–167.
[32] Z.A. Wang, Y. Wang, W.-J. Cai, S.-Y. Liu, Talanta 57 (2002) 69–80.
[33] Z.A. Wang, W.-J. Cai, Y.C. Wang, B.L. Upchurch, Mar. Chem. 84 (2003) 73–84.
[34] J.-Z. Zhang, Anal. Sci. 22 (2006) 57–60.

[35] W. Yao, R.H. Byrne, R.D. Waterbury, Environ. Sci. Technol. 32 (1998) 2646–2649.
[36] W. Yao, R.H. Byrne, Talanta 48 (1999) 277–282.
[37] J.-Z. Zhang, C. Kelble, F.J. Millero, Anal. Chim. Acta 438 (2001) 49–57.
[38] J.-Z. Zhang, J. Chi, Environ. Sci. Technol. 36 (2002) 1048–1053.
[39] L.D. Guo, J.-Z. Zhang, C. Gueguen, Global Biogeochem. Cycles 18 (2004) GB1038, doi:10.1029/2003GB002152.
[40] Q.P. Li, J.-Z. Zhang, F.J. Millero, D.A. Hansell, Mar. Chem. 96 (2005) 73–85.
[41] J.-Z. Zhang, R. Wanninkhof, K. Lee, Geophys. Res. Lett. 28 (2001) 1579–1582.
[42] Q.P. Li, D.A. Hansell, J.-Z. Zhang, Limnol. Oceanogr.: Methods 6 (2008) 319–326.
[43] M.D. Patey, M.J.A. Rijkenberg, P.J. Statham, M.C. Stinchcombe, E.P. Achterberg, M. Mowlew, Trends Anal. Chem. 27 (2008) 169–182.
[44] R.L. Miller, M. Belz, C.D. Castillo, R. Trzaska, Cont. Shelf Res. 22 (2002)1301–1310.
[45] E.J. D'sa, R.G. Sterward, A. Vodacek, N.V. Blough, D. Phinney, Limnol. Oceanogr. 44 (1999) 1142–1148.
[46] K. Grasshoff, Deep-Sea Res. 11 (1964) 597–604.
[47] J.-Z. Zhang, Deep-Sea Res. I 47 (2000) 1157–1171.
[48] K.A. Fanning, M.E.Q. Pilson, Anal. Chem. 45 (1973) 136–140.
[49] X.L. Huang, J.-Z. Zhang, Microchem. J. 89 (2008) 58–71.

Talanta 79 (2009) 963–966

Contents lists available at ScienceDirect

Talanta

journal homepage: www.elsevier.com/locate/talanta

Short communication

Millisecond analysis of double stranded DNA with fluorescent intercalator by micro-thermocontrol-device

Hideyuki F. Arata[a,b,*], Frederic Gillot[a,c,1], Dominique Collard[a,c], Hiroyuki Fujita[a]

[a] Institute of Industrial Science (IIS), The University of Tokyo, 4-6-1 Komaba, Meguro-ku, Tokyo 153-8505, Japan
[b] Japan Society for the Promotion of Science (JSPS), Japan
[c] LIMMS-CNRS/IIS, France, Japan

ARTICLE INFO

Article history:
Received 18 February 2009
Received in revised form 15 April 2009
Accepted 16 April 2009
Available online 3 May 2009

Keywords:
Intercalator
DNA
Denaturation
Microheater
Millisecond

ABSTRACT

Study of interaction between DNA and intercalator at molecular level is important to understand the mechanisms of DNA replication and repair. A micro-fabricated local heating thermodevice was adapted to perform denaturation experiments of DNA with fluorescent intercalator on millisecond time scale. Response time of complete unzipping of double stranded DNA, 16 μm in length, was measured to be around 5 min by commercial thermocycler. Response time of quenching of double stranded DNA with fluorescent intercalator SYBR Green was measured to be 10 ms. Thus, quenching properties owing to strand unzipping and denaturation at base pair level were distinguished. This method has provided easy access to measure this parameter and may be a powerful methodology in analyzing biomolecules on millisecond time scale.

1. Introduction

Aromatic molecules of planer structure are known to intercalate between base pairs of double stranded DNA (hereinafter dsDNA) [1]. These intercalators inhibit DNA replication and repair, thus playing a substantial role in controlling cancer development and genotoxicity [2]. Therefore, study of intercalation mechanism and its application has attracted great interests in genetics and medical researches. SYBR Green (hereinafter SG) is an intercalator which is commonly used to monitor dsDNA [3]. It shows strong fluorescent intensity when intercalated between base pairs of a dsDNA whereas it shows almost negligible fluorescence when a dsDNA is denatured and structurally unzipped [4]. A dsDNA starts separating into single strands at a temperature higher than 90 °C without any external mechanical force [5]; this phenomenon is commonly used in the first stage of the polymerase chain reaction (PCR) cycle. Fluorescent intercalators can verify unzipping of dsDNA into two single strand DNAs (hereinafter ssDNAs). This process takes a few seconds to a few minutes, mainly depending on length of DNA. However, dynamic properties of the quenching process have not been precisely studied. The main reason is due to the difficulties in observing phenomena at molecular level, such as DNA and SG interaction or denaturation at base pair level, which may happen on an extremely short time scale. Thus, the terminology "denaturation" has been used both as "unzipping of double strands" and "denaturation at base pair level". To analyze quenching dynamics on millisecond time scale is inevitable for further genetic researches.

Microfabrication technology has realized miniaturized devices of several kinds, such as sensors [6,7], reactors [8,9], and actuators [10]. In addition, these devices have fast response and high sensitivity due to the merits of miniaturization. Application of microdevices to chemical or biological experiments has realized integrating multiple functional units onto a small chip, so-called micrototal analysis systems (μTAS) [11]. μTAS allows rapid chemical or biological analysis with small amounts of samples [12,13]. Therefore, applications aiming at manipulations and characterization of biomaterials by microsystem have become one of the major trends in this field [14]. Some procedures which require rapid temperature switching, for example on-chip PCR [15,16], have been improved by miniaturization. This is because miniaturization enables rapid temperature control simultaneously with real-time observation owing to the small amount of volume that must be heated [17–21]. Thermal control by micro-thermodevice has various advantages, such as compactness and simple operation, to that of laser heating system [22,23] which requires manual operation and adjustments from one run to another.

A square-shaped micro-thermodevice for biological applications with side length of 20 μm was manufactured (Fig. 1(a)) [24] (Precise fabrication process and evaluation of the device will be reported elsewhere). This device consisted of a microheater and

* Corresponding author. Current address: Curie Institute, 11 rue P. et M. Curie, Paris, France.
E-mail address: arata@sanken.osaka-u.ac.jp (H.F. Arata).
[1] Current address: Ecole Centrale de Lyon, France.

0039-9140/$ – see front matter © 2009 Elsevier B.V. All rights reserved.
doi:10.1016/j.talanta.2009.04.045

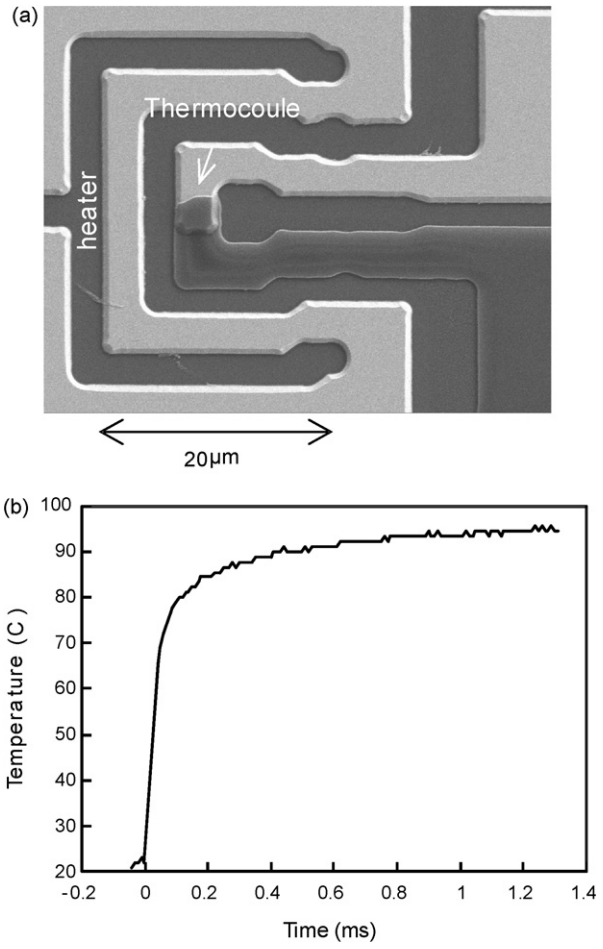

Fig. 1. Micro-thermocontrol-device of millisecond response time. (a) Scanning electron microscope image of the device. The micro heater was designed rectangle of 20 μm × 20 μm. The width of the heater is 2 μm. The thermosensor is a Pt–Cr thin film thermocouple (TFTC) with a hot junction area of 2 μm × 2 μm. (b) Step response of the micro-thermodevice. This device realized real-time temperature switching in about 1 ms under microscopic observation.

a micro-thermocouple integrated on a Si wafer covered with a 100 nm thick SiO_2 insulation layer. The platinum microheater was designed rectangle of 20 μm squared. The width of microheater was 2 μm. The thermosensor was a Pt–Cr thin film thermocouple (TFTC) with a hot junction area of 2 μm × 2 μm. The temperature calibration of the thermocouple can be carried out by either immersing the device into a hot water [18] or using 8CB liquid crystal that shows a distinctive phase change at 313 K [24]. This micro-thermodevice has realized real-time temperature switching under the microscope in 1 ms (Fig. 1(b)). Thermal characteristics and temperature distribution of a heater in the micrometer scale were investigated by numerical simulations previously [24,25]. We firstly used our micro-thermodevice of this design coupled with microcontainers to reveal the millisecond dynamics of fluorescent proteins denaturation [26].

In this report, this micro-thermodevice was used to measure the response time of fluorescent quenchings of dsDNAs/SG and free SG on millisecond time scale. Consequently, "unzipping of double strands" and "denaturation at base pair level" were clearly distinguished by measuring their response time. Thus, hereinafter, we use a term "denaturation" as denaturation at base pair level to distinguish from mechanical unzipping of dsDNA. Response time of unzipping was measured by commercial thermocycler on a time scale of minutes and denaturation was measured by micro-thermodevice on millisecond time scale.

2. Materials and methods

2.1. Double stranded DNA

λ-Phage DNA of 16 μm length (3010: TAKARA) was chosen for denaturation experiments. A relatively long dsDNA may take longer time for unzipping into ssDNAs compared to a shorter dsDNA because 2 strands require a certain time to be mechanically unzipped by thermal energy whereas melting of base pairs does not depend on the length of DNA. The melting temperature of this λDNA at which half of the base pairs break is 66 °C calculated from an established formula [27]. However, to unzip dsDNA completely and irreversibly, temperature higher than 90 °C is required [5].

2.2. Unzipping measurements on long time scale

To measure the response time for dsDNA to unzip completely and irreversibly, dsDNA/SG were exposed at high temperatures for various time spans. SYBR Green (SYBR Green 1 Nucleic Acid Gel Stain: Molecular Probes) diluted 10,000 times was mixed with a 4.6 pM solution of λDNA—a concentration low enough to prevent unzipped ssDNAs from reforming dsDNA—and sustained in TE buffer (Tris + EDTA, pH 7.4). The buffer containing dsDNA/SG was aliquot (5 μL in each tube) and was exposed at high temperatures on a thermocycler (Chill Heat CHT-102HT: Iwaki); 10 min at various temperatures and various time spans at 91 °C. Temperatures of the samples were measured by a commercial thermocouple immersed in the solution. Each tube was mounted on ice immediately after the heating to prevent from renaturation. The solution was poured onto a glass plate (36 mm × 24 mm: Matsunami) and a cover glass (18 mm × 18 mm: Matsunami) was mounted without any spacer; this created a flow cell of less than 5 μm in height to facilitate counting numbers of DNAs under the microscope. The sample was exposed by a mercury lamp through filters (WIG, ND6). Fluorescent quenching effect by the exposure was limited to 0.4% in 1 s which is negligible in our experiment. Images were captured by CCD camera (Cascade 2: Photometrix). Number of non-denatured dsDNA per microscopic view was counted manually in 12–16 buffer droplets in each condition.

2.3. Denaturation measurements on millisecond time scale

To observe quenching dynamics of dsDNA/SG, we mounted the micro-thermodevice on a fluorescent microscope (Olympus, BX51). dsDNAs dyed by SG were maintained in a TE buffer at the same condition as in the unzipping experiments. The solution was poured onto the micro-thermodevice and a cover glass (Matsunami 2 mm × 2 mm) was mounted onto the solution without any spacers. Images were captured by a high speed CCD camera (Cascade 2: Photometrix) with a frame rate of 10.5 ms per frame. The time courses of fluorescent intensities of each dsDNA were analyzed with commercial software (Metamorf). Analysis at single DNA molecule level allows us to measure the dynamics on short time scales. The response time of SG dye free in solution was measured by analyzing the intensity of fluorescent solution where no DNA exists.

To measure the delay of the optical systems (i.e. the microscope and the camera), we measured the step response by switching an LED on and off under the microscope with the same camera condition as in the experiment but with faster frame rate. The time response was measured to be less than 5 ms. We concluded that all the experimental data obtained at frame rate larger than this value were not affected by the delay of the optical setup.

3. Results and discussions

Fig. 2(a) shows the number of dsDNA per microscopic view after 10 min exposure at various temperatures. The number of

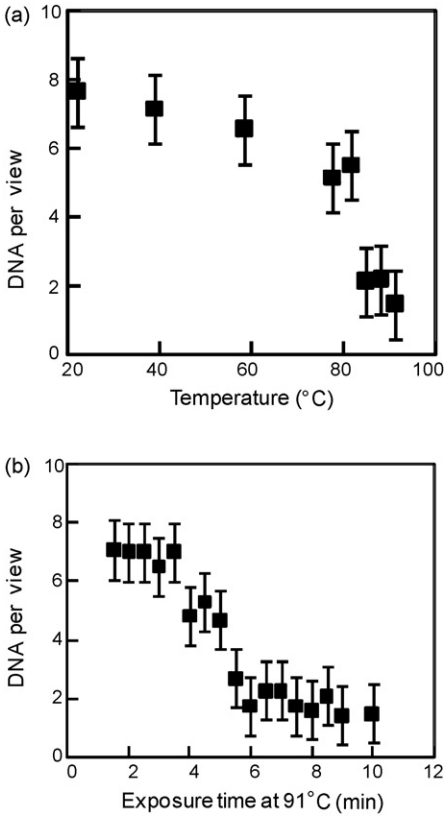

Fig. 2. Statistical measurement of complete and irreversible unzipping of 16 μm long λDNA at high temperatures. The vertical axis represents the average number of non-denatured DNA per microscopic view. (a) dsDNAs unzipped completely at temperatures higher than 90 °C. (b) The unzipping completed in around 4–6 min after exposing to the temperatures higher than 90 °C.

non-denatured DNA decreased at the temperature higher than 90 °C. This means that the critical temperature for complete unzipping is around 90 °C. Fig. 2(b) shows the number of dsDNA images per microscopic view after exposing at 91 °C for various exposure times. The number of non-denatured DNA decreased drastically after 4–6 min. This means that unzipping of 16 μm-long λDNA completes between 4 and 6 min at 91 °C.

Fig. 3 shows the time courses of fluorescent intensity of dsDNA/SG when the temperature was raised from room temperature to slightly under 100 °C in 1 ms at elapse time of 0 s. Inset shows the same data over a longer time span, which shows quenching owing to the UV illumination is negligible in this experiment. The fluorescent intensity of dsDNA/SG quenched within one camera frame, 10.5 ms, when the temperature switching was synchronized with the camera frame as in Fig. 3 but the quenching occurred during 2 frames when the equipments were not synchronized. This shows that the response time of this quenching was around 10 ms. 10.5 ms per frame is the fastest time resolution for DNA measurement with this camera because a faster frame rate degrades the image resolution which makes it impossible to recognize a single DNA molecule. The quenching cannot be attributed to unzipping of dsDNAs because it completes in 4–6 min. On the other hand, time response of SG free in solution was measured to be slightly larger than 20 ms which is obviously larger than that of DNA/SG (Fig. 4).

Dissociation of the intercalator from dsDNA, denaturation of dsDNA, and change of the intercalator structure in higher temperature can be attributed to the fluorescent quenching of DNA/SG. The difference in time response between DNA/SG and SG may suggest that data shown in Fig. 3 are the quenching owing to dissociation of intercalator from dsDNA or denaturation of dsDNA when the

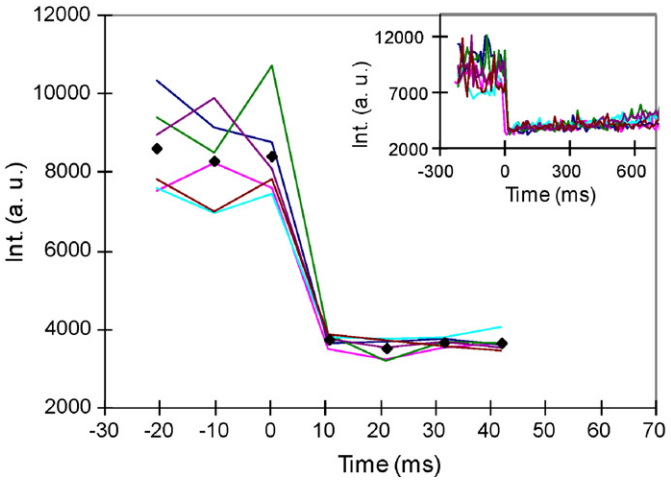

Fig. 3. Time courses of each single dsDNA/SG quenching by rapid exposure to high temperatures. The average intensities of 6 DNAs are plotted in diamond. The temperature was switched from room temperature to slightly under 100 °C at an elapse time of 0 ms. Inset shows the same data over a longer time span. Response time of this quenching was 10 ms.

response time of SG itself has no difference between the free-state and the DNA-conjugated state. Nevertheless, there is a possibility that the conformation of SG is alerted by heat shock when intercalated between base pairs of dsDNA. If this is the case, difference in response time is derived from a change of intercalator structure at the higher temperature. Certainly, quenching of DNA/SG shown in Fig. 3 happened during an interaction between DNA and SG. It is not due to unzipping of dsDNA nor quenching of SG alone. Because DNA/SG and SG alone have different quenching dynamics, the intensity may have a second order decay due to both time constants. However, since the fluorescent intensity of SG is much lower than that of DNA/SG, we did not recognize second order decay in our data. At this stage, we do not have sufficient evidence to prove which of those effects plays a major role in the quenching mechanism. Although further studies are required to understand this mechanism at SG molecule level, this micro-thermodevice has provided access to measure the response times of thermal quenching of dsDNA/SG and SG. To the best of our knowledge, this is the first time to measure those parameters on millisecond time scale. Further research by this methodology might provide important information in understanding mechanisms of DNA intercalation related to DNA replication, repair and cancer development.

High speed heating measurements of DNA with intercalator can be applied to sequence dependent analysis such as search

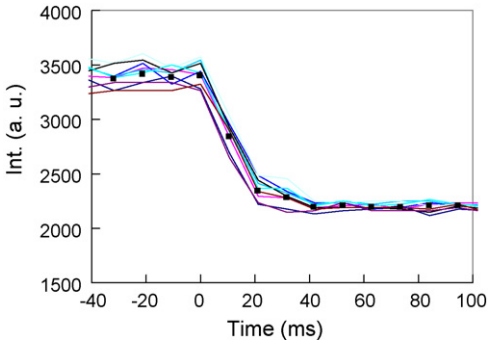

Fig. 4. Time courses of SG quenching by rapid exposure to high temperatures. The average intensities of 9 areas in solution were plotted in square. The temperature was switched from room temperature to slightly under 100 °C at an elapse time of 0 ms. Response time was slightly larger than 20 ms which is clearly larger than that of dsDNA/SG.

for mismatch [28], diagnostics [29], AT/GC contents analysis, etc. Therefore, it also has a potential for contribute to development of new materials such as DNA detecting reagents and DNA nanowires. Quick heating of short DNA may realize ultrafast PCR with real-time monitoring of single DNA molecule. One of the most prominent merits of thermal control is its adaptability with other tools/techniques to manipulate/measure biomaterials at molecular level such as AFM, optical tweezers, microfluidics, etc. AFM and optical tweezers enable to measure physical parameters on millisecond to microsecond time scale [30]. Combining with millisecond thermal control device will add another tuneable parameter. Since physical properties of DNA have a strong correlation with its surrounding temperature [5], this kind of experiments may elucidate important information hidden under time averaging.

4. Conclusion

In summary, denaturation response times of dsDNA/SG complex and free SG dye at high temperatures were measured to be 10 ms and slightly larger than 20 ms, respectively. Those parameters were measured by the micro-thermodevice, which has 1 ms response speed in altering the temperature. Considering that mechanical unzipping of dsDNA completes on time scale of a few minutes, the quenching of dsDNA/SG complex cannot be attributed to strands unzipping of the dsDNA. Although, the quenching properties of dsDNA/SG complex at base pair level is not yet well understood, this micro-thermodevice has provided easy access to measure this parameter. We believe that millisecond temperature switching experiments based on this methodology and device herein described might be a powerful tool to study dynamics of biomaterials on short time scales which might attract wide interests both in industrial research and pure scientific research such as genetics, molecular biology and biophysics.

Acknowledgements

This work was supported by Japan Society for the Promotion of Science (JSPS). We thank Dr. M. Kumemura for providing DNA. We thank Dr. N. Sakaki, Dr. T. Nojima, and Dr. M. Kumemura for useful discussions. This paper was reviewed and revised while HA was working in J.-L. Viovy's group at Curie Institute, Paris.

References

[1] L.B. Hendry, V.B. Mahesh, E.D. Bransome Jr., D.E. Ewing, Mutat. Res. Fundam. Mol. Mech. Mutagen. 623 (2007) 53–71.
[2] R.D. Snyder, L.B. Hendry, Environ. Mol. Mutagen. 45 (2005) 100–105.
[3] J.H. Schefe, K.E. Lehmann, I.R. Buschmann, T. Unger, H. Funke-Kaiser, J. Mol. Med. 84 (2006) 901–910.
[4] H. Zipper, et al., Nucleic Acids Res. 32 (2004) 103.
[5] D. Danilowicz, Y. Kafri, R.S. Conroy, V.W. Coljee, J. Weeks, M. Prentiss, Phys. Rev. Lett. 93 (2004) 078101.
[6] M.C. Wu, Proc. IEEE 85 (1997) 1833.
[7] M. Kimura, K. Toshima, Sens. Actuators A: Phys. 108 (2003) 239–243.
[8] L.R. Arana, S.B. Schaevitz, A.J. Franz, M.A. Schmidt, K.F. Jensen, J. MEMS 12 (2003) 600.
[9] Y. Rondelez, et al., Nat. Biotechnol. 23 (2005) 361–365.
[10] I. Amato, Science 282 (1998) 402.
[11] D.R. Reyes, D. Iossifidis, P.-A. Auroux, A. Manz, Anal. Chem. 74 (2002) 2623.
[12] G.M. Whitesides, Nature 442 (2006) 368.
[13] D. Janasek, J. Franzke, A. Manz, Nature 442 (2006) 374.
[14] H.F. Arata, M. Kumemura, N. Sakaki, H. Fujita, Anal. Bioanal. Chem. 391 (2008) 1618–2642.
[15] E.T. Lagally, I. Medintz, R.A. Mathies, Anal. Chem. 73 (2001) 565–570.
[16] P. Belgrader, et al., Anal. Chem. 73 (2001) 286.
[17] H.F. Arata, Y. Rondelez, H. Noji, H. Fujita, Anal. Chem. 77 (2005) 4810.
[18] H.F. Arata, H. Noji, H. Fujita, Appl. Phys. Lett. 88 (2006) 083902.
[19] S. Yamaguchi, et al., Chem. Eur. J. 14 (2008) 1891–1896.
[20] L. Lam, et al., Biomed. Microdev. 10 (2008) 539–546.
[21] H.F. Arata, H. Fujita, Integr. Biol. 2009, doi:10.1039/b901902b.
[22] H. Kato, T. Nishizaka, T. Iga, K. Kinosita Jr., S. Ishiwata, Proc. Natl. Acad. Sci. U.S.A. 99 (1999) 9602–9606.
[23] K. Kawaguchi, S. Ishiwata, Cell Motil. Cytoskeleton 49 (2001) 41–47.
[24] F. Gillot, F.O. Morin, H.F. Arata, R. Guegan, H. Tanaka, H. Fujita, Lab Chip 7 (2007) 1–4.
[25] H.F. Arata, et al., Sens. Actuators B: Chem. 117 (2006) 339–345.
[26] H.F. Arata, et al., Lab Chip 8 (2008) 1436–1440.
[27] Current Protocols in Molecular Biology, Copyright© 2007 by John Wiley and Sons, Inc.
[28] B.A. Jackson, J.K. Barton, J. Am. Chem. Soc. 119 (1997) 12986–12987.
[29] R.K. Saiki, D.H. Gelfund, S. Stoffel, S.J. Scharf, R. Higuchi, G.T. Horn, K.B. Mullis, H.A. Erlich, Science 239 (1988) 487–491.
[30] K.C. Neuman, A. Nagy, Nat. Met. 5 (2008) 491.

Talanta 79 (2009) 863–870

Contents lists available at ScienceDirect

Talanta

journal homepage: www.elsevier.com/locate/talanta

Batch and flow measurement of hydrogen ions in highly acidic media using 2-(4-methoxy phenyl) 6-(4-nitrophenyl)-4-phenyl-1,3-diazabicyclo [3.1.0] hex-3-ene as an H^+-selective ionophore

Majid Arvand*, Khatereh Ghaiuri

Department of Chemistry, Faculty of Science, University of Guilan, P.O. Box: 1914, Rasht, Iran

ARTICLE INFO

Article history:
Received 13 January 2009
Received in revised form 11 May 2009
Accepted 12 May 2009
Available online 21 May 2009

Keywords:
pH sensor
Acidic media
Sandwich membrane method
Equilibrium water content
Flow injection analysis

ABSTRACT

A hydrogen ion-selective poly(vinyl chloride) (PVC) membrane electrode was developed using 2-(4-methoxy phenyl) 6-(4-nitrophenyl)-4-phenyl-1,3-diazabicyclo [3.1.0] hex-3-ene as ionophore. Effects of experimental parameters such as membrane composition, nature and amount of plasticizer, and the amount of additive on the potential response of pH sensor were investigated. This H^+-selective membrane electrode gave a linear response over the pH range 0–4 (10^{-4} to 1 mol L^{-1} HCl) with slope of 57.4 ± 0.3 mV pH^{-1} and limit of detection 6.3×10^{-5} mol L^{-1} at 20 °C. Also, hydrofluoric acid did not influence the surface of this electrode and thus it was maintained without showing any changes in potentials after being used in a hydrofluoric acid solution. The equilibrium water content of the electrode was determined in the presence of two different plasticizers as membrane solvent. The alkaline cation binding affinity of ionophore was very low that prove these cations do not have specific interaction with this ionophore. The electrode had fairly low electrical resistance, good potential stability and reproducibility. It has a rapid potential response to changes of pH (10 s), easily used in a single channel wall-jet flow injection system with good reproducibility (RSD% = 1.67%) and high reversibility. It was used as indicator electrode in potentiometric determination of pH in real samples.

1. Introduction

A glass electrode is the most popular electrode in the determination of acidity owing to its high selectivity, reliability and dynamic pH range. Although pH-sensitive glass electrode has distinguished response characteristics and has been in use for such a long period, it has certain setbacks such as its high resistance, fragility, its instability in hydrofluoric acid or fluoride solutions and its unsuitability to serve as a microelectrode for biological applications. Accordingly, there have been huge developments in design of non-glass pH-sensitive electrodes over the past two decades [1–20].

The first neutral carrier based solvent polymeric membrane pH electrodes containing an ionophore, instead of glass, have been developed in Simon's laboratory, where tridodecylamine and other compounds containing basic nitrogen groups have been discovered as selective membrane compounds in pH electrodes [21–27]. Later, other authors continued this work, thus other various compounds (aliphatic, heteroaromatic and their derivatives) have been studied as carriers of hydrogen ions [1–20,28,29]. Among these, alkyl pyrazoles [4], phenoxazine derivatives [3,13–15], amines [5–10,24,27–29], hexabutyl-tri-amidophosphate [11], azobenzenes [12], 4′,5′-dibromofluorescein octadecylester [16], calix[4]arene [17,18], calix[4]-aza-crowns [19], zeolite [20], long-chain alkyl picolinamides [21,22] and octadecyliso-nicotinate [25] appear to be promising.

Flow injection potentiometry (FIP) by ion-selective electrodes (ISEs) is well known to possess several advantages, including low cost, simple instrumentation, rapid response, high reproducibility of the analysis, high selectivity and sensitivity. Moreover, the transient nature of the signal in FIA may help to overcome the effects of interfering ions if the electrode's response to these ions is slower than that to the target analyte and the lifetime of electrodes may be extended as the surface is predominantly exposed to carrier solution. Because of the above-mentioned advantages, in recent years, several reports on flow injection potentiometry have been published in the literature [30,31].

Recently, we used a new class of ionophores containing nitrogen atoms such as 6-(4-nitrophenyl)-2-phenyl-4-(thiophen-2-yl)-3,5-diaza-bicyclo[3.1.0] hex-2-ene [32], 6-(4-nitrophenyl)-2,4-diphenyl-3,5-diaza-bicyclo[3.1.0] hex-2-ene [33], 6-(4-nitrophenyl)-2-phenyl-4,4-dipropyl-3,5-diaza-bicyclo[3,1,0] hex-2-ene [34], (2E, 4E)-5-(2,4-dinitrophenyl amino)penta-2,4-dienal [35], and N^5-(2,4-dinitro-phenyl)-N^1,N^1-diethyl-penta-1,3-diene-1,5-diamine [36] as carrier in developing of ion-selective electrodes

* Corresponding author. Tel.: +98 131 3233262; fax: +98 131 3233262.
E-mail address: arvand@guilan.ac.ir (M. Arvand).

0039-9140/$ – see front matter © 2009 Elsevier B.V. All rights reserved.
doi:10.1016/j.talanta.2009.05.015

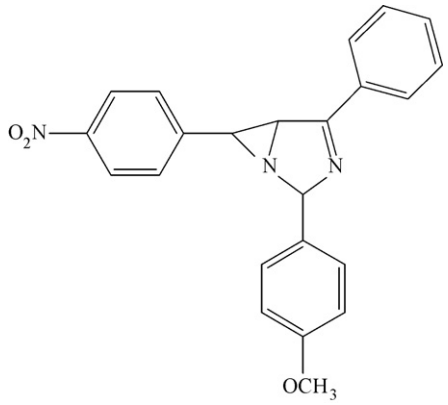

Fig. 1. Structure of 2-(4-methoxy phenyl) 6-(4-nitrophenyl)-4-phenyl-1,3-diazabicyclo [3.1.0] hex-3-ene (MNDH) used as ionophore.

[32–34] and optodes [35,36]. As organic compounds with nitrogen atoms such as amines [5–10,24,27–29], alkyl pyrazoles [4], azobenzenes [12], calix[4]-aza-crowns [19], long-chain alkyl picolinamides [21,22], and octadecyliso-nicotinate [25] used as ionophore in construction of pH sensors, we thought that the new compound 2-(4-methoxy phenyl) 6-(4-nitrophenyl)-4-phenyl-1,3-diazabicyclo [3.1.0] hex-3-ene with two nitrogen atoms in its structure could also be utilized in development of hydrogen ion-selective electrodes. Therefore, we focused on the possibility of using synthesized 2-(4-methoxy phenyl) 6-(4-nitrophenyl)-4-phenyl-1,3-diazabicyclo [3.1.0] hex-3-ene (MNDH) in the construction of a hydrogen-selective electrode. The structure of MNDH is given in Fig. 1. For this purpose, membranes with various combinations were prepared by the change of the ratio of ionophore, PVC, plasticizer and lipophilic anion in order to determine the optimum membrane composition. The response time and the lifetime of the electrode and its selectivity against some anions and cations were investigated. The electrode performance is similar to that of glass pH electrodes and the electrodes are robust, resistant to hydrofluoric acid, with high potential response stability and can be used as an indicator electrode in potentiometric determination of pH in real samples.

2. Experimental

2.1. Reagents and solutions

All reagents used were of analytical reagent grade. High relative molar mass poly(vinyl chloride) (PVC), acetophenone (AP), *o*-nitrophenyl octyl ether (*o*-NPOE), dibuthyl phthalate (DBP), dibuthyl sebacate (DBS), nitro benzene (NB), oleic acid (OA), potassium tetrakis(*p*-chlorophenyl)borate (KT*p*ClPB), tetrahydrofuran (THF), sodium hydroxide (NaOH), hydrochloric acid (HCl), hydrofluoric acid (HF), acetic acid (CH_3COOH), and other reagents were obtained all from Merck (Darmstadt, Germany) or Fluka chemical company (Switzerland). All solutions and buffers were prepared by dissolving the salts in distilled deionized water.

2.2. Synthesis of the ionophore

The ionophore 2-(4-methoxy phenyl) 6-(4-nitrophenyl)-4-phenyl-1,3-diazabicyclo [3.1.0] hex-3-ene (MNDH) used in this work, was synthesized according to the previously reported method with some modification in the described procedure [37]. To prepare the compound, 2-benzoyl-3-(4-nitrophenyl)-aziridine (0.268 g, 1 mmol), NH_4Br (0.1 g, 1 mmol) and 4-methoxy benzaldehyde (1 mmol) were dissolved in 10 mL of absolute ethanol and stirred at room temperature. Anhydrous gaseous ammonia is gently blown into reaction mixture for several hours. A color change in the reaction mixture from orange into turquoise is characteristic for product formation. The reaction mixture was filtered, washed with ethanol, dried in the air and the resulting solid recovered 0.33 g, purified by silica gel column chromatography and recrystallized from methanol (61.2% yield). The product has mp = 156–158 °C, IR (KBr): 3050 and 3000 (=CH), 2950 and 2850 (C–H), 1600 (C=N), 1570 and 1450 (C=C), 1510 and 1340 (NO_2), 1250 and 1030 (C–O–C) cm^{-1}; ^1H NMR (500 MHz, $CDCl_3$): 2.54 (s, 1H), 3.79 (s, 1H), 3.81 (s, 3H), 6.78 (s, 1H), 6.9 (d, J = 8.44 Hz, 2H), 7.42 (d, J = 8.45 Hz, 2H), 7.45 (d, J = 8.41 Hz, 2H), 7.52 (t, J = 7.48 Hz, 2H), 7.58 (t, J = 7.2 Hz, 1H), 8.02 (d, J = 7.6 Hz, 2H), 8.19 (d, J = 8.43 Hz, 2H).

2.3. Electrode preparation

The sensor membrane was prepared with the following composition: the ionophore MNDH (m/m, ~3%), plasticizer *o*-NPOE (m/m, ~63%), PVC (m/m, ~31%) and additive KT*p*ClPB (m/m, ~3%) were mixed and the components were dissolved in THF (2 mL). The solution was mixed well and the solvent was evaporated slowly until an oily concentrated mixture was obtained. A Pyrex tube (3 mm o.d.) was dipped into the mixture for about 15 s so that a transparent membrane of about 0.5 mm thickness was formed. The tube was then pulled out from the solution and kept at room temperature for about 3 h. The tube was then filled with internal solution buffer pH 2.5 (CH_3COOH and NaOH). The electrode was finally conditioned for 4 h by soaking in solution buffer pH 3 (CH_3COOH and NaOH). The ratios of various ingredients, concentration of equilibrating solution and time of contact were optimized to provide a membrane that was reproducible, noiseless and stable potential.

2.4. Emf measurements

All emf measurements were carried out with the following assembly:

Hg–Hg_2Cl_2/internal buffer solution of pH 2.5 (CH_3COOH and NaOH)/PVC membrane/test solution/Hg–Hg_2Cl_2, KCl (sat'd). The reference electrode was obtained from Azar electrode Co. (Urmia, Iran). Potentiometric measurements were carried out with a digital pH/millivoltmeter (Jenway, Model 3305) at constant temperature (20.0 ± 0.5 °C).

2.5. Equilibrium water content

The equilibrium water content (EWC) of PVC membranes based on both *o*-NPOE and AP as plasticizers was evaluated using the gravimetric method [15]. Dry membranes weighing about 100 mg (w_1) were immersed in the appropriate soaking medium for 5 days and the swollen membranes were blot dried with a paper towel and immediately weighed (w_2). Then, the swollen membranes were dried at room temperature to a constant weight (w_3). The EWC values were calculated using the following equation:

$$\mathrm{EWC}(\%) = \left[\frac{(w_2 - w_3)}{w_2}\right] \times 100 \quad (1)$$

The loss of plasticizer from the membrane into the water phase was evaluated from the difference between w_1 and w_3.

2.6. Flow injection system

The scheme of the flow injection system is shown in Fig. 2. Water was pumped with a peristaltic pump (Scharlau HP4) (A) by using standard Tygon tubing coupled to the flow rate controller (B) and flow-cell which was the polyethylene (PE) canal where were

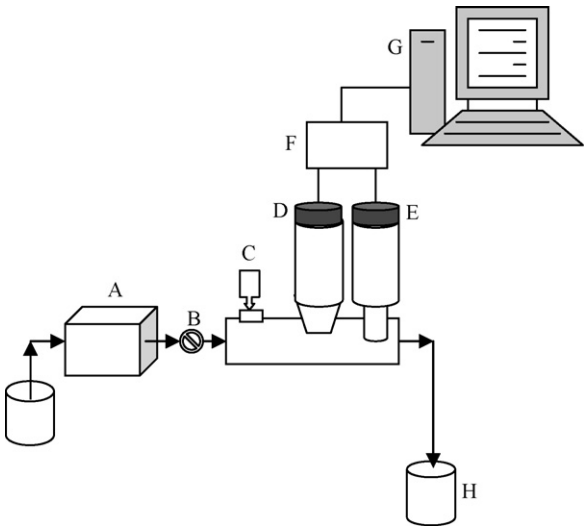

Fig. 2. Setup of the flow system used: (A) peristaltic pump (Scharlau HP4), (B) flow rate controller, (C) injector, (D) H^+-selective electrode, (E) reference electrode, (F) potentiometer, (G) data processor (computer), (H) output flow and waste.

set H^+-selective electrode (D) include (membrane cell and internal reference electrode) and reference electrode (E). Samples were injected using an injector 2.5 mL of canal (C). The sample injection into water carried and further dispersion process produced a highly reproducible pH which was here advantageously exploited for the determination of pH. The corresponding potential change was measured (F) and recorded vs. time. Then data by computer (G) were indicated to form peak. (H) was output flow and waste.

3. Results and discussion

3.1. Effect of membrane composition

The literature survey showed that the usual range of composition in the preparation of PVC matrix membrane electrodes was 0–5% ionophore, 30% PVC (matrix), 58–66% plasticizer (solvent) and 0–8% lipophilic ion [38]. Therefore, the optimum membrane composition was sought for within this composition range. In addition, the contribution of the matrix (without ionophore) to the overall pH-response was studied by membranes without any MNDH.

The first series of studies was carried out by the membranes prepared by keeping constant the ionophore and changing the amount lipophilic anion. In the second series of studies, the effect of the ionophore ratios upon the response of the electrode was investigated by changing its content. The properties of plasticizer affect on the sensitivity, selectivity and linearity of H^+-ISEs [39]. Since the nature of plasticizer influences the dielectric constant of the membrane phase both the mobility of the ionophore molecule and the state of the ligand [38,39] it was expected to play a key role in the characteristics of the ion-selective electrode. For this purpose, the effect of the plasticizer was verified by keeping constant the content of the ionophore and additive and using AP, NB, DBP, DBS and *o*-NPOE. As it is seen from Table 1, among five different plasticizers used, *o*-NPOE resulted in a best Nernstian slope. In the other hand, the linear range for the electrode constructed with *o*-NPOE was better than to the other plasticizers. In other experiments, the effect of the lipophilic anion was evaluated by the addition of lipophilic salt KT*p*ClPB and fatty acid OA. It was found that the sensitivity towards the hydrogen ion showed a significant decrease from 57.4 ± 0.3 with KT*p*ClPB to 37.1 ± 0.3 mV pH^{-1} with OA at 20 °C (Table 1). This is due to the protonation of weak acid OA in acidic media. In this case the OA cannot act as cation exchanger very well. The role of additive has been deeply discussed in Section 3.2.

The results obtained from the electrode prepared with the membrane having a plasticizer/PVC ratio of 1.87–2.13 were examined. The membrane prepared with an *o*-NPOE/PVC ratio of 2.0 was found to have the highest sensitivity and the widest linear range. Collective results are given in Table 1. Moreover 3 mg of ionophore was chosen as the optimum amount of ionophore in the PVC-membrane. Further addition of ionophore, had no effect on the electrode response. The high amount of the ionophore may also induce strong interactions between polymeric chains and ionophore, preventing mobility of the segments as explained by Reinhoudt and co-workers [40].

In general, the thickness and hardness of the membrane depend upon the amount of PVC used. At higher PVC content, the membrane becomes too dense, which makes the transport of cations into the membrane more difficult and results in the increased resistance. At lower PVC content, the membrane becomes mechanically weak and swells up easily in aqueous solution. As shown in Table 1 the linear pH ranges were that 0.0–4.0 for MNDH-based ISE. Also, its Nernstian slopes showed, 57.4 ± 0.3 mV pH^{-1} with detection limit of 6.3×10^{-5} mol L^{-1} at 20.0 ± 0.5 °C (No. 2). It is also noteworthy that the optimum conditioning time for the membrane electrode was obtained 4 h, afterward it then generates stable potentials when placed in contact with buffer solutions.

3.2. Electric resistance of the membrane

The resistance of the electrode is much lower than that of a glass electrode and is favorable for electrode miniaturization. The amounts of MNDH as neutral ionophore in membranes had no effect on the electric resistance of membrane electrodes. Since the

Table 1
Effect of the membrane composition on the slope of MNDH based-pH electrode.

No.	Membrane composition (%w/w)				Plasticizer/PVC	Slope[a]	Linear range
	MNDH	Plasticizer	Additive	PVC	ratio	(mV pH^{-1})	(mol L^{-1})
1	3	66 (*o*-NPOE)	0	31	2.13	31.2 ± 0.6	1×10^{-4} to 1
2	3	63 (*o*-NPOE)	3 (KT*p*ClPB)	31	2.0	57.4 ± 0.3	1×10^{-4} to 1
3	3	60 (*o*-NPOE)	6 (KT*p*ClPB)	31	1.94	55.0 ± 0.3	1×10^{-4} to 1
4	3	58 (*o*-NPOE)	8 (KT*p*ClPB)	31	1.87	52.7 ± 0.3	1×10^{-4} to 1
5	0	66 (*o*-NPOE)	3 (KT*p*ClPB)	31	2.13	13.2 ± 1.1	5×10^{-3} to 1
6	1	65 (*o*-NPOE)	3 (KT*p*ClPB)	31	2.1	44.5 ± 0.4	1×10^{-4} to 1
7	5	61 (*o*-NPOE)	3 (KT*p*ClPB)	31	1.97	53.2 ± 0.2	1×10^{-4} to 1
8	3	63 (DBS)	3 (KT*p*ClPB)	31	2.0	47.1 ± 0.9	2×10^{-3} to 1
9	3	63 (AP)	3 (KT*p*ClPB)	31	2.0	51.3 ± 1.3	1×10^{-4} to 1
10	3	63 (DBP)	3 (KT*p*ClPB)	31	2.0	46.3 ± 0.3	1×10^{-4} to 1
11	3	63 (NB)	3 (KT*p*ClPB)	31	2.0	43.9 ± 0.8	5×10^{-3} to 1
12	3	63 (*o*-NPOE)	3 (OA)	31	2.0	37.1 ± 0.3	1×10^{-4} to 1

[a] Mean values of slopes for three replicate measurements.

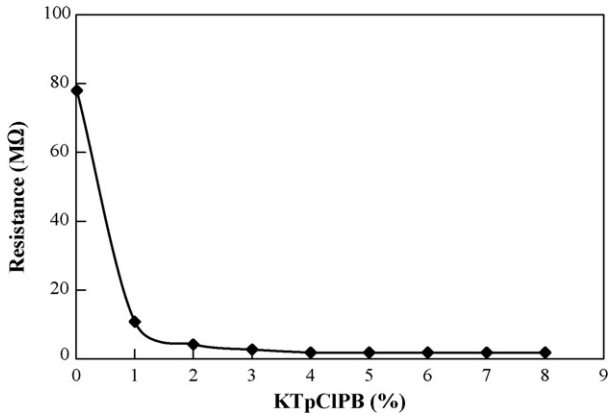

Fig. 3. Electrical resistance of hydrogen ion-selective membrane electrode based on MNDH with varying amounts of KT*p*ClPB.

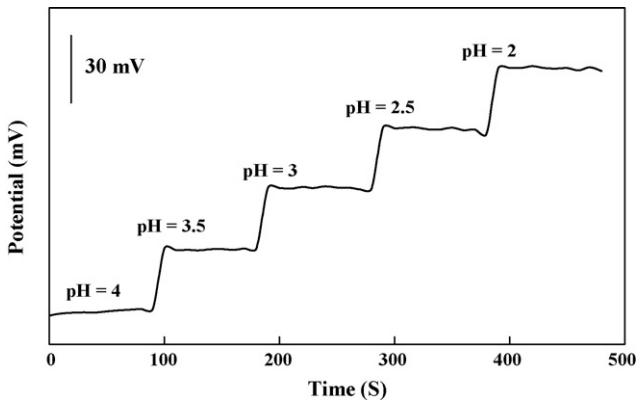

Fig. 4. Dynamic response of membrane electrode for step changes in pH (electrode number 2).

values of membrane thickness was constant so variations of electrical resistance were small compared to input resistance. It is also known that the presence of lipophilic anions in cation-selective membrane electrodes not only diminishes the ohmic resistance and enhances the response behavior, selectivity, and sensitivity of the membrane electrodes, but also may catalyze the exchange kinetics at the sample-membrane interface [41,42]. Without such additives, many electrodes do not respond properly toward a cation. The use of ionic additives such as different tetraphenyl borate salts and its more lipophilic derivative, KT*p*ClPB and also fatty acids such as OA as lipophilic additives is widely reported in the preparation of different ion-selective electrodes [43–45]. Their main role is attributed to the inducing permselectivity to some PVC membrane selective electrodes [45]. Addition of 3.0 mg of KT*p*ClPB as a lipophilic additive showed better Nernstian response and linear range (No. 2). OA was also investigated as additive. The data given in Table 1 shows that KT*p*ClPB is more suitable additive than OA. However, increasing the amount of KT*p*ClPB shows no beneficial influence on the membrane electrode response, furthermore the observed potential was seen to be unstable. The membrane electrodes to which KT*p*ClPB as lipophilic agent were not added did not respond selectively to hydrogen ions and the membranes showed high electric resistance as much as 78 MΩ. But more than 8 wt.% of KT*p*ClPB, the composition of membranes could not use as electrodes by mechanical leaking because KT*p*ClPB is freely soluble in water. The data in Fig. 3 show, respectively, that the electrical resistance of polymer membranes based on MNDH was dependent on varying the amount of lipophilic agent.

3.3. Response time, lifetime and reversibility of the electrode

The time for the electrode to reach a stable potential after it was immersed into the calibration solutions (response time) was recorded starting from 1.0×10^{-4} mol L^{-1} HCl to 1.0×10^{-2} mol L^{-1} HCl solution. The response time of the electrode was found to be longer in pH 4 than the pH 2 (approximately 15 s). This value is comparable to, or even shorter than those hydrogen-selective electrodes, which give a linear response in a similar concentration range [5,6,18–20]. The actual potential vs. time traces is shown in Fig. 4. As can be seen, the electrode reaches the equilibrium response in an average time of about 10 s.

Reproducibility of the electrode was examined by using six similar constructed electrodes under the optimum conditions. The results showed good reproducibility for proposed electrode. For instance, the slopes observed were 57.4 ± 0.3 mV pH^{-1}. The long-term stability of the electrode was studied by periodically recalibrating in standard solutions and calculating the response slope. The slope of the electrode responses was reproducible over a period of atleast 6 weeks. Therefore the proposed electrode can be used for more than 6 weeks without a considerable change in its response characteristics towards pH.

To evaluate the reversibility of the electrode, a similar procedure with opposite direction was adopted. The measurements were performed in the sequence of low to high pHs. The results showed that the potentiometric responses of the sensor was reversible and had any memory effect, although the time needed to reach equilibrium values were longer than that of high to low pHs. Noteworthy, it is well documented that, in the case of low to high pH, the time needed to attain a stable potential is some 100 times larger than that required for the case of high to low pH (for a 1 time change in the pH) [38].

3.4. Selectivity of the electrode

It is reported in literature that the working range of neutral ionophore-based electrodes was adversely affected by the anions and the cations. It is known that the cations such as lithium, sodium and potassium narrow in the lower and anions such as bromide, iodide and thiocyanate in the upper limit of the working range of the cation-selective electrodes. In short, many ionic impurities are expected to reduce the working range of the electrode [6,46,47].

Whether or not the hydrogen electrode prepared is sensitive to lithium, sodium and potassium ions, and its selectivity coefficients against these ions were evaluated by the use of the fixed interference method [3]. That is, the emf of a cell comprising an ion-selective electrode and a reference electrode is measured for solutions of constant activity of the interfering ion, a_B, and varying activity of the primary ion, a_A. The emf values obtained are plotted vs. the logarithm of the activity of the primary ion. The intersection of the extrapolated linear portions of this plot indicates the value of a_A that is to be used to calculate $K^{Pot}_{A,B}$ from the following equation:

$$K^{Pot}_{A,B} = \frac{a_A}{a_B^{z_A/z_B}} \quad (2)$$

A perusal of selectivity coefficient data presented in Table 2 indicates that the electrode is sufficiently selective over a number of anions and cations. This behavior may be due to the selective uptake of H^+ by ionophore in comparison to the other species.

The effect of bromide, iodide, thiocyanate and perchlorate as background electrolyte upon the working range of the electrode was also determined by the use of the mixed run method, and the data is given in Fig. 5. As seen from Fig. 5, the deviation of curves from the theoretical plot is small at the presence of these anions and thus these ions do not disturb the functioning of the H^+-selective electrode significantly.

Table 2
Selectivity coefficients of the proposed hydrogen ion-selective electrode based on MNDH.

M^{n+}	Log $K^{Pot}_{M,H}$	X^{m-}	Log $K^{Pot}_{X,H}$
Li^+	−3.60	ClO_3^-	−5.22
K^+	−3.69	BrO_3^-	−5.73
Na^+	−0.30	ClO_4^-	−4.94
Ca^{2+}	−3.40	SCN^-	−5.28
Ba^{2+}	−4.67	I^-	−5.32
Ni^{2+}	−4.89	Br^-	−5.63
Cu^{2+}	−4.62	NO_2^-	−4.89
Al^{3+}	−3.79	NO_3^-	−5.19
Cr^{3+}	−3.61	SO_4^{2-}	−6.52
Co^{2+}	−5.42	SO_3^{2-}	−6.60
Mn^{2+}	−5.49		
Fe^{2+}	−5.14		

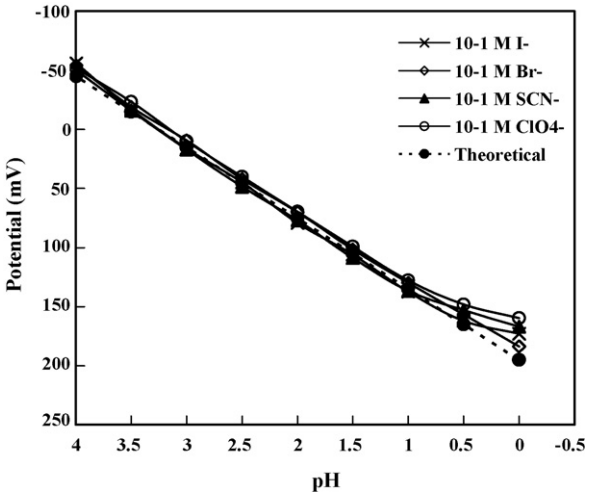

Fig. 5. Effect of the nature of background electrolyte on the electrode response of H^+-ISE based on MNDH (electrode number 2).

3.5. Association constant (pK_a) and cation binding affinity of H^+-selective ionophore

To determine the pK_a value for MNDH ionophore, the sandwich membrane experiments were performed as reported by Pungor et al. [48]. For this purpose, two single membranes with and without ionophore were conditioned in 0.01 mol L^{-1} HCl and the combined sandwich membrane was measured in a symmetrical cell with 0.01 mol L^{-1} HCl as sample and inner filling solutions to observe a Nernstian response. Table 3 shows the observed sandwich membrane potentials of ionophore and its pK_a value, which were calculated from the following established equation:

$$E_M = \frac{RT}{F}\ln\left\{\frac{(L_T - R_T)}{K_a}\right\} - \frac{RT}{F}\Delta pH \quad (3)$$

where L_T and R_T are the total concentration of ionophore and ionic additive in the membrane and ΔpH is the pH of the sample subtracted by that of the inner filling solution (while ionophore-free membranes show a pH response only in pure acid solutions therefore $\Delta pH = 0$). The symbols R, T and F are the gas constant, the absolute temperature and the Faraday constant, respectively. The stoichiometry for the ionophore protonation is here assumed to be 1:1. The cation binding affinity was also studied quantitatively by the same method to test the previous assumption that the metal cations do not have specific interaction with such H^+-ionophore. The observed sandwich membrane potentials are shown in Table 3. The complex formation constants were calculated from the following equation:

$$\beta_{IL_n} = \left(L_T - \frac{nR_T}{Z_I}\right)^{-n} \exp\left(\frac{\Delta emf Z_I F}{RT}\right) \quad (4)$$

where R, F, T, L_T and R_T have the same meaning as mentioned above and Z_I is interference ion charge, Δemf sandwich membrane potential, n, the stoichiometry coefficient of the complex. The ion I^+ is singly positively charged and forms a 1:1 complex with the corresponding lipophilic ionophore in the polymer membrane. The small association constant values shown in Table 3 for the neutral ionophore MNDH confirmed the extremely weak interaction between the Li^+, Na^+ and K^+ ions and the neutral ionophore. These experiments give quantitative evidence for the fact that the highly selective ionophore can be used as a suitable H^+-selective ionophore in potentiometric and optical methods in polymer membranes without introducing significant errors.

Table 4
Equilibrium water content (EWC) and loss of plasticizer (LP) from dummy membranes.

	PVC/*o*-NPOE membrane	PVC/AP membrane
EWC (%)		
In H_2O	2.13	0.8
In 10^{-3} mol L^{-1} NaCl	1.12	2.94
LP (%)		
In H_2O	0.32	3.9
In 10^{-3} mol L^{-1} NaCl	0.94	1.06

3.6. Water uptake by dummy membranes

The water uptake depends on the polarity of the plasticized membrane as well as on the aqueous solvent (solution) used to hydrate the membrane. Higher EWC values were observed in pure water when a polar solvent such as *o*-NPOE ($\varepsilon = 23.9$), was used as the solvent plasticizer. With AP ($\varepsilon = 17.4$), the water uptake was less from pure water than from 10^{-3} mol L^{-1} NaCl solution (Table 4). Freshly prepared membranes were oily and this plasticizer was exuded when the membrane was placed in contact with aqueous solutions. The exuded plasticizer surface layer was greater for AP than for *o*-NPOE plasticizer (Table 4). These membranes also showed unstable potentiometric readings. This effect was also found in membranes containing ETH5294 as reported by Cosofret et al. [15]. The high surface membrane resistance could be reduced significantly by adding the lipophilic salt additive KT*p*ClPB in our optimal compositions.

3.7. Flow injection potentiometry

The flow cell used for detection of pH was designed to accommodate small size of the sensor to avoid large dispersion of the sample in the cell and give good response and recovery times with a constant geometry and a minimum "dead" space. With short tubing (10 cm between injector and cells), low total volume between

Table 3
Sandwich membrane potentials and calculated properties of H^+-selective ionophore.

	PVC/*o*-NPOE membrane		K^+		Na^+		Li^+	
	Δemf	pK_a	Δemf	log β_1	Δemf	log β_1	Δemf	log β_1
MNDH	184 ± 2	9.31 ± 0.03	7 ± 1	2.60 ± 0.01	8 ± 1	2.62 ± 0.01	7 ± 2	2.60 ± 0.03

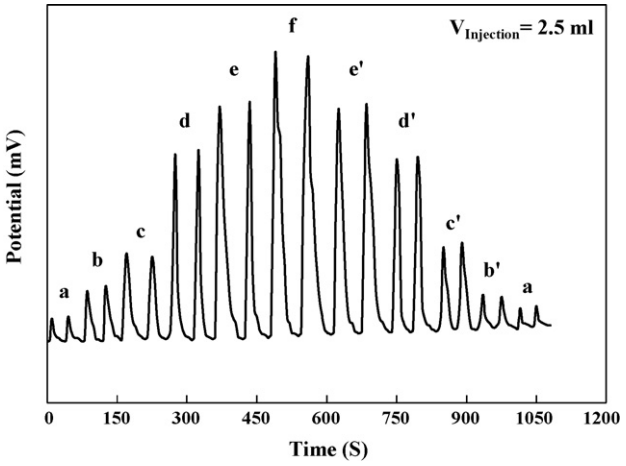

Fig. 6. FIP peaks obtained using an optimized H^+-selective electrode (electrode number 2) in standard HCl solutions (flow rate 1.32 mL min^{-1}). (a,a') pH 5, (b,b') pH 4, (c,c') pH 3, (d,d') pH 2, (e,e') pH 1, (f) pH 0.

injector and sensor (10 mL) and relatively large injection volume (2.5 mL), dispersion in this system is kept to be minimum. The effect of carrier buffer flow rate was examined over a range of flow rates from 0.98 to 2.5 mL min^{-1} for buffers solutions ranging from pH 0 to 5 using the small membrane electrode. The potentiometric response (slope in mV pH^{-1}) was recorded against the flow rate. The optimal flow rate was chosen to be 1.32 mL min^{-1}. In flow rates lower than 1.32 mL min^{-1}, the small detector showed a slight memory effect, long washing times and low analytical frequency. At flow rates higher than 1.32 mL min^{-1}, the detector response decreases and the peak width become narrow because high flow rates decrease the residence time of the sample. The formation of the potentiometric signal is based, in general, on dynamic equilibrium reactions, thus the magnitude of the signal is independent of the rate of the transport process. Accordingly, the flow rate affects only the transient signal produced at rapid concentration changes [30]. A dynamic response with the detector was studied at a settled flow rate at 1.32 mL min^{-1} (Fig. 6). The results of Fig. 6 showed good reversibility and reproducibility (RSD% = 1.67%, n = 5).

3.8. Effect of temperature

To study the thermal stability of the electrodes, calibration graphs [$E_{electrode}$ vs. pH] were constructed at different test solution temperatures covering the range 10–50 °C (representative graphs are given in Fig. 7). At higher temperatures, the slope of electrode did not show a good Nernstian behavior. This behavior may be due to the following reason: at such high temperatures, the phase boundary equilibrium at the gel layer-test solution interface is disturbed by the thermal agitation of the solution [49].

The standard cell potentials E^o were determined at different temperatures from the respective calibration plots as the intercepts of these plots at pH 0, and were used to determine the isothermal temperature coefficient (dE^o/dt) of the cell with the aid of the following equation [50]:

$$E^o_{cell} = E^o_{cell\,(25^\circ C)} + \left(dE^o/dt\right)_{cell}(t-25) \quad (5)$$

Plot of E^o vs. (t – 25) produced a straight line. The slope of this line was taken as the isothermal temperature coefficient of the cell. It amounts to 0.00043 V/°C. The standard potentials of the reference electrode (Hg/Hg_2Cl_2; KCl (sat'd)) were calculated using the following equation:

$$E^o = 0.241 - 0.00066\,(t-25) \quad (6)$$

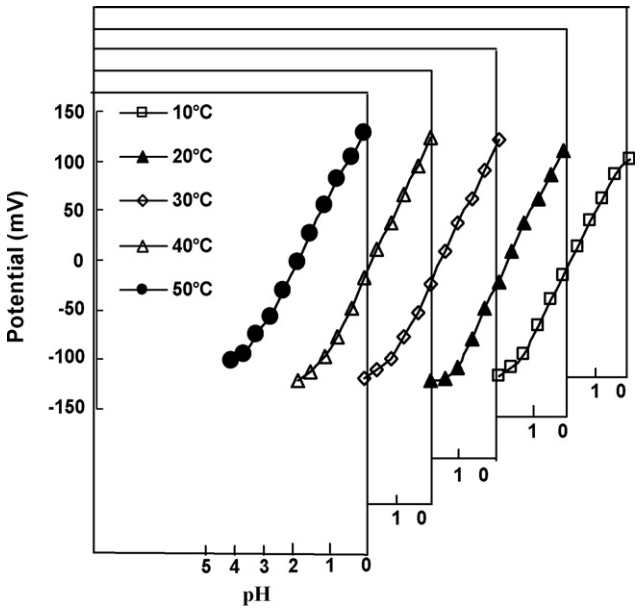

Fig. 7. Calibration graphs for H^+-selective electrode (electrode number 2) at test solution temperatures 10 °C, 20 °C, 30 °C, 40 °C and 50 °C.

The values of the standard potentials of H^+-electrode were calculated at the different temperatures from the following relation:

$$E^o_{cell} + E^o_{reference} = E^o_{electrode} \quad (7)$$

Plot of $E^o_{electrode}$ vs. (t – 25) gave a straight line. The slope of the line was taken as the isothermal temperature coefficient of the pH electrode. It amounts to 0.00023 V/°C. The small values of $(dE^o/dt)_{cell}$ and $(dE^o/dt)_{electrode}$ reveal the high thermal stability of the electrode within the investigated temperature range.

4. Analytical application of the electrode

The electrode was used in the titration of standard hydrochloric acid with sodium hydroxide. The titration curve was plotted and the concentration of sodium hydroxide was determined in order to elucidate whether the prepared hydrogen ion-selective electrode can be employed as an indicator electrode in acid–base

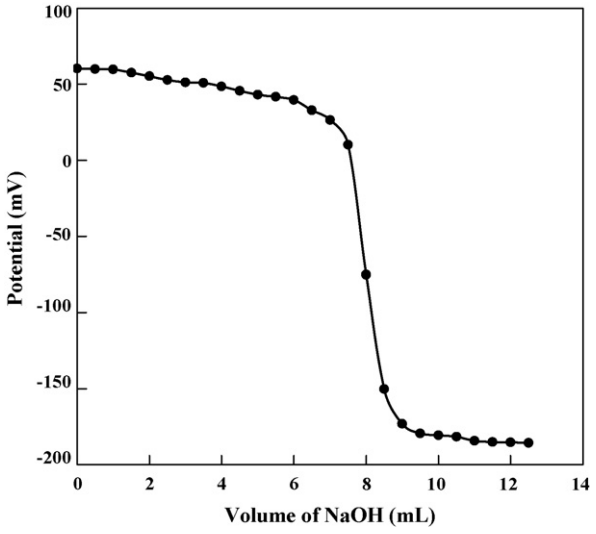

Fig. 8. Potentiometric titration curve for 20 mL of 0.02 mol L^{-1} HF solution with 0.05 mol L^{-1} NaOH, using the proposed sensor (electrode number 2) as an indicator electrode.

Table 5
Error in pH measurement by using the commercial and the new electrode.

Buffer pH	Proposed electrode	Error (%)	HANNA (HI 8519N)	Error (%)	TOA (HM-5ES)	Error (%)	SCHOTT (CG710)	Error (%)
3.70	3.63	−1.9	3.68	−0.5	3.75	1.4	3.80	2.7
2.40	2.27	−5.4	2.30	−4.2	2.30	−4.2	2.58	7.5
1.60	1.70	6.3	1.88	17.5	1.70	6.3	1.79	11.9
0.75	0.8	5.3	0.88	17.3	0.90	20.0	0.91	21.3

Table 6
Comparison of the proposed electrode with glass pH-electrode in complex matrix samples.

Sample	pH (glass electrode)	pH (proposed electrode)	ΔpH
Industrial vinegar	2.6	2.7	0.1
Orange juice	2.2	2.0	−0.2
Lemon juice	2.1	1.9	−0.2

titrations. The same titration was also carried out by the use of a commercial combined glass pH electrode and the novel hydrogen ion-selective electrode was found to be reliable at 95% confidence level. The electrode can be used for end-point indication in titrations of hydrofluoric acid with sodium hydroxide. Fig. 8 shows the E–V curve for this type of titration using a sample of 20 mL of 0.02 mol L^{-1} HF titrated with 0.05 mol L^{-1} NaOH. After a measurement with this electrode in hydrofluoric acid, the working range and the Nernstian slope remained the same. We can say that the electrode prepared could be successfully employed in acid–base titrations.

The newly prepared hydrogen selective electrode is also compared with three different commercial glass pH electrodes at low pH values 0.75–3.70. Buffers in various pH (0.75, 1.60, 2.40, 3.70) were prepared. Their pH were determined both with glass pH electrodes and the newly prepared pH sensor. The results are given in Table 5. Here the pH values measured with the glass pH electrodes are compared with pH of buffers. Their relative errors and the error made with the new electrode are given in Table 5. As can be seen and as expected the error made with glass pH electrodes is high at low pHs. On the other hand, the new electrode can be used safely at very low pH values (0–4).

In order to compare the applicability of the electrode response with that of the pH-glass electrodes in real sample analysis, measurements were made in complex matrices. Industrialized fruit juices of different found in supermarket were used as matrices. As seen in Table 6, an agreement was obtained between electrodes. However, this favorable response should be seen with some care in the sense that the use of this electrode in complex media can occasionally lead to error due to complexation or redox effects.

5. Conclusions

On the basis of the results presented here, the 2-(4-methoxy phenyl) 6-(4-nitrophenyl)-4-phenyl-1,3-diazabicyclo [3.1.0] hex-3-ene can be used as an ionophore in hydrogen ion-selective electrodes. The proposed hydrogen ion-selective electrode can be a good alternative for glass electrodes and it can reliably be employed as an indicator electrode in acid–base titrations especially fluoride-containing solutions. It has low sensitivity towards lithium, sodium and potassium ions when compared with the glass electrodes. For this electrode, the following points are important. The resistance of the proposed membrane electrode is much lower than that of a glass electrode and is favorable for electrode miniaturization. The hydrogen ion-selective PVC membrane exhibits fast response and a good reproducibility and stability. The prepared electrodes were shown to have pH values near the theoretical value, in the range of pH 0–4. In the case of neutral ionophores containing a basic nitrogen atom, the pK_a of the nitrogen atom will determine the position of the dynamic range of the electrode. The small pK_a of the proposed ionophore has been shifted the dynamic range to small pH values. The accurate and precise measurement of acidic pH by using a flow injection system with potentiometric detection could also be accomplished. The results obtained in this work enable to conclude that this electrode can be used to the analysis of acids pH in real samples rapidly and accurately. All these characteristics point to the usefulness of the new electrode for measurements in acidic range.

Acknowledgement

The authors are thankful to the post-graduate office of Guilan University for the support of this work.

References

[1] V.V. Cosofret, E. Linder, R.P. Buck, R.P. Kusy, J.Q. Whitley, J. Electroanal. Chem. 345 (1993) 169.
[2] V.V. Cosofret, T.M. Nahir, E. Linder, R.P. Buck, J. Electroanal. Chem. 327 (1992) 137.
[3] E. Linder, V.V. Cosofret, R.P. Kusy, R.P. Buck, Talanta 40 (1993) 957.
[4] J. Chojnacki, J.F. Biernat, J. Electroanal. Chem. 277 (1990) 159.
[5] D.-H. Cho, K.-C. Chung, M.Y. Park, Talanta 47 (1998) 815.
[6] D.-H. Cho, K.-C. Chung, S.-S. Jeong, M.-Y. Park, Talanta 51 (2000) 761.
[7] W.-S. Han, M.-Y. Park, K.-C. Chung, D.-H. Cho, T.-K. Hong, Talanta 54 (2001) 153.
[8] W.-S. Han, M.-Y. Park, D.-H. Cho, T.-K. Hong, D.-H. Lee, J.-M Park, K.-C. Chung, Anal. Sci. 17 (2001) 727.
[9] A. Michalska, A. Hulannicki, A. Lewenstam, Analyst 119 (1994) 2417.
[10] C. Espedas-Torre, M.E. Meyerhoff, Anal. Chem. 67 (1995) 3108.
[11] V.M. Lutov, K.N. Mikhelson, Sens. Actuators B 18–19 (1994) 400.
[12] R. Yuan, Y.-Q. Chai, R.-Q. Yu, Analyst 117 (1992) 1891.
[13] V.V. Cosofret, T.M. Nahir, E. Lindner, R.P. Buck, J. Electroanal. Chem. 327 (1992) 137.
[14] E. Lindner, T. Rosatzin, J. Jeney, V.V. Cosofret, W. Simon, R.P. Buck, J. Electroanal. Chem. 352 (1993) 309.
[15] V.V. Cosofret, M. Erdosy, J.S. Raleigh, T.A. Johnson, M.R. Neuman, R.P. Buck, Talanta 43 (1996) 143.
[16] Y. Mi, E. Bakker, J. Electrochem. Soc. 144 (1997) L28.
[17] D. Kuruoğlu, E. Canel, S. Memon, M. Yılmaz, E. Kılıc, Anal. Sci. 19 (2003) 217.
[18] A. Demirel, A. Doğan, E. Canel, Sh. Memon, M. Yilmaz, E. Kiliç, Talanta 62 (2004) 123.
[19] X.-J. Liu, B. Peng, F. Liu, Y. Qin, Sens. Actuators B 125 (2007) 656.
[20] J.-P. Li, T.-Z. Peng, C. Fang, Anal. Chim. Acta 455 (2002) 53.
[21] D. Erne, D. Ammann, W. Simon, Chimica 33 (1979) 88.
[22] D. Erne, K.V. Schenker, D. Ammann, E. Pretsch, W. Simon, Chimica 35 (1981) 178.
[23] P. Anker, D. Ammann, W. Simon, Mickrochim. Acta 1 (1983) 237.
[24] U. Oesch, Z. Brzozka, A. Xu, B. Rusterholz, G. Suter, H.V. Pham, D.H. Welti, D. Ammann, E. Pretsch, W. Simon, Anal. Chem. 58 (1986) 2285.
[25] U. Oesch, Z. Brzozka, A. Xu, W. Simon, Med. Biol. Eng. Comput. 25 (1987) 414.
[26] P. Chao, D. Ammann, U. Oesch, W. Simon, F. Lang, Pflugers Arch. 411 (1988) 216.
[27] P. Schlthess, Y. Shijo, H.V. Pharm, E. Pretsch, D. Ammann, W. Simon, Anal. Chim. Acta 131 (1981) 111.
[28] D. Amman, F. Lanter, R.A. Steiner, P. Schulthess, Y. Shijo, W. Simon, Anal. Chem. 53 (1981) 2267.
[29] N. Oyama, T. Hirokawa, S. Yamaguchi, N. Ushizawa, T. Shimomura, Anal. Chem. 59 (1987) 258.
[30] J. Ruzicka, E.H. Hansen, Flow Injection Analysis, 2nd Ed., Wiley, New York, 1988.
[31] P.W. Alexander, T. Dimitrakopoulos, D.B. Hibbert, Talanta 44 (1997) 1397.
[32] M. Arvand, S.A. Asadollahzadeh, Talanta 75 (2008) 1046.
[33] M. Arvand, A.M. Moghimi, A. Afshari, N. Mahmoodi, Anal. Chim. Acta 579 (2006) 102.
[34] M.A. Zanjanchi, M. Arvand, A. Islamnezhad, N. Mahmoodi, Talanta 74 (2007) 125.
[35] M. Arvand, M. Eskandarnejad, Anal. Lett. 41 (2008) 2877.
[36] M. Arvand, T.M. Gholizadeh, N. Mahmoodi, Intern. J. Environ. Anal. Chem. in press.
[37] N.O. Mahmoodi, M.A. Zanjanchi, H. Kiani, J. Chem. Res. (2004) 438.
[38] E. Bakker, P. Bühlmann, E. Pretsch, Chem. Rev. 97 (1997) 3083.

[39] X. Yang, N. Kumar, H. Chi, D.D. Hibbert, P.N.W. Alexander, Electroanalysis 9 (1997) 549.
[40] P.L.H.M. Cobben, R.J.M. Egberink, J.B. Bomer, P. Bergveld, W. Verboom, D.N. Reinhoudt, J. Am. Chem. Soc. 114 (1992) 10573.
[41] E. Bakker, E. Pretsch, Anal. Chim. Acta 309 (1995) 7.
[42] S. Wakida, T. Masadome, T. Imato, Y. Shibutani, K. Yakabe, T. Shono, Y. Asano, Anal. Sci. 15 (1999) 47.
[43] U. Schaller, E. Bakker, U.E. Spichiger, E. Pretsch, Anal. Chem. 66 (1994) 391.
[44] M. Arvand, M.F. Mousavi, M.A. Zanjanchi, M. Shamsipur, S. Taghvaei, Anal. Lett. 35 (2002) 767.
[45] M. Arvand, A. Pourhabib, R. Shemshadi, M. Giahi, Anal. Bioanal. Chem. 387 (2007) 1033.
[46] E. Bakker, A. Xu, E. Pretsch, Anal. Chim. Acta 295 (1994) 253.
[47] V.V. Egorov, Y.V. Sin'kevich, Talanta 48 (1999) 23.
[48] E. Pungor, Z. Fether, G. Nagy, K. Toth, G. Horvai, M. Gratzl, Anal. Chim. Acta 109 (1979) 1–24.
[49] S. Khalil, S. Abd El-Aliem, J. Pharm. Biomed. Anal. 27 (2002) 25.
[50] L.I. Antropov, Theoretical Electrochemistry, Mir, Moscow, 1972.

Talanta 79 (2009) 639–647

Contents lists available at ScienceDirect

Talanta

journal homepage: www.elsevier.com/locate/talanta

Poly(3-methylthiophene)/palladium sub-micro-modified sensor electrode. Part II: Voltammetric and EIS studies, and analysis of catecholamine neurotransmitters, ascorbic acid and acetaminophen

Nada F. Atta*, Maher F. El-Kady

Department of Chemistry, Faculty of Science, University of Cairo, 1 Al Gamaa Street, Post Code 12613 Giza, Egypt

ARTICLE INFO

Article history:
Received 23 January 2009
Received in revised form 21 April 2009
Accepted 21 April 2009
Available online 3 May 2009

Keywords:
Poly(3-methylthiophene)
Pd nanoparticles
Electrochemical impedance spectroscopy
Catecholamine neurotransmitters
Ascorbic acid
Acetaminophen (paracetamol)

ABSTRACT

Promising voltammetric sensors based on the modification of Pt and poly(3-methylthiophene) (PMT) electrodes with Pd nanoparticles were achieved for the determination of catecholamine neurotransmitters, ascorbic acid and acetaminophen. Electrochemistry of the indicated compounds was studied at these electrodes and interesting electrocatalytic effects were found. Furthermore, simple, easily prepared one electrochemical step Pd-modified Pt electrode (Pt/Pd) is reported for the first time. Cyclic voltammetry (CV) and chronocoulometry (CC) were used for the determination of the apparent diffusion coefficients in different electrolytes at these electrodes and the values are in the range from 10^{-4} to 10^{-5} cm^2 s^{-1}. Furthermore, it was found that the method of polymer formation had a substantial effect on the synergism between the polymer film and the loaded metal particles towards the oxidation of dopamine (DA) in different supporting electrolytes. This was confirmed by the CV, CC and EIS (electrochemical impedance spectroscopy) as well as SEM (Scanning Electron Microscopy) results. Pt and PMT electrodes modified with Pd nanoparticles showed excellent results for the simultaneous determination of tertiary and quaternary mixtures of the studied compounds.

1. Introduction

Conducting polymers (CPs) are widely employed as coatings conferring the electrode systems antifouling properties and possibly activating electrocatalytic redox processes [1,2]. Among different CPs, PMT showed unusual characteristics towards the determination of catecholamine neurotransmitters compared to commonly used electrodes such as Pt, Au, glassy carbon, and chemically modified electrodes [3,4]. A step forward with respect to 'simple' modification with pristine CPs consist of the inclusion of metal functionalities inside the polymeric matrix, in order to further increase the performances of the resulting composite material. In particular, inclusion of noble metal nanoparticles (NPs), whose catalytic properties are well known [5], constitutes one of the most interesting possibilities. Similar composites based on polypyrrole and polyaniline have been recently reported [6–10]. Polythiophenes/NPs composites are even less studied [11–13]. Among polythiophenes, poly(3,4-ethylenedioxythiophene) (PEDOT) is presumably the most studied one but few recent papers are reported on PMT/NPs composites [14–16] in spite of its interesting properties. Among the reported conducting polymer–metal composites, platinum (Pt) is probably the most studied one. The fabrication and the subsequent characterization of palladium (Pd)-modified CP nanocomposites are not extensively reported in the literature [16,17]. On the other hand, the rate of charge or mass transport associated with redox reactions in modified films is commonly studied by determining the apparent diffusion coefficient (D_{app}) [18].

The development of voltammetric sensors for the determination of catecholamine neurotransmitters and specially dopamine (DA) has received considerable interest during the last few years [15]. They include dopamine (DA), epinephrine (E), and norepinephrine (NE). They play important roles in various biological, pharmacological and physical processes [19]. Recently, attention has been paid to develop a new generation of modified electrodes involving monolayers, conducting polymers and nanoparticles able to solve efficiently the problems encountered in the conventional unmodified electrodes.

Electrochemical impedance spectroscopy (EIS) is an effective technique for probing the features of chemically modified electrodes and for understanding electrochemical reaction rates [20,21]. EIS was used to characterize Pt-modified polyaniline (PAN) film in H_2SO_4 solution [22]. The results showed that compared with the pure polyaniline film|H_2SO_4 solution interface, the deposition of platinum in the polyaniline matrix greatly reduces the electrochemical charge transfer resistance (R_{ct}) in the platinum-modified polyaniline film|H_2SO_4 solution interface.

* Corresponding author. Tel.: +20 2 37825266.
E-mail address: nada_fah1@yahoo.com (N.F. Atta).

0039-9140/$ – see front matter © 2009 Elsevier B.V. All rights reserved.
doi:10.1016/j.talanta.2009.04.040

In the first part of this work, we have reported the modification of PMT polymer films with Pd particles [16]. In this paper, the electrochemistry of dopamine and other catecholamine neurotransmitters as well as ascorbic acid, acetaminophen and some organic compounds at the Pd nanoparticles modified PMT electrode are considered. Different methods were used for the formation of PMT films and the deposition of Pd nanoparticles. The effect of supporting electrolyte on the electrochemistry of these compounds is addressed as well. CV and CC are used for the determination of the apparent diffusion coefficient values for these compounds at different electrodes and electrolytes as it gives some information about the kinetics of charge transfer during the redox reactions of these compounds. The effect of the method of polymer film formation on the synergism between the polymer film and the subsequently loaded Pd particles is thoroughly studied. CV, CC, SEM and EIS measurements were used to address this point. EIS was used to study the capacitance and resistance of the metal modified polymer composites. Finally, this novel modified sensor electrode is used for the simultaneous detection of tertiary and quaternary mixtures of these compounds.

2. Experimental

2.1. Chemicals and reagents

All chemicals were used as received without further purification. 3-Methylthiophene (distilled under rotary evaporation prior to use) tetrabutyl ammonium hexafluorophosphate (Bu_4NPF_6), acetonitrile (HPLC grade), hydroquinone, catechol, dopamine, epinephrine, norepinephrine, methyl-L-DOPA, p-aminophenol, acetaminophen, ascorbic acid, sulfuric acid, nitric acid, hydrochloric acid, phosphoric acid, perchloric acid, sodium sulfate, sodium nitrate, sodium chloride, and sodium phosphate were supplied by Aldrich Chem. Co. (Milwaukee, WI, USA). Palladium (II) chloride was supplied by Scherimg Kaul Paum AG, Berlin, Germany. Aqueous solutions were prepared using double distilled water.

2.2. Electrochemical cells and equipments

Electrochemical polymerization and characterization were carried out with a three-electrode/one-compartment glass cell. Experimental details can be found elsewhere [16]. All experiments were performed at 25 °C.

Electrochemical impedance spectroscopy was performed using a Gamry-750 system and a lock-in-amplifier that are connected to a personal computer. The data analysis software was provided with the instrument and applied non-linear least square fitting with Levenberg-Marquardt algorithm. All impedance experiments were recorded between 0.1 Hz and 100 kHz with an excitation signal of 10 mV amplitude.

2.3. Electrodeposition of the polymer film on Pt electrode and further modification with Pd particles

Two electrochemical methods were employed for the deposition of the polymer film from a solution of 0.05 M 3-methylthiophene and 0.05 M Bu_4NPF_6 in acetonitrile. In the first method (BE method) the potential applied between the platinum disc working electrode and the reference (Ag/AgCl) is held constant at +1.8 V for 30 s (the electrode is indicated Pt/PMT(BE)). The second alternative (CV method) is to vary the potential with time, namely 50 mV s^{-1}, between two potential limits, ca. $E_i = -0.1$ V and $E_f = +1.8$ V for 15 cycles (the electrode is indicated Pt/PMT(CV)).

Further modification with Pd particles involves the following: a polymer film is prepared and washed with doubly distilled water. This was followed by the electrochemical deposition of Pd particles from a solution of 2.5 mM $PdCl_2$ in 0.1 M $HClO_4$ by applying a double potential step (BE) or cyclic voltammetric program (CV) to the polymer. The double potential step conditions are ($E_i = -0.05$ V, $\Delta t_i = 30$ s, $E_f = +0.01$ V, $\Delta t_f = 300$ s). In the cyclic voltammetric (CV) method, on the other hand, the electrode is cycled between −0.25 V and +0.65 V at a scan rate of 50 mV s^{-1} for 25 cycles [16]. Moreover, Pd particles were also deposited directly over Pt electrode.

3. Results and discussion

3.1. Electrochemistry of DA at Pt/PMT/Pd-modified electrodes

Initial studies of the voltammetric behavior of DA were performed using cyclic voltammetry. Fig. 1(A) compares typical cyclic voltammograms of 5 mmol L^{-1} dopamine in 0.1 mol L^{-1} H_2SO_4 recorded at four different working electrodes (i.e. bare Pt, Pt/PMT(BE), Pt/PMT(BE)/Pd(BE), and Pt/PMT(BE)/Pd(CV) electrodes). At bare Pt electrode, a poorly defined oxidation peak was observed at 664 mV whereas at Pt/PMT(BE) electrode the potential shifts negatively to 543 mV. Further, an increase in peak current is also observed due to the improvements in the reversibility of the electron transfer processes and the larger real surface area of the polymer film. The porous structure of conducting polymer allows dispersing the metal particles into the polymer matrix and generates additional electrocatalytic sites [23–25]. The electrodeposition of Pd particles on the polymer film causes a remarkable

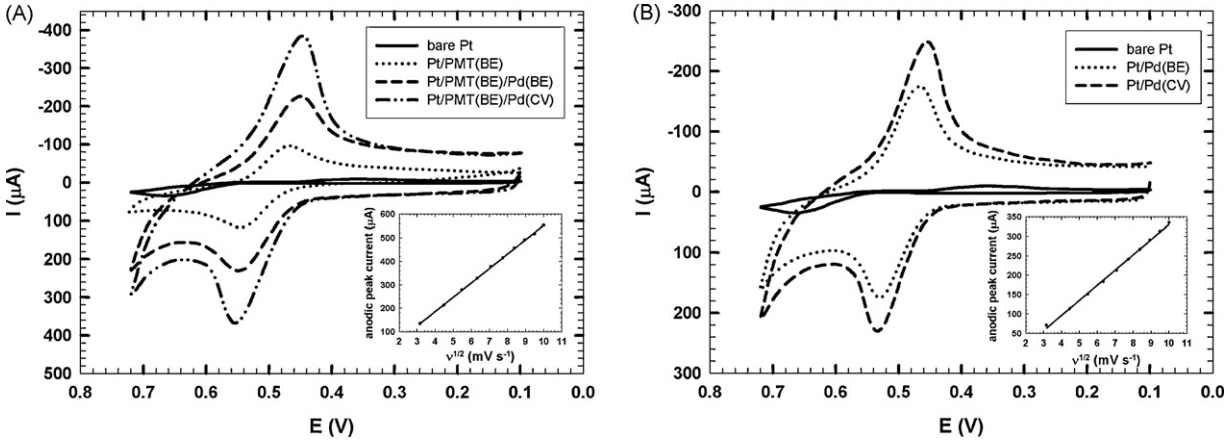

Fig. 1. Cyclic voltammetric behavior of 5 mmol L^{-1} DA/0.1 mol L^{-1} H_2SO_4 at: (A) bare Pt, Pt/PMT(BE), Pt/PMT(BE)/Pd(BE), and Pt/PMT(BE)/Pd(CV) electrodes. (B) Bare Pt, Pt/Pd(BE) and Pt/Pd(CV) electrodes. Scan rate = 50 mV s^{-1}. (Inset: relationship between the square root of scan rate and anodic peak current.)

Table 1
Summary of the cyclic voltammetry results obtained at Pt/PMT(BE), Pt/PMT(CV), Pt/PMT(BE)/Pd(BE), and Pt/PMT(BE)/Pd(CV) in 5 mmol L^{-1} analyte/0.1 mol L^{-1} H_2SO_4.

Compound	Pt/PMT				Pt/PMT(BE)/Pd			
	BE[a]		CV[a]		BE[b]		CV[b]	
	E_{pa} (mV)	I_{pa} (μA cm^{-2})	E_{pa} (mV)	I_{pa} (μA cm^{-2})	E_{pa} (mV)	I_{pa} (μA cm^{-2})	E_{pa} (mV)	I_{pa} (μA cm^{-2})
Hydroquinone	446	103.2	473	80.3	443	164.1	455	262.2
Catechol	551	120.4	591	105.2	555	188.8	553	289.3
Dopamine	543	110.3	572	89.5	549	193.7	556	321.5
Methyl-L-DOPA	565	125.1	594	90.1	566	188.6	579	292.4
Epinephrine	574	99.6	596	79.9	561	144.4	561	249.2
Norepinephrine	573	110.9	593	80.2	556	134.2	556	215.1
p-Aminophenol	532	119.5	551	82.3	528	153.1	556	330.8
Acetaminophen	693	135.3	718	121.4	696	213.5	692	361.7
Ascorbic acid	360	58.5	362	47.4	311	128.6	314	197.6

[a] The method of formation of the polymer film.
[b] The method of deposition of Pd particles.

increase in peak currents. Thus, the deposition of the polymer film on Pt electrode decreases the potential of oxidation substantially (i.e. thermodynamically feasible reaction). Further, the electrodeposition of Pd particles over PMT film enhances the redox current effectively indicating an improvement in the electrode kinetics by the presence of Pd particles. The remarkable enhancement in current response followed by a drop in peak potential provides clear evidence of the catalytic effect of the Pd-modified PMT electrodes that acts as a promoter to enhance the electrochemical reaction, considerably accelerating the rate of electron transfer.

Now, what about the catalytic effect of Pd particles when Pd is deposited directly to Pt electrode? CVs of 5 mmol L^{-1} DA were recorded at Pt/Pd(BE) and Pt/Pd(CV) electrodes in 0.1 mol L^{-1} H_2SO_4, Fig. 1(B). DA exhibits well-defined redox peaks at the Pd-modified electrodes with the oxidation potential shifted negatively to 466 and 456 mV at Pt/Pd(BE) and Pt/Pd(CV) electrodes, respectively. A substantial increase in the peak currents is also observed but it is still less than the corresponding values at Pt/PMT/Pd electrodes. The aforementioned results confirm the key role played by Pd particles on the catalytic oxidation of DA.

Further, the linear relationship between the peak current and square root of scan rate (Fig. 1, insets) in the scan rate range from 10 to 100 mV s^{-1} points to the diffusion-controlled nature of DA oxidation on Pt/Pd and Pt/PMT/Pd electrodes.

3.2. Electrochemistry of catecholamine neurotransmitters, acetaminophen, and ascorbic acid

Initial studies of the voltammetric behavior of all compounds were performed using cyclic voltammetry. Tables 1 and 2 summarize the electrochemical data for the oxidation of some molecules of biological interest, namely, dihydroxy compounds (hydroquinone, catechol), catecholamine neurotransmitters (dopamine, epinephrine, and norepinephrine), methyl-L-DOPA, as well as p-aminophenol, acetaminophen and ascorbic acid. The data were collected from the cyclic voltammograms at Pt/PMT(BE), Pt/PMT(CV), Pt/PMT(BE)/Pd(BE), Pt/PMT(BE)/Pd(CV) and Pt, Pt/Pd(BE), Pt/Pd(CV) electrodes for the compounds indicated (BE refers to formation using bulk electrolysis and CV refers to formation using cyclic voltammetry of the corresponding interface). The scan rate is 50 mV s^{-1}, and the analyte concentration is 5 mmol L^{-1} in 0.1 mol L^{-1} H_2SO_4 for the electrodes studied. Except for ascorbic acid and acetaminophen (undergo irreversible oxidation) all test substances displayed reversible behavior in 0.1 mol L^{-1} H_2SO_4 electrolyte. From the biosensor point of view, the oxidation peak potential values, E_{pa}, for these substances as well as their corresponding oxidation peak current values, I_{pa}, are more important than their reversible behavior. Thus, all compounds show significant decrease in the E_{pa} values at the Pd-modified electrodes. Moreover, the I_{pa} increased in the following order: I_{pa} values at Pt < Pt/PMT(BE) < Pt/PMT(BE)/Pd(BE) < Pt/PMT(BE)/Pd(CV) and Pt < Pt/Pd(BE) < Pt/Pd(CV). The electrodeposition of Pd over bare Pt- or PMT-modified electrode effectively enhances its electrocatalytic activity towards the oxidation of the indicated compounds. Furthermore, Pd-modified electrodes show excellent stability of the redox signal in the repeated cyclic voltammograms in solutions containing the compounds of study up to 50 cycles.

3.3. Effect of solution pH

The redox system should be affected by changes in pH because of the involvement of protons in the overall electrode reaction. The effect of changing the pH of the medium on the response of

Table 2
Summary of the cyclic voltammetry results obtained at Pt, Pt/Pd(BE), and Pt/Pd(CV) electrodes in 5 mmol L^{-1} analyte/0.1 mol L^{-1} H_2SO_4.

Compound	Pt		Pt/Pd			
			BE[a]		CV[a]	
	E_{pa} (mV)	I_{pa} (μA cm^{-2})	E_{pa} (mV)	I_{pa} (μA cm^{-2})	E_{pa} (mV)	I_{pa} (μA cm^{-2})
Hydroquinone	562	42.4	429	99.5	431	156.4
Catechol	686	32.9	536	120.1	538	177.2
Dopamine	664	34.7	530	160.2	534	214.1
Methyl-L-DOPA	689	31.2	543	80.5	558	165.9
Epinephrine	737	29.8	537	78.6	555	148.1
Norepinephrine	756	32.2	538	75.1	545	145.5
p-Aminophenol	617	25.1	523	109.8	532	160.4
Acetaminophen	728	38.8	695	173.6	694	226.9
Ascorbic acid	–[b]	–[b]	296	55.2	294	90.5

[a] The method of deposition of Pd particles.
[b] No value was observed up to 1.2 V.

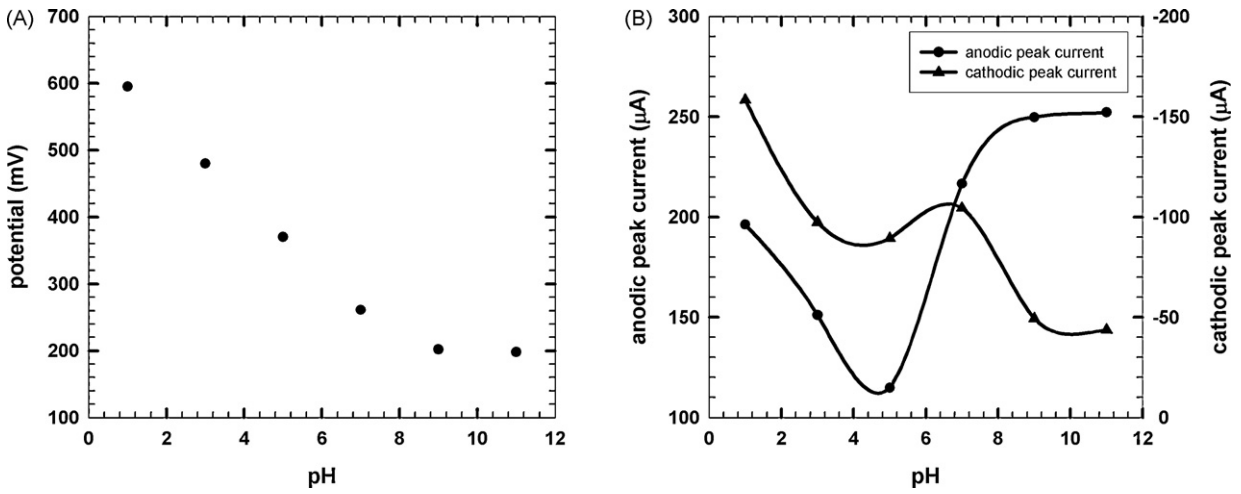

Fig. 2. Effect of solution pH on the electrochemical behavior of Pt/PMT(BE)/Pd(CV) electrode. (A) Dependence of the anodic peak potential of dopamine oxidation on solution pH. (B) Dependence of the anodic peak current of dopamine oxidation on solution pH.
Results were taken from cyclic voltammograms carried out in 5 mmol L^{-1} dopamine/0.1 mol L^{-1} phosphate buffer of different pH values at a scan rate of 50 mV s^{-1}.

electrodes was examined in phosphate buffers. As illustrated in Fig. 2(A), the anodic peak potential shifts linearly to more negative values as pH increases over a range from 1 to 7. The slope is −55.6 mV/pH unit for Pt/PMT(BE)/Pd(CV) electrode. The nearly Nernstian slope obtained here suggests two-proton, two-electron process for dopamine oxidation [26–28]. According to the Nernst equation, the slope of −55.6 mV/pH reveals that the proportion of the electron and proton involved in the reactions is 1:1. As the dopamine oxidation is a two-electron process, the number of protons involved is also predicted to be two. In solution, the pK_a's of dopamine are 8.9 (pK_{a1}) and 10.6 (pK_{a2}) [29]. A linear behavior was observed for pH values in the range from 1 to 7 and just a little deviation was obtained at pH 9. This indicates the deprotonation of dopamine at pH 9 so that it is no longer a two-proton, two-electron process at this point and other equilibria should be taken into account. At pH 11 the redox reaction of DA is no longer pH dependent as dopamine is completely deprotonated at this pH.

Fig. 2(B) shows that from pH 1 to 5 the anodic peak current decreases with increasing solution pH value. Dopamine exists in the protonated form at low pH values. The current of oxidation increases abruptly as the pH increases from 5 to 7. Further, beyond pH 7 the current increases with pH but at a lower rate.

3.4. Apparent diffusion coefficients of the studied compounds

The presence of the polymer film on the surface of an electrode tends to complicate the mathematical treatment required for the diffusion coefficient calculation [30]. It has been assumed, by many researchers, that the polymer film is another layer that the analyte or a counter anion has to penetrate in order for the electron to move through the film for a redox reaction to be observed. This movement of the charges through the polymer layer is known as the "electron hopping process" [31]. Effective diffusion coefficients for redox reactions at various polymer films were, as expected, much lower (10^{-10} to 10^{-15} cm^2 s^{-1} [32]) than those typically found in aqueous solution (ca. 10^{-5} cm^2 s^{-1} [33]). Furthermore, the effective diffusion coefficient values for different polymers can vary by several orders of magnitudes for the same analyte [34].

In this study, the dependence of the anodic peak current density on the scan rate has been used for the estimation of the "apparent" diffusion coefficient, D_{app}, of various organic species. For a diffusion-controlled process, a plot of the anodic peak current values versus the square root of the scan rate results in a straight-line relationship. The slope of these lines should result in an estimation

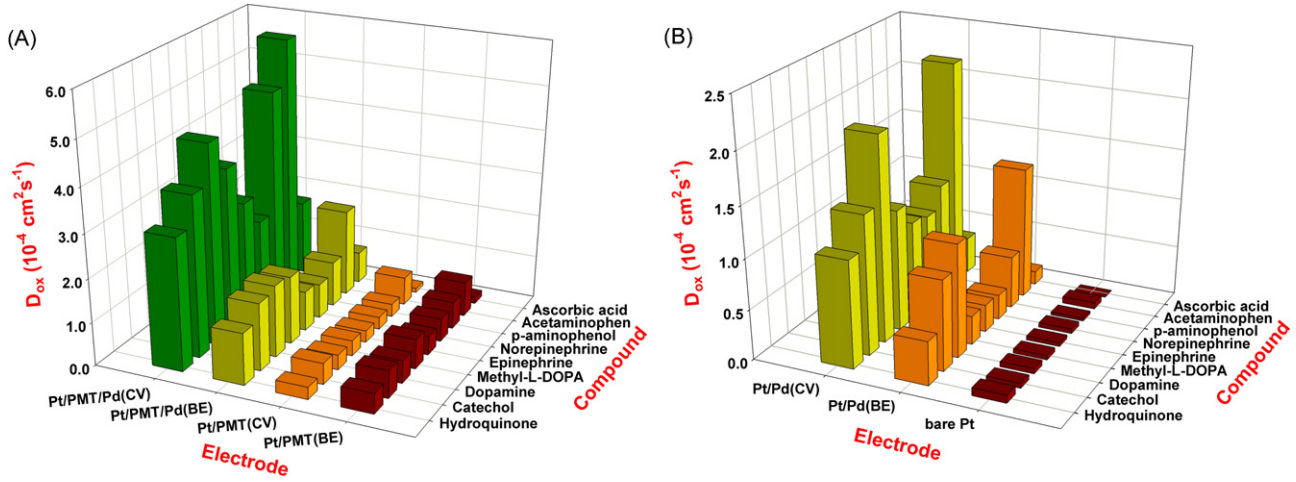

Fig. 3. Apparent diffusion coefficient values for all studied compounds as calculated from the oxidation segment of the corresponding CVs at: (A) bare Pt, Pt/Pd(BE), and Pt/Pd(CV) electrodes. (B) Pt/PMT(BE), Pt/PMT(CV), Pt/PMT(BE)/Pd(BE), and Pt/PMT(BE)/Pd(CV) electrodes.

of the value of D_{app} according to Randles Sevcik equation [35]:

$$i_p = 2.69 \times 10^5 n^{3/2} A\, C^0 D^{1/2} \nu^{1/2} \quad (1)$$

where i_p is the peak current density ($A\,cm^{-2}$), n is the number of electrons transferred, at $T = 298\,K$, A is the geometrical electrode area ($0.0176\,cm^2$), C^0 is the analyte concentration ($5 \times 10^{-6}\,mol\,cm^{-3}$), D is the diffusion coefficient of the electroactive species ($cm^2\,s^{-1}$), and ν is the scan rate ($V\,s^{-1}$). It is important to notice that the apparent surface area used in the calculations did not take into account the surface roughness, which is an inherent characteristics for all polymer films formed using the electrochemical technique. Fig. 3 shows D_{app} values at different electrodes for the studied compounds.

The calculated D_{app} values are between 10^{-4} and $10^{-7}\,cm^2\,s^{-1}$. Those values were observed for the following electrodes: PMT-modified electrodes (Pt/PMT(BE), Pt/PMT(CV)), Pd-modified PMT electrodes (Pt/PMT(BE)/Pd(BE), Pt/PMT(BE)/Pd(CV)), bare Pt-, Pd-modified Pt electrodes (Pt/Pd(BE), and Pt/Pd(CV)). D_{app} values are higher than those reported earlier in the literature [36,37]. This is possibly due to the quick mass transfer of the analyte molecules towards electrode surface from bulk solutions and/or fast electron transfer process of electrochemical oxidation of the analyte molecule at the interface of the electrode surface and the solutions [38,39]. These results are consistent with recent publications [40–42]. Furthermore, it also shows that the redox reaction of the analyte species takes place at the surface of the electrode under the control of the diffusion of the molecules from solution to the electrode surface and not within the polymer and polymer/Pd matrices. From the data of Fig. 3 the following trends can be noticed:

- D_{app} values for bare Pt and Pt electrodes modified with Pd increase in the following order: Pt < Pt/Pd(BE) < Pt/Pd(CV) which confirms the role of Pd particles in improving the electron transfer kinetics at the electrode/solution interface.
- D_{app} values for PMT-modified Pt electrodes increases in the following order: Pt/PMT (CV) < Pt/PMT(BE) for all analytes studied. SEM micrographs show that Pt/PMT(BE) is more compact than Pt/PMT(CV), which seems to be more porous [16]. The compact structure of Pt/PMT(BE) enhances the diffusion of molecules at the electrode/solution interface. The diffusional current and the diffusion coefficients are therefore higher at the relatively more homogeneous Pt/PMT(BE) electrode.
- D_{app} values for PMT electrodes modified with Pd particles using different methods increase in the following order: Pt/PMT(BE)/Pd(BE) < Pt/PMT(BE)/Pd(CV) for all analytes. SEM micrographs [16] show that the Pd particles are smaller and homogenously distributed in the case of Pt/PMT(BE)/Pd(CV) electrode, while larger Pd particles with dendritic shape are observed in the case of Pt/PMT(BE)/Pd(BE) electrode. This confirms that the size and homogeneity of the deposited particles affect the electroactivity of these modified electrodes [43].
- D_{app} values at the polymer modified electrodes increase in the following order: Pt/PMT(CV) < Pt/PMT(BE) < Pt/PMT(BE)/Pd(BE), Pt/PMT(BE)/Pd(CV) which is in agreement with the cyclic voltammetry results of Section 3.2.

3.5. Effect of the supporting electrolyte

In this section a study of the effect of different supporting electrolytes on the electrochemical behavior of different electrodes and the calculated diffusion coefficient values of dopamine at the studied electrodes are presented. It was reported that both redox potential and current depend on the kind of electrolyte used [4]. The supporting electrolytes used were acids (H_2SO_4, HNO_3, $HClO_4$, HCl, and H_3PO_4) and their corresponding sodium salts (Na_2SO_4, $NaNO_3$, NaCl, and Na_3PO_4). Furthermore, the effect of the method of polymerization on the synergistic electrocatalytic effect between the polymer film and the loaded metal particles towards the oxidation of DA in different supporting electrolytes is considered. For this reason, a comparison is made between the behavior of Pt/PMT(BE)/Pd and Pt/PMT(CV)/Pd, where Pd was deposited by the CV method.

The anodic peak potentials, E_{pa}, of DA for all the modified electrodes are much less positive than those obtained at the conventional Pt bare electrode in all electrolytes, Table 3. This confirms the catalytic effect of the modified surfaces over conventional electrodes. It is also important to notice that for Pt/PMT/Pd electrodes, where PMT is deposited by BE and CV methods, E_{pa} values are always lower at this electrode for which PMT is formed by BE method in all electrolytes. This suggests the higher catalytic activity of the PMT/Pd composite in which PMT is formed by BE method over that with CV method. In addition, this difference increases when the sodium salts were used as electrolytes. Moreover, the anodic peak currents, I_{pa} (Table 3) obtained at these electrodes increases in the following order irrespective of the electrolyte type Pt < Pt/PMT(BE) < Pt/Pd < Pt/PMT(BE)/Pd. This result agrees with the cyclic voltammetry data (Fig. 1) and it also shows that the relative electrocatalytic behavior of these electrodes is constant in all electrolytes.

3.5.1. Diffusion coefficients of dopamine in different electrolytes

The diffusion coefficients, D_{app}, of DA in different electrolytes were calculated from cyclic voltammetry (CV), chronocoulometry (CC) experiments and the results were compared. D_{app} values were calculated from CV as in Section 3.4, while CC data were used to calculate the value of D_{app} according to the formula given by Anson [44]:

$$Q = \frac{2nFACD^{1/2}t^{1/2}}{\pi^{1/2}} \quad (2)$$

From the slope of the linear relationship between Q and $t^{1/2}$, D can be determined if C (concentration, $mol\,cm^{-3}$), A (surface area of the electrode, cm^2), and n (electron transfer number) are known. Chronocoulometric experiments were performed in the solution

Table 3
Summary of the cyclic voltammetry results obtained at Pt, Pt/PMT(BE), Pt/Pd(CV), Pt/PMT(CV)/Pd, and Pt/PMT(BE)/Pd in 5 mmol L^{-1} DA/0.1 mol L^{-1} electrolyte.

Electrolyte	Pt		Pt/PMT(BE)		Pt/Pd		Pt/PMT(CV)/Pd		Pt/PMT(BE)/Pd	
	E_{pa} (mV)	I_{pa} ($\mu A\,cm^{-2}$)	E_{pa} (mV)	I_{pa} ($\mu A\,cm^{-2}$)	E_{pa} (mV)	I_{pa} ($\mu A\,cm^{-2}$)	E_{pa} (mV)	I_{pa} ($\mu A\,cm^{-2}$)	E_{pa} (mV)	I_{pa} ($\mu A\,cm^{-2}$)
H_2SO_4	664	34.7	543	109.2	536	207.9	583	193.2	556	321.1
HNO_3	688	29.4	540	117.7	540	194.9	613	220.4	566	324.5
$HClO_4$	686	32.2	545	132.0	537	193.2	582	216.7	562	287.9
H_3PO_4	734	28.2	545	69.3	543	153.1	623	139.1	573	215.1
HCl	675	34.5	541	77.4	545	223.0	585	35.8	575	253.7
Na_2SO_4	605	22.56	466	49.2	451	118.9	580	73.7	493	184.2
$NaNO_3$	636	24.1	500	32.5	490	113.8	620	35.6	533	176.0
NaCl	671	23.5	530	45.4	496	110.1	601	32.6	539	163.2
Na_3PO_4	−72	12.1	−87	57.1	−88	99.7	−80	36.1	−85	148.4

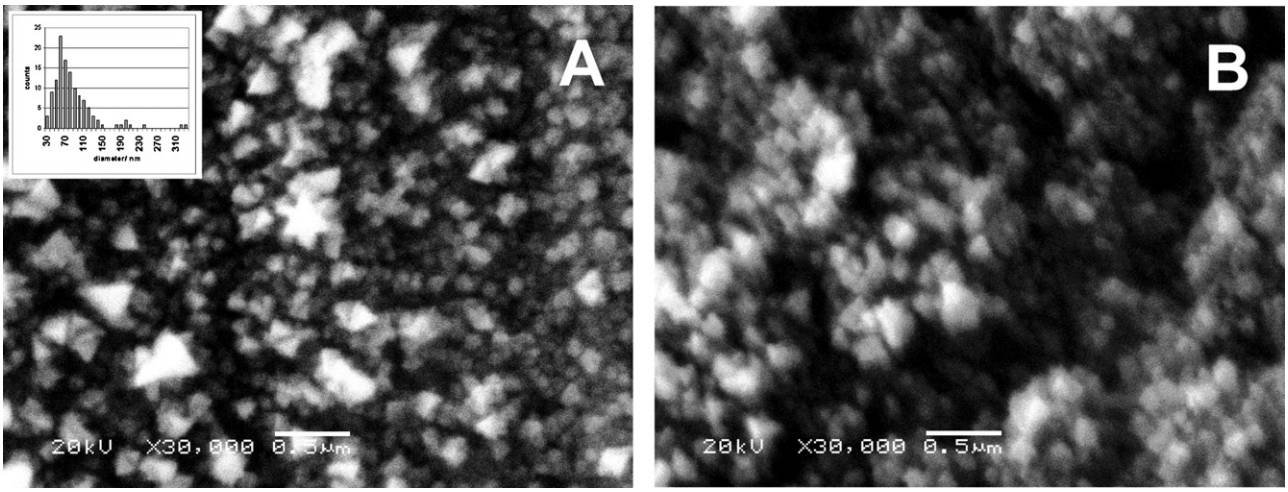

Fig. 4. SEM for (A) Pt/PMT(BE)/Pd(CV) and (B) Pt/PMT(CV)/Pd(CV). The inset: a histogram showing the particle size distribution.

containing dopamine and then the slope of the Anson plot is subtracted from the slope of the Anson plot of the same experiment carried out in the supporting electrolyte without the electroactive species. The resulting slope was then used to calculate D_{app} from the Anson equation shown above. D_{app} values obtained from CC were in close agreement with those calculated from CV measurements. D_{app} values range from 10^{-7} to 10^{-4} cm^2 s^{-1}. These values are close to the values of D_{app} in solution. Again, this is possibly due to the fast mass transfer of the analyte molecules towards electrode surface from bulk solutions and/or fast electron transfer process of electrochemical oxidation of the analyte molecule at the interface of the electrode surface and the solutions [38,39].

D_{app} values of DA increase in the following order in all electrolytes Pt < Pt/PMT(BE) < Pt/Pd(CV) < Pt/PMT(BE)/Pd(CV). However, the diffusion coefficients at Pt/PMT(CV)/Pd(CV) electrode are always lower than Pt/PMT(BE)/Pd(CV). The difference between these two electrodes increases in neutral and alkaline media in which D_{app} values at Pt/PMT(CV)/Pd(CV) are even lower than the individual Pt/PMT and Pt/Pd electrodes. SEM analysis can be used to confirm the difference in morphology between Pt/PMT(CV)/Pd(CV) and PT/PMT(BE)/Pd(CV) electrodes, Fig. 4. Thus, higher loading of Pd with smaller particle size is achieved at the latter electrode. The particle size distribution obtained at Pt/PMT(BE)/Pd(CV) indicates that the most frequent particle size is around 60 nm. Thus, the amount of Pd, particle size, better distribution as well as the different morphologies of the polymer substrate and the difference in the doping level of the polymer films [16] may be the reason for the difference between these two electrodes.

3.6. Analysis of mixtures

The determination of catecholamines in biological samples is crucial for the diagnosis of many diseases [45]. However, electrochemical oxidation of catecholamines especially dopamine (DA) at conventional electrodes is found difficult because of (a) fouling of the electrode surface due to the adsorption of oxidation products, (b) interference due to the co-existence of interfering compounds such as ascorbic acid (AA) and others in the biological fluids, which also undergoes oxidation more or less at the same potential [46].

Acetaminophen (paracetamol), APAP, is also likely to interfere with DA and AA determination [47]. To our knowledge, only one report was published for the analysis of AA, DA, and APAP mixture [41]. The differential pulse voltammograms (DPV) for the analysis of a tertiary mixture of 5 mmol L^{-1} AA, 5 mmol L^{-1} DA, and 5 mmol L^{-1} APAP in 0.1 mol L^{-1} H_2SO_4 over bare Pt and Pt/Pd (CV) electrodes was measured. An unresolved oxidation peak was observed in the potential range from 0.1 to 0.75 V illustrating that the oxidation peaks of AA, DA, and APAP cannot be separated on the bare Pt. When the Pt/Pd(CV) electrode was used, three well-separated signals were obtained. The anodic peak potentials of AA, DA, and APAP oxidations on the Pt/Pd(CV) electrode were at approximately 256, 500, and 656 mV, respectively. DPVs for the analysis of the same mixture of AA, DA, and APAP, at Pt/PMT(BE) and Pt/PMT(BE)/Pd(CV) electrodes were also measured. Three oxidation peaks appeared on each electrode corresponding to AA, DA, and APAP. The oxidation potentials on Pt/PMT are observed at 268, 500, and 664 mV for AA, DA, and APAP, respectively. On the other hand, the oxidation peaks of AA, DA, and APAP on Pt/PMT(BE)/Pd(CV) electrode appeared at 260, 508, and 670 mV, respectively. Therefore, better separation of the signals was achieved on Pt/PMT(BE)/Pd(CV) electrode. Furthermore, Pt/PMT(BE)/Pd(CV) electrode has high selectivity for the determination of DA in the presence of AA and APAP. This can be checked by investigating the values of oxidation current on both electrodes. Lower oxidation current for AA and APAP, higher oxidation current for DA was achieved at Pt/PMT/Pd(CV) electrode with respect to Pt/PMT electrode. Hence, DA can be easily determined on Pt/PMT/Pd electrode even in the presence of higher concentration of AA and APAP (analysis of DPV results indicate that DA/AA current ratio = 19.1:1 on Pt/PMT/Pd(CV) and 2.98:1 on Pt/PMT). A comparison of the behavior of these electrodes with respect to the oxidation of DA and AA shows the synergism between the polymer matrix and the embedded Pd nanoparticles.

Fig. 5 shows the DPV results for the analysis of a quaternary mixture containing 5 mmol L^{-1} AA, 5 mmol L^{-1} hydroquinone (HQ), 5 mmol L^{-1} DA, and 5 mmol L^{-1} APAP in 0.1 mol L^{-1} H_2SO_4. When this mixture is analyzed on bare Pt electrode (Fig. 5(A)), a rather broad oxidation peak was obtained and the peak potentials of the existing species were indistinguishable. It is therefore impossible to determine the individual concentrations of these compounds because of the merged voltammetric oxidation peak. However, modification of the Pt electrode with Pd particles resolved the merged voltammetric peak into four well-defined peaks at potentials around 264, 408, 504, and 656 mV for AA, HQ, DA, and APAP, respectively. Fig. 5(B) shows the same results as in Fig. 5(A) but on Pt/PMT(BE) and Pt/PMT(BE)/Pd (CV) electrodes. Again, better selectivity for the resolved determination of DA was achieved at Pt/PMT(BE)/Pd(CV) electrode as the current due to the interferences (AA and APAP) has been decreased while at the same time the current due to DA has been increased.

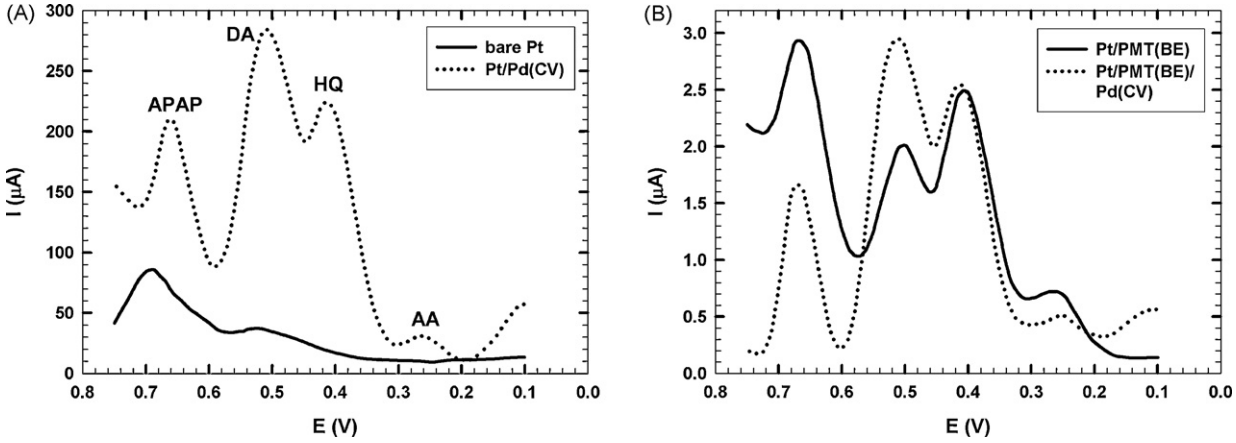

Fig. 5. DPVs for a quaternary mixture of 5 mmol L^{-1} AA, 5 mmol L^{-1} HQ, 5 mmol L^{-1} DA and 5 mmol L^{-1} APAP in 0.1 mol L^{-1} H_2SO_4 at: (A) bare Pt and Pt/Pd(CV) electrodes and (B) Pt/PMT(BE) and Pt/PMT(BE)/Pd(CV) electrodes. DPV conditions: pulse amplitude = 50 mV, scan rate = 20 mV s^{-1}, sample width = 17 ms, pulse width = 50 ms.

3.7. Electrochemical impedance spectroscopy (EIS) studies

EIS data were obtained for PMT modified with Pd particles at ac frequency varying between 0.1 Hz and 100 kHz with an applied potential in the region corresponding to the electrolytic oxidation of dopamine in 0.1 mol L^{-1} H_2SO_4. Effect of the method of formation of PMT on the synergistic effect between the polymer film and the loaded metal particles was studied. The data are presented as a relation between the impedance and the frequencies, the Bode plot. In all cases the experimental data will be compared to an "equivalent circuit" that uses some of the conventional circuit elements, namely: resistance, capacitance, diffusion and induction elements. Thus, it is anticipated that the changes in the conditions of the experiments, as will be described, are reflected on the electrochemical parameters. The equivalent circuit is shown in Fig. 6A. In this circuit, R_u is the solution resistance. Capacitors in EIS experiments often do not behave ideally; instead they act like a constant phase element (*CPE*). Therefore, *CPE1* and *CPE* are constant phase elements and *m* and *n* are their corresponding exponents (*m*, *n* are less than one). C_p and C_f represent the capacitance of the double layer. Diffusion can create an impedance known as the Warburg impedance, *W*.

Table 4 lists the best fitting values calculated from the equivalent circuit (Fig. 6A) for the impedance data of Fig. 6(B and C). The average error (χ^2) of the fits for the mean error of modulus was in the range: $\chi^2 = (1.5–3.8) \times 10^{-2}$. The following observations and conclusions could be drawn from Table 4:

- For PMT films formed by CV and relatively high applied potentials, the capacitive component of the film increases as expected and is in good agreement with the CVs' that depicts a behavior similar to a capacitor with relatively large capacitance value [48,49]. On the other hand, PMT films formed by BE show relatively decreased values of the capacitive component indicating a more porous character of the films as confirmed by SEM pictures.
- It is important to notice that ionic species are solvated and their migration within the polymeric film depends on the pore size of the film. And since anionic species are the major components

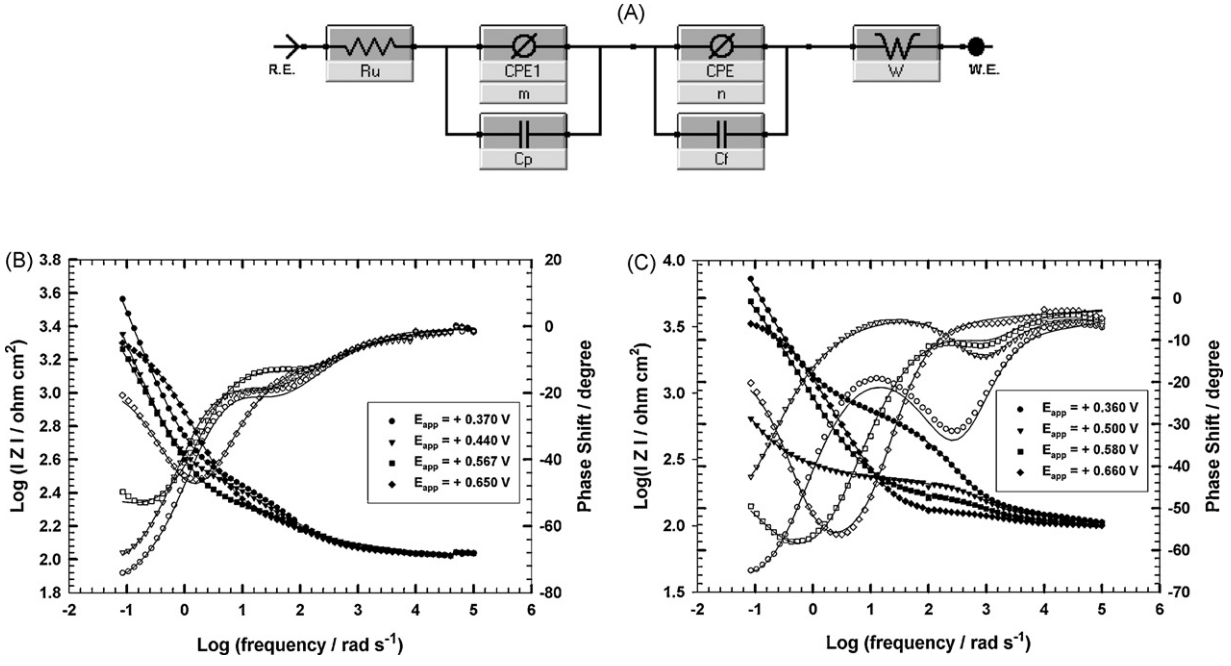

Fig. 6. (A) Equivalent circuit used in the fit procedure of the impedance spectra. The results were analyzed using Levenberg-Marquardt/simplex algorithms based on a complex non-linear least squares procedure. The Bode plot of impedance spectra for (B) Pt/PMT(BE)/Pd(CV), (C) Pt/PMT(CV)/Pd(CV) all tested in 5 mmol L^{-1}/0.1 mol L^{-1} H_2SO_4.

Table 4
EIS fitting data corresponding to Fig. 6(B and C), where I = Pt/PMT(BE)/Pd(CV), II = Pt/PMT(CV)/Pd(CV).

Electrode	E/V	R_u (Ω cm^2)	*CPE1* (F cm^{-2})	m	C_p (μF cm^{-2})	*CPE* (F cm^{-2})	n	C_f μF cm^{-2})	W (Ω s$^{-1/2}$)
I	+0.370	110.5	13,990	0.700	509	383.7	0.227	11.29	101.7
	+0.440	110.6	16,230	0.199	996	431.9	0.269	7.789	10.0
	+0.567	109.2	246.3	0.219	8.29	2146	0.284	762.5	40.0
	+0.650	108.3	30.8	0.280	6.59	1371	0.131	239.3	60.0
II	+0.360	116.7	899	0.15	2.22	29,170	0.10	353	987.1
	+0.500	111.2	181	0.10	1.59	544	0.52	2780	40.0
	+0.580	104.7	56	0.05	3.17	4123	0.35	234	786.6
	+0.660	99.8	2796	0.17	0.978	200	0.26	1.69	60.0

compensating for the charge within the polymer film [48,50], contribution of solvent used that may catalytically decompose at the film/electrolyte interface is not expected except at relatively high applied potentials. Thus, polarization resistance appreciably decreases with increase in applied potential for films formed by CV or BE. The change in polarization resistance is more pronounced in the case of films prepared by BE. This could be attributed to a change in morphology that is mainly dictated by the porosity of the films. The shape and compactness of each film, namely those formed by two different synthetic methods, should also contribute to the rate and mechanism of charge transfer leading to the remarkable impedance characteristics of each film.

- Moreover, the impedance response of the films at the low-frequency domain should be controlled by the capacitive elements. However, the deposition of the film layer for instance leads to depreciated effect for applied potential for various polymer types and electrochemical method used for deposition.
- From the data indicated in Table 4, the value of solution resistance, R_u, is almost constant within the limits of the experimental errors. On the other hand, the ionic/electronic charge transfer resistance, *CPE*, shows gradual increase then decrease in value with the applied potential indicating that the migration of ionic species within the film pores is not the only mean of charge exchange at the polymer/electrolyte interface. This is also observed with the relative change in the value of the Warburg impedance, *W*, which changes accordingly with the charge transfer resistances. The last observation indicates the key role played by the morphology, film composition, and its thickness in the charge transfer. Another indication of this model is proved by the noticed increase in the capacitance values with applied potential and whether the film is formed by CV or BE methods.
- It is important to notice that for all films, the charge transfer shows relatively small changes before reaching full oxidized polymer films. This indicates that while the ionic conductance within the film is a function of potential and nature of the film, the electronic conductance is not affected with the same conditions. Therefore, *CPE* represents mainly electronic resistance while *CPE1* represents the predominant diffusion influence on the charge transfer process.

Although the general trend for all films indicate a gradual shift to lower impedance values with applied potential, it would be difficult within the scope of this study to clarify the relation between the pore size and the film morphology and their influence on the subsequent effect on the metal deposition.

4. Conclusions

The electrochemistry of DA and other catecholamines as well as ascorbic acid and acetaminophen at Pt/PMT/Pd electrodes was studied. A remarkable enhancement in current response followed by a drop in peak potential was observed which provide clear evidence of the catalytic effect of the Pd-modified PMT electrodes. What was interesting is the Pt electrodes modified with Pd particles (Pt/Pd) which resulted in well-defined redox peaks with low oxidation potential and high peak current values. This result puts this kind of metal modified Pt electrodes in the category of promising and highly electroactive modified electrodes. The apparent diffusion coefficients were also calculated at different electrodes and electrolytes for the compounds studied. D_{app} values indicate quick mass transfer of the analyte molecules towards electrode surface from bulk solutions and/or fast electron transfer process of electrochemical oxidation of the analyte molecule at the interface of the electrode surface and the solutions. Furthermore, it was found that the method of polymerization had a substantial effect on the synergism between the polymer film and the loaded metal particles towards the oxidation of DA in different supporting electrolytes. This was confirmed from the CV, CC, EIS and SEM results. Pt/PMT(BE)/Pd(CV) and Pt/Pd(CV) electrodes showed excellent results for the simultaneous determination of tertiary and quaternary mixtures of the studied compounds. EIS was used to study the capacitance and resistance of the metal modified polymer composites.

Acknowledgements

The authors would like to acknowledge the financial support from Cairo University through the Vice President Office for Research Funds and “MUCSAT” for SEM measurements.

References

[1] U. Lange, N.V. Roznyatovskaya, V.M. Mirsky, Anal. Chim. Acta 614 (2008) 1.
[2] A. Malinauskas, R. Garjonyte, R. Mazeikiene, I. Jureviciute, Talanta 64 (2004) 121.
[3] A. Kelley, B. Angolia, I. Marawi, J. Solid State Electrochem. 10 (2006) 397.
[4] H.B. Mark Jr., N. Atta, Y.L. Ma, K.L. Petticrew, H. Zimmer, Y. Shi, K.L. Lunsford, J.F. Rubinson, A. Galal, Bioelectrochem. Bioenerg. 38 (1995) 229.
[5] G.C. Bond, C. Louis, D.T. Thompson, Catalysis by Gold, Catalytic Science Series, vol. 6, World Scientific Publishing, 2006.
[6] J. Li, X. Lin, Sens. Actuators B 124 (2007) 486.
[7] K. Jüttner, K.-M. Mangold, M. Lange, K. Bouzek, Russ. J. Electrochem. 40 (2004) 317.
[8] S. Domínguez-Domínguez, J. Arias-Pardilla, A. Berenguer-Murcia, E. Morallón, D. Cazorla-Amorós, J. Appl. Electrochem. 38 (2008) 259.
[9] Y. Leroux, E. Eang, C. Fave, G. Trippe, J.C. Lacroix, Electrochem. Commun. 9 (2007) 1258.
[10] N.F. Atta, A. Galal, F. Khalifa, Appl. Surf. Sci. 253 (2007) 4273.
[11] F. Terzi, C. Zanardi, V. Martina, L. Pigani, R. Seeber, J. Electroanal. Chem. 619 (2008) 75.
[12] S.S. Kumar, J. Mathiyarasu, K.L. Phani, J. Electroanal. Chem. 578 (2005) 95.
[13] J. Mathiyarasu, S. Senthilkumar, K.L.N. Phani, V. Yegnaraman, Mater. Lett. 62 (2008) 571.
[14] B. Rajesh, K.R. Thampi, J.-M. Bonard, A.J. McEvoy, N. Xanthopoulos, H.J. Mathieu, B. Viswanathan, J. Power Sources 133 (2004) 155.
[15] X. Huang, Y. Li, Y. Chen, L. Wang, Sens. Actuators B 134 (2008) 780.
[16] N.F. Atta, M.F. El-Kady, J. Solid State Electrochem., submitted for publication.
[17] L. Kong, X. Lu, E. Jin, S. Jiang, C. Wang, W. Zhang, Compos. Sci. Technol. 69 (2009) 561.
[18] C.R. Martin, I. Rubinstein, A.J. Bard, J. Am. Chem. Soc. 104 (1984) 4817.
[19] B.H.C. Westerink, W. Timmerman, Anal. Chim. Acta 379 (1999) 263.
[20] S.M. Park, J.S. Yoo, Anal. Chem. 75 (2003) 455A.

[21] E. Katz, I. Willner, Electroanalysis 15 (2003) 913.
[22] L. Niu, Q. Li, F. Wei, X. Chen, H. Wang, J. Electroanal. Chem. 544 (2003) 121.
[23] S. Tian, J. Liu, T. Zhu, W. Knoll, Chem. Mater. 16 (2004) 4103.
[24] L. Zhang, M. Wan, J. Phys. Chem. B 107 (2003) 6748.
[25] A.I. Gopalan, K.-P. Lee, K.M. Manesh, P. Santhosh, J.H. Kim, J.S. Kang, Talanta 71 (4) (2007) 1774.
[26] X. Lin, Y. Zhang, W. Chen, P. Wu, Sens. Actuators B 122 (2007) 309.
[27] T. Yin, W. Wei, J. Zeng, Anal. Bioanal. Chem. 386 (2006) 2087.
[28] G. Jin, Y. Zhang, W. Cheng, Sens. Actuators B 107 (2005) 528.
[29] D.R. Lide (Ed.), Handbook of Chemistry and Physics, 84th edition, CRC Press, 2004.
[30] J.Q. Chambers, J. Electroanal. Chem. 130 (1981) 381.
[31] W.T. Yap, L.M. Doanne, Anal. Chem. 54 (1982) 1437.
[32] F.C. Anson, T. Ohsaka, J.M. Saveant, J. Am. Chem. Soc. 105 (1983) 4883.
[33] A.H. Schroeder, F.B. Kaufman, J. Electroanal. Chem. 113 (1980) 209.
[34] P.T. Kissinger, W.R. Heineman (Eds.), Laboratory Techniques in Electroanalytical Chemistry, Marcel Dekker, 1984, p. 82.
[35] N. Yang, Q. Wan, J. Yu, Sens. Actuators B 110 (2005) 246.
[36] N.F. Atta, I. Marawi, K.L. Petticrew, H. Zimmer, H.B. Mark, A. Galal, J. Electroanal. Chem. 408 (1996) 47.
[37] A. Galal, J. Solid State Electrochem. 2 (1998) 7.
[38] Q. Wan, N. Yang, X. Zou, H. Zhang, B. Xu, Talanta 55 (2002) 459.
[39] V.S. Vasantha, S.-M. Chen, J. Electroanal. Chem. 592 (2006) 77.
[40] M. Hasik, E. Wenda, C. Paluszkiewicz, A. Bernasik, J. Camra, Synth. Metal 143 (2004) 341.
[41] S.-F. Wang, F. Xie, R.-F. Hu, Sens. Actuators B 123 (2007) 495.
[42] F. Ye, J. Nan, L. Wang, Y. Song, K.-B. Kim, Electrochim. Acta 53 (2008) 4156.
[43] A. Mourato, S.M. Wong, H. Siegenthaler, L.M. Abrantes, J. Solid State Electrochem. 10 (2006) 140.
[44] A.W. Bott, W.R. Heineman, Curr. Sep. 20 (2004) 4.
[45] T. Hashitani, K. Mizukawa, M. Kumazaki, H. Nishino, Neurosci. Res. 30 (1998) 43.
[46] V.S. Ijeri, P.V. Jaiswal, A.K. Srivastava, Anal. Chim. Acta 439 (2001) 291.
[47] S.A. Kumar, C.-F. Tang, S.-M. Chen, Talanta 76 (2008) 997.
[48] C. Gabrielli, M. Keddam, N. Nadi, H. Perrot, J. Electroanal. Chem. 485 (2000) 101.
[49] A. Galal, J. Appl. Polym. Sci. 102 (2006) 2416.
[50] H. Sakai, R. Baba, K. Hashimoto, A. Fujishima, A. Heller, J. Phys. Chem. 99 (1995) 11896.

Talanta 79 (2009) 583–589

Contents lists available at ScienceDirect

Talanta

journal homepage: www.elsevier.com/locate/talanta

Dual purpose laser ablation-inductively coupled plasma mass spectrometry for pulsed laser deposition and diagnostics of thin film fabrication: Preliminary study

Mersida Janeva Azdejković [a], Johannes Teun van Elteren [a,*], Kristina Žužek Rožman [b], Radojko Jaćimović [b], Evangelia Sarantopoulou [c], Spomenka Kobe [b], Alkiviadis Constantinos Cefalas [c]

[a] National Institute of Chemistry, Hajdrihova 19, 1001 Ljubljana, Slovenia
[b] Jožef Stefan Institute, Jamova 39, 1001 Ljubljana, Slovenia
[c] National Hellenic Research Foundation, TPCI, 48 Vassileos Constantinou Ave., Athens 11635, Greece

ARTICLE INFO

Article history:
Received 22 October 2008
Received in revised form 10 April 2009
Accepted 16 April 2009
Available online 3 May 2009

Keywords:
PLD
Thin film fabrication
LA-ICPMS
Nanoparticles
Stoichiometry
Size distribution

ABSTRACT

PLD (pulsed laser deposition) is an attractive technique to fabricate thin films with a stoichiometry reflecting that of the target material. Conventional PLD instruments are more or less black boxes in which PLD is performed virtually "blind", i.e. without having great control on the important PLD parameters. In this preliminary study, for the first time, a 213 nm Nd–YAG commercial laser ablation-inductively coupled plasma mass spectrometer (LA-ICPMS) intended for microanalysis work was used for PLD under atmospheric pressure and in and ex situ ICPMS analysis for diagnostics of the thin film fabrication process.

A PLD demonstration experiment in a He atmosphere was performed with a $Sm_{13.8}Fe_{82.2}Ta_{4.0}$ target–Ta-coated silicon wafer substrate (contraption with defined geometry in the laser ablation chamber) to transfer the permanent magnetic properties of the target to the film. Although this paper is not dealing with the magnetic properties of the film, elemental analysis was applied as a means of depicting the PLD process. It was shown that in situ ICPMS monitoring of the ablation plume as a function of the laser fluence, beam diameter and repetition rate may be used to ensure the absence of large particles (normally having a stoichiometry somewhat different from the target). Furthermore, ex situ microanalysis of the deposited particles on the substrate, using the LA-ICPMS as an elemental mapping tool, allowed for the investigation of PLD parameters critical in the fabrication of a thin film with appropriate density, homogeneity and stoichiometry.

1. Introduction

In contrast to its conceptual technical simplicity, pulsed laser deposition (PLD) is very complex from a physical–chemical point of view. PLD offers several advantages over other deposition techniques, e.g., preservation of stoichiometry, film homogeneity and high-quality crystalline structure of the deposited films. The good structural quality is attributed to the large kinetic energy of the ablated atoms and molecules upon arrival at the substrate surface [1]. The efficiency of nanocrystallization of the films depends on the properties of the laser beam (wavelength, energy, intensity, etc.), deposition geometry, type and purity of initial target and substrate. Furthermore, the laser ablation process is strongly affected by the ambient conditions such as temperature, background pressure and gas composition.

PLD is commonly carried out in ultra-high vacuum with no auxiliary analytical equipment attached to the PLD instrument although for research purposes various, mostly optical detectors have been tried [2] and in some cases mass spectrometry detectors [3,4]. Commercial laser ablation-inductively coupled plasma mass spectrometer (LA-ICPMS) systems for elemental microanalysis have similar lasers as PLD instruments but not the possibility to work under high vacuum conditions although low vacuum laser ablation chambers have been reported [5]. However, in many instances PLD has been successfully executed under atmospheric conditions in the presence of an inert gas [6], even for the target material ($Sm_{13.8}Fe_{82.2}Ta_{4.0}$) used in this study [7,8]. This suggests that commercial LA-ICPMS systems may be used to good effect as well, with the added advantage of in situ analysis of the ablation plume and ex situ analysis of the deposited particles. However, to be able to use the ICPMS as a detector for laser ablation generated aerosols representative for the fabricated thin film one has to understand the various processes occurring from ablation evaporation to ICP evaporation.

A sequence of events takes place which may lead to elemental fractionation due to (a) formation of non-stoichiometric aerosol particles, (b) selective particle transport phenomena as a result of diffusion, gravitational settling and inertial deposition and (c)

* Corresponding author. Tel.: +386 1 4760288; fax: +386 1 4760300.
E-mail address: elteren@ki.si (J.T. van Elteren).

0039-9140/$ – see front matter © 2009 Elsevier B.V. All rights reserved.
doi:10.1016/j.talanta.2009.04.031

incomplete atomization of particles as a result of particle size distribution [9]. When a target is ablated, material gets heated far above the melting and boiling point and evaporates into the surrounding atmosphere. Small aerosol particles with a size up to 100 nm can be produced by gas-to-particle conversion processes such as nucleation and condensation followed by coarsening due to particle collision and coalescence causing the total number of particles to reduce and the average size to increase [10]. Additionally, a certain amount of material remains melted and may act as a source for larger particles produced by hydrodynamic sputtering, a sort of plasma-initiated splashing [11]. Fractionated evaporation causes an enrichment of the more volatile components in the condensable vapor phase and a depletion in the mechanically removed droplets from the melt. Multi-stage cascade impactor experiments have shown that particles leaving the laser ablation chamber have at least a bimodal size distribution with a smaller fraction around 10 nm (consisting of spherical particles) and a larger fraction in the μm range (consisting of agglomerated particles) [12].

Horn and Günther [13] have investigated the influence of particle size distribution on the transport efficiency of laser ablation-induced aerosols in various gases (He, Ne and Ar) ablating NIST glasses and found that He essentially yields smaller particles sizes due to a high thermal conductivity (compared to the other gases) and therefore a faster spread of thermal energy away from the sampling position, leading to a more rapid end of condensational growth. This was confirmed by cascade impactor experiments performed by Koch et al. [12]. As far as the influence of particle size in the ICP is concerned, particles in the micrometer range can give rise to ICP-induced fractionation with lower wavelength lasers yielding smaller particles [14]. It was shown that by filtering certain particle fractions (>ca. 1 μm) better stoichiometric excitation and ionization is obtained. Fs lasers yield smaller particles then ns lasers with an overall composition closer to that of the target material [12]. Furthermore, mass load effects in the ICP may influence the fractionation due to localized vaporization and ion generation of the material in the plasma [15]. Optimal laser conditions for minimized fractionation can be summarized by reduction of the large particle fraction [10].

The aim of this preliminary work was to investigate the potential of a commercial LA-ICPMS system (213 nm Nd:YAG laser) for PLD purposes, i.e. using a target–substrate contraption to fabricate a thin film in the ablation chamber (in He under atmospheric pressure). Additionally, the hyphenated ICPMS instrument was tested for its analytical capabilities for in situ elemental analysis of the ablation plume and ex situ elemental analysis of the deposited film. The elemental signal ratios in the ablation plume were monitored to ensure the absence of large particles; this was independently checked by multi-stage cascade impaction of particles leaving the laser ablation chamber. Additionally, the film density, homogeneity and stoichiometry were investigated and the PLD parameters optimized using the LA-ICPMS instrument as an elemental mapping tool in combination with image analysis. Since permanent-magnet films are promising materials for structured microelectromagnetic devices, a $Sm_{13.8}Fe_{82.2}Ta_{4.0}$ target with high coercivity and a Ta-coated silicon wafer substrate were used to demonstrate the potential of a commercial LA-ICPMS system for both synthesis and analysis. A suite of other techniques was used to verify the properties of the particles generated and the thin films fabricated.

2. Experimental

2.1. Laser ablation ICPMS equipment

The modular laser ablation ICPMS system for PLD synthesis-diagnostics comprised a laser ablation device (New Wave Research UP 213, Fremont, USA) interfaced with a quadrupole ICPMS (Agilent 7500ce, Palo Alto, CA, USA) by a piece of Tygon tubing (1 m × i.d. 3 mm) for transport of the particles from one to the other. The laser ablation device contained a frequency-quintupled Nd:YAG laser (wavelength, 213 nm; pulse width, 4 ns) and had a motorized stage to be moved (programmable) in the *x*, *y* and *z* direction (with sub-micrometer resolution) for precise focusing of the laser beam. A CCD camera with a high magnification and a computer-controlled zoom allowed for adjusting of the focus and viewing of the ablation process on a monitor. PLD took place in a so-called SuperCell™ (New Wave Research), a chamber with a small void volume especially designed for optimal flow dynamics, containing the target–substrate contraption (see Section 2.2). He (5.0) was used as a PLD background gas (at atmospheric pressure) and also to transport the ablated material from the ablation chamber to the ICP for elements to be vaporized/atomized/ionized; argon was added as a make-up gas before the torch of the ICP. The ions formed in the ICP were extracted into the quadrupole MS and separated according to their mass-to-charge ratios.

2.2. Target/substrate materials and PLD geometry

As a target material $Sm_{13.8}Fe_{82.2}Ta_{4.0}$ was used, actually a cast obtained by induction melting of Sm (13.8 at.%), Fe (82.2 at.%) and Ta (4.0 at.%) and characterized as a number of phases ($SmFe_2$, $SmFe_3$, Sm_2Fe_{17} and $TaFe_2$) with clearly defined boundaries between them [16]. The target's dimensions were 10 mm × 5 mm with a thickness of 2 mm. The target was polished before each experiment to remove the oxidized surface layer. As a substrate a Si wafer coated with a ca. 100 nm thick layer of Ta was employed. The substrate's dimensions were ca. 6 mm × 3 mm with a thickness of 0.21 mm. Fig. 1 shows the target–substrate contraption which angled both the target and substrate at 45° with respect to the laser beam, keeping the target and substrate parallel at distances from 2 to 4 mm. The laser beam was focused on the target, half-way from the base of the target, and rastering was performed during laser ablation. The thin film fabricated was stored under hexane to prevent oxidation as Sm is very susceptible to reaction with oxygen.

2.3. ICPMS diagnostics of the PLD process

In situ elemental ICPMS analysis of the PLD plume was performed as a function of the laser fluence (0.1–15 J cm^{-2}), crater size (8–100 μm) and repetition rate (1–20 Hz) under the following operational parameters: He flow rate, 0.95 L min^{-1}; Ar make up flow rate, 0.75 L min^{-1}; scanning speed, 10 μm s^{-1}; time-resolved analysis of ^{57}Fe and ^{147}Sm (both 0.1 s acquisition time). Ex situ elemental analysis of the thin films fabricated was performed using the LA-ICPMS as a mapping tool with subsequent image analysis (Origin 7.5 SR4, OriginLab Corporation, Northampton, USA) to investigate the film density, homogeneity and stoichiometry as a function of the laser fluence, He flow rate and target–substrate distance at 30 min deposition times. Mapping was performed under the following rastering/acquisition conditions: laser fluence, ca. 4 J cm^{-2}; laser beam

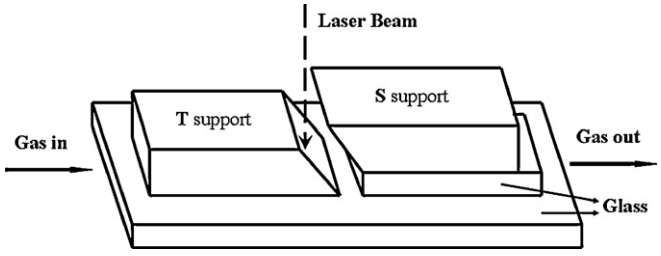

Fig. 1. Target–substrate geometry for PLD.

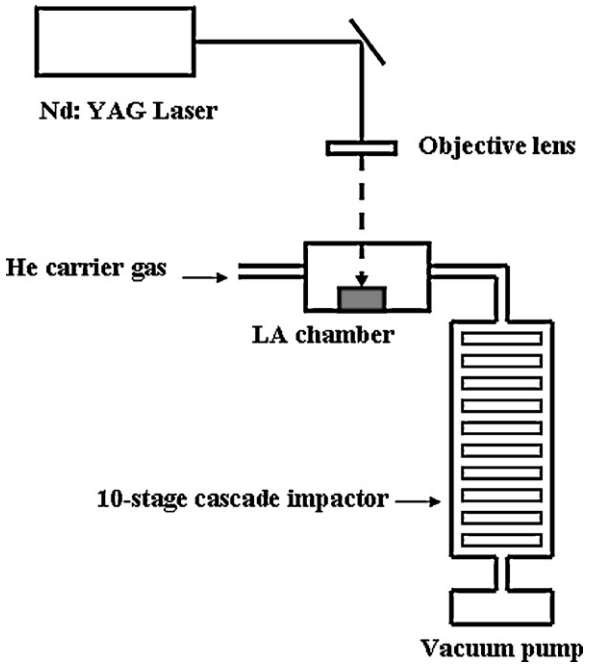

Fig. 2. Experimental setup for size-segregation of laser ablation generated aerosol particles using a cascade impactor.

diameter, 80 μm; scanning speed, 150 μm s^{-1}; pulse rate, 10 Hz; line distance, 100 μm; He flow rate, 1.0 L min^{-1}; acquisition time, 0.2 s ^{57}Fe and 0.4 s ^{147}Sm.

2.4. Verification of the particle size distribution

To investigate the size and composition of particles generated in the laser ablation process the above described laser ablation device was disconnected from the ICMPS and attached to a Berner ten-stage low-pressure cascade impactor which covers the sizes between 38 nm and 16 μm by simply hovering the outlet tube of the laser ablation cell in the inlet part of the impactor. A vacuum pump was adjusted to create a pressure gradient which resulted in a throughput of 25 L min^{-1}. In Fig. 2 a schematic diagram of the setup is given. Clean Tedlar impaction foils were used and particles were collected for 30 min. For determination of the elements in the deposited size fractions by k_0-standardized instrumental neutron activation analysis (k_0INAA), the Tedlar foils were irradiated in the TRIGA Mark II reactor, Ljubljana, at a neutron flux of 1.1×10^{12} n cm^{-2} for 20 h [17].

2.5. Thin film characterization

The surface morphology of the films was examined using FE-SEM SUPRA 35VP scanning electron microscopy (SEM), and the chemical composition of the deposits was investigated with energy dispersive X-ray spectroscopy (EDXS).

3. Results and discussion

3.1. Target homogeneity

Under conditions optimal for LA-ICPMS microanalysis (high He flow rate to minimize transport losses and a high ICP RF power to maximize the evaporation of particles) the $Sm_{13.8}Fe_{82.2}Ta_{4.0}$ target was ablated and the ^{57}Fe, ^{147}Sm and ^{181}Ta signals monitored upon traversing the target. From Fig. 3 it can be observed that Ta is less homogeneously distributed than Fe and Sm. The target material

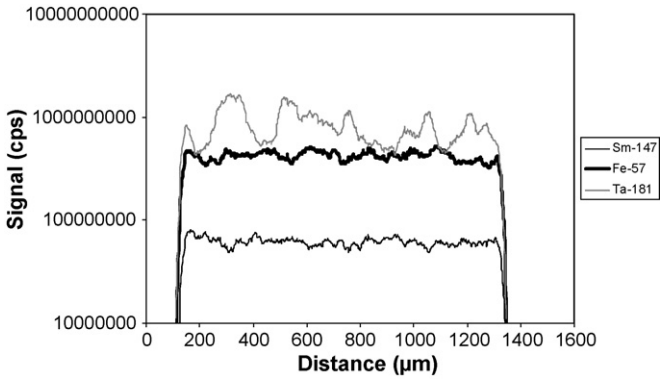

Fig. 3. Elemental signals upon traversing the $Sm_{13.8}Fe_{82.2}Ta_{4.0}$ target. Operational LA-ICPMS parameters: fluence, 10 J cm^{-2}; laser beam diameter, 100 μm; repetition rate, 10 Hz; scanning speed, 10 μm s^{-1}; He gas flow rate, 0.95 L min^{-1}, RF power, 1500 W; acquisition time, 0.1 s for each mass.

is a melt composite of $SmFe_2$, $SmFe_3$, Sm_2Fe_{17} and $TaFe_2$ with a low amount of Ta (4.0 at.%) present in only one of the phases [16]. Since the (much) more abundant Sm (13.8 at.%) and Fe (82.2 at.%) are present in three and four of the phases, respectively, it is obvious that Ta is less homogeneously distributed in the target than Sm and Fe. The Ta heterogeneity may have consequences for the homogeneity of the final film fabricated although films with appropriate characteristics (magnetic properties) have been fabricated from the very target using conventional PLD [7,8]. In the remainder of this work mostly ^{57}Fe and ^{147}Sm signals and their ratios were monitored.

3.2. In situ elemental monitoring of the PLD plume

In the in situ PLD diagnostics procedure the majority of particles from the ablation plume (>99%) [18] is transferred to the ICPMS. In PLD one wishes to deposit small particles on the substrate only, as arrival of macroscopic globules of molten material, up to ca. 10 μm diameter, is detrimental to the properties of the film. The use of ICPMS as an on-line detector may aid in the optimization of the PLD parameters for generation of small particles with an appropriate stoichiometry. Guillong and Günther [14] have shown that the U/Th ratio upon ablation of NIST glass 610 (measured as a cps ratio), using a 266 nm Nd:YAG system, dramatically depends on the conditions for ablation as a result of the particle size. They claim that their fractionation findings are due to ICP-enhanced processes related to particle size, critically limited to diameters above 1 μm. Filtering the large particles resulted in all instances in a better U/Th ratio (closer to unity as implicated by almost identical first ionization potentials for U and Th). In our case, using an opaque target instead of a transparent target and a 213 nm Nd:YAG system instead of a 266 nm Nd:YAG system, we can guesstimate that a large proportion of the particles has a diameter below 0.2 μm [19], and is therefore less influenced by the ICP.

From Fig. 4 it can be observed that experiments with an ICPMS tuned for normal LA-ICPMS microanalysis work do not show significant differences in the ^{57}Fe/^{147}Sm ratios (measured as cps ratios) upon ablation of the $Sm_{13.8}Fe_{82.2}Ta_{4.0}$ target as a function of the following PLD parameters: laser fluence (0.1–15 J cm^{-2}, Fig. 4A), laser beam diameter (8–100 μm, Fig. 4B) and pulse rate (1–20 Hz, Fig. 4C). The average ^{57}Fe/^{147}Sm ratio for all experiments was 0.16, with a maximum deviation of ±5%. None of the PLD parameters tested appears to compromise the average stoichiometry of the particles in the plume as governed by the ^{57}Fe/^{147}Sm ratio measured. It seems as if fractionation due to formation of non-stoichiometric particles, selective particle transport phenomena and/or incomplete atomization, and consequently a highly variable ^{57}Fe/^{147}Sm ratio, is not

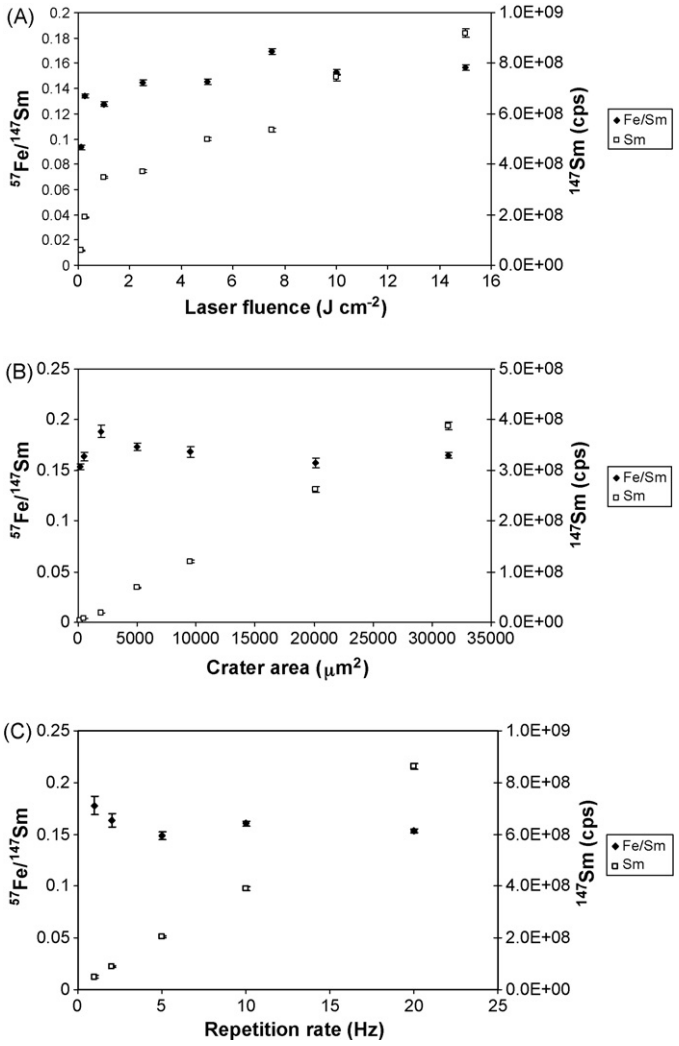

Fig. 4. Influence of laser fluence (A), crater area (B) and repetition rate (C) on the ^{147}Sm signal and the $^{57}Fe/^{147}Sm$ ratio. For operational default LA-ICPMS parameters see Fig. 3. Error bars denote the uncertainty in the measurement.

an important issue with this specific target material and under the laser conditions applied. The elemental signals (in cps) in Fig. 4, given for Sm but similar for Fe and Ta, augment these observations by their linear proportionality with regard to laser fluence (after overcoming an initial threshold), crater area and repetition rate. It seems logical to conclude that for all PLD parameters tested (for a range of conditions) the nominal particle size is below 1 μm which is supposed to be the limit for the occurrence of ICP-enhanced processes [14]. The validity of this assumption was verified by size-segregation of particles in a ten-stage cascade impactor.

3.3. Verification of the particle size distribution

The laser ablation outlet was sampled by a ten-stage cascade impactor and the distribution data obtained by INAA are given in Fig. 5. It is clear that the particle size distribution under a laser fluence of 9 J cm^{-2} results in the generation of small particles (Fig. 5A), with ca. 95% [w/w] having an aerodynamic diameter $D_{ae} \leq 0.75$ μm. By ablating a target of $Sm_{13.8}Fe_{82.2}Ta_{4.0}$ we expect to collect aerosol particles which resemble the composition of the target (28.1% [w/w] Sm, 62.1% [w/w] Fe and 9.8% [w/w] Ta). The average particle composition is fairly similar to this target composition with 26.7% [w/w] Sm, 65.1% [w/w] Fe and 9.8% [w/w] Ta. However, the elemental distribution is not identical for all particle sizes (Fig. 5B). The

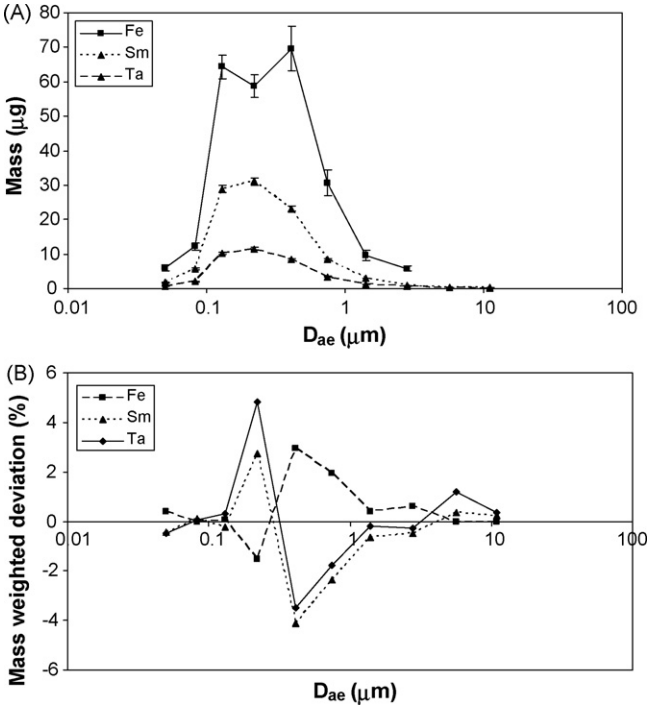

Fig. 5. Mass size distributions (A) and mass-weighted deviations from the target composition (B) for Fe, Sm and Ta upon ablation of the $Sm_{13.8}Fe_{82.2}Ta_{4.0}$ target and size-segregation in the cascade impactor. Since the target composition is not exactly the same as the average composition of the particles found, the graphs in (B) are slightly offset in the vertical direction (see the text for details). LA conditions: laser fluence, 9 J cm^{-2}; laser beam diameter, 100 μm; pulse rate, 10 Hz; scanning speed, 10 μm s^{-1}; He flow rate, 0.6 L min^{-1}. Error bars denote the uncertainty in the measurement.

mass-weighted deviation from the measured average particle composition for each size fraction indicates that Sm and Ta are more or less equally distributed over the particle sizes whereas Fe shows a reverse trend to make the mass balance neutral (neutral here means in accordance with the measured average particle composition). It is unclear why Sm and Ta behave similarly, especially since they are the most and least volatile of the three elements investigated, respectively. In general, smaller particles tend to be enriched with more volatile elements and larger ones tend to be depleted [12,20]. However, the mass-weighted composition of the various particle sizes never differs more than ca. 10%. The findings not only confirm that nanoparticles are generated in the LA setup used but also that the composition of the particles reflects that of the target with little mass-weighted inter-particle heterogeneity. This is encouraging information for the optimization of the film fabrication process which will be studied in the next section.

3.4. Ex situ LA-ICPMS of the deposited particles

When particles are deposited on a substrate and a film is generated one wishes to maximize the film density and at the same time minimize the film heterogeneity. Furthermore, one strives for an average stoichiometry which reflects that of the target. Using the LA-ICPMS as an elemental mapping tool the influence of laser fluence, He flow rate and target–substrate distance on these film properties were investigated. In Fig. 6 the findings of the mapping are given for ^{57}Fe (similar for ^{147}Sm), as an indication of the film density, and for $^{57}Fe/^{147}Sm$, as and indication of the film homogeneity and stoichiometry. The ^{57}Fe maps are given in so-called JET colors to display the range of concentrations in a illustrative way. The $^{57}Fe/^{147}Sm$ maps are expressed in 256 shades of gray with the actual target stoichiometry ($^{57}Fe/^{147}Sm$ ratio of 0.16 as found by

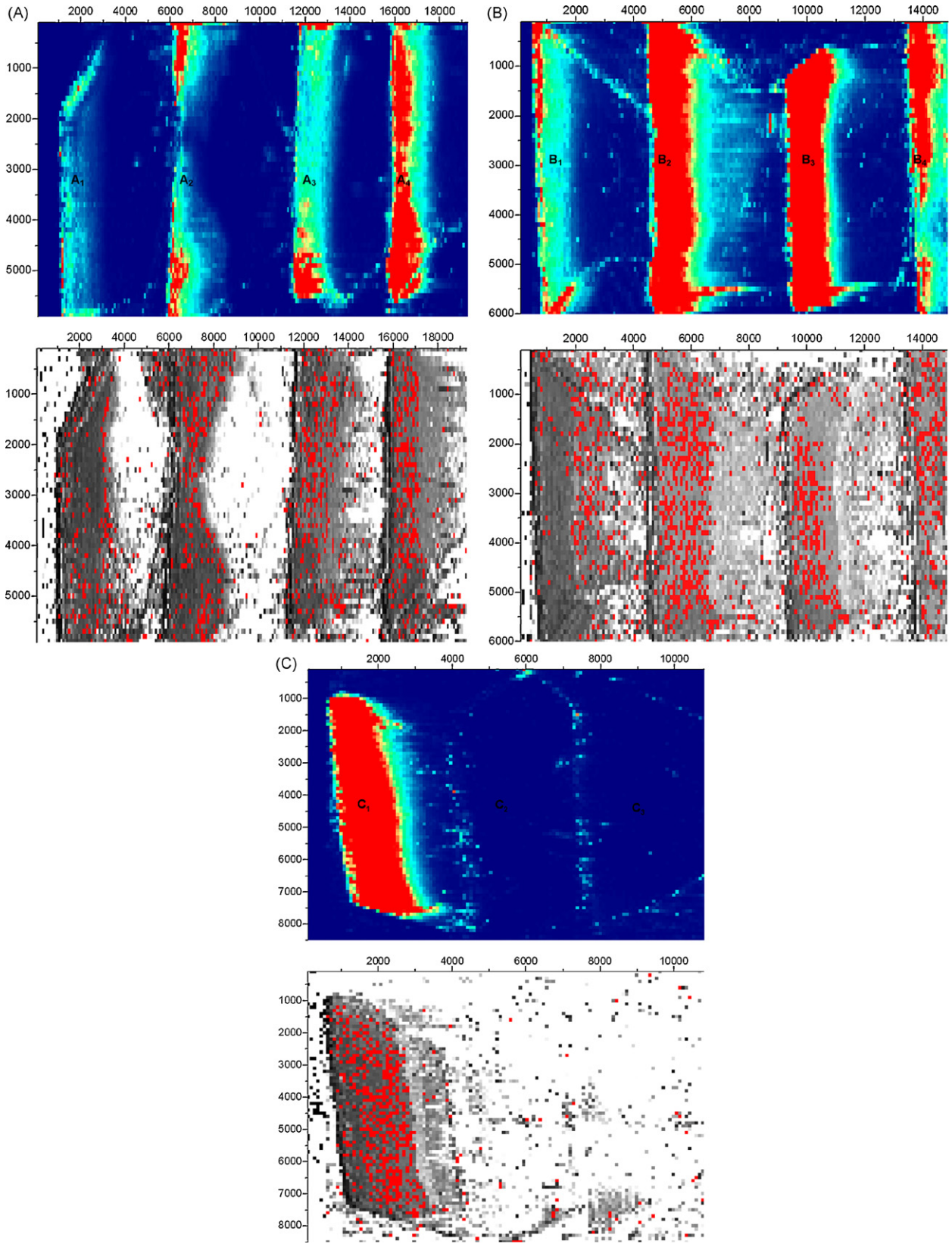

Fig. 6. Element maps (scale in μm) of ^{57}Fe and ^{57}Fe/^{147}Sm for substrates generated at varying fluence (A_1 = 1.7 J cm^{-2}, A_2 = 3.9 J cm^{-2}, A_3 = 6.1 J cm^{-2}, A_4 = 9.3 J cm^{-2}), He flow rate (B_1 = 0 L min^{-1}, B_2 = 0.3 L min^{-1}, B_3 = 0.6 L min^{-1}, B_4 = 1.0 L min^{-1}) and target–substrate distance (C_1 = 2 mm, C_2 = 3 mm, C_3 = 4 mm), with the first image (in JET colors) denoting the ^{57}Fe maps and the second image (in shades of gray, with red pixels indicating the target stoichiometry [±5%]) the ^{57}Fe/^{147}Sm maps. For JET colors: lower image densities are mapped onto "cool" colors and higher densities onto "hot" colors; low density images are shown in blue or violet, and high density images appear as orange or red. Operational default PLD parameters: fluence, 9 J cm^{-2}; He gas flow rate, 0.3 L min^{-1}; target–substrate distance, 2 mm; laser beam diameter, 100 μm; repetition rate, 10 Hz; scanning speed, 10 μm s^{-1}, deposition time, 30 min. The size of the substrates was ca. 6 mm × 3 mm. (For interpretation of the references to color in this figure legend, the reader is referred to the web version of the article.)

analysis of the plume upon ablation of the target, see Section 3.2) indicated as red pixels with a deviation of ±5% from this value. Since the laser fluence is more or less directly proportional to the amount of particles generated above a certain threshold (Fig. 2A) it is no surprise that in Fig. 6A the largest fluence (9 J cm^{-2}) yields the highest film density (A_4). The average stoichiometry for this fluence is also very close to the target's stoichiometry as can be seen from the red pixel distribution in the section referring to this film. In Fig. 6B one sees that a He flow rate of 0.3 L min^{-1} yields the thickest film (B_2) with a stoichiometry closest to that of the target. From Fig. 6C it can be observed that the target–substrate distance is very critical in the generation of a thick film; 2 mm is the only distance which yields a film altogether, having a composition close to that of the target (C_1). For other background gases the findings are most probably different due to the effect of the thermal conductivity of the gas on the particle diameter and the size of the laser-induced plasma [13]. The optimized PLD parameters (A_4, B_2 and C_1) were used to fabricate films for further characterization.

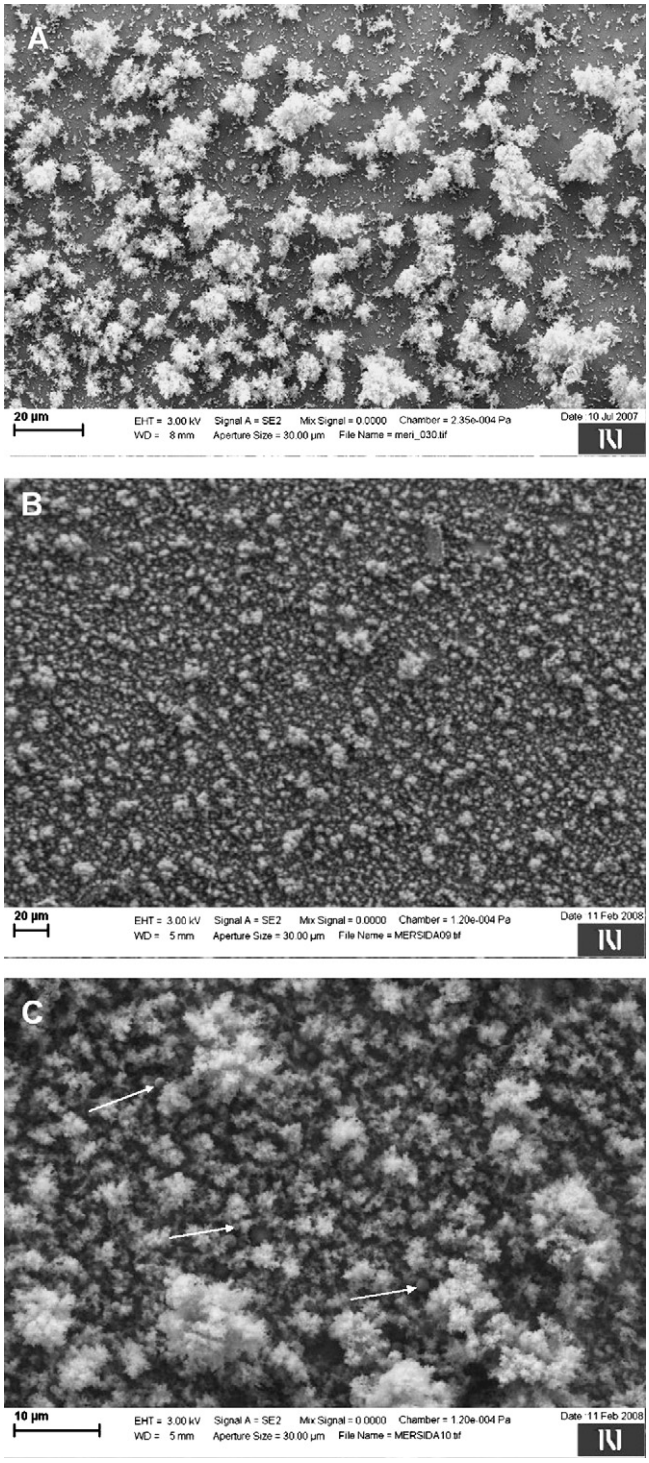

Fig. 7. SEM images of particles deposited on the substrate for 30 min (A) and 2 h (B and C); some larger spherical particles of different sizes are indicated by arrows. For operational default PLD parameters see Fig. 6.

3.5. Thin film characterization

In Fig. 7 the SEM micrographs of the deposited material are presented. It can be seen that the film growth is three-dimensional with particles forming clusters on the substrate. This so-called Volmer-Weber growth [21] occurs by ripening and coalescence of clusters until eventually a continuous film has been produced [21]. This type of island growth is the most common growth mode and prevails when the thin film and substrate are composed of dissimilar materials, have different crystal structure and chemistry, and no epitaxial relationship exists between them. In Fig. 7A the coalescence process has not been completed yet due to a too short deposition time (30 min) whereas in Fig. 7B the deposition time of 2 h suffices to produce a continuous film. Zooming in on the deposits (Fig. 7C) shows that besides nanoparticles also larger spherical particles of different sizes have been formed. From SEM-EDXS characterization measurements it follows that the Fe/Sm ratio in larger particles was in general somewhat higher than in the target. This is in accordance with cascade impactor findings for the fractions between 0.41 and 2.8 µm or higher (Fig. 5B). The results seem to agree with the literature as far as mechanisms for formation of particles are concerned. Small particles are formed by nucleation and condensation from the vapor while larger particles may be ejected from the melted liquid due to hydrodynamic instability or recoil pressure from the expanding vapor plume [11]. The vaporization enthalpy of Fe is much higher than that of Sm causing Sm to vaporize readily upon laser heating leaving a melted residue that is rich in lower volatility Fe. Hence, particles ejected from the melt are expected to have a higher Fe/Sm ratio than the target.

4. Conclusions

Nd:YAG lasers (213 nm) intended for analytical microanalysis are suitable for PLD of $Sm_{13.8}Fe_{82.2}Ta_{4.0}$ under atmospheric conditions, with the added advantage of in situ ICPMS monitoring of the ablation plume and ex situ LA-ICPMS of the deposited particles on the substrate. In this way the size distribution and elemental composition of particles in the plume may be probed, next to the elemental density, homogeneity and stoichiometry of the thin film fabricated. Since this diagnostics approach is generic it may be used to investigate PLD (under atmospheric conditions) of other novel materials as well.

Acknowledgements

This work has been supported by the Slovenian Research Agency (Contracts J2-7133-0104 and 1000-06-310052). The authors wish to thank Dr. V.S. Šelih, Dr. M.P. Beeston and Dr. I. Grgić for assistance with the measurements and constructive discussions.

References

[1] J.C.S. Kools, T.S. Baller, S.T. De Zwart, J. Dieleman, J. Appl. Phys. 71 (1992) 4547.
[2] H.J. Dang, M.F. Zhou, Q.Z. Qin, Appl. Surf. Sci. 140 (1999) 118.
[3] H.Y. Fan, W. Ho, S.A. Reid, Int. J. Mass Spectrom. 230 (2003) 11.
[4] T. Mathews, J.R. Sellar, B.C. Muddle, Chem. Mater. 12 (2000) 917.
[5] D. Fliegel, D. Günther, Spectrochim. Acta B 61 (2006) 841.

[6] M. Rusop, T. Soga, T. Jimbo, M. Umeno, Appl. Surf. Sci. 197 (2002) 426.
[7] S. Kobe, E. Sarantopoulou, G. Dražič, J. Kovač, M. Janeva, Z. Kollia, A.C. Cefalas, Appl. Surf. Sci. 254 (2007) 1027.
[8] E. Sarantopoulou, S. Kobe, K. Žužek Rožman, Z. Kollia, G. Dražić, A.C. Cefalas, IEEE Trans. Magn. 40 (2004) 2943.
[9] R. Hergenröder, Spectrochim. Acta B 61 (2006) 284.
[10] R. Hergenröder, J. Anal. At. Spectrom. 21 (2006) 1016.
[11] R. Hergenröder, J. Anal. At. Spectrom. 21 (2006) 517.
[12] J. Koch, A. Von Bohlen, R. Hergenröder, K. Niemax, J. Anal. At. Spectrom. 19 (2004) 267.
[13] I. Horn, D. Günther, Appl. Surf. Sci. 207 (2003) 144.
[14] M. Guillong, D. Günther, J. Anal. At. Spectrom. 17 (2002) 831.
[15] I. Kroslakova, D. Günther, J. Anal. At. Spectrom. 22 (2007) 51.
[16] K. Žužek, P.J. Mcguiness, S. Kobe, J. Alloys Compd. 289 (1999) 213.
[17] R. Jaćimović, B. Smodis, T. Bučar, P. Stegnar, J. Radioanal. Nucl. Chem. 257 (2003) 659.
[18] M. Janeva Azdejković, J.T. van Elteren, unpublished results.
[19] I. Horn, M. Guillong, D. Günther, Appl. Surf. Sci. 182 (2001) 91.
[20] C.Y. Liu, X.L. Mao, S.S. Mao, R. Greif, R.E. Russo, Anal. Chem. 77 (2005) 6687.
[21] R.J. Stokes, D. Fennell Evans, Fundamentals of Interfacial Engineering, John Wiley and Sons, 1997.

Talanta 79 (2009) 712–722

Contents lists available at ScienceDirect

Talanta

journal homepage: www.elsevier.com/locate/talanta

Multi-residue analysis and ultra-trace quantification of 36 priority substances from the European Water Framework Directive by GC–MS and LC-FLD-MS/MS in surface waters

Sami Barrek[a,b], Cécile Cren-Olivé[a,c,*], Laure Wiest[a], Robert Baudot[a], Carine Arnaudguilhem[a], Marie-Florence Grenier-Loustalot[a]

[a] Service Central d'Analyse du CNRS – USR59, Chemin du Canal, BP 22, 69360 Solaize, France
[b] Institut National de Recherche et d'Analyse physico-chimique (INRAP), pôle technologique de Sidi Thabet, 2020 Sidi Thabet, Tunisia
[c] Université Claude Bernard Lyon 1, UMR 5180, CPE, Bâtiment 308, 43 Bd du 11 Novembre 1918, 69100 Villeurbanne, France

ARTICLE INFO

Article history:
Received 6 January 2009
Received in revised form 22 April 2009
Accepted 28 April 2009
Available online 5 May 2009

Keywords:
European Water Framework Directive
Priority substances
GC–MS
LC–MS/MS
Fluorescence
Surface waters

ABSTRACT

A multi residue analysis was developed for screening, quantification and confirmation of 36 priority organic compounds included in the 2000/60/EC European Water Framework Directive. The compounds analyzed included 19 pesticides, 8 PAH, 5 endocrine-disruptors and 4 organochlorine compounds. The method was developed in three steps. First, automated off-line solid-phase extraction using Strata X cartridges was optimized to trap simultaneously the 36 studied compounds. Second, the more volatile compounds were analysed by gas chromatography coupled to mass spectrometry with electron impact ionisation in selected ion monitoring mode (SIM). Third, the last 20 compounds were detected and quantified, in one run, by liquid chromatography coupled to fluorescence detector and tandem mass spectrometry. The excellent selectivity and sensitivity allowed us satisfactory quantification and confirmation at levels as low as 0.2–67 ng L^{-1} with recoveries between 59 and 105%. Such methodology was then applied to French surface waters: all the waters present organic contaminants, and their concentration varied according to the origin and nature of substances.

1. Introduction

Organic contaminants present in the environment are a result of different sources of pollution from anthropogenic activities such as industrial chemical production, agricultural application, domestic activities to natural origins [1]. Many of these contaminants are characterized by a strong persistence which explain their wide presence in the soil–water environment [1,2] and their accumulation in fatty tissue [1,3,4] So due to these physicochemical characteristics and their extensive use, many of these compounds end-up in surface and ground water and have to be considered as a potential risk for ecosystems as well as for drinking water quality.

In this context, strict regulations for the control of contaminants' concentration levels in environment have been established. In the field of water policy, the European Union adopted the Water Framework Directive 2000/60/EC, whose objectives are to improve, protect and prevent further deterioration of water quality across Europe [5]. The Water Framework Directive recommends, in this aim, the development of new procedures for the identification of substances and of the set up of control measures of 54 compounds of concern listed under 33 priority substances in the Annex X [5] and 8 substances in the Annex IX [5]. This list includes 4 metals, 20 pesticides, 8 polycyclic aromatic hydrocarbons (PAHs), 13 organochlorine compounds and 5 endocrine-disruptors and 4 other organic compounds [5]. The maximal concentrations authorized for these contaminants which vary from 0.1 ng/L to 20 μg/L depending on the chemical nature of the compound, establish the environmental quality standards and define the "good ecological and chemical status" [5].

Analytical methods based on gas chromatography [6–15] or liquid chromatography [6,7,12,13,15,16] followed by mass spectrometry [6–9,11,13–15] or tandem mass spectrometry [6,7,10,12,13,15,16] are the most commonly used techniques for the quantification of organic micro-contaminants in water. However, in spite of the recent technical progress, the instrumental quantification limits of the micro-contaminants are still high, around μg/L. Therefore the micro-contaminants quantification in water requires a first step of extraction and preconcentration in order to detect a threshold down to 0.1 ng/L (Directive 2000/60/EC) [5]. This sample preparation step is, in fact, the critical step of the whole analysis. The most common method is solid-phase extraction (SPE) [6–12,15,16], which can be used to determine a broad range of

* Corresponding author.
E-mail address: c.cren@sca.cnrs.fr (C. Cren-Olivé).

0039-9140/$ – see front matter © 2009 Elsevier B.V. All rights reserved.
doi:10.1016/j.talanta.2009.04.058

contaminants in one analysis. While liquid–liquid extractions (LLE techniques) [6,7] are time-consuming, expensive and hazardous to health due to the high volume of potentially toxic solvents used, SPE methods are rapid, present good recoveries and low detection limits [6–12,15,16]. In addition, SPE methods can be automated by using laboratory robotic systems that do all or part of the sample preparation steps. Modern trends in sample preparation are towards the simplification of the process and minimising the organic solvent used with the development and application to environmental samples of liquid-phase microextraction (LPME) [6,7,17], the microextraction in solid phase (SPME) [6,7,17,18] and stir bar sorptive extraction (SBSE) [6,7,14,19], and biosensors [20], and semipermeable membrane devices (SMPD) [6,7,21].

The large majority of the developed methods focused on specific contaminant classes such as pesticides [22], polycyclic aromatic hydrocarbons [23], alkylphenols [24,25], phthalates [24]. Few offer the simultaneous determination of environmental contaminants belonging to different chemical families [8–16], and only three are related to compounds relevant of the Water Framework Directive [8,10,14]. They all proposed the determination of twenty or so compounds (24 [8,14] and 26 [10]) by GC–MS or GC–MS/MS, which limits the analysis only to the more volatile and apolar contaminants of the list.

Therefore, the purpose of this paper is to discuss the development of a multi-residue analysis of 36 priority substances from the European Water Framework Directive [5] by gas and liquid chromatographies coupled to mass spectrometry in surface waters. By the comparison of three types of extractions, we demonstrate that a single solid-phase extraction can be used to extract all the compounds of different physicochemical properties. The compounds were then analyzed by GC–MS and/or LC-FLD-MS/MS according to their main characteristics (volatility, polarity, fluorescence). These methods were applied to survey of the 36 substances in real surface waters from France. To our best knowledge, this is the first time that a multi-residue method has been developed which can analyse 36 compounds from the European Water Framework Directive and from a wide variety of chemical families with ng L^{-1} reporting limits.

2. Experimental section

2.1. Chemical and reagent

All standards were of high purity (99.9%). The 19 selected pesticides were purchased from Dr Ehrensdorfer (Augsburg, Germany), PAHs standards from Supelco (Supelco, France), alkyl-phenols compounds from Riedel-del-Haën (Seelze, Germany) and the 4 organochlorine compounds and the di(2-ethylhexyl)phthalate from Sigma–Aldrich (Saint Quentin Fallavier, France). Methanol, acetonitrile, and isopropanol of HPLC-MS grade were obtained from Carlo Erba (Milan, Italy), dimethylsulfoxide (DMSO) of Analytical Grade, isooctane and toluene of Pesticide Grade were from Riedel de-Haën (Seelze, Germany) and dichloromethane from Sigma–Aldrich (Saint Quentin Fallavier, France). Ammonium acetate added as an ionic additive to eluents was purchased from Merck (Lyon, France). Ultra pure (UP) water was produced from a Direct-Q system (Millipore, Molsheim, France).

Stock solutions were prepared in brown glass bottles at a concentration of 20 mg/L in isopropanol and stored at −20 °C. Ultrapure water samples were spiked with aliquots of these solutions to achieve final concentrations at 100 ng/L.

2.2. Sample collection and pre-treatment

Samples were collected in 1L brown glass bottles from Rhône-Alpes region (France) and kept on ice immediately. Samples were analysed not later than 48 h after sampling and were stored in brown glass bottles at 4 °C until extraction. As soon as their arrivals in the laboratory, the samples were filtered using a Millipore YT30 142 HW device (Bedford, USA) under nitrogen pressure and through 3 different porosity filters: a glass fibre prefilter, and 8 μm, 0.45 μm nitrocellulose filters all provided by Millipore (Molsheim, France). Prior to extraction, 10% (v/v) of isopropanol were added to the water samples to prevent the adsorption of analytes.

2.3. Sample extractions

The SPE procedure was performed with an Auto-Trace SPS Workstation (Caliper, Roissy Charles De Gaulle, France). Four commercially available SPE cartridges were tested: Oasis HLB cartridges (3 mL, 60 mg) from Waters (Milford, MA, USA), Strata-X (3 mL, 200 mg), Strata-C18E (3 mL, 200 mg) from Phenomenex (Le Pecq, France) and Supelclean Envi-Carb (3 mL, 250 mg) from Supelco (Supelco, France). Each SPE cartridge was conditioned with 4 mL of acetonitrile, 4 mL of 1/1/1 (v/v/v) methanol/isopropanol/acetonitrile and 20 mL of ultrapure water. 500 mL of samples were loaded onto the cartridge at a flow rate of 5 mL/min. immediately after, the cartridge was air-dried for 15 min. Elution was then carried out with 4 mL of 1/1/1 (v/v/v) methanol/isopropanol/acetonitrile and then with 4 mL of acetonitrile, which allows highest recovery of all target compounds.

One commercially available Solid Phase Extraction Disks Envi-C18 DSK from Supelco was tested. The disc was pre-conditioned with 8 mL of methanol, and then rinsed by 20 mL of ultrapure water in the filtration system. 500 mL of sample was passed through the disc at a flow rate about 20–25 mL/min. The contaminants were then eluted with 6 mL of methanol.

For the adsorption experiments, 500 mL of spiked water was transferred to a clean 1 L amber glass bottle and approximately 200 mg (measured in a 2 mL-bottomed autosampler vial) of Ambersorb 572 (Rohm and Haas Canada Inc., Supelco, France) was added to sample. The bottles were stirred magnetically at 650 rpm to reduce the liquid-phase resistance between the adsorbent particles. The Ambersorb 572 was isolated from the water by filtering the bottle contents through a 45 mm Whatman No 4 filter paper (VWR, France) on a filtration apparatus. The sample bottle and filtration apparatus walls were rinsed with high purity solvents (isopropanol, water and methanol) and then by ultrapure water to ensure complete transfer of the Ambersorb 572. The filtration apparatus was left under vacuum for 3 min to remove as much water as possible from the Ambersorb 572. The filter paper with the Ambersorb 572 was transferred using forceps to a 20 mL vial and 5 mL of dichloromethane was added. The Ambersorb 572 was then recovered by filtration.

For the SBSE extraction procedure, the commercial TwisterTM stir bar for sorptive extraction was obtained from Gerstel (Lille, France). It consists of a 20 mm length glass-encapsulated magnetic stir bar, externally coated with 0.5 mm of PDMS. Prior to the first use, the stir bar was placed into a vial containing 1 mL of a mixture of methylene chloride–methanol (1:1) for 15 min followed by a drying step using a lint-free tissue. The twister was then conditioned at 280 °C with a helium stream of 40 mL/min for 3 h. To perform the extraction, the stir bar was introduced into a 500 mL Erlenmeyer containing 100 mL of water and submitted to a stirring speed of 650 rpm for 4 h. Then stir bar was drying using a lint-free tissue and placed 10 min into 5 mL of acetonitrile for the analyte desorptions.

After extraction, the preparation of the resulting extracts varies depending on the nature of the following analysis: GC–MS or LC-FLD-MS/MS. For GC–MS analysis, the extracts obtained during each procedure were concentrated under a gentle stream of N_2 at 40 °C. Then, 500 μL of a mixture of isooctane–toluene (90/10, v/v)

was added. For LC-FLD-MS/MS, 200 μL of DMSO was added to the different resulting extracts which were then concentrated to a volume of ~200 μL under a gentle stream of N_2 at 40 °C. 100 μL of isopropanol were added, and the extract was brought to a final volume of 1 mL using ultra pure water.

2.4. Gas chromatography–mass spectrometry

GC–MS was carried out with a 6890 Agilent gas chromatograph coupled to a 5973N Agilent mass spectrometer with an Agilent 7683 autosampler (Agilent Technologies, Heilbronn, Germany). Chromatographic separation was performed on a 30 m × 0.25 mm I.D., 0.25 μm film thickness HP-5MS capillary column (Agilent Technologies, Avondale, USA). Helium (purity 99.999%) was used as a carrier gas at a constant pressure of 18.2 psi. Initial oven temperature was set at 70 °C for 2 min, followed by a linear ramp to 150 °C at a rate of 25 °C/min. Subsequently, the temperature was raised to 200 °C at a rate of 3 °C/min followed by a ramp to 280 at a rate of 8 °C/min and a hold time of 10 min. A split–spitless injector set at 280 °C was always used and injections of 1 μL were performed in the pulsed splitless mode. Transfer line temperature was set at 280 °C and the source temperature at 230 °C. The mass spectrometer was operated in the electron impact mode (EI, 70 eV). Electron multiplier voltage was set at 1900 V and the dwell time at 25 ms. Acquisition was performed in the selected ion monitoring (SIM) mode according to the parameters shown in Table 1. Three product ions were selected among the more abundant and one was chosen for quantification. The selected ions were checked with the retention time and must respect relative intensities of the standard in the range of ±10%. The quantification was carried out by double injection.

2.5. Liquid chromatography–Fluorescence detection-mass spectrometry

Analyses were performed on Agilent 1100 series HPLC (Agilent Technologies, Heilbronn, Germany) equipped with a reversed column C18 Isis Nucleodur EC (125 mm × 2.1 mm, pore size 3 μm) from Macherey-Nagel (Macherey-Nagel, Hoerdt, France). The column was kept at 27 °C and the sample injection volume was set at 20 μL. A binary mobile phase gradient with 1 mM NH_4Ac in Milli-Q water (A) and pure MeOH (B) was used at a flow rate of 0.25 mL min^{-1}. The gradient was as follows: 40% of B, increased linearly to 100% by 33 min, and held for 10 min. A 10 min equilibration step at 40% B was used at the end of each run to bring the total run time per sample to 53 min.

The fluorescence detection was performed using a multi-excitation and multi-emission mode. Finally the wavelengths used for detection of the 8 PAHs compounds included in this study were reported in Table 2. The interface between the computer and the fluorescence detector was a PCI accession card purchased to connect the analogic output. Electric signal collected from the output of detector was treated then by the Analyst software. This detection is carried out by an acquisition card. Detector announces is recorded on the analogical exit of the card. The maximum of the current tension on this exit is +1 V. A high concentration of PAHs can saturate the signal. To cope with this problem and to have an answer flax field of the detector for concentrations ranging between 2 and 100 μg/L, we optimized the gain value for each one of PAHs. The optimum gain values obtained are (number between bracket): naphthalene (9), anthracene (7), fluoranthene (9), benzo (b) fluoranthene (7), benzo (K) fluoranthene (7), benzo (A) pyrene (7), indeno (1,2,3-Cd) pyrene (10) and benzo (g, h, i) perylene (10).

The mass spectrometer used was a 3200 Q-Trap LC/MS/MS system (Applied Biosystems, Foster City, CA, USA) equipped with an ESI (TurboV) source. The operating parameters were: ion spray voltage 5 kV and −4.2 kV for positive and negative mode respectively, the temperature of the source 500 °C, the nitrogen flow 50 psig for the nebulizer gas (GS1) and 60 psig for the turbo gas (GS2). For each compound, declustering potential (DP) and collision energy (CE) of the main transitions were optimised from a continuous flow of a standard injection (10 mg/L solution at 10 μL min^{-1}) to obtain the maximum intensities (Table 2). Two MS/MS transitions were acquired for each analyte, using the Q/q intensity ratio as confirmatory parameter. The quantification was carried out by double injection.

3. Results and discussion

The aim of this paper is to develop a multi-residue analysis and ultra-trace quantification of different classes of chemicals in environmental waters identified by the EU as priority substances. We selected 36 substances among the European

Table 1
GC–MS conditions (retention time and *m/z* selected for SIM mode) and the Limit Of Detection (LOD) and Quantification (LOQ) for natural waters (expressed in ng L^{-1} for 500 mL for surface water).

Compounds	Number	Retention time	T Ion	Q Ions	ILR (μg/L)	r^2	LOD (ng/L)	LOQ (ng/L)
1,2,4-trichlorobenzene (TCL)	1	5,330	180	182; 147; 145	40–900	0.9989	6.0	25
Naphtalene (NAP)	2	5,353	128	129; 102; 64	40–900	0.9985	8.0	30
Hexachlorobutadiene (HCBD)	3	5,611	225	260; 227; 190	40–900	0.9985	6.0	27
Trifluralin (TFLA)	4	11,692	306	335; 290; 264	100–1300	0.9997	12.0	45
α-Hexachlorocyclohexane (a-HCH)	5	12,109	183	219; 145; 111	50–1200	0.9989	10.0	35
Hexachlorobenzene (HCB)	6	12,400	284	286; 249; 142	40–1100	0.9987	8.0	36
Atrazine (ATRA)	7	13,028	200	215; 202; 173	50–1200	0.9994	20.0	45
β-Hexachlorocyclohexane (b-HCH)	8	13,224	183	219; 109	50–1200	0.9990	11.0	35
γ-Hexachlorocyclohexane (c-HCH)	9	13,484	181	219; 217; 111	50–1200	0.9988	11.0	35
δ-Hexachlorocyclohexane (d-HCH)	10	14,566	181	219; 183; 109	50–1200	0.9992	12.0	35
Alachlor (ALA)	11	17,068	160	269; 237; 188	40–1000	0.9995	20.0	45
Aldrin (ALD)	12	18,556	263	298; 293; 265	40–1000	0.9990	7.0	32
Chlorpyrifos (CPF)	13	19,277	199	314; 286; 258	60–1600	0.9995	25.0	53
Isodrin (ISD)	14	20,067	193	293; 263; 195	60–1400	0.9990	23.0	49
Chlorfenvinphos (CFP)	15	21,598	267	323; 295; 269	50–1200	0.9998	32	56
Endosulfan A (ENF-1)	16	22,644	241	339; 277; 265	70–1600	0.9990	41.0	67
Dieldrin (DLD)	17	23,893	263	380; 279; 79	45–1100	0.9992	6.0	28
Endrin (END)	18	24,781	263	345; 317; 245	50–1200	0.9991	18.0	42
op-DDT	19	25,810	235	246; 237; 165	35–800	0.9996	9.0	30
pp-DDT	20	27,015	235	246; 237; 165	60–1600	0.9998	12.0	41

ILR: Instrument linearity range (μg/L); T Ion: Quantification ion; Q Ion: Qualification ion.

Table 2
LC-FLD-MS/MS conditions (retention time, ES mode used, transitions selected, Declustering Potential (DP) and Collision energy, Wavelength (nm)) and the Limit Of Detection (LOD) and Quantification (LOQ) for natural waters (expressed in ng L^{-1} for 500 mL for surface water).

Compounds	No.	RT	Instrument linearity range (μg/L)	r^2	LOD (ng/L)	LOQ (ng/L)	Detection parameters			
			Detection by mass spectrometry				ESI Mode	MRM transition (precursor/product ion)	DP (V)	CE (eV)
Simazine (SIM)	1	8.79	2–140	0.9996	0.01	0.2	+	202/132 202/124	41	25 23
Atrazine (ATRA)	2	12.97	3–160	0.9995	0.1	1	+	216/96 216/132	41	31 33
Isoproturon (IPT)	3	13.70	5–150	0.9995	0.7	2	+	207/165 207/134	46	25 31
Diuron (DIU)	4	14.60	4–140	0.9995	1.6	6	+	233/160 233/133	41	41 65
Pentachlorophenol (PCP)	5	18.80	3–110	0.9995	0.2	0.7	−	265/35 265/202	−45	−50 −44
Alachlor (ALA)	6	20.60	5–105	0.9985	1.0	9	+	270/238 270/147	26	17 33
Chlorfenvinphos (CFP)	8	23.50	4–170	0.9995	0.1	0.5	+	359/170 359/155	31	55 19
Para-ter-octylphenol (POP)	9	27.10	15–150	0.9992	4.0	15	−	205/133 205/117	−45	−36 −80
Nonylphenol (NP)	11	29.33	20–180	0.9996	4.0	30	−	219/133 219/147	−45	−44 −34
Octylphenol (OP)	12	30.40	18–170	0.9987	3.0	10	−	205/106 205/119	−40	−28 −48
4-para-nonylphenol (4NP)	14	31.97	15–150	0.9990	1.4	6	−	219/106 219/119	−50	−28 −52
Di(2-ethylhexyl)phthalate (DEHP)	15	35.58	1–160	0.9984	5.0	17	+	391/149 391/167	21	27 17

Compounds	No.	RT	Instrument linearity range (μg/L)	r^2	LOD (ng/L)	LOQ (ng/L)	Wave length (nm) (excitation/emission)
			Detection by fluorescence				
Naphtalene (NAP)	7	21.75	5–150	0.9939	–	–	220/335
Anthracene (ANTH)	10	29.31	4–100	0.9962	0.5	1	247/400
Fluoranthene (FLUA)	13	30.87	6–140	0.9909	1.0	2	236/450
Benzo(b)fluoranthene (BBF)	16	36.29	6–135	0.9989	0.5	1	236/450
Benzo(k)fluoranthene (BKF)	17	36.66	7–142	0.9983	0.5	1	251/428
Benzo(a)pyrene (BPY)	18	37.31	6–130	0.9991	0.5	3	251/428
Benzo(g,h,i)perylene (BBE)	19	39.60	5–120	0.9986	0.5	1	270/426
Indeno(1,2,3-cd)pyrene (IPY)	20	39.80	5–120	0.9987	0.5	1	270/426

Water Framework Directive: 19 pesticides (alachlor, aldrin, atrazine, chlorfenvinphos, chlorpyrifos, op-DDT, pp-DDT, dieldrin, diuron, endosulfan, endrine, α-hexachlorocyclohexane (α-HCH), β-hexachlorocyclohexane (β-HCH), γ-hexachlorocyclohexane (γ-HCH), δ-hexachlorocyclohexane (δ-HCH), isodrin, isoproturon, simazine, trifluralin), 8 PAHs (anthracene, fluoranthene, naphthalene, benzo(a)pyrene, benzo(b)fluoranthene, benzo(g,h,i)perylene, benzo(k)fluoranthene, indeno(1,2,3-cd)pyrene), 5 endocrine-disruptors (di(2-ethylhexyl)phthalate, nonylphenol, 4-para-nonylphenol, octylphenol and para-ter-octylphenol), 4 organochlorine compounds (1,2,4-trichlorobenzene, hexachlorobenzene, hexachlorobutadiene, pentachlorophenol).

As illustrated in Fig. 1, the method was developed in three steps. First, automated off-line solid-phase extraction was optimized to trap simultaneously the 36 studied compounds. Second, the 20 more volatile compounds were analysed by gas chromatography coupled to mass spectrometry with electron impact ionisation in selected ion monitoring mode (SIM). Third, the last 20 compounds were detected and quantified, in one run, by liquid chromatography coupled to fluorescence detector and mass spectrometry. So, four substances (naphtalene, atrazine, alachlor, and chlorfenvinphos) are analyzed both in GC–MS and LC-FLD-MS/MS.

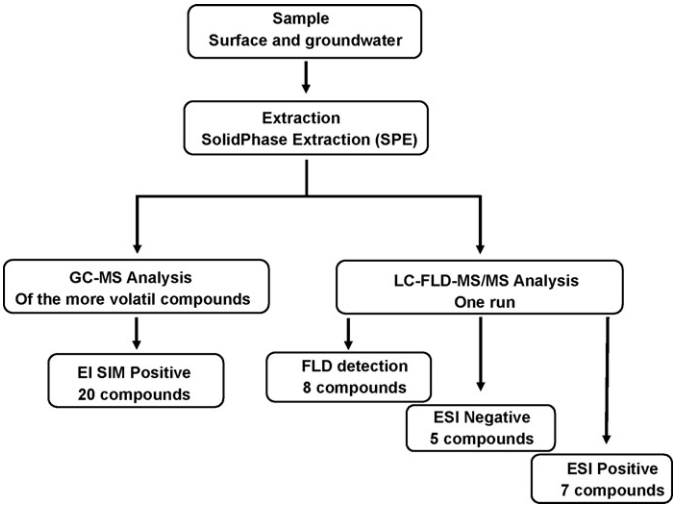

Fig. 1. Flow chart of the analytical strategy developed for the sample extraction process and analysis.

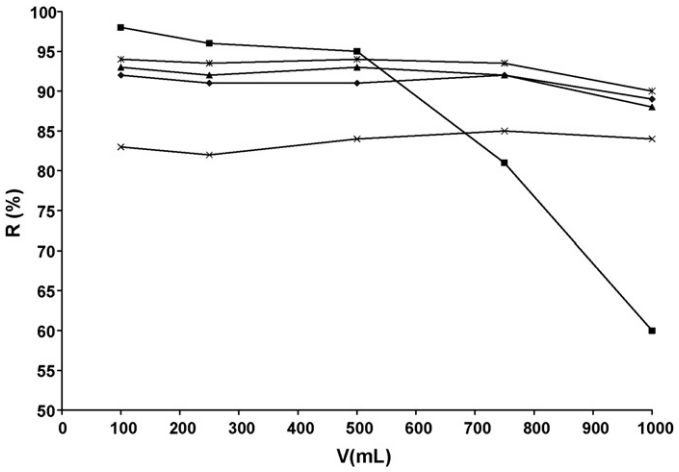

Fig. 2. Extraction recovery obtained for the loaded volume between 100 and 1000 mL with different cartridges: (♦) Strata X, (■) HLB, (▲) Strata C18, (x) Envi-carb, (*) Envi-disk.

3.1. Multi-residue extraction method

During multi-residue analysis development, the extraction step optimisation is a real analytical challenge due to the fact that compounds of different polarities, solubilities, volatilities and pK_a values have to be simultaneously extracted and analyzed. In this case, the objective of this first step was to develop a single extraction method in order to extract the 36 compounds. In this aim, we studied three types of extractions: the Solid Phase Extraction (SPE), the Stir Bar Sorptive Extraction (SBSE) and the use of adsorption media. More precisely, we tested five SPE supports: four SPE cartridges (two polymeric phases (Oasis HLB and Strata-X), one modified silica based material (Strata-C18), and one carbon based materials (Envi-carb)), and one solid phase extraction disk (Envi-C18 DSK). For the adsorption experiment, we chose one synthetic carbonaceous adsorbent (Ambersorb 572) and the SBSE extraction was performed using 20 mm length commercial TwisterTM stir bar externally coated with 0.5 mm of PDMS.

To be able to compare the SPE supports, which did not present the same quantity of phase, we had to verify the maximum volume loadable onto each SPE cartridge. This operation was carried out using typical ground waters fortified with atrazine at a concentra-

Table 3
Comparison between different types of extractions in the case of spiked surface water (100 ng L^{-1} for each compound).

Compounds	Extractions recovery (%)[a]						
	Ambersorb 572	Strata-C18	HLB	Envi-Carb	Strata-X	SBSE	Envi-disk
LC-FLD-MS/MS							
Simazine	nt	90	98	7	95	50	90
Atrazine	nt	96	99	86	88	59	99
Isoproturon	nt	90	89	78	90	57	12
Diuron	nt	51	92	85	95	52	7
Pentachlorophenol	nt	82	18	nd	105	69	9
Alachlor	nt	94	75	40	74	58	100
Naphtalene	nt	44	52	nd	75	49	45
Chlorfenvinphos	nt	84	89	73	83	50	93
Para-ter-octylphenol	nt	59	14	nd	70	50	6
Anthracene	nt	41	55	nd	65	47	45
Nonylphenol	nt	71	43	89	77	72	61
Octylphenol	nt	56	34	28	59	49	95
Fluoranthene	nt	35	38	nd	76	38	28
4-para-nonylphenol	nt	33	18	9	66	41	18
Di(2-ethylhexyl)phthalate	nt	155	140	nd	170	68	99
Benzo(b)fluoranthene	nt	38	29	nd	82	45	35
Benzo(k)fluoranthene	nt	60	12	nd	74	47	54
Benzo(a)pyrene	nt	29	22	nd	77	48	30
Benzo(g,h,i)perylene	nt	57	71	nd	75	32	58
Indeno(1,2,3-cd)pyrene	nt	65	55	nd	83	57	56
GC–MS							
1,2,4-trichlorobenzene	43	63	101	100	99	nt	98
Naphtalene	nd	40	44	nd	72	nt	40
Hexachlorobutadiene	24	31	45	63	64	nt	46
Trifluralin	51	86	99	92	102	nt	74
α-Hexachlorocyclohexane	27	83	85	94	95	nt	55
Hexachlorobenzene	28	52	60	32	61	nt	70
Atrazine	85	92	102	80	88	nt	99
β-Hexachlorocyclohexane	33	97	78	83	86	nt	54
γ-Hexachlorocyclohexane	27	87	95	78	96	nt	55
δ-Hexachlorocyclohexane	31	75	80	80	85	nt	59
Alachlor	49	96	86	35	79	nt	92
Aldrin	57	77	92	75	74	nt	86
Chlorpyrifos	50	103	83	71	76	nt	79
Isodrin	35	95	97	90	100	nt	95
Chlorfenvinphos	85	89	90	82	89	nt	96
Endosulfan A	nd	78	98	84	93	nt	87
Dieldrin	81	90	88	75	99	nt	86
Endrin	79	80	93	86	80	nt	82
op-DDT	40	75	88	70	76	nt	48
pp-DDT	48	68	76	65	73	nt	51

nd: Not detected; nt: Not tested.

[a] $n = 6$ three time by duplicate, RSD < 10%.

tion level of 0.5 μg/L. We varied the loaded volume between 100 and 1000 mL in order to determine the influence of different phenomena of interference due to the saturation of the cartridge or the loss of a fraction of contaminants by elution. As seen on Fig. 2, no significant losses by breakthrough were observed for Strata-X, Strata-C18, Envi-carb cartridges and the C18 discs, while a significant loss appears for the Oasis HLB cartridges after 500 mL, which can be related to the tiniest quantity of phase (60 mg) and not to its nature. So the maximum sample volume loadable into the cartridge is 750 mL for the Strata-X, Strata-C18, Envi-carb cartridges and the C18 discs, and 500 mL for the Oasis HLB ones. On the basis on this result, we chose to compare the different extraction method working on a volume of 500 mL of surface water spiked with the mixture of the 36 studied contaminants at a concentration of 100 ng/L. The different procedures of extraction were carried out three times and the recovery was determined by a double injection.

The Table 3 presents the extraction recovery obtained for the different types of extractions and supports tested. These results show that by SBSE and Ambersorb 572, we could extract the compounds with a range for recovery, respectively, from 32 to 72% and from 24% to 85% according to the compounds. These results are acceptable for a multi-residue procedure but they are insufficient for the analysis of ultratraces (1–10 ng/L). The recovery obtained on the Envi-carb cartridges is acceptable for pesticides but remained very weak for the phenolic compounds. We can also notice that the elution of PAHs is impossible on this support. This is related to the strong interaction between PAHs and the extraction phase. Even if the extraction on discs of the Envi-disk type has the advantage of reducing the time of extraction because it could be put on line during the filtration of the samples, the results obtained on PAHs and some products phenolic remain too modest. For three cartridges HLB, Strata-X and Strata-C18, the results obtained are acceptable for the pesticides with a better performance for the Strata-X cartridges on the phenolic compounds and PAHs. The recovery very high noted for Di (2-ethylhexyl) phthalate is due to the leaching of this product by the cartridge body. This problem could be eliminated by using Teflon cartridges. Based on these results, Strata-X cartridges were chosen to perform the SPE procedure.

In environmental matrix, analyte recoveries using Strata-X cartridges were determined on 30 ng/L fortified typical surface waters, representative of real environmental scenario, by adding known and appropriate volumes of the working standard solution. The recoveries were also greater than 60% for the target compounds ranging from 59% to 105%, with relative standard deviation inferior to 10%.

3.2. Analytical strategy

3.2.1. Gas chromatography/mass spectrometry

With the GC conditions optimized, a single run in GC/EI/MS permitted the multi-residue analysis of the 20 more volatile compounds in 28 min, and it offered good sensitivity and selectivity. Fig. 3 displays the GC/MS total ion chromatogram of surface water spiked with a standard mixture at 100 ng/μL using the HP-5MS capillary column. Characterization of all 20 compounds was performed before establishing the time-scheduled SIM conditions. Table 1 depicts the two or three qualification ions and the quantification ion of each compound.

3.2.2. Liquid chromatography/fluorescence/mass spectrometry detections

The last 20 compounds were detected and quantified, in one run, by liquid chromatography coupled to fluorescence detector and mass spectrometry (Fig. 4). The optimization of the chromatographic conditions was carried out on a mixture of standards at a concentration of 2 mg/L by UV detection. We tested two organic solvents (methanol and acetonitrile) and the best gradient was obtained using a mixture of water and methanol. Retention times of the compounds were determined by injecting the pure standards. The determination of excitation and emission wavelengths for the detection of PAHs by fluorescence was carried out using a mixture of standards. Detection by mass spectrometry was carried out in a FIA mode on pure compounds in a mixture of water and methanol (50/50) then on the mixture of the 20 products under the same conditions.

We chose to separate the different compounds using a stationary phase with a particle diameter of 3 μm and a mobile phase

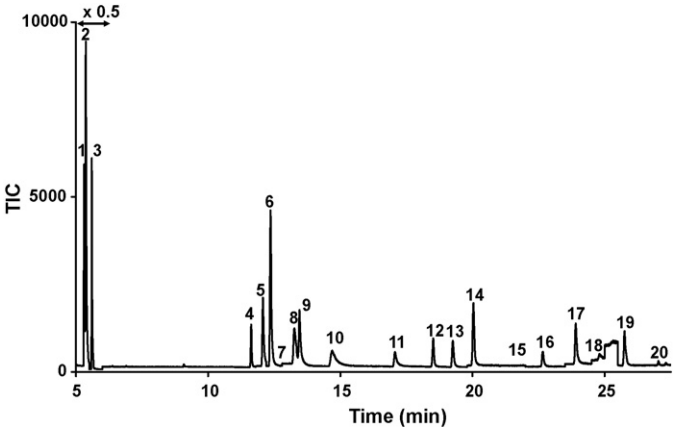

Fig. 3. GC–MS chromatogram of surface water spiked with a standard mixture at 100 μg/mL acquired in the selected ion monitoring (SIM) (compounds number cf Table 1).

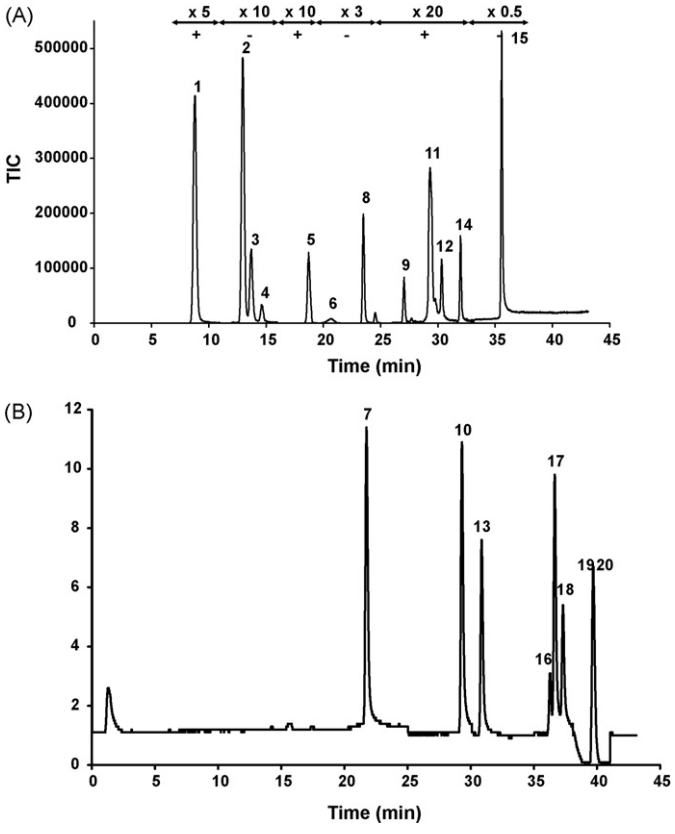

Fig. 4. LC-FLD-MS/MS chromatogram of surface water spiked with (A) a standard mixture at 40 μg L^{-1} acquired in MRM mode and (B) a standard mixture at 20 μg L^{-1} detected in fluorescence mode (injection of 20 μL) (compounds number cf Table 2).

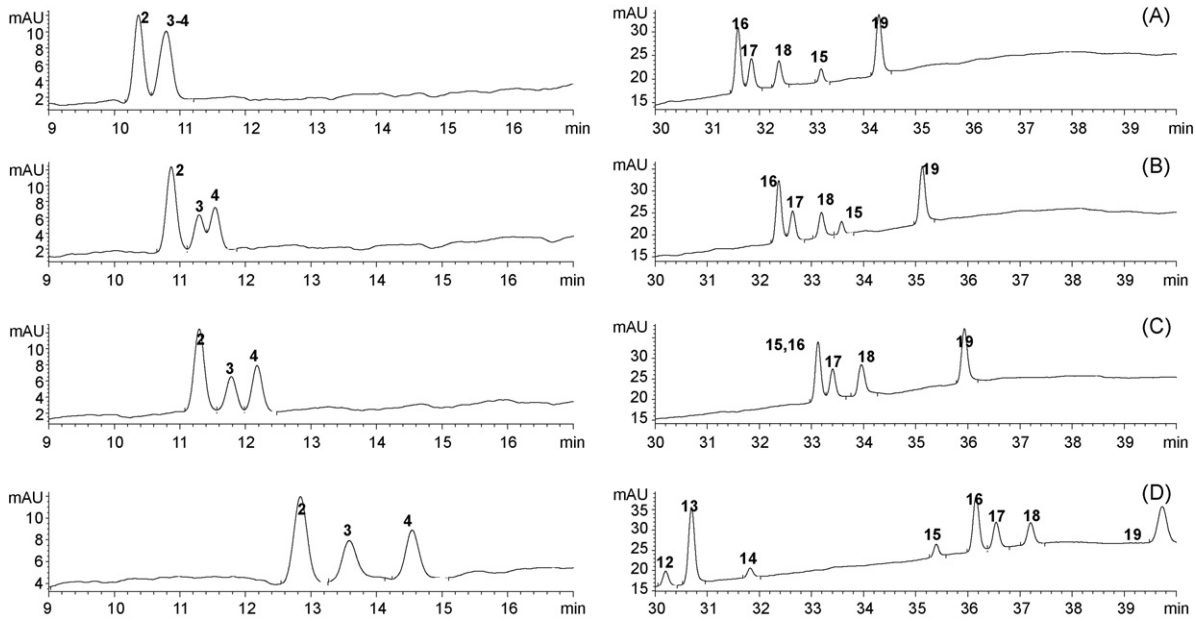

Fig. 5. Influence of the temperature onto the separation of standard mixture at 5 mg L^{-1} acquired in UV mode obtained at: (A) 50 °C, (B) 40 °C, (C) 35 °C, (D) 25 °C (injection of 2 μL, detection at 220 nm) (compounds number cf Table 2).

made up of ultrapure water plus methanol at 40% of methanol in the beginning of the gradient. Under these conditions the pressure is very high. To reduce it, we modified the temperature and studied its influence onto the separation. The temperature of separation was determined by a series of injection from 25 to 50 °C by step of 5 °C (Fig. 5A–D). The Fig. 5 shows the possibility of a good resolution for the separation of the isoproturon (**3**) and the diuron (**4**) between 25 and 35 °C (Fig. 5C–D). Nevertheless, at 35 °C, the separation between the benzo (b) fluoranthene (**16**) and the di(2-ethylhexyl)phthalate (**15**) is badly affected (Fig. 5C). So, the best condition for the whole separation is a temperature about 25 °C (Fig. 5D). But, under these conditions, the pressure is always too high onto the column due to the low temperature and the important viscosity of the starting mixture solvents. So to reduce the pressure, we had to increase the temperature finding a compromise for the separation. Since the detection and the quantification of the benzo (b) fluoranthene and the di(2-ethylhexyl)phthalate (**15**) are carried out by two different modes of detections, fluorescence and mass spectrometry respectively, we made a point of having a resolution of 1.5 to avoid any ion suppression in the mass spectrometer source. In conclusion, to have a resolution of 1.5 between the benzo (b) fluoranthene and the di(2-ethylhexyl)phthalate and to reduce the pressure we chose to work at 27 °C.

Besides, the mass spectrometry method was developed using the possibility offered by the 3200 Q-Trap LC–MS/MS system to switch the mode used (positive or negative) during the run. Based on the chromatographic separation obtained, we defined five different periods: (i) in the first one from 0 to 17 min, ESI positive mode, (ii) from 17 to 20 min, ESI negative mode to detect Pentachlorophenol, (iii) from 20 to 26 min, positive mode, (iv) from 26 to 34 min, ESI negative mode to detect alkylphenols, (v) before returning to positive mode for the final 9 min.

In conclusion, we reported, on Fig. 4, an example of chromatogram obtained by coupling HPLC-FLD-MS/MS under the optima conditions of separation and detection on surface water spiked with mixture of the 20 contaminants at concentration level of 10 μg/L. In a single run of forty minutes, the multi-residue analysis of 20 compounds is performed: 8 compounds (the PAHs) were detected with a fluorescence detector, 7 in ESI positive mode and 5 in ESI negative mode (Figs. 1 and 4).

3.3. Matrix effects, surfactant and analyte protectant

During real sample analysis, sample matrix may cause serious problems at different steps of the analysis process, notably the SPE extraction step and the GC–MS or LC–MS/MS analyses. On the one hand, in fresh waters systems, organic micropollutants are bound to natural organic matter, which is responsible for a decrease in their recoveries by solid-phase extraction [26]. On the other hand, one of the limitations of GC–MS and LC–MS/MS analyses is their susceptibility to coextracted matrix components, which results typically in the suppression or the enhancement of the analyte signal [27–29].

The negative effect of organic macromolecules observed in water on the SPE of PAHs, n-alkanes, steroids seems to be due to clogging phenomenon, which induces a competition between organic macromolecules (DNA, polysaccharides, humic acids ...) and organic pollutants for the available sorption sites [26]. The addition of surfactant like cetyltrimethylammonium bromide [30] or isopropanol [26] to water sample has been proved to prevent this negative effect. Isopropanol was chosen in this study because it is less noxious and environmentally hazardous than cetyltrimethylammonium bromide.

In order to assess the efficiency of the surfactant (isopropanol) to improve the efficiency of SPE, recoveries were evaluated on a surface water sample spiked with analytes at a concentration of 30 ng/L with and without isopropanol (Table 4). The addition of isopropanol prior to the extraction step induces an increase in the recovery for the majority of target compounds. Four pesticides (trifluralin, α-hexachlorocyclohexane, aldrin, isodrin) are extracted only in presence of isopropanol. The efficiency of the SPE of PAHs (anthracene and fluoranthene) and alkyphenols (NP, OP, 4-NP) has been improved by ~20% compared to the results for water without isopropanol. For the other compounds, the recoveries obtained with isopropanol are in the range of those obtained without isopropanol.

Matrix components can severely compromise another step of the analysis, which is the analysis, itself, either by GC–MS or LC–MS/MS. In GC–MS, the use of analyte protectants to avoid the matrix-induced response enhancement was first proposed by Erney and Poole [28] before being re-introduced by Anastassiades and coworkers [27]. Analyte protectants are compounds that strongly interact with active sites in GC system, thus decreasing degrada-

Table 4
Isopropanol impact on the recovery of the target molecules from spiked surface water (30 ng L^{-1} for each compound).

Compounds	Isopropanol impact (%)[a]
LC-FLD-MS/MS	
Simazine	−8
Atrazine	0
Isoproturon	5
Diuron	3
Alachlor	6
Chlorfenvinphos	2
Para-ter-octylphenol	7
Anthracene	25
Nonylphenol	23
Octylphenol	15
Fluoranthene	26
4-para-nonylphenol	21
Benzo(b)fluoranthene	1
Benzo(k)fluoranthene	9
Benzo(a)pyrene	3
Benzo(g,h,i)perylene	2
Indeno(1,2,3-cd)pyrene	5
GC–MS	
1,2,4-trichlorobenzene	0
Naphtalene	3
Hexachlorobutadiene	−1
Trifluralin	88
α-Hexachlorocyclohexane	97
Hexachlorobenzene	0
Atrazine	5
β-Hexachlorocyclohexane	7
γ-Hexachlorocyclohexane	10
δ-Hexachlorocyclohexane	6
Alachlor	0
Aldrin	82
Chlorpyrifos	6
Isodrin	65
Chlorfenvinphos	5
Endosulfan A	2
Dieldrin	2
Endrin	−1
op-DDT	0
pp-DDT	3

[a] $n = 6$ three time by duplicate, RSD < 15%.

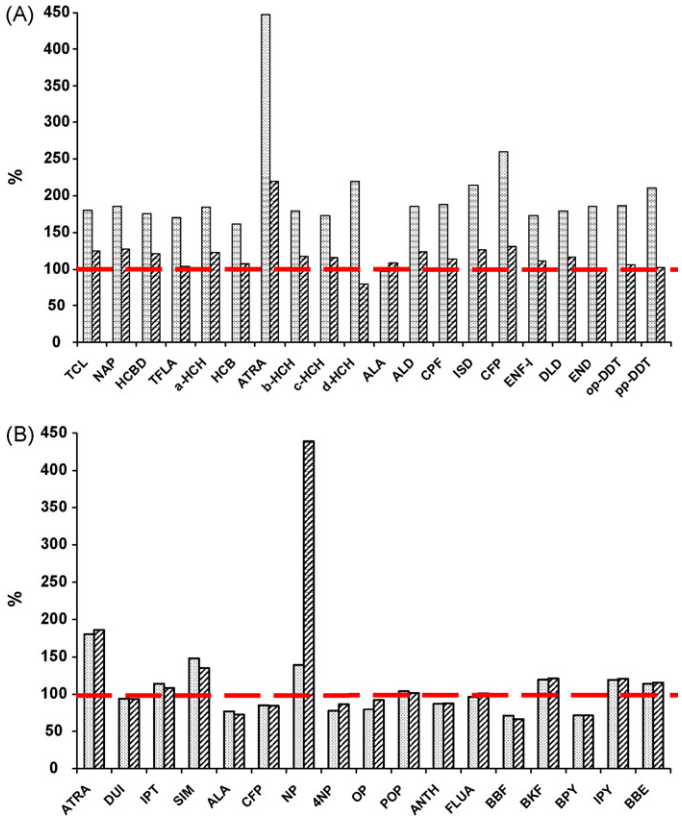

Fig. 6. The percentage of signal intensity in a sample matrix versus the signal of the same concentration in the pure solvent in absence (dot) or presence (line) of isopropanol: (A) for GC–MS analysis (used solvent: isooctane–toluene (90/10, v/v)), and (B) for LC-FLD-MS/MS (used solvent: DMSO–isopropanol–water (20/10/70, v/v)) (compounds abbreviation cf Tables 1 and 2).

tion and/or adsorption of co-injected analytes [27,28]. Different mixtures were proposed; we decided to evaluate the application of isopropanol, used previously.

First, the evaluation of the extent of ion suppression/enhancement was conducted using a spiked ground-water sample at a concentration of 30 ng/L (experiment in duplicate). The signal change was calculated for each individual compounds as the percentage of signal intensity in a sample matrix versus the signal of the same concentration in standard solution (for GC–MS in isooctane–toluene (90/10, v/v); and for LC–MS/MS in DMSO–isopropanol–water (20/10/70, v/v)).

Fig. 6 shows the change in analyte signal in GC–MS (Fig. 6A) and in LC–MS/MS (Fig. 6B). In LC–MS/MS analysis, for the majority of the compounds the signal modification was less than 30% except for atrazine, simazine and nonylphenol. But on the other hand, the signal enhancement observed in GC–MS analysis was superior to 60% for the all compounds except for alachlor and β-Hexachlorocyclohexane.

The evaluation of the efficiency of the analyte protectant to compensate the matrix-induced response enhancement observed in GC–MS was conducted again using a spiked ground-water sample at a concentration of 30 ng/L in presence of isopropanol (experiment in duplicate). Fig. 6 clearly demonstrates the beneficial effect of the analyte protectant addition, resulting in signal modification inferior to 30% for all the compounds in GC–MS (except atrazine). For the LC–MS/MS analysis, no change was observed, preserving the good analytical performances previously obtained. So these results demonstrate that isopropanol is a good surfactant to prevent the negative effect of matrix on SPE stage as well as an efficient analyte protectant for GC–MS analysis.

3.4. Validation studies of the analytical method

Statistical validation of the method was performed evaluating the limits of detection (LOD) and quantification (LOQ) as well as the accuracy, the precision and the linearity.

The limits of detection and quantification were estimated as the analyte concentration with a signal-to-noise-ratio of respectively 3 and 10 when injecting the real sample extract. For the GC–MS analyses (Table 1), the limits of detection for the majority of the compounds are below 40 ng/L for natural waters, ranging from 6 ng/L for 1,2,4-trichlorobenzene to 41 ng/L for endosulfan. The low sensitivity for endosulfan A, chlorpyrifos, and trifluralin was previously observed in recent wok based on analysis using GC-(EI)-MS/MS [10]. This behaviour can be explained by the very high fragmentation by electron ionisation in the mass spectrometer resulting in poor response concentration ratios. Moreover, for the LC-FLD-MS/MS analysis, Table 2 shows that the limits of detection obtained allows environmental studies, without any ambiguity, since for the 8 compounds detected by fluorescence, the limit of detection (LOD) vary from 0.5 to 8 ng/L while the limit of detection of the 12 last compounds detected by mass spectrometry vary from 0.01 to 5 ng/L.

Regarding LOD and LOQ, it is troublesome to make a realistic comparison with those reported in the literature using other GC or

Table 5
Accuracy and precision of the developed method.

LC-FLD-MS/MS	Repeatability				Reproducibility			
	1st day ($n=6$)		2nd day ($n=6$)		3rd day ($n=6$)		($n=18$)	
	R (%)	RSD (%)	R (%)	RSD (%)	R (%)	RSD (%)	R (%)	RSD (%)
1,2,4-trichlorobenzene	94.0	2.1	91.8	5.2	92.6	3.8	92.8	3.5
Naphtalene	71.6	2.9	69.8	3.8	70.5	2.7	70.6	3.0
Hexachlorobutadiene	59.8	3.3	58.4	6.1	58.9	4.8	59.1	4.3
Trifluralin	101.3	2.4	98.9	3.7	99.8	2.5	100.0	2.8
α-Hexachlorocyclohexane	93.6	3.2	91.4	6.0	92.2	4.7	92.4	4.3
Hexachlorobenzene	60.1	5.2	58.7	7.7	59.2	6.6	59.3	5.8
Atrazine	91.2	2.6	89.0	5.6	89.8	4.2	90.0	3.9
β-Hexachlorocyclohexane	87.6	3.3	85.6	6.1	86.3	4.8	86.5	4.4
γ-Hexachlorocyclohexane	92.0	2.6	89.9	5.6	90.7	4.2	90.9	3.9
δ-Hexachlorocyclohexane	89.6	2.6	87.4	5.6	88.2	4.2	88.4	3.9
Alachlor	72.1	2.3	70.6	5.3	71.2	3.9	71.3	3.6
Aldrin	78.2	4.3	76.4	7.0	77.1	5.8	77.2	5.1
Chlorpyrifos	78.1	2.8	76.2	5.8	76.9	4.4	77.0	4.0
Isodrin	95.7	2.0	93.4	5.1	94.2	3.7	94.4	3.4
Chlorfenvinphos	85.5	3.4	83.5	6.2	84.2	4.9	84.4	4.4
Endosulfan A	97.8	3.0	95.5	5.9	96.4	4.6	96.6	4.1
Dieldrin	97.1	2.5	94.8	5.5	95.6	4.2	95.8	3.8
Endrin	83.4	3.4	81.4	6.2	82.1	4.9	82.3	4.4
op-DDT	70.7	3.0	69.0	5.9	69.6	4.5	69.8	4.1
pp-DDT	76.0	4.4	74.2	7.0	74.8	5.8	75.0	5.2
GC-MS	**Repeatability**				**Reproducibility**			
	1st day ($n=6$)		2nd day ($n=6$)		3rd day ($n=6$)		($n=24$)	
	R (%)	RSD (%)	R (%)	RSD (%)	R (%)	RSD (%)	R (%)	RSD (%)
Simazine	93	2.2	93	2.2	94	1.3	93	4.1
Atrazine	90	1.5	89	1.3	92	0.6	91	3.4
Isoproturon	90	1.8	86	3.3	88	3.3	88	2.2
Diuron	90	4.2	89	4.3	91	2.5	90	3.6
Pentachlorophenol	99	4.0	102	5.3	101	4.7	101	9.1
Alachlor	85	4.7	83	6.2	89	1.7	86	3.6
Naphtalene	72	3.4	68	1.6	70	2.8	70	3.4
Chlorfenvinphos	83	6.5	84	7.8	88	0.9	85	2.1
Para-ter-octylphenol	66	3.9	70	4.0	68	4.3	68	3.6
Anthracene	63	9.4	68	11.2	69	4.3	66	4.9
Nonylphenol	72	3.7	72	3.3	73	5.1	72	3.6
Octylphenol	57	5.2	55	2.9	55	2.6	56	4.4
Fluoranthene	73	3.6	74	2.3	74	2.2	74	16.8
4-para-nonylphenol	61	3.9	62	4.2	62	7.4	62	4.0
Di(2-ethylhexyl)phthalate	191	6.4	138	4.7	124	12.8	148	4.9
Benzo(b)fluoranthene	81	2.0	79	0.8	81	2.4	80	4.0
Benzo(k)fluoranthene	70	5.5	78	0.7	77	0.8	76	4.2
Benzo(a)pyrene	74	3.3	74	3.9	72	0.6	73	4.9
Benzo(g,h,i)perylene	76	3.5	77	2.6	78	3.2	76	2.0
Indeno(1,2,3-cd)pyrene	86	3.5	87	2.6	88	3.2	86	5.5

R: Recovery; RSD: Relative Standard Deviation.

LC techniques since LOD and LOQ are dependent on the methodology used for their estimation (initial volume of sample, method of sample preparation, type of mass spectrometer, type of studied water). However, compared with other methodologies concerning the Water Framework Directive [8,10,14], we achieved comparable LOD, even better ones [10].

We carried out the study of precision, expressed as repeatability and accuracy, expressed as reproducibility using spiked water at a concentration of 100 ng/L. The accuracy was estimated by means of recovery experiments analyzing deionised water ($n=18$ for GC–MS or 24 for LC-FLD-MS/MS) in different days (Table 4). The precision of the method was determined in terms of relative standard deviation (RSD, %) from the recovery experiments ($n=6$) of analyses performed in the same day. Table 5 shows the results obtained for the GC–MS and LC-FLD-MS/MS methods. Concerning the GC–MS method, results for repeatability show the good precision of the method with a RSD mean value of 3.1, 5.8 and 4.5 for the 1st day, 2nd day and 3rd day respectively. The results for reproducibility indicate the good robustness of the method with RSD mean values of 4.1. For the LC-FLD-MS/MS, the precision is very good with a RSD mean value of 4.1, 3.8 and 3.34 for the 1st day, 2nd day and 3rd day respectively while the reproducibility is better than 17% for all the compounds varying from 2.1% for Chlorfenvinphos to 16.8% for Fluoranthene, with a mean value of 4.7.

For the linearity study, the range of concentration studied in GC–MS was 40-1600 μg/L analyzing reference standard solution at six concentration levels (40, 100, 300, 800 and 1600 μg/L). As shown in Table 1, correlation coefficients (r^2) were higher than 0.998 for all the compounds. On the other hand, the calibration curves were obtained, for the LC-FLD-MS/MS method, analyzing reference standard solutions whose concentration varies from 0.4 to 150 μg/L. Linearity was assumed when regression coefficient was superior to 0.99 (Table 2) and is in the range of concentration of 1-180 μg/L, which corresponded to 2–360 ng/L in the water sample applying the SPE concentration factor of 500 in this case.

Table 6
Occurrence and concentration of target compounds in waters analysed.

	TV (μg/L)	LOD (ng/L)	% of contaminated samples	% CCS > TV	% TV > CCS > 0.5TV	% 0.5TV > CCS > 0.2TV	% 0.2TV > CCS
Alachlor	300	1.0	95.4	–	–	–	100
Aldrin	10	7.0	41.7	20.0	80.0	–	–
Anthracene	100	0.5	95.8	–	–	–	100
Atrazine	600	0.1	100	–	–	–	100
Benzo(b)fluoranthene	50	0.5	16.6	–	–	25	75
Benzo(k)fluoranthene	30	0.5	29.1	–	–	–	100
Benzo(g.h.i)perylene	16	0.5	100	–	–	–	100
Benzo(a)pyrene	50	0.5	87.5	–	–	4.7	95.2
Chlorfenvinphos	60	0.1	36.4	–	–	12.5	87.5
Chlorpyrifos	30	25.0	95.8	73.9	26.1	–	–
Dieldrin	10	6.0	58.3	28.5	71.5	–	–
Di(2-ethylhexyl)phthalate	1 300	5.0	95.4	–	–	19	81
Diuron	200	1.6	72.7	–	–	6.2	93.7
op-DDT	10	9.0	54.2	100.0	–	–	–
pp-DDT	10	12.0	4.2	100.0	–	–	–
Endosulfan A	5	41.0	0.0	–	–	–	–
Endrin	5	18.0	12.5	100.0	–	–	–
Fluoranthene	90	1.0	95.8	–	–	–	100
Hexachlorobenzene	30	8.0	0.0	–	–	–	–
Hexachlorobutadiene	100	6.0	0.0	–	–	–	–
α-Hexachlorocyclohexane	100	10.0	33.3	–	–	12.5	87.5
β-Hexachlorocyclohexane	100	11.0	91.7	–	–	4.5	95.5
γ-Hexachlorocyclohexane	100	11.0	75.0	–	–	11.1	88.9
δ-Hexachlorocyclohexane	100	12.0	0.0	–	–	–	–
Indeno(1.2.3-cd)pyrene	16	0.5	100	–	–	–	100
Isodrin	5	23.0	62.5	100.0	–	–	–
Isoproturon	300	0.7	31.8	–	–	–	100
Naphtalene	2 400	8.0	87.5	–	–	–	100
Nonylphenol	300	4.0	100	4.5	9.1	18	68.2
4-para-nonylphenol	300	1.4	68.1	–	–	–	100
Octylphenol	60	3.0	63.6	–	–	28.6	71.4
Para-ter-octylphenol	60	4.0	100	82	4.6	14	–
Pentachlorophenol	2 000	0.2	0	–	–	–	–
Simazine	700	0.01	77.3	–	–	–	100
1,2,4-trichlorobenzene	400	6.0	8.3	100.0	–	–	–
Trifluralin	30	12.0	4.2	100.0	–	–	–

TV: Threshold value; CCS: Concentration of Contaminated Samples.

3.5. Application to real samples

The multiresidue methodology optimized was applied in a study carried out in France (Rhône-Alpes Region) in order to accomplish the Water Framework Directive 2000/60/EC concerning the survey of the Directive target contaminants in surface water. 20 samples were analyzed for the 36 compounds as depicted above. The results obtained are presented in the Table 6.

None of the water was organic-contaminant-free. Three different groups of compounds appear. Seventeen compounds found in almost all the analysed samples but usually at very low concentration form the first group. These substances contaminating between 63.8 and 100% of the samples are 7 pesticides (β-Hexachlorocyclohexane, γ-Hexachlorocyclohexane, chlorpyrifos, simazine, atrazine, diuron, alachlor), 6 PAH (anthracene, benzo(a)pyrene, benzo(g,h,i)perylene, fluoranthene, naphthalene, indeno(1,2,3-cd)pyrene), and 4 endocrine-disruptors (octylphenol, nonylphenol, 4-para-nonylphenol, di(2-ethylhexyl)phthalate). Fortunately, the concentration found for these 17 compounds in the surface waters are inferior to 20% of the threshold values fixed by the 2000/60/EC directive, except for the chlorpyrifos and the nonylphenol, for which 73.9% and 4.5% of the sample contaminated present a concentration superior to the threshold value. This widespread trace level pollution has been described in most countries including Portugal, [31] Greece [32–35] and Spain [10]. For example, concerning the contamination of freshwaters by pesticides, it is apparent [35] that the three most commonly encountered compounds in Europe are atrazine, simazine and alachlor, in agreement with our results.

On the other hand, the second groups constitutes 9 other substances contaminating few samples but at a level higher than the threshold values fixed by the 2000/60/EC directive: 7 pesticides (dieldrine, endrine, trifluralin, aldrin, isodrin, op-DDT, pp-DDT), one endocrine-disruptor (para-ter-octylphenol) and one organochlorine compound (1,2,4-trichlorobenzene). These results can be explained by the choice of the threshold values. These compounds present, indeed, the lowest values in the Water Framework (from 0,005 to 0,060 μg/L) [5]. This pattern is in agreement with previously reported results published in France [15] or Greece [32–34].

Finally, the last group regroups five target products which were not found in any sample: hexachlorobutadiene, γ-hexachlorocyclohexane, hexachlorobenzene, endosulfan, and pentachlorophenol.

4. Conclusion

With the growing attention to contaminants in the environment, there is a need for quick and sensitive analytical method that can screen for a wide variety of compounds simultaneously. The analytical methodology described above provides a sensitive method for the detection of a wide range of priority organic compounds included in the 2000/60/EC European Water Framework Directive: pesticides, PAH, endocrine-disruptors and organochlorine compounds. The automated SPE followed by GC–MS and LC-FLD-MS/MS gives the sensitivity and selectivity necessary to the detection of these compounds at environmental relevant concentration in the nanogram per litre range. The development of a single extraction procedure for all samples and all analytes, sensitive and robust,

irrespective of concentration levels and water physico-chemical properties is a real analytical challenge and a real advance in environmental sciences. This methodology will allow the monitoring launched by the EU on water quality, and will make possible to analyze temporal and/or spatial distributions of organic contaminants in the aquatic environment.

Acknowledgments

The authors thank the CNRS (Centre National de la Recherche Scientifique) for S.B.'s post-doctoral stage's funding and the Rhône-Alpes Region for the Rhodanos program funding on the DEMA study (Development of analytical methods for priority substances).

References

[1] T. Reemtsma, M. Jekel, Organic Pollutants in the Water Cycle, Wiley-VCH Verlag GmBH & Co. KGaA, Weinheim, 2006.
[2] J.A.C. Barth, P. Grathwohl, K.C. Jones, Environmental Pollution 148 (2007) 693.
[3] J.L. Domingo, A. Bocio, Environment International 33 (2007) 397.
[4] M.S. Evans, D. Muir, W.L. Lockhart, G. Stern, M. Ryan, P. Roach, Science of the Total Environment 351 (2005) 94.
[5] Directive 2000/60/EC, Off. J. Eur. Commun., October 23, L327 (2000).
[6] S.D. Richardson, Analytical Chemistry 79 (2007) 4295.
[7] C.J. Koester, A. Moulik, Analytical Chemistry 77 (2005) 3737.
[8] S. Lacorte, I. Guiffard, D. Fraisse, D. Barcelo, Analytical Chemistry 72 (2000) 1430.
[9] H.B. Lee, T.E. Peart, M.L. Svoboda, Journal of Chromatography A 1094 (2005) 122.
[10] E. Pitarch, C. Medina, T. Portoles, F.J. Lopez, F. Hernandez, Analytica Chimica Acta 583 (2007) 246.
[11] S.Y. Zhang, Q.A. Zhang, S. Darisaw, O. Ehie, G.D. Wang, Chemosphere 66 (2007) 1057.
[12] R.A. Trenholm, B.J. Vanderford, J.C. Holady, D.J. Rexing, S.A. Snyder, Chemosphere 65 (2006) 1990.
[13] T.A. Ternes, M. Bonerz, N. Herrmann, D. Loffler, E. Keller, B.B. Lacida, A.C. Alder, Journal of Chromatography A 1067 (2005) 213.
[14] C. Huertas, J. Morillo, J. Usero, I. Gracia-Manarillo, Talanta 72 (2007) 1149.
[15] J.-B. Baugros, B. Giroud, G. Dessalces, C. Cren-Olivé, M.-F. Grenier-Loustalot, Analytica Chimica Acta 607 (2008) 191.
[16] B.J. Vanderford, R.A. Pearson, D.J. Rexing, S.A. Snyder, Analytical Chemistry 75 (2003) 6265.
[17] D.A. Lambropoulou, I.K. Konstantinou, T.A. Albanis, Journal of Chromatography A 1152 (2007) 70.
[18] G. Ouyang, J. Pawliszyn, Trac-Trends in Analytical Chemistry 25 (2006) 692.
[19] F. David, P. Sandra, Journal of Chromatography A 1152 (2007) 54.
[20] S. Rodriguez-Mozaz, M.J.L. de Alda, D. Barcelo, Journal of Chromatography A 1152 (2007) 97.
[21] F.A. Esteve-Turrillas, A. Pastor, M. de la Guardia, Analytical and Bioanalytical Chemistry 387 (2007) 2153.
[22] L. Alder, K. Greulich, G. Kempe, B. Vieth, Mass Spectrometry Reviews 25 (2006) 838.
[23] D.L. Poster, M.M. Schantz, L.C. Sander, S.A. Wise, Analytical and Bioanalytical Chemistry 386 (2006) 859.
[24] M. Petrovic, E. Eljarrat, M.J.L. de Alda, D. Barcelo, Journal of Chromatography A 974 (2002) 23.
[25] M.J.L. de Alda, S. Diaz-Cruz, M. Petrovic, D. Barcelo, Journal of Chromatography A 1000 (2003) 503.
[26] L. Jeanneau, P. Faure, E. Jarde, Journal of Chromatography A 1173 (2007) 1.
[27] K. Mastovska, S.J. Lehotay, M. Anastassiades, Analytical Chemistry 77 (2005) 8129.
[28] D.R. Erney, C.F. Poole, Hrc-Journal of High Resolution Chromatography 16 (1993) 501.
[29] W.M.A. Niessen, P. Manini, R. Andreoli, Mass Spectrometry Reviews 25 (2006) 881.
[30] N.Q. Li, H.K. Lee, Journal of Chromatography A 921 (2001) 255.
[31] S. Lacorte, P. Viana, M. Guillamon, R. Tauler, T. Vinhas, D. Barcelo, Journal of Environmental Monitoring 3 (2001) 475.
[32] A.D. Nikolaou, S. Meric, D.F. Lekkas, V. Naddeo, V. Belgiorno, S. Groudev, A. Tanik, Desalination 226 (2008) 306.
[33] T. Lekkas, G. Kolokythas, A. Nikolaou, M. Kostopoulou, A. Kotrikla, G. Gatidou, N.S. Thomaidis, S. Golfinopoulos, C. Makri, D. Babos, M. Vagi, A. Stasinakis, A. Petsas, D.F. Lekkas, Environment International 30 (2004) 995.
[34] T. Lekkas, M. Kostopoulou, A. Petsas, M. Vagi, S. Golfinopoulos, A. Stasinakis, N. Thomaidis, G. Pavlogeorgatos, A. Kotrikla, G. Gatidou, N. Xylourgidis, G. Kolokythas, C. Makri, D. Babos, D.F. Lekkas, A. Nikolaou, Journal of Environmental Monitoring 5 (2003) 593.
[35] I.K. Konstantinou, D.G. Hela, T.A. Albanis, Environmental Pollution 141 (2006) 555.

Talanta 79 (2009) 657–664

Contents lists available at ScienceDirect

Talanta

journal homepage: www.elsevier.com/locate/talanta

Implementation of enhanced correlation maps in near infrared chemical images: Application in pharmaceutical research

Carlos Cairós[a], José Manuel Amigo[b,*], Robert Watt[c], Jordi Coello[a], Santiago Maspoch[a]

[a] Departament de Química, Facultat de Ciències, Universitat Autònoma de Barcelona, 08193 Bellaterra, Barcelona, Spain
[b] Department of Food Science, Faculty of Life Sciences, University of Copenhagen, Rolighedsvej 30, DK-1958 Frederiksberg-C, Denmark
[c] The School of Pharmacy-University of London, 29/39 Brunswick Square, London WC1N 1AX, UK

ARTICLE INFO

Article history:
Received 4 February 2009
Received in revised form 16 April 2009
Accepted 21 April 2009
Available online 3 May 2009

Keywords:
Chemical imaging
Enhanced contrast function
Tablets
Singularities
Hyperspectral near infrared

ABSTRACT

Recent developments in Hyperspectral Imaging equipment have made possible the use of this analytical technique for fast scanning of sample surfaces. This technique has turned out to be especially useful in Pharmacy, where information about the distribution of the components in the surface of a tablet can be obtained. One particular application of Hyperspectral Chemical Imaging is the search for singularities inside pharmaceutical tablets, e.g. coating defects. Nevertheless, one problem has to be faced: how to analyze a sample without any previous knowledge about it, or having only the minimum information about the tablet.

In this work a new methodology, based on correlation coefficients, is introduced to obtain valuable information about one Hyperspectral Image (detection of defects, punctual contaminants, etc.) without any previous knowledge. The methodology combines Principal Component Analysis (PCA), correlation coefficient between one specific pixel included in the image and the rest of the image; and a new enhanced contrast function to obtain more selective chemical and spatial information about the image. To illustrate the applicability of the proposed methodology, real tablets of ibuprofen have been studied.

The proposed methodology is presented as a control technique to detect batch variability, defects in final tablets and punctual contaminants, being a potential supplementary tool for quality controls. In addition, the usefulness of the proposed methodology is not exclusive to NIR-CI devices, but to any hyperspectral and multivariate image system.

1. Introduction

In the last years the traditional single point spectroscopy (mainly focused on near infrared, Fourier Transform Infrared and Raman Spectroscopy) has been successfully combined with mapping devices that allow obtaining a spectral pattern in each area unit of one surface (commonly denoted as pixel). With the inclusion of these techniques, Hyperspectral Chemical Imaging devices have increased the possibilities in a number of research fields, especially in pharmaceutical research [1–5]. The opportunity to obtain quality spectral information of tablets surface in a short period of time allows the direct analysis of the sample without needing further chemical analysis. In this sense, the targets are focused in two different aspects: to study the distribution of the analytes in the surface of the tablet; and to detect and locate anomalies, defects, contaminants or thickness of coatings.

Analysis of chemical images with mathematical tools makes possible to extract the desirable information from the raw data [1,6]. For example, a number of research works have been recently published focusing the interest in the analysis of pharmaceutical mixtures being blended to assure the perfect distribution of all the analytes on the surface of the product tablet [7–10]. In this sense, techniques like Partial Least Squares Regression (PLS-R), Classical Least Squares (CLS) or even Multivariate Curve Resolution-Alternating Least Squares (MCR-ALS) are being applied [1,2,10].

Nevertheless, the execution of these tasks presents several drawbacks, being the main one the lack of any prior information about the components forming the tablet, or that the pure analytes available in a research laboratory are not identical to the analytes used for manufacturing the tablets. This is the case, for example, when adulterated samples are studied or when unknown contaminants are present in one tablet/surface. Consequently, pharmaceutical researchers are continuously looking for robust and reliable working methodologies that allow obtaining the maximum information of interest of the tablet with the minimum previous knowledge.

In this sense, several methods have been already proposed to extract valuable information about the Hyperspectral Images without further information. The main ones are Principal Component Analysis (PCA) [11] and its variant, the Fixed Size Image

* Corresponding author. Tel.: +45 353 32570; fax: +45 353 33245.
E-mail address: jmar@life.ku.dk (J.M. Amigo).

0039-9140/$ – see front matter © 2009 Elsevier B.V. All rights reserved.
doi:10.1016/j.talanta.2009.04.042

Window-Evolving Factor Analysis (FSIW-EFA) [6]. These techniques are aimed to extract the main sources of variability in the tablet and to study the local and global rank (i.e. the number of sources of variability in the tablet).

In this paper, a new working methodology is proposed to study chemical image samples using only self-contained information. The general scope is to introduce a new approach for better visualization of anomalies in surfaces as well as to study the surface itself, locating different zones, etc. The methodology is based on the mutual correlation between one specific pixel and the rest of the image. The main advantage of using correlation coefficients is that it is a mathematical parameter that measures the similarity between two spectra. However, one of the main problems working with correlation coefficients is that, usually, many of the spectra in the image are highly correlated with each other, making the interpretability of the correlation map a complicated task. This is the case, for example, when the analysis of the tablet is performed by using near infrared chemical image (NIR-CI), where the spectra are usually highly correlated with each other. To overcome this problem and improve the information obtained with the correlation maps, a new enhanced contrast function is proposed to normalize the scale of the correlation coefficient and to enhance the differences between a target spectrum in the image and the rest of image's spectra. This method is based on the scaling of the Pearson correlation index to improve contrast in chemical images where the composition of the target sample is unknown.

Another possibility studied in this work is the calculation of the enhanced correlation maps when the pure spectra are available. This perspective offers direct information about the qualitative distribution of a determined analyte in the sample without needing further modeling (for example with MCR-ALS or PLS) and in an understandable way.

The proposed working procedure is fulfilled with a prior Principal Component Analysis to obtain a first visualization of the tablet and to allow the selection of the pixel of interest. To test the effectiveness and prove the benefits of the methodology, a real commercial tablet of ibuprofen was tested. To accomplish the applicability of the proposed methodology, an analysis of the tablet by using pure spectra of components has also been performed. The enhanced correlation maps are calculated and thoughtfully studied.

2. Working methodology

The proposed methodology can be summarized in three well defined steps. The combination of all of them may increase the knowledge about the image and the distribution of the component or mixture of components represented by each pixel. This point is discussed further on in this paper. The three steps, preceded by a preprocessing data stage are:

(1) A previous visualization of the surface by using Principal Component Analysis.
(2) Selection of the pixel of interest and calculation of the correlation surface between the selected pixel and the rest of the pixels in the image.
(3) Calculation, whether needed, of the enhanced correlation surface.

In some cases a transformation of the image into a binary one can be useful to obtain the particle/size domain or other sample characteristics.

2.1. Structure of the image: preprocessing

The structure of an Hyperspectral Image is a three-dimensional data cube, $\underline{D}\,(X \times Y \times \lambda)$ where X and Y represent the spatial axes and λ the spectral profile obtained for each pixel [12,13]. Each pixel of the image, $a(x,y)$, corresponds to one spectrum in the defined spatial coordinates x and y and has the structure of a vector of dimensions $(1 \times \lambda)$ (Fig. 1).

Before applying any methodology, two previous steps are mandatory: the unfolding of the image and the preprocessing of the spectral information. The unfolding step is crucial to adapt the three-dimensional structure to Principal Component Analysis. Consequently, the new unfolded image D will have the dimension $(XY \times \lambda)$. Preprocessing is necessary in order to avoid the influence of undesirable phenomena classically encountered in Hyperspectral Images such as scattering and/or spatial noise. Different methods, such as smoothing/derivatives (Savitzky–Golay or Norris algorithms), Standard Normal Variate (SNV), Multiplicative Scatter Correction (MSC) and normalizing to unit vector length are frequently used [14,15].

2.2. Initial visualization: Principal Component Analysis

Principal Component Analysis (PCA) is an unsupervised technique of visualization and classification that has already been successfully used in Image Analysis [1,5,11,16,17]. Herein, PCA is performed to obtain a first overview of the main sources of variability on the surface studied in an easy way. In PCA applied to Hyperspectral Images, the scores maps are obtained by refolding the scores vectors obtained for each factor; whereas the loadings are related to the spectral variability. Usually, the association of one Principal Component loading to a pure analyte is a difficult task, because PCA is aimed to explain variability sources, which include the influence of chemical components and physical aspects (as illumination or roughness of the surface). Nevertheless, PCA is the most straightforward method to obtain a first impression of the tablet and to select the pixel under consideration (Fig. 1, step 1).

2.3. Correlation maps

The key part of constructing useful correlation maps is to select an adequate pixel to calculate its correlation with all other pixels. Once the pixel of interest, $a(x',y')$, has been selected, an correlation map $R(X \times Y)$ is created by calculating the correlation coefficient between each spectrum on the image $b(x,y)$ and the selected spectrum. In this work, the Pearson correlation coefficient for each pixel, ρ_{xy}, is calculated as follows:

$$\rho_{xy} = \frac{\mathrm{Cov}(a_{x'y'}, b_{xy})}{\sigma_{a_{x'y'}} \sigma_{b_{xy}}} \tag{1}$$

where $\mathrm{Cov}(a_{x'y'}, b_{xy})$ accounts for the covariance between both spectra, $a_{x'y'}$ being the spectrum in the selected pixel and b_{xy} each of the pixels of the image (Eq. (2)); whereas $\sigma_{a_{x'y'}}$ and $\sigma_{b_{xy}}$ account for the standard deviation of $a_{x'y'}$ and b_{xy}, respectively.

$$\mathrm{Cov}(a_{x'y'}, b_{xy}) = \frac{1}{(\lambda - 1)} \sum_{\lambda=1}^{\lambda} (a_{x'y'} - \bar{a}_{x'y'})(b_{x'y'} - \bar{b}_{x'y'}) \tag{2}$$

The correlation coefficients are scaled from 0 to 1 (lowest and highest similarity, respectively) for better interpretation (Eq. (3)):

$$\rho'_{xy} = \frac{\rho_{xy} - \min(R)}{\max(R) - \min(R)} \tag{3}$$

Therefore, a new correlation map R' $(X \times Y)$ is obtained, having into consideration that the only difference between R and R' is the scale of correlation coefficients. This transformation helps to the interpretation of the correlation values and, therefore, the correlation histogram, since the values are quoted between 0 and 1 (Fig. 1, step 2).

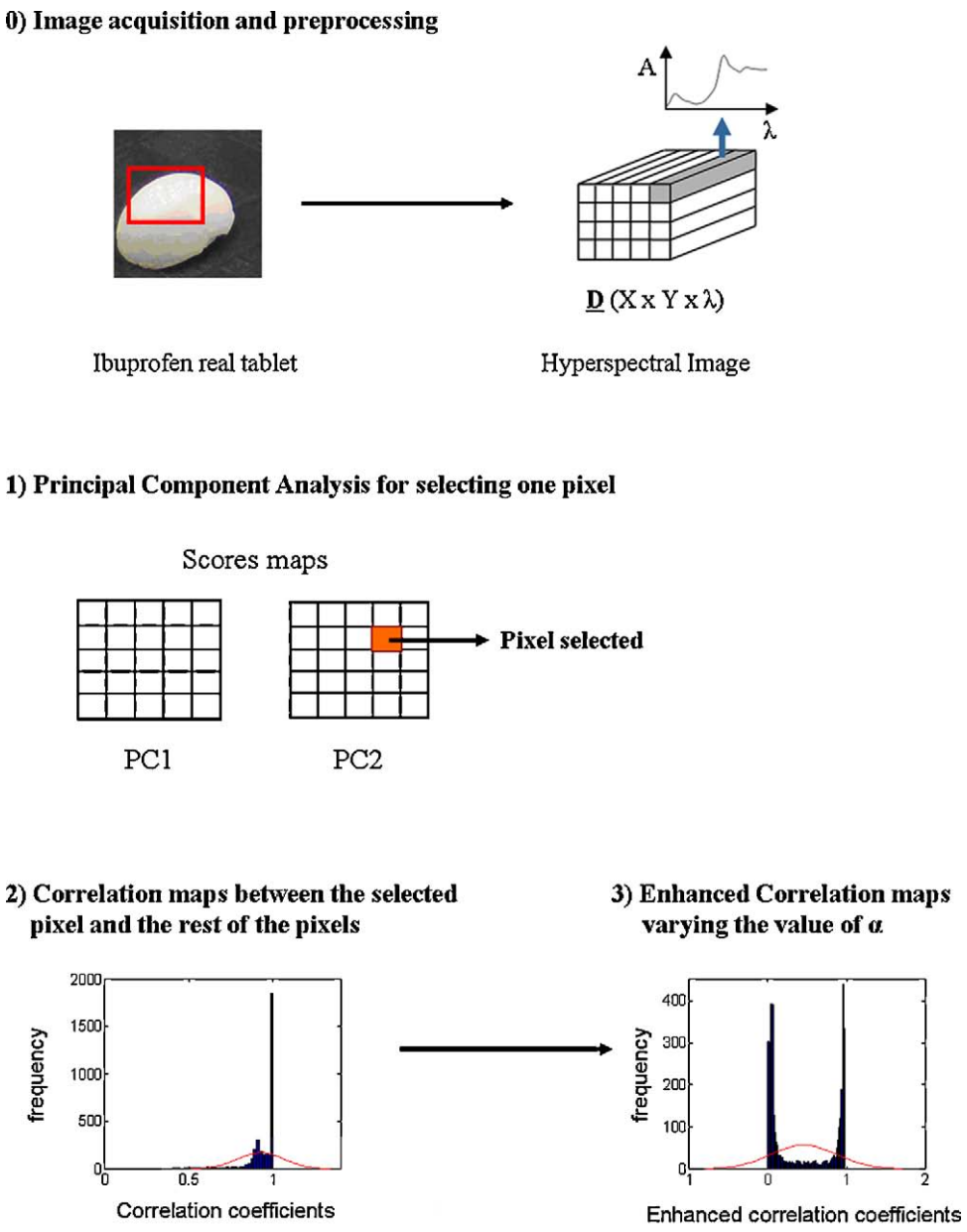

Fig. 1. General scheme of the application of the proposed methodology. The scheme has been divided into three steps: Principal Component Analysis and selection of the pixel of interest, calculation of the correlation coefficients and, finally, the enhancing of the correlation histogram.

2.4. Enhanced correlation maps

As we pointed out in Section 1, the information that the correlation map offers may be difficult to interpret. The enhancing contrast function proposed in this work (Eq. (4)) uses the calculated correlation coefficients from Eq. (1) to calculate a new parameter for each pixel e_{xy}. This new enhanced correlation map, $E(X \times Y)$ is obtained in the following way:

$$e_{xy} = \frac{\rho'_{xy} - \min(R')}{(\max(R') + \alpha) - \rho'_{xy}} \quad (4)$$

The obtained enhanced coefficients can be re-scaled (in the same way as in Eq. (3)) for better interpretation. This new function tries to increase the discrimination between correlation coefficients by using the maximum and the minimum value of correlation coefficients in R' (Fig. 1, step 3). Basically, the transformation stretches the distribution of the correlation coefficients. The discrimination power is controlled by one parameter, α. The valued of this parameter ranges from 0 to infinite, but 1 is convenient upper limit (see Section 4.4). As it will be shown later on, α values close to 0 means higher discrimination power; whereas values of α close to 1 indicate that almost no discrimination is being performed in the correlation coefficients.

2.5. Binary images

In order to calculate the particle/domain statistics of the image a complementary step is to translate the chemical image into a binary image (two component easy-to-compute image defined only by 1 and 0), setting a threshold on the enhanced correlation coefficient scale of the chemical image. Nevertheless, setting this threshold is not an easy task and to our knowledge no objective method has been reported so far. The enhanced function facilitates this; as the new scale of enhanced coefficients is normalized to emphasize the different between the target spectrum and the rest of image's spectra.

3. Experimental

3.1. Tablet

To illustrate the working procedure of this methodology, a commercial tablet of ibuprofen was randomly selected from a commercial package of ibuprofen 200 mg. The nominal concentration of ibuprofen was 55% (versus total weight of the tablet). The tablet contained a sucrose coating and the core of the tablet (ibuprofen and excipients).

The tablet was sectioned using a cutting blade coupled to a microscope. First, the tablet must be immobilized on a microscope slide. Even if a cutting blade could cut a tablet perfectly flat, that flat surface needs to be made parallel to the image plane. By mounting the tablet and then cutting with respect to the microscope slide plane, the surface of the prepared tablet is automatically in line with the image plane.

Pure spectra of ibuprofen and sucrose were registered by scanning a flat surface of compacted pure component simulating tablet conditions.

3.2. Instruments and software

The transverse section of the tablet was scanned with an Auto Image Microscope connected to a Fourier Transform Near Infrared (FT-NIR) spectrometer (PerkinElmer). The area of the image corresponds to 4.2 mm × 4.2 mm divided into 60 × 60 pixels of 70 μm size. The wavelength range was from 4000 to 7500 cm^{-1} with a spectral resolution of 4 cm^{-1}.

Images were preprocessed before the analysis. Standard Normal Variate and Savitzky–Golay smoothing with a window size of 9 points and a polynomial order 2 were applied. PCA have been performed after mean centering the data in order to emphasize variability between spectra. All the preprocessing methods used as well as the methodology proposed in this paper have been implemented in several easy-to-use MATLAB routines (version 2008b, The MathWorks, Massachussetts) and they are freely available upon request or via web [18].

4. Working procedure: analyzing the main parts of an ibuprofen tablet

The corresponding image, due to the shape of the sample, included information about coating and core (parts of interest), with the features that the core part was perpendicular to NIR light plane and some coating part was not perpendicular to scan plane and component of the metal sample holder (Fig. 1).

One of the main features of this approach is that is not sensible to bad pixel, in the sense that noisy or not expected spectra do not change final results, allowing a fast visualization of tablet surface.

4.1. Principal Component Analysis and selection of one pixel of interest

As it can be seen in Fig. 2, the PCA analysis of the tablet offered important information. Only the first four factors score maps are depicted. These four factors explained more than the 80% of the variance, while the first factor contains more than 70%.

Loadings profiles are difficult to associate to a pure spectrum of the two main components of the tablet. The first, second and third scores maps emphasized two different areas of the tablet: the central part of the tablet (PC 1) and an area surrounding the central part (PC 2 and 3). Consequently, it is suggested that the tablet was composed by three parts mainly: its main mixture, the coating edge and the external coverage surrounding the tablet. Also, an unexpected singular point was detected in the main part of the tablet (blue circle in the second factor of the scores maps). Therefore, further investigation was necessary to determine the nature of this part of the tablet and correlation coefficient maps were performed.

4.2. Correlation map for finding singularities in the tablet

In our case, one of the pixels of the unexpected area was selected (pixel in position (26 × 40)) and the correlation map was determined (Fig. 3a).

As it can be observed in Fig. 3a the correlation map seemed not to offer really good information at first sight. This result is due to

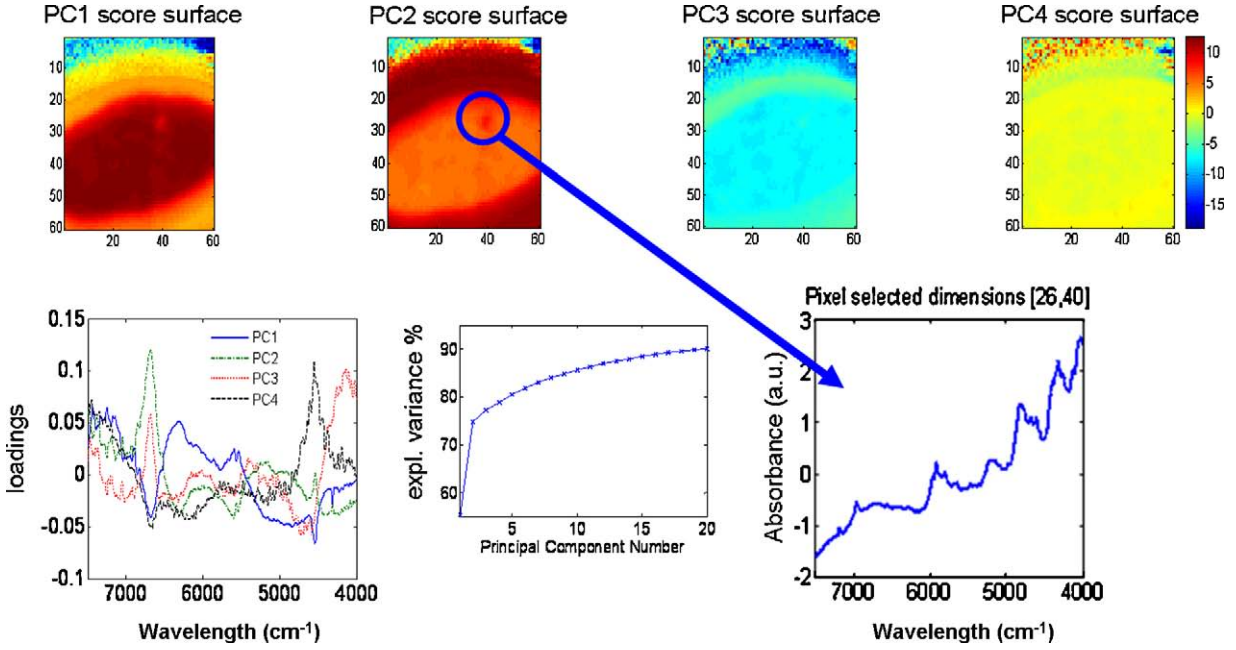

Fig. 2. First part of the graphical output. PCA analysis of the tablet. Upper row, first 4 PC's scores surfaces (blue, low intensity; red, high intensity). Lower row, loadings plot for the first 4 factors, cumulative variance plot and the spectrum of selected pixel (26 × 40). (For interpretation of the references to color in this figure legend, the reader is referred to the web version of the article.)

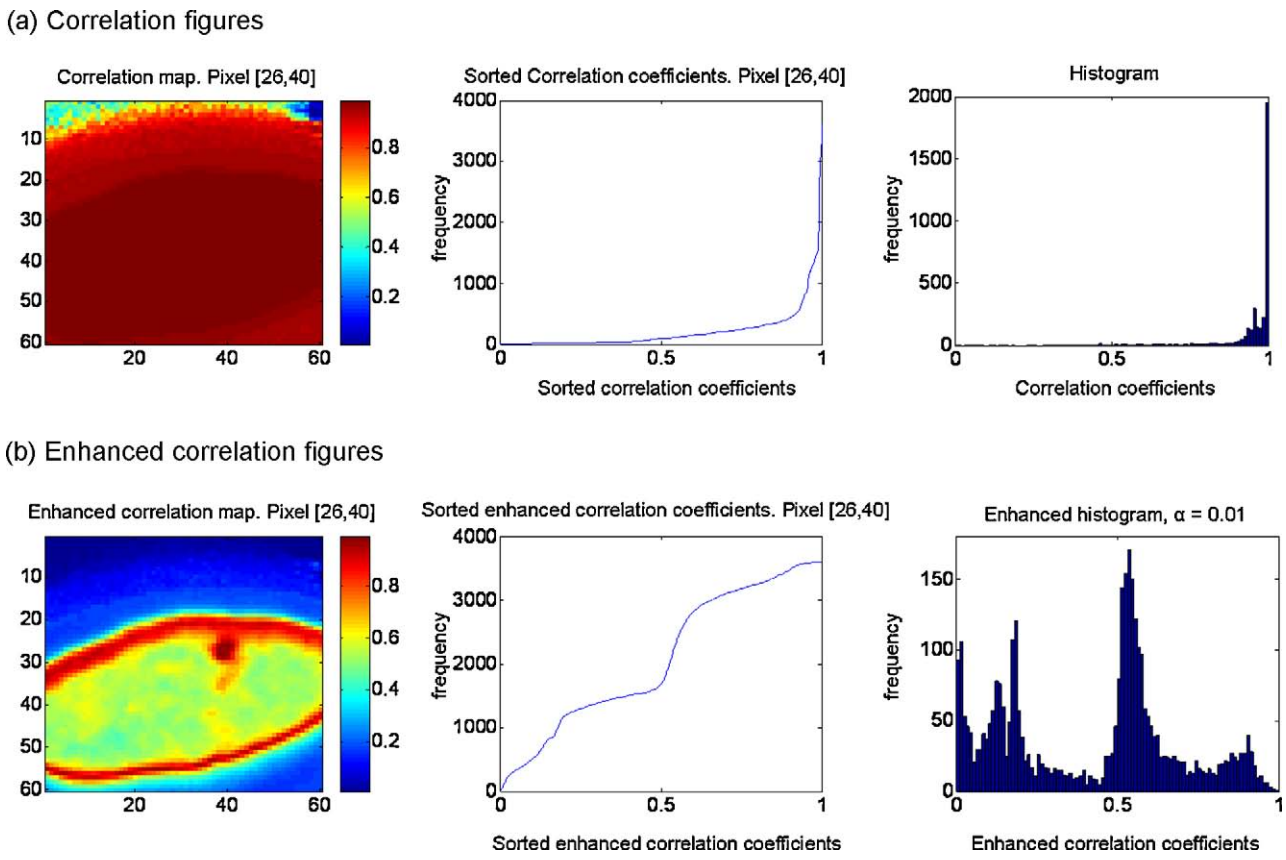

Fig. 3. (a) Correlation map, sorted correlation coefficients and histogram of the correlation coefficients. (b) Enhanced correlation map, sorted enhanced correlation coefficients and its corresponding histogram.

the high correlation between the selected spectrum and the main part of the tablet, and the low correlation coefficient between the selected spectrum and the coverage part. The large scale makes complicated a visual representation of the results. By plotting the attained distribution of correlation coefficients as accumulative frequency diagram or histogram (Fig. 3a), the inadequate contrast of the image can be understood. Most of the values of correlation were found around 0.99 but values from 0 to 0.98 can be found in different proportions. This distribution makes impossible to reduce the scale and consequently, the whole range (from 0 to 1) should be used. As it is showed, the contrast of the obtained map depends on the minimum and maximum value of correlation coefficients.

4.3. Enhanced correlation map

Trying to improve the visualization of the correlation maps, the enhancing transformation was applied by imposing an α value of 0.01. The results (Fig. 3b) were impressive: now the enhanced correlation map clearly shows the coating contour, correlation zone in where the pixel of interest was located. The sorted enhanced correlation coefficients and the corresponding histogram showed a new distribution, as well. It was possible to observe how the enhanced function divided the sample into very distinguishable areas. Also it is seen that the unexpected area encountered in the tablet was chemically related to the coating components: the maximum similarity of the selected pixel was found in the area surrounding the central part of the tablet, area expected to be the coating zone.

4.4. The effect of varying the value of α

To illustrate discrimination power of α, correlation maps of two target spectra, one corresponding to the coating zone, pixel in position (19×39), and the other corresponding to core zone, pixel in position (40×30) were performed by varying the α value. Target spectra are plotted in Fig. 4a. It can be observed the high similarity between these two spectra and the pure spectra of ibuprofen and sucrose (Fig. 4b).

Correlation maps for pixel (19×39) depicted in Fig. 5 showed correlation with the coating zone target spectrum. A high correlation with the coating and the core of the tablet is observed in correlation map using $\alpha = 1$. In this case, the information of the enhanced correlation map is very similar than the information given by the correlation map itself. Nevertheless, the discrimination power increased with the decreasing the value of α. This offered valuable information about the composition and general distribution of the coating, allowing the study of this chemical distribution with different discrimination levels.

Fig. 6 illustrates the enhanced correlation maps of the sample with a target spectrum of the core tablet (pixel (40×30)). Once more, a decreasing in α value was translated into an increasing in the discrimination. The anomaly was again detected and identified as a low correlation region inside of core zone, but the rest of the core seemed to be well distributed. Increasing the discrimination power, small differences within core region could be appreciated. In general, the enhanced correlation maps shown in Figs. 5 and 6 allowed obtaining the coating size and the core area of the tablet, checking the chemical distribution of both areas.

4.5. Binary images: finding a good threshold

One of the main advantages of the enhanced correlation function is the improvement in the interpretability of the enhanced histogram, with the purpose of setting an appropriate threshold to obtain binary images that may show the zones of interest. Fig. 3

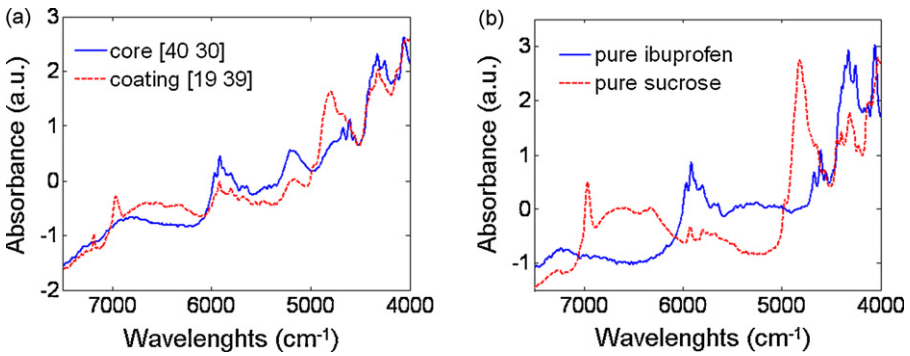

Fig. 4. (a) Core and coating target spectra used to perform correlation and enhanced correlation maps. (b) Pure spectra of ibuprofen and sucrose.

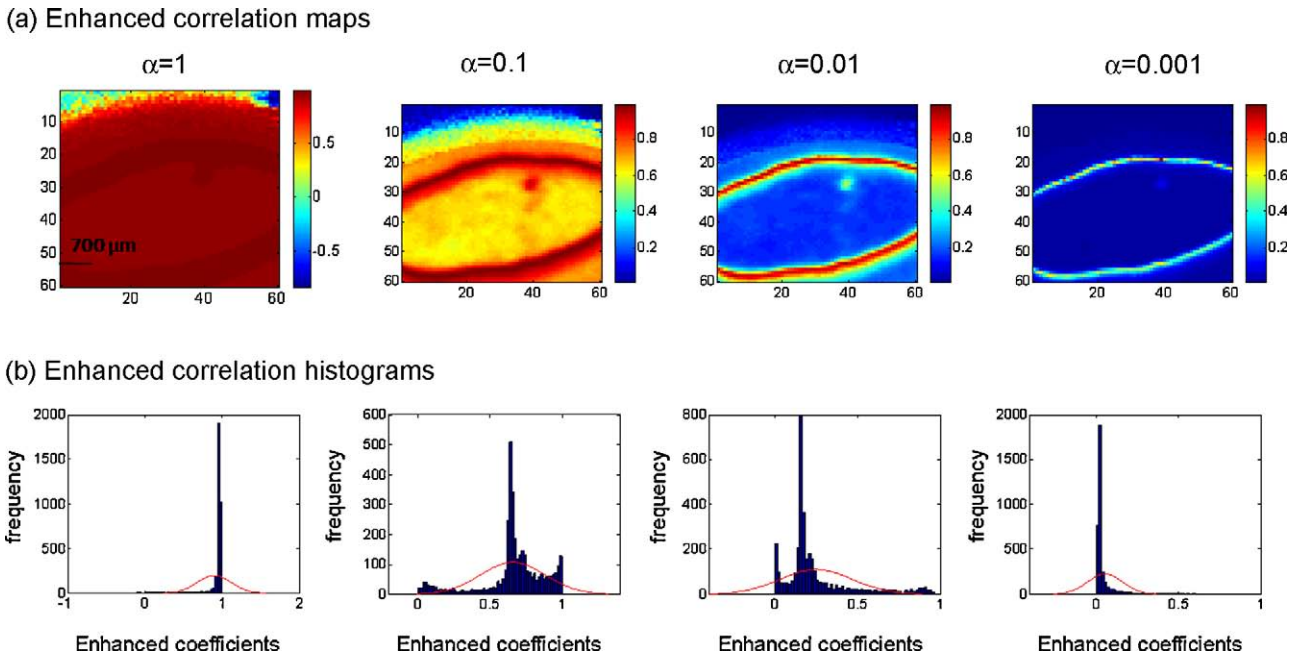

Fig. 5. (a) Enhanced correlation maps and (b) the corresponding histograms calculated for pixel (26 × 39) by varying the value of α.

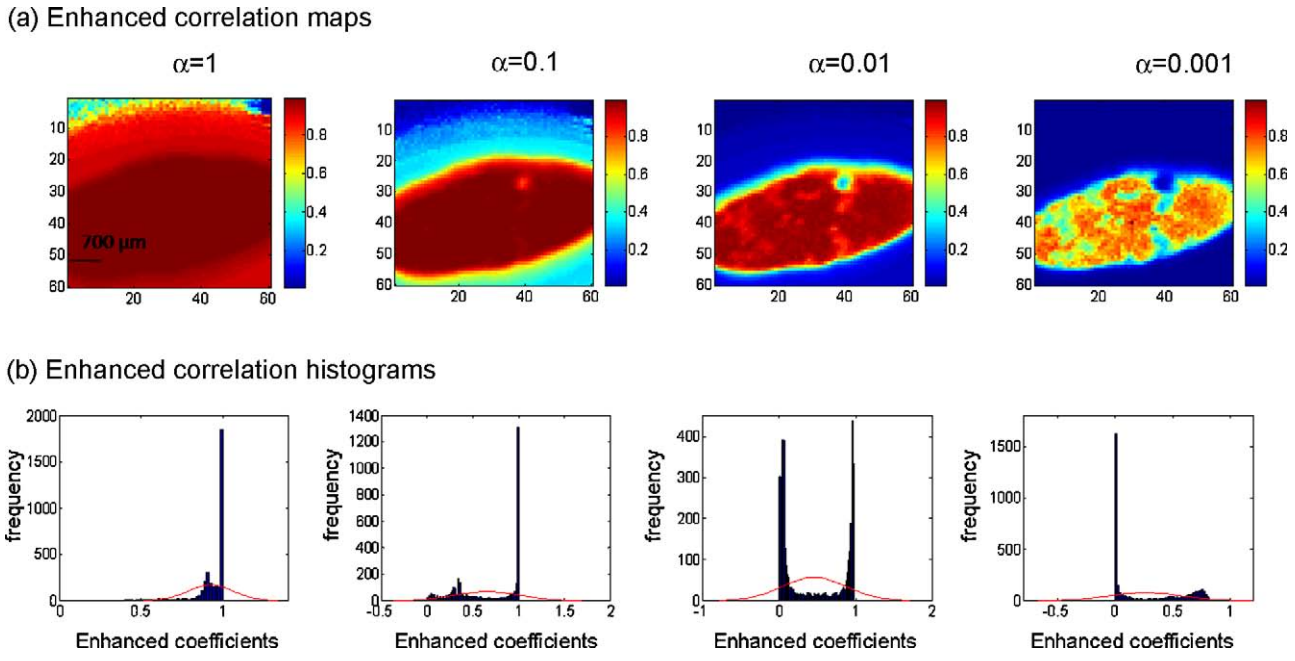

Fig. 6. (a) Enhanced correlation maps and (b) the corresponding histograms calculated for pixel (40 × 30) by varying the value of α.

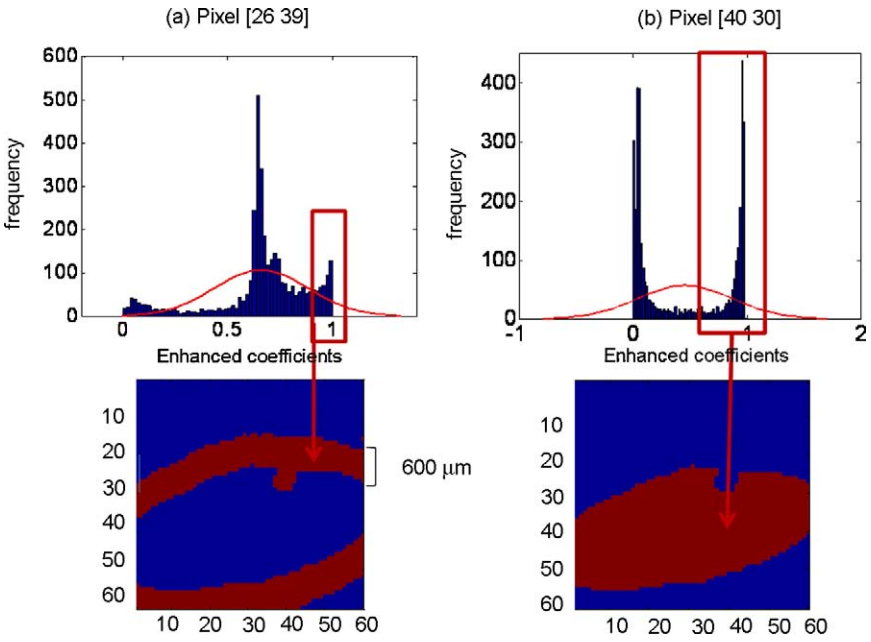

Fig. 7. Selection of the enhanced coefficients range to obtain binary image for (a) pixel (26 × 39) and (b) pixel (40 × 30).

already showed the benefits of working with the enhanced correlation histogram (Fig. 3b) instead of working with the standard correlation histogram (Fig. 3a). The effect of α in the coefficient distribution was clearly observed in the histograms in Figs. 5 and 6. When α decreased, the enhanced correlation coefficients, initially grouped around 0.99, shifted to lower values in the histogram. Consequently, the distribution was expanded along the x-axis, but with different discrimination grade. This amplification effect with

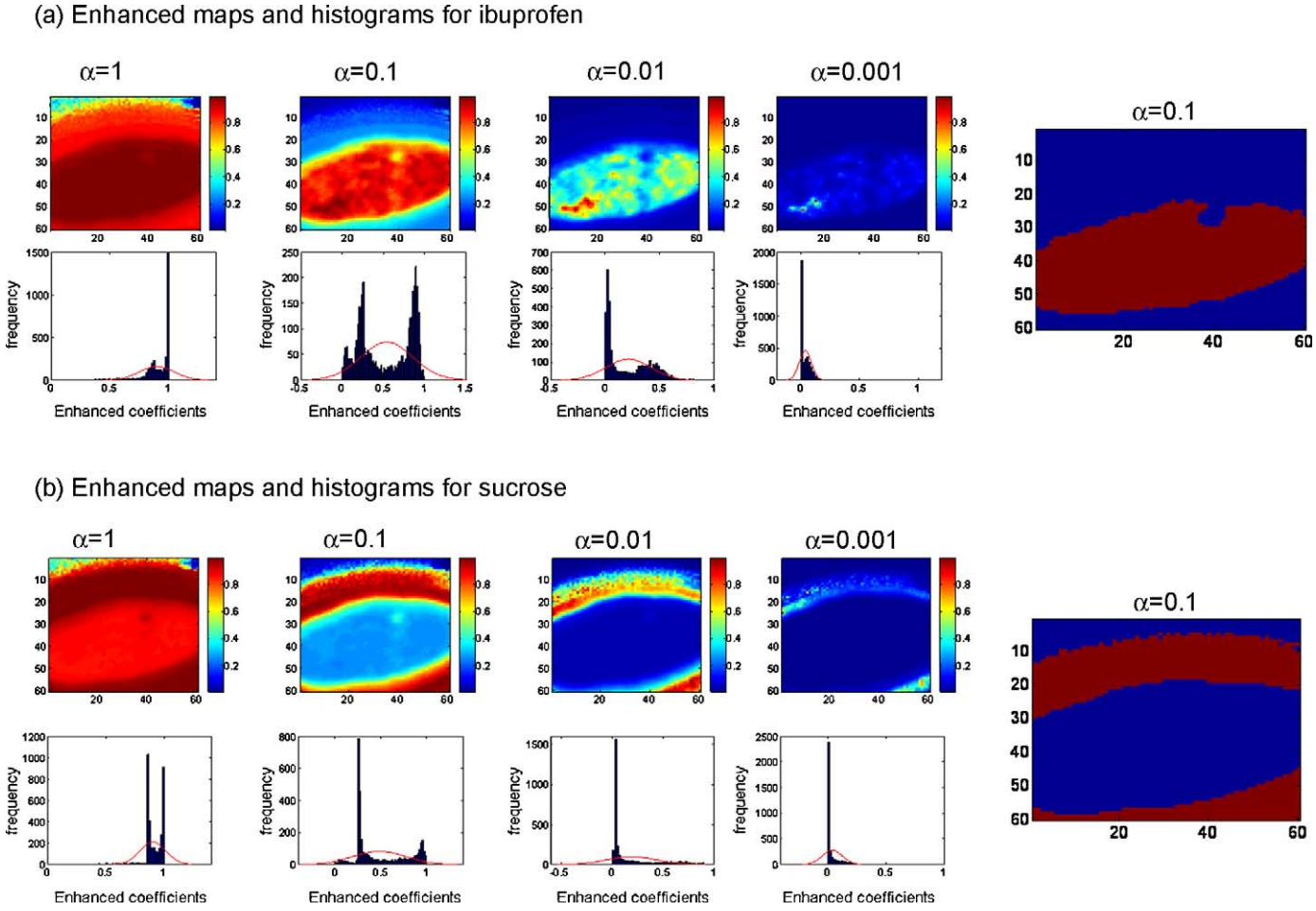

Fig. 8. (a) Enhanced correlation maps and histograms of the sample using ibuprofen and (b) sucrose with different α values.

α allows a better assignment of the threshold to build a binary image.

Nevertheless, there are not optimum values of α. Calculating various enhanced correlation maps with different α values, and making the transformation to a binary image with the one that clearly discriminates the zones is a recommended task.

Even if many zones are clearly depicted in one histogram, the right procedure to obtain binary images is performing correlation maps with as many target spectra as zones should be located. In this particular case, the chosen values of enhanced correlation coefficients ranged from 0.78 to 1, over coefficients obtained using $\alpha = 0.1$ for the coating zone (Fig. 5) and from 0.6 to 1 using $\alpha = 0.01$ for the core zone (Fig. 6). These results are shown in Fig. 7, where it is possible to distinguish between the coating edge of the tablet and ibuprofen zone.

5. Enhanced correlation maps using pure spectra

Fig. 8 shows the enhanced correlation maps and the corresponding histograms obtained for two of the main components in the tablet (Fig. 4b): ibuprofen (API) and sucrose (unique coating component). The ibuprofen enhanced correlation maps showed similar information as the enhanced correlation maps obtained with the target pixel (40×30) (see Section 4.4). It is remarkable that the enhanced contrast function was a useful tool to distinguish small differences on ibuprofen concentration at the tablet surface.

On the other hand, the sucrose enhanced correlation maps did not provide good information about the coating zone parallel to the plane of tablet section. The sucrose pure spectrum was highly correlated with the external part of the tablet (coating), necessarily in the image because of the sample shape (Fig. 1). The zone of study was difficult to define, and it was not possible to obtain a representative binary image of the coating zone (Fig. 8b). Indeed, one of the conclusions of this study was that the coating zone is not represented by sucrose pure spectrum, but by a mixture spectrum mainly composed of sucrose, ibuprofen and excipients responses. Thus, correlation coefficient maps demonstrated to be a more useful tool to establish chemical distribution assessment and size of this type of tablets coating than pure component correlation maps.

This new methodology can be very useful in initial phases of image studies, and in other specific situations as it has been previously shown, where different zones or components want to be identified in a sample. Correlation maps offer another fast-computing possibility to obtain information about the large amount of data achieved using these new chemical image techniques.

6. Conclusions

A new, simply implemented approach for obtaining spatial information of pharmaceutical tablets without any previous knowledge has been presented by using near infrared chemical image and information contained only in the sample under analysis. The fact that previous information about the sample is not needed makes the proposed methodology especially useful in analysis of unknown samples, strange contaminants localization, and locating anomalies in different samples.

The basic idea is to explore how spectral or other properties of each pixel in the image differ from the others, and that was achieved through the application of Pearson's correlation coefficient. The proposed function allows changing the correlation scale in order to obtain a good contrast for the image for any combination of correlation coefficient maximum and minimum.

The proposed methodology can detect a deviation by comparing the spectra obtained from one tablet. As we pointed out beforehand, the main feature of this methodology is that the operator has the opportunity of selecting different pixels as well as different α values in an easy way. This dynamic iteration allows studying different areas of the image and increasing and decreasing the discrimination with the selected pixel. Therefore, the methodology can be used as a control technique to detect defects in final tablets and punctual contaminants, being a potential supplementary tool for quality controls. In addition, it has to be pointed out that the usefulness of the proposed methodology is not exclusive to NIR-CI devices, but it can be applied to any hyperspectral and multivariate image system.

Acknowledgements

José Manuel Amigo wants to thank the Danish Research Council for Technology and Production Sciences for his post-doctoral fellowship. Santiago Maspoch, Jordi Coello and Carlos Cairós are grateful to Spain's Ministry of Science and Technology for funding this research within the framework of Project CTQ2007-62528. Carlos Cairós thanks the Spain's Ministry of Science and Technology for his predoctoral fellowship BES2005-9614.

References

[1] J.M. Amigo, J. Cruz, M. Bautista, S. Maspoch, J. Coello, M. Blanco, Trac-Trends in Analytical Chemistry 27 (2008) 696.
[2] J.M. Amigo, C. Ravn, European Journal of Pharmaceutical Sciences 37 (2009) 76.
[3] C. Gendrin, Y. Roggo, C. Collet, Talanta 73 (2007) 733.
[4] N. Jovanovic, A. Gerich, A. Bouchard, W. Jiskoot, Pharmaceutical Research 23 (2006) 2002.
[5] Y. Roggo, A. Edmond, P. Chalus, M. Ulmschneider, Analytica Chimica Acta 535 (2005) 79.
[6] A. de Juan, R. Tauler, R. Dyson, C. Marcolli, M. Rault, M. Maeder, Trac-Trends in Analytical Chemistry 23 (2004) 70.
[7] H. Ma, C.A. Anderson, Journal of Near Infrared Spectroscopy 15 (2007) 137.
[8] H. Ma, C.A. Anderson, Journal of Pharmaceutical Sciences 97 (2008) 369.
[9] A.A. Gowen, C.P. O'Donnell, P.J. Cullen, S.E.J. Bell, European Journal of Pharmaceutics and Biopharmaceutics 69 (2008) 10.
[10] C. Ravn, R. Bro, E. Skibsted, Journal of Pharmaceutical and Biomedical Analysis 48 (2008) 554.
[11] Y. Roggo, N. Jent, A. Edmond, P. Chalus, M. Ulmschneider, European Journal of Pharmaceutics and Biopharmaceutics 61 (2005) 100.
[12] A.A. Gowen, C.P. O'Donnell, P.J. Cullen, G. Downey, J.M. Frias, Trends in Food Science & Technology 18 (2007) 590.
[13] G. Reich, Advanced Drug Delivery Reviews 57 (2005) 1109.
[14] R.J. Barnes, M.S. Dhanoa, S.J. Lister, Applied Spectroscopy 43 (1989) 772.
[15] P. Geladi, H. Grahn, Multivariate Image Analysis, John Wiley & Son Ltd., New York, 1997.
[16] P. Geladi, H. Isaksson, L. Lindqvist, S. Wold, K. Esbensen, Chemometrics and Intelligent Laboratory Systems 5 (1989) 209.
[17] L. Zhang, M.J. Henson, S.S. Sekulic, Analytica Chimica Acta 545 (2005) 262.
[18] http://www.models.kvl.dk/users/jose_manuel_amigo/index.htm.

Talanta 79 (2009) 598–602

Contents lists available at ScienceDirect

Talanta

journal homepage: www.elsevier.com/locate/talanta

Pressurized liquid extraction followed by gas chromatography with atomic emission detection for the determination of fenbutatin oxide in soil samples

P. Canosa[a], R. Montes[a], J.P. Lamas[a], M. García-López[a], I. Orriols[b], I. Rodríguez[a,*]

[a] Departamento de Química Analítica, Nutrición y Bromatología, Instituto de Investigación y Análisis Alimentario, Universidad de Santiago de Compostela, Santiago de Compostela 15782, Spain
[b] EVEGA, Estación de Viticultura e Enoloxía de Galicia, Leiro 32427, Ourense, Spain

ARTICLE INFO

Article history:
Received 7 January 2009
Received in revised form 3 April 2009
Accepted 16 April 2009
Available online 3 May 2009

Keywords:
Pressurized liquid extraction
Fenbutatin oxide
Ethylation
Soil samples
Gas chromatography atomic emission detection

ABSTRACT

A novel method for the determination of the miticide bis[tris(2-methyl-2-phenylpropyl)tin] oxide, also known as fenbutatin oxide (FBTO), in agricultural soils is presented. Pressurized liquid extraction (PLE) followed by analyte derivatization and extraction into isooctane was the used sample preparation approach. Selective determination was achieved by gas chromatography with atomic emission detection (GC-AED). Influence of different parameters on the performance of the extraction process is thoroughly discussed; moreover, some relevant aspects related to derivatization, determination and quantification steps are also presented. As regards PLE, the type of solvent and the temperature were the most relevant variables. Under optimized conditions, acetone, without any acidic modifier, was employed as extractant at 80 °C. Cells were pressurized at 1500 psi, and 2 static cycles of 1 min each were applied. Acetone extracts (ca. 25 mL) were concentrated to 1 mL, derivatized with sodium tetraethyl borate ($NaBEt_4$) and the FBTO derivative, resulting from cleavage of the Sn–O–Sn bond followed by ethylation of the hydroxyl fragments, extracted into isooctane and determined by GC-AED. Under final working conditions, the proposed method provided recoveries from 76 to 99% for spiked soil samples, a limit of quantification of 2 ng g^{-1} and an acceptable precision. Analysis of samples from vineyards sprayed with FBTO, confirmed the persistence of the miticide in soil for more than 1 year after being applied.

1. Introduction

Fenbutatin oxide (bis[tris(2-methyl-2-phenylpropyl)tin] oxide, FBTO), also known as bis(trineophyltin) oxide, is a non-systemic, selective insecticide used for the protection of crops, particularly fruits, against mites [1,2]. Its large molecular weight (1053 amu), extremely high octanol–water partition coefficient ($\log K_{ow}$ 12.8), negligible vapour pressure and chemical stability convert FBTO into a persistent compound in plants and soil. The European Union has set maximum allowable residues of FBTO up to 5 μg g^{-1} in some fruits [3], which can be considered a relatively high level, taking into account that this compound remains on the surface of vegetables [4] and thus, it could be removed during raining or through photochemical degradation reactions. Although, in presence of water traces, FBTO breaks down rendering two molecules of tris(2-methyl-2-phenylpropyl)tin hydroxide [5], this reaction is reversible and the resulting tri-substituted organotin species is still relatively lipophilic ($\log K_{ow}$ 7.9); thus, its mobility in the environment it is expected to be low. FBTO is highly toxic to some aquatic organisms with lethal concentration doses (LC_{50}) in the low ng mL^{-1} range for several fish species [6].

Conversely to other organotin compounds, particularly tributyl and triphenyltin, whose analytical determination and environmental fate have been exhaustively investigated during last 20 years, little attention has been paid to FBTO. In the middle of the 1990s, FBTO was included in generic sample preparation methodologies for the determination of organotin species in environmental samples using gas chromatography (GC) based techniques [7,8]. In these early works, time and solvent-consuming sample preparation approaches such as Soxhlet and liquid–solid extraction, using manual shaking, followed by concentration of the extracts and analyte alkylation with Grignard reagents were employed [7–9]. Although FBTO was found in sediments and agricultural soils [7–9], further works dealing with improvements in the analytical methodology for the determination of FBTO in these solid matrices were not found. In fact, the applicability of sodium tetraethyl borate ($NaBEt_4$) to the derivatization of FBTO in aqueous solutions was not demonstrated until 2005 by Devos et al. [10], who developed a method for the sensitive determination of this compound in water samples using in situ derivatization followed by headspace extraction of the ethyl derivative with solid-phase microextraction (SPME). On the other hand, $NaBEt_4$ has been employed in GC analysis of butyl

* Corresponding author. Tel.: +34 981 563100x14387; fax: +34 981 595012.
E-mail address: isaac.rodriguez@usc.es (I. Rodríguez).

0039-9140/$ – see front matter © 2009 Elsevier B.V. All rights reserved.
doi:10.1016/j.talanta.2009.04.033

and phenyl tin species since long time ago [11]. In the same way, the usefulness of modern extraction techniques requiring moderate consumption of organic solvents, e.g. microwave assisted extraction (MAE), sonication or pressurized-liquid extraction (PLE), and systematically evaluated for the extraction of other organotin compounds from solid matrices [12–17], has not been demonstrated for FBTO. Among the above techniques, PLE does not only achieve high recoveries in the extraction of organotin compounds from environmental samples [14–17]; in addition, it provides filtrated extracts, avoiding the risk of analytes re-adsorption on the particles of the solid residue after finishing the extraction step and before phases separation.

The aim of this work was to develop a fast and sensitive procedure for the determination of FBTO in agricultural soils and to investigate the levels and persistence of this compound in vineyards treated with commercial formulations containing this miticide as active ingredient. After extraction, using an aqueous miscible solvent, FBTO was derivatized with $NaBEt_4$ and selectively determined by GC with atomic emission detection (AED). Effects of different factors on the performance of the extraction process and influence of the quantification method on the accuracy of measured concentrations are thoroughly discussed.

2. Experimental

2.1. Solvents and reagents

Acetone, ethyl acetate, dichloromethane, isooctane and n-hexane, trace analysis grade solvents, were obtained from Merck (Darmstadt, Germany). FBTO, $NaBEt_4$, glacial acetic acid, sodium acetate, potassium dihydrogen phosphate and activated alumina (0.1 mm particle size) were purchased from Aldrich (Milwaukee, WI, USA). Diatomaceous earth and acid washed quartz sand were bought from Aldrich and Riedel-de Haën (Seelze, Germany), respectively. A standard solution of triphenyl pentyltin (Ph_3SnPe) in n-hexane (10 $\mu g\,mL^{-1}$) was provided by IRMM (Geel, Belgium) with occasion of a former intercomparison exercise, further dilutions of this compound, used as internal standard (IS), were made in isooctane. The stock solution of FBTO (200 $\mu g\,mL^{-1}$) was prepared in acetone. Diluted standards and solutions used to fortify soil samples were made in the same solvent. Except otherwise is stated, concentrations of FBTO and Ph_3SnPe are referred to tin.

Sodium acetate solutions (1 M) were prepared in ultrapure water, obtained from a Milli-Q system (Millipore, Billerica, MA, USA). Their pH was adjusted at different values in the range from 4.5 to 6 units with acetic acid. Buffers at higher pHs (6.5 and 7.5 units) were obtained using potassium dihydrogen phosphate. $NaBEt_4$ was dissolved in NaOH (0.1 M in ultrapure water) to get a solution with a concentration of 1%. This reagent is stable for a maximum of 5 days when stored at 4 °C.

Derivatization, ethylation, of FBTO was carried out in 20 mL volume glass tubes furnished with PTFE layered caps. An aliquot of a FBTO standard in acetone, or a soil extract in the same solvent, was poured in the tube, 10 mL of sodium acetate/acetic acid buffer at pH 5.5 and 1 mL of $NaBEt_4$ were then added. The tube was capped and shaken vigorously for 5 min. After that, the ethylated derivative of FBTO (trineophyl ethyltin) was extracted with 2 mL of isooctane containing a known concentration of Ph_3SnPe. If necessary, this extract can be evaporated (ca. 100 μL), using a gentle stream of nitrogen, before injection in the GC-AED system. Changes in the final volume of the concentrated extract, and differences in the sensitivity of the GC-AED for standards and soil extracts, were compensated using Ph_3SnPe as IS.

Glassware and PLE cells, used during sample preparation, were washed with a common detergent followed by thorough rinsing with ultrapure water and acetone.

2.2. Samples and sample preparation

Soil from fields non-treated with FBTO was used during optimisation of extraction conditions. Samples were sieved and the fraction below 0.3 mm considered for analysis. Spiked samples were prepared adding a standard mixture of FBTO, made in acetone, to a known mass of soil. After thorough homogenization, the slurry was left in a hood, at room temperature, for 1 week. Spiked samples were then aged at 4 °C, for at least 1 month, before analysis. Soil samples from vineyards treated with plaguicides containing FBTO, as acaricide against red mites (*Tetranichus urticae*), were processed under optimised conditions. Normally, samples were sieved and extracted as received and the concentration of FBTO corrected with the humidity of the soil; however, those samples collected after intense rain episodes were previously lyophilized.

Extractions were accomplished using a pressurized liquid extractor, ASE 200 Dionex (Sunnyvale, CA, USA), equipped with 11 mL capacity stainless-steel cells. Two cellulose filters followed by 2 g of quartz sand were placed at the bottom of each cell, 0.4 g of soil, previously mixed with 2 g of diatomaceous earth, were then loaded. Finally, the remaining free volume was filled with quartz sand and another cellulose filter was placed on top. Under final working conditions, FBTO was recovered from soil samples with acetone, employing 2 static extraction cycles of 1 min each. Pressure and temperature of extraction cells were set at 1500 psi and 80 °C, respectively. The flush volume and purge time (using nitrogen) were 11 mL (equivalent to 100% of the cell's capacity) and 1 min, respectively. The acetone extract was evaporated and adjusted to 1 mL. A fraction of 0.5 mL was submitted to same derivatization conditions as FBTO standards prepared in acetone.

2.3. Determination

Levels of FBTO in spiked and non-spiked samples were determined by GC-AED using an Agilent (Wilmington, DE, USA) 6890 GC system, equipped with a split/splitless injector and connected to a G2350A atomic emission detector. Separations were carried out with an Agilent HP-5 type capillary column (30 m × 0.32 mm i.d., d_f 0.25 μm) operated at a constant helium flow of 1.4 mL min^{-1}. The GC oven was programmed as follows: 80 °C (held for 2 min), 15 °C min^{-1} to 300 °C (held for 5 min). Injections (1–2 μL volume) were made in the pulsed splitless mode (40 psi, 2 min) using an autosampler. The injection port, the transfer line between the GC and the helium microwave-induced plasma, and the plasma cavity, were set at 300 °C. Helium was used as make-up gas in the plasma at 270 mL min^{-1}. O_2 and H_2 were also added to the plasma as auxiliary gases at pressures of 30 and 20 psi, respectively. Chromatograms were recorded at 303 nm; moreover, the 301 and 271 nm wavelengths were monitored occasionally for elemental identity confirmation.

Two different quantification techniques were considered, (1) addition of known concentrations of FBTO to acetone extracts from soil samples, previously to the derivatization step, and (2) comparison with FBTO standards submitted to same derivatization conditions as soil extracts. In both cases, peak areas obtained for the ethyl derivative of FBTO were corrected with the signal of the IS.

3. Results and discussion

3.1. Ethylation of FBTO and characterization of GC-AED determination

Optimisation of GC-AED conditions was carried out with ethylated standards of FBTO in isooctane. The derivatization reaction

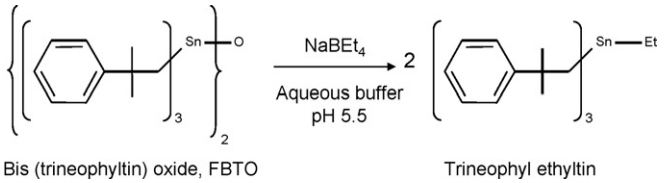

Fig. 1. Chemical structures of FBTO and its ethyl derivative after reaction with sodium tetraethyl borate.

was accomplished under similar conditions to those reported for other organotin compounds, such as tributyl, triphenyltin and their degradation products [11,14,18]. In summary, 0.5 mL of a FBTO standard in acetone were diluted with 10 mL of buffer and then 1 mL of derivatization solution was added. This mixture was shaken vigorously for 5 min. During this process, the Sn–O–Sn bond breaks down rendering two molecules of trineophyltin hydroxide, which further react with sodium tetraethyl borate to give the ethyl derivative, Fig. 1. Then, this derivative is extracted into isooctane. The yield of the reaction remained unchanged between pH 5.0 and 6.5, decreasing significantly at lower and higher values. Experimentally, it was found necessary to complete first the ethylation reaction, in aqueous solution, and then adding the isooctane phase. If both, isooctane and $NaBEt_4$, are added simultaneously over the buffered solution of FBTO, as usually carried out for butyl and phenyl tin species [14,15], a significant reduction (30–40%) in the response of the trineophyl ethyltin derivative was noticed. Probably, in the second situation, a fraction of FBTO, as distannoxane compound, is rapidly transferred to the organic phase impairing the reaction with $NaBEt_4$, which remains in the lower aqueous layer.

As regards GC-AED determination, the combination of pulsed splitless injection (40 psi) with a high temperature in the injector (300 °C) improved significantly the achieved limit of quantification (LOQ). This behaviour is in agreement with the still relatively high molecular weight of the ethylated derivative of FBTO (547 amu). Pressure of auxiliary gases (hydrogen and oxygen) in the helium plasma also affected significantly to the intensity of the emission signal. The best sensitivity (defined as the ratio between peak area and concentration) was observed using relatively high oxygen pressures (30 psi) and medium values for hydrogen (20 psi); whereas, the combination of high hydrogen and low oxygen values, suggested for the GC-AED determination of other organotin compounds [8,19,20], led to calibration graphs with two to three times lower slopes. Under optimized instrumental conditions, an excellent linearity was obtained in the range between 5 and 1000 ng mL^{-1}, with a correlation coefficient (R^2) higher than 0.999. Repeatability of injection and derivatization processes remained around 2 and 4%, respectively. The limit of quantification for FBTO, defined for a signal to noise ratio (S/N) of 10, was 2 ng mL^{-1} as tin, for an injection volume of 2 μL.

3.2. PLE conditions

3.2.1. Extraction solvent

Optimisation of extraction conditions was carried out using a soil sample, with a total organic carbon (TOC) content of 5.3%, spiked with FBTO at 1 μg g^{-1}. Four different solvents with increasing polarities, previously recommended for the extraction of FBTO from sediments and vegetable samples using the Soxhlet technique and manual solid–liquid extraction [1,7–9], were initially compared. The size of sample was 0.4 g. A single static extraction cycle of 10 min, with the cell at 100 °C and 1500 psi and a flush volume of 100%, was employed. These departure conditions were adopted considering previous applications of PLE to the extraction of butyl and phenyltin compounds from environmental samples [14,21]. Extracts were evaporated to dryness, reconstituted with 1 mL of acetone, and then a fraction of 0.5 mL derivatized as described in the experimental section. An aliquot (1 μL) of the upper isooctane layer was injected in the GC-AED system without additional concentration. Fig. 2 compares the responses (peak areas) measured for the ethyl derivative of FBTO in each case. Despite the extremely high lipophilic character of FBTO, ethyl acetate and acetone provided higher responses than dichloromethane and n-hexane. This trend can be explained assuming the existence of equilibrium between FBTO and trineophyltin hydroxide in the soil sample [5], with the latter species showing a higher affinity for medium polarity solvents. Moreover, acetone and ethyl acetate are able to displace water traces from the pores of the soil achieving a better solubilisation of FBTO. Between them, acetone was preferred since it is miscible with the aqueous solution of $NaBEt_4$; thus, dryness evaporation of extracts was not necessary.

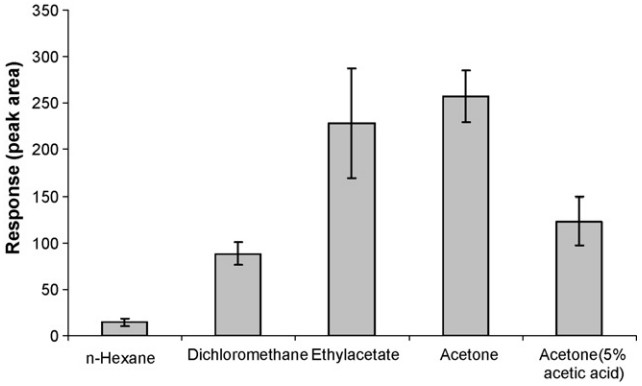

Fig. 2. Responses (peak areas) obtained for fractions (0.4 g) of the same spiked soil sample. Static PLE for 10 min (1 cycle) at 100 °C and 1500 psi, $n = 4$ replicates.

Further extractions with acetone containing a 5% of acetic acid showed an important reduction in the response of the FBTO derivative, Fig. 2. Extra peaks for other organotin species did not appear in the corresponding chromatograms (figure not shown); therefore, this result cannot be attributed to partial decomposition of FBTO under acidic conditions. Very likely, it is just the consequence of a too polar extraction solution. Consequently, acetone was maintained as extraction solvent.

3.2.2. Instrumental PLE parameters

Once acetone was set as extraction solvent, the effect of different instrumental variables on the performance of the process was examined using experimental factorial designs. Pressure and purge time of PLE cells (nitrogen was used as purge gas) were fixed at 1500 psi and 60 s, respectively. The first variable has demonstrated to exert little influence on the yield of PLE methods [15]; whereas, 60 s of purge were enough to remove any trace of solvent (acetone) impregnating samples packed inside PLE cells.

In a first optimisation stage, a 2^3 experimental factorial design, with two central points, was used to investigate the influence of temperature (70–130 °C), number of static extraction cycles (1–3) and time per cycle (2–10 min) on the efficiency of the PLE process. The flush volume was maintained at 100%. The signal (peak area) obtained for FBTO in each of the experiments comprised in this first design was used as variable response. Although none of the investigated factors played a significant effect, at the 95% confidence level, on the performance of the process, the stronger the extraction conditions the lower the response obtained for FBTO. Partial decomposition of the analyte and/or increasing in the complexity of the extract, leading to a decrease in the efficiency of the further ethylation reaction, might be responsible for the observed trend. Although Ruiz-Encinar et al. [17] have demonstrated that the use of high temperatures might led to partial decomposition of tri- and

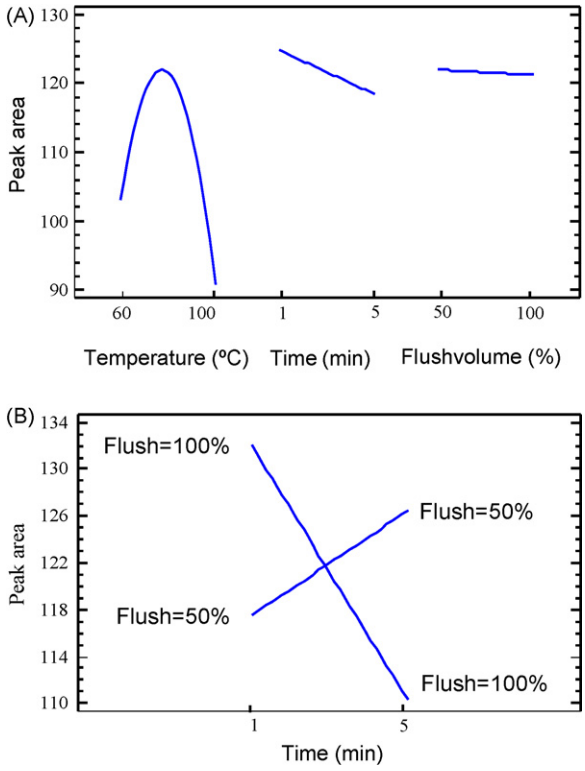

Fig. 3. Main effects (A) and interaction time–flush volume (B) plots obtained from the mixed mode experimental factorial design.

dibutyltin during PLE extractions, this fact could not be confirmed for FBTO since additional peaks, corresponding to other organotin species were not noticed in the GC-AED chromatograms.

On the basis of above comments, it was decided to fix the number of extraction cycles at 2 and to shift the other two factors (extraction time per cycle and temperature) to lower values; moreover, the percentage of flush was included in a second experimental design. In this case, a mixed mode $3^1 \times 2^2$ design, with the factor temperature considered at three levels (60, 80 and 100 °C), was used. Low and high levels for factors time and percentage of flush were 1–5 min and 50–100%, respectively. Fig. 3 shows the main effect of each factor and the interaction between the variables time and flush volume on the response obtained for FBTO. As observed, a clear maximum was achieved at the intermediate temperature (80 °C), Fig. 3A. Time and flush volume played negligible effects on the extraction; however, the interaction between both factors indicated that the combination of short extraction cycles (1 min) with a high flush volume (100%) is preferred to the opposite situation, Fig. 3B. The other two interactions (temperature–time and temperature–flush volume) did not affect to the performance of the extraction, figure not shown.

Thus, two static extraction cycles, at 80 °C, for 1 min, with a total flush of 100% were adopted as optimal PLE parameters. Using these conditions, around 25 mL of acetone were consumed in the extraction step, the repeatability of the whole sample preparation process remained below 11% ($n = 4$ replicates), and the response for FBTO in the re-extraction of PLE cells, containing the spiked soil, represented less than 2% of that obtained in the first extraction.

3.3. Recoveries and other figures of merit

Initially, the recoveries of the proposed method were evaluated by external calibration, comparing the responses obtained for FBTO, as ethyl derivative, in the extracts from spiked soil samples and in calibration standards. Surprisingly, considering that (1) procedural blanks did not show cross contamination problems and that (2) the GC-AED system presents an excellent selectivity for organotin compounds, unacceptable high recoveries (values between 200 and 250%) were obtained for spiked soil samples with different carbon contents, considering several emission lines of tin (271 and 301 in addition to 303 nm) to record the corresponding chromatograms. Clean-up of isooctane extracts using alumina packed in a Pasteur pipette [15] did not overcome the above problem.

When Ph_3SnPe was added, as IS, to the isooctane used to recover the trineophyl ethyltin from calibration standards and soil extracts, an increment in the peak area of this compound for soil extracts versus pure standards was noticed. As Ph_3SnPe did not undergo any derivatization reaction, it was assumed that enhancement of mass transference from the body of the splitless injector to the head of the column, for soil extracts versus calibration standards, could explain the above behaviour. The same fact might be responsible for recoveries higher than 100% obtained for FBTO with external calibration. Although, matrix induced response enhancement is a well-known phenomenon in the determination of organic pesticides using GC-based techniques [22,23], for the best of our knowledge, it had not been previously reported for organotin compounds.

Table 1 summarizes the recoveries of the proposed method for aged, spiked agricultural soil samples. Values between 76 and 99% were measured in the four investigated samples, with an acceptable concordance between pairs of results obtained with standard addition over soil extracts and comparison with pure standards, after correction of FBTO responses with those measured for the IS (Ph_3SnPe). Thus, both, FTBO and the IS, underwent similar signal enhancements. As the latter quantification method increases the sample throughput, it was adopted for further studies. The isooctane extract obtained from sample code 4 (Table 1) was concentrated around 10 times using a gentle stream of nitrogen (1 mL was evaporated to approximately 0.1 mL). Found recoveries (91 ± 9 and 87 ± 4 using standard addition and comparison against pure standards, respectively) proved the lack of losses, for both trineophyl ethyltin and the IS, during the evaporative concentration step.

Procedural blanks did not reveal the existence of contamination problems (Fig. 4A), thus the limit of quantification (LOQ) of the method, for a sample intake of 0.4 g and considering a 10-fold concentration of the isooctane extract, was 2 ng g^{-1} expressed as tin (equivalent to 9 ng g^{-1} as FBTO). This value is similar to those reported for butyltin compounds in sediment and biota samples using PLE as extraction technique and different GC-based detection techniques [14,15,21].

Table 1
Recoveries of the developed method for spiked soil samples as function of the quantification technique, after signal normalization with Ph_3SnPe, $n = 4$ replicates.

Code	TOC (%)	Addition level (ng/g)	Recovery (%) ± standard deviation	
			Standard addition	Calibration with standards
1	5.3	1000	79 ± 5	76 ± 5
2	5.3	200	99 ± 8	88 ± 8
3	2.9	200	92 ± 4	94 ± 4
4	1.4	100	91 ± 9	87 ± 4

TOC, total organic carbon.

Table 2
Concentrations of FBTO (ng g^{-1} as tin, referred to dry weight) in soils from vineyards treated with this acaricide, $n = 4$ replicates.

Vineyard	Fumigation dates	Sample code	Sampling date	Conc. (ng g^{-1}) ± standard deviation
1	July 2007	1[a]	October 2007	57 ± 6
		2[a]	March 2008	58 ± 7
		3[a]	June 2008	29 ± 1
		4[a]	October 2008	5 ± 1
2	July 2007 and July 2008	5[a]	June 2008	42 ± 1
		5[b]	June 2008	36 ± 4
		6[a]	October 2008	157 ± 6
		6[b]	October 2008	120 ± 10

[a] Fraction under 0.3 mm.
[b] Fraction between 0.3 and 1 mm.

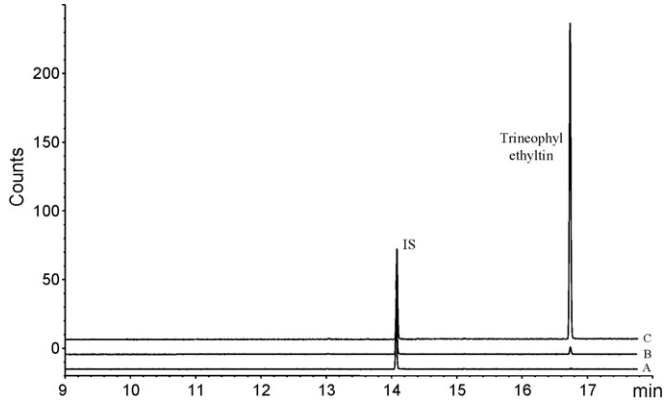

Fig. 4. Overlay of chromatograms for a procedural blank (A) and soil samples codes 4 (B) and 6 (C) from Table 2.

3.4. Application to real samples

The developed method was applied to soil samples from two vineyards which had been fumigated with FBTO (55 g of active ingredient per hectolitre of water). Samples were taken from the upper 5 cm soil layer and sieved. Details about sampling dates and found concentrations, corrected with the percentage of humidity presented in the soil, are summarized in Table 2. Percentages of total organic carbon (TOC) in these samples varied between 1.4 and 2.5%. FBTO was detected in all samples at concentrations in the range from 5 to 157 ng g^{-1} depending on the number of applied treatments, and the time passing since fumigation until sampling. Chromatograms corresponding to two soil samples containing low and high levels of FBTO are depicted in Fig. 4. Values measured in sample codes 1–4 showed a steady, although slow, temporal diminution in the residues of FBTO. Concentrations found in samples 1 and 2, from vineyard number 1, were practically equivalent. In practise, this does not necessary mean that FBTO was not degraded during this period, since vine leaves contain high loads of the miticide, which is transferred to soil at the end of autumn. Application of the developed method to leaves from vineyard number 2 revealed a concentration of FBTO as high as 2.8 ± 0.4 μg g^{-1} ($n = 3$ replicates). Data obtained for fractions from samples codes 5 and 6, with different particle sizes, showed a slight reduction in the concentration of FBTO with the increase in the size of soil particles, Table 2.

4. Conclusions

A novel and sensitive method for the determination of FBTO in soil samples is presented. This miticide reacts with $NaBEt_4$ under similar conditions than more polar, lower molecular weight organotin species; however, its high lipophilicity and limited volatility, even after derivatization, conferred FBTO noticeable differences during extraction and determination by GC-AED. PLE provided quantitative recoveries in the extraction of soil samples, consuming a moderate volume of acetone and, when Ph_3SnPe is used as IS, quantification can be performed against standards in acetone, derivatized under same conditions as sample extracts. As far as we could trace, this work constitutes the first application of PLE to the extraction of FBTO. Analysis of a limited number of samples confirmed the slow degradation of this acaricide in soils with the risk of accumulation in agricultural fields sprayed every year. Additional studies are necessary to determine the degradation pathways of FBTO, and the persistence of its potential by-products.

Acknowledgment

This study has been supported by Xunta de Galicia (project PGIDIT06RAG50501PR-2).

References

[1] K.A. Barnes, R.J. Fussell, J.R. Startin, H.J. Mobbs, R. James, S.L. Reynolds, Rapid Commun. Mass Spectrom. 11 (1997) 159.
[2] A.D. Teodoro, M.A.M. Fadini, W.P. Lemos, R.N.C. Guedes, A. Pallini, Exp. Appl. Acarol. 36 (2005) 61.
[3] Commission Directive 53/2006/EC of 7 June 2006, Off. J. Eur. Commun. 8.6.2006, L 154/11.
[4] P. Cabras, M. Melis, C. Tuberoso, D. Falqui, M. Pala, J. Agric. Food Chem. 40 (1992) 901.
[5] T.P. Lockhart, J. Organomet. Chem. 287 (1985) 179.
[6] USA Environmental Protection Agency, R.E.D. Facts (Fenbutatin-oxide), EPA-738-F-94-021 (September, 1994).
[7] J.A. Stäb, W.P. Cofino, B. van Hattum, U.A.T. Brinkman, Fresenius J. Anal. Chem. 347 (1993) 247.
[8] J.A. Stäb, W.P. Cofino, B. van Hattum, U.A.T. Brinkman, Anal. Chim. Acta 286 (1994) 335.
[9] A. Gray, A.J. Dutton, C.V. Eadsforth, Pestic. Sci. 43 (1995) 295.
[10] C. Devos, L. Moens, P. Sandra, J. Sep. Sci. 28 (2005) 665.
[11] P. Michel, B. Averty, Appl. Organomet. Chem. 5 (1991) 393.
[12] L. Wang, J.W.H. Lam, J. Anal. Atom. Spectrom. 16 (2001) 724.
[13] M. Gallego-Gallegos, M. Liva, R. Muñoz Olivas, C. Cámara, J. Chromatogr. A 1114 (2006) 82.
[14] J. Heroult, T. Zuliani, M. Bueno, L. Denaix, G. Lespes, Talanta 75 (2008) 486.
[15] A. Wasik, T. Ciesielski, Anal. Bional. Chem. 378 (2004) 1357.
[16] S. Chiron, S. Roy, R. Cottier, R. Jeannot, J. Chromatogr. A 879 (2000) 137.
[17] J. Ruiz-Encinar, P. Rodríguez-González, J. Rodríguez-Fernández, J.I. García Alonso, S. Diez, J.M. Bayona, A. Sanz-Medel, Anal. Chem. 74 (2002) 5237.
[18] M. Ceulemans, R. Lobinski, W.M.R. Dirkx, F.C. Adams, Fresenius J. Anal. Chem. 347 (1993) 256.
[19] M. Zabaljauregi, A. Delgado, A. Usobiaga, O. Zuloaga, A. de Diego, J.M. Madariaga, J. Chromatogr. A 1148 (2007) 78.
[20] R. Lobisnki, W.M.R. Dirkx, M. Ceulemans, F.C. Adams, Anal. Chem. 64 (1992) 159.
[21] C.G. Arnold, M. Berg, S.R. Müller, U. Dommann, R.P. Schwarzenbach, Anal. Chem. 70 (1998) 3094.
[22] T. Schmeck, B.W. Wenclawiak, Chromatographia 62 (2005) 159.
[23] C.F. Poole, J. Chromatogr. A 1158 (2007) 241.

Talanta 79 (2009) 916–925

Contents lists available at ScienceDirect

Talanta

journal homepage: www.elsevier.com/locate/talanta

Extending the working calibration ranges of four hexachlorocyclohexane isomers in gas chromatography–electron capture detector by radial basis function neural network

Yanfei Chen [1], Jin He [1], Jibin Zhang, Ziniu Yu *

State Key Laboratory of Agricultural Microbiology and National Engineering Research Center of Microbial Pesticides, Huazhong Agricultural University, Wuhan 430070, PR China

ARTICLE INFO

Article history:
Received 19 March 2009
Received in revised form 13 May 2009
Accepted 15 May 2009
Available online 22 May 2009

Keywords:
Radial basis function neural network
Hexachlorocyclohexane
Working calibration range
Gas chromatography–electron capture detector

ABSTRACT

A radial basis function neural network (RBFNN) method was developed for the first time to model the nonlinear calibration curves of four hexachlorocyclohexane (HCH) isomers, aiming to extend their working calibration ranges in gas chromatography–electron capture detector (GC–ECD). Other 14 methods, including seven parametric curve fitting methods, two nonparametric curve fitting methods, and five other artificial neural network (ANN) methods, were also developed and compared. Only the RBFNN method, with logarithm-transform and normalization operation on the calibration data, was able to model the nonlinear calibration curves of the four HCH isomers adequately. The RBFNN method accurately predicted the concentrations of HCH isomers within and out of the linear ranges in certified test samples. Furthermore, no significant difference ($p > 0.05$) was found between the results of HCH isomers concentrations in water samples calculated with RBFNN method and ordinary least squares (OLS) method ($R^2 > 0.9990$). Conclusively, the working calibration ranges of the four HCH isomers were extended from 0.08–60 ng/ml to 0.08–1000 ng/ml without sacrificing accuracy and precision by means of RBFNN. The outstanding nonlinear modeling capability of RBFNN, along with its universal applicability to various problems as a "soft" modeling method, should make the method an appealing alternative to traditional modeling methods in the calibration analyses of various systems besides the GC–ECD.

1. Introduction

Electron capture detector (ECD) is widely applied in the determination of analytes containing halogen atoms, cyano groups or nitro groups. It has been recognized to be an indispensable, simple, sensitive and selective detector for gas chromatography (GC) in the past four decades [1]. Nevertheless, it also suffers from various disadvantages, one of them being its narrow linear dynamic range (LDR) [2]. Quantification in GC–ECD is mostly done from calibration curves in LDR based on the linear regression hypothesis of ordinary least squares (OLS). It may lead to inaccurate results if analyte concentration in a sample exceeds the upper concentration limit on the calibration curve. In that case the analyst may be forced to dilute the sample or reduce the sensitivity of the analytical measurement with the ensuing risk of contamination, increase of time consumption and analysis costs [3]. These procedures, however, are not always practical especially in the multi-component or multi-sample analyses where analyte concentrations may cover very wide concentration ranges. Moreover, there remain some questions as to whether the increased accuracy of fitting a linear calibration curve compensates for the loss in signal-to-noise ratio (S/N) that may result from dilution or sensitivity reduction [4].

Fortunately, several instrumental, analytical, and mathematical methods with various degrees of success have been proposed to tackle the above problems [5–9]. Apparently, the mathematical approach, which is actually the focus of the present work, exhibits more advantages in cost, time consumption and universality than the former two. Because of the potential nonlinearity of calibration curve in GC–ECD, various curve fitting methods were employed as alternatives to OLS method. Table 1 lists several curve fitting methods available in the software packages of four leading world GC instrument manufactures. These methods could be

Abbreviations: ANN, artificial neural network; ANNs, artificial neural networks; ANOVA, analysis of variance; BPNN, back propagation neural network; ECD, electron capture detector; EI, electron impact; GC, gas chromatography; GRNN, generalized neural network; HCH, hexachlorocyclohexane; I.S., internal standard; LDR, linear dynamic range; r, correlation coefficient; LOD, limit of detection; LODs, limit of detections; MS, mass spectrometer; LOQ, limit of quantification; LOQs, limit of quantifications; m/z, mass-to-charge ratio; OLS, ordinary least squares; PCNB, pentachloronitrobenzene; R2, coefficient of determination; RBF, radial basis function; RBFNN, radial basis function neural network; RMSE, root mean square error; RMSPD, root mean square of the percentage deviations; RSD, relative standard derivation; S/N, signal-to-noise ratio; SIM, selected ion monitoring.

* Corresponding author. Tel.: +86 27 87280802; fax: +86 27 87393882.
E-mail address: yz41@mail.hzau.edu.cn (Z. Yu).

[1] Both the authors contributed equally and both are co-first authors.

0039-9140/$ – see front matter © 2009 Elsevier B.V. All rights reserved.
doi:10.1016/j.talanta.2009.05.027

Table 1
Curve fitting methods adopted in the software packages of different GC instrument manufactures.

Manufacturer	Software	Curve fitting method
Agilent Technologies	ChemStation A.09	Linear, quadratic, log, power, exponent, piecewise linear
Thermo Electron	Xcalibur 1.4	Linear, quadratic, linear log–log, quadratic log–log, average response factor, point-to-point, cubic spline, locally weighted
Shimadzu	GCsolution 2.0	Linear, quadratic, cubic, point-to-point, average response factor, exponent, manual response factor
Varian	Star Workstation 6.0	Linear, quadratic, cubic

generally classified into two groups: parametric and nonparametric methods. The former commonly involves the use of polynomial, logarithm, power, exponent, linear log–log, and quadratic log–log. Theoretically, parametric curve fitting method will perform well if the assumed structure of the function is sufficiently close to the global relation of **y**–**x** (**y** and **x** indicating response and quantum, respectively). Unfortunately, if such precondition does not meet, parametric curve fitting method will not achieve satisfactory results [10].

Nonparametric curve fitting method, in contrast, tries to avoid modeling the global relation of **y**–**x**. It focuses only on the local relation around a point of interest. If the global relation of **y**–**x** to be modeled is unknown, however, it can be expected that a nonparametric method will, on average, have better performance than the parametric counterpart [10]. Linear interpolation and cubic spline are the commonly utilized nonparametric curve fitting methods [7].

Recently, artificial neural networks (ANNs) are increasingly applied in analytical chemistry as a powerful complement to traditional statistical and modeling methods [11–14]. ANNs represent so-called "soft" modeling without the need to know or establish a mathematical model. The models have an ability to learn and extract **y**–**x** mapping relations from the presentation of a set of training samples [15]. Among the types of ANN already applied in calibration method, back propagation neural network (BPNN) is the most widely used one. Radial basis function neural network (RBFNN) and generalized regression neural network (GRNN) are ANNs, which both use radial basis functions as transfer functions, offering interesting alternatives to BPNN in the sense that they allow local and fast training [16].

ANNs have been widely applied in chemometrics, concerning the fields of modeling [17,18], signal processing [19], curve resolution [20], calibration [21,22], parameter estimation [23–25], quantitative structure activity relationship [26–28], pattern recognization [29–31], and artificial intelligence [32]. As for the section of calibration, ANNs have been employed as very typical way to improve the working calibration ranges in different analytical techniques, such as voltammetry [20,21], optical sensor [22], spectrometry [3,33] and GC [19]. Taking the work of Fu et al. as an example, the performance of a thermoionic detector in GC was improved 10-fold in its detection limit thanks to the employment of an ANN processing [19]. Nevertheless, as far as we know, no literature has been reported on the ANNs applied to extend the working calibration range of GC–ECD up to now.

Hexachlorocyclohexane (HCH) used to be extensively applied as a broad-spectrum organochlorine pesticide. It has been listed as the persistent organic pollutant in the Stockholm Convention for its tendency to accumulate along the food chain, together with harmful effects on human beings and the environment [34]. Its residues in diverse environmental samples were distributed in wide concentration ranges [35–38]. Its linear range in GC–ECD, however, is relatively narrow.

In this study, seven parametric curve fitting methods, two nonparametric curve fitting methods and six ANN methods belonging to three types of ANN (i.e. BPNN, GRNN and RBFNN) were developed and evaluated for modeling the nonlinear calibration curves of four HCH isomers, aiming to explore the best method that could extend the working calibration ranges of HCH in GC–ECD. The accuracy and precision of the best method was further validated by analyses of certified test samples and comparison with OLS method in the determination of HCH residues in water samples.

2. Materials and methods

2.1. Standards and reagents

Five certified analytical standards of α-HCH, β-HCH, lindane, δ-HCH in petroleum ether (100.00 ± 0.13 μg/ml) and pentachloronitrobenzene (PCNB) in benzene (100.00 ± 0.10 μg/ml) were purchased from China Standard Technology Development Corporation (Beijing, China). *n*-Hexane was HPLC grade and other reagents were analytical grade. These were purchased from Sinopharm Chemical Reagent Co., Ltd. (Shanghai, China). PCNB was used as internal standard (I.S.).

Individual stock standard solutions of each HCH isomer (10 μg/ml) and PCNB (1 μg/ml) were prepared in *n*-hexane and stored in a freezer at −20 °C. Composite stock standard solutions containing four HCH isomers at concentration of 1 μg/ml were prepared by diluting the individual stock standard solutions with *n*-hexane and stored at 4 °C in the dark. Calibration standards were made up, which covered five orders of magnitude of concentrations using 26 standards. These were prepared by serial dilution of composite stock standard solutions with *n*-hexane and adding a constant amount of I.S. stock standard solution. Concentration ranges of HCH isomers were 0.010–1000 ng/ml. I.S. was at the constant concentration of 100 ng/ml. Each order of magnitude of concentration was characterized using five standards (1, 2, 4, 6, 8 series). Certified test samples were prepared by serial dilution of each HCH individual stock standard solution with *n*-hexane and adding a constant amount of I.S. stock standard solution to yield each HCH concentration at three levels: 1 ng/ml, 10 ng/ml and 100 ng/ml and I.S. concentration of 100 ng/ml. The concentrations of HCH were selected to be inside and outside their linear calibration ranges in GC–ECD.

2.2. Samples preparation

Water samples were collected from four lakes around Huazhong Agricultural University in Hubei province of China. They were prefiltered through Millipore PTFE-membrane filters of 0.45 μm pore size to remove algae and suspended materials. The method of sample extraction and concentration was referred to US EPA Method 3510C [39]. The final volume of extraction, extracted from 250 ml water sample, was concentrated to 2 ml in *n*-hexane by nitrogen blowdown technique. No clean-up was required as no interferences were observed during analysis. Spike certain volume of I.S. stock standard solution to each sample extract to obtain PCNB concentration of 100 ng/ml.

Spiked water samples, used for calculating recovery rates of sample pretreatment method, were prepared by spiking three different levels of HCH standards (8 ng/l, 60 ng/l and 160 ng/l for α-HCH, β-HCH and lindane; 6 ng/l, 30 ng/l and 80 ng/l for δ-HCH) into water sample blank. Spiked water samples, used for validat-

ing the curve fitting method, were also prepared by spiking three different levels of HCH standards into water sample blank. The three levels selected to be in and out linear calibration ranges were: 1.5 ng/l, 5 ng/l and 15 ng/l for α-HCH, 2 ng/l, 20 ng/l and 45 ng/l for β-HCH, 0.5 ng/l, 25 ng/l and 90 ng/l for lindane, 0.5 ng/l, 15 ng/l, and 40 ng/l for δ-HCH. Same pretreatments above were employed to treat spiked water samples before introduced to GC.

2.3. Instrumental and analytical conditions

A Finnigan Trace GC Ultra (Thermo Finnigan, Milan, Italy) equipped with ^{63}Ni electron capture detection (ECD) and a Finnigan Trace DSQ (Thermo Electron Co., Austin, TX, USA) mass spectrometer (MS) was used. Helium of purity greater than 99.999 % was used as carrier gas and the makeup gas of ECD. For separation, a DB-1 MS capillary column of 30 m length × 0.25 mm i.d. × 0.25 μm film thickness (J&W Scientific Co., Folsom, CA, USA) was employed.

GC conditions: injection volume: 1 μl, splitless with surge injection mode, splitless time: 1.10 min, surge pressure: 200 kPa, surge time: 1.00 min, injector temperature: 250 °C, constant carrier gas pressure: 150 kPa, oven temperature programme: initial temperature 70 °C (held for 1.00 min), increased by 40 °C/min to 140 °C (without hold), then increased by 5 °C/min to 190 °C (held for 3 min), and finally, increased to 260 °C at the rate of 30 °C/min and held at this temperature for 3 min. ECD conditions: detector base temperature: 260 °C, ECD temperature: 300 °C, and makeup gas flow rate: 30 ml/min. MS conditions: transfer line temperature: 250 °C, ion source temperature: 200 °C, reagent delay time: 8 min, selected ion monitoring (SIM) mode with electron impact (EI) ionization (electron energy 70 eV), scan in segments, namely monitoring *m*/*z* 109, 181, 183 and 219 for HCH isomers from 8 min to 10.68 min during the whole run time, and *m*/*z* 237, 239, 249 and 295 for PCNB after 10.68 min. Peak identification was conducted by the accurate retention time of each standard and further confirmed by MS.

In the processes of calibration, responses were measured as the peak areas of HCH isomers relative to that of the internal standard. Quantitation of HCH is based on the response using internal standard calibration method.

2.4. Determination of HCH isomers by GC–ECD and GC–MS

Twenty-six calibration standards prepared, with a concentration range from 0.01 ng/ml to 1000 ng/ml for HCH isomers and a constant concentration of 100 ng/ml for I.S., were injected sequentially into GC–ECD and GC–MS system, respectively. Three replicates for each calibration standard were taken. Calibration data pairs (i.e. response data *vs*. concentration data) acquired from GC–ECD were employed to establish the calibration curves, and evaluate the various curve fitting methods including ANNs. While calibration data pairs acquired from GC–MS were only used in the comparison of HCH linear ranges in GC–ECD and GC–MS.

1 μl of certified test samples, extracts of water samples or spiked water samples was injected into GC–ECD for the determination of HCH isomers. Three replicates for each sample were taken. The acquired calibration data pairs were utilized to evaluate the accuracy and precision of the selected curve fitting method, which exhibited the best performance to model calibration curves of HCH isomers in the 15 methods.

2.5. Quality control and quality assurance

The limits of detection (LOD) of HCH isomers were defined as three times of the S/N. Similarly, the limit of quantification (LOQ) was defined as 10 times of the S/N. For every set of 10 samples, a procedure blank and a spiked sample consisting of all standards were run to check for interference and cross contamination. HCH isomers recovery studies were undertaken to demonstrate the efficiency of the method. The recoveries of four HCH isomers in spiked water varied from 76% to 115% and the relative standard derivation (RSD) was in the range from 3% to 10% ($n = 5$). LODs and LOQs for HCH isomers in water sample were 0.18–0.34 ng/l and 0.60–2.25 ng/l, respectively. The RSD of injection was 0.8–1.5% ($n = 5$). Retention time shifts of I.S. were less than 3 s and changes in I.S. areas were no more than 10% in each batch of analysis.

2.6. Modeling the calibration curves of four HCH isomers

Samples or calibration standards producing peaks of S/N larger than 10 were then evaluated using various curve fitting methods. The acquired calibration data pairs of each HCH isomers, covering the entire working range, were divided randomly into a training data set and test data set by the percentages of 80% and 20%, respectively. Training data set was used for constructing the models of calibration curves by different curve fitting methods, while test data set was employed to evaluate the prediction abilities of the models. A total of 15 curve fitting methods were employed and compared.

2.6.1. Modeling the calibration curves by parametric methods

The most common approach to model the calibration curves has been to fit a global parametric function (Eq. (1))

$$\mathbf{y} = f(\mathbf{x}, \theta) \tag{1}$$

with finite length parameter vector θ to the data $(\mathbf{x}, \mathbf{y})$. The modeling procedure minimizes some error function J so that $\theta = \min(\sum J_i)$ for all data pairs $(\mathbf{x}_i, \mathbf{y}_i)$ in a training data set. Very often, J is a least squares criterion. If f is linear in the parameters θ, least squares minimization corresponds to linear regression and the parameters can be calculated in closed form. In more interesting applications, however, f is nonlinear in the parameters and the error function J must be minimized iteratively [10].

Six parametric methods, namely quadratic polynomial, cubic polynomial, logarithm, power, exponent, linear log–log, and quadratic log–log, were selected to model the calibration curves of HCH isomers in this paper.

2.6.2. Modeling the calibration curves by nonparametric methods

Nonparametric methods do not assume any particular distribution for the population of experimental data. The most popular nonparametric methods applied to calibration methods are the linear interpolation and cubic spline, which seek to fit the experimental data with a series of linear and cubic curved portions, respectively. These portions are connected at points called "knots", at each of which the two linked linear or cubic functions and their corresponding first or second derivatives must be continuous [40]. The result is a linear or smooth curve passing through all data points. Linear interpolation and cubic spline are generally used when data points are known exactly and are widely free from random errors. They were both adopted to model the calibration curves of HCH isomers in present work.

2.6.3. Modeling the calibration curves by artificial neural networks

ANNs are pseudo-parallel information-processing systems, inspired by biological nervous networks. Commonly, they can be trained with certain learning rule to perform a particular function and solve problems that are difficult for conventional computers or human beings.

Three types of ANN were evaluated for modeling the calibration curves, namely BPNN, RBFNN and GRNN. Response data set and concentration data set acquired from GC–ECD were treated as input variables and target variables in the training of ANNs, respectively. ANNs were all trained under supervised learning mode [41].

Table 2
Results of the optimizations of ANN architectures.

Methods	Data transformations	Architecture parameters
BPNN01	Logarithm	ANN architectures: 1-8-1, 1-3-1, 1-12-1 and 1-12-1[a,b]; transfer functions of neurons in hidden layer and output layer: both were "tansig"; learn function: "learngdm"; train function: "trainlm", performance function: mean square error; train goal: 1.0E-6; other parameters were the default values
BPNN02	Logarithm and normalization	ANN architectures: 1-8-1, 1-9-1, 1-10-1 and 1-11-1[a,b]; other parameters were the same as above.
GRNN01	Logarithm	ANN architectures: 1-48-1, 1-44-1, 1-46-1 and 1-52-1[a,b]; values of SPREAD: 10E-2, 10E-2.4, 10E-2 and 10E-3[b]; other parameters were the default values
GRNN02	Logarithm and normalization	ANN architectures: 1-48-1, 1-44-1, 1-46-1 and 1-52-1[a,b]; values of SPREAD: 10E-2, 10E-2.4, 10E-2 and 10E-3[b]; other parameters were the default values
RBFNN01	Logarithm	ANN architectures: 1-2-1, 1-2-1, 1-2-1 and 1-2-1[a,b]; values of SPREAD: 1.0, 1.7, 1.3 and 1.5[b]; other parameters were the default values
RBFNN02	Logarithm and normalization	ANN architectures: 1-2-1, 1-2-1, 1-2-1 and 1-2-1[a,b]; values of SPREAD: 1.0, 1.7, 1.3 and 1.5[b]; other parameters were the default values

[a] ANN architectures are presented in the form of N_{input}-N_{hidden}-N_{output}, where N_{input}, N_{hidden} and N_{output} are the neuron numbers of input layers, the neuron numbers of hidden layers and the neuron numbers of output layers, respectively.
[b] Parameters for α-HCH, β-HCH, lindane and δ-HCH, respectively.

BPNN is a multi-layer feed-forward network with the error back propagation learning rule. It usually consists of three layers: input, hidden and output. Data "flows" exclusively from the input to the output layer, and thus this particular topology is usually referred to as "feed-forward ANN". While the adjustment of the weights is performed on the opposite direction, i.e. it is "back propagated" [42]. The process is iteratively repeated until the error reaches a predetermined goal or after a selected number of learning/validation cycles.

RBFNN can be also described as a three-layer feed-forward structure. The hidden layer of RBFNN consists of a number of radial basis function (RBF) units (n_h) and bias (b_k). Gaussian function was selected as the radial basis function in this study. The RBF measures the Euclidean distance between input vector ($\mathbf{x}$) and the radial basis function center (c_j) and perform the nonlinear transformation with RBF in the hidden layer as given in Eq. (2):

$$h_j(\mathbf{x}) = \exp\left(-\frac{\left\|\mathbf{x} - c_j\right\|^2}{r_j^2}\right) \quad (2)$$

In which, h_j is the notation for the output of the jth RBF unit. For the jth RBF c_j and r_j are the center and width respectively. The operation of the output layer is linear, which is given in Eq. (3):

$$y_k(\mathbf{x}) = \sum_{j=1}^{n_h} w_{kj} h_j(\mathbf{x}) + b_k \quad (3)$$

where y_k is the kth output unit for the input vector $\mathbf{x}$, w_{kj} is the weight connection between the kth output unit and the jth hidden layer unit, and b_k is the bias [26]. The latter is in turn estimated according to (0.8326/SPREAD). RBFNN can require more neurons than standard feed-forward back propagation networks, but often they can be designed in a fraction of the time it takes to train standard feed-forward networks. They work best when many training vectors are available [43].

GRNN is a variation of the RNFNN that is based on the Nadaraya–Watson kernel regression. It is also a one-pass learning algorithm (same to the former RBFNN) with a highly parallel structure. GRNN can be used for any regression problem in which an assumption of linearity is not justified [44].

The most important problem in developing a neural network is generalization: a neural network is expected to make good predictions when data not present in the training data set is used as an input. Generally, generalization depends on the size and efficiency of training data set, architecture of the network and the physical complexity of the problem [45].

Preliminary work had been done to improve the generalization of ANNs. (1) Normalized response and concentration data to [0 1] separately, in order to uniform their different magnitudes and ensure the training starts within the active range of the nonlinear transfer functions; (2) Multiplied response and concentration data by 1000 and 10, respectively, and then each of them was transformed with logarithm. The transformation could make the distribution of response and concentration data more uniform in a new compressed numerical range; (3) Introduced leave-one-out cross-validation to the training of ANNs; (4) Optimized the ANNs architectures with training data set (Table 2). Six ANN methods developed in this paper were classified by their types of ANN (i.e., BPNN, RBFNN and GRNN) and whether data sets were transformed by log function.

2.7. Evaluating the method performance

Some criteria were required by which the performance of various curve fitting methods could be compared. These are referred to as "goodness-of-fit" measures. Because the primary goal of quantitative analyses is the accurate reporting of concentration values, the fitting abilities and prediction abilities of curve fitting methods are of primary interests.

Firstly, evaluate the fitting abilities by two goodness-of-fit statistics, namely the fitting correlation coefficient (*fitting r*) and root mean square percentage deviation (RMSPD) of fitting (Eq. (4)). *fitting r* was used to evaluate the quality of a linear regression analysis of HCH isomers concentrations predicted by different methods with the training data set versus the actual concentrations in the calibration standards. It was different from the correlation coefficient (r) obtained in the fitting of the parametric model to experimental data. RMSPD represents the fitting precision over the entire curve. It is based on percentage deviations in the concentrations and unbiased towards any part of the curve, for which RMSPD was employed here instead of the commonly used statistic root mean square error (RMSE).

$$\mathrm{RMSPD} = \left(\frac{1}{N}\sum_{i=1}^{N}\left(\frac{C^i_{\mathrm{pred}} - C^i_{\mathrm{real}}}{C^i_{\mathrm{real}}} \times 100\right)^2\right)^{1/2} \quad (4)$$

where C^i_{pred} and C^i_{real} correspond to the ith predicted and actual concentrations, respectively, and N is the number of data used in the training data set or test data set [33].

Secondly, evaluate the prediction abilities by the RMSPD of prediction (Eq. (4)) and relative error. The calculations were based on the test data set.

Finally, the best curve fitting method to model nonlinear calibration curves was determined through the first two steps. Its accuracy and precision was further validated by analyses of certified test samples and comparison with OLS method in the determination of HCH residues in water samples.

All curve fitting and statistical evaluation were conducted with Matlab 7.3 software (MathWorks Co., Natick, MA, USA).

3. Results and discussion

3.1. Linear ranges comparison of HCH isomers in GC–ECD and GC–MS

The term of linear range is defined as the concentration range over which the intensity of the signal obtained is directly proportional to the concentration of the species producing the signal [46]. It can be expressed by the range from lower concentration limit to upper concentration limit. The concentration limits are generally derived from the linear regression formulation at a specific confidence level. The adjusted coefficient of determination (adjusted R^2) was employed to assess the goodness-of-fit of linear regression formulation. The adjusted R^2 takes into account the variation in the degrees of freedom experienced by the residuals with the inclusion of further terms in a regression formulation. Therefore, it provides a statistically more accurate reflection of the regression formulation fitness than the coefficient of determination (R^2) [33].

Fig. 1 is a typical chromatogram with the four HCH compounds plus the I.S. obtained with GC–ECD. Fig. 2 shows the nonlinear behaviors of the response for the four HCH isomers with increasing concentrations in GC–ECD. A total of 60, 54, 57 and 66 calibration data pairs for α-HCH, β-HCH, lindane and δ-HCH standards were acquired from GC–ECD, respectively. And their entire concentration ranges were 0.2–1000 ng/ml, 0.6–1000 ng/ml, 0.4–1000 ng/ml and 0.08–1000 ng/ml, separately. In general, the calibration curves are linear at low concentrations, but show curvature towards the concentration axis at higher analyte levels. All the linear ranges of the four HCH isomers in GC–ECD were significantly narrow, spanning 0.2–20 ng/ml, 0.6–60 ng/ml, 0.4–20 ng/ml and 0.08–20 ng/ml, respectively (see insets in Fig. 2). The adjusted R^2 of each regression formulation for HCH isomers was larger than 0.9950 but no

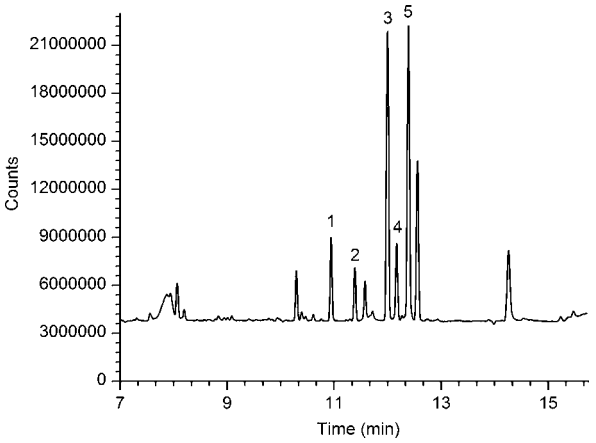

Fig. 1. The chromatogram of a spiked water sample obtained with GC–ECD. The spiked concentrations of α-HCH, β-HCH, lindane and δ-HCH were 15 ng/l, 20 ng/l, 90 ng/l and 15 ng/l. The I.S. concentration in the extract from 250 ml spiked water sample was 100 ng/ml. The peaks marked by 1, 2, 3, 4 and 5 were represented α-HCH, β-HCH, lindane, δ-HCH and I.S.

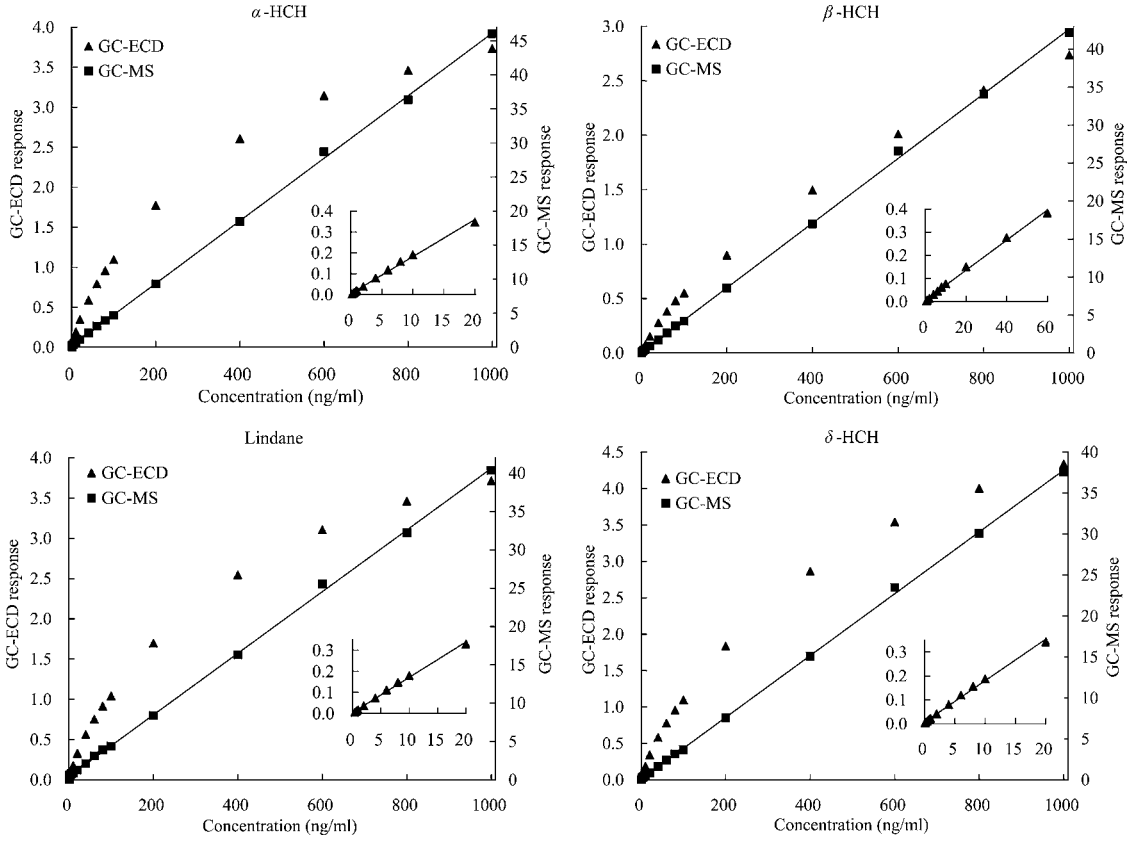

Fig. 2. Scatter plots of response *vs.* concentration for α-HCH, β-HCH, lindane and δ-HCH in GC–ECD (▲) and GC–MS (■). The solid lines through data point (▲) and data point (■) were fitted by OLS method. Insets show the linear ranges of the four HCH isomers in GC–ECD, namely 0.2–20 ng/ml, 0.6–60 ng/ml, 0.4–20 ng/ml and 0.08–20 ng/ml for α-HCH, β-HCH, lindane and δ-HCH, respectively.

Table 3
Fitting abilities comparison between 15 different curve fitting methods.

Method	*fitting r*				RMSPD of fitting (%)			
	α-HCH	β-HCH	Lindane	δ-HCH	α-HCH	β-HCH	Lindane	δ-HCH
Quadratic polynomial	0.9929 ± 0.0001	0.9996 ± 0.0000	0.9937 ± 0.0001	0.9959 ± 0.0000	1219.30 ± 211.84	67.26 ± 15.81	673.53 ± 88.43	1891.00 ± 315.78
Cubic polynomial	0.9989 ± 0.0000	0.9996 ± 0.0000	0.9988 ± 0.0000	0.9993 ± 0.0000	530.22 ± 68.59	109.71 ± 14.75	320.46 ± 31.64	1034.4 ± 103.74
Logarithm	0.4584 ± 0.0240	0.5312 ± 0.0263	0.4848 ± 0.0248	0.4794 ± 0.0244	25062.00 ± 2896.90	9662.20 ± 635.61	12698.00 ± 1255.50	54124.00 ± 6810.80
Power	0.9948 ± 0.0007	0.9992 ± 0.0001	0.9947 ± 0.0006	0.9956 ± 0.0004	1678.40 ± 180.13	251.94 ± 21.82	970.50 ± 95.49	3422.90 ± 469.09
Exponent	0.9995 ± 0.0001	0.5948 ± 0.2645	0.9994 ± 0.0001	0.9996 ± 0.0001	269.27 ± 35.50	6941.40 ± 5456.00	188.55 ± 20.24	722.82 ± 62.40
Linear log–log	0.9189 ± 0.0081	0.9764 ± 0.0032	0.9282 ± 0.0080	0.9415 ± 0.0057	6203.20 ± 757.23	1886.30 ± 189.41	3690.50 ± 328.28	12882.00 ± 1085.70
Quadratic log–log	0.9929 ± 0.0010	0.9996 ± 0.0000	0.9936 ± 0.0007	0.9958 ± 0.0004	1249.00 ± 168.10	67.85 ± 16.16	672.15 ± 105.04	2011.50 ± 298.92
Linear interpolate	1.0000 ± 0.0000	1.0000 ± 0.0000	1.0000 ± 0.0000	1.0000 ± 0.0000	0.00 ± 0.00	0.00 ± 0.00	0.00 ± 0.00	0.00 ± 0.00
Cubic spline	1.0000 ± 0.0000	1.0000 ± 0.0000	1.0000 ± 0.0000	1.0000 ± 0.0000	0.00 ± 0.00	0.00 ± 0.00	0.00 ± 0.00	0.00 ± 0.00
BPANN01	0.9999 ± 0.0000	0.9999 ± 0.0000	0.9999 ± 0.0000	0.9999 ± 0.0000	65.00 ± 64.63	72.40 ± 41.39	36.67 ± 47.4128	169.32 ± 195.96
BPANN02	0.9960 ± 0.0011	0.9980 ± 0.0001	0.9966 ± 0.0010	0.9983 ± 0.0012	2.65 ± 0.03	2.19 ± 17	2.18 ± 0.30	2.89 ± 0.14
GRANN01	1.0000 ± 0.0000	1.0000 ± 0.0000	1.0000 ± 0.0000	1.0000 ± 0.0000	68.65 ± 7.00	17.79 ± 2.21	36.12 ± 3.77	19.91 ± 2.10
GRANN02	0.9952 ± 0.0016	1.0000 ± 0.0000	0.9961 ± 0.0012	1.0000 ± 0.0000	2.48 ± 0.44	0.00 ± 0.00	2.02 ± 0.32	0.00 ± 0.00
RBFANN01	0.9999 ± 0.0000	1.0000 ± 0.0000	0.9998 ± 0.0000	0.9999 ± 0.0000	56.75 ± 15.94	6.78 ± 2.71	14.65 ± 4.34	41.15 ± 17.22
RBFANN02	0.9996 ± 0.0001	1.0000 ± 0.0000	0.9998 ± 0.0000	0.9997 ± 0.0001	1.87 ± 0.08	1.54 ± 0.13	1.22 ± 0.05	5.89 ± 0.95
OLS01[a]	0.9954 ± 0.0005	0.9954 ± 0.0005	0.9961 ± 0.0005	0.9961 ± 0.0005	43.92 ± 6.49	62.37 ± 5.76	24.86 ± 3.29	97.34 ± 11.17
OLS02[b]	0.9991 ± 0.0002	0.9992 ± 0.0002	0.9991 ± 0.0001	0.9991 ± 0.0001	2.86 ± 0.27	3.78 ± 0.56	2.72 ± 0.34	7.49 ± 1.67

All results correspond to the average ± standard deviation. n = number of training data, namely 48, 43, 46 and 53 for α-HCH, β-HCH, lindane and δ-HCH, respectively.

[a] OLS01, used as a control, represents ordinary least squares method with $R^2 > 0.9950$ in linear ranges of 0.2–20 ng/ml, 0.6–60 ng/ml, 0.4–20 ng/ml and 0.08–20 ng/ml for α-HCH, β-HCH, lindane and δ-HCH, respectively.

[b] OLS02, used as a control, represents ordinary least squares method with $R^2 > 0.9990$ in linear ranges of 0.8–10 ng/ml, 2–20 ng/ml, 1–10 ng/ml and 0.2–10 ng/ml for α-HCH, β-HCH, lindane and δ-HCH, respectively.

more than 0.9960. Inclusion of an extra calibration data pair will deteriorate the adequacy of the linear model (adjusted R^2 less than 0.9950). In addition, the shapes of four calibration curves were various considering the spans of linear part and nonlinear part, and the curvature in nonlinear part.

For the purpose to compare, calibration curves of the four HCH isomers in GC–MS were also plotted in Fig. 2. Apparently, a sharp contrast was formed between the linear ranges of the four HCH isomers in GC–ECD and GC–MS. The calibration curves in GC–MS exhibit great linearity towards the concentration ranged from 1 ng/ml to 1000 ng/ml for α-HCH, β-HCH and lindane, and 2 ng/ml to 1000 ng/ml for δ-HCH. Moreover, the adjusted R^2 of every regression formulation for HCH isomers was larger than 0.9993.

Such narrow linear range of HCH isomers in GC–ECD entails those samples with concentrations higher than the upper limit would require dilution, with all the disadvantages already mentioned. An alternative could be to extend the working calibration range by modeling the entire nonlinear calibration curve with appropriate curve fitting method.

3.2. Modeling performance comparison between different nonlinear curve fitting methods

A total of 15 curve fitting methods were developed and compared in present work. Those methods consisted of seven parametric methods, two nonparametric methods, and six ANN methods. In ANN methods, BPNN01, GRNN01 and RBFNN01 denoted only normalization were implemented on calibration data in the modeling by the three types of ANN. While BPNN02, GRNN02 and RNFNN02 denoted both logarithm-transformation and normalization were implemented. Additionally, OLS01 and OLS02, representing two ordinary least squares methods with $R^2 > 0.9950$ and $R^2 > 0.9990$ in linear ranges, respectively, were utilized as controls. The modeling performance of curve fitting method was indicated by its fitting ability and prediction ability.

3.2.1. Fitting abilities comparison

Fitting ability reflects the approximating level of models to the training data, and it can be simply measured by the *fitting r* and RMSPD of fitting in the process of constructing the model of calibration curve.

Referring to Table 3, nonparametric methods and ANN methods possess higher values of *fitting r* than parametric methods in modeling calibration curves of four HCH isomers generally. Values of *fitting r* for the two nonparametric methods employed are both equal to 1.0000 exactly. Meanwhile, the same precision level of *fitting r* was obtained by BPNN01, GRNN01, RBFNN01 and RBFNN02. Other ANN methods also get the approximate values of *fitting r*; however, such cases were only occurred in parts of the four isomers. In contrast, no parametric methods employed possess the values of *fitting r* higher than 0.9990 for all the four HCH isomers, and only one method of cubic polynomial obtains the values of *fitting r* higher than 0.9950 for the four standards simultaneously. Similar results were found when it came to the RMSPD of fitting. Nonparametric methods and ANN methods possess smaller RMSPD of fitting than parametric methods. Furthermore, only two nonparametric methods and three ANN methods of BPNN02, GRNN02 and RBFNN02 obtained smaller RMSPD of fitting than the control of OLS02 for all the four analytes.

Generally, the fitting abilities of parametric methods are extremely depended on whether their assumed structures of the functions are sufficiently close to the global relation of **y**–**x**. Apparently, a fixed function is difficult to simultaneously model the four calibration curves with different shapes. Therefore, their fitting abilities to modeling the various partial nonlinear calibration curves of HCH isomers in the entire working calibration range are, on aver-

Table 4
Prediction abilities comparison between 15 different curve fitting methods.

Method	RMSPD of prediction (%)			
	α-HCH	β-HCH	Lindane	δ-HCH
Quadratic polynomial	1088.50 ± 544.69	64.72 ± 28.58	589.69 ± 255.06	1753.00 ± 960.69
Cubic polynomial	523.11 ± 275.69	88.50 ± 55.43	291.78 ± 133.33	953.71 ± 509.03
Logarithm	18838.00 ± 14913.00	8840.2 ± 5061.70	9453.60 ± 6477.00	49346.00 ± 30603.00
Power	1465.30 ± 783.25	237.10 ± 90.21	970.60 ± 473.48	2892.80 ± 1467.5
Exponent	240.98 ± 127.04	6940.10 ± 6067.30	179.61 ± 88.68	660.75 ± 337.19
Linear log–log	5327.30 ± 2732.10	1696.30 ± 729.92	3382.30 ± 1428.20	10647.00 ± 4770.8
Quadratic log–log	1125.70 ± 629.61	63.14 ± 34.85	625.62 ± 302.25	1861.90 ± 926.07
Linear interpolate	2.86 ± 6.24	1.84 ± 0.92	1.67 ± 3.35	5.92 ± 7.57
Cubic spline	8.54 ± 43.22	9.27 ± 43.80	8.58 ± 39.44	17.24 ± 90.28
BPANN01	60.56 ± 68.94	70.81 ± 51.78	36.47 ± 48.39	167.26 ± 230.57
BPANN02	4.86 ± 2.90	4.20 ± 3.97	4.74 ± 4.22	10.09 ± 14.46
GRANN01	56.05 ± 40.45	20.02 ± 11.12	36.06 ± 18.45	24.24 ± 11.27
GRANN02	4.27 ± 4.02	3.67 ± 11.69	3.56 ± 4.75	8.79 ± 15.61
RBFANN01	41.34 ± 33.99	5.73 ± 4.04	13.71 ± 9.97	33.54 ± 28.37
RBFANN02	2.31 ± 0.40	1.83 ± 0.57	1.49 ± 0.30	5.41 ± 3.38
OLS01[a]	44.31 ± 22.92	53.43 ± 30.17	20.84 ± 9.60	73.23 ± 51.06
OLS02[b]	2.47 ± 0.88	2.80 ± 2.48	2.12 ± 0.90	5.63 ± 4.14

All results correspond to the average ± standard deviation. n = number of test data in test data set (20% of the total calibration data), namely 12, 11, 11 and 13 for α-HCH, β-HCH, lindane and δ-HCH, respectively.

[a] OLS01, used as a control, represents ordinary least squares method with $R^2 > 0.9950$ in linear ranges of 0.2–20 ng/ml, 0.6–60 ng/ml, 0.4–20 ng/ml and 0.08–20 ng/ml for α-HCH, β-HCH, lindane and δ-HCH, respectively.

[b] OLS02, used as a control, represents ordinary least squares method with $R^2 > 0.9990$ in linear ranges of 0.8–10 ng/ml, 2–20 ng/ml, 1–10 ng/ml and 0.2–10 ng/ml for α-HCH, β-HCH, lindane and δ-HCH, respectively.

age, lower than nonparametric method and ANN methods. Of the latter two types of method, linear interpolate, cubic spline, BPNN02, GRNN02 and RBFNN02 were free from the constraint of fixed model framework, so they possess the strongest fitting abilities.

3.2.2. Prediction abilities comparison

Prediction ability is probably the most important index of curve fitting method. By comparing the RMSPDs of prediction of the 15 methods and OLS02, RBFNN02 has the optimal prediction ability for each individual test data of four HCH isomers. Linear interpolate provided nearly identical results but only for β-HCH and lindane. Although cubic spline, BPNN02, GRNN02 and RBFNN01 possess the strong fitting abilities, their prediction abilities are relatively poor, just little better than BPNN01 and GRNN01 in ANN methods. While the prediction abilities of parametric methods are the worst in all methods (see details in Table 4). Additionally, the relative errors of RBFNN02 were randomly distributed around zero line, and no tendency to fall on a curve in entire concentration ranges. The absolute values of the averages of relative errors were less than 0.49%, 0.45%, 0.26% and 1.01% for α-HCH, β-HCH, lindane and δ-HCH, respectively (Fig. 3). Those reconfirmed the suitability of RBFNN02 to model the calibration curves of HCH isomers.

As nonlinear calibration curves often arise from a combination of physico-chemical effects and failure of mathematical approximations etc., it is perhaps unrealistic to expect that any single curve will adequately describe whole calibrate data. The poor prediction abilities of parametric methods just verified such assumption. Although linear interpolation and cubic spline are quick and easy, it is not very precise in prediction. The errors are proportional to the square and cubic of the distance between the data points, respectively. What is worse, the calculation and interpretation of those lines are complicated by the presence of possible outliers [40]. Those may be the causes for their higher fitting abilities but relative lower prediction abilities. With regard to ANN methods, averages and standard deviations of RMSPD of prediction were both decreased when logarithm-transform and normalization operation on calibration data were utilized. It confirmed that the generalization of ANN can be improved by narrowing data numerical ranges and uniforming their different magnitudes. The great of standard deviations of RMSPD of prediction in BPNN02 is partially resulted from too many random weight/bias initialization functions in its architecture. While the different results acquired by GRNN02 and RBFNN02 possible originate from their minor differences in weight function.

In addition, it is worth mentioning that some workers may argue against the application of such curve fitting methods due to their lack of physical meaning and may be difficult to interpret. Nevertheless, as long as they provide results that could be proved to be accurate and satisfied an acceptable degree of precision, we consider that they should not be disregard as alternatives calibration methods [3,33]. Clearly, RBFNN02 provided the best performance on all of the four calibration curves in terms of fitting and prediction abilities in present work. Its accuracy and precision would be further validated.

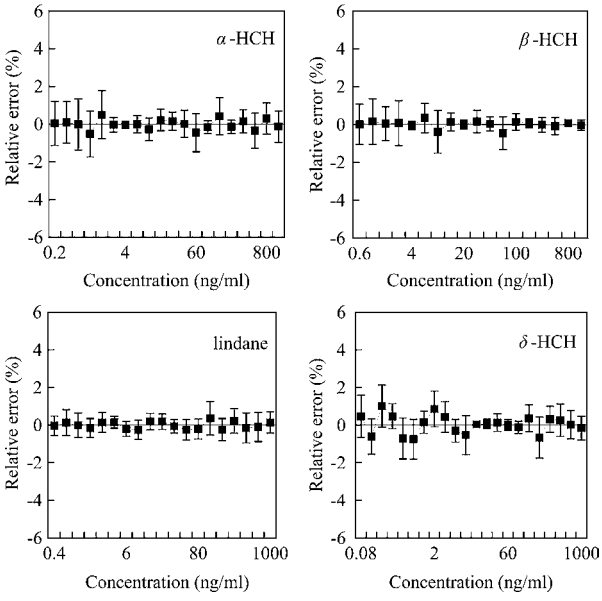

Fig. 3. Relative error (average ± standard deviation) of the predicted concentrations for the four HCH isomers by RBFNN02. n = number of test data, namely 12, 11, 11 and 13 for α-HCH, β-HCH, lindane and δ-HCH, respectively.

Table 5
Determination of HCH isomers in certified test samples with RBFNN method and its results compared to nominal values.

Concentration (μg/l)	α-HCH[a]			β-HCH[a]			Lindane[a]			δ-HCH[a]		
	Level 1	Level 2	Level 3	Level 1	Level 2	Level 3	Level 1	Level 2	Level 3	Level 1	Level 2	Level 3
Nominal	1.00 ± 0.01	10.00 ± 0.07	100.00 ± 0.76	1.00 ± 0.02	10.00 ± 0.09	100.00 ± 0.52	1.00 ± 0.01	10.00 ± 0.05	100.00 ± 0.50	1.00 ± 0.01	10.00 ± 0.05	100.00 ± 0.25
Predicted	0.99 ± 0.02 (1.71)	9.89 ± 0.09 (0.87)	100.02 ± 0.78 (0.78)	1.00 ± 0.02 (2.04)	9.93 ± 0.09 (0.88)	99.06 ± 0.77 (0.78)	1.00 ± 0.01 (1.28)	9.91 ± 0.05 (0.50)	99.10 ± 0.97 (0.98)	1.01 ± 0.01 (0.83)	9.98 ± 0.01 (0.07)	99.47 ± 0.49 (0.49)
p-value[b]	0.2932	0.1483	0.9815	0.8906	0.3649	0.1528	0.4108	0.0808	0.2254	0.6569	0.5335	0.1699

[a] Values correspond to the average ± standard deviation ($n = 3$). Relative standard deviation (%RSD) is given in parenthesis.
[b] One-way ANOVA at the 5% significance level.

Table 6
Determination of HCH isomers in spiked water samples with RBFNN method and OLS method.

Method	Sample 1[a]				Sample 2[a]				Sample 3[a]			
	α-HCH	β-HCH	Lindane	δ-HCH	α-HCH	β-HCH	Lindane	δ-HCH	α-HCH	β-HCH	Lindane	δ-HCH
RBFANN02	1.36 ± 0.01 (0.87)	1.71 ± 0.06 (3.68)	0.42 ± 0.01 (1.75)	0.48 ± 0.02 (4.52)	12.40 ± 0.19 (1.53)	19.00 ± 0.42 (2.22)	87.42 ± 0.63 (0.72)	11.92 ± 0.35 (2.94)	4.79 ± 0.04 (0.75)	41.75 ± 0.90 (2.16)	24.75 ± 0.16 (0.65)	35.04 ± 0.59 (1.70)
OLS	1.38 ± 0.01 (0.83)	1.70 ± 0.07 (3.89)	0.42 ± 0.01 (2.20)	0.47 ± 0.02 (3.79)	12.28 ± 0.17 (1.40)	19.03 ± 0.41 (2.14)	87.94 ± 0.75 (0.85)	12.09 ± 0.37 (3.07)	4.79 ± 0.04 (0.75)	41.96 ± 1.00 (2.38)	24.78 ± 0.20 (0.82)	35.77 ± 0.56 (1.56)
p-value[b]	0.1420	0.8219	0.4891	0.7528	0.4981	0.9302	0.4150	0.5824	0.9783	0.7953	0.8694	0.1719

[a] Values correspond to the average ± standard deviation ($n = 3$). Relative standard deviation (% RSD) is given in parenthesis.
[b] One-way ANOVA at the 5% significance level.

3.3. Determination of HCH isomers in certified test materials and water samples

The accuracy and precision of RBFNN02 were validated by analysis of the certified test materials and comparison with the standard method of OLS in the determination of HCH isomers in water samples.

3.3.1. Analysis of HCH isomers in certified test materials

RBFNN02 was employed to model the calibration curve of each HCH isomer in the entire working calibration ranges from 0.08–0.4 ng/ml to 1000 ng/ml. And then it was utilized to predict the concentrations of HCH isomers in certified test samples with HCH isomers concentrations below and above the maximum linear calibration limit. The results obtained in such a way are presented in Table 5. A statistical evaluation of one-way analysis of variance (ANOVA) revealed no significant differences ($p > 0.05$) in accuracy between the nominal concentrations and those obtained by RBFNN02 method at all levels. And good precision was attained in all cases ($\leq$2.04% RSD).

3.3.2. Comparison of RBFNN02 and OLS method

Two strategies were employed in the determination of HCH isomers in water samples: (1) dilute the extracts of water samples or spiked water samples with the concentrations of HCH isomers outside the linear ranges, and then quantify the concentrations of analytes with OLS method in the linear portions of calibration curves; (2) model the calibration curves of each HCH isomers in the entire working calibration ranges from 0.08–0.4 ng/ml to 1000 ng/ml by RBFNN02, then determine the analytes directly. The results obtained by OLS method ($R^2 > 0.9990$) with those obtained by RBFNN02 were to be compared.

No residues of HCH were detected in water samples. Therefore, the concentrations of HCH isomers in three spiked water samples determined by the two different methods were statistically compared. It can be seen from the results summarized in Table 6 that good precision is obtained in all samples ($\leq$4.52% RSD). The accuracy, on the other hand, is good (i.e., the results are not significantly different ($p > 0.05$)) for the concentrations at all levels obtained by the means of RBFNN02 and OLS.

The results indicated that RBFNN can adequately model the nonlinear calibration curve in a wide range of concentration, thus extending the working calibration range without loss of either accuracy or precision. For the specific case of HCH isomers, four working calibration ranges of 0.2–20 ng/ml, 0.6–60 ng/ml, 0.4–20 ng/ml and 0.08–20 ng/ml have been extended to those of 0.2–1000 ng/ml, 0.6–1000 ng/ml, 0.4–1000 ng/ml and 0.08–1000 ng/ml, respectively. Meanwhile, the high sensitivity in linear portion of the calibration curves was still preserved. Determination of HCH at both low (linear portion) and relatively high (nonlinear portion) concentrations can be accomplished with only one RBFNN model. This is unlike to some approaches which involve extra specimen manipulations (such as dilution) or decrease of the sensitivity of analytical measurements, thus allowing only the determination of HCH at high concentrations.

4. Conclusions

A RBFNN method was developed for the first time to model each calibration curve of four HCH isomers in GC–ECD. The working calibration ranges of the four analytes had been successfully extended from 0.08–60 ng/ml to 0.08–1000 ng/ml, without sacrificing accuracy and precision. Contrary to some instrumental and analytical methods hitherto developed, the RBFNN approach can be easily developed, allows less specimen manipulations (such as dilution) and retains the high sensitivity of the measurements at the linear portion of the calibration curve. This will be more valuable and practical especially in the multi-component or multi-sample simultaneous analyses where analytes concentrations may cover very wide concentration ranges. Another characteristic of RBFNN method is robustness, that is, it is able to predict the exact concentration in various samples, disregarding dispersion intrinsic to the input variable [3]. What is more, no *a priori* knowledge of the problem is required modeling by RBFNN method ("soft" modeling), as is different to the conventional mathematical methods.

Modeling the calibration curve by RBFNN represents a promising alternative to traditional modeling methods in calibration analysis. Although the working calibration ranges and actual values of RBFNN parameters may be specific for the HCH isomers and the ECD used in this study, we believe the present modeling method to be also applicable to other analytes and systems.

Acknowledgement

This work was funded by the self-determination project of State Key Laboratory of Agricultural Microbiology of Huazhong Agricultural University.

References

[1] E.S. Chen, E.C. Chen, J. Chromatogr. A 952 (2002) 173.
[2] A. Uyanık, J. Chromatogr. B: Biomed. Appl. 693 (1997) 1.
[3] E.A. Hernandez-Caraballo, F. Rivas, R.M.A. de Hernandez, Anal. Bioanal. Chem. 381 (2005) 788.
[4] N.J. Miller-Ihli, T.C. O'Haver, J.M. Harnly, Spectrochim. Acta Part B 39B (1984) 1603.
[5] J. Simon, K. Richard, U.S. Patent 5,479,022, 1995.
[6] M.S. Klee, M.D. Williams, I. Chang, J. Murphy, J. High Resolut. Chromatogr. 22 (1999) 24.
[7] K. Booij, M.T.J. Hillebrand, E.M.v. Weerlee, Analyst 123 (1998) 415.
[8] E. Storr-Hansen, J. Chromatogr. 558 (1991) 375.
[9] W.E. Wentworth, E. Chen, J.E. Lovelock, J. Phys. Chem. 70 (1966) 445.
[10] S. Schaal, in: H. Ritter, O. Holland, B. Möhl (Eds.), Prerational Intelligence in Strategies, High-Level Processes and Collective Behavior, Kluwer Academic Press, 1999, p. 595.
[11] M. Jalali-Heravi, Methods Mol. Biol. 458 (2008) 81.
[12] H.M. Cartwright, Methods Mol. Biol. 458 (2008) 1.
[13] M. Hasani, F. Emami, Talanta 75 (2008) 116.
[14] A.T.K. Tran, R.V. Hyne, F. Pablo, W.R. Day, P. Doble, Talanta 71 (2007) 1268.
[15] M. Kompany-Zareh, H. Tavallali, M. Sajjadi, Anal. Chim. Acta 469 (2002) 303.
[16] A. Afkhami, M. Abbasi-Tarighat, M. Bahram, Talanta 75 (2008) 91.
[17] S. Sremac, A. Popovic, Z. Todorovic, D. Cokesa, A. Onjia, Talanta 76 (2008) 66.
[18] M.H. Fatemi, J. Chromatogr. A 955 (2002) 273.
[19] C.Y. Fu, L.I. Petrich, P.F. Daley, A.K. Burnham, Anal. Chem. 77 (2005) 4051.
[20] A. Gutes, F. Cespedes, R. Cartas, S. Alegret, M. del Valle, J.M. Gutierrez, R. Munoz, Chemom. Intell. Lab. Syst. 83 (2006) 169.
[21] T. Khayamian, A.A. Ensafi, A. Benvidi, Talanta 69 (2006) 1176.
[22] M.N. Taib, R. Andres, R. Narayanaswamy, Anal. Chim. Acta 330 (1996) 31.
[23] R.M. Balabin, R.Z. Safieva, E.I. Lomakina, Chemom. Intell. Lab. Syst. 88 (2007) 183.
[24] R.M. Balabin, R.Z. Safieva, E.I. Lomakina, Chemom. Intell. Lab. Syst. 93 (2008) 58.
[25] M. Jalali-Heravi, Z. Garkani-Nejad, J. Chromatogr. A 950 (2002) 183.
[26] H.F. Chen, Anal. Chim. Acta 609 (2008) 24.
[27] F. Luan, H.T. Liu, Y.Y. Wen, X.Y. Zhang, Anal. Chim. Acta 612 (2008) 126.
[28] F. Luan, H.T. Liu, Y.Y. Wen, X.Y. Zhang, Analyst 133 (2008) 881.
[29] D. Kruzlicova, J. Mocak, B. Balla, J. Petka, M. Farkova, J. Havel, Food Chem. 112 (2009) 1046.
[30] P. Esseiva, F. Anglada, L. Dujourdy, F. Taroni, P. Margot, E. Du Pasquier, M. Dawson, C. Roux, P. Doble, Talanta 67 (2005) 360.
[31] R. Lleti, L.A. Sarabia, M.C. Ortiz, R. Todeschini, M.P. Colombini, Analyst 128 (2003) 281.
[32] C.-L. Chang, M.-Y. Hsu, Expert Syst. Appl. 36 (2009) 10663.
[33] E.A. Hernandez-Caraballo, R.M. Avila-Gomez, F. Rivas, M. Burguera, J.L. Burguera, Talanta 63 (2004) 425.
[34] M. Porta, E. Puigdomenech, F. Ballester, J. Selva, N. Ribas-Fito, S. Llop, T. Lopez, Environ. Int. 34 (2008) 546.
[35] J.L. Junior, N. Re-Poppi, Talanta 72 (2007) 1833.
[36] O.S. Fatoki, R.O. Awofolu, J. Chromatogr. A 983 (2003) 225.
[37] J. Gao, L. Liu, X. Liu, J. Lu, H. Zhou, S. Huang, Z. Wang, P.A. Spear, Environ. Int. 34 (2008) 1097.
[38] S.K. Sarkar, B.D. Bhattacharya, A. Bhattacharya, M. Chatterjee, A. Alam, K.K. Satpathy, M.P. Jonathan, Environ. Int. 34 (2008) 1062.
[39] United States Environmental Protection Agency, Separatory funnel liquid–liquid extraction (US EPA Method 3510C Revision 3), 1996.

[40] J.N. Miller, Analyst 116 (1991) 3.
[41] S. Gosav, M. Praisler, D.O. Dorohoi, G. Popa, Talanta 70 (2006) 922.
[42] B.J. Wythoff, Chemom. Intell. Lab. Syst. 18 (1993) 115.
[43] S. Chen, C.N. Cowan, P.M. Grant, IEEE Trans. Neural Netw. 2 (1991) 302.
[44] D.F. Specht, IEEE Trans. Neural Netw. 2 (1991) 568.
[45] S. Haykin, Neural Networks: A Comprehensive Foundation, Prentice Hall, Englewood Cliffs, NJ, 1994.
[46] A.D. McNaught, A. Wilkinson, IUPAC Compendium of Chemical Terminology, second ed., Blackwell Scientific Publications, Oxford, UK, 1997.

Talanta 79 (2009) 877–886

Contents lists available at ScienceDirect

Talanta

journal homepage: www.elsevier.com/locate/talanta

Factors affecting the reactivity of thiol-functionalized mesoporous silica adsorbents toward mercury(II)

Cyril Delacôte[a,b], Fabrice O.M. Gaslain[c], Bénédicte Lebeau[c], Alain Walcarius[a,*]

[a] Laboratoire de Chimie Physique et Microbiologie pour l'Environnement, UMR 7564, CNRS – Nancy-Université, 405 rue de Vandoeuvre, F-54600 Villers-les-Nancy, France
[b] Chimie Et Interdisciplinarité: Synthèse, Analyse, Modélisation, UMR 6230, CNRS – Université de Nantes, 2 rue de la Houssinière, BP 92208, F-44322 Nantes Cedex 3, France
[c] Equipe Matériaux à Porosité Contrôlée, Institut de Science des Matériaux de Mulhouse, LRC 7228, CNRS-UHA-ENSCMu, 3 rue Alfred Werner, F-68093 Mulhouse, France

ARTICLE INFO

Article history:
Received 9 March 2009
Received in revised form 6 May 2009
Accepted 13 May 2009
Available online 22 May 2009

Keywords:
Mercury(II) adsorbent
Thiol
Mesoporous silica
MCM-41
MCM-48
Speciation
Diffusion kinetics

ABSTRACT

Numerous mercaptopropyl-functionalized silica spheres have been prepared by either post-synthesis grafting of MCM-41 and MCM-48 or self-assembly co-condensation of mercaptopropyltrimethoxysilane (MPTMS) or mercaptopropyltriethoxysilane (MPTES) and tetraethoxysilane (TEOS) precursors in hydroalcoholic medium in the presence of a cationic surfactant as templating agent and ammonia as catalyst. These materials of approximately the same particle size and morphology featured different functionalization levels, various degrees of structural order, and variable distribution of thiol groups in the mesopores. Their reactivity in solution has been studied using Hg(II) as model analyte. Total accessibility (on a 1:1 S:Hg stoichiometry basis) was demonstrated and quantified for well-ordered materials whereas less open and less organized structures with high degrees of functionalization were subject to less-than-complete loadings. Capacities measured at pH 2 were lower than at pH 4 because of distinct mercury-binding mechanisms. Kinetics associated to the uptake process were studied by *in situ* electrochemical monitoring of Hg(II) consumption from aqueous suspensions containing the various adsorbents. They indicate only little difference between materials of the MCM-41 and MCM-48 series at similar functionalization levels, fast mass transport in well-ordered mesostructures in comparison to the poorly or non-ordered ones (except at pH 2 where charge formation induced some restriction in materials characterized by long-range structural order), and even faster processes in the wormlike frameworks (characterized by shorter range structural order). Hg(II) binding to thiol-functionalized materials obtained by post-synthesis grafting was found to occur more rapidly in the early beginning of the uptake process as a result of a higher concentration of binding sites at the pore entrance in comparison to the more homogeneous distribution of these groups in the mesochannels of materials obtained by co-condensation.

1. Introduction

Ordered mesoporous silicas have been discovered in the 1990s by Kresge *et al.* [1,2]. These materials are typically obtained in the presence of surfactant as structure-directing agent and they are characterized by high specific surface areas (700–1500 $m^2\,g^{-1}$), by uniform and controlled pore sizes and by long-range order. Functionalization with mercaptopropyl groups can be achieved by covalent grafting of mercaptopropylsilyl groups to the framework pore walls [3–9] or in one step by template self-assembly co-condensation of mercaptopropyl-containing organosilane and tetraalkoxysilane precursors [10–15]. Various mesostructure types have been obtained by this direct route, including MCM-41 [14–16], MCM-48 [16], SBA-15 [17–19], SBA-16 and KIT-6 [20], HMS [21], MSU [11,13], SBA-1 [22,23]. Such functionalized materials have been widely studied with respect to mercury(II) binding and some advantages over non-templated homologues have been reported: (1) better accessibility to binding sites due to open framework and regular structure [4,9,10,24]; (2) high adsorption capacities because of large surface areas and numerous functional groups [3,4,15,19]; (3) better selectivity for Hg(II) (with respect to other metal species) [10,12]; (4) faster adsorption rates [7,9,12,13,15]. Great capacities and good selectivity are attractive for environmental remediation purposes [25,26] while fast diffusional kinetics is of paramount importance for applications in electroanalytical chemistry [27] (e.g., development of mercury sensors based on analyte preconcentration prior to voltammetric detection [28–30]).

In spite of these results, rationalization of the main parameters affecting the accessibility and rates of access of target probes to the active centers remains somewhat difficult as investigations were usually made on materials exhibiting distinct composition, structure, particle size and morphology, porosity, and the conditions applied to perform adsorption experiments were also variable.

* Corresponding author.
E-mail address: alain.walcarius@lcpme.cnrs-nancy.fr (A. Walcarius).

0039-9140/$ – see front matter © 2009 Elsevier B.V. All rights reserved.
doi:10.1016/j.talanta.2009.05.020

One already knows that the degree of structural order in the adsorbent, its pore size, the density of organo-functional groups, as well as the particle size can have a significant influence on the recognition properties of the hybrid material (capacity, apparent diffusion coefficients [9,11,13,15]). Mercury(II) coordination to thiol-functionalized mesoporous silica was also largely studied [3,24,31,32] and it was notably shown that varying pH (and therefore Hg(II) speciation in solution) led to the formation of positively charged or neutral complexes on the mesopore walls (Eqs. (1) and (2) [24]).

$$\equiv Si{-}C_3H_6{-}SH + Hg^{2+}, 2NO_3^- \rightarrow \equiv Si{-}C_3H_6{-}S{-}Hg^+, NO_3^- + HNO_3 \quad (1)$$

$$\equiv Si{-}C_3H_6{-}SH + Hg(OH)_2 \rightarrow \equiv Si{-}C_3H_6{-}S{-}HgOH + H_2O \quad (2)$$

The −S−HgOH complex has been evidenced by EXAFS and XANES [31] and −S−Hg^+, NO_3^- by CE (NO_3^- detection) [24]. Such distinction between neutral and charged complexes might be of great importance as enhanced resistance to mass transfer of ions into channels containing charged moieties on their mesopore walls has been reported as a consequence of electrostatic shielding [9,24,33].

In this work, we have thus characterized the accessibility and rates of access to the active centers in a wide range of hybrid materials exhibiting the same particle morphology (spheres of approximately the same diameter) and comparable pore sizes but prepared in such a way to get materials with different pore structure (hexagonal, cubic or wormlike), various functionalization levels (up to 5.8 mmol g^{-1}) and distinct distribution organo-functional groups (grafted *versus* co-condensed solids). Mercury(II) binding to mercaptopropyl-functionalized silica samples has been chosen as a model system likely to point out the effect of these parameters on the reactivity of the materials. Experiments will be performed at pH 2 and 4 in order to distinguish the cases where a charged complex is formed inside the porous structures to those involving only neutral species. The wide range of physico-chemical characteristics of materials prepared on the basis of a unique synthetic approach is expected to enable defining the key parameters likely to affect the performance of functionalized mesoporous silica with respect to possible applications in analytical chemistry (high capacity adsorbent) or in electrochemistry (fast diffusion rates ensuring high sensitivity).

2. Experimental

2.1. Chemicals and reagents

All reagents were analytical grade and used as received from the suppliers. The following chemicals were used for preparation of adsorbent samples: tetraethoxysilane (TEOS, >98%, Aldrich), mercaptopropyltrimethoxysilane (MPTMS, 95%, Lancaster), mercaptopropyltriethoxysilane (MPTES, 95%, Lancaster), cetyltrimethylammonium bromide (CTAB, 98%, Fluka), ammonia (33% aqueous solution, Riedel de Haën), ethanol (95%, Riedel de Haën), hydrochloric acid (HCl, 37%, Riedel de Haën) and toluene (99%, Merck). A mercury(II) stock solution 0.10 M (in 0.1 M HNO_3) was prepared by dissolving the corresponding nitrate salt ($Hg(NO_3)_2$, Prolabo) in nitric acid solution (diluted from HNO_3, 68%, Prolabo). Solutions were daily prepared by diluting the stock solution and their concentration was checked using a certified standard solution (Hg^{2+} 1.001 ± 0.002 g L^{-1} in HNO_3 3 M, Merck). Partial neutralization of these acidic solutions was made by adding NaOH (Prolabo) and final pH values were measured using the Metrohm 691 pH meter (combined glass electrode no. 6.0222.100). No buffer was used for adsorption experiments to avoid any eventual complexation of mercury by one of the buffer components. For electrochemical determination of mercury(II) concentration in solution on gold electrode (see Section 2.4), the electrolyte solution was made of 1.2×10^{-4} M EDTA (ethylenediaminetetraacetate, disodium form, 99%, from Prolabo), 7.2×10^{-4} M NaCl (Prolabo), and 2.8×10^{-2} M $HClO_4$ (70%, Prolabo). High purity water (18 MΩ cm) obtained from a Millipore Milli-Q water purification system was used for all experiments.

2.2. Mesoporous materials preparation

Mesoporous silica materials have been prepared according to a previously published procedure implying polycondensation of alkoxysilane reagents in hydroalcoholic medium in the presence of CTAB as template and ammonia as catalyst, which is known to provide spherical particles with MCM-41 or MCM-48 architecture depending on the sol composition [14,34,35]. Two synthetic routes were then followed to get functionalized materials: (1) the co-condensation reaction of TEOS and MPTMS or MPTES in conditions as above [14–16] and (2) the post-synthesis grafting of MCM-41 and MCM-48 samples with MPTMS [3,9].

2.2.1. Preparation of mesoporous silica and thiol-functionalized hybrid materials by self-assembly (co-)condensation

Typical molar composition for the synthesis of MCM-41 type materials are 1:0.41:14.5:53:180 of precursor(s):CTAB: ammonia:ethanol:water [15]. The precursor(s) was(were) TEOS alone (to get unmodified MCM-41) or mixtures of MPTMS with TEOS at molar ratios varying from 0 to 50% (MPTMS/(MPTMS + TEOS)). Typically, 1.2 g of CTAB was dissolved in a mixture of 25 mL of ultra pure water, 20 mL of ethanol and 6.5 mL of ammonia solution under vigorous stirring. Then the precursor mixture with appropriate ratios of MPTMS and TEOS (total amount: 8 mmol) in 5 mL of ethanol was added. Condensation occurred within 2 min and the resulting white precipitate was stirred for 2 h. The product was then isolated by vacuum filtration on a Büchner funnel and washed alternatively with water and ethanol. The resulting powder was dried under vacuum (<10^{-2} bar) for 24 h at 60 °C. The surfactant was then removed from the hybrid material by acid/solvent extraction by suspending the solid particles in 1 M HCl in ethanol (1 g of solid powder in 100 mL of solution), which was then allowed refluxing for 24 h. Finally, solid products were recovered by filtration, washed with ethanol and dried according to the aforementioned conditions. Functionalized MCM-41 materials have been named herein as $MPS_{(HEX)}$ (mercaptopropyl-silica synthesized via a procedure which promotes an hexagonal mesoporous geometry), followed by the MPTMS ratio (*n*%) found in the starting sols: MPS_{HEX}-*n*%; MPS_{HEX}-0% was also named MCM-41.

To promote the formation of MCM-48 type architecture, a similar procedure to the above one was applied except that the amount of water was doubled compared to the quantity used for MCM-41 materials and MPTMS was replaced by MPTES [16]. Again TEOS was used alone (to get unmodified MCM-48) or mixtures of MPTES with TEOS at molar ratios varying from 0 to 50% (MPTES/(MPTES + TEOS)). The rest of the experimental procedure was the same as aforementioned. Comparatively to the precedent series, the resulting functionalized MCM-48 materials have been named herein as $MPS_{(CUB)}$ (mercaptopropyl-silica synthesized via a procedure which promote cubic mesoporous geometry), followed by the MPTES ratio (*n*%) found in the starting sols: MPS_{CUB}-*n*%; MPS_{CUB}-0% was also named MCM-48.

2.2.2. Post-synthesis grafting of mesoporous silica materials

A second series of materials was synthesized by grafting MPTMS to the above-obtained mesoporous MCM-41 and MCM-48 silica

spheres, using a classical procedure [9,36]. Typically, 500 mg of silica was dried at 130 °C for 48 h to remove excess of adsorbed water. The sample was dispersed with ultrasonic stirring in 50 mL of toluene to which 0.9 or 2 mmol (large excess) of MPTMS was added. The mixture was heated and maintained in refluxing toluene for 24 h under argon to avoid oxidation of thiol groups into disulfide moities. The resulting product was recovered by filtration and washing with toluene. This was followed by heat treatment at 60 °C for 12 h under vaccum (<10^{-2} bar). Materials have been named MCM-41-$SH_{grafted}$, MCM-41-$SH_{grafted}$-excess, MCM-48-$SH_{grafted}$, MCM-48-$SH_{grafted}$-excess, according to their structure and amount of MPTMS used.

In addition, two samples functionalized with an excess of MPTMS have been prepared by another procedure involving the formation of a self-assembled monolayer (SAM) of the organosilane prior to its grafting. This approach is expected to give rise to a huge amount of organo-functional groups homogeneously coated onto the mesopore walls [3] whereas the "classical" grafting process may lead to hererogeneous distribution of organic moieties (i.e., preferential location at the pore entrance [21,37,38]). Briefly, a silica-MPTMS mixture (2 mmol of MPTMS and 500 mg of MCM-41 or MCM-48) was stirred in toluene at room temperature under argon for 24 h to enable the formation of a self-assembled MPTMS monolayer onto the internal surfaces of mesoporous silica. Then, the suspension was heated at reflux for an additional 24 h period to condense the adsorbed MPTMS moieties with the surface silanol groups. The resulting materials have been named MCM-41-$SH_{grafted}$-SAMMS and MCM-41-$SH_{grafted}$-SAMMS (SAMMS = Self-Assembled Monolayers on Mesoporous Supports [26]).

2.3. Instrumentation

All materials have been characterized by various physicochemical techniques in order to get the necessary information on structural, composition and porosity parameters useful to enable appropriate discussion of the analytical results. Specific surface areas and pore volumes were calculated by the BET method from nitrogen adsorption–desorption experiments performed at 77 K with a Coulter instrument (model SA 3100), in the relative pressure range from about 10^{-5} to 0.99. Pore size distributions were calculated by using the BJH (Barrett, Joyner and Halenda) approach modified by the KJS (Kruck, Jaroniec and Sayari) method from the desorption branch of isotherms measured with a Micromiretics instrument (model Tristar), in the same relative pressure range. All samples were dried at 60 °C for a minimum of 12 h under vacuum before carrying out the adsorption experiments. The level of structural order in the materials was evaluated by powder X-ray diffraction (XRD): the data were collected at room temperature using a classical powder diffractometer (X'PERT PRO, Philips), equipped with a Cu anode (Kα radiation, λ = 0.15418 nm, scanning range, 0.5–10° (2θ), step size: 0.02° per 2 s). CHNS elemental analyses were obtained from the "Service Central d'Analyse" of the CNRS at Lyon, France and the "Service Commun d'Analyse" of the University Henri Poincaré at Nancy, France. They have been carried out on final materials (i.e., after template removal for those prepared by the co-condensation route) for determining the amount of thiol groups and checking the total removal of CTAB used in the synthesis. The electrochemical experiments were carried out at room temperature in an undivided three-electrode cell using μ-Autolab potentiostat associated to the GPES electrochemical analysis system (Eco Chemie). The working electrodes were a rotating gold or glassy carbon disk electrode (model PAR 636, 4 mm diameter), the silver/silver chloride electrode (Ag/AgCl, Metrohm, no. 6.0733.100) was used as reference, while a platinum wire served as the counter electrode. Particle size distribution was measured just at the end of kinetic experiments with using a light scattering analyzer (model LA920, Horiba), based on the Mie scattering theory. Average particle sizes have been calculated on distributions expressed in number and in volume. They were usually characterized by isolated particles of narrow particle size distribution and some bigger aggregates.

2.4. Electrochemical monitoring of Hg(II) adsorption

2.4.1. Adsorption capacities: batch experiments at various pH and Hg(II) concentrations

Adsorption capacities of the materials were evaluated from batch experiments (Hg(II) solutions containing the adsorbent particles in suspension). Typically 8 mg of material was suspended in 100 mL or 250 mL of solution containing Hg(II) at a selected concentration adjusted at pH 2 or 4. After sonication and continuous stirring for 48 h, the solid particles were filtered off and the remaining metal concentrations in solution were determined by anodic stripping voltammetry (ASV) on a gold disk electrode according to a published procedure [39]. Stripping voltammograms were recorded after 30 s electrolysis at +0.3 V, by scanning potentials in the differential pulse mode up to +1.0 V. Analysis was performed after appropriate dilution of sample in electrolyte described above to fall into the linear range of the technique (5×10^{-8} to 1.2×10^{-6} M). The amounts of adsorbed species on the solid phases were easily calculated by difference with respect to the starting concentrations taking into account the solid-to-solution ratio. Capacities were measured by adjusting the initial mercury amount at 100% and 150% of the amount of thiol groups in the materials (i.e., 1:1 stoichiometry and 50% excess).

2.4.2. Kinetics experiments: in situ monitoring of Hg(II) adsorption as a function of time

Because uptake processes in mesoporous materials are known to be very fast, our group has developed an original electrochemical method to continuously monitor the solution-phase Hg(II) directly in MPS suspensions [9,15,40]. This was preferred over the more classical method involving intermittent sampling and discontinuous analyses of remaining Hg(II) in solution after solid filtration, which was used elsewhere [7,13], in order to follow mercury binding during the first seconds of the experiment. The method is based on the continuous amperometric analysis of Hg(II) species at a rotating disk electrode in conditions where steady-state currents are directly proportional to their concentration. The procedure consists in applying a constant potential of −0.5 V (*versus* SCE) to a glassy carbon rotating disk electrode (2000 rpm) until reaching a steady-state current. The starting solution contains Hg(II) at a selected concentration and pH was fixed at 2 or 4. At time $t = 0$, the adsorbent (5 mg MPS previously dispersed in a 5 mL solution at pH 2 or 4, under sonication to ensure a homogeneous distribution of particles) was added into the cell. Hg(II) consumption was monitored by recording the decrease in transient currents at the rotating electrode (two sampling points per second). At the end of the measurement, a fraction of the suspension is filtered and the remaining mercury concentration is determined by ASV on gold electrode (to check the accuracy of the continuous monitoring). A second fraction of the suspension is used for measuring the particle size distributions. The starting Hg(II) concentrations were adjusted to have an amount of mercury in the medium corresponding to the amount of accessible thiol groups in the materials (capacity values determined as above). Solution volumes were 30 mL except at pH 4 in the case of highly functionalized materials (MPS-20% to MPS-50%) for which 100 mL was necessary to avoid precipitation of mercury hydroxide (occurring at concentrations upper than 2×10^{-4} M [41]). Other calibration details and control experiments have been reported previously [40].

Table 1
Some physico-chemical characteristics of MPS samples.

Sample name	BET analysis			Particle size		XRD	$-SH_{groups}$	
	Surf. area ($m^2\,g^{-1}$)	Pore vol. ($cm^3\,g^{-1}$)	Pore size (nm)	Indiv. (μm)	Agreg. (μm)	2θ main line (°)	Calculated ($mmol\,g^{-1}$)	Measured ($mmol\,g^{-1}$)
MPS_{HEX}-3%	1368	0.89	2.91	0.51	3.0	2.51	0.5	0.4
MPS_{HEX}-6%	1538	0.84	2.80	0.39	2.9	2.64	0.9	0.8
MPS_{HEX}-9%	1713	0.75	2.69	0.45	2.9	2.69	1.4	1.3
MPS_{HEX}-12%	1615	0.72	2.66	0.39	3.9	2.77	1.8	1.6
MPS_{HEX}-15%	1465	0.66	2.69	0.39	4.6	2.81	2.2	1.9
MPS_{HEX}-20%	1162	0.56	2.74	0.39	5.5	2.91	2.8	2.5
MPS_{HEX}-25%	843	0.43	2.87	0.30	6.5	3.00	3.3	3.2
MPS_{HEX}-30%	760	0.39	n/m	0.34	7.6	3.13	3.8	3.8
MPS_{HEX}-40%	546	0.28	n/m	0.26	12.6	3.26	4.7	4.7
MPS_{HEX}-50%	353	0.18	n/m	<0.26	12.7	3.43	5.5	5.8
MPS_{CUB}-3%	1193	0.83	3.04	0.39	3.1	2.61	0.5	0.4
MPS_{CUB}-6%	1079	0.73	2.99	0.39	2.1	2.59	0.9	0.8
MPS_{CUB}-9%	966	0.58	2.90	0.39	3.6	2.58	1.4	1.3
MPS_{CUB}-12%	946	0.52	2.82	0.39	4.6	2.59	1.8	1.8
MPS_{CUB}-15%	860	0.47	2.81	0.34	5.3	2.59	2.2	2.1
MPS_{CUB}-20%	691	0.37	2.85	0.34	5.8	2.61	2.8	2.5
MPS_{CUB}-25%	607	0.32	2.76	0.34	5.6	n/m	3.3	2.9
MPS_{CUB}-30%	584	0.30	n/m	5.12	9.8	n/m	3.8	3.6
MPS_{CUB}-40%	488	0.25	n/m	7.70	10.6	n/m	4.7	4.7
MPS_{CUB}-50%	322	0.17	n/m	10.10	12.3	n/m	5.5	5.5
MCM-41	884	0.68	3.14	–	–	2.39	–	–
MCM-41-$SH_{grafted}$-1.8	867	0.59	2.91	0.45	2.7	2.39	(1.8)	0.9
MCM-41-$SH_{grafted}$-excess	809	0.52	2.89	0.48	2.7	2.39	(4)	1.2
MCM-41-$SH_{grafted}$-SAMMS	848	0.56	2.92	0.51	2.6	2.39	(4)	1.4
MCM-48	986	0.80	3.19	–	–	2.51	–	–
MCM-48-$SH_{grafted}$-1.8	973	0.66	2.93	0.51	1.2	2.51	(1.8)	0.9
MCM-48-$SH_{grafted}$-excess	911	0.63	2.96	0.51	1.2	2.51	(4)	1.4
MCM-48-$SH_{grafted}$-SAMMS	995	0.61	2.84	0.51	1.1	2.51	(4)	2.0

n/m: non-measurable; calculated–SH_{groups} represent the maximal amounts of thiol groups that are likely to be present on the materials on the basis of the organosilane contents in the synthesis media.

3. Results and discussion

Even if this paper is primarily devoted to the analytical examination of the main parameters affecting the adsorption properties of thiol-functionalized materials towards Hg(II) species, it is important to describe beforehand the physico-chemical characteristics of the large series of adsorbents used in this work. This will help drawing conclusions from accessibility and kinetic measurements.

3.1. Adsorbent characterization

A detailed characterization of mercaptopropylsilyl-functionalized mesoporous silica spheres (MPS) prepared through the direct assembly pathway can be found in our previous paper [16]. The synthesis conditions have been adjusted to generate either hexagonal (MPS_{HEX}) or cubic (MPS_{CUB}) mesostructures and MPTMS/TEOS or MPTES/TEOS ratios were varied in order to get materials with a wide range of functionalization levels (MPS_{HEX}-*n*% or MPS_{CUB}-*n*%). Fig. 1 illustrates some XRD patterns obtained for these two series of materials. Part A of the figure shows that MPS_{HEX}-*n*% (with $n<15$) samples were indeed characterized by a hexagonal mesostructure of MCM-41 type, as evidenced by a main reflection at 2θ angles between 2.5° and 3.5° and the presence of two weaker reflections at higher 2θ values. These lines correspond respectively to diffraction plans that could be indexed as (1 0 0), (1 1 0), and (2 0 0) in a *P6mm* hexagonal symmetry. The shift of the main line to higher 2θ angles reveals some lattice contraction upon increasing the functionalization level. Rising further the MPTMS content in the reaction mixture (more than 20%) resulted a single peak at low angle, which broadened as functionalization level increased. This is attributed to a continuous decrease of long-range structural order and to the formation of mesoporous wormhole framework structures (short-range order). The MPS_{CUB}-*n*% series was characterized by totally different patterns (Fig. 1B). Materials synthesized with low thiol contents (up to MPS_{CUB}-15%) showed reflection peaks indexed as (2 1 1), (2 2 0), (3 2 1), (4 0 0), (4 2 0), (3 3 2), (4 2 2) and (4 3 1), which are characteristic of *Ia3d* cubic mesostructure. This time, however, increasing further the MPTES content in the synthesis medium caused a rapid loss of XRD signals, indicating that MPS_{CUB}-20% was poorly organized and MPS_{CUB}-25–50% not at all. Other physico-chemical characteristics of MPS_{HEX} and MPS_{CUB} materials are given in Table 1. As expected from the place occupied by the organo-functional groups, the pore volume of these solids was found to continuously decrease when rising up the functionalization level. On the other hand, the mesopore size was kept rather high (i.e., 2.7–2.9 nm) independently on the mesostructure type (hexagonal, wormlike, cubic), indicating the successful templating role played by CTAB surfactant. All materials were made of spherical particles (shown from electron microscopy [16]) of approximately the same size (~350–400 nm), which had however the tendency to agglomerate (~3–12 μm), especially at high thiol content because of increased hydrophobicity. Table 1 also reports the amounts of mercaptopropyl groups in the final solids, indicating effective and almost quantitative functionalization as measured values were very close to those calculated from MPTMS/TEOS or MPTES/TEOS ratios in the starting sol. These data have been completed by ^{29}Si solid-state NMR measurements (see some illustrative results in Table 2) to confirm that mercaptopropyl groups have been readily incorporated into the materials via covalent bonding and not simply physi-sorbed or impregnated in the solids. Good agreement between results of elemental analysis and NMR evaluation of thiol group contents was indeed observed.

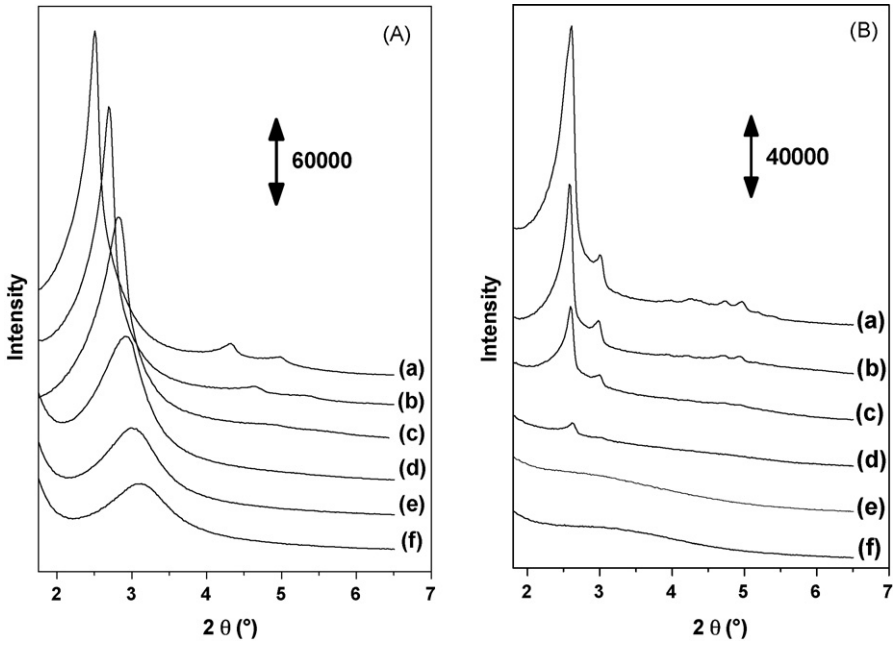

Fig. 1. XRD patterns of some MPS samples (both HEX and CUB series). (A) MPS_{HEX}-*n*% series: (a) *n* = 3, (b) *n* = 9, (c) *n* = 15, (d) *n* = 20, (e) *n* = 25, (f) *n* = 30; (B) MPS_{CUB}-*n*% series: (a) *n* = 3, (b) *n* = 9, (c) *n* = 15, (d) *n* = 20, (e) *n* = 25, (f) *n* = 30.

A series of grafted materials was also prepared for comparison purposes. To this end, MCM-41 and MCM-48 prepared as above (but without MPTMS or MPTES) and thus exhibiting approximately the same particle size and morphology and pore size (yet a little bit larger because of the absence of organo-functional moieties), have been grafted with mercaptopropyl groups. This has been made by both a "classical" grafting procedure using distinct amounts of MPTMS (to get materials with different thiol contents) and by a particular approach (SAMMS) ensuring homogeneous distribution of organic moieties onto the mesopore walls [3] whereas the "classical" one often leads to preferential location of these groups at the pore entrance [21,37,38]. The second approach (SAMMS) is thus expected to provide materials resembling more to those obtained by co-condensation. Table 1 gives the main characteristics of grafted materials, showing notably a small decrease in porosity upon grafting and maximal organic group contents that were much lower than functionalization levels obtained by the direct synthesis pathway.

A wide range of materials with same morphology and comparable porosity, 2 distinct mesostructure types, as prepared according to 2 different ways (post-synthesis grafting or co-condensation), and containing variable amounts of ligand, is thus available. These adsorbents can now be used for Hg(II) uptake in a fully comparative approach to point out the main parameters likely to affect their reactivity in terms of accessibility to the binding sites and mass transfer rates, which constitute two main parameters influencing the analytical and electrochemical applications of such organic–inorganic hybrids [27].

3.2. Hg(II) uptake capacities: accessibility to the binding sites and effect of pH

Uptake capacity of a material likely to adsorb target species by complexation is controlled by both the strength of the complex (how the equilibrium is shifted to the right) and the accessibility to the binding sites. In the present case, the first point if fully fulfilled due to the very high stability of thiol–mercury(II) complexes whereas the second one (accessibility) is likely to be influenced by pH [24] and by the degree of organization of the mesoporous adsorbent [15]. Hg(II) uptake by MPS materials was thus studied at two pH values (2 and 4, where positively charged and neutral complexes are respectively formed, see Eqs. ((1) and (2)) and at distinct Hg(II)/thiol ratios (equimolar and 1.5 excess Hg(II) over the thiol groups content in the material).

Fig. 2 illustrates the results obtained from the series of adsorbents prepared by co-condensation. Several conclusions can be drawn from these data.

First, the amount of immobilized Hg(II) species was always lower at pH 2 (where Hg(II) is in the form of Hg^{2+}) than at pH

Table 2
^{1}H decoupled ^{29}Si MAS NMR data for selected MPS_{HEX}-*n*% and MPS_{CUB}-*n*% materials: corresponding relative peak areas obtained by curve deconvolution and amounts of mercaptopropyl groups calculated from T^n/Q^n ratios (error for $\%Q^n$ and $\%T^n$ values is about 5%).

Sample	Q^4	Q^3	Q^2	T^3	T^2	Q^n	T^n	T^n/Q^n	Grafted SH groups (mmol g^{-1})
MPS_{HEX}-9%	0.52	0.40		0.08		0.92	0.08	0.09	1.2
MPS_{HEX}-12%	0.54	0.35		0.12		0.88	0.12	0.14	1.8
MPS_{HEX}-30%	0.47	0.26		0.23	0.05	0.72	0.28	0.39	3.6
MPS_{HEX}-50%	0.36	0.18		0.42	0.04	0.53	0.47	0.89	5.3
MPS_{CUB}-9%	0.46	0.40	0.05	0.06	0.03	0.92	0.08	0.09	1.4
MPS_{CUB}-12%	0.48	0.35	0.04	0.11	0.02	0.87	0.13	0.15	1.9
MPS_{CUB}-30%	0.38	0.29		0.16	0.17	0.67	0.33	0.49	4.0
MPS_{CUB}-50%	0.42	0.15		0.42		0.58	0.42	0.73	4.9

Q^n and T^n are resonances observed for the siloxane [Q^n = Si–$(OSi)_n$–$(OH)_{4-n}$, *n* = 2–4; Q^4 at −110 ppm, Q^3 at −101 ppm and Q^2 at −91 ppm] and organosiloxane [T^m = RSi–$(OSi)_m$–$(OH)_{3-m}$, *m* = 1–3; T^3 at −65 ppm, T^2 at −56 ppm] centers.

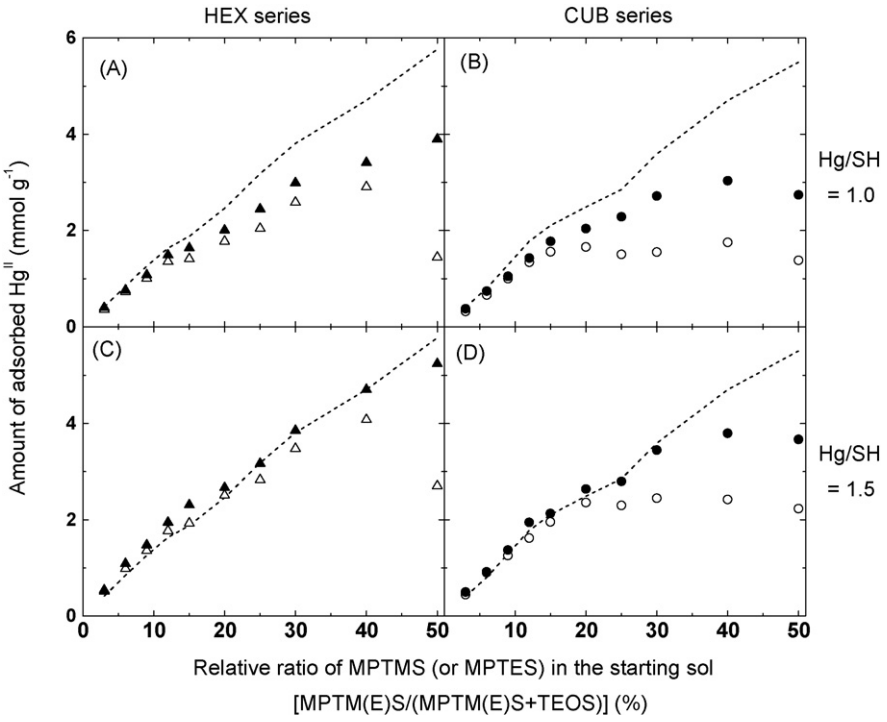

Fig. 2. Variation of Hg(II) uptake by MPS materials, as a function of the relative molar ratio of MPTMS (or MPTES) in the starting sol at pH 2 (open symbols △ and ○) and pH 4 (solid symbols ▲ and ●). (A and C) MPS_{HEX}-*n*% materials (△ and ▲); (B and D) MPS_{CUB}-*n*% materials (○ and ●). Data have been obtained for 2 different ratios between the initial mercury amount in solution and thiol groups content in the adsorbent: Hg/SH = 1.0 (A and B) and Hg/SH = 1.5 (C and D); the dotted lines represent the thiol contents in the various materials.

4 (where Hg(II) is in the form of $Hg(OH)_2$) and differences were more marked with poorly ordered and non-organized materials (see, e.g., MPS_{CUB}-25–50% on Fig. 2 B and D). This is due to the formation of positively charged complexes inducing repulsive electrostatic effects against Hg^{2+} attempting to reach the remaining thiol groups located deeply in the material. This effect might be dramatic in some cases as nearly 50% decreases were observed for MPS_{Hex}-50%, MPS_{CUB}-40% and MPS_{CUB}-50%. Even more impres-

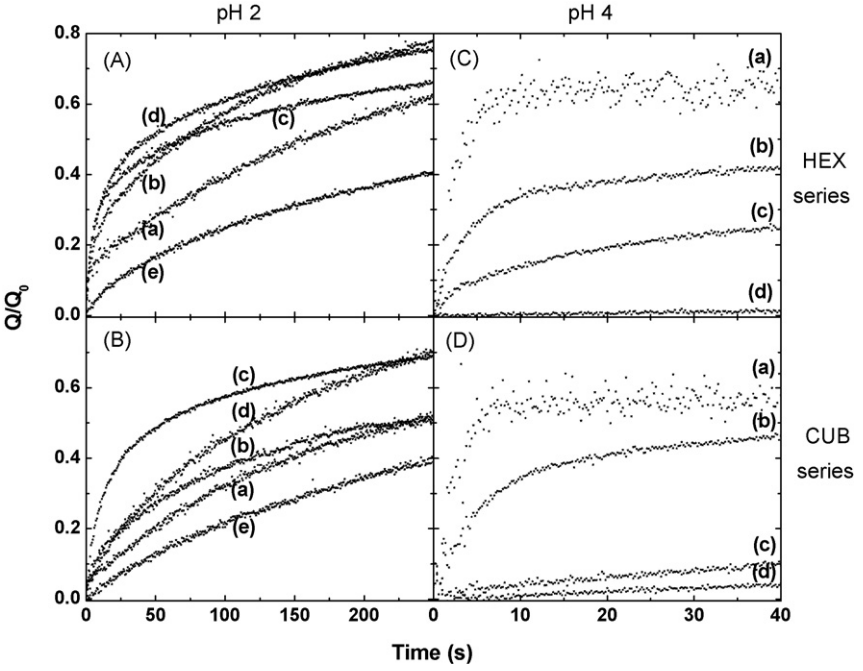

Fig. 3. Variation of Hg(II) uptake by MPS materials as a function of time. Immobilized Hg(II) is expressed as Q/Q_0 values where Q is the amount of Hg(II) consumed by the material at time t, and Q_0 is the maximum amount of Hg(II) likely to be bound to the adsorbent at equilibrium. Uptake experiments have been carried out at pH 2 (A and B) and at pH 4 (C and D). Both MPS_{HEX}-*n*% and MPS_{CUB}-*n*% materials have been used and data presented here correspond to various functionalization levels (various *n*% values):
[A] MPS_{HEX}-3% (a); −6% (b); −12% (c); −20% (d); −40% (e).
[B] MPS_{CUB}-3% (a); −6% (b); −12% (c); −20% (d); −40% (e).
[C] MPS_{HEX}-3% (a); −15% (b); −30% (c); −50% (d).
[D] MPS_{CUB}-3% (a); −15% (b); −30% (c); −50% (d).

sive is the fact that decrease in capacity for Hg(II) can be observed when increasing the amount of mercaptopropyl groups in the adsorbent, which could be explained by lower porosity (Table 1). Thus, materials should be engineered depending on the application and not simply by considering that larger capacity would be straightforward with materials bearing larger amounts of thiol groups.

Secondly, even if trends were similar, excess of Hg(II) in solution with respect to the amount of thiol groups in the material was necessary to get the maximal capacity values (1.5 excess Hg(II) over thiol groups was enough; increasing further this ratio did not result in significant change in the data). On the basis of 1:1 complex stoichiometry [3], data in Fig. 2 demonstrate that total accessibility to binding sites can be achieved in mesostructured materials independently on the structure type (hexagonal, cubic, wormlike) while less-than-complete binding was observed with non-ordered solids (i.e., MPS_{CUB}-30–50%). This confirms the advantage belonging to ordered mesoporous materials in terms of enhanced binding capacities with respect to non-organized adsorbents [4,9,10,15]. The maximal capacity values at pH 4 were 5.2 mmol g^{-1} (4.1 mmol g^{-1} at pH 2) and 3.8 mmol g^{-1} (2.4 mmol g^{-1} at pH 2), respectively in MPS_{HEX} and MPS_{CUB} series, the difference being explained by a mesostructural order maintained up to higher thiol group contents in MPS_{HEX} than in MPS_{CUB} materials. These values are the highest ever reported for Hg(II) adsorption: they correspond to 1.04 g Hg(II) per g of MPS_{HEX}-50% and to 0.76 g Hg(II) per g of MPS_{CUB}-40% at pH 4, being very promising for remediation purposes. By comparison, highest values previously reported were 2.5 mmol g^{-1} for thiol-functionalized monolayers on mesoporous silica [3], 3.8 mmol g^{-1} for thiol-functionalized mesoporous silica of MCM-41 type [15] or 4.1 mmol g^{-1} for thiol-functionalized mesoporous silica of SBA-15 type [19]. Strictly speaking, comparison to well-ordered mesostructures is not meaningful as MPS_{HEX}-50% and MPS_{CUB}-40% are poorly organized but these materials have been prepared by the surfactant template route so that sufficient porosity has been created to ensure good accessibility to the binding sites, and thereby high capacity, as in well-structured mesoporous materials.

Thirdly, the amount of immobilized Hg(II) species can be even higher than the thiol groups content in the material, especially in well-ordered hexagonal or cubic mesostructures and at pH 4 (see parts C and D in Fig. 2). This can be explained by possible interaction of $Hg(OH)_2$ with the surface silanol groups on mesoporous silica according to Eq. (3) [42], which comes in addition to complexation with thiol groups.

$$\equiv \mathrm{Si{-}OH} + \mathrm{Hg(OH)_2} \rightarrow \equiv \mathrm{Si{-}O{-}HgOH} + \mathrm{H_2O} \quad (3)$$

This contribution is however restricted because of much lower stability of ≡Si—O—HgOH in comparison to ≡Si—C_3H_6—S—HgOH [24]. Formation of Hg(II)-thiolate complexes of other stoichiometry may also contribute to explain the observed higher loadings but this is difficult to take this possibility into account here as such complexes have been reported from experiments performed at pH values where both Hg^{2+} and $Hg(OH)_2$ are likely to co-exist [32].

Hg(II) binding to grafted solids was also investigated and 100% accessibility (i.e., each thiol group chelating one Hg(II)) was always observed at pH 4, confirming that grafting organofunctional groups onto the internal surface of regular mesopore channels does not prevent them from being reached by species from the external solution. On the other hand, 20–30% less uptake was observed at pH 2 as a result of aforementioned electrostatic repulsions. The highest capacities were for thiol-functionalized monolayers on mesoporous silica (MCM-41-$SH_{grafted}$-SAMMS and MCM-48-$SH_{grafted}$-SAMMS) because they bear more thiol groups than materials grafted by the "classical" procedure (Table 1), with values of respectively 1.4 and 2.0 mmol g^{-1} at pH 4.

To conclude, surfactant-templated thiol-functionalized silica materials obtained by co-condensation (MPS) are characterized by much higher capacities for Hg(II) in comparison to those prepared by post-synthesis grafting because the direct sol–gel route enables larger ligand loadings. Adsorbents prepared in conditions leading to hexagonal mesostructures (MPS_{HEX}-*n*%) exhibit better performance than those based on cubic structures (MPS_{CUB}-*n*%) because they can be manufactured with very high thiol group contents while maintaining a good level of mesostructural order, ensuring thereby optimal accessibility to the binding sites. Decreasing pH in a region where Hg(II) binding leads to the formation of positively charged complexes in the mesopore channels (i.e., pH 2) results in significant decrease in capacity due to unfavourable electrostatic interactions.

3.3. Kinetics associated to Hg(II) uptake: effect of mesostructural order and pH

The speed of Hg(II) uptake by MPS materials has been evaluated and compared by *in situ* monitoring of Hg(II) consumption from MPS suspensions as a function of time, using a previously developed method [9,40]. Illustrative data are depicted in Fig. 3 in the form of Q/Q_0 *versus* time curves, where Q is the amount of Hg(II) consumed by the material at time t, and Q_0 is the maximum amount of Hg(II) likely to be bound to the adsorbent at equilibrium (values determined after 48 h reaction). Q/Q_0 is thus expected to vary from 0 at $t = 0$, corresponding to the moment when MPS particles have been dispersed in Hg(II) solution, to unity at the maximum (i.e., if equilibrium can be reached in the time-scale of the experiment). It can be seen from these data that the rate of Hg(II) uptake is dramatically dependent on the adsorbent type, on its functionalization level (and consequently its level of mesostructural order) and on pH. At first sight, on can notice a global trend indicating slower processes when using highly functionalized and/or poorly ordered materials, and some distinct behaviour at pH 2. These variations can be interpreted in terms of different mass transfer rates in the mesoporous solids, which have been demonstrated to be determining for Hg(II) binding to thiol-functionalized silica because the complexation reaction by itself is very fast [13,33]. More accurate description and comparison of data requires however some mathematical treatment. Diffusion in homogenous spherical particles displaying a particle size a_x is expressed by the following equation [40,43]:

$$\frac{Q}{Q_0} = \sum_{x=1}^{x=n} f_{a_x} \left[6 \left(\frac{D_{app} t}{a_x^2} \right)^{\frac{1}{2}} \left\{ \pi^{\frac{-1}{2}} + 2 \sum_{n=1}^{\infty} (-1)^n \mathrm{ierfc} \frac{n a_x}{\sqrt{D_{app} t}} \right\} - 3 \frac{D_{app} t}{a_x^2} \right] \quad (4)$$

where D_{app} is the apparent diffusion coefficient, *ierfc* the error function, f_{ax} the relative fraction of particles having the same size a_x (determined from particle size distribution analysis).

At the early beginning of the experiments ($t \rightarrow 0$), one can reasonably assume that the main contribution of the uptake process is that of the individual spheres (much more numerous than the aggregates). In such case, one can assimilate particles as a unique population characterized by a unique size (that of individual particles) and Eq. (4) can be simplified as follow:

$$\lim \left(\frac{\partial (Q/Q_0)}{\partial (\sqrt{t})} \right)_{t \rightarrow 0} = 6 \sqrt{\frac{D_{app}}{\pi a^2}} \quad (5)$$

From the slope of "Q/Q_0 versus $\sqrt{t}$" plots, it is thus easy to calculate D_{app} values by taking into account experimentally determined particle sizes of isolated particles (Table 1).

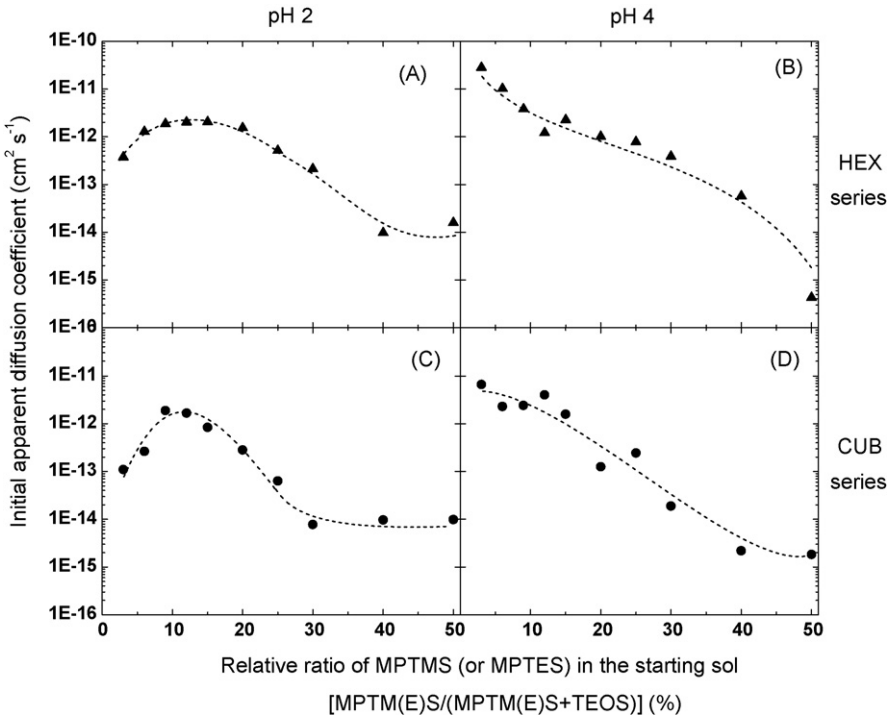

Fig. 4. Variation of the initial apparent diffusion coefficient ($D_{app,0}$) for Hg(II) in MPS spheres as a function of the relative molar ratio of MPTMS (or MPTES) in the starting sol, as evaluated from uptake experiments performed at pH 2 (A and C) and pH 4 (B and D). Parts A and B correspond to MPS_{HEX}-*n*% materials while parts C and D are related to MPS_{CUB}-*n*% series. Data were estimated from kinetic curves at the early times of the experiments when the uptake process is dominated by the smaller spherical particles (see text for calculus details).

Fig. 4 shows the variation of such apparent diffusion coefficients evaluated at time $t \rightarrow 0$ (called "initial D_{app}" or "$D_{app,0}$" values hereafter) for MPS_{HEX}-*n*% and MPS_{CUB}-*n*% series, at pH 2 and 4, as a function of the functionalization level of the materials. Let's first consider results obtained at pH 4 (parts B and D in Fig. 4). They clearly indicate faster mass transport in materials characterized by low levels of functionalization and then a progressive decrease in $D_{app,0}$ values at MPTMS contents above 30–40% (for MPS_{HEX}-*n*%) and MPTES contents above 15–20% (for MPS_{CUB}-*n*%). Such decrease can be attributed to lower pore volumes (less place for Hg(II) to diffuse) but the main parameter controlling this variation seems to be the structural order of the adsorbents as breakthrough occurred when passing from mesostructured solids to poorly ordered or non-organized materials. In fact, in the MPS_{HEX}-*n*% series (Fig. 4B), one can distinguish three categories: the highly organized hexagonal mesostructures (MPS_{HEX}-3–15%) exhibiting highest values of $D_{app,0}$, the wormlike mesostructures characterized by short-range order (MPS_{HEX}-15–40%) giving rise to intermediate $D_{app,0}$ values, and the poorly ordered MPS_{HEX}-40–50% materials leading to dramatic decrease in $D_{app,0}$ values. In the MPS_{CUB}-*n*% series (Fig. 4D), highest $D_{app,0}$ values were obtained for the highly organized cubic mesostructures (MPS_{CUB}-3–15%), which were then found to rapidly decrease as fast as the level of structural organization decreased. Comparing hexagonal with cubic mesostructures also reveals slightly faster transport in the MCM-41 family with respect to the MCM-48 one. This suggests that long mesochannels parallel to each other are more favourable to the transport of analytes in comparison to a more interconnected 3D arrangement of mesopores, in agreement with previous observations made with thiol-functionalized SBA-15 and SBA-16 materials [44]. This

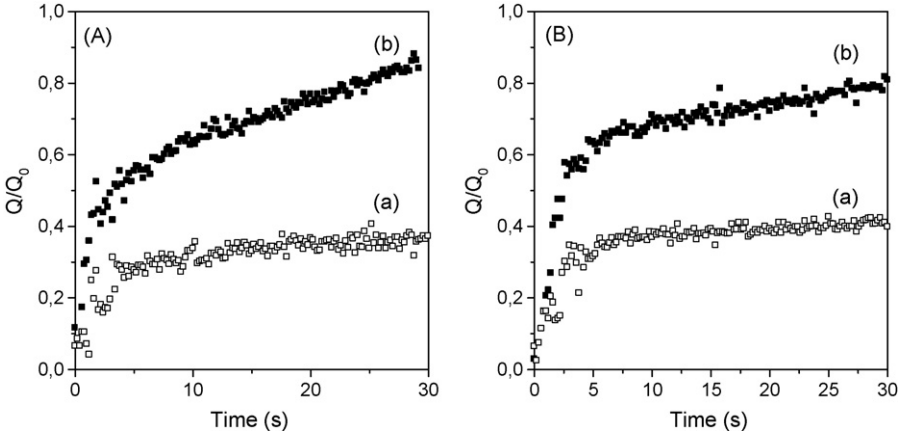

Fig. 5. Variation of Hg(II) uptake by mercaptopropyl-grafted MCM-41 (**A**) and MCM-48 (**B**) samples, as a function of time. Immobilized Hg(II) is expressed in the form of Q/Q_0 values as in Fig. 3. Uptake experiments have been carried out at pH 2 (a) and at pH 4 (b).

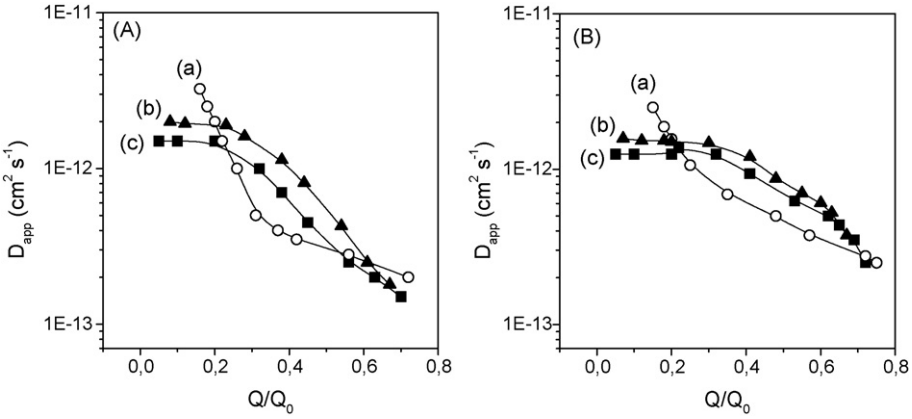

Fig. 6. Variation of the apparent diffusion coefficient (D_{app}) for Hg(II) in mercaptopropyl-grafted MCM-41 (**A**) and MCM-48 (**B**) samples, expressed as a function of the filling level (Q/Q_0). Data have been obtained from uptake experiments performed at pH 2 using adsorbents grafted by the conventional method (a) or by the SAMMS approach (b), and data obtained for MPS samples prepared by the one step co-condensation route (respectively MPS_{HEX}-9% and MPS_{CUB}-9%) have been added for comparison purposes (c).

rather unexpected trend (cubic mesophases are usually recognized to facilitate faster diffusion in comparison to the hexagonal ones [45,46]) is however borderline significant (compare parts B and D in Fig. 4) and might be explained by lower pore volumes in the cubic series than in the hexagonal one (Table 1).

The above conclusions are still valid when considering Hg(II) binding at pH 2 (see parts A and C in Fig. 4), except one overwhelming difference for highly organized mesostructures displaying long-range order (MPS-*n*% with $n \leq 15$). In these materials exhibiting a mesostructural order at very long distance, the formation of positively charged species ($\equiv Si–C_3H_6–S–Hg^+$) upon Hg^{2+} binding acts as an electrostatic barrier slowing down further ingress of the positively charged probes (Hg^{2+}) to reach binding sites, yet accessible but located deeper in the material. Optimal values have been observed for mesostructured materials exhibiting short-range order. This was already observed in the MCM-41 family [15,47] and confirmed here for the MCM-48 one. The subsequent decrease in $D_{app,0}$ values with increasing the functionalization level is due to both lack of mesostructural order and enhanced hydrophobicity, with again a breakthrough appearing at lower thiol contents in the MPS_{CUB}-*n*% series than in MPS_{HEX}-*n*%, in agreement with structural data (Fig. 1).

Grafted MCM-41 and MCM-48 samples behaved similarly with pH. This is illustrated in Fig. 5, showing much faster Hg(II) binding at pH 4 than at pH 2 for both hexagonal and cubic mesostructures. Differences were even more marked than for adsorbents prepared by co-condensation, which can be attributed to better long-range mesostructural order. Mass transfer resistance at pH 2 is again explained by the formation of positively charged moieties on the mesopore walls, consistent with results reported for Hg(II) uptake by mercaptopropyl-grafted SBA-15 and SBA-16 samples [44] and in good agreement with what was previously observed for protonation of aminopropyl-grafted mesoporous silica materials [9].

3.4. Dynamics of the process: effect of adsorbent preparation mode

Eq. (4) can be used to evaluate apparent diffusion coefficients at different stages of the uptake reaction (i.e., as a function of Q/Q_0) if one assumes that spherical diffusion dominates at any moment of the process. This assumption is not fully correct here as spherical particles have the tendency to form aggregates (Table 1). One could however consider it acceptable in first approximation, at least to compare materials between them, as interparticle diffusion in the small aggregates should be much faster than diffusional rates in the individual mesoporous particles (intraparticle diffusion). Fig. 6 illustrates typical comparative data obtained at pH 2 for adsorbents prepared by grafting (classical or SAMMS method) or by co-condensation for both hexagonal (Fig. 6A) and cubic (Fig. 6B) mesostructures. In all cases, D_{app} values were found to decrease as soon as Hg(II) loading increased as a result of less and less free place available for the ingress of additional Hg(II) species [9,15]. However, the shape of these variations was strongly dependent on the adsorbent preparation mode. Thiol-functionalized mesoporous silica samples obtained by post-synthesis grafting of MCM-41 and MCM-48 by the "classical" route (curves "a" on Fig. 6) were characterized by Hg(II) uptake rates higher than their homologues prepared by one-step co-condensation (curves "c" on Fig. 6) at the beginning of the uptake process but these rates fell down rapidly afterwards. This can be explained by the fact that post-synthesis grafting occur preferentially at mesopore entrance [21,37,38], generating thereby a greater density of organofunctional groups at the boundaries of the particles, which are more easily accessible for Hg(II) species at the beginning of the uptake process. Complexation at these binding sites located at mesopore entrance is thus expected to induce some bottleneck effect, slowing down the access rate to other binding sites located deeper in the mesoporous particle. The more homogeneous distribution of organic groups in the whole volume of materials prepared by co-condensation [21,37,38] induces much less variations in D_{app} values up to *ca.* 30% filling in MPS_{HEX} and 40% in MPS_{CUB}, the subsequent decrease in diffusion rates being attributed to the presence of more and more $\equiv Si–C_3H_6–S–Hg^+$ species formed in the mesochannels. Results obtained with grafted materials prepared according to the SAMMS method (in which organic groups are uniformly distributed as self-assembled monolayers on the whole internal surface of the material [26]) further support the above interpretation: variations of D_{app} values *versus* Q/Q_0 follow the same trend as for materials obtained by co-condensation (compare curves "b" and "c" in Fig. 6). This demonstrates the importance of the design of the mesoporous adsorbent on its properties and performance.

4. Conclusion

Functionalized mesoporous silica prepared by the surfactant template route are attractive adsorbents and the present work, yet based on a physico-chemical approach, has highlighted the main parameters likely to affect key issues for applications in the fields of analytical chemistry (remediation and sensing). This has been made on the basis of a wide range of solids of approximately the same size and shape, comparable pore sizes (i.e., same CTAB template used

for all syntheses), but distinct mesostructures, functionalization levels, and functionalization modes. Performance of these materials in analytical and electroanalytical chemistry are dependent on both their capacity (number of accessible binding sites) and mass transfer kinetics (rate of access to active centers). Capacities of thiol-functionalized mesoporous silica for Hg(II) species were higher with adsorbents prepared by co-condensation than for grafted materials due to larger amount of incorporated ligands. Hexagonal (MCM-41 type) mesostructures gave rise to higher Hg(II) loadings than the cubic ones (MCM-48 type) because the mesostructural order was maintained over wider organo-functional group contents in the MCM-41 series. Some restrictions in capacity were also observed at low pH values where thiol–Hg(II) complexes are positively charged. Diffusion rates were usually higher in well-ordered materials except when positively charged complexes were formed for which short range order was found to be optimal. Binding kinetics were also affected by ligands distribution in the material (mainly at pore entrance in grafted solids or more homogeneously dispersed in the co-condensed ones).

Acknowledgments

This work was supported by the French Ministry of Research and FOMG acknowledges financial support from the French ACI NMAC and ANR programs. We are also grateful to J.P. Emeraux for recording XRD patterns.

References

[1] C.T. Kresge, M.E. Leonowicz, W.J. Roth, J.C. Vartuli, J.S. Beck, Nature 359 (1992) 710.
[2] J.S. Beck, J.C. Vartuli, W.J. Roth, M.E. Leonowicz, C.T. Kresge, K.D. Schmitt, C.T.W. Chu, D.H. Olson, E.W. Sheppard, S.B. McCullen, J.B. Higgins, J.L. Schlenker, J. Am. Chem. Soc. 114 (1992) 10834.
[3] X. Feng, G.E. Fryxell, L.Q. Wang, A.Y. Kim, J. Liu, K.M. Kemmer, Science 276 (1997) 923.
[4] L. Mercier, T.J. Pinnavaia, Adv. Mater. 9 (1997) 500.
[5] L. Mercier, T.J. Pinnavaia, Environ. Sci. Technol. 32 (1998) 2749.
[6] X. Chen, X. Feng, J. Liu, G.E. Fryxell, M. Gong, Sep. Sci. Technol. 34 (1999) 1121.
[7] S. Mattigod, X. Feng, G.E. Fryxell, J. Liu, M. Gong, Sep. Sci. Technol. 34 (1999) 2329.
[8] A.M. Liu, K. Hidajat, S. Kawi, D.Y. Zhao, Chem. Commun. (2000) 1145.
[9] A. Walcarius, M. Etienne, B. Lebeau, Chem. Mater. 15 (2003) 2161.
[10] J. Brown, L. Mercier, T.J. Pinnavaia, Chem. Commun. (1999) 69.
[11] J. Brown, R. Richer, L. Mercier, Microporous Mesoporous Mater. 37 (2000) 41.
[12] B. Lee, Y. Kim, H. Lee, J. Yi, Microporous Mesoporous Mater. 50 (2001) 77.
[13] A. Bibby, L. Mercier, Chem. Mater. 14 (2002) 1591.
[14] M. Etienne, B. Lebeau, A. Walcarius, New J. Chem. 26 (2002) 384.
[15] A. Walcarius, C. Delacôte, Chem. Mater. 15 (2003) 4181.
[16] F. Gaslain, C. Delacote, B. Lebeau, A. Walcarius, J. Sol-Gel Sci. Technol. 49 (2009) 112.
[17] Q. Wei, Z. Nie, Y. Hao, Z. Chen, J. Zou, W. Wang, Mater. Lett. 59 (2005) 3611.
[18] R.M. Grudzien, S. Pikus, M. Jaroniec, J. Phys. Chem. C 113 (2009) 4875.
[19] J. Aguado, J.M. Arsuaga, A. Arencibia, Microporous Mesoporous Mater. 109 (2008) 513.
[20] B. Nohair, S. MacQuarrie, C.M. Crudden, S. Kaliaguine, J. Phys. Chem. C 112 (2008) 6065.
[21] L. Mercier, T.J. Pinnavaia, Chem. Mater. 12 (2000) 188.
[22] H.M. Kao, T.Y. Shen, J.D. Wu, L.P. Lee, Microporous Mesoporous Mater. 110 (2008) 461.
[23] H.M. Kao, L.P. Lee, A. Palani, Anal. Chem. 80 (2008) 3016.
[24] A. Walcarius, C. Delacote, Anal. Chim. Acta 547 (2005) 3.
[25] A. Stein, B.J. Melde, R.C. Schroden, Adv. Mater. 12 (2000) 1403.
[26] G.E. Fryxell, S.V. Mattigod, Y. Lin, H. Wu, S. Fiskum, K. Parker, F. Zheng, W. Yantasee, T.S. Zemanian, R.S. Addleman, J. Liu, K. Kemner, S. Kelly, X. Feng, J. Mater. Chem. 17 (2007) 2863.
[27] A. Walcarius, C. R. Chim. 8 (2005) 693.
[28] S. Sayen, M. Etienne, J. Bessière, A. Walcarius, Electroanalysis 14 (2002) 1521.
[29] W. Yantasee, Y. Lin, T.S. Zemanian, G.E. Fryxell, Analyst 128 (2003) 467.
[30] A. Walcarius, M. Etienne, S. Sayen, B. Lebeau, Electroanalysis 15 (2003) 414.
[31] C.C. Chen, E.J. McKimmy, T.J. Pinnavaia, K.F. Hayes, Environ. Sci. Technol. 38 (2004) 4758.
[32] S.J.L. Billinge, E.J. McKimmy, M. Shatnawi, H.J. Kim, V. Petkov, D. Wermeille, T.J. Pinnavaia, J. Am. Chem. Soc. 127 (2005) 8492.
[33] C. Amatore, A. Oleinick, O. Klymenko, C. Delacôte, A. Walcarius, I. Svir, Anal. Chem. 80 (2008) 3229.
[34] M. Grün, I. Lauer, K.K. Unger, Adv. Mater. 9 (1997) 254.
[35] M. Grün, K.K. Unger, A. Matsumoto, K. Tsutsumi, Microporous Mesoporous Mater. 27 (1999) 207.
[36] E.F. Vansant, P. Van Der Voort, K.C. Vrancken, Stud. Surf. Sci. Catal. 93 (1995).
[37] M.H. Lim, A. Stein, Chem. Mater. 11 (1999) 3285.
[38] R.J.P. Corriu, E. Lancelle-Beltran, A. Mehdi, C. Reyé, S. Brandès, R. Guilard, J. Mater. Chem. 12 (2002) 1355.
[39] Y. Bonfil, M. Brand, E. Kirowa-Eisner, Anal. Chim. Acta 424 (2000) 65.
[40] A. Walcarius, M. Etienne, J. Bessière, Chem. Mater. 14 (2002) 2757.
[41] C.F. Baes Jr., R.E. Mesmer, The Hydrolysis of Cations, Wiley, New York, 1976, pp. 301–312.
[42] A. Walcarius, J. Bessière, Chem. Mater. 11 (1999) 3009.
[43] J. Crank, The Mathematics of Diffusion, Clarendon Press, Oxford, 1975.
[44] F. Gaslain, C. Delacote, B. Lebeau, C. Marichal, J. Patarin, A. Walcarius, Stud. Surf. Sci. Catal. 165 (2007) 417.
[45] J.W. Lee, W.G. Shim, H. Moon, Microporous Mesoporous Mater. 73 (2004) 109.
[46] Sujandi, S.E. Park, Stud. Surf. Sci. Catal. 170B (2007) 1446.
[47] A. Walcarius, C. Delacote, S. Sayen, Electrochim. Acta 49 (2004) 3775.

Talanta 79 (2009) 967–970

Contents lists available at ScienceDirect

Talanta

journal homepage: www.elsevier.com/locate/talanta

Short communication

Evaluation of the suitability of sampling on Tenax TA and polydimethylsiloxane for the analysis of combustion gases

Koen Desmet[a], Marc Schelfaut[a], Tadeusz Górecki[b], Pat Sandra[a,*]

[a] Laboratory of Separation Sciences, Department of Organic Chemistry, Ghent University, Krijgslaan 281 S4, B-9000 Gent, Belgium
[b] Department of Chemistry, University of Waterloo, Waterloo, ON, N2L 3G1 Canada

ARTICLE INFO

Article history:
Received 25 February 2009
Received in revised form 17 April 2009
Accepted 21 April 2009
Available online 3 May 2009

Keywords:
Sorptive sampling
Combustion gases
Tenax TA
Polydimethylsiloxane

ABSTRACT

Two sorbents commonly employed for air sampling were selected for the evaluation of their suitability for the analysis of combustion gases namely Tenax TA as adsorbent and polydimethylsiloxane (PDMS) as absorbent. Target compounds were selected among the gaseous combustion products of polyurethane foam and fire-retarded polystyrene. The combustion gases were generated by burning test materials in the flame of a Bunsen burner. Gaseous combustion products were sampled simultaneously with the two sorbents using a two-way adapter, thereby exposing each sorbent to the same combustion gas atmosphere. Special attention was given to the deterioration encountered in the Tenax TA performance upon repeated combustion gas exposure, limiting its use for sampling reactive atmospheres.

1. Introduction

Gas chromatography is the method of choice when analyzing volatile and semi-volatile organic compounds in the gas phase. Sampling, which involves collecting a representative amount of the analyte(s) from the atmosphere and transferring it to the gas chromatograph, remains the bottleneck of most procedures. Two strategies can generally be used. Whole air samples can be collected using e.g. Tedlar bags, Summa-passivated canisters, impingers or airtight syringes. Alternatively, the analytes can be collected through sorption on a suitable preconcentration material (sorbent), and the later desorbed thermally or using a solvent. Analyte preconcentration on solid sorbents is often preferred because of better sensitivity of the method and ease of handling of the samples. More detailed discussion of the techniques used in air sampling and analysis can be found in many review papers (e.g. [1,2]).

Commonly used sorbents include carbon-based materials, such as activated carbon and carbon molecular sieves, and organic polymers like Tenax and Chromosorb. All of them collect the analytes through the process of physical adsorption. Recently, polydimethylsiloxane (PDMS) was introduced as a promising alternative. Analyte sorption onto this material is based on partitioning of the analytes into its bulk, i.e. it works as an absorbent rather than adsorbent [3,4].

Sorbents need to fulfill a number of requirements. They should allow complete enrichment and fast desorption of the analytes of interest. Artifact formation and/or irreversible sorption are not tolerable. Low affinity to water, high inertness and high thermal stability are preferred. Furthermore, the sorbent materials should be reusable [2,3,5].

Analyte trapping generally does not create any problem as breakthrough volumes are quite high for most analytes of interest. Fast and complete desorption of the analytes can be difficult when the analyte–sorbent interaction is too strong. This can lead to the decomposition of some trapped components (e.g. α-pinene and sabinene on Carboxen 569, Carbotrap and Tenax [6,7]), or to the irreversible adsorption of polar analytes (e.g. alcohols, on activated carbon [8]). Artifacts creation on carbon-based materials was also demonstrated in the analysis of thiols [9]. Water retention can disturb the chromatography or lead to hydrolysis of the compounds retained. Most carbon-based materials (with the exception of graphitized carbon black, i.e. Carbotraps) tend to retain large volumes of water and should not be used in exceedingly humid atmospheres [2,5].

Porous organic adsorbents normally fulfill most of the requirements formulated above. However, they often lack thermal stability, and characteristic degradation peaks occur when sorbents such as Tenax or Chromosorb are reused. In many cases the products formed include analytes of interest, such as benzene, toluene and xylene from Chromosorb [3] and benzaldehyde and acetophenone from Tenax [10].

PDMS-based sorbents absorb the analytes into liquid-like phase rather than retaining them on the surface, as is the case with

* Corresponding author. Tel.: +32 56 204031; fax: +32 56 204859.
E-mail address: pat.sandra@richrom.com (P. Sandra).

0039-9140/$ – see front matter © 2009 Elsevier B.V. All rights reserved.
doi:10.1016/j.talanta.2009.04.044

classical adsorbents. As a consequence, mild thermal desorption conditions can be used to liberate the analytes. Thermal decomposition of PDMS produces readily identifiable siloxane products, which usually do not interfere with the analytes of interest, but might coelute with them. This problem can be easily overcome by using mass spectrometry for analyte detection and identification. In addition, PDMS is a very hydrophobic material, which makes it suitable for sampling under humid conditions [4].

Our research focuses on rapid fingerprinting of combustion gases (e.g. emitted during fires) based on volatile and semi-volatiles organic compounds produced. Sampling methodology had to be devised to address problems arising from the dynamic sampling environment. Sampling based on Tedlar bags, Summa canisters or airtight syringes was not considered, as fast and flexible sampling was requested. Methodologies based on Tenax TA and on PDMS were evaluated and their performances compared.

2. Experimental

2.1. Chemicals

Polyurethane and polystyrene samples were donated by the manufacturers, BASF (Antwerp, Belgium) and Recticel (Wetteren, Belgium), respectively. A standard solution was prepared in anhydrous methylene chloride (Biosolve, Valkenswaard, The Netherlands) at a concentration of 10 μg/mL of each component. 2-Bromostyrene, 2-bromophenol, 2,6-dibromophenol, 2,4,6-tribromophenol, 2-tolylisocyanate and 2,4-toluenediisocyanate were obtained from Fluka (Buchs, Switzerland).

2.2. Sampling

Sampling was performed using an SKC air sampler (Sercolab, Mechelen, Belgium), accompanied with a low flow needle valve (SKC). Flow through the sampling tubes was measured using a mass flow meter (Aalborg, Alltech, Lokeren, Belgium). Tenax TA (150 mg) and PDMS (200 mg) sorbent tubes were obtained from Gerstel (Mülheim a/d Ruhr, Germany). New and used tubes were conditioned before sampling at 320 °C for 8 h with a helium flow of 30 mL/min. During sampling, the tubes were protected against particle contamination by insertion of a small amount of deactivated glass wool (Supelco). The glass wool plug was removed before analysis.

In order to test the performance of the sorbents in combustion gas sampling, a home made two-way manifold was connected to a sampling pump, which allowed a similar flow to be pulled through the sorbent tubes. The experimental set-up is illustrated in Fig. 1.

To overcome the differences in backpressure caused by the much larger particle size of the PDMS sorbent (0.5 mm) compared to the Tenax TA, a low flow needle valve was installed in-line with the PDMS-filled tube. The flow rate through each sampling tube was set at 100 mL/min using a mass flow meter.

Extruded polystyrene (10 cm × 10 cm × 3 cm) and polyurethane (10 cm × 10 cm × 5 cm) samples were placed in contact with a Bunsen burner flame in an enclosed, but not activated fume hood (60 cm × 135 cm × 120 cm) during the sampling period of 10 min. With this set-up, each of the tubes was exposed to the same volume of the smoke gas.

2.3. Thermal desorption and analysis

Sorbent tubes were desorbed thermally using a TDS-2 thermal desorber from Gerstel. To achieve desorption of the analytes from the sampling tube, the thermal desorption unit was heated from 50 °C to 300 °C at 60 °C/min with an initial time of 1 min and a final time of 5 min. Compounds were swept towards a programmed temperature vaporizer (PTV, CIS-4 from Gerstel) where the split valve was open at 100 mL/min and trapped at 150 °C in an empty baffled liner. When desorption was completed, the PTV was heated from −150 °C to 300 °C at 12 °C/s. The PTV temperature program started after an additional 30 s at 150 °C to allow full flow stabilization inside the PTV liner after closure of the split valve. The total splitless time was 1 min. The TDS-2 was mounted on a 6890 HP GC-5973 MSD (Agilent Technologies, Little Falls, DE, USA). The MSD was used in the electron impact mode (70 eV), generating full scan spectra between 50 amu and 450 amu. Ion extraction was applied for the elucidation of the target compounds. Separation was carried out on an HP-5MS fused silica capillary column, 30 m L × 0.25 mm I.D. × 0.25 μm d_f (Agilent Technologies). Carrier gas was helium at a constant flow of 1.2 mL/min. The oven was programmed from 40 °C (1 min) to 300 °C at 10 °C/min and held for 3 min.

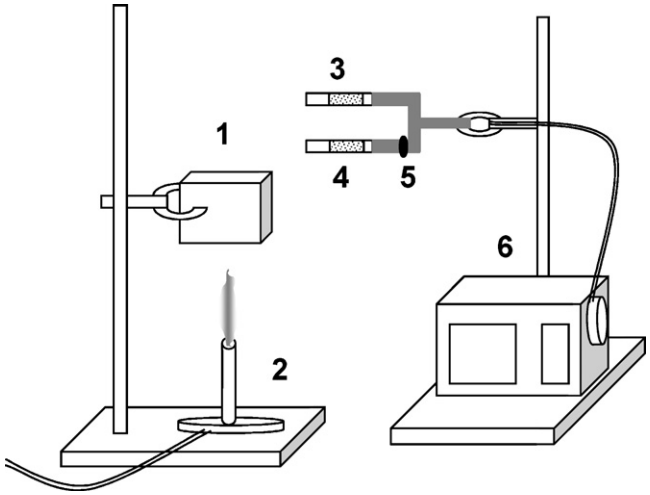

Fig. 1. Schematic representation of the experimental set-up for sampling of smoke gases. 1. Sample, 2. Bunsen burner, 3. Tenax TA, 4. PDMS, 5. Needle valve, 6. Air sampler.

3. Results and discussion

Initial experiments were performed on tubes exposed to smoke for at least five samplings of 1 L. The performance comparison of the two sorbents was based on the selection of target compounds with high toxicity, hence environmental importance. Some nitrogen containing compounds were selected for the combustion gases of polyurethane, while brominated species were selected for the fire-retarded extruded polystyrene (FR-polystyrene). Tables 1 and 2 list the selected compounds, the ions used for ion extraction and relative enrichment factor on PDMS and Tenax TA for polyurethane versus FR-polystyrene smoke, respectively. Relevant parts of the chromatograms are shown in Figs. 2 and 3 for polyurethane and FR-polystyrene, respectively. The results revealed some striking differences.

For polyurethane derived smoke, large differences between the two sorbents were found for 2,4-toluenediisocyanate (peak 1), with much higher response on PDMS. This difference is probably due to the high reactivity of the isocyanate group and its tendency to

Table 1
Relative quantities ($area_{PDMS}/area_{Tenax}$) of the target analytes in polyurethane derived smoke gas.

Peak no	Selected ion	Compound	$Area_{PDMS}/area_{Tenax}$
1	174	2,4-Toluenediisocyanate	16.20
2	153	1-Naphtalenecarbonitrile	0.88
3	153	2-Naphtalenecarbonitrile	0.94

Table 2
Relative quantities ($area_{PDMS}/area_{Tenax}$) of the target analytes in FR-polystyrene-derived smoke gas.

Peak no	Selected ion	Compound	$Area_{PDMS}/area_{Tenax}$
1	170	Bromomethylbenzene	2.32
2	172	3-Bromophenol	1.98
3	196	1-Allyl-2-bromobenzene	0.74
4	169	Dibromomethylbenzene	2.10
5	252	Dibromophenol	1.96
6	206	Bromonaphtalene	3.12
7	206	Bromonaphtalene	2.38
8	330	Tribromophenol	42.3

bind to available amine or hydroxyl functions. The latter are either present or can be formed on the surface of Tenax, as it is made of a 2,6-diphenyleneoxide polymer. Recoveries for the less reactive nitriles (peaks 2 and 3) seem very similar.

Combustion of fire-retarded extruded polystyrene resulted in the emission of various brominated aromatic species. The formation of these compounds is linked to the simultaneous oxidative decomposition of the polystyrene backbone to various benzene or phenol radical species [11] and the decomposition of hexabromocyclododecane [12] used as the fire-retardant, and their consequent radical–radical interaction. All the target brominated species were detected on PDMS and Tenax TA, although in lower quantities on Tenax, but tribromophenol (peak 8), a known dioxin-precursor [13], was barely detectable on Tenax. Important to note is that a second heating of the sample tubes, Tenax TA and PDMS, did not release any of the target solutes for both polyurethane and FR-polystyrene.

These results were somewhat surprising and consequently, further comparisons were made to confirm these findings.

One microliter of the standard solution, corresponding to 10 ng per compound loaded on the tube, containing 2-bromostyrene, 2-bromophenol, 2,6-dibromophenol and 2,4,6-tribromophenol (representing polystyrene combustion products) and 2-tolylisocyanate and 2,4-toluenediisocyanate (representing polyurethane combustion products) were directly injected on the previously used tubes and on new Tenax TA and PDMS tubes. The results are illustrated in Fig. 4, depicting the relative responses in relation to the sorbent giving the largest response.

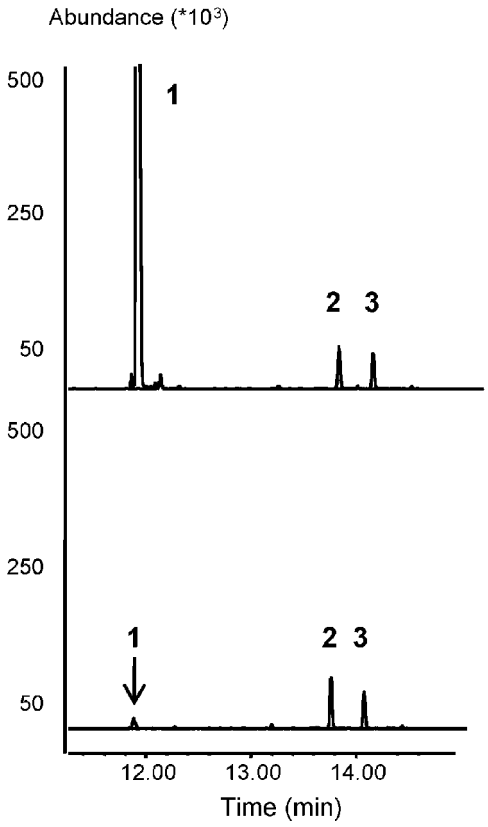

Fig. 2. Relevant part of the ion extracted chromatograms for the analysis of polyurethane smoke. Upper chromatogram PDMS, lower chromatogram Tenax TA. Conditions see text. Peak identification Table 1.

Large differences in recovery were observed when comparing the results obtained for the Tenax tubes while this is not observed

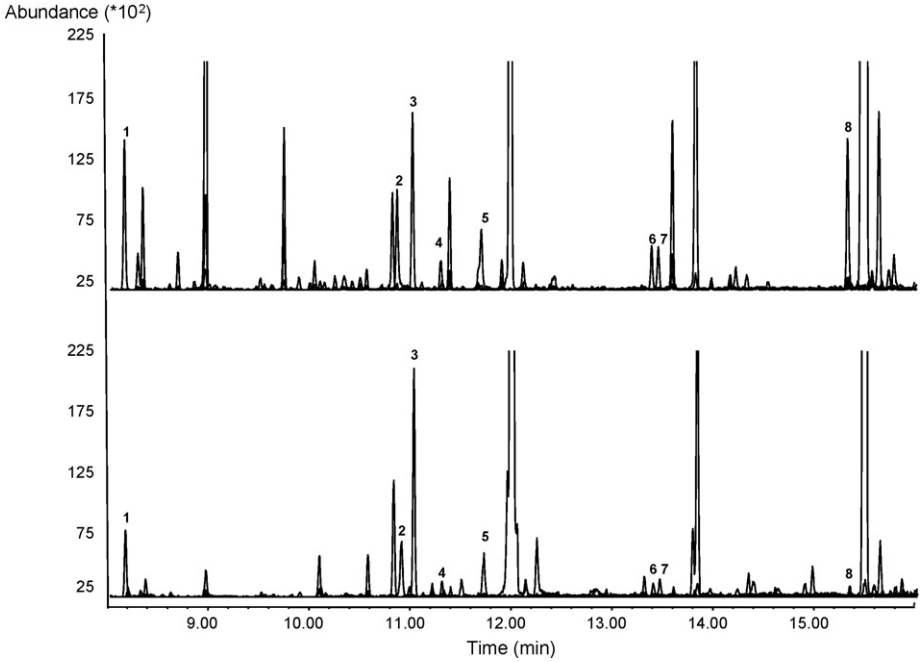

Fig. 3. Relevant part of the extracted ion chromatograms for the analysis of FR-polystyrene smoke. Upper chromatogram PDMS, lower chromatogram Tenax TA. Conditions see text. Peak identification Table 2.

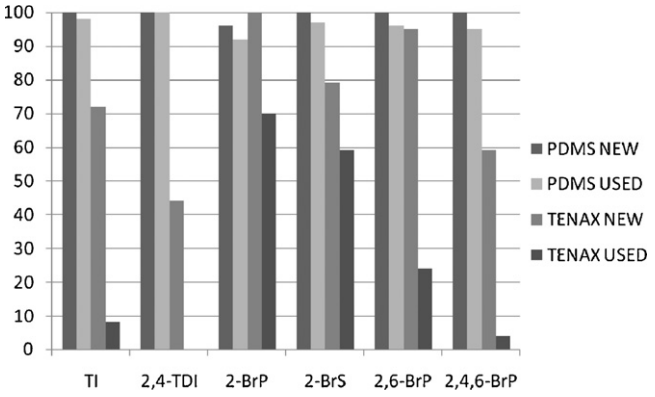

Fig. 4. Relative responses (% of the largest response) of 2-tolylisocyanate (TI), 2,4-toluenediisocyanate (2,4-TDI), 2-bromophenol (2-BrP), 2-bromostyrene (2-BrS), 2,6-dibromophenol (2,6-BrP) and 2,4,6-tribromophenol (2,4,6-BrP) upon direct injection onto PDMS and Tenax tubes previously exposed to smoke and new PDMS and Tenax tubes.

for the PDMS tubes. These data point to a devastating effect of combustion gases on the performance of Tenax. The new Tenax tube generally followed the PDMS trend in retention capacity, although it should be pointed out that the response for 2,4-toluenediisocyanate on the new Tenax tube was already less than 50% of that for PDMS. The relative standard deviations of the results obtained by the direct injection of the standards ($n = 6$) onto the smoke-exposed Tenax tube were as high as 50% in the analysis of the bromophenols, while the RSD values for the new Tenax tube and the old and new PDMS tubes were in the 10–12% range. A comparison of the RSD values for the isocyanate species was deemed less meaningful due to the high reactivity of these compounds. Fig. 4 clearly indicates that the PDMS sorbent outperformed Tenax TA in the overall recovery of the selected compounds. The inertness or the sorption (partitioning) mechanism, inherent to PDMS, seems to allow the sampling of reactive atmospheres without the deterioration of the sorbent performance, making PDMS an ideal sampling medium for the analysis of smoke gases.

4. Conclusions

Tenax TA and PDMS were simultaneously exposed to the combustion gases of polyurethane foam and fire-retarded polystyrene. In addition to these analyses, direct injection of standard solutions onto the sorbent tubes was used to evaluate their performance.

Large discrepancies in the performance between the two adsorbents and PDMS were observed in the analysis of reactive species, such as 2,4-toluenediisocyanate. This was most likely related to the presence of reactive groups on the surfaces of the adsorbents. Further investigation of Tenax revealed that exposure to combustion gases degrades its performance considerably. This limits the usefulness of Tenax in sampling of reactive atmospheres. On the other hand, PDMS, for which sampling is based on partitioning of the solutes into the bulk material, did not seem to be affected even after repeated sampling of the smoke gas atmosphere, which points to its usefulness in this type of analysis.

References

[1] M. Michulec, W. Wardencki, M. Partyka, J. Namieśnik, Crit. Rev. Anal. Chem. 35 (2005) 117.
[2] K. Dettmer, W. Engewald, Anal. Bioanal. Chem. 373 (2002) 490.
[3] E. Baltussen, F. David, P. Sandra, C.A. Cramers, J. High Res. Chromatogr. 21 (1998) 332.
[4] E. Baltussen, C.A. Cramers, P. Sandra, Anal. Bioanal. Chem. 373 (2002) 3.
[5] K. Dettmer, W. Engewald, Chromatographia 57 (Suppl.) (2003) S339.
[6] H. Rothweiler, P.A. Wäger, C. Schlatter, Atmos. Environ. 25 (1991) 231.
[7] C. Coeur, V. Jacob, I. Dennis, P. Foster, J. Chromatogr. A 786 (1997) 185.
[8] J. Rudling, J. Chromatogr. 503 (1990) 33.
[9] E. Baltussen, F. David, P. Sandra, C. Cramers, J. Chromatogr. A 864 (1999) 345.
[10] P.A. Clausen, P. Wolkoff, Atmos. Environ. 31 (1997) 715.
[11] K. Desmet, B. Tienpont, M. Schelfaut, P. Sandra, Chromatographia 57 (2003) 385.
[12] F. Barontini, V. Cozzani, L. Petarca, Rapid Commun. Mass Spectrom. 15 (2001) 690.
[13] S. Sidhu, L. Masquid, B. Dellinger, G. Mascolo, Combust. Flame 100 (1995) 11.

Talanta 79 (2009) 762–767

Contents lists available at ScienceDirect

Talanta

journal homepage: www.elsevier.com/locate/talanta

Development and validation of a simple stability-indicating high performance liquid chromatographic method for the determination of miconazole nitrate in bulk and cream formulations

María M. De Zan[a,b,*], María S. Cámara[a], Juan C. Robles[a], Silvina V. Kergaravat[a], Héctor C. Goicoechea[b]

[a] Laboratorio de Control de Calidad de Medicamentos, Cátedra de Química Analítica I, Facultad de Bioquímica y Ciencias Biológicas Universidad Nacional del Litoral, C.C. 242, S3000ZAA Santa Fe, Argentina

[b] Laboratorio de Desarrollo Analítico y Quimiometría (LADAQ), Cátedra de Química Analítica I, Facultad de Bioquímica y Ciencias Biológicas Universidad Nacional del Litoral, C.C. 242, S3000ZAA Santa Fe, Argentina

ARTICLE INFO

Article history:
Received 13 March 2009
Received in revised form 29 April 2009
Accepted 30 April 2009
Available online 7 May 2009

Keywords:
Miconazole
HPLC
Validation
Cream
Stability-indicating method

ABSTRACT

A simple and stability-indicating high performance liquid chromatographic method was developed and validated for the determination of miconazole nitrate in bulk and cream preparations. The extraction step for cream samples consisted in a warming, cooling and centrifugation procedure that assures the elimination of the lipophilic matrix component, in order to avoid further precipitation in the chromatographic system. Separation was achieved on a ZORBAX Eclipse XDB – C18 (4.6 mm × 150 mm, 5 μm particle size) column, using a mobile phase consisting of water, methanol and acetonitrile, in a flow and solvent gradient elution for 15 min. The column was maintained at 25 °C and 10 μL of solutions were injected. UV detection was performed at 232 nm, although employment of a diode array detector allowed selectivity confirmation by peak purity evaluation. The method was validated reaching satisfactory results for selectivity, precision and accuracy. Degradation products in naturally aged samples could be simultaneously evaluated, without interferences in the quantitative analysis.

1. Introduction

Miconazole, 1H-imidazole,1-[2-(2,4-dichlorophenyl)-2-[(2,4-dicholophenyl)methoxy]ethyl]-(±) (Fig. 1) is an antimycotic-imidazole derivative [1]. With a wide activity spectrum, it is endowed with a powerful activity against dermatophytes and *Candida albicans*, as well as against several Gram-positive germens [2].

The generally accepted mode of action of azole antifungals is the inhibition of 14-alpha-lanosterol demethylase, a key enzyme in ergosterol biosynthesis, resulting in depletion of ergosterol and accumulation of toxic 14-alpha-methylated sterols in the membrane of susceptible yeast species [3].

Miconazole has been extensively applied in the management of dermal, oral, and vaginal mycosis. Currently, it is used in a variety of pharmaceutical formulations such as injections, tablets, oral gels, creams, ointments, topical powders and vaginal suppositories. The most usual application forms include creams, ointments or gels at 2.0% concentration level, alone or associated with anti-inflammatory steroids, or other antimicrobials such as gentamicine for the treatment of dermatitis. Diaper dermatitis, a common dermatologic disorder of infancy, frequently associated with *C. albicans* infections, is currently treated with ointments containing 0.25% miconazole nitrate [3]. Moreover, mucoadhesive buccal patches containing miconazole nitrate have been developed, and very recently an extended release miconazole bioadhesive buccal tablet was reported to be effective in the treatment of oropharyngeal candidiasis [4]. Pessaries containing a combination of metronidazol and miconazol nitrate are used in treatment of vulvovaginal infections [4].

USP [1] (United States Pharmacopoeia) and British [5] Pharmacopoeia methods for the assay of miconazole nitrate and related substances or degradation products in bulk and pharmaceutical dosage forms are diverse. The bulk material assay is performed by a potentiometrical titrimetry in both pharmacopoeias, whereas related compounds are evaluated through an isocratic high performance liquid chromatography (HPLC) method. This method employs 0.2 mol L^{-1} ammonium acetate, methanol, and acetonitrile (38:32:30) as the mobile phase at a flow rate of 2 mL min^{-1} and a 4.6 mm × 100 mm column containing 3 μm C18 packing. Under these conditions, the chromatographic analysis requires

* Corresponding author at: Laboratorio de Control de Calidad de Medicamentos, Cátedra de Química Analítica I, Facultad de Bioquímica y Ciencias Biológicas Universidad Nacional del Litoral, C.C. 242, S3000ZAA Santa Fe, Argentina.
Tel.: +54 342 4575205; fax: +54 342 4575205.
E-mail address: mmdezan@fbcb.unl.edu.ar (M.M. De Zan).

0039-9140/$ – see front matter © 2009 Elsevier B.V. All rights reserved.
doi:10.1016/j.talanta.2009.04.060

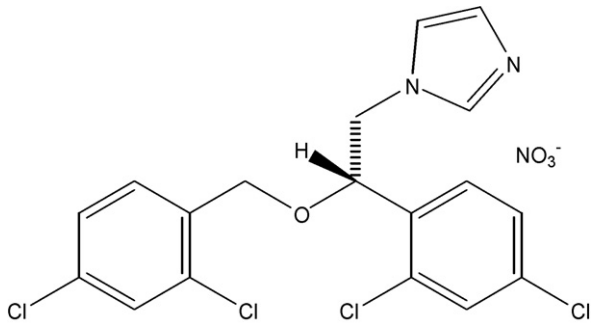

Fig. 1. Structural formulae for miconazole nitrate (MW = 479.1).

a considerable time for equilibration and for obtaining results (ca. 30 min). On the other hand, the same method is described in British Pharmacopoeia for the simultaneous determination of related substances, such as for the assay of miconazole in cream preparations. However, a gradient of 0.01 mol L^{-1} ammonium dihydrogen orthophosphate pH 6.0, tetrahydrofuran and acetronitrile is employed in the latter method for assaying miconazole and hydrocortisone in creams. The 30th edition of the USP suggests an HPLC based method to analyze cream and vaginal ovule formulations containing miconazole nitrate, which employs a mobile phase consisting of triethylamine and phosphoric acid in a mixture of acetonitrile, tetrahydofuran and methanol. When analysing injections, the mobile phase in the USP method is an ammonium acetate buffer in acetonitrile and methanol, whereas a GC method is suggested for powders. To the best of our knowledge, no analytical chromatographic methods were reported in the literature for the routine quantitative assay of miconazole nitrate in bulk form, and only a limited number of methods for its assay in pharmaceutical dosage forms have been presented. Colorimetry [6], derivative spectrophotometry [7,8], HPLC [9] and magnetic resonance spectroscopy [10] were applied in tablets, powders and ovules containing miconazole nitrate. On the other hand, solid phase extraction (SPE) prior HPLC with post-column photochemical reaction [11] and supercritical fluid extraction followed by derivative spectroscopy [12] were described for cream preparation analysis.

Cream analysis generally represents a difficult task for analysts, essentially due to the complexity of the base cream or matrix in which the analyte of interest is immersed. It usually contains vaseline, paraffine, cetoestearilic alcohol or other lipophilic components which are poorly soluble in the solvents commonly used in HPLC. For this reason, the assay method requires an extractive procedure prior to the chromatographic step in order to ensure the elimination of interfering components, avoiding the precipitation in the chromatographic system.

In the present report, we present a strategy which allows for the simultaneous quantification and stability evaluation of miconazole nitrate in bulk and cream formulations through a simple, rapid, precise, accurate and specific HPLC-UV method with an efficient and extremely easy extractive procedure. It is interesting to note that a reversed-phase HPLC method for determination of econazole nitrate in cream formulations has been recently developed using miconazole nitrate as an internal standard [13]. However, in the presently proposed method, the separation was achieved in a shorter retention time and consuming a lower amount of solvent. On the other hand, the results obtained in the validation step suggest that it is not necessary to employ an internal standard, simplifying the work. Moreover, in comparison with the methods described in the literature, our chromatographic system needs a simpler mobile phase composition and no buffer, reaching excellent resolution and peak symmetry.

It is internationally admitted that analytical measurements should be made using methods which have been tested to ensure they are fit for the purpose. In this regard, method validation is an important requirement in the practice of chemical analysis, and it should be an integral part of any good analytical practice. Recommendations provided for scientific organizations such as EURACHEM (European Analytical Chemistry) [14,15] and IUPAC (International Union Of Pure and Applied Chemistry) [16,17] can be considered in this way. Moreover, for pharmaceutical analysis, guidelines from the USP [1], ICH [18] (International Conference on Harmonisation), and the FDA [19,20] (Food and Drug Administration) provide a framework for performing such validations. Taking into account these considerations, the proposed methodology has been extensively validated.

2. Experimental

2.1. Chemicals and reagents

A miconazole nitrate working standard was prepared in our laboratory from a raw material, which was characterized and assayed according to specifications of the 30th edition of the USP. Miconazole nitrate bulk material, creams containing (i) 2.0 g% p/p of miconazole (nitrate) or (ii) 2.0 g% of miconazole (nitrate), 0.1% of betamethasone (17-valerate) and 0.1% gentamicine (sulphate), and the base cream utilized in the formulation, were all obtained from LAFORMED SA, Formosa, Argentina. The base cream formulation includes liquid and solid paraffin, cetostearyl alcohol, benzyl alcohol, cetomacrogol 1000, monobasic sodium phosphate, phosphoric acid, propylene glycol, methylparaben, propylparaben and triethanolamine. Raw material of all this compounds was provided by LAFORMED SA (Formosa, Argentina). Methanol and acetonitrile (HPLC grade) were purchased from Aberkon Quimica, Argentina. Glacial acetic acid (analytical grade) was purchased from Laboratorios Cicarelli, Argentina, while purified HPLC grade water was obtained from a Milli-Q® system (Millipore, Milford, MA, USA). Acidic methanol was prepared by diluting glacial acetic acid in methanol to obtain a final concentration of 0.1% (v/v).

2.2. HPLC instrumentation and conditions

The HPLC system was an Agilent 1100 Series equipped with a quaternary pump, membrane degasser, thermostated column compartment, autosampler and diode array detector (DAD) (Agilent Technologies, Waldbronn, Germany). For data acquisition and processing, the Chemstation version B 0103 was used. The HPLC column was a ZORBAX Eclipse XDB – C18 (4.6 mm × 150 mm, 5 μm particle size), Agilent Technologies. The chromatographic separation was performed using a mobile phase consisting of water, methanol and acetonitrile, in a flow and solvent gradient elution of 15 min (see Table 1). Solvents were filtered through 0.45 μm pore Nylon filter before use. The column was maintained at 25 °C and an injection volume of 10 μL was used. The photodiode array detector was set at 232 (4) nm with reference in 360 (100) nm and used in scan mode in the range of 200–500 nm for selectivity and stability studies. Peak purity was evaluated from spectral analysis performed with the instrument software.

Table 1
Gradient program used for the separation of miconazole.

Time (min)	Water (%)	Methanol (%)	Acetonitrile (%)	Flow rate (mL min^{-1})
0.0	30	30	40	1.0
2.0	20	35	45	1.0
4.5	20	35	45	1.0
7.0	10	40	50	1.5
10.0	30	30	40	1.0

2.3. Stock and standard solutions

A stock standard solution of miconazole nitrate 11.0 mg mL^{-1} was prepared by exactly weighing and dissolving a portion of the working standard in HPLC grade methanol. This solution, which proved to be stable for a period of 2 month, was stored at 4 °C and protected against light in a refrigerator. The latter solution was left to attain room temperature before use. Working standard solution was prepared daily by dilution of appropriate amount of the stock standard solution in water:methanol:acetonitrile (30:30:40) reaching a final concentration of 0.53 mg mL^{-1}.

2.4. Cream pre-treatment

Portions of ca. 2.2 g of previously well-homogenised cream samples were accurately weighed in 250 mL vessels and 15 mL of acidic methanol were added. Vessels were covered by a watch glass and placed in a water bath at 90 °C with agitation and kept there until the cream components were melted. Afterwards, they were removed from the bath, vigorously shaken for 5 min in a magnetic stirrer plate and kept at room temperature until the specimen resolidified. The heating–shaking–cooling procedure was repeated twice to guarantee the complete solubilization and extraction of miconazole nitrate from the matrix components. The obtained suspensions were then transferred to 25.0 mL volumetric flask, washing the vessels with acidic methanol aliquots that were collected in the same flasks. Suspensions were then made up to volume with the same solvent and 10.0 mL of them were placed in centrifuge tubes with caps. The tubes were kept at −20 °C in freezer during 20 min and then centrifugated at 2000 × *g* for 15 min. This procedure assures the complete precipitation of the lipophilic components of the base cream, whereas miconazole nitrate remains soluble in acidic methanol. After that, 3.0 mL of the supernatants (at room temperature) were transferred to a 10.0 mL flask and made up to volume with a mix of water:acetonitrile (30:40) to achieve a final composition of solvents equal to the initial composition of the mobile phase. The solutions were poured again in new caped centrifuge tubes and kept at −20 °C in freezer for 20 min. Remaining lipophilic components, completely precipitated in this step, were separated by centrifugation at 2000 × *g* for 15 min. Finally, suitable amounts of the solutions, containing about 0.53 mg mL^{-1} of miconazole nitrate, were filtered through a 0.45 μm nylon filter into an injector vial.

2.5. Validation samples

2.5.1. Matrix and excipient solutions

A portion of base cream (blank) of ca. 2.2 g, containing neither miconazole nitrate nor other active ingredients, was processed in the same manner as indicated above for cream pre-treatment.

Cetostearyl alcohol, benzyl alcohol, propylene glycol, methylparaben, propylparaben and triethanolamine solutions 0.5 mg mL^{-1} were prepared in methanol.

2.5.2. Linearity standard solutions

Adequate amounts of the stock standard solution of miconazole nitrate were diluted to obtain solutions with the following concentrations: 0.26, 0.40, 0.53, 0.66 and 0.79 mg mL^{-1}, all of them covering the range from 50.0 to 150.0% of the expected concentration of the analyte in the assay solution (triplicates).

2.5.3. Linearity cream solutions

Portions of base cream of ca. 2.2 g were processed in the same manner as indicated above for cream pre-treatment, and were spiked with appropriate volumes of the miconazole nitrate stock standard solution. Water:acetonitrile mixture was then added to a final volume of 10.0 mL in order to obtain solutions of concentrations which were analogous with those of the linearity standard solutions (triplicates).

2.5.4. Recovery solutions

Laboratory cream samples were prepared by spiking base cream portions with appropriate known amounts of miconazole nitrate standard powder to reach concentrations of 80.0, 100.0 and 120.0% of the expected amount of the analyte in real samples. Triplicates were prepared for each concentration level. The resulting samples were then processed in the same manner as indicated above for cream pre-treatment.

3. Results and discussion

3.1. Method development

3.1.1. Extraction

The sample pre-treatment procedures described in pharmacopoeias for creams containing miconazole nitrate to be assayed by an HPLC method consist in obtaining a suspension of the sample in pure methanol or in a solvent mixture, either by agitation or sonication at room temperature or in a water bath at 40–45 °C. The suspension is then rapidly filtered through a glass microfiber or a membrane filter. This procedure produces a foamy emulsion of the formulation under test, which makes filtration difficult, leading to both low recoveries and low precision. In addition, a late precipitation of excipients in the injector vials was observed, putting the column and equipment safety at risk. On the other hand, the procedure described in the present report (see Section 2), although longer and more laborious than those described in pharmacopoeias, can be straightforwardly implemented. Additionally, it does not need expensive equipment or materials, as those required in the literature methods (i.e. SPE or supercritical extraction fluid) [15,16].

3.1.2. Chromatography

The use of an extra-densely covered column, packed with double end-capping and prepared with an ultra high purity silica support, allowed us to use a pure solvent as the mobile phase, originating both sharp and symmetric peaks. This fact provides the following advantages to the proposed methodology: (a) no buffer solutions are needed, (b) shorter stabilization times are required, and (c) the column lifetime is enlarged.

Several proportions of water:methanol:acetonitrile and flow gradients were evaluated in order to achieve an optimum separation of the analyte from excipients that remain soluble (paraben and degradation products) in a short time of analysis. With the optimized gradient system, the retention time corresponding to miconazole was 8.3 min, being extremely stable among injections. However, the analysis time was set to 15 min, allowing elution of all possible degradation products which could be retained, without the need of a further stabilization time between injections. The wavelength was set at 232 (4) nm, the absorption maximum of miconazole in the elution solvent.

3.2. Method validation

Following ICH recommendations, detection limit and quantitation limit were not evaluated since the developed method is for quantitation of a major component in bulk or in pharmaceutical products.

3.2.1. Selectivity

The selectivity of the method was evaluated injecting by triplicate the following solutions: (a) injection solvent

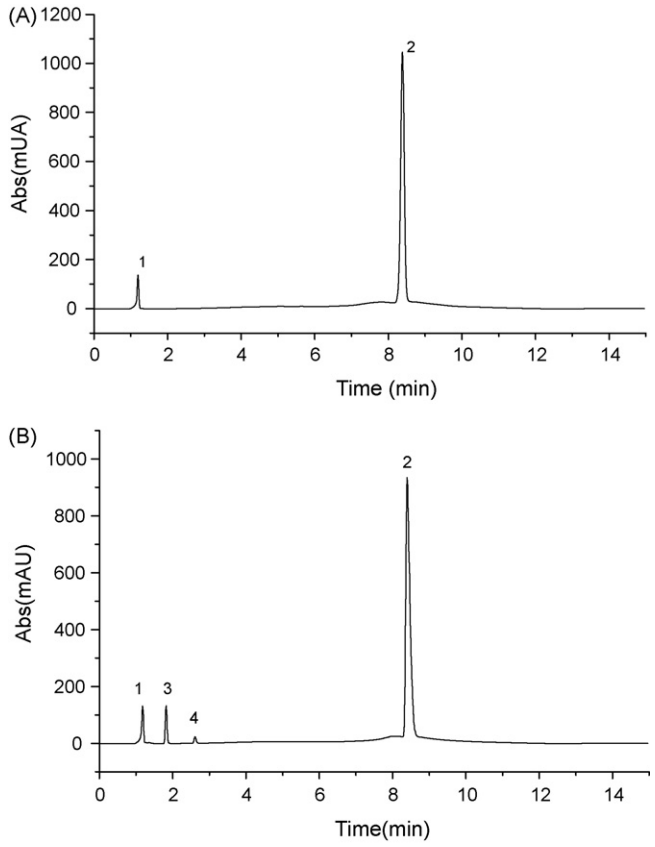

Fig. 2. Typical chromatograms obtained at 232 nm for (A) standard solution of miconazole nitrate 0.53 mg mL^{-1} and (B) miconazole nitrate cream sample showing (1) nitrate ion, (2) miconazole, (3) methylparaben, (4) propylparaben.

(water:metanol:acetonitrile, 30:30:40), (b) a pure standard solution of miconazole nitrate 0.53 mg mL^{-1}, (c) solutions of excipients, (d) solution of matrix, and (e) a cream sample solution. No peaks were observed in solvent chromatograms, whereas two peaks were obtained with the standard solution, corresponding to nitrate ion with retention time (t_r) equal to 1.19 min and miconazole (t_r = 8.38 min). Only methylparaben and propylparaben solutions showed peaks at the selected wavelength. Two peaks were observed in chromatograms for matrix solutions. They were identified by comparing both the retention times and the UV spectra to those for the reference excipient solutions, and corresponded to methylparaben (t_r = 1.80 min) and propylparaben (t_r = 2.60 min). Interestingly, no peaks were observed at t_r values near the miconazole retention time. Finally, when analysing a cream sample solution, the resolution between the analyte and propylparaben peaks was highly satisfactory. Typical chromatograms for standard and sample solutions are shown in Fig. 2.

On the other hand, the peak purity of the analyte was evaluated by the following procedure: (a) recording all spectra in the peak by using a diode array detector, (b) computing the average spectrum, and (c) comparing the difference values between each spectrum and the average with an estimation of the noise threshold. A peak purity factor was calculated as the mean value of all spectra in the peak that are within the threshold [21]. Peak purity factors were 99.95% for miconazole in sample solutions and 99.93% in standard solutions, computed on 135 spectra for each peak. Moreover, spectral matching between analyte peak in standard and sample solutions was of 99.96%. On the basis of these results, it can be concluded that there are no interfering components in the analyte peak.

Table 2
System suitability parameters.

Parameter	Value
Theoretical plates (N)	28,400
Asymmetry (A)	1.117
Tailing (T)	0.922
Capacity factor (K')	3.946
R.S.D. of repeated injections (n = 6) (%)[a]	0.25

[a] Relative standard deviation.

In order to study the degradation of the active ingredient and to get insight into the stability-indicating power of the analytical procedure, ICH recommendations were applied [22]. Three different batches of miconazole nitrate cream, which had previously undergone natural aging during 18 months, were analysed by triplicate, following the above-described procedure. Secondary peaks were also evaluated. A small secondary peak was observed, which was well resolved from the main peaks. Also peak purity of the analyte was maintained, and no interference in the assay was observed.

3.2.2. System suitability

A system suitability evaluation was performed by six standard solution injections, following ICH guidance. Evaluation of analyte peak parameters provided high quality results, as can be appreciated in Table 2. The results agree with those specified in pharmacopoeias and ICH guidelines, demonstrating that the chromatographic system is adequate and reliable.

3.2.3. Solution stability

In order to assure stability of miconazole solution during a period of time considered to be usual in routine analysis, standard and sample solutions were fractionated in four injector vials and left in the injector tray. Each solution was injected every 2 h from a new vial during a total time of 6 h. Percentages of areas respect to the initial area, i.e. t = 0, were calculated and the validity times were established as the time in which the area percentage ranged from 98.0 to 102.0% of the initial value. This study produced the following validity times: 6 h for standard solution and 4 h for sample solution.

3.2.4. Linearity

Linearity was studied for both pure standard and analyte in sample matrix using standard and sample solutions prepared as described in Section 2.5. Peak areas of miconazole were plotted versus concentration, and a least-squares analysis was performed.

For determining the data homoscedasticity, an F-test was employed to compare the extreme variances. The difference between the observed and critical value of F was not significant. The linearity between the response and the concentration over the analyzed range was evaluated using the statistical test suggested by IUPAC [23]. The results obtained showed that the calculated F-values did not exceed the tabulated values.

In order to compare the computed intercepts with the zero value, the confidence intervals were determined. In addition, a t-test was used to compare both the intercept and the slope of regression lines and no significant difference was observed. Results are summarized in Table 3.

3.2.5. Precision

Precision was evaluated at the repeatability and intermediate precision levels. For repeatability analysis, six independent portions of a cream sample were processed through the full analytical method and results were evaluated obtaining an associated R.S.D. (%) value of 0.58.

On the other hand, intermediate precision was evaluated with a new series of six portions of the same sample used in the repeatabil-

Table 3
Statistical analysis for calibration graphs of pure standard and analyte in sample matrix.

Item	Results	
	Standard	Sample matrix
F-Test for homoscedasticity evaluation	4.89 (19)[a]	7.78 (9.12)[b]
F-Test for linearity evaluation	1.13 (4.7)[c]	3.8 (3.8)[d]
t-Test[e] to compare intercepts	0.12 (2.45)	
t-Test[f] to compare slopes	0.02 (2.45)	
Intercept[g]	−29 (76)	27 (122)
Confidence interval for the intercept	[−271; 212]	[−359; 414]

The values between parentheses correspond to critical values at $\alpha = 0.05$ and the following degrees of freedom: [a]($\upsilon_1 = 2$, $\upsilon_2 = 2$), [b]($\upsilon_1 = 4$, $\upsilon_2 = 3$), [c]($\upsilon_1 = 3$, $\upsilon_2 = 6$), [d]($\upsilon_1 = 4$, $\upsilon_2 = 8$), [e]($\upsilon = 6$), [f]($\upsilon = 6$). [g]The values between parentheses correspond to the standard deviation.

ity assay, processed in a different day, 1 week later and by a different analyst. The corresponding R.S.D. (%) was 0.54. A statistical *F*-test was applied to compare the variance with the one computed in the repeatability analysis. The computed *F* value was equal to 1.29, whereas the critical $F_{crit(5,5,\alpha=0.05)}$ is 5.05. Therefore, it can be concluded that no differences exist between the variances obtained. On the other hand, both variances are lower than 2%, indicating the extremely good repeatability of the proposed methodology.

In addition, an R.S.D. (%) value was computed using the mean values of the analysed series; the resulting R.S.D. was 0.90. Owing to the fact that the latter value is lower than 2.8%, the maximum value accepted for AOAC in a recommendation for active ingredients [24], we conclude that the intermediate precision can be considered as excellent.

3.2.6. Accuracy

Solutions prepared as described in Section 2.5 were injected, and the recovery of the known amount of added analyte was computed for each sample. The results obtained are indicative of the good accuracy reached with the proposed methodology, since the mean recovery was included in the interval 100 ± 2%, at each level over the range of 80–120% of the target concentration [24]. Detailed results are shown in Table 4.

In addition, the global recovery, computed for the nine determinations (of the total analytical procedure), was 100.5% (R.S.D.% = 1.70). A statistical Student's *t*-test was applied, which allows us to conclude that no significant difference exists between the recovery obtained and the ideal value 100 at a confidence level of 95%.

3.2.7. Application: assay of commercial cream preparations

Once validated, the developed method was applied to the assay of miconazole nitrate and to the evaluation of degradation products in commercial cream preparations. The obtained results, corresponding to three batches of miconazole nitrate cream, are shown in Table 5. The percentage drug recovery, with respect to the label claimed by the manufacturer, indicates that the active ingredient in samples was present at a level included within the USP requirements of 90.0–110.0 of the labelled amount of miconazole nitrate.

With the aim of performing a further estimation of the potentiality of the developed methodology, three batches, corresponding to aged creams containing miconazole nitrate, gentamicin sulphate and betamethasone 17-valerate were subjected to the whole analytical procedure. As can be observed in Fig. 3, several additional peaks are present, which correspond to betamethasone 17-valerate and both its degradation and isomerization products. Min Li and colleagues demonstrated, through a strategy combining LC–MS with stress studies (forced degradation), that betamethasone 17-valerate follows, at least, two degradation pathway. The isomerization mechanism produces betamethasone 21-valerate, dexamethasone 17-valerate and dexamethasone 21-valerate, since the hydrolytic pathway gives bethametasone and dexamethasone as degradants [25]. By means of DAD employment, we confirmed that all degradants peaks observed in these aged samples chromatograms, showed a high spectral correlation with bethametasone 17-valerate.

Interestingly, miconazole stands perfectly separated from the remaining components. Furthermore, the peak purity is the same as that observed for the standard solution. On the other hand, as can be appreciated in Fig. 3, gentamicin does not interfere in the

Table 4
Recoveries obtained in the accuracy assay.

Level (% of expected concentration)	Recovery (%)	Mean recovery (%)	R.S.D. (%)
80.0	103.2–101.3–101.7	102.2	0.98
100.0	98.5–99.1–100.9	99.5	1.26
120.0	100.9–99.0–99.1	99.7	1.07

Table 5
Results obtained when analysing commercial samples.

Batch	Claimed label (% p/p)	Found[a] (% p/p)	Percentage of claimed label (%)
1	2.00	2.04 (0.03)	102.0
2	2.00	1.98 (0.01)	99.0
3	2.00	1.99 (0.02)	99.5

[a] Average computed for triplicates. Standard deviations are informed between parentheses.

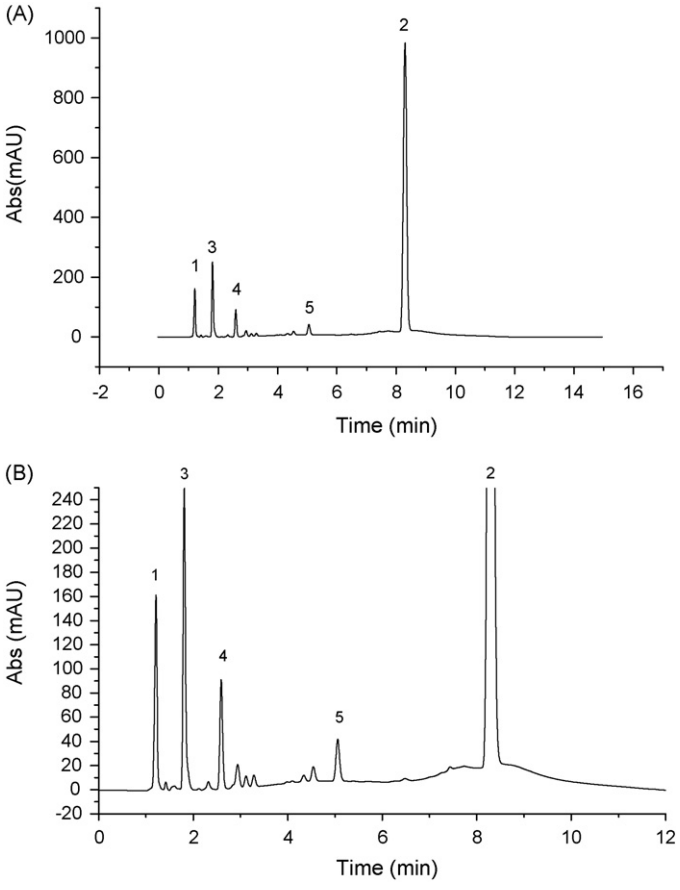

Fig. 3. Chromatogram obtained for a degradated cream sample containing 2.0 g% of miconazole (nitrate), 0.1% of betamethasone (valerate) and 0.1% gentamicine (sulphate). (A) Full scale. (B) Expansion plot in the base line region showing (1) nitrate ion, (2) miconazole, (3) methylparaben, (4) propylparaben, (5) betamethasone and several degradation peaks.

analysis, owing to the fact that the absorbance in the UV region for this compound is negligible.

4. Conclusions

A validated stability-indicating HPLC analytical method for the routine analysis of miconazole nitrate in bulk and cream formulations has been developed. The extractive step of cream samples is simple, requires no sophisticated procedures, and produces excellent analyte recoveries, without the late precipitation of lipophilic compounds occurring in the procedures recommended by pharmacopoeias. The chromatographic method is accurate, precise and specific, and has the ability to separate the analyte from degradation products and excipients which are usually found in cream dosage forms. The analytical procedure has been successfully applied to the determination of miconazole in commercial bulk materials and cream preparations. In addition, the procedure can be applied to the analysis of aged samples to evaluate stability, and to formulations containing other active ingredients.

Acknowledgments

Financial support from Universidad Nacional del Litoral (Project CAI+D No. 12/B407) and Consejo Nacional de Investigaciones Científicas y Técnicas (CONICET) is gratefully acknowledged. The authors thank LAFORMED S.A. for providing drugs and pharmaceuticals.

References

[1] The United States Pharmacopeia, 30th ed., United States Pharmacopeia Convention, Rockville (2007).
[2] G. Piel, B. Evrard, M. Fillet, G. Llabres, L. Delattre, Int. J. Pharm. 169 (1998) 15.
[3] N.A. Nafee, F.A. Ismail, N.A. Boraie, L.M. Mortada, Int. J. Pharm. 264 (2003) 1.
[4] E. Ozyurt, M.B. Toykuliyeba, I.L. Danilyans, O. Morton, G. Baktir, Int. J. Gynecol. Obstet. 74 (2001) 35.
[5] British Pharmacopeia, The Stationary Office, London, UK (2007).
[6] P.Y. Khashba, S.R. El-Shabori, K.M. Emara, A.M. Mohamed, J. Pharm. Biomed. Anal. 22 (2000) 363.
[7] K. Wróbel, K. Wróbel, I.M. de la Garza Rodriguez, P.L. López de Alba, L. López Martinez, J. Pharm. Biomed. Anal. 20 (1999) 99.
[8] N. Erk, M. Levent-Altun, J. Pharm. Biomed. Anal. 25 (2001) 115.
[9] C. Akay, S.A. Ozkan, Z. Senturk, S. Cevheroglu, Il Fármaco 57 (2002) 953.
[10] A.A. Salem, H.A. Mossa, B.N. Barsoum, J. Pharm. Biomed. Anal. 41 (2006) 654.
[11] A.M. Di Pietra, V. Cavrini, V. Andrisano, R. Gatti, J. Pharm. Biomed. Anal. 10 (1992) 873.
[12] D. Bonazzi, V. Cavrini, R. Gatti, E. Boselli, M. Caboni, J. Pharm. Biomed. Anal. 18 (1998) 8235.
[13] A.A. Gaona-Galdos, P.L. García, M.S. Aurora-Prado, M.I.R.M. Santoro, E.R.M. Kedor-Hackmann, Talanta 77 (2008) 673.
[14] EURACHEM Guide: The Fitness for Purpose of Analytical Methods. A Laboratory Guide to Method Validation and Related Topics, EURACHEM Secretariat, Teddington (1998).
[15] CITAC/EURACHEM Guide: Guide to Quality in Analytical Chemistry, An Aid to Acreditation, EURACHEM Secretariat, Teddington (2002).
[16] IUPAC Technical Report, Pure Appl. Chem. 74 (5) (2002) 835.
[17] IUPAC Recommendations, Anal. Chim. Acta 391 (1999) 105.
[18] International Conference on Harmonization of Technical Requirements for the Registration of Pharmaceutical for Human Use: Validation of Analytical Procedures. Text and Methodology – Q2 (R1) (2005).
[19] FDA Guidance for Industry (draft): Analytical Procedures and Methods Validation (2000).
[20] FDA Guidance for Industry: Bioanalytical Method Validation (2001).
[21] C.F. Poole, The Essence of Chromatography, Elsevier, Amsterdam, 2003.
[22] International Conference on Harmonization for Stability Testing of New Drug Substances and Products – Q1A (R2) (2003).
[23] K. Danzer, L.A. Currie, Pure Appl. Chem. 70 (1998) 993.
[24] AOAC Peer-Verified Method Program, Manual on Policies and Procedures, Arlington, VA, USA (November 1993).
[25] M. Li, M. Mingxiang, A. Rustum, J. Pharm. Biomed. Anal. 48 (2008) 1451.

Talanta 79 (2009) 887–892

Contents lists available at ScienceDirect

Talanta

journal homepage: www.elsevier.com/locate/talanta

Determining the adulteration of spices with Sudan I-II-II-IV dyes by UV–visible spectroscopy and multivariate classification techniques

Carolina V. Di Anibal [a], Marta Odena [b], Itziar Ruisánchez [a], M. Pilar Callao [a,*]

[a] Department of Analytical and Organic Chemistry, Rovira i Virgili University, Marcel·lí Domingo s/n Campus Sescelades, E-43007 Tarragona, Spain
[b] Public Health Laboratory, C/M, Cristina No. 54, 43002 Tarragona, Spain

ARTICLE INFO

Article history:
Received 2 April 2009
Received in revised form 8 May 2009
Accepted 13 May 2009
Available online 22 May 2009

Keywords:
Sudan dyes
KNN
PLS-DA
SIMCA
Spices
Multivariate analysis

ABSTRACT

We propose a very simple and fast method for detecting Sudan dyes (I, II, III and IV) in commercial spices, based on characterizing samples through their UV–visible spectra and using multivariate classification techniques to establish classification rules. We applied three classification techniques: *K*-Nearest Neighbour (KNN), Soft Independent Modelling of Class Analogy (SIMCA) and Partial Least Squares Discriminant Analysis (PLS-DA). A total of 27 commercial spice samples (turmeric, curry, hot paprika and mild paprika) were analysed by chromatography (HPLC-DAD) to check that they were free of Sudan dyes. These samples were then spiked with Sudan dyes (I, II, III and IV) up to a concentration of 5 mg L^{-1}. Our final data set consisted of 135 samples distributed in five classes: samples without Sudan dyes, samples spiked with Sudan I, samples spiked with Sudan II, samples spiked with Sudan III and samples spiked with Sudan IV.

Classification results were good and satisfactory using the classification techniques mentioned above: 99.3%, 96.3% and 90.4% of correct classification with PLS-DA, KNN and SIMCA, respectively. It should be pointed out that with SIMCA, there are no real classification errors as no samples were assigned to the wrong class: they were just not assigned to any of the pre-defined classes.

1. Introduction

Sudan I (1-[(2,4-dimethylphenyl)azo]-2-naphthalenol), Sudan II (1-(phenylazo)-2-naphthol), Sudan III (1-(4-phenylazophenylazo)-2-naphthol) and Sudan IV (*o*-tolyazo-*o*-tolyazo-betanaphthol) are an azo-family of synthetic dyes that are widely used for colouring agents such as waxes, floor and shoe polishes. They are categorized as class 3 carcinogens by the International Agency for Research on Cancer (IARC) [1]. As a result, Sudan dyes are illegal as additives in foodstuffs destined for human consumption according to both the FSA (Food Standards Agency) [2] and the European Union. Unfortunately, in some countries, these dyes are still being used as additives in some foodstuffs to improve the colour for commercial benefits. Reports have indicated that high amounts of Sudan dyes, at least 1 g L^{-1}, are required to have an impact on visual colour [3].

Several methods have been proposed to detect the presence of some of these synthetic dyes in foodstuffs: for example, high performance liquid chromatography-diode array detection HPLC-DAD [4,5], gel permeation chromatography–mass spectrometry [6], pressurized capillary electrochromatography (CEC) with amperometric detection [7], HPLC with electrochemical detection [8], liquid chromatography–mass spectrometry [9–11], tandem mass spectroscopy and isotope dilution [12], multi-wall carbon nanotube-based electrochemical sensing [13], and the ELISA method [14]. Also, second order multivariate techniques that use a data matrix for each sample have been applied to determine Sudan I in chilly powder [15]. In most of these methods, time-consuming pre-separations are often needed, analysis is not so fast and the instrumentation is no so affordable.

Multivariate techniques have been successfully applied to the analysis of foodstuffs. Some recent papers on this issue are: the multivariate prototype approach for authenticating red wines [16], the classification of milks according to their origin [17], the authentication of salmon and salmon-based products [18], characterisation and discrimination among butters according to their fat content [19], the authentication and classification of olive oil [20–22], the classification of vinegar [23] and the classification of apple fruits and ciders [24,25].

In this study, we propose a very simple and fast method for detecting Sudan dyes in commercial spices, based on characterizing samples through their UV–visible spectra and using multivariate classification techniques to establish classification rules. Five classes are considered: class 1: samples without Sudan dyes, class 2: samples spiked with Sudan I, class 3: samples spiked with Sudan II, class 4: samples spiked with Sudan III, and class 5: samples spiked with Sudan IV. Therefore, an unknown sample (the possible Sudan dye content of which is unknown) is assigned to one of the five classes considered in this study.

* Corresponding author. Tel.: +34 977558199; fax: +34 977558446.
E-mail address: mariapilar.callao@urv.cat (M.P. Callao).

0039-9140/$ – see front matter © 2009 Elsevier B.V. All rights reserved.
doi:10.1016/j.talanta.2009.05.023

Table 1
Type of errors made according to the decision taken satisfying the accomplishment of a null hypothesis.

	H_0 TRUE	H_0 FALSE
Statistical decision: reject H_0	*Type I error*	*Correct decision*
Statistical decision: do not reject H_0	*Correct decision*	*Type II error*

First of all, we applied an exploratory analysis based on the well-known principal component analysis (PCA) technique [26,27] in order to detect natural sample grouping with no previous information. Then, we applied classification techniques, both hard (discriminating) and soft (modelling) techniques. In the first, the hyperspace is divided in as many regions as the number of existing classes so, if a sample falls in the region of space corresponding to a particular class; it is classified as belonging to only this class. In the last, frontiers are built between each class and the rest of the space [28], modelling each class separately. The decision rule for a given class is a class box that envelopes the position of the class and an object can be assigned in more than one class or not assigned to a class [29]. We applied *K*-Nearest Neighbours (KNN) [30,31], Soft Independent Modelling of Class Analogy (SIMCA) [32,33] that is a soft classification technique and Partial Least Squares Discriminant Analysis (PLS-DA) that are hard classification techniques. PLS-DA is a variant of PLS [34] in which instead of predicting a quantitative parameter a qualitative assignation (class) is done [35–37].

We are dealing with a contamination problem, so it is important to consider the type of classification error because the associated cost and practical implications are different. From a practical point of view, then, stating that a sample does not contain Sudan dye when it does is not the same as stating that a sample contains Sudan dye when it does not. In this scenario, we will present the results on the basis of the following null hypothesis, H_0: "Sample does not contain Sudan dye". Therefore, as is shown in Table 1, type I and type II errors will be studied when each classification technique is applied. Type I errors might have economic implications as samples will be removed from the market with no real need. The consequences of type II errors are worse as they involve a health risk: consumers will buy samples contaminated with Sudan dye. Type I and II errors are related with sensitivity and specificity [38].

To the best of our knowledge, the one-step determination of the four Sudan dyes on the basis of their UV–visible spectra and multivariate classification has yet to be reported.

2. Experimental

2.1. Reagents and samples

Table 2 shows the chemical structure of the four Sudan dyes. It can be seen that all four Sudan dyes have some common structure but that Sudan III and IV have an additional azo and benzene group. Also, Sudan II and IV have two methyl groups more than Sudan I and III. The Sudan I standard was purchased from ACROS (Geel, Belgium) and the other Sudan dyes were purchased from SIGMA (St. Louis, MO, USA). A total of 27 spices from different commercial trade were purchased from markets. Acetonitrile and chloroform (for HPLC and UV–visible analysis) and acetic acid (for HPLC) were all of HPLC grade.

Samples contaminated with Sudan dye were obtained from the non-contaminated samples. To prepare the working solutions that were to be used to spike the commercial spices, appropriate amounts of Sudan I, II, III and IV were diluted in acetonitrile. Sudan III and Sudan IV were initially dissolved in a small fraction of chloroform and then diluted with acetonitrile.

The samples to be analysed, either by HPLC or UV–visible, followed an extraction process: one gram of sample was weighed and

Table 2
Chemical structure of Sudan dyes.

Dye	Structure
Sudan I	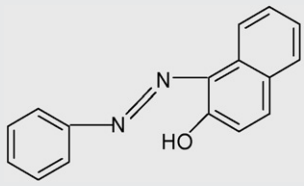
Sudan II	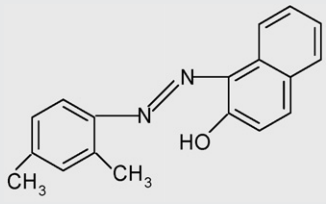
Sudan III	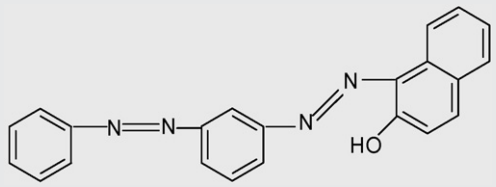
Sudan IV	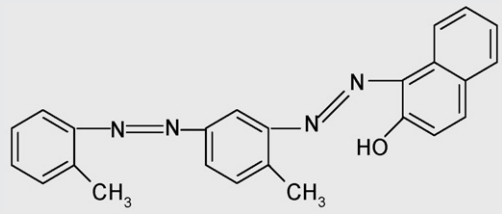

50 mL of acetonitrile was added. The sample was extracted with magnetic stirring. Each extract was obtained by filtering twice, first with glass microfibre filters and then with syringe filters. In order to obtain the UV–visible spectra, a volume of this extract (350 μL for mild and hot paprika, 300 μL for curry and 70 μL for turmeric) was spiked with the appropriate amount of one Sudan dye in such a way that the final concentration was 5 mg L^{-1}. Table 3 contains the list of the commercial samples analysed, the corresponding spiked samples and the numbers assigned to them all.

2.2. Apparatus and software

The HPLC is a Varian Star (Varian Inc., USA) model equipped with the following modules: a Prostar 240 pump; a Prostar 410 automatic injector and a Prostar 335 diode array detector (DAD). The relevant parameters were: column, Agilent Zorbax ODS (Agilent Technologies, USA) 250 mm × 4.6 mm (5 μm particle size); mobile phase, acetonitrile/acid acetic 16% (70:30, v/v) in gradient mode; flow rate 1.0 mL min^{-1}; temperature 40 °C. Photometric detection was performed at 478 nm for Sudan I and 510 nm for Sudan II, III and IV. The software used was the STAR 6.41 Chromatography Workstation.

The UV–visible spectrophotometer (Agilent 8453, United States) was equipped with a diode array detector (DAD). UV–visible spectrum scanning was carried out in the wavelength range of 260–600 nm (each nm) which represents 340 variables.

The data measured was processed with Matlab 6.5 software (Version 6.5, The Math Works Inc., Natick, USA) and PLS Toolbox 3.5 (Eigenvector Research Incorporated). Data was pre-processed with mean centering before each chemometric treatment.

Table 3
Description of the samples studied: commercial name and assigned number.

Spice	Commercial Trade	Original and spiked spices				
		Original	Sudan I	Sudan II	Sudan III	Sudan IV
Turmeric	Hacendado	1	28	55	82	109
	Jugosan	2	29	56	83	110
	Corbella	3	30	57	84	111
	Non-branded	4	31	58	85	112
	Non-branded	5	32	59	86	113
Curry	Eroski	6	33	60	87	114
	Carmencita	7	34	61	88	115
	Bonpreu	8	35	62	89	116
	Caprabo	9	36	63	90	117
	Hacendado	10	37	64	91	118
	Dia	11	38	65	92	119
Mild paprika	Carmencita	12	39	66	93	120
	Bonpreu	13	40	67	94	121
	Caprabo	14	41	68	95	122
	Hacendado	15	42	69	96	123
	Carrefour	16	43	70	97	124
	"De la Vera" Carrefour	17	44	71	98	125
	Dani	18	45	72	99	126
	Gourmet	19	46	73	100	127
Hot paprika	Eroski	20	47	74	101	128
	Carmencita	21	48	75	102	129
	Bonpreu	22	49	76	103	130
	Caprabo	23	50	77	104	131
	Hacendado	24	51	78	105	132
	Dani	25	52	79	106	133
	Gourmet	26	53	80	107	134
	"De la Vera" El Reu	27	54	81	108	135

3. Results and discussion

Fig. 1a and b show, respectively, the spectra of a standard solution of the four Sudan dyes at 5 mg L^{-1} and one spectrum for each of the four spices studied (turmeric, curry, hot paprika and mild paprika), randomly chosen. It can be seen that the spectra of the four Sudan dyes have different shapes although there is considerable overlap. Sudan I and Sudan II (as well as Sudan III and Sudan IV) have similar spectra according to their chemical structure. Mild and hot paprika present similar spectra shape at the same wavelength interval, as do turmeric and curry but with a slight blue-shift of the absorption peak.

Fig. 2a and b show the HPLC chromatograms of a mixture of the four Sudan standards and a random paprika sample, respectively. It should be pointed out that all paprika samples have similar behaviour. Sudan I, II and IV are not present in the sample analysed as there is no chromatographic peak at the expected retention time. There is some uncertainty, however, about the presence of Sudan III in the paprika samples as the sample chromatogram has a peak at its expected retention time. When turmeric and curry samples are

Table 4
SIMCA model details: number of principal components (PC's) and percentage of correct classifications and predictions. The values corresponding to the no. of PC's chosen for each model are shown in bold.

	No. of principal components	Classification ability	Prediction ability
Class 1: unspiked spices	1	88.9	85.2
	2	96.3	81.5
	3	**96.3**	**92.6**
	4	96.3	85.2
Class 2: spices spiked with Sudan I	1	37.0	18.5
	2	**92.6**	**85.2**
	3	92.6	85.2
Class 3: spices spiked with Sudan II	1	18.5	7.4
	2	92.6	85.2
	3	96.3	85.2
	4	**96.3**	**88.9**
	5	96.3	88.9
Class 4: spices spiked with Sudan III	1	33.3	18.5
	2	92.6	88.9
	3	92.6	85.2
	4	**96.3**	**96.3**
	5	96.3	92.6
Class 5: spices spiked with Sudan IV	1	29.6	29.6
	2	**92.6**	**88.9**
	3	92.6	88.9

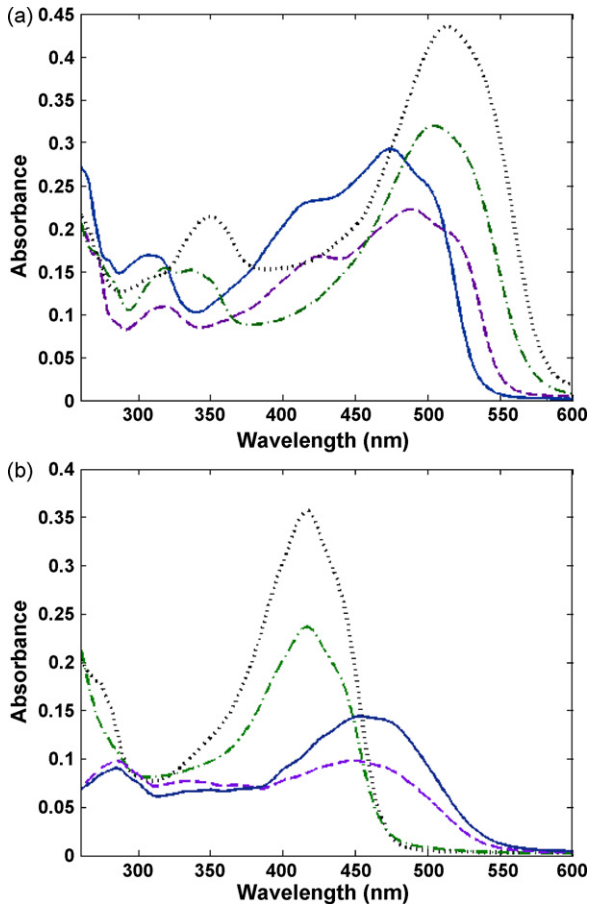

Fig. 1. (a) UV–visible spectra of Sudan I, II, III and IV at 5 ppm (mg L^{-1}). Sudan I (solid line), Sudan II (dashed line), Sudan III (dotted-dashed line) and Sudan IV (dotted line). (b) UV-visible spectra of turmeric sample (dotted line), curry sample (dashed-dotted line) hot paprika sample (solid line) and mild paprika sample (dashed line).

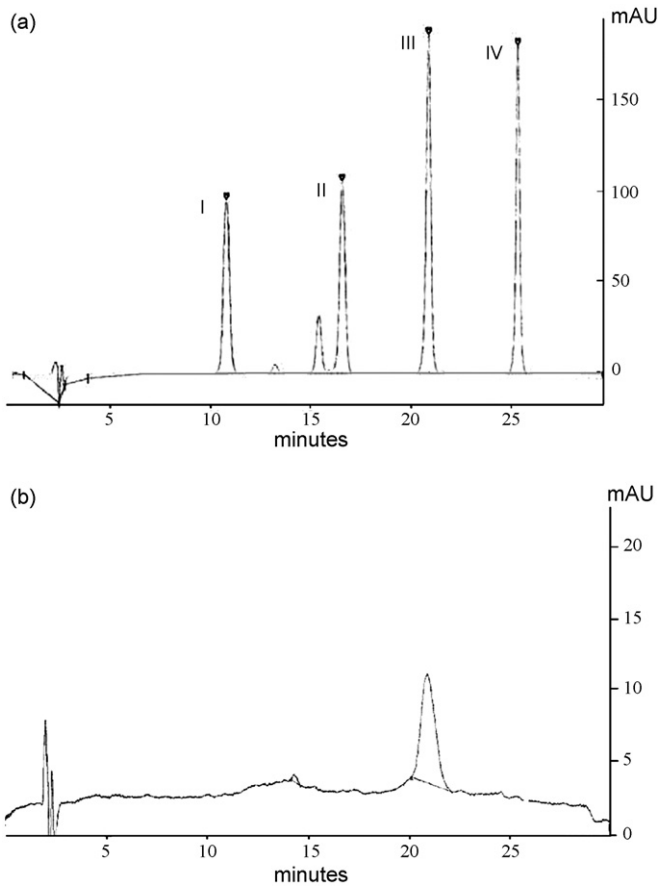

Fig. 2. (a) Chromatogram of Sudan standard dyes at 5 mg L^{-1}. (b) Chromatogram of mild paprika (sample no. 15).

analysed, there is only one chromatographic peak but its retention time is lower than that of the peaks associated with any of the four Sudan dyes. In this case, these samples are free of any kind of Sudan.

First of all, an exploratory analysis of the 135 UV–visible spectra corresponding to samples indicated in Table 3 was made by principal component transformation. The PCA score plot is shown in Fig. 3, with 86.13% of the total variance explained by the first two principal components. The plot shows that samples that do not contain Sudan are well separated from those that do, with the exception of samples no. 17 and no. 27 which overlap the samples that contain Sudan II. These samples are a special variety of mild and hot paprika called "De la Vera". It should be stressed that none of the samples without Sudan are placed in the group of samples that contain Sudan III, which indicates that, as expected, the commercial samples analysed do not contain Sudan III.

The samples spiked with the Sudan dyes tended to be grouped according to the type of dye they contain, but the different classes are not clearly separated. Also, in each of the five classes considered, there is a grouping corresponding to the type of spice. So, in the case of samples without Sudan, curries (no. 6–11) and turmeric (no. 1–5) are spread along PC2, and have similar PC1 score values, whereas the group corresponding to mild (no. 12–19) and hot paprika (no. 20–27) are more compact and have similar PC2 score values. Likewise, samples spiked with the four Sudan dyes have a similar behaviour that is translated linearly to the different classes.

KNN, SIMCA and PLS-DA were used to make the classifications to the five categories. The models built during the study were validated using the leave-one-out cross validation approach [39].

The KNN classification rule is based on the similarity between neighbours calculated from the Euclidean distance. Therefore, an unknown sample is classified to the class to which belongs the majority of k neighbours closer to it. The classification percentage for each class is the parameter used to determine how many neighbours (k) need to be considered. The results were best when five neighbours were considered. The only exception was class 1 (sam-

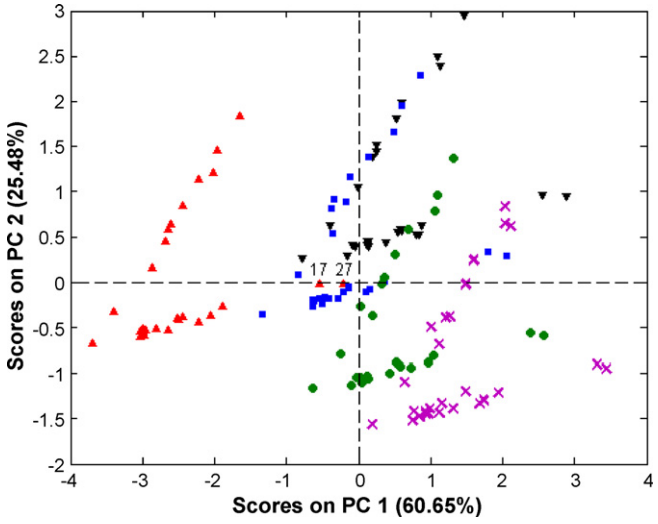

Fig. 3. Score plot of commercial unspiked samples (triangles up) and samples spiked at 5 mg L^{-1} with Sudan I (triangles down), Sudan II (squares), Sudan III (circles) and Sudan IV (crosses).

Table 5
PLS-DA model details: number of latent variables (LV's), percentage of cumulative variance for the X and Y block and prediction ability. The values corresponding to the number of LV's chosen are shown in bold.

No. of LV	% Cumulative variance		Prediction ability				
	X-block	Y-block	Class 1	Class 2	Class 3	Class 4	Class 5
1	60.10	16.15	92.6	11.1	81.5	44.4	85.1
2	84.01	30.02	92.6	81.5	70.4	81.5	92.6
3	96.41	36.97	92.6	96.3	77.8	81.5	100
4	99.14	41.75	100	96.3	77.8	71.4	100
5	99.58	57.25	100	96.3	85.2	81.5	100
6	**99.79**	**69.94**	**100**	**100**	**96.3**	**100**	**100**
7	99.79	78.59	100	100	96.3	100	100

ples without Sudan dyes) in which the classification results were best with three neighbours. So $K = 5$ was always considered for all the classes in the classification step.

Similarly, the number of principal components required to build the SIMCA model in each of the five pre-defined classes, is determined by the maximum prediction ability. Table 4 shows the details of the SIMCA model for each class and the number of PC's retained for each class are indicated in bold.

The SIMCA approach enables the T^2 Hotelling and Q statistics to be studied. T^2 gives a measure of the fit of each sample to the obtained model, while Q is a measure of the residuals, and is therefore related to the sample information not included in the model. The T^2 and Q limits allow establishing the sample relation with the model [40]. In the five classes studied, some samples are out of the limits of T^2: samples no. 27 for class 1, no. 44 and no. 54 for class 2, and no. 125 and no. 135 for class 5 and some samples are out the limits of Q: no. 1 for class 1, no. 33 for class 2, no. 60 and 77 for class 3, no. 87 for class 4, and no. 114 for class 5. Sample no. 62 is at the limit of the class to which it belongs (class 3). Finally, almost all samples belonging to class 3 (samples which contain Sudan II), are close to the limits of class 2 (samples which contain Sudan I).

According to the best prediction ability (see Table 5), the PLS-DA model was performed using six latent variables. The PLS-DA model consists of building a conventional PLS model, but with class indicator variables as Y matrix. PLS-DA is carried out using an exclusive binary coding scheme with one bit per class, so to discriminate between five classes, a response encoded {1, 0, 0, 0, 0} means that the sample belongs to class 1, to discriminate between five classes, a response and a response encoded {0, 1, 0, 0, 0} means that the sample belongs to class 2, and so on. During the modelling process, the PLS-DA method is trained to compute the five "membership values", one for each class. The class assignment result is expressed in terms of a value that is normally distributed around 0 when the prediction is that the sample is not in a class and around 1 when the prediction is that it is in a class. For this reason it is possible to obtain prediction values below 0 (negative values) and also above 1.

PLS-DA uses the distribution of calibration-sample predictions to determine a threshold value based on the Bayes theorem, which will best split those classes with the least probability of false classifications for future predictions. It is assumed that the predicted values for each class are approximately normally distributed. From this distribution the probability of a sample to belong to each class is calculated and is then assigned to the class that has the highest probability value.

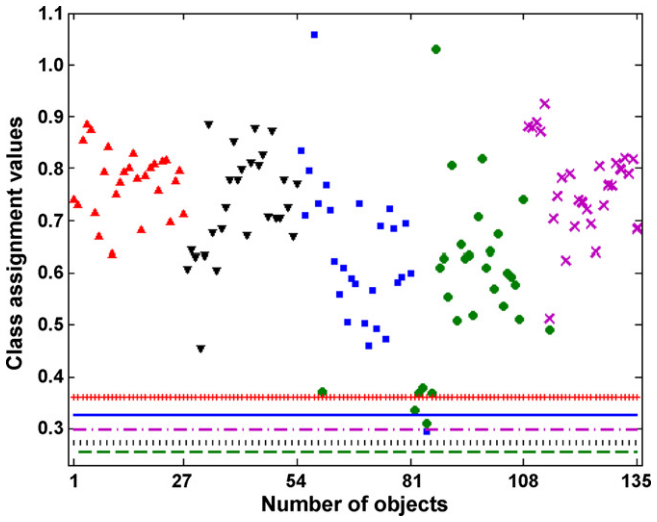

Fig. 4. Assigned class values vs objects number according to Table 3. Class 1, samples without Sudan dyes (triangles up); class 2, samples spiked with Sudan I (triangles down); class 3, samples spiked with Sudan II (squares); class 4, samples spiked with Sudan III (circles); class 5, samples with Sudan IV (crosses). Threshold values: class 1 (vertical dashed line); class 2 (dotted line); class 3 (solid line); class 4 (dashed line); and class 5 (dotted-dashed line).

Fig. 4 shows the PLS-DA assigned values for each sample and the threshold value for each class (presented as horizontal lines). For the sake of clarity, only samples with an assignation value higher than a threshold value are depicted. According to those values, there are two samples assigned to more than one class. One is sample no. 85 (non-branded turmeric spiked with Sudan III), which belongs to class 4 and it is assigned to its own class and to class 3. In that case, the probability values are 88% and 52%, respectively, so this sample is considered as belonging to class 4. The other is sample no. 114 (Curry Eroski spiked with Sudan IV), which belongs to class 5 and it is assigned to its own class and to class 4. In that case, the probability values are 100% and 98%, respectively, so, assignation to only one of the predefined classes is not possible. Finally, sample 60 (Curry Eroski spiked with Sudan II), which belongs to class 3 has an assignation value above the threshold value for class 4 and the probability value is 89%, so it is wrongly assigned as belonging to class 4.

Table 6
Class assignment for each sample with KNN, SIMCA and PLS-DA. Wrongly and not assigned samples are indicated in bold.

	Assignment to class 1	Assignment to class 2	Assignment to class 3	Assignment to class 4	Assignment to class 5	Samples not assigned to any class
PLS-DA	1–27	28–54	55–59, 61–81	82–108, **60**	109–135	–
KNN	1–16, 18–26	28–30, 32–54, **65**, **71**	55–64, 66–70, 72–81, **17**, **27**, **31**	82–108	109–135	–
SIMCA	2–26	28–30, 32, 34, 35–43, 45–53	55–59, 61, 63–76, 78–81	82–86, 88–108	109–113, 115–124, 126–134	**1**, **27**, **31**, **33**, **44**, **54**, **60**, **62**, **77**, **87**, **114**, **125**, **135**

Finally, Table 6 shows the class assignments for each sample when the three classification techniques are used. The wrongly classified samples are shown in bold. The sample numbers are the same as the ones in Table 3.

From the results, several overall conclusions can be drawn: (a) no samples containing Sudan dye (samples in classes 2–5) are assigned to class 1 (samples that do not contain Sudan dye). This is of great importance from the point of view of the type of error, which will be discussed later; (b) the SIMCA approach does not assign any samples to the wrong class, although it does not assign 13 samples to any class at all. In our opinion this is a clear advantage over the other classification techniques (KNN, for instance, will always assign a sample to one of the predefined classes; (c) the classification results, in terms of classification percentage, were best with the PLS-DA approach (only sample no. 60 was wrongly assigned).

Another general trend is that all samples spiked with Sudan dye from the non-contaminated Curry sample called "Eroski" (samples no. 33, no. 60, no. 87 and no. 114) were not assigned to any class when the SIMCA approach was used. Sample no. 60 (which contains Sudan II) was wrongly assigned when the PLS-DA approach was used. With the mild and hot paprika samples called "De la Vera", the original and some spiked samples are not assigned or wrongly assigned. This might be due to a special behaviour or sample composition. For the other wrongly assigned samples, no general trends are observed.

From the point of view of the null hypothesis, H_0 ("The analysed sample is not contaminated. It does not contain Sudan") and based on Table 1, the following situations have to be discussed. The null hypothesis was rejected when it was true for two samples when using the KNN approach (no. 17 and no. 27), two samples when using SIMCA (no. 1 and no. 27) and no samples when using PLS-DA approach. So with the first two techniques, type I error is 7.4%. From a practical point of view, the normal procedure with samples that are detected as contaminated is to submit them to a confirmatory analysis (in our case HPLC-MS). This means additional time and cost. In our particular case, the key error is type II error, which means that the sample is said to be not contaminated, that it does not contain Sudan, when it does. Our results show that we have 0% of type II error, which is important because no confirmatory method will ever be applied.

4. Conclusions

The use of UV–visible spectroscopy with multivariate classification techniques is a simple and inexpensive methodology for determining the possible contamination of foodstuffs, such as culinary spices, with Sudan dyes I–IV.

Considering the null hypothesis approach, the consequences of wrongly assigning a contaminated sample as non-contaminated (type II error) might involve a health risk. It should be pointed out that the results are extremely positive as no wrong assignments are made whenever one of the three classification techniques is applied.

A comparison between the three classification techniques shows that the results were best with PLS-DA, as only one sample was wrongly assigned. What is more, this wrong assignment involves no health or economic risk as it is a contaminated sample assigned to a different group of contaminated samples. The KNN and SIMCA approaches assign some non-contaminated samples as contaminated. Finally, three contaminated samples are wrongly assigned by KNN because of a mistaken Sudan assignation. The SIMCA approach does not assign some samples to any class. In these cases a confirmatory method would be required.

When the paprika samples without Sudan dyes (class 1) were subject to chromatographic analysis, it could not be stated whether Sudan III was present or not (class 4). With the proposed methodology, however, it is clear that Sudan III is not present because no samples without Sudan are within or close to the samples that contain Sudan III.

Acknowledgments

The authors would like to thank the Spanish Ministry of Education, Culture and Sports (Project CTQ2007-61474/BQU) for economic support, and the Management Agency for University and Investigation Support of the Catalan Government for providing Carolina Di Anibal's doctoral fellowship.

References

[1] IARC, Monographs on the Evaluation of the Carcinogenic Risk of Chemical to Man: Some Aromatic Azo Compounds, Vol. 8, International Agency for Research on Cancer, Lyon, France, 1975, pp. 224–231.
[2] http://www.food.gov.uk/foodindustry/guidancenotes/foodguid/sudanguidance.
[3] http://www.astaspice.org/pubs/sudanwhitepaper.pdf.
[4] M. Mazzetti, R. Fascioli, I. Mazzoncini, G. Spinelli, I. Morelli, A. Bertoli, Food Additives & Contaminants, Part A 21 (2004) 935–941.
[5] M. Ma, X. Luo, B. Chen, S. Su, S. Yao, Journal of Chromatography A 1103 (2006) 170–176.
[6] H. Sun, F. Wang, L. Ai., Journal of Chromatography A 1164 (2007) 120–128.
[7] L. Shaofeng, Z. Xue, L. Xucong, W. Xiaoping, F. Fengfu, X. Zenghong, Electrophoresis 28 (2007) 1696–1703.
[8] O. Chailapakul, W. Wonsawat, W. Siangproh, K. Grudpan, Y. Zhao, Z. Zhu, Food Chemistry 109 (2008) 876–882.
[9] H. Limin, S. Yijuan, F. Binghu, S. Xiangguang, Z. Zhenling, L. Yahong, Analytica Chimica Acta 594 (2007) 139–146.
[10] O. Pardo, V. Yusà, N. León, A. Pastor, Talanta 78 (2009) 178–186.
[11] M.R.V.S. Murty, N. Sridhara Chary, S. Prabhakar, N. Prasada Raju, M. Vairamani, Food Chemistry 115 (2009) 1556–1562.
[12] L. Di Donna, L. Maiuolo, F. Mazzotti, D. De Luca, G. Sindona, Analytical Chemistry 76 (2004) 5104–5108.
[13] T. Gan, K. Li, K. Wu, Sensors and Actuators B 132 (2008) 134–139.
[14] Y. Wang, D. Wei, H. Yang, Y. Yang, W. Xing, Y. Li, A. Deng, Talanta 77 (2009) 1783–1789.
[15] Y. Jintao, L. Lifu, L. Yingwu, D. Changai, H. Bo, Analytica Chimica Acta 607 (2008) 160–167.
[16] S. Preys, E. Vigneau, G. Mazerolles, V. Cheynier, D. Bertrand, Chemometrics and Intelligent Laboratory Systems 87 (2007) 200–207.
[17] P. Ciosek, W. Wróblewski, Talanta 76 (2008) 548–556.
[18] S. Masoum, C. Malabat, M. Jalali-Heravi, C. Guillou, S. Rezzi, D.N. Rutledge, Analytical and Bioanalytical Chemistry 387 (2007) 1499–1510.
[19] B. Jaillais, V. Morrin, G. Downey, Chemometrics and Intelligent Laboratory Systems 86 (2007) 179–188.
[20] M. Casale, C. Casolino, G. Ferrari, M. Forina, Journal of Near Infrared Spectroscopy 16 (2008) 39–47.
[21] F. Fernandes Gambarra-Neto, G. Marino, M.C. Ugulino Araújo, R. Kawakami Harrop Galvão, M.J. Coelho Pontes, E.P. de Medeiros, R. Sousa Lima, Talanta 77 (2009) 1660–1666.
[22] M. Casale, C. Armanino, C. Casolino, M. Forina, Analytica Chimica Acta 589 (2007) 89–95.
[23] M. Casale, C. Armanino, C. Casolino, C. Oliveros, M. Forina, Food Science and Technology Research 12 (2006) 223–230.
[24] R.M. Alonso-Salces, C. Herrero, A. Barranco, L. Berrueta, B. Gallo, F. Vicente, Food Chemistry 93 (2005) 113–123.
[25] R.M. Alonso-Salces, S. Guyot, C. Herrero, L. Berruela, J. Drilleau, B. Gallo, F. Vicente, Food Chemistry 91 (2005) 91–98.
[26] D.L. Massart, B.G.M. Vandeginste, L.M.C. Buydens, S. De Jong, P.J. Lewi, J. Smeyers-Verbeke, Handbook of Chemometrics and Qualimetrics, Part A, Elsevier, Amsterdam, 1997.
[27] R.G. Berenton, Chemometrics: Data Analysis for the Laboratory and Chemical Plant, John Wiley & Sons, Chichester, 2003.
[28] D. González-Arjona, A.G. González, Analytica Chimica Acta 363 (1998) 89–95.
[29] M.P. Derde, D.L. Massart, Mikrochimica Acta II (1986) 139–152.
[30] R. Duda, P. Hart, D. Stork, Pattern Classification, 2nd ed., John Wiley & Sons, New York, 2001.
[31] W. Wu, D. Massart, Analytica Chimica Acta 349 (1997) 253–261.
[32] B.G.M. Vandeginste, D.L. Massart, L.M.C. Buydens, S. De Jong, P.J. Lewi, J. Smeyers-Verbeke, Handbook of Chemometrics and Qualimetrics, Part B, Elsevier, Amsterdam, 1998.
[33] S. Wold, M. Sjöström, in: B.R. Kowalski (Ed.), ACS Symposium Series No. 52, American Chemical Society, Washington, DC, 1977.
[34] P. Geladi, B. Kowalski, Analytica Chimica Acta 185 (1986) 1–17.
[35] F. Liu, Y. He, L. Wang, Analytica Chimica Acta 615 (2008) 10–17.
[36] M. Barker, W. Rayens, Journal of Chemometrics 17 (2003) 166–173.
[37] K. Hovde Liland, U. Geir Nidal, Journal of Chemometrics 23 (2009) 7–18.
[38] M.C. Ortiz, L. Sarabia, R. García-Rey, M.D. Luque de Castro, Analytica Chimica Acta 558 (2006) 125–131.
[39] M. Stone, Journal of the Royal Statistical Society B 36 (1974) 111–147.
[40] A. Rius, M.P. Callao, F.X. Rius, Analyst 122 (1997) 737–741.

Talanta 79 (2009) 734–738

Contents lists available at ScienceDirect

Talanta

journal homepage: www.elsevier.com/locate/talanta

Speciation of selenomethionine and selenocystine using online micro-column containing Cu(II) loaded nanometer-sized Al_2O_3 coupled with ICP-MS detection

Jiankun Duan, Bin Hu*

Department of Chemistry, Wuhan University, Wuhan 430072, China

ARTICLE INFO

Article history:
Received 15 December 2008
Received in revised form 24 April 2009
Accepted 29 April 2009
Available online 7 May 2009

Keywords:
Selenized yeast
Human urine and serum
Cu(II) loaded nanometer-sized Al_2O_3
Selenomethionine
Selenocystine
ICP-MS

ABSTRACT

A flow injection online speciation procedure by using micro-column packed with Cu(II) loaded nanometer-sized Al_2O_3 coupled to inductively coupled plasma mass spectrometry (ICP-MS) for the separation and determination of selenomethionine (SeMet) and selenocystine ($SeCys_2$) has been developed. The main factors affecting the separation and preconcentration of SeMet and $SeCys_2$ including pH value, sample flow rate, eluent concentration, eluent volume and flow rate, and interfering ions have been investigated. It was found that $SeCys_2$ could be selectively retained by micro-column packed with Cu(II) loaded nanometer-sized Al_2O_3 at pH 4.0, and the retained $SeCys_2$ could be eluted by 1.0 mol L^{-1} HNO_3, while SeMet was not retained and passed through the micro-column directly at this pH. Both SeMet and $SeCys_2$ could be quantitatively adsorbed by the micro-column at pH 9.0, and the retained SeMet and $SeCys_2$ could be easily eluted with 1.0 mol L^{-1} HNO_3. The content of SeMet was obtained by subtracting the $SeCys_2$ from the total content of seleno amino acids. With the enrichment factor of 7.8 and 7.7, the limits of detection (LODs) for SeMet and $SeCys_2$ were found to be 24 pg Se mL^{-1} and 21 pg Se mL^{-1}, respectively. The relative standard deviations (RSDs) for $SeCys_2$ and SeMet with seven replicate determinations of 1.0 ng mL^{-1} SeMet and $SeCys_2$, were 2.1% and 1.6%, respectively, the sampling frequency of 8 h^{-1} was obtained. The proposed method was applied to the speciation of SeMet and $SeCys_2$ in selenized yeast, human urine and serum with satisfactory results.

1. Introduction

Selenium (Se) is an essential nutrient in a very narrow concentration range [1]. Dietary studies have shown that selenium in amino acids is absorbed more readily by the body than its inorganic species. Organo seleno compounds, mainly seleno amino acids, were widely existed in biological samples [2]. One of the seleno amino acids, selenocysteine (SeCys), the 21st essential amino acid, is considered to be biologically active, in contrast to the other major form, selenomethionine (SeMet), which can replace methionine to participate in the synthesis of protein [3]. The biological and toxicological effects of selenium are strongly dependent on its chemical forms ("species"). Therefore, interest in the differentiation of selenium species (inorganic and organic) is increasing, either in foodstuff and supplements, or in body fluids such as serum and urine.

The general methods for the selenium speciation are based on combining a very efficient separation technique with a sensitive detection technique. In order to avoid the interference of sulfur-containing amino acids due to their similarity to seleno amino acids, elemental specific detectors, such as atomic emission spectrometry (AES) [4], atomic absorption spectrometry (AAS) [5], atomic fluorescence spectrometry (AFS) [6] and inductively coupled plasma mass spectrometry (ICP-MS) [7] have been commonly used to detect seleno amino acids. Of all these elemental specific detection methods, ICP-MS has been increasingly widespread in selenium speciation because of its several advantages for selenium speciation analysis over more traditional detectors, including multi-element and multi-isotope detection and high sensitivity with a wide linear dynamic range.

Numerous separation methods including liquid chromatography (LC) [8–11], gas chromatography (GC) [12,13], capillary electrophoresis (CE) [14,15] and solid phase extraction (SPE) [16–19], have been utilized for speciation of seleno amino acids. Analysis of seleno amino acids by GC requires derivatization of the carboxylic and amino groups in order to increase their volatility using some derivatization reagents, such as chloroformate, etc. [12,13]. HPLC in conjunction with various elemental-selective detectors (especially ICP-MS) is one of the most used techniques for the speciation of seleno amino acids, and the limits of detection (LODs) are typically at the levels of nanogram per milliliter or sub nanogram per milliliter. CE is a good alternative for the speciation of seleno amino acids, but it suffered from the insufficient sensitivity when it was used for real world sample analysis. Compared to

* Corresponding author. Fax: +86 27 68754067.
E-mail address: binhu@whu.edu.cn (B. Hu).

0039-9140/$ – see front matter © 2009 Elsevier B.V. All rights reserved.
doi:10.1016/j.talanta.2009.04.063

Table 1
Optimum operating conditions for ICP-MS.

Plasma	
Rf power	1200 W
Plasma gas flow rate	15 L min^{-1}
Carrier gas flow rate	1.08 L min^{-1}
Sampling depth	7.0 mm
Sampler/skimmer diameter orifice	Nickel 1.0 mm/0.4 mm
Time-resolved data acquisition	
Scanning mode	Peak-hopping
Dwell time	0.1 s
Points per spectral peak	1
Isotopes	^{77}Se, ^{82}Se

chromatographic methods, SPE possessed some special merits like easy to operate, time saving, reduced solvent utilization and low cost. Unfortunately, SPE methods for separation/preconcentration of organo seleno compounds are scarce. Preconcentration of four seleno amino acids (SeMet, selenoethionine (SeEth), selenocystine ($SeCys_2$), selenocystamine (SeCysta)) on a porous graphitic carbon column was obtained by Abbas-Ghaleb et al. [20], however, the separation of seleno amino acids in this method was achieved by HPLC. Latva et al. [19] separated SeMet from inorganic selenium with metal-loaded activated charcoals. Huang et al. [16] have developed a novel, fast, and cheap non-chromatographic method for speciation of dissolved inorganic and organic selenium species in environmental and biological samples by flow injection (FI) dual-column preconcentration/separation on-line coupled with ICP-MS determination. These results demonstrated that SPE was a good alternative for separation/preconcentration of seleno amino acids. Besides, considering the same functional groups (amino and carboxyl groups) existing in seleno and conventional amino acids, some other methods for preconcentration conventional amino acids are supposed to be adopted for seleno amino acids.

It is reported that Cu(II) can form stable complexes with seleno amino acids [21] as well as can be easily adsorbed on the surface of nanometer-sized Al_2O_3 [22]. In view of that, the aim of this work was to achieve online preconcentration and separation of SeMet and $SeCys_2$ using Cu(II) loaded nanometer-sized Al_2O_3 coupled to ICP-MS and apply the proposed method to the determination of SeMet and $SeCys_2$ in real samples.

2. Experimental

2.1. Instrumentation

An Agilent 7500a ICP-MS (Agilent Technologies, Takatura, Japan) system with Babington nebulizer was used for the determination of target analytes. The optimum operation conditions were summarized in Table 1. ^{77}Se and ^{82}Se were monitored, but only isotope ^{82}Se was used for quantification in this work. The pH values were controlled with a Mettler Toledo 320-S pH meter (Mettler Toledo Instruments Co. Ltd., Shanghai, China) supplied with a combined electrode. An IFIS-C flow injection system (Ruimai Tech. Co. Ltd., Xi'an, China) and a self-made PTFE micro-column (20 mm × 2.0 mm i.d.) packed with nanometer-sized Al_2O_3 were used in the online separation/preconcentration process. A minimum length of PTFE tubing with an i.d. of 0.5 mm was used for all connections in order to minimize the dead volume.

2.2. Standard solution and reagents

All reagents used were of highest purity or at least analytical reagent grade. The stock standard solutions (1.000 mg Se mL^{-1}) were prepared by dissolving 62.1 mg of DL-selenomethionine and 52.9 mg L-selenocystine (Acros Organics, Geel, Belgium) in 25 mL of high-purity de-ionized water and 0.01 mol L^{-1} hydrochloride, respectively. Work solutions were prepared daily by stepwise dilution of their stock solutions with high-purity de-ionized water. High-purity de-ionized water obtained by Milli-Q system (18.2 MΩ cm, Millipore, Molsheim, France) was used throughout the whole experiments. Nanometer-sized Al_2O_3 was prepared in our laboratory, and the details on its synthesis and characterization were described in Ref. [23].

2.3. Column preparation and experimental procedure

50 mg of nanometer-sized Al_2O_3 was filled into a PTFE micro-column (20 mm × 2.0 mm i.d.) plugged with a small portion of degreased cotton at both ends. The schematic diagram was shown in Fig. 1, as described in Ref. [22].

Before use, 0.1 mol L^{-1} NaOH and high-purity de-ionized water were passed through the column (1 mL min^{-1}) in sequence in order to clean and condition it. Then, 1.0 mol L^{-1} $CuSO_4$ solution and high-purity de-ionized water was sequentially passed through the column (1 mL min^{-1}) to modify the surface of the nanometer-sized Al_2O_3. The sample solution was divided into two portions; one was adjusted to pH 4.0, and the other to pH 9.0. For the determination of $SeCys_2$ (C_1), sample solution with pH 4.0 was passed through the column, the retained $SeCys_2$ on the micro-column was eluted with HNO_3 and the eluent was directly introduced into ICP-MS for determination of selenium. For the total content of SeMet and $SeCys_2$ (C_2), sample solution with pH 9.0 was processed with the same procedure as mentioned above. The concentration of SeMet was calculated as the difference of C_1 and C_2.

For the regeneration of the nanometer-sized Al_2O_3 packed micro-column, 0.5 mol L^{-1} NaOH solution and high-purity de-ionized water were passed through the column, followed by passing through the column with 1.0 mol L^{-1} $CuSO_4$ solution. By this treatment, the column could be reused for at least 20 times, and no obvious reduce on the recoveries of analytes was found.

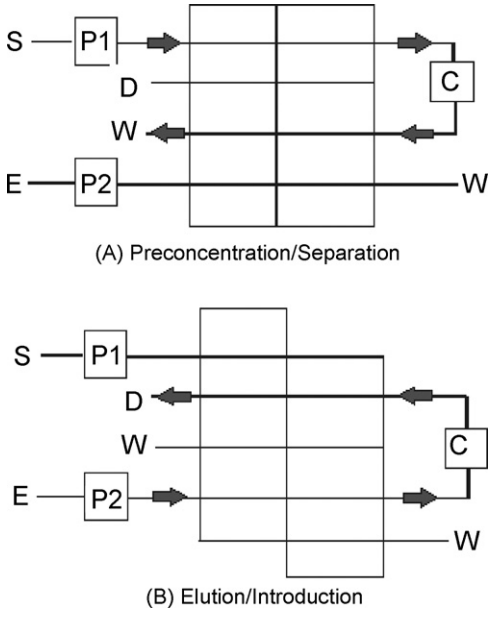

Fig. 1. Flow injection manifold and operation for on-line SPE and ICP-MS determination. (A) Preconcentration/separation step; (B) elution/introduction step. S: sample; E: elution; W: waste; C: micro-column packed with nanometer-sized Al_2O_3; P1, P2: peristaltic pumps; D: detector.

2.4. Sample treatment

A yeast certified reference material (SELM-1) purchased from National Research Council of Canada (NRCC, Ottawa, Canada) was pretreated by the recommended method developed by McSheehy et al. [24]. Briefly, methanesulfonic acid (10 mL, 4 mol L^{-1}) was added to the sample of the SELM-1 (0.1 g). The mixtures were heated at reflux for 16 h, and then transferred to the volumetric flask, and the volume was made up to 100 mL. This solution was adjusted to the desired pH and diluted by 1:1000 with water prior to determination.

The selenized yeast was purchased from the Department of Food Technology of Huazhong Agricultural University (Wuhan, China). The sample treatment recipe was based on the recommended method [25]. 0.02 g sample was treated with 10 mL high-purity deionized water and then shaken at 50 °C for 2 h and centrifuged at 4000 rpm for 0.5 h. 1 mL of supernatant was diluted to 100 mL and adjusted to the desired pH.

The urine and serum sample (provided by Hospital of Wuhan University, Wuhan, China) were centrifuged for 10 min at 4000 rpm, then 2.5 mL and 1.0 mL of the supernatant was pipetted and adjusted to the desired pH, respectively. Afterwards, they are diluted to 10 mL with water prior to analysis [8,26].

The total content of selenium in samples was determined by pneumatic nebulization (PN)-ICP-MS after sample digestion. The sample digestion procedure was described as follows: 0.1 g of yeast samples or 0.5 mL urine and serum sample were put into PTFE digestion vessels, and 5 mL of HNO_3 and 1 mL of H_2O_2 were added, respectively. The mixture was covered and left overnight, and then evaporated to near dryness at 80 °C. The residue was dissolved with 1% (v/v) HNO_3 and diluted to 10 mL. The yeast sample solution was diluted by 1:100 prior to PN-ICP-MS determination.

The blank samples were operated as the same experimental procedure without addition of the target analytes.

3. Results and discussion

3.1. Optimization of adsorption variables

The adsorption variables were optimized using a solution containing 20 ng mL^{-1} of target analytes. The pH value plays an important role with respect to the adsorption of different compounds on the Cu(II) loaded nanometer-sized Al_2O_3 powder. Fig. 2 shows the effects of pH value on adsorption percentage of SeMet and $SeCys_2$. It can be seen that a quantitative adsorption of both seleno amino acids can be obtained above pH 8.0 due to the formation of Cu-seleno amino acids complexes. However, $SeCys_2$ could also be adsorbed quantitatively by Cu(II) loaded nanometer-sized Al_2O_3 micro-column in the pH range of 3–5 while SeMet can be hardly retained and passed through the micro-column. The different adsorption behaviors for $SeCys_2$ and SeMet on the Cu(II) loaded nanometer-sized Al_2O_3 micro-column might ascribe to their different molecular structures. There is a Se–Se bond in the $SeCys_2$, and the bond energy of Cu–Se (376 kJ mol^{-1} [27]) is higher than that of Se–Se (206 kJ mol^{-1} [28]), therefore, a Se–Cu bond could be easily formed, which results in a retention of $SeCys_2$ at pH 3–5. In subsequent experiments, pH 4.0 was selected to separate SeMet and $SeCys_2$ and pH 9.0 was employed to preconcentrate both SeMet and $SeCys_2$. The concentration of SeMet was then calculated as the respective concentration difference between the above two results.

The effect of flow rates of sample solutions on adsorption percentage of analytes was examined by passing the sample solution through the micro-column with the flow rates changing from 0.2 to 1.2 mL min^{-1}. The experimental results showed that 1.0 mL min^{-1} was the maximum flow rate at which the analytes could be quantitatively adsorbed at either of the pH values 4.0 or 9.0. Thus, 1.0 mL min^{-1} was selected as the optimal sample flow rate in subsequent work.

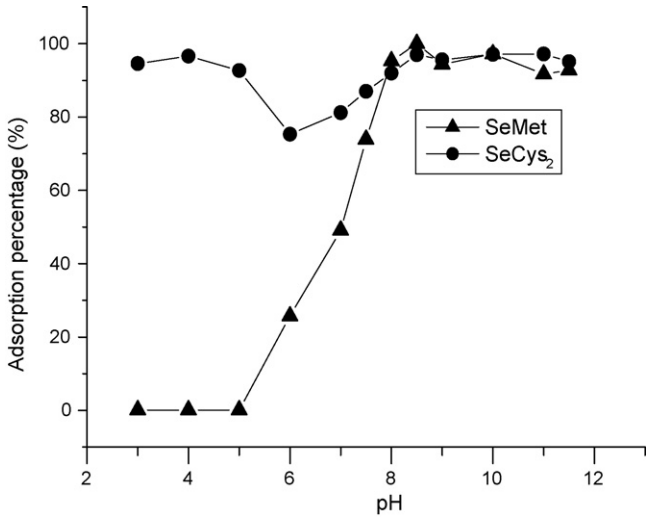

Fig. 2. Effect of pH on the adsorption percentage (%) of SeMet and $SeCys_2$ on Cu(II) loaded nanometer-sized Al_2O_3. SeMet and $SeCys_2$: 20 ng mL^{-1}; sample volume: 3 mL; sample flow rate: 1.0 mL min^{-1}.

3.2. Optimization of eluting conditions

As reported in Ref. [20], Cu^{2+} retained on the nanometer-sized Al_2O_3 could be desorbed easily using acid solution as eluent. As a result, HNO_3 was utilized as eluent to desorb Cu^{2+} and seleno amino acids from the micro-column simultaneously. In order to study the effects of the concentration and volume of HNO_3 on the desorption, three portions of 0.2 mL HNO_3 were sequentially used to elute the target seleno amino acids adsorbed on the micro-column. Fig. 3 is the effect of HNO_3 concentration and volume on the recoveries of SeMet and $SeCys_2$. As can be seen, either $SeCys_2$ retained at pH 4.0 or SeMet and $SeCys_2$ adsorbed at pH 9.0 could be eluted from the micro-column effectively with 0.2 mL of 0.5 mol L^{-1} HNO_3. Finally, 0.3 mL of 1.0 mol L^{-1} HNO_3 was used in order to ensure the analytes desorbed completely.

For quantitative desorption of the retained analytes in a small eluent volume, a low elution flow rate should be used, providing sufficient time for equilibrium between the solid-phase and the eluent. Therefore, the effect of eluent flow rate was investigated and the recovery was decreased if the eluent flow rate was above 0.5 mL min^{-1}. As a result, 0.5 mL min^{-1} was selected as the flow rate of elution for the further studies.

3.3. Optimization of sample volume

A large sample volume used is in favor of enhancing the enrichment factor, thus leading to an improvement of sensitivity. To study the effect of sample volume on recovery of the analytes, various volumes of sample solutions containing SeMet and $SeCys_2$ were operated according to the general procedure, and the experimental results showed that when the sample volume of SeMet and $SeCys_2$ were lower than 20 mL and 25 mL, respectively, the recoveries of SeMet and $SeCys_2$ were all above 90% and kept unchanged, whereas a decrease was observed with further increase of sample volume for both SeMet and $SeCys_2$. In the flow injection (FI) system, 3 mL of sample was used in order to increase the sampling frequency.

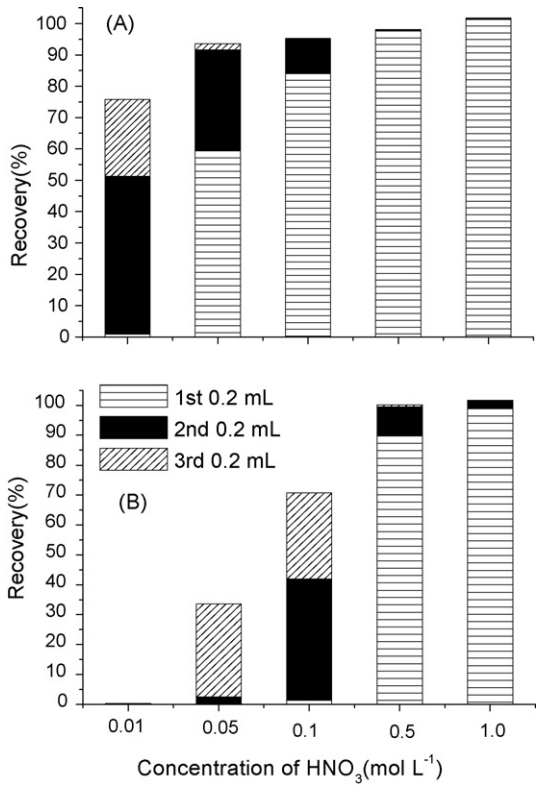

Fig. 3. Effect of HNO_3 volume and concentration on recovery (%) of SeMet and $SeCys_2$ on Cu(II) loaded nanometer-sized Al_2O_3. A: SeMet; B: $SeCys_2$; SeMet and $SeCys_2$: 20 ng mL^{-1}; pH 9.0; sample volume: 3 mL; sample flow rate: 1.0 mL min^{-1}; elution flow rate: 0.5 mL min^{-1}.

3.4. Interferences of foreign ions

The effects of some common coexisting ions on preconcentration, separation and determination of SeMet and $SeCys_2$ were studied. In these experiments, corresponding salts were added into solutions containing 20 ng mL^{-1} of SeMet and $SeCys_2$. The experimental results indicated that 5000 mg L^{-1} of Na^+, K^+, NH_4^+, 2000 mg L^{-1} of Mg^{2+}, 1000 mg L^{-1} Ca^{2+} and 100 mg L^{-1} Zn^{2+} have little interference on the separation/preconcentration of target analytes. Besides, the tolerance limits of NO_3^-, SO_4^{2-} and Cl^- for the studied analytes were all found to be above 5 g L^{-1}. The above tolerance limits for the studied coexisting ions are higher than the average level of these coexisting ions found in human serum and urine as reported in Ref. [29]. Further studies showed that 20 ng mL^{-1} of Se(IV) and Se(VI) could be hardly adsorbed on the column at the pH 4.0 or 9.0, which clearly indicates that there was no interference caused by Se(IV) and Se(VI).

Table 2
Analytical performance.

	$SeCys_2$[a]	SeMet[b]
LOD (ng Se mL^{-1})	0.021	0.024
RSD (%)[c]	2.1	1.6
Linear range (ng Se mL^{-1})	0.1–5	0.1–10
R	0.998	0.999
Linear equations	$y = 43{,}064x + 12{,}635$	$y = 38{,}465x + 12{,}972$
Enrichment factor	7.7	7.8

[a] pH 4.0.
[b] pH 9.0.
[c] C = 1.0 ng mL^{-1}, n = 7.

Table 3
Comparison of limits of detection (ng mL^{-1}) found in the literatures for selenium speciation following different analytical techniques.

Analytical technique	SeMet	$SeCys_2$	Reference
SPE-ICP-MS	0.021	0.024	This work
IPC-ICP-MS[a]	0.34	0.44	[8]
SPME-GC–ICP-MS	0.014	0.029	[12]
SPE-ICP-MS	0.21	0.05	[16]
HPLC-UV/nano-TiO_2-CL[b]	6.4	12	[30]
HPLC–ICP-CRC-MS	0.028[c]/0.014[d]	0.016[c]/0.008[d]	[31]
UV-HG-HPLC–ICP-CRC-MS[e]	0.015[c]/0.008[d]	0.011[c]/0.006[d]	
HPLC–ICP-CRC-MS	0.022–0.37	0.026–0.30	[32]
HPLC-UV-HG-AFS	2.9	1.1	[33]
HPLC–ICP-MS	>5	>5	[34]
HPLC–ICP-MS	1.2	–	[35]

[a] IPC-ICP-MS = ion-pairing reversed chromatography-ICP-MS.
[b] HPLC-UV/nano-TiO_2-CL = high performance liquid chromatography-UV irradiation–nano-TiO_2-chemiluminescence.
[c] ^{78}Se.
[d] ^{80}Se.
[e] UV-HG-HPLC–ICP-CRC-MS = UV irradiation-hydride generation-high performance liquid chromatography–ICP-collision and reaction cell-MS.

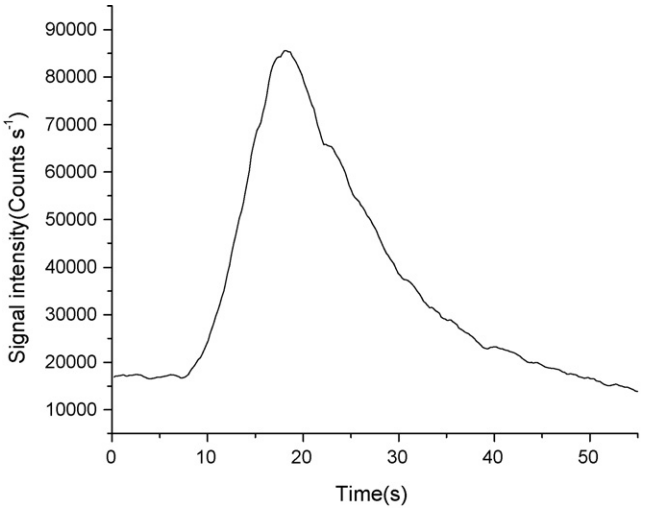

Fig. 4. Peak profile of SeMet (2 ng mL^{-1}) as an example obtained by the online SPE-ICP-MS. Sample loaded: 1.0 mL min^{-1} for 3 min; elution: 0.5 mL min^{-1} for 0.6 min.

3.5. Analytical performances

Under the optimal conditions, the signal profile of SeMet was examined, and Fig. 4 was the typical elution profile obtained for 2 ng mL^{-1} SeMet (as Se). The analytical performance of online FI-ICP-MS for the determination of SeMet and $SeCys_2$ was evaluated, and the performance data are given in Table 2. The limits of detection (LODs) were calculated by three times of standard deviation of the blank signals according to the definition of IUPAC. With 3 min for preconcentration and 36 s for elution, the sampling frequency was 8 h^{-1}. Further studies showed that the concentration ratio of SeMet and $SeCys_2$ in the range of 1:10–10:1 has little effect on recoveries. The adsorption capacity of the solid extractant for SeMet and $SeCys_2$ was 36.7 μg Se g^{-1} and 62.5 μg Se g^{-1}, respectively, which is suffi-

Table 4
Selenium analysis in NRCC certified reference material of SELM-1.

SELM-1	Analyte	Found	Certified
SELM-1(μg g^{-1}) (mean ± SD, n = 3)	SeMet	3355 ± 69	3389 ± 173
	$SeCys_2$	ND[a]	–
	Total selenium	2026 ± 8.0	2049 ± 55

[a] ND = not detected.

Table 5
Determination of seleno amino acids in the real samples (mean ± SD, $n = 3$).

	Added		Determined		Recovery (%)	
	$SeCys_2$	SeMet	$SeCys_2$	SeMet	$SeCys_2$	SeMet
Yeast ($mg\,kg^{-1}$)	–	–	52.5 ± 3.1	55.5 ± 3.0	–	–
	25.0	25.0	76.0 ± 4.1	81.0 ± 1.6	94.0	102
Urine ($ng\,mL^{-1}$)	–	–	1.24 ± 0.11	0.37 ± 0.01	–	–
	1.60	1.60	3.01 ± 0.13	2.03 ± 0.06	109	104
Serum ($ng\,mL^{-1}$)	–	–	5.76 ± 0.23	1.29 ± 0.24	–	–
	6.00	1.20	12.1 ± 0.87	2.47 ± 0.70	107	98.3

cient for the analysis of most real samples. A comparison of LODs obtained by this method with several other approaches reported in the literatures for selenium speciation is shown in Table 3. As could be seen, the LODs of this method are much lower than that obtained by the other methods except HPLC-ICP-collision reaction cell-MS.

3.6. Method validation and real sample analysis

This method was applied for the determination of seleno amino acids in a certified reference material (CRM) of SELM-1 yeast, and the results were listed in Table 4. As could be seen, a good agreement between the determined values and the certified values was obtained for both SeMet and total selenium.

The proposed method was applied to the determination of SeMet and $SeCys_2$ in selenized yeast. The analytical results, together with the recoveries for the spiked samples, are given in Table 5. The total selenium content in yeast, determined by PN-ICP-MS using external calibration, was found to be $2519\,mg\,kg^{-1}$. The contents of $SeCys_2$ and SeMet in the extracts of yeast were found to be $52.5 \pm 3.1\,mg\,Se\,kg^{-1}$ and $55.5 \pm 3.0\,mg\,Se\,kg^{-1}$, respectively. Furthermore, both human serum and urine samples were also analyzed, and the results were listed in Table 5. As can be seen, the total contents of selenium in urine and serum samples were $12.6\,ng\,mL^{-1}$ and $109\,ng\,mL^{-1}$, respectively, which were in accordance with the values reported in Ref. [29]. The contents of $SeCys_2$ and SeMet are at the $ng\,mL^{-1}$ or sub $ng\,mL^{-1}$ levels in human serum and urine, demonstrating that seleno amino acids (mainly SeMet and $SeCys_2$) usually existing in human serum and urine are the minority species of selenium [8,26,36–38].

4. Conclusion

The FI on-line separation and preconcentration system using Cu(II) loaded nanometer-sized Al_2O_3 as a sorbent material for ICP-MS determination of SeMet and $SeCys_2$ has been evaluated, and it was demonstrated to be promising for routine preconcentration, separation and determination of selenomethionine and selenocystine in yeast sample and human body fluids. Compared with the established method for the speciation of seleno amino acids, the following advantages can be achieved with this newly proposed method such as no chromatographic system required, simplicity, rapidness, high sensitivity and low running cost.

Acknowledgements

Financial supports from National Nature Science Foundations of China (No. 20575048), the Science Fund for Creative Research Groups of NSFC (No. 20621502) and MOE of China (NCET-04-0658, 20030486101) are gratefully acknowledged.

References

[1] M.P. Rayman, Lancet 356 (2000) 233.
[2] E. Dumont, F. Vanhaecke, R. Cornelis, Anal. Bioanal. Chem. 385 (2006) 1304.
[3] Y. Shiobara, T. Yoshida, K.T. Suzuki, Toxicol. Appl. Pharmacol. 152 (1998) 309.
[4] B.Y. Deng, J.R. Feng, J. Meng, Anal. Chim. Acta 583 (2007) 92.
[5] D.E. Nixon, T.P. Moyer, M.F. Burritt, Spectrochim. Acta Part B 54 (1999) 931.
[6] M. Vilano, R. Rubio, J. Anal. At. Spectrom. 15 (2000) 177.
[7] C. B'Hymer, J.A. Caruso, J. Chromatogr. A 1114 (2006) 1.
[8] S. Afton, K. Kubachka, B. Catron, J.A. Caruso, J. Chromatogr. A 1208 (2008) 156.
[9] J.M. Marchante-Gayón, I. Feldmann, C. Thomas, N. Jakubowski, J. Anal. At. Spectrom. 16 (2001) 457.
[10] E.H. Larsen, M. Hansen, T. Fan, M. Vahl, J. Anal. At. Spectrom. 16 (2001) 1403.
[11] Y. Ogra, K.T. Suzuki, J. Anal. At. Spectrom. 20 (2005) 35.
[12] A.P. Vonderheide, M. Montes-Bayon, J.A. Caruso, Analyst 127 (2002) 49.
[13] C. Haberhauer-Troyer, G. Álvarez-Llamas, E. Zitting, P. Rodriguez-González, E. Rosenberg, A. Sanz-Medel, J. Chromatogr. A 1015 (2003) 1.
[14] L. Bendahl, B. Gammelgaard, O. Jùns, O. Farver, S.H. Hansen, J. Anal. At. Spectrom. 16 (2001) 38.
[15] B. Graû, R. Hergenröder, A. Neyer, D. Siepe, J. Sep. Sci. 25 (2002) 135.
[16] C.Z. Huang, B. Hu, M. He, J.K. Duan, J. Mass Spectrom. 43 (2008) 336.
[17] M. Siwek, A. Bari Noubar, R. Erdmann, B. Niemeyer, B. Galunsky, Chromatographia 67 (2008) 305.
[18] S.V.K. Yathavakilla, M. Shah, S. Mounicou, J.A. Caruso, J. Chromatogr. A 1100 (2005) 153.
[19] S. Latva, S. Peräniemi, M. Ahlgrén, Anal. Chim. Acta 478 (2003) 229.
[20] K. Abbas-Ghaleb, N. Gilon, G. Cretier, J.M. Mermet, Anal. Bioanal. Chem. 377 (2003) 1026.
[21] G. Feroci, A. Fini, R. Badiello, A. Breccia, Microchem. J. 57 (1997) 379.
[22] J. Yin, Z.C. Jiang, G. Chang, B. Hu, Anal. Chim. Acta 540 (2005) 333.
[23] G. Chang, Z.C. Jiang, T.Y. Peng, B. Hu, Acta Chim. Sinica 61 (2003) 100.
[24] S. McSheehy, L. Yang, R. Sturgeon, Z. Mester, Anal. Chem. 77 (2005) 344.
[25] B. Iscioglu, E. Henden, Anal. Chim. Acta 505 (2004) 101.
[26] B. Michalke, P. Schramel, J. Chromatogr. A 807 (1998) 71.
[27] S. Mahadevan, A. Giridhar, J. Non-Cryst. Solids 221 (1997) 281.
[28] Ishu, S.K. Tripathia, P.B. Barman, Chalcogenide Lett. 3 (2006) 121.
[29] S. Caroli, A. Alimonti, E. Coni, F. Petrucci, O. Senofonte, N. Violante, Crit. Rev. Anal. Chem. 24 (1994) 363.
[30] Y.Y. Su, H. Chen, Y. Gao, X.H. Li, X.D. Hou, Y. Lv, J. Chromatogr. B 870 (2008) 216.
[31] J. Darrouzès, M. Bueno, S. Simon, F. Pannier, M. Potin-Gautier, Talanta 75 (2008) 362.
[32] J.M. Marchante-Gayón, C. Thomas, I. Feldmanna, N. Jakubowski, J. Anal. At. Spectrom. 15 (2000) 1093.
[33] Ó. Muñiz-Naveiro, R. Domínguez-González, A. Bermejo-Barrera, P. Bermejo-Barrera, J.A. Cochob, J.M. Fraga, Talanta 71 (2007) 1587.
[34] C. Kahakachchi, H.T. Boakye, P.C. Uden, J.F. Tyson, J. Chromatogr. A 1054 (2004) 303.
[35] J. Zheng, M. Ohata, N. Furuta, J. Anal. At. Spectrom. 17 (2002) 730.
[36] D. Kuehnelt, D. Juresa, K.A. Francesconi, M. Fakih, M.E. Reid, Toxicol. Appl. Pharmacol. 220 (2007) 211.
[37] R.Y. Wang, Y.L. Hsu, L.F. Chang, S.J. Jiang, Anal. Chim. Acta 590 (2007) 239.
[38] J.R. Encinar, D. Schaumlöffel, Y. Ogra, R. Lobinski, Anal. Chem. 76 (2004) 6635.

Talanta 79 (2009) 905–910

Contents lists available at ScienceDirect

Talanta

journal homepage: www.elsevier.com/locate/talanta

Use of QSAR methods for predicting the chemiluminescent behaviour of organic compounds upon reaction with potassium permanganate in an acid medium

M.J. Duart[a], G.M. Antón Fos[b], L. Lahuerta Zamora[b], J. Martínez Calatayud[c,*]

[a] Departamento de Ingeniería, División de Farmacia y Tecnología Farmacéutica, Facultad de Farmacia, Universidad Miguel Hernández, Alicante, Spain
[b] Departamento de Química, Bioquímica y Biología Molecular, Universidad CEU Cardenal Herrera, Moncada (Valencia), Spain
[c] Departamento de Química Analítica, Universidad de Valencia, Burjassot (Valencia), Spain

ARTICLE INFO

Article history:
Received 19 January 2009
Received in revised form 5 May 2009
Accepted 13 May 2009
Available online 22 May 2009

Keywords:
Molecular topology
QSAR
Chemiluminescence intensity
Continuous flow
Pharmaceuticals

ABSTRACT

In previous work, molecular connectivity computations were successfully used to predict the chemiluminescent behaviour of organic compounds upon reaction with common strong oxidants and the native fluorescence too; both of them in a liquid phase. The obtained results were used to develop new analytical procedures to the given compounds. For the first time, connectivity methods were used for a purely analytical purpose. In this work, we went deeper into the knowledge of direct chemiluminescence processes by using molecular connectivity in the form of QSAR methods to predict the chemiluminescence intensity produced by reactions between organic compounds (pharmaceuticals mainly) and potassium permanganate in a liquid phase. The choice of this oxidant was dictated by its being the most active by far in producing chemiluminescence.

We used discriminant analysis to examine the results for 63 substances the emission intensity of which upon reaction with acid potassium permanganate was experimentally measured in a continuous-flow manifold. Descriptors were chosen by applying *stepwise linear dicriminant analysis* (LDA) to Snedecor *F*-values, using the smallest Mahalanobis distance, the minimum error on the test set and the lowest value of the Wilks'lambda as sorting criterion.

The theoretical predictions thus obtained were checked against the experimental results for a set of 16 compounds not used in the previous theoretical computations the chemiluminescent behaviour of which was also experimentally assessed. The result was a hit rate of 87.5% in the predictions.

1. Introduction

Chemiluminescence is the emission of electromagnetic (ultraviolet, visible or near infrared) light by effect of a chemical reaction. Chemiluminescence-based methods exhibit a high sensitivity, very low detection limits and broad linear dynamic ranges, and can be implemented with simple, robust equipment. In fact, some methods can detect analytes at the femtomol or even attomol level, and amounts as small as 120 molecules for some enzymes [1].

Chemiluminescence methods have been used to determine both organic (pharmaceuticals, biomolecules) and inorganic substances in a wide variety of industrial, environmental, clinical and biotechnological matrices, among others [2–5].

A number of chemiluminescence methods are of the direct type (i.e. they measure light emitted in an analyte–oxidant reaction where the analyte acts as the substrate). Such methods are the most simple and usually provide a high sensitivity and low detection limits. Thus, morphine has been determined in this way at levels as low as 28.5 parts per trillion [6], and so has ergonovine maleate at 0.07 parts per billion [7]. The oxidants used for this purpose include such common species as $KMnO_4$, Ce(IV), $K_3[(CN)_6Fe]$, H_2O_2, Br_2, NaClO, O_2 and *N*-bromosuccinimide.

The development of direct chemiluminescence methods entails the previous experimental elucidation of the chemiluminescent behaviour of the analyte in its reaction with various oxidants in different liquid media. This experimental tasks involve time-consuming reactivity screening tests of the trial-and-error type and hence substantial time and money investments. This problem can be avoided or at least lessened by using molecular connectivity computations; which are able to predict the chemiluminescent behaviour of some substances upon reaction with common strong oxidants in a liquid phase. The predictions thus obtained in previous work were quite consistent with their experimental counterparts [8–11]. Using molecular connectivity to predict chemiluminescent behaviour has allowed us and other authors to develop new analytical methods for biomedical and environmental determinations.

Most analytical methods based on direct chemiluminescence measurements involve oxidizing the analyte with potassium per-

* Corresponding author.
E-mail address: jose.martinez@uv.es (J. Martínez Calatayud).

0039-9140/$ – see front matter © 2009 Elsevier B.V. All rights reserved.
doi:10.1016/j.talanta.2009.05.017

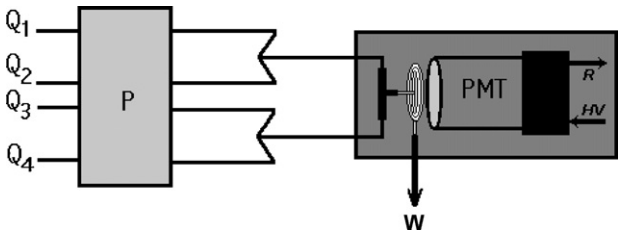

Fig. 1. Manifold used for chemiluminescence intensity measurements. Q_1, $KMnO_4$ flow-rate; Q_2 and Q_3, H_2SO_4 flow-rate; Q_4, analyte flow-rate (400 ppm in deionized water—blank). $Q_1 = Q_2 = Q_3 = Q_4 = 2.8$ ml min^{-1}. HV, high-voltage power supply; R, recorder; P, peristaltic pump; W, waste.

manganate in a strong (sulfuric or pyrophosphoric) acid. In fact, permanganate has been widely used as a chemiluminescent reagent [12,13]. The greatest advantage of this oxidant over others is that it is the source of the chemiluminescence produced in the reaction; with slight discrepancies, there is wide consensus that the actual emitting agent is an intermediate product of the reduction of Mn (VII) rather than the oxidation product of the analyte. The mechanism behind the emission remains controversial, however. The central role of this oxidant in the production of chemiluminescence justifies its extensive analytical use; however, why it exhibits no emission under specific conditions where other oxidants do remains unexplained.

This paper does not engage in the previous debate. Rather, in this work we set to expand the use of molecular connectivity in this field by deriving semi-quantitative predictions of not only the chemiluminescent behaviour of organic compounds (pharmaceuticals mainly), but also the emission intensity obtained upon oxidation of the substrates by potassium permanganate in an acid medium. To this end, we use QSAR methods (quantitative–structure activity relationship) as molecular topology to construct a topological mathematical model in order to classify the studied compounds into four groups or classes according to chemiluminescence intensity.

Within the framework of QSAR methods, which establish quantitative relations between structure and activity, molecular connectivity has widely demonstrated its ability for an easy and efficient characterization of molecular structure through the so-called topological indices (TIs). In this mathematical formalism a molecule is assimilated to a graph, where each vertex represents one atom and each axis one bond. Starting from the interconnections among the different vertexes, an adjacency topological matrix can be built whose elements *ij* take the values 1 or 0, depending whether the vertex *i* is connected to the vertex *j* or not, respectively. The manipulation of this matrix gives origin to a set of topological indices or topological descriptors. When these indices are selected adequately, it is possible to have a very specific characterization of each chemical compound [14–19].

Molecular connectivity has been tested on several properties of different classes of organic, bioorganic and inorganic compounds. This topological method has been applied to the determination of biological activities [20], physical [21] and chemical properties [22]. Also, molecular connectivity has been applied to the prediction of analytical properties with developed analytical applications, basically to chromatographic processes [23,24] and recently to liquid-phase chemiluminescence and fluorescence [9,25,26].

1.1. Experimental reagents, apparatus and procedures

All reagents used were of analytical-grade unless stated otherwise. Solutions were prepared in water that was purified by reverse osmosis and then deionized to 18 MΩ cm in a Sybron/Barnstead Nanopure II water purification system furnished with a fibre filter of 0.2 μm pore size. The pharmaceuticals and pesticides studied were purchased from different manufacturers. All other chemicals (strong inorganic acids and alkalis, and oxidants such as $KMnO_4$) were obtained from Panreac (Barcelona, Spain).

Table 1
Symbols and definitions of the topological indices.

Symbol	Name	Definition	Refs.
${}^k\chi_t$, k = 0–4, t = p, c, pc	Randić-like indices of order k and type path (p), cluster (c) and path-cluster (pc)	${}^k\chi_t = \sum_{j=1}^{k n_t} \left(\prod_{i \in S_j} \delta_i \right)^{-1/2}$, δ_i, number of bonds, σ or π of the atom i to non-hydrogen atoms. S_j, jth sub-structure of order k and type t	[27]
${}^k\chi_t{}^v$, k = 0–4, t = p, c, pc	Kier-Hall indices of order k and type path (p), cluster (c) and path-cluster (pc)	${}^k\chi_t{}^v = \sum_{j=1}^{k n_t} \left(\prod_{i \in S_j} \delta_i^v \right)^{-1/2}$, $\delta_i{}^v$, Kier-Hall valence of the atom i. S_j, jth sub-structure of order k and type t	[27]
${}^kD_t$, k = 0–4, t = p, c, pc	Connectivity differences of order k and type path (p), cluster (c) and path-cluster (pc)	${}^kD_t = {}^k\chi_t - {}^k\chi_t^v$	[27]
G_k, k = 1–5	Topological charge indices of order k	$G_k = \sum_{i=1}^{N-1} \sum_{j=i+1}^{N} \lvert M_{ij} - M_{ji} \rvert \, \delta(k, D_{ij})$, M = AQ, product of the adjacency and inverse squared distance matrices for the hydrogen-depleted molecular graph. D, distance matrix; δ, Kronecker delta	[28]
$G_k{}^v$, k = 1–5	Valence topological charge indices of order k	$G_k^v = \sum_{i=1}^{N-1} \sum_{j=i+1}^{N} \lvert M_{ij}^v - M_{ji}^v \rvert \, \delta(k, D_{ij})$, $M^v = A^vQ$, product of the electronegativity-modified adjacency and inverse squared distance matrices for the hydrogen-depleted molecular graph. D, distance matrix; δ, Kronecker delta	[28]
J_k, $J_k{}^v$, k = 1–5	Weighted topological charge indices of order k	$J_k = \frac{G_k}{N-1}$ $J_k^v = \frac{G_k^v}{N-1}$	[28]
W	Wiener Index	Total number of bonds between all pairs of atoms in the graph	[29]
L	Length	Maximal distance between atoms in terms of bonds	[30]

Fig. 1 depicts the continuous-flow manifold used to measure the chemiluminescence emission intensity in the reactions between acid potassium permanganate and the different target substances. The manifold consisted of a Minipuls-2 peristaltic pump from Gilson (Middleton, WI) that was used to propel the oxidant solution (0.02 mol l^{-1} $KMnO_4$, Q_1 = 2.8 ml min^{-1}), reaction medium (1 mol l^{-1}, $Q_2 = Q_3$ = 2.8 ml min^{-1}) and analyte (400 ppm, Q_4 = 2.8 ml min^{-1}) through PTFE tubing of 0.8 mm i.d. The solutions were merged at a T-piece located 2 cm from the flow-cell, which was a quartz tube of 1.0 mm i.d. tightly coiled as a flat spiral with no gaps between successive turns, the overall cell diameter being 3 cm. A mirror was positioned at the back of the cell in order to maximize the amount of light collected and the cell was placed 2 mm from the photomultiplier tube (a 9902 end window model from Electron Tubes, Co., Middlesex, UK). The T-piece, flow-cell and photomultiplier tube (PMT) were accommodated in a light-tight custom-made box. The PMT was operated at a voltage of −1273 V that was supplied by a PHV-40 programmable high-voltage generator from Acton Research Corporation (Acton, MA); the output was interfaced to a computer equipped with a dedicated board and software.

1.2. Computational methods: calculation of topological descriptors

The topological indices (TIs) used in this work are shown in Table 1 together with their definition and the references describing in detail how to be calculated [27,30]. All descriptors were computed from the adjacency topological matrix obtained from the hydrogen depleted graph using the programmes Desmol11 [31] and Molconn-Z [32]. Each compound was characterized from 132 TIs. We used molecular connectivity, geometric, loading, atomic electrotopological and various other types of indices.

Table 2
Results of the LDA study and classification of the compounds in the training set.

Compound	Prob. 1[a]	Prob. 2[b]	Prob. 3[c]	Prob. 4[d]	Signal (a.u.)	Predicted class
Inactive						
Alanine	0.973	0.022	0.004	0.001	0	I
Ampicilline	0.866	0.100	0.004	0.031	3.5	I
Asparagine	0.999	0.001	0	0	0	I
Aspartic acid	0.998	0.002	0	0	0	I
Atropine	0.435	0.186	0.163	0.216	0	I
Biguanide	0.981	0.012	0	0.007	0	I
Captopril	0.972	0.019	0.008	0.001	7.4	I
Iproniazide	0.881	0.012	0.104	0.003	6.8	I
Lidocaine	0.908	0.002	0.081	0.009	0	I
Lysine	0.999	0	0	0	0	I
Metronidazol	1.000	0	0	0	0	I
Minoxidil	0.897	0.008	0.018	0.077	6.1	I
Pirazinamide	0.978	0.021	0	0	0	I
Piridoxine	0.867	0.039	0	0.094	3.1	I
Proline	0.995	0.005	0	0	0	I
Arginine	0.999	0.001	0	0	0	I
Ciprofloxacine	0.050	0.473	0.415	0.062	0	A
Mentol	0.900	0.009	0.021	0.070	0	I
Metformine	1.000	0	0	0	0	I
Metomile	0.972	0.001	0.027	0	0	I
Moderately active						
Flufenazine	0.022	0.665	0.078	0.235	26.6	MA
Folic acid	0	0.980	0.005	0.014	52.0	MA
Isoxicam	0.008	0.919	0.003	0.070	33.4	MA
Isoniazide	0.890	0.098	0.005	0.007	44.6	I
Emetine	0	0.047	0.943	0.010	18.3	A
Active						
Antipirine	0.205	0.103	0.674	0.018	73.4	A
Benzydamine	0	0.020	0.966	0.014	65.8	A
Bromhexine	0	0	0.998	0.002	83.2	A
Chlorpheniramine	0.011	0.007	0.973	0.010	156.5	A
Sulfametoxazol	0.020	0.337	0.408	0.236	161.1	A
Chlorpromazine	0.008	0.017	0.373	0.602	93.9	HA
Vitamin D3	0.059	0.376	0.548	0.017	96.0	A
Indometacine	0	0.044	0.951	0.005	176.1	A
Highly active						
Acriflavine	0	0.039	0.002	0.959	417.7	HA
Trimetoprim	0	0.004	0.003	0.992	471.4	HA
Ergonovine	0.001	0.098	0.892	0.009	486.8	A
Flufenamic acid	0.001	0.165	0	0.833	650.0	HA
Syringaldazine	0	0.100	0.139	0.761	881.2	HA
Salicylamide	0	0.030	0.014	0.956	1938.4	HA

Prob., probability; I, inactive; MA, moderately active; A, active; HA, highly active.
a.u., arbitrary units (from the detector display) directly connected with the emission intensity; estimated accuracy ±0.1.
[e]Measured experimentally.
[a] Calculated from Eq. (1).
[b] Calculated from Eq. (2).
[c] Calculated from Eq. (3).
[d] Calculated from Eq. (4).

Table 3
Results of the LDA study and classification of the compounds in the test set.

Compound	Prob. 1[a]	Prob. 2[b]	Prob. 3[c]	Prob. 4[d]	Signal (a.u.)[e]	Class
Inactive						
Cyclohexylamine	0.995	0.003	0	0.002	0	I
Cysteine	0.939	0.045	0.009	0.007	2.0	I
Dextrometrorphan	0.83	0.007	0.108	0.055	0	I
Nicotinic acid	0.965	0.033	0.001	0.001	0	I
Pentotal	0.948	0.002	0.046	0.004	6.9	I
Acetyl cisteine	1.000	0	0	0	2.7	I
Amoxicillin	0.575	0.252	0.003	0.170	7.4	I
Cystine	1.000	0	0	0	3.0	I
Nicotinamide	0.966	0.032	0.001	0.001	0	I
Nortriptiline	0.065	0.457	0.385	0.094	3.9	MA
Moderately active						
Ninhydrin	0.012	0.924	0.053	0.010	12.5	MA
Terramycin	0	0.999	0	0.001	9.1	MA
Hydrocortisone	0.713	0.244	0.007	0.035	10.7	I
Active						
Piramidon	0.066	0.114	0.746	0.073	95.9	A
Probucol	0	0	1.000	0	67.8	A
Ondansetron	0.001	0.005	0.994	0	143.3	A
Guayafenesine	0.021	0.117	0.115	0.748	102	HA
Barbituric acid	0.875	0.115	0.008	0.002	189.5	I
Captan	0	0.005	0.994	0	70.5	A
Highly active						
Proflavin	0	0.009	0	0.991	398.3	HA
Sulfadiazine	0.014	0.098	0.009	0.879	254.4	HA
Phenylephrine	0.277	0.056	0.014	0.653	1028.7	HA
Thioridazine	0.022	0.02	0.835	0.122	513.4	A
Sulfamerazine	0.012	0.144	0.030	0.815	407.3	HA

Prob., probability; I, inactive; MA, moderately active; A, active; HA, highly active.
a.u., arbitrary units (from the detector display) directly connected with the emission intensity; estimated accuracy ±0.1.
[a] Calculated from Eq. (1).
[b] Calculated from Eq. (2).
[c] Calculated from Eq. (3).
[d] Calculated from Eq. (4).
[e] Calculated experimentally.

1.3. Linear discriminant analysis

Stepwise linear discriminant analysis, LDA, is a useful technique for finding discriminant functions (DF). It is a pattern-recognition method, which permits (facilitates), by combining variables, the evaluation of the ability to distinguish among two or more groups of populations. In our work the independent variables were the topological indices and the discrimination property was the chemiluminescent emission intensity.

The study was performed on a former group containing 63 compounds; this group was randomly divided into two different groups known as training and test group, respectively. The selection is a step of the software process. Once selected the compounds from the initial group of 63, the LDA study was performed with the training set containing 39 compounds which were classified according to the obtained information from experimental work; this classification consisted of several groups according to the observed chemiluminescence emission intensity [viz. highly active (6 compounds), active (8 compounds), moderately active (5 compounds) and inactive (20 compounds)]. A compound was classified as inactive (I, Class 1), moderately active (MA, Class 2), active (A, Class 3) or highly active (HA, Class 4) depending on whether its chemiluminescence intensity was 0–9, 9–60, 60–200 or more than 200 a.u. (arbitrary units, see footnote in Tables 2 and 3), respectively. The test set, which facilitates the evaluation of the quality of the discriminant function (DF) obtained, included 24 compounds (10 I, 3 MA, 6 A and 5 HA).

LDA was performed with the BMDP 7M package [33]. The selection of the descriptors was based on the highest value of Fisher–Snedecor parameter (F), and the classification criterion was the shortest Mahalanobis distance (distance of each case to the average of all cases used in the regression equation) and the minimum error on the test set. The 7M software chooses the variables used in computing the linear classification functions in a stepwise manner; at each step the variable that adds the most to the separation of the groups is entered into (or the variable that adds the least is removed from) the discriminant function. The quality of the discriminant function is evaluated by the Wilks' lambda parameter, λ, which is a multivariate analysis of variance statistic that tests the equality of group means for the variable(s) in the discriminant function. The Wilks' lambda for the overall discrimination is computed as the ratio of the determinant of the within-groups variance/covariance matrix over the determinant of the total variance/covariance matrix [34]:

$$\lambda = \frac{\det(W)}{\det(T)}$$

λ ranges between 0 and 1. The lower is this parameter better is the discriminant capacity of the selected function.

To this end, we applied the linear discriminant analysis (LDA) to the training set to construct a predictive mathematical model connecting molecular descriptors and activity.

2. Results and discussion

The continuous-flow manifold of Fig. 1 was used to conduct the experimental screening tests. Chemiluminescence signals (sample minus blank) were measured by using the above-described luminometer. A reaction was deemed not chemiluminescent when the signal difference (sample minus blank) was less than twice background noise.

We obtained four equations with 9 independent variables (Eqs. (1)–(4)). Each equation categorized the studied compounds as inactive (DFI), moderately active (DFMA), active (DFA) or highly active (DFHA). The statistical figures of merit for the selected equation were $N = 39$, $F = 6.50$ and $\lambda = 0.139$. The training set consisted of 39 compounds of which 20 were inactive [19 (i.e. 95%) being accurately predicted], 5 moderately active [3 (60%) being accurately predicted], 8 active [7 (87.5%) being accurately predicted] and 6 highly active [5 (83.3%) being accurately predicted]. We applied to the test group ($N = 24$) the DF to evaluate the quality of the function and we obtained 90%, 66.7%, 66.7% and 80% of success for the groups of inactives, moderately actives, actives and highly actives, respectively.

$$\mathrm{DF_I} = -25.78 - 1.95G_4 + 8.28G_5 + 76.79J_1 + 7.21J_2^V - 167.42J_5^V - 5.98\Delta^0\chi + 8.52\Delta^3\chi_p - 0.01W + 3.65L \quad (1)$$

$$\mathrm{DF_{MA}} = -38.78 - 3.35G_4 + 19.25G_5 + 93.18J_1 + 3.76J_2^V - 370.31J_5^V - 9.03\Delta^0\chi + 13.24\Delta^3\chi_p - 0.02W + 4.90L \quad (2)$$

$$\mathrm{DF_A} = -40.24 - 7.33G_4 + 23.57G_5 + 105.75J_1 + 0.22J_2^V - 297.94J_5^V - 12.64\Delta^0\chi + 16.03\Delta^3\chi_p - 0.02W + 4.86L \quad (3)$$

$$\mathrm{DF_{HA}} = -41.44 - 0.94G_4 + 12.89G_5 + 109.13J_1 - 9.58J_2^V - 338.47J_5^V - 9.48\Delta^0\chi + 14.44\Delta^3\chi_p - 0.02W + 5.13L \quad (4)$$

$$N = 39 \qquad l = 0.139 \qquad F = 6.50 \qquad p < 0.0001$$

Table 4
Application of the topological mathematical model to a set of compounds and experimental verification of the results.

Compound	Prob. 1[a]	Prob. 2[b]	Prob. 3[c]	Prob. 4[d]	Theoretical prediction	Signal (a.u.)	Experimental class
Metochlorpramide	0.015	0.056	0.615	0.313	A	353.0	HA
Sulfamtoxipiridazine	0	0.040	0.004	0.957	HA	320.3	HA
Trimetoprim	0	0.004	0.003	0.992	HA	471.4	HA
Eskacine	0.004	0.465	0.112	0.419	MA	41.1	MA
Caffeine	0.576	0.211	0.153	0.06	I	0	I
Histamine	0.983	0.015	0.001	0	I	0	I
Histidine	0.956	0.037	0.006	0.001	I	0	I
Tetracaine	0	0.085	0.804	0.110	A	231.6	HA
Ergonovine	0.001	0.098	0.009	0.892	HA	486.8	HA
Phenylpropanolamine	0.511	0.160	0.064	0.266	I	0	I
Tolbutamide	0.588	0.043	0.025	0.343	I	0	I
Prometacine	0.014	0.016	0.897	0.072	A	82.9	A
Propifenazone	0.067	0.180	0.682	0.071	A	188.7	A
Codeine	0.057	0.157	0.057	0.729	HA	318.4	HA
Epinephrine	0.016	0.033	0.006	0.945	HA	778.8	HA
Tyrosine	0.170	0.156	0.015	0.660	HA	528.3	HA

Prob., probability; I, inactive; MA, moderately active; A, active; HA, highly active.
[e]Calculated experimentally.
[a] Calculated from Eq. (1).
[b] Calculated from Eq. (2).
[c] Calculated from Eq. (3).
[d] Calculated from Eq. (4).

The descriptors in the selected discriminant function (DF) are charge indices, G_i, J_i, which take account of intra-molecular charge transfers, connectivity indices, $^{m}\chi_t$, and graph length, L, which encode topological information on molecular assembling. As expected, chemiluminescence is related to both, pure structural as well as electronic features.

Tables 2 and 3 summarize the sorting results obtained by applying the discriminant functions (Eqs. (1)–(4)) to each set. Each compound was assigned to the class for which the discriminant function (DF) exhibited the highest probability. Based on the results, predictions were accurate for more than 80% of compounds in both the training set and test set. Also, probability values (prob.) exceeded 80% in most instances (see columns 2–5 (prob.) in Tables 2 and 3). The accuracy of the selected equation is clearly apparent from the fact that 75% of the studied compounds were assigned to a specific class with a probability greater than 0.85.

The discriminant capacity provided by the DF was confirmed by applying the function to a set of 16 compounds used in none of the previous theoretical computations. The predictions thus obtained (Table 4) were compared with the experimental values for the 16 compounds as determined in the above-described continuous-flow assembly. The reactions involved solutions of each individual compound (Q_1), the reaction medium (H_2SO_4, Q_2 and Q_3) and the oxidant ($KMnO_4$, Q_4). The comparison revealed that 14 of the 16 compounds were accurately classified.

And finally, the resulting equation was checked versus the experimental results for a set of 16 chemicals (these compounds were not previously used to obtain the equation) to test the theoretical prediction of the chemiluminescent intensity; which at the end it should be confirmed by experimental assays (see Table 4).

3. Conclusions

Fourteen of the 16 compounds the chemiluminescence intensity of which was correctly predicted, this is equivalent to a hit rate of 87.5% and testifies to the validity of the used topological descriptors, which in addition, were readily selected by applying simple algorithms to the topological adjacency matrix. The theoretical model was not able to establish the correct group for two active compounds, metochlorpramide and tetracaine which were predicted as active while from the experimental assays they resulted highly active.

These results clearly reflect the potential of molecular topology as a theoretical tool for predicting chemiluminescence intensity and hence in the search for not only chemiluminescent, but also highly chemiluminescent reactions.

The results obtained so far by applying molecular connectivity computations to chromatographic and chemiluminescence data testify their usefulness to predict the chemical behaviour of substances in a variety of analytical chemical fields. Research intended to expand existing applications is currently under way in our laboratory.

References

[1] T. Jonsson, M. Emteborg, K. Irgum, Anal. Chim. Acta 361 (1998) 205.
[2] Y. Fuster Mestre, L. Lahuerta Zamora, J. Martínez Calatayud, Luminescence 15 (2000) 1.
[3] K. Robards, P.J. Worsfold, Anal. Chim. Acta 266 (1992) 147.
[4] J. Martínez Calatayud, Flow Injection Analysis of Pharmaceuticals, Taylor and Francis, UK, 1996, p. 171.
[5] L.J. Kricka, G.H.G. Thorpe, Analyst 108 (1983) 1274.
[6] R.W. Abbott, A. Townshend, R. Gill, Analyst 111 (1986) 635.
[7] Y. Fuster Mestre, B. Fernández Band, L. Lahuerta Zamora, J. Martínez Calatayud, Analyst (Cambridge, UK) 124 (1999) 413.
[8] L. Lahuerta Zamora, Y. Fuster Mestre, M.J. Duart, G.M. Antón Fos, R. García Doménech, J. Gálvez Álvarez, J. Martínez Calatayud, Anal. Chem. 73 (2001) 4301.
[9] B. Gómez-Taylor Corominas, G.M. Antón Fos, J.V. García Mateo, L. Lahuerta Zamora, J. Martínez Calatayud, Talanta 60 (2003) 623.
[10] B. Li, L. Ma, Ch. Xu, J. Luminescence 128 (2008) 1484.
[11] M. Catalá Icardo, L. Lahuerta Zamora, G.M. Antón-Fos, J. Martínez Calatayud, M.J. Duart, Trends Anal. Chem. 24 (8) (2005) 782.
[12] J.L. Adcok, P.S. Francis, T.A. Smith, N.W. Barnett, Analyst 133 (2008) 49.
[13] O. Rubio Pons, D. Martínez Gregorio, J.V. García Mateo, J. Martínez Calatayud, Anal. Chim. Acta 438 (2001) 149.
[14] M.J. Duart, R. García-Domenech, J. Gálvez, P.A. Alemán, R.V. Martín-Algarra, G.M. Antón-Fos, J. Med. Chem. 49 (12) (2006) 3667.
[15] M. Karelson, in: R. Todeschini, V. Consonni (Eds.), Molecular Descriptors in QSAR/QSPR, John Wiley & Sons, New York, 2000.
[16] R. Mannhold, H. Kubinyi, H. Timmerman (Eds.), Handbook of Molecular Descriptors, Methods and Principles in Medicinal Chemistry, vol. 11, Wiley VCH Verlag GmbH, Weinheim, Germany, 2000.
[17] J. Devillers, A.T. Balaban, Topological Indices and Related Descriptors in QSAR and QSPAR, Overseas Publishers Association, Amsterdam, 1999.
[18] H. Hosoya, M. Gotoh, M. Murakami, S. Ikeda, J. Chem. Inf. Comput. Sci. 39 (39) (1999) 192.
[19] L.B. Kier, L.H. Hall, J. Chem. Inf. Compt. Sci. 40 (2000) 792.
[20] L.B. Kier, W.J. Murray, L.H. Hall, J. Med. Chem. 18 (1975) 1272.
[21] R. García Domenech, A. Villanueva, J. Gálvez, R. Gozalbes, J. Chim. Phys. 96 (1999) 1172.
[22] M. Catalá Icardo, L. Lahuerta Zamora, G.M. Anton Fos, J. Martínez Calatayud, M.J. Duart, TrAC Trends Anal. Chem. 24 (2005) 782.
[23] L.B. Kier, L.H. Hall, J. Pharm. Sci. 68 (1979) 120.

[24] R. Gozalbes, J.V. Julian Ortiz, G.M. Antón Fos, J. Gálvez Alvarez, R. García Domenech, Chromatographia 51 (2000) 331.
[25] L. Lahuerta Zamora, Y. Fuster Mestre, J.M. Duart, G.M. Anton Fos, R. García Domenech, J. Gálvez Alvarez, J. Martínez Calatayud, Anal. Chem. 73 (2001) 4301.
[26] J.R. Albert-García, G.M. Antón-Fos, M.J. Duart, L. Lahuerta Zamora, J. Martínez Calatayud, Talanta 79 (2009) 412.
[27] L.B. Kier, L.H. Hall, J. Pharm. Sci. 72 (1983) 1170.
[28] J. Gálvez, R. García-Domenech, M.T. Salabert, R. Soler, J. Chem. Inf. Comput. Sci. 34 (1994) 520.
[29] H. Wiener, J. Am. Chem. Soc. 69 (1947) 17.
[30] R. Moliner, F. García, J. Gálvez, R. García Doménech, C. Serrano, An. Real Acad. Farm. 57 (1991) 287.
[31] Desmol13 Software, Unidad de Investigación de Diseño de Fármacos y Conectividad Molecular, Facultad de Farmacia, Universitat de Valencia, Spain, 2000.
[32] L.H. Hall, MOLCONN–Z software, Eastern Nazarene College, Quincy, MA, 1995.
[33] W.J. Dixon, M.B. Brown, L. Engelman, BMDP Statistical Software Manual, vol. I, University of California Press, 1990, pp. 3390–4358.
[34] W.W. Cooley, P.R. Lohnes, Multivariate Data Analysis, John Wiley & Sons, Inc., 1971.

Talanta 79 (2009) 830–835

Contents lists available at ScienceDirect

Talanta

journal homepage: www.elsevier.com/locate/talanta

A versatile total internal reflection photometric detection cell for flow analysis

Peter S. Ellis, Brady S. Gentle, Michael R. Grace, Ian D. McKelvie*

Water Studies Centre, School of Chemistry, P.O. Box 23, Monash University, Clayton, Vic. 3800, Australia

ARTICLE INFO

Article history:
Received 9 April 2009
Received in revised form 6 May 2009
Accepted 7 May 2009
Available online 15 May 2009

Keywords:
Multi-reflection cell
Flow analysis
Liquid core waveguide
Schlieren

ABSTRACT

A total internal reflection (TIR) flow-through cell that is highly tolerant of schlieren effects, has limited hydrodynamic dispersion and does not trap gas bubbles, and which is suitable for sensitive photometric measurements in flow analysis, is described. Light from an optical fibre is introduced into a short length of quartz capillary through the sidewall at an incident angle of ca. 53°. Under this condition, incident light undergoes total internal reflection from the external air–quartz interface and is propagated by successive reflections from the external walls through the aqueous liquid core of the cell. Detection of the transmitted beam is enabled by intentionally introducing an optical coupling medium at a predetermined distance along the capillary wall, which allows the internally reflected light to be captured by a second optical fibre connected to a charge-couple device detector.

This configuration embodies a number of the desirable features of a liquid core waveguide cell (i.e. total internal reflection), a multi-reflection (MR) flow cell (i.e. minimum susceptibility to schlieren effects, low hydrodynamic dispersion and little tendency to trap bubbles), and a conventional Z-cell (wide dynamic range). When employed with a flow injection system, a limit of detection of 2.0 $\mu g\,PL^{-1}$ was achieved for the determination of reactive phosphate using the TIR cell, compared with LOD values of 3.8 $\mu g\,PL^{-1}$ and 4.9 $\mu g\,PL^{-1}$ obtained using the MR and Z-cells with same manifold.

The combined advantages of schlieren-tolerance and lack of bubble entrapment of the MR cell with the higher S/N ratio and wider dynamic range of a conventional Z-cell, make the TIR cell eminently useful for photometric measurements of samples with widely differing refractive indices.

1. Introduction

Of the diverse range of detection methods that are utilized in flow analysis, photometry is probably the single most commonly applied detection method [1]. This is because of the wide range of chromophoric detection reactions that can be utilized, and the relative ease with which simple photometric detectors can be constructed using cheap components such as light emitting diodes and photodiodes.

Commercially available photometric flow-through cells typically have a Z- or U-configuration, most commonly with an optical pathlength of 10 mm [2]. There are several limitations associated with this design; these include poor sensitivity due to pathlength restrictions and sometimes large hydrodynamic dispersion. Stray gas bubbles in solution can also accumulate at the inlet or outlet of the flow cell, which in Z- and U-cells are usually at ≤90° to the optical path. Trapped bubbles cause light scattering in the optical path which results in noisy baseline signals, and can also generate large signal spikes when the bubbles detach and pass through the flow cell. Both effects are highly undesirable, especially in systems that are designed for unattended automated field measurements.

Two approaches have been explored to enhance the sensitivity of photometric detection cells, both of which rely on the use of an extended optical pathlength using either long capillaries, or cells that are internally reflective due either to total internal reflection or reflective wall coatings. For example Lei et al. [3] used capillaries of one meter in length in different configurations (straight, coiled) with laser, W and Xe sources to perform sensitive measurement of absorbance, and reported a detection limits of as low as 5 $ng\,L^{-1}$ for phosphate. Similarly Ormaza-González and Statham [4] used a high power LED with a 0.6-m straight capillary to achieve an LOD of 1 $ng\,L^{-1}$ for phosphate. However, even with the use of high intensity light sources, substantial light loss can occur due to scattering in the capillary walls, and the sensitivity enhancement achieved is usually not commensurate with the pathlength enhancement.

A variation on this approach is the use of liquid core waveguide (LCW) cells. These comprise a low refractive index, polymeric tubing material (e.g. Teflon AF2400®, or fused silica capillary-coated either internally or externally with the same polymer) that allows for total internal reflection through the liquid core. These cells can be manufactured with optical pathlengths of up to several metres [5], and provide considerably enhanced sensitivity [6].

* Corresponding author. Tel.: +61 3 99054558; fax: +61 3 99054196.
E-mail address: ian.mckelvie@sci.monash.edu.au (I.D. McKelvie).

0039-9140/$ – see front matter © 2009 Elsevier B.V. All rights reserved.
doi:10.1016/j.talanta.2009.05.008

However, the geometry of both Z and liquid core waveguide cells makes them especially prone to refractive index (RI) or schlieren effects [2,7]. These occur when the refractive indices of the carrier liquid and injected sample differ, which under laminar flow conditions results in the formation of parabolic liquid-lenses at the sample–carrier interfaces. Depending on the relative refractive indices of injected sample and carrier, light passing through these lenses may be refracted either away from or focused onto, the detection element. These aberrations in the transmitted light rays produce substantial "ghost" absorbance peaks, even when no chromophore is present [8], and can generate sizeable errors.

A number of methods have been reported for the reduction or compensation of schlieren effects. These include measurement of absorbance in the central part of a large injection where it is largely unaffected by refractive index effects [9], dual wavelength spectrophotometry [10,11] and on-line salinity compensation [12]. Refractive index effects may also be minimized by introduction of the light into the flow cell transverse to the flow axis, a condition under which there is little refraction of the light beam by the sample zone as it passes [13]. However because of the inherently shorter optical pathlength, this results in decreased sensitivity.

The use of mirror-coated helical [14] or straight [15] capillaries that exhibit multi-reflective or multi-path behaviour has also been investigated as a means of achieving enhanced sensitivity. Ellis et al. [15] developed a multi-reflective flow cell that consisted of a short length of glass capillary-coated externally with a silver reflective surface. Two windows were etched into the silvered surface to allow the introduction and collection of light at an angle of ca. 60° to the axis of flow. A light beam entering the capillary would therefore undergo multiple reflections from one mirrored sidewall to the next until the exit aperture was reached. This cell was found to have markedly improved sensitivity compared with a Z-cell because of its longer optical pathlength and lower dispersion. It also displayed much less susceptibility to the refractive index effect. In addition, the connections between the cell and the flow system are longitudinal to the flow axis, and any stray gas bubbles entering the flow cell will simply pass through, without becoming trapped.

However, a disadvantage of the multi-reflective cell is that the external silver mirror coating absorbs a certain fraction of the light upon each reflection. In the 400–1000 nm wavelength range a silvered surface will typically absorb 5% of incident light [16], and while this may be tolerable in the visible range, use of these cells for measurements in the UV range is precluded because of increased light absorption by silver coatings at these shorter wavelengths [16]. Use of aluminium coating may improve reflective performance, but as much as 20% light absorption may still occur for each reflection in the 200–400 nm range [17], which for a multi-reflection cell will cause significant light attenuation even after only a few reflections.

Hence the challenges in designing a photometric detection cell for trace analysis are to devise one that embodies high sensitivity and minimum susceptibility to schlieren effects and bubble entrapment, and that is not prone to significant light attenuation due to absorption either by reflective coatings or the capillary wall material.

An alternative approach to the use of either reflective wall-coated cells or liquid core waveguides is to use a design that embodies the characteristics of both; namely, the total internally reflecting behaviour of liquid core waveguides, and the angular introduction and collection of light through the side walls of the capillary that is employed in the multi-reflection cell.

Total internal reflection only occurs when a ray of light passes from a medium of higher refractive index to one of lower refractive index and it strikes the medium interface at an angle larger than the critical angle, which is calculated from:

$$\theta_c = \arcsin\left(\frac{n_2}{n_1}\right) \quad (1)$$

where n_2 and n_1 are the refractive indices of the least and most dense media, respectively. Tsunoda et al. [18] demonstrated the feasibility of using total internal reflection from the air–quartz interface at the outside of the glass capillary as the basis of extended, multipath photometric detection.

From Eq. (1), the critical angle, $\theta_{1,\min}$ for total internal reflection at a quartz–air interface can be estimated to be 43.45° using the refractive index data shown in Table 1. Similarly, it may be shown that if the angle of incidence, $\theta_{1,\max}$, exceeds 66.06° (the critical angle for the liquid core–quartz interface) that total internal reflection will occur at both the air–quartz and quartz–core liquid interfaces, and the light will be transmitted within the capillary walls without further contact with the liquid core.

Thus if light is directed into the wall of a quartz capillary from an optical fibre at an incident angle, θ_1, of between 43.45° and 66.06°, then it is predicted that total internal reflection will occur from the external quartz–air interface, and light will be reflected back and forth through the liquid core and provide the means of light propagation through the cell. The reflection nodes along the capillary can be predicted by simple geometric modeling, and if a connection is made at one such node with an optical fibre, using optical cement with a suitable refractive index, then light will pass out through the capillary wall into the fibre and thence to a photodetector.

This design is analogous to a liquid core waveguide, except that light is internally reflected from the external air–quartz interface rather than the internal liquid–tube interface. In liquid core waveguides and optical fibres, it is highly desirable to avoid any light leakage from the optical core and the refractive index of the core, and cladding materials are selected according to the suitabil-

Table 1
Parameters used in the simulation of the optical performance of the TIR flow cell (see Fig. 1).

Parameter	Symbol	Value
Refractive index of air (λ = 589 nm)	n_1	1.0030
Refractive index of quartz (λ = 589 nm)	n_2	1.4585
Refractive index of liquid core (λ = 589 nm)	n_3	1.3330
Refractive index of coupling medium (λ = 589 nm)	n_4	1.5700
OD of capillary (mm)	d_1	1.9500
ID of capillary (mm)	d_2	0.8400
Wall thickness (mm)	$(d_1 - d_2)/2$	0.5550
Minimum (critical) angle for TIR to occur at air/quartz interface (deg)	$\theta_{1,\min} = \arcsin(n_1/n_2)$	43.45
Corresponding refraction angle at core/quartz interface (deg)	$\theta_2 = \arcsin(n_1/n_3)$	48.80
Predicted entry angle at quartz/glue interface (deg)	$\theta_3 = \arcsin(n_1/n_4)$	39.71
Maximum (critical) angle to avoid TIR at liquid core/quartz interface (deg)	$\theta_{1,\max} = \arcsin(n_3/n_2)$	66.06
Actual entry angle at quartz/glue interface (deg)	$\theta_3 = \arcsin(n_1/n_4)$	53.00
Actual refraction angle at glue/quartz interface (deg)	$\theta_1 = \arcsin(n_3/n_2)\sin\theta_2$	59.28
Actual angle at the quartz/core interface (deg)	$\theta_2 = \arcsin(n_2/n_3)\sin\theta_3$	70.16
Actual angle at the quartz/air interface (deg)	$\theta_1 = \arcsin(n_3/n_2)\sin\theta_2$	59.28
Distance along capillary wall (mm)	$L_1 = 0.5(d_1 - d_2)\tan\theta_1$	0.934
Distance along capillary core (mm)	$L_2 = d_2\tan\theta_2$	2.328
Ray length through capillary wall (mm)	$R_1 = L_1/\sin\theta_1$	1.086
Ray length through capillary core (mm)	$R_2 = L_2/\sin\theta_2$	2.475
Reflection length	$2L_1 + L_2$	4.196
Length of capillary between light entry and exit windows (mm)	D	18.00
Number of reflections	$N = D/(2L_1 + L_2)$	4.29
Total optical pathlength (mm)	$l = NR_2$	10.62

ity of their refractive indices. In this instance, two light leakage points have been intentionally introduced to facilitate illumination of the liquid core and collection of the emergent light. An important advantage of using total internal reflection rather than reflective capillary walls is that the only loss of light that occurs is due to the absorption by the capillary medium, and not by reflective coatings as is the case in the multi-reflection cell.

The objectives of this study were to design and construct a total internal reflection flow-through cell for use in photometric flow analysis measurements, and to determine the conditions for optimal sensitivity, with least dispersion and susceptibility to schlieren effects. These characteristics of the TIR flow cell been evaluated and compared with corresponding data for Z- and multi-reflective cells.

2. Experimental

2.1. Design and construction of flow-through cells

2.1.1. Total internal reflection cell

The total internal reflection cell was constructed from a 60 mm length of circular GE 214 fused silica quartz tubing (Momentive performance materials, Albany, New York, USA) 1.95 mm o.d. and 0.85 mm i.d. mounted on a dovetail slide to ensure the stability of the optics. The total volume of the cell including connectors was 71 μL. Quartz optical fibres (P1000-2-UV/VIS, Ocean Optics Inc, Dunedin, FL, USA, 1000 μm diameter) were mounted at 53° to the normal of the capillary surface 18 mm apart to introduce light and to collect emergent light. The fibres were cemented to the capillary walls using N3 UV curing optical adhesive (Norland Products, Cranbury, NJ, USA). The assemblage was contained within a light-tight plastic enclosure. A red light emitting diode diode (Serial #1513SRCE, λ_{max} = 660 nm; 2800 mCd at 20 mA, Kingbright Corporation, City of Industry, CA, USA) was used as the lightsource, and the absorbance was measured with an USB-ISS-UV/Vis CCD detector (Ocean Optics, Dunedin, FL, USA).

2.1.2. Multi-reflective cells and Z-cells

A silver-coated borosilicate capillary (0.8 mm i.d. and 1.3 mm o.d., total volume 49 μL) with incident and transmitted light apertures 13 mm apart was used [15]. Ocean Optics 1000 μm diameter quartz fibres clamped at 30° to the normal of the capillary walls were used to introduce and collect light.

A 10 mm pathlength optical glass Z-cell with a 1.5 mm diameter optical aperture, an illuminated volume of 18 μL and a total volume of 377 μL (Starna Ltd., Hainault, Essex, UK, Model No 75.15) was used for comparative measurements. Optical fibres for introduction and collection of the light were positioned normal to the cell windows using a purpose-built cell holder, and the same red LED was used as that listed in Section 2.1.1.

2.2. Flow injection apparatus and reagents

An automated flow injection analysis system was used for the comparison the sensitivity and dispersion of the different cells, and for the determination of dissolved reactive phosphate. This system comprised two peristaltic pumps (Ismatec CA5E, Glattbrugg, Switzerland) and an electrically driven injection valve (Model 5020, Rheodyne, Rohnert Park, CA 94928, USA), using a LabView® program for computerized system control and data acquisition. The manifold configurations used were those described by Karlberg and Pacey [19] for measurement of dispersion and phosphate determination, respectively. Standards of bromothymol blue in the range 1–10 mgL^{-1} were prepared in 0.01 mol L^{-1} sodium tetraborate [20] and used to measure the sensitivity and dispersion of the Z-configuration cell, the multi-reflective cell and the total internal reflection cell.

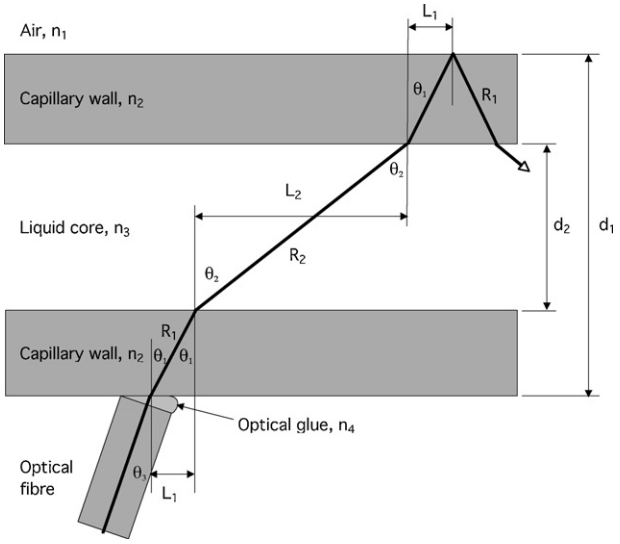

Fig. 1. Partial schematic diagram of the total internal reflection (TIR) cell showing the strategy for transverse introduction of incident light. The same arrangement is used at the other end of the capillary to measure the transmitted light intensity. Symbols are defined in Table 1.

All reagents and standards for measurement of phosphate as phosphomolybdenum blue were prepared according to the method of Lyddy-Meaney et al. [21]. Sea water used to test the refractive index effect and for preparation of phosphate standards was collected from Port Phillip Bay at Mornington, SE Australia, filtered using a 0.22 μm membrane (Acrodisc®, PALL Biosciences, Ann Arbor, MI 48103, USA), and refrigerated at ≤4 °C pending use.

2.3. Estimation of optical pathlength of the total internal reflection and multi-reflective cells

The effective optical pathlength of a reflective flow-through cell can be estimated by application of the laws of refraction and from a knowledge of the dimensions and refractive indices of the capillary and the liquid contained therein. The axial distance that a beam is displaced along the capillary wall, L_1 at each reflection point (see Fig. 1 and Table 1) is given by

$$L_1 = \frac{[(d_1 - d_2 \tan\theta_1)]}{2} \quad (2)$$

where d_1 and d_2 are the inner and outer diameters of the capillary, respectively, and θ_1 is the incident angle. For both the TIR and MR cells, the length of the light path through the liquid core, R_2, for a single reflection can be determined from the beam angle at the core–quartz interface, θ_2, and the corresponding longitudinal displacement, L_2, of the beam through the liquid core (Fig. 1):

$$R_2 = \frac{L_2}{\sin\theta_2} \quad (3)$$

Hence the number of reflected ray segments, N, and the total optical pathlength, l, within the liquid core are calculated from:

$$N = \frac{D}{2L_1 + L_2} \quad (4)$$

and hence

$$l = NR_2 \quad (5)$$

Pathlength calculations were performed for both the TIR and MR flow cells, and exemplar data for the TIR cell is shown Table 1.

Table 2
Mean molar absorptivity values corrected for dispersion and pathlength and normalized against the Z-cell. $\varepsilon_{Meas} = 22700\,mol^{-1}L\,cm^{-1}$, and was determined by batch spectrophotometric measurement.

Flow cell type	Calibration slope, $S\,(M^{-1})$	Measured/calculated pathlength, $l\,(cm)$	Apparent molar absorptivity, $\varepsilon' = S/l\,(M^{-1}cm^{-1})$	Dispersion, D	Molar absorptivity corrected for D, $\varepsilon_{corr} = \varepsilon' D$	ε_{corr}: ε_{Meas}
Z	14030 ± 120	1.000 ± 0.000	14030 ± 120	1.63 ± 0.01	22850 ± 260	1.01 ± 0.01
MR	30540 ± 250	2.242 ± 0.043	13620 ± 280	1.47 ± 0.01	19980 ± 420	0.88 ± 0.02
TIR	13940 ± 320	1.062 ± 0.013[a]	13134 ± 346	1.47 ± 0.01	19346 ± 515	0.85 ± 0.02

[a] See Table 1.

3. Results and discussion

3.1. Sensitivity of multi-reflective cells and accuracy of optical pathlength estimations

Two major factors that influence the sensitivity of a flow analysis system are the optical pathlength of the flow-through cell and the hydrodynamic dispersion of the manifold, which includes the intrinsic dispersion of the detector. Therefore an increase in the optical pathlength and a decrease in the dispersion of the flow cell might be reasonably expected to give improved sensitivity.

The calibration gradient (sensitivity), calculated optical pathlength and measured dispersion are shown for each cell type in Table 2. These data show that despite multi-path optical properties (cf. $N \approx 4$, Table 1), the optical pathlength and sensitivity of the TIR cell are similar to the Z-cell. The reason for this apparent contradiction is that for each reflection, much of the path traversed by a ray is through the walls of the capillary (i.e. $2R_1$) rather than the core (R_2, cf. Fig. 1). The pathlength through the liquid is thus dictated by the minimum critical entry angle required for total internal refraction, and by the ratio of the wall thickness to the inner diameter of the capillary. This is illustrated in Fig. 2, where the calculated pathlength to physical capillary length is plotted versus the entry angle for the capillary in question. It is evident that even for the most acute entry angles, the estimated pathlength of the TIR cell is always less than the total length of the capillary, and at the entry angle of 53° the pathlength is almost at a minimum. Similar calculations involving decreasing wall thickness suggest that a pathlength: capillary length of >1 will be achieved only for capillaries with the thinnest of walls (i.e. <0.044 mm). This is in marked contrast to the mirror-coated MR cell for which the use of a more acute entry angle will result in enhancement of the optical pathlength because of the correspondingly large increase in the number of reflections that occurs (Fig. 2).

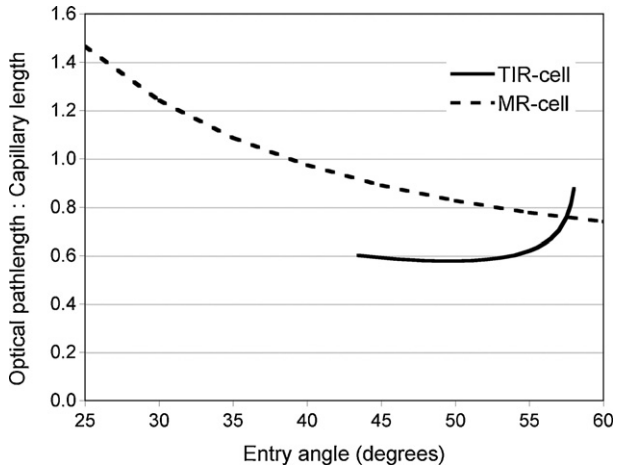

Fig. 2. Plot of estimated optical pathlength: capillary length as a function of entry angle for TIR and MR cells with the same physical dimensions (cf. Table 1). The TIR plot is constrained by the minimum entry angle necessary to achieve total internal reflection at the air–quartz interface, and the maximum entry angle permitted in order to avoid total internal reflection within the capillary walls.

Fig. 2 also implies that entry angles of somewhat greater than 53° would result in somewhat longer pathlengths for the TIR cell, and while this is true, in practice it was found that this angle was the one that gave the greatest optical transmission through the flow cell, and therefore the best signal to noise ratio and limit of detection. At angles greater than 53°, there is presumably incipient internal reflection and loss within the capillary at the liquid–quartz interface that increases as the calculated critical angle of 66.06° is approached.

There are at least two potential sources of error in the optical pathlength estimations for both the MR and TIR flow cells. Firstly, LED light sources are non-collimated, and thus there will be a range of incident angles because the optical fibre will emit light at the same angle as it is accepted from the source. Secondly, simple ray-tracing calculations like these assume that the reflections occur in only one plane. While this might be a reasonable assumption if square capillaries were used, the use of circular capillaries results in rotation of the rays about the longitudinal axis as they progress through the cell because of reflection from the curved walls.

The accuracy of the computed pathlength can be verified experimentally by determining the apparent molar absorptivity, ε' of a dye solution using both the MR and TIR cells. If the hydrodynamic dispersion, D, is measured, then the dispersion-corrected absorptivity can be determined, ε_{corr}, and the ratio of this value and the measured (true) absorptivity values will provide a measure of the error in the calculated and actual pathlengths. The ε_{corr} value for the Z-cell obtained in this manner is within experimental error of the measured value of $22700\,mol^{-1}L\,cm^{-1}$, which verifies the legitimacy of this approach (Table 2). The ε_{corr} values for the MR and TIR cells show that the optical pathlengths determined by simple geometric ray-tracing overestimate the true value by 12% and 15%, respectively. This is obvious given that the estimated number of reflections is 4.29, when it should be an integer value, and the four reflection nodes can be observed along the quartz capillary. However these nodal zones are noticeably diffuse, which is further evidence of the non-collimated nature of the light source, and the radial reflections that occur within the flow cell.

A major advantage of using total internal reflection to create a transversely illuminated cell is that a light beam undergoes less attenuation than it would during multiple reflections from a metal-coated wall, especially in the UV spectral range where even Al coatings exhibit a high degree of absorption.

3.2. Schlieren behaviour

Fig. 3 indicates that the schlieren effect of the TIR and MR cells is relatively small in comparison to that experienced by the Z-configuration cell. Of the TIR and MR cells, the latter showed the least schlieren effect, which is consistent with transmission of the light through the cell by multiple acute reflections. The slightly greater refractive index effect observed in the TIR cell results from a reflected light path which is more closely aligned to the longitudinal axis of the cell than in the MR cell. Under these conditions, the

Table 3
Comparison of the analytical performance for the determination of reactive phosphorus by flow analysis using the three different flow cell configurations.

Cell type	Calibration range ($\mu g P L^{-1}$)	R^2	Limit of detection[a] ($\mu g P L^{-1}$)	Reproducibility (%RSD for 100 ($\mu g P L^{-1}$), $n=5$)
Z	10–100	0.9993	4.9	0.80
MR	10–100	0.9995	3.8	0.27
TIR	10–100	0.9999	2.0	0.66

[a] Calculated from the calibration data using the linear regression method of Miller and Miller [23].

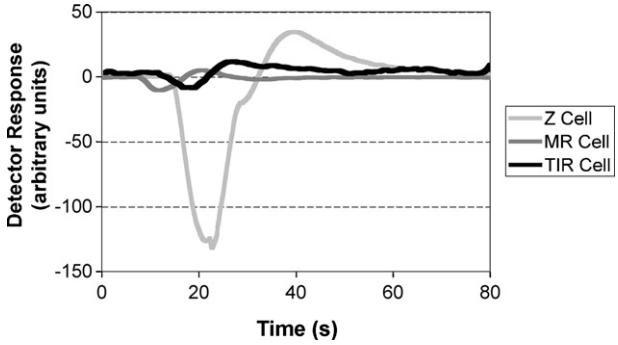

Fig. 3. Schlieren effects for Z-, multi-reflective and total-internal reflection cells for injection of sea water ($n = 1.3394$) into an ultra-pure water carrier stream ($n = 1.3330$). Measurements were performed at 660 nm.

schlieren lensing effect is more likely to occur. This is illustrated by Fig. 4 which compares the peak shapes obtained for the determination of reactive phosphorus in marine water using the TIR and the Z-configuration cells. There is no obvious indication of any schlieren effect occurring in the peaks collected using the TIR cell, whereas these effects are very evident when the Z-cell is employed. In waters where there are marked variations in salinity, such as occurs in estuaries, the schlieren effect can cause anomalous peaks when a Z-cell is used, which can lead to quite erroneous results. A cell that exhibits a reduction of the schlieren effect on peak shape will therefore measurably improve the accuracy of spectrophotometric measurement in such samples.

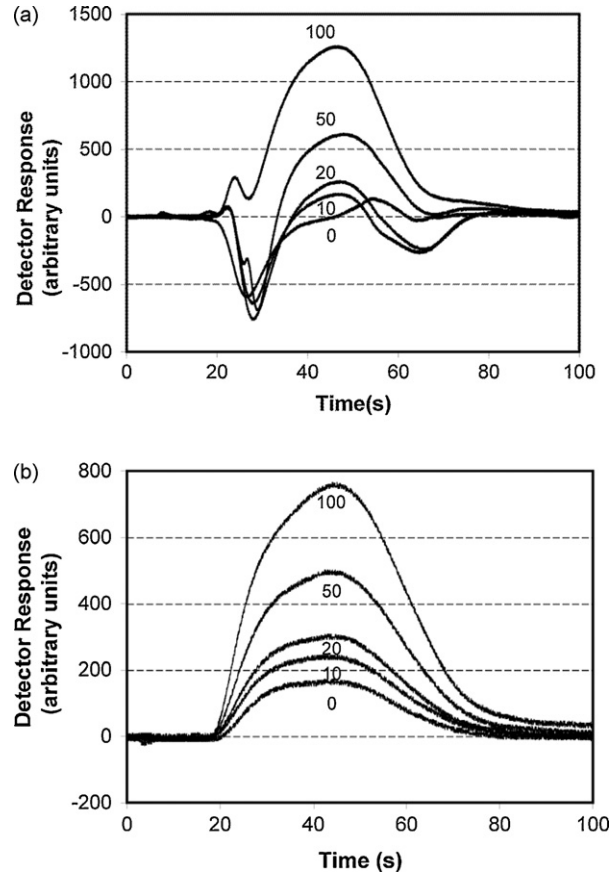

Fig. 4. Flow injection peaks for reactive phosphorus calibration using the (a) Z-cell and (b) the total internal reflection cell. Reactive phosphorus concentrations are shown as $\mu g P L^{-1}$, and were measured as phosphomolybdenum blue at 660 nm.

3.3. *Evaluation of the total internal reflection cell for the determination of reactive phosphate in seawater*

The reproducibility and limit of detection of the photometric determination of reactive phosphate in seawater were used as measures of the analytical performance of the total internal reflection cell. Identical flow injection manifold conditions were used in the evaluation of each flow cell, save that the cells themselves were exchanged between calibration experiments (Table 3). The measured detection limit of 2.0 $\mu g P L^{-1}$ and reproducibility of RSD = 0.66% for 100 $\mu g P L^{-1}$ ($n = 5$), indicate that the TIR cell has an analytical performance that is marginally better limit of detection that of MR cell and somewhat better than the Z-cell. While the optical pathlength of the TIR, and hence the sensitivity, are somewhat less than for the MR and Z cells, this is offset by the higher signal to noise ratio achieved for the TIR cell, with a commensurate improvement in the LOD.

4. Conclusion

A total internal reflection flow-through cell has been constructed and the optical and hydrodynamic characteristics have been evaluated using a series of dye studies. The practical advantages of this cell have been assessed in the photometric determination of reactive phosphorus using flow injection analysis. The performance of this new cell was compared with a silver-coated multi-reflective cell and a conventional Z-cell. A silver-coated MR cell showed superior sensitivity compared with the TIR cell because the pathlength of the latter is necessarily shorter due to the requirement for a greater entry angle in order to achieve total internal reflection. However, a better limit of detection was achieved for the TIR compared with either the MR or Z-cells, because the more efficient transmission of light through the cell results in an improved signal to noise ratio. There is also scope for further improvement of the sensitivity of the TIR cell by careful optimization of the internal diameter and wall thickness of the capillary used, and by modest increases in capillary length. The ray-tracing method employed to calculate the optical pathlength for the internally and mirror-coated reflective cells [15,18,22] has also been shown to provide estimates that are accurate to within 15% of those derived from dye studies.

The TIR is therefore more versatile than the MR cell, in that it does not rely for its operation on reflective coatings that only function efficiently within a particular and limited spectral range. However, unlike the MR cell, the TIR cell is not restricted to measurements of low absorbances, because its optical path is similar to that of a conventional Z-cell. In comparison with the Z-cell, the TIR cell shows much less susceptibility to the schlieren effect and a reduced potential for bubble entrapment.

Thus the TIR cell combines the advantages of schlieren-tolerance and lack of bubble entrapment of the MR cell with the higher S/N

ratio and wider dynamic range of a conventional Z-cell. This TIR optical configuration also offers the prospect for photometric detection in the UV range given an appropriate choice of light source, capillary material and optical coupling media.

Acknowledgements

This research was supported by an Australian Research Council Linkage Project grant (LP0669359) and EPA (Victoria).

References

[1] G.D. Christian, A.C. Tr, Trends Anal. Chem. 24 (2005) 560.
[2] W. Frenzel, I.D. McKelvie, in: S.D. Kolev, I.D. McKelvie (Eds.), Advances in Flow Injection Analysis and related Techniques, Elsevier, Amsterdam, 2008, p. 311.
[3] W. Lei, K. Fujiwara, K. Fuwa, Anal. Chem. 55 (1983) 951.
[4] F.I. Ormaza-González, P.J. Statham, Anal. Chim. Acta 244 (1991) 63.
[5] H. Takiguchi, A. Tsubata, M. Miyata, T. Odake, H. Hotta, T. Umemura, K. Tsunoda, Anal. Sci. (2006) 1017.
[6] Z.A. Wang, W.-J. Cai, Y. Wang, B.L. Upchurch, Mater. Chem. 84 (2003) 73.
[7] W. Yao, R.H. Byrne, Talanta 48 (1999) 277.
[8] A.C.B. Dias, E.P. Borges, E.A.G. Zagatto, P.J. Worsfold, Talanta 68 (2006) 1076.
[9] T. Yamane, J. Flow Injection Anal. 12 (1995) 176.
[10] E.A.G. Zagatto, M.A.Z. Arruda, A.O. Jacintho, I.L. Mattos, Anal. Chim. Acta 234 (1990) 153.
[11] H. Liu, P.K. Dasgupta, Anal. Chim. Acta 289 (1994) 347.
[12] I.D. McKelvie, D.M.W. Peat, G.P. Matthews, P.J. Worsfold, Anal. Chim. Acta 351 (1997) 265.
[13] S. Jambunathan, P.K. Dasgupta, D.K. Wolcott, G.D. Marshall, D.C. Olson, Talanta 50 (1999) 481.
[14] P.K. Dasgupta, Anal. Chem. 56 (1984) 1401.
[15] P.S. Ellis, A.J. Lyddy-Meaney, P.J. Worsfold, I.D. McKelvie, Anal. Chim. Acta 499 (2003) 81.
[16] J. Sebag, V.L. Krabbendam, G. Poczulp, D. Neill, T. Vucina, M. Boccas, Opt. Eng. 6273 (2006) 62730X.
[17] G. Hass, J.B. Heaney, H. Herzig, J.F. Osantowski, J.J. Triolo, Appl. Opt. 14 (1975) 2639.
[18] K.-I. Tsunoda, A. Nomura, J. Yamada, S. Nishi, Appl. Spectrosc. 43 (1989) 49.
[19] B. Karlberg, G.E. Pacey, Flow Injection Analysis—A Practical Guide, Elsevier, Amsterdam, 1989.
[20] J. Ruzicka, E.H. Hansen, Flow Injection Analysis, John Wiley and Sons, N.Y., 1981.
[21] A.J. Lyddy-Meaney, P. Ellis, P.J. Worsfold, E.C.V. Butler, I.D. McKelvie, Talanta 58 (2002) 1043.
[22] T. Wang, J.H. Aiken, C.W. Huie, R.A. Hartwick, Anal. Chem. 63 (1991) 1372.
[23] J.C. Miller, J.N. Miller, Statistics and Chemometrics for Analytical Chemistry, Pearson Education Limited, Harlow, England, 2005.

Talanta 79 (2009) 681–686

Contents lists available at ScienceDirect

Talanta

journal homepage: www.elsevier.com/locate/talanta

Screen-printed immunosensor modified with carbon nanotubes in a continuous-flow system for the *Botrytis cinerea* determination in apple tissues

Martín A. Fernández-Baldo, Germán A. Messina, Maria I. Sanz, Julio Raba*

INQUISAL, Departamento de Química, Universidad Nacional de San Luis, CONICET, Chacabuco y Pedernera, D5700BWS San Luis, Argentina

ARTICLE INFO

Article history:
Received 7 January 2009
Received in revised form 23 April 2009
Accepted 23 April 2009
Available online 7 May 2009

Keywords:
Enzyme immunoassays
Botrytis cinerea
Amperometric immunosensor
Carbon-based screen-printed electrodes
Multi-walled carbon nanotubes
Flow injection analysis

ABSTRACT

Botrytis cinerea is a plant-pathogenic fungus that produces the disease known as grey mould in a wide variety of agriculturally important hosts in many countries. This paper describes the development of an immunosensor coupled to carbon-based screen-printed electrodes (SPCE) modified with multi-walled carbon nanotubes (CNTs), which show a rapid and sensitive determination of *B. cinerea* in apple tissues (Red-delicious) using a competitive immunoassay method.

Both the infected plant tissue sample and the *B. cinerea*-specific monoclonal antibody are allowed to react immunologically with the *B. cinerea* purified antigens immobilized on a rotating disk. Then, the bound antibodies are quantified by a horseradish peroxidise (HRP) enzyme labeled second antibodies specific to mouse IgG, using 4-tertbutylcatechol (4-TBC) as enzymatic mediators. The HRP, in the presence of hydrogen peroxide, catalyses the oxidation of 4-TBC to 4-tertbutyl o-benzoquinone. The electrochemical reduction back to 4-TBC is detected on SPCE-CNT at −0.15 V. The response current is inversely proportional to the amount of the *B. cinerea* antigens present in the fruit sample. The time consumed per assay was 30 min and the calculated detection limits for electrochemical method and the ELISA procedure are 0.02 and 10 $\mu g\,mL^{-1}$, respectively. Moreover the intra- and inter-assay coefficients of variation were below 7%. This electrochemical immunosensor promises to be usefully suited to the detection and quantification of *B. cinerea* in apparently healthy plant prior to the development of the symptoms.

1. Introduction

A wide range of plant species, including economically important crops such as vegetables, ornamentals, bulbs and fruits can be affected by grey mould caused by the fungal pathogen *Botrytis cinerea* [1,2].

B. cinerea is a ubiquitous pathogen, present often as latent infections, which can in some cases can produce a development symptomatic infections in the plant. The latency between infection and the appearance of visible symptoms can be long and variable in the case of *B. cinerea*. Consequently, an apparently healthy plant can deteriorate suddenly due to the development of latent or quiescent infection into visible disease [3].

Gray mould is difficult to be controlled satisfactorily with fungicides because the fungus is genetically variable and some strains has developed resistance to many of the chemicals introduced in the last 20 years [4]. In addition, there are also pressures from consumers to reduce pesticides in the food chain [5,6]. For these reasons, there is an increased interest in alternatives to fungicides for disease detection and control. To prevent the indiscriminate use of fungicides, a sensitive and reliable methods to determinate the fungus in plant tissue become crucial.

Detection and quantification of specific fungus in plant tissues in the presence of other fungus are difficult. Classical methods such as isolation on selective media are useful but they have limitations, i.e., many pathogens are masked by overgrowth of faster growing fungi. Quantitative nucleic acid-based methods have been developed [3], but these methods are expensive and not easy to perform routinely. Immunological methods provide a promising alternative. The fungus was detected by enzyme-linked immunosorbent assay (ELISA) [7–9]. But unfortunately, these techniques require highly qualified personnel, consume a lot of time, or need sophisticated instrumentation. Therefore, development of a new method with high sensitivity and specificity for direct detection of *B. cinerea* is highly desirable.

Heterogeneous enzyme immunoassays, coupled with flow injection (FI) system and electrochemical detection, represent a powerful analytical tool for the determination of low levels of many analytes such as antibodies, hormones, drugs, tumor markers, and viruses [10].

Electrochemical biosensors based on screen-printed-single-use electrodes are in tune with the requirements of in situ screen-

* Corresponding author. Tel.: +54 2652 425385; fax: +54 2652 430224.
E-mail address: jraba@unsl.edu.ar (J. Raba).

0039-9140/$ – see front matter © 2009 Elsevier B.V. All rights reserved.
doi:10.1016/j.talanta.2009.04.059

ing devices and all the equipment needed for the electrochemical analysis is portable. Also, they have the major performance characteristics of biosensors, the minimum sample preparation, the simplicity of the apparatus, obtaining of fast results, the cost effectiveness, small and becoming miniaturized with new technologies [11]. However, in recent years, analyses with electrochemical detection constitute a methodology used extensively [12–15]. The advantages of this approach include the speed, accuracy, and precision with which many electrochemical measurements can be made.

Carbon nanotubes (CNTs) are a novel type of carbon material and can be considered as the result of folding graphite layers into carbon cylinders. The CNTs have generated great interest in future applications based on their field emission and electronic transport properties [16,17], their high mechanical strength and their chemical properties [18].

This work has been focused on their electrocatalytic behaviours toward the oxidation of biomolecules and their performance has been found to be much superior to those of other carbon electrodes in terms of reaction rate, reversibility and detection limit [19]. In view of the excellent properties of carbon nanotubes, they have been used to modify different electrodes for preparation of carbon nanotube nanoelectrode arrays and electrochemical sensing of chemical and biological species [20].

The advantages of carbon-based screen-printed electrodes (SPCEs), such as simple and low-cost fabrication and conveniently practical application in the detection of biomolecules, have been extensively illustrated [21–24]. The uses of CNTs for the preparation of CNT-modified screen-printed electrodes have been reported previously [25–28].

The objective of the current study was the development of an immunosensor coupled SPCEs modified with multi-walled-CNTs (SPCE-CNT) for rapid and sensitive determination of *B. cinerea* in plant tissues.

The detection of *B. cinerea* was carried out using a competitive immunoassay method based on the use of purified *B. cinerea* antigens that are immobilized on a rotating disk. The *B. cinerea* purified antigens or plant tissue sample (prepared in buffer PBS) and the *B. cinerea*-specific monoclonal antibody (BC-12.CA4) are allowed to react immunologically with the immobilized antigens, and the bound antibodies are quantified by a horseradish peroxidase (HRP) enzyme labeled second antibodies specific to mouse IgG, using 4-tertbutylcatechol (4-TBC) as enzymatic mediators. HRP in the presence of hydrogen peroxide (H_2O_2) catalyses the oxidation of 4-TBC to 4-tertbutyl o-benzoquinone (4-TBBQ) [29]. The electrochemical reduction back to 4-TBC is detected on SPCE-CNT at −0.15 V. The response current obtained from the product of enzymatic reaction is proportional to the activity of the enzyme and consequently, to the amount of antibodies bound to the surface of the immunosensor of interest, but the response current is inversely proportional to the amount of the *B. cinerea* antigens present in the fruit sample.

The assays were used for the detection and quantification of the fungus in infected apple fruits (Red Delicious) tissues before and after symptom induction, and does not require highly skilled technicians or expensive and dedicated equipment.

2. Materials and methods

2.1. Reagents and solutions

All reagents used were of analytical reagent grade. The monoclonal antibody BC-12.CA4 and secondary antibody-enzyme conjugate (anti-mouse polyvalent immunoglobulins peroxidase conjugate) were obtained from *ADGEN* diagnostics (Scotland, UK) and Sigma Chemical (St. Louis, MO, USA), respectively. Glutaraldehyde (25% aqueous solution) and H_2O_2 were purchased from Merck, Darmstadt. 3-Aminopropyl-modified controlled pore glass, 1400 Å mean pore diameter and 24 $m^2\ mg^{-1}$ surface area, was from Electro Nucleonics (Fairfield, NJ) and contained 48.2 $\mu mol\ g^{-1}$ of amino groups. 4-Tert-butylcatechol was purchased from Sigma Chemical Co., St. Louis and all other reagents employed were of analytical grade and were used without further purifications. Aqueous solutions were prepared using purified water from a Milli-Q-system.

The SAPS ELISA kit for Botrytis was purchased from SAPS offices, Cambridge University Botanic Garden, Cambridge, England and was used in accordance with manufacture instructions [30].

2.2. Flow-through reactor/detector unit

The main body of the cell was made of Plexiglas. Fig. 1 illustrates the design of the Flow-through chamber containing the rotating disk and the detector system with a final cell volume of 20 μL. The SPCE is on the top of the rotating reactor. The rotating reactor is a disk of Plexiglas into which a miniature magnetic stirring bar has been embedded. Rotation of the lower reactor was effected with a laboratory magnetic stirrer with control of temperature (Metrohm AG, Herisau, Switzerland) and controlled with a variable transformer with an output between 0 and 250 V and maximum amperage of 7.5 A (Waritrans, Argentina). All solutions and reagents were conditioned to 37 °C before the experiment, using a laboratory water bath Vicking Mason Ii (Vicking SRL, Argentina).

Amperometric detection was performed using the BAS LC-4C and the BAS 100 B (electrochemical analyzer Bioanalytical System, West Lafayette, IN) was used for cyclic voltammetric analysis. The potential applied to the CNT-GCE detection was −0.15 V versus Ag/AgCl, 3.0 mol L^{-1} NaCl reference electrode (BAS RE-6), and a Pt wire was the counter electrode. At this potential, a catalytic current was well established.

A pump (Wilson Minipuls 3 peristaltic pump, Gilson Electronics, Middleton, WI, USA) and a Baby Bee Syringe Pump (Bioanalytical System, West Lafayette, IN) were used for pumping, introducing the sample, and stopping the flow.

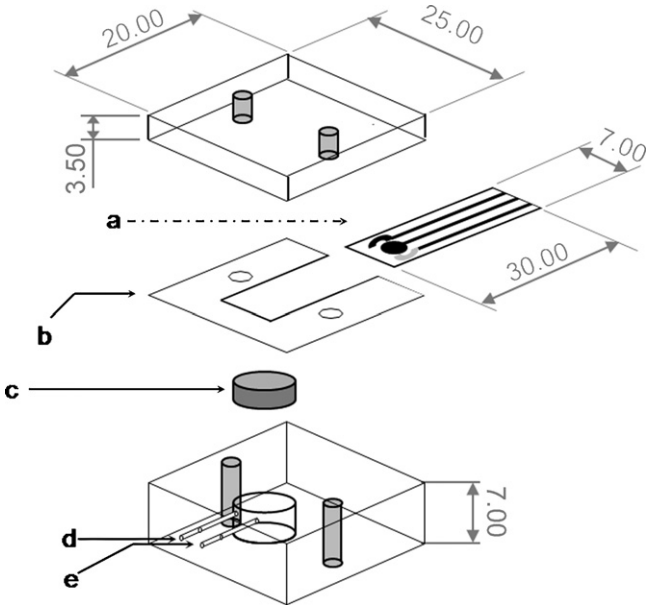

Fig. 1. Schematic representation of components in the bioreactor flow cell. (a) SPCE-CNT, (b) Gasket: Teflon, thickness 0.3 mm, (c) rotating disk, (d) flow out, and (e) flow in. All measurements are given in millimeters.

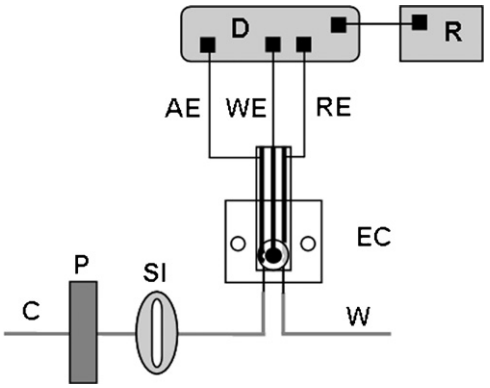

Fig. 2. Block diagram of the continuous-flow system and detection arrangement. P: pump (Gilson Minipuls 3 peristaltic pump, Gilson Electronics, Inc. Middleton, WI). C: carrier buffer line. SI: sample injection. W: waste line. EC: cell containing the rotating disk and GSPE. WE: SPGE-CNT. RE: pseudo-reference electrode. AE: auxiliary electrode. D: BAS LC-4C potentiostat (Bioanalytical Systems, West Lafayette, IN, USA). R: recorder.

Fig. 2 illustrates schematically the components of the single-line continuous-flow setup. The pump tubing was Tygon (Fisher Accu Rated, 0.25 mm i.d., Fisher Scientific, Pittsburgh, PA, USA), and the remaining tubing used was Teflon (0.25 mm i.d. from Cole–Parmer, Chicago, IL, USA).

All pH measurements were made with an Orion Expandable Ion Analyzer (model EA 940, Orion Research, Cambridge, MA, USA) equipped with a glass combination electrode (Orion Research).

2.3. Preparation of the B. cinerea antigens

A *B. cinerea* strain was recovered from apple tissues and it was used in this study. The isolates were maintained on potato dextrose agar (PDA) at 4 °C. For micelial production, the *B. cinerea* were grown on PDA, for 8–12 days at 21 ± 2 °C. After that, the mycelial mat was removed; snap frozen in liquid nitrogen, blended in a warring blendor and freeze dried to obtain a fine powder and resuspended in 0.01 mol L^{-1} PBS, pH 7.2. The antigen preparation was centrifuged at 1000 × *g* for 10 min, and the supernatant was stored in the 0.01 mol L^{-1} PBS (pH 7.2), at −20 °C between uses.

For conidial production, *B. cinerea* were grown on PDA at 21 ± 2 °C. When the mycelium appeared, cultures were kept at 15 °C for inducing sporulation. After a week, spores were harvested and suspended in 10 mL of sterile the 0.01 mol L^{-1} PBS (pH 7.2) containing 0.05% (v/v) Tween 80. The concentration of spore suspension was determined with a Neubauer chamber and adjusted with PBS to 1×10^5 spores mL^{-1}.

2.4. Preparation of the SPCE-CNT

An electrode pretreatment was carried out before each voltammetric experiment in order to oxidize the graphite impurities and to obtain a more hydrophilic surface [31], with the aim of improving the sensitivity and reproducibility of the results.

The graphite electrode surface is pretreated applying a potential +1.6 V (versus Ag-SPE) for 120 s and +1.8 V (versus Ag-SPE) for 60 s in 5 mL of 0.25 mol L^{-1} acetate buffer, containing 0.01 mol L^{-1} KCl (pH 4.75), under stirred conditions. Then, the electrodes were washed using 0.01 mol L^{-1} PBS, pH 7.2 and stored in the same buffer at 4 °C.

One milligram of MWCNT was dispersed with the aid of ultrasonic stirring for 45 min in methanol/water (50:50, v/v) in an aqueous 0.1% Nafion solution. A 5 μL aliquot of this dispersion was dropped on the screen-printed graphite working electrode surface and then the solvent was evaporated under an infrared heat lamp [32].

2.5. Immunosensor preparation

The rotating disk reactor (bottom part) was prepared by immobilizing *B. cinerea* antigens on 3-aminopropyl-modified controlled-pore glass (APCPG). The APCPG, smoothly spread on one side of a double-coated tape affixed to the disk surface, was allowed to react with an aqueous solution of 5% (w/w) glutaraldehyde at pH 10.00 (0.20 mol L^{-1} carbonate) for 2 h at room temperature. After washing with purified water and 0.10 mol L^{-1} phosphate buffer of pH 7.00, 25 μL of antigens preparation (10 μg mL^{-1} 0.01 mol L^{-1} PBS, pH 7.2) was coupled to the residual aldehyde groups overnight at 5 °C. The immobilized antibodies preparation was finally washed with phosphate buffer (pH 7.00) and stored in the same buffer at 5 °C between uses. The immobilized antigen preparations were perfectly stable for at least 1 month.

2.6. Amperometric analysis of B. cinerea in apple fruits tissues samples

This method was applied in the determination of *B. cinerea* in 24 commercials apple fruits tissues samples and in the detection of *B. cinerea* in control infected plant tissues.

The control apples were infected using a spore suspension of 1×10^5 spores mL^{-1}. Fruit were wounded (3 mm × 3mm × 3 mm) with a punch, and 20 μL of the spore suspension were pipetted into a wound. The apples were kept at 25 °C and evaluations of rot incidence and lesion diameters were made along 10 days. Ten fruit per the assays were used with three wounds each one. Each experiment was repeated three times.

Infected and uninfected apples tissues were ground to a fine powder in liquid N_2. The PBS extracts were prepared from powdered apples tissues extracts by adding 0.1 g plant tissue into 0.9 mL PBS and vortexed for 1 min to ensure homogeneous suspensions before using for the immunological assay.

The unspecific binding (on the surface of the rotating disc) was blocked by 5 min treatment at 37 °C with 3% skim milk in a 0.01 mol L^{-1} PBS, pH 7.2. The apples PBS extracts were diluted twofold with a solution of the monoclonal antibody IgG mouse anti-*B. cinerea* at a concentration of 15 μg mL^{-1} (0.01 mol L^{-1} PBS, pH 7.2) and then 25 μL of this solution were injected into the PBS carrier stream at a flow rate of 100 μL min^{-1} and incubated 10 min at 25 °C with stirring.

The immunosensor was washed with 0.01 mol L^{-1} PBS, pH 7.2. After washing, 25 μL of the anti-mouse IgG-HRP conjugate (dilution of 1/2000 in 0.01 mol L^{-1} PBS, pH 7.2) was injected and incubated 10 min at 25 °C with stirring. The immunosensor was then washed free of any traces of unbound enzyme conjugate with 0.01 mol L^{-1} PBS (pH 7.2). Finally the substrate solution (25 μL of a 0.1 mol L^{-1} phosphate–citrate buffer, pH 5.0 containing 1.0×10^{-3} mol L^{-1} H_2O_2 and 1.0×10^{-3} mol L^{-1} 4-TBC) was injected into the carrier stream and the enzymatic product was detected by amperometric flow injection analysis. For the next analysis the immunoreactor was conditioned by injection of desorption buffer (0.1 mol L^{-1} glycine–HCl, pH 2) for 2 min and then washed with 0.01 mol L^{-1} in PBS, pH 7.2. The SPCE-CNTs were reused for five consecutive determination.

A standard curve for the amperometric procedure was produced by following our protocol with a series of purified antigens that covered the relevant range of antigen concentration (0–100 μg mL^{-1}). When not in use, the immunosensor was stored in 0.01 mol L^{-1} PBS (pH 7.2) containing sodium azide (0.01%) at 4 °C.

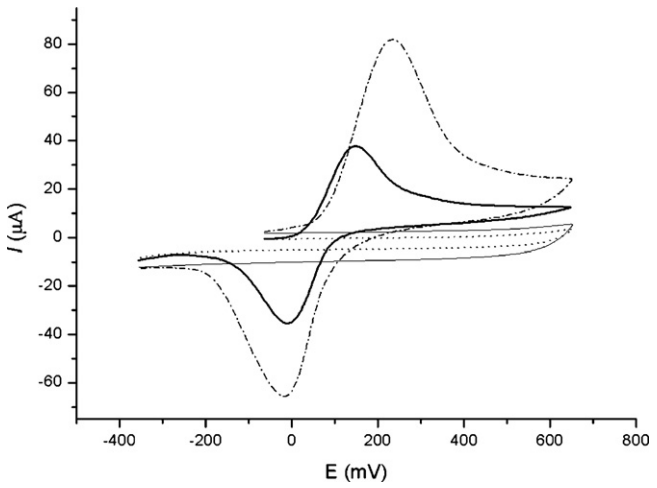

Fig. 3. Cyclic voltammograms at a CNT-SPCE (·–·–·) and at a bare GCE (—) for 1.0×10^{-3} mol L^{-1} 4-TBC in aqueous solution containing 0.1 mol L^{-1} phosphate–citrate buffer (pH 5.0). The background voltammograms of CNT-SPCE (···) and a bare GCE (—) was made in aqueous solution containing 0.1 M phosphate–citrate buffer (pH 5.0). Scan rate: 0.1 V s^{-1}, $T = (25 \pm 1)$ °C.

3. Results and discussion

3.1. Electrochemical study of 4-TBC with the SPCE-CNT

Fig. 3 shows the comparison of cyclic voltammograms obtained at a SPCE-CNT and at an unmodified SPCE for 1 mM solution of 4-tertbutylcatechol (4-TBC) in an aqueous solution containing 0.10 mol L^{-1} phosphate buffer pH 7.0 as supporting electrolyte. As it can be seen, 4-TBC exhibit well-defined one anodic and a corresponding cathodic peak versus Ag/AgCl at the CNT-GCE, which corresponds to the transformation of 4-TBC to 4-TBBQ and vice-versa within a quasi-reversible two-electron process, whose peak currents are considerably larger than those obtained at the bare GCE. The modification of the electrode surface with CNTs produced an enhancement of the electrochemical response for this compound.

The improved amperometric response at the CNT-modified electrode is attributed to the increased surface area upon electrode modification [33]. Other relevant advantages of the amperometric detection at CNTs-GCE are the high repeatability and very low and stable background currents of the measurements achieved over the whole potential range [33]. The ability of carbon nanotubes to circumvent electrode surface fouling during amperometric sensing has been recognized for molecules such as NADH [34] and can be attributed to the unique spatial structure of CNTs.

The effect of the concentration of CNT on the surface of GCE was studied in range of 0.1–3 mg of CNTs, which were dispersed in 1 mL of methanol/water (50:50 v/v) in an aqueous 0.1% Nafion solution. A 10 μL aliquot of this dispersion was dropped on the graphite working electrode surface and then the solvent was evaporated under an infrared heat lamp. A significant increase of electric signal was observed between 0.5 and 1 mg mL^{-1}. Insignificant differences were obtained for greater concentrations. For convenience 1 mg mL^{-1} of CNT was used to electrode modifications.

3.2. Optimum conditions for the immune reactions and the determination of enzymatic products

It has been shown that the theoretical framework developed for static ELISA system cannot be applied to describe the kinetics of antibody–antigen interactions occurring in a continuous-flow immunoassay [35]. The buffer flow reduces the limitations of diffusion as observed in static ELISA systems [36], the controlled pore glass increase the area for antigens immobilization about three orders of magnitude [37] and a high sensitivity can be attained by a rotating bioreactor and continuous-flow/stopped-flow/continuous-flow processing [38].

The proposed method manifolds follow the EIA principles, but instead of using a microtiter plate, the reagents and washing buffers were pumped consecutively through the immunosensor containing immobilized antibodies, coupled to electrochemically detection for the determination of *B. cinerea*. The HRP enzyme-labeled second antibody specific to mouse IgG was used as conjugate and the product of the enzymatic indicator reaction was measured using electrochemical detection.

The implementation of continuous-flow/stopped-flow programming and the location of two facing independent reactors (Fig. 1) permits: (a) utilization of relatively low immunoreactants loading conditions, (b) instantaneous operation under high initial rate conditions, (c) easy detection of accumulated products, and (d) reduction of apparent Michaelis–Menten constant, K'_M.

A more complete reagent homogenization is achieved [39], because the cell works as a mixing chamber by facilitating the arrival of immunoreactants, the arrival of enzymatic substrate at the active sites and the release of products from the same sites. The net result is high values of current.

The effect of the rotation rate was evaluated in a range of 60–300 rpm. A significant increase of electric signal was observed between 60 and 180 rpm. Insignificant differences were obtained for greater rotation velocities. For convenience a rotation rate of 180 rpm was used to evaluate other parameters. If the rotating disk in the cell is devoid of rotation, the response is lower because diffusional reactions are too slow to be observed in the time scale of electrochemical analysis. If a rotation of 180 rpm is imposed on the rotating disc at the bottom of the cell, the signal is dramatically enlarged.

The sample size was studied in the range 5–40 μL. Sensitivity is almost tripled in the range between 5 and 25 μL. Insignificant differences were obtained for greater sample size. A sample size of 25 μL was used to evaluate other parameters.

The rate of enzymatic response under stopped-flow conditions was studied in the pH range 4–7 and shows a maximum value of activity at pH 5. The pH value used was 5.00 in 0.1 mol L^{-1} phosphate–citrate buffer.

The effect of varying H_2O_2 concentration from 1.0×10^{-4} to 1.0×10^{-2} mol L^{-1}, for 1.0×10^{-3} mol L^{-1} 4-TBC solution and the effect of varying 4-TBC concentration from 1.5×10^{-4} to 2.5×10^{-2} mol L^{-1} for 1.0×10^{-3} mol L^{-1} H_2O_2 solution on the bioreactor response were evaluated. The optimum concentrations of H_2O_2 and 4-TBC were 1.0×10^{-3} mol L^{-1}, respectively. Those concentrations were then used.

3.3. Quantitative test for the detection of B. cinerea

Under the selected conditions described above, the electrochemical response of the enzymatic product is proportional to the activity of the enzyme and consequently is inversely proportional to the amount of the *B. cinerea* antigens present in the fruit sample.

A standard curve for the amperometric procedure was produced by following our protocol with a series of purified antigens that covered the relevant range of antigen concentration (0–100 μg mL^{-1}). The linear regression equation was $i = 526.03 + -4.78 \times C_{B.\ cinerea}$, with the linear regression coefficient $r = 0.996$. The coefficient of variation (CV) for the determination of 25 μg mL^{-1} *B. cinerea* was below 4% (six replicates). The detection limit (DL) was considered to be the concentration that gives a signal three times the standard deviation (SD) of the blank. For the proposed method the DL was 0.02 μg mL^{-1}. The commercial spectrophotometric

Table 1
Within-assay precision (five measurements in the same run for each control serum) and between-assay precision (five measurements for each control, repeated for three consecutive days).

Control solution[a]	Within-assay		Between-assay	
	Mean	CV%	Mean	CV%
5	5.22	2.20	5.61	4.41
25	24.78	3.78	25.40	6.54
75	76.01	2.86	76.94	5.86

[a] ($\mu g\,mL^{-1}$) *B. cinerea* antigen.

system SAPS-ELISA Kit for Botrytis permit to make quantitative estimates of the fungal antigen present in a fruit sample within a 1 h practical session. The SAPS-ELISA Kit for Botrytis detecting in a linear manner, between 10 and 30 $\mu g\,mL^{-1}$ with a DL of 3.5 $\mu g\,mL^{-1}$ of *B. cinerea* purified antigens concentrations. This result shows that electrochemical detection was more sensitive than spectrophotometric method.

The precision of the electrochemical assay was checked with a control solution at 5, 25 and 75 $\mu g\,mL^{-1}$ *B. cinerea* purified antigens concentrations. The within-assay precision was tested with five measurements in the same run for each sample. These series of analyses were repeated for three consecutive days in order to estimate the between-assay precision. The results obtained are presented in Table 1. The *B. cinerea* assay showed good precision; the CV within-assay values were below 4% and the between-assay values were below 7%.

The accuracy was tested with dilution and recovery tests. A dilution test was performed with a control solution of 100 $\mu g\,mL^{-1}$ *B. cinerea* purified antigens concentrations with 0.01 mol L^{-1} PBS, pH 7.2 (Fig. 4).

The electrochemical system was compared with a commercial spectrophotometric system SAPS-ELISA Kit for Botrytis for the determination of *B. cinerea* in 24 commercials apple fruits tissues samples. Reproducibility assays were made using a repetitive standard ($n = 6$) of 25 $\mu g\,mL^{-1}$ *B. cinerea* (Table 2).

3.4. Correlations with ELISA assay procedure

The electrochemical system was compared with a commercial spectrophotometric system for the quantification of *B. cinerea* in 24 commercials apple fruits tissues samples. The slopes obtained were reasonably close to 1, indicating a good correspondence between

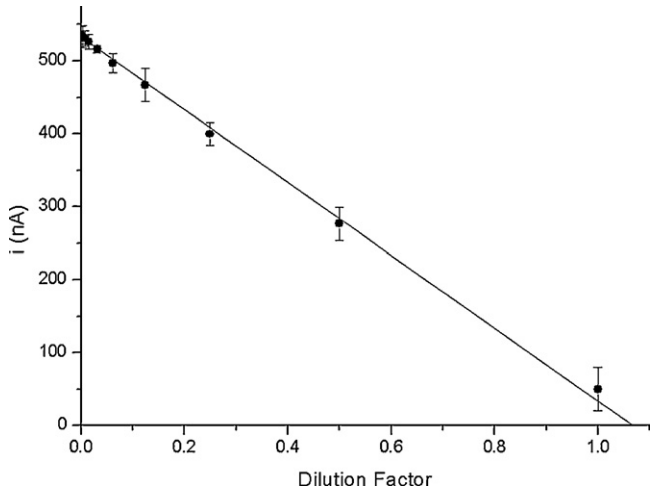

Fig. 4. Dilution test results for the control solution of 100 $\mu g\,mL^{-1}$ *B. cinerea* purified antigens concentrations with 0.01 mol L^{-1} PBS, pH 7.2. Each value of current is based on five determinations.

Table 2
Reproducibility assays using repetitive standards ($n = 6$) of 25 $\mu g\,mL^{-1}$ *B. cinerea* antigen concentration.

Standards of 25 $\mu g\,mL^{-1}$ *B. cinerea* antigen	Proposed method ($\mu g\,mL^{-1}$)	EIA ($\mu g\,mL^{-1}$)
1	25.11	24.31
2	25.57	25.57
3	24.82	24.44
4	25.34	25.54
5	25.79	25.98
6	24.27	26.47
$X \pm SD$[a]	25.15 ± 0.549	25.38 ± 0.853

[a] X ($\mu g\,mL^{-1}$), mean ± SD, standard deviation.

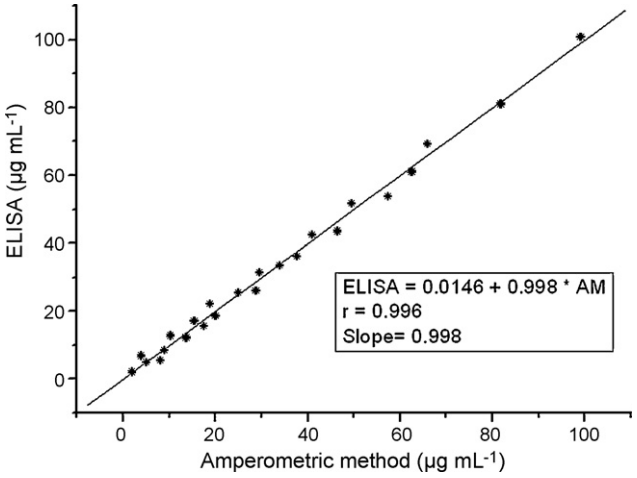

Fig. 5. Correlation between proposed method and commercial photometric assays.

the two methods (Fig. 5). Compared with the SAPS-ELISA Kit for Botrytis, our method shows large enhancement in sensitivity, low detection limit, speed and simplicity. These results suggest that the sensitivity reached for this procedure allow to determine very low level of *B. cinerea* antigens in apparently healthy plant that can deteriorate suddenly due to the development of latent or quiescent infection into visible disease.

4. Conclusions

In this work, a microfluidic immunosensor coupled with flow injection (FI) system for rapid, sensitive and selective quantification with very low levels of *B. cinerea* in commercials apple fruits tissues samples was developed using electrochemical detection.

The overall assay time (30 min) was shorter than the time reported for ELISA commercial test kits (60 min), with no reduction on the selectivity, being these important advantages. Also minimizes the waste of expensive reagents; shows physical and chemical stability, low background current, wide working potential range, and accuracy. Modification of SPCE with CNTs produced an enhancement of the electrochemical responses obtained for reduction of 4-tertbutyl o-benzoquinone to 4-TBC.

In conclusion, this method promises to be particularly useful in the analysis of symptomless plants, either to locate latent infections (avoiding conventional culturing techniques which are not only time-consuming but also not able to give a quantitative result) or to assess disease development before symptoms become visible.

Acknowledgements

The authors wish to thank the financial support from the Universidad Nacional de San Luis, the Agencia Nacional de Promoción

Científica y Tecnológica, and the Consejo Nacional de Investigaciones Científicas y Técnicas (CONICET).

References

[1] J.R. Coley-Smith, K. Verhoeff, W.R. Jarvis, The Biology of Botrytis, Academic Press, NewYork, 1980, p. 318.
[2] M.L. Daughtrey, R.L. Wick, J.L. Paterson, Compendium of Flowering Potted Plant Diseases, American Phytopathological Society Press, 1995, p. 11.
[3] M. Belen Suarez, K. Walsh, N. Boonham, T. O'Neill, S. Pearson, I. Barker, Plant Physiol. Biochem. 43 (2005) 890.
[4] R. Staples, A. Mayer, FEMS Microbiol. Lett. 134 (1995) 1.
[5] B. Hileman, Chem. Eng. News 71 (1993) 3.
[6] W. Leibinger, B. Breuker, M. Hahn, K. Mendgen, Phytopathology 87 (1997) 1103.
[7] U.M. Meyer, R.A. Spotts, F.M. Dewey, Plant Dis. 84 (2000) 1099.
[8] F.M. Dewey, S.E. Ebeler, D.O. Adams, A.C. Noble, U.M. Meyer, Am. J. Enol. Vitic. 51 (2000) 276.
[9] F.A. Obanor, M. Walter, N.W. Waipara, R. Cernusko, N. Z. Plant Prot. 55 (2002) 150.
[10] G. Gübitz, C. Shellum, Anal. Chim. Acta 283 (1993) 421.
[11] G. Bagni, D. Osella, E. Sturchio, M. Mascini, Anal. Chim. Acta 573 (2006) 81.
[12] A.L. Lasalle, B. Limoges, C. Degrand, J. Electroanal. Chem. 379 (1994) 281.
[13] L. Dellaciana, G. Bernacca, F. Bordin, S. Fenu, F. Garetto, J. Electroanal. Chem. 382 (1995) 129.
[14] K. Jiao, W. Sun, H.Y. Wang, Chinese Chem. Lett. 13 (2002) 69.
[15] R.E. Gyurcsanyi, A. Bereczki, G. Nagy, M.R. Neuman, E. Lindner, Analyst 127 (2002) 235.
[16] Q. Zhao, Z. Gan, Q. Zhuang, Electroanalysis 14 (2002) 1609.
[17] M.M. Treachy, T.W. Ebbesen, J.M. Gibson, Nature (London) 381 (1996) 678.
[18] H. Murakami, M. Hirakawa, C. Tanaka, H. Yamakawa, Appl. Phys. Lett. 76 (2000) 1776.
[19] G. Li, J.M. Liao, G.Q. Hu, N.Z. Ma, P.J. Wu, Biosens. Bioelectron. 20 (2005) 2140.
[20] N.Q. Li, J.X. Wang, M.X. Li, Rev. Anal. Chem. 22 (2003) 19.
[21] M.A.T. Gilmartin, J.P. Hart, D.T. Patton, Analyst 120 (1995) 1973.
[22] J.P. Hart, S.A. Wring, Trends Anal. Chem. 16 (1997) 89.
[23] J. Wang, P.V.A. Pamidi, K.R. Rogers, Anal. Chem. 70 (1998) 1171.
[24] M.P. O'Halloran, M. Pravda, G.G. Guilbault, Talanta 55 (2001) 605.
[25] P. Fanjul-Bolado, P. Queipo, P.J. Lamas-Ardisana, A. Costa-García, Talanta 74 (2007) 427.
[26] N. Sato, H. Okuma, Sens. Actuators B Chem. 129 (2008) 188.
[27] C. Lee, S. Wang, C. Yuan, M. Wen, K. Chang, Biosens. Bioelectron. 22 (2007) 877.
[28] Y. Ye, H. Ju, Biosens. Bioelectron. 21 (2005) 735.
[29] C. Ruan, Y. Li, Talanta 54 (2001) 1095.
[30] Instruction Manual for SAPS ELISA kit for Botrytis (Student Guide), Cambridge University Botanic Garden, Cambridge, England, 2000.
[31] J. Wang, X. Cai, C. Jonsson, M. Balakrishnan, Electroanalysis 8 (1996) 20.
[32] D. Vega, L. Agüí, A. González-Cortés, P. Yáñez-Sedeño, J.M. Pingarrón, Talanta 71 (2007) 1031.
[33] L. Agüí, C. Peña-Farfal, P. Yáñez-Sedeño, J.M. Pingarrón, Electroanalysis 19 (2007) 237.
[34] M. Musameh, J. Wang, A. Merkoci, Y. Lin, Electrochem. Commun. 4 (2002) 743.
[35] G.A. Wemhoff, S.Y. Rabbany, A.W. Kusterbeck, R.A. Ogert, R. Bredehorst, F.S. Ligter, J. Immunol. Methods 156 (1992) 223.
[36] E. Salinas, A. Torriero, F. Battaglini, M.I. Sanz, R. Olsina, J. Raba, Biosens. Bioelectron. 21 (2005) 313.
[37] M.C. Gosnell, R.E. Snelling, H.A. Mottola, Anal. Chem. 58 (1986) 1585.
[38] A. Lapierre, F. Battaglini, J. Raba, Anal. Chim. Acta 443 (2001) 17.
[39] G.A. Messina, A. Torriero, I.E. De Vito, J. Raba, Talanta 64 (2004) 1009.

Talanta 79 (2009) 824–829

Contents lists available at ScienceDirect

Talanta

journal homepage: www.elsevier.com/locate/talanta

Determination of organophosphate flame retardants and plasticizers in sediment samples using microwave-assisted extraction and gas chromatography with inductively coupled plasma mass spectrometry

M. García-López [a,b], I. Rodríguez [a], R. Cela [a], K.K. Kroening [b], J.A. Caruso [b,*]

[a] Departamento de Química Analítica, Nutrición y Bromatología, Facultad de Química, Instituto de Investigación y Análisis Alimentario (IIAA), Universidad de Santiago de Compostela, Santiago 15782, Spain
[b] University of Cincinnati/Agilent Technologies Metallomics Center of the Americas, Department of Chemistry, University of Cincinnati, Cincinnati, OH 45221-0172, USA

ARTICLE INFO

Article history:
Received 18 February 2009
Received in revised form 6 May 2009
Accepted 7 May 2009
Available online 15 May 2009

Keywords:
Inductively coupled plasma mass spectrometry
Microwave extraction
Organophosphate compounds
Flame retardants
Sediment

ABSTRACT

A procedure for the determination of 10 organophosphates, used as flame retardants and plasticizers, in sediment samples is presented. Microwave-assisted extraction (MAE) and gas chromatography with inductively coupled plasma mass spectrometry (GC–ICP-MS) were used for sample preparation and analytes determination, respectively. Influence of different variables on the performance of extraction and determination processes is thoroughly discussed. Temperature, type and amount of organic solvent showed a major effect on the yield of MAE. Regarding GC–ICP-MS detection, the combination of pulsed splitless injection with low radio frequency (rf) power, hard extraction conditions (referred to lens voltage) and addition of nitrogen (0.03 L min^{-1}) to the argon plasma provided the best sensitivity. Under final working conditions, recoveries between 78% and 105%, for samples spiked at different concentration levels, and limits of quantification from 2 to 4 ng g^{-1} were achieved. Analysis of unspiked sediments confirmed the excellent selectivity of the proposed method for real-life polluted sample analysis.

1. Introduction

Organophosphate esters (OPs) are a heterogeneous group of compounds in terms of physical and chemical properties and applications [1]. They are commonly used as flame retardants and plasticizers and can be found in a wide variety of products, such as varnishes, polyurethane foams, upholstery and textiles. OPs are normally employed as additives, not chemically bonded; therefore, they can easily be released to the surrounding area [2]. After that, air, particulate matter, and wastewater contribute to their spread into the environment. As a result of their increasing usage, persistence of some species, particularly chlorinated OPs, low water solubility and high adsorption to particulate matter of some of them, they can be concentrated in sediment samples [3–8]. So far, little work has been conducted for the extraction of OPs from sediments and the available procedures, which have been developed for just a few of them, are time-consuming and require large amounts of organic solvent. Soxhlet extraction using methanol–water (2:1) for 24 h [3], reflux heating with methanol–water (9:1) for 16 h [4], ultrasound-assisted solvent extraction with ethyl acetate–acetonitrile (3:7), 2 × 30 mL, for 30 min [5], shaking with acetone for 30 min [6] or combination of sonication (20 min) and shaking (15 min) with acetone (100 mL) first and methanol (50 mL) second [7], have been proposed for OPs extraction from sediments. Further clean-up of raw extracts provided by above techniques normally involved dilution with water and partition into dichloromethane [7], and/or solid-phase extraction using normal [4,6] or reversed-phase sorbents [3]. To the best of our knowledge, the only microwave-assisted extraction (MAE) protocol for this matrix was proposed by De Geus et al. [8]. The researchers used a domestic microwave oven to perform the extraction of a few OPs in open vials, thus irradiation time was limited by the boiling point of the selected solvent mixture.

Gas chromatography (GC) with nitrogen phosphorus detection (NPD) [9,10], mass spectrometry using electron impact ionization (GC–EI-MS) [11,12] or positive chemical ionization (GC–PCI-MS) [13,14] have been proposed for the determination of OPs in environmental samples. Unsatisfactory selectivity of NPD detection, excessive fragmentation of some OPs in EI-MS, rendering ions with low m/z ratios, and limited sensitivity in PCI-MS are some of the most important drawbacks of these techniques when applied to the determination of OPs in complex environmental matrices [15]. Conversely, inductively coupled plasma mass spectrometry (ICP-MS) provides a good combination of sensitivity and selectivity, which has been exploited not only for OPs analysis in complex matrices, such as blood [16] or wastewater [17], but also

* Corresponding author.
E-mail address: joseph.caruso@uc.edu (J.A. Caruso).

0039-9140/$ – see front matter © 2009 Elsevier B.V. All rights reserved.
doi:10.1016/j.talanta.2009.05.006

for phosphorus-containing pesticides in different beverages and environmental samples [18–21].

On the other hand, as far as could be ascertained, the ICP-MS capability for the determination of triisobutyl phosphate (TiBP), tris(chloropropyl)phosphate (TCPP), tris(dichloropropyl) phosphate (TDCP) and triphenyl phosphine oxide (TPPO) has not been evaluated yet. Furthermore, published papers for the remaining OPs do not deal with the direct injection of an organic solvent in the GC–ICP-MS system but use solid-phase microextraction (SPME) as sample introduction technique [16,17]. Therefore, this work is the first approach using direct solvent injection for OPs determination by means of GC–ICP-MS.

Available data related to the presence of OPs in sediments are very limited; moreover, these compounds are usually found at low level, which poses an additional challenge to their determination. The Office of Health studies from Tokyo on its surveys from 1977 to 1979 reported levels of tributyl phosphate (TBP) between 2 and 240 ng g^{-1} [6]. Ishikawa et al. determined levels of tris(2-chloroethyl)phosphate (TCEP) ranging from 13 to 28 ng g^{-1} [6]. Martinez-Carballo et al. [5] analyzed several Austrian sediments determining concentrations of TBP, TCEP, tris(2-butoxyethyl)phosphate (TBEP), triphenyl phosphate (TPP) and tris(2-ethylhexyl)phosphate (TEHP) between 2.4 and 160 ng g^{-1} and up to 1300 ng g^{-1} for TCPP. TDCP was also detected in some of the analyzed samples. However, high levels of some OPs were measured in bottom sediment from a waste disposal site and the surrounding area in Japan: TBP, TCEP, TCPP, TDCP, TBEP and TEHP determined concentrations ranged from 2 to 7395 ng g^{-1} [7]. The aim of this work was to develop a procedure to extract a group of 10 OPs from sediment samples. MAE was the technique of choice and GC–ICP-MS was used for determination purposes. Several variables affecting the extraction efficiency were evaluated in detail and ICP-MS parameters were optimized. Finally, the performance of the method was demonstrated with real-life polluted sediments.

2. Experimental

2.1. Reagents, standards and samples

Acetone, ethyl acetate, *n*-hexane and dichloromethane were acquired from Pharmco-Aaper (Brookfield, CT, USA). Acetonitrile was purchased from Tedia (Fairfield, OH, USA). Tripropyl phosphate (TPrP), TiBP, TBP, TCEP, TDCP, TBEP, TPP, TEHP and TPPO were acquired from Aldrich (Milwaukee, WI, USA). TCPP, as a technical mixture of three isomers, was provided by the chemical company Dr. Ehrenstorfer (Augsburg, Germany). For quantitative purposes only the first isomer was considered. Tripentyl phosphate (TPeP) was obtained from TCI Europe (Zwijndrecht, Belgium) and used as internal standard (IS). Individual stock solutions of each analyte and the IS were prepared in acetone. Diluted standards and mixtures of target OPs were made in *n*-hexane, when used to prepare spiked samples, and in ethyl acetate, when employed as calibration standards. The stock solution of the IS was also diluted with ethyl acetate and added to calibration standards and sample extracts. Normal-phase silica cartridges (50 mg) were provided by Waters (Milford, MA, USA).

Sediment samples were obtained from rivers located in Spain and USA: Sarela (Santiago de Compostela, Spain), Asma (Chantada, Spain) and Ohio River on its way through three different states: Ohio, Kentucky and Indiana (USA). Samples were dried (freeze-dried or air dried) and sieved. Fractions with particle sizes below 300 μm were considered for this study.

Preliminary assays were performed with sediment from the Ohio river spiked with 1000 ng g^{-1} for each compound. For the experimental factorial design and method performance evaluation, the sediment from the Sarela was used; the spiked levels were 1000, 200 and 50 ng g^{-1}. The spiking procedure consisted of mixing a fraction of sediment with a standard solution of OPs in *n*-hexane, using a volume of solvent which guaranteed that the sediment was completely covered. This slurry was thoroughly stirred and left in a hood until complete evaporation of the solvent. Then, it was stored in amber glass vessels at 4 °C, for at least 2 weeks before extraction.

GC–ICP-MS determination conditions were optimized using a standard solution of OPs, with a concentration of 200 ng mL^{-1}, prepared in ethyl acetate.

2.2. Sample preparation

Extractions were performed using a CEM Explorer-Discoverer (Matthews, NC, USA) focused microwave extractor device, equipped with 10 mL glass vessels, sealed with polytetrafluoroethylene layered septum caps. A Sorvall RC-5B Refrigerated Superspeed Centrifuge (Dupont Instruments, ON, Canada) was used to centrifuge supernatants after microwave extraction. Under optimized conditions, 0.5 g of accurately weighed sample were extracted at 150 °C in two sequential steps of 15 min duration, using 5 mL of solvent. The first extraction was performed with acetone and the second with acetonitrile. The sealed extraction vessels were allowed to cool before being released from the microwave cavity to prevent evaporation losses. Both supernatants were combined and centrifuged at 4000 rpm, for 4 min. After that, 1 mL of ethyl acetate was added and the extract was evaporated under nitrogen stream to ca. 0.5 mL. Finally, it was purified on 50 mg silica cartridges. Analytes were recovered from the cartridge with 1 mL of ethyl acetate. The IS was added to an aliquot of the extracts. For real sample analysis, the final extract was further concentrated to 200 μL due to the low levels of OPs found in the analyzed sediments.

Soxhlet extractions were performed with 90 mL of acetone for 16 h. Extracts were evaporated and the solvent changed to ethyl acetate. Then, they were submitted to same clean-up procedure as microwave extracts.

2.3. Determination

Analytes were determined using an Agilent (Santa Clara, CA, USA) 6890 gas chromatograph connected, through a heated interface (Agilent Technologies, Santa Clara, CA), to an Agilent 7500cs ICP-MS system (Agilent Technologies, Santa Clara, CA, USA), equipped with shielded torch and collision/reaction cell technology. Chromatographic separations were carried out with an HP-5 capillary column (30m × 0.32 mm i.d., df: 0.25 μm) purchased from Agilent (Santa Clara, CA, USA). The temperature of the column was programmed at 15 °C min^{-1} from 70 °C (held for 1 min) to 270 °C (held for 5 min). Helium (99.999%) was used as carrier gas in the GC column at a constant flow rate of 1.5 mL min^{-1}. The injector was kept at 270 °C and a pulse of 30 psi, for 0.5 min, was employed to improve the efficiency of the injection process. Aliquots (2 μL) of standard solutions and sample extracts were injected in the splitless mode (2 min). The GC–ICP-MS interface was kept at 290 °C. In the ICP-MS, argon flow rates were 15 and 0.8 L min^{-1} for the plasma and carrier gases, respectively. Nitrogen, with a flow rate of 0.03 L min^{-1}, was used as additional gas in the central argon channel. The forward radio frequency (rf) power was 700 W and the sampling depth 7 mm. The extraction lens 1 was kept at −155 V and quadrupole and octopole bias were set at −9 and −12 V, respectively.

3. Results and discussion

3.1. Chromatographic conditions

The temperature gradient for baseline separation of target compounds was optimized in a previous work [9]. Moreover, con-

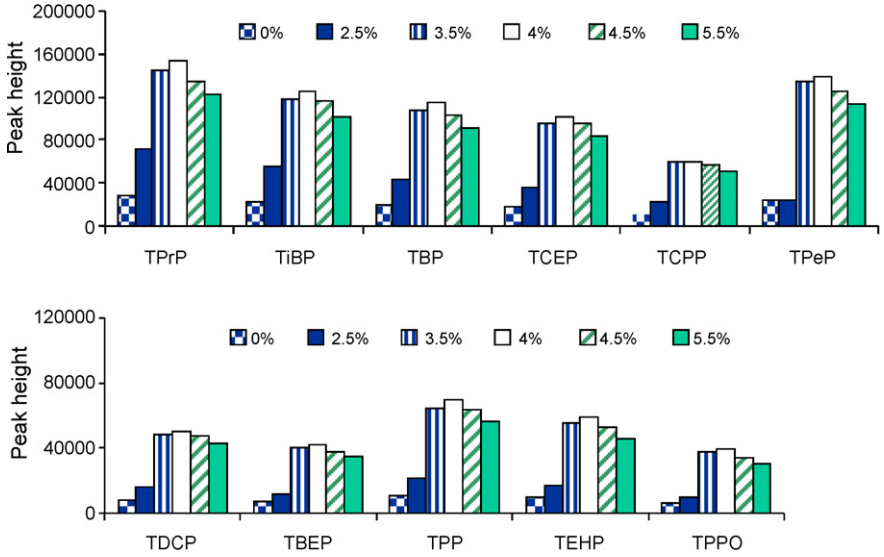

Fig. 1. Influence of nitrogen addition to the central argon plasma channel on phosphorus ionization. Percentage of nitrogen referred to an Ar flow of 0.8 L min^{-1}. Obtained response for a 200 ng mL^{-1} OPs standard solution in ethyl acetate.

ventional and pulsed splitless were compared as injection modes. The latter increases inlet pressure just before the beginning of a run and returns it to the set value (corresponding to the selected column flow) after a pre-established time. The pressure pulse sweeps the sample out of the inlet and into the column faster, reducing the chance of analyte decomposition and/or adsorption in the internal surface of the liner. In addition, it provides a narrow injection band in the head of the GC column.

Increasing the pressure in the injector to 30 psi led to a 2–3-fold improvement in the peak height of target species when compared to conventional splitless. Higher pressure values did not affect chromatographic responses of selected OPs and increased the risk of leaks in the injector, thus 30 psi was maintained as optimal pressure during injection.

3.2. ICP-MS detection

Several parameters affecting the ICP-MS performance were studied in detail. Moreover, as in previous studies, nitrogen was used as additional gas in the central argon plasma channel to enhance phosphorus ionization [16–21]. The addition of small amounts of alternate gases (N_2, O_2, He) is usually employed to improve the detection limits of elements with high ionization potentials such as phosphorus. Although the mechanism is not completely clear, it is attributed to changes in the bulk properties of the plasma [20].

3.2.1. Carrier gas flow, N_2 addition and collision cell conditions

The effect of the argon carrier gas flow on the response of target compounds was investigated in the range between 0.65 and 0.95 L min^{-1}. The optimum value was 0.8 L min^{-1} (data not shown).

As previously stated, nitrogen was added to the carrier gas. Fig. 1 shows the responses obtained with 0.8 L min^{-1} of Ar containing percentages of nitrogen from 0% to 5.5%. The addition of nitrogen provided an important improvement in sensitivity. Maximum peak heights were noticed when the carrier gas flow contained between 0.02 and 0.04 L min^{-1} of N_2, and they slightly dropped down at higher flows. On the other hand, N_2 contributed also to increase the baseline noise of the corresponding chromatograms. An intermediate flow of 0.03 L min^{-1} of N_2 (equivalent to a percentage of 4% relative to the carrier gas flow) was selected because it guaranteed a good signal to noise ratio and good stability versus slight changes on nitrogen flow. This trend matched with that reported in previous studies, where the addition of nitrogen was also found beneficial at low percentages [16–20].

Detection of phosphorus-containing species by ICP-MS is affected by polyatomic interferences consisting of nitrogen, oxygen and hydrogen atoms combinations. Obviously, the use of nitrogen, to enhance phosphorus ionization, worsens the spectral background at 31 *m/z* units. In systems furnished with collision cell technology, such interferences usually can be minimized using helium as collision gas. It was found that introducing just 0.5 mL min^{-1} (the lower flow allowed by the instrument) of this gas into the collision cell gave a similar decrease in the baseline noise and in the responses of OPs; consequently, the S/N ratio of chromatographic peaks remained unchanged and, thus, He was not used in the collision cell.

3.2.2. Forward rf power

Fig. 2 shows the effect of the rf power on the responses of TCEP and TPP. The rest of species followed a similar trend. In contrast to relatively high values reported in previous articles for OPs or phosphorus-containing pesticides detection [16–20], the highest responses were obtained in the power range between 600 and 700 W, with an exponential decay of signals measured at higher powers, which matched with the trend reported by other researchers for phosphorus and halogen detection in dry plasma conditions [21]. Considering that low forward powers, 600 and 700 W, performed more or less the same, 700 W was selected as

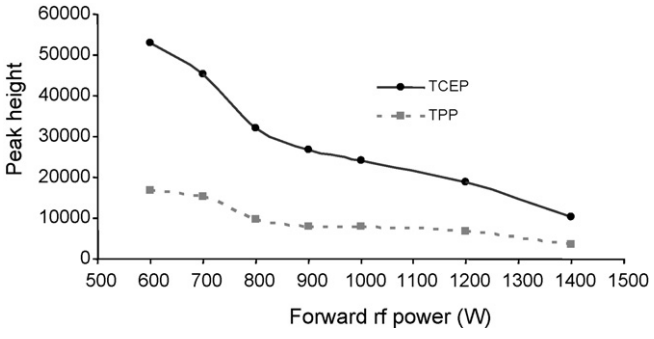

Fig. 2. Effect of the rf forward power on OPs response.

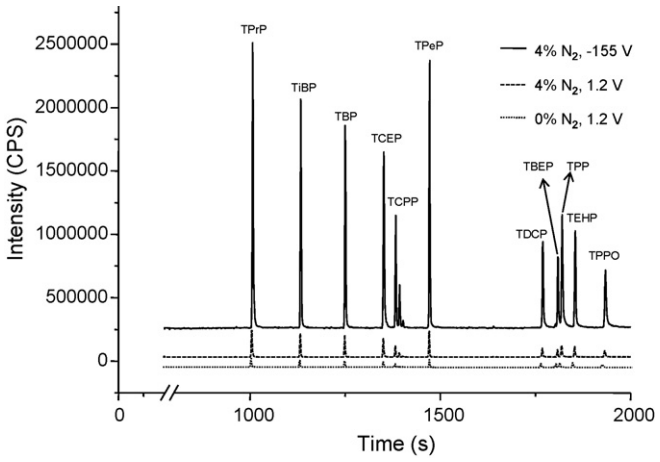

Fig. 3. Overlapped chromatograms for a 200 ng mL^{-1} OPs standard solution obtained with the ICP-MS operated under soft conditions (extraction lens 1 at 1.2 V) and hard (extraction lens 1 at −155 V).

working value in order to ensure plasma stability which might be affected by the injection of complex matrices with high organic contents.

3.2.3. Extraction lens 1 voltage and makeup gas flow

As stated by Pröfrock et al. [21], the ICP-MS 7500cs system shows high dependency between its sensitivity and the extraction mode when coupled to GC. The ICP-MS instrument used can be operated with different extraction modes, namely soft extraction (positive extraction lens 1 voltage up to +10 V) or hard extraction (highly negative extraction lens 1 voltage down to −200 V). In our research, a dramatic improvement was noticed operating the ICP-MS under hard extraction conditions (Fig. 3), which were not exploited in previous studies dealing with some of the OPs involved in this research [16,17].

The effect of the auxiliary (intermediate) argon flow in the ICP plasma was also evaluated. Flows between 0.5 and 1.3 L min^{-1} were assayed and any noticeable difference was found neither in phosphorus response nor in the background signal with the use of makeup gas, data not shown, so it was avoided.

3.3. Microwave-assisted extraction optimization

3.3.1. Extraction solvent

Based on previous studies [9,10,15,2] three medium-polarity organic solvents: ethyl acetate, dichloromethane and acetone, were tested as extractants in the MAE process. Initially, extractions were performed at 80 °C for 10 min using 0.5 g of sediment and 5 mL of organic solvent. Obtained extracts were concentrated (ca. 0.5 mL), purified using a 50 mg silica SPE cartridge and adjusted to a final volume of 1 mL. In the case of acetone and dichloromethane extracts, 1 mL of ethyl acetate was added when they were concentrated, prior to silica purification.

Table 1
Experimental factorial design $3^1 \times 2^2$ domain.

Factor	Levels		
	Low	Medium	High
Volume (mL)	4	–	8
Time (min)	5	–	15
Temperature (°C)	60	95	130

In general, acetone provided better responses than ethyl acetate and dichloromethane, Fig. 4. For instance, TPPO was poorly extracted with ethyl acetate and not detected in dichloromethane extracts. On the basis of these results, acetone was selected for further experiments. These findings are in agreement with those reported previous works. Martínez-Carballo et al. determined 9 OPs in the Austrian aquatic environment and reported that dichloromethane was unsuitable for OPs extraction from sediment samples [5] using sonication as extraction technique. On the other hand, acetone was also the best solvent for OPs extraction from dust samples using both MAE [9] and matrix solid-phase dispersion (MSPD) [10].

3.3.2. Microwave extraction parameters

In a second step, the optimization of the extraction temperature and time, as well as the acetone volume, was simultaneously performed using an experimental factorial design type $3^1 \times 2^2$, involving a total of 12 experiments as shown in Table 1. The mass of sediment was kept at 0.5 g. Obtained extracts were processed as in the preliminary assays. Standardized values of main effects, obtained after analyzing the responses for each analyte in the experiments of the design, are presented in Table 2. The absolute value of the main effect for a given compound is proportional to the variation in the efficiency of the extraction for this species, when the considered factor changes from the low to the high level established in the design domain. Its sign means whether the extraction yield increases (positive sign) or decreases (negative sign). For all compounds, the volume of solvent showed a negative effect on the efficiency of the process, meaning that 4 mL provides higher extraction yields than 8 mL. Moreover, this factor was statistically significant (95% confidence level) for TBP, TCEP, TDCP, TBEP, TEHP and TPPO. On the other hand, the effect of extraction time was positive, except for TPP, and statistically significant for TCEP, TCPP, TDCP, TEHP and TPPO. Finally, temperature showed a positive effect for all the compounds and was statistically significant except for TBP and TPP. According to these results, acetone volume was kept at 4 mL and the extraction time was set at 15 min. Some additional assays were carried out to ensure that the better performance of the lower volume of acetone (4 mL) compared to the higher level of

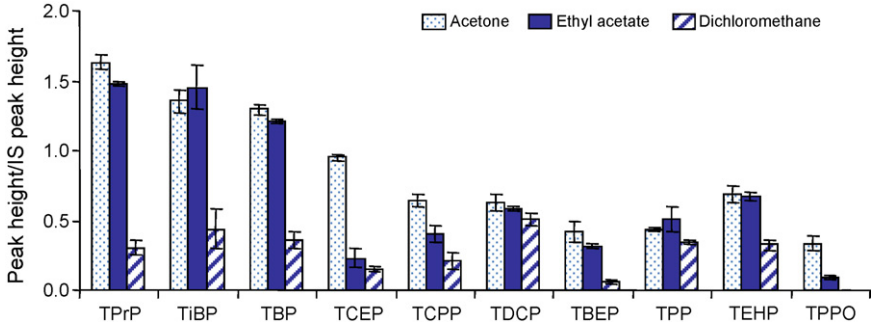

Fig. 4. Comparison of responses using different extraction solvents. Data for a spiked (1000 ng g^{-1}) sediment sample. MAE at 80 °C for 10 min using 5 mL of each solvent. Mean values with their standard deviations, $n = 3$ replicates, for 0.5 g samples.

Table 2
Standardized values for major effects considered in the $3^1 \times 2^2$ experimental factorial design.

Factor	Compound									
	TPrP	TiBP	TBP	TCEP	TCPP	TDCP	TBEP	TPP	TEHP	TPPO
Volume (mL)	−2.67	−2.16	−2.90*	−4.17*	−1.50	−4.58*	−4.28*	−1.98	−3.35*	−3.26*
Time (min)	0.41	0.41	0.33	2.77*	3.05*	4.86*	2.51	−2.33	3.74*	3.26*
Temperature (°C)	3.25*	3.04*	2.51	5.81*	4.47*	5.78*	3.22*	2.74	5.06*	3.39*

* Statistically significant effects at the 95% confidence level.

the design (8 mL) was not due to evaporation losses of the analytes affecting more to the latter situation. No evaporation losses were observed in any case. The better performance of lower solvent volumes when using MAE is not new and has been already reported for other organic compounds [22,23].

On the basis of above comments, temperatures higher than those explored within the design domain were tested in further experiments. In comparison with data obtained at 130 °C, slightly higher responses were measured for TPrP, TDCP, TPP and TEHP at 150 °C, whereas further improvement was not noticed using a temperature of 170 °C (data not shown). Thus, 150 °C was selected as optimal temperature in the extraction step.

Extractions performed under above conditions provided recoveries above 84% except for TPrP and TCEP, for which a 70% recovery was achieved. Exposing the sample to the microwave radiation for a longer period was evaluated as a possible way of improvement. However, comparison between 15 and 30 min of MAE revealed no significant difference (data not shown) so 15 min was kept as extraction time.

The CEM MW system employed in this work offers the possibility of stirring the sample contained in the closed vessels, using Teflon coated stir bars, while they are exposed to the microwave field. It was observed that stirring did not improve the extraction efficiency (data not provided) therefore, this option was not further employed.

As stated before, the lower recoveries were found for TPrP and TCEP, which are two of the more polar OPs [1]. Therefore, the use of a more polar organic solvent might be a way to improve the extraction efficiency. A first extraction was performed with 4 mL of acetone under already optimized conditions (15 min, 150 °C), the supernatant removed and a second extraction with acetonitrile, under the same conditions, was carried out. Recoveries achieved for the more polar compounds rose to values above 80%. The use of acetone in both cycles was also evaluated but provided lower recoveries than acetonitrile in the case of TPrP, so the use of a different solvent for each extraction step was needed.

In an attempt to reduce the amount of solvent employed to perform the extractions, the use of 2 mL per cycle, instead of 4 mL, was evaluated (data not shown). Recoveries were the same, except in the case of TPPO, for which the extraction yield dropped to 50% when using the lower volume. Therefore, it was not possible to decrease the solvent amount.

3.4. Method performance and real sample analysis

Instrumental limits of quantification (LOQs) of the GC–ICP-MS system, calculated as the concentration of analyte giving a signal 10 times the standard deviation of the background noise of the chromatographic signal, were 10 ng mL^{-1} for TCPP (0.9 ng mL^{-1}, as phosphorus) and 5 ng mL^{-1} for the remaining OPs (equivalent to 0.4–0.7 ng mL^{-1} when calculated for phosphorus). These values are in the same order of magnitude as the limit of detection previously reported for TPP [21]. Injection repeatability was evaluated at 25 ng mL^{-1} and remained between 3% and 8%. Linearity was evaluated with standards prepared in ethyl acetate at concentrations from 5 to 3000 ng mL^{-1}. Correlation coefficients between 0.993 and 0.999 were obtained.

Recoveries of the proposed sample preparation method were evaluated with sediment samples spiked at three different concentration levels. Fractions of the spiked samples, as well as a non-spiked fraction of the same sediment, were extracted in triplicate under optimal conditions given in the experimental section. As shown on Table 3, recoveries ranged from 78% to 105%, with relative standard deviations (RSD) below 12%. Those values were calculated with standard addition over sample extracts, since different slopes were noticed for calibration graphs corresponding to solutions of OPs in ethyl acetate and matrix matched standards (spiked microwave-assisted extracts from unpolluted sediment samples). This behavior is probably related to differences in the efficiency of mass transfer processes from the body of the injector to the GC column for pure standards and sample extracts [24].

Re-extraction of solid residues after MAE of the sediment spiked at 1000 ng g^{-1}, using the Soxhlet technique, confirmed the efficiency of the developed extraction method. On the other hand, procedural blanks demonstrated the absence of contamination problems. On the basis of these results, LOQs of 10 ng g^{-1} (20 ng g^{-1} for TCPP) were obtained for the overall method. In practice, these values can be reduced until 2 and 4 ng g^{-1}, respectively, if the final extract is concentrated from 1 to 0.2 mL. A difference with other techniques employed in the determination of OPs in solid matrices, such as GC-NPD and GC–EI-MS, for which baseline level is strongly affected by the presence of co-extracted organic compounds, is the selectivity of ICP-MS detection which ensures an improvement in the S/N ratio of chromatographic peaks directly proportional to the final volume reduction of the sample extract. The above mentioned LOQs are slightly lower than those provided by Ishikawa et al. [6] using a GC-FPD system, with the advantage of a much more straightforward sample preparation procedure and similar to those reported for ultrasound-assisted extraction followed by LC–MS/MS (between 0.48 and 11 ng g^{-1}) [5]. Several sediment samples, collected from the different rivers in Spain and USA, were extracted following the optimized procedure. Chromatograms revealed the presence of traces of most OPs considered in this work, being TBP (2.8–8 ng g^{-1}) and TCPP (4–10 ng g^{-1}) the most abundant species. Fig. 5 shows the overlapped chromatograms of a 50 ng mL^{-1} standard and a real sediment sample, concentrated to 200 μL.

Table 3
Recoveries, as percentage, of the optimized method for three different spike levels, $n = 3$ replicates.

	Recovery ± SD		
	50 ng g^{-1}	200 ng g^{-1}	1000 ng g^{-1}
TPrP	100 ± 2	83 ± 1	89 ± 2
TiBP	98 ± 12	93 ± 2	96 ± 7
TBP	105 ± 4	83 ± 4	95 ± 2
TCEP	103 ± 7	78 ± 6	81 ± 4
TCPP	92 ± 9	81 ± 3	100 ± 2
TDCP	94 ± 6	91 ± 2	98 ± 2
TBEP	94 ± 3	78 ± 3	96 ± 1
TPP	103 ± 5	90 ± 6	97 ± 1
TEHP	103 ± 4	103 ± 4	101 ± 1
TPPO	99 ± 1	100 ± 4	92 ± 5

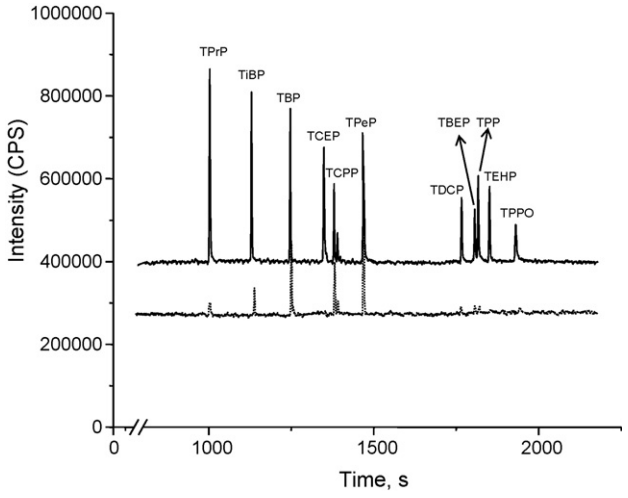

Fig. 5. Overlay of chromatograms of a 50 ng g^{-1} standard (solid line) with a concentrated sediment sample (dotted line).

4. Conclusions

MAE followed by GC–ICP-MS represents a valuable alternative for the determination of OPs in sediment samples. The proposed method presents a low consumption of organic solvents and requires a simple additional clean-up to preserve the performance of the GC column. Careful optimization of ICP-MS conditions, particularly with respect to the rf power and extraction lens voltage, resulted in quantification limits in the low ng mL^{-1} range for the OPs considered in this study. These values are similar to those reported for other techniques as GC-NPD, GC–MS and even LC–MS/MS. ICP-MS provides much less complex chromatograms, almost free of interferences, especially when compared to the above mentioned mass spectrometric techniques. These features point to GC–ICP-MS as a suitable technique for the reliable determination of OPs in samples with higher organic matter content than sediments, such as settled dust and particulate matter from indoor and outdoor environments, where OPs are ubiquitous pollutants, and sludge from sewage treatments plants, whose OPs content remains mostly unknown.

Acknowledgements

MGL acknowledges a FPU grant from the Spanish Ministry of Science and Innovation. MGL is also grateful to Professor Caruso's group for hosting her study period at the University of Cincinnati. The researchers are grateful to Agilent Technologies and CEM for their continuing support and to Professors Mack and Gudmundsdottir and their groups for their assistance.

References

[1] T. Reemtsma, J.B. Quintana, R. Rodil, M. García-López, I. Rodríguez, Trends Anal. Chem. 27 (2008) 727.
[2] A. Marklund, B. Andersson, P. Haglund, Chemosphere 53 (2003) 1137.
[3] H. Weil, K. Haberer, Fresenius J. Anal. Chem. 339 (1991) 405.
[4] D.C.G. Muir, N.P. Grift, J. Solomon, J. Assoc. Off. Anal. Chem. 64 (1981) 79.
[5] E. Martínez-Carballo, C. González-Barreiro, A. Sitka, S. Scharf, O. Gans, Sci. Tot. Environ. 388 (2007) 290.
[6] S. Ishikawa, M. Taketome, R. Shinohara, Water Res. 19 (1985) 119.
[7] Y. Kawagoshi, I. Fukunaga, H. Itoh, J. Mater. Cycles Waste Manage. 1 (1999) 53.
[8] H. De Geus, B.N. Zegers, H. Lingeman, U.A.Th. Brinkman, Int. J. Environ. Anal. Chem. 56 (1994) 119.
[9] M. García, I. Rodríguez, R. Cela, J. Chromatogr. A 1152 (2007) 280.
[10] M. García, I. Rodríguez, R. Cela, Anal. Chim. Acta 590 (2007) 17.
[11] A. Marklund, B. Andersson, P. Haglund, J. Environ. Monit. 7 (2005) 814.
[12] J. Andresen, K. Bester, Water Res. 40 (2006) 621.
[13] J. Björklund, S. Isetun, U. Nilsson, Rapid Commun. Mass Spectrom. 18 (2004) 3079.
[14] J.B. Quintana, R. Rodil, P. López-Mahía, S. Muniategui-Lorenzo, D. Prada-Rodríguez, Anal. Bioanal. Chem. 388 (2008) 1283.
[15] J.B. Quintana, R. Rodil, T. Reemtsma, M. García-López, I. Rodríguez, Trends Anal. Chem. 27 (2008) 904.
[16] M. Shah, J. Meija, B. Cabovska, J.A. Caruso, J. Chromatogr. A 1103 (2006) 329.
[17] J. Ellis, M. Shah, K.M. Kubachka, J.A. Caruso, J. Environ. Monit. 9 (2007) 1329.
[18] N. Fidalgo-Used, M. Montes-Bayón, E. Blanco-González, A. Sanz-Medel, J. Anal. At. Spectrom. 20 (2005) 876.
[19] N. Fidalgo-Used, M. Montes-Bayón, E. Blanco-González, A. Sanz-Medel, J. Anal. At. Spectrom. 21 (2006) 876.
[20] A.P. Vonderheide, J. Mejia, M. Montes-Bayón, J.A. Caruso, J. Anal. At. Spectrom. 18 (2003) 1097.
[21] D. Pröfock, P. Leonhard, S. Wilbur, A. Prange, J. Anal. At. Spectrom. 19 (2004) 623.
[22] K.K. Chee, M.K. Wong, H.K. Lee, J. Chromatogr. A 723 (1996) 259.
[23] C.S. Eskilsson, E. Björklund, J. Chromatogr. A 902 (2000) 227.
[24] C.F. Poole, J. Chromatogr. A 1158 (2007) 241.

Talanta 79 (2009) 768–774

Contents lists available at ScienceDirect

Talanta

journal homepage: www.elsevier.com/locate/talanta

Simultaneous voltammetric determination of prednisone and prednisolone in human body fluids

Rajendra N. Goyal*, Sunita Bishnoi

Department of Chemistry, Indian Institute of Technology Roorkee, Roorkee 247 667, India

ARTICLE INFO

Article history:
Received 1 April 2009
Received in revised form 29 April 2009
Accepted 30 April 2009
Available online 9 May 2009

Keywords:
Prednisone
Prednisolone
Voltammetry
Doping
Biological fluids

ABSTRACT

A sensitive, rapid and reliable electrochemical method based on voltammetry at single wall carbon nanotube (SWNT) modified edge plane pyrolytic graphite electrode (EPPGE) is proposed for the simultaneous determination of prednisolone and prednisone in human body fluids and pharmaceutical preparations. The electrochemical response of both the drugs was evaluated by osteryoung square wave voltammetry (OSWV) in phosphate buffer medium of pH 7.2. The modified electrode exhibited good electrocatalytic properties towards prednisone and prednisolone reduction with a peak potential of ~−1230 and ~−1332 mV respectively. The concentration versus peak current plots were linear for both the analytes in the range 0.01–100 μM and the detection limit (3σ/slope) observed for prednisone and prednisolone were 0.45×10^{-8}, 0.90×10^{-8} M, respectively. The results of the quantitative estimation of prednisone and prednisolone in biological fluids were also compared with HPLC and the results were in good agreement.

1. Introduction

Corticosteroids affect biochemical events and cellular processes in tissues and organ of the body, hence, play a crucial role in human physiology [1]. Synthetic corticosteroids also have important physiological activities, such as anti-inflammatory and anti-stress action and are regarded as the most effective treatment for topical diseases [2,3] and these drugs also have the potential positive effects on sports performance. Hence, synthetic corticoids are extensively abused by athletes in competitive games and their use has been forbidden by the International Olympic Committee and World Anti-Doping Agency [4–6]. Prednisone (I) and prednisolone (II) are synthetic corticosteroids usually prescribed in the treatment of a wide variety of inflammatory diseases such as asthma, rheumatoid arthritis, various kidney diseases including nephritic syndrome, allergies and cluster headache [7–11]. These are available in market in the form of tablets, capsules, injections, ointments and creams and the use of both the compounds is banned in sports under anti-doping rules [12–14]. Simultaneous determination of prednisolone and prednisone has great significance to bioscience and clinical diagnosis since prednisone is a biologically inactive 11-dehydro metabolite of prednisolone. In human system prednisone is converted to the bioactive moiety prednisolone, via reduction of the 11-oxo group by the liver enzyme, 11-β-hydroxydehydrogenase [15,16]. In mammals including humans interconversion of prednisone to prednisolone was found after oral administration of either of them with somewhat favoured prednisolone [17–19]. In view of the clinical importance and increased abuse of prednisolone and prednisone by athletes, it is considered desirable to analyze their concentrations in body fluids as well as in pharmaceutical formulations.

In view of the importance of corticosteroids in human physiology many methods such as spectroscopy and chromatographic methods coupled with spectroscopy or diode array detector and chemiluminescence have been developed for the simultaneous or individual determination of prednisone and prednisolone in biological fluids [20–23]. However, inspite of the fact that above methods are sensitive and widely used, they require special sample preparation, time consuming extraction steps and long derivatization procedures. Polarography has also been attempted for determination of prednisone and prednisolone, however, the two peaks were found to be seriously overlapping [24]. In view of the increasing cases of doping by the athletes, simple, efficient, sensitive and reproducible analytical technique is needed to detect such cases at the site of games. Osteryoung square wave voltammetry has been used for the sensitive determination of large number of anabolic steroids [25,26]. However, the determination in these studies is based on oxidation of steroids. Since blood and urine possess uric acid, dopamine, xanthine and ascorbic acid, etc., a major problem is encountered due to interference of their oxidation signals with analyte signal. Hence, attempts in the present method are focused on determination based on reduction of prednisone and prednisolone.

* Corresponding author. Tel.: +91 1332 285794; fax: +91 1332 273560.
E-mail addresses: rngcyfcy@iitr.ernet.in, rngcyfcy@rediffmail.com (R.N. Goyal).

0039-9140/$ – see front matter © 2009 Elsevier B.V. All rights reserved.
doi:10.1016/j.talanta.2009.04.067

The present paper presents determination of prednisone and prednisolone in biological fluids using edge plane pyrolytic graphite electrode after modification with single wall carbon nanotube.

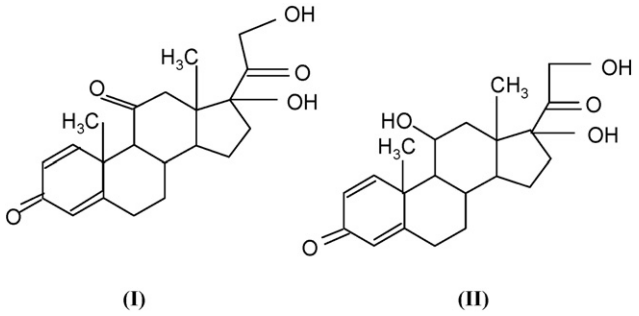

2. Materials and methods

2.1. Instrumentation

Voltammetric experiments were carried out using a computerized BAS (Bioanalytical Systems, West Lafayette, USA) CV-50W analyzer. A three-electrode single compartment cell system was employed, with a platinum wire as counter electrode and Ag/AgCl electrode (3 M NaCl) as reference (Model MF-2052 RB-5B). The edge plane pyrolytic graphite electrode (~6 mm^2) used as the working electrode was prepared in the laboratory by the reported method [27]. The pH of the buffers was measured using a Century India Ltd., digital pH meter (Model CP-901). All potentials reported are referred to Ag/AgCl electrode at an ambient temperature of 27 ± 2 °C. High performance liquid chromatography (HPLC) experiments were performed on Agilent 1100 series system with reverse phase column RP-18e (5 μM). The mobile phase used for HPLC experiments was a mixture of water:methanol (60:40) at a flow rate of 1.4 ml min^{-1} and absorbance of the eluent was monitored at 254 nm. The JEOL JSM-7400F field emission scanning electron microscopy (FE-SEM) instrument was used to study the surface morphology of SWNT modified EPPGE.

2.2. Chemicals and reagents

Prednisone and prednisolone were obtained from Sigma (St. Louis, MO, USA). Prednisolone containing tablets manufactured by different pharmaceutical companies were purchased from the local market. Single-wall carbon nanotube (SWNT) of purity >95% was purchased from Bucky, USA. Phosphate buffers of desired pH and ionic strength (0.5 M) were prepared according to the method of Christian and Purdy [28] using analytical grade chemicals from Merck. The stock solutions of desired concentration of prednisone and prednisolone were prepared in methanol (A.R.). Other solvents and chemicals used were of analytical grade.

2.3. Procedure

Voltammograms were recorded after mixing 2 mL of the stock solution of appropriate compound with 2 mL of phosphate buffer. The solution was deoxygenated by bubbling nitrogen for 8–10 min before recording the voltammograms. The optimized operating parameters to record osteryoung square voltammograms (OSWVs) were: initial E: 0.0 mV and final E: −1600 mV, square wave frequency (f): 15 Hz, square wave amplitude (E_{SW}): 25 mV and potential step (E): 4 mV.

Control urine sample were received from healthy laboratory personnel and urine samples of patients undergoing treatment with prednisolone were obtained from the Institute Hospital. The samples were obtained after 4 h of administration of prednisolone tablet (Nucort Forte 10 mg). The human blood samples from three healthy volunteers were obtained from the Institute Hospital. The blood with EDTA as anticoagulant was ultra-centrifuged and the supernatant blood plasma obtained was taken for the analysis of prednisone and prednisolone. Urine and blood plasma samples were used for voltammetric analysis without any dilution since biological samples did not show any reduction peak on scanning from 0.0 to −1600 mV.

2.4. Fabrication of SWNT modified PGE

The bare edge plane pyrolytic graphite electrode was rubbed on an emery paper and washed with double distilled water and then touched softly onto tissue paper. The electrode was then ready for modification. A 0.05 mg mL^{-1} suspension of SWNT was prepared by dispersing 0.05 mg SWNT in 1.0 mL N,N-dimethylformamide (DMF) by ultrasonic agitation. Initially 10–100 μL of the solution was casted at the surface of EPPGE using a microsyringe and dried in a stream of hot air. It was found that the peak current for prednisone as well as prednisolone did not increase after 40 μL. Hence, for further studies 40 μL of this solution was coated onto the surface of the clean pyrolytic graphite electrode. The electrode was then kept in air for 8–10 h and now the working electrode with a well-coated layer of SWNT on its surface was ready for experimental purpose. Initially the response of modified electrode was recorded in a solution containing 2 mL phosphate buffer solution of pH 7.2 and 2 mL methanol, which was previously de-oxygenated with nitrogen for at least 10 min. The absence of peak in voltammogram in the region 0.0 to −1.6 V versus Ag/AgCl and very low current values indicate that the modified electrode can be safely used for experimental purposes. A comparison of typical FE-SEM images of bare edge plane PGE with SWNT modified EPPGE is presented in Fig. 1.

3. Results and discussion

3.1. Electrochemical behaviour of prednisone and prednisolone

Fig. 2 presents a comparison of typical osteryoung square wave voltammograms of 10 μM of prednisolone and prednisone at the bare and modified edge plane pyrolytic graphite electrodes in phosphate buffer of pH 7.2. Well defined peaks for the reduction of prednisone and prednisolone were observed at potentials ~−1299 and ~−1412 mV respectively at the bare electrode. The peak obtained for both the compounds is rather broad, suggesting slow electron transfer kinetics. However, with increase in concentration of prednisolone the second peak merged with background, hence, the attempts to use bare EPPGE for determination of the two steroids failed. At the SWNT modified electrode, well-defined reduction peaks were obtained, where, the reduction peak potential of prednisone and prednisolone shifted to less negative potentials, ~−1230 and ~−1332 mV respectively and the peak current also increased. The above results suggested that the SWNT modified electrode promoted the electrochemical reduction of prednisone and prednisolone by considerably accelerating the rate of electron transfer. One of the reasons for this catalysis is that metallic impurities in nanotubes act as a promoter by increasing the rate of electron transfer, thus, a negative shift in their reduction potentials is observed. The electrocatalytic activity of SWNT has been assigned by many workers to entrapped metals in the cavity [29,30].

3.2. Effect of pH and square wave frequency

The effect of pH on the reduction of both the drugs was studied in the pH range 2.4–10.0. The peak potential (E_p) of both the drugs

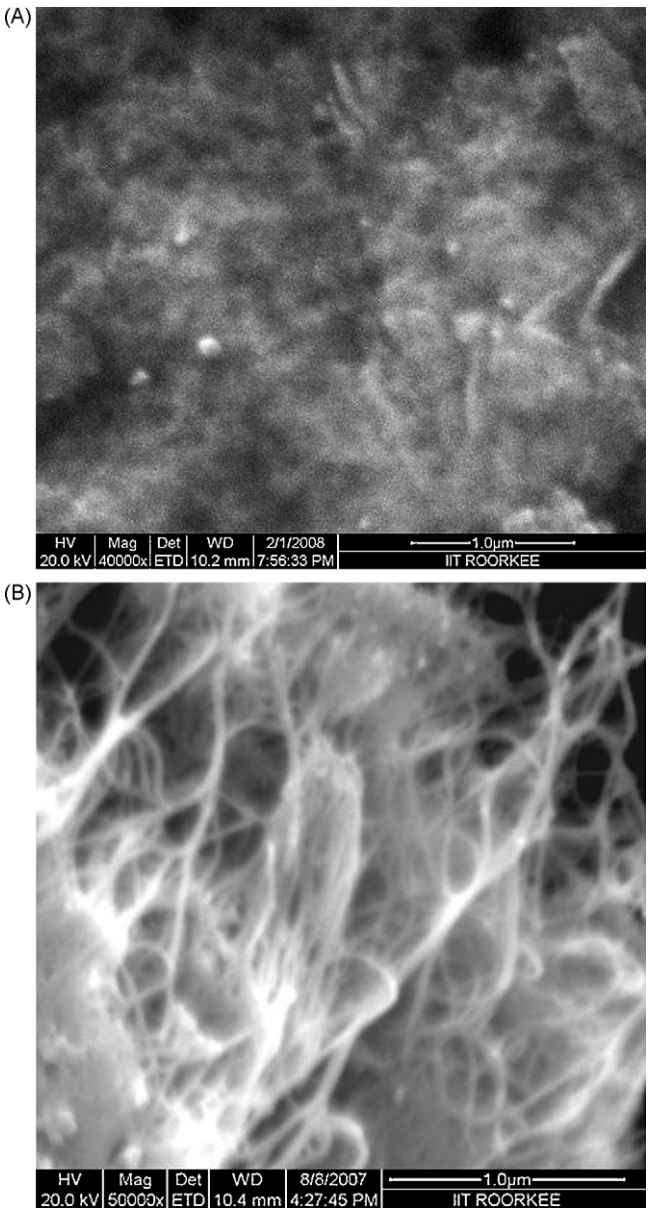

Fig. 1. A comparison of typical FE-SEM image of (A) bare edge plane PGE and (B) SWNT modified edge plane pyrolytic graphite electrode.

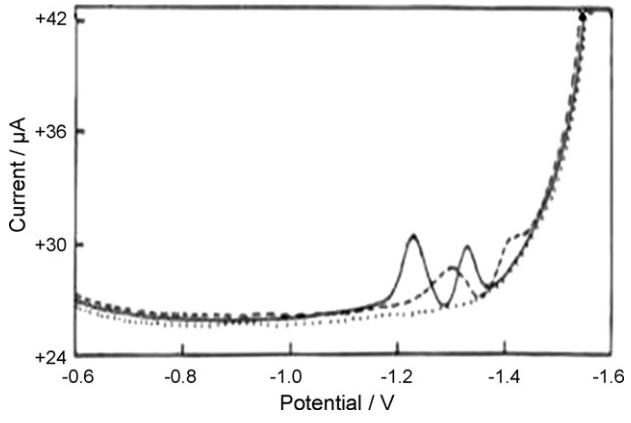

Fig. 2. Observed osteryoung square wave voltammograms for the reduction of 10 μM of prednisolone and prednisone at bare EPPGE (––), SWCNT modified EPPGE (—) and background PBS (pH 7.2) at SWNT modified EPPGE (. . . . . .).

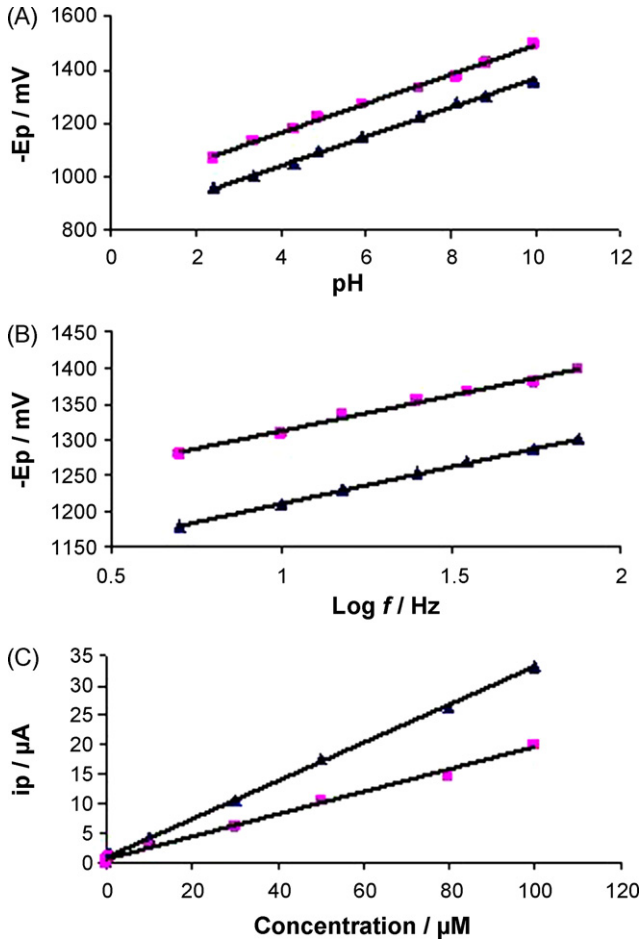

Fig. 3. (A) Observed dependence of peak potential ($-E_p$) on pH for 10 μM prednisone (▲) and 10 μM prednisolone (■) at SWNT modified EPPGE. (B) Plot of $-E_p$ versus logarithm of frequency (log$f$) of 10 μM prednisone (▲) and 10 μM prednisolone (■) at SWNT modified EPPGE. (C) Calibration plot observed for prednisone (▲) and prednisolone (■) at SWNT modified EPPGE at pH 7.2.

was found to shift towards more negative potentials with increase in pH (Fig. 3A). The variation of peak potential (E_p) with pH was linear for both the analytes and the dependence of E_p on pH obey the relations:

$$-E_p\,(\text{pH}\,2.4-10.0) = [825.52 + 54.53\,\text{pH}]\ \text{versus Ag/AgCl for prednisone}$$

$$-E_p\,(\text{pH}\,2.4-10.0) = [944.52 + 54.58\,\text{pH}]\ \text{versus Ag/AgCl for prednisolone}$$

having correlation coefficients 0.9973 and 0.9968 respectively.

The slope of the $-E_p$ versus pH curves was ~55 mV/pH for both the analytes, indicating that equal number of protons and electrons are involved in the electrode reaction.

The influence of square wave frequency (f) on the peak current (i_p) of both analytes was examined in the range of 5–75 Hz. At frequency higher than 75 Hz, the peaks merged with the background. The peak current (i_p) of both the analytes was found to increase with increase in square wave frequency (f). The dependence of peak current on square wave frequency was linear suggesting thereby that the electrode reaction for both the compounds is adsorption controlled [31,32]. The variation of i_p with f can be expressed by the

equations:

$$i_p\,(\mu A) = 0.2268\,f + 0.4283 \quad \text{for prednisone}$$

$$i_p\,(\mu A) = 0.2215\,f + 0.1444 \quad \text{for prednisolone}$$

having correlation coefficients 0.9958 and 0.9991 respectively.

The peak potential of prednisone and prednisolone were also found to shift towards more negative potentials with increase in square wave frequency and the plots of E_p versus log$f$ were linear in the frequency range 5–75 Hz (Fig. 3B). The variation of E_p with log$f$ can be expressed by the equations:

$$-E_p\,(\text{mV}) = 103.22\,\log f + 1107.4 \quad \text{for prednisone}$$

$$-E_p\,(\text{mV}) = 98.775\,\log f + 1212.6 \quad \text{for prednisolone}$$

with correlation coefficients 0.9988 and 0.9929 respectively. Such a behaviour indicates the nature of redox reaction as reversible [32].

3.3. Individual determination of prednisone and prednisolone

The square wave voltammograms were recorded for prednisone as well as prednisolone at different concentrations in the range 0.01–100 μM. It was found that the peak currents increased linearly with increasing concentration (Fig. 3C). The graphs between peak current (i_p) and concentration from the data generated during OSWV studies were linear and the relation can be represented by the equations:

$$i_p\,(\mu A) = 0.3233C\,(\mu M) + 0.8415 \quad \text{for prednisone}$$

$$i_p\,(\mu A) = 0.1897C\,(\mu M) + 0.5815 \quad \text{for prednisolone}$$

with correlation coefficients 0.9993 and 0.9945 respectively, where i_p is current in μA and C is concentration in μM. The observed sensitivities for prednisone and prednisolone are 0.33 and 0.19 μA μM^{-1} respectively, indicating that both analytes can be safely estimated in the given concentration range. The detection limit of prednisone and prednisolone was calculated by using the formula $3\sigma/b$, where σ is standard deviation of the blank and b is slope of the calibration curve, and found to be 0.45×10^{-8} and 0.90×10^{-8} M respectively.

3.4. Simultaneous determination of prednisone and prednisolone

The main aim of the present study was to simultaneously investigate the electrochemical response of prednisone and prednisolone in human body fluids, as metabolism of prednisolone in human system proceeds through prednisone. The main problem encountered with simultaneous determination in earlier reports was close reduction potentials due to which it was difficult to resolve the overlapped voltammograms [33]. This problem was resolved in the present studies using SWNT modified edge plane pyrolytic graphite electrode.

The simultaneous determination of prednisone and prednisolone at modified EPPGE was carried out by fixing the concentration of one compound and varying the concentration of other at pH 7.2. Fig. 4A shows square wave voltammograms for different concentration of prednisone keeping the concentration of prednisolone constant (10 μM). The figure clearly depicts that the voltammetric peak of prednisolone remains unaltered and the peak current remained practically constant. The peak current of prednisone increased with increase in its concentration. Similarly, Fig. 4B shows square wave voltammograms obtained by varying the concentration of prednisolone keeping the concentration of prednisone constant (10 μM). The prednisolone signal increases with

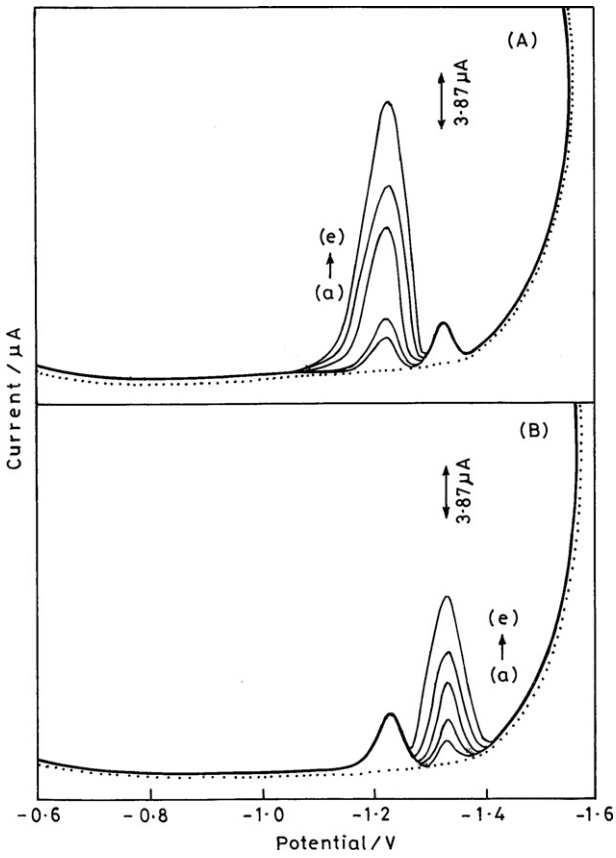

Fig. 4. (A) Square wave voltammograms of mixture of prednisolone and prednisone at modified electrodes in 0.1 M phosphate buffer (pH 7.2); (A) prednisone at a fixed concentration of prednisolone 10 μM; [prednisone]: $a = 5$, $b = 10$, $c = 30$, $d = 40$, $e = 60$ μM and (B) prednisolone at a fixed concentration of prednisone; [prednisone] 10 μM; [prednisolone]: $a = 5$, $b = 10$, $c = 30$, $d = 40$, $e = 60$ μM.

increase in its concentration without affecting the prednisone signal, which remains almost constant. Currents observed in both the cases for the varied component were essentially same as observed during the individual determination and obeyed the relation for the calibration plot. It was found that the reduction peak of neither prednisone nor prednisolone interferes with each other in the studied concentration range and thus, the proposed method can be safely applied for their simultaneous determination.

3.5. Interference study

It was considered necessary to evaluate the influence of some electroactive interferents such as, uric acid, ascorbic acid, xanthine, albumin and hypoxanthine in the determination of prednisone and prednisolone, since these are common biological compounds present in noticeable amount in living systems. Study of their influence on voltammetric response of prednisone and prednisolone was carried out by recording voltammograms for mixtures containing fixed quantity (10 μM) of the analytes (prednisone or prednisolone) and varying concentration of each interferent in the range 10–1000 μM. The addition of these interferents did not affect the peak current of prednisone or prednisolone and no new reduction peaks were observed in the range 0 to −1.6 V. This behaviour suggested that prednisone and prednisolone can be safely determined in biological fluids. As determination is based on reduction of prednisone and prednisolone, it is understandable that common metabolites present in biological fluids do not interfere because none of them are reducible.

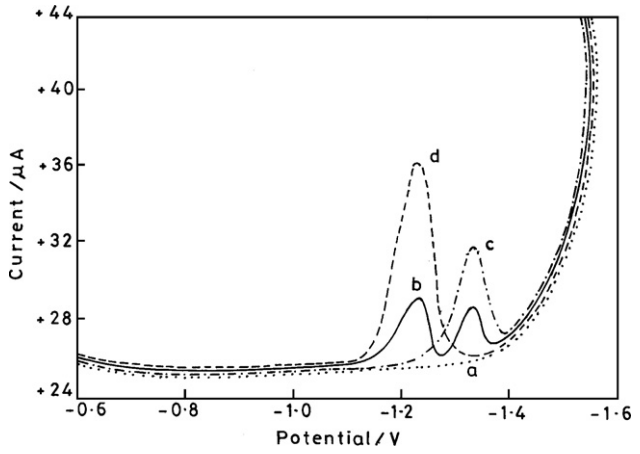

Fig. 5. Square wave voltammograms of control urine sample (a), urine sample after administration of prednisolone tablet (b), control urine spiked with 30 μM prednisolone (c) and control urine spiked with 30 μM prednisone (d) at SWNT modified EPPGE.

3.6. Analytical applications

3.6.1. Real sample analysis

To establish the utility of the developed method, prednisone and prednisolone was determined in human urine samples. In mammals including humans, interconversion of prednisolone to prednisone, has been reported, hence, residues of both steroids are found after oral administration of either of them [17–19]. Square wave voltammograms of control urine sample from healthy volunteer (a), urine sample (sample 1) from patient undergoing treatment with prednisolone after 4 h of administration of single dose of 10 mg prednisolone tablet (Nucort Forte) (b), control urine sample spiked with 30 μM of prednisolone (c) and control urine sample spiked with 30 μM of prednisone (d) at SWNT modified edge plane pyrolytic graphite electrode are depicted in Fig. 5. As can be seen, two clear peaks at −1230 and −1332 mV are observed in voltammograms (c) and (d), which are due to reduction of prednisone and prednisolone respectively. Curve (a) presents voltammogram of control urine and does not exhibit peaks corresponding to prednisone and prednisolone, however, peaks at same potentials in curve (b) indicate that both these steroids are excreted in urine sample (sample 1) from the patient undergoing treatment with prednisolone. The concentrations of both the compounds in urine sample 1 were determined using developed method and were found as 12.48 and 7.12 μM for prednisolone and prednisone respectively. Three urine samples were analyzed and the results obtained are presented in Table 1.

The concentrations of prednisone and prednisolone in human urine samples were also determined using HPLC and the results were compared with the ones observed by present method. For this purpose, various concentrations of prednisone and prednisolone standards were analyzed using HPLC and the calibration curves were obtained by plotting the peak area of the analytes peaks against concentrations. Typical HPLC chromatograms of prednisone and prednisolone are presented by curves A and B in Fig. 6 and exhibit peaks at retention time ~7.990 and ~9.432 min respectively. Urine samples were diluted 6 times prior to analysis to minimize the complexity of matrix. Curve C in Fig. 6 presents chromatogram of control urine and does not exhibit peaks corresponding to prednisone and prednisolone. The urine samples obtained from patients undergoing treatment with prednisolone after 4 h of administration of prednisolone tablet were then injected. Samples were then analyzed using HPLC method and a typical chromatogram observed for sample 1 is presented by curve D. Two well-defined peaks at retention time ~7.990 and ~9.432 min were noticed corresponding to prednisone and prednisolone respectively. Other prominent peaks in chromatogram were observed at R_t ~ 1.090 and ~1.223 min, most probably due to the presence of major urine metabolites like uric acid, xanthine, etc., however, no attempts were made to identify them. Finally, the concentrations of prednisolone and prednisone in human urine samples were determined using calibration curves and found as 2.00 and 1.2 μM respectively. As urine sample was diluted 6 times before injection in HPLC, the concentration of prednisone and prednisolone in urine (sample 1) was determined as 12.0 and 7.2 μM respectively. A comparison of prednisone and prednisolone determined by the developed method and HPLC is presented in Table 1 and clearly indicates that the proposed method is in good agreement with those obtained by HPLC method.

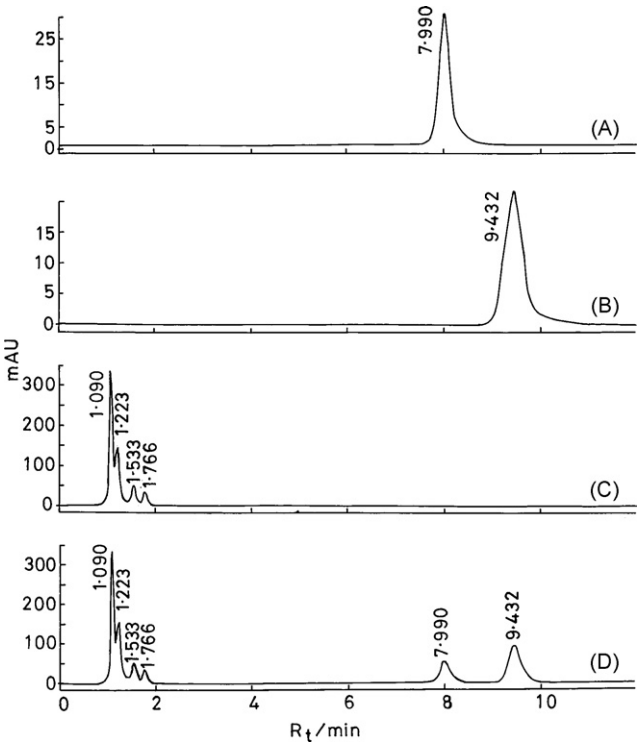

Fig. 6. A comparison of typical HPLC chromatograms observed for (A) standard solution of prednisone, (B) standard solution of prednisolone, (C) control urine sample, (D) urine sample obtained from patient undergoing treatment with prednisolone after 4 h of administration of 10 mg prednisolone tablet.

Table 1
A comparison of prednisone and prednisolone concentration determined by SWNT modified EPPGE and HPLC in human urine after 4 h of administration of 10 mg of prednisolone tablet.

Sample	Prednisolone		Prednisone	
	Modified EPPGE	HPLC	Modified EPPGE	HPLC
1	12.48	12.00	7.12	7.20
2	12.06	12.20	7.44	7.80
3	12.80	12.60	7.60	6.60

3.6.2. Analysis of prednisolone in pharmaceutical preparations

Prednisolone is normally prescribed for the treatment of various diseases, hence, the modified EPPGE was also used to analyze the prednisolone content in three common commercial medicinal samples, viz. Nucort Forte (Unimax Laboratories, Mfg. Lic. No.; 32-B (H)), Omnacortil – 10 (Macleods Pharmaceuticals Ltd., Mfg. Lic. No.; DD/313) and Wysolone* 10, (Wyeth Ltd., Mfg. Lic. No.; 545). The tablets were grounded to powder, dissolved in methanol and then diluted so that the concentration of prednisolone falls in the

Table 2
Determination of prednisolone in commercial tablets using SWNT modified edge plane pyrolytic graphite electrode.

Sample	Stated content (mg/tablet)	Detected content (mg/tablet)	Error (%)
Nucort Forte	10	9.83	−1.7
Wysolone	10	9.94	−0.6
Omnacortil-10	10	9.62	−3.8

working range. Following the proposed method the concentration of prednisolone in three commercial samples was determined using modified EPPGE. The results are summarized in Table 2 and clearly indicate that the prednisolone content determined by the proposed method is in good agreement with the claimed prednisolone content in pharmaceutical preparations. It is also expected that the SWNT modified EPPGE has great potential for the determination of prednisone and prednisolone in pharmaceutical sample analysis.

3.6.3. Recovery test

Recovery experiments were also performed using standard addition method to evaluate the accuracy of the proposed method. The recovery tests of both drugs ranging from 10 to 50 μM were carried out utilizing SWNT modified EPPGE. Three human plasma samples obtained from healthy volunteers were spiked with known amounts of standard prednisone and prednisolone subsequently followed by recording their voltammograms. In all the cases two separate well-defined peaks were observed with E_p −1230 and −1332 mV corresponding to prednisone and prednisolone respectively. The concentration of the two compounds was calculated using calibration plots and the results observed are listed in Table 3. The recoveries varied in the range from 97.60% to 101.50% in the case of prednisolone and from 96.60% to 103.28% in case of prednisone. The recoveries indicate that the accuracy of the proposed voltammetric method is good.

3.7. Stability and reproducibility of modified EPPGE

The stability and reproducibility of the modified electrode was evaluated by monitoring the peak current responses daily at a constant prednisolone or prednisone concentration over a period of 15 days. The experimental results indicated that the current responses showed a relative standard deviation of 3.24% and 4.12% for prednisone and prednisolone respectively. After 15 days, reduction peak potentials shifted towards more negative potentials and current values were also decreased. These results suggest that the modified electrode can be safely used up to 15 days of its preparation, hence, possesses good stability.

Table 3
Recovery results obtained for prednisone and prednisolone in human plasma samples at the modified electrode.

	Prednisolone		Prednisone	
Spiked (μM)	Detected (μM)	Recovery (%)	Detected (μM)	Recovery (%)
Sample 1				
10.0	10.15	101.50	9.88	98.80
30.0	29.84	99.47	30.24	100.80
50.0	50.60	101.20	51.64	103.28
Sample 2				
10.0	9.76	97.60	9.66	96.60
30.0	30.34	101.13	30.96	103.20
50.0	49.95	99.90	51.08	102.16
Sample 3				
10.0	10.00	100.00	9.76	97.60
30.0	30.09	100.30	30.16	100.53
50.0	49.50	99.00	50.0	100.00

To examine the intraday reproducibility, repetitive measurements were carried out in a solution of fixed concentration of either prednisolone or prednisone. The results of seven successive scans show a relative standard deviation of 1.06% and 1.64% respectively for prednisone and prednisolone. To ascertain the reproducibility of the results further, four electrodes with almost same area were modified with the same volume of SWNT solution in DMF and their response towards the reduction of fixed concentration of prednisolone and prednisone was observed. The current obtained for the four independent electrodes showed a relative standard deviation of 2.08% and 1.84% respectively, confirming thereby that the results are reproducible. Thus, the modified electrode exhibits good reproducibility and stability for the determination of prednisone and prednisolone.

4. Conclusions

The results presented above clearly demonstrate that prednisone and prednisolone can be simultaneously determined using square wave voltammetric technique at SWNT modified edge plane pyrolytic graphite electrode. The most promising result of the proposed method is the use of pyrolytic graphite electrode. The modified electrode not only exhibited strong catalytic activity towards the simultaneous reduction of prednisone and prednisolone, but also increased the peak currents. Several studies have been devoted to investigate the reason of electrocatalytic activity of SWNT. It is now generally accepted that embedded metals present in SWNT and accessible to fluids are responsible for such catalysis. The impurity of metals in SWNT has been assigned to cause electrocatalysis [29]. Hurt et al. [34] and Liu et al. [35] have reported that metal which is completely encapsulated in impermeable carbon shells and not in contact with fluid does not play any role during bioavailability studies of nickel in SWNT. It is also reported that with purification of carbon nanotubes, the peak potential of dopamine shifts to more negative potential [30]. Hence, such a metal is expected not to be electrochemically active. Thus, the "fluid accessible metal" is probably an important property of carbon nanotubes (rather than total metal present) and is believed to be responsible for electrocatalytic activity of CNT.

The method has been successfully applied for the determination of prednisolone in commercial preparations. Both the steroids have also been determined in human blood and urine samples with adequate reproducibility and sensitivity. As both drugs are extensively abused by athletes for doping and both are interconvertable to each other, therefore, it is expected that the simultaneous determination of these corticosteroids in body fluids would provide a simple and fast method for detecting the cases of doping at the site of competitive games. Thus, the proposed method is a fast, sensitive and reliable approach for simultaneous determination of both synthetic corticosteroids and a promising substitute to other reported methods owing to its simplicity, rapidity and low financial input.

The available sites for reduction in prednisolone are the keto groups at positions 3 and 20 and in prednisone the keto groups at positions 3, 11 and 20. Ketosteroid having a carbonyl group conjugated with a double bond has been reported to undergo easier reduction in comparison to isolated keto groups [36]. In prednisone reduction at carbonyl group, C-11 has been reported to be hindered due to the presence of methyl group at position 10 [23,37]. Thus, the probable active site for reduction in both ketosteroids is carbonyl groups at position 3. Therefore, peaks at −1230 and −1332 mV are assigned to the reduction of carbonyl groups at position 3 to give corresponding hydroxyl groups in a $2H^+$, $2e^-$ reaction. Their interconversion in liver indicates that carbonyl group at position 11 is reduced to CHOH group [17–19] in prednisone and hydroxyl group in prednisolone is oxidized to C=O.

Acknowledgements

One of the authors (SB) is thankful to the Council of Scientific and Industrial Research, New Delhi for awarding Junior Research Fellowship. Financial assistance for this work was provided by the Department of Science and Technology, New Delhi vide grant no. SR/S1/IC-21/2007.

References

[1] D. Qi, B. Rodrigues, Am. J. Physiol. Endocrinol. Metab. 292 (2007) E654.
[2] O. Nozaki, J. Chromatogr. A 935 (2001) 267.
[3] P.J. Barnes, Nature (Suppl) 402 (1999) B31.
[4] M.H. Spyridaki, P. Kiousi, A. Vonaparti, P. Valavani, V. Zonaras, M. Zahariou, E. Sianos, G. Tsoupras, C. Georgakopoulos, Anal. Chim. Acta 573 (2006) 242.
[5] M.E. Touber, M.C. van Engelen, C. Geogakopoulos, J.A. van Rhijn, M.W.F. Nielen, Anal. Chim. Acta 586 (2007) 137.
[6] V. Cirimele, P. Kintz, V. Dumestre, J.P. Goulle, B. Ludes, Forensic Sci. Int. 107 (2000) 381.
[7] A. Nikai, Medicina 44 (2007) 1700.
[8] T. Hasegawa, K. Ishihara, S. Takakura, H. Fujii, T. Nishimura, M. Okazaki, N. Miki, B. Umeda, Int. Med. 39 (2000) 794.
[9] I. Hafstroem, M. Rohani, S. Deneberg, M. Woernert, T. Jogestrand, J. Frostegaard, J. Rheumatol. 34 (2007) 1810.
[10] B. Peng, Q. Li, D. Luyo, S.M. Whitcup, F.G. Roberge, C.C. Chan, Int. Congr. Ser. 1068 (1994) 249.
[11] P.T. Hansen, H.J. Rigmor, Ugeskrift fot laeger 168 (2006) 4417.
[12] < http://grg51,typead.com/steroid_nation/2007/01/soccer_pro_bann.html, >.
[13] E. Pujos, M.M.F. Waton, O. Paisse, M.F.G. Loustalot, Anal. Bioanal. Chem. 381 (2005) 244.
[14] World Antidoping Code 2007 prohibited list, Australian Sports anti doping authority, Australia, 2007.
[15] M. Conti, F.J. Frey, G. Escher, C. Marone, B.M. Frey, Endocrinology 139 (1998) 1533.
[16] O. Fruchter, E. Zoumakis, S. Alesci, M.D. Martino, G. Chrousos, Z. Hochberg, Steroids 71 (2006) 1001.
[17] M. Vogt, H. Derendorf, J. Kramer, H.E. Junginger, K.K. Midha, V.P. Shah, S. Stavchansky, J.B. Dressman, D.M. Barends, J. Pharm. Sci. 96 (2007) 27.
[18] V.G. Hale, L.Z. Benet, Pharmacology 44 (1992) 273.
[19] U.F. Legler, F.J. Frey, L.Z. Benet, J. Clin. Endocrinol. Metab. 55 (1982) 762.
[20] S. Mazurek, R. Szostak, J. Pharm. Biomed. Anal. 40 (2006) 1225.
[21] H. Shibasaki, H. Nakayama, T. Furuta, Y. Kasuya, M. Tsuchiya, A. Soejima, A. Yamada, T. Nagasawa, J. Chromatogr. B 870 (2008) 164.
[22] Y. Zhang, H.-L. Wu, Y.-J. Ding, A.-L. Xia, H. Cui, R.-Q. Yu, J. Chromatogr. B 840 (2006) 116.
[23] L. Amendola, F. Garribba, F. Botre, Anal. Chim. Acta 489 (2003) 233.
[24] H.S.D. Boer, J.D. Hartigh, H.H.J.L. Ploegmakers, W.J.V. Oort, Anal. Chim. Acta 102 (1978) 141.
[25] R.N. Goyal, V.K. Gupta, N. Bachheti, Anal. Chim. Acta 597 (2007) 82.
[26] S. Yilmaz, S. Skrzypek, Y. Dilgin, S. Yagmur, M. Coskun, Curr. Anal. Chem. 3 (2007) 41.
[27] F.J. Miller, H.E. Zittel, Anal. Chem. 35 (1963) 1866.
[28] G.D. Christian, W.C. Purdy, J. Electroanal. Chem. 3 (1962) 363.
[29] C.E. Banks, A. Crossley, C. Salter, S.J. Wilkins, R.G. Compton, Angew. Chem. Int. Ed. 45 (2006) 2533.
[30] R.N. Goyal, S.P. Singh, Carbon 46 (2008) 1556.
[31] M.R.C. Massaroppi, S.A.S. Machado, L.A. Avaca, J. Braz. Chem. Soc. 14 (2003) 113.
[32] F. Quentel, C. Elleouet, Electroanalysis 13 (2001) 1030.
[33] Y. Ni, S. Li, S. Kokot, Anal. Lett. 41 (2008) 2058.
[34] R.H. Hurt, M. Monthioux, A. Kane, Carbon 44 (2006) 1028.
[35] X. Liu, V. Gurel, D. Morris, D.W. Murray, A. Zhitkovich, A. Kane, Adv. Mater. 19 (2007) 2790.
[36] P. Zuman, M. Kolthoff, Progress in Polarography, vol. 2, Interscience Publishers, New York, 1962.
[37] Y.-R. Chiang, W. Ismail1, S. Gallien, D. Heintz, A.V.G. Dorsselaer, G. Fuchs, Appl. Environ. Microbiol. 74 (2007) 107.

Talanta 79 (2009) 775–779

Contents lists available at ScienceDirect

Talanta

journal homepage: www.elsevier.com/locate/talanta

Highly sensitive fluorescent sensor for mercury ion based on photoinduced charge transfer between fluorophore and π-stacked T–Hg(II)–T base pairs

Liangqia Guo, Hong Hu, Ruiqing Sun, Guonan Chen*

Ministry of Education Key Laboratory of Analysis and Detection Technology for Food Safety (Fuzhou University), Fuzhou University, Fuzhou, Fujian, 350002, China

ARTICLE INFO

Article history:
Received 2 March 2009
Received in revised form 4 May 2009
Accepted 4 May 2009
Available online 12 May 2009

Keywords:
Mercury ion
Photoinduced charge transfer
Fluorescence quenching
M-DNA

ABSTRACT

A novel and simple oligodeoxyribonucleotide-based sensor with single fluorophore-labeled for mercury ion sensing was reported. An oligodeoxyribonucleotide poly(dT) was labeled with fluorescein as donor. Based on the specific binding of Hg(II) to T–T mismatch base pairs, the formation of π-stacked [T–Hg(II)–T] with "sandwich" structure on the addition of Hg(II) ions facilitates the electron transfer via photoinduced charge transfer (PCT), which creates an additional nonradiative decay channel for excited fluorophore and triggers the fluorescence to be quenched. The π-stacked [T–Hg(II)–T] functioned not only as mercury ion recognition but also as an electron acceptor to quench the donor. A linear relationship was observed over the range of 0–1.0 μM with the detection limit of 20 nM for mercury ions. The fluorescence quenching phenomenon and quenching mechanism, reliability and selectivity of the system were investigated in detail.

1. Introduction

Recently, the interactions of metal ions with nucleic acids, proteins are recognized as an important topic [1], as they are involved in RNA folding, mechanisms of ribozymes action [2], gene mutations [3] and the design of biomolecular devices with metal cofactors [4]. Recent efforts to align metal ions along DNA helix have demonstrated that metal ions, such as Cu(II), Zn(II), Ag(I), Ni(II), Co(II), bind to nucleobases, deoxyribose, or phosphodiester backbone and have provided potential applications of the metallised DNA (M-DNA) to nanomaterials and biosensors [5–7]. In this regard, mercury ions preferentially bind to thymine–thymine (T–T) mismatch base pairs, in which imino protons of the bases are replaced by Hg(II), to generate stable mercury-mediated base pairs [T–Hg(II)–T] [8–11]. The formation of stable DNA π-stacks containing mercury-mediated thymine–thymine pairs suggests a new approach to the development of M-DNA.

In the past few years this preferential binding property of thymidines has successfully been applied in the design of oligonucleotide-based mercuric ion fluorescent sensors [12–19]. Combining with the high extinction coefficient and unique distance dependent optical properties of DNA–Au nanoparticles, colorimetric sensing systems [20–24] for mercury have also been demonstrated in aqueous media. Furthermore, UO_2^{2+}-dependent DNAzyme [25] and self-cleaving DNAzyme [26] for mercury ions have also been reported. In these sensing systems, the thymidine–Hg(II)–thymidine coordination chemistry only played a role in mercury ion recognition.

Till now, research related to mercury-mediated thymine–thymine pairs [T–Hg(II)–T] has mostly been focused on the structure confirmation [8–11] and application of this coordination chemistry to recognise mercury ions [12–26]. Nevertheless, effect of [T–Hg(II)–T] on DNA-mediated charge transfer (CT) efficiency has rarely been explored [27–29]. During our studies of thymine derivatives we unexpectedly found that the fluorescence of single fluorophore-labeled oligodeoxyribonucleotide containing consecutive thymines can be quenched on the addition of mercury ion. Encouraged by this finding, we designed an oligodeoxyribonucleotide-based sensor for mercury ions in aqueous solution with high sensitivity and selectivity. At the presence of Hg(II) ions, the formation of π-stacked [T–Hg(II)–T] with "sandwich" structure facilitates the electron transfer via photoinduced charge transfer (PCT), which creates an additional nonradiative channel for the excited fluorophore and triggers the fluorescence to be quenched. The π-stacked [T–Hg(II)–T] functioned not only as mercury ion recognition but also as an electron acceptor to quench the fluorescence. The fluorescence quenching phenomenon and quenching mechanism, reliability and selectivity of the system were investigated in detail in this study. To the best of our knowledge, this is the first example of single fluorophore-labeled oligodeoxyribonucleotide to study fluorescence phenomena in M-DNA and making use of M-DNA as electron acceptor for metal ions sensing.

* Corresponding author. Tel.: +86 591 87893315; fax: +86 591 83713866.
E-mail address: gnchen@fzu.edu.cn (G. Chen).

0039-9140/$ – see front matter © 2009 Elsevier B.V. All rights reserved.
doi:10.1016/j.talanta.2009.05.001

Table 1
Sequence of oligonucleotides used in this study.

$(T)_7$–F	Fluorescein-5′-TTTTTTT-3′
C-DNA	5′-TTTTTTT-3′

2. Experimental

2.1. Chemicals

All oligonucleotides were obtained from Shanghai Sangon Biological Engineering Technology & Services Co., Ltd. of China. The sequence of oligonucleotides was listed in Table 1. The $Hg(NO_3)_2$ stock solution (1.0×10^{-3} M) was prepared by measuring the appropriate amount of $Hg(NO_3)_2{\cdot}H_2O$ into a 250 mL volumetric flask and adding 2 or 3 drops of concentrated nitric acid, followed by deionized water. All chemicals used were analytical grade or better. All buffers were prepared by using metal free reagents and water was purified with MilliQ purification system (Millipore).

2.2. Fluorescence measurements

The fluorescence measurements were performed at room temperature on a Varian Cary Eclipse Fluorescence Spectrophotometer except specific indication. Before conducting fluorescence measurements, aliquots of Hg(II) aqueous(0–50.0 μM) were added separately to 10 mM 3-(N-morpholino) propanesulfonic acid (MOPS, pH 6.8) buffer containing 20 nM $(T)_7$–F and equilibrated for 24 h. The emission spectra were collected from 500 to 600 nm with the excitation wavelength of 480 nm.

2.3. Fluorescence lifetime measurements

Fluorescence lifetime measurements were obtained using an Edinburgh Analytical Instruments FL/Fs920 combined TCSPC lifetime spectrometer and spectrofluorimeter system (Edinburgh Instruments Ltd.). Fluorescence lifetime data were obtained with a free running discharge flash lamp (nF900 Nanosecond Flash lamp) operating at 7.0 kV, 0.40 bar, and a frequency of 40 kHz. The decay profiles were collected over 1024 channels of the multichannel analyzer with a time-channel of 0.048 ns until 1100 counts were collected in the peak channel. The instrument response function (IRF) was measured after recording the sample nanosecond emission graph collection (1100 counts in the peak channel) with a light scattering solution (LUDOX Colloidal silica, Sigma) in the sample compartment. The IRF and decay profiles were collected with a bandwidth of 1.0 nm for both the excitation and emission monochromators. The fluorescence decay data were performed with 273 nm excitation wavelength and 519 and 527 nm emission wavelength for $(T)_7$–F and Hg(II)-mediated $(T)_7$–F, respectively and were fitted to give the fluorescence lifetimes of $(T)_7$–F and Hg(II)-mediated $(T)_7$–F. The reduced χ^2 and residual plots were used to judge the quality of the fits. The χ^2 values of these fittings were kept as close to 1 as possible.

3. Results and discussion

3.1. Strategy of sensing

The sensor, $(T)_7$–F, consists of 7-mer thymine carrying a fluorescent residue (fluorescein, F) at the 5′-termini with an intervening six-carbon spacer. As a proof-of-concept experiment, the number of thymine in the prototype is seven but not limited to seven. Fluorescein was selected as the fluorophore due to its superior brightness ($\Phi \approx 1$, high ε) and water solubility [30]. Fluorescence spectra of $(T)_7$–F at the absence and presence of $Hg(NO_3)_2$ are shown in Fig. 1.

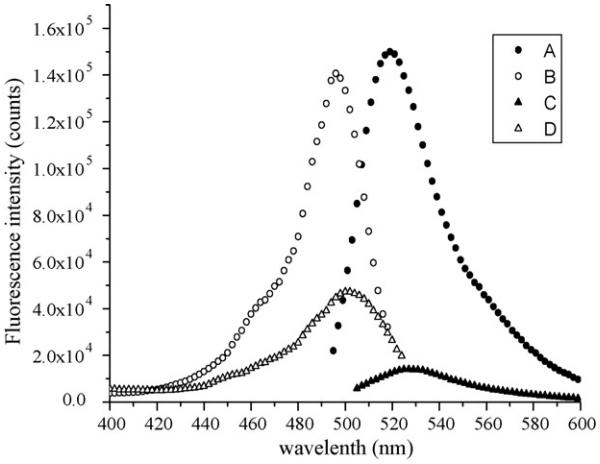

Fig. 1. Fluorescence spectra of $(T)_7$–F at the absence and presence of $Hg(NO_3)_2$ curves (A) and (B) are emission and excitation spectra of 20 nM $(T)_7$–F at the absence of $Hg(NO_3)_2$, respectively; curves (C) and (D) are emission and excitation spectra of 20 nM $(T)_7$–F at the presence of 10 μM $Hg(NO_3)_2$, respectively.

The emission profile of $(T)_7$–F is identical to that of free fluorescein, except a spectral shift [31] to longer wavelength about 6 nm and a decrease in quantum yield [32]. When $Hg(NO_3)_2$ was added, the fluorescence decreased with the red shift of the excitation and emission wavelength from 496 to 501 nm and 519 to 527 nm, respectively.

For the sensor does not contain guanosine residue, the fluorescence quenching via photoinduced electron transfer due to the good electron-donating property of guanosine [33] could be excluded. Furthermore, the absorption of [T–Hg(II)–T] pairs (at 240–300 nm [9]) does not overlap with the emission of fluorescein, the quenching by Förster fluorescence resonance energy transfer could also be ruled out. In addition, in the same condition Hg(II) ions do not quench the fluorescence of free fluorescein which was not incorporated into the oligodeoxyribonucleotide. For mercury ions preferentially bind to T–T pairs, when $(T)_7$–F was exposed to Hg(II) ions, Hg(II) ions bind directly to N_3 of thymidine in place of the imino proton and bridge two thymidine residues [8–11] to form the [T–Hg(II)–T] pairs between two molecules of the sensor. The structure of [T–Hg(II)–T] [8–11] is shown in Fig. 2(a). Therefore, two molecules of $(T)_7$–F form "sandwich" structure with Hg(II) ions with the help of [T–Hg(II)–T] pairs. The interaction of neighboring [T–Hg(II)–T] base pairs considerably increased the electron hole transfer efficiency [27] and facilitates electron transfer over long distances along the helix [34–36]. Thus π-stacked [T–Hg(II)–T] accepts and mediates the electron transfer along the DNA, creates an additional nonradiative decay channel via PCT for the excited

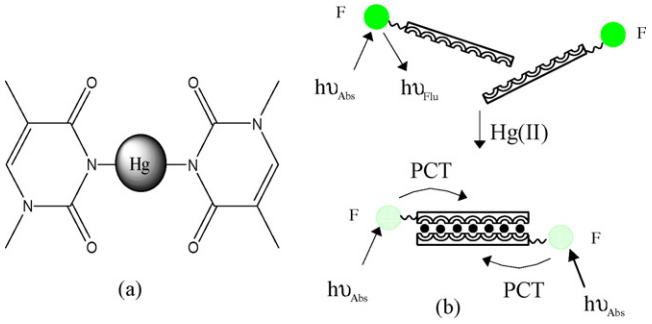

Fig. 2. (a) The structure of [T–Hg(II)–T]. (b) The rationale of the prototype (F: fluorescein; $h\upsilon_{Abs}$: fluorophore was excited at absorption wavelength; $h\upsilon_{Flu}$: fluorescence emission; PCT: photoinduced charge transfer).

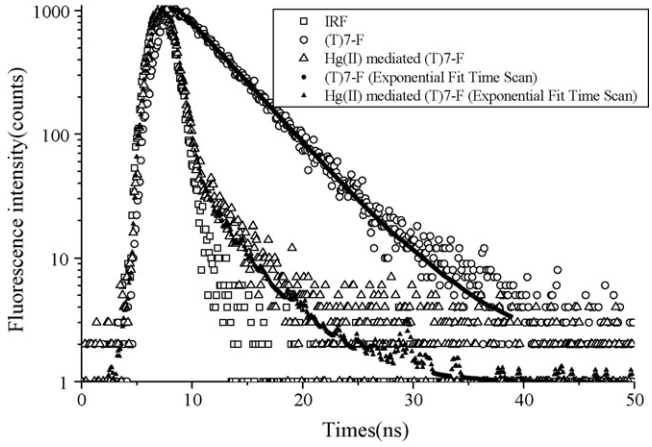

Fig. 3. Fluorescence decay curves of 20 nM $(T)_7$–F and 20 nM $(T)_7$–F + 10.0 μM $Hg(NO_3)_2$ in pH 7.0 buffer containing 10 mM 3-(N-morpholino) propanesulfonic acid and 0.3 M $NaNO_3$ monitored at 519 and 527 nm, respectively.

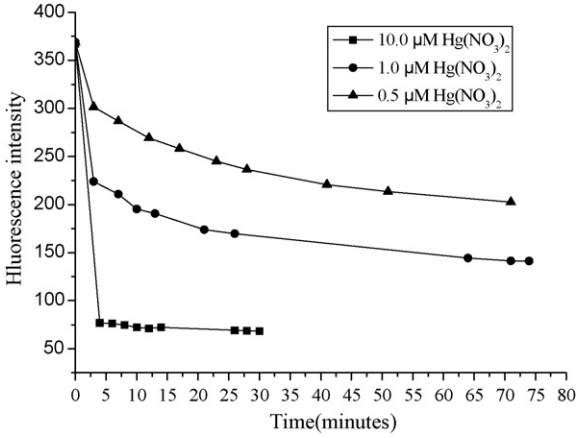

Fig. 4. Kinetics curve of Hg(II) sensing process (20 nM $(T)_7$–F).

state of fluorescein, which results in the fluorescence quenching. The rationale of the prototype is illustrated in Fig. 2(b).

3.2. Fluorescence lifetime

To further understand the quenching mechanism, fluorescence lifetimes (see Fig. 3) of $(T)_7$–F and Hg(II)-mediated $(T)_7$–F were conducted.

The parameters are listed in Table 2. For $(T)_7$–F, the decay data exhibit a single exponential decay kinetic of the general form [37]

$$f(t) = A + B_1 e^{-t/\tau} \quad (1)$$

A is the variable background, B_1 is the preexponential factor and t the observed lifetime. The decay exhibits a single exponential decay kinetic with τ of 4.401 ns. The single lifetime displays the fluorescein dianion lifetime which correlates well with that of free fluorescein [38]. For Hg(II)-mediated $(T)_7$–F, the decay data exhibit biexponential decay kinetic of the general form [37]

$$f(t) = A + B1e^{-t/\tau_1} + B_2 e^{-t/\tau_2} \quad (2)$$

A is the variable background, B_1 and B_2 are preexponential factors of the two components with lifetimes τ_1 and τ_2. The lifetime (τ_2 = 4.202 ns) of the long one, which accounts for 7.86% and is close to that of uncomplexed form, is assigned to that of $(T)_7$–F. The lifetime (τ_1 = 0.1170 ns) of the short one, which accounts for 92.14% and is due to the residual fluorescence from excited fluorescein in Hg(II)-mediated form whose population has been depleted by electron transfer [35], is assigned to that of the Hg(II)-mediated form. The fluorescence decay elucidates the π-stacked [T–Hg(II)–T] accepts and mediates the electron transfer through the DNA backbone [27,39], and provides an additional nonradiative decay channel for the excited state of fluorescein, which results in fluorescence quenching.

3.3. Optimization of sensing condition

The optimum pH of quenching efficiency might correlate with the pKa of the fluorophore and the form of Hg(II) ions which exist in solution. Effect of different buffer at pH 7.0 such as Tris–HCl, MOPS, phosphate buffer solution (PBS), N-2-hydroxyethylpiperazine-N′-2-ethanesulfonic acid (HEPES) on the quenching efficiency of the sensor in the presence of 1.0 μM $Hg(NO_3)_2$ were investigated, and the result showed that in MOPS buffer solution the sensing of Hg(II) ions had the best quenching efficiency. This may be due to the formation of an insoluble product between Hg(II) ions and anions such as Cl^-, PO_4^{3-} in other buffer, a process that breaks the association of the Hg(II) ions with the T-bases [24]. Subsequently, effect of pH on Hg(II) ions sensing was also examined, and the result showed that the optimized value of $(F - F_0)/F_0$ could be obtained at pH 6.8.

When Hg(II) ions were added, Hg(II) ions bring the ssDNA to form the duplex. The kinetics of the process was conducted by collecting the fluorescence of the system at intervals of some time after addition of Hg(II) ions at three concentration of 0.5, 1.0 and 10.0 μM (see Fig. 4). The equilibrium process of 95% quenching efficiency was within 5 min for 10.0 μM Hg(II) ions and about 75 min for 0.5 μM Hg(II) ions, respectively. The lower concentration of Hg(II) ions results in the slower sensing process. For the sensing to reach the equilibrium especially at low concentration of Hg(II) ions, the incubation time was selected for 24 h before fluorescence collecting in this study.

3.4. Sensitivity

Under the optimum condition (10 mM MOPS buffer pH 6.8, incubation time for 24 h), the fluorescence of $(T)_7$–F (20 nM) decreased with the increasing of the concentration of $Hg(NO_3)_2$ (see Fig. 5(A)). From Fig. 5(B), a linear relationship was observed over the range of 0–1.0 μM (R^2 = 0.97) with the limit of detection of 20 nM (defined as S/N = 3). The sensitivity is better than previously reported Au

Table 2
Fluorescence lifetime parameters of $(T)_7$–F and Hg(II)-mediated $(T)_7$–F.

	A	B	B Std Dev	τ (ns)	τ Std Dev	χ^2
$(T)_7$–F	1.904	6.030E-2	1.041E-3	4.401	3.048E-11	1.274

	A	B_1	B_1 Std Dev	B_2	B_2 Std Dev
Hg(II)-mediated $(T)_7$–F	0.9630	0.7796	0.1252	1.852E-3	1.651E-4

	τ_1 (ns)	τ_1 Std Dev	τ_1 Rel%	τ_2 (ns)	τ_2 Std Dev	τ_2 Rel%	χ^2
Hg(II)-mediated $(T)_7$–F	0.1170	2.089E-11	92.14	4.202	2.202E-10	7.86	1.171

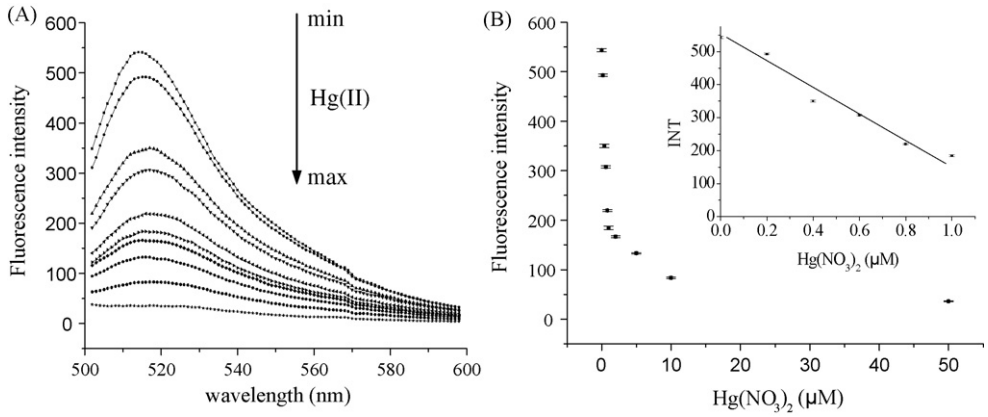

Fig. 5. (A) Fluorescence spectra of $(T)_7$–F (20 nM) on adding different concentration of $Hg(NO_3)_2$ (0, 0.2, 0.4, 0.6, 0.8, 1.0, 2.0, 5.0, 10.0, 50.0 μM); (B) maximum fluorescence intensity value of $(T)_7$–F (20 nM) vs the concentration of $Hg(NO_3)_2$ (0, 0.2, 0.4, 0.6, 0.8, 1.0, 2.0, 5.0, 10.0, 50.0 μM). Inset: calibration curve.

Table 3
Comparison of optical sensors for mercury detection.

Hg(II) ions sensor	Limit of detection	Method	Solvent	Reference
MSO oligonucleotide (double labeled)	40 nM	Fluorometric	Water	[12]
D-$(T)_{21}$–F	–	Fluorometric	Water	[13]
PTT	30 μM	Fluorometric	Organic	[14]
Pyrene–thymine dyad	0.1 μM	Fluorometric	Organic-water	[15]
MSO–PMNT	42 nM	Fluorometric	Water	[16]
DNA–Au nanoparticles	100 nM	Colorimetric	Water	[20]
DNA–Au nanoparticles	3 μM	Naked eye	Water	[21]
T_{33}–Au nanoparticles	250 nM	Colorimetric	Water	[22]
Au nanoparticles with thiolated thymine oligonucleotides	5 μM	Colorimetric	Water	[23]
$(T)_7$–F	20 nM	Fluorometric	Water	This work

MSO: mercury-specific oligonucleotide; PTT: poly[3-(N-thymin-1-ylacetyl)ethylamine-thiophene]; PMNT: poly(3-(3′-*N*,*N*,*N*-triethylamino-1′-propyloxy)-4-methyl-2,5-thiophene hydrochloride).

nanoparticle based colorimetric Hg(II) sensors [20–23] and some of the other sensors [12–16] based on the formation of [T–Hg(II)–T], even one fold higher than the double dyes labeled system [12]. Comparison of several major optical sensors for mercury detection based on the preferential binding property of thymidines was listed in Table 3, which shows that our mercury sensor compares favorably to previously reported ones.

3.5. Reliability

The reliability of the Hg(II) sensing can be corroborated by using label-free $(T)_7$ (C-DNA) as a control. On addition of Hg(II) ions to the free fluorescein solution, the fluorescence did not quench whether in the presence of C-DNA or not. The result revealed that only when fluorescein was incorporated into oligodeoxyribonucleotide poly(dT), the six-carbon linker in the sensor brings the excited state of fluorescein and the π-stacked [T–Hg(II)–T] in close proximity to each other, fluorescence quenching via photoinduced charge transfer occurs from the excited singlet state of fluorescein to the π-stacked [T–Hg(II)–T].

As a "turn-off" sensor, fluorescence intensity decreased in the presence of Hg^{2+} ions, which might give "false positive" results caused by external quenchers or other environmental factors that could also induce fluorescence decrease. To differentiate the "false positive" signal, the control could be conducted (see Fig. 6). In the presence of excess C-DNA, the fluorescence of $(T)_7$–F quenched only slightly upon addition of Hg(II) ion due to C-DNA competing for the Hg(II) ion with $(T)_7$–F. If the fluorescence of $(T)_7$–F quenches in the absence of C-DNA, but does not quench in the presence of C-DNA, the sample contains Hg(II) ions. Conversely, when the fluorescence of $(T)_7$–F is quenched in the presence and the absence of C-DNA, the quenching is most likely caused by unexpected contaminants and the presence of Hg(II) in the sample is uncertain [12]. Thus, by using C-DNA as control, false positive signal can be distinguished from Hg(II)-mediated quenching during the analysis of practical samples.

3.6. Selectivity

Transition-metal ions are well-known as fluorescence quenchers and work via numerous mechanisms, including ground-state complexation, collisional conversion of electronic to kinetic energy, heavy atom effects, magnetic perturbations, charge-

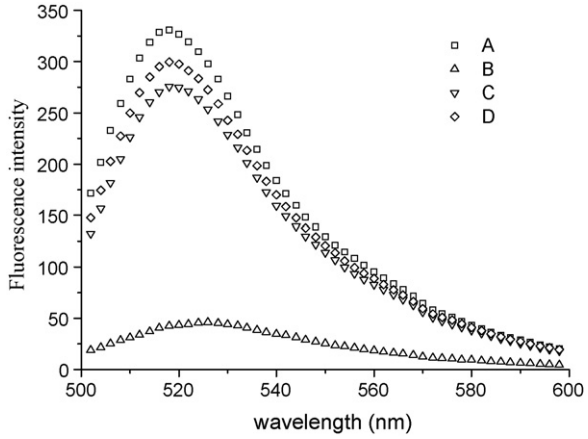

Fig. 6. Fluorescence spectra of the sensor at the present of C-DNA. A: 20 nM $(T)_7$–F; B: 20 nM $(T)_7$–F + 10 μM $Hg(NO_3)_2$; C: 20 nM $(T)_7$–F + 10 μM $Hg(NO_3)_2$ + 10 μM C-DNA; D: 20 nM $(T)_7$–F + 10 μM $Hg(NO_3)_2$ + 30 μM C-DNA.

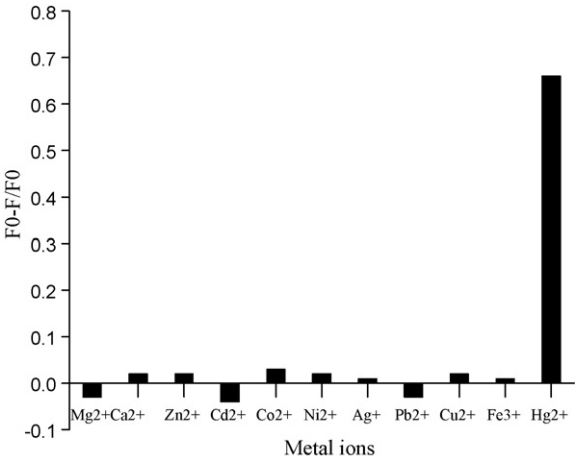

Fig. 7. Fluorescence quenching efficiency of $(T)_7$–F (20 nM) in the presence of 200 μM $Mg(NO_3)_2$ (1), 200 μM $Ca(NO_3)_2$ (2), 100 μM $Zn(NO_3)_2$ (3), 100 μM $Cd(NO_3)_2$ (4), 100 μM $Co(NO_3)_2$ (5), 100 μM $Ni(NO_3)_2$ (6), 10.0 μM $AgNO_3$ (7), 1.0 μM $Pb(NO_3)_2$ (8), 1.0 μM $Cu(NO_3)_2$ (9), 1.0 μM $Fe(NO_3)_3$ (10), 1.0 μM $Hg(NO_3)_2$ (11).

Table 4
Determination of Hg(II) ions in water samples using the proposed method.

	Added (nM)	Founded (nM) mean[a] ± SD[b]	Recovery (%)
Sample1	300	278 ± 20	92.7
Sample2	600	626 ± 20	104.3

[a] Mean of three determinations.
[b] SD, standard deviation.

transfer phenomena, electronic energy transfer, and fluorescence resonance energy transfer [40]. The selectivity of the sensor for Hg(II) over alkaline earth metal and transition-metal ions (Mg^{2+} and Ca^{2+} at 200 μM, Zn^{2+}, Cd^{2+}, Co^{2+} and Ni^{2+} at 100 μM, Ag^{+} at 10.0 μM, Pb^{2+}, Cu^{2+} and Fe^{3+} at 1.0 μM) was investigated under the optimum condition (Fig. 7). Little change in the fluorescence intensity of the sensor was observed on addition of the these metal ions, in contrast to significant quenching as observed for Hg(II) ions. The results demonstrate excellent selectivity over alkaline earth and transition-metal ions.

3.7. Assay of Hg(II) ions concentrations in water samples

The application of the proposed method was evaluated for determination of Hg(II) ions in river water samples obtained from Minjiang river. The sample collected was first filtered through a 0.22 μm filter membrane to remove insoluble substance. For the response range of the proposed method is not yet adequate for environment monitoring in the 10^{-8}–10^{-9} M range. The water samples were spiked with Hg(II) ions at different concentration levels. The results were summarized in Table 4 and indicated that our sensor was able to detect mercury in river water.

4. Conclusions

In summary, a novel and simple fluorescence sensor for Hg(II) ions was proposed based on Hg(II) preferential binding to T–T mismatch base pairs. Upon addition of Hg(II) ions, the formation of π-stacked [T–Hg(II)–T] with "sandwich" structure accepts and mediates the electron transfer via PCT and creates an additional nonradiative decay channel for the excited state of fluorescein, which induces the fluorescence to be quenched. In this study, the π-stacked [T–Hg(II)–T] functioned not only as selective recognition, but also as an electron acceptor for mercury ion sensing. Although the equilibrium time was a little long at low concentration for mercury ion sensing, a short incubation time might also been achieved at the cost of the sensitivity. We hope our findings could be further applicable to DNA-inspired metal-ion sensors and M-DNA materials for nanoelectronic applications.

Acknowledgements

The authors are grateful to the National Natural Science Foundation (50503006, 20575011 and 20735002) and Science foundation of Fujian Province (2008J0149) of China for financial support.

References

[1] Y. Tanaka, K. Taira, Chem. Commun. (2005) 2069–2079.
[2] N.K. Lee, H.R. Koh, K.Y. Han, S.K. Kim, J. Am. Chem. Soc. 129 (2007) 15526–15534.
[3] M.E. Ariza, M.V. Williams, J. Biochem. Mol. Toxicol. 3 (1999) 107–112.
[4] P. Cheng, C. He, J. Am. Chem. Soc. 126 (2004) 728–729.
[5] K. Tanaka, A. Tengeiji, T. Kato, N. Toyama, M. Shionoya, Science 299 (2003) 1212–1213.
[6] H.A. Wagenknecht, Angew. Chem. Int. Ed. 42 (2003) 3204–3206.
[7] A. Rakitin, P. Aich, C. Papadopoulos, Y. Kobzar, A.S. Vedeneev, J.S. Lee, J.M. Xu, Phys. Rev. Lett. 86 (2001) 3670–3673.
[8] Z. Kuklenyik, L.G. Marzilli, Inorg. Chem. 35 (1996) 5654–5662.
[9] Y. Miyake, H. Togashi, M. Tashiro, H. Yamaguchi, S. Oda, M. Kudo, Y. Tanaka, Y. Kondo, R. Sawa, T. Fujimoto, T. Machinami, A. Ono, J. Am. Chem. Soc. 128 (2006) 2172–2173.
[10] Y. Tanaka, S. Oda, H. Yamaguchi, Y. Kondo, C. Kojima, A. Ono, J. Am. Chem. Soc. 129 (2007) 244–245.
[11] A. Bagno, G. Saielli, J. Am. Chem. Soc. 129 (2007) 11360–11361.
[12] A. Ono, H. Togashi, Angew. Chem. Int. Ed. 43 (2004) 4300–4302.
[13] Y. Miyake, A. Ono, Tetrahedron Lett. 46 (2005) 2441–2443.
[14] Y. Tang, F. He, M. Yu, F. Feng, L. An, H. Sun, S. Wang, Y. Li, D. Zhu, Macromol. Rapid Commun. 27 (2006) 389–392.
[15] Z. Wang, D. Zhang, D. Zhu, Anal. Chim. Acta 49 (2005) 10–13.
[16] X. Liu, Y. Tang, L. Wang, J. Zhang, S. Song, C. Fan, S. Wang, Adv. Mater. 19 (2007) 1471–1474.
[17] C.K. Chiang, C.C. Huang, C.W. Liu, H.T. Chang, Anal. Chem. 80 (2008) 3716–3721.
[18] B.C. Ye, B.C. Yin, Angew. Chem. Int. Ed. 47 (2008) 8386–8389.
[19] J. Wang, B. Liu, Chem. Commun. (2008) 4759–4761.
[20] J.S. Lee, M.S. Han, C.A. Mirkin, Angew. Chem. Int. Ed. 46 (2007) 4093–4096.
[21] X. Xue, F. Wang, X. Liu, J. Am. Chem. Soc. 130 (2008) 3244–3245.
[22] C.W. Liu, Y.T. Hsieh, C.C. Huang, Z.H. Lin, H.T. Chang, Chem. Commun. (2008) 2242–2244.
[23] S. He, D. Li, C. Zhu, S. Song, L. Wang, Y. Long, C. Fan, Chem. Commun. (2008) 4885–4887.
[24] D. Li, A. Wieckowska, I. Willner, Angew. Chem. Int. Ed. 47 (2008) 3927–3931.
[25] J. Liu, Y. Lu, Angew. Chem. Int. Ed. 46 (2007) 7587–7590.
[26] M. Hollenstein, C. Hipolito, C. Lam, D. Dietrich, D.M. Perrin, Angew. Chem. Int. Ed. 47 (2008) 4346–4350.
[27] A.A. Voityuk, J. Phys. Chem. B 110 (2006) 21010–21013.
[28] J. Joseph, G.B. Schuster, Org. Lett. 9 (2007) 1843–1846.
[29] T. Ito, G. Nikaido, S. Nishimoto, J. Inorg. Biochem. 101 (2007) 1090–1093.
[30] E.M. Nolan, S.J. Lippard, J. Am. Chem. Soc. 125 (2003) 14270–14271.
[31] R. Sjöback, J. Nygren, M. Kubista, Biopolymers 46 (1998) 445–453.
[32] J.L. Mergny, A.S. Boutorine, T. Garestier, F. Belloc, M. Rougee, N.V. Bulychev, A.A. Koshkin, J. Bourson, A.V. Lebedev, B. Valeur, N.T. Thuong, C. Helene, Nucleic Acids Res. 22 (1994) 920–928.
[33] T. Heinlein, J.P. Knemeyer, O. Piestert, M. Sauer, J. Phys. Chem. B 107 (2003) 7957–7964.
[34] B.Q. Spring, R.M. Clegg, J. Phys. Chem. B 111 (2007) 10040–10052.
[35] P. Aich, S.L. Labiuk, L.W. Tari, L.J.T. Delbaere, W.J. Roesler, K.J. Falk, R.P. Steer, J.S. Lee, J. Mol. Biol. 294 (1999) 477–485.
[36] S.D. Wettig, G.A. Bare, R.J.S. Skinner, J.S. Lee, Nano Lett. 3 (2003) 617–622.
[37] L.E. Cramer, K.G. Spears, J. Am. Chem. Soc. 100 (1978) 221–227.
[38] L. Flamigni, J. Phys. Chem. 97 (1993) 9566–9572.
[39] B. Liu, A.J. Bard, C.Z. Li, H.B. Kraatz, J. Phys. Chem. B 109 (2005) 5193–5198.
[40] N. Rupcich, W. Chiuman, R. Nutiu, S. Mei, K.K. Flora, Y. Li, J.D. Brennan, J. Am. Chem. Soc. 128 (2006) 780–790.

Talanta 79 (2009) 570–575

Contents lists available at ScienceDirect

Talanta

journal homepage: www.elsevier.com/locate/talanta

Synthesis and photocatalytic applications of Ag/TiO_2-nanotubes

Guangmei Guo [a], Binbin Yu [b], Ping Yu [c], Xi Chen [b,*]

[a] College of Sciences, Hebei University of Science and Technology, Shijiazhuang 050018, China
[b] State Key Laboratory of Marine Environmental Science, Xiamen University, Siming South Rd. 422, Xiamen 361005, China
[c] Fujian Research Institute of Metric Science, Fuzhou 350003, China

ARTICLE INFO

Article history:
Received 3 December 2008
Received in revised form 13 April 2009
Accepted 16 April 2009
Available online 3 May 2009

Keywords:
Ag/TiO_2-nanotubes
Photocatalytic degradation
Rhodamine dyes
Organochlorine pesticides

ABSTRACT

TiO_2- and Ag/TiO_2-nanotubes (NTs) were synthesized by hydrothermal methods and microwave-assisted preparation, respectively. Scanning electron microscopy, high resolution transmission electron microscopy, Brunauer–Emmett–Teller particle surface area measurement and X-ray diffraction were used to characterize the nanotubes. Rutile TiO_2-NTs with $Na_2Ti_5O_{11}$ crystallinity had a length range of 200–400 nm and diameters of 10–20 nm. TiO_2- and Ag/TiO_2-NTs with a 0.4% deposition of Ag had high surface areas of 270 and 169 $m^2\,g^{-1}$, respectively. The evaluation of photocatalytic activity showed that Ag/TiO_2-NTs displayed higher photocatalytic activity than pure TiO_2-NTs and a 60.91% degradation of Rhodamine-B with 0.8% deposition of Ag species. Also 60% of Rhodamine-6G was physisorbed and 40% chemisorbed on the surface of TiO_2-NTs. In addition, the photocatalytic degradations of organochlorine pesticides taking α-hexachlorobenzene (BHC) and dicofol as typical examples, were compared using Ag/TiO_2-NTs, and found that their degradations rates were all higher than those obtained from commercial TiO_2.

1. Introduction

In recent decades, the study of TiO_2-nanotubes (TiO_2-NTs) has become an important research field due to their special chemical and physical characteristics, including high ion-exchange capability, high special surface area due to their open mesoporous nature, enhanced proton conductivity and relative stability [1]. These multilayered nanotubes have several crystal structures, such as $H_2Ti_3O_7$, $H_2Ti_2O_4(OH)_2$ and $H_2Ti_4O_9{\cdot}H_2O$, and are used in hydrogen sensors [2,3], the catalysis of CO [4], photocatalysis [5], ion-exchange [5], and the preparation of lithium batteries [6].

Recently, there has been growing interest in catalysis of TiO_2-NTs, including photocatalysis and catalytic oxidation. Shao et al. [7], utilized TiO_2-NTs in the photocatalytic degradation of sodium dodecyl benzene sulfonate. In Hodos et al.'s report [5], CdS was applied to the outer and inner surfaces of TiO_2-NTs, resulting in a higher photocatalytic capability than that of pure TiO_2-NTs for methyl orange degradation. Generally, Pd/TiO_2-NTs show high catalytic activity for methanol electro-oxidation in direct methanol fuel cells [8]. The catalytic performance of Au/TiO_2-NTs, Cu/TiO_2-NTs and Au–Cu/TiO_2-NTs have been compared for low-temperature CO oxidation [4]. Ultrahigh crystalline TiO_2-NTs were produced and applied to photocatalytic oxidation of trimethylamine gas [9]. Furthermore, $TiO_{2-x}C_x$-nanotube arrays displayed higher photocurrent densities and more efficient water splitting under visible-light illumination (>420 nm) [10]. The high surface-to-volume ratio of TiO_2-NTs shows great potential for application, but it has still not been studied extensively.

In the present study, we prepared TiO_2-NTs via methods and Ag/TiO_2-NTs by deposition of Ag onto the surface of TiO_2-NTs. The adsorption and photocatalytic degradation of Rhodamine dyes were carried out as a function of different TiO_2 systems were investigated. To reveal the potential application of Ag/TiO_2-NTs in analytical chemistry, the photocatalytic degradations of organochlorine pesticides taking α-hexachlorobenzene (BHC) and dicofol as typical examples, were compared. Compared with pure TiO_2-NTs and commercial TiO_2 particles, 0.8% Ag/TiO_2-NTs exhibited a good degree of photocatalytic activity and could be separated easily.

2. Experimental

2.1. Reagents and solutions

Rhodamine-B (R-B) and Rhodamine 6G (R-6G) were purchased from Wake Pure Chemicals, Co. Ltd. (Osaka, Japan). Their stock solutions with 2.0 $g\,L^{-1}$ were prepared by pure water. α-BHC (95.5–100%) and dicofol (97%) were obtained from Accustandard Co. Ltd. (USA). Acetone and hexane were of pesticide residue grade and purchased from Tedia Co. Ltd. (USA). Stock solutions of BHC and dicofol with 100 $\mu g\,mL^{-1}$ were prepared and dissolved in acetone.

* Corresponding author. Tel.: +86 592 2184530; fax: +86 592 2186401.
E-mail address: xichen@xmu.edu.cn (X. Chen).

0039-9140/$ – see front matter © 2009 Elsevier B.V. All rights reserved.
doi:10.1016/j.talanta.2009.04.036

TiO_2 nano-particles (*Degussa P*-25, Germany) were 70% in anatase and 30% in rutile phases, and their primary particle diameters were in the range of 30–50 nm.

2.2. Preparation of TiO_2- and Ag/TiO_2-NTs

A hydrothermal method for TiO_2-NTs preparation was applied according to Lin et al. [2], so that 2.0 g TiO_2 nano-particles was added into 100 mL NaOH solution with a concentration of 10 mol/L, and the mixture refluxed for 24 h at 140 °C. After filtration, the white product was treated with 0.1 mol/L HCl and distilled water, until the pH value of the washing solution was lower than 7. Subsequently the nanotube was dried at room temperature and calcined at 300 °C for 1 h to remove any impurity on the TiO_2-NTs surface. Finally, the product of TiO_2-NTs with a range of 300–800 nm in length and 15–30 nm in diameter was obtained (Fig. 1a).

A microwave-assisted approach was selected to produce Ag/TiO_2-NTs [11,12] and 0.10 g TiO_2-NTs and 30 mL glycol containing 4.0×10^{-4} mol KOH were mixed ultrasonically and put into a Teflon lined autoclave. A designated amount of $AgNO_3$ was added into the mixture and it was exposed to microwave irradiation for 45 s at high level. After cooling the resulting powder was filtered and oven dried. From the HRTEM image shown in Fig. 2b, the depositing Ag nano-particles on TiO_2-NTs with a range of 12–20 nm in diameter could be found.

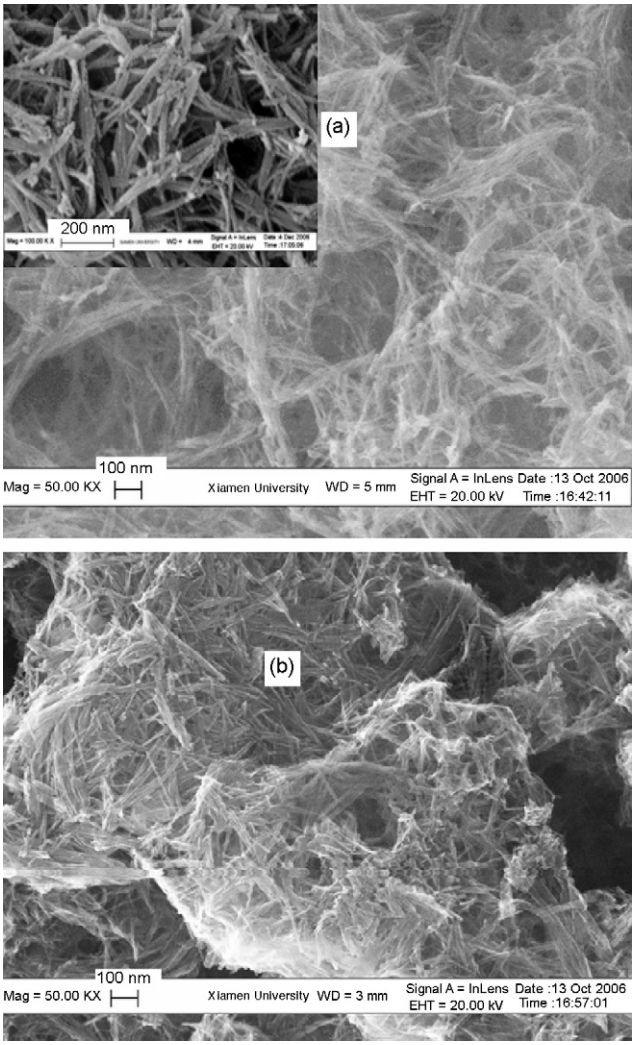

Fig. 1. SEM images of TiO_2 and Ag/TiO_2-NTs. (a) TiO_2-NTs, insert: higher magnification (b) 0.4% Ag/TiO_2-NTs.

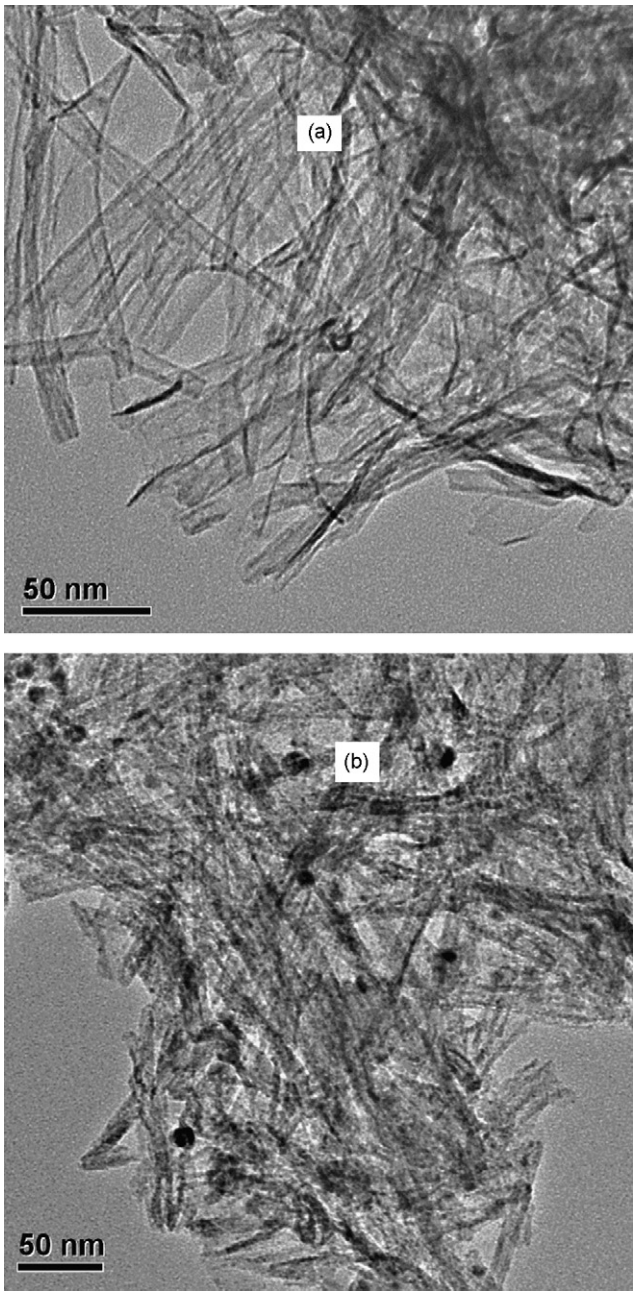

Fig. 2. HRTEM of (a) TiO_2-NTs; (b) 0.4% Ag/TiO_2-region A; and (c) 0.4% Ag/TiO_2-region B.

2.3. Measurement of Rhodamine-6G adsorption

Static adsorption isotherms of R-6G onto TiO_2-NTs were prepared by determining the amount of dye in an aqueous solution, which was extracted in a given time interval. The adsorptive content of dye q was calculated according to the following formula (1), where C_0 and C represent the original and residual concentration of R-6G; W is the amount of TiO_2-NTs; and V is the bulk volume of the solution.

$$q = \frac{(C_0 - C) \times V}{W} \ (\mathrm{g/g}) \quad (1)$$

After adsorption equilibrium on the TiO_2-NTs surface was achieved, the absorber TiO_2-NTs saturated with dye was separated. To obtain a rapid desorption equilibrium, a mixed solution containing ethanol and water (v/v, 1:1) was used as with elution solvent.

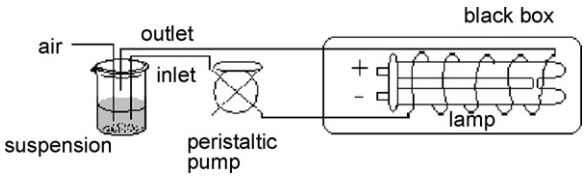

Fig. 3. Setup for photocatalytic experiment.

The desorption content of R-6G from TiO_2-NTs could be determined on the basis of formula (2), where W is the total adsorptive content of dye and V is the bulk volume of the solution. All experiments were held at 30 °C.

$$\text{Desorption rate}\,(\%) = \frac{C \times V}{W} \times 100 \quad (2)$$

2.4. Photocatalytic degradation of Rhodamine dyes and pesticides

As shown in Fig. 3, a peristaltic pump was used to transfer the suspension into a flow system for more effective photocatalytic degradation. As the irradiation source, a 9 W ultraviolet lamp with a main wavelength of 365 nm was placed into a black box to avoid environmental irradiation. After photocatalysis, the sample was centrifuged and the residual amount of R-B in the solution was detected using a fluorescence spectrometer (Hitachi, F-4500).

A Shimadazu GC-2010 gas chromatograph (GC) equipped with an electron capture detector (ECD) and a DB-5 column (30 m × 0.25 mm × 0.25 μm) was applied to detect the original and residual pesticides. The temperature program of the GC-ECD was selected as follows: 100–220 °C at 20 °C min^{-1}, 220–240 °C at 5 °C min^{-1}, 240–300 °C at 20 °C min^{-1} for BHC; 200–300 °C (10 min) at 10 °C min^{-1} for cypermethrin; 150–280 °C (1 min) at 20 °C min^{-1}, 280–300 °C at 10 °C min^{-1} for dicofol. The temperature of ECD and injector was held at 300 and 280 °C, respectively. Each sample with 1 μL was repeatedly injected twice, and the data were collected and averaged.

2.5. Characterization of samples

SEM (LEO-1530, Oxford Co., UK) was used to observe the surface morphologies, and HRTEM (TECNAI F-30) was used to obtain three-dimensional observations. The analysis of Ti, O and Ag was implemented by energy dispersive X-ray spectrometry (EDS).

X-ray diffraction (XRD) images were obtained using X' Pert diffractometer (Philips, Netherlands), employing Cu Kα radiation λ = 0.154 nm. The patterns were recorded in a range from 20° to 85° (2θ). BET specific surface area analysis was performed using measurements of nitrogen adsorption–desorption at −195 °C by surface area and porosimetry analyzer (Micromeritics ASAP-2000, USA). Before adsorption the samples were degassed at 300 °C for 2 h. UV–vis DRAS were recorded on a UV-2501 (Shimadazu Ltd., Japan) against a $BaSO_4$ reference. A microwave oven (RE-S560NT, SHARP, Japan) with an output power of 500 W was used to prepare Ag/TiO_2-NTs.

3. Results and discussion

3.1. SEM and TEM images of TiO_2- and Ag/TiO_2-NTs

SEM images of TiO_2- and Ag/TiO_2-NTs (Fig. 1) demonstrated that TiO_2-NTs have a length range of 200–400 nm and a diameter of 10–20 nm, and that the TiO_2-NTs were loosely tangled together, which can be observed more clearly in the insert in Fig. 1a. The large number of cavities which appeared on the surface of the TiO_2-NTs confirmed their porous characteristic, consistent with the results of BET analysis shown below. In Fig. 1b, the morphological appearance of Ag/TiO_2-NTs was similar to that of TiO_2-NTs, indicating that samples maintained their appearance after microwave reaction.

Table 1
EDS analysis results of TiO_2-NTs and 0.4% Ag/TiO_2-NTs.

TiO_2-NTs			0.4% Ag–TiO_2-NTs		
Element	wt.%	at.%	Element	wt.%	at.%
O(K)	34.955	59.667	O(K)	37.461	64.822
Ti(K)	56.973	32.484	Ti(K)	56.223	32.495
Na(K)	1.125	1.330	Ag(K)	5.195	1.333
			Na(K)	1.119	1.348

The HRTEM technique was applied to observe the deep nanostructure inside TiO_2-NTs and Ag/TiO_2-NTs. In Fig. 2a, as in a previous report [13], open-ended TiO_2-NTs with a wall thickness of about 2–3 nm and uniform inner diameters of about 10 nm could be observed. Due to the incomplete growth of the nanotubes, a small number of shorter TiO_2-NTs was obtained. As seen in Table 1, EDS results showed that the atomic number ratio of Ti/O was nearly 1:2 with a certain amount of Na, which confirmed that the material was composed of TiO_2-NTs.

As shown in Fig. 2b, Ag particles with sizes of about 10 nm were distributed on the TiO_2-NTs. Based on the EDS analysis result, the content of Ag was found to be 5.195% (wt.%) and 1.333% (at.%). During the microwave-polyol process, polyol acted as a reducing agent to form aldehyde, which reacted with Ag(OH) to generate nano-Ag particles, which precipitated on the TiO_2-NTs [11].

3.2. XRD analysis

XRD results illustrated that the crystallinity of nanotubes was generally poor. Peaks marked R and $Na_2Ti_5O_{11}$ corresponded to the rutile phase of TiO_2 and the $Na_2Ti_2O_5$ phase, respectively. The ordered structure of nano-TiO_2 was destroyed during the curing process and amorphous nanotubes were formed. However, a small amount of rutile material was still observed in Fig. 4 due to its high stable properties, whereas, no anatase was found. Besides, there was a new diffraction peak ranging from 23° to 25° of 2θ, which was attributed to $Na_2Ti_5O_{11}$ according to the comparison with the standard JCPDs card. The observation was consistent with the results of EDS.

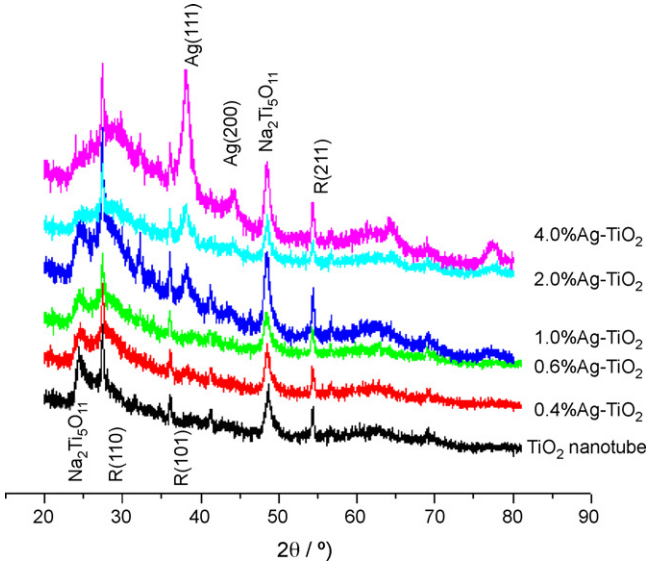

Fig. 4. XRD patterns of Ag–TiO_2 at different doping ratios.

Table 2
BET results of TiO_2 and Ag–TiO_2-NTs.

Sample	BET surface area (m^2/g)	Pore volume (cm^3/g)	Pore size (nm)
TiO_2 particle (*Dugussa P*-25)	50 (provided by Degussa Corp.)		
TiO_2-NTs	270	1.03	13.68
0.4% Ag-TiO_2-NTs	169	0.35	6.57
1% Ag-TiO_2-NTs	144	0.25	5.28
4% Ag-TiO_2-NTs	137	0.25	5.25

An Ag crystal phase appeared and showed good crystallinity. The peak intensity of Ag(1 1 1) obviously increased with the increase in amount of Ag in the TiO_2-NTs, when the additional amount of Ag into the TiO_2-NTs was more than 1%. No obvious Ag(1 1 1) peak appeared for the 0.4% and 0.6% addition Ag/TiO_2-NTs samples due to the lower deposition content of Ag. No obvious phase transformation between rutile phase and $Na_2Ti_2O_5$ phase could be found with the increase in amount of Ag species. The result indicated that most of the Ag nano-particles were deposited on the surface of the TiO_2-NTs, and not in the crystal lattice of the nanotubes, which was in accordance with the phenomena observed by SEM and TEM.

3.3. BET special surface area analysis

TiO_2-NTs were characterized by N_2 adsorption–desorption at −195 °C. Results including the BET surface area, pore volume and BET pore size are listed in Table 2. As shown in Fig. 5, the N_2 adsorption–desorption isotherm of TiO_2-NTs presented a type IV isotherm according to the IUPAC classification, displaying the porous characteristics of nanotubes. An adsorption–desorption hysteresis loop was observed at $P/P_0 \approx 0.78$, indicating capillary condensation inside the mesoporous nanotubes. After TiO_2 particles were converted into nanotubes, the BET surface area enlarged from 50 to 270 $m^2\ g^{-1}$. With increase in the amount of Ag deposited, BET surface area, pore volume and outright pore size decreased. Correspondingly, the BET surface area changed from 270 $m^2\ g^{-1}$ of TiO_2-nanotubes to 137 $m^2\ g^{-1}$ of 4% Ag/TiO_2-NTs, and the pore volume from 1.03 to 0.25 $cm^3\ g^{-1}$. It could be deduced that Ag particles occupied the pores of the TiO_2-NTs and caused blockage of the pore volume during the microwave process [14]. Furthermore, the BET surface area declined as the sample became more compact under higher pressure. The average pore size for TiO_2-NTs was 13.7 nm, which was in accordance with the HRTEM observation.

3.4. Adsorption of R-6G

Experimental results indicated that R-6G was evidently adsorbed on the TiO_2-NTs surface in a neutral environment, and this affected the photocatalytic efficiency of TiO_2-NTs in R-6G degradation. In contrast, there was no obvious adsorption of R-B dye onto the TiO_2-NTs surface. No analogous phenomenon for the R-6G dye was observed in the nano-TiO_2 particle system. The influence of R-6G adsorption on TiO_2-NTs photocataysis was investigated using adsorption and desorption amounts of R-6G on the TiO_2-NTs surfaces. As shown in Fig. 6a, R-6G displayed a higher affinity for the TiO_2-NTs surfaces in aqueous solution. The adsorptive amount of R-6G with 10 mg g^{-1} (R-6G: TiO_2-NTs, w/w) was up to 18 mg g^{-1} after 20 h immersion. The adsorption equilibrium was attained when adsorption reached 21 mg g^{-1} at 30 °C, at which time 83.68% of the R-6G had been absorbed onto the TiO_2-NTs. This result indicated that TiO_2-NTs provided an effective adsorptive site for R-6G adsorption.

The desorption isotherm of R-6G as a function of time is shown in Fig. 6b. With the increase of elution time, R-6G dye was extracted slowly from TiO_2-NTs. After a 40 h elution, the content of R-6G in solution showed a 60% decrease and remained constant with longer elution time. No obvious desorption was observed even when the elution solution was replaced. In general, the desorption process is considered to be an endothermic reaction, and a higher temperature improves the desorption of dyes. Fortunately, no more desorption was found for R-6G dye on TiO_2-NTs at a temperature of 40 °C. It could be deduced that 60% physical- and 40% chemical-adsorption of R-6G occurred on the surface of the nanotubes [2].

3.5. Evaluation of photocatalytic activity

Photocatalytic activities of TiO_2-NTs and Ag–TiO_2-NTs with different amounts of Ag deposition were evaluated by comparing their R-6G degradation efficiencies. The results showed that no obvious degradation was observed in the TiO_2-NTs/UV system since the surfaces of TiO_2-NTs were covered by R-6G, which prevented the generation of electrons and development of holes in the TiO_2-NTs under UV irradiation. However, no adsorption was observed for R-B under the same conditions and, consequently, R-B was selected as the target for evaluating photocatalytic activity in the TiO_2-NTs and Ag/TiO_2-NTs. It could be concluded that an appropriate amount of adsorption is favorable for photocatalysis, but full adsorption would have the opposite effect.

The degradation of R-B under different photocatalysis systems is shown in Table 3. C represented the residual content and C_0 was the original content of R-B, while $(1 - C/C_0)$ was regarded as the degradation efficiency. An R-B degradation efficiency of 70.34% and 3.79% was found with and without commercial TiO_2 particles (*Degussa P*-25) as catalyst, respectively. The degradation comparisons from Table 3 revealed that the deposition of nano-Ag particles onto the TiO_2-NTs surfaces enhanced remarkably the photocatalytic activity. The 0.8% Ag/TiO_2-NTs resulted in the highest degradation ratio (87.91%) among materials with different amounts of nano-Ag particle deposition. The degradation ratio of 87.91% using 0.8% Ag/TiO_2-NTs is obviously higher than that using the *Degussa*

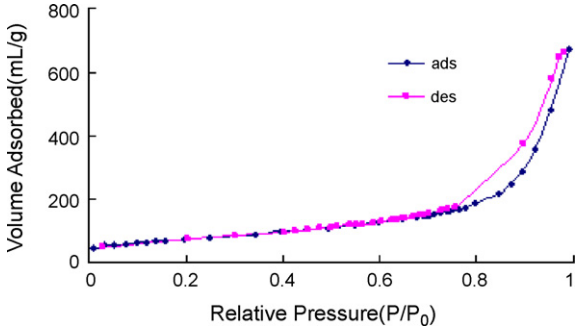

Fig. 5. Isotherm of nitrogen adsorption–desorption at −195 °C on the surface of TiO_2-NTs.

Table 3
Residual Rhodamine-B % using different photocatalytic systems.

Catalyst	C/C_0 (%)
No catalyst	96.21
TiO_2 particles	29.66
TiO_2-NTs	54.30
0.2% Ag–TiO_2-NTs	38.62
0.4% Ag–TiO_2-NTs	32.55
0.6% Ag–TiO_2-NTs	28.21
0.8% Ag–TiO_2-NTs	12.09
1.0% Ag–TiO_2-NTs	26.97
2.0% Ag–TiO_2-NTs	37.58

C_0 = original and C = residual content of R-B.

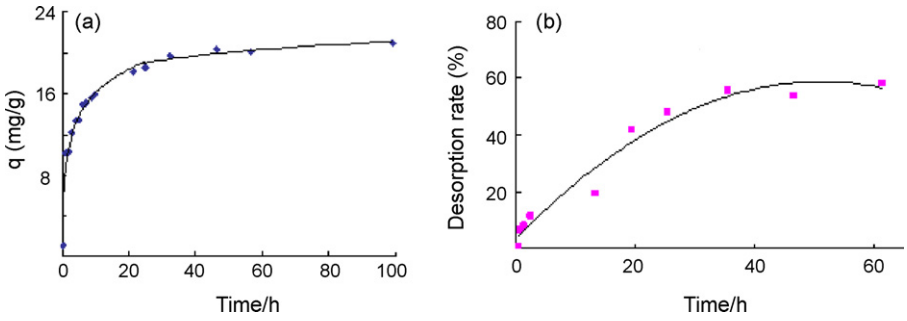

Fig. 6. Absorption (a) and desorption (b) amounts of Rhodamine-6G as a function of time, TiO_2-NTs: 0.04 g/50 mL.

P-25 TiO_2 particles system (degradation ratio with 70.34%), and that value of 45.70% obtained for TiO_2-NTs. The lower degradation activity of TiO_2-NTs was caused by their low crystallinity, which effectively generated electrons and produced holes. An appropriate deposition of nano-Ag particles onto the TiO_2-NTs surface improved the degradation activity, for the following reasons: (a) TiO_2-NTs supported an appropriate content of nano-Ag particles well due to their high special surface area, which could obviously capture the photoinduced electrons and so prevent their recombination [15]; and (b) photoinduced electrons could be transferred to reactants effectively due to the two dimensional structure of TiO_2-NTs. A higher deposition of Ag species caused an increase of photodegradation efficiency, but an excess content of nano-Ag particles resulted in the reverse, that is a decrease of R-B degradation. It could be that an excess content of nano-Ag particles re-combined electrons and holes. Furthermore, Ag deposition on nanotubes may have acted as a site where electrons could accumulate, and this could induce an electric field to attract holes. Therefore the site of Ag species becomes a combined center for electron and hole production instead of a center for electron capture [16]. Although the commercial nano-TiO_2 particles, *Degussa P*-25, showed a definite photocatalytic activity, it was difficult to separate them from the photocatalytic medium after application. TiO_2-NTs and Ag/TiO_2-NTs could be centrifugally separated even at a relatively low rotation speed. According to the above experimental results, 0.8% Ag/TiO_2-NTs exhibited a reasonable degree of photocatalytic activity and indicated good application potential.

In order to reveal the analytical potential of Ag/TiO_2-NTs, in atmosphere, the degradations of α-BHC and dicofol, which were taken as typical examples and their rudimental contents were detected by GC approach [17], were compared using the commercial nano-TiO_2 particles, *Degussa P*-25, TiO_2-NTs and 0.8% Ag/TiO_2-NTs. In general, Cl^-, a final degradations product of organochlorine pesticides, could be detected by other convenient approaches such as electroanalytical chemistry [18] or chemiluminescence [19]. A higher degradation rate of organochlorine pesticides means high concentration of Cl^-, resulting in a higher sensitive for the determination of the organochlorine pesticides. As the results presented in Table 4, after the 20 min irradiation under a 9 W ultraviolet lamp, without any TiO_2, α-BHC and dicofol would almost keep their original state. 57.2% ($1 - C/C_0$) of α-BHC and 58.5% of dicofol were degraded using *Degussa P*-25, but, analogously, 50.7% for α-BHC and 52.4% for dicofol under TiO_2-NTs photocatalysis. Obviously, the degradations efficiency of α-BHC or dicofol was higher than that obtained by *Degussa P*-25when 0.8% Ag/TiO_2-NTs was applied in the photocatalysis. Correspondingly, their degradations efficiencies with 67.9% and 72.5% for α-BHC and dicofol were found under the same conditions. These results showed that 0.8% Ag/TiO_2-NTs obviously increased the photocatalytic degradation efficiency of organochlorine pesticides, indicating this material is with a great potential in the development of the rapid determination of organochlorine pesticides.

Table 4
Degradation efficiency of α-BHC and dicofol under different TiO_2 photocatalysis ($n = 5$).

TiO_2 material	C/C_0 (%)	
	α-BHC	Dicofol
No TiO_2	96.2 ± 2.3	97.8 ± 1.6
Degussa P-25	42.8 ± 1.3	41.5 ± 1.8
TiO_2-NTs	49.3 ± 2.1	47.6 ± 2.0
0.8% Ag/TiO_2-NTs	32.1 ± 1.6	27.5 ± 2.8

4. Conclusions

In conclusion, TiO_2-NTs and Ag/TiO_2-NTs were synthesized using a hydrothermal method and microwave-assisted preparation, respectively. The photocatalytic activity of TiO_2-NTs was enhanced by the deposition of a certain amount of nano-Ag particles. In addition, TiO_2-NTs showed an interesting adsorption for R-6G, including 60% physisorption and 40% chemisorption in a neutral solution. In the degradations of Rhodamine dyes, α-BHC and dicofol, 0.8% Ag/TiO_2-NTs displayed good prospective advantages for use in photocatalytic degradation. This result indicates that some pollutants or pesticides would be photo-degradation or transformation by Ag/TiO_2-NTs to detectable states in analytical mean.

Acknowledgements

This research work was financially supported by the Science and Technology Project of Hebei Province (No. 07246751D), the National Nature Scientific Foundations of China (Nos. 20775064, 20735002), the Program for New Century Excellent Talents in University of China (NCET). Furthermore, we would like to extend our thanks to Professor John Hodgkiss of the University of Hong Kong for his assistance with English.

References

[1] D.V. Bavykin, A.A. Lapkin, P.K. Plucinski, L. Murciano, J.M. Friedrich, F.C. Walsh, Top. Catal. 39 (2006) 151.
[2] S.H. Lim, J. Luo, Z. Zhong, W. Ji, J. Lin, Inorg. Chem. 44 (2005) 4124.
[3] H.S. Kim, W.T. Moon, Y.K. Jun, S.H. Hong, Sens. Actuator B: Chem. 120 (2006) 63.
[4] B. Zhu, Q. Guo, X. Huang, S. Wang, S. Zhang, S. Wu, W. Huang, J. Mol. Catal. A: Chem. 249 (2006) 211.
[5] M. Hodos, E. Horvath, H. Haspel, A. Kukovecz, Z. Konya, I. Kiricsi, Chem. Phys. Lett. 39 (2004) 512.
[6] L. Kavan, M. Kalbac, M. Zukalova, I. Exnar, V. Lorenzen, R. Nesper, M. Graetzel, Chem. Mater. 16 (2004) 477.
[7] Y. Shao, K.H. Xue, C.J. He, Q.L. Chen, F.F. Tao, W. Shen, Y.Y. Feng, Chin. Chem. World 4 (2003) 174.
[8] M. Wang, D.J. Guo, H.L. Li, J. Solid State Chem. 178 (2005) 1996.
[9] M.A. Khan, H.T. Jung, O.B. Yang, J. Phys. Chem. B 110 (2006) 6626.
[10] J.H. Park, S. Kim, A.J. Bard, Nano Lett. 6 (2006) 24.
[11] S. Komarneni, D. Li, B. Newalkar, H. Katsuki, A.S. Bhalla, Langmuir 18 (2002) 5959.

[12] H.H. Bao, Z.D. Xu, H.Y. Yin, Y.F. Zheng, W.X. Chen, Chin. J. Inorg. Chem. 3 (2005) 374.
[13] L.Q. Weng, S. Song, S. Hodgson, A. Baker, J. Yu, J. Eur. Ceram. Soc. 26 (2006) 1405.
[14] A. Jitianu, T. Cacciaguerra, R. Benoit, S. Delpeux, F. Beguin, S. Bonnamy, Carbon 42 (2004) 1147.
[15] B. Xin, L. Jing, Z. Ren, B. Wang, H. Fu, J. Phys. Chem. A 109 (2005) 2805.
[16] V. Vamathevan, R. Amal, D. Beydoum, G. Low, S. McEvoy, J. Photochem. Photobiol. A 148 (2002) 233.
[17] B.B. Yu, J.B. Zeng, L.F. Gong, M.S. Zhang, X. Chen, Talanta 72 (2007) 1667.
[18] X.M. Chen, Z.J. Lin, Z.M. Cai, X. Chen, X.R. Wang, Talanta 76 (2008) 1083.
[19] J.N. Wang, C. Zhang, H.X. Wang, F.Z. Yang, X.R. Zhang, Talanta 54 (2001) 1185.

Talanta 79 (2009) 959–962

Contents lists available at ScienceDirect

Talanta

journal homepage: www.elsevier.com/locate/talanta

Short communication

Surface modification of poly(dimethylsiloxane) microchips using a double-chained cationic surfactant for efficiently resolving fluorescent dye adsorption

Bingyan Han, Yuanhong Xu, Lixue Zhang, Xiurong Yang, Erkang Wang*

State Key Laboratory of Electroanalytical Chemistry, Changchun Institute of Applied Chemistry, Chinese Academy of Sciences, Graduate School of the Chinese Academy of Sciences, Changchun, Jilin 130022, China

ARTICLE INFO

Article history:
Received 2 March 2009
Received in revised form 10 April 2009
Accepted 16 April 2009
Available online 24 April 2009

Keywords:
Double-chained cationic surfactants
DDAB
Surface modification
Poly(dimethylsiloxane)
Microchip

ABSTRACT

This paper described a double-chained cationic surfactant, didodecyldimethylammonium bromide (DDAB), for dynamic surface modification of poly(dimethylsiloxane) (PDMS) microchips to reduce the fluorescent dyes adsorption onto the microchannel. When DDAB with a high concentration was present as the dynamic modification reagent in the running and sample buffer, it not only reversed the direction of electroosmotic flow, but also efficiently suppressed fluorescent dyes pyronine Y (PY) or rhodamine B (RB) adsorption onto the chip surface. In addition, vesicles formed by DDAB in the buffer with higher surface charge density and electrophoretic mobility could provide wider migration window and potential for the separation of compounds with similar hydrophobicity. Factors affecting modification, such as pH and concentrations of the buffer, DDAB concentration in the buffer were investigated. Compared with commonly used single-chained cetyltrimethylammonium bromide, DDAB provided a better modification performance. Furthermore, PY and RB were separated successfully on a PDMS microchip at the appropriate conditions with DDAB.

1. Introduction

Microfluidic chips attracted researchers' wide interest because they could achieve rapid detection with low sample and reagent consumption, and at the same time combined various techniques to carry out miniaturization of the instrument system [1–4]. Poly(dimethylsiloxane) (PDMS) as a low-cost polymer has increasingly become a versatile material to fabricate microfluidic chips in the past years because of its well-known advantages such as low-temperature polymerization, good elasticity, optical transparency, biological inertness and nontoxicity, permeability, etc. [5–8]. However, PDMS adsorbs some organic solvents and hydrophobic analytes such as fluorescent dyes and proteins due to its quite hydrophobic surface, porous nature and incompatibility with aqueous separation media, thus causes fouling of the material and hampers its wide applications in lab-on-a-chip, especially in electrophoresis. It is evident, therefore, that the biggest problem in using PDMS for microfluidics lies in the surface hydrophobicity. Up to now, much effort has been made to improve its hydrophilicity by surface modification of PDMS microchannel, for example, exposure to energy, using polyelectrolyte multilayers, radiation-induced graft polymerization, silanization [2,9–14]. Among them, the surfactant-based dynamic modification is a favorable method owing to its versatility and low cost. Single-chained surfactants have been introduced to PDMS modification in several reports [9,15]. In the recent years, double-chained surfactants, which are also called lipid or supported lipid bilayer membranes, are developed gradually to PDMS microchip for the different biological applications based on their biomimetic properties [16,17]. Then, they have been reported for use in microchip electrophoresis to separate the small molecules, peptides, and proteins by Allbritton group [18]. Herein, we adopt a double-chained cationic lipid, didodecyldimethylammonium bromide (DDAB), to the microchip in order to form the more favorable modification coating than the positively charged phospholipid membranes on the microchannel, improving the hydrophilicity and efficiently resolving fluorescent dye adsorption. Lucy's group put forward its characterization that could induce a reverse electroosmotic flow (EOF) in capillary electrophoresis [19–22]. Liu et al. reversed a EOF by DDAB dynamic modification to achieve ATP analysis, because the EOF in the PDMS channel was not strong enough to deliver ATP, whose mobility was larger than that of EOF in the reversed direction [23]. This provided an effective reference for us to carry out the purpose of suppressing fluorescent dye adsorption.

In this paper, DDAB as dynamic coating additive in the running and sample buffer induced a strong reversal and stable EOF,

* Corresponding author. Tel.: +86 431 85262003; fax: +86 431 85689711.
E-mail address: ekwang@ciac.jl.cn (E. Wang).

0039-9140/$ – see front matter © 2009 Elsevier B.V. All rights reserved.
doi:10.1016/j.talanta.2009.04.030

and suppressed fluorescent dye adsorption onto the PDMS/glass chip channel. Although glass and PDMS have different surface properties, DDAB can stably coat both glass and PDMS. Electrostatic attraction and hydrophobic interaction between the DDAB bilayer or molecule and the PDMS or glass surface contributed to the channel modification. It not only proved the hydrophilicity of the microchip; but also could be called a kind of micellar electrokinetic capillary chromatography (MEKC) in the microchip electrophoresis, which was different from the case where Lucy and co-workers or Liu and co-workers used DDAB as a semi-permanent coating to coat the channel prior to the separation [20,23]. Vesicles formed by double-chained surfactant have higher surface charge density and electrophoretic mobility than micelles formed by single-chained surfactant, so it can provide wider migration window and potential for the separation of compounds with similar hydrophobicity [24]. In a word, direction of EOF was reversed by the positive charges of DDAB and the adsorption of fluorescent dye pyronine Y (PY) onto the PDMS channel was resolved. Sharp and reproducible PY signals were obtained by microchip electrophoresis with laser-induced fluorescence (LIF) detection method within less than 30 s. It provided a better modification performance than single-chained CTAB on the PDMS surface. Furthermore, the mixture of PY and another fluorescent dye rhodamine B (RB) was separated successfully in the modified PDMS microchip.

2. Experimental

2.1. Chemicals and materials

DDAB was obtained from Acros (Belgium). Cetyltrimethylammonium bromide (CTAB) and PY were purchased from Sigma–Aldrich Co. (St. Louis MO, USA). RB was obtained from the British Drug Houses Ltd. (Poole, UK). Sylgard 184 and curing agent were obtained from Dow Corning (Midland, MI, USA). Sodium phosphate (Na_2HPO_4/NaH_2PO_4) buffer (PB) was used as both electrophoresis running buffer and sample buffer. pH of PB was adjusted with orthophosphoric acid. All chemicals were analytical reagent grade and used as received without further purification. All solutions were dissolved in the Milli-Q water gotten by Milli-Q ultra-high purity water system (Millipore, Bedford, MA, USA) and stored in the refrigerator at 4 °C for use. Experimental solutions were prepared by stock solutions of 1 mM PY or RB and 20 mM DDAB.

2.2. Electrophoresis procedure on PDMS microchips

Detailed process to design and fabricate the hybrid PDMS/glass microchip was described in our previous work [24]. The obtained PDMS replica with cross-electrophoresis channels showed a trapezoidal shape. It was 60 μm wide on the bottom layer, 75 μm on the upper layer and 10 μm deep. After drilled four reservoirs at each end of the across-channel using a hole punch, the PDMS replica was sealed onto a glass slide to create a hybrid PDMS/glass chip. Before electrophoresis, the channels were rinsed with 0.1 M NaOH, Milli-Q water and running buffer with DDAB for 3 min, respectively. Then running buffer was added into buffer reservoir (BR), sample waste (SW), and waste reservoir (WR), respectively, and the sample was placed in the sample reservoir (SR) (see Fig. S1). Sample loading and electrophoretic process were carried out on the two different modes of the high voltages, respectively. Sample loading: V_{BR} = float, V_{BW} = float, V_{SR} = ground, V_{SW} = 0.3 kV. Sample was loaded for 10 s. Electrophoretic process: V_{BR} = ground, V_{BW} = 1.2 kV, V_{SR} = 0.3 kV, V_{SW} = 0.3 kV. In this process, 0.3 kV high voltages were set at the SR and SW to reduce peak tailing.

2.3. Apparatus

Experiments were performed on the Micralyne Microfluidic Tool Kit (μTK) (Micralyne Inc., Edmonton, Alta., Canada). It consisted of high-voltage (HV) power supplies, which could be set at ground, floating or HV state, and a LIF detection system using the 532 nm ν-doubled Nd-YAG laser (4 mW). A 40 × 0.55 NA lens focused the beam onto the channel of a microchip to excite fluorescent dyes. The optical path into the photomultiplier tube (PMT) has a 10 nm bandpass filter centered at 568.2 nm. Data acquisition and manipulation were performed by a LabView (National Instruments, Austin, TX) software. Acquisition frequency of PMT and the gain were set at 25 Hz and 0.400 throughout all the experiments, respectively.

2.4. EOF measurement

The current monitoring method was used to measure the EOF in the PDMS microchannel [26]. The electroosmotic mobility, μ_{eo}, was calculated by the Eq. (1): where L is the length of the microchannel, V is the total applied voltage and t is the time of C (C > 1.0) mM PB to be completely displaced by C' (where C' = 0.9 C) mM PB in the microchannel.

$$\mu_{eo} = \frac{L^2}{Vt} \quad (1)$$

3. Results and discussion

If the PDMS channel was not dealt with any modification, fluorescent dye PY would adsorb greatly to the channel surface with the hydrophobic interaction between PY and PDMS. When DDAB was added into the running buffer and sample solution, signals of the PY were detected by LIF on a microchip. This phenomenon proved the DDAB could be chosen for the PDMS surface modification. In order to obtain the optimized modification conditions, factors that influenced forming modification coating on the surface were investigated. It should be noted that optimized condition might depend on the channel shape or dimension used in the experiment.

3.1. Influence factors of surface modification coating

3.1.1. Buffer pH

First of all, three pH values of the buffer (i.e. 2.0, 5.0, and 8.0, respectively) were studied by evaluating peak height and migration time (t_{mig}) of PY to demonstrate the modification effect of DDAB. As shown in Fig. 1A, peaks of 20 μM PY decreased with increasing pH, and even disappeared at pH 8.0 and peak tailing became serious at pH 5.0. t_{mig} increased significantly with increasing pH, from less than 30 s at pH 2.0 to more than 60 s at pH 5.0. We found μ_{eo} decreased gradually with increasing pH in the experiments, and DDAB in the varying pH values would not change the fluorescence intensity of PY. Therefore, decreased μ_{eo} resulted in an increasing t_{mig} [27]. From the Fig. 1B and C, reproducibility of peak heights and t_{mig} at pH 2.0 (relative standard derivation (RSD) was 12.93% and 2.33%, respectively) was much better than that at pH 5.0 (RSD was 77.06% and 9.84%, respectively) from the consecutive three-time electropherograms. Besides, the sharp peak of another fluorescent dye RB conformed this excellent modification effect at pH 2.0. Compared with the previous reports [15,28,29], DDAB reversed the direction of EOF, which was the same with electrophoretic mobility of analyte, thus t_{mig} was greatly shortened.

3.1.2. Concentration of DDAB

DDAB concentration was investigated as well in 10.0 mM PB at pH 2.0. As shown in Fig. 2a, it would not obtain the signal of PY at

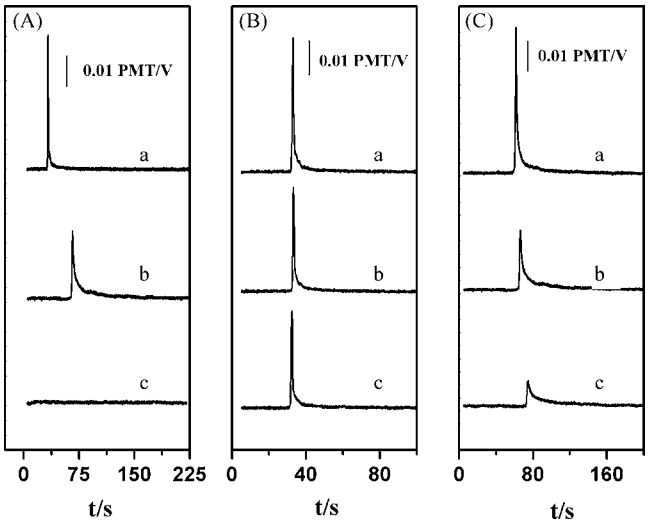

Fig. 1. Electropherograms of 20 μM PY with 10.0 mM PB at (A) (a) pH 2.0, (b) pH 5.0 and (c) pH 8.0 containing 1.0 mM DDAB, (B) pH 2.0 for the (a) 2nd, (b) 3rd and (c) 4th sample loading and (C) pH 5.0 for the (a) 2nd, (b) 3rd and (c) 4th sample loading containing 1.0 mM DDAB.

the concentration of 0.1 mM DDAB. Although in Liu et al.'s work [23] DDAB could strongly reverse the EOF at this very low concentration level, it cannot efficiently suppress fluorescent dye adsorption on the PDMS wall. As expected, increasing DDAB concentration could improve modification effect. Peak height of PY gradually increased with increasing the concentration, and achieved maximum value at 0.5 mM (Fig. 2). With the increase in the DDAB concentration, t_{mig} decreased due to the increase in EOF, for example from 7.87×10^{-3} cm^2/V s at the 0.3 mM DDAB to 5.66×10^{-2} cm^2/V s at the 0.5 mM DDAB. The enhanced DDAB density on the PDMS surface led to the increased μ_{eo} and decreased t_{mig}. At last 0.5 mM was throughout used. Meanwhile, due to the strong hydrophobicity of PDMS, only the larger DDAB concentration than that used in the capillary could effectively suppress adsorption [20].

3.1.3. Concentration of PB

Fig. 3 depicted the effects of PB concentration ranging from 2.0 to 12.0 mM at the given pH and DDAB concentration. The current was rapidly rising while the PB concentration was increasing in the

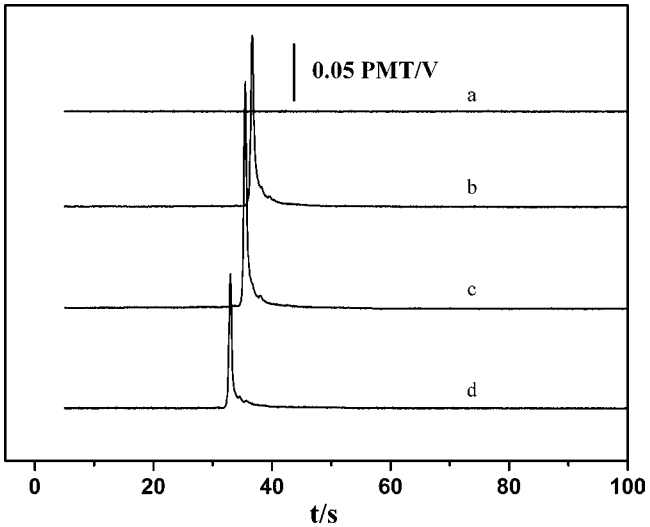

Fig. 2. Electropherograms of 20 μM PY with 10.0 mM PB at pH 2.0 containing (a) 0.1, (b) 0.3, (c) 0.5 and (d) 1.0 mM DDAB.

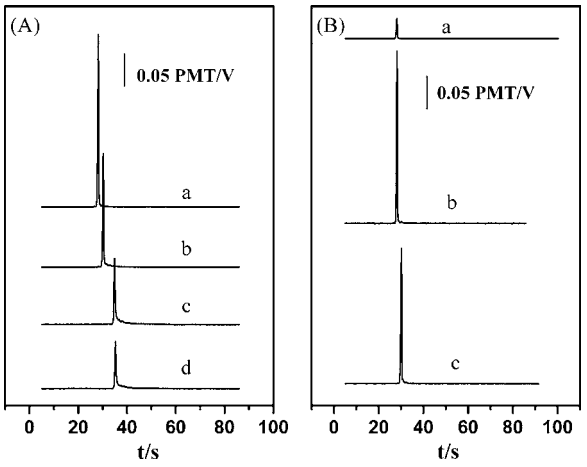

Fig. 3. Electropherograms of 20 μM PY with (A) (a) 3.0, (b) 6.0, (c) 9.0 and (d) 12.0 mM PB, (B) (a) 2.0, (b) 3.0 and (c) 4.0 mM PB at pH 2.0 containing 0.5 mM DDAB.

experiment. The high current would affect peak signal stability that the signal intensity (peak height or peak area) decreased or disappeared [28]. As shown in Fig. 3A, peaks of PY decreased gradually with increasing the PB concentration from 3.0 to 12.0 mM. Meanwhile, the high Joule heat at the higher PB concentration caused the serious peak tailing and a long t_{mig} [30]. Reducing or increasing PB concentration at 3.0 mM would not enhance PY signals, and t_{mig} prolonged a little with increasing PB concentration (shown in Fig. 3B). Nevertheless, there was no peak tailing from 2.0 to 4.0 mM because the Joule heat was not remarkable any longer. Thus, 3.0 mM PB was chosen at last.

3.2. Reproducibility and linear relationship

Under the optimized condition as mentioned above, 0.5 mM DDAB in 3.0 mM PB at pH 2.0, RSD of t_{mig} and the peak height showed excellent reproducibilities by consecutively injecting 20 μM PY ten times, which was 0.71% and 4.14%, respectively. Moreover, μ_{eo} didn't have significant change over a period of 6 h within six-time measures at random, whose RSD was 4.65%. The results indicated DDAB induced a reproducible and stable EOF and could effectively modify the PDMS microchip to reduce adsorption of the fluorescent dyes. Otherwise, the limit of detection we obtained (S/N = 3) was approximately 100 nM and linear calibration curve between the intensity based on peak height and the concentration of PY ranged from 6 to 60 μM. The sensitivity and linear calibration curve of our method was comparable to the reported methods with nonionic surfactant Triton X-100, but not better than that with mixture of ionic liquid/nonionic surfactant [28,29]. Despite that, in our work the reversed EOF which was the same with electrophoretic mobility of analyte markedly shortened t_{mig}.

3.3. Comparison between DDAB and CTAB

The modification effect with double-chained DDAB was superior to that with single-chained CTAB under the same conditions. Compared with DDAB (RSD of t_{mig} and the peak height of PY was 0.71% and 4.14%, respectively; $n = 10$), RSD of t_{mig} and the peak height of PY with CTAB was up to 5.40% and 25.54%, respectively ($n = 10$). μ_{eo} with DDAB was larger 8-fold than that of CTAB, from 6.57×10^{-2} cm^2/V s to 7.36×10^{-3} cm^2/V s. Due to the bilayer structure, the DDAB vesicles had a higher charge density than that of the typical micelles. Hence, they had greater electrophoretic mobility in the opposite direction of EOF [24]. In addition, the theoretical

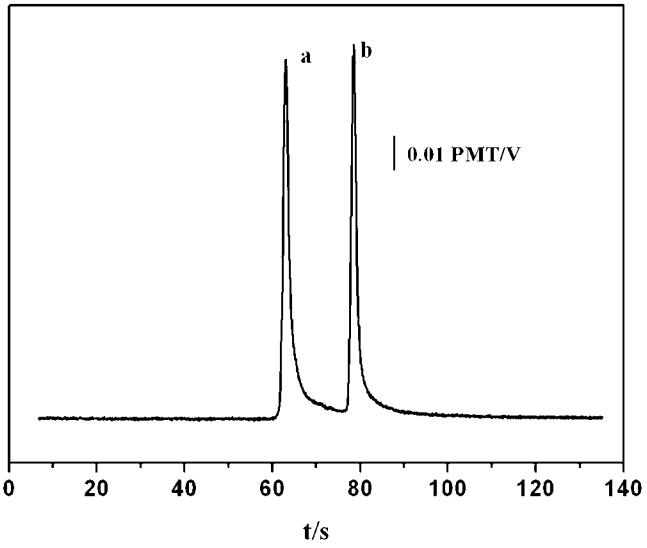

Fig. 4. Electropherograms of the mixture of 50 μM RB (a) and 10 μM PY (b) in 9 mM PB at pH 3.0 containing 0.3 mM DDAB.

plates number, N, was calculated by Eq. (2):

$$N = 5.54\left(\frac{t_{mig}}{W_{1/2}}\right)^2 \quad (2)$$

where N is the theoretical plates number and $W_{1/2}$ is the width of the component peak at 50% peak height. The obtained N was greatly enhanced from 5110 with CTAB to 22,870 with DDAB. As the same discussions above, double-chained DDAB provides a better modification performance than single-chained CTAB on the PDMS surface. It was consistent with the modification effect of DDAB in the capillary [21].

3.4. Separation of PY and RB

We performed two kind of fluorescent dyes' separation, PY and RB, on the modified PDMS microchip. The optimized conditions above was only appropriate for detection of PY, thus separation efficiency of the mixture was poor because of the large μ_{eo}. As shown in Fig. 4, 10 μM PY and 50 μM RB succeeded to be separated by increasing PB and decreasing DDAB concentration, which decreased μ_{eo} and improved the resolution [31]. Besides, the wide migration window and the strong partitioning of the analytes with the DDAB yielded a better resolution for the analytes in MEKC [24].

4. Conclusions

We succeeded in resolving the adsorption of the fluorescent dye onto the microchannel of the PDMS chip with a cationic lipid DDAB. When DDAB with a high concentration was present in the running and sample buffer, it not only reversed the direction of electroosmotic flow, which significantly shorten t_{mig}, but also efficiently suppressed fluorescent dyes PY or RB adsorption onto the chip surface. Factors influencing the modification effect on the PDMS surface were studied. Under the optimized conditions of 0.5 mM DDAB in 3.0 mM PB at pH 2.0, detection limit of PY on the optimized condition was 100 nM. The standard curve was linear in the range of 6–60 μM. t_{mig} and the peak height showed excellent reproducibilities. Furthermore, double-chained DDAB was proved to bring better modification than single-chained CTAB. Two kinds of fluorescent dyes PY and RB were separated successfully on a PDMS microchip at the appropriate conditions with DDAB as modification coating. This simple dynamic modification could be extended to biology analysis.

Acknowledgement

This work is supported by National Natural Science Foundation of China Grant No. 20890020, and 973 Project 2007 CB 714500 as well as 863 Project No. 2006 AA 020701.

Appendix A. Supplementary data

Supplementary data associated with this article can be found, in the online version, at doi:10.1016/j.talanta.2009.04.030.

References

[1] D.J. Harrison, K. Fluri, K. Seiler, Z.H. Fan, C.S. Effenhauser, A. Manz, Science 261 (1993) 895–897.
[2] T.J. Johnson, D. Ross, M. Gaitan, L.E. Locascio, Anal. Chem. 73 (2001) 3656–3661.
[3] T. Vilkner, D. Janasek, A. Manz, Anal. Chem. 76 (2004) 3373–3386.
[4] H. Becker, L.E. Locascio, Talanta 56 (2002) 267–287.
[5] H. Makamba, J.H. Kim, K. Lim, N. Park, J.H. Hahn, Electrophoresis 24 (2003) 3607–3619.
[6] D. Qin, Y. Xia, G.M. Whitesides, Adv. Mater. 8 (1996) 917–919.
[7] M.A. Unger, H.P. Chou, T. Thorsen, A. Scherer, S.R. Quake, Science 288 (2000) 113–116.
[8] S.K. Sia, G.M. Whitesides, Electrophoresis 24 (2003) 3563–3576.
[9] G. Ocvirk, M. Munroe, T. Tang, R. Oleschuk, K. Westra, D.J. Harrison, Electrophoresis 21 (2000) 107–115.
[10] Y. Liu, J.C. Fanguy, J.M. Bledsoe, C.S. Henry, Anal. Chem. 72 (2000) 5939–5944.
[11] S. Hu, X. Ren, M. Bachman, C.E. Sims, G.P. Li, N. Allbritton, Anal. Chem. 74 (2002) 4117–4123.
[12] A. Papra, A. Bernard, D. Juncker, N.B. Larsen, B. Michel, E. Delamarche, Langmuir 17 (2001) 4090–4095.
[13] J.M. Cunliffe, N.E. Baryla, C.A. Lucy, Anal. Chem. 74 (2002) 776–783.
[14] A.J. Wang, J.J. Xu, H.Y. Chen, J. Chromatogr. A 1107 (2006) 257–264.
[15] C.D. García, B.M. Dressen, A. Henderson, C.S. Henry, Electrophoresis 26 (2005) 703–709.
[16] K.S. Phillips, Q. Cheng, Anal. Chem. 77 (2005) 327–334.
[17] K.S. Phillips, Y. Dong, D. Carter, Q. Cheng, Anal. Chem. 77 (2005) 2960–2965.
[18] K.S. Phillips, S. Kottegoda, K.M. Kang, C.E. Sims, N.L. Allbritton, Anal. Chem. 80 (2008) 9756–9762.
[19] C.A. Lucy, R.S. Underhill, Anal. Chem. 68 (1996) 300–305.
[20] J.E. Melanson, N.E. Baryla, C.A. Lucy, Anal. Chem. 72 (2000) 4110–4114.
[21] M.M. Yassine, C.A. Lucy, Anal. Chem. 76 (2004) 983–2990.
[22] M.M. Yassine, C.A. Lucy, Anal. Chem. 77 (2005) 620–625.
[23] B.-F. Liu, M. Ozaki, H. Hisamoto, Q. Luo, Y. Utsumi, T. Hattori, S. Terabe, Anal. Chem 77 (2005) 573–578.
[24] Y. Li, Q. Liu, S. Yao, Talanta 75 (2008) 677–683.
[26] X. Huang, M.J. Gordon, R.N. Zare, Anal. Chem. 60 (1988) 1837–1838.
[27] R.T. Kennedy, I. German, J.E. Thompson, S.R. Witowski, Chem. Rev. 99 (1999) 3081–3132.
[28] J. Kang, J. Liu, H. Qiu, X.-B. Yin, X. Yang, E. Wang, Talanta 66 (2005) 1018–1024.
[29] Y. Xu, H. Jiang, E. Wang, Electrophoresis 28 (2007) 4597–4605.
[30] Y. Li, C. Wang, J. Sun, Y. Zhou, T. You, E. Wang, Y.S. Fung, Anal. Chim. Acta 550 (2005) 40–46.
[31] Y. Gao, Y. Tian, E. Wang, Anal. Chim. Acta 545 (2005) 137–141.

Talanta 79 (2009) 633–638

Contents lists available at ScienceDirect

Talanta

journal homepage: www.elsevier.com/locate/talanta

Dynamic hollow-fibre liquid phase microextraction of dinitrophenols from human plasma: Optimization of an extraction flow system using experimental design methodology

Helena Hansson, Malene Lagerström, Magnus Åberg, Ulrika Nilsson*

Department of Analytical Chemistry, Stockholm University, 106 91 Stockholm, Sweden

ARTICLE INFO

Article history:
Received 15 December 2008
Received in revised form 16 April 2009
Accepted 21 April 2009
Available online 3 May 2009

Keywords:
Supported liquid membrane
Hollow-fibre liquid phase microextraction
Nitrophenols
Human blood plasma
Optimization

ABSTRACT

The utility of a dynamic hollow-fibre liquid phase microextraction method (optimized using a four-variable experimental design and response surface modelling) for extracting dinitrophenolic compounds from human plasma samples was evaluated. The investigated variables were donor phase salt concentration (10–400 mM), donor phase pH (2–6), acceptor phase pH (7–12), and donor/acceptor phase flow rates (30/7.5 to 70/17.5 μL min^{-1}). Four dinitrophenol pesticides were used as model substances at concentrations of 0.1 μg mL^{-1} in spiked human plasma samples. Extraction efficiencies ranging from 42 to 77% with RSDs below 9 were achieved with the optimized method. The flow rate and acceptor pH were shown to strongly affect the extraction efficiency for all compounds, while the donor phase pH and salt concentration had minor effects. With a well-defined acceptor phase pH and flow rate the system exhibited high robustness. The limits of quantification for the investigated compounds, using the presented extraction method followed by liquid chromatography/electrospray ionization mass spectrometry in selected ion monitoring mode, ranged from 0.05 to 0.1 μg mL^{-1} plasma.

1. Introduction

In this study we use a miniaturized version (wall thickness 50 μm, inner diameter 280 μm) of the XT-extractor [1,2], a liquid membrane-based system for dynamic hollow-fibre liquid phase microextraction (HF-LPME), previously designed by Jonsson et al. [1]. The XT-extractor had larger hollow-fibre dimensions (wall thickness 100 μm, inner diameter 330 μm). The name is due to a cross (X)-connector and a tee (T)-connector and a PTFE tubing with a hollow fibre mounted in between. The version presented in this work is similar, but has two T-connectors instead of X and T. Miniaturization offers several obvious advantages, including the scope to extract analytes from samples with smaller volumes and to reduce solvent consumption. The utility of the minituarized system for extracting nitrophenol pesticides from aqueous standard solutions was subsequently evaluated [2], but no attempt was made in the cited study to optimize the system for extracting plasma samples.

HF-LPME resembles classical liquid–liquid extraction, but the liquid phases in HF-LPME are separated by a hollow fibre, typically made of polypropylene, with pores in which an organic solvent of sufficiently low vapour pressure (e.g. undecanone or dihexyl ether [3]) is immobilized by capillary forces, thereby forming a liquid membrane. Thus, the system can be used for a form of three-phase liquid–liquid–liquid extraction, known as supported liquid membrane extraction (SLM), of either acidic or basic compounds. The analytes in the sample (donor phase, or simply donor) are neutralized and extracted across the organic liquid membrane into the extracting solvent (acceptor phase, or simply acceptor). Generally the efficiency is highest for compounds with log *P* values in the range −1 to +3 [4]. HF-LPME based extraction procedures for basic compounds in stagnant systems have been reported by Bårdstu et al. [5] and Pedersen-Bjergaard et al. [6].

Nitrophenolic pesticides, used as model compounds in the present study, are acidic and have log *P* values ranging between 1.7 and 5.6. This group of compounds were used globally in agriculture and as raw industrial materials before they were banned both by the EU and the American Environmental Protection Agency (US EPA) [7,8]. However, they are still used in several countries outside the EU and US, and are widely spread in the environment because of their high water solubility [7,8].

Tremp et al. identified and quantified nitrated phenols in exhausts from motor vehicles and studied the transfer process of these compounds between air and water bodies [9]. Morville et al. [10] have recently presented measurements to show variations of concentration and the role of traffic in the emission of phenols and nitrophenols to the atmosphere.

In the early 1930s dinitrophenols were used as weight loss drugs, but this was shown to pose serious health risks [11]. Although the

* Corresponding author.
E-mail address: ulrika.nilsson@anchem.su.se (U. Nilsson).

0039-9140/$ – see front matter © 2009 Elsevier B.V. All rights reserved.
doi:10.1016/j.talanta.2009.04.051

use of 2,4-dinitrophenol (DNP) as drug is illegal nowadays it can still be purchased for weight loss. It is sold under names as Sulfo black, Nitro Klenup or Caswell No. 392 without warnings [12]. The enlarged interest in weight loss drugs has caused an increase in case reports [13]. Recently, there have been several fatalities due to the use of 2,4-dinitrophenol (DNP), sold over the Internet as a dietary supplement for bodybuilders or as weight loss drug [12,14]. Exposure limits for the substances set to 10 $\mu g\,mL^{-1}$ serum and 5 $\mu g\,mL^{-1}$ whole blood have been proposed by the EU [15].

Recently, several on-line and off-line microextraction techniques were reviewed by Hyötyläinen and Riekkola [16], and Lambropoulou et al. [17] have reviewed several liquid-phase microtechniques specifically for extracting pesticides, mostly applied to pesticides in aqueous matrices. In addition, a static HF-SLM method for detecting dinitrophenolic compounds in water samples has been developed and optimized by Lezamiz and Jönsson [18], and an HF-SLM method for extracting short-chain fatty acids from human serum, followed by GC/FID detection, has been developed by Zhao et al. [19]. For detection of DNP Leftwich et al. has presented a UV method for serum from a man poisoned after crop spraying [20] and Miranda et al. used a GC/MS a method for serum from a 17-yerar-old female and a 28-year-old male using DNP as weight loss drug [12]. In the latter case reported admission blood levels were 36 and 28 $mg\,L^{-1}$, respectively, and fatal [12].

The aim of the study presented here was to optimize the efficiency of the dynamic micro-HF-LPME system for extracting nitrophenols from human plasma, using LC/ESI-MS to detect the analytes, due to its high selectivity and lack of any need for derivatization prior to analysis.

2. Experimental

2.1. Chemicals and material

All standard compounds, i.e. 4,6-*o*-dinitrocresol (DNOC), 2-sec-butyl-4,6 dinitrophenol (Dinoseb), 2-*tert*-butyl-4,6 dinitrophenol (Dinoterb), 2,4-dinitrophenol (DNP) and 3-methyl-4-nitrophenol (IS) (all of 98% purity) were purchased from Sigma–Aldrich (Seelze, Germany). Dihexyl ether (97%) and acetonitrile of analytical grade were from Sigma–Aldrich (Steinheim, Germany).

Sodium hydrogen carbonate, sulphuric acid, sodium hydroxide and sodium chloride were obtained from Merck (Darmstadt, Germany), formic acid (98–100%) from Scharlau Chemie S.A. (Barcelona, Spain) and normapure acetone from VWR International (Lutterworth, UK). Plasma was obtained from Karolinska Hospital (Stockholm, Sweden). The polypropylene hollow fibre (Accurel PP, 50/280, porosity 40%, i.d. 280 μm) used to construct the microextraction system was purchased from Membrana GmbH (Wuppertal, Germany), the polyetheretherketone (PEEK) T-connectors, low-pressure polyacetal fittings, o-rings and PTFE tubing (1/16″ 0.5 mm i.d.) from Vici Jour (Schenkon, Switzerland), the cyanoacrylate glue from Casco AB (Stockholm, Sweden), the fused-silica capillary (TSP 100245) from Polymicro Technologies Inc. (Phoenix, AZ, USA) and the TL-105 column heater from Timberline Instruments Inc. (Boulder, CO, USA).

Water used to prepare aqueous solutions was purified using a Milli-Q system (Millipore, Billerica, MA, USA).

2.2. The extractor and extraction procedure

The extractor is easy to assemble from cheap, commercially available parts. A 12-cm hollow fibre glued to a fused-silica capillary at both ends was placed in PTFE tubing, which was then connected to two T-connectors. The extractor was placed vertically and was filled with the organic phase (dihexyl ether) to saturate the pores of the hollow fibre. The extractor was then placed in a column heater and connected to a syringe pump with two syringes to control the flow of the donor and acceptor, respectively. The donor flow rate was always set four times higher than the acceptor flow. The flow rate of both donor and acceptor was measured ($n = 6$, RSD = 1 and RSD = 7, respectively).

Plasma was kept at −20 °C until use, and was then thawed at room temperature. Portions of 1 mL plasma and 0.5 mL of aqueous standard solutions were mixed on a mixing table for 30 min. After mixing, 0.9 mL water, 0.1 mL isopropanol and two drops of sulphuric acid were added to each plasma sample, which was then ultrasonicated for 1 min. Plasma samples were kept at room temperature during the day of analysis. Blank plasma samples were treated identically, except that 0.5 mL of ultra pure water was added instead of the standard solution.

The plasma sample pretreatment and extraction system have been recently described in detail [2].

2.3. LC/ESI-MS

The analytes were separated from other constituents of 5-μL portions of the samples by high-performance liquid chromatography using an LC 10 AD vp chromatograph with a SIL-10 AD vp autoinjector (Shimadzu, Japan) and a Hypersil-Gold C_{18} column (50 mm × 2.1 mm i.d., 3 μm particle size; Thermo, Cheshire, UK). The mobile phase (flow rate 200 $\mu L\,min^{-1}$, total run time 18 min) consisted of 20% A for 5 min, a step change to 50% A, held for 10 min, followed by a step change to 20% A, held for 3 min, where A was acetonitrile and the balance was provided by Milli-Q water (both acidified with 0.01% formic acid). An ESI triple-quadrupole API 2000 mass spectrometer from Applied Biosystems (MDS SCIEX, Foster City, Canada) was then used in negative mode to monitor the quasi-molecular ions $[M-H]^-$ of the analytes (m/z 152 for IS, 183 for DNP, 197 for DNOC and 239 for both Dinoseb and Dinoterb). The following settings were used: desolvation temperature, 350 °C; declustering potential, −40 V; focusing potential, −400 V; entrance potential, −10 V; ion spray voltage, −4500 V; nebulizer gas, 10 psi; curtain gas, 20 psi; ion source gases, 20 psi. Reconstructed ion chromatograms (RICs) for extracted human plasma samples are shown in Fig. 1. A volumetric internal standard (3-methyl-4-nitrophenol) and single-point calibration with an external standard solution were used to calculate the extraction efficiency.

2.4. Optimization and experimental design

A full-factorial experimental design, as described in Table 1, was set up to evaluate the influence of the following four controlled variables on the extraction efficiency: donor pH (2 and 6, adjusted with sulphuric acid), salt concentration in the donor phase (10 and 400 mM sodium chloride), flow rates of the acceptor and donor phases (30/7.5 and 70/17.5 $\mu L\,min^{-1}$), and acceptor pH (7 and 12, adjusted with sodium hydroxide). In all experiments the acceptor solution contained 60mM sodium hydrogen carbonate and the donor flow rate was four times higher than the acceptor flow rate. The experimental design included 17 permutations of conditions, obtained by varying each of the investigated variables at the lower and upper levels (designated − and + in Table 1, respectively). Four experiments were performed for each of these permutations of conditions, and an additional set of 12 replicate experiments were performed with central settings of the variables (designated 0).

The design was subsequently complemented with 8 further permutations of experimental conditions to complete a central composite face (CCF) design, with one experiment per permutation. The CCF design allows a quadratic model for extraction efficiency to be fitted as a function of the four controlled variables, thereby improving the optimization. The experimental design was set up

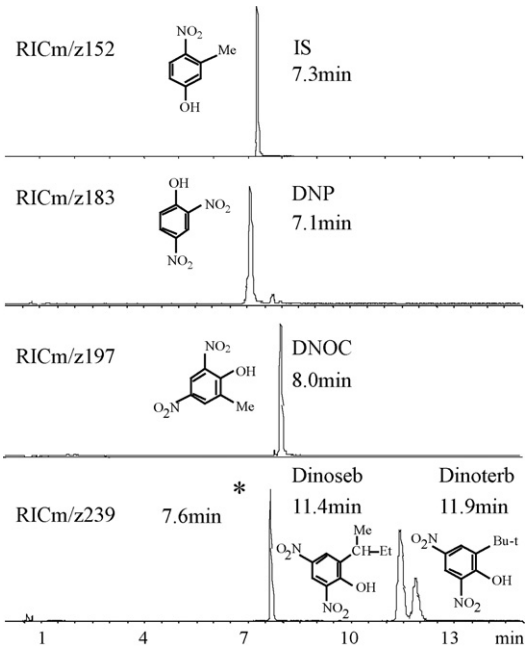

Fig. 1. Reconstructed ion chromatograms (RICs) of extracted human plasma samples obtained using LC/ESI-MS in negative mode. *Unidentified compound detected in all plasma samples.

and evaluated using the chemometric software MODDE 6.0 (Umetrics AB, Umeå, Sweden).

2.5. Linearity, detectability and carry-over

Instrumental linearity was investigated for aqueous solutions of standards at six concentration levels, ranging from 0.06 to 0.6 μg mL^{-1} (per analyte), in triplicate.

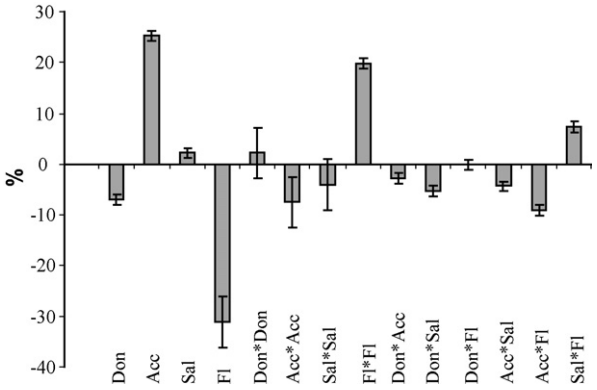

Fig. 2. Scaled, zero-centred coefficient plot for the combined extraction efficiency. The parameters are donor phase pH (Don), acceptor phase pH (Acc), salt concentration in the donor phase (Sal) and acceptor/donor phase flow rates (Fl).

To estimate the limit of quantification (LOQ) for the method samples with concentrations in the range 0.01–2.0 μg mL^{-1} were extracted at optimal settings and analyzed.

To reduce carry-over a 30-min wash cycle was applied between consecutive extractions.

3. Results and discussion

3.1. Optimization and experimental design

The extraction efficiency for each of the compounds individually, and the overall extraction efficiency for all of the compounds (calculated as the sum of the individual extraction efficiencies), as a function of the investigated variables was modelled by least squares regression. The coefficients of the models obtained show that the most important parameters are the pH of the acceptor phase and the flow rates (see Fig. 2 for the overall model, the results for the indi-

Table 1
The full-factorial design ($N = 2^4 + 3$ centre points) with 19 experiments (N), two levels, three replicates, n (number of runs) = 4, four variables, and nine complementary experiments to complete a central composite face (CCF) design (C).

Experiment no.	Experiment designation	Acceptor pH	Donor pH	Donor salt (mM)	Donor/acceptor flow rate (μL min^{-1})
1	N1	+	–	–	–
2	N2	+	+	–	–
3	N3	+	–	+	–
4	N4	+	+	+	–
5	N5	+	–	–	+
6	N6	+	+	–	+
7	N7	+	–	+	+
8	N8	+	+	+	+
9	N9	–	–	–	–
10	N10	–	+	–	–
11	N11	–	–	+	–
12	N12	–	+	+	–
13	N13	–	–	–	+
14	N14	–	+	–	+
15	N15	–	–	+	+
16	N16	–	+	+	+
17	N17	0	0	0	0
18	N18	0	0	0	0
19	N19	0	0	0	0
20	C77	0	–	0	0
21	C78	0	+	0	0
22	C79	–	0	0	0
23	C80	+	0	0	0
24	C81	0	0	–	0
25	C82	0	0	+	0
26	C83	0	0	0	–
27	C84	0	0	0	+
28	C85	0	0	0	0

In all experiments, the donor flow rate was four times the acceptor flow rate. The N- and C-experiments were performed on two different occasions.

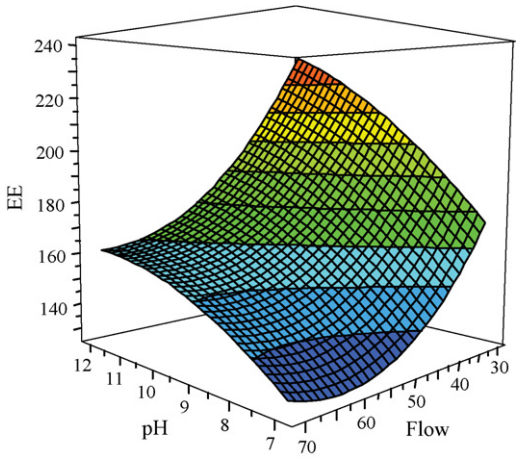

Fig. 3. Response surface obtained for the overall extraction efficiency (EE) plotted vs. flow and acceptor pH. Response surface for the individual EE are presented in the supplementary material.

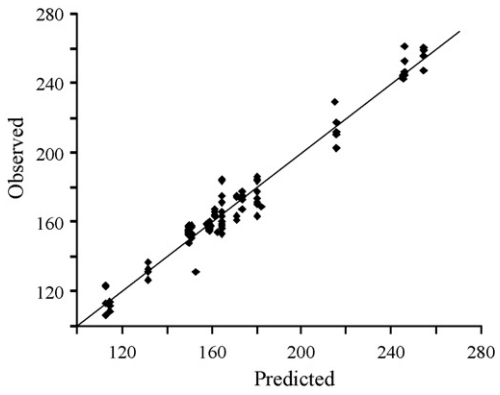

Fig. 4. Plot of observed vs. predicted values for the overall extraction efficiency (%). Results for the individual models are presented in the supplementary material.

vidual models are presented in the supplementary material). The higher the acceptor pH, the higher was the extraction efficiency, which is in accordance with theoretical expectations. Fig. 3 shows the overall response surface, while the results for the individual analytes are presented in the supplementary material. Increasing the pH pushes the system further from equilibrium and thus creates a stronger force driving transfer from the donor to the acceptor phase, while a low flow rate is beneficial because it prolongs the extraction time and thus improves the extraction efficiency. The donor pH has a weakly negative coefficient, because although increasing the acidity of the donor phase enhances the protonation of the analytes, thereby slightly increasing their rate of transfer into the organic phase, their neutralization is not the rate-determining step of the system.

The optimal settings for each analyte investigated and for the overall analyte extraction efficiency are shown in Table 2.

The highest efficiency was obtained with an acceptor pH of 12. However, such a high pH should be avoided to preserve both the extractor and the LC/MS equipment. The practical acceptor pH limit for routine analysis would be 10, and optimal settings for pH 10 are shown in Table 3. In this region of high acceptor pH the method is rather robust with only small differences in efficiency when changing pH. Therefore, an acceptor pH of 10 was chosen. As shown in Table 4, there were no significant differences between predicted and obtained efficiencies, for acceptor pH settings of both 10 and 12 ($p < 0.05$), indicating that the model had high quality. The experimental data could be explained well by the quadratic model, as shown in Fig. 4.

3.2. Linearity, limit of quantification and carry-over

The efficiency of the method for extracting all of the analytes from the plasma samples was highly repeatable, with RSDs consistently below 10, except for the lowest concentrations. At concentrations below 0.05 μg mL^{-1} for DNP and DNOC, and below 0.1 μg mL^{-1} for Dinoseb and Dinoterb, the extraction efficiency exhibited concentration-dependence (see Fig. 5). The LOQ values, defined as the thresholds of concentration-dependence, were 0.05 μg mL^{-1} for both DNP and DNOC, and 0.1 μg mL^{-1} for both

Table 2
The optimal parameters found for each of the analytes and the overall optimum point.

Analyte	Flow rate donor/acceptor (μL min^{-1})	pH donor	pH acceptor	Donor salt concentration (mM)
DNP	30/7.5	2	12	10
DNOC	30/7.5	6	12	10
Dinoseb	30/7.5	2	12	322
Dinoterb	30/7.5	2	12	400
Overall optimum	30/7.5	2	12	88

Table 3
Optimal parameter settings with an acceptor pH of 10.

Analyte	Flow rate donor/acceptor (μL min^{-1})	pH donor	pH acceptor	Donor salt concentration (mM)
DNP	30/7.5	2	10	49
DNOC	30/7.5	6	10	10
Dinoseb	30/7.5	2	10	239
Dinoterb	30/7.5	2	10	400
Overall optimum	30/7.5	2	10	186

Table 4
Experimentally determined and predicted extraction efficiencies (Obt. EE and Pred. EE, respectively).

	DNP		DNOC		Dinoseb		Dinoterb		Overall	
Acc. pH	Pred. EE (%)	Obt. EE (%)	Pred. EE (%)	Obt. EE (%)	Pred. EE (%)	Obt. EE (%)	Pred. EE (%)	Obt. EE (%)	Pred. EE (%)	Obt. EE (%)
10	65	61 (1)	73	64 (4)	49	42 (4)	44	40 (2)	230	205 (2)
12	71	68 (6)	85	77 (5)	53	46 (3)	45	42 (9)	255	233 (4)

RSD values ($n = 3$) are shown in parenthesis.

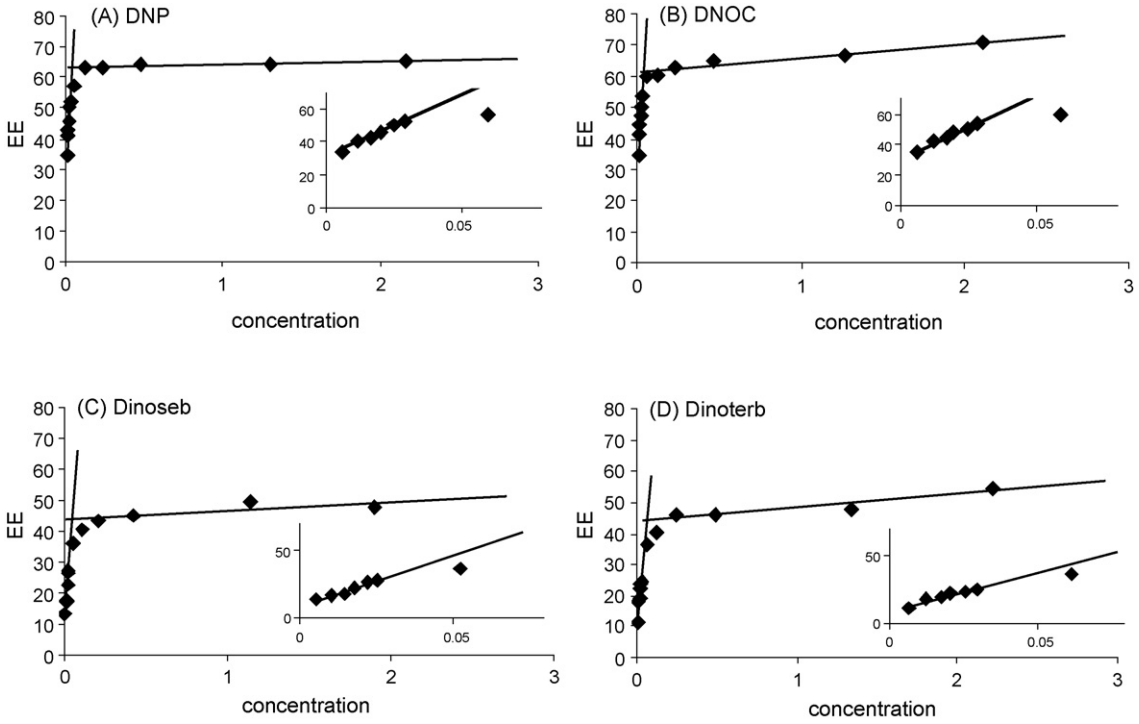

Fig. 5. Extraction efficiency (EE) of spiked analytes vs. their concentration, in the range 0.01–2.0 μg mL^{-1}, extracted with a 15-min stagnant acceptor and optimal settings, $n = 3$. The insets show enlargements of the regions spanning 0.01–0.06 μg mL^{-1} for DNP and DNOC, and 0.01–0.1 μg mL^{-1} for Dinoseb and Dinoterb.

Dinoseb and Dinoterb. The concentration-dependence is due to carry-over in the membrane, which is greater for the more lipophilic Dinoseb and Dinoterb compared to DNP and DNOC. Thus, such carry-over should be eliminated to maximize the reliability of consecutive extractions. A wash cycle of 30 min was therefore applied between extractions. After a complete wash cycle the levels of the analytes in extracted blank samples were sub-detectable.

4. Conclusion

This dynamic hollow-fibre extraction method has been optimized, for the first time, for extracting analytes from small volumes of human plasma samples using a four-variable CCF experimental design. The results indicate that the system is robust with respect to variations in donor salt concentration and donor pH, but substantially more strongly affected by the flow rate and acceptor pH, therefore it is of highest importance to maintain tight control of the flow rate and to maintain high acceptor buffer capacity to obtain repeatable results. However, the absolute true optimum would probably be at infinitely low flow rates, with an infinitely high pH difference between the acceptor and donor phases. On the other hand, a high acceptor pH affects the syringe piston material and perturbs the flow rate, and should therefore be avoided.

Without applying a wash cycle a carry-over effect was observed in a blank sample extracted directly after the sample. This is probably due to hydrophobic interactions between the analytes and the polyproplylene membrane surface, which affects the reliability of the results. The carry-over could be effectively eliminated by a 30-min wash cycle. In addition, the method LOQ could be simply reduced by increasing the size of the samples.

This dynamic system offers opportunities for fully automated extractions with a minimum of manual handling and the ability to repeatably extract plasma samples without reducing efficiency and minimal carry-over, making it highly suitable for on-line coupling.

Acknowledgments

We thank Erik Alm and Ralf Torgrip (Department of Analytical Chemistry, Stockholm University, Sweden) for setting up the experimental design and Dr. Maria Athanasiadou (Department of Environmental Chemistry, Stockholm University, Sweden) for providing the plasma samples.

Appendix A. Supplementary data

Supplementary data associated with this article can be found, in the online version, at doi:10.1016/j.talanta.2009.04.051.

References

[1] O.B. Jonsson, U. Nordlöf, U.L. Nilsson, Anal. Chem. 75 (2003) 3506–3511.
[2] H. Hansson, U. Nilsson, Talanta 77 (2009) 1309–1314.
[3] J.Å. Jönsson, L. Matthiasson, J. Sep. Sci. 24 (2001) 495–507.
[4] J.Å. Jönsson, L. Matthiasson, LCGC N. Am. vol. 21 (5) (2003) 424–438.
[5] K.F. Bårdstu, T.S. Ho, K.E. Rasmussen, S. Pedersen-Bjergaard, J.Å. Jönsson, J. Sep. Sci. 30 (2007) 1364–1370.
[6] S. Pedersen-Bjergaard, T.S. Ho, K.E. Rasmussen, J. Sep. Sci. 25 (2002) 141–146.
[7] UNEP, FAO, Inclusion of Chemicals in the Interim Prior Informed Consent Procedure—Review of Notifications of Final Regulatory Actions to Ban or Severely Restrict A Chemical—Dinoterb, UNEP/FAO/PIC/ICRC.3/15, Geneva, 2001.
[8] EPA, Decision and emergency order suspending the registrations of all pesticides products containing dinoseb, Feb Reg. 51 (1986) 36634.
[9] J. Tremp, P. Mattrel, S. Fingler, W. Gigler Eawag, Water, Air Soil Pollut. 68 (1993) 113–123.
[10] S. Morville, A. Scheyer, P. Mirabel, M. Millet, Environ. Sci. Pollut. Res. 13 (2) (2006) 83–89.
[11] E. Colman, Regul. Toxicol. Pharmacol. 48 (2007) 115–117.
[12] E. Miranda, I. McIntyre, D. Parker, R. Gary, B. Logan, J. Anal. Toxicol. 30 (2006) 219–222.
[13] R. McFee, T. Caraccio, M. McGuigan, S. Reynolds, P. Bellanger, Vet. Hum. Toxicol. 45 (5) (2004) 251–254.
[14] L. Politi, C. Vignali, A. Polettini, J. Anal. Toxicol. 31 (2007) 55–61.

[15] A. Moretto, in: T.C. Marrs, B. Ballantyne (Eds.), Pesticide Toxicology and International Regulation, Wiley, Chichester, England, 2004, p. 457.
[16] T. Hyötyläinen, M.L. Riekkola, Anal. Chim. Acta 614 (2008) 27–37.
[17] D.A. Lambropoulou, T.A. Albanis, J. Biochem. Biophys. Methods 70 (2007) 195–228.
[18] J. Lezamiz, J.Å. Jönsson, J. Chromatogr. A 1152 (2007) 226–233.
[19] G. Zhao, J. Lui, M. Nyman, J.Å. Jönsson, J. Chromatogr. B 846 (2007) 202–208.
[20] R. Leftwich, J. Floro, R. Neal, A. Wood, Southern Med. J. 75 (2) (1982) 182–189.

Talanta 79 (2009) 746–751

Contents lists available at ScienceDirect

Talanta

journal homepage: www.elsevier.com/locate/talanta

Electrochemically deposited boronate affinity extracting phase for covalent solid phase microextraction of cis-diol biomolecules

Jiangang He, Zhen Liu*, Peng Dou, Jing Liu, Lianbing Ren, Hong-Yuan Chen**

Key Lab of Analytical Chemistry for Life Science, School of Chemistry and Chemical Engineering, Nanjing University, 22 Hankou Road, Nanjing 210093, China

ARTICLE INFO

Article history:
Received 1 February 2009
Received in revised form 27 April 2009
Accepted 29 April 2009
Available online 7 May 2009

Keywords:
Solid phase microextraction
Boronate affinity
Covalent extraction
Cis-diol compound
High-performance liquid chromatography
Riboflavin

ABSTRACT

A new format of solid phase microextraction (SPME), boronate affinity SPME, was proposed for the first time for covalent extraction of cis-diol containing biomolecules. This new SPME format is based on the reversible complex formation between boronic acids and 1,2- and 1,3-cis-diols. The complex formation and dissociation can be facilely controlled by changing pH. An extracting phase of poly-3-aminophenylboronate (polyAPBA) electrochemically deposited on a metal wire was employed to demonstrate the concept of this new methodology. Catechol and riboflavin were used as the test analytes, and the SPME extraction was combined off-line with high-performance liquid chromatographic (HPLC) separation followed by UV absorbance or fluorescence detection. Fundamental aspects, such as selectivity, extraction/desorption equilibrium, linearity, effect of competing compounds, reproducibility and life-time, were first investigated. Then the developed method was applied to beer samples since the content of riboflavin plays an important role in the flavor stability of beverages. Excellent performance of the SPME fibers was observed for both standard and real samples. Particularly, the expected excellent features of the polyAPBA extracting phase were experimentally verified, which include specific selectivity, eliminated matrix effect and manipulable capture/release. The new methodology of SPME can be a promising tool since a lot of 1,2- and 1,3-cis-diol-containing compounds are of great biological importance.

1. Introduction

Solid phase microextraction (SPME) [1,2] has developed to be an important micro-scale sampling and sample preparation technology. Extracting phase is the core of this technology. Although there have been a series of commercial extracting phases and a large number of home-made ones, one of the generally accepted drawbacks of SPME is its lack of selectivity [3]. Therefore, development of novel extracting phases with desirable selectivity and properties had been a key aspect since early stage of SPME.

So far, SPME is extensively combined with gas chromatography (GC) analysis. When SPME is combined with liquid phase separation such as high-performance liquid chromatography (HPLC) and capillary electrophoresis (CE), extracting phases are subject to more critical requirements. First, non-volatile compounds are more different in their properties than volatile compounds, and the current extracting phases for GC analysis cannot work well for many non-volatile analytes especially biomolecules. Therefore, specific selectivity is highly desirable. To meet such a need, some novel extracting phases have been developed, for instance, polypyrrole coating [4], mesoporous silica [5], immobilized antibody [6], molecular imprinted polymer (MIP) [7] and polymer monolith [8]. Second, an extracting phase immersed into an aqueous environment involves plentiful interactions with abundant water and solvent molecules and other co-present molecules in the sample as well. To effectively eliminate the interference from the sample matrix becomes a more important issue as compared with gas phase separation. Restricted-access material [9] is a representative material for eliminating interference from biological macromolecules, which can solely extract small molecules while excluding macromolecules in sample matrix. Third, fast desorption kinetics becomes a more significant concern. In GC analysis, the analyte desorption can be completed in a short duration by virtue of quick diffusion of analyte in gas phase, which can be notably facilitated by using a high temperature. In comparison, the diffusion of analytes in liquid phase is much slower and the separation is usually performed at room temperature. That is to say, release of analytes from an extracting phase in liquid phase separation is inherently controlled by a much slower desorption kinetics, causing apparent peak broadening and carryover. A solution to this problem is the introduction of a heated interface which increases the desorption rate by elevating the temperature [10]. Unfortunately, such an interface has not yet become a standard accessory for SPME–HPLC coupling. Clearly, an ideal SPME extracting phase for use in liquid phase separation should possess all the following features:

* Corresponding author. Tel.: +86 25 8368 5639; fax: +86 25 8368 5639.
** Corresponding author. Fax: +86 25 8359 4862.
E-mail addresses: zhenliu@nju.edu.cn (Z. Liu), hychen@nju.edu.cn (H.-Y. Chen).

0039-9140/$ – see front matter © 2009 Elsevier B.V. All rights reserved.
doi:10.1016/j.talanta.2009.04.061

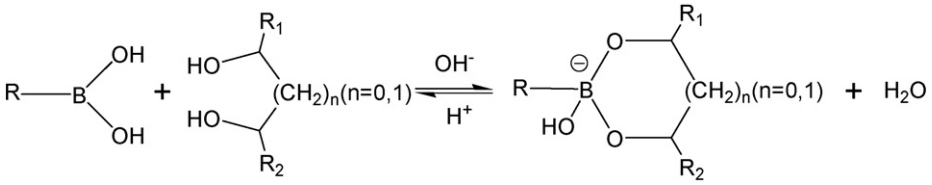

Scheme 1.

specific selectivity, eliminated matrix effect and easy-to-control capture/release.

Boronic acids can be ideal extracting phase substances due to their unique chemistry. In a non-aqueous or basic aqueous medium, boronic acids can form covalent bonds with 1,2- or 1,3-cis-diol to generate five- or six-membered cyclic esters; while in an environment of acidic pH, the complexation reversibly releases boronic acids and the cis-diol compounds [11,12]. The reaction is given in Scheme 1. Boronic acids have been successfully used as ligands for molecular recognition in chemical sensing [13–17] and for affinity separation in liquid chromatography [18–23]. An extracting phase of boronic acid may possess all the features that an ideal SPME extracting phase should have. First, the extraction selectivity is highly specific. Second, compounds adsorbed by non-covalent interactions can be removed by washing the resulting fiber under an appropriate condition, providing eliminated matrix effect. Third, the capture/release process can be gently manipulated by changing the pH conditions, avoiding use of harsh conditions, such as high temperature and high content of organic solvent or salt, which may cause denaturation of biomolecules.

In this study, we for the first time report boronate affinity SPME extraction phase for specifically extracting 1,2- and 1,3-cis-diol-containing compounds. The extracting phase, poly-3-aminophenylboronic acid (polyAPBA), was readily prepared using the existing electrochemical deposition approach [24–27] (see Scheme 2 for the polymerization reaction and the structure of polyAPBA). The boronate affinity SPME was off-line combined with HPLC analysis. Fundamental aspects were first evaluated, including the extraction selectivity, extraction/desorption equilibrium, linearity, effect of competing compounds, reproducibility and lifetime. The established method was finally applied to analysis of riboflavin in beer, which is in good agreement with literature result. The boronate affinity SPME extracting phase exhibited the advantages such as specific selectivity, eliminated matrix effect and manipulable capture/release. Because a lot of 1,2- and 1,3-cis-diol-containing compounds are of great biological importance, such as carbohydrates, RNA, nucleosides and glycoproteins, the boronate affinity SPME proposed in this study can be a promising method for bioanalysis.

2. Experimental

2.1. Reagents

3-Aminophenylboronic acid (3-APBA), riboflavin and sodium fluoride were obtained from Alfa Aesar (Ward Hill, MA, USA). Quinol and catechol were purchased from Sigma (St. Louis, MO, USA). Water was purified with a Milli-Q Advantage A10 System (Millipore, Milford, MA, USA), and was used to prepare all solutions. The other reagents and solvents were purchased as HPLC or AR grade reagents from normal commercial sources. The beer samples were purchased directly from the market in Nanjing.

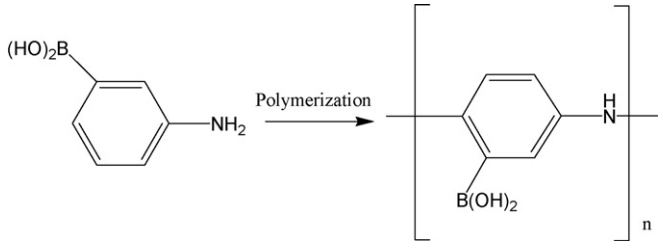

Scheme 2.

2.2. Instruments

Electrochemical deposition of polymer was performed using a CHI 750C electrochemical analyzer (CH Instruments, Austin, TX, USA), which was controlled by an electrochemical software (version 8.03) from the same company. Scanning electron microscopy (SEM) analyses were performed on a field emission SEM S-4800 instrument (Hitachi, Tokyo, Japan). A 1200 HPLC system equipped with a diode array detector (DAD) and a fluorescence detector (Agilent Technologies, Waldbronn, Germany) was employed for the separation. The HPLC system was controlled by a LC 3D ChemStation (version B.02.01-SR1). A ZORBAX Eclipse XDB-C8 analytical column (150 mm × 4.6 mm i.d., 5 μm particle size) from Agilent Technologies was used for the separation of quinol and catechol. The HPLC conditions were as follows: column temperature, 20 °C; mobile phase, methanol/50 mM acetic acid (60:40, v/v); flow rate, 0.5 mL/min; volume injected; 10 μL; DAD detection wavelength, 275 nm. A Venusil XBP-C18 analytical column (250 mm × 4.6 mm i.d., 5 μm particle size) from Agela Technologies (Newark, DE, USA) was employed for the analysis of riboflavin. The HPLC conditions were as follows: column temperature, 20 °C; mobile phase, methanol/water (60:40, v/v); flow rate, 0.5 mL/min; volume injected; 10 μL; fluorescence detection excitation wavelength, 450 nm; emission wavelength, 524 nm.

2.3. Preparation of polyAPBA extracting phase

A calomel electrode and a platinum electrode were employed as the reference electrode and the counter electrode, respectively. A silver wire or silver-coated copper wire (8 cm × 500 μm) was used as the working electrode. To prepare the silver-coated copper wire, a clean copper wire was dipped into a heated (95 °C) mixture solution of 40 μL 10% H_2SO_4 and 10 mL 25 mM $AgNO_3$ for 20 s, and then the copper wire was drawn out and the powdery silver was wiped off using absorbent cotton, leaving the white silver coating firmly deposited on the surface of the copper wire. Prior to the deposition, the metal wire was cleaned with acetone and water in ultrasonic bath (10 min for each). The deposition of polyAPBA was carried out in an electrochemical cell according to a recently reported cyclic voltametric (CV) procedure [23]. Briefly, a solution consisting of 3-APBA (40 mM) and sodium fluoride (120 mM) prepared with 10 mM sodium phosphate buffer (adjusted to pH 5.0) was added into the electrochemical cell. The three electrodes were placed in this solution and the cyclic voltammetry conditions used for polymerization were −0.2 to +0.7 V, with a scan rate of 0.1 V/s for 10 cycles. After deposition, the resulting fibers were rinsed with water then soaked in water for 24 h to allow the un-deposited polymer to dissolve.

2.4. Preparation of sample solutions

A mixture of quinol (0.6 mg/mL) and catechol (0.4 mg/mL) dissolved in 100 mM sodium phosphate buffer (pH 9.0) was prepared. Fresh mixture solution was used to reduce possible influence due to oxidation of quinol and catechol. A stock solution of riboflavin (0.2 mg/mL) dissolved in 100 mM sodium phosphate buffer (pH 9.0) was prepared and stored in a freezer. Fresh solutions of riboflavin (2 mg/L) were prepared each day by diluting the stock solution with the sodium phosphate buffer. To prepare the beer samples, 10 mL of beer and 10 mL of 200 mM sodium phosphate buffer (pH 9.0) were added in a 50-mL beaker, and then the pH of mixed solution was adjusted to 9.0 using 100 mM sodium hydroxide. SPME process was performed in 5 mL of the prepared solution immediately after the preparation.

2.5. Extraction and desorption

Before the extraction, the SPME fibers were rinsed with water and a 100-mM sodium phosphate buffer (pH 9.0); then the SPME fibers were put into 5 mL of sample solution to extract the analyte without stirring. To optimize the extraction condition, extraction time range from 5 to 60 min was studied. After extraction, the SPME fiber was rinsed with 100 mM sodium phosphate buffer (pH 9.0) and water. Desorption was carried out with inserting the SPME fiber into a glass tube (1 mm i.d. × 10 cm length) filled with 30 μL 10 mM acetic acid (pH 3.5). The extraction and desorption was performed in the dark to avoid decomposition due to light exposure. After desorption, the resulting final solution was transferred into a microcentrifugal tube (0.2 mL). A 10-μL final solution was injected into the HPLC system for analysis. To eliminate possible sample carryover, the used SPME fiber was immersed into acetic acid for 30 min, followed by a rinse with water. Then the fiber was ready for the next use.

3. Results and discussion

3.1. Preparation and characterization of extracting phase

Although polyAPBA coating deposited on platinum, gold and glassy carbon electrodes has been reported [26], silver wire was first chosen as a support for SPME in this study because it is less expensive as compared with platinum and gold meanwhile it has better roughness as compared with glassy carbon. Fig. 1 illustrates typical CV curves associated with the electrochemical deposition process, along with CV curves for the same process without the presence of 3-APBA in the working solution for comparison. Traces A indicate the CV curves when 3-APBA was absent in the working solution, in which the peaks at 0.55 and 0.12 V can be assigned to the oxidization and reduction of silver, respectively. Traces B show the CV curves for the case with the addition of 3-APBA into the electrochemical cell, in which reduction peaks were observed at 0.12 and 0.02 V while the oxidation peak at 0.55 V disappeared. The peak at 0.02 V can be assigned to the reduction of 3-APBA, according to previous reports [27]. Since the formation of polyAPBA coating on the silver wire blocked the oxidation of the silver, the peak at 0.55 V disappeared. After the electrochemical deposition process, the surface of silver wire became dark, indicating the formation of a polyAPBA coating on the metal rod. The SEM photographs of the cross-section and the side surface of a prepared SPME fiber are shown in Fig. 2, which further confirm the deposited polyAPBA coating on the silver wire. The rough surface observed with the SEM is favorable for a high extraction capacity. The thickness of the coating was estimated to be about 7 μm.

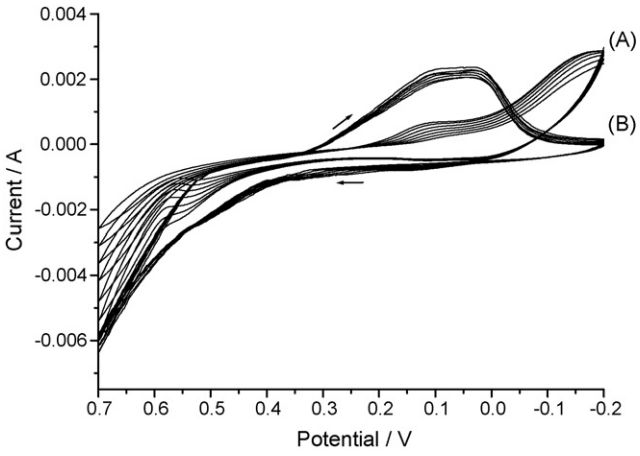

Fig. 1. Comparison of CV curves of silver wire in a working solution containing 120 mM sodium fluoride, 10 mM sodium phosphate buffer (pH 5.0) in the absence of 3-APBA (A) and in the presence of 40 mM 3-APBA (B). Cyclic voltammetry scanned from −0.2 to +0.7 V, scan rate 0.1 V/s.

To reduce the cost of the SPME fibers, a copper wire with a predeposited silver coating was used as an alternative of the silver wire. The experimental results showed that this substitute could be a useful supporting material for SPME fibers, but additional optimization procedure is needed to control the properties of the silver coating. Thus, silver wire was used as the sole supporting material in further investigations in this study.

3.2. Extraction selectivity and extracting capability

The extraction selectivity of the prepared SPME fibers was investigated through extracting catechol and quinol from a mixture of these two compounds. Catechol and quinol are much common in their structure but the only difference is that catechol is a cis-1,2-diol compound while quinol is not. According to the boronate affinity, catechol will be extracted by a polyAPBA-coated SPME fiber, while quinol will be excluded. As shown in Fig. 3, only catechol was extracted from the mixture by the SPME fiber. Thus, the predicted specific selectivity of the polyAPBA coating was confirmed.

To investigate the extracting capability of the prepared SPME fibers, riboflavin, 1,3-cis-diol-containing compound, was further chosen as a test analyte. Since 1,3-cis-diols formed six-membered cyclic esters are generally less stable than 1,2-cis-diols formed five-membered cyclic esters, if riboflavin can be extracted, then the prepared SPME fiber should be applicable for a broad range of cis-diol compounds. Riboflavin in an aqueous solution as diluted as 2 μg/mL was effectively extracted by the boronate affinity SPME fiber. When a saturated riboflavin solution was used, the extraction capacity of the SPME fiber was determined to be 2.0 ± 0.2 ng riboflavin/fiber. The high extraction capacity benefits from the rough surface of the polyAPBA coating.

3.3. Extraction and desorption equilibrium

Experiments were complemented to investigate the extraction profile and desorption profile. The pH for the extraction and desorption was 9.0 and 3.5, respectively. The extraction and desorption were carried out in the dark at room temperature, without any agitation. Fig. 4A shows the extraction time profile with extraction time ranged from 5 to 60 min. The desorption time was set at 60 min to ensure that the extracted analyte can be released almost completely. The peak area increased with increase in the extraction time within the range of 5–30 min, then kept nearly constant with further increase in the extraction time. This means that the equilibrium was reached in 30 min. Fig. 4B shows the desorption

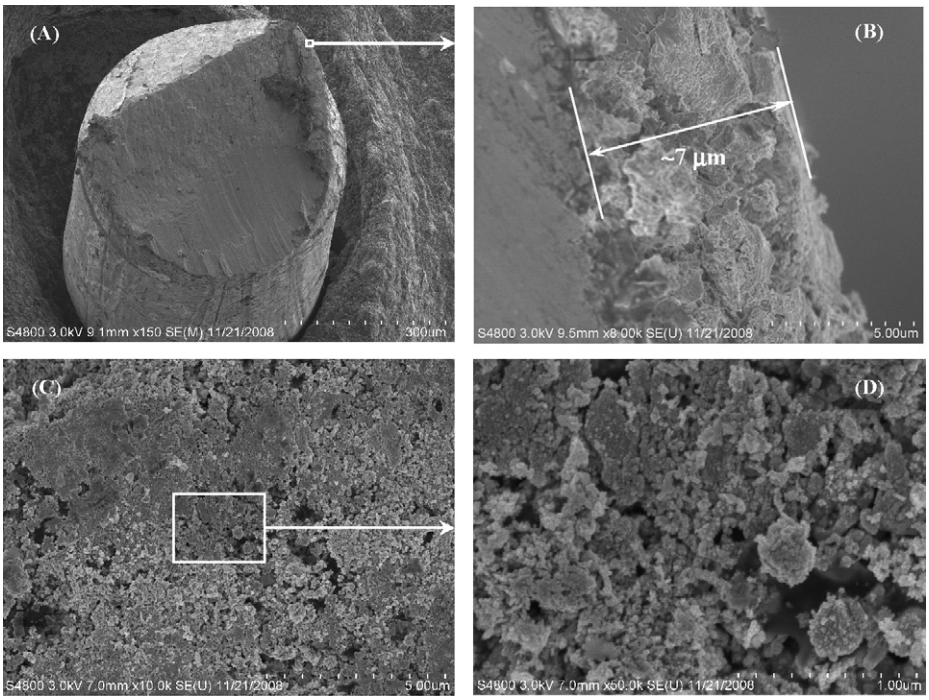

Fig. 2. SEM photographs of the cross-section (A and B) and the side surface of a prepared SPME fiber (C and D). Magnification: (A) 150×; (B) 8000×; (C) 10,000×; (D) 50,000×.

time profile with the desorption time ranged from 2.5 to 60 min. The extraction time was set as 60 min to ensure a nearly constant extracted amount for experiments at different desorption times. The peak area increased with the desorption time within initial 30 min and then the increasing speed became much slower with further increasing the desorption time. The equilibrium time can be roughly considered to be 30 min. For later investigations, both extraction and desorption were carried out for 30 min. The only one experimental factor that controlled the capture and release of the analyte in these experiments was the pH condition. The similar trends of the extraction profile and the desorption profile indi-

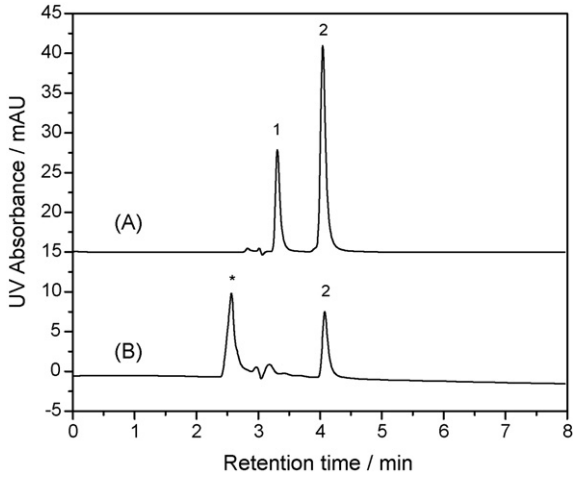

Fig. 3. Comparison of the chromatograms for a mixture of quinol and catechol (A) and analytes extracted by a polyAPBA-coated SPME fiber from the mixture (B). Sample: (A) 0.04 mg/mL quinol and 0.06 mg/mL catechol in 50 mM acetic acid solution; (B) analytes extracted by a polyAPBA-coated SPME fiber from a mixture of 0.04 mg/mL quinol and 0.06 mg/mL catechol in 100 mM sodium phosphate buffer, pH 9.0; extraction time: 30 min, desorption time: 30 min. HPLC conditions: mobile phase, methanol/50 mM acetic acid (60:40, v/v); flow rate, 0.5 mL/min; volume injected, 10 μL; DAD wavelength, 275 nm. Peak identity: 1, quinol; 2, catechol; *, sodium phosphate.

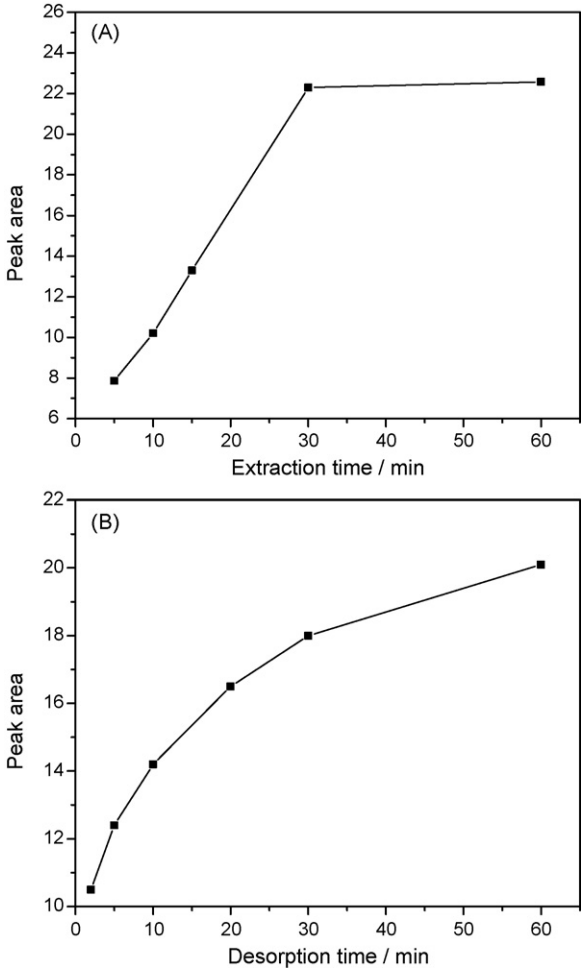

Fig. 4. Dependence of peak area for riboflavin on extraction time (A) and desorption time. Sample: 2 μg/mL riboflavin in 100 mM sodium phosphate buffer, pH 9.0; desorption time in (A): 60 min; extraction time in (B): 60 min.

cate the reversible feature of the covalent reaction between the polyAPBA and the analyte.

3.4. Analytical features

3.4.1. Carryover

Because the volume of the desorbing solution was small (30 μL) and no agitation was applied during the desorbing step in this study, sample carryover was possible. The carryover was estimated to be about 10% when the desorption time was set at 30 min. For consecutive use of the same fiber, a pre-rinse step was applied to eliminate the carryover. The used SPME fiber was immersed into acetic acid for 30 min, followed by a wash with water. Using this pre-rinse step, the carryover was effectively eliminated, as indicated by the excellent linearity as follows.

3.4.2. Linearity

To investigate the linear range of prepared SPME, sample solutions containing 10 ng/mL to 20 μg/mL riboflavin were used for extraction. Fig. 5 shows the dependence of the peak found for the extracted riboflavin on the concentration of riboflavin present in the sample solutions. Although the SPME fiber began to be saturated as the riboflavin concentration increased to 10 μg/mL, there was an excellent linearity within the range of 10–1000 ng/mL, with a squared correlation coefficient of 0.9992 ($n = 7$).

3.4.3. Effect of sugars

In many samples, especially clinic and food samples, sugars are usually present in plenty. Since a lot of sugars belong to cis-diol compounds, their existence in the sample may influence the extraction of the analyte under interest. Glucose and sucrose, which have one pair of 1,3-cis-diol in the molecular structures, are two typical sugars that can be commonly found in clinic and food samples, so they were chosen as competing analogues and added to the riboflavin samples to evaluate their effects on the extraction. The presence of the two sugars in the sample, up to 100 mg/mL (or 10%, w/w), did not significantly influence the extraction of riboflavin. The limited competition capability of glucose and sucrose is beyond the common knowledge that monosaccharide has certain affinity to boronic acids. This is probably related to the structures of the sugars and the conformation of boronic acid on the coating surface as well. Unlike catechol and riboflavin, which can be considered as two-dimensional molecules, the monosaccharides are of boat or chair conformation, which are three-dimensional molecules. In this study, the boronic acid ligands were directly attached to the network of the polymer (no spacer arm). Steric hindrance effect might have prevented glucose and sucrose from forming stable complexes with the boronic acid ligand.

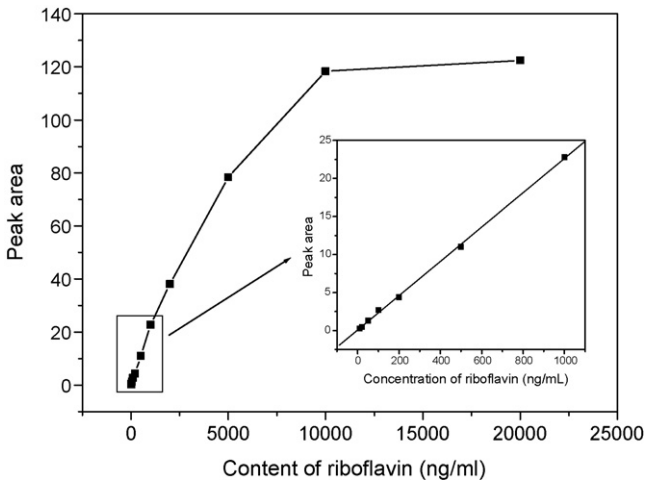

Fig. 5. Dependence of the peak area for the extracted riboflavin on the concentration of riboflavin in the samples. The intersection shows a close-up of the linear range.

3.4.4. Reproducibility and life-time

Reproducibility was examined with an aqueous solution of 2 μg/mL riboflavin. For run-to-run reproducibility, the relative standard deviation (R.S.D.) value for peak area was found to be 6.4% ($n = 12$). For fiber-to-fiber reproducibility, the R.S.D. value was found to be 12.5% ($n = 12$). The reproducibility was acceptable since the off-line desorption manually operated might have contributed to a portion of the deviation. It should also be emphasized that extracting phase preparation procedure used in this study have not optimized yet. With further efforts, the reproducibility can be improved significantly through optimization of experimental factors of the electrochemical deposition process. The fibers were found to be able to endure for 2 months with at least 150 uses while keeping run-to-run R.S.D. less than 10%. The limit of detection of the boronate affinity SPME–HPLC method with fluorescence detection was determined to be about 10 ng/mL (S/N = 3).

3.5. Application to real sample

Like other vitamins, riboflavin plays significant roles for the health of humans and animals. It is involved in helping protection cells from oxygen damage, supporting cellular energy production and maintaining the supply for other B vitamins. Although riboflavin deficiency increases the risk of some diseases and a variety of riboflavin-rich foods have been suggested [28], ironically too much riboflavin in beverages is associated with the occurrence of an unpleasant taste, generally described as “sunstuck flavor”, “off-flavor” and “reduced flavor” [29,30], which is found in many beverages such as sparkling and white wines, beer, cider, milk and fruit juices, upon exposure to light. Therefore, it is important to determine the concentration of riboflavin in beverages. Among many beverages, beer is a special one as it naturally contains a high concentration of riboflavin, coming from barley and yeast as well. In this study, beer was used as a real sample to verify the extracting capability of the boronate affinity SPME established in this study. Since riboflavin decomposes under light exposure, its light-degraded products may contain some fragments that are still fluorescent but have no 1,2- or 1,3-cis-diol groups. These fragments can be used as negative controls to confirm the specific extraction selectivity. Budweiser and Tsingtao beers were chosen real samples.

A certain volume of the beer under test was taken out from the bottle and the pH was adjusted to 9.0. The prepared solution, stored in the dark, was used as a stock sample solution for later analysis. An appropriate volume of the stock solution was injected into the HPLC instrument to build a chromatogram for it components. As shown in Fig. 6A, four major fluorescent compounds are observed. The peak for riboflavin was located at 6.2 min, while other three compounds were eluted earlier. Although the identities of the earlier eluted compounds are not exactly known, they are likely the light-induced decomposition compounds of riboflavin. An aliquot of the stock solution was taken out for the extraction with a polyAPBA-coated fiber. After desorption, the finally obtained solution was injected for analysis. As shown in Fig. 6B, a peak located at 6.2 min for riboflavin was observed while other peaks found in Fig. 6A were not observed. This result confirms the highly specific extraction selectivity to riboflavin and powerful extraction capability to the real sample of the polyAPBA extracting phase. To quantitate the riboflavin concentration in the real samples, an appropriate volume of concentration-known standard riboflavin solution was spiked to an aliquot of the stock beer solution, followed with the same SPME extraction and HPLC analysis. As shown in Fig. 6C, the spiked sample gave a peak at 6.2 min with increased peak area. By com-

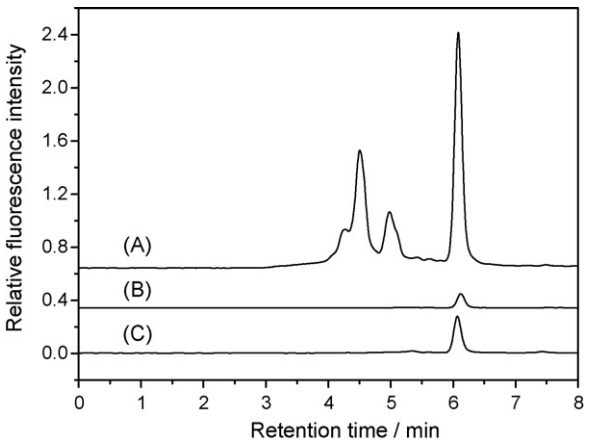

Fig. 6. Comparison of the chromatograms for directly injected beer sample (A), riboflavin extracted from a beer sample (B) and from a riboflavin-spiked beer sample (C). Sample: (A) beer sample (pH adjusted to 9.0); (B) beer sample with pH adjusted to 9.0; (C) beer sample spiked with 200 ng/mL riboflavin, then the pH adjusted to 9.0; extraction time: 30 min, desorption time: 30 min. HPLC conditions: mobile phase, methanol/water (60:40, v/v); flow rate, 0.5 mL/min; volume injected, 10 μL; fluorescence detection excitation wavelength, 450 nm; emission wavelength, 524 nm.

Table 1
Riboflavin in beers determined by boronate affinity SPME–HPLC ($n = 3$).

Brand	Riboflavin found (mean ± S.D., ng/mL)
Budweiser	175.9 ± 16.9
Tsingtao	153.2 ± 14.7

parison of the peak areas for the un-spiked and spiked samples, the concentration of riboflavin in the beer was determined. The results are shown in Table 1. This is in good agreement with literature report which found riboflavin concentration levels in the range of $(0.5–1.0) \times 10^{-6}$ M for beers of a variety of brands [30]. Thus the extraction capability for practical use of the boronate affinity SPME fiber proposed in this study was verified.

4. Conclusions

In this study, we report for the first time boronate affinity SPME. The extracting phase polyAPBA was prepared by electrochemical deposition and successfully applied for covalent SPME of 1,2- and 1,3-cis-diol compounds. Preliminary experiments have demonstrated excellent performance of the boronate affinity extracting phase. Although we demonstrated the concept with an electrochemically prepared extracting phase, this new SPME format does not necessarily exclude other extracting phase preparation methods. The boronate affinity SPME exhibited three significant advantages, including high specificity, eliminated matrix effect and easy-to-control capture/release. It is worthy to point out that a drawback at current stage is that the extraction has to be performed in an alkaline pH condition, which may give rise to degradation of labile compounds. However, such a limitation can be overcome through introducing a special functional group into the molecules of boronic acids [31–34]. Since a lot of important biomolecules contain 1,2- or 1,3-cis-diol, the boronate affinity SPME can develop into a promising tool for bioanalysis especially clinic analysis. In our lab, boronate affinity SPME-based new methodologies are being ongoing for microextraction and analysis of biologically significant molecules such as glycoproteins.

Acknowledgements

We gratefully acknowledge the financial support of the General Grant (No. 20675038) from the National Natural Science Foundation of China and the Key Grant of 973 Program (No. 2007CB914102) from the Ministry of Science and Technology of China to Z.L.

References

[1] J. Pawliszyn, Solid-Phase Microextraction: Theory and Practice, Wiley, New York, 1997.
[2] J. Pawliszyn, Anal. Chem. 75 (2003) 2543.
[3] C. Dietz, J. Sanz, C. Cámara, J. Chromatogr. A 1103 (2006) 183.
[4] J. Wu, H. Lord, J. Pawliszyn, Talanta 54 (2001) 655.
[5] J.Q. Hou, Q. Ma, X.Z. Du, H.L. Deng, J.Z. Gao, Talanta 62 (2004) 241.
[6] M.E.C. Queiroz, E.B. Oliveira, F. Breton, J. Pawliszyn, J. Chromatogr. A 1174 (2007) 72.
[7] X.G. Hu, Y.L. Hu, G.K. Li, J. Chromatogr. A 1147 (2007) 1.
[8] Y. Wen, Y.Q. Feng, J. Chromatogr. A 1160 (2007) 90.
[9] W.M. Mullett, K. Levsen, D. Lubda, J. Pawliszyn, J. Chromatogr. A 963 (2002) 325.
[10] J.C. Rodrigues, A.J.S. Neto, C. Fernandes, C. Alves, A.S. Contadori, F.M. Lanças, J. Chromatogr. A 1105 (2006) 208.
[11] L.C. Clark, C. Lyons, Ann. N. Y. Acad. Sci. 102 (1962) 29.
[12] H.L. Weith, J.L. Wiebers, P.T. Gilham, Biochemistry 9 (1970) 4396.
[13] W.H. Wu, C. Greene, Clin. Chem. 32 (1986) 1193.
[14] J.-Y. Yoon, A.W. Czarnik, J. Am. Chem. Soc. 114 (1992) 5874.
[15] M. Takeuchi, T. Imada, S. Shinkai, J. Am. Chem. Soc. 118 (1996) 10658.
[16] E. Shoji, M.S. Freund, J. Am. Chem. Soc. 123 (2001) 3383.
[17] R. Flueckiger, T. Woodtli, W. Berger, Diabetes 33 (1984) 73.
[18] C.J. Hawkins, M.F. Lavin, D.L. Parry, I.L. Ross, Anal. Biochem. 159 (1986) 187.
[19] S. Hjerten, J.-P. Li, J. Chromatogr. 500 (1990) 543.
[20] X.-C. Liu, W.H. Scouten, Methods Mol. Biol. 147 (2000) 119.
[21] W.L. Roberts, Clin. Chem. 53 (2007) 142.
[22] Q. Zhang, N. Tang, J.W.C. Brock, H.M. Mottaz, J.M. Ames, J.W. Baynes, R.D. Smith, T.O. Metz, J. Proteome Res. 6 (2007) 2323.
[23] J. Rick, T.-C. Chou, Biosens. Bioelectron. 22 (2006) 329.
[24] J. Mathiyarasu, S. Senthilkumar, K.L.N. Phani, V. Yegnaraman, J. Appl. Electrochem. 35 (2005) 513.
[25] S.R. Ali, R.R. Parajuli, Y. Ma, Y. Balogun, H. He, J. Phys. Chem. B 111 (2007) 12275.
[26] E. Shoji, M.S. Freund, J. Am. Chem. Soc. 124 (2002) 12486.
[27] S. Liu, L. Bakovic, A. Chen, J. Electroanal. Chem. 591 (2006) 210.
[28] H.J. Powers, Am. J. Clin. Nutr. 77 (2003) 1352.
[29] C. Andrés-Lacueva, F. Mattivi, D. Tonon, J. Chromatogr. A 823 (1998) 355.
[30] M.G. Duyvis, R. Hilhorst, C. Laane, D.J. Evans, D.J.M. Schmedding, J. Agric. Food Chem. 50 (2002) 1548.
[31] R.P. Singhal, B. Ramamurhy, N. Govindraj, Y. Sarwar, J. Chromatogr. A 543 (1991) 17.
[32] X. Li, J. Pennington, J.F. Stobaugh, C. Schoeich, Anal. Biochem. 372 (2008) 227.
[33] G. Wulff, Pure Appl. Chem. 54 (1982) 2093.
[34] G. Wulff, M. Lauer, H. Bohnke, Angew. Chem. Int. Ed. 23 (1984) 741.

Talanta 79 (2009) 648–656

Contents lists available at ScienceDirect

Talanta

journal homepage: www.elsevier.com/locate/talanta

Second-order calibration of excitation–emission matrix fluorescence spectra for determination of glutathione in human plasma

Bahram Hemmateenejad [a,*], Zahra Rezaei [b], Sasan Zaeri [b]

[a] Department of Chemistry, Shiraz University, Shiraz 71454, Iran
[b] Department of Medicinal Chemistry, Faculty of Pharmacy, Shiraz University of Medical Sciences, Shiraz, Iran

ARTICLE INFO

Article history:
Received 24 January 2009
Received in revised form 18 April 2009
Accepted 21 April 2009
Available online 3 May 2009

Keywords:
Glutathione
Fluorescence
Excitation–emission
Second-order calibration
Standard addition
Plasma

ABSTRACT

A rapid non-separative spectroflourimetric method based on the second-order calibration of the excitation–emission data matrix was proposed for the determination of glutathione (GSH) in human plasma. In the phosphate buffer solution of pH 8.0 GSH reacts with *ortho*-phthaldehyde (OPA) to yield a fluorescent adduct with maximum fluorescence intensity at about 420 nm. To handle the interfering effects of the OPA adducts with aminothiols other than GSH in plasma as well as intrinsic fluorescence of human plasma, parallel factor (PARAFAC) analysis as an efficient three-way calibration method was employed. In addition, to model the indirect interfering effect of the plasma matrix, PARAFAC was coupled with standard addition method. The two-component PARAFAC modeling of the excitation–emission matrix fluorescence spectra accurately resolved the excitation and emission spectra of GSH, plasma (or plasma constituents). The concentration-related PARAFAC score of GSH represented a linear correlation with the concentration of added GSH, similar to that is obtained in simple standard addition method. Using this standard addition curve, the GSH level in plasma was found to be $6.10 \pm 1.37\ \mu mol\ L^{-1}$. The accuracy of the method was investigated by analysis of the plasma samples spiked with $1.0\ \mu mol\ L^{-1}$ of GSH and a recovery of 97.5% was obtained.

1. Introduction

Glutathione (GSH) is a tri-peptide consisting of three amino acids: glutamate, cysteine and glycine. It has a key role in the defense system of many mammalian tissues. A look at the literature will introduce us to an extensive variety of functions attributed to GSH among which antioxidant activity against both endogenous and exogenous reactive species outstands [1,2]. GSH can be considered as a redox buffer [3,4]; it scavenges free radicals and detoxifies xenobiotics and is a strong defense against oxidative and nitrosative stresses [5–7]. GSH has also role in regulating cell proliferation [8] as well as cell apoptosis, the programmed death of cells [9–11]. Glutathione has two main redox forms; GSH is the reduced form of glutathione and is actually the predominant form of it over other oxidized forms [12,13]. Among the oxidized forms, GSSG is known more and is both enzymatically and non-enzymatically formed by GSH [14]. In most of the cells, GSSG accounts for only 1% of the depleted GSH whereas it comprises more than 25% of the oxidized GSH in the subcellular parts, e.g. in the mitochondria [15,16].

For some reasons, reported reference levels of glutathione seem to vary from one work to another in the literature. These differences are mainly derived from different methodologies adopted [17]. So, a good sample preparation including, for example, avoidance of unwanted hemolysis of the red blood cells (RBCs) or the storage of whole blood or plasma samples under an appropriate temperature condition [18] is of crucial importance in the assay of glutathione. In almost all of the methods for glutathione determination, a deproteinization step is necessary [14]. Apart from that, such methods mostly adopt a derivatizing agent that can be either colorimetric or fluoregenic. Sometimes when the determination of total glutathione is desired, a disulfide reduction step is also included [19]. Therefore, all these types of sample interventions can be responsible for the variations seen in the determination results. Such fluctuations from one work to another may be well recognized when blood and plasma samples are concerned; and out of these two assay environments, plasma data show more diversity; maybe because plasma undergoes more manipulations than whole blood in the preparation step [17].

There are different methodologies that are adopted in the quantification of glutathione and its analogues. These methods are classified mainly as separative and non-separative techniques. Chromatographic approaches including high performance liquid chromatography (HPLC), thin layer chromatography (TLC) and gas chromatography (GC), together with capillary electrophoresis (CE) serve as separative ones while spectrophotometric, spectrofluorimetric and electrochemical methods fall in the second category

* Corresponding author. Tel.: +98 711 2284822; fax: +98 711 2286008.
E-mail address: hemmatb@sums.ac.ir (B. Hemmateenejad).

0039-9140/$ – see front matter © 2009 Elsevier B.V. All rights reserved.
doi:10.1016/j.talanta.2009.04.041

[14]. Chromatographic techniques take the advantage of high specificity and selectivity for they physically neutralize the interfering effects of artifacts and when used in combination with sensitive detectors like fluorimetric ones, they become so sensitive and that is why there have been so increasing attention towards them. On the other hand, non-separative approaches are not very well reflected in the works of recent investigators mainly because of the problem of unsatisfactory specificity caused by other aminothiols present in the biological matrices. Although non-separative techniques lack enough specificity, they are very promising with respect to the matter of their simplicity and low cost if we manipulate the assay system in a way so as to somehow separate and probably recognize the interferences contributing to the final instrumental signals.

GSH and its analogues do not present any strong chromophores or fluorophores in their structures and hence, are frequently derivatized by either colorometric or fluoregenic tags to exhibit convincing sensitivity [20]. Except for the electrochemical-based detection methods which do not rely on the derivatization of glutathione, other methods lack enough sensitivity when no derivatization has been considered and therefore have either a chromophore or fluorophore introduction step in their protocols [14]. Fluoregenic labeling agents are commonly used in the assay of glutathione. They offer high sensitivity compared to UV–vis labeling agents. These fluoregenic agents are *o*-phthaldehyde (OPA) [21–25], monobromobimane (BrB) [26], fluorobenzofurazan derivatives [27,28], Rhodamine-based probes [29,30], etc., among which OPA (not fluorescent by itself) is widely used to form a highly fluorescent, stable derivative of GSH and other aminothiols. The mild laboratory conditions required for the reaction of OPA with GSH have made this reagent much attractive to be used by many investigators involved in glutathione determination [21–25,31]. The introduction of OPA as a derivatizing agent in the assay of glutathione was done by Cohn and Lyle [23] and was then modified by other authors [24]. Although OPA serves as a good labeling tag as mentioned before, it is very active towards amino acids as well as aminothiols other than GSH, putting a challenge in front of its applications in the GSH assay [17,31–35].

Since the introduction of chemometrics methods in analytical chemistry the problem of spectral overlapping has been diminished thanks to the resolving power of various multivariate calibration methods. In contrast to univariate calibration, measuring of multivariate signals per sample enables one to compensate for contributions of interferences in an unknown sample. While the first-order multivariate calibration methods are able to handle the spectral interferences of the compounds whose variations are taking into account in the calibration process [36–41], the second- or higher order data analyses methods can compensate for potential interferences not included in the calibration set [42–45]. This is universally recognized as the second-order advantage. The second-order methods need a matrix of response data per sample and thus a three-way array of data is obtained by staking the data matrices of different samples under each other. These types of data can be provided by hyphenated instruments such as HPLC-DAD, GC–MS and LC–MS, excitation–emission fluorescence spectra and spectroscopic monitoring of the reaction kinetic. Parallel factor (PARAFAC) analysis is one of the second-order calibration methods, in which the trilinearity of the measured analytical data is a necessary condition. For a detailed discussion on PARAFAC and its basis and applications, the reader is referred to the literature [42–47]. The excitation–emission matrix of fluorescence spectra is a kind of trilinear data and such data have been extensively used in the recent years to achieve second-order advantage.

In this work, we developed a non-separative spectrofluorimetric-based method, with OPA as the labeling agent for the determination of plasma GSH using PARAFAC as a second-order data analysis method. We adopted a second-order standard addition method to compensate both the contributions of other aminothiols, potentially presented in plasma, and the effect of plasma matrix on the spectrofluorimetric determination of GSH. The experimental conditions were optimized to achieve the best sensitivity for the direct determination of GSH in plasma.

2. Experimental

2.1. Reagents

o-Phthaldehyde (OPA), trichloroacetic acid (TCA), Na_2HPO_4 and EDTA were obtained from Merck Co. (Germany). GSH was purchased from Sigma Chemical Company (St. Louis, MO). Doubly distilled water was used to make disodium hydrogen phosphate buffer solution.

The buffer pH was set at 8.0 by dissolving 1.780 g of disodium hydrogen phosphate in doubly distilled water and the final volume of it was made to 100.0 mL. Apart from disodium hydrogen phosphate, 0.1 g of EDTA was also dissolved in the buffer solution to inhibit the autoxidation phenomenon of GSH which is actually common and problematic in its assay.

The mother OPA solution used for derivatization was prepared by dissolving 0.025 g OPA in 25.0 mL methanol (reagent grade, Merck) to yield a concentration of 0.1% (w/v) of OPA. This solution seemed to maintain its activity for several weeks when kept in the refrigerator. GSH stock solution was prepared by dissolving 0.015 g in 100.0 mL of phosphate buffer solution to yield a concentration of 500.0 $\mu mol\,L^{-1}$ and stored at 4 °C until used. The 10% (w/v) TCA solution was prepared by dissolving 10.0 g of cold TCA crystals in doubly distilled water and made to 100.0 mL.

2.2. Instrumentation

A Perkin-Elmer LS 50B Luminescence Spectrophotometer was used for the fluorimetric measurements. A refrigerator-equipped centrifuge model SIGMA 3K30 was used for precipitating plasma proteins at high ($10{,}000 \times g$) revolution. Data manipulation was performed employing Microsoft Excel (2003) and MATLAB 7.0.

2.3. Plasma samples and sample preparation

Daily based fresh frozen plasma (FFP) samples prepared from the venous blood of random healthy male and female blood donors of the Central Blood Transfusion Organization (Shiraz, Iran) were gathered. The process of RBC removal and other necessary steps in preparing plasma samples were done and checked by the staff of that organization. Frozen plasma samples with a temperature lower than −80 °C were put into standard cold boxes and quickly transported to the laboratory freezers until the day of experiment.

As suggested by many authors that have worked on the glutathione determination, one of the necessary steps in plasma preparation is protein removal that is done by different strategies including the use of acids (trichloroacetic acid (TCA), perchloric acid (PCA), 5-sulfosalicylic acid (5-SSA) and metaphosphoric acid (MPA)), organic solvents (methanol, acetonitrile, etc.) and ultrafiltration, among which acidic reagents are, by far, more popular than others [14]. TCA with a concentration of 10% (w/v), served as the protein precipitant in our study. Before adding appropriate volumes of acid to plasma samples, it was given enough time for the frozen plasma to gradually melt at the room temperature (25 °C). After centrifugation of acidic plasma samples at $10{,}000 \times g$ (twice for each sample) in a refrigerator-equipped centrifuge maintained at 4 °C, the supernatant liquid was carefully pipetted into laboratory tubes and frozen at −80 °C before the spectrofluorimetric measurements. Such frozen supernatants are supposed to contain GSH and

other non-macromolecular plasma constituents such as ions, amino acids, some small peptides etc., but no proteins.

2.4. Excitation–emission spectrofluorimetric setup

All samples were measured in a dark condition because of the GSH–OPA adduct susceptibility to exposure to the direct light. Measurements were done in a 10 mm × 10 mm quartz cuvette at the room temperature. Excessive care was taken to fully clean the cuvette to reduce any fluorescent interfering hand-transported contaminations on its external wall. The wavelength range of 370–600 nm with 0.5 nm intervals was selected for obtaining the emission spectra of the assay samples. For each sample, an excitation–emission data matrix was generated by exciting that sample at 10-nm intervals from 310 to 360 nm. It was found that the best intensities were gained if the excitation and emission slit widths were set at 10 nm and 3.5 nm, respectively. A scan speed of 1500 nm/min was employed. It should be noted that for univariate calibration the excitation and emission wavelengths were set at 340 nm and 420 nm, respectively. The data produced by the instrument were smoothed using the Savitski-Golay smoothing approach and subsequently analyzed by PARAFAC.

2.5. Calibration of the GSH–OPA adduct in buffer solution

Prior to going to GSH measuring in real samples, a calibration step in the phosphate buffer medium was thought to be necessary to firstly evaluate the fluorescence of the GSH–OPA adduct as well as the appropriate excitation–emission wavelength pair reported in the literature and secondly to draw a calibration curve for the determination of the detection limit in the phosphate buffer solution. To do so, various GSH solutions with concentrations of 0.20, 1.00, 2.00, 4.00, 5.00, 10.00, 20.00 and 40.00 μmol L^{-1} were prepared in the aqueous buffer of pH 8.0. Equal volumes (i.e., 2.0 mL) of 0.1% OPA and GSH solutions of desired concentration were directly mixed in the well-wrapped laboratory tubes and after mixing gently, appropriate portion of the reaction mixture was transferred into the spectroflourimeter cuvette. It should be noted the concentrations of GSH in the resulting solutions are one-half of the above mentioned concentrations. The fluorescence intensity of each reaction solutions was then measured at the excitation and emission wavelengths of 340 nm and 420 nm, respectively. Three independent measurements were performed for each solution at the same lab conditions. Calibration curve was derived by plotting the averaged fluorescence intensity *vs*. GSH concentration.

2.6. General procedure for GSH assay in plasma

A standard addition approach coupled with PARAFAC as three-way calibration method was adopted here for the assay of GSH in plasma. In a series of six well-wrapped laboratory tubes were added 0.50 mL diluted plasma and 3.25 mL aqueous buffer of pH 8.0. Then minute and variable amounts of GSH stock solution (i.e., 0.0, 8.0, 24.0, 40.0, 80.0 and 160.0 μL) were added to the above solutions to make the added GSH concentrations of 0.0, 1.0, 3.0, 5.0, 10.0 and 20.0 μmol L^{-1}, respectively. Finally, 0.25 mL of 0.10% (w/v) OPA was added to reach to the final volume of 4.00 mL. The reaction mixture was then allowed to stand in darkness for 10 min at the room temperature for the reaction to be completed. Since the plasma also contains GSH, the actual concentrations of GSH in the resulting solutions were not equal to the added concentrations. The degree of plasma dilution was optimized to obtain the best results with respect of both accuracy and sensitivity. Under the specified instrumental setup, an excitation–emission data matrix was generated for each of six calibrator samples by successively exciting each sample at 360, 350, 340, 330, 320 and 310 nm and obtaining the corresponding emission intensities through 370–600 nm.

To show that the analysis of the GSH concentration in the plasma is valid, i.e., to check the model recovery power, the plasma samples were spiked with 1.0 μmol L^{-1} of standard GSH and the complete standard addition procedure discussed in the previous paragraph was employed and the percent of recovery was calculated.

2.7. PARAFAC modeling

The PARAFAC analysis was performed using the N-way toolbox of MATLAB provided by Professor Rasmus Bro. It was taken from the website of Faculty of Life Sciences, University of Copenhagen (http://www.models.kvl.dk/source/). The recorded three-dimensional excitation–emission fluorescence data of standard addition samples were denoised employing Savitsky–Golay smoothing method. The six two-dimensional matrices were rearranged into a three-dimensional array required for PARAFAC analysis. Final data were the average of the three independent runs at the same experimental conditions. Core consistency, percent of the explained variances (or residual sum of square errors) and number of PARAFAC iterations were used to obtain the optimum number of PARAFAC factors. To obtain the best results, PARAFAC was run using different applied constraints.

3. Results and discussion

The unique properties of GSH–OPA adduct (i.e., mild reaction condition, no fluorescence emission of OPA and intense fluorescence emission of adduct) made it as a routine detection method for glutathione by liquid chromatographic methods [31]. Thanks to the resolving power of three-way calibration methods even in the presence of non-modeled interferences, here, PARAFAC calibration was used to develop a rapid analytical method for quantization of GSH in plasma without need to separate the analyte from interferences. First of all, the fluorescence property of GSH–OPA adduct was studied in the buffer solution. It was found that the best excitation–emission wavelength pair is 340 nm and 420 nm, respectively as also suggested by the literature [21–25,48]. The excitation and emission fluorescence spectra of GSH–OPA adduct in buffer of pH 8.0 are shown in Fig. 1. The excitation and emission spectra exhibit distinct peak maxima at 340 nm and 420 nm, respectively. It should be noted that pH was not optimized in this work and the previously reported optimized value (pH 8.0) was used.

By plotting emission intensities (with excitation and emission wavelengths of 340 nm and 420 nm, respectively) *vs*. GSH concentrations, a linear calibration curve in the GSH concentration range of 0.05–10.00 μmol L^{-1} with calibration equation of ($y = 34.63 \times -1.14$) and correlation coefficient (R^2) of 0.990 was obtained. The averaged emission intensity of the blank sample containing no GSH was 3.51 with a standard deviation of 0.077 ($n = 5$). Three times of the blank standard deviation was added to the average of blank emission intensity to obtain the detection limit (DL) signal. Accordingly, a detection limit (DL) of 0.039 μmol L^{-1} was obtained for GSH determination in buffer solution by transferring the DL signal into the calibration equation.

The next step is studying the fluorescence property of GSH–OPA adduct in the human plasma solution. There are numerous known and unknown biological compounds such as SH-bearing amino acid, cysteine, and other thiol-containing peptides as well as many fluorescent compounds present in the plasma matrix that may severely interfere with the analyte under assay. The excitation and emission spectrum of plasma is also shown in Fig. 1. Plasma, when untreated with OPA, shows an excitation spectrum having maximum intensity at 280 nm and a descending emission pattern

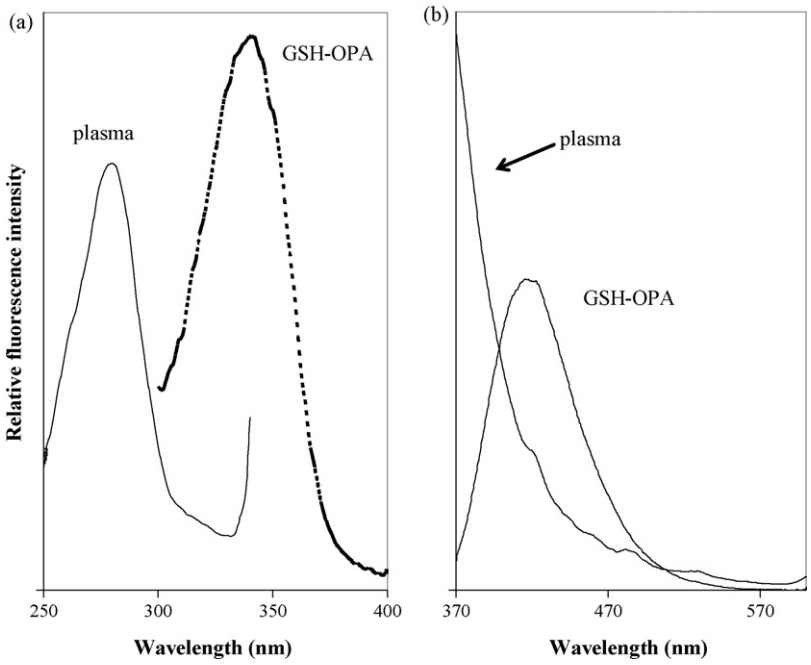

Fig. 1. Excitation (a) and emission (b) spectra of GSH–OPA adduct and plasma (untreated with OPA).

through the wavelengths of 370–600 nm. Surprisingly, a relatively significant shoulder at around 420 nm was also observed in the plasma emission profile.

In addition to fluorescence emission, plasma also imposes its quenching effects on the fluorimetric quantification of the analytes present in it. This phenomenon becomes very problematic in deriving satisfactory models because quenching effects severely reduce enough sensitivity required for the assay. In addition, the plasma constitutes can also show interfering effects through reaction with OPA. To investigate the effects of plasma on the fluorescence property of GSH–OPA adduct, two separate experiments were run: (a) firstly, OPA and GSH solutions were mixed and after the completion of the reaction, plasma solution was added and (b) secondly GSH standard solution was added to plasma and then they were mixed with OPA solution. Both experiments were achieved with variable volumes of the plasma solution. The resulted emission spectra are shown in Fig. 2. It should be noted that in the above experiments, the concentrations of GSH and OPA were constant and only the added volumes of plasma solution in the total of 4.0 mL reaction mixtures were varied between 0.0 and 2.5 mL. Moreover, the plasma itself

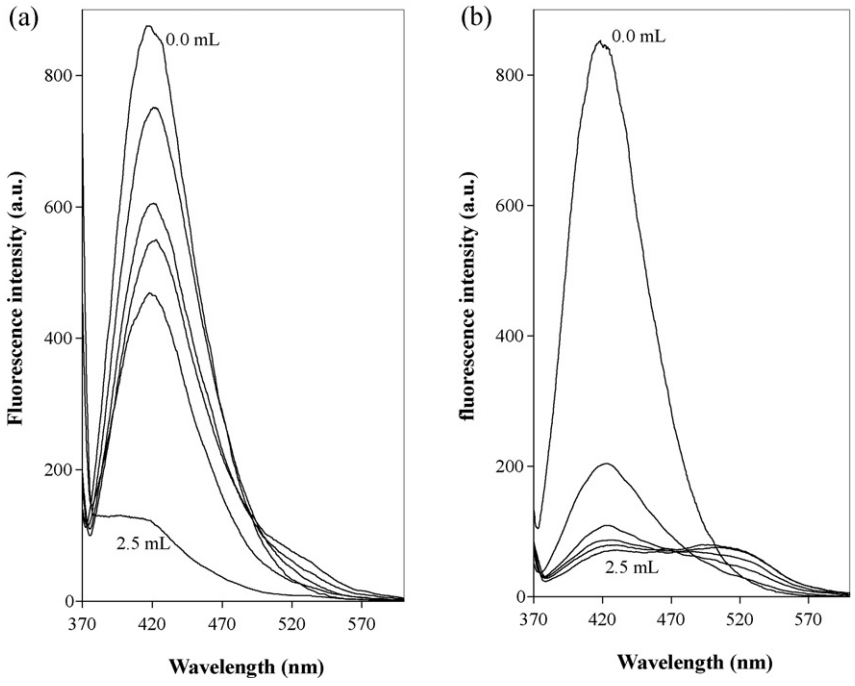

Fig. 2. Quenching of GSH–OPA adduct by plasma. The order of addition of reagents is (a) OPA and GSH solutions were mixed and after the completion of the reaction, plasma solution was added, (b) firstly GSH standard solution was added to plasma and then they were mixed with OPA solution. The volumes of added plasma are between 0.0 mL (the highest spectrum) and 2.5 mL (the lowest spectrum) with 0.5 mL intervals in a total volume of 4.0 mL.

contains some GSH but at very lower level of that added to the reaction mixture so that the contribution of plasma GSH in the GSH–OPA fluorescence can be ignored.

The left part of Fig. 2 shows a gradual decreasing in the fluorescence intensity of GSH–OPA adduct (at 420 nm) upon increasing addition of plasma, accompanying with the appearance of new peak at about 520 nm. The new peak can be attributed to the reaction of OPA with other plasma constituents. This is confirmed by the spectral changes shown in the right part of Fig. 2. As it is evident, by the addition of OPA to the mixture of plasma and GSH, the fluorescence intensity of GSH–OPA is decreased dramatically accompanying with a clear formation of new florescent peak at 520 nm. The substantial decreasing of the fluorescence intensity upon addition of minute amount of plasma can be attributed to two factors: consumption of OPA by plasma constitutes and quenching effect of plasma on the GSH–OPA fluorescence.

3.1. Optimization of OPA concentration

The above observations indicated significant quenching effect of plasma constituents on the GSH–OPA fluorescence. The major result of this effect is a decreased sensitivity of the proposed method for GSH assay in plasma. While PARAFAC is able to handle the non-modeled interfering effects of the unknown plasma constituents (i.e., those produced fluorescent products upon reaction with OPA), the mentioned matrix effect cannot be resolved by PARAFAC. To decrease matrix effect, two different criteria were employed: (a) since the tendency of OPA to GSH is more than other plasma constituents [21–26], the amounts of added OPA was decreased to the levels necessary for GSH reaction in order to decrease the formation of plasma constituents–OPA adducts and hence their interfering effects and (b) according to the emission spectra shown in Fig. 2, the volume of the added plasma to the reaction mixture was decreased in order to lower the concentration of quenchers. Up to now, the reaction mixtures contained 1.50 mL of 0.10% OPA, 0.50 mL plasma and 2.00 mL aqueous buffer to reach to the total volume of 4.00 mL.

To investigate the effect of OPA concentration, the volume of added OPA in the total of 4.00 mL reaction mixture was lowered from 1.50 to 0.13 mL step by step. In addition, the effect of plasma dilution was investigated by using 0.50 mL of undiluted plasma taking directly from the deprotonization step and 2.5-fold diluted plasma. Since the studied florescence producing system is complex here (i.e., having signal from both background and analyte in addition to quenching matrix effect) in each examined experimental

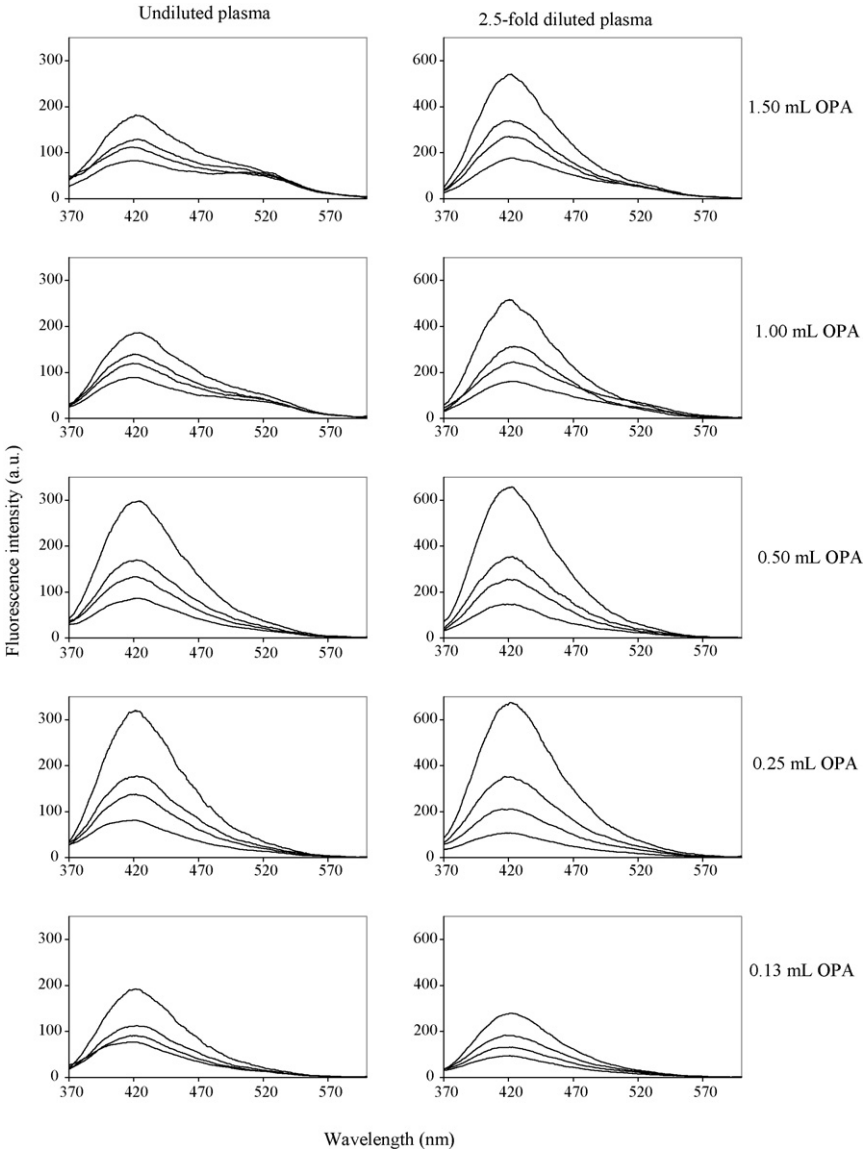

Fig. 3. Changes in the emission spectra as the function of GSH concentration in the different amounts of OPA and plasma.

Table 1
The slope and intercept of calibration curves obtained at different amounts of OPA and plasma.

OPA volume (mL)	Undiluted plasma		2.5-Fold diluted plasma	
	Slope	Intercept	Slope	Intercept
1.50	10.31	76.11	40.06	140.57
1.00	10.41	83.61	39.32	119.56
0.50	23.24	60.33	56.62	82.99
0.25	26.20	53.78	63.67	32.96
0.13	13.12	55.22	20.45	73.30

condition a calibration curve was derived and its slope and intercept were used as scoring functions for optimization. The changes in the emission spectra as the function of GSH concentration in the different amounts of OPA and plasma are shown in Fig. 3 and the slope and intercept of the corresponding calibration graphs are represented in Table 1. As it is observed from Fig. 3, when undiluted plasma is used two clear emission peaks are observed for high levels of OPA volume (i.e., 1.50 and 1.00 mL): one for GSH–OPA (420 nm) and another for plasma constituents–OPA adducts (520 nm). The peak at 520 nm is changed to a weak shoulder for OPA volume of 0.5 mL and it disappears when lower levels of OPA are used. This can be related to decreasing in the concentration of plasma constituents–OPA adduct by lowering the OPA level in the reaction mixtures. The decrease in the emission intensity at 520 nm is accompanying with increasing in the emission intensity at 420 nm due to the decreasing in the concentration of absorbing species at 420 nm (i.e., plasma constituents-OPA adduct). However, for OPA volume lower than 0.25 mL, a reduction in the signal intensity at 420 nm is observed, which can be attributed to no sufficient OPA for reaction with GSH. Thus, OPA volume of 0.25 mL can be considered as the optimum value.

Although the quenching effects of plasma-OPA adducts were lowered dramatically by lowering OPA volume from 1.5 to 0.25 mL, the plasma quenching effect is still present. As it is observed from right part of Fig. 3, a significant enhancement in the fluorescence emission intensity of GSH–OPA adduct was obtained by 2.5-fold dilution of plasma before addition to reaction mixture. In addition, a decrease in peak intensity is observed at 520 nm for diluted plasma. The changes in the emission intensity at 420 nm as a function of OPA volume for diluted plasma represented the similar trend as undiluted plasma and the emission intensity reached to its maximum value when OPA volume decreased from 1.5 to 0.25 mL.

The slope and intercept of the calibration curves reported in Table 1 reveal the same trend as discussed in Fig. 3. The largest slope (or the best sensitivity) is observed for OPA volume of 0.25 mL. The intercept values indicate the contribution of plasma constituents (both GSH and other constituents) in the plasma fluorescence. For diluted plasma it reaches to its minimum value at OPA volume of 0.25 mL. At higher OPA levels, large intercepts are observed, which can be attributed to fluorescence of plasma–OPA adducts. According to the aforementioned results and discussion, a 0.25 mL of 0.10% (w/v) OPA and 0.5 mL of 2.5-fold diluted plasma in a total volume of 4.0 mL were considered as optimum condition for GSH assay in plasma.

3.2. PARAFAC analysis

According to the aforementioned optimization results, at the suggested optimum condition the direct and indirect interferering

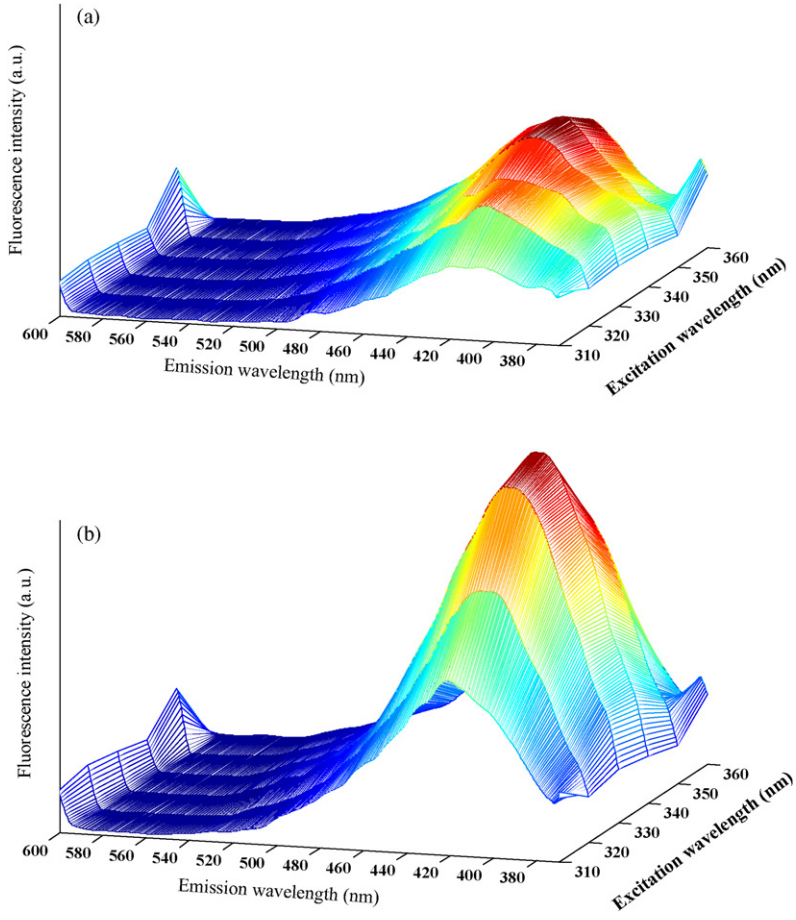

Fig. 4. The excitation–emission spectral profile of the mixtures of plasma constituents–OPA and GSH–OPA adducts: (a) without external GSH and (b) with 1.0 μM added GSH.

effects of plasma constituents are at the lowest levels. However, they still exist and thus exert their interfering effects on GSH determination in plasma. Thus, we employed PARAFAC as a multivariate calibration method to handle non-modeled interfering effects of plasma–OPA adducts. Also, PARAFAC was combined with standard addition method to overcome plasma matrix effects. For a detailed understanding of the basis of such analytical approach, the reader is referred to the literature [42–47]. However, as a short description, we expect the calibration line (i.e., PARAFAC score in the direction of added analyte concentration) to cross the *Y*-axis (with a statistically significant positive intercept) because there is always a basic amount of endogenous analyte (here, GSH) in the assay sample. As can be mathematically proved, the point at the intersection of the calibration curve with the horizontal axis representing, in our case, the added GSH concentrations, will be considered as the intrinsic plasma GSH level.

The three-dimensional excitation–emission fluorescence spectra of plasma–OPA is shown in Fig. 4a and those of plasma added to it 1.0 μmol L^{-1} standard GSH (the first standard addition solution) is shown in Fig. 4b. Similar spectra were recorded for the other standard addition samples. The three-way data array of the excitation–emission-added GSH concentration fluorescence data were subjected to PARAFAC analysis for obtaining the relevant scores of the mentioned ways. A non-negativity constraint was exerted on the excitation and emission ways thus allowing the fitting process to work in such a way that the outcoming emission and excitation spectra follow a conventional peak shape with no negative values. No other types of constraints were found to be necessary; maybe because of the matter of PARAFAC uniqueness. A critical step in PARAFAC calibration method, similar to other factor analysis-based calibration methods, is obtaining the number of significant principal factors. For determining the proper number of components in PARAFAC, several powerful tools are available among which we used residual sum of squares, core consistency [46] and the number of iterations. A five-level repetition with random initialization strategy was specified to separately derive models based on 1–4 components. Such repetition level could ideally give opportunity to well evaluate model stability in any of the four factors. In fact, if too many components (or factors) are chosen, the number of local minima will drastically increase and as a consequence, the model becomes unstable on each run. The results are depicted in Fig. 5. All employed criteria suggest that our three-way data set is best represented by two-component PARAFAC model.

We expect residual sum of squares to continually decrease upon the increase in the number of components. However, if such decrease is not statistically significant, then it will not mean that the corresponding component(s) fall(s) among the true number of components [46]. As it is observed from Fig. 5, by moving from the first component to the second one, we observe a relatively significant decrease whereas this is not so when the next two components are considered. Core consistency is another diagnostic tool. Values obtained from this test fall in a range between zero (and maybe even negative values) and 100. If an *n*-component model generates core consistency values as 100 or near it, then *n* is very probable to be the right number of components. Values approaching zero are representative of the models the component number of which is not properly chosen. Returning to Fig. 5, we encounter a very sharp fall in the core consistency value from a two-component model to a three-component one thus indicating that there are actually two underlying factors in our fluorescence data. Models which do not converge at the same minimum mostly require an increased number of iterations to fit the data. This is probably because of the too many components selected. That is also the case when we consider the number of iterations as a determining criterion in our study. As shown in the last part of Fig. 5, a drastic scattering is clearly detectable in the values of the iteration number just after the second component. All these findings together with the visual evaluation of the three resolved modes confirm that there are only two types of chemical undergoing factors in the reaction mixture. These components can be attributed to GSH–OPA and plasma constituents–OPA adducts. Since in the experimental setup of standard addition method the concentration of all plasma constituents, except GSH was remained constant, PARAFAC was not able to discriminate between these constituents and all of them are considered as a single component, we refer to them plasma (or matrix) component.

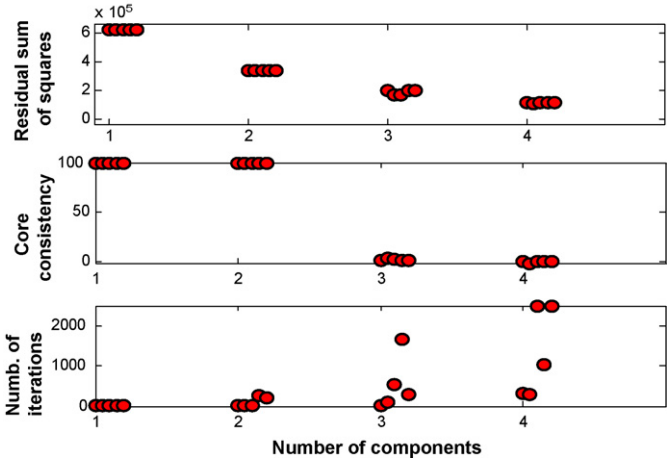

Fig. 5. PF-test plots for the determination of number of factors in PARAFAC.

The PARAFAC scores of the resolved components for emission and excitation profiles are represented in Fig. 6. The unimodal emission profile (labeled as factor 1), representing the highest intensity at 420 nm, is definitely belonging to the GSH–OPA adduct as was also instrumentally confirmed in the phosphate buffer solution (see Fig. 1). The second emission profile does not seem to belong to only one chemical entity. Based on the fact that plasma texture also has emission properties as shown earlier in this work, the first descending part of the resolved spectrum, from wavelengths 370 nm to almost 420 nm, can be very well attributed to the plasma background emission. However, the relatively broad-peak spectrum just following that of plasma, reflects the presence of the other SH-carrying moieties that react with OPA in the same way as GSH does but presenting their emission peak intensities at wavelengths longer than 420 nm. Russel and Scaduto [35] have also reported such interfering phenomenon by presenting similar broad-peak spectra of the interfering agents.

The excitation profiles resolved by the two-component PARAFAC fitting (Fig. 6) are also in harmony with the experimental findings. According to the emission profiles, the first factor can be attributed to the excitation spectrum of GSH–OPA adduct. It shows a peak at wavelengths around 340 nm, which is the same as that found for GSH–OPA adduct in the buffer solution of pH 8.0. The second excitation factor is supposed to be that of both plasma background and interfering OPA-derivatives of the plasma compounds. It exhibits a peak at 340 nm and a probable one at the higher wavelengths. However, we were not allowed to extend the excitation wavelengths higher than that of the starting wavelength of the emission profile. Russel and Scaduto have also reported that OPA-derivatives of both GSH and other potential interfering species have nearly similar excitation spectra [35].

3.3. Application to plasma sample

Once the PARAFAC scores of emission and excitation profiles were assigned to the relevant species (i.e., they were used for

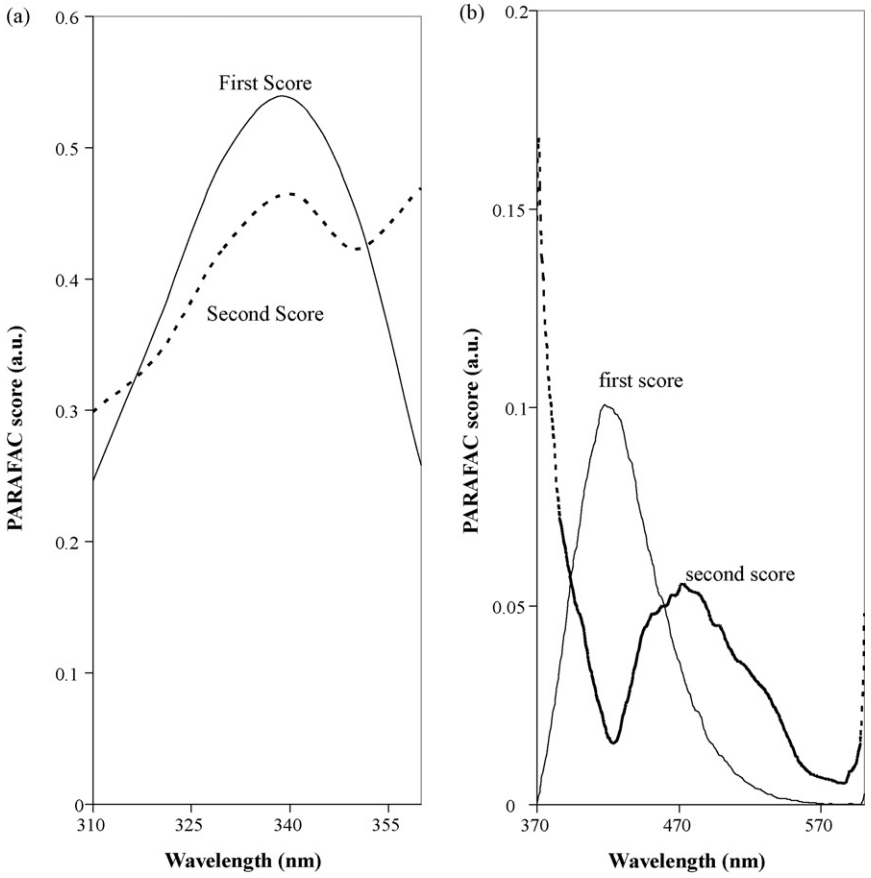

Fig. 6. The resolved two-component PARAFAC scores in the directions of (a) excitation and (b) emission wavelengths. First and second scores can be attributed to GSH–OPA and plasma–OPA adducts, respectively.

qualitative analysis), the PARAFAC scores of the third way (i.e., concentration mode) was used for quantitative analysis of GSH in plasma. As it is observed from Fig. 7, the first factor is actually related to GSH while the second factor could be attributed to the other fluorescent derivative(s) generated upon reaction with OPA. As it is expected, the concentration profile of the second factor is almost constant at near zero values since there have been no change in the amount of other plasma constituents upon addition of OPA. The analytical appraisals of the resulted standard addition line are given in Table 2. There is observed a fairly linear relationship ($R^2 = 0.999$) between the first score and the added GSH concentration. As it is shown in the lower part of Fig. 7, this calibration curve has an intercept of 444.53, which is much higher than the three times of its standard error (102.1) and therefore it can be considered significantly different from zero. Extrapolation of the calibration curve makes an intersecting point on the concentration axis with a value of 0.305 ± 0.069. This value can also be calculated by dividing intercept by slope. The standard deviation in the predicted concentration was calculated based on standard errors of the slope and intercept of the standard addition graph. This is not really the plasma intrinsic GSH concentration since we have not yet corrected this value for the dilutions plasma samples underwent. These plasma samples were 2.5 times diluted during optimization process and then 0.50 mL portions of such plasma samples were made up to 4.0 mL as the final reaction mixture volume. Therefore, considering such successive dilutions ($2.5 \times 8 = 20$-fold dilution), we found the plasma GSH concentration to be 6.10 ± 1.37 μmol L^{-1}. The plasma GSH concentrations reported in the literature [49–53] are in the range of 2.22–11.26 μmol L^{-1}. Thus the obtained value by the PARAFAC method complies with the literature values.

To validate the accuracy of the proposed method for the assay of GSH in plasma and to obtain a confidence about the obtained GSH concentration in plasma the following procedure was employed. The series of six plasma solutions containing variable amounts of GSH standard solutions (i.e., those used for the assay of GSH in plasma) were spiked with a constant amount of standard GSH (final concentration of 1.00 μmol L^{-1}). The three-way excitation–emission spectra of the resulting solutions were subjected to PARAFAC calibration in the same manner as described for non-spiked samples. The analytical appraisals of the resulted standard addition line (plotting the first concentration-related PARAFAC score against the concentration of added standard) are also given in Table 2. It is observed that the calibration graph of the spiked plasma has a slope very close to the non-spiked plasma solution. This explains that the amount of GSH in plasma dose not affect on the sensitivity of the PARAFAC calibration. The recovery of GSH assayed in the spiked plasma is relatively equal to the sum of that found in the non-spiked plasma and that added to it. There is observed a

Table 2
Analytical appraisals of the PARAFAC standard addition calibration lines for the analysis of GSH in plasma.

	Slope	Intercept	R^2	Found GSH	Recovery
Non-spiked plasma	1453.7 (±21.3)	444.53 (±102.1)	0.9991	0.305 (±0.069)	–
Plasma spiked with 1.00 μM GSH	1440.7 (±24.4)	1844.0 (±130.7)	0.9989	1.280 (±0.09)	97.5%

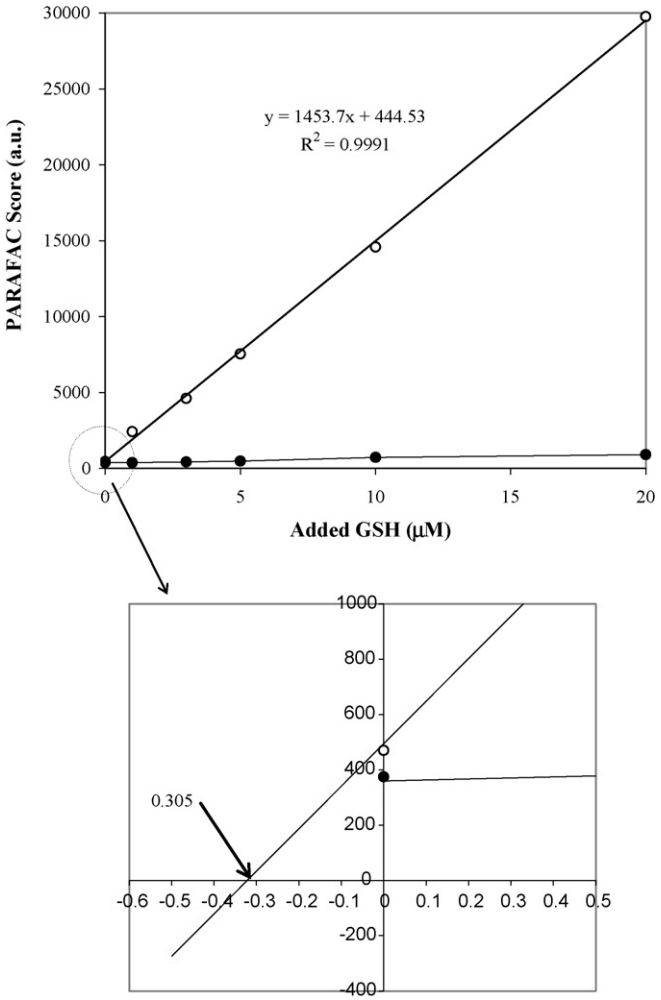

Fig. 7. Plot of the concentration-related two-component PARAFAC scores against the concentration of added GSH to plasma. The filled markers denote the score of the plasma constituents.

high percent of recovery for the spiked plasma (i.e., 97.5%) indicating the high accuracy of the proposed PARAFAC calibration method for the assay of GSH in plasma.

4. Conclusion

We developed a rapid, simple and selective method for the direct determination of GSH in plasma. It works based on PARAFAC analysis of the excitation–emission matrix fluorescence spectra of GSH upon reaction with OPA. While PARAFAC analysis could overcome the spectral interfering effects of fluorescent plasma constituents (other than GSH), its combination with standard addition method enabled us to handle the indirect interfering effect of plasma matrix. The two-component PARAFAC model resulted in pure excitation and emission fluorescence spectra of GSH–OPA and plasma constituents–OPA adducts. The first component of the third PARAFAC score represented a fair linear correlation with the concentration of added GSH (similar to that obtained in univariate standard addition method) and the second component remained unchanged as function of GSH concentration. The concentration of GSH in plasma, estimated from the regression equation of the resulted standard addition plot, was found to be $6.10 \pm 1.37\ \mu mol\ L^{-1}$. The accuracy of the proposed method was validated by spiking standard GSH to plasma and recovering the spiked value. A recovery of 97.5% confirmed the ability of the employed method for the direct determination of GSH in plasma without need for separation.

Acknowledgement

Financial support of this project by the Iran National Science Foundation (INSF) is appreciated.

References

[1] A. Meister, Biochim. Biophys. Acta 1271 (1995) 35.
[2] D.J. Reed, M.K. Savage, Biochim. Biophys. Acta 1271 (1995) 43.
[3] A. Meister, Science 220 (1983) 472.
[4] A.J.L. Cooper, B.S. Kristal, Biol. Chem. 378 (1997) 793.
[5] A. Meister, Cancer Res. 54 (1994) 1969.
[6] A. Jain, J. Martensson, E. Stole, P.A. Auld, A. Meister, Proc. Natl. Acad. Sci. U.S.A. 88 (1991) 1913.
[7] S. Luprecio, S. Tamir, S.R. Tannebaum, Free Radic. Biol. Med. 21 (1996) 513.
[8] M. Poot, H. Teubert, P.S. Rabinovitch, T.J. Kavanagh, J. Cell Physiol. 163 (1995) 555.
[9] D.J. van den Dobbelsteen, C.S.I. Nobel, J. Schlegel, I.A. Cotgreave, S. Orrenius, A.F. Slater, J. Biol. Chem. 271 (1996) 15420.
[10] L. Ghibelli, C. Fanelli, G. Rotilio, E. Lafa via, S. Coppolia, C. Colussi, FASEB J. 12 (1998) 479.
[11] A.G. Hall, Eur. J. Clin. Invest. 29 (1999) 238.
[12] G. Bellomo, F. Mirabelli, D. Di Monte, P. Richelmi, H. Thor, C. Orrenius, S. Orrenius, Biochem. Pharmacol. 36 (1987) 1313.
[13] Y.C. Chai, S.S. Ashraf, K. Rokutan, R.B. Johnston Jr., J.A. Thomas, Arch. Biochem. Biophys. 310 (1994) 273.
[14] E. Camera, M. Picardo, J. Chromatogr. B 781 (2002) 181.
[15] K.J. Lenton, H. Therriault, J.R. Wagner, Anal. Biochem. 274 (1999) 125.
[16] B.R. Shivakumar, S.V. Kolluri, V. Ravindranath, Mol. Cell. Biochem. 111 (1992) 125.
[17] A. Patore, G. Federici, E. Bertini, F. Piemonte, Clin. Chim. Acta 333 (2003) 19.
[18] B.J. Mills, J.P.J. Richie, C.A. Lang, Anal. Biochem. 184 (1990) 263.
[19] M. Floreani, M. Petrone, P. Debetto, P. Palatini, Free Radic. Res. 26 (1997) 449.
[20] M. Koller, H. Eckert, Anal. Chim. Acta 352 (1997) 31.
[21] D. Tsikas, J. Sandmann, D. Holzberg, P. Pantazis, M. Raida, J.C. Frolich, Anal. Biochem. 273 (1999) 32.
[22] I. Molnar-Perl, J. Chromatogr. A 913 (2001) 283.
[23] V.H. Cohn, Lyle, Anal. Biochem. 14 (1966) 434.
[24] P.J. Hissin, R. Hilf, Anal. Biochem. 74 (1976) 214.
[25] A.R. Ivanov, I.V. Nazimov, L. Baratova, A.P. Lobazov, G.B. Popkovich, J. Chromatogr. A 913 (2001) 315.
[26] M.A. Raggi, R. Mandrioli, C. Sabbioni, F. Mongiello, M. Marini, S. Fanali, J. Microcolumn Sep. 10 (1998) 503.
[27] K. Imai, S. Uzu, T. Toyo'oka, J. Pharm. Biomed. Anal. 7 (1989) 1395.
[28] I.K. Abukhalaf, N.A. Silvestrov, J.M. Menter, J. Pharm. Biomed. Anal. 28 (2002) 637.
[29] B. Tang, Y. Xing, P. Li, N. Zhang, F. Yu, G. Yang, J. Am. Chem. Soc. 129 (2007) 11666.
[30] M. Marcos, P.J. Chmielewski, Org. Lett. 10 (2008) 837.
[31] R. Paroni, E. De Vecchi, G. Cighetti, et al., Clin. Chem. 41 (1995) 448.
[32] P.C. Jocelin, A. Kamminga, Anal. Biochem. 37 (1970) 417.
[33] E. Beutler, C. West, Anal. Biochem. 81 (1977) 458.
[34] R. Brigelius, C. Muckel, T.P.M. Akerboom, H. Sies, Biochem. Pharmacol. 32 (1983) 2529.
[35] C. Russel, J.R. Scaduto, Anal. Biochem. 174 (1988) 265.
[36] M. Hasani, M. Moloudi, F. Emami, Anal. Biochem. 370 (2007) 68.
[37] A.A. Ensafi, T. Khayamian, R. Tabaraki, Talanta 71 (2007) 2021.
[38] B. Hemmateenejad, A. Abbaspour, H. Maghami, R. Miri, M.R. Panjehshahin, Anal. Chim. Acta 575 (2006) 290.
[39] Z. Rezaei, B. Hemmateenejad, S. Khabnadideh, M. Gorgin, Talanta 65 (2005) 21.
[40] M. Shamsipur, J. Tashkhourian, B. Hemmateenejad, H. Sharghi, Talanta 64 (2004) 590.
[41] K. Kargosha, A.H.M. Sarrafi, J. Pharm. Biomed. Anal. 26 (2001) 273.
[42] G.M. Escandar, A.C. Olivieri, N.M. Faber, H.C. Goicoechea, A.M. de la Peña, R.J. Poppi, Trends Anal. Chem. 26 (2007) 752.
[43] H. Abdollahi, A. Safavi, S. Zeinali, Chemometr. Intell. Lab. Syst. 94 (2008) 112.
[44] K. Vatsavai, H.C. Goicoechea, A.D. Campiglia, Anal. Biochem. 376 (2008) 213.
[45] A. Espinosa-Mansilla, A.M. de la Peña, F. Cañada-Cañada, D.G. Gómez, Anal. Biochem. 347 (2005) 275.
[46] Rasmus Bro, Chemometr. Intell. Lab. Syst. 38 (1997) 149.
[47] C.M. Anderson, R. Bro, J. Chemometr. 17 (2003) 200.
[48] A. Brent, T. Neuschwander, F. Jozeph Roll, Anal. Biochem. 179 (1989) 236.
[49] F. Michelet, R. Gueguen, P. Leroy, et al., Clin. Chem. 41 (1995) 1509.
[50] J.D. Adams, J.N. Johannesen, J.P. Bacon, Clin. Chem. 33 (1987) 1675.
[51] J.D. Adams, E. Khaw, G. Jaresko, et al., Res. Commun. Subst. Abuse 11 (1990) 153.
[52] M. Kretzschmar, D. Muller, J. Hubscher, et al., Int. J. Sports Med. 12 (1991) 218.
[53] M.A. Mansoor, A.M. Svardal, P.M. Ueland, Anal. Biochem. 200 (1992) 218.

Talanta 79 (2009) 576–582

Contents lists available at ScienceDirect

Talanta

journal homepage: www.elsevier.com/locate/talanta

Improvement of extraction capability of magnetic molecularly imprinted polymer beads in aqueous media via dual-phase solvent system

Yuling Hu*, Ruijin Liu, Yi Zhang, Gongke Li*

School of Chemistry and Chemical Engineering, Sun Yat-sen University, 135 Xingang Xi Road, Guangzhou 510275, China

ARTICLE INFO

Article history:
Received 14 February 2009
Received in revised form 10 April 2009
Accepted 16 April 2009
Available online 24 April 2009

Keywords:
Magnetic molecularly imprinted polymer beads
Dual-phase solvent system
High-performance liquid chromatography
Triazines

ABSTRACT

In this study, a novel and simple dual-phase solvent system for the improvement of extraction capability of magnetic molecularly imprinted polymer (MIP) beads in aqueous sample was proposed. The method integrated MIP extraction and micro-liquid–liquid extraction (micro-LLE) into only one step. A magnetic MIP beads using atrazine as template was synthesized, and was applied to aqueous media by adding micro-volume of n-hexane to form a co-extraction system. The magnetic MIP beads preferred to suspend in the organic phase, which shielded them from the disturbance of water molecule. The target analytes in the water sample was extracted into the organic phase by micro-LLE and then further bound to the solid-phase of magnetic MIP beads. The beads specificity was significantly improved with the imprinting efficiency of template increasing from 0.5 to 4.4, as compared with that in pure aqueous media. The extraction capacity, equilibration process and cross-selectivity of the MIP dual-phase solvent extraction system were investigated.

The proposed method coupled with high-performance liquid chromatography was applied to the analysis of atrazine, simazine, propazine, simetryn, prometryne, ametryn and terbutryn in complicated sample such as tomato, strawberry juice and milk. The method is selective, sensitive and low organic solvent-consuming, and has potential to broaden the range of MIP application in biological and environmental sample.

1. Introduction

Molecularly imprinted polymers (MIPs) are synthetic artificial receptors produced by the cross-linking of functional monomers in the presence of the template molecule. Removal of the template yields imprinted cavity capable of recognizing template molecule under appropriate conditions. By mimicking bio-system, molecular imprinting technology provides a promising alternative way to create highly selective materials with the additional advantages of reusability and low-cost [1]. MIPs have found wide applications in chromatographic separation [2], sensors [3], solid-phase extraction (SPE) [4,5] and solid-phase microextraction (SPME) [6–8].

However, MIPs always demonstrate their best performance in hydrophobic organic solvents such as n-hexane or toluene. A well documented obstacle to the wider application of MIPs is the issue of aqueous compatibility, because the presence of polar solvents, especially water, will inevitably weaken the interaction forces formed between the template and the functional monomers resulting in poorer selectivity [9]. Unfortunately, there are many applications which require MIPs capable of operating in more polar solvents such as acetonitrile, methanol, and ultimately water. Development of new strategies for use of MIPs in aqueous environment is desirable, as most environmental or biological samples exist in an aqueous matrix.

One of the strategies was focused on development of water-compatible MIPs. A representative approach was preparing imprinted polymer in aqueous media. Recently Yan et al. [10] prepared a water-compatible MIPs in water–methanol systems for selective extraction and separation of ciprofloxacin from human urine samples, and the results revealed that the obtained MIPs have high affinity for ciprofloxacin in aqueous environment. Not always however, the method was effective to allow practical application of the synthesized polymer. Traditional MIP preparation methods are usually carried out in organic phase. An alternative approach for imprinting of water-soluble molecules is to use organic-soluble analogues complementary to substructures of the target as dummy template [11]. Other reports focused on development of water-compatible MIP using novel monomers, such as polymerisable β-cyclodextrin. This unique monomer comprised a hydrophobic moiety capable of screening interactions between monomers and template from adverse effect of an aqueous media. Selective recognition was successfully obtained with β-cyclodextrin as monomer for some biomolecules such as tryptophan, steroids and

* Corresponding authors. Tel.: +86 20 84110922; fax: +86 20 84112245.
E-mail addresses: ceshyl@mail.sysu.edu.cn (Y. Hu), cesgkl@mail.sysu.edu.cn (G. Li).

0039-9140/$ – see front matter © 2009 Elsevier B.V. All rights reserved.
doi:10.1016/j.talanta.2009.04.029

cholesterol in aqueous media [12–15]. Different imprinting methods, such as metal ion-mediated imprinting [16], stoichiometric imprinting [17–19] have also been investigated during the past few years.

Another practical strategy to solve the problem of MIP water-compatibility was to employ two-step extraction method. Martínez et al. [20] investigated the using of propazine-MIP as a clean-up sorbent for organic extracts obtained in a prior SPE procedure. The analytes percolate through the propazine-MIP in an organic media coming from the previous SPE step, which successfully avoided the disturbance from water. In addition, liquid–liquid extraction (LLE), were more commonly applied as an additional extraction step to transfer analytes from aqueous media to organic phase prior to MIP-SPE or MIP-SPME [7,8]. However, these procedures are complicate, time-consuming and analytes may be partly lost in sample preparation steps. Piletska et al. [21] employed a simple method by depositing a layer of mineral oil onto the surface of the polymer to create a hydrophobic environment and to improve the recognition properties of MIP in polar solvent. The effect in water media however was less pronounced.

Triazines are a kind of controlled herbicides for its risks of healthy harm. Many authors have employed MIPs for selective extraction of triazine [22–24]. However, when the analyte is present in an aqueous media, the analyte and other interfering compounds are retained non-specifically on the MIP [8,24]. It is necessary to include a clean-up step with an organic solvent to enhance the selectivity of MIP prior to the elution step but resulting in a reduced recovery.

The aim of this work was to develop a simple and low organic solvent-consuming method for enhancing selectivity of the MIP beads in aqueous sample. For the purpose of this study magnetic molecularly imprinted polymer beads using atrazine as template was synthesized by suspension polymerization with microwave irradiation, and subsequently employed in a dual-phase solvent system in which small amount of organic solvent was added in the sample matrix. The analytes of interest was transferred from the aqueous media to the organic phase and then onto the magnetic MIP beads which was protected by organic phase around them. This method integrated micro-LLE and MIP extraction into only one step, and was applied to the pretreatment of triazines in tomato, strawberry juice and milk before chromatographic analysis.

2. Experimental

2.1. Chemicals

Atrazine, simazine, propazine, simetryn, prometryne, ametryn and terbutryn standards were obtained from Bingzhou Pesticide Plant (Shandong, China). Stock solutions of triazines were prepared at a concentration of 200 mg/L in methanol, and the standard solutions of lower concentration were prepared by the serial dilution of the stock solutions. Methacrylic acid (MAA) and azo(bis)-isobutyronitrile (AIBN) were provided by Damao Reagent Plant (Tianjin, China). Styrene (St) was purchased from Tianjin Reagent Plant (Tianjin, China). Divinylbenzene (DVB) was obtained from Qunli Reagent Chemical Industry Corporation (Shanghai, China). Ethylene glycol (PEG 6000) was purchased from Xilong Chemical Plant (Shantou, China). Ferric chloride ($FeCl_3{\cdot}6H_2O$) and ferrous sulfate ($FeSO_4{\cdot}7H_2O$) was obtained from Shenyang Chemical Industry Corporation (Shenyang, China). Acetonitrile, methanol and n-hexane were HPLC grade solvents, and were purchased from Merck (Darmstadt, Germany). Water was doubly distilled. All other reagents were of analytical grade. All solutions used for HPLC were filtered through a nylon 0.45 μm filter before use.

2.2. Magnetic MIP beads production under microwave irradiation

Magnetite particles were synthesized by co-precipitation with a mixture solution containing $FeCl_3$ (1.0 mol/L) and $FeSO_4$ (0.5 mol/L) in ammonia aqueous solution (28 wt.%), which have been reported in the literature [25].

Magnetic MIP beads were prepared under microwave irradiation following the procedure of our recent study [26]. Atrazine (0.215 g, 1.0 mmol) and MAA (0.34 mL, 4.0 mmol) were dissolved in toluene (4.0 mL, 37.7 mmol). The solution was sparged with oxygen-free nitrogen and then stored in dark for 12 h. The magnetite particles were modified by PEG. The pre-polymer solutions, PEG–Fe_3O_4 particles suspended solution, dispersing media (water, 80 mL), St (9.14 mL, 79.6 mmol), cross-linker (TRIM, 2.55 mL, 8 mmol and DVB 1.13 mL, 8 mmol) and initiator (AIBN, 0.100 g, 0.6 mmol) were adequately mixed in a 300 mL single-necked flask and dispersed by vigorous agitation (600 rpm), bubbled with a nitrogen stream throughout the procedure. Polymerization was carried out in the MAS-I microwave synthesizer (Sineo, Shanghai), with a programmed temperature control under nitrogen protection. The polymeric mixture was firstly heated by microwave heating from 25 to 45 °C within 2 min, rise to 60 °C in 2 min, then achieved 70 °C in 1 min, and finally kept at 70 °C for 120 min.

The template was removed by extensive washing with 10% (v/v) acetic acid in methanol with ultrasonic agitation, until no atrazine leakage was observed from the magnetic MIP beads. Non-imprinted polymer (NIP) magnetic beads were prepared in the same way but without the addition of the template to the polymerization mixture.

2.3. MIP extraction performance in a dual-phase solvent system

The imprinted polymer beads were screened for the particle size fractions at the range of 120–150 μm. The particle size distribution was tested by a Malvern Master Sizer 2000 particle size analyzer from Malvern (Malvern, Britain). The polymer beads were cleaned up with methanol before use, and then placed in 120 °C in vacuum oven 12 h.

0.040 g magnetic imprinted beads were suspended in 0.5 mL n-hexane in a glass sample vial, to which 3.0 mL of de-ionized water containing 15 μg/L triazines was added. This resulted in the formation of two immiscible phases with the polymer beads suspended in the organic phase because of the hydrophobic surface characteristic of the polymer. Samples were agitated by rocking at room temperature. After appropriate extraction time, the polymer was separated from the solution by a magnetic separation step and cleaned by n-hexane to remove non-specifically adsorbed analytes on the polymer surface. The target analytes were desorbed by 1.0 mL methanol, dealt with a nitrogen drying step and re-dissolved in a 100 μL methanol. Then 20 μL of the portion were injected in HPLC system and analyzed. Control experiments were conducted with the magnetic NIP beads instead of magnetic MIP beads or in the absence of any polymer particles.

2.4. Chromatographic separation

HPLC–UV was performed on a Shimadzu LC-2010 system consisted of a low-pressure gradient solvent pump, an auto-sampler and a UV–vis detector. The analytical column was a C_{18} column 250 mm × 4.6 mm I.D., 5 μm (Dikma) with an attached 7.5-mm C_{18} security guard column (Phenomenex, USA). The mobile phase was acetonitrile/water (30:70, v/v) and then changed linearly to acetonitrile/water (68:32, v/v) within 28 min at a flow rate of 1.0 mL/min. The detection wavelength was 225 nm for triazines.

Table 1
The extraction amounts of atrazine on magnetic MIP beads, magnetic NIP beads and the imprinting efficiency (binding ratio of MIP and NIP) in different extraction solvents and the corresponding Snyder polarity index of extraction solvents.

	Water	Methanol	Chloroform	n-Hexane	Dual-phase solvent[a]	Dual-phase solvent[b]
Snyder polarity index	10.2	6.6	4.4	0.1	–	–
MIP (ng)	1.2 ± 0.1	2.8 ± 0.1	4.0 ± 0.3	9.5 ± 0.3	10.1 ± 0.3	20.6 ± 0.1
NIP (ng)	2.3 ± 0.2	2.4 ± 0.1	1.3 ± 0.1	2.1 ± 0.2	2.3 ± 0.2	3.1 ± 0.1
Imprinting efficiency	0.5	1.2	3.0	4.5	4.4	6.6

[a] The dual-phase solvent system composed of 3 mL n-hexane and 3 mL water.
[b] The dual-phase solvent system composed of 0.5 mL n-hexane and 3 mL water.

2.5. Sample applications

The tomatoes of each sample (700 g) was chopped, triturated and homogenized in a blender, sifted and a portion of 50 g was placed into a glass bottle. The solution was spiked with triazines at concentration of 0.005, 0.015 and 0.030 mg/kg. Then 1 g polyvinyl pyrrolidone (PVP) was added to the sample solution. The blended solution was subsequently shaken for 3 min in a vortex mixer at high speed. After filtration through a Buchner funnel, the sample was submitted to MIP extraction mentioned above.

The strawberry juice purchased from market was pretreated by PVP following the same procedure as tomatoes.

35 mL milk was diluted by 15 mL de-ionized water and then blended with 0.1 g active carbon with vigorous stirring to remove protein. After filtration through a Buchner funnel, the sample was extracted by magnetic MIP beads in a dual-phase solvent extraction system.

3. Results and discussions

3.1. Evaluation of MIP binding performance in different media

In this study, microwave heating was utilized for synthesizing magnetic imprinted beads with promoting selectivity and capacity, which was studied in our previous work recently [26]. Magnetic separation provides a simple and convenient method as an alternative to filtration. In this study, the molecularly imprinting recognition was combined with magnetic separation as an approach for triazines analysis in complicated samples.

The binding of template molecule atrazine on both magnetic MIP and NIP beads was assessed in a range of polar, non-polar and intermediate solvents. Table 1 illustrated the binding amounts of atrazine on the magnetic MIP and NIP beads and the imprinting efficiency that was calculated as the binding ratio of MIP and NIP in different extraction solvents. The corresponding Snyder polarity index of the extraction solvents was also illustrated. As shown in Table 1, the magnetic MIP beads exhibited entirely different binding behavior in the solvents with different polarity. Best selectivity on magnetic MIP beads was obtained with n-hexane as extraction solvent. This happens because n-hexane decreases to a minimum the non-specific hydrophobic interactions and creates the suitable environment for electrostatic interactions, which play a very important role in molecular recognition. The imprinting efficiency decreases with increase of the polarity of the solvents. When the polymer beads was performed extraction in pure water environment, the extraction amounts of template on magnetic MIP beads was even less than that on magnetic NIP beads. This was unsurprising due to the strong disturbance from the hydrogen bond interaction between the aqueous molecule and the imprinting sites. One possibility would be to find a way to restrict access of aqueous molecules into the binding sites of MIP beads.

3.2. Establishment of the MIP dual-phase solvent extraction system

The initial excellent performance of magnetic MIP beads in n-hexane and the essential immiscible nature of the solvent in water enlightened us to develop a MIP extraction method in a dual-phase solvent system. As illustrated in Fig. 1, the polymer beads were suspended in the micro-volume of n-hexane and mixed with water sample. The extraction was then performed by rocking. It was observed that the magnetic MIP and NIP beads preferred to remain in the organic phase because of the considerably hydrophobic nature of the divinylbenzene based polymer. This resulted in dispersion of small drops of organic phase with the enveloped polymer beads core. This was key phenomenon which largely inhibits water molecules from entering the MIP pores and template specific binding sites. n-Hexane functioned both as a shielding and an extraction reagent. The target analytes in the water sample was extracted into the organic phase by micro-LLE and then further bound onto the solid-phase of magnetic MIP beads. It can be seen from Table 1 that the imprinting efficiency (binding ratio of MIP:NIP) of template molecule increased significantly from 0.5 in the pure aqueous environment to 4.4 in the dual-phase solvent

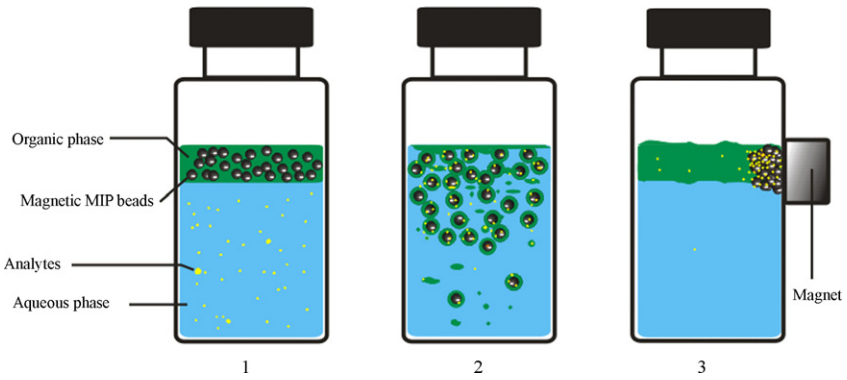

Fig. 1. Extraction procedure of the magnetic MIP beads in the dual-phase solvent system. (1) Adding the magnetic MIP beads suspended in the n-hexane to aqueous solution; (2) agitation of the solution and extraction and (3) magnetic separation.

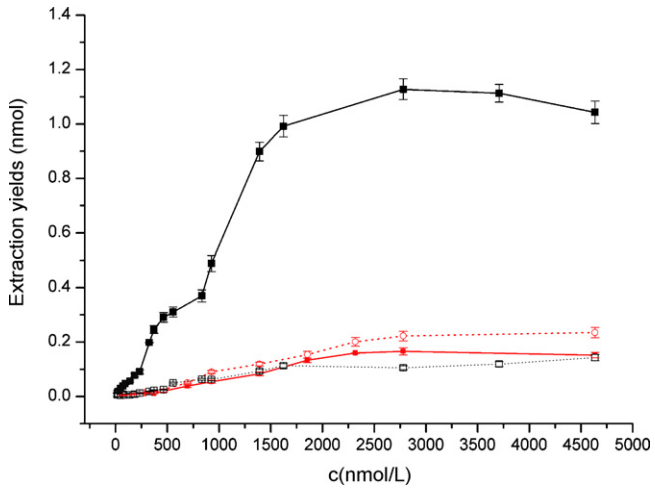

Fig. 2. Binding isotherm for adsorption of atrazine on the magnetic MIP beads (solid line and symbol) and the magnetic NIP beads (dash line and open symbol) in dual-phase solvent system (■) and water (●).

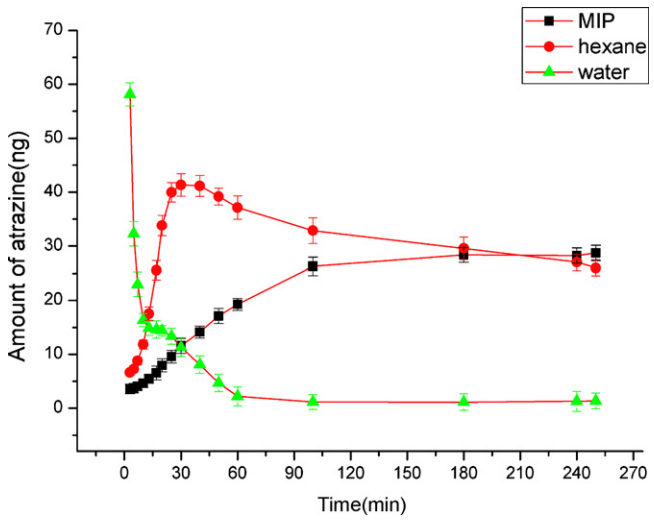

Fig. 3. The amount of atrazine in the polymer phase (■), the organic phase (●) and the aqueous phase (▲) with increase of extraction time. The original concentration in the aqueous phase was 50 μg/L.

system when the volume ratio of n-hexane:water was 1:1. This was found to be extremely close to that in the n-hexane alone. The results illustrated that specificity of the magnetic MIP beads was protected by the surrounding organic phase while exposed to the aqueous environment in the dual-phase solvent system. In the case of the dual-phase solvent system when the volume ratio of n-hexane:water was 1:6, higher imprinting efficiency was obtained. This phenomenon may therefore arise due to the difference in free concentration of atrazine in the organic phase at equilibrium in the presence of a second solvent.

3.3. Binding capacity of the magnetic MIP beads in dual-phase solvent system

The binding capacity of the magnetic MIP beads in dual-phase solvent system was evaluated. Fig. 2 shows the binding isotherm for adsorption of atrazine on magnetic MIP beads and the control polymer in dual-phase solvent system with 0.5 mL n-hexane added to 3 mL water sample, and was compared with that in pure water. As seen, the binding amounts increases gradually with the increase of the concentration of atrazine in the initial solution for each case. However, it is obvious that the binding capacity of the atrazine on MIP in dual-phase solvent system was much higher than that in water alone. In addition, MIP and NIP showed completely different binding behavior with the increase of atrazine concentration in dual-phase solvent system, whereas the binding isotherms of MIP and NIP were similar in water. The slight adsorption of atrazine on MIP and NIP in water was mostly ascribed to non-specific binding such as hydrophobic interaction. As a proof of concept, the results indicated that the specificity of the imprinted polymer beads was retained and strengthened in the dual-phase solvent system.

3.4. Equilibrium and kinetic consideration

As in traditional MIP evaluation in the single-phase solvent system, equilibrium is established between the bound and free analytes. In the case of this current system, equilibrium is established among the three phases. There are two equilibriums in the system, and the extraction equations for analyte *i* can be written as

$$i_w \overset{k_{org/w}}{\longleftrightarrow} i_{org} \overset{k_A}{\longleftrightarrow} i_p$$

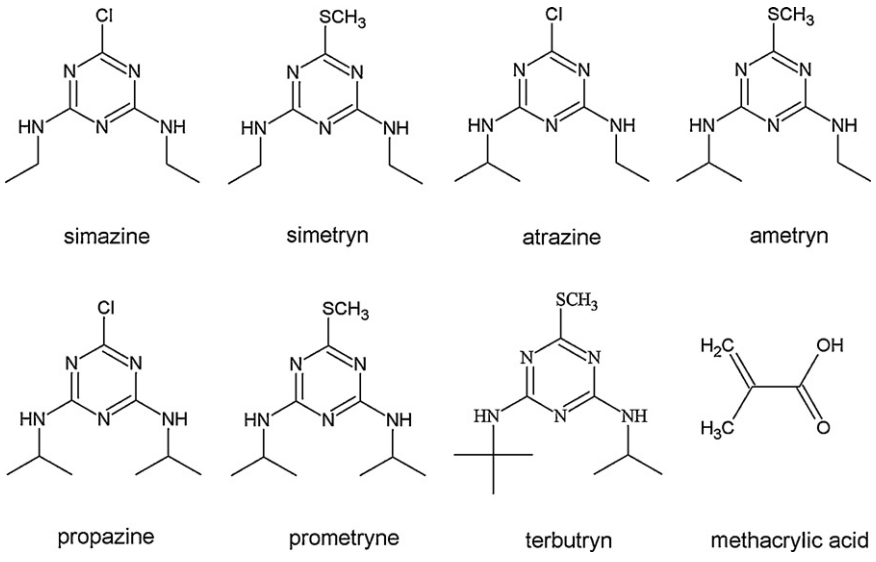

Fig. 4. The structures of the triazines and the monomer.

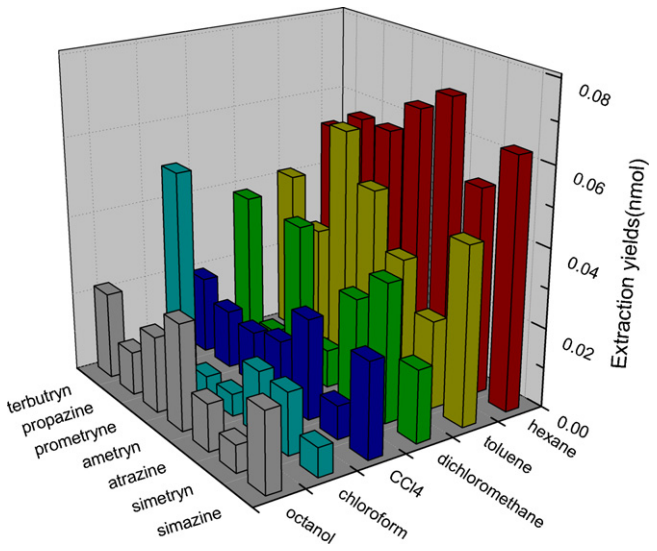

Fig. 5. The extraction yields of seven triazines in different dual-phase solvent system. The concentration of each triazine in the aqueous phase was 50 μg/L.

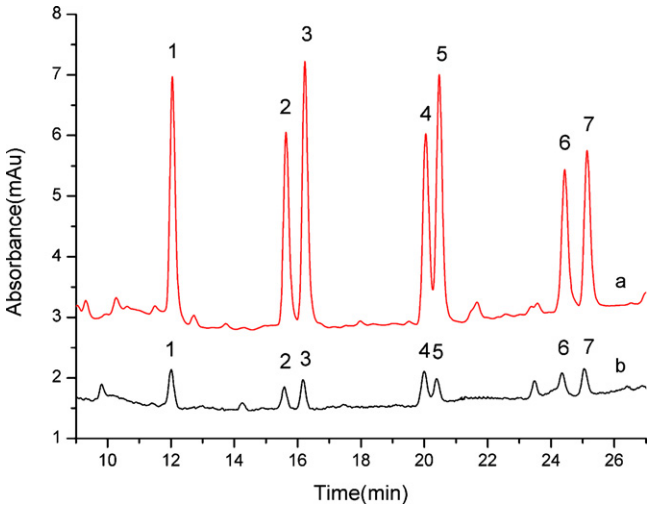

Fig. 6. Chromatogram of the triazines mixed standard solution after extraction by the magnetic imprinted beads in a dual-phase solvent system (a) and in pure water (b). 1 simazine, 2 simetryn, 3 atrazine, 4 ametryn, 5 prometryne, 6 propazine and 7 terbutryn.

where the subscript w represents the aqueous phase, org, the organic phase and p the polymer phase. The constants, $k_{org/w}$ and k_A are equilibrium constants.

Fig. 3 depicted the amount of atrazine in the aqueous phase, the organic phase and the polymer phase with the increase of extraction time from 3 to 250 min. As shown in Fig. 3, the micro-LLE between the aqueous phase and the organic phase and the MIP extraction between the organic phase and the polymer was performed simultaneously. The mass transfer is relative a faster procedure for the first extraction process and slower for the latter. It should take about 240 min to reach equilibrium among the three phases. The partition coefficient of solute between the organic phase and the aqueous phase was calculated at 125.9. The distribution coefficient, which was defined as the ratio of the concentration of the solute between the polymer phase and the organic phase at equilibrium, was 13.1 mL/g. Although the equilibration time was relatively long, it was not necessary to take such a long time in practical analysis [27], because quantitative analysis is feasible in nonequilibrium situations once the extraction conditions, such as agitation speed and adsorption time, are held constant.

3.5. Extraction of structural analogues

The synthetic MIPs usually show cross-selectivity towards its structural analogues besides the template molecule. Consequently, simultaneous extraction of the template and six other structural analogues, including simazine, propazine, simetryn, prometryne, ametryn and terbutryn, by the magnetic MIP beads in the dual-phase solvent system was investigated. The structures of the triazines and the monomer were shown in Fig. 4.

Firstly, the extraction behavior of seven triazines in different dual-phase solvent system was investigated. For the purpose of the present study six water-immiscible solvents were tested and the results were illustrated in Fig. 5. The experimental results showed that n-hexane exhibits the best extraction performance to most of the triazines. The extraction yields were low with octanol as organic phase due to the disturbance of the hydroxyl group in the octanol molecule to hydrogen bonding interaction between triazines and the imprinted polymer.

The magnetic MIP beads showed considerable high cross-reactivity to the analogues of the template in the n-hexane/water dual-phase solvent system. The imprinting efficiency was calculated at 4.4 (atrazine), 4.2 (simazine), 3.6 (simetryn), 3.0 (ametryn), 3.2 (propazine), 2.9 (terbutryn) and 2.4 (prometryne), respectively. Consequently the method can be applied to the simultaneous extraction of these triazine herbicides.

The sensitivity of the triazines also increased significantly owing to double enrichment process. Fig. 6 compared chromatogram of the seven triazines after extraction by the magnetic MIP beads in a dual-phase solvent system and in pure water. It can be seen in Fig. 6 that the amount of triazines extracted by MIP in the dual-phase solvent system were 3.1–6.6-fold of that in pure water samples.

3.6. Investigation of the extraction conditions

In order to obtain the optimized extraction conditions and best extraction efficiency we used the peak areas of analyte as the HPLC response to evaluate the extraction efficiency under different conditions.

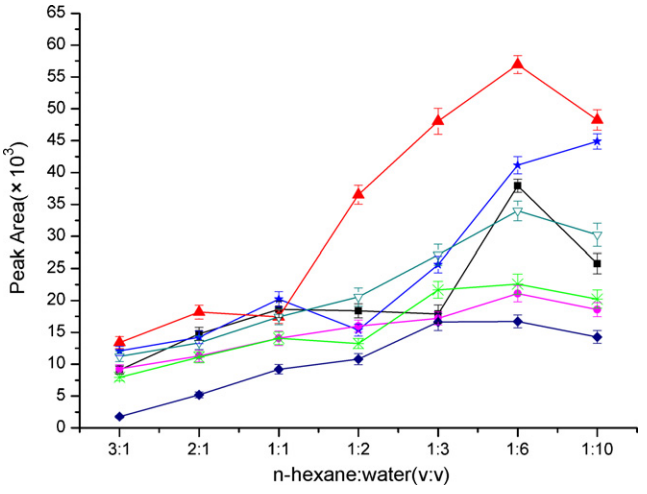

Fig. 7. Binding of triazines on the magnetic imprinted beads with different ratio of n-hexane and water. Triazines are simazine (■), simetryn (★), atrazine (▲), ametryn (▽), prometryne (●), propazine (*), prometryne (♦).

Table 2
Recoveries (*R*) and RSD of triazines for spiked tomato, strawberry juice and milk samples ($n = 6$).

Compounds	Tomato						Strawberry juice						Milk					
	0.005 mg/kg		0.015 mg/kg		0.030 mg/kg		0.005 mg/kg		0.015 mg/kg		0.030 mg/kg		0.005 mg/kg		0.015 mg/kg		0.030 mg/kg	
	R%	RSD%	*R*%	RSD%	*R*%	RSD%	*R*%	RSD%	*R*%	RSD%	*R*%	RSD%	*R*%	RSD%	*R*%	RSD%	*R*%	RSD%
Simazine	115.9	9.7	90.3	7.5	116.9	9.6	111.2	5.7	88.0	8.3	91.0	7.6	101.0	9.8	94.5	7.9	111.4	4.9
Simetryn	101.9	8.3	81.4	7.6	82.8	7.8	84.7	5.2	104.7	9.7	95.2	7.4	89.4	8.9	99.9	3.8	90.2	7.9
Atrazine	102.0	5.9	111.3	3.3	96.0	2.6	101.8	8.7	112.9	9.1	80.2	6.6	88.0	3.4	104.2	8.9	90.3	5.1
Ametryn	118.5	7.4	91.7	3.8	90.2	8.3	115.6	9.8	103.0	7.9	81.4	8.2	113.2	8.5	93.2	4.8	98.9	6.5
Prometryne	71.6	8.9	83.5	4.6	86.0	7.0	84.3	6.0	80.3	9.9	82.2	5.8	82.1	9.2	103.4	7.3	86.3	6.5
Propazine	89.9	10.6	81.3	5.9	107.2	6.9	93.4	9.8	95.2	9.7	110.4	4.2	87.5	9.9	99.8	6.4	85.2	5.6
Terbutryn	93.3	10.7	81.5	4.8	85.7	6.5	91.3	8.5	110.2	6.9	91.2	8.2	83.3	9.5	98.5	10.3	95.2	6.1

The optimized amount of organic solvent in the MIP dual-phase solvent extraction system was investigated by evaluation of peak areas of triazines with different ratio of n-hexane and water. The results, shown in Fig. 7, indicated that the extraction efficiency was the highest in the mixture of n-hexane and water with volume ratio of 1:6. That is, for extraction of 3 mL water sample, only 0.5 mL organic solvent was required for addition.

The effect of polymer amounts for extraction was examined in the range of 10–60 mg polymer beads at room temperature with constant shaking rate. The results indicated that the extraction efficiency increased with the polymer increasing from 10 to 40 mg and approximately no changes up to 60 mg. Therefore, a 40-mg magnetic MIP beads was selected for extraction.

Shaking rate is one of the important parameters that affect the extraction efficiency. The effect of sample agitation was evaluated using a shaking rate of between 40 and 200 period/min. The result showed that the extraction efficiency of the triazines improved with the shaking rate being increased until 160 period/min. Therefore, a shaking rate of 160 period/min was selected for sample extraction.

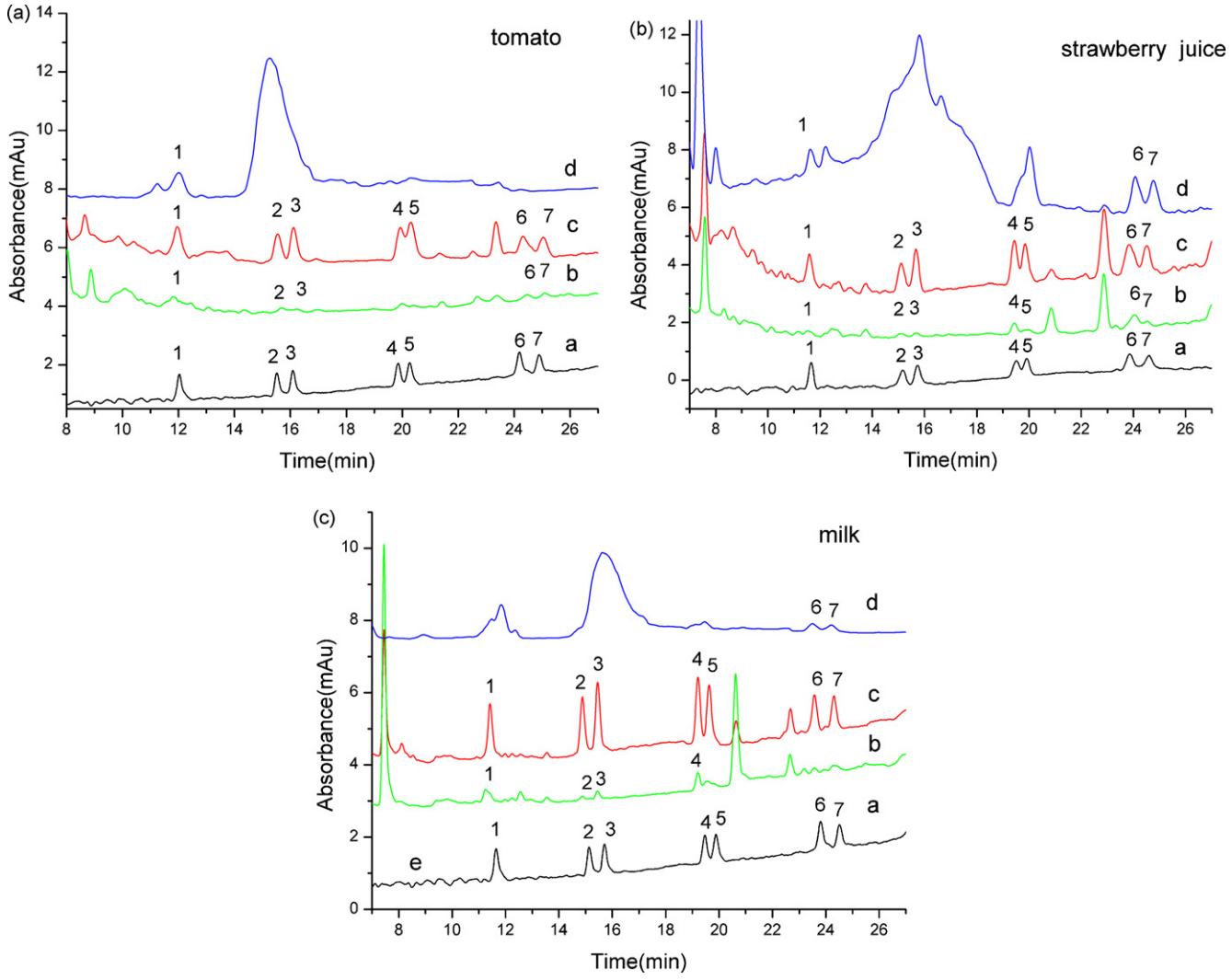

Fig. 8. The chromatogram of the standard triazines (a) and the spiked tomato, strawberry juice and milk samples with 0.015 mg/kg triazines after extraction in the dual-phase solvent system with magnetic NIP beads (b), magnetic MIP beads (c) and without polymer in the sample solution (d). 1 simazine, 2 simetryn, 3 atrazine, 4 ametryn, 5 prometryne, 6 propazine and 7 terbutryn.

3.7. Application in real sample analysis

To validate the applicability of the proposed method, the linearity and limits of detection were investigated using the optimum extraction conditions. Good linearity was achieved in the range of 1.0–40.0 μg/L for the triazines studied, and the detection limits were in range of 0.20–0.63 μg/L.

The established method was applied to analysis of complicated sample such as tomato, strawberry juice and milk. The sample was spiked with atrazine, simazine, simetryn, ametryn, propazine, terbutryn and prometryne and subsequently analyzed. In order to validate the molecular recognition effect of the magnetic MIP beads, the magnetic NIP beads and micro-LLE with n-hexane were used for comparison, respectively. Fig. 8 illustrated the chromatogram of the spiked tomato, strawberry juice and milk samples with 0.015 mg/kg triazines after extraction with magnetic MIP beads, magnetic NIP beads and without polymer in the sample with addition of 0.5 mL n-hexane in the aqueous samples. As shown in Fig. 8, the chromatogram of triazines by solvent extraction was complex due to the complicated matrix effect of the sample solution. Triazines could not be totally detected in the spiked sample solutions by the micro-LLE with 0.5 mL n-hexane as organic solvent although the method showed some enrichment for a few triazines such as simetryn, propazine and terbutryn. The result is easily understood due to the poor selectivity of the solvent extraction method. Similarly, most of the triazines cannot be detected or determined with very low sensitivity by extraction with magnetic NIP beads. The high selectivity was observed for the MIP extraction in dual-phase solvent followed by HPLC analysis owing to the special recognition to template molecules and its structural analogues. The recoveries of the samples spiked with seven triazines at three levels (0.005, 0.015, and 0.030 mg/kg) was found to be from 71.6 to 118.5% with the relative standard deviation (RSD) from 2.6 to 10.7% with six parallel replicate analysis (Table 2).

4. Conclusions

A novel and simple extraction method in a dual-phase solvent system for the improvement of recognition ability of molecularly imprinted polymer in aqueous sample media was proposed. By adding small amount of n-hexane in the aqueous sample, the imprinted polymer specificity was significantly improved by creating a non-polar environment around the binding sites, which could facilitate the interaction between analytes and the synthetic receptor. The imprinting efficiency of template increased from 0.5 to 4.4 and the sensitivity for seven trazines increased 3.1–6.6 times in the dual-phase solvent system, as compared with that in pure aqueous media. The proposed method was applied to selective enrichment of triazines in tomato, strawberry juice and milk before HPLC analysis. Disturbance of hydrogen interaction from the water was prevented and the selectivity and sensitivity was greatly enhanced by the integrated extraction procedure. The method generates possibilities for further use of MIP in other aqueous media such as biological fluids and environmental water.

Acknowledgements

The authors would like to thank the National Natural Science Foundation of China for financially supporting this research under grant numbers 20705042, 20775095, respectively. Thanks to Qisheng Zhong for his kind help to accomplish some of the figures.

References

[1] P.K. Owens, L. Karlsson, E.S.M. Lutz, L.I. Andersson, Trends Anal. Chem. 18 (1999) 146.
[2] F.G. Tamayo, A. Martin-Esteban, J. Chromatogr. A 1098 (2005) 116.
[3] G. D'Agostino, G. Alberti, R. Biesuz, M. Pesavento, Biosens. Bioelectron. 22 (2006) 145.
[4] E. Caro, R.M. Marcé, F. Borrull, P.A.G. Cormack, D.C. Sherrington, Trends Anal. Chem. 25 (2006) 143.
[5] A.C.B. Dias, E.C. Figueiredo, V. Grassi, E.A.G. Zagatto, M.A.Z. Arruda, Talanta 76 (2008) 988.
[6] W.M. Mullett, P. Martin, J. Pawliszyn, Anal. Chem. 73 (2001) 2383.
[7] X.G. Hu, Y.L. Hu, G.K. Li, J. Chromatogr. A 1147 (2007) 1.
[8] X.G. Hu, J.L. Pan, Y.L. Hu, Y. Huo, G.K. Li, J. Chromatogr. A 1188 (2008) 97.
[9] O.K. Castell, C.J. Allender, D.A. Barrow, Biosens. Bioelectron. 22 (2006) 526.
[10] H.Y. Yan, K.H. Rowa, G.L. Yang, Talanta 75 (2008) 227.
[11] X.J. Wang, Z.L. Xua, J.L. Feng, N.C. Bing, Z.G. Yang, J. Membr. Sci. 313 (2008) 9.
[12] X.W. He, W.Y. Li, Y.K. Zhang, L. Qin, J. Chromatogr. A 1187 (2008) 94.
[13] T. Hishiya, M. Shibata, M. Kakazu, H. Asanuma, M. Komiyama, Macromolecules 32 (1999) 2265.
[14] H. Asanuma, T. Akiyama, K. Kajiya, T. Hishiya, M. Komiyama, Anal. Chim. Acta 435 (2001) 25.
[15] Y. Yang, Y.Y. Long, Q. Cao, K. Li, F. Liu, Anal. Chim. Acta 606 (2008) 92.
[16] N. Bereli, M. Andac, G. Baydemir, R. Say, I.Y. Galaev, A. Denizli, J. Chromatogr. A 1190 (2008) 18.
[17] C. Lubke, M. Lubke, M.J. Whitcombe, E.N. Vulfeon, Macromolecules 33 (2000) 5098.
[18] J.L. Urraca, M.C. Moreno-Bondi, A.J. Hall, B. Sellergren, Anal. Chem. 79 (2007) 695.
[19] J.L. Urraca, A.J. Hall, M.C. Moreno-Bondi, B. Sellergren, Angew. Chem. Int. Ed. 45 (2006) 5158.
[20] R. Carabias-Martínez, E. Rodríguez-Gonzalo, E. Herrero-Hernández, J. Chromatogr. A 1085 (2005) 199.
[21] E.V. Piletska, M. Romero-Guerra, A.R. Guerreiro, K. Karim, A.P.F. Turner, S.A. Piletsky, Anal. Chim. Acta 542 (2005) 47.
[22] I. Ferrer, F. Lanza, A. Tolokan, V. Horvath, B. Sellergren, G. Horvai, D. Barceló, Anal. Chem. 72 (2000) 3934.
[23] F. Chapuis, V. Pichon, F. Lanza, S. Sellergren, M.C. Hennion, J. Chromatogr. A 999 (2003) 23.
[24] R. Carabias-Martínez, E. Rodríguez-Gonzalo, E. Herrero-Hernández, Anal. Chim. Acta 559 (2006) 186.
[25] R.Y. Hong, T.T. Pan, H.Z. Li, J. Magn. Magn. Mater. 303 (2006) 60.
[26] Y. Zhang, R.J. Liu, Y.L. Hu, G.K. Li, Anal. Chem. 81 (2009) 967.
[27] J. Ai, Anal. Chem. 69 (1997) 1230.

Talanta 79 (2009) 804–809

Contents lists available at ScienceDirect

Talanta

journal homepage: www.elsevier.com/locate/talanta

Magnesium effect on the acetylcholinesterase inhibition mechanism: A molecular chromatographic approach

F. Ibrahim, Y.C. Guillaume*, M. Thomassin, C. André

Equipe des Sciences Séparatives, Biologiques et Pharmaceutiques (2SBP/EA-4267), Laboratoire de Chimie Analytique, Faculté de Médecine-Pharmacie, CHU-Jean Minjoz, Université de Franche-Comté, Place Saint Jacques, 25030 Besançon Cedex, France

ARTICLE INFO

Article history:
Received 19 January 2009
Received in revised form 30 April 2009
Accepted 5 May 2009
Available online 15 May 2009

Keywords:
Acetylcholinesterase
Inhibitors
Association
Magnesium
Column liquid chromatography

ABSTRACT

The acetylcholinesterase enzyme (AChE) was immobilized on a chromatographic support to study the effect of magnesium on the binding mechanism of five AChE inhibitors (donepezil, tacrine, galanthamine, physostigmine and huperzine). The determination of the enthalpy and entropy changes of this binding at different magnesium concentration values suggested that van der Waals interactions and hydrogen bonds predominated the donepezil and tacrine association to AChE. As well, hydrophobic and electrostatic forces seemed to be the major interactions controlling the huperzine, galanthamine and physostigmine association with AChE. In addition, it appeared that magnesium cation increased the binding affinity of galanthamine and physostigmine to the active site gorge of AChE. A comparison of the inhibitors hydrophobicity to their relative bound percentage with AChE showed an affinity enhanced with the increase in the molecule hydrophobicity and confirmed that the hydrophobic forces played an important role in the AChEI–AChE binding process. This novel biochromatographic column could be useful to find a specific inhibitor for this enzyme and so open new perspectives to be investigated.

1. Introduction

Alzheimer's disease (AD) is a common age-related neurodegenerative pathology with neurological and psychiatric manifestations. The greatly reduced presence of acetylcholine in the cerebral cortex is a significant factor in AD [1,2]. The enzyme acetylcholinesterase (AChE) catalyzes the hydrolysis of the ester bound of acetylcholine (ACh) to terminate the impulse transmitted action of ACh through cholinergic synapses, therefore the inhibition of acetylcholinesterase (AChE) activity may be one of the most realistic approaches to the symptomatic treatment of AD [3]. Many medicinal agents, as donepezil, huperzine or rivastigmine, used for treatment of Alzheimer's disease, belong to the important class of acetylcholinesterase inhibitors (AChEIs) [3,4]. The three-dimensional structure for *Torpedo californica* AChE was resolved in 1991 [5]. Sussman and co-workers have shown that, structurally, there is a narrow active site gorge about 20 Å deep which consists of two separated ligand binding sites, the acylation (or active) site which is located at the bottom of the gorge and the peripheral anionic binding site which is located close to the mouth of the active site gorge. The in vivo and in vitro cholinesterase activity and the effect of inhibitors and cations on this activity have been widely studied in the biomedical literature [6–8], but few studies have examined the mechanism of inhibitors association with AChE and the effect of biological conditions on this association [9]. Magnesium, in particular, seems to have a profound effect on dementias of various types. Cilliler et al. [10] suggested that there is a relationship between serum magnesium levels and the degree of Alzheimer's disease. Glick [11] of the Bionix Corporation reviewed the effects of magnesium in patients with Alzheimer's disease and other dementias. He reported that magnesium may improve memory and alleviate other symptoms in patients with Alzheimer's disease. Therefore, recognition of forces during the AChEI–AChE binding process provides us valuable models for further understanding of acetylcholinesterase inhibitions processes and may open unexplored avenues to other AD treatment. In this study the AChE enzyme was immobilized on amine support by cross-linking reaction with a suitable bifunctional reagent (i.e. glutaraldehyde). This chromatographic support was used to determine and quantify the forces driving association between a series of acetylcholinesterase inhibitors and this enzyme. The energetic of binding of the inhibitor to the enzyme as both a function of temperature and magnesium concentration (x) was studied using a biochromatographic approach.

2. Experimental method

2.1. Reagents and solvents

The five drugs AChEIs were depicted in Fig. 1. Galanthamine and donepezil were obtained from Interchim (Montluçon, France),

* Corresponding author. Tel.: +33 3 81 66 55 44; fax: +33 3 81 66 56 55.
E-mail address: yves.guillaume@univ-fcomte.fr (Y.C. Guillaume).

0039-9140/$ – see front matter © 2009 Elsevier B.V. All rights reserved.
doi:10.1016/j.talanta.2009.05.005

Donepezil	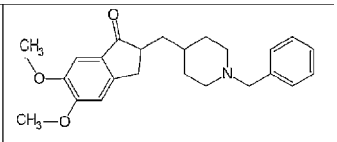
Tacrine	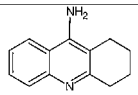
Galanthamine	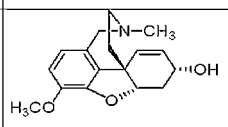
Huperzine A	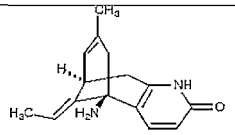
physostigmine	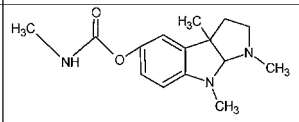

Fig. 1. Chemical structures of AChEIs.

physostigmine and huperzine were purchased from Sigma (Paris, France) and tacrine from Cayman Chemical-Interchim (Montluçon, France).

Acetylcholinesterase from Electrophorus Electricus (electric eel) was purchased from Sigma (Paris, France), glutaraldehyde, Ellman's reagent and sodium cyanoborohydride from Interchim (Montluçon, France) and S-acetylthiocholine from ALFA AESAR-Interchim (Montluçon, France). Monoethanolamine was obtained from Aldrich–Sigma (Paris, France). Water was obtained from an Elgastat option water purification system (Odil, Talant, France) fitted with a reverse osmosis cartridge. Sodium dihydrogenophosphate and di-natriumhydrogenophosphate were obtained from Prolabo and Merck (Paris, France) respectively. The mobile phase consisted of 0.1 M sodium phosphate buffer adjusted at pH 7.4 with magnesium concentrations (x) equal to 0.0, 0.5, 0.75, 1.0, 1.5, 2.0 and 2.5 mmol L^{-1} (including its biological concentration range i.e. 0.75–1.0 mmol L^{-1}). Experiments were carried out over the temperature range 278–308 K (278, 283, 288, 293, 298, 303 and 308 K). The detection wavelength was at 280 nm for donepezil, 210 nm for huperzine and 254 nm for the other molecules. The mobile phase flow-rate was 0.5 mL/min. AChEIs solutions were prepared in the mobile phase, and 20 μL was injected into the chromatographic system. For the determination of the adsorption isotherms, for each AChEI studied, the equilibration of the column was carried out with 15 concentrations of AChEI (0–7 μM) in the mobile phase to obtain a stable detection. 20 μL of the most concentrated AChEI sample was injected at least three times and the retention time was measured.

2.2. Apparatus

The high performance liquid chromatography (HPLC) system consisted of a Hewlett-Packard quaternary pump (1050), an Agilent (G1365B, serie 1100) UV-Visible detector (Paris, France) and a Rheodyne 7725i injection valve (Cotati, CA, USA) fitted with a 20-μL sample loop. The Modulo-Cart HS Uptisphere3 NH2 (50 mm × 4.6 mm) was purchased from Interchim (Montluçon, France), where the propylamino groups were bound onto 3 μm silica particles of 120 Å pore size. The acetylcholinesterase stationary phase (i.e., the AChE column) prepared via the in situ technique is given below.

2.3. Covalent immobilization technique of AChE

The in situ immobilization technique was considered in this study [12–14]. The immobilization of AChE via the amino groups of the enzyme on aminopropyl silica pre-packed column activated with glutaraldehyde was carried out as follows. Briefly, the column was first washed with phosphate buffer (50 mM, pH = 7.0) for 30 min at 0.5 mL/min. Then the stationary phase was activated by recycling glutaraldehyde 10% in phosphate buffer (50 mM, pH 6.0) for 12 h in the dark, followed by washing with phosphate buffer (50 mM, pH 6.0) for 30 min at 0.5 mL/min. A solution of 250 U AChE in 80 mL phosphate buffer (50 mM, pH 6.0) was recirculated through the column at a flow-rate of 0.5 mL/min for 24 h. After immobilization, the enzyme solution was analysed with the Ellman's assay in order to determine the unreacted enzyme units. The Schiff bases were reduced by recycling the derivatized of 0.1 M cyanoborohydride solution in phosphate buffer (50 mM, pH 6.0) for 2 h at 25 °C. The matrix was then washed with phosphate buffer (50 mM, pH 6.0) and then with 0.2 M monoethanolamine solution in phosphate buffer (50 mM, pH 6.0) for 3 h at room temperature. Then the column was rinsed for 1 h with phosphate buffer (pH 7.4, 50 mM) at a flow-rate of 0.5 mL/min and was stored at 4 °C after rinsing with phosphate buffer (50 mM, pH 7.4) containing 0.1% sodium azide. By analysing the enzymatic activity of the enzyme solutions before and after the immobilization using Ellman's assay, the activity decreased about 70%, this means that about 70% of the enzyme in the AChE solution were immobilized on the column stationary phase.

2.4. Langmuir distribution isotherms

Single and multi-component isotherms are now measured by dynamic methods. The most widespread of this is frontal analysis, but this technique is time consuming and requires large amounts of pure compounds [15]. Another popular method, elution by characteristic point (ECP), derives the isotherm from the profile of the diffuse front of the band obtained in response to a single injection of a highly concentrated sample [16]. This method is fast and needs only small amounts of sample, but it requires accurate calibration of the detector and an efficient column. Distribution isotherms can also be apprehended using the perturbation technique originally developed for measuring gas-adsorbent equilibria. The perturbation technique makes possible the determination of adsorption isotherms by measuring the retention times of small sample sizes injected onto a column equilibrated with sample solutions at different concentration levels. The column used for the determination of the isotherm is first equilibrated with a solution containing the compound dissolved in a non-adsorbable solvent. Then a small sample volume containing higher concentration of the compound is injected onto the column. After the injection, the equilibrium condition is disturbed and the perturbation waves reaches the column outlet, a peak is registered by the detector. In the case of a single component equilibrium of a compound dissolved in a non-adsorbable solvent, one peak is observed and the distribution isotherms depends only on the concentration of a single solute [17,18]. The well-known Langmuir theoretical approach relates the total concentration of the sample in the stationary phase (C_S) and

Table 1
Values of the retention contribution of the two kind of sites k'_A and k'_B, the retention factor k'($k' = k'_A + k'_B$) (extrapolated at $C_m = 0$), the relative bound percentage b%, the log P and the non-linear regression coefficients r^2 and F (Langmuir model; Lang and bi-Langmuir model; bi-Lang), for the five AChEIs at a bulk solvent pH = 7.4 and T = 298 K, standard deviations are in parentheses.

AchEI	k'_A	k'_B	k'	b (%)	log P	r^2; F-Lang	r^2; F-bi-Lang
Huperzine	0.54 (0.01)	0.01 (0.01)	0.55 (0.01)	35.40 (0.09)	0.20	0.9993; 2990	0.9996; 6281
Physostigmine	0.73 (0.01)	0.02 (0.01)	0.75 (0.01)	43.00 (0.10)	1.70	0.9998; 8980	0.9999; 600310
Galanthamine	0.73 (0.01)	0.03 (0.01)	0.76 (0.01)	43.30 (0.11)	1.80	0.9998; 7710	0.9998; 8820
Tacrine	2.28 (0.01)	0.02 (0.01)	2.30 (0.01)	69.74 (0.12)	2.20	0.9998; 9040	0.9999; 423930
Donepezil	2.98 (0.02)	0.03 (0.01)	3.01 (0.01)	75.10 (0.12)	3.70	0.9998; 9980	0.9999; 530896

that in the mobile phase (C_m) [17–19]:

$$C_S = \frac{\alpha K C_m}{1 + K C_m} \quad (1)$$

where α is the column saturation capacity and K is the association constant between AChEI in the sample and the AChE stationary phase. The sample AChEI retention factor k' was directly proportional to the slope of its adsorption isotherm and can be thus given by the following equation [17–19]:

$$k' = \frac{t - t_0}{t_0} = \phi \frac{dC_S}{dC_m} = \frac{\phi \alpha K}{(1 + K C_m)^2} \quad (2)$$

where t is the retention time of the solute determined from the peak maximum, t_0 is the column hold up time, i.e., the elution time of a non-retained compound, and ϕ is the column phase ratio (V_S/V_m) (V_S is the volume of the stationary phase in the column and V_m the void volume). By plotting the k' value vs. the sample concentration in the bulk solvent, the parameters $\phi\alpha K$ corresponding to the retention contribution of the AChE binding site under linear condition (i.e., the k' value extrapolated at $C_m = 0$) were calculated using Eq. (2) [17–19]. The main advantage of the perturbation technique consists in using a simpler instrumentation for the acquisition of the experimental data than frontal analysis method: the determination of the concentration of the individual compounds at the intermediate plateaus of the frontal analysis curves is no longer needed [17,18]. As well, using the AChE stationary phase, AChEI could tightly bind to the matrix of the column. Then if AChEI bound on two sites on the stationary phase, i.e. a specific site (site A with an adsorption constant K_A) and a column saturation capacity α_A and second site which is non-specific (sites B with an adsorption constants K_B and a column saturation capacity α_B), then the AChEI retention factor (k') directly proportional to the slope of its adsorption isotherm is given by the following equation [17–19]:

$$k' = \frac{t - t_0}{t_0} = \phi \frac{dC_S}{dC_m} = \phi \left(\frac{\alpha_A K_A}{(1 + K_A C_m)^2} + \frac{\alpha_B K_B}{(1 + K_B C_m)^2} \right) \quad (3)$$

Eq. (3) was fitted to the solute retention factor k' by a non-linear regression and the parameters $k'_A = \phi K_A \alpha_A$ and $k'_B = \phi K_B \alpha_B$ corresponding to the retention contributions of the two kinds of sites under linear conditions were calculated. Valuable informations about the processes driving AChEI–AChE association mechanism can be further gained by examining the temperature dependence of AChEI retention [20,21]. Under linear conditions, the temperature dependence of the retention factor is given by the following relationship:

$$\ln k' = \left(-\frac{\Delta H^\circ}{RT} \right) + \left(\frac{\Delta S^\circ}{R} \right) + \ln \phi \quad (4)$$

where R is the gas constant, T is the column temperature in Kelvin, ΔH° and ΔS° are, respectively, the solute enthalpy and entropy changes accompanying the transfer of the AChEIs from the bulk solvent to the AChE surface. If the AChE stationary phase, AChEI and solvent properties are temperature invariant, a linear van't Hoff plot is obtained and from the slope and intercept ΔH° and ΔS° can be calculated.

3. Results and discussion

3.1. Langmuir distribution isotherms

The Langmuir distribution isotherms were calculated at pH = 7.4 and 298 K. For each AChEI and for each AChEI concentration in the bulk solvent, the most concentrated AChEI sample was injected into the chromatographic system and its retention factor was determined (see Section 2.1). The variation coefficients of the k' values were <0.3%, indicating a high reproducibility and a good stability for the chromatographic system. Using a weighted non-linear regression (WNLIN) procedure, the constants of Eq. (2) were used to estimate the retention factors. The slope of the curve representing the variation of the estimated retention factors (k') (Eq. (2)) vs. the experimental values (0.998; ideal is 1.000) and r^2 (0.996) indicate that there is an excellent correlation between the predicted and experimental retention factors. The non-linear regression coefficient r^2 and the F value (from the Fisher test with the confidence level at 95%) were determined. These are shown in Table 1. The F value constitutes a more discriminating parameter than the r^2 value when assessing the significance of the model equation. From the full regression model, a Student's t-test was used to provide the basis for the decision as to whether or not the model coefficients were significant. Results of the Student's t-test show that no variable can be excluded from the model. These results showed that the Langmuir model describes accurately the association behaviour of AChEI with AChE. However, the immobilization of AChE on silica support could lead to non-specific interactions. Using the non-linear regression, the retention contributions of the two kind of sites k'_A and k'_B were determined from Eq. (3). The corresponding non-linear regression coefficients r^2 and F values of this bi-Langmuir model were determined and given in Table 1. The non-linear coefficient results ($r^2 > 0.99$) and the F values proved that the two Langmuir model described accurately the binding mechanism of AChEI with the AChE stationary phase. As well, the results showed that the interactions between ACEI and the matrix of the stationary phase were neglected (the k'_A and k'_B values were given in Table 1 and $k'_B \ll k'_A$).

3.2. Thermodynamic origins of the AChEI binding to AChE

The k' values were determined for a sample concentration in the mobile phase equal to zero; i.e. $C_m = 0$. The van't Hoff plots ($\ln k'$ vs. $1/T$) of Eq. (4) were drawn for all the AChEI molecules. Linear van't Hoff plots were obtained with correlation coefficients r^2 higher than 0.91 for donepezil, tacrine and huperzine. An example of plot was given for tacrine in Fig. 2. For galanthamine the variations of $\ln k'$ vs. $1/T$ were negligible (Fig. 2). These van't Hoff plot behaviours were thermodynamically expected when the solute–AChE association mechanism was independent of temperature. According to Eq. (4) these van't Hoff plots provided a conventional way of calculating the thermodynamic parameters (ΔH°, ΔS°). For donepezil and tacrine which are dual acetylcholinesterase inhibitors that could bind simultaneously to the peripheral and catalytic sites of the enzyme [22], both ΔH°, ΔS° were negative values (Table 2). Nega-

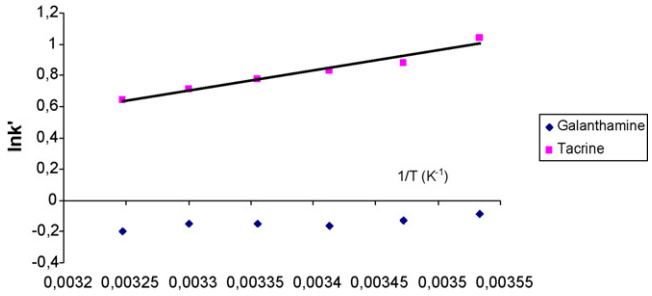

Fig. 2. Plot of $\ln k'$ vs. $1/T$ for tacrine and galanthamine at pH = 7.4 and a magnesium concentration equal to 0.75 mM.

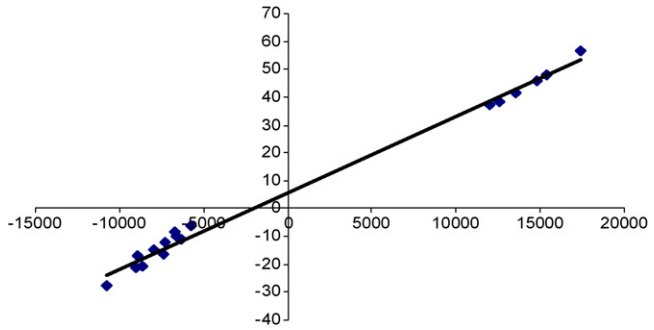

Fig. 3. Plot of ΔH° (J/mol) vs. ΔS° (J/mol K) for donepezil, tacrine and huperzine binding on AChE at all the magnesium concentrations.

tive ΔH° values indicated that it was energetically more favourable for these drugs to be linked to AChE rather to be in the bulk solvent. Negative ΔS° values showed an increase in the order of the chromatographic system when these drugs were included in the AChE binding gorge. The negative ΔH° and ΔS° values demonstrated that the binding was controlled enthalpically, i.e., hydrogen bonds and van der Waals forces were the major interactions stabilizing the AChE–drug (i.e., donepezil, tacrine) association [23–25]. The ΔS° values obtained for tacrine were more negative than for donepezil (Table 2), showing that the tacrine molecule was more organized in the binding gorge of AChE than donepezil due to the hydrophobic interactions. These results in accordance with other studies [26,27] showed that donepezil was fixed inside the gorge by direct hydrogen bonds, water bridges, and hydrophobic interactions. Niu et al. [26] showed that all oxygen and nitrogen atoms of donepezil take part in the formation of hydrogen bonds, but mostly, donepezil forms hydrogen bonds with the enzyme residues through its carbonyl oxygen atom of the dimethoxyindanone group. At the same time, the aromatic residues lining the enzyme gorge wall were the major components contributing to hydrophobic interactions with donepezil [26] and tacrine [28,29]. Tacrine can be bind with the aromatic amino acid lining the gorge by π–π stacking. Moreover the aromatic nitrogen of tacrine and the tacrine amino NH group can be hydrogen-bonded to the main-chain carbonyl oxygen of some amino acids (His, Trp, ...) of the binding gorge [28,29]. For huperzine, the positive ΔH° and ΔS° values indicated predominant hydrophobic forces between AChE and this molecule, and draw attention to the role that solvent reorganization must be playing in determining the strength of the huperzine–AChE complex [30–32]. In addition to the hydrophobic interactions which govern the huperzine–AChE association, other interactions as the hydrogen bonds due to the huperzine electronegative atoms (O, N) can get involved in this association. This result in accordance with a previous study [33] showed that huperzine engaged favourable interactions in the hydrophobic core and electrostatic region of the active site gorge of the enzyme.

Enthalpy–entropy compensation (EEC) temperature is a useful thermodynamic approach to the analysis of physico-chemical data [34]. Mathematically the entropy-enthalpy compensation can be expressed by the following equation:

$$\Delta H^\circ = \beta \Delta S^\circ + \Delta G^\circ_\beta \quad (5)$$

Table 2
Values of ΔH° (kJ/mol) and ΔS° (J/mol K) for the five AChEIs binding on AChE at a magnesium concentration equal to 0.75 mM. Standard deviations are in parentheses.

AChEIs	ΔH° (kJ/mol)	ΔS° (J/mol K)
Donepezil	−6.59 (0.05)	−9.73 (0.08)
Tacrine	−10.73 (0.09)	−27.73 (0.07)
Galanthamine	–	+0.99 (0.01)
Huperzine	+14.76 (0.10)	+45.74 (1.01)

ΔG°_β is the corresponding Gibbs free energy variation at the compensation temperature β. According to this last equation, when enthalpy–entropy compensation is observed with a group of compounds in a particular chemical interaction, all the compounds have the same free energy ΔG°_β at temperature β [35,36]. The plot of ΔH° vs. ΔS° obtained for donepezil, tacrine and huperzine was linear at all the magnesium concentration values of the bulk solvent ($r^2 > 0.99$) (Fig. 3). The correlation coefficient of this plot was higher than 0.99, and this value can be considered adequate to verify enthalpy–entropy compensation [37]. It can be deduced that the relative contributions of enthalpy and entropy to the overall free energy are the same for this three AChEIs (donepezil, tacrine and huperzine) and the magnesium concentrations in the bulk solvent. But, since different mechanisms could result in the same proportion of enthalpy and entropy relative to the overall free energy, it cannot be deduced rigorously that the association mechanism of these molecules with the AChE was independent of their structures and the magnesium concentration in the bulk solvent [38]. However, donepezil, tacrine and huperzine have similar inhibitor activity for AChE. These two conditions (EEC and similar biological effects) seem to imply a similarity of properties of these three AChEIs.

For galanthamine the $\ln k'$ vs. $1/T$ variations were negligible (Fig. 2). Thus, for this molecule, hydrophobic and electrostatic interactions were the major interactions governing its association with AChE (entropically driven mechanism). Greenblatt et al. [39] have solved the X-ray crystal structure of galanthamine bound in the active site of *Torpedo californica* acetylcholinesterase (TcAChE) at 2.3 Å resolution. They have shown that galanthamine binds at the base of the gorge interacting with both the acyl-binding pocket and the principal quaternary ammonium-binding site, the indole ring of Trp-84. The relatively tight binding of galanthamine to AChE appears to arise from a number of moderate to weak interactions with the protein, coupled to a low entropy cost for binding due to the rigid nature of the inhibitor [39,40]. These interactions came from polar and non-polar interactions of the tertiary amino group, the terminal hydroxyl group and the aromatic rings of galanthamine with the active binding gorge of the enzyme. In addition, two principal hydrogen bonds could be formed with some amino acid of the active site gorge (Trp, Asp, ...) thanks to the hydroxyl group and the O-methyl group of galanthamine.

Physostigmine (AB) combined also with both the peripheral and catalytic sites of the enzyme (EH) active gorge, this association involves a reversible complex (EH–AB) formation. Barak et al. [41] have shown that the accommodation of physostigmine and its analogues by AChE is dominated by hydrophobic interactions [41,42]. The reversible complex is followed by carbamoylation of the enzyme, and production of a covalent adduct (EA). The carbamoylated enzyme is then hydrolyzed to regenerate the free enzyme as

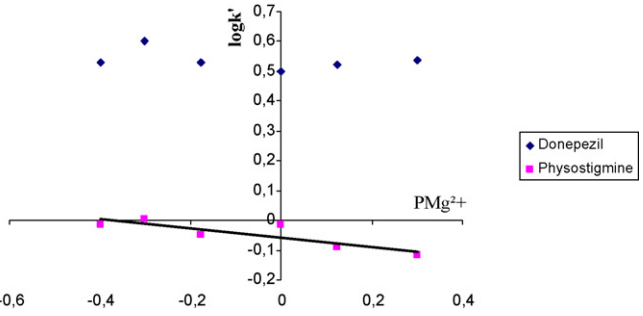

Fig. 4. Plot of $\ln k'$ vs. $P\mathrm{Mg}^{2+}$ for donepezil and physostigmine at a column temperature equal to 308 K.

following [40,41]:

$$\mathrm{EH} + \mathrm{AB} \underset{k_{-1}}{\overset{k_1}{\rightleftarrows}} \mathrm{EH}\cdots\mathrm{AB} \xrightarrow{k_2} \mathrm{EA} + \mathrm{BH} \xrightarrow{k_3} \mathrm{EH} + \mathrm{AOH}$$

k_i represents the rate constant of the different equilibrium. The decarbamoylation phase of the reaction is considerably slow than the other phases and is therefore the most clarified step of the interaction [40]. Therefore, concerning the physostigmine molecule, the determination of the retention parameters with the AChE stationary phase, give only an initial evaluation of its association mechanism.

The relative bound percentages of the AChEIs with the enzyme (b%) were calculated at 298 K using the following equation [43]:

$$b\% = \frac{k'}{1+k'}\% \tag{6}$$

These values were given in Table 1. Eq. (6) has been shown to give a good correlation vs. reference methods for compounds with medium-to-strong binding to protein [43,44]. The corresponding log P (partition coefficient octanol/water) values were exposed by many scientific sites (Pubchem, Drugbank, Chemspider, . . .). Table 1 presents the log P values (http://pubchem.ncbi.nlm.nih.gov/) which have been derived from an atomic fragment database using $X\log P$ (a program for the prediction of the octanol/water partition coefficients of organic compounds). A significant linear relationship correlating the AChE relative bound percentage to log P taken as a measure of lipophilicity was obtained (r upper than 0.87). This result showed an affinity enhanced with the increase in the molecule hydrophobicity and confirmed that the hydrophobic forces play an important role in the AChEI–AChE binding processes [44].

3.3. Magnesium cation effect on the AChEI–AChE association mechanism

The magnesium effects on association mechanism between the AChEIs and the enzyme can be modelled at a thermodynamic level in terms of the direct stoichiometric participation of the magnesium cations in the association reaction. The dependence of k' on the magnesium concentration (x) can be formulated as follows [45,46]:

$$\frac{\partial \log k'}{\partial P\mathrm{Mg}^{2+}} = n_{\mathrm{Mg}^{2+}} \tag{7}$$

where $n_{\mathrm{Mg}^{2+}}$ was the number of magnesium cations displaced or bound upon AChEI–AChE complex formation.

The $\log k'$ vs. $P\mathrm{Mg}^{2+}$ (=$-\log x$) were plotted for all AChEIs. These plots showed that for donepezil, tacrine and huperzine the retention was magnesium concentration independent. An example of plot for donepezil was given in Fig. 4. For galanthamine and physostigmine the retention was magnesium concentration dependent and increased significantly with salt concentration increase in the bulk solvent (Fig. 4). This increase of the binding intensity with magnesium concentration can be explained by a change in the water activity (i.e. the hydrophobic effect) classically attributed to salt effect [45,46]. This trend of the hydrophobic interaction intensity of galanthamine and physostigmine with the active site gorge with magnesium concentration is affected by the binding of magnesium cations to the anionic groups of the peripheral anionic binding site. From Eq. (7), the slope of the curve $\log k'$ vs. $P\mathrm{Mg}^{2+}$ (Fig. 4) gives the number of magnesium at the AChEIs–AChE interface implied in the binding process. Negatives values of $n_{\mathrm{Mg}^{2+}}$ were obtained for galanthamine and physostigmine at all temperatures of the bulk solvent. For example, at 35 °C the corresponding $n_{\mathrm{Mg}^{2+}}$ value for galanthamine was −0.10, and for physostigmine was −0,16. The negative values of $n_{\mathrm{Mg}^{2+}}$ reflected that the galanthamine or physostigmine displacement to their AChE active binding gorge was accompanied with magnesium exclusion. Many studies showed that AChE can bind divalent inorganic cations (Mg^{2+}, Ca^{2+}, . . .) [9,47] and this binding was showed to have a competitive effect against cationic substrates and inhibitors binding on AChE [9]. Our results showed that the ionic competitive effect of magnesium for galanthamine and physostigmine binding on AChE was less important than the hydrophobic interactions. In addition, these hydrophobic interactions were increased as the magnesium concentration in the bulk solvent increased. These results demonstrated that in the biological magnesium concentration range (0.75–1 mmol L^{-1}), an increase in the magnesium concentration led an enhancement of the galanthamine and physostigmine association with AChE and consequently an increase of the AChE inhibition. Thus, a magnesium supplementation for patients who suffer from Alzheimer disease can be useful during the treatment with these AChEIs.

4. Conclusion

The mechanism of donepezil, tacrine, galanthamine, huperzine and physostigmine binding to AChE was analyzed. The determination of the thermodynamic data of this association showed that for donepezil and tacrine the inhibitor binding with AChE was governed principally by hydrogen bonding and van der Waals forces. Whereas for huperzine, galanthamine and physostigmine, the association was dominated by hydrophobic interactions. The effect of magnesium on the association with AChE was studied. No important change in the donepezil, tacrine and huperzine association with AChE stationary phase was observed. On the other hand an increase of the magnesium concentration led an enhancement of the galanthamine and physostigmine association with the enzyme and consequently an increase of the AChE inhibition. This study demonstrated that it seems to be interesting to test in vivo, the magnesium supplementation during galanthamine and other AChEIs treatment for patients who suffer from Alzheimer disease.

References

[1] B.A. Yankner, A. Caceres, L.K. Duffy, Proc. Natl. Acad. Sci. U.S.A. 87 (1990) 9020.
[2] D.C. German, U. Yazdani, S.G. Speciale, P. Pasbakhsh, D. Games, C.L. Liang, J. Comp. Neurol. 462 (2003) 371.
[3] J. Kao, G. Grossberg, Alzheimer's Disease, vol. 2, Springer, Berlin, Heidelberg, 2008, p. 25.
[4] J. Kaur, M.Q. Zhang, Curr. Med. Chem. 7 (2000) 273.
[5] J.L. Sussman, M. Harel, F. Frolow, C. Oefner, A. Goldman, L. Toker, I. Silman, Science 253 (1991) 872.
[6] M. Alcalá Mdel, N.M. Vivas, S. Hospital, P. Camps, D. Muñoz-Torrero, A. Badia, Neuropharmacology 44 (2003) 749.
[7] I. Silman, J.L. Sussman, Chem.-Biol. Interact. 175 (2008) 3.
[8] F. Stock, J. Hoffmann, J. Ranke, R. Störmann, B. Ondruschka, B. Jastorff, Green Chem. 6 (2004) 286.
[9] V. Tõugu, T. Kesvatera, Biochim. Biophys. Acta 1298 (1996) 12.
[10] A.E. Cilliler, S. Ozturk, S. Ozbakir, Gerontology 53 (2007) 419.
[11] J.L. Glick, Med. Hypotheses 31 (1990) 211.
[12] M. Bartolini, V. Cavrini, V. Andrisano, J. Chromatogr. A 1031 (2004) 27.
[13] A.M. Girelli, E. Mattei, J. Chromatogr. B 819 (2005) 3.

[14] T. Bagnost, Y.C. Guillaume, M. Thomassin, J.F. Robert, A. Berthelot, A. Xicluna, C. André, J. Chromatogr. B 856 (2007) 113.
[15] G. Guiochon, S. Golshan-Shirazi, A.M. Katti, Academic Press, Boston, 1994.
[16] J.F.K. Huber, R.G. Gerriste, J. Chromatogr. 58 (1971) 137.
[17] C. Blumel, P. Hugo, A. Seidel Morgenstern, J. Chromatogr. A 865 (1999) 51.
[18] P. Jandera, S. Berncekova, K. Mihlbachler, G. Guiochon, V. Backovska, J. Planeta, J. Chromatogr. A 925 (2001) 19.
[19] C. André, Y.C. Guillaume, Chromatographia 58 (2003) 193.
[20] Y.C. Guillaume, C. Guinchard, Anal. Chem. 68 (1996) 2869.
[21] C. André, Y.C. Guillaume, J. Chromatogr. A 1029 (2004) 21.
[22] D. Alonso, I. Dorronsoro, L. Rubio, P. Muñoz, E. García-Palomero, M. Del Monte, A. Bidon-Chanal, M. Orozco, F.J. Luque, A. Castro, M. Medina, A. Martínez, Bioorg. Med. Chem. 13 (2005) 6588.
[23] C. Andre, M. Thomassin, C. Guyon, T.T. Truong, Y.C. Guillaume, J. Pharm. Biomed. Anal. 32 (2003) 217.
[24] S. Urien, P. Nguyen, S. Berlioz, F. Brée, F. Vacherot, J.P. Tillement, J. Biochem. 302 (1994) 69.
[25] E. Peyrin, Y.C. Guillaume, N. Morin, C. Guinchard, J. Chromatogr. A 808 (1998) 113.
[26] C. Niu, Y. Xu, Y. Xu, X. Luo, W. Duan, I. Silman, J.L. Sussman, W. Zhu, K. Chen, J. Shen, H. Jiang, J. Phys. Chem. B 109 (2005) 23730.
[27] G. Kryger, I. Silman, J.L. Sussman, Structure 7 (1999) 297.
[28] P. Muñoz-Ruiz, L. Rubio, E. García-Palomero, I. Dorronsoro, M. del Monte-Millán, R. Valenzuela, P. Usán, C. de Austria, M. Bartolini, V. Andrisano, A. Bidon-Chanal, M. Orozco, F.J. Luque, M. Medina, A. Martínez, J. Med. Chem. 48 (2005) 7223.
[29] D. Han, P. Yang, J. Mol. Struct. (Theochem.) 668 (2004) 25.
[30] D.M. Wong, H.M. Greenblatt, H. Dvir, P.R. Carlier, Y.F. Han, Y.P. Pang, I. Silman, J.L. Sussman, J. Am. Chem. Soc. 125 (2003) 363.
[31] D. Zhong, A. Douhal, A.H. Zewail, Proc. Natl. Acad. Sci. U.S.A. 97 (2000) 14056.
[32] F. Darrouzain, C. André, L. Ismaili, M. Matoga, Y.C. Guillaume, J. Chromatogr. B 820 (2005) 283.
[33] A. Saxena, N. Qian, I.M. Kovach, A.P. Kozikowski, Y.P. Pang, D.C. Vellom, Z. Radić, D. Quinn, P. Taylor, B.P. Doctor, Protein Sci. 3 (1994) 1770.
[34] W. Melander, C.S. Horvath, Academic Press, New York. 23, 1986.
[35] R.R. Krug, Ind. Eng. Chem. Fundam. 19 (1980) 50.
[36] C. André, L. Ping, M. Thomassin, J.F. Robert, Y.C. Guillaume, Anal. Chem. Acta 542 (2005) 199.
[37] L.A. Cole, J.G. Dorsey, K.A. Dill, Anal. Chem. 64 (1992) 1324.
[38] R. Ranatunga, M.F. Vitha, P.W. Carr, J. Chromatogr. A 946 (2002) 47.
[39] H.M. Greenblatt, G. Krygera, T. Lewisb, I. Silmanc, J.L. Sussman, FEBS Lett. 463 (1999) 321.
[40] J. Stojan, M. Zorko, Biochim. Biophys. Acta (BBA)—Protein Struct. and Mol. Enzymol. 1337 (1997) 75.
[41] D. Barak, A. Ordentlich, D. Stein, Q.S. Yu, N.H. Greig, A. Shafferman, Biochem J. 417 (2009) 213.
[42] A. Shafferman, D. Barak, D. Stein, C. Kronman, B. Velan, N.H. Greig, A. Ordentlich, Chem.-Biol. Interact. 175 (2008) 166.
[43] D.S. Hage, J. Chromatogr. B 768 (2002) 3.
[44] F. Darrouzain, P. Dallet, J.P. Dubost, L. Ismaili, F. Pehourcq, B. Bannwarth, M. Matoga, Y.C. Guillaume, J. Pharm. Biomed. Anal. 41 (2006) 228.
[45] F.S. Sarr, Y.C. Guillaume, C. André, J. Pharm. Biomed. Anal. 47 (2008) 651.
[46] C.J. Van Oss, Interfacial Forces in Aqueous Media, Marcel dekker, New York, 1994.
[47] A.C.D. Bainy, M.H.G. de Medeiros, P. Di Mascio, E.A. de Almeida, Biotemas 19 (2006) 35.

Talanta 79 (2009) 818–823

Contents lists available at ScienceDirect

Talanta

journal homepage: www.elsevier.com/locate/talanta

A practical method for sensitive determination of the fluorescent water-tracer uranine by reversed phase HPLC under alkaline conditions

Tohru Ikeya [a,*], Naho Horimoto [b], Yasuhiro Kashino [c]

[a] Ocean Research Institute, The University of Tokyo, 1-15-1 Minamidai, Nakano-ku, Tokyo 164-8639, Japan
[b] Department of Ocean Sciences, Tokyo University of Marine Science and Technology, Konan, 4-5-7 Minato-ku, Tokyo 108-8477, Japan
[c] Graduate School and Faculty of Science, University of Hyogo, 3-2-1 Kohto, Kamigohri, Ako-gun, Hyogo 678-1297, Japan

ARTICLE INFO

Article history:
Received 1 April 2009
Received in revised form 4 May 2009
Accepted 6 May 2009
Available online 15 May 2009

Keywords:
Chemical tracer
Fluorescent dye
Uranine
Fluorescein
HPLC
SPE

ABSTRACT

A stable and highly sensitive HPLC method for uranine has been developed. Because of unstableness of silica-based octadecyl-C18 columns at high pH condition, a reversed phase HPLC analysis under alkaline conditions has not necessarily taken as a usual method. However, the application for uranine seems to be advantageous, since the fluorescence yield of uranine is markedly enhanced at high pH condition. The detection limit of the HPLC system was 0.9 pg. The analytical consideration was also paid for the solid phase extraction (SPE) prior to the HPLC analysis with careful consideration of the recently revised pK_a values of uranine. The recovery rate of uranine by SPE was found to depend on the sample volume and a few ml of seawater was applied to SPE in order to maintain the recovery rate during SPE. A combination of HPLC and SPE methods achieved detection of uranine at concentrations as low as 0.2 ng l^{-1} (0.5 pM), which was comparable to the background concentration of uranine in coastal water off Japan. For the practical use of the detected tracer-uranine concentration values after substantial duration after release, the photodegradation of uranine in surface water was also evaluated in terms of incident solar radiation dose as an exponential rate constant of −0.135 mol photon^{-1} m^2.

1. Introduction

Fluorescent dyes have been widely used as tracers in hydrography because the stained water can be visually observed and the concentration of the tracer readily determined with bench-top or *in situ* sensors. Among various tracer dyes, uranine has been preferred in hydrographic research as well as in industrial and health care applications, because of its high solubility in water, relatively low expense [1,2] and low toxicity [3–5].

The fluorescence yield of tracer dyes has been shown to be a function of temperature, ion strength (salinity) and pH [1]. *In situ* determination of concentrations in field water is also affected by interference from suspended particles, and fluorescence from coexisting dissolved and colloidal organic substances as well as phytoplankton pigments (chlorophylls and phycobiliproteins) [1]. As for uranine, the emission band of the fluorescence is similar to that of a major component of hydrophilic phycobiliproteins (phycoerythrin) in oceanic cyanobacteria of the genus *Synechococcus* [6], which commonly occur from the surface to near the bottom of euphotic layer in the ocean [7,8]. Thus, *in situ* detection of uranine fluorescence at low concentrations might be interfered by the background fluorescence both in surface and subsurface seawater. To avoid these problems in detecting a series of fluorescent tracers in field waters, a two-step separation procedure involving HPLC analysis following concentration with solid phase extraction (SPE) has been applied to specifically detect dyes such as rhodamine B, rhodamine WT, sulphorhodamine B, sulphorhodamine G and uranine [9–13].

Uranine (disodium fluorescein, acid yellow 73, IC45530) is one of the xanthene dyes with an OH-group as auxochrome. It has three pK_a points comprising cation, monoanion, dianion and neutral species [14,15]. Based on the pK_a values 1.95, 5.05 and 7.00, which were determined by Zanker and Peter [14] for uranine in the aprotic polar solvent dioxan, phthalate buffer at pH 3 was used as an extraction buffer with the aim of facilitating concentration of neutral uranine by an octadecyl-C_{18} (C_{18}) column for SPE [12]. Recently, Smith and Pretorius [15] re-examined the pK_a values of uranine in an aqueous medium and confirmed them to be 2.22, 4.34 and 6.68 at 25 °C after correction for ionic activity. Accordingly, the conditions for extraction of uranine during SPE require re-examination in order to achieve better recovery of uranine.

Because the specific absorbance and fluorescence of dianionic species are greater than for other uranine species, the

Abbreviations: ISUS, *in situ* ultraviolet spectrophotometer; SPE, solid phase extraction.

* Corresponding author. Tel.: +81 3 5351 6507; fax: +81 3 5351 6506.
E-mail addresses: ctikeya@ori.u-tokyo.ac.jp (T. Ikeya), nahori@kaiyodai.ac.jp (N. Horimoto), kashino@sci.u-hyogo.ac.jp (Y. Kashino).

0039-9140/$ – see front matter © 2009 Elsevier B.V. All rights reserved.
doi:10.1016/j.talanta.2009.05.007

fluorescence yield increases under alkaline condition [1,15,16]. The pH-dependence of fluorescence of uranine is especially greater than that of other tracer dyes [1]. However, the high pH-dependence of the fluorescence yield of uranine has not been considered as a factor controlling the detection limit [12]. From the reported pK_a values of uranine, we can predict that the highest fluorescence yield will be achieved under a pH greater than 9. Therefore, reversed phase HPLC analysis under alkaline conditions above pH 9 was made using an ethylene-bridged hybrid HPLC column that is highly stable, even under alkaline condition [17]. The fluorescence of elute from HPLC column was then measured under combination of excitation and emission wavelengths that are optimized to detect uranine.

In this study, we developed a method comprising reversed phase HPLC analysis under alkaline conditions to separate and detect uranine and measure its concentration using SPE. The recovery rate through the SPE procedure was also examined in relation to the affinity of uranine species on the reversed phase SPE column. To assess the practical application of the method for field seawater under natural sunlight, the degradation rate of uranine in seawater was experimentally determined under natural solar radiation. Finally, these methods were applied to measure the background concentration of uranine in coastal waters from Sagami Bay, Japan.

2. Experimental

2.1. Reagents and analytical procedures

HPLC-grade methanol was obtained from Wako Pure Chemical (Osaka, Japan). All other chemicals including uranine were reagent-grade from Wako Pure Chemical.

For determining the potential recovery rate of SPE, seawater at 20 m depth was collected from the middle of Sagami Bay, Japan (35°05′N, 139°26′E) by T/V *Seiyo Maru* of the Tokyo University of Marine Science and Technology, and filtered with GF/F filter (Whatman, Maidstone, England) before use. Seawater samples were also taken from 12 depths between the surface and 200 m depth during a research cruise KT-06-16 of the R/V *Tansei-Maru* of the Japan Agency for Marine-Earth Science and Technology involving a tracer discharge experiment in Sagami Bay.

A Bond Elut C_{18} cartridge (100 mm × 4.6 mm, Varian; Palo Alto, CA) was used for solid phase extraction (SPE) after equilibration with 10 ml of equilibration medium (0.08 mM acetic acid–ammonium acetate) (pH 3.0) for 1–4 days. Extraction was performed in the dark (0.08–0.8 μmol photon m^{-2} s^{-1}). After equilibration for 15 min the test seawater was adjusted to pH 3.0 as described below and was passed through the SPE cartridge at a rate of 1–2 ml min^{-1}. The cartridge was further rinsed by 10 ml of equilibration medium and dried for 10 min by passing air using a chemically tolerant diaphragm pump. To elute uranine, 2 ml of methanol/acetic acid–ammonium acetate (20/0.11, v/v) buffer (pH 9.0) was applied to the SPE cartridge by syringe. For the estimation of recovery rate, filtered seawater was used by adding a given amount of standard aqueous uranine solution (10 mg l^{-1}) and 0.55% (v/v) of 15 M acetic acid–ammonium acetate (pH 3.0) to adjust the pH. The eluted solution was mixed with 50 mM of sodium carbonate buffer (pH 10) (0.15/1, v/v) and the fluorescence was measured with a spectrofluorometer (RF5300PC; Shimadzu, Kyoto, Japan) to assess the bulk recovery after SPE. The excitation and detection wavelengths were 493 and 510 nm, respectively.

Chromatographic separation of uranine was carried out using a 150 mm × 4.6 mm XBridge C_{18} column (5 μm) with a 20 mm × 4.6 mm guard column (Waters, Milford, MA). Mobile phases A and B comprised 50 mM acetic acid–ammonium acetate (pH 9) and 4 mM triethylamine as an ion pairing reagent in 30/70 (v/v) methanol/water (Milli-Q water; Millipore, Bedford, MA) (mobile phase A) or in methanol (mobile phase B). The pH of the buffer solution was adjusted with acetic acid to 7.0, 8.0 or 9.0. The pH of the mobile phases were checked after stabilizing for several hours. After equilibration with mobile phase A, the proportion of mobile phase B was linearly increased to 100% taking 6 min and then decreased to 0% at 7 min. After concentrating the test sample by SPE as described above, the eluted methanol/buffer solution was dried in dark micro-tubes. The resulting residual solids were then dissolved with a fixed volume of methanol and mixed with 75 mM acetic acid–ammonium acetate (pH 9) and 6 mM triethylamine at a volume ratio of 2:1, and up to 200 μl was applied for HPLC analysis. The field seawater sample was filtered by 0.2 mm PTFE filter (Whatman, Maidstone, England) before injection into the HPLC column.

2.2. Apparatus for chromatographic analysis

The HPLC system consisted of a solvent delivery system LC-10ADVP equipped with a fluorescence detector RF-10AXL, a photodiode array detector SPD-M10AV and the analyzing software CLASS-M10A (Shimadzu). The analog signal from the fluorescence detector was recorded by a pen-recorder and a personal computer through a 14-bit A/D converter at a frequency of 1 Hz. For the fluorometric analysis with RF-10AXL, the excitation and detection wavelengths were 476 and 515 nm, respectively.

2.3. Experimental procedures for the photodegradation of uranine

Seawater at 20 m depth from the middle of Sagami Bay was divided into 100 ml transparent Nalgene (Thermo Fisher, Rochester, NY) polycarbonate bottles, and uranine was added at 10 μg l^{-1} (26.6 nM) to each bottle. The bottles were incubated in a water bath under sunlight with circulating surface seawater to maintain the *in situ* surface water temperature. Light quantity was adjusted to 100%, 45%, 16% and 5% by wrapping the bottles with different sheets of black nylon cloth. An aliquot of seawater was collected from each bottle and the concentration of uranine was measured with a Model-10 Field Fluorometer (Turner-Designs, Sunnyvale, CA). Two band-pass filters (5-56, Corning, Glendale, AZ) were used for excitation (357–494 nm) and a 4-96 Corning band-pass filter with two interference filters (Y-52, AGC Techno Glass, Tokyo, Japan) were used for emission (513–612 nm). The light intensity inside each bottle was measured with a QSL-2200 Quantum Scalar Laboratory irradiance sensor (Biospherical Instruments, San Diego, CA). Total solar irradiance at the water bath was monitored with a cosine Quantum Sensor (LI-COR, Lincoln, NE) at 5 min intervals.

3. Results

3.1. Reversed phase HPLC under alkaline conditions

The aim of the current investigation is to obtain a stable and highly sensitive HPLC method for the detection of uranine. The uranine fluorescence yield should be higher in the alkaline mobile phase than in lower pH conditions. The dianion uranine species that are the dominant forms of uranine in alkaline conditions should have a lower affinity for the hydrophobic groups of the column surface under reversed phase condition than the less-ionized uranine species. Therefore, a normal phase column was tested first. However, it gave low retention of uranine (data not shown). Contrary to the above assumption, uranine was retained by the column under reversed phase conditions and eluted with a sharp single peak at around 8 min when a XBridge C_{18} column was used with an alkaline mobile phase in the presence of 4 mM triethylamine as an ion pairing reagent (Fig. 1). When the pH of the mobile phase was

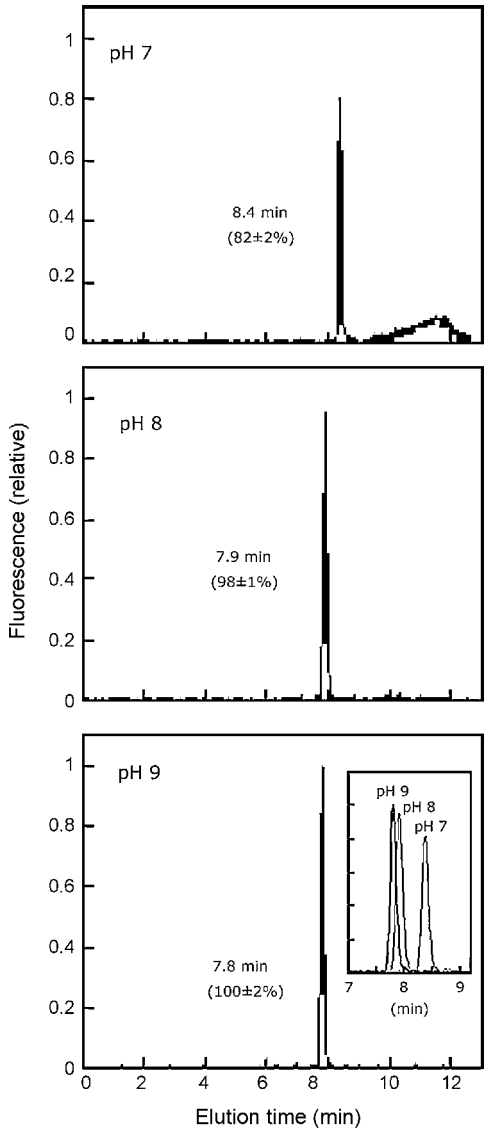

Fig. 1. Elution profile of uranine (100 pg) using pH 7, pH 8 and pH 9 buffer for the mobile phase. Triplicate measurements were averaged for each profile. The separation was performed using an XBridge C_{18} column (150 mm × 4.6 mm). Gradient conditions: 0.01 min = 100% A, 0% B; 6 min = 0% A, 100% B; 7 min = 100% A, 0% B. For each peak, the peak elution time (in min) and in parenthesis the value of the relative peak height are given. The inset in the lowest panel shows the fluorescence peaks with the three pH buffer conditions between 7 and 9 min.

increased from 7 to 9, uranine eluted slightly faster and the emitted uranine fluorescence increased (Fig. 1). The elution profile of uranine indicates that the main fluorescence peak at around 8 min was reinforced by dianion uranine species that are the dominant form in alkaline conditions. The broad and diminutive peak which appeared at around 11.5 min when a neutral mobile phase was used could be due to the higher affinity of less-ionized uranine species under neutral pH conditions.

The 95% confidence interval of the determination of 10 pg uranine was 0.2 pg (n = 5) under the reversed phase HPLC using pH 9 buffer. The detection limit, which was defined as 2-fold of standard deviation of baseline-noise (Fig. 1), was as low as 0.9 pg.

3.2. Examination of factors affecting the recovery rate of SPE

To concentrate uranine prior to the HPLC analysis, SPE was introduced by Franke et al. [12] on the basis of pK_a values reported by Zanker and Peter [14]. According to the corrected pK_a values of uranine in acidic aqueous medium by Smith and Pretorius [15], the relative abundance of uncharged neutral uranine species amounts to 60% rather than 70%, as derived from the pK_a values reported by Zanker and Peter [14]. This estimation implies that the affinity of neutral uranine species for the SPE C_{18} column is not as high as expected even under the acidic conditions. Thus the recovery rate of uranine was examined to evaluate the effect of pH of the extraction buffer on SPE (Table 1). Acetate was used to adjust the pH of test seawater for SPE, as well as the methanol elution buffer solution, in order to minimize any potential acidic contamination of the HPLC injection buffer solution. To adjust the pH to 5, phosphate was also used. Compared with the non-treated uranine solution containing 1.5 ng as a control (500 ng l^{-1}; 1.33 nM), around 90% of the uranine was recovered from 3 ml of filtered field seawater after SPE by using a pH 3 buffer (Table 1). The recovery rate was scarcely affected by the concentration of acetate buffer at pH 3.0. When the pH of the extraction medium increased, the recovery rate of uranine decreased to 80% at pH 4.0 and 50% at pH 5.0 in accordance with the decrease in the proportion of neutral uranine species as calculated from the reported pK_a values.

Table 1
Effect of extraction buffer on the recovery rate of uranine after SPE.

Conditions	Fluorescence at 510 nm (relative)
Control	100
pH 3.0, 0.08 M acetate	91.2
pH 3.0, 0.1 M acetate	88.7
pH 4.0, 0.08 M acetate	80.3
pH 5.0, 0.08 M phosphate	52.6

After passing through the 3 ml test seawater sample containing 1.5 ng uranine (500 ng l^{-1}; 1.33 nM), the SPE columns were washed with 10 ml of 0.08 mM acetate buffer (pH 3.0). The trapped uranine was eluted with 2 ml of methanol/acetic acid–ammonium acetate (20/0.11, v/v) buffer (pH 9.0). The eluted solution was mixed with 50 mM sodium carbonate buffer (pH 10) (0.15/1, v/v). Fluorescence of uranine was measured with a RF5300PC spectrofluorometer by exciting at 493 nm.

The capacity of the current SPE C_{18} cartridge for uranine was investigated (Fig. 2). Various amount of uranine dissolved in 3 ml of filtered natural seawater were subjected to SPE and the fluorescence intensity emitted from the resulting substances measured. The linear relationship between the spiked amount of uranine and the fluorescence intensity indicates that the current SPE C_{18}

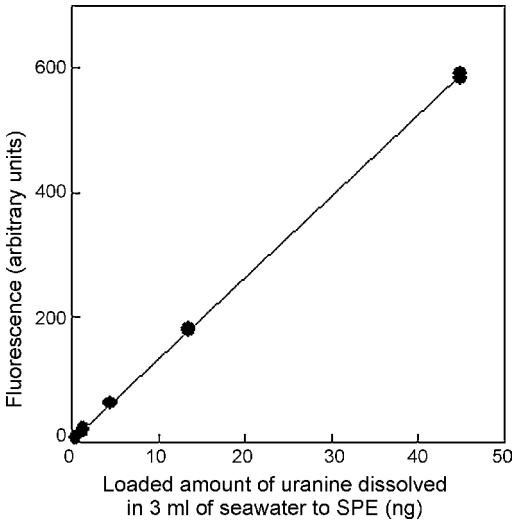

Fig. 2. Recovery of uranine after SPE using 0.08 M acetate buffer at pH 3.0. The amounts of loaded uranine were 0.45, 1.4, 5, 14 and 45 ng (0.40, 1.2, 4.0, 11.9 and 39.8 nM) in 3 ml of filtered natural seawater. Duplicate measurements were made for each condition. Other analytical procedures were the same as those in Table 1.

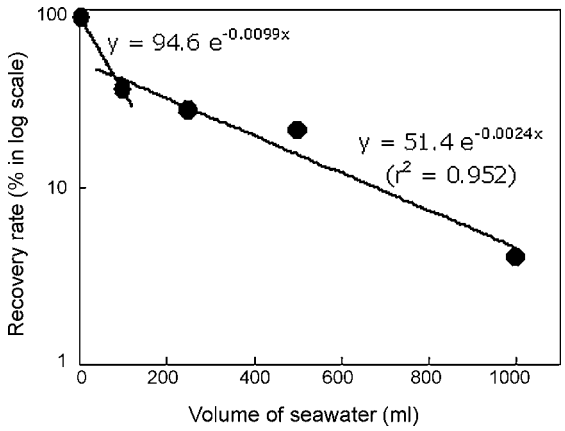

Fig. 3. Effect of sample volume of seawater on the recovery of uranine by SPE. Uranine (83 pg) was dissolved in filtered natural seawater (pH 3.0) of variable volumes whose pH was adjusted by 0.08 M acetate (44, 2.2, 0.88, 0.44 and 0.22 pM uranine for 5, 100, 250, 500 and 1000 ml of seawater, respectively). The eluted solutions of SPE were subjected to HPLC analysis. Other analytical procedures were the same as in Table 1. Each recovery rate value is an average of duplicate measurements.

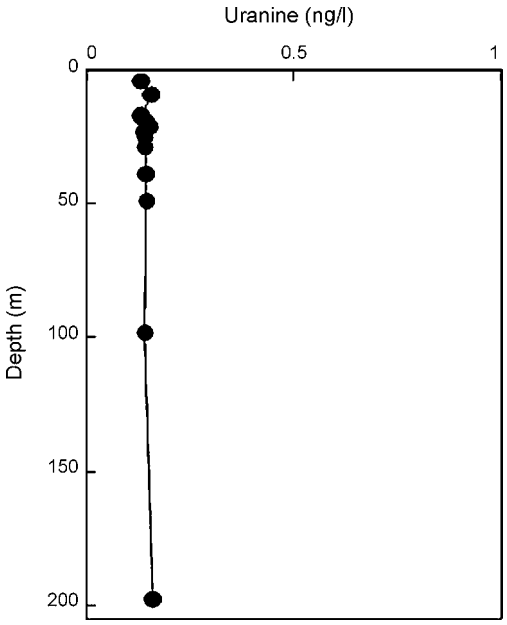

Fig. 4. Vertical profile of uranine concentration in Sagami Bay, coastal Japan, during a tracer study in July, 2006. Fifteen milliliters of seawater sample was concentrated by SPE and subsequently analyzed by HPLC. The detected concentrations showed no signal of the discharged water-mass and were interpreted as background.

cartridge recovers up to 50 ng of uranine at pH 3.0 which is in proportion to the added uranine. However, it was also found that the volume of loaded sample affected the recovery rate. For 5 ml of added seawater containing 83 pg (44 pM) uranine, the recovery rate was 90% (Fig. 3). When the volume of the seawater containing the same amount of uranine increased, the recovery rate was decreasing (respectively 35%, 27%, 21% and 4% for the volumes of 100 ml (2.2 pM), 250 ml (0.88 pM), 500 ml (0.44 pM) and 1000 ml (0.22 pM)). The decrease of recovery rate within the examined range of volume of seawater showed a biphasic logarithmic curve (two different regression equations in Fig. 3).

3.3. Detection of uranine in coastal seawater by SPE and HPLC

The SPE and HPLC methods developed in this study were applied to water collected during the tracer experiment in Sagami Bay, Japan (around 2700 km^2). Uranine was used to trace discharged water from a density current generator [18], which was moored in the middle of Sagami Bay and pumped up 10^5 tons of seawater per day from a depth of 200 m. The experiment was carried out in July, 2006. Fifty-six kilograms uranine was released into the intake of the discharger. Ninety-six hours after its discharge, uranine was detected at 0.2–1 ng l^{-1} (0.5–2.7 pM) at the target density layer of 5 stations among 9 observation stations located within 8 km of the discharge point (unpublished work). There was no fluorescence signal in the HPLC elution profiles other than the marked peak at 8 min. However, a relatively constant concentration of uranine (0.14 ± 0.01 (s.d.) ng l^{-1}; 0.37 ± 0.03 pM) was measured beside the targeted density layer. Fig. 4 shows the typical vertical profile of uranine where no discharged water was detected. The uranine concentrations were similar from the surface to 200 m depth.

3.4. Photodegradation of uranine under sunlight in coastal seawater

In order to analyze the dispersion of uranine distribution over several days, photodegradation by solar radiation should be taken into account. The photodegradation rate of uranine has been expressed as a rate constant incorporating only exposure time under full sun or cloudy conditions [1,16]. However, in order to evaluate the rate of photodegradation of uranine throughout a water column under fluctuating irradiance, a rate constant determined by quantum dose is necessary. Since it has been shown that the specific absorption of uranine depends on pH and redox potential [16], uranine was dissolved in *in situ* seawater, and the photodegradation rate was measured in transparent bottles with different attenuations of sunlight (Fig. 5). The rate of decrease in uranine concentration was proportional to the irradiance, and showed an almost identical trend when plotted against the integrated quantum dose. The rate constant for the exponential decay of uranine against quantum dose was -0.135 mol $photon^{-1}$ m^2.

4. Discussion

In this study, we have developed an improved method to measure uranine concentrations. The detection limit by HPLC analysis using an alkaline buffer with triethylamine was improved to 0.9 pg which is 2.5 times better than that previously reported by Franke et al. [12].

Based on the pK_a values reported by Smith and Pretorius [15], the relative abundance of dianion species is, at most, half of all species of uranine at pH 7.0, increasing to around 75% at pH 8 and more than 90% at pH 9. In spite of increasing negative charge states of uranine, we have shown that uranine can be separated by reversed phase HPLC under alkaline conditions, which allows detection of uranine in the high fluorescence yield state with improved sensitivity. The fluorescence peak from uranine during the elution increased as the proportion of dianion species increased with increased pH in the mobile phase (Fig. 1), although it did not quantitatively correspond to the estimates of the proportion of ion species of uranine at different pH values.

As indicated by the previous study [12], the optimal pH condition for SPE of uranine was around pH 3 (Table 1) in accord with the estimated pK_a values [15]. The constant recovery was confirmed for up to 50 ng of uranine loaded on SPE column (Fig. 2). However, the recovery rate of uranine during SPE for a large amount of natural seawater was apparently expressed as a combination of first-order reaction rate ($-dB/dv = (k_1 + k_2))B$; where B is the amount of uranine molecules bounded within the SPE column, v the volume of seawater, k_1 the rate constant of initial rapid loss of uranine and k_2 is the rate constant of second slow loss of uranine) (Fig. 3). The

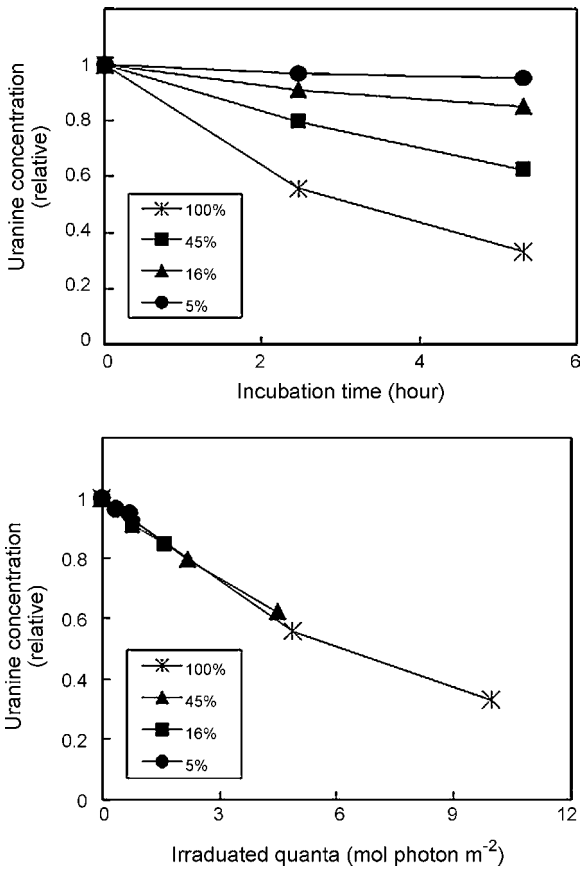

Fig. 5. Photodegradation of uranine dissolved in seawater (10 μg l^{-1}; 26.6 nM) under attenuated sunlight (100%, 45%, 16% and 5%). The concentration of uranine was plotted as a function of the incubation time (top panel) or the integrated quantum irradiance (bottom panel). Samples were collected at a given time interval and the uranine concentration was immediately measured with a Turner-Designs Model-10 fluorometer (wavelengths for excitation and emission was in a band of 357–494 nm, and 513–612 nm, respectively).

apparent loss of uranine during SPE for natural seawater might be explained by the presence of some competitive binding material in natural seawater and a relatively low affinity of bulk of uranine species even in pH 3 medium as predicted from pK_a values [15]. Thus, the biphasic logarithmic curve might due to different affinity of uranine species; the rapid loss rate in initial phase for less charged (cation and monoanion) species (42% of total under pH 3) and second phase for neutral species (58% of total under pH 3).

Because the detection limit of uranine by our HPLC method is 0.9 pg, the overall detection limit of uranine in the initial seawater would be 0.2 ng l^{-1} (0.5 pM) if a 5 ml sample of seawater was used for SPE. If the sample volume for SPE was greater than 5 ml, the minimum detectable concentration would exceed the background concentration of uranine in Sagami Bay (Fig. 4) and the recovery rate of SPE would also decline (Fig. 3). The detection limits obtained in the present study are comparable to those for sulphorhodamine B, rhodamine B and rhodamine WT [11], if the same sample volume was applied.

We have confirmed that pH seriously affects the affinity of uranine in both SPE- and HPLC-reversed phase columns. The lesser recovery rate of uranine by SPE for larger volumes of filtered field seawater suggests that the affinity of uranine for the C_{18} surface of the SPE column is not as high as that of other components in the seawater. This may be because there is insufficient uncharged neutral uranine species at pH 3.0. Our research shows that the volume of sample seawater is important for quantitative determination of uranine. Around 90% recovery was achieved when a few ml of seawater was applied to SPE under our conditions. Since the maximum volume of HPLC was around 0.2 ml, the concentration of uranine from coastal seawater during SPE should be around 20-fold. Suijlen et al. [11] pointed out that the precision of measurements of field samples was 3 times less than that of artificially prepared samples. Similar loss of target dyes by competition with neutral components in field seawater during the SPE procedure might be one cause of lower precision irrespective of the target dyes. Much larger volumes of seawater than used in our current study might cause lower precision when concentrating uranine by SPE.

A background concentration of uranine at 0.14 ± 0.01 (s.d.) ng l^{-1} (0.37 ± 0.03 pM) in coastal water was measured in Sagami Bay (Fig. 4). When the apparent loss of uranine during SPE for 15 ml of natural seawater was estimated by a regression in Fig. 3, the corrected value amounts to 0.17 ng l^{-1} (0.45 pM). Since the tracer uranine released from the moored discharger was found in depth layers from 17 to 49 m within 104 h (data not shown), and the water column was stratified above 70 m depth (data not shown), the uniform distribution of uranine from the surface to 200 m could not be explained by the discharged water-mass. Thus a method to detect uranine as a tracer should be practically designed and consider the background concentration of uranine in seawater. Furthermore, the solubility of uranine and the possibility of toxic effect of uranine should also be considered. The toxic effect of uranine on fish, zooplankton and bacteria has been considered when using uranine as a tracer dye and insecticide, and in health care applications [1,4,5]. The lethal concentrations of uranine inducing 50% mortality were much higher than its recommended concentration in field applications (1–2 mg l^{-1}; 2.7–5.3 μM) [3–5].

Another factor affecting the detection limit of uranine is the photodegradation caused by sunlight since uranine has a high photodegradation decay constant [1]. The extent of photodegradation of uranine under sunlight in the tested seawater completely depended on photon dose irrespective of the intensity of incident irradiance (Fig. 5 lower panel). Based on the estimated decay constant of uranine (Fig. 5 lower panel), the solar radiation in the summer in the central part of Japan, and the light attenuation constant (0.11 m^{-1}), such as in the typical waters in Sagami Bay [19], the uranine concentration, 100 h after discharge, would not be significantly affected by photodegradation process below a depth of 75 m although it would decrease to 90%, 10% and less than 1% at 48, 20 and 12 m depths, respectively. Thus the light environment should also be considered when designing the detection range of uranine and the scale of tracer experiments.

5. Conclusion

Two-step separation and detection of uranine by SPE and HPLC was examined by considering the equilibrium behavior of uranine at different pH values. High uranine concentrations can be determined by *in situ* (ultraviolet) spectrophotometers (ISUS) [20]. Since uranine has a characteristic absorption spectrum in the ultraviolet region, initial high (0.08–1 mg l^{-1}; 0.2–3 μM) concentrations could be determined by ISUS. After the release of uranine, it was detected at around 0.24 mg l^{-1} (0.64 μM) in a water-mass (unpublished work). The detection limit of uranine in seawater was improved to 0.2 ng l^{-1} (0.5 pM) for a 5 ml sample of seawater. Thus concentration ranges within an order of 10^7 can be covered by HPLC after SPE (10^{-7} to 10^{-2} mg l^{-1}; 3×10^{-7} to 3×10^{-2} μM) in combination with *in situ* fluorometry and spectrophotometry (10^{-4} to 1 mg l^{-1}; 3×10^{-4} to 3 μM). Such a potentially wide detection range of a target dye is suitable for consistent determination of tracer experiment at large scale in time and space.

Acknowledgments

This work was partly supported by the Ministry of Education, Culture, Sports, Science and Technology, Japan (MEXT) and a grant from Hyogo Prefecture for Y.K., and by the Marino-Forum 21 (Tokyo).

References

[1] P.L. Smart, I.M.S. Laidrow, Water Resour. Res. 13 (1977) 15–33.
[2] M.L. Viriot, J.C. André, Analusis 17 (1989) 97–111.
[3] H. Pouliquen, M. Algoet, V. Buchet, H. Bris, Vet. Hum. Toxicol. 37 (1995) 527–529.
[4] H. Wang, L. Lu, S. Zhu, Y. Li, W. Cai, Curr. Microbiol. 52 (2006) 1–5.
[5] J. Carré, M. Joyeux, A. Montiel, Environ. Risques Santé 6 (2007) 443–452.
[6] B.B. Prezelin, B.A. Boczar, in: F.E. Round, D.J. Chapman (Eds.), Progress in Phycological Research, vol. 4, Biopress Ltd., Bristol, 1987, pp. 349–464.
[7] L.S. Murphy, E.M. Haugen, Limnol. Oceanogr. 30 (1985) 47–58.
[8] T. Ikeya, K. Ohki, M. Takahashi, Y. Fujita, J. Oceanogr. Soc. Jpn. 47 (1991) 1–6.
[9] R.W.P.M. Laane, M.W. Manuels, W. Staal, Water Res. 18 (1984) 163–165.
[10] J.W. Hofsttraat, M. Steendijl, G. Vriezekolk, W. Schreurs, G.J.A.A. Broer, N. Wijnstok, Water Res. 25 (1991) 883–890.
[11] J.M. Suijlen, W. Staal, P.M. Houpt, A. Draaier, Cont. Shelf Res. 14 (1994) 1523–1538.
[12] C. Franke, H. Weserholm, R. Niessner, Water Res. 31 (1997) 2633–2637.
[13] R.C. Upstill-Goddard, J.M. Suijlen, G. Malin, P.D. Nightingale, Limnol. Oceanogr. 46 (2001) 927–934.
[14] V. Zanker, W. Peter, Chem. Ber. 91 (1958) 572–580.
[15] S.A. Smith, W.A. Pretorius, Water S.A. 28 (2002) 395–402.
[16] S.A. Smith, W.A. Pretorius, Water S.A. 28 (2002) 403–406.
[17] Waters. Waters Xbridge™ HPLC columns whitepaper, 2004, http://www.waters.com/.
[18] K. Ouchi, T. Yamatogi, K. Kobayashi, M. Nakamura, Proceedings of the Ocean Community Conference '98, Marine Technology Society, Baltimore, 1998, pp. 129–136.
[19] Y. Yamada, K. Matsushita, Bull. Jpn. Soc. Fish. Oceanogr. 69 (2005) 206–229.
[20] K.S. Johnson, L.J. Coletti, Deep-Sea Res. 49 (Pt. 1) (2002) 1291–1305.

Talanta 79 (2009) 613–620

Contents lists available at ScienceDirect

Talanta

journal homepage: www.elsevier.com/locate/talanta

Comparison of several solid-phase extraction sorbents for continuous determination of amines in water by gas chromatography–mass spectrometry

Beatriz Jurado-Sánchez [a], Evaristo Ballesteros [b,*], Mercedes Gallego [a]

[a] Department of Analytical Chemistry, Campus of Rabanales, University of Córdoba, E-14071-Córdoba, Spain
[b] Department of Physical and Analytical Chemistry, E.P.S. of Linares, University of Jaén, Alfonso X, El Sabio, 28, E-23700 Linares, Jaén, Spain

ARTICLE INFO

Article history:
Received 3 February 2009
Received in revised form 3 April 2009
Accepted 16 April 2009
Available online 3 May 2009

Keywords:
Solid-phase extraction
Gas chromatography
Amines
Waters

ABSTRACT

A semiautomatic method has been proposed for the determination of different types of amines in water samples including anilines, chloroanilines, N-nitrosamines and aliphatic amines. The analytes were retained on a solid-phase extraction sorbent column and after elution, 1 μL of the extract was analysed by gas chromatography coupled with electron impact ionization mass spectrometry. A systematic overview is given of the advantages and disadvantages of several sorbents (LiChrolut EN, Oasis HLB, RP-C_{18}, graphitized carbon black, fullerenes and nanotubes) in the retention of amine compounds and based on sensitivity, selectivity and reliability. The retention efficiency for the studied amines was higher (ca. 100%) with LiChrolut EN and Oasis HLB than it was with RP-C_{18} and fullerenes (53 and 62%, respectively, on average). Detection limits of 0.5–16 ng L^{-1} for the 27 amines studied were obtained when using a sorbent column containing 75 mg of LiChrolut EN for 100 mL of sample, the RSD being lower than 6.5%. The method was applied with good accuracy and precision in the determination of amines in various types of water including river, pond, tap, well, drinking, swimming pool and waste.

1. Introduction

Amines such as anilines, their substituted chloro-derivates and N-nitrosamines (NAms), often occur at trace levels in a number of ambient environments including air, water, soil and waste [1–3]. They can be released directly into the environment from anthropogenic sources including cattle feed, waste incineration, automobile exhaust, cigarette smoke and various industries. Naturally occurring aliphatic, aromatic and polyamines are formed as metabolic products in microorganisms, plants and animals. These compounds are also widely used as raw materials in the production of dyes, polymers, surfactants, cosmetics and corrosion inhibitors. In addition, chlorinated anilines such as p-chloroaniline and 3,4-dichloroaniline can also be found as degradation products and intermediates of various phenylurea and phenylcarbamate pesticides. NAms are usually formed by nitrosation or oxidation reactions of amine precursors and as disinfection by-products [4,5]. Aromatic amines are suspected carcinogenic compounds; in fact, several anilines have been found to be carcinogenic in animal experiments [6]. Also, the European Union 76/464/CEE Directive [7] has included many amines in the list of priority pollutants which should be monitored in environmental waters. Aliphatic amines, not toxic in themselves, are well known for their odour and as precursors of NAms, which are classified as probable human carcinogens by the US Environmental Protection Agency (US EPA). This Agency has also established control levels for these compounds in drinking water at nanogram per liter [8].

The widespread use and harmfulness of amines make their analysis in environmental matrices important [9,10]. Several analytical methods for the determination of amines in water samples have been proposed, such as gas chromatography (GC) [3,9] liquid chromatography (LC) [11,12], capillary electrophoresis [13], spectrofluorimetry [14] and UV spectrophotometry [15]. In general, GC is superior to LC for the determination of amines with regard to resolution, and very often also in terms of separation time and sensitivity [16]. A wide variety of detectors can be used for the GC analysis of amines, including nitrogen–phosphorous [2,17], flame-photometry and electron-capture detectors [18], which offer increased selectivity for specific amines. Furthermore, GC with a mass-spectrometry detector (MS) can provide structural information for the unequivocal identification of amines [19–22]. In order to obtain limits of detection at nanogram per liter levels, a preconcentration step is mandatory in all instances. Amines have high polarity and solubility in water, so their extraction from water samples is difficult thus liquid–liquid extraction has been replaced by solid-phase microextraction [2,18,19,21,23,24] or solid-phase extraction (SPE) [25–27].

* Corresponding author. Tel.: +34 953648560; fax: +34 953648560.
E-mail address: eballes@ujaen.es (E. Ballesteros).

0039-9140/$ – see front matter © 2009 Elsevier B.V. All rights reserved.
doi:10.1016/j.talanta.2009.04.035

From a structural point of view, different amine groups such as aliphatic, aromatic and heterocyclic amines can be distinguished. The basic amine character depends on the amine compound, so aliphatic and heterocyclic amines often have pK_a around 9–11 while aromatic amines and NAms have pK_a between acid and a near-neutral range. The different pK_a values can influence amine retention on a SPE sorbent, so it is hard to find a universal sorbent for the big amine family, although probably non-polar sorbents in a basic medium are the best choice. In this context, SPE based on styrene–divinylbenzene copolymers [1,9,20,28] seemed especially promising because of their higher capacities and pH stability in comparison with common RP-C_{18} phases [12,26,29]. Fullerenes are hydrophobic sorbents which can establish π–π interactions with aromatic compounds and derivatized organometallic compounds [30,31]. From that premise, the aim of this work was the development of a continuous SPE system for the simultaneous preconcentration of various groups of amines (i.e., aliphatic amines, anilines, chloroanilines and N-nitrosamines). For this purpose a comparative study of several sorbent materials including conventional (LiChrolut EN, Oasis HLB, RP-C_{18} and graphitized carbon black), and non-conventional sorbents (C_{60} and C_{70} fullerenes, and nanotubes) were tested in order to select the best option in terms of universality, sensitivity and precision for amine retention.

2. Experimental

2.1. Chemical and standards

All amines were purchased by Sigma–Aldrich (Madrid, Spain) in the highest purity available. The compounds with their pK_a and $\log K_{o/w}$ values, as well as the retention times and the masses used for their detection are listed in Table 1. Triphenylphosphate (internal standard), sodium aluminosilicate and inert material of poly-(tetrafluoroethylene) white beads (pore diameter, 4 Å) were purchased from Fluka (Madrid, Spain). 2-*tert*-butyl-4-methylphenol was purchased from Merck (Darmstadt, Germany) and bromophos-methyl from Riedel-de-Haën (Seelze, Germany). Solvents (acetonitrile, ethyl acetate, *n*-hexane and methanol) were supplied by Merck, all in chromatographic grade. As amines are potential or actual carcinogens, all products were handled with care, using efficient fume hoods, avoiding inhalation or skin contact and wearing protective latex gloves. C_{60} fullerene (99.9%. particle size 50–70 μm), C_{70} fullerene (99%, particle size 50–70 μm), and multiwall carbon nanotubes (MWCNTs) (2–15 nm in diameter, 1–10 μm long, with 5–20 graphic layers) were supplied by MER Corp. (Tucson, AZ, USA). LiChrolut EN (particle size 40–120 μm) was purchased from Merck; Oasis HLB (particle size 30–60 μm) was obtained from Waters (Madrid, Spain); graphitized carbon black (GCB) (particle size 80–100 μm) and silica-reverse-phase sorbent with octadecyl functional groups (RP-C_{18}, particle size 60–80 μm) were provided by Supelco (Madrid, Spain).

Individual stock standard of all amines (10 g L^{-1}) were prepared in methanol and stored at 4 °C in the dark. Two standard working solutions were prepared by sequential dilution of each standard solution with water purified by a Milli-Q system (Millipore, Bedford, MA, USA), one for NAms and anilines adjusted at pH 7.4 with dilute $NaHCO_3$ and the other for aliphatic amines adjusted at pH 12 with dilute NaOH. The eluent was a mixture of ethyl acetate–acetonitrile 9:1 (v/v) containing 1 mg L^{-1} of triphenylphosphate as internal standard (IS), which was freshly prepared on a daily basis.

2.2. Instruments and apparatus

Amine determinations were done by using a Focus GC instrument interfaced to a DSQ II mass spectrometer and controlled by a computer running XCalibur software (Thermo Electron SA, Madrid, Spain). The GC instrument was equipped with a polydimethylsiloxan (95%) cross-linked DB-5 capillary column (Supelco, 30 m × 0.25 mm I.D. × 0.25 μm film thickness) using helium (purity >99.999%) as carrier gas (1 mL min^{-1}). For the determination of NAms and anilines, the injection port was kept at 250 °C and the oven temperature program was as follows: 50 °C, held for 1 min; ramp to 100 °C at 5 °C min^{-1}; ramp to 220 °C at 9 °C min^{-1}.The determination of low-molecular-weight amines (i.e., propylamine, butylamine and pentylamine) by gas chromatography is particularly difficult due to their high volatility; for this reason, soft GC conditions are required [32]. The injector port was kept at 200 °C, and to separate/determine aliphatic amines the next oven temperature program was programmed: 40 °C; ramp to 50 °C at 3 °C min^{-1}; ramp to 240 °C at 40 °C min^{-1}. The sample injection for all amines was done in the split mode (1:20 ratio), using an injection volume of 1 μL. The mass spectrometer was used in the following conditions: ion source temperature, 200 °C; transfer line temperature, 220 °C; electron impact ionization mode, 70 eV; scan

Table 1
Studied amines with pK_a, retention times, t_r and mass values used for detection.

Amine	$\log K_{o/w}$	pK_a	t_r (min)	Detected (m/z)[a,b]
N-nitrosamines				
N-nitrosodimethylamine (NDMA)	0.57	–	4.50	42, 43, **74**
N-nitrosodiethylamine (NDEA)	0.48	–	5.88	42, 44, **102**
N-nitrosopyrrolidine (NPYR)	−0.19	–	10.80	41, 42, **100**
N-nitrosomorpholine (NMOR)	−0.44	–	10.90	**56**,86,116
N-nitrosopiperidine (NPIP)	0.36	–	11.96	**42**, 55, 114
N-nitrosodibutylamine (NDBA)	2.63	–	15.37	57, **84**, 158
N-nitrosodiphenylamine (NDPhA)	3.13	–	21.18	42, 167, **168**
N-nitrosodimethylaniline (NDMAN)	–	3.56	20.50	42, 105, **150**
N-nitrosodiethylaniline (NDEAN)	–	0.67	21.03	**133**, 163, 178
4-Nitrosodiphenylamine (4-NDPhA)	–	–	22.50	**167**, 168, 198
Anilines				
Aniline (A)	0.9	4.6	8.02	65, 66, **93**
2-Chloroaniline (2-CLA)	1.92	2.66	12.43	65, **127**,129
3-Chloroaniline (3-CLA)	1.88	3.52	13.90	65, **127**,129
4-Chloroaniline (4-CLA)	1.83	3.97	19.08	65, **127**,129
2,3-Dichloroaniline (2,3-DCLA)	2.78	–	14.93	90, **161**, 163
2,4-Dichloroaniline (2,4-DCLA)	2.78	2	16.71	90, **161**, 163
2,5-Dichloroaniline (2,5-DCLA)	2.75	–	15.00	90, **161**, 163
2,6-Dichloroaniline (2,6-DCLA)	2.82	0.71	14.80	90, **161**, 163
3,4-Dichloroaniline (3,4-DCLA)	2.69	2.9	17.02	90, **161**, 163
3,5-Dichloroaniline (3,5-DCLA)	2.90	–	16.91	90, **161**, 163
2,4,5-Trichloroaniline (2,4,5-TCLA)	3.45	0.96	17.96	**195**, 197, 199
2,4,6-Trichloroaniline (2,4,6-TCLA)	3.52	0.07	19.98	**195**, 197, 199
3,4,5-Trichloroaniline (3,4,5-TCLA)	3.32	1.85	21.50	**195**, 197, 199
2-Nitroaniline (2-NA)	1.85	0.26	18.15	65, 92, **138**
Aliphatic amines				
Propylamine (PA)	0.15	10.71	4.8	28, **30**, 59
Butylamine (BTA)	0.86	10.68	4.9	28, **30**, 41
Pentylamine (PTA)	1.49	10.69	5.2	**30**, 41, 87

[a] The base peaks used for quantification are boldfaced.
[b] m/z for IS (triphenylphosphate): 77, 325, **326**.

range, from m/z 30 to 326. Peak area was chosen as the analytical signal for quantification purposes. The time for solvent delay was set to 4 min.

The continuous flow configuration were assembled from a Gilson Minipuls-3 peristaltic pump (Villiers-le-Bel, France) fitted with poly(vinylchloride) pumping tubes, two Rheodyne 5041 injection valves (Cotati, CA, USA) and PTFE (3 mm I.D.) laboratory-made columns of different lengths packed with each sorbent material. In order to avoid abrupt changes in column compactness when LiChrolut EN or Oasis HLB sorbents were soaked, each sorbent segment (1.0 cm long) were separated by one segment of an inert material (i.e., PTFE beads, segments of ~0.5 cm long). The sorbents column were conditioned as follows: 0.5 mL of acetonitrile and then 1 mL of purified water for LiChrolut EN and Oasis HLB; 1 mL of methanol and 1 mL of purified water for RP-C_{18}; and 0.5 mL of *n*-hexane–acetonitrile (1:1) and 1 mL of purified water for fullerenes and MWCNTs. Columns prepared sequentially exhibited analytical signals with similar analyte-to-internal standard areas ratio which confirm their high reproducibility.

2.3. Sampling procedure

Water samples were collected from various locations in 1 L opaque PTFE bottles. Ascorbic acid (20 mg L^{-1}) was added as a preservative. Samples were then stored at 4 °C until analysis (within 2 weeks of collection). Before the analysis, water samples (if required) were filtered through a 0.45 μm membrane filter (mixed cellulose esters, Millipore) and the pH values adjusted at 7.4 or 12 with an appropriate amount of diluted $NaHCO_3$ or NaOH, respectively.

2.4. Solid-phase extraction method

The continuous SPE system employed for the continuous preconcentration/elution of amines in water is depicted in Fig. 1. Sample volumes up to 300 mL (for 75 mg of LiChrolut EN sorbent) or standard solutions at pH 7.4 (for NAms and anilines) or at pH 12 (for aliphatic amines) containing between 0.2 and 2000 ng of amines were aspirated at 5.5 mL min^{-1} through the sorbent column. All amines were sorbed and the sample matrix was sent to waste. Simultaneously, the loop of the second valve (IV_2) was filled with the eluent (ethyl acetate–acetonitrile 9:1 with the IS) by means of a syringe. Any residual water remaining inside the column and the connectors was flushed by passing an air stream through the carrier line at 3 mL min^{-1} for 2 min. Next, IV_2 was switched to pass the loop contents (150 μL) through the column, in the opposite direction of the sample, in order to elute amines. The organic extract was collected in a safe-lock tube of 0.5 mL containing sodium aluminosilicate (desiccator), and aliquots of 1 μL were manually injected into the gas chromatograph for analysis. Under these conditions, the sorbent column was serviceable for about 6 months.

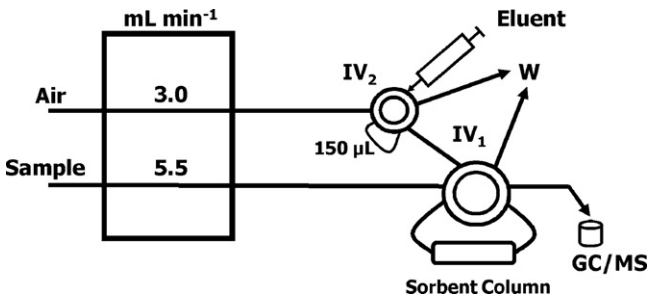

Fig. 1. Continuous flow system developed for the preconcentration/clean-up of amines in water samples. IV: injection valve; W: waste; IS: internal standard, GC/MS: gas chromatograph with mass-spectrometric detector.

3. Results and discussion

3.1. Selection of the sorbent using a flow system

In a previous work, we developed an SPE system for the preconcentration of seven NAms in water by using LiChrolut EN as the sorbent material [27]. This system was initially used for the simultaneous retention of 27 amines, including NAms, anilines and aliphatic amines. Reversed phase SPE involves the partitioning of organic solutes from a polar mobile phase, in our case the water sample, into a non-polar phase, such as bonded hydrocarbon phases (RP-C_{18}), GCB and polymeric sorbents (LiChrolut EN and Oasis HLB). The hydrophobic or partitioning mechanism is a low-energy process (5 kcal mol^{-1}) analogous to a molecule being removed from water in a liquid–liquid extraction [33]. The graphitized carbon sorbents apparently not only have a hydrophobic effect but also the potential for specific interactions with the analyte; thus, they can act as a mixed-mode sorbent (reversed-phase and anion exchange) [33]. Polymeric sorbents contain aromatic rings which permit electron–donor interactions between the sorbent and π bonds of the solute; furthermore, these materials are often "doped" with a hydrophilic group, such as sulfonic acid, which imparts a somewhat polar character to the matrix of the sorbent. Therefore polymeric sorbents can act as a mixed-mode sorbent having more capacity for polar compounds. Fullerenes normally have been used as sorbents in reversed phase, and they only interact with organic compounds by π–π interactions [34]. Based on these premises, the above sorbents materials were selected for the retention of aliphatic and aromatic amines with a variable log of octanol–water partition coefficient (to predict analyte behaviour based on its hydrophobicity) and pK_a values (to predict analyte behaviour based on its polar interactions), as can be seen in Table 1.

Conventional sorbents (RP-C_{18}, GCB, LiChrolut EN and Oasis HLB) and non-conventional ones such as C_{60} and C_{70} fullerenes, and MWCNTs were selected in this study. For this purpose each column was packed with 80 mg of the sorbent and the sorption efficiency was assessed by comparing the amount of each amine present in fractions of 5 mL of standard solutions containing 15 ng of each amine before (100% recovery) and after (unsorbed) the sorbent column. Each aqueous solution fraction was extracted by hand with 1 mL of ethyl acetate, and 1 μL aliquots were injected into the gas chromatograph for their analysis. Taking into account that the three aliphatic amines (propylamine, butylamine and pentylamine) require different GC conditions than the other 24 amines studied (anilines and NAms), we also selected two standard solutions at different pH considering the different pK_a values of the two groups of amines. The standard solution of the three aliphatic amines was adjusted at pH 12 with diluted NaOH (pH higher than their pK_a values) whereas the standard solution for the other 24 anilines and NAms were adjusted at pH 7.4 with diluted $NaHCO_3$. The average sorption efficiency ($n = 3$) for all amines was dependent on the individual sorbent as listed in Table 2. As can be observed, the maximum amine sorption (ca. 100%) was obtained for LiChrolut EN and Oasis HLB, whereas for the other sorbents the sorption was variable ranging from less than 10 to 100%. Aliphatic amines were unretained on GCB, fullerenes and MWCNTs, whereas on RPC_{18} there was under 12% retention.

With regard to RP-C_{18}, the retention of anilines was similar to that of fullerenes and MWCNTs, as will be discussed later. Surprisingly, RP-C_{18} interacts with all NAms but it would only be useful for four NAms: two aliphatics (NDMA and NDBA) and the two diphenylamines. The retention of NAms on GCB was similar to that of fullerenes and MWCNTs since the higher percent sorption (ca. 80%) was obtained for the aromatic fraction. This sorbent is not valid for the retention of anilines as shown in Table 2, since its sorption per-

Table 2
Percent sorption of amines on different sorbent materials[a,b].

Amine	LiChrolut EN	Oasis HLB	RP-C_{18}	GCB	C_{60} fullerene	C_{70} fullerene	MWCNTs
N-nitrosamines							
NDMA	99.9	99.9	100.0	5.0	0	0	0
NDEA	100.0	99.9	52.8	4.6	0	0	0
NPYR	99.0	99.5	12.5	27.7	0	0	0
NMOR	100.0	99.9	14.0	4.0	0	0	0
NPIP	99.5	90.2	25.5	4.0	0	0	0
NDBA	99.5	100.0	100.0	28.0	0	0	0
NDPhA	99.9	100.0	100.0	82.1	100.0	98.9	99.9
NDMAN	99.0	90.0	58.0	79.9	99.0	98.8	99.0
NDEAN	99.8	100.0	54.5	80.0	99.9	99.9	99.8
4-NDPhA	99.9	100.0	100.0	79.7	100.0	100.0	99.9
Aliphatic amines							
PA	99.8	99.9	11.0	0	0	0	0
BTA	99.9	99.8	6.0	0	0	0	0
PTA	100.0	99.9	7.0	0	0	0	0
Aromatic amines							
A	100.0	98.0	8.0	22.3	4.0	3.9	3.8
2-CLA	100.0	98.0	28.0	13.3	15.0	12.0	17.0
3-CLA	100.0	95.0	30.0	7.3	19.0	18.0	17.0
4-CLA	100.0	100.0	34.5	12.8	34.0	34.0	32.0
2,3-DCLA	100.0	99.0	11.0	13.5	15.0	12.0	11.0
2,4-DCLA	100.0	100.0	99.9	14.0	99.0	94.5	90.0
2,5-DCLA	100.0	99.9	11.0	14.3	6.0	6.0	5.0
2,6-DCLA	100.0	99.5	55.2	13.0	57.1	55.0	50.0
3,4-DCLA	99.8	99.9	10.0	2.0	18.0	17.0	16.0
3,5-DCLA	100	99.6	70.4	11.0	78.0	71.0	72.0
2,4,5-TCLA	99.9	99.5	95.0	31.3	100.0	100.0	100.0
2,4,6-TCLA	100.0	100.0	100.0	4.5	100.0	100.0	100.0
3,4,5-TCLA	100.0	99.5	100.0	5.2	99.9	99.8	100.0
2-NA	99.9	99.5	90.0	5.7	90.0	88.9	87.0

[a] For 80 mg SPE sorbents.
[b] Sample pH adjusted at pH 7.4 (for NAms and anilines) or at pH 12 (for aliphatic amines).

cent is the lowest of all the sorbents tested. This can be ascribed to the fact that the bond strength is generally lower in graphitized carbon than with other sorbents, probably because only non-specific Van der Waals forces are the main sorption mechanism [35].

Fullerenes and MWCNTs characteristics were unlike those of sorbents, thus, as mentioned above, they could only establish π–π interactions with aromatic compounds and therefore non-aromatic compounds were not retained in these materials. For the four aromatic N-nitrosamines (N-nitrosodiphenylamine, N-nitrosodimethylaniline, N-nitrosodiethylaniline and 4-nitrosodiphenylamine), the sorption efficiency was ca. 100%, while it was 0% for the non-aromatic ones. With regard to anilines, the three sorbents show similar behaviour, thus sorption efficiency increases with the number of chlorine atoms, since the polarity of the aromatic ring also increases along with, as a consequence, the number of π–π interactions. Surprisingly 2,4- and 3,5-dichloroaniline are retained more than 90 and 70%, respectively, unlike the other disubstituted anilines studied. This fact can be explained through the presence of chlorine atoms in a more accessible position to establish anion–π interactions. In an effort to comprehend the underlying basis of this interaction, Kim et al. [36] researched the interaction of various anions (including complexes of halide) with several representative π systems. Anion–π interactions are marked by substantial contributions from dispersion energies, which increase for aromatic anions. In addition, for halide anions the interactions are dominated by electrostatic and induction forces.

According to the results obtained with the six sorbents listed in Table 2, it can be seen that GCB is the worst of all and the least selective, followed by RP-C_{18}. Fullerenes and MWCNTs mainly interact with aromatic NAms and trichloroanilines. Only LiChrolut EN and Oasis HLB sorbents retain the 27 amines selected in this study because they act as a mixed-mode sorbent with more capacity for polar compounds such as amines. Therefore both polymeric sorbents were selected for further experiments.

The first variable studied was the sample pH over the range 2–14. In the above experiments for NAms [27], a mixture of ethyl acetate–acetonitrile (9:1) was found to be the most effective eluent, and was initially adopted for the 27 amines. For this purpose, 25 mL of standard solutions containing 1 μg L^{-1} of each amine were prepared at variable pH adjusted with diluted HCl or NaOH, and preconcentrated into the SPE system depicted in Fig. 1. As could be expected, the compounds were retained in neutral form; thus, anilines and all NAms exhibited an optimum interval in neutral medium (6.5–8.5), whereas the three aliphatic amines were only retained above pH 12. By way of example, Fig. 2 shows the effect

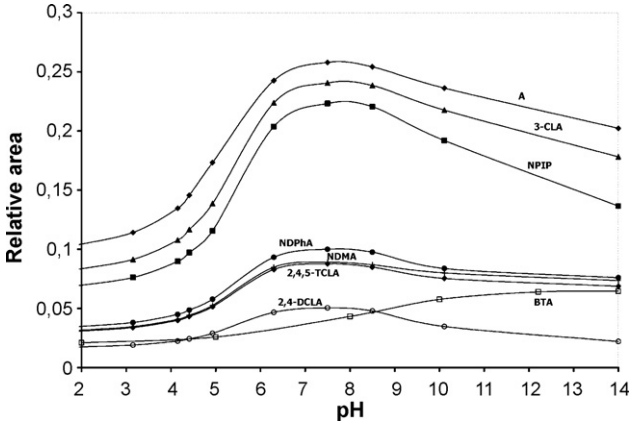

Fig. 2. Influence of sample pH on the retention of amines. Analyte concentration: 1 μg L^{-1}; relative area: ratio of analyte area to internal standard (1 mg L^{-1} of triphenylphosphate).

of pH on the retention of a representative amine from each studied group on the LiChrolut EN sorbent. This behaviour was similar for the two sorbents, LiChrolut EN and Oasis HLB, which can be ascribed to the fact that the retention mechanism of the amines in the two sorbents is mainly due to hydrophobic interactions. When an analyte is in neutral form, it becomes more hydrophobic, and retention strengthens under reverse-phase conditions. For amines, when the sample pH is adjusted at 2 pH units above its pK_a values, the compounds are neutralized. As can be seen in Table 1 (where only the pK_a values found in the bibliography are listed), aliphatic amines had pK_a values over 10.7 and thus required a sample pH value of 12 or higher. For this reason, the simultaneous determination of 27 amines in one sample was not possible because NAms and anilines should be determined at a pH lower than 8.5 (pH 7.4 was selected by adjusting with diluted $NaHCO_3$), whereas aliphatic amines required pH 12 (adjusted with diluted NaOH). However, this is not a shortcoming of the method since, as mentioned above in Section 2, the chromatographic conditions employed for aliphatic amines were very different for other amines.

The optimum amount of each type of sorbent was established by using various columns containing 25–100 mg of LiChrolut EN or Oasis HLB. A series of calibration graphs were constructed for each organic extract by passing 25 mL of aqueous standard solutions containing variable amounts of the amines and eluting with 150 μL of 9:1 ethyl acetate–acetonitrile in each case. The amount of sorbent used was found to be quite influential; thus, the sensitivity (slope of the calibration graph) was 8 times higher with 75 mg than it was with 25 mg of LiChrolut EN sorbent. Similarly, the sensitivity was 7 times with 60 mg of Oasis HLB than it was with 25 mg of the same sorbent. Columns containing more than 80 or 65 mg of LiChrolut EN or Oasis HLB, respectively, required increased volumes of eluent for complete elution of the amines. This was confirmed by a second injection (150 μL) of eluent subjected to no preconcentration, which resulted in an extent of carryover that increased with increasing amount of sorbent above 80 mg of LiChrolut EN and 65 mg of Oasis HLB. Working columns packed with 75 mg of LiChrolut EN or 60 mg of Oasis HLB were therefore used in subsequent tests. Also, the elution efficiency with several organic solvents of variable polarity was evaluated, but the mixture of ethyl acetate–acetonitrile (9:1) was the eluent that provided no carryover for a 150 μL volume. The sample and eluent flow rates were similar for the two sorbents, selecting the highest values 5.5 and 3.0 mL min^{-1}, respectively.

The breakthrough volume of the sample was the last variable evaluated in the optimized system. This parameter is crucial in SPE methods because it is directly related to the enrichment factor, and therefore to the sensitivity of the method. This study was carried out by preparing 15 ng of each amine in variable volumes of purified water (from 10 to 400 mL) at pH 12 (aliphatic amines) or pH 7.4 (anilines and NAms). Sorption efficiency of ca. 100% was obtained with aqueous volumes of up to 300 and 180 mL for LiChrolut EN and Oasis HLB, respectively.

Finally, among the different internal standards assayed (triphenylphosphate, bromophos-methyl and 2-*tert*-butyl-4-methylphenol), triphenylphosphate was finally selected because its chromatographic peak was the only one that did not overlap with any of the analytes.

3.2. Calibration and statistical study

The performance and reliability of the proposed off-line SPE-GC/MS method (Fig. 1) were assessed by determining the regression equation, linear range, analyte detectability and relative standard deviation for the 27 amines studied and for both sorbent columns. For this purpose, 50–200 μL of working standard solutions containing 24 NAms and anilines or three aliphatic amines at variable concentrations were spiked to individual 100 mL of uncontamined drinking water, in the interval 2–20,000 ng L^{-1}, and extracted as in Section 2.4. Figures of merit of the proposed method are listed in Table 3; the correlation coefficient was higher than 0.995 (12 points per calibration) in all instances. Limits of detection (LOD), defined at the concentration of the analyte that provides a chromatographic peak equal to three times the regression standard deviation ($S_{y/x}$) divided by the slope of the calibration graph, ranged from 0.5 to 6.9, and 3.9 to 17.0 ng L^{-1} for anilines and NAms and aliphatic amines, respectively. The precision was calculated as the relative standard deviation obtained by measuring 11 samples at pH 12 or 7.4 containing the amines at concentrations within the lower range of the calibration graphs (60–100 ng L^{-1}) and ranged from 4.0 to 6.0% (within-day precision) and from 5.4 to 6.5% (between day precision).

Recoveries of the method were calculated by using various types of water (river, pond, tap, well, drinking, swimming pool and waste) that did not have amines at detectable values, by spiking two different concentrations of each amine (60 and 200 ng L^{-1}) to 100 mL of sample by triplicate ($n = 3$) for both class of sorbents (LiChrolut EN and Oasis HLB). As can be observed in Table 4, recoveries ranged from 95 to 103%, which testify the applicability of the proposed method to any water sample because favourable results were obtained even in complex matrixes (viz. wastewater). By way of example, Fig. 3 shows the chromatograms obtained for the analysis of 100 mL of an uncontamined drinking water sample spiked with 100 ng L^{-1} of anilines and NAms (pH 7.4, Fig. 3A) and aliphatic amines (pH 12, Fig. 3B), using the LiChrolut EN column. As can be observed in Fig. 3A, 24 amines could be separated in a single chromatographic run in about 23 min without difficulty in the separation of positional isomers (mono-, di- and trichloroanilines). Aliphatic amines separation was achieved in less than 5 min. It should be also noticed that the resulting chromatograms were very clean due to the mass spectrometer was set in the SIM mode.

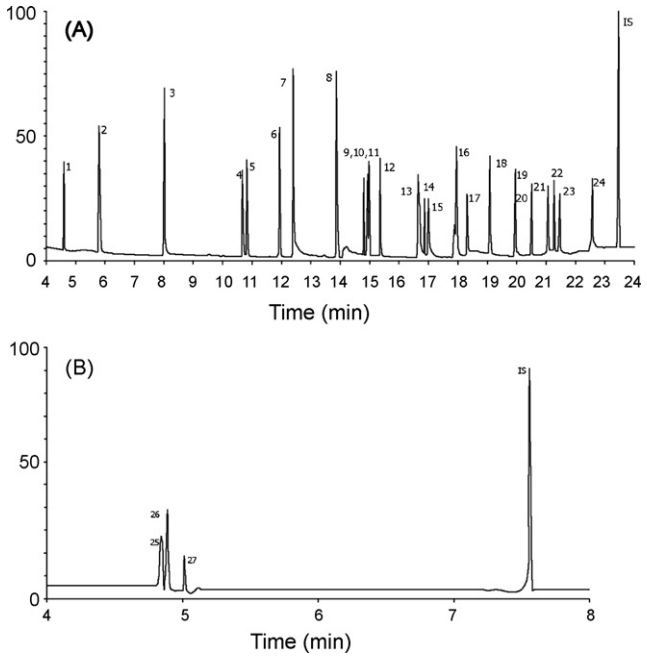

Fig. 3. GC/MS chromatograms in SIM mode for (A) a drinking water fortified with 100 ng L^{-1} of anilines and N-nitrosamines and (B) of aliphatic amines. 1: NDMA; 2: NDEA; 3: A; 4: NPYR; 5: NMOR; 6: NPIP; 7: 2-CLA; 8: 3-CLA; 9: 2,6-DCLA; 10: 2,3-DCLA; 11: 2,5-DCLA; 12: NDBA; 13: 2,4-DCLA; 14: 3,5-DCLA; 15: 3,4-DCLA; 16: 2,4,5-TCLA; 17: 2-NA; 18: 4-CLA; 19: 2,4,6-TCLA; 20: NDMAN; 21: NDEAN; 22: NDPhA; 23: 3,4,5-TCLA; 24: 4-NDPhA; 25: PA; 26: BTA; 27: PTA; IS: internal standard.

Table 3
Limits of detection, linearity and precision of the investigated amines[a].

Amine	LOD[b] (ng L^{-1})		Linear range (ng L^{-1})				RSD[c] (%)			
	LiChrolut EN	Oasis HLB	LiChrolut EN	r[d]	Oasis HLB	r[d]	Within-day		Between day	
							LiChrolut EN	Oasis HLB	LiChrolut EN	Oasis HLB
NDMA	2.7	2.8	8–20,000	0.9999	10–20,000	0.9999	5.9	6.0	6.4	6.5
NDEA	1.1	1.2	3–20,000	0.9998	4–20,000	0.9997	5.4	5.8	6.0	6.4
NPYR	3	3.3	10–20,000	0.9997	11–20,000	0.9996	5.7	5.6	6.0	6.1
NMOR	2.7	2.8	8–20,000	0.9996	9–20,000	0.9998	5.8	5.7	6.1	6.4
NPIP	1.2	1.5	4–20,000	0.9997	5–20,000	0.9998	5.5	5.4	6.0	6.2
NDBA	3.0	3.3	10–20,000	0.9996	11–20,000	0.9999	6.0	5.9	6.3	6.5
NDPhA	2.4	2.5	8–20,000	0.9999	9–20,000	0.9999	4.2	4.0	5.8	5.9
NDMAN	3.1	3.0	10–20,000	0.9996	10–20,000	0.9996	5.4	5.4	6.0	6.1
NDEAN	3.7	3.8	15–20,000	0.9999	15–20,000	0.9999	4.2	4.0	5.9	5.6
4-NDPhA	3.1	3.2	10–20,000	0.9998	10–20,000	0.9999	5.3	4.9	6.0	6.1
A	0.8	0.8	3–20,000	0.9996	3–20,000	0.9998	4.6	4.9	5.8	5.9
2-CLA	0.5	0.5	2–20,000	0.9999	2–20,000	0.9997	4.0	4.1	5.9	5.6
3-CLA	1.0	1.0	3–20,000	0.9998	3–20,000	0.9996	4.1	4.4	5.9	5.8
4-CLA	2.2	2.5	8–20,000	0.9996	9–20,000	0.9999	5.6	5.5	6.4	6.5
2,3-DCLA	4.5	4.0	15–20,000	0.9999	14–20,000	0.9998	4.0	4.0	5.4	5.2
2,4-DCLA	5.0	5.1	16–20,000	0.9997	16–20,000	0.9998	4.9	4.0	5.4	5.3
2,5-DCLA	2.8	2.8	10–20,000	0.9998	10–20,000	0.9997	4.7	4.2	5.8	5.6
2,6-DCLA	4.1	4.2	15–20,000	0.9996	15–20,000	0.9999	5.9	5.2	6.5	6.3
3,4-DCLA	6.5	6.5	22–20,000	0.9998	22–20,000	0.9996	4.8	4.8	5.6	5.7
3,5-DCLA	6.7	6.9	22–20,000	0.9999	22–20,000	0.9998	4.8	4.8	5.7	5.6
2,4,5-TCLA	2.7	2.8	8–20,000	0.9997	8–20,000	0.9998	5.3	5.3	6.2	6.1
2,4,6-TCLA	3.2	3.3	10–20,000	0.9998	10–20,000	0.9999	5.0	5.0	6.0	6.2
3,4,5-TCLA	4.3	4.5	14–20,000	0.9999	14–20,000	0.9999	5.0	5.2	6.1	6.0
2-NA	5.1	4.8	16–20,000	0.9996	15–20,000	0.9996	5.1	5.3	6.0	6.2
PA	8.2	8.3	28–20,000	0.9999	28–20,000	0.9997	5.4	5.1	6.2	6.4
BTA	3.9	4.3	14–20,000	0.9998	17–20,000	0.9998	5.1	4.9	6.4	6.4
PTA	16.1	17.0	55–20,000	0.9999	60–20,000	0.9999	5.2	4.7	6.3	6.1

[a] Sample adjusted at pH 7.4 (for NAms and anilines) or at pH 12 (for aliphatic amines); volume, 100 mL.
[b] Limit of detection.
[c] Relative standard deviation (n = 11).
[d] Correlation coefficient.

Table 4
Average recoveries of amines spiked to water samples[a].

Amine	Pond water (ng L^{-1})		Wastewater (ng L^{-1})		Well water (ng L^{-1})		Tap water (ng L^{-1})		River water (ng L^{-1})		Swimming pool (ng L^{-1})	
	60	200	60	200	60	200	60	200	60	200	60	200
NDMA	98 ± 5	103 ± 4	102 ± 5	95 ± 5	95 ± 5	97 ± 4	101 ± 5	96 ± 4	101 ± 5	102 ± 6	100 ± 5	97 ± 4
NDEA	100 ± 6	97 ± 4	103 ± 5	103 ± 6	100 ± 4	102 ± 5	96 ± 4	99 ± 4	100 ± 4	99 ± 5	103 ± 4	97 ± 5
NPYR	98 ± 5	97 ± 4	99 ± 4	98 ± 4	99 ± 4	102 ± 4	103 ± 4	101 ± 5	101 ± 4	99 ± 4	101 ± 6	100 ± 5
NMOR	98 ± 6	102 ± 5	103 ± 5	102 ± 5	101 ± 6	102 ± 6	99 ± 5	101 ± 6	99 ± 5	97 ± 4	99 ± 5	99 ± 5
NPIP	98 ± 5	96 ± 4	98 ± 4	100 ± 6	98 ± 4	100 ± 4	101 ± 6	102 ± 4	103 ± 4	97 ± 5	98 ± 4	100 ± 6
NDBA	101 ± 5	99 ± 4	99 ± 5	100 ± 6	97 ± 5	98 ± 5	101 ± 4	101 ± 5	101 ± 6	100 ± 5	99 ± 5	100 ± 6
NDPhA	103 ± 4	99 ± 5	98 ± 6	103 ± 6	102 ± 4	103 ± 5	97 ± 5	96 ± 6	100 ± 5	99 ± 5	98 ± 6	103 ± 6
NDMAN	101 ± 4	100 ± 5	103 ± 4	99 ± 5	103 ± 4	98 ± 4	99 ± 5	102 ± 5	103 ± 4	98 ± 5	100 ± 6	97 ± 4
NDEAN	99 ± 4	103 ± 5	102 ± 4	99 ± 5	99 ± 6	99 ± 6	98 ± 4	97 ± 4	100 ± 6	100 ± 4	102 ± 5	97 ± 4
4-NDPhA	98 ± 4	101 ± 5	100 ± 5	99 ± 5	103 ± 4	97 ± 4	97 ± 4	99 ± 5	97 ± 4	100 ± 5	101 ± 4	99 ± 5
A	101 ± 5	96 ± 4	99 ± 5	97 ± 5	100 ± 6	98 ± 5	95 ± 5	102 ± 5	99 ± 5	103 ± 6	102 ± 5	102 ± 5
2-CLA	101 ± 6	98 ± 4	103 ± 5	99 ± 6	102 ± 4	100 ± 5	97 ± 5	102 ± 6	99 ± 6	103 ± 4	100 ± 6	99 ± 6
3-CLA	99 ± 5	103 ± 4	98 ± 4	101 ± 4	103 ± 5	103 ± 4	99 ± 4	98 ± 4	97 ± 6	102 ± 5	97 ± 4	103 ± 6
4-CLA	102 ± 6	98 ± 5	98 ± 5	96 ± 5	103 ± 4	102 ± 5	102 ± 5	97 ± 5	100 ± 6	102 ± 4	99 ± 6	103 ± 4
2,3-DCLA	10 1 ± 5	96 ± 6	100 ± 4	103 ± 6	97 ± 6	98 ± 4	101 ± 4	96 ± 6	96 ± 5	102 ± 5	98 ± 5	100 ± 4
2,4-DCLA	99 ± 5	103 ± 4	99 ± 5	103 ± 6	97 ± 4	100 ± 4	101 ± 5	99 ± 4	101 ± 5	99 ± 6	100 ± 6	98 ± 5
2,5-DCLA	98 ± 4	101 ± 5	102 ± 6	103 ± 6	97 ± 5	99 ± 5	99 ± 4	103 ± 5	98 ± 5	101 ± 4	102 ± 5	99 ± 6
2,6-DCLA	103 ± 4	102 ± 5	103 ± 4	99 ± 5	99 ± 5	100 ± 6	98 ± 6	101 ± 5	99 ± 5	100 ± 4	99 ± 5	98 ± 4
3,4-DCLA	99 ± 4	102 ± 5	98 ± 4	100 ± 5	98 ± 6	103 ± 6	103 ± 5	102 ± 5	102 ± 6	98 ± 5	99 ± 4	102 ± 5
3,5-DCLA	98 ± 4	103 ± 5	97 ± 4	100 ± 5	97 ± 6	100 ± 4	100 ± 4	99 ± 5	98 ± 5	97 ± 6	103 ± 5	101 ± 5
2,4,5-TCLA	103 ± 4	99 ± 5	98 ± 4	102 ± 6	97 ± 5	102 ± 4	101 ± 5	102 ± 6	98 ± 5	99 ± 4	98 ± 5	101 ± 6
2,4,6-TCLA	100 ± 4	100 ± 5	101 ± 4	99 ± 5	100 ± 4	99 ± 5	99 ± 5	100 ± 4	102 ± 4	96 ± 5	97 ± 5	98 ± 5
3,4,5-TCLA	103 ± 4	97 ± 5	95 ± 4	102 ± 5	102 ± 4	99 ± 5	103 ± 4	97 ± 5	99 ± 6	101 ± 6	99 ± 5	100 ± 4
2-NA	101 ± 4	97 ± 5	102 ± 6	99 ± 5	95 ± 4	98 ± 5	102 ± 5	96 ± 4	97 ± 6	103 ± 4	98 ± 5	101 ± 5
PA	101 ± 4	100 ± 5	98 ± 4	97 ± 4	100 ± 5	102 ± 5	99 ± 5	102 ± 6	102 ± 5	99 ± 5	98 ± 4	99 ± 5
BTA	99 ± 4	100 ± 5	98 ± 5	99 ± 5	100 ± 4	100 ± 5	103 ± 6	98 ± 4	99 ± 5	100 ± 6	97 ± 4	101 ± 5
PTA	98 ± 5	97 ± 5	95 ± 5	101 ± 5	102 ± 4	98 ± 5	99 ± 4	100 ± 5	102 ± 6	98 ± 4	103 ± 6	96 ± 4

[a] 75 mg of LiChrolut EN sorbent, sample adjusted at pH 7.4 for NAms and anilines or at pH 12 for aliphatic amines; volume, 100 mL (n = 3, ±SD).

3.3. Analysis of water samples

Usually drinking water samples do not contain amines or these are present at concentrations so low that it is necessary to use high sample volumes for their detection. In this sense, the LiChrolut EN column shows the highest enrichment factors as it has a breakthrough volume up to 300 mL compared to those of Oasis HLB, which only tolerate volumes up to 180 mL. In addition, according to the literature, Oasis HLB material is a polymer with lipophilic divinylbenzene and hydrophilic N-vinylpyrrolidine groups that retains all kinds of non-polar and polar pollutants, giving low recoveries in the analysis of wastewater samples [37]; thus it was discarded in the application of the proposed method.

The proposed method was applied to determine 27 amines (aliphatic, anilines and N-nitrosamines) in several types of water samples, namely: river, pond, tap, well, drinking, swimming pool and waste. Initially, 100 mL of each sample was analysed following the method described and LiChrolut EN sorbent; when negative results were obtained, the sample volume was increased up to 300 mL to confirm the absence of amines at detectable levels. Only four samples were found to contain residues of amines although the concentrations were lower than the maximum admissible concentration established (excepting wastewaters). The results obtained are listed in Table 5. N-nitrosamines were only detected in wastewaters whereas anilines were present in the four positive samples; none of the analysed water contained aliphatic amines. Fig. 4 shows the chromatogram (SIM mode) obtained for a wastewater where 15 amines were detected. The full chromatogram is very clean since only five peaks from the matrix were detected.

Table 5
Analysis of water samples by SPE/GC/MS[a].

Water	Amine	Concentration found ($ng\,L^{-1}$)
Well	2,6-DCLA	40 ± 3
	2,4,5-TCLA	35 ± 2
	3,4,5-TCLA	70 ± 4
Swimming pool	3-CLA	160 ± 10
	4-CLA	200 ± 15
	2,4,5-TCA	40 ± 2
Waste 1	4-CLA	70 ± 3
	2,4,5-TCLA	25 ± 1
	2,4,6-TCLA	30 ± 2
	3,4,5-TCLA	50 ± 3
	NDMA	60 ± 4
	NDEA	30 ± 2
	NPYR	100 ± 6
	NMOR	300 ± 15
	NPIP	20 ± 1
	NDBA	320 ± 20
	NDPhA	90 ± 6
	4-NDPhA	200 ± 15
Waste 2	2-CLA	220 ± 15
	3-CLA	160 ± 10
	4-CLA	20 ± 1
	2,4-DCLA	350 ± 20
	2,4,5-TCLA	30 ± 2
	2,4,6-TCLA	25 ± 2
	3,4,5-TCLA	60 ± 4
	NDMA	50 ± 3
	NDEA	20 ± 1
	NPYR	100 ± 8
	NMOR	90 ± 5
	NPIP	70 ± 4
	NDBA	45 ± 3
	NDPhA	480 ± 30
	4-NDPhA	40 ± 3

[a] Sample volume, 100 mL ($n = 3$); 75 mg of LiChrolut EN; sample pH, 7.4.

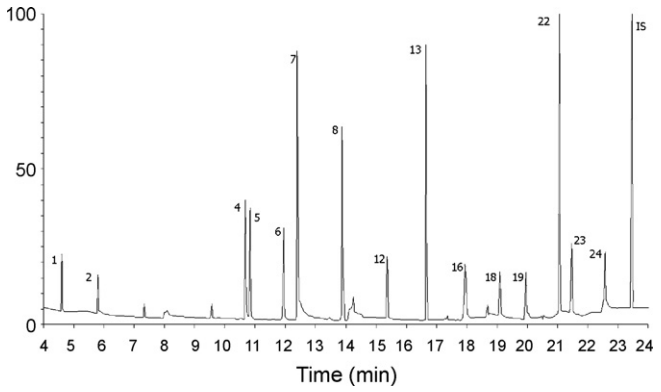

Fig. 4. Chromatogram in SIM mode for amines obtained in the analysis of 100 mL of the contaminated wastewater 2 (see Table 5). For peaks identification see Fig. 3.

4. Conclusions

An exhaustive study has been performed with several sorbent materials that can interact with amines, namely: LiChrolut EN, Oasis HLB, RP-C_{18}, graphitized carbon black (conventionals), fullerenes and nanotubes (non-conventionals). From this study, the following conclusions can be drawn: (i) fullerenes and MWCNTs are adequate to retain aromatic compounds such as aromatic NAms, and despite amine aromaticity, they only interact with trichloroanilines and 2-nitroaniline, through π–π interactions, and with some dichloroanilines that contain chlorine atoms in accessible positions for establishing anion–π interactions, and are thus highly selective; (ii) sorbents that can interact with analytes by various types of mechanisms including ion exchange (LiChrolut EN and Oasis HLB) were the only materials in which all the amines assayed were quantitatively retained due to their polar character and are therefore are universal and valid sorbent materials for the preconcentration of these types of compounds; (iii) the breakthrough volume is determined by these interactions, increasing from fullerenes to LiChrolut EN, this thus being the last sorbent selected; (iv) a simple automatic SPE unit for sample volumes up to 300 mL and with a sampling frequency of 55 min per sample has been proposed; when only 100 mL sample volumes are required, the sampling frequency is considerably increased (ca. 20 min); (v) the SPE-GC/MS method developed allowed the quantifying of 27 amines in water samples at a low nanogram per liter level, without matrix effects and with recovery nearly to 100%, which is considerably higher than other methods described in the bibliography (recovery ≤80%) [18,21,29] or is more accurate and precise (recoveries above 120%) [21,29]; (vi) the sensitivity of the proposed method (LOD 0.5–16 $ng\,L^{-1}$) is similar to that of other methods using SPME and GC/MS (2–13 $ng\,L^{-1}$) [21], but higher than that achieved by Liu et al. [23], who determined four amines by in-tube SPME-LC/UV with LODs ranging from 40 to 130 $ng\,L^{-1}$.

Acknowledgements

The authors would like to thank to the DGI of the Spanish Ministry of Science and Technology for financial support awarded in the form of Grant CTQ2007-63962/BQU. B.J.S would like to thank DGI for awarding a predoctoral Grant.

References

[1] A. Pielesz, in: L.M.L. Nollet (Ed.), Chromatographic Analysis of the Environment, CRC Press–Taylor & Francis, Boca Raton, FL, 2006, p. 377 (Chapter 11).
[2] M. Ábalos, J.M. Bayona, F. Ventura, Anal. Chem. 71 (1999) 3531.
[3] M. Akyüz, Talanta 71 (2007) 486.
[4] S.D. Richardson, M.J. Plewa, E.D. Wagner, R. Schoeny, D.M. DeMarini, Mutat. Res. 636 (2007) 178.

[5] Y.Y. Zhao, J.M. Boyd, M. Woodbeck, R.C. Andrews, F. Qin, S.E. Hrudey, X.F. Li, Environ. Sci. Technol. 42 (2008) 4857.
[6] L.S. Gold, E. Zeiger, Handbook of Carcinogenic Potency and Genotoxicity Databases, CRC Press, Boca Raton, 1997.
[7] Directive 76/464/CEE, Dangerous Substances Discharged into the Environment, OJ no. L129, Brussels, 1976.
[8] Iris Substance List, US Environmental Protection Agency, http://cfpub.epa.gov/ncea/iris/index.cfm?fuseaction=iris.showSubstanceList.Last, up-date January 20, 2009.
[9] C.J. Smith, G.L. Dooly, S.C. Moldoveanu, J. Chromatogr. A 991 (2003) 99.
[10] H.M. Pinheiro, E. Touraud, O. Thomas, Dyes Pigments 61 (2004) 121.
[11] M. Cobo, M. Silva, J. Chromatogr. A 848 (1999) 105.
[12] S. Meseguer Lloret, C. Molins Legua, P. Campins Falcó, J. Chromatogr. A 978 (2002) 59.
[13] J. Zhang, X. Wu, W. Zhang, L. Xu, G. Chen, Electrophoresis 29 (2008) 796.
[14] Dj. Djozan, M.A. Faraj-Zadeh, Anal. Lett. 31 (1998) 2093.
[15] N.A. Zatar, A.Z. Abu-Zuhri, A.A. Abu-Shaweesh, Talanta 47 (1998) 883.
[16] I. Molnar-Perl (Ed.), Quantitation of Amino Acids and Amines by Chromatography, Elsevier, Amsterdam, 2005, p. 365.
[17] H. Kataoka, M. Miyake, K. Mitani, J. Sep. Sci. 30 (2007) 90.
[18] A. Fromberg, T. Nilsson, B.R. Larsen, L. Montanarella, S. Facchetti, J.O. Madsen, J. Chromatogr. A 746 (1996) 71.
[19] L. Müller, E. Fattore, E. Benfenati, J. Chromatogr. A 791 (1997) 221.
[20] S. Mishra, V. Singh, A. Jain, K.K. Verma, Analyst 126 (2001) 1663.
[21] T. Zimmermann, W.J. Ensinger, T.C. Schmidt, Anal. Chem. 76 (2004) 1028.
[22] M. Akyüz, S. Ata, J. Chromatogr. A 1129 (2006) 88.
[23] X.Y. Liu, Y.S. Jin, H.X. Zhang, M.C. Liu, J. Chromatogr. A 1212 (2008) 10.
[24] H. Lin, C. Deng, X. Zhang, J. Sep. Sci. 31 (2008) 3225.
[25] C. Molins-Legua, P. Campins-Falcó, Anal. Chim. Acta 546 (2005) 206.
[26] P. Kusch, G. Knupp, M. Hergarten, M. Kozupa, M. Majchrezak, J. Chromatogr. A 1113 (2006) 198.
[27] B. Jurado-Sánchez, E. Ballesteros, M. Gallego, J. Chromatogr. A 1154 (2007) 66.
[28] V. Singh, M. Gupta, A. Jain, K.K. Verma, J. Chromatogr. A 1010 (2003) 243.
[29] M. Less, T.C. Schmidt, E.V. Löw, G. Stork, J. Chromatogr. A 810 (1998) 173.
[30] J. Lee, J.D. Fortner, J.B. Hughes, J.H. Kim, Environ. Sci. Technol. 41 (2007) 2529.
[31] J.R. Baena, M. Gallego, M. Valcárcel, Trends Anal. Chem. 21 (2002) 187.
[32] M. Ábalos, R. Mas, V. Suc, J.M. Bayona, Chromatographia 54 (2001) 109.
[33] E.M. Thurman, M.S. Mills, Solid-Phase Extraction, Principles and Practice: Chemical Analysis Series, vol. 147, John Wiley & Sons, Inc., New York, 1998.
[34] R.T. Yang, Adsorbents: Fundamentals and Applications, John Wiley & Sons, Inc., New Jersey, 2003, p. 84 (Chapter 5).
[35] A. Serrano, M. Gallego, J. Sep. Sci. 29 (2006) 33.
[36] D. Kim, P. Tarakeshwar, K.S. Kim, J. Phys. Chem. A 108 (2004) 1250.
[37] M. Krauss, J. Hollender, Anal. Chem. 80 (2008) 834.

Talanta 79 (2009) 940–946

Contents lists available at ScienceDirect

Talanta

journal homepage: www.elsevier.com/locate/talanta

Non-chromatographic determination of ultratraces of V(V) and V(IV) based on a double column solid phase extraction flow injection system coupled to electrothermal atomic absorption spectrometry

Manuela Leticia Kim, Mabel Beatríz Tudino*

Laboratorio de Análisis de Trazas, Departamento de Química Inorgánica, Analítica y Química Física, INQUIMAE, Universidad de Buenos Aires, Pabellón 2, Ciudad Universitaria, (1428) Buenos Aires, Argentina

ARTICLE INFO

Article history:
Received 7 April 2009
Received in revised form 18 May 2009
Accepted 19 May 2009
Available online 27 May 2009

Keywords:
V(V)
V(IV)
Hybrid mesoporous silica
Solid phase extraction
Electrothermal atomic absorption spectrometry

ABSTRACT

In this work, a non-chromatographic procedure for the on-line determination of ultratraces of V(V) and V(IV) is presented. The method involves a solid phase extraction-flow injection system coupled to electrothermal atomic absorption spectrometry (SPE-FI-ETAAS). The system holds two microcolumns (MC) set in parallel and filled with lab-made mesoporous silica functionalized with 3-aminopropyltriethoxy silane (APS) and mesoporous silica MCM-41, respectively. The pre-concentration of V(V) is performed by sorption onto the first MC (C1) filled with APS at pH 3, whilst that of V(IV) is performed by sorption onto the second column (C2) filled with mesoporous silica MCM-41 at pH 5. Aqueous samples containing both analytes are loaded and, after pre-concentration (pre-concentration factor PCF = 10, sorption flow rate = 1 mL min^{-1}, sorption time = 10 min), they are eluted in separate vessels with hydroxylammonium chloride (HC) 0.1 mol L^{-1} in HCl 0.5 mol L^{-1} (elution volume = 1 mL, elution flow rate = 0.5 mL min^{-1}). Afterwards, both analytes are determined through ETAAS with graphite furnace. Under optimized conditions, the main analytical figures of merit for V(V) and V(IV) are, respectively: detection limits (3 s): 0.5 and 0.6 μg L^{-1}, linear range: 2–100 μg L^{-1} (both analytes), sensitivity: 0.015 and 0.013 μg^{-1} L and sample throughput: 6 h^{-1} (both analytes). Recoveries of both species were assayed in different water samples. Validation was performed through certified reference materials for ultratraces of total vanadium in river water.

1. Introduction

Vanadium is highly distributed in the Earth's crust and deserves great attention in industrial applications such as those concerning the manufacturing of alloys, glasses, pigments, etc. Particularly, it is present in fossil fuels which release the metal to the environment when it is burnt [1].

Generally, the metals toxicity depends on the oxidation state. Vanadium is present in natural waters in concentrations ranging between 1×10^{-7} and 5×10^{-7} mol L^{-1} [2], being the more relevant species V(V) and V(IV). V(V) is present as VO_2^+ and VO_4^{3-} in acid and alkaline media, respectively. However, at the above mentioned concentrations and the pH values usually occurring in natural waters, it should be present as $H_2VO_4^-$. V(IV) lives as VO^{2+} in a reductive and acid media but it can be oxidized by the atmospheric oxygen.

Considering the low concentrations present in natural waters, it becomes necessary the employment of pre-concentration systems before its determination by UV–vis [3], ICP-OES [4], ET AAS [5], etc. The literature describes several approaches for on-line or off-line vanadium preconcentration employing solid phase extraction (SPE). Gil et al. employed carbon nanotubes after complexation with 1.2-ciclohexandiaminetetraacetic acid for the determination of V(IV) [6]. Polymeric solids holding immobilized ligands are also popular amongst retention materials. Polyestiren-divinylbenzene resins functionalized with 4.5-dicarboxy imidazol have been employed for the simultaneous retention of V(IV) and V(V) followed by sequential elution of both analytes [7]. Other approaches involve the employment of molecular sieves for the retention of the complex between V(IV) and Eriochrome cyanine R followed by the sequential reduction of V(V) into V(IV) for sequential speciation [8], etc. Regarding hybrid mesoporous materials, they have been widely employed for the retention of metals for decontamination purposes [9–11]. Mostly of studies reported in the literature involve off-line determination of organic [12] and inorganic analytes [13–15]. On-line analytical applications are scarce [16–20] probably due to problems related to the inefficient release

* Corresponding author. Tel.: +54 1145763360; fax: +54 1145763341.
E-mail address: tudino@qi.fcen.uba.ar (M.B. Tudino).

0039-9140/$ – see front matter © 2009 Elsevier B.V. All rights reserved.
doi:10.1016/j.talanta.2009.05.032

of the analytes once sorbed. In the particular case of vanadium, no papers involving either total vanadium determination or analytical speciation at ultratrace levels by retention onto this kind of solids are reported up to date.

In this work, we present a new methodology for the non-chromatographic determination of V(V) and V(IV) by SPE-FI-ETAAS. Lab-made hybrid mesoporous silica functionalized with 3-aminopropyltriethoxy silane (APS) [17,18] and mesoporous silica MCM-41 were employed for the retention of V(V) and V(IV), respectively. A flow injection system holding two microcolumns (MC) set in parallel was designed in order to retain both analytes at a suitable pH onto each one of the fillings, employing just one sample loading. Once retained, the analytes were sequentially eluted by means of a solution with strong redox properties in highly acidic media. Afterwards, both inorganic species were off-line determined by ETAAS.

The advantages of this methodology will be presented in terms of analytical figures of merit. Results involving the determination of V(V) and V(IV) in natural waters and the validation of the analytical methodology will be provided.

2. Experimental

2.1. Reagents

Standard solutions of 1.000 g L^{-1} of V(V) were prepared by dissolving 0.1148 g of ammonium metavanadate (99.9%, Merck Darmstadt, Germany) in 50 mL de double deionized water (DDW) (18 MΩ cm^{-1}, MilliQ Water System, Millipore, Bedford, MA, USA). 1.000 g L^{-1} of V(IV) standards were prepared by dissolving 0.2484 g of vanadyl sulfate (Merck) in 50 mL of DDW.

5×10^{-3} mol L^{-1} ammonia solutions were prepared by a suitable dilution of concentrated NH_3 (Merck). Concentrated HCl (Merck) was employed for preparing solutions at pH 3. The eluent solution was prepared by dissolving 0.6949 g of hydroxylammonium chloride (HC) in 100 mL of HCl 0.5 mol L^{-1}.

Sodium tetraethylorthosilicate (TEOS) 98% (Mr = 208.33, d = 0.934 g mL^{-1}), cetyl trimethylammonium bromide (CTAB) (Mr = 364.46) and 3-aminopropyltriethoxisilane (APTES) (Mr = 221.37, d = 0.942) (Sigma–Aldrich, St Louis, MO, USA) were employed for the synthesis of hybrid mesoporous solids.

All operations were performed in a laminar flow hood. Nalgene glassware (Nalge, Rochester, NY, USA) was washed with a nitric acid solution (1 + 1) and rinsed with DDW, ethanol and acetone.

2.2. Sample treatment

Water samples were previously filtrated through nylon membranes (0.45 μm). Afterwards, standard additions of 50 μg L^{-1} of both, V(V) and V(IV), were performed in order to test recoveries in real samples.

The reference material (NIST, SRM 1643e, total vanadium certified concentration = 37.86 ± 0.56 μg L^{-1}) was diluted 1:2 with DDW and kept at pH 3 by the addition of NaOH (Merck) 1 mol L^{-1}.

2.3. Apparatus

The flow system FI (Fig. 1) was assembled with a peristaltic pump (IPC, Ismatec, Glattbrugg-Zürich, Switzerland), a ten-ports rotatory valve VICI (Valco Instruments, Houston, TX, USA), 0.5 mm i.d. PTFE® tubings (Cole Parmer, Chicago, IL, USA) and two acrylic microcolumns (MC) with the inner part drilled to obtain a 7.9 μL bed volume (10 mm long, 1.0 mm internal diameter). Both MC were fixed through 0.25–28 female connectors to the FI tubing, keeping the aspect ratio optimized in order to obtain minimal dispersion together with minimal resistance to the solutions flow. Two plugs of polystyrene foam were placed at both sides of the MC and the solids were slurry loaded (0.1 g) into the MC with a plastic syringe.

Samples were analyzed by graphite furnace atomic absorption spectrometry (GFAAS) with a Shimadzu graphite furnace atomic absorption spectrometer AA6800 (Shimadzu, Kyoto, Japan) equipped with an autosampler Shimadzu ASC-6100. Vanadium hollow cathode lamp (Hamamatsu, Japan), deuterium lamp background correction and pyrolitic graphite furnaces (platform atomization) were employed throughout the measurements. Instrumental conditions are listed in Table 1a and b.

2.4. Procedure

2.4.1. Synthesis of hybrid mesoporous solids

The solid APS was prepared according to the methodology described by Fowler et al. [19] and previously reported elsewhere [16,17].

2.4.2. Preconcentration and determination of V(V) and V(IV)

Fig. 1 shows the SPE-FI system employed for V(V) and V(IV) preconcentration.

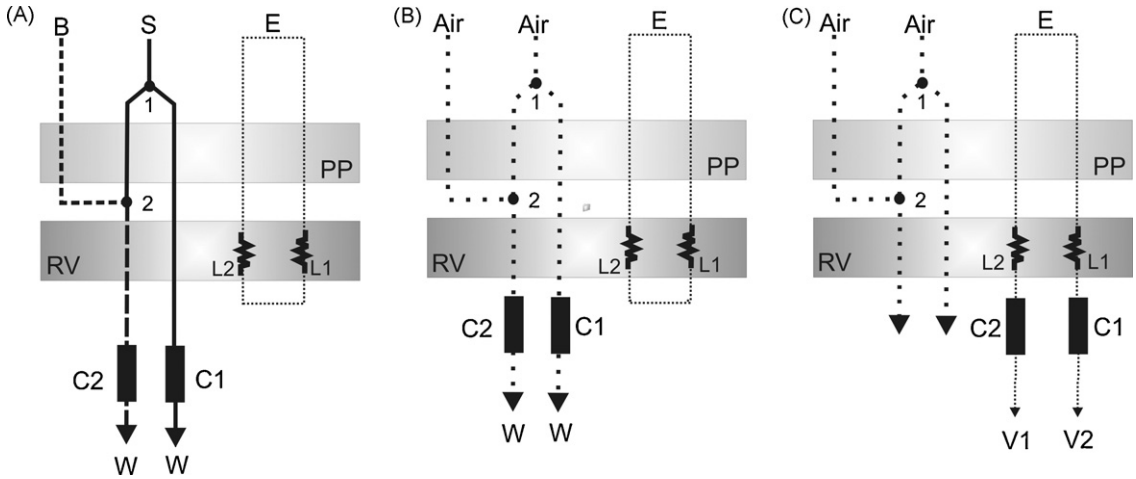

Fig. 1. FI system for vanadium speciation. (a) Sample loading position onto microcolumns C1 and C2. Sample loading flow rate: 1 mL min^{-1}, ammonia solution (B) flow rate: 0.2 mL min^{-1}, waste (W), peristaltic pump (PP), sample (S), ten-ports rotatory valve (RV), eluent solution (E), eluent loops (L1 = L2), sample bifurcation (1), pH conditioning confluence (2), vessels (V1 and V2). (b) Sample and ammonia streams are emptied before eluent injection. (c) Elution position: elution flow rate: 0.5 mL min^{-1}.

Table 1
Instrumental conditions for total V determination and graphite furnace temperature program.

Parameter				
(a)				
Wavelength		318.5 nm		
Spectral bandpass		0.2 nm		
Lamp current		10 mA		
Background correction		Deuterium lamp		
Sample volume		80 μL		
Stage	Temperature (°C)	Ramp time (s)	Hold time (s)	Argon gas flow (L min^{-1})
(b)				
Drying	120	30	–	1.00
	250	10	–	1.00
Pyrolysis	650	40	–	1.00
	650	–	5	0.00
Atomization	2650	–	2	0.00 (read)
	2650	–	1	0.30

Sample and standard solutions are introduced in the microcolumns C1 and C2 at pH 3 and pH 5, respectively, at 1 mL min^{-1} flow rate and a preconcentration time of 10 min. The confluence carrying 5×10^{-3} mol L^{-1} ammonia solution at 0.2 mL min^{-1} (point 2) allows pH conditioning of the sample when passing through C2 at a total flow rate of 1.2 mL min^{-1} in this MC. Even though C2 is loaded at a higher flow rate than C1, the total mass of each analyte loaded onto C1 and C2 respectively, remains the same. Fig. 1 A shows the FI system in loading position. Whilst the samples are going through the microcolumns, two separate loops (1.0 mL volume, 0.5 mm i.d, 127 cm length) are filled with the eluent which is recycled in a closed circuit.

After 10 min, the sample and ammonia solutions are removed allowing air to enter into the flow system lines (Fig. 1B). Once all lines are filled with air, the valve is commutated and the elution loops are emptied by a simple air displacement. Thus, the solution containing hydroxylammonium chloride (HC) 0.1 mol L^{-1} in HCl 0.5 mol L^{-1} (elution volume = 1 mL, flow rate = 0.5 mL min^{-1}) is carried towards both MCs, allowing the release of V(V) from C1 and V(IV) from C2. Eluates are collected in separate vessels and measured off-line by ETAAS (Fig. 1C).

2.4.3. Adsorption kinetic studies of V(V) and V(IV)

Batch experiments were performed by suspending 500 mL of solutions 5 mg L^{-1} of V(V) and V(IV) in 100 mg of APS. Measurements were carried out by taking 100 μL aliquots of the supernatant at different times of contact between the analyte and the filling.

3. Results and discussion

3.1. Optimization of pH for sorption of V(V) and V(IV)

Several batch experiments were conducted with the aim of evaluating the influence of pH on the sorption of V(V) and V(IV) onto APS. HCl or NaOH solutions were employed for pH conditioning. For doing this, 500 μg L^{-1} solutions of V(V) and V(IV) in separate vessels were contacted with APS at pH values ranging between 1 and 9. Suspensions were agitated during 24 h and then centrifugated at 3200 rpm. Remaining vanadium was measured in the supernatant solution by ETAAS.

Fig. 2 shows the sorption behaviour of both forms of vanadium vs. pH.

The maximum adsorption capacities q (mmol g^{-1}) of V(V) and V(IV) were observed at pH 5, being q lower for the latter. At pH 5 and concentrations below 10^{-6} mol L^{-1}, V(V) is present as $H_2VO_4^-$ whilst the net surface charge of APS is positive. In this way, it is retained by electrostatic interaction with the filling. At lower pH, sorption capacity diminishes due to the protonation of V(V) which lives as the cationic form VO_2^+ [20] whilst the net surface charge of APS is still positive. At pH above 5, V(V) remains in the anionic form and q decreases mainly because the surface charge of silica is negative and the aminopropyl groups are now not charged. Since the most remarkable difference of sorption capacities was observed at pH 3, it was selected for conditioning of C1.

For pH values between 0 and 5, V(IV) is mostly present as VO^{2+} and $(VO)_2(OH)_2^{2+}$. In this pH range, the net surface charge of the solid changes from positive (pH < 2) to negative with not charged aminopropyl groups for pH above 5. So, the larger the net negative charge of the surface, the higher the absorption of V(IV) by electrostatic interaction with the filling. The decrease of q at higher pH values is attributed to the precipitation of oxo-hydroxo species with a general formula $VO_2 \cdot nH_2O$ ($Kps \approx 10^{-22}$). In extremely basic conditions, the anionic form $VO(OH)_3^-$ is obtained and thus, the oxo-hydroxo species solubilized [20].

The same experiments were carried out in order to study the influence of pH on the adsorption of both analytes onto silica MCM-41 (Fig. 3). In this case, the filling achieves net charge zero (at low pH) or negative charge (pH 2 or above) and still, some retention of V(V) species was observed. In the case of V(IV), the positive charged species showed larger q values when raising pH up to 5–6. From 6 onwards, the analyte precipitates as told above. So, pH 5 was selected for conditioning C2. However, the aptitude of MCM 41 for specific retention of V(IV) seemed not enough for its determination with no interference of V(V) through batch operations.

In this way, flow through experiments were assayed in order to reach specificity by kinetic discrimination. The same experiments were carried out on line by simply passing through the flow sys-

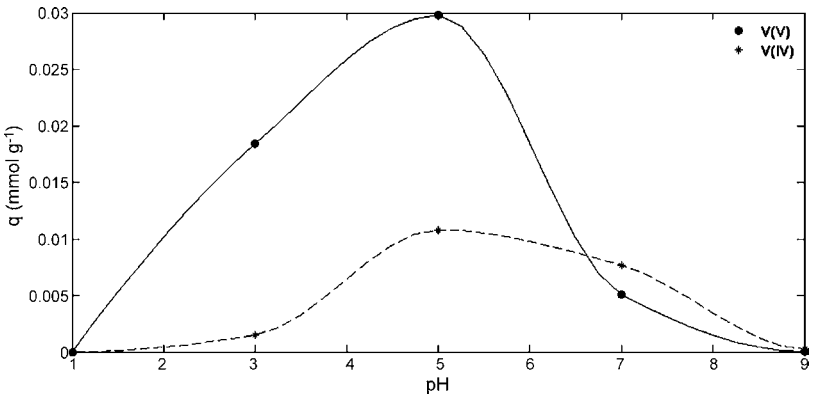

Fig. 2. Influence of pH on the retention of V(V) and V(IV) onto APS (batch). [V(V)]: 500 μg L^{-1}, [V(IV)]: 500 μg L^{-1}.

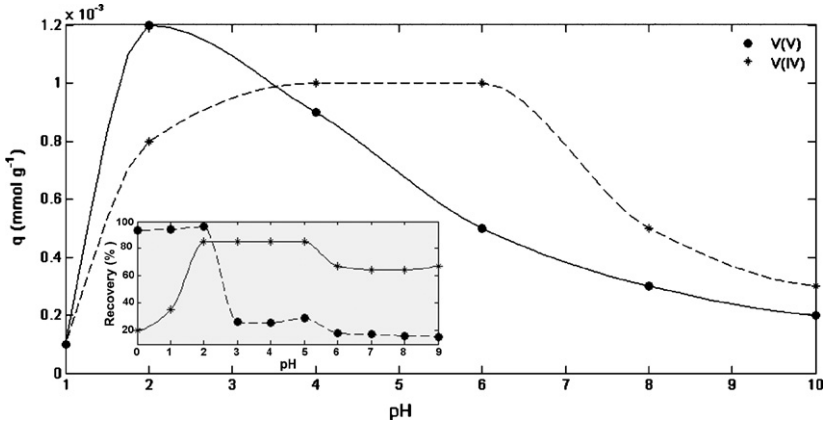

Fig. 3. Influence of pH on the retention of V(V) and V(IV) onto MCM-41 (batch). [V(V)]: 500 μg L^{-1}, [V(IV)]: 500 μg L^{-1}. Inset: flow through experiments.

tem, solutions of V(V) and V(IV) 50 μg L^{-1} with a preconcentration factor (PCF= V_{sample}/V_{eluent}) = 10, adsorption flow rate = 1 mL min^{-1} and elution flow rate = 0.5 mL min^{-1}). The findings obtained under flow through conditions and thus, the influence of the adsorption kinetics on the determination of both analytes with no mutual interference, will be discussed in the next section.

3.2. Influence of the adsorption flow rate on the retention of V(V) and V(IV) and kinetic studies

It was observed that the percentages of recovery remained relatively constant and equal to 95% for V(V) onto C1 and 85% for V(IV) onto C2 up to 1 mL min^{-1} loading flow rate (Fig. 4a and b). The adsorptions of V(IV) onto C1 and V(V) onto C2 were neglectable. Note that, whilst the specificity on V(V) retention onto APS was obtained by pH discrimination, the specificity on V(IV) sorption onto MCM-41 was only obtained under flow through conditions. This last circumstance should be assigned to a remarkable difference between adsorption kinetics of both analytes onto MCM-41 under the experimental conditions: a contact time of about 0.4 s. Neither filling compactation nor pressure enhancement were observed for this flow rate value. Loading flow rate of 1 mL min^{-1} was selected in order to optimize the sample throughput without enlarging the time of preconcentration. In order to keep PCF constant and equal to 10, the loaded mass of the analytes was kept constant along the experiments. Taking into account that the adsorption kinetics influence the specificity, the effect of the loading flow rate on the retention of V(V) and V(IV) onto both fillings at the optimized pHs, were carried out. Fittings of experimental data were calculated by the Pseudo Second order kinetic model (PO2) [21–23] which showed the best correlation.

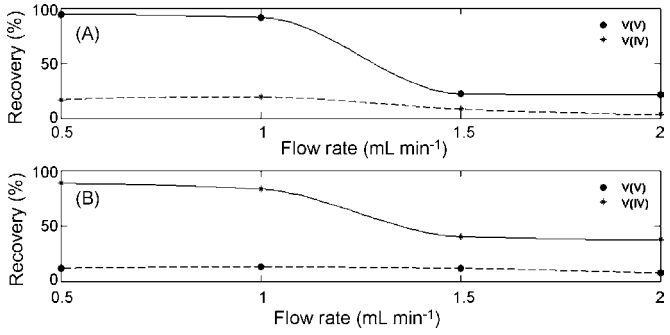

Fig. 4. (a and b) Influence of the flow rate on: (a) the adsorption of V(V) and V(IV) onto APS (C1) at pH 3 and (b) the adsorption of V(V) and V(IV) onto MCM-41 (C2) at pH 5. [V(V)] and [V(IV)] = 30 μg L^{-1}, elution flow rate: 0.5 mL min^{-1}, elution volume: 1 mL, PCF = 10.

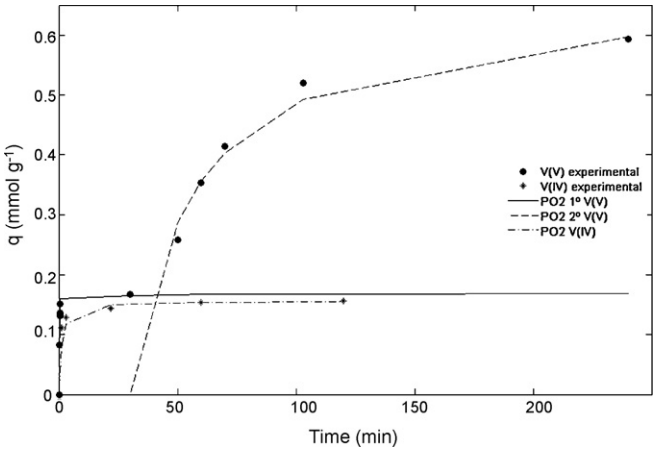

Fig. 5. Adsorption kinetics of V(V) and V(IV) onto APS at pH 3. [V(V)] = [V(IV)] = 5 mg L^{-1}. APS = 100 mg (slurry loaded onto C1). Experimental and calculated data (PO2 kinetic model). V(IV) experimental and calculated data are 100 times enhanced in order to keep the same scale.

The figures show that the adsorption kinetic curves of V(V) and V(IV) at pH 3 onto APS20% (Fig. 5) are significantly different from those onto MCM-41 at pH 5 (Fig. 6). Fig. 5 shows two well differentiated steps: a first plateau up to 50 min and a second one up to 300 min where two q_{max} values are obtained. This circumstance should probably be related to the existence of two predominant species of V(V), VO_2^+ and $H_2VO_4^-$ (log K = 2.6) [20], that interact differently with the solid at pH 3. Under these conditions, the

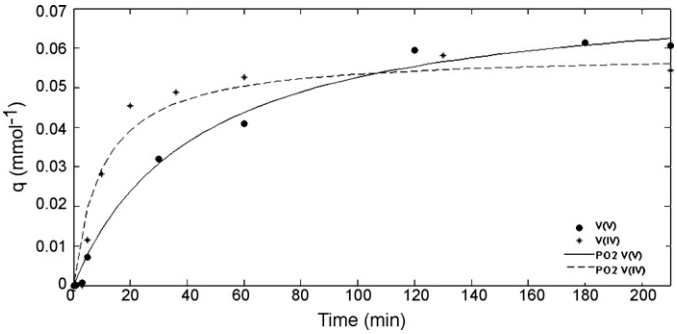

Fig. 6. Experimental and calculated data (PO2 kinetic model) for adsorption kinetics of V(V) and V(IV) onto MCM-41 at pH 5. [V(V)] = [V(IV)] = 5 mg L^{-1}. MCM-41 = 100 mg (slurry loaded onto C2).

silanols deprotonation should be responsible for the first portion of the curve corresponding to the electrostatic interaction of VO_2^+ with the negatively charged silanols [2]. The second part should be attributed to the interaction of $H_2VO_4^-$ with the positively charged aminopropyl groups. This should be the reason why two different approaches were needed for explaining the whole response: PO2 1° for 0–50 min and PO2 2° for 50 min onwards At pH 5 (Fig. 6), $H_2VO_4^-$ is the predominant specie of V(V) so, the *q* vs. *t* plot shows only one step corresponding to the adsorption of negatively charged V(V) onto MCM-41. In the case of V(IV) no differences on the shape of the adsorption kinetic curves were observed. This should be explained by taking into account that, as said above, V(IV) is present as VO^{2+} and/or $(VO)_2(OH)_2^{2+}$ and thus, no different adsorption behaviors onto the negative surface charge of the solid should be expected. Thus, only one step kinetic curve is observed, and just one fitting is needed. Note that, at the selected contact times between both analytes and MCM-41 the adsorption of V(V) is now unimportant due to the differences of the initial adsorption rates ($V^0_{V(IV)} = 3\,V_{V(V)}$).

Flow through studies were carried out in order to re-evaluate the influence of pH onto adsorption capacities when kinetic discrimination is taken into account. Experiments involving adsorption of V(V) and V(IV) onto APS showed no significant differences with respect to the findings in Fig. 2. Regarding the flow through behavior onto MCM-41, adsorption was seriously affected by the time of contact analyte/filling, allowing in these way, V(IV) retention with no interference of V(V) (Fig. 3 inset).

3.3. Studies on the optimum preconcentration factor

The variation of PCF was achieved keeping the adsorption flow rate constant and changing the preconcentration time. As shown in Fig. 7, recoveries of V(V) and V(IV) remain practically constant and around 95% and 85% respectively, up to PCF = 10. Above this, a decrease is noticed with PCF values close to 60% and 50% for V(V) and V(IV) respectively.

3.4. Influence of the eluent characteristics on the analytes recoveries

Several solutions were assayed in order to accomplish an efficient release of V(V) and V(IV) by employing low volumes of an ETAAS friendly eluent. On the belief that changes in pH and redox environment should produce good liberation of the analytes by species conversions, the solutions listed in Table 2 were tested in terms of percentage of recovery of V(V) and V(IV).

Even though E2 and E5 showed the best performance for V(V) elution, E2 was preferred considering that the nitric acid in E5 should probably oxidize APS, reducing in this way the filling lifetime. In order to prevent oxidation of the filling, E5 in HCl [16] was also tested but a relatively high background signal in the detector was observed even when the time of pyrolysis was enlarged. It was also observed that changes of pH were not enough to release efficiently V(V) and that changes of the redox properties (conversion of the negatively charged $H_2VO_4^-$ into the cation VO^{2+}) were also needed.

Table 2
Eluents for V(V) and V(IV), sorbed onto C1 and C2, respectively. V(V)] = [V(IV)] = 50 μg L^{-1}, elution flow rate: 0.5 mL min^{-1}, eluent volume: 1 mL, adsorption flow rate: 1 mL min^{-1}, PCF: 10.

Eluent	Eluent solution	Recovery V(V) (%)	Recovery V(IV) (%)
E1	HCl 1 mol L^{-1}	69.2	100
E2	HC 0.1 mol L^{-1} + HCl 1 mol L^{-1}	91.8	99
E3	HNO_3 1 mol L^{-1}	42.6	98
E4	Ascorbic acid 1%w/v	29.1	56
E5	1.5-Diphenylcarbazide in 0.5 mol L^{-1} HNO_3 [24]	99.1	100

V(IV) was completely recovered under strong acid conditions showing that the release is possible by simply changing the surface charge of MCM-41. E2 was also selected in order to employ the same eluent for both species, making simpler the flow manifold design. It was found that HC 0.1 mol L^{-1} in HCl 0.5 mol L^{-1} was optimum for 100% elution of V(V) and V(IV). Moreover, E2 was an excellent solvent for ETAAS as HC easily decomposes into the graphite furnace.

3.5. Elution volume

In order to obtain the best PCF together with the use of the minimum volume of reagents and the production of the minimum volume of waste, the eluent volume was optimized by changing the dimensions of the eluent loops of the flow system (see Fig. 1) and keeping constant the adsorption flow rate and the elution flow rate. Results for V(V) and V(IV) recoveries are shown in Fig. 8.

A 95% V(V) and 85% V(IV) recovery was obtained for 1 mL onwards for both analytes and this value was selected as optimum. Note that lower volumes showed a poor response which obliged us to off-line injection into the GF which handles upmost 100 μL (sample injected volume: 80 μL).

3.6. Optimization of the elution flow rate

Fig. 9 shows the influence of elution flow rate on the analytes release, keeping constant the eluent volume. Best results were obtained for 0.5 mL min^{-1} or below. Again, it was observed that the times of contact between the analytes and the fillings and those of the analytes and the eluent determine the efficiency of the whole analytical procedure. As told before, the adsorption kinetic is slow

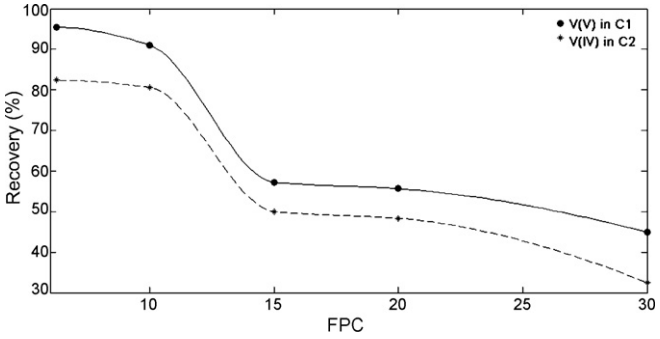

Fig. 7. Optimum preconcentration factor (PCF) for V(V) in C1 and V(IV) in C2. [V(V)] = [V(IV)] = 50 μg L^{-1} pH 3 in C1 and pH 5 in C2, adsorption flow rate: 1 mL min^{-1}, elution flow rate: 0.5 mL min^{-1}, eluent volume: 1 mL.

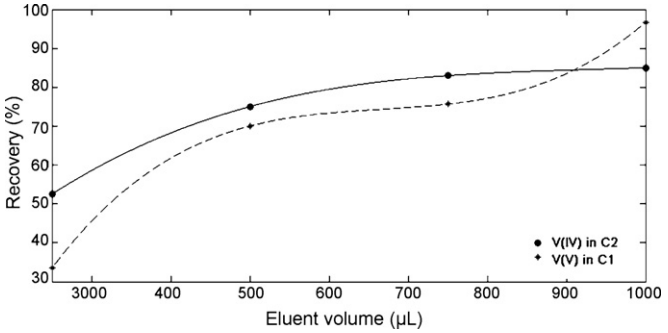

Fig. 8. Optimization of the eluent volume. [V(V)] = [V(IV)] = 50 μg L^{-1}, eluent flow rate: 0.5 mL min^{-1}, adsorption flow rate: 1 mL min^{-1}, PCF: 10, eluent: E2.

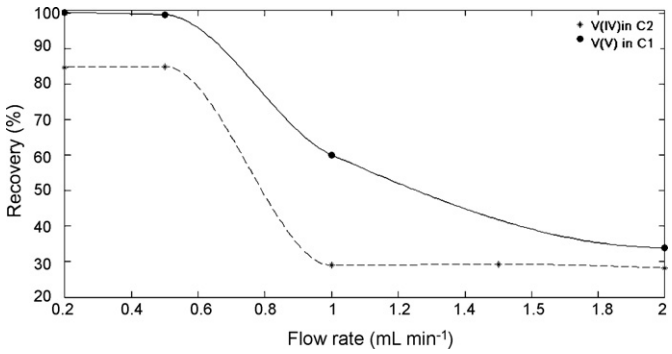

Fig. 9. Influence of the elution flow rate on the recovery of vanadium. [V(V)] = [V(IV)] = 50 μg L^{-1}, adsorption flow rate: 1 mL min^{-1}, PCF: 10, eluent: E2, eluent volume: 1000 μL.

Table 3
MTL of interferences for the determination of V(V) and V(IV).

Interferences	MTL for V(V) determination (μg L^{-1})	MTL for V(IV) determination (μg L^{-1})
Cr (VI)	>100	>100
Fe (III)	>1000	>100
Al (III)	>100	>100
Zn (II)	>100	>100
Cu (II)	>200	>20
Mg (II)	>50,000	>50,000
Ca (II)	>50,000	>50,000
Na (I)	>100,000	>100,000
Cl^-	>50,000	>350,000
SO_4^{2-}	>100,000	>500,000
NO_3^-	>100,000	>200,000
PO_4^{3-}	>50,000	>200,000

[V(V)] = [V(IV)] = 50 μg L^{-1}.

but, once sorbed, the interaction between the analytes and the filling is strong (even stronger for V(V) onto APS). In this way, elution needs to enlarge the times of contact analytes/E2 in order to free them from the solids.

3.7. Influence of interferences

Table 3 shows the influence (expressed as maximum tolerable limit, MTL) of different ions usually present in real water samples, on V(V) and V(IV) analytical signal. It shows that MTLs in C2 at pH 5 (V(IV) determination) are higher for anions which is compatible with the negative surface charge of the filling. On the other hand, MTLs in C1 at pH 3 (V(V) determination) are equal or higher for cations when compared to C2, which is consistent with the positive charge of APS. Regarding Cr(V), an important decrease on V(V) signal is observed probably due to the presence of $HCrO_4^-$ as predominant specie which competes with HVO_4^- for sorption onto the filling [18]. Table 3 also shows the great tolerance to a high concentration of concomitant ions of the system, which enhances the probability of good vanadium quantification in real samples.

3.8. Analytical figures of merit

Under optimized conditions (adsorption flow rate = 1 mL min^{-1}, elution flow rate = 0.5 mL min^{-1}, pH_{C1} 3, pH_{C2} 5, elution volume = 1000 μL, preconcentration time = 10 min) an PCF of 10 with a preconcentration efficiency of 95% of V(V) and 85% of V(IV) was obtained. Detection limits (calculated as $3S_b$) were 0.5 and 0.6 μg L^{-1} for V(V) and V(IV), respectively. The characteristic masses were 23 pg for V(V) and 25 pg for V(IV). The relevant figures of merit in comparison to others already reported are listed in Table 4.

Even though the analytical methodologies reported by Aureli et al. [25] and Gil et al. [6] show better limits of detection (other figures of merit are barely shown), two main advantages should be addressed with this proposal: a lower cost of equipment (in comparison to the approach in [25] and a much more simpler sample pretreatment (in comparison with the approaches in [25] and [6]). Moreover, in comparison with the results in [25], vanadium speciation instead of total vanadium determination is performed here. To enhance: V(V) and V(IV) determination is simply performed by changing the chemical environment (redox potential and pH) during *flow through* experiments of preconcentration and elution of both forms, with no need of chromatographic separations which usually enlarge the analytical frequency.

3.9. Vanadium determination in real samples

In order to study the matrix effect on V(V) and V(IV) recoveries in real samples, DDW, osmosis, mineral and tap waters were spiked with 50 μg L^{-1} of each one of the analytes. The percentages of recovery obtained for the assayed samples are shown in Table 5.

Good results, within the experimental error allowed for ultratrace analysis, were obtained for both analytes. In the case of V(IV), the standard addition methodology should be applied if more accurate and precise results were needed. The determination of total vanadium in a certified reference material (NIST, SRM 1643e) was also performed by employing the standard addition methodology. The total vanadium content was simply obtained through the sum of the individual concentrations of V(V) and V(IV). The total vanadium concentration was equal to (38.7 ± 0.5) μg L^{-1} which is in good agreement with the certified value of (37.63 ± 0.44) μg L^{-1} (95% confidence level, n = 3).

Table 4
Comparison of analytical performance of the proposed methodology with data taken from bibliography or others already reported.

Analytical performance	Proposed methodology FI-SPE-ETAAS		ETAAS[a]	HPLC-ICP MS [25]		FI-SPE ETAAS [6]	
	V(V)	V(IV)	Total V	V(IV)	V(V)	V(IV)	V(V)
Speciation	Yes	No	Yes	Yes			
LOD (μg L^{-1})	0.5	0.6	3.5	0.16	0.025	0.019	
Regression equation	0.015C + 0.006	0.013C + 0.004	0.0024C + 0.0007	NR	NR		
Sensitivity (μg^{-1} L)	0.015	0.013	0.0024	NR	NR		
Dynamic range (μg L^{-1})	2–100	2–100	10–600	0.16–16	0.025–50	NR	
Maximum PCF	10	10	–	NR	NR	900	
RSD % (n = 5, 50 μg L^{-1})	1.8	2.3	3	5.5	1.4	2	
Characteristic mass (pg)	23	25	145	–	–	63000	
Sample throughput (h^{-1})	6	6	30	2	2	20	
Column lifetime (sorption/desorption cycles)	200	200	–	–	–	50	

NR: not reported.
[a] Measured in our laboratory.

Table 5
Studies of recovery of V(V) and V(IV) in different water samples spiked with 50 μg L^{-1} of each analyte (n = 3, 95% confidence level).

Sample	Added (μg L^{-1})		Found (μg L^{-1})		Recovery (%)	
	V(V)	V(V)	V(VI)	V(IV)	V(V)	V(IV)
DDW	0	0	0.0 ± 0.1	0.0 ± 0.6	0	0
	50	50	48.5 ± 1.8	40.1 ± 3,1	97	80
Osmosis water	0	0	0.0 ± 0.1	0.0 ± 0.1	0	0
	50	50	47.5 ± 2.1	39.1 ± 4.2	95	78
Mineral water	0	0	0.0 ± 0.1	0.0 ± 0.1	0	0
	50	50	48.5 ± 2.7	36.2 ± 3.4	94	72
Tap water	0	0	0.0 ± 0.9	0.0 ± 0.1	0	0
	50	50	47.6 ± 2.7	38.4 ± 4.3	95	77

4. Conclusions

A simple and reliable methodology for the inorganic speciation of vanadium was developed. The non-chromatographic method, based on sorption of V(V) and V(IV) onto a lab-made hybrid mesoporous solid (silica based), is presented here for the first time. The method requires just one sample loading and just one eluent solution for performing both determinations, making easier the analyst work.

The dual column FI-SPE-ETAAS system showed an excellent performance at the moment of the determination of both forms of vanadium in water samples, even under high ionic strength conditions.

So, the lab-made hybrid mesoporous solids look promising for analytical determinations if their unquestionable sorption capacities [26,27] are combined with: (a) kinetic discrimination schemes for selectivity enhancement [28] and (b) the choice of suitable eluents able to easily liberate the retained analytes by changing the physico-chemical environment of sorption. In this way, the experiments presented here in order to study the adsorption kinetic of both analytes onto the solid materials and their desorption kinetics, should help on advancing in new analytical applications.

Acknowledgment

To the University of Buenos Aires (UBA) and the National Council of Science and Technology (CONICET) for financial support.

References

[1] Z. Chen, G. Owens, Anal. Chim. Acta 607 (2008) 1.
[2] J. Cruywagen, J. Heyns, A. Westra, Inorg. Chem. (1996) 1556.
[3] L. Rostampour, M. Taher, Talanta 75 (2008) 1279.
[4] G. Abbasse, B. Ouddane, J. Fischer, Anal. Bioanal. Chem. 374 (2002) 873.
[5] K. Pyrzyńska, T. Wierzbicki, Talanta 64 (2004) 823.
[6] R. Gil, S. Goyanes, G. Polla, P. Smichowski, R. Olsina, L. Martinez, J. Anal. At. Spectr. 22 (2007) 1290.
[7] D. Banerjee, B. Mondal, D. Das, A. Das, Microchim. Acta 141 (2003) 107.
[8] J. Bosque-Sendra, M. Valencia, S. Boudra, Fresenius J. Anal. Chem. 360 (1998) 31.
[9] R. Nooney, M. Kalyanaraman, G. Kennedy, E. Maginn, Langmuir 17 (2001) 528.
[10] M. Mureseanu, A. Reiss, I. Stefanescu, E. David, V. Parvulescu, G. Renard, V. Hulea, Chemosphere 73 (2008) 1499.
[11] H. Yoshitake, New J. Chem. 29 (2005) 1107.
[12] X.Z. Du, Y.R. Wang, X.J. Tao, H.L. Deng, Anal. Chim. Acta 543 (2005) 9.
[13] M.R. Jamali, Y. Assadi, F. Shemirani, M.R. Milani Hosseini, R.R. Kozani, M. Masteri-Farahani, M. Salavati-Niasari, Anal. Chim. Acta 579 (2006) 68.
[14] M.R. Ganjali, L.H. Babaei, A. Badiei, G.M. Ziarani, A. Tarlani, Anal. Sci. 20 (2004) 725.
[15] O. Kaftan, M. Açıkel, A. Eroglu, T. Shahwan, L. Artok, C. Ni, Anal. Chim. Acta 547 (2005) 31.
[16] M. Kim, J. Stripeikis, M. Tudino, Talanta 77 (2009) 1068.
[17] M. Kim, J. Stripeikis, M. Tudino, Spectrochim. Acta Part B (2009) in press, doi:10.1016/j.sab.2009.01.006.
[18] D. Pérez-Quintanilla, A. Sánchez, I. del Hierro, I. Sierra, Microchim. Acta 165 (2009) 291.
[19] C. Fowler, S. Burkett, S. Mann, Chem. Commun. (1997) 1769.
[20] A.S. Tracey, G.R. Willsky, E.S. Takeuchi, Vanadium: Chemistry, Biochemistry, Pharmacology and Practical Applications, CRC press, Taylor & Francis Group, Boca Raton, FL, USA, 2007.
[21] Y.S. Ho, G. McKay, Water Res. 34 (2000) 735.
[22] J. Li, X. Miao, Y. Hao, J. Zhao, X. Sun, L. Wang, J. Colloid Interface Sci. 318 (2008) 309.
[23] Y. Ho, J. Hazard. Mater. 136 (2006) 681.
[24] F. Andrade, M. Tudino, O. Troccoli, Analyst 121 (1996) 613.
[25] F. Aureli, S. Ciardullo, M. Pagano, A. Raggi, F. Cubadda, J. Anal. At. Spectr. 23 (2008) 1009.
[26] J. Seneviratne, J. Cox, Talanta 52 (2000) 801.
[27] D. Chen, C. Huang, M. He, B. Hu, J. Hazard. Mater 164 (2009) 1146.
[28] E.H. Hansen, M. Miró, TrAC Trends Anal. Chem. 26 (2007) 18.

Talanta 79 (2009) 695–699

Contents lists available at ScienceDirect

Talanta

journal homepage: www.elsevier.com/locate/talanta

Multivariate optimization of hydrodistillation-headspace solvent microextraction of thymol and carvacrol from *Thymus transcaspicus*

Vahid Kiyanpour[a], Ali Reza Fakhari[a,b,*], Reza Alizadeh[b], Behvar Asghari[a], Mehdi Jalali-Heravi[c]

[a] Department of Phytochemistry, Medicinal Plants and Drugs Research Institute, Shahid Beheshti University, G. C., Evin, Tehran, Iran
[b] Department of Chemistry, Faculty of Sciences, Shahid Beheshti University, G. C., Evin, Tehran, Iran
[c] Department of Chemistry, Sharif University of Technology, Azadi Avenue, P.O. Box 11155-9516, Tehran, Iran

ARTICLE INFO

Article history:
Received 26 November 2008
Received in revised form 25 April 2009
Accepted 27 April 2009
Available online 9 May 2009

Keywords:
Thymol
Carvacrol
Hydrodistillation
Headspace solvent microextraction
Response surface methodology
Thymus transcaspicus

ABSTRACT

In this paper multivariate response surface methodology (RSM) has been used for the optimization of hydrodistillation-headspace solvent microextraction (HD-HSME) of thymol and carvacrol in *Thymus transcaspicus*. Quantitative determination of compounds of interest was performed simultaneously using gas chromatography coupled with flame ionization detector (GC-FID). Parameters affecting the extraction efficiency were assessed and the optimized values were 5 min, 2 μL and 3 min for the extraction time, micro-drop volume and cooling time after extraction, respectively. The amounts of analyte extracted increased with plant weight. The calibration curves were linear in the ranges of 6.25–81.25 and 1.25–87.50 mg L^{-1} for thymol and carvacrol, respectively. Limit of detection (LOD) for thymol and carvacrol was 1.87 and 0.23 mg L^{-1}, respectively. Within-day and between-day precisions for both analytes were calculated in three different concentrations and recoveries obtained were in the range of 89–101% and 95–116% for thymol and carvacrol, respectively.

1. Introduction

Essential oils are naturally occurring compounds extracted from vegetal materials and due to their various properties such as antimicrobial, antioxidant and antifungal have been used in pharmaceutical and food industries [1]. The thyme essential oil is one of the most important oils used in traditional medicine to treat cold, flu and cough [2]. New properties of thyme oil such as strong acetylcholinesterase (Alzheimer disease agent) inhibitory effect have been reported [3]. Based on our previous research, the above mentioned properties of thyme oil are related to its high phenolic content (thymol, carvacrol, linalool, etc.) [4].

A wide variety of extraction method has been used for the isolation of the essential oil from plant materials. Common techniques for the isolation and extraction of the essential oils include hydrodistillation and steam distillation, supercritical-fluid extraction (SFE), solid-phase microextraction (SPME), headspace solvent microextraction (HSME) and hydrodistillation-headspace solvent microextraction (HD-HSME). HD-HSME is a rapid, simple and cost effective method for extracting volatile compounds. There are various parameters such as extraction time, micro-drop volume, sample mass, etc., affecting the extraction efficiency of this method [5–11].

Different chromatographic methods have been used for the determination of thymol and carvacrol in various matrixes. The method of quantitative thin-layer chromatography (TLC) combined with densitometry has been used to determine the thymol and carvacrol content of *Oleum thymi* essential oil [12]. Vinas and coworkers have determined phenol, thymol and carvacrol in honey using high performance liquid chromatography with fluorimetric detection [13]. These compounds have also been determined using gas chromatographs equipped with flame ionization [14,15] and mass spectrometric detection [2,16].

The aim of the present work was optimizing a HD-HSME method for the extraction of thymol and carvacrol in *Thymus transcaspicus* followed by their quantitative determination using a simple and reliable GC-FID analysis procedure.

2. Experimental

2.1. Reagents and materials

Aerial parts of *T. transcaspicus* were collected in June 2007 from Aladagh Mountains, Bojnourd, Iran. The plant materials were air dried in the absence of light at ambient temperature and stored at 4 °C.

* Corresponding author at: Department of Chemistry, Faculty of Sciences, Shahid Beheshti University, G. C., Evin, Tehran, Iran. Tel.: +98 21 22431683; fax: +68 21 22431661.
E-mail address: a-zavareh@sbu.ac.ir (A.R. Fakhari).

0039-9140/$ – see front matter © 2009 Elsevier B.V. All rights reserved.
doi:10.1016/j.talanta.2009.04.068

Table 1
Factors and their notations together with their levels used in central composite design.

Factors	Key	Levels		
		−1	0	+1
Drop volume (μL)	A	1	2	3
Extraction time (min)	B	1	3	5
Plant weight (g)	C	0.1	0.55	1
Cooling time after distillation (min)	D	1	2.5	4

Thymol and carvacrol standards were purchased from Merck (Darmstadt, Germany) and Fluka (Buchs, Switzerland), respectively. The extracting solvents *n*-tetradecane (>99%), *n*-pentadecane (>99%), *n*-hexadecane (>99%), *n*-heptadecane (>99%) and 1-phenyl decane (>99%) were purchased from Merck (Darmstadt, Germany) and Fluka (Buchs, Switzerland).

2.2. Apparatus

The detailed description of the procedure and apparatus used for HD-HSME has been reported previously [5]. In brief, extraction and injection were performed with a Hamilton Model 1701N 10-μL gas-tight syringe with fixed bevelled-point needle. A 100-mL round-bottomed flask containing dried plant in water was heated on a mantle. After refluxing the mixture for 10 min, the syringe needle was located into the headspace of the sample. After cooling, the syringe plunger was depressed and a micro-drop of extraction solvent was suspended from the needle tip. When the optimum time was reached the plunger was withdrawn and the micro-drop was retracted back into the syringe. The needle was removed from the headspace and the sample was injected into the GC injection port.

2.3. GC analysis condition

GC analysis was performed by using a Thermoquest-Finnigan Trace GC instrument equipped with a 60 m × 0.25 mm i.d., 0.25 μm film thickness, DB-1 fused silica capillary column. Nitrogen was used as carrier gas at a constant flow rate of 1.1 mL min^{-1}. The oven temperature was increased from 60 to 250 °C at 5 °C min^{-1}. The temperatures of injection and detection systems (FID) were 250 and 280 °C, respectively.

2.4. Experimental design

Central composite face-centered design (CCF) was used to optimize the extraction of thymol and carvacrol from *T. transcaspicus*. Four variables including drop volume (A), extraction time (B), the plant sample weight (C) and cooling time after hydrodistillation (D) were studied at three levels (Table 1) with repeating six experiments at the center of the design. The number of runs (*N*) is defined by the following equation:

$$N = 2^{k-p} + 2k + C_p \quad (1)$$

where *k* is the number of studied variables, *p* is the fractionalization element (in full factorial design, $p = 0$) and C_p is the number of central points [17]. The levels along with the notation for the factors studied in the present study are given in Table 1. Table 2 shows the relative peak areas for thymol and carvacrol together with the design matrix with coded variables.

Design generation and statistical analyses were performed using the software package Statgraphics Plus version 5.1 for windows (Rockvill, MD, USA).

3. Results and discussion

3.1. Optimization of the extraction conditions

The success of HD-HSME strongly depends on the selection of an appropriate solvent. The extraction solvent should not evaporate during the extraction; also it must have a good ability to extract the analyte. Moreover, the solvent must be chosen in such a way that its peaks do not overlap with those of analyte in the chromatogram. In order to select the best extraction solvent, preliminary experiments were performed under the same operating conditions (drop volume = 2 μL; extraction time = 2 min; sample weight = 1 g; and cooling time after distillation = 2 min), with different solvents namely *n*-tetradecane, *n*-pentadecane, *n*-hexadecane, *n*-heptadecane and 1-phenyldecane. Among these solvents, *n*-pentadecane showed the best results and was selected as extraction solvent for the following experiments. *n*-Heptadecane was used as internal standard to correct the variation of the injection volumes.

Multivariate optimization methods provide advantages over more traditional optimization designs, including the fact that a smaller set of experiments produce more information and allow identification of the interactions among the variables. Previous studies have shown that several variables such as drop volume, extraction time, sample weight and cooling time after hydrodistillation could potentially affect the efficiency of the HD-HSME method [5–9].

By considering four parameters at three levels, the number of experiments would normally be 81. However, this number has been reduced to 30 by using a central composite design face center (CCF) approach. The statistical model, resulted from this limited number of experiments, was used to identify the high yield trends for the extraction process. The variables together with the values

Table 2
The relative peak areas for thymol and carvacrol together with the design matrix with coded variables.

Run	A	B	C	D	Response (relative peak area[a])	
					Thymol	Carvacrol
1	0	0	0	+1	0.035	0.022
2	0	0	0	0	0.111	0.065
3	0	0	0	0	0.112	0.073
4	−1	−1	−1	+1	0.046	0.022
5	0	0	0	0	0.010	0.063
6	+1	+1	−1	+1	0.065	0.029
7	0	0	0	0	0.107	0.077
8	−1	−1	+1	+1	0.276	0.140
9	−1	0	0	0	0.034	0.015
10	−1	−1	+1	−1	0.059	0.024
11	+1	0	0	0	0.114	0.075
12	+1	−1	+1	+1	0.147	0.070
13	−1	−1	−1	−1	0.047	0.006
14	−1	+1	−1	+1	0.032	0.015
15	+1	+1	+1	+1	0.380	0.213
16	−1	+1	−1	−1	0.025	0.008
17	0	0	0	0	0.098	0.057
18	+1	+1	+1	−1	0.368	0.178
19	+1	−1	+1	−1	0.044	0.042
20	−1	+1	+1	−1	0.241	0.145
21	+1	+1	−1	−1	0.084	0.040
22	−1	+1	+1	+1	0.430	0.263
23	+1	−1	−1	+1	0.021	0.009
24	0	0	0	−1	0.136	0.079
25	0	−1	0	0	0.137	0.076
26	0	0	0	0	0.100	0.046
27	0	0	+1	0	0.742	0.379
28	+1	−1	−1	−1	0.001	0.003
29	0	+1	0	0	0.092	0.059
30	0	0	−1	0	0.089	0.038

[a] The relationship between the peak area of thymol and carvacrol and internal standard (*n*-heptadecane).

Table 3
Analysis of variance (ANOVA) study for the thymol.

Source	Sum of squares	d.f.	Mean square	*F*-Ratio	*P*-Value
A: Volume	0.00007	1	0.00007	0.01	0.9320
B: Time	0.04923	1	0.04923	5.28	0.0364
C: Weight	0.28792	1	0.28792	30.88	0.0001
D: T cooling	0.01014	1	0.01014	1.09	0.3134
AA	0.02405	1	0.02405	2.58	0.1291
AB	0.00919	1	0.00919	0.99	0.3365
AC	0.00048	1	0.00048	0.05	0.8229
AD	0.00542	1	0.00542	0.58	0.4572
BB	0.00815	1	0.00815	0.87	0.3645
BC	0.04023	1	0.04023	4.31	0.0554
BD	0.00137	1	0.00137	0.15	0.7068
CC	0.15551	1	0.15551	16.68	0.0010
CD	0.01665	1	0.01665	1.79	0.2013
DD	0.01875	1	0.01875	2.01	0.1765
Total error	0.13985	15	0.00932		
Total (corr.)	0.72026	29			

of the responses are shown in Table 2. The relationship between the peak areas of thymol and carvacrol and internal standard (*n*-heptadecane) for each experiment was used as response value to measure the extraction efficiency.

Analysis of variance (ANOVA) was used to assess the significance of the model. The initial summary of the statistic experiment for thymol and carvacrol, is shown in Tables 3 and 4, respectively.

The *F*-ratio in this table shows the ratio of the mean–squares error to the pure error obtained from the replication of experiment replicates at the center of the design. The significance of the *F* value depends on the number of degrees of freedom (d.f.) in the model and is given in the *P*-value column. Confidence level of 95% was chosen in this design. Therefore, the effects <0.05 in the *P*-value column are statistically significant. Fig. 1 shows the pareto chart of thymol and carvacrol based on the results illustrated in Tables 3 and 4. It can be seen that extraction time (B), sample weight (C), sample weight square effect (CC) and the interaction between the sample weight and extraction time (BC) show a positive effect on the extraction efficiency of both thymol and carvacrol. However, except for the interaction between C and D factors, there was no interaction between the other factors (Fig. 1).

The optimum range for each factor was obtained from the main effect plots along with the three-dimensional estimated response surfaces. To this end, two variables were fixed at their central point values. Fig. 2 shows the effect of different parameters on the extraction efficiency of carvacrol. The same results were obtained for thymol (data not shown). As can be seen from these plots, maximum values were achieved for three out of four factors within the inves-

Table 4
Analysis of variance (ANOVA) study for the carvacrol.

Source	Sum of squares	d.f.	Mean square	*F*-Ratio	*P*-Value
A: Volume	0.00002	1	0.00002	0.01	0.9178
B: Time	0.01728	1	0.01728	7.04	0.0181
C: Weight	0.09193	1	0.09193	37.47	0.0000
D: T cooling	0.00372	1	0.00372	1.52	0.2368
AA	0.00596	1	0.00596	2.43	0.1400
AB	0.00059	1	0.00059	0.24	0.6282
AC	0.00060	1	0.00060	0.25	0.6259
AD	0.00250	1	0.00250	1.023	0.3285
BB	0.00170	1	0.00170	0.70	0.4170
BC	0.01391	1	0.01391	5.67	0.0309
BD	0.00001	1	0.00001	0.01	0.9293
CC	0.03436	1	0.03436	14.00	0.0020
CD	0.00480	1	0.00480	1.96	0.1822
DD	0.00465	1	0.00465	1.90	0.1887
Total error	0.03680	15	0.00245		
Total (corr.)	0.20827	29			

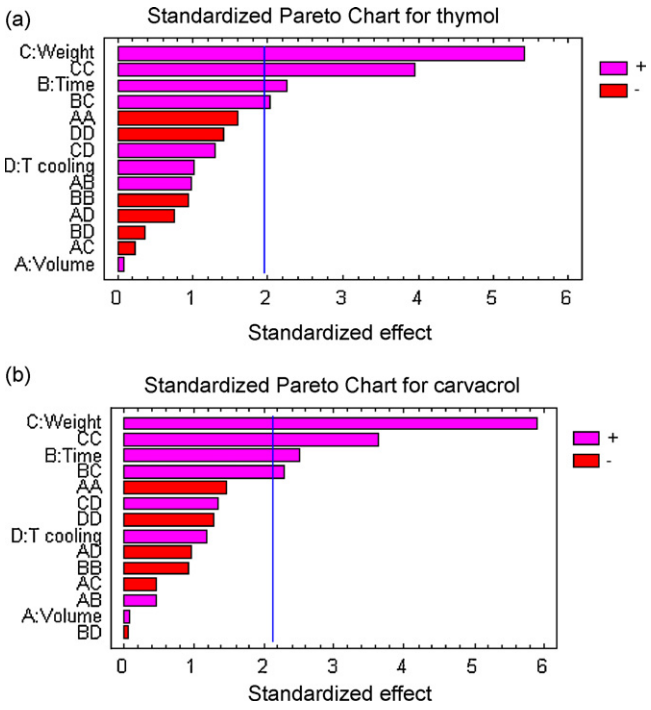

Fig. 1. Standardized pareto charts for (a) thymol and (b) carvacrol.

tigated ranges. As the plant weight increases the amounts of the extracted thymol and carvacrol increase. Since we have to choose a small extract container to establish a fast equilibrium between the drop and unoccupied space area of the container, the maximum amount of the plant used within the experiment was chosen as 1 g.

Table 5 shows the optimum extraction conditions of the thymol and carvacrol confirmed by the contour maps of the estimated response surface (Fig. 2(c) and (d)). The optimum conditions for both compounds were apparently very close (Table 5).

According to the calibration curves, thymol and carvacrol amounts in thyme for the optimum condition were found to be 1.168 and 0.859 mg, respectively, per 1 g of dried plant sample. These values show that 0.1168% and 0.0859% (W/W) of thyme are thymol and carvacrol. The chromatogram of the extracted essential oil from *T. transcaspicus* by using HD-HSME method is presented in Fig. 3.

3.2. Analytical figures of merit

Under the optimum conditions, the following validation methods were addressed for both thymol and carvacrol: limit of detection (LOD), limit of quantification (LOQ), linearity range, accuracy and between-day and within-day precisions.

Linearity of the method was confirmed by preparing standard curves for the analytical ranges of 6.25–81.25 mg L^{-1} for the thymol and 1.25–87.50 mg L^{-1} for the carvacrol. The standard curves were linear in the above mentioned ranges with regression coeffi-

Table 5
Optimized values of factors affecting the extraction of thymol and carvacrol.

Factor	Low level	High level	Optimum		Experimental conditions
			Thymol	Carvacrol	
Volume (μL)	1.0	3.0	2.06	1.92	1.0
Time (min)	1.0	5	4.8	4.9	1.0
Weight (g)	0.1	1.0	1.0	1.0	1.0
Cooling time after distillation (min)	1.0	4.0	2.9	3.1	3.0

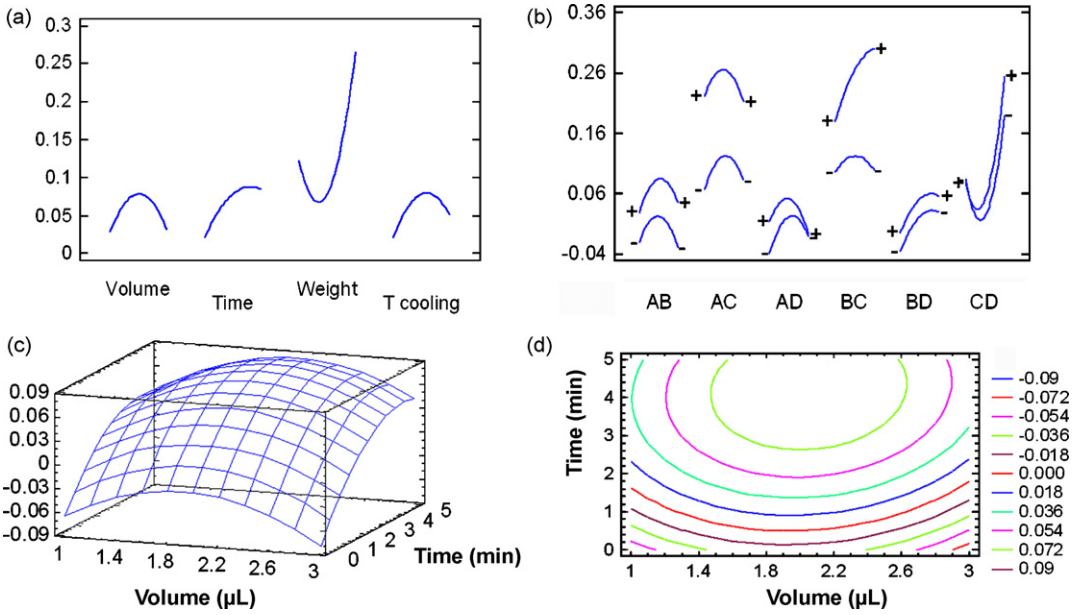

Fig. 2. (a) Main effect plots for carvacrol, (b) Interaction plots for carvacrol, (c) estimated response surface, and (d) counters of estimated response surface plot for the extraction of carvacrol.

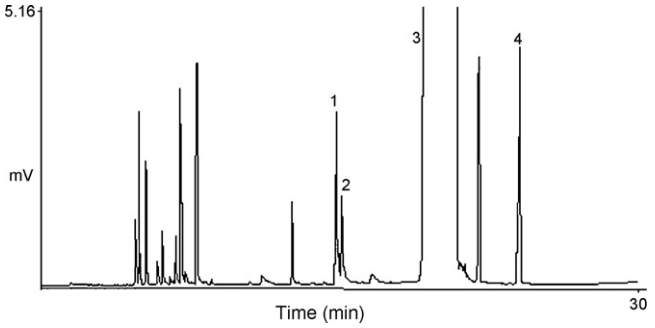

Fig. 3. GC chromatogram of *T. transcaspicus* essential oil. (1) Thymol, (2) carvacrol, (3) solvent, and (4) internal standard.

cients of 0.994 and 0.998 for thymol and carvacrol, respectively (Table 6).

Limit of detection (LOD) for both compounds were calculated using Eq. (2):

$$\mathrm{LOD} = \frac{3s_b}{m} \quad (2)$$

where s_b is the standard deviation of the blank signal, and m is the slope of the calibration curve. The LOD was found to be 1.87 and 0.23 mg L^{-1} for the thymol and carvacrol, respectively.

The limit of quantification (LOQ), defined as $10 \times \mathrm{LOD}/3$, was 6.23 and 0.77 mg L^{-1} for the thymol and carvacrol, respectively (Table 6).

Table 6
The range of linearity, calibration equation, limits of detection (LOD) and limits of quantification (LOQ) for the thymol and carvacrol extracted by HD-HSME method.

Parameter	Thymol	Carvacrol
Linearity range (mg L^{-1})	6.25–81.25	1.25–87.5
Slope	0.0694	0.0306
% R.S.D. of slope	6.37	11.8
Intercept	0.3054	0.1170
Correlation (R^2)	0.9944	0.9979
LOD (mg L^{-1})	1.87	0.23
LOQ (mg L^{-1})	6.23	0.77

Table 7
Within-day precision and between-day precisions.

	Thymol			Carvacrol		
Concentration (mg L^{-1})	12.50	15.62	18.75	12.48	15.00	20.00
Within-day (n = 5) % R.S.D.	10.10	7.27	11.97	9.22	7.11	5.09
Between-day (n = 3) % R.S.D.	9.20	9.16	10.16	9.32	8.35	9.43

LOD and LOQ of HD-HSME method are closed to the other methods such as SPME and SPE but its dynamic range is wider compared to the others [15,18–21].

The precision of the method was estimated from the six runs repeated at the center points of the factors. Relative standard deviations for the thymol and carvacrol were found to be 6.37% and 11.80%, respectively. Five measurements were made for the within-day precision. Between-day precision was calculated from the average of measurements for each day. Three concentrations were chosen for the determination of between-day and within-day precisions (Table 7).

Accuracy, based on recovery of thymol and carvacrol was calculated by comparing the peak areas obtained from the spiked plant sample, at the concentrations of 130 and 180 mg L^{-1} for thymol and carvacrol, respectively with those obtained from the unspiked solutions. Recoveries (n = 3) were in the ranges of 89–101% and 95–116% for thymol and carvacrol, respectively.

These results show the precision for the determination of the thymol and carvacrol are better than of the other mentioned methods [15,18–21] and accuracy of HD-HSME method is comparable to other methods [15,18–21].

4. Conclusion

Response surface methodology has been used for optimizing HD-HSME method to extract the thymol and carvacrol from *T. transcaspicus*. It was found that there are various parameters affecting the extraction efficiency of HD-HSME. In order to reduce the number of experiments and to assess the existence of interaction between the affecting parameters, multivariate approach was used for the optimization of the extraction condition. Four parameters of drop volume, extraction time, plant weight and cooling time after distillation were optimized using CCF technique. The optimized

method was evaluated and found to be efficient and reliable for the extraction of thymol and carvacrol from the plant materials.

Acknowledgment

The authors gratefully acknowledge the Research Council of Shahid Beheshti University for financial support.

References

[1] P.L. Teissedre, A.L. Waterhouse, J. Agric. Food Chem. 48 (2000) 3605.
[2] S. Abu-Lafi, I. Odeh, H. Dewik, M. Qabajah, L.O. Hanus, V.M. Dembitsky, Bioresour. Technol. 99 (2007) 3914.
[3] M. Jukic, O. Politeo, M. Maksimovic, M. Milos, M. Milos, Phytother. Res. 21 (2007) 259.
[4] S.I. Dimitrijevic, K.R. Mihajlovski, D.G. Antonovic, M.R. Milanovic-Steva-Novic, D.Z. Mijin, Food Chem. 104 (2007) 774.
[5] A.R. Fakhari, P. Salehi, R. Heydari, S.N. Ebrahimi, P.R. Haddad, J. Chromatogr. A 1098 (2005) 14.
[6] P. Salehi, B. Asghari, F. Mohammadi, Chromatographia 65 (2007) 119.
[7] P. Hashemi, M.M. Abolghasemi, A.R. Fakhari, S.N. Ebrahimi, S. Ahmadi, Chromatographia 66 (2007) 283.
[8] P. Salehi, F. Mohammadi, B. Asghari, Chem. Nat. Compd. 44 (2008) 111.
[9] P. Salehi, A.R. Fakhari, S.N. Ebrahimi, R. Heydari, Flavour Fragr. J. 22 (2007)280.
[10] A. Besharati-Seidani, A. Jabbari, Y. Yamini, Anal. Chim. Acta 530 (2005) 155.
[11] A. Besharati-Seidani, A. Jabbari, Y. Yamini, M.J. Saharkhiz, Flavour Fragr. J. 21 (2006) 502.
[12] A. Bazylko, H. Strzelecka, Chromatographia 52 (2000) 112.
[13] P. Vinas, M.J. Soler-Romera, M. Hernandez-Cordoba, Talanta 69 (2006) 1063.
[14] M.J. Nozal, J.L. Bernal, J.J. Jimenez, M.J. Gonzalez, M. Higes, J. Chromatogr. A 954 (2002) 207.
[15] C. Kohlert, G. Abel, E. Schmid, M. Veit, J. Chromatogr. B 767 (2002) 11.
[16] M. Lodesani, A. Pellacani, S. Bergomi, E. Carpana, T. Rabitti, P. Lasagni, Apidologie 23 (1992) 257.
[17] T.B. Barket, Quality by Experimental Design, Marcel-Dekker, New York, 1978.
[18] A.C. Martel, S. Zeggane, J. Chromatogr. A 954 (2002) 173.
[19] E.Y. Backheet, Phytochem. Anal. 9 (1998) 134.
[20] L. Dong, C. Deng, J. Wang, X. Shen, Anal. Chim. Acta 585 (2007) 76.
[21] A. Michelitsch, A. Rittmannsberger, A. Hüfner, U. Rückert, W. Likussar, Phytochem. Anal. 15 (2004) 320.

Talanta 79 (2009) 851–855

Contents lists available at ScienceDirect

Talanta

journal homepage: www.elsevier.com/locate/talanta

Establishing linear solvation energy relationships between VOCs and monolayer-protected gold nanoclusters using quartz crystal microbalance

Chi-Lin Li [a], Chia-Jung Lu [b,*]

[a] Department of Chemistry, Fu-Jen Catholic University, Hsinchuang, Taiwan, ROC
[b] Department of Chemistry, National Taiwan Normal University, Taipei 11677, Taiwan, ROC

ARTICLE INFO

Article history:
Received 4 February 2009
Received in revised form 9 May 2009
Accepted 11 May 2009
Available online 20 May 2009

Keywords:
Gold nanoparticles
Gas sensor
Linear solvation energy relationships
Volatile organic compounds

ABSTRACT

Linear solvation energy relationships (LSERs) have been recognized as a useful model for investigating the chemical forces behind the partition coefficients between vapor molecules and absorbents. This study is the first to determine the solvation properties of monolayer-protected gold nanoclusters (MPCs) with different surface ligands. The ratio of partition coefficients/MPC density (K/ρ) of 18 volatile organic compounds (VOCs) for four different MPCs obtained through quartz crystal microbalance (QCM) experiments were used for the LSER model calculations. LSER modeling results indicate that all MPC surfaces showed a statistically significant ($p < 0.05$) preference to hydrogen-bond acidic molecules. Through dipole–dipole attraction, 4-methoxythiophenol-capped MPCs can also interact with polar organics ($s = 1.04$). Showing a unique preference for the hydrogen bond basicity of vapors ($b = 1.11$), 2-benzothiazolethiol-capped MPCs provide evidence of an intra-molecular, proton-shift mechanism on surface of nano-gold.

1. Introduction

With the introduction, by Brust et al., of the synthesis of monolayer-protected nanoclusters (MPCs) [1,2], a tremendous amount of research effort has been devoted to the investigation of the versatile properties of these novel materials. MPCs consist of a nano-gold core with a diameter in the range of 3–10 nm and a thiolate self-assembled monolayer (SAM) on the surface. Murray et al. [3–6] have extensively investigated the conductivity, surface chemistry and electrochemical properties of MPCs.

Use of MPCs as chemiresistors for the detection of organic vapors was first explored by Wohltjen and Snow [7,8]. An octane thiol-capped MPC was spray-coated as a thin film on a micro-fabricated interdigit electrode (IDE). The resistance of the MPC thin film increased as the VOCs absorbed into the film (e.g., toluene and chloroform). An interesting feature of MPC vapor sensors is that versatile selectivity can be easily achieved by replacing surface thiolates. Zellers et al. demonstrated the first dual MPC chemiresistors as a detector array for capillary GC and studied the resistive response model of MPC-coated chemiresistors [9–11]. Zhong et al. investigated a series of cross-linked MPCs as vapor-sensing films for use in both chemiresistors and in quartz crystal microbalances (QCM), and also tested the pattern recognition of a chemiresistor array consisting of various MPCs [12–14]. In addition to QCM and chemiresistors, the vapor-sensing selectivity of MPCs is also demonstrated using localized surface plasmon resonance (LSPR) sensors [15,16].

Although the versatile vapor selectivity of MPC-based sensors has been demonstrated in numerous studies [9,14,17–19], the actual chemical interactions between the MPC surface and the test vapors has never been studied quantitatively. Other sorption-type vapor sensors, such as polymer-coated QCM and surface acoustic wave (SAW) sensors, have faced the same challenge. The solution is the use of linear solvation energy relationship (LSER) modeling to quantify the chemical force coefficients of the sensing materials [20,21]. The LSER model can be described as follows [22–24]:

$$\log K = c + rR_2 + s\pi_2^H + a\sum \alpha_2^H + b\sum \beta_2^H + l\log L^{16} \quad (1)$$

where K is the partition coefficient for the sorption process. K can be obtained by various means: GLC [22–24], gravimetric methods [25], or QCM [26,27]. K values obtained by gravimetric microbalance (i.e., using Kahn microbalance) are found to agree better with those obtained from QCM experiments. However, the gravimetric approach requires a large absorbent mass to detect significant weight changes on the microbalance scale during vapor sorption. In contrast, the QCM approach requires only a small absorbent mass to achieve similar results [27].

The sorption process can be treated as a dissolution behavior. Thus, by definition, the VOCs are solutes and the sensing/absorbent films are solvents. R_2, π_2^H, $\sum \alpha_2^H$, $\sum \beta_2^H$, and $\log L^{16}$ in Eq. (1) are solute parameters that can be determined and calculated via other independent methods [22–24]. R_2 is the excess molar refraction, as

* Corresponding author. Tel.: +886 2 29030749x406; fax: +886 2 29324249.
E-mail address: cjlu@ntnu.edu.tw (C.-J. Lu).

0039-9140/$ – see front matter © 2009 Elsevier B.V. All rights reserved.
doi:10.1016/j.talanta.2009.05.012

compared to saturated hydrocarbons, which indicates the polarizability of the solute. π_2^H is the dipole moment of the solute. $\sum \alpha_2^H$ and $\sum \beta_2^H$ are the hydrogen-bond acidity and basicity of the absorbed molecule. $\log L^{16}$ indicates the effectiveness of the dispersion force and the solvent cage stability. This term is determined by measuring the energy change of the solute in the hexadecane solvent. The regression coefficients (i.e., *r*, *s*, *a*, *b* and *l*) show the importance of the contribution of the corresponding chemical forces to the partition coefficient between a given vapor/sorbent pair. The regression constant, *c*, is a residual product of multiple linear regressions that has no significance in relation to the chemical forces.

Through the years, the LSER model has been successfully applied in the investigation of the response mechanism of polymer-based sorption sensors such as SAW and QCM. Hierlemann et al. extensively investigated the limiting condition of polymer-coated sensor arrays employing LSER [27]. Grate et al. developed a novel strategy to predict the category of an unknown vapor based on LSER descriptors [28,29].

Our previous report described the synthesis of MPCs capped with functionally distinct thiolates for vapor-sensor applications. The initial results of tests of rapid response, reproducibility, and selectivity were also presented [19]. The present study utilized the LSER model to investigate the surface chemical interactions of the same set of materials, and we investigated the influences of chemical forces on the response patterns of a MPC-coated QCM array. To establish LSER coefficients for MPCs, 18 organic vapors with divergent functional groups were tested.

2. Experimental

2.1. Materials

Hydrogen tetrachloroaurate ($HAuCl_4$) was purchased from Alfa Aesar. Tetraoctylammonium bromide (TOAB) was obtained from Arcos. 4-Methoxythiophenol (MOP) and dichloromethane-d2 were obtained from Lancaster. Other organic thiolates such as n-octanethiol (C8SH), 2-naphthalenethiol (NAP), and 2-benzothiazolethiol (MBT) were purchased from TCI. Organic solvents for vapor generation and MPC synthesis were obtained from Aldrich with 99%, or higher, purity. Water was purified with a system from Millipore Bedford.

2.2. Nanocluster synthesis

Monolayer-protected nanoclusters (MPCs) were synthesized using a water/toluene two-phase approach [1]. TOAB was used as a phase-transfer agent. $NaBH_4$ was used to reduce the $AuCl_4^-$. The molar ratio used in our synthesis was Au/TOAB/thiolate = 3/3/1. Detailed procedures regarding the concentration, temperature and reaction time were reported elsewhere [19]. The final MPC product was purified by re-precipitation in cold ethanol (~300 mL) and separated by centrifugation. Complete removal of undesired TOAB and thiolates was confirmed by monitoring the H-NMR spectrum of rinse-off residual dissolved in dichloromethan-d2. Typically, three cycles of re-dissolve in toluene and re-precipitation in ethanol are needed.

2.3. Preparation of QCM sensor devices

10 MHz, AT-cut, gold surface electrode quartz crystals (Taitein electronics, CO., Taiwan) were used for the QCM test in this study. Prior to use, crystals were cleaned with a H_2SO_4/H_2O_2 solution to remove any surface organic residue, followed by rinsing in deionized water. MPCs were dissolved in dichloromethane and spray-coated on QCM. The frequency shifts due to spray-coating were recorded for the calculations of MPC film mass.

2.4. Test vapor generation and calibration

A three mass-flow controller system was constructed to provide a high flow-rate and rapid-switching test vapor atmosphere. Compressed-house air (~30 psi) was scrubbed using a molecular sieve trap, a charcoal trap, and a high-efficiency particle filter. The humidity of the air stream was monitored with a humidity meter (DO9861T-R1, Delta Ohm, Padua, Italy) and was always kept below the lowest readable humidity value (<1%). The concentration of organic vapor was generated by passing the background air through a bubbler to produce a saturated vapor concentration at room temperature, which was then diluted with different flow ratios of background air. Mass flow controllers (5850i, Brooks Instrument, PA, USA) were calibrated with a bubble burette prior to installation in the vapor generation system. 3-way solenoid valves were connected in front of the test cell, which allowed computer-controlled switching between the background air and the test vapor concentration. The vapor concentrations were calibrated with GC-FID (HP-5890, Agilent) by comparisons made to the mass-response of calibration curves obtained from CS_2 solution injection of the same compound. For polar compounds having a boiling point greater than 120 °C, the vapor generation system showed considerable negative bias (i.e., approximately −20 to −30%). This was due to incomplete evaporation of compounds with high boiling points at room temperature. Effective concentrations were corrected using CS_2 calibration data under the same GC-FID operating conditions. The scheme for the vapor testing system can be found in one of our previous reports [15].

2.5. MPC-coated QCM sensor testing

All vapor exposure tests were performed at room temperature (25 ± 1 °C) in an air conditioned lab. The temperatures of all tests were recorded to calculate the effective vapor concentration generated by the system. A data acquisition system employing a frequency counter interface (PXI-1031, National Instruments, TX, USA) and a LabView program written in-house were used to simultaneously record the frequency change of four different MPC-coated QCM sensors.

3. Results and discussion

This study investigated the surface chemical forces of four different types of nano-Au particles capped with either MOP, C8SH, MBT or NAP monolayers. Fig. 1 shows examples of calibration lines of the QCM array coated with the four MPCs and tested with two very different vapors: n-octane and n-butanol. The original vapor on/off response signals are not presented here, since similar data can be found in either our previous report [19] or in the studies of other researchers who examined different MPCs [10,13]. The *Y*-axis unit in Fig. 1 is ppm of $\Delta f\nu/\Delta fs$ where Δfs is the frequency shift that resulted from spraying the MPC film on a QCM device, $\Delta f\nu$ is the frequency shift caused by vapor sorption onto the MPC film on the QCM device. $\Delta f\nu/\Delta fs$ means that the QCM responses were normalized to the film coating mass, because the quantity of absorbed molecules is proportional to the coating mass under a given vapor concentration.

After accounting for the different coating thickness on each sensor, some selectivity is evident based on the results presented in Fig. 1. In general, n-butanol (Fig. 1b) was more sensitive than n-octane (Fig. 1a) for all MPC-QCM sensors. However, while MOP–Au, MBT–Au, and NAP–Au all showed a much lower sensitivity to

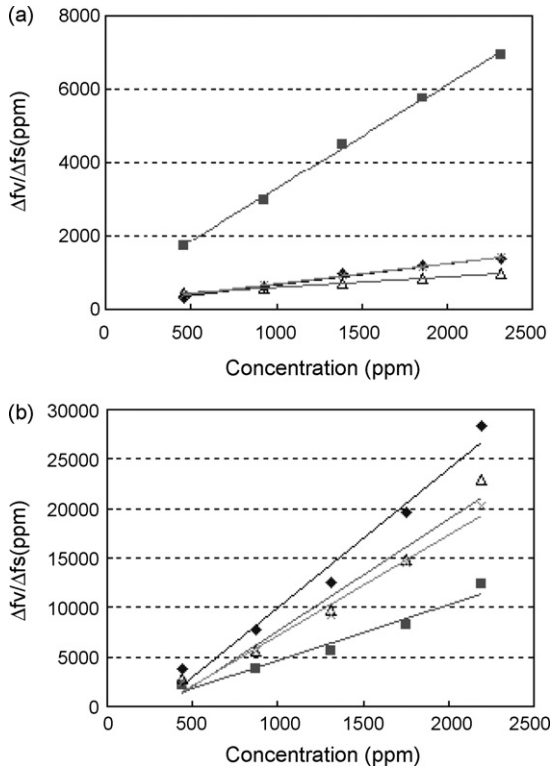

Fig. 1. Examples of QCM sensor calibration curves: (a) octane and (b) butanol (♦: MOP–Au; △: MBT–Au; ■: C8–Au; ×: NAP–Au).

n-octane than C8SH–Au did, they all outperformed C8SH–Au in n-butanol QCM sensing.

The frequency shift of QCM due to MPC spray-coating was controlled in a range of from 7.21 to 9.52 kHz. Using the Sauerbrey equation [31] and a theoretical density (ρ = 3–6 g/cm^3) of MPC [30], the film thickness was estimated to be approximately 100 nm. When the film is acoustically thin, the response of QCM can only be attributed to mass change. If the film is acoustically thick, the QCM responds to changes in both mass and modules due to asynchronous motion across the film thickness. Hierlemann et al. [27] coated a rubbery polymer, polyisobutylene (PIB, ρ = 0.92 g/cm^3), on QCM with a frequency shift of between 10 and 15 kHz (i.e., 150–200 nm based on literature values), which proved to be acoustically thin. It is clear that the MPC films used in this study were much thinner than the polymer film in the preceding reference, based on the lower frequency shift after coating. Also, the metal (i.e., nano-gold)-loaded MPC film was much denser than the PIB film. Thus, we are confident that the MPC-coated QCM used in this study responds only to the mass increase during vapor testing.

Table 2
Ratios of partition coefficients to MPC densities (K/ρ_s).

Vapor	MOP–Au	C8SH–Au	MBT–Au	NAP–Au
Chloroform	78.9	111.1	76.0	100.3
Tetrahydrofuran	255.4	201.7	422.7	260.5
Ethyl acetate	377.5	387.1	398.8	361.5
2-Butanone	199.6	89.4	265.5	175.1
Benzene	112.1	259.7	119.7	152.3
Cyclohexane	73.2	143.1	56.0	40.5
Acetonitrile	149.8	44.1	124.2	110.7
2-Methyl-1-propanol	781.4	450.3	656.7	466.6
Toluene	290.3	503.2	254.0	282.2
n-Butanol	3812.8	1665.8	2980.8	2755.9
n-Octane	133.5	661.2	99.2	134.6
Butyl acetate	1414.9	1685.1	1472.3	1504.3
Chlorobenzene	1711.1	2181.3	1795.0	1725.7
n-Pentanol	3144.7	2243.3	2260.7	1707.6
Anisole	2523.2	2457.4	2502.9	2550.9
1,2-Dichloroethane	420.6	388.5	483.4	418.2
1,4-Dioxane	334.3	236.7	311.5	266.9
n-Butyl amine	1219.5	445.6	1272.4	1812.5

Table 1 summarizes the calibration data of all 18 vapors tested with the QCM array. Most of the R^2 values in Table 1 are greater than 0.99 except for a few highly volatile, or extremely polar, compounds. Basically, the linearity of the QCM results is quite acceptable; therefore, the slopes can be used further in the estimation of the partition coefficients (K). The K value can be calculated using a previously reported equation [20]:

$$\Delta fv = \frac{\Delta fs C v K}{\rho_s} \quad (2)$$

where Cv is the vapor concentration and ρ_s is the density of the MPC film. Eq.2 can be rearranged as $K/\rho_s = (\Delta fv/\Delta fs)Cv$, with the term on the right representing the slope of the QCM calibration line, except the unit of concentration must be changed to g/cm^3. As a result, the partition coefficient has no unit and the unit of ρ_s remains g/cm^3.

After conversion of the unit of concentration, the values for K/ρ_s were obtained and are listed in Table 2. Unfortunately, ρ_s values were not previously reported for all of the MPCs examined, because they are new materials. It is impractical and expensive to synthesize a large amount of MPC for the sole purpose of density measurement. Grate et al. have calculated the theoretical densities of MPCs to

Table 1
Calibration slope and R^2 of 18 VOCs tested on four MPC-coated QCM sensors.

VOCs	MOP–Au	C8SH–Au	MBT–Au	NAP–Au
Chloroform	0.31 (0.9910)	0.40 (0.9978)	0.24 (0.9973)	0.33 (0.9792)
Tetrahydrofuran	0.61 (0.9972)	0.52 (0.9999)	1.05 (0.9908)	0.71 (0.9970)
Ethyl acetate	1.11 (0.9998)	1.41 (0.9987)	1.17 (0.9975)	1.23 (0.9952)
2-Butanone	0.48 (0.9968)	0.26 (0.9949)	0.61 (0.9987)	0.43 (0.9967)
Benzene	0.31 (0.9956)	0.65 (0.9972)	0.29 (0.9942)	0.40 (0.9973)
Cyclohexane	0.21 (0.9829)	0.45 (0.9995)	0.17 (0.9999)	0.13 (0.9897)
Acetonitrile	0.18 (0.9908)	0.07 (0.9928)	0.15 (0.9653)	0.11 (0.9825)
2-Methyl-1-propanol	1.95 (0.9955)	1.42 (0.9844)	1.68 (0.9967)	1.25 (0.9992)
Toluene	0.91 (0.9956)	1.84 (0.9974)	0.81 (0.9942)	1.00 (0.9983)
n-Butanol	14.02 (0.9820)	5.72 (0.9872)	11.33 (0.9843)	10.17 (0.9835)
n-Octane	0.57 (0.9889)	2.85 (0.9984)	0.30 (0.9999)	0.55 (0.9999)
Butyl acetate	5.66 (0.9981)	8.81 (0.9936)	5.53 (0.9963)	6.87 (0.9986)
Chlorobenzene	6.50 (0.9957)	9.57 (0.9982)	6.59 (0.9993)	6.78 (0.9968)
n-Pentanol	9.83 (0.9906)	8.56 (0.9949)	6.70 (0.9938)	6.36 (0.9966)
Anisole	9.86 (0.9984)	11.35 (0.9989)	9.39 (0.9980)	11.11 (0.9945)
1,2-Dichloroethane	1.40 (0.9958)	1.50 (0.9996)	1.63 (0.9944)	1.57 (0.9978)
1,4-Dioxane	0.97 (0.9965)	0.74 (0.9991)	0.90 (0.9982)	0.88 (0.9817)
n-Butyl amine	2.92 (0.9847)	1.15 (0.9919)	2.79 (0.9965)	3.91 (0.9921)

be approximately 3–6 g/cm^3 [30]. Under constant temperature and pressure, MPC density should remain constant even if it is undetermined. At this point, we could not directly obtain K; instead, we used the ratio of K/ρ_s in the LSER modeling. The method of calculation used is as follows: first, we take $\log(K/\rho_s)$:

$$\log\left(\frac{K}{\rho_s}\right) = \log K - \log \rho_s \quad (3)$$

Then, replace $\log K$ using original LSER Eq. (1):

$$\log\left(\frac{K}{\rho}\right) = c + rR_2 + s\pi_2^H + a\sum \alpha_2^H + b\sum \beta_2^H + l\log L^{16} - \log \rho_s \quad (4)$$

Since ρ_s is a constant, it does not vary with the solvation properties of the different vapors (i.e., R_2, π_2^H, $\sum \alpha_2^H$, $\sum \beta_2^H$, and $\log L^{16}$) used in the experiments. Therefore, ρ_s does not contribute to the LSER coefficients obtained from regression versus solvation parameters. Therefore, we can combine ρ_s with another constant, c, as follows:

$$\log\left(\frac{K}{\rho_s}\right) = (c - \log \rho_s) + rR_2 + s\pi_2^H + a\sum \alpha_2^H + b\sum \beta_2^H + l\log L^{16} \quad (5)$$

$$\log\left(\frac{K}{\rho_s}\right) = c' + rR_2 + s\pi_2^H + a\sum \alpha_2^H + b\sum \beta_2^H + l\log L^{16} \quad (6)$$

The original constant "c" is a regression residual that does not represent any chemical force, as is the case for ρ_s. In the above equations, $\log \rho_s$ and c are combined to become a new regression residual. Thus, we can model the chemical force interaction without knowing the actual value of the MPC density. In fact, using simulated densities of 3 and 6 (g/cm^3) in the LSER model proved that only the c' value changed with different densities. All the other force coefficients (e.g., r, s, a, b and l) remained the same.

Table 3 lists the solvation parameters of the vapors used in this study. All values are compiled from previous LSER literature [22–24]. As Table 3 shows, we selected test vapors with a reasonable range of volatility and with diverse solvation properties. The results of the LSER modeling are shown in Table 4. The statistically significant values ($P < 0.05$) are labeled with an asterisk. The dispersion force term (l) was statistically significant for all tested materials.

Table 3
Solvation parameters of tested vapors.

Tested vapors	R_2	π_2^H	$\sum \alpha_2^H$	$\sum \beta_2^H$	$l\log L^{16}$
Chloroform	0.425	0.49	0.15	0.02	2.48
Tetrahydrofuran	0.289	0.52	0	0.48	2.636
Ethyl acetate	0.106	0.62	0	0.45	2.314
2-Butanone	0.166	0.7	0	0.51	2.287
Benzene	0.61	0.52	0	0.14	2.786
Cyclohexane	0.305	0.1	0	0	2.964
Acetonitrile	0.237	0.9	0.07	0.32	1.739
2-Methyl-1-propanol	0.22	0.42	0.37	0.48	2.413
Toluene	0.601	0.52	0	0.14	3.325
n-Butanol	0.224	0.42	0.37	0.48	2.601
n-Octane	0	0	0	0	3.677
Butyl acetate	0.071	0.6	0	0.45	3.353
Chlorobenzene	0.718	0.65	0	0.07	3.657
n-Pentanol	0.219	0.42	0.37	0.48	3.106
Anisole	0.708	0.75	0	0.29	3.89
1,2-Dichloroethane	0.416	0.64	0.1	0.11	2.573
1,4-Dioxane	0.329	0.75	0	0.64	2.892
n-Butyl amine	0.224	0.35	0.16	0.61	2.618

All values are complied from refs. [22–24].

This is not surprising since the dispersion force represents a fundamental interaction among all substances. It is noteworthy that the vapor hydrogen-bond acidity was also significantly favored by all MPCs. There are two possible sites on MPCs that can accept an incoming hydrogen bond provider: the metal surface and the sulfur atom in the thiol group. The direct adsorption of alcohols (i.e., the hydrogen bond provider in this study) on a nano-metal surface has been previously reported [32]. Hydrogen bond interaction between alcohols and thiolates can still be effective even when the sulfur is bonded to a gold surface [33]. Also noteworthy was that MOP–Au had a higher affinity ($a = 2.61$) for the hydrogen-bond acidity than did the other three MPCs ($a = 1.98$–2.20). This can be attributed to the exterior, terminal —O—CH_3 group that increased the propensity to form hydrogen bonds with acidic compounds.

Aside from the dispersion force and the hydrogen-bond acidity, the dipole moment of the solute (i.e., $s\pi_2^H$) showed a significant interaction only for MOP–Au. MOP–Au attracted incoming polar molecules due to dipole–dipole interaction on its —O—CH_3 group. MBT–Au was the only material in this study that showed a unique preference for incoming molecules with hydrogen bond basicity ($b = 1.11$). This result indicates that the 2-benzothiazolethiol mono-

Table 4
Linear solvation energy relationships (LSERs) modeling results.

MPC	c'	r	s	a	b	l	R^2	S.E.	F
MOP–Au	−0.54	−0.14	1.05*	2.61*	0.91	0.77*	0.82	0.278	11.2
C8SH–Au	−0.54	−0.30	0.63	1.98*	0.24	0.95*	0.84	0.245	12.8
MBT–Au	−0.45	0.01	1.00	2.20*	1.11*	0.71*	0.78	0.306	8.6
NAP–Au	−0.51	0.04	0.95	2.18*	1.00	0.74*	0.75	0.327	7.3

* $P < 0.05$.

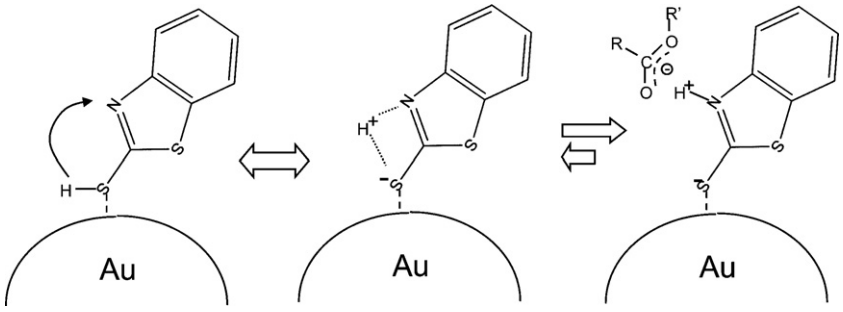

Fig. 2. Mechanism of hydrogen-bond acidity on 2-benzothiazolethiol capped MPCs.

layer on the nano-gold acts as a hydrogen-bond acid. Our proposed mechanism for this interaction is illustrated in Fig. 2. The proton on the thiol group is shifted to an amino site. When an incoming hydrogen-bond base (e.g., acetate) is absorbed by the 2-benothiazolethiol monolayer, it will be attracted to the proton on the amine site and will form a hydrogen bond. Donation of hydrogen-bond acidity directly from the thiol group is unlikely, since we did not observe significant affinity for any of the other MPCs.

4. Conclusion

In the present study, we investigated the surface properties of MPCs using QCM experiments and LSER modeling. Although the actual density values of MPCs are not yet available, we have shown that this does not impair the use of LSER modeling. This study also demonstrated how the surface affinity of nanoparticles is altered by the monolayer functional groups. Another noteworthy aspect of this study was the observation and corroboration that all MPCs examined exhibited a tendency to interact with hydrogen-bond acids. Qualitatively, researchers can always predict the surface polarity or the hydrogen bond affinity based on functional group structure and basic knowledge of organic chemistry. However, the LSER coefficients provide quantitative information about the magnitude of the affinity for certain chemical forces. Furthermore, LSER modeling can assist with the understanding of the results of vapor selectivity using a MPC-coated QCM array.

Acknowledgement

The authors thank the National Science Council (NSC) of Taiwan R.O.C. for its funding support of this project under contract number NSC 96-2113-M-003-009-MY2.

References

[1] M. Brust, M. Walker, D. Bethell, D. Schiffrin, R. Whyman, J. Chem. Soc. Chem. Commun. (1994) 801.
[2] M. Brust, D. Bethell, D. Schiffrin, C. Kiely, Adv. Mater. 7 (1995) 795.
[3] W.P. Wuelfing, R.W. Murray, J. Phys. Chem. B 106 (2002) 3139.
[4] M.C. Leopold, R.L. Donkers, D. Georganopoulou, M. Fisher, F.P. Zamborini, R.W. Murray, Faraday Discuss. 125 (2004) 63.
[5] S. Chen, J. Mater. Chem. 17 (2007) 4115.
[6] T.A. Postlethwaite, J.E. Hutchison, K.W. Hathcock, R.W. Murray, Langmuir 11 (1995) 4109.
[7] H. Wohltjen, A.W. Snow, Anal. Chem. 70 (1998) 2856.
[8] A.W. Snow, H. Wohltjen, Chem. Mater. 10 (1998) 947.
[9] Q.Y. Cai, E.T. Zellers, Anal. Chem. 74 (2002) 3533.
[10] W.H. Steinecker, M.P. Rowe, E.T. Zellers, Anal. Chem. 79 (2007) 4977.
[11] M.P. Rowe, W.H. Steinecker, E.T. Zellers, Anal. Chem. 79 (2007) 1164.
[12] L. Wang, X. Shi, N.N. Kariuki, M. Schadt, G.R. Wang, Q. Rendeng, J. Choi, J. Luo, S. Lu, C.-J. Zhong, J. Am. Chem. Soc. 129 (7) (2007) 2161.
[13] L. Han, D.R. Daniel, M.M. Maye, C.-J. Zhong, Anal. Chem. 73 (2001) 4441.
[14] L. Han, X. Shi, W. Wu, F.L. Kirk, J. Luo, L. Wang, D. Mott, L. Cousineau, S.I. Lim, C.-J. Zhong, Sens. Actuators B 106 (2005) 431.
[15] C.-S. Cheng, Y.-Q. Chen, C.-J. Lu, Talanta 73 (2007) 358.
[16] Y.-Q. Chen, C.-J. Lu, Sens. Actuators B 135 (2009) 492.
[17] P.F. Pang, Z.D. Guo, Q.Y. Cai, Talanta 65 (2005) 1343.
[18] H.L. Zhang, S.D. Evans, J.R. Henderson, R.E. Miles, T.H. Shen, Nanotechnology 13 (2002) 439.
[19] C.-Y. Yang, C.-L. Lin, C.-J. Lu, Anal. Chim. Acta 565 (2006) 17.
[20] S.J. Patrash, E.T. Zellers, Anal. Chem. 65 (1993) 2055.
[21] J.W. Grate, S.J. Patrash, M.H. Abraham, Anal. Chem. 67 (1995) 2162.
[22] J.W. Grate, M.H. Abraham, Sens. Actuators B 3 (1991) 85.
[23] M.H. Abraham, Chem. Soc. Rev. 22 (1993) 73.
[24] J.W. Grate, Chem. Rev. 108 (2008) 726.
[25] C.-J. Lu. Ph.D. Thesis, University of Michigan, Ann Arbor (2002).
[26] J.W. Grate, E.T. Zellers, Anal. Chem. 72 (2000) 2861.
[27] A. Hierlemann, E.T. Zellers, A.J. Ricco, Anal. Chem. 73 (2001) 3458.
[28] J.W. Grate, B.M. Wise, Anal. Chem. 73 (2001) 2239.
[29] J.W. Grate, B.M. Wise, M.H. Abraham, Anal. Chem. 71 (1999) 4544.
[30] J.W. Grate, D.A. Nelson, R. Skaggs, Anal. Chem. 75 (2003) 1868.
[31] G. Sauerbrey, Z. Phys. A: Hadrons Nucl. 155 (1959) 206.
[32] M.-M. Yang, X.-H. Bao, W.-X. Li, J. Phys. Chem. C 111 (2007) 7403.
[33] Y. Joseph, B. Guse, A. Yasuda, T. Vossmeyer, Sens. Actuators B 98 (2004) 188.

Talanta 79 (2009) 935–939

Contents lists available at ScienceDirect

Talanta

journal homepage: www.elsevier.com/locate/talanta

In situ PEI and formic acid directed formation of Pt NPs/MWNTs hybrid material with excellent electrocatalytic activity

Jing Li[a,b], Wen Yang[a,b], Hui Zhu[a,b], Xiaolei Wang[a,b], Fan Yang[a], Bailin Zhang[a], Xiurong Yang[a,*]

[a] State Key Laboratory of Electroanalytical Chemistry, Changchun Institute of Applied Chemistry, Chinese Academy of Sciences, Changchun 130022, PR China
[b] Graduate School of the Chinese Academy of Sciences, Beijing 100039, PR China

ARTICLE INFO

Article history:
Received 26 February 2009
Received in revised form 16 May 2009
Accepted 19 May 2009
Available online 27 May 2009

Keywords:
Pt/MWNTs hybrid material
PEI
Formic acid
Electrocatalysis
Oxygen reduction
Dopamine redox

ABSTRACT

A hybrid material based on Pt nanoparticles (Pt NPs) and multi-walled carbon nanotubes (MWNTs) was fabricated with the assistance of PEI and formic acid. The cationic polyelectrolyte PEI not only favored the homogenous dispersion of carbon nanotubes (CNTs) in water, but also provided sites for the adsorption of anionic ions $PtCl_4^{2-}$ on the MWNTs' sidewalls. Deposition of Pt NPs on the MWNTs' sidewalls was realized by in situ chemical reduction of anionic ions $PtCl_4^{2-}$ with formic acid. The hybrid material was characterized with TEM, XRD and XPS. Its excellent electrocatalytic activity towards both oxygen reduction in acid media and dopamine redox was also discussed.

1. Introduction

Due to large surface area, good physical and chemical stability, and high electrical conductivity, carbon nanotubes (CNTs) have attracted considerable attention as the supporting materials of metal nanoparticles in hybrid materials [1]. Over the past years, various noble metal nanoparticles such as Pt, Au, Pd, have been constructed on the CNTs' sidewalls via different methods [1,2]. Pt/CNTs hybrid material possessed exceptional catalytic ability and holded great promise for application in various areas, including fuel cells [3–5], selective hydrogenation [6], and the preparation of pure hydrogen [7].

It was well known that the catalytic activity of Pt/CNTs hybrid material depended on not only the size and uniformity of Pt nanoparticles (Pt NPs), but also their distribution on the CNTs' sidewalls [8]. Therefore, numerous synthetic methods have been explored to fabricate Pt/CNTs hybrid material with high electrocatalytic activity [9–13]. Among these strategies, noncovalent functionalization method [13,14], especially polyethyleneimine (PEI)-assisted method [15,16], gradually became an effective and promising method in fabricating high performance electrocatalyst. PEI, an amino-rich cationic polyelectrolyte, has been known to effectively interact with CNTs via both physisorption and electrostatic adsorption on the CNTs' sidewalls without affecting the electronic network of the CNTs [15]. Based on PEI-assisted method, the decoration of metal nanoparticles on the CNTs' sidewalls could be further achieved by in situ chemical reduction of metal precursors with reductants. Recently, Dong and co-workers [15] presented a facile route to coat CNTs with controllable coverage of Au NPs, in which PEI acted as both a functional agent to ease the CNTs' dispersion and a reductant.

In addition, reductant was also an important factor in the PEI-assisted method to fabricate the Pt/CNTs hybrid material with uniform and well-dispersed Pt NPs. Up to now, various reductants such as hydrogen (H_2) [17], ethylene glycol (EG) [18], sodium borohydride ($NaBH_4$) [19] have been used for preparing Pt NPs. Nowadays, as a moderate reductant, formic acid has aroused great attention because of its controllable reductions and adjustable morphologies for Pt NPs. Recently, Yang et al. [20] and Sun et al. [21] developed template- and surfactant-free routes to fabricate a porous Pt NPs froth and 3D Pt nanoflowers. Moreover, formic acid has been explored to deposit high-density Pt NPs and Pt nanowires on the CNTs [22,23]. However, formic acid, as a reductant, was not used in PEI-assisted methods mentioned above.

With the assistance of PEI and formic acid, here we present a facile and efficient route to in situ decoration of the sidewalls of multi-walled carbon nanotubes (MWNTs) with Pt NPs under mild conditions ($\leq$85 °C). The obtained hybrid materials were characterized with transmission electron microscope (TEM), X-ray diffraction (XRD) and X-ray photoelectron spectroscopy (XPS).

* Corresponding author. Tel.: +86 431 85262056; fax: +86 431 85689278.
E-mail address: xryang@ciac.jl.cn (X. Yang).

0039-9140/$ – see front matter © 2009 Elsevier B.V. All rights reserved.
doi:10.1016/j.talanta.2009.05.029

The electrochemical performance of the as-prepared Pt/MWNTs hybrid material was studied. Moreover, the electrocatalytic activity towards both oxygen reduction in acid media and dopamine redox was also investigated.

2. Experimental

2.1. Reagents and chemicals

Potassium tetrachloroplatinate(II) (K_2PtCl_4) was purchased from Shanghai Jiushan Chemical Co. Ltd. (Shanghai, China). Polyethyleneimine (PEI, Mw. 10,000), was obtained from Alfa Aesar (USA). Multi-walled carbon nanotubes (MWNTs, D = 40–60 nm) were purchased from Shenzhen Nanotech. Port. Co. Ltd. (Shenzhen, China). Commercial catalyst with the Pt-loading of 20 wt.% on the carbon black was obtained from Alfa Aesar (USA). Formic acid (88%), sulfuric acid (98%), nitric acid (65–68%), Na_2HPO_4 and NaH_2PO_4 were purchased from Beijing Beihua Fine Chemicals Co. Ltd. (Beijing, China) and were used without further purification. Nafion (5 wt.% of lower aliphatic alcohols/water mixture) was available from Aldrich (USA). Dopamine was obtained from Fluka (USA).

2.2. Preparation of PEI-modified MWNTs

The preparation of PEI-modified MWNTs (PEI-MWNTs) was performed according to the reported method [14] with a little modification. Firstly, MWNTs were purified by fluxing the as-received MWNTs in 3 M HNO_3 for 48 h. Then, the 30 mg purified MWNTs were dispersed in 200 ml of 1 wt.% aqueous solution of PEI with the help of stirring and sonication. The suspension was stored at 50 °C for more than 24 h. After that, the suspension was filtered via cellulose filter (pore diameter, 0.22 μm). Finally, the product was thoroughly washed with double distilled water to obtain a neutral state and was dried at 60 °C in a vacuum oven.

2.3. Preparation of Pt/MWNTs hybrid material

For the reduction of 62.9 wt.% Pt NPs on the MWNTs, the PEI-MWNTs (6 mg) and K_2PtCl_4 solution (0.1 M, 0.46 ml) were dispersed into 40 ml double distilled water with the help of sonication. After 20 min sonication, the moderate reductant formic acid (4 ml) was added into the solution. To speed the reaction, the above mixture was heated to 80 °C and refluxed for 30 min. Finally, the Pt/MWNTs hybrid material (Pt/MWNT) was separated from solution by centrifugation, washed three times with distilled water, and dried at 60 °C in a vacuum oven. The Pt/MWNTs with different Pt-loadings were prepared through adjusting the mass ratio between PEI-MWNTs and K_2PtCl_4.

2.4. Preparation of Pt/MWNTs hybrid material modified electrode

The glassy carbon electrode (GCE) was carefully polished with 1.0 μm and 0.3 μm alumina slurry successively and then was cleaned with the help of sonication in double distilled water for a few minutes. The as-prepared Pt/MWNT was homogeneously dispersed in double distilled water to a concentration of 2 mg/ml by the sonication. Then, a 10 μl of suspension was dropped on to the clean GCE surface. After the evaporation of water under ambient temperature, a 10 μl of diluted nafion solution (0.05 wt.% in ethanol) was pipetted on to the suspension modified GCE surface and was dried in air. For comparison, commercial catalyst modified electrode and PEI-MWNTs modified electrode were also prepared under the same condition.

2.5. Instrumentations

Transmission electron microscopy (TEM) was carried out with Hitachi Model H-8100 operating at 200 kV accelerating voltage. Sample for TEM was prepared by dropping the as-prepared Pt/MWNT solution onto a carbon film-coated copper grid and allowed to dry at room temperature. X-ray diffraction (XRD) pattern of the sample was recorded on a Rigaku-Dmax 2500 diffractometer equipped with graphite monochromatized Cu Kα (λ = 0.15405 nm) radiation at a scanning speed of 4° min^{-1} in the range from 20° to 90°. X-ray photoelectron spectroscopy (XPS) measurement was carried out with an ESCLAB MK II spectrometer (VG Co., UK) with Mg Kα radiation ($h\gamma$ = 1253.6 eV) as the X-ray source and pass energy of 20 eV. Sample for XPS was deposited onto a piece of silicon wafer and air-dried. A weighted out sample was dissolved in aqua regia overnight [14], and the concentration of Pt ions was characterized by a Thermo Scientific ICAP 6000 inductively coupled plasma-optical emission spectrometer (ICP-OES).

Electrochemical experiments were performed with a CHI 660 electrochemical workstation (Chenhua, Shanghai). A three-electrode system was employed with a glass carbon electrode (3 mm in diameter) as working electrode, a platinum foil as counter electrode and an Ag/AgCl (saturated KCl) electrode as reference electrode. All the potentials in this paper were versus Ag/AgCl electrode.

3. Results and discussion

3.1. Schematic procedure of the preparation of Pt/MWNTs hybrid material

Fig. 1 illustrated the schematic procedure of the preparation of Pt/MWNT, which involved three main steps. Firstly, MWNTs were modified by cationic polyelectrolyte PEI via the electrostatic interaction and physisorption [15]. With the help of PEI, MWNTs can be dispersed in water, and imino-groups can also be introduced onto the MWNTs' sidewalls. Secondly, PEI-modified MWNTs can provide sites for the adsorption of anionic $PtCl_4^{2-}$ via electrostatic attraction. Thirdly, formic acid was selected as a reductant to ease the decoration of Pt NPs on the MWNTs' sidewall uniformly. As a moderate reductant, the following reaction took place slowly at room temperature [21,23], the reaction speed can thus be adjusted substantially.

$$PtCl_4^{2-} + 2HCOOH \rightarrow Pt + 4Cl^- + 2H^+ + 2CO_2$$

To speed the reaction, the reaction mixture was heated to 80 °C and refluxed for 30 min [20,22]. Finally, Pt NPs were directly in situ deposited onto the MWNTs' sidewalls.

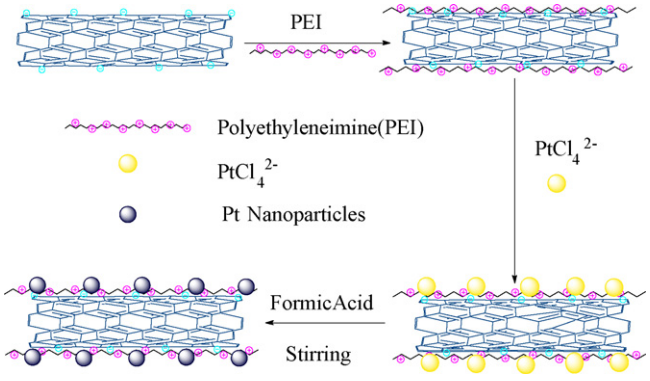

Fig. 1. Schematic procedure of the preparation of the as-prepared Pt/MWNT.

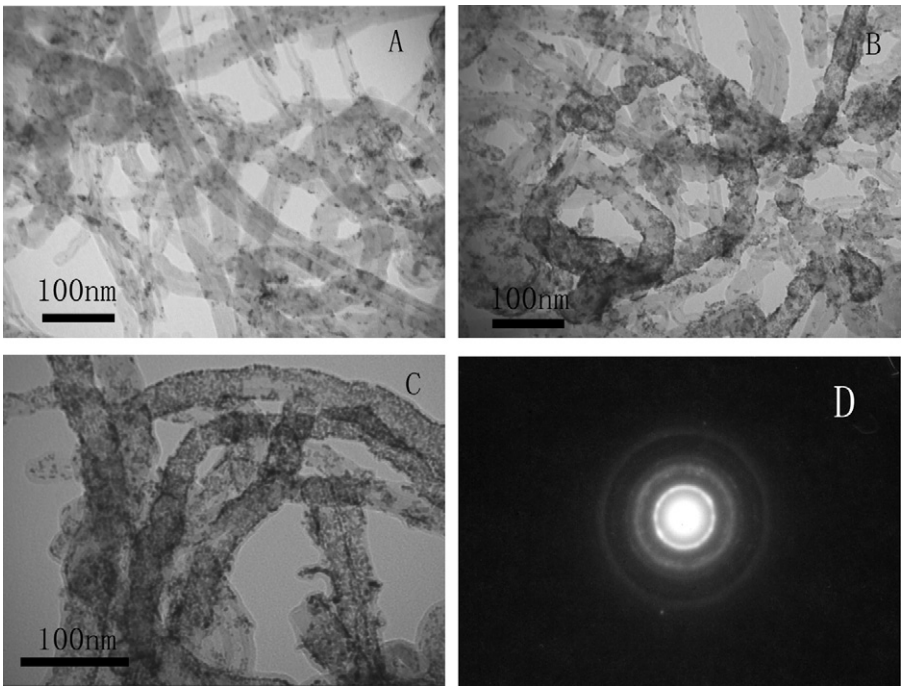

Fig. 2. Typical TEM images of the as-prepared Pt/MWNTs with Pt-loadings of 15 wt.% (A), 41.6 wt.% (B) and 62.9 wt.% (C). (D) The selected area electron diffraction of the as-prepared Pt/MWNT with a Pt-loading of 15 wt.%.

3.2. Characterization of Pt/MWNTs hybrid material

The as-prepared Pt/MWNTs were characterized with TEM (Fig. 2). Fig. 2A depicted the representative TEM image of the as-prepared Pt/MWNT with a Pt-loading of 15 wt.%. Spherical Pt NPs have been successfully adhered to the MWNTs' sidewalls. The density of the decorated Pt NPs positively increased with the Pt-loading amount (Fig. 2A–C). Additionally, it was worth to notice that the size and distribution of the decorated Pt NPs were not influenced significantly by previous Pt-loading amount (Figure S-1). Pt NPs (approx. 3.70 nm in diameter) could be homogenously deposited on the MWNTs' sidewalls without any aggregation in each case. Moreover, all those Pt NPs were preferentially decorated on the MWNTs' sidewalls and were not found at the area without MWNTs. This experiment was repeated on two separate occasions, and similar results were still present (data not shown). Further selected area electron diffraction (SAED) of as-prepared Pt/MWNT with a Pt-loading of 15 wt.% (Fig. 2D) revealed that there were four clear rings, attributed to the diffraction facets of (1 1 1), (2 0 0), (2 2 0), and (3 1 1) crystal planes of face-centered cubic (fcc) Pt [14,21,24]. According to previous report, metal/MWNT hybrid material with high-density metal NPs can be prepared with the assistance of polymer [15,25]. Following the similar protocols, it was also possible to order some optimum hybrid materials with high-density Pt NPs via the presented PEI-assisted method.

To obtain the crystallographic information of the as-prepared Pt/MWNT, XRD measurement was also carried out (Figure S-2). It was observed that the peak near 2θ value of 26° originated from the graphitic carbon of MWNTs [25,26]. The diffraction peaks at 2θ values of 40.1°, 46.4°, 67.8°, 81.8° can be attributed to the (1 1 1), (2 0 0), (2 2 0) and (3 1 1) reflection of the fcc crystal lattice of Pt, consistent with the SAED data. The expanded diffraction peaks revealed that the crystalline phase would be nanosized. The XRD result confirmed

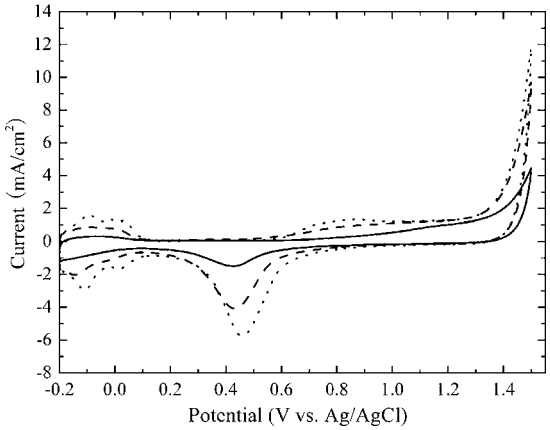

Fig. 3. Cyclic voltammograms of the as-prepared Pt/MWNTs with Pt-loadings of 15 wt.% (solid line), 41.6 wt.% (dash line), 62.9 wt.% (dot line) modified GCEs. Measurements were performed in nitrogen-saturated 0.5 M H_2SO_4 solution. Scan rate: 20 mV/s.

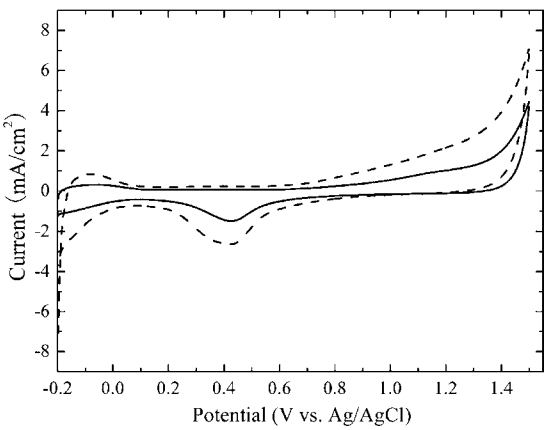

Fig. 4. Typical cyclic voltammograms of the as-prepared Pt/MWNT with a Pt-loading of 15 wt.% (solid line) modified GCEs and commercial catalyst with a Pt-loading of 20 wt.% (dash line) modified GCE. Measurements were performed in nitrogen-saturated 0.5 M H_2SO_4 solution. Scan rate: 20 mV/s.

that Pt NPs with the fcc crystal lattice were successfully deposited on the MWNTs' sidewalls.

In order to analyze the chemical composition of Pt NPs deposited on the MWNTs' sidewalls, XPS experiment was carried out to investigate the surface of sample (Figure S-3). From Figure S-3A, it displayed the XPS spectrum of the Pt_{4f} region. The binding energies of Pt ($4f_{5/2}$) and Pt ($4f_{7/2}$) were 74.4 ± 0.2 eV and 71.1 ± 0.2 eV, respectively. In addition, no obvious shoulder at higher binding energy was found. The XPS spectrum of Pt_{4f} region revealed that the deposited Pt NPs were in a metallic form, instead of ionic forms [21]. Thus, the zero-valence Pt NPs were decorated on the MWNTs' sidewalls [14]. The binding energy of C_{1s} was detected at 284.6 eV (Figure S-3B). The peak at 400.5 eV corresponded to the binding energy of N_{1s} (Figure S-3C), which indicated that PEI successfully modified the MWNTs' sidewalls. All of those XPS results verified that the zero-valence Pt NPs were successfully decorated on the PEI-MWNTs' sidewalls.

3.3. Electrochemical property and electrocatalytic activity of Pt/MWNTs hybrid material

The electrochemical property of the as-prepared Pt/MWNT was investigated. Fig. 3 depicted cyclic voltammograms (CVs) of the as-prepared Pt/MWNTs with Pt-loadings of 15 wt.% (solid line), 41.6 wt.% (dash line) and 62.9 wt.% (dot line) confined onto GCE. Their shapes of CVs, which were similar to the typical CV with pure Pt electrode in H_2SO_4 solution [27], associated with hydrogen adsorption and desorption event in the potential range from −0.2 V to 0.1 V as well as the formation of Pt oxide (more anodic than 0.6 V) and the reduction of Pt oxide (centered at around 0.4 V) [22]. From Fig. 4, it showed CV of the as-prepared Pt/MWNT with a Pt-loading of 15 wt.% (solid line) confined onto GCE, and that of the commercial catalyst (Alfa Aesar) with a Pt-loading of 20 wt.% (dash line) for comparison. According to the formula reported in literature [21,22], the electrochemical surface area (ESA) of the as-prepared Pt/MWNT modified GCE from the hydrogen desorption peak, which was observed in Refs. [14,17], was 38.3 m^2/g and the reduction peak potential of Pt oxide was at about 0.430 V. For comparison, the ESA of Alfa Aesar catalyst modified GCE was 41.0 m^2/g, and the reduction peak potential of Pt oxide was at about 0.425 V. Thus, the utilization of Pt NPs in the as-prepared Pt/MWNT was comparable to that of commercial catalyst.

The electrocatalytic activity of the as-prepared Pt/MWNT towards oxygen reduction was also investigated. Typical CVs towards oxygen reduction obtained at the as-prepared Pt/MWNT with a Pt loading of 15 wt.% modified GCE were shown in Fig. 5. No distinct catalytic reduction peak was observed from 0.6 V to 0 V in nitrogen-saturated H_2SO_4 solution (dot line). In the presence of oxygen, a remarkable catalytic reduction peak current occurred at 0.430 V (solid line) [4,14], which indicated that the as-prepared Pt/MWNT possessed excellent electrocatalytic activity towards oxygen reduction. Additionally, the electrocatalytic activity towards oxygen reduction for different concentrations of oxygen at the as-prepared Pt/MWNT with a Pt loading of 15 wt.% modified GCE was further studied as shown in Figure S-4. With the increase of oxygen concentration, the peak currents for oxygen reduction increased significantly. But the peak potentials for oxygen reduction, centered at around 0.430 V, had no obvious change (curve a–e). These results further proved that the as-prepared Pt/MWNT might be applied potentially in fuel cells and many other electrochemical devices.

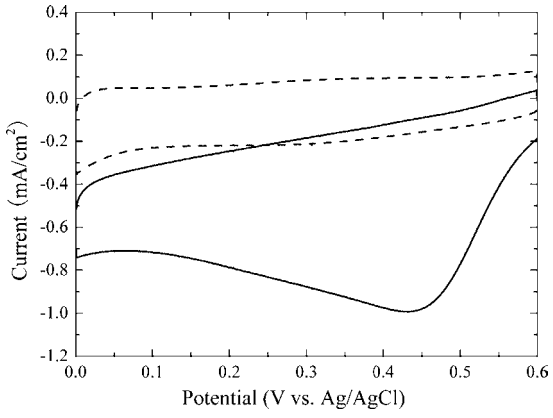

Fig. 5. Typical cyclic voltammograms of oxygen reduction obtained at the as-prepared Pt/MWNT with a Pt-loading of 15 wt.% modified GCE in 0.5 M nitrogen-saturated (dash line) and oxygen-saturated (solid line) H_2SO_4 solution. Scan rate: 20 mV/s.

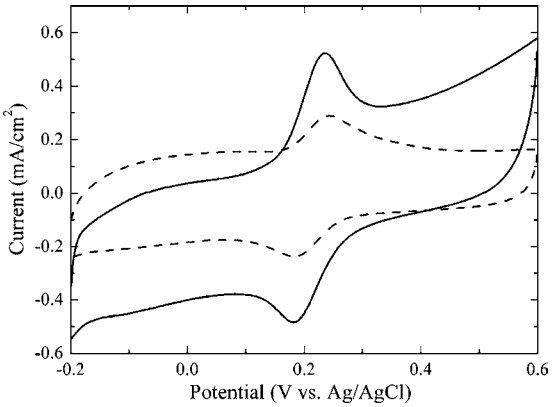

Fig. 6. Typical cyclic voltammograms obtained at the PEI-MWNTs modified GCE (dash line) and the as-prepared Pt/MWNT with a Pt-loading of 15 wt.% modified GCE (solid line) for 0.5 mM dopamine in 0.1 M phosphate buffer solution (pH 7.0). Scan rate: 50 mV/s.

Dopamine, as one of the most important neurotransmitter, played significant role in the functioning of the central nervous, cardiovascular, renal and hormonal systems [28]. Due to the diseases such as schizophrenia, Parkinson's disease caused by the abnormal level of dopamine [29,30], the determination of dopamine has attracted great attention recently. Here, the electrochemical behavior of PEI-MWNTs modified GCE and that of the as-prepared Pt/MWNT with a Pt-loading of 15 wt.% modified GCE to dopamine redox were also studied (Fig. 6). For the PEI-MWNTs modified GCE, dopamine showed a smaller CV peak response with a potential difference of 61 mV (dash line), while for the as-prepared Pt/MWNT modified GCE, the oxidation peak was shifted to more negative potential with a potential difference of 55 mV and threefold enhancement of redox peak currents (solid line). The smaller potential difference and enhanced redox peak currents indicated that the as-prepared Pt/MWNT modified GCE exhibited higher catalytic activity than that of the PEI-MWNTs modified GCE. Therefore, the as-prepared Pt/MWNT exhibited favorable electrocatalytic activity towards dopamine redox, and holded great potential for the electrochemical sensor application.

4. Conclusion

In summary, based on PEI-assisted method, Pt/MWNT has been successfully prepared by in situ chemical reduction of K_2PtCl_4 with formic acid under mild conditions (≤85 °C). The uniform Pt NPs (approx. 3.70 nm in diameter) with face-centered cubic crystal lattice were homogenously deposited onto the MWNTs' sidewalls with controllable coverage, and even the Pt/MWNT with high-density Pt NPs could be obtained. With high EAS, which was comparable to

that of commercial catalyst, the as-prepared Pt/MWNT exhibited excellent electrocatalytic activity towards both oxygen reduction in acid media and dopamine redox. The as-prepared Pt/MWNT might be a promising material for the application in catalyst for fuel cell technology and electrochemical sensor.

Acknowledgements

This work was supported by the National Natural Science Foundation of China (No. 90713022), the National Key Basic Research Development Project of China (No. 2007CB714500) and the Project of Chinese Academy of Sciences (No.KJCX2-YW-H11).

Appendix A. Supplementary data

Supplementary data associated with this article can be found, in the online version, at doi:10.1016/j.talanta.2009.05.029.

References

[1] V. Georgakilas, D. Gournis, V. Tzitzios, L. Pasquato, D.M. Guldie, M. Prato, J. Mater. Chem. 17 (2007) 2679.
[2] G.G. Wildgoose, C.E. Banks, R.G. Compton, Small 2 (2006) 182.
[3] W.Z. Li, C.H. Liang, W.J. Zhou, J.S. Qiu, Z.H. Zhou, G.Q. Sun, Q. Xin, J. Phys. Chem. B 107 (2003) 6292.
[4] Y.H. Lin, X.L. Cui, C. Yen, C.M. Wai, J. Phys. Chem. B 109 (2005) 14410.
[5] Z.H. Wen, Q. Wang, J.H. Li, Adv. Funct. Mater. 18 (2008) 959.
[6] G.Q. Guo, F. Qin, D. Yang, C.C. Wang, H.L. Xu, S. Yang, Chem. Mater. 20 (2008) 2291.
[7] Y.G. Wang, N. Shah, G.P. Huffman, Energy Fuels 18 (2004) 1429.
[8] Z.Q. Tian, S.P. Jiang, Y.M. Liang, P.K. Shen, J. Phys. Chem. B 110 (2006) 5343.
[9] H.C. Choi, M. Shim, S. Bangsaruntip, H.J. Dai, J. Am. Chem. Soc. 124 (2002) 9058.
[10] B.M. Quinn, C. Dekker, S.G. Lemay, J. Am. Chem. Soc. 127 (2005) 6146.
[11] Y.Y. Mu, H.P. Liang, J.S. Hu, L. Jiang, L.J. Wan, J. Phys. Chem. B 109 (2005) 22212.
[12] Y.-T. Kim, K. Ohshima, K. Higashimine, T. Uruga, M. Takata, H. Suematsu, T. Mitani, Angew. Chem. Int. Ed. 45 (2006) 407.
[13] A. Kongkanand, K. Vinodgopal, S. Kuwabata, P.V. Kamat, J. Phys. Chem. B 110 (2006) 16185.
[14] W. Yang, X.L. Wang, F. Yang, C. Yang, X.R. Yang, Adv. Mater. 20 (2008) 2579.
[15] X.G. Hu, T. Wang, X.H. Qu, S.J. Dong, J. Phys. Chem. B 110 (2006) 853.
[16] X.G. Hu, T. Wang, L. Wang, S.J. Guo, S.J. Dong, Langumir 23 (2007) 6352.
[17] M.M. Waje, X. Wang, W.Z. Li, Y.S. Yan, Nanotechnology 16 (2005) S395.
[18] Y.C. Xing, J. Phys. Chem. B 108 (2004) 19255.
[19] H. Lee, S.E. Habas, S. Kweskin, D. Butcher, G.A. Somorjai, P.D. Yang, Angew. Chem. Int. Ed. 45 (2006) 7824.
[20] D.Q. Yang, S.H. Sun, H. Meng, J.-P. Dodelet, E. Sacher, Chem. Mater. 20 (2008) 4677.
[21] S.H. Sun, D.Q. Yang, D. Villers, G.X. Zhang, E. Sacher, J.-P. Dodelet, Adv. Mater. 20 (2008) 571.
[22] D.-Q. Yang, S.H. Sun, J.-P. Dodelet, E. Sacher, J. Phys. Chem. C 112 (2008) 11717.
[23] S.H. Sun, D.Q. Yang, G.X. Zhang, E. Sacher, J.-P. Dodelet, Chem. Mater. 19 (2007) 6376.
[24] L.T. Qu, L.M. Dai, E. Osawa, J. Am. Chem. Soc. 128 (2006) 5523.
[25] K.P. Gong, P. Yu, L. Su, S.X. Xiong, L.Q. Mao, J. Phys. Chem. C 111 (2007) 1882.
[26] Z.Y. Sun, Z.M. Liu, B.X. Han, Y. Wang, J.M. Du, Z.L. Xie, G.J. Han, Adv. Mater. 17 (2005) 928.
[27] A.J. Bard, L.R. Faulkner, Electrochem. Methods, 2nd ed., John Wiley & Sons Inc., New York, 2001, pp. 569–571.
[28] P.E.M. Phillips, G.D. Stuber, M.L.A.V. Heien, R.M. Wightman, R.M. Carell, Nature 422 (2003) 614.
[29] Y.X. Li, X.Q. Lin, Sens. Actuators B: Chem. 115 (2006) 134.
[30] S.R. Ali, Y.F. Ma, R.R. Parajuli, Y. Balogun, W.Y.-C. Lai, H.X. He, Anal. Chem. 79 (2007) 2583.

Talanta 79 (2009) 845–850

Contents lists available at ScienceDirect

Talanta

journal homepage: www.elsevier.com/locate/talanta

Simple and rapid voltammetric determination of morphine at electrochemically pretreated glassy carbon electrodes

Fei Li, Jixia Song, Dongmei Gao, Qixian Zhang, Dongxue Han, Li Niu*

State Key Laboratory of Electroanalytical Chemistry, Changchun Institute of Applied Chemistry, and Graduate University of the Chinese Academy of Sciences, Chinese Academy of Sciences, Changchun 130022, PR China

ARTICLE INFO

Article history:
Received 18 January 2009
Received in revised form 9 May 2009
Accepted 11 May 2009
Available online 20 May 2009

Keywords:
Morphine
Electrochemical pretreatment
Voltammetric detection
Glassy carbon electrode

ABSTRACT

A simple and rapid method for morphine detection has been described based on electrochemical pretreatment of glassy carbon electrode (GCE) which was treated by anodic oxidation at 1.75 V, following potential cycling in the potential range from 0 V to 1.0 V *vs.* Ag|AgCl reference electrode. The sensitivity for morphine detection was improved greatly and the detection limit was 0.2 μM. The reproducibility of the voltammetric measurements was usually less than 3% RSD for six replicate measurements. Moreover, this method could readily discriminate morphine from codeine. And an electrochemical detection of morphine in spiked urine sample was succeeded with satisfactory results.

1. Introduction

Morphine as a major component in opium is frequently used to relieve severe pain in patients, especially those undergoing a surgical procedure. However, it is toxic in excess and when abused. To prevent overdose-induced toxication, it is necessary to sensitively monitor the concentrations of morphine in a patient's blood or urine. Various analytical methods have been developed for the determination of morphine and its major metabolites. The most common analytical techniques currently used include gas chromatography [1,2], high-performance liquid chromatography (HPLC) [3–8] and their combination with other detection methods. Benefited from high efficient separation, they have the advantage of high sensitivity, but suffer from time-consuming and expensive equipment. Use of capillary electrophoresis and microchip capillary electrophoresis [9–11] have partially solved this problem. However, the difficulty in preparing capillary column and its short life restrict its development. Immunoassay, such as surface plasmon resonance (SPR) based immunosensors [12,13] and radioimmunoassay (RIA) [14] are also reported for morphine detection, although they are very sensitive but antibody cross-reactivity may exist. Research in more depth has been devoted to develop a simple, economical, fast and efficient method for detecting morphine.

The electrochemical method is widely used because it is highly sensitive, cheap, simple, easily miniaturized and convenient. The use of bare electrodes such as glassy carbon electrode [15], platinum electrode and graphite electrode [16] are proved to be straightforward and simple on detecting morphine. However, there are a number of limitations, such as slow electron transfer, low sensitivity and electrode contamination, etc. To avoid those shortcomings, combination of HPLC and electrochemical detection has been designed [17]. Recently, some new electrochemical detection methods have been proposed for morphine detection. For example, an adsorptive differential pulse stripping method [18] and its conjugation with least-squares support vector machines [19] have been developed for trace morphine detection. Fast Fourier transformation with continuous cyclic voltammetry at Au microelectrode [20,21] has been devised for morphine detection in a flow injection system. Furthermore, different modified electrodes have been developed for morphine detection. For example, Jin and co-workers prepared a kind of cobalt hexacyanoferrate modified carbon paste electrode, combined it with HPLC and successfully detected morphine *in vivo* [22]. Ho et al. devised a Prussian blue-modified indium tin oxide (ITO) electrode [23] and molecularly imprinted electrodes for morphine determination [24,25]. Multiwalled carbon nanotubes modified preheated glassy carbon electrode has also been used for the morphine detection [26]. Prussian blue film modified-palladized aluminum electrode [27] has recently been used for morphine detection.

It is also well known that electrochemical pretreatment of glassy carbon electrode (PGCE) are usually prepared by potentiostatic polarization at oxidizing potentials or by potential cycling in a wide potential range. The pretreatment introduces oxygen-containing

* Corresponding author. Fax: +86 431 8526 2800.
E-mail address: lniu@ciac.jl.cn (L. Niu).

0039-9140/$ – see front matter © 2009 Elsevier B.V. All rights reserved.
doi:10.1016/j.talanta.2009.05.011

functional groups on the electrode surface. These functional groups exhibit certain interaction, such as electron donor–acceptor, hydrogen bonding, electrostatic, dispersive and solvophobic interactions [28,29], with various species. For example, PGCE has been applied in the preconcentration and electroanalysis of copper [28] and manganese species [30]. A number of organic molecules such as erythromycin [31], vitamin B_2 [29] have also been adsorbed strongly at such activated glassy carbon electrodes. Besides, PGCE has also been used to determine biomolecules, such as DNA [32,33]. However, to our best knowledge, the report concerning the detection of morphine at PGCE is quite few. In this work, it was found that morphine could also be effectively adsorbed and accumulated on the electrochemically pretreated glassy carbon electrode. So a simple, rapid and sensitive voltammetric method for morphine detection was explored. The method could readily discriminate morphine even from coexist codeine. As a potential application, the electrochemical detection of morphine in spiked urine sample was performed too.

2. Experimental

2.1. Reagents

Morphine hydrochloride and codeine phosphate were supplied by the Institute of Forensic Science Ministry of Public Security (China). Unless otherwise stated, other reagents were of analytical grade and used as received. Phosphate buffer solution (0.05 M PBS), which was prepared by mixing different volume of Na_2HPO_4 solution (0.05 M) and KH_2PO_4 solution (0.05 M), was employed as supporting electrolyte. Britton–Robinson (B–R) buffer was prepared by dissolving the same concentrations (0.04 M) of orthophosphoric acid, boric acid and glacial acetic acid in water and adjusting to the desired pH value with sodium hydroxide (0.2 M). All aqueous solutions were prepared with high pure water from a Millipore system (>18 MΩ cm).

2.2. Apparatus

Scanning electron microscopy (SEM) pictures were imaged by an XL30 ESEM FEG field emission scanning electron microscope. X-ray photoelectron spectroscopy (XPS) was conducted with a VG ESCALAB MKII spectrometer (VG Scientific, UK) employing a monochromatic Mg-Kα source ($h\nu$ = 1253.6 eV) and the elemental content ratio was evaluated by using the software installed with the instrument. Cyclic voltammetric (CV) measurements were performed in a conventional three-electrode cell with a platinum wire as the auxiliary electrode and an Ag|AgCl (saturated KCl) as the reference electrode with a CHI 660 Electrochemical Workstation (CHI, USA). The working electrode was bare or pretreated glassy carbon electrode (GCE, d = 3 mm). All potentials reported here refer to the Ag|AgCl (sat. KCl) reference electrode.

2.3. Pretreatment of the glassy carbon electrode

The glassy carbon electrode was polished carefully with 1.0 μm, 0.3 μm, and 0.05 μm alumina slurry to a mirror finish, respectively. And it was cleaned in an ultrasonicating bath for 2 min before use. The general procedure for electrochemical pretreatment of glassy carbon electrode was modified from previously published procedures [32]. The preparation of PGCE was performed by anodic oxidation at 1.75 V for 200 s in 0.05 M PBS at pH 5. The electrode was then cycled between 0 and 1.0 V at a scan rate of 0.1 V/s until a stable current–voltage curve was obtained.

2.4. Procedure for determination of morphine

The electrochemical experiments were performed in 0.05 M PBS (pH 7.4) with different concentrations of morphine. The adsorptive accumulation of morphine at the working electrode was done in a stirred solution at open circuit for 90 s. After a 2 s quiet time, the cyclic voltammograms were recorded from 0 V to 0.7 V at 0.1 V/s. The electrode can be used for next measurement after continuous sweep for four cycles at potential range from 0 V to 1.0 V in 0.05 M PBS (pH 7.4).

2.5. Sample preparation

Urine samples were obtained from healthy laboratory volunteers without any pretreatment, except that they were diluted by 100 times with 0.05 M PBS (pH 7.4). A quantity of the morphine was added to the diluted urine and the resulting drug urine solutions were used for voltammetric analysis. The content of the morphine was determined by the standard addition method [31].

3. Results and discussion

3.1. Morphology and surface composition after pretreatment

Through the electrochemical pretreatment a thin layer was found on the electrode surface, which was in agreement with the previous report [34,35]. This layer is composed of carbon oxidation products of the electrode itself and has been termed electrochemical graphite oxide. The morphology of the glassy carbon electrode before and after the anodic oxidation pretreatment was examined by SEM (data not shown here). Both of them were flat and uniform in the submicrometer scale, indicating that the pretreatment was mild and did not cause significant changes in GCE surface morphology. The surface of the glassy carbon electrode was further examined by XPS measurement. As shown in Fig. 1, the O_{1s} spectra show an increase in amplitude after the pretreatment (dotted), although the peak shape changed little. The major peak in the C_{1s} spectrum (284.6 eV) changed in shape as a result of pretreatment. The width at half-maximum height went from 0.86 eV at the polished electrode (solid) to 1.42 eV at the pretreatment electrode. New C_{1s} peaks were also found at the binding energy centered at ca. 286.9 eV, 288.6 eV, 292.9 eV and 295.8 eV, indicating the presence of different forms of carbon having higher binding energy, such as carbonyl, carboxyl and quinone [36,37]. Calculations indicated that the oxygen-to-carbon ratio of the electrode surface were 0.12 and 0.33 for the freshly polished and pretreated electrode, respectively. The increase in the O/C ratio and the O_{1s} amplitude showed

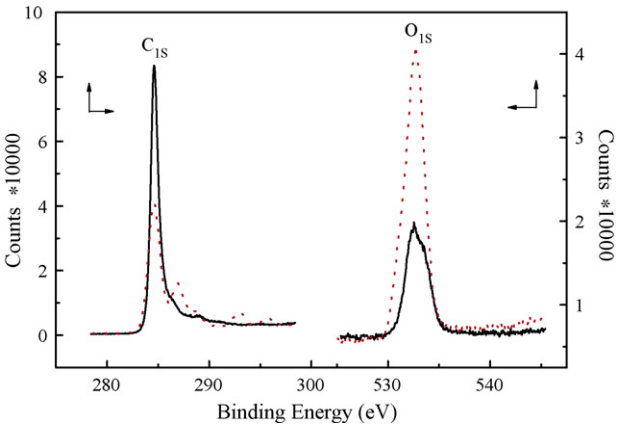

Fig. 1. XPS spectra of freshly polished GCE (solid) and pretreated GCE (dotted).

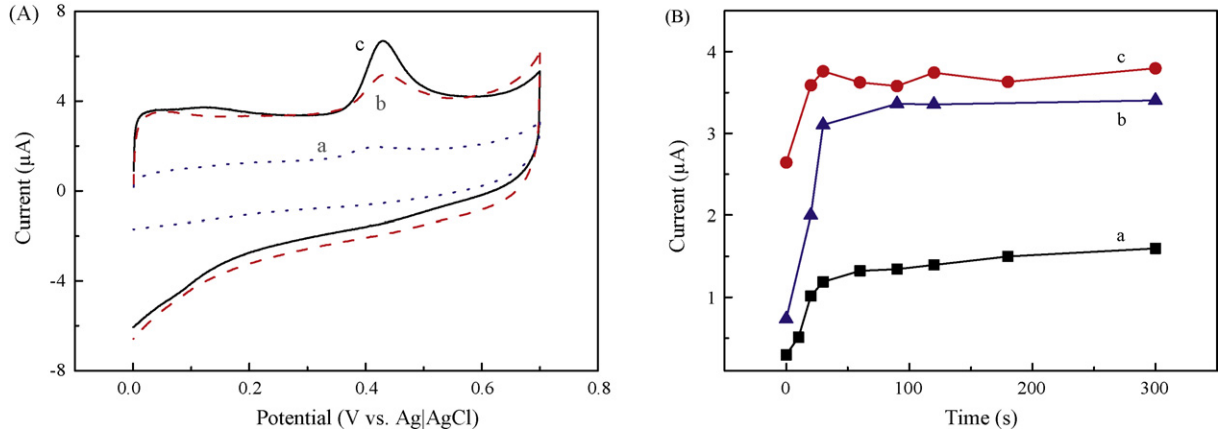

Fig. 2. (A) Cyclic voltammograms of 25 μM morphine in 0.05 M PBS (pH 7.4) (A) at (a) unpretreated GCE (dotted) and (b and c) pretreated GCE without (dash) and with accumulation (solid) at 0.1 V/s. Accumulation was performed in open circuit for 90 s. (B) Influence of accumulation time on the peak current of morphine at different concentrations. (a) 5 μM; (b) 10 μM; (c) 25 μM. Scan rate: 0.1 V/s.

that the surface became oxygenated during pretreatment, which was consistent with previous reports, i.e. oxygen-containing groups could be created on the surface of glassy carbon electrodes through pretreatment [34,36,37]. Thus, the environment of surface carbon became more complicated upon pretreatment [36]. According to previous report [34], the pretreatment of GCE involved the formation of a new phase, which contained a significant amount of microcrystallinity and graphite oxide.

3.2. Voltammetric behaviour of morphine at pretreated glassy electrode

Morphine is a kind of phenolic compounds, which can transfer electrons to electrodes at a certain potential. Fig. 2A shows the cyclic voltammograms of 25 μM morphine at the unpretreated GCE (dotted) and pretreated GCE without (dash) and with accumulation (solid) in 0.05 M PBS (pH 7.4). At this pretreated GCE, the morphine gave a well-defined oxidation peak at ca. 0.43 V. The oxidation reaction of the phenolic group at the 3-position involving one-electron transferring is responsible for the major peak. The oxidation of the phenolic group leads to the formation of pseudomorphine as the main product. The oxidation of morphine can be described by the following mechanism (Scheme 1).

The peak potential of the oxidation of morphine at the pretreated GCE was slightly more negative than that obtained at unpretreated GCE. The peak current of pretreated GCE was higher than that of the unpretreated GCE, although the background current of the pretreated GCE was somewhat higher than the unpretreated GCE. From curve b, it could be seen that morphine was quickly oxidized at the pretreated GCE without accumulation, and the peak current was 4-fold larger than that at the unpretreated GCE. And after a 90 s accumulation (curve c), an approximately twice enhancement of the peak current was observed over that obtained without accumulation. Therefore a considerable enhancement in sensitivity could be obtained by applying adsorption step.

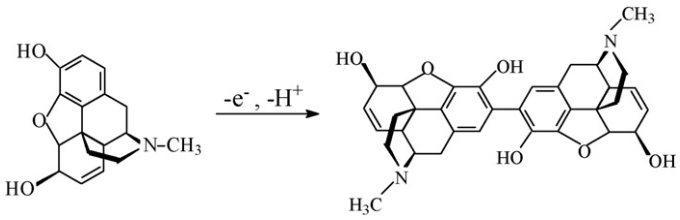

Scheme 1. The reaction scheme of morphine.

Moreover, it was also found that the adsorption efficiency of morphine was affected strikingly by preanodization time, accumulation time and stirring. It is generally accepted that the number of active adsorption sites increases with the preanodization time [28,29]. We have investigated the influence of the activation time. Longer activation time usually resulted in larger number of adsorption sites. However, the thickness of the activated film became larger and the adsorption ability of morphine at the electrode decreased. Meanwhile, thicker film might result in memory effects of the electrode and thus affected the reproducibility too. We found that the adsorptive ability of morphine at the electrode decrease when the time duration for electrode pretreatment exceeds over 200 s (data not shown here). So a preanodization time of 200 s was selected. The influence of accumulation time of morphine at different concentrations (i.e. 2 μM, 10 μM and 25 μM) to the peak current was employed. When the accumulation time was less than 90 s, the peak currents increased with the time, and after that it reached a platform. It indicated that the equilibrium between the concentration of morphine in solution and that on the surface of the electrode occurred at ca. 90 s. Thus, the accumulation of 90 s was selected as the optimum condition at open circuit (Fig. 2B). The peak current obtained under constant stirring also increased with stirring assistance. The results also showed that the peak currents decreased to a constant with succeeding potential scan, as previously reported [33], which was attributed to adsorption of oxidation product at this PGCE. So it is necessary to renew the electrode surface by potential cycling before each measurement.

As shown in Fig. 3, the peak currents (i_p) at the pretreated electrode in 25 μM morphine solution (pH 7.4) varied with change of scan rate (υ). In the range of 10–150 mV/s, the relations obey the following question ($R = 0.9964$, where υ is in mV/s and i_p is in μA),

$$\log i_p = -1.342 + 0.888 \log \upsilon \quad (1)$$

This indicated that the electrode process was controlled simultaneously both by diffusion and adsorption [31].

3.3. Effects of pH

Effect of pH on the peak current and peak potential (as shown in Fig. 4) for the morphine oxidation was also investigated. The peak potential shifted negatively with increase of pH. It could be explained by the consequence of deprotonation involved in the oxidation process which was facilitated at higher pH values [26]. A plot of peak potentials *vs.* pH value was found to be linear over the pH range of 3–9, corresponding to a mechanism involving the same number of electrons and protons (as shown in Fig. 4B). It

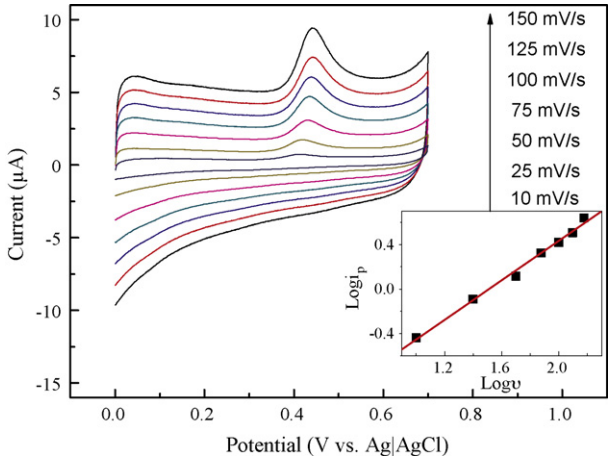

Fig. 3. Cyclic voltammograms of 25 μM morphine in 0.05 M PBS (pH 7.4) at pretreated GCE at various scan rates: 10 mV/s, 25 mV/s, 50 mV/s, 75 mV/s, 100 mV/s, 125 mV/s and 150 mV/s from inner to outer, respectively. Inset is the calibrated plot of $\log i_p$ *vs.* $\log \upsilon$.

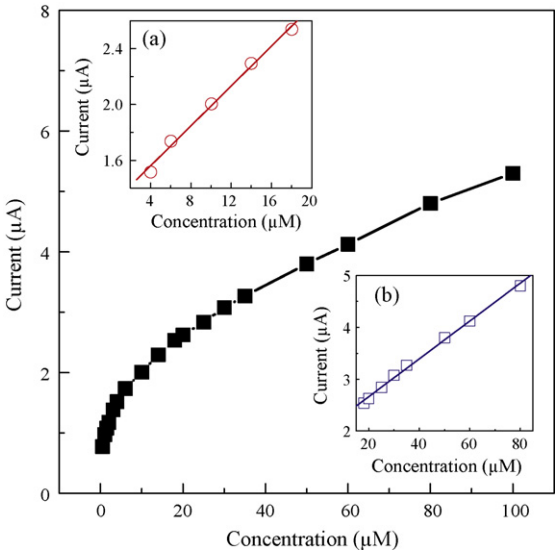

Fig. 5. Calibration curves of current response *vs.* morphine concentration. Inset is the calibration curve corresponding (a) to 4–18 μM morphine and (b) to 18–100 μM morphine. Accumulation was performed in open circuit for 90 s. Scan rate: 0.1 V/s.

was found in Fig. 4A that the current increased with the decrease of the pH. Our results showed that morphine adsorbed readily on pretreatment glassy carbon electrode in acidic medium, while morphine was usually easily adsorbed on bare electrode under alkaline medium. Firstly, this might be related to the differences in the surface properties of the electrodes and the adsorption interactions between morphine and the electrode surfaces. According to previous report [34], the pretreatment of GCE involved the formation of a new phase, which contained a significant amount of microcrystallinity and graphite oxide. This graphite oxide film probably acts as a reservoir for morphine and causes the observed adsorption. But this graphite oxide film would be partially dissolved in alkaline medium [35] and resulted in the decrease of morphine adsorption. Secondly, the variation of electrostatic interaction and hydrogen bonding between morphine and the electrode surface at different pH could also be responsible for this phenomenon. Thirdly, the decrease of the peak current might be resulted from the decomposition of morphine in alkaline medium. Based on above reasons, the current decreased with the increase of the pH.

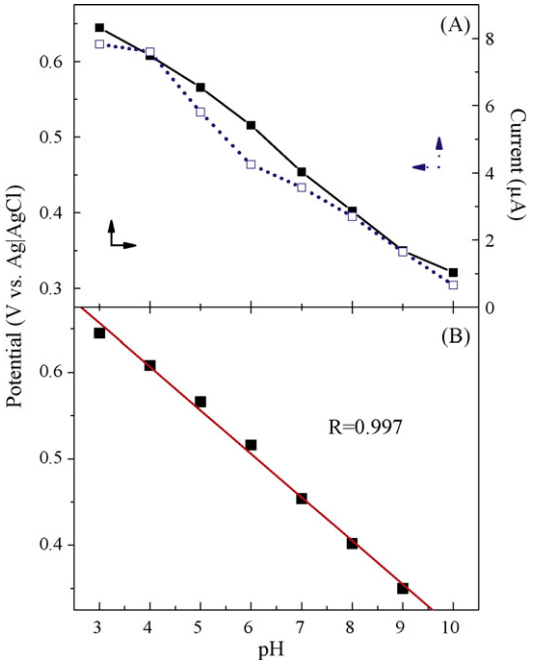

Fig. 4. (A) Influences of pH values on the peak current (□) and peak potential (■) of 25 μM morphine in B–R buffers at 0.1 V/s. (B) Calibration plot of pH *vs.* potential.

3.4. Calibration curve

Fig. 5 displays the calibration curve for morphine determination at PGCE. The peak current increased with the morphine concentration up to 100 μM. There were two linear relations with different slopes in the range of 4–100 μM. In the low concentration, the linear range (4–18 μM) gave a large slope of 0.0715 A L mol^{-1}, and a correlation coefficient of 0.997. When the concentration exceeded 18 μM, it deviated from the linear relationship (4–18 μM) and followed another linear relationship (18–100 μM) which gave a relative small slope of 0.0353 A L mol^{-1} and a correlation coefficient of 0.998. Due to the limited adsorption sites, the saturated coverage of the electrode surface was reached and peak current tended to immovability when the morphine concentration is more than 400 μM. The detection limit was estimated to be ca. 0.2 μM based on the signal corresponding to three times the noise of the response following the accumulation of 90 s. Reproducibility of the PGCE for determination of morphine was also investigated. It was performed in the solution of 10 μM morphine in 0.05 M PBS (pH 7.4). A relative standard deviation of 2.77% was obtained for six replicate measurements.

3.5. Discrimination of morphine from codeine

Voltammetric response at the PGCE in morphine solution containing codeine was also examined further. Codeine, with the methyl ether group (–OCH_3) substituted for the phenolic group (–OH) in the 3-position, is very similar to morphine in structure (as shown in Fig. 6 inset). It usually interferes with morphine analysis in urine or blood. The oxidation peak of codeine was found at 0.96 V (data not shown here) due to the absence of phenolic group at the 3-position. Therefore, the pretreated electrode operating at 0.43 V (as shown in Fig. 2A) can easily discriminate morphine from codeine.

The adsorption of morphine by the PGCE involved interactions between morphine molecules and the activated surfaces. The presence of codeine may affect such detection of morphine due to its

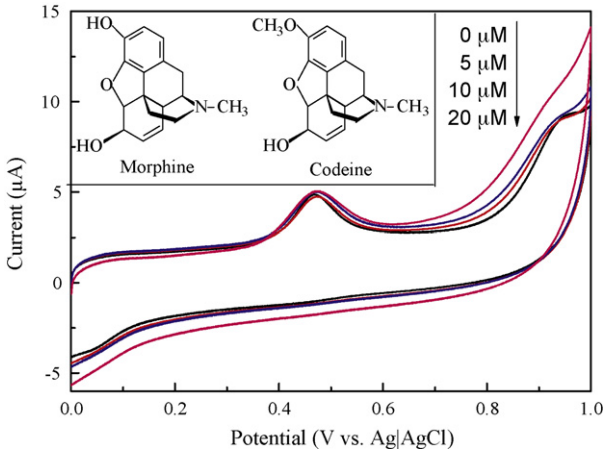

Fig. 6. Cyclic voltammograms of 10 μM morphine in the presence of various concentrations of codeine: 0 μM, 5 μM, 10 μM and 20 μM at the pretreated GCE, respectively. Accumulation was performed in open circuit for 90 s. Scan rate: 0.1 V/s. Inset: the molecular structure of morphine and codeine.

competitive adsorption. The degree of interference was explored at various codeine concentrations. The results, as shown in Fig. 6, exhibited that codeine did not show significant interference while its concentration was lower than 2-fold concentration of morphine. It was well known that it was important criteria for judging recent heroin use while the morphine-to-codeine ratio was higher than 2 [38]. And morphine was the major component in opium poppy. Therefore, the PGCE may be used for the quantitative and qualitative determination of morphine in opium poppy and for judging heroin abusers. When the concentration of codeine was 100 times larger than that of morphine, the PGCE was still available to detect morphine qualitatively.

3.6. Determination of morphine in urine

The proposed method in real sample analysis was also examined in human urine samples. The recovery was evaluated by comparing the analytic signals of morphine obtained from the spiked urine with those of the same concentration standard solution ($n = 5$) (Table 1). The recovery of the spiked samples ranged between 95.1% and 106.6%. The R.S.D. ($n = 5$) was less than 6.0%.

In Table 2, response characteristics of the proposed method are compared with those obtained by some reported methods. In comparison with some other voltammetric methods of morphine determination, our method showed advantages in several aspects. For example, Prussian blue film modified-palladized aluminum electrode [27] has been recently used for morphine detection. Here the PGCE has lower detection limit. Moreover, the preparation process of PGCE was simpler and the reproducibility was also good. Meanwhile, it could be reused through the simple electrochemical treatment and also could be even used in real sample. Niazi et al. [19] reported using of adsorptive differential pulse stripping voltammetric method on a hanging mercury drop electrode for determination of morphine with excellent detection limit (0.01 μM). But the mercury is very poisonous and it was only used

Table 1
Results of determination of morphine in urine sample.

Urine sample	Spike (μmol L^{-1})	Found (μmol L^{-1})	Recovery (%)	R.S.D. (%)[a]
1	5.0	4.76	95.1	3.4
2	10.0	10.65	106.6	4.8
3	15.0	14.62	97.5	5.3

[a] Average of five replicate measurements.

Table 2
Comparison the proposed method with other reported methods.

Detection method	Limit of detection	Sample	Recovery (%)	Reference
Microchip CE[a]	0.2 μmol L^{-1}	Urine	96.2	[11]
LPME[b]–HPLC[c]	0.05 mg L^{-1}	Urine	92.4–106.8	[39]
Amperometry	0.2 mmol L^{-1}	Not applied	–	[24]
Amperometry-MIP[d]	0.3 mmol L^{-1}	Not applied	–	[25]
SIA[e]	0.076 μg mL^{-1}	Urine	96.3	[40]
DPV[f]	0.01 μmol L^{-1}	Plasma	98.5–102.5	[19]
Voltammetry	0.2 μmol L^{-1}	Urine	95.1–106.6	This work

[a] Capillary electrophoresis.
[b] Liquid phase microextraction.
[c] High-performance liquid chromatography.
[d] Molecularly imprinted polymer.
[e] Sequential injection analysis.
[f] Differential pulse voltammetry.

in the pretreated plasma sample. Compared with other methods to determine morphine in urine, such as microchip electrophoresis [11], liquid phase microextraction-HPLC [39] and sequential injection analysis [40], this method had the similar detection limit and the accuracy. At the same time, it also show extra advantages: simple preparation process of PGCE; short time and low cost for the analysis; and no pretreatment needed before the measurement.

4. Conclusion

Voltammetric determination of morphine has been performed at the electrochemically pretreated GCE. The main advantage of the proposed method is simple and fast compared to other determination methods. Furthermore, a low detection limit and a wide range of concentrations are enough for usual analytical purpose. The method has been demonstrated that it easily discriminate morphine from codeine. Moreover, the determination morphine in real human urine without any sample pretreatment has been succeeded with consistent result with those of HPLC and microchip electrophoresis. The proposed method provides the basis for designing portable morphine sensor due to its easy and fast preparation, and low cost.

Acknowledgement

The authors are most grateful to the NSFC, China (No. 20827004) and Ministry of Science and Technology (Nos. 2006BAKB05 and 2007BAK26B06) for their financial support.

References

[1] B. Fryirs, M. Dawson, L.E. Mather, J. Chromatogr. B 693 (1997) 51.
[2] U. Hofmann, S. Seefried, E. Schweizer, T. Ebner, G. Mikus, M. Eichelbaum, J. Chromatogr. B 727 (1999) 81.
[3] P.P. Rop, F. Grimaldi, J. Burle, M.N. Desaintleger, A. Viala, J. Chromatogr. B 661 (1994) 245.
[4] S.R. Edwards, M.T. Smith, J. Chromatogr. B 814 (2005) 241.
[5] M. Mabuchi, S. Takatsuka, M. Matsuoka, K. Tagawa, J. Pharm. Biomed. Anal. 35 (2004) 563.
[6] K.L. Crump, I.M. McIntyre, O.H. Drummer, J. Anal. Toxicol. 18 (1994) 208.
[7] R. Aderjan, S. Hofmann, G. Schmitt, G. Skopp, J. Anal. Toxicol. 19 (1995) 163.
[8] S.O. Mashayekhi, M. Ghandforoush-Sattari, R.D.W. Hain, J. Clin. Pharm. Ther. 33 (2008) 419.
[9] J.Q. Mi, X.X. Zhang, W.B. Chang, J. Immunoass. Immunochem. 25 (2004) 57.
[10] J.L. Tsai, W.S. Wu, H.H. Lee, Electrophoresis 21 (2000) 1580.
[11] Q.L. Zhang, J.J. Xu, X.Y. Li, H.Z. Lian, H.Y. Chen, J. Pharm. Biomed. Anal. 43 (2007) 237.
[12] G. Sakai, K. Ogata, T. Uda, N. Miura, N. Yamazoe, Actuators Sens. B 49 (1998) 5.
[13] N. Miura, K. Ogata, G. Sakai, T. Uda, N. Yamazoe, Chem. Lett. (1997) 713.
[14] D.J. Chapman, S.P. Joel, G.W. Aherne, J. Pharm. Biomed. Anal. 12 (1994) 353.
[15] R.S. Schwartz, C.R. Benjamin, Anal. Chim. Acta 141 (1982) 365.
[16] B. Proksa, L. Molnár, Anal. Chim. Acta 97 (1978) 149.
[17] P.H. Jordan, J.P. Hart, Analyst 116 (1991) 991.
[18] A. Niazi, A. Yazdanipour, Chin. Chem. Lett. 19 (2008) 465.

[19] A. Niazi, J. Ghasemi, M. Zendehdel, Talanta 74 (2007) 247.
[20] P. Norouzi, M.R. Ganjali, A.A. Moosavi-movahedi, B. Larijani, Talanta 73 (2007) 54.
[21] M.R. Ganjali, P. Norouzi, R. Dinarvand, R. Farrokhi, A.A. Moosavi-movahedi, Mater. Sci. Eng. C 28 (2008) 1311.
[22] F. Xu, M.N. Gao, L. Wang, T.S. Zhou, L.T. Jin, J.Y. Jin, Talanta 58 (2002) 427.
[23] K.C. Ho, C.Y. Chen, H.C. Hsu, L.C. Chen, S.C. Shiesh, X.Z. Lin, Biosens. Bioelectron. 20 (2004) 3.
[24] W.M. Yeh, K.C. Ho, Anal. Chim. Acta 542 (2005) 76.
[25] K.C. Ho, W.M. Yeh, T.S. Tung, J.Y. Liao, Anal. Chim. Acta 542 (2005) 90.
[26] A. Salimi, R. Hallaj, G.R. Khayatian, Electroanalysis 17 (2005) 873.
[27] M.H. Pournaghi-Azar, A. Saadatirad, J. Electroanal. Chem. 624 (2008) 293.
[28] K.K. Shiu, K. Shi, Electroanalysis 10 (1998) 959.
[29] K.K. Shiu, K. Shi, Electroanalysis 12 (2000) 134.
[30] J.W. Di, F. Zhang, Talanta 60 (2003) 31.
[31] H.S. Wang, A.M. Zhang, H. Cui, D.J. Liu, R.M. Liu, Microchem. J. 64 (2000) 67.
[32] H.S. Wang, H.X. Ju, H.Y. Chen, Electroanalysis 13 (2001) 1105.
[33] H.S. Wang, H.X. Ju, H.Y. Chen, Anal. Chim. Acta 461 (2002) 243.
[34] L.J. Kepley, A.J. Bard, Anal. Chem. 60 (1988) 1459.
[35] D.M. Anjo, M. Kahr, M.M. Khodabakhsh, S. Nowinski, M. Wanger, Anal. Chem. 61 (1989) 2603.
[36] R.C. Engstrom, V.A. Strasser, Anal. Chem. 56 (1984) 136.
[37] K.M. Sundberg, W.H. Smyrl, J. Electrochem. Soc. 136 (1989) 434.
[38] F. Moriya, K.M. Chan, Y. Hashimoto, Legal Med. 1 (1999) 140.
[39] Z. Zhang, C. Zhang, X. Su, M. Ma, B. Chen, S. Yao, Anal. Chim. Acta 621 (2008) 185.
[40] A.M. Idris, A.O. Alnajjar, Talanta 77 (2008) 522.

Talanta 79 (2009) 590–597

Contents lists available at ScienceDirect

Talanta

journal homepage: www.elsevier.com/locate/talanta

Ionic liquids as mobile phase additives in high-performance liquid chromatography with electrochemical detection: Application to the determination of heterocyclic aromatic amines in meat-based infant foods

Aurora Martín-Calero, Verónica Pino, Juan H. Ayala, Venerando González, Ana M. Afonso*

Department of Analytical Chemistry, Nutrition and Food Science, University of La Laguna, 38205 La Laguna, Spain

ARTICLE INFO

Article history:
Received 11 December 2008
Received in revised form 6 April 2009
Accepted 16 April 2009
Available online 3 May 2009

Keywords:
Heterocyclic aromatic amines
Ionic liquids
High-performance liquid chromatography
Electrochemical detection
Meat-based infant foods

ABSTRACT

The beneficial effects of several ionic liquids (ILs) as mobile phase additives in high-performance liquid chromatography with electrochemical detection for the determination of six heterocyclic aromatic amines (HAs) have been evaluated for first-time. The studied ionic liquids were 1-butyl-3-methylimidazolium tetrafluoroborate (BMIm-BF_4), 1-hexyl-3-methylimidazolium tetrafluoroborate (HMIm-BF_4) and 1-methyl-3-octylimidazolium tetrafluoroborate (MOIm-BF_4). Several chromatographic parameters have been evaluated in the presence or absence of ILs, or using ammonium acetate as the most common mobile phase additive, with three different C18 stationary phases. The effect of the acetonitrile content was also addressed. In general, best resolution, lower peak-widths (up to 72.1% lower) and lower retention factors are obtained when using ILs rather than ammonium acetate as mobile phase additives. The main improvement was obtained in the baseline noise, being 360% less noisy for BMIm-BF_4, 310% for HMIm-BF_4, and 227% for MOIm-BF_4, when compared to ammonium acetate at +1000 mV. Different chromatographic methods using the best conditions for each IL were also evaluated and compared. Finally, the best chromatographic conditions using 1 mM of BMIm-BF_4 as mobile phase additive, the Nova-Pak® C18 column, 19% (v/v) of acetonitrile content in the mobile phase, and +1000 mV in the ECD, have been applied for the chromatographic analysis of six HAs contained in meat-based infant foods. The whole extraction method of meat-based infant foods using focused microwave-assisted extraction and solid-phase extraction has also been optimized. Extraction efficiencies up to 89% and detection limits ranged between 9.30 and 0.165 ng g^{-1} have been obtained under optimized conditions.

1. Introduction

The separation of basic compounds in high-performance liquid chromatography (HPLC) still remains problematic due to the silanol interactions [1,2]. The poor performance seen with basic compounds has been partially addressed through the development and introduction of the so-called base-deactivated materials [3,4]. Nevertheless, addition of alkylamines and other amino quenchers to the mobile phase does not fully remove the deleterious effect of free silanols on the retention of basic analytes, even when employing the purified and least acidic silica supports [5].

A new alternative to reduce or suppress the silanol activity is based on the utilization of ionic liquids (ILs) as additives of the mobile phase [6–13]. ILs are a class of low melting point ionic compounds which have a variety of properties allowing many of them to be sustainable green solvents. ILs possess high thermal stabilities and negligible vapor pressures making them attractive alternatives to environmentally unfriendly solvents that produce volatile organic compounds [14]. They have been used in a number of analytical applications, including some extraction processes [15–19].

ILs evidently lose many of their original properties when they are diluted to act as eluent additives. In some cases, they may keep several of their intermolecular interactions, which may be useful for chromatographic separations [9]. The beneficial effects of ILs in the separation of basic compounds have been described as it follows: ILs cations could interact and compete for the silanol groups with the basic groups of the analytes. In addition, the nonpolar alkyl groups of the stationary phase can interact with different alkyl groups of the heterocyclic ring or quaternary cation of the IL [6]. At the same time, the chaotropic character of the anions constituting ionic liquids is responsible for possible ion-paring with cationic solutes [10]. All these interactions could efficiently shield the residual silanols and improve the peak shapes while reducing the chromatographic retention times of the basic analytes [9].

* Corresponding author. Fax: +34 922318090.
E-mail address: aafonso@ull.es (A.M. Afonso).

0039-9140/$ – see front matter © 2009 Elsevier B.V. All rights reserved.
doi:10.1016/j.talanta.2009.04.032

All the reported applications of ILs as mobile phase additives include HPLC with UV or diode array detection [6–8,10]. To our knowledge, there are not reported studies using HPLC with electrochemical detection (ECD) and ILs. Electrochemical detection of analytes is based on the electrochemical response of the compounds at the operating potential, and it requires the presence of an ionic mobile phase in order to have an adequate electrolyte solution. Therefore, it results necessary to evaluate the effect of the ionic liquids in such ionic mobile phase.

The main aim of this work was to study for first-time the beneficial effect of a group of alkylimidazolium-based ILs as mobile phase additives in HPLC with ECD in the determination of a group of heterocyclic aromatic amines (HAs). HAs are known for their potent mutagenic response and they have also been linked to cancer [20–22]. These basic compounds are usually determined by HPLC using triethylamine (TEA) [23] or ammonium acetate [24,25] as mobile phase additives. Several specific columns have been developed to analyze these amines [26], and in this way, this study includes the effect of ILs in three different C18 stationary phases (with low and moderate silanol activity). Several chromatographic parameters including resolution, efficiency, peak-width, peak-area, peak-height, and retention factor have been evaluated in the presence or absence of ILs. Furthermore, both the influence of the acetonitrile content and the effect of the ILs on the relationship between the applied potential *versus* the obtained intensity of the ECD, have been treated. Finally, an application of the method using the best chromatographic conditions and the most adequate IL (1-butyl-3-methylimidazolium tetrafluoroborate, BMIm-BF_4) has been conducted in meat-based infant foods to determine six HAs. The overall extraction process using focused microwave-assisted extraction and solid-phase extraction in combination with HPLC–ECD has also been optimized. ILs are also proposed for first time as eluting agents in SPE.

2. Experimental

2.1. Reagents

The studied amines were: 3-amino-1-methyl-5*H*-pyrido[4,3-*b*]indole (Trp-P-2), 3-amino-1,4-dimethyl-5*H*-pyrido[4,3-*b*]indole (Trp-P-1), and 2-amino-9*H*-pyrido[2,3-*b*]indole (AαC), purchased from Toronto Research Chemicals (North York, ON, Canada); 2-amino-3-methyl-9*H*-pyrido[2,3-*b*]indole (MeAαC), 9*H*-pyrido[4,3-*b*]indole (NH), and 1-methyl-9*H*-pyrido[4,3-*b*]indole (H), purchased from Aldrich-Chemie (Beerse, Belgium). Stock standard solutions in methanol were prepared containing 92 μg mL^{-1} of H; 520 μg mL^{-1} of NH; 400 μg mL^{-1} of Trp-P-2, Trp-P-1, AαC and MeAαC. These solutions were kept refrigerated at 0 °C and protected from light, and they were used for the preparation of working standard solutions.

The studied ionic liquids were: 1-butyl-3-methylimidazolium tetrafluoroborate (BMIm-BF_4), 1-methyl-3-octylimidazolium tetrafluoroborate (MOIm-BF_4), and 1-hexyl-3-methylimidazolium tetrafluoroborate (HMIm-BF_4), purchased from Fluka (Buchs, Switzerland).

Ethylenediaminetetraacetic acid (EDTA), ammonium acetate and potassium chloride, were of pro-analysis grade quality and supplied by Merck (Darmstadt, Germany). Acetonitrile and methanol were of HPLC-grade supplied by Scharlau (Barcelona, Spain) and Merck, respectively. Water was purified using a Milli-Q gradient A10 system from Millipore (Billerica, MA, USA). All solvents were filtered through a 0.45 μm Durapore® membrane filter (Millipore) before being used in the chromatographic system.

2.2. Instrumentation

Focused microwave-assisted extractions were performed at atmospheric pressure using the Discover model of the CEM Focused Microwave™ Synthesis System (Matthews, NC, USA) equipped with an infrared temperature control system, stirring and cooling options. The ChemDriver™ software (CEM) was used for data acquisition.

C18 cartridges (100 mg) were purchased from Supelco (Bellefonte, PA, USA). The cartridges were conditioned using 5 mL of methanol, followed by 5 mL of water and then 500 μL of ammonium acetate. Elution was accelerated with a Visiprep™ solid-phase extraction vacuum manifold from Supelco.

The HPLC system was a liquid chromatograph consisting of a solvent delivery system ProStar 230 from Varian (Palo Alto, CA, USA) equipped with a Rheodyne valve (Supelco) with a 20 μL injection loop. The detection of HAs was carried out using a ProStar 370 Electrochemical Detector (Varian). It was provided with a working electrode (glassy carbon), a reference electrode (Ag/AgCl, 2 M) and an auxiliary electrode (stainless steel). Three analytical columns were used: a TSK Gel® ODS-80TM column (5 mm, 150 mm × 3.9 mm i.d.) from Tosoh Biosep (Stuttgart, Germany), a Nova-Pak® C18 column (4 mm, 150 mm × 3.9 mm i.d.) from Waters (Milford, MA USA), and a ABZ+ plus column (5 mm, 150 mm × 2.1 mm i.d) from Supelco. All these columns were used in combination with a Pelliguard LC-18 guard column (Supelco). Data were acquired with the Star 5.51 chromatography workstation software (Varian).

2.3. Focused microwave-assisted extraction and solid-phase purification procedures

Meat-based infant foods samples were bought in a local supermarket, and used without being subjected to any further manipulation. The spiking process of infant foods was as it follows: the spiking solution was slowly added to form a dough which was mechanically stirred for several minutes. Afterwards, it was stored in the dark for 24 h. The spiked levels were: 1.45 μg g^{-1} for NH, 0.490 μg g^{-1} for H, 0.443 μg g^{-1} for Trp-P-2, 1.40 μg g^{-1} for Trp-P-1, 1.38 μg g^{-1} for AαC, and 0.583 μg g^{-1} for MeAαC.

The optimum extraction process of the samples was as it follows: a 6 mL aliquot of extractant phase (composed by 20%, v/v of methanol in 0.8 M of NaOH) was added to 1 g of infant food sample (spiked or non-spiked), and placed in a Pyrex® tube of 40 mL. After ensuring that an agitation bar was placed in the tube, the extraction tube was introduced into the microwave cavity. The microwave-assisted extraction step was conducted as described in a previous work [25]. Afterwards, the tube was allowed to cool at room temperature and was placed in a water-ice bath for several minutes. This purification step was required for the extraction of lipids and fats, and it has been described in several works [25,27]. Then, the supernatant was introduced in a tube, and centrifuged during 20 min at 4000 rpm. 4 mL of the centrifuged supernatant were then diluted at 20 mL with ammonium acetate 0.5 M, and subjected to the SPE purification step.

The optimized procedure with the C18 SPE cartridge was as it follows: the diluted phase with ammonium acetate coming from the previous step (20 mL) was then loaded on the C18 (100 mg SPE) cartridge. This SPE cartridge was then washed with 5 mL of Milli-Q water, and eluted with 1 mL of the mixture 10 mM BMIm-BF_4:acetonitrile (1:1). An aliquot of 20 μL of this eluted extract was then directly injected in the HPLC system.

2.4. HPLC–ECD procedure

The working potential of the electrochemical detector was set at +1000 mV. The chromatographic separation of the HAs was car-

ried out under isocratic conditions at a flow rate of 1 mL min^{-1}. The mobile phases were prepared with Milli-Q water and acetonitrile and containing in all cases 2 mM of KCl, as the electrolyte solution for the Ag/AgCl reference electrode of the ECD, and 0.1 mM of EDTA for complexation of possible metal ions present in solution.

Mobile phases with additives include ionic liquids (1, 2, 4, 6, 10 and 12 mM) or ammonium acetate (50 mM). Mobile phases prepared with ILs were adjusted to pH = 3.6 with either 10% (v/v) of hydrochloric acid or 0.01 M of sodium hydroxide. Mobile phases prepared with ammonium acetate were adjusted to pH = 6 using acetic acid. These mobile phases also contain KCl and EDTA, as it was mentioned before. The purpose to compare ammonium acetate at pH 6 and the ILs at pH 3.6 was based in the fact than both kinds of additives must be compared at their optimum separation conditions. 50 mM ammonium acetate at pH = 6 is the most common condition in HPLC–ECD for the determination of amines when using this traditional additive [24]. On the other hand, ILs can be considered similar silanol blockers than TEA, and this additive has been successfully employed at pH 3.6, as it has been shown in several works by our group [28,29].

Mobile phases without additives were also employed for comparative purposes, and were adjusted to pH = 3.6 with either 10% (v/v) of hydrochloric acid or 0.01 M of sodium hydroxide. These mobile phases also contain KCl and EDTA, as it was early mentioned.

The optimum chromatographic conditions employed with the meat-based infant foods were: 1 mM of BMIm-BF_4 as mobile phase additive, the Nova-Pak stationary phase, and a value of 19% (v/v) for the acetonitrile content in the mobile phase. This mobile phase also contains KCl and EDTA, and the pH was 3.6, as it was mentioned before.

3. Results and discussion

3.1. Intensity versus potential in the ECD when using ILs as mobile phase additives

Three different ILs (butyl-, hexyl-, and octyl- methylimidazolium tetrafluoroborate) have been studied and compared with the common mobile phase additive ammonium acetate. The utilization of ILs as mobile phase additives rather than ammonium acetate clearly changes the ionic characteristics of the mobile phase. This aspect must be investigated in conjunction with the ECD used in the determination of HAs. Hence, several studies were conducted to investigate the relationships between the potential applied and the mobile phase background current generated. Eluents (with 18%, v/v of acetonitrile) containing 1 mM of ILs, 50 mM of ammonium acetate, or mobile phases free of additives, were tested. Fig. 1A shows the curves of intensity *versus* potential obtained when varying the applied potential between 0 and +1200 mV. It can be observed that all eluents containing ILs produced similar background currents, lower than 60 nA, within the range 0–800 mV. The background currents increased exponentially when working with potential values higher than +900 mV. At +1000 mV, which is a common working potential of the ECD for HAs [25], mobile phases containing 50 mM of ammonium acetate showed much higher background currents than those containing ILs (around three times higher). In fact, the improvement was 360% for BMIm-BF_4, 310% for HMIm-BF_4, and 227% for MOIm-BF_4, when compared to ammonium acetate at +1000 mV. This decrease in the background current ensured much cleaner baselines and less noise in the chromatograms when using ILs as additives. It should be noted that these studies have been carried out using the same kind of mobile phases (with KCl and EDTA), being the only difference the substitution of ammonium acetate (used at common working concentrations) by ILs. Therefore, the decreasing in the background signal could be only attributed to the beneficial effects of ILs.

The same comparative study between ILs and ammonium acetate was carried out with mobile phases free of acetonitrile (100% of water), and the obtained results were the same: much lower background noise when using ILs. These results also point out the low influence of the organic solvent content of the mobile phase in the intensity *versus* potential plots (Fig. 1B).

3.2. Effect of ILs on several chromatographic parameters

Isocratic elution is usually employed in combination with HPLC–ECD for the determination of HAs [24,30]. All the studies with ILs were carried out using isocratic conditions.

Several chromatographic parameters were studied to establish the influence of the ILs as mobile phase additives, among them, the retention factor, the peak-area, the peak-height, and the peak-width of the HAs studied. Table 1 summarizes some of these chromatographic parameters at a representative concentration for the three ILs (2 mM) in each column studied. The additive ammonium acetate has also been included in the table for comparative purposes.

All the HAs presented a similar trend in their retention factors when increasing the IL concentration in the mobile phase, independently of the kind of IL. In general, an increase in the IL concentration generated a decrease in the retention factors of the HAs. This effect was especially significant when compared to eluents free of additives. Nevertheless, this effect was less important at high IL concentrations, and in fact, the retention factors remained practically constant at IL concentrations higher than 2 mM. The change in the retention factors when using ILs as mobile phase additives was lower when the ABZ+ plus stationary phase was being used. In fact, the retention factors of the HAs practically did not change when varying the IL concentrations for this stationary phase. This

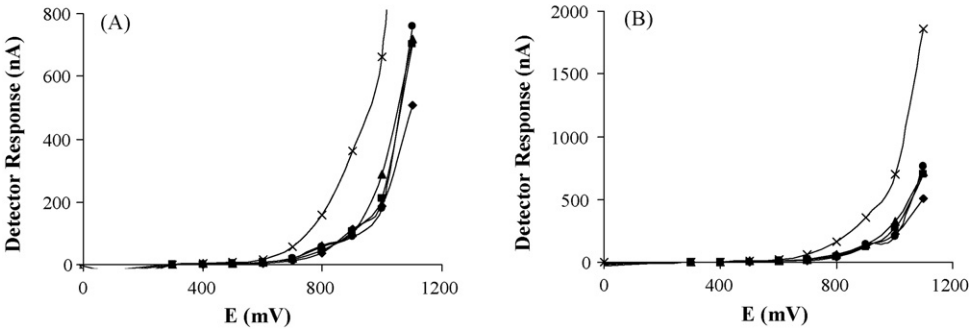

Fig. 1. Potential windows of the ECD when using mobile phases (A) with 18% (v/v) of acetonitrile or (B) free of acetonitrile, composed of (♦) 1 mM BMIm-BF_4, (■) 1 mM HMIm-BF_4, (▲) 1 mM MOIm-BF_4, (×) 50 mM ammonium acetate, and (●) no additives (neither ILs nor ammonium acetate).

Table 1
Effects of ILs at a concentration of 2 mM as mobile phase additives on several chromatographic parameters for the HAs in the three columns.

HA	Additive	Retention factor			Efficiency (N)		
		Nova-Pak	ABZ+	ODS	Nova-Pak	ABZ+	ODS
	$BMIm\text{-}BF_4$						
NH		1.94	0.904	2.28	3,510	2,663	21,202
H		2.40		2.95	13,362		29,364
Trp-P-2		3.88	1.73	4.77	15,265	16,612	31,366
Trp-P-1		5.72	2.63	7.24	17,673	14,246	33,573
AαC		12.8	8.70	15.5	30,445	29,513	39,559
MeAαC		25.0	14.4	30.3	63,658	33,775	45,604
	$HMIm\text{-}BF_4$						
NH		0.937	0.656	1.28	6,481	2,581	14,233
H							
Trp-P-2		1.41	1.24	2.01	25,131	15,434	21,525
Trp-P-1		2.12	1.88	3.15	21,726	12,273	20,257
AαC		12.0	11.8	14.3	53,798	33,932	37,259
MeAαC		23.1	19.6	25.1	90,987	39,611	46,476
	$MOIm\text{-}BF_4$						
NH		0.525	0.786	0.610	2,765	965	8,697
H							
Trp-P-2		0.818		0.885	17,621		15,172
Trp-P-1			1.18	1.20		10,564	19,580
AαC		13.6	14.1	14.6	40,938	43,365	30,822
MeAαC		26.6	22.4	–	79,091	51,743	–
	50 mM ammonium acetate						
NH		4.46	6.27	7.36	27,925	20,329	31,498
H		6.49	8.97	11.3	24,628	17,227	27,464
Trp-P-2		9.18	11.3	17.2	70,834	35,457	76,203
Trp-P-1		14.1	16.1	23.9	86,006	46,484	113,583
AαC		21.3	25.1	32.4	88,074	48,929	137,005
MeAαC		53.6	53.7	–	161,922	62,346	–

HAs concentrations: NH (1.45 μg mL^{-1}), H (0.490 μg mL^{-1}), Trp-P-2 (0.443 μg mL^{-1}), Trp-P-1 (1.40 μg mL^{-1}), AαC (4.92 μg mL^{-1}) and MeAαC (0.583 μg mL^{-1}).

fact is concordant with the characteristics of this stationary phase: high purity silica and low silanol activity.

It should be noted that the retention factors obtained with ammonium acetate as mobile phase additive were much higher than the ones obtained with any IL (Fig. 2) and any stationary phase for all the HAs studied. This noticeable decrease in the retention factors when using ILs as mobile phase additives instead of ammonium acetate must to be highlighted. The addition of ILs improved the retention factor, independently in the pH value, although it is obvious that an increase in the pH produced an enhancement of retention factor, due to a decrease in the amines ionization.

It should also be noted that the lowest retention factors were obtained with the ABZ+ plus stationary phase for all the ILs studied. Fig. 2 shows representative chromatograms obtained when ILs and ammonium acetate were used as eluent additives in the Nova-Pak stationary phase. A chromatogram obtained without any mobile phase additive has also been included. It can also be observed that the retention factors of amines greatly decrease with the increase in the lengths of the alkyl substituent of imidazolium cation from butyl, hexyl to octyl. $BMIm\text{-}BF_4$ ionic liquid provided better resolution for the first four amines (see Fig. 2).

It must be highlighted that the peak-widths observed with ammonium acetate were much higher than those obtained with ILs in all the stationary phases and at any IL concentration. Therefore, ILs improved the peak-shape of the HAs studied. Fig. 3 shows a representative example for Trp-P-1 with the Nova-Pak stationary phase and MeAαC with the ABZ+, with respect to the influence of ILs or ammonium acetate as mobile phase additives in the variation of the peak-width.

In general, and with a few exceptions, the use of ILs as mobile phase additives generated higher peak-areas for NH and H when compared with ammonium acetate. But for the other HAs, similar or lower peak-areas were obtained. All HAs presented the same trend with respect to peak-heights: in general, the highest peak-heights

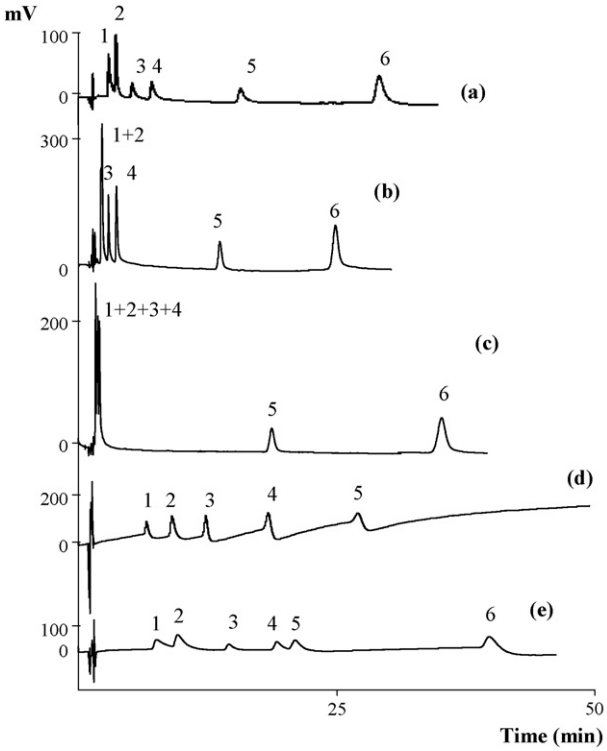

Fig. 2. Chromatograms of all amines in a Nova-Pak stationary phase using (a) 10 mM $BMIm\text{-}BF_4$, (b) 10 mM $HMIm\text{-}BF_4$, (c) 10 mM $MOIm\text{-}BF_4$, (d) 50 mM ammonium acetate, (e) without additives in the mobile phase. HAs and concentrations: (1) NH (1.45 μg mL^{-1}), (2) H (0.490 μg mL^{-1}), (3) Trp-P-2 (0.443 μg mL^{-1}), (4) Trp-P-1 (1.40 μg mL^{-1}), (5) AαC (4.92 μg mL^{-1}), and (6) MeAαC (0.583 μg mL^{-1}). Retention time of MeAαC in (d) is higher than 50 min. The acetonitrile content was 18% (v/v).

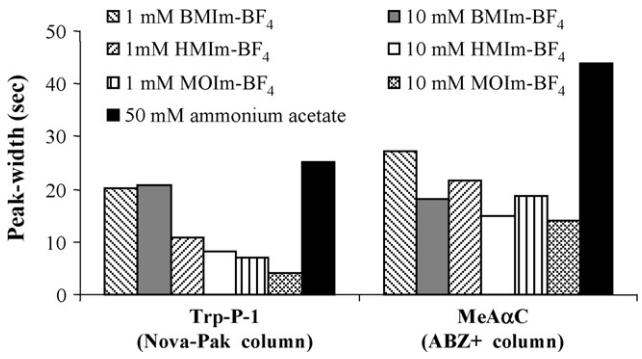

Fig. 3. Influence on the peak-widths of ILs and ammonium acetate for Trp-P-1 in the Nova-Pak column (left) and MeAαC in the ABZ+ column (right). The concentration of HAs is as indicated in Fig. 2.

were obtained with the ABZ+ plus, independently of the additive. For NH and H, the peak-heights observed with ammonium acetate were much lower than those obtained with ILs.

As a general trend, it can be concluded that the increases in the IL concentration caused decreases in both the retention factors and the peak-widths of the studied amines, especially when compared with ammonium acetate. At a representative concentration of IL (1 mM) and with the Nova-Pak column, the decrease in peak-widths ranged from 15.0% (H) to 31.1% (MeAαC) for BMIm-BF_4; from 11.2% (H) to 58.5% (Trp-P-2) for HMIm-BF_4; and from 6.46% (H) to 72.1% (Trp-P-1) for MOIm-BF_4, when compared with the peak-width of these HAs obtained using ammonium acetate as mobile phase additive. The exception was NH, which had the same peak-width with all mobile phase additives. It can clearly be observed in Fig. 2 that the total analysis time was lower when using ILs (at 10 mM concentration in the figure) than with ammonium acetate (50 mM).

Two different effects on the efficiency (calculated as plate number) [31] can be observed depending on the kind of amine. NH, H, Trp-P-1 and Trp-P-2 experimented slight increases in the efficiency when increasing the IL concentration. This effect was more significant at high IL concentrations. Furthermore, the increases were higher for the IL BMIm-BF_4 and for the ODS stationary phase. On the other hand, AαC and MeAαC present no differences in efficiencies among columns, but they presented slight increases in the efficiencies with the IL concentration for all the ILs. If these efficiencies are compared with those obtained with the additive ammonium acetate, several effects can be observed. In general, NH and H presented higher efficiencies with ammonium acetate in all the stationary phases, being the exception H in the stationary phase ODS with the BMIm-BF_4. Trp-P-1 and Trp-P-2 always present higher efficiencies when ammonium acetate was used as mobile phase additive. AαC and MeAαC presented similar efficiencies with ILs and ammonium acetate for all the stationary phases studied at higher concentrations of ILs. Table 1 shows several of these efficiencies obtained for all the HAs at a representative concentration of 2 mM for all the ILs in the three stationary phases studied. Ammonium acetate is also included for comparative purposes. As it can be seen from Table 1, in general, there were not significant improvements in the efficiencies when ILs were used as mobile phase additives.

Consequently, ILs seem to be more favorable than ammonium acetate as mobile phase additives for the chromatographic determination of HAs by HPLC–ECD, decreasing the chromatographic retention time and improving the peak-shapes.

3.3. Influence of the acetonitrile content in the mobile phase when using ILs as additives

The retention data of the studied HAs were examined to elucidate the role of the organic modifier (acetonitrile in our case) in the separation of HAs on the three studied columns when using HPLC–ECD and ILs as mobile phase additives.

To carry out this study, the percentage of acetonitrile was varied from 5 to 50% (v/v) for the studied ILs and columns. The obtained plots of $\log k$ *versus* the percentage of acetonitrile were acceptably linear in the whole studied range ($0.96 < R < 0.99$), following the well-known Soczewinski–Wachmaister's equation [32,33]. Table 2 lists the obtained values for $\log k_w$ (the retention factor of the analyte when the mobile phase is free of acetonitrile), S (the elution strength in aqueous-organic eluents without additives) and R for each amine in the Nova-Pak column, as a representative example, when using mobile phases with or without ILs. ILs concentration was 1 mM in all cases.

As a general trend, the three ILs as mobile phase additives decreased the $\log k_w$ term and increased the S term when compared to mobile phases without additives. These two effects were opposite. At constant S, when $\log k_w$ decreases there will be a decrease in the analyte retention. On the other hand, at constant $\log k_w$, an increase in S will produce an increase in the analyte retention [10]. For each HAs, the calculated $\log k_w$ for each ILs and each column were different from those obtained in absence of IL additives in the mobile phase. These differences in the $\log k_w$ values probably reflect differences in the way that ILs interact with the bonded phases, that is, differences in the solvation of the stationary phases due to the ILs [34]. Another explanation can lie in the presence of selective analyte-IL interactions in the mobile phase. In this case of ILs as mobile phase additives, it seems that both effects: adsorption on the stationary phase, and ion-pairing with the basic analytes, are taking place [10].

All the studied amines showed the expected behavior, the retention factor decreased linearly as the concentration of the organic modifier increased. The six studied amines can be classified in two groups depending on their behavior when comparing among them. One group is constituted by NH, H, Trp-P-2 and Trp-P-1, and the second group by the amines AαC and MeAαC. In the first group of amines it was observed important differences in the $\log k_w$ values for the three ILs and the three columns. In addition, the S values were very similar for each compound with the three ILs when using the Nova-Pak column (see Table 2). This is the reason why there were important differences in the obtained $\log k$ values with this

Table 2
Extrapolated zero organic phase retention factor ($\log k_w$) and elution strength (S) changes induced by BMIm-BF_4, HMIm-BF_4 and MOIm-BF_4 (at a concentration of 1 mM) in a Nova-Pak stationary phase.

HA	Absence of ILs additives			BMIm-BF_4			HMIm-BF_4			MOIm-BF_4		
	$\log k_w$	S	R	$\log k_w$	S	R	$\log k_w$	S	R	$\log k_w$	S	R
NH	1.24	−0.060	0.99	1.38	−0.048	0.98	0.899	−0.042	0.96	0.570	−0.052	0.99
H	1.30	−0.062	0.99	1.48	−0.050	0.97	1.02	−0.046	0.97	0.763	−0.065	0.99
Trp-P-2	1.58	−0.073	0.99	1.77	−0.056	0.97	1.33	−0.052	0.98	1.02	−0.064	0.99
Trp-P-1	1.93	−0.083	0.99	1.76	−0.046	0.97	1.60	−0.057	0.98	1.31	−0.070	0.99
AαC	2.25	−0.051	0.99	2.27	−0.056	0.99	2.10	−0.053	0.98	2.11	−0.064	0.99
MeAαC	2.58	−0.055	0.99	2.04	−0.041	0.99	2.29	−0.051	0.98	2.52	−0.071	0.99

group of amines when using the Nova-Pak stationary phase. However, there were differences in the *S* values when the ABZ+ plus or the ODS stationary phases were used, and therefore the differences in the obtained log *k* values were not so important. In the second group of amines (AαC and MeAαC), it can be observed similar values for log k_w values with the three ILs, as well as similar log *k* values.

3.4. Analytical characteristics of the chromatographic method when using ILs as additives

Once the chromatographic behavior of some HAs by HPLC–ECD was studied in the presence of ILs as mobile phase additives, it resulted interesting to select the best chromatographic conditions for each IL, and then to compare the quality parameters of the chromatographic methods obtained under these optimum conditions. The selection of the optimum chromatographic parameters for each IL was focused in maximizing the chromatographic resolution of the studied amines, considering optimum values when $R_s > 1.5$ [31]. This resolution was especially monitored with H and NH, because the separation of these HAs is in general problematic.

The Nova-Pak column was selected in this comparative study and the selected ionic liquid concentration was 1 mM. In general, the best peak resolution and enhancement were obtained with this column, as well as the adequate retention times and baseline. The ABZ+ plus column gave the lowest retention times; however, the amines H and NH could not be resolved at any IL concentration. The ODS column gave the highest retention times for the three ILs.

The optimal mobile phase composition was selected attending to the results obtained when studying the effect of the acetonitrile content, and intending to improve the peak resolution at different eluent composition. The selected acetonitrile contents were 19% (v/v) for BMIm-BF_4 (R_s value of 3.34 for NH–H), 20% (v/v) for HMIm-BF_4 (R_s value of 1.5 for NH–H), and 15% (v/v) for MOIm-BF_4 (NH and H could not be resolved but the Rs was excellent for the rest of HAs studied).

Table 3 lists the quality parameters of the chromatographic method for the three ILs in the optimal conditions early mentioned. It can be observed that the precision of the proposed chromatographic methods, calculated as relative standard deviations, ranged between 2.2 and 8.3%. In addition, all the calibrations presented good linearity ($R > 0.99$), with the exception of Trp-P-1 when using MOIm-BF_4. Fig. 4 shows some representative chromatograms obtained under the optimal conditions. It should be noted that the total chromatographic time was lower than 40 min in all cases.

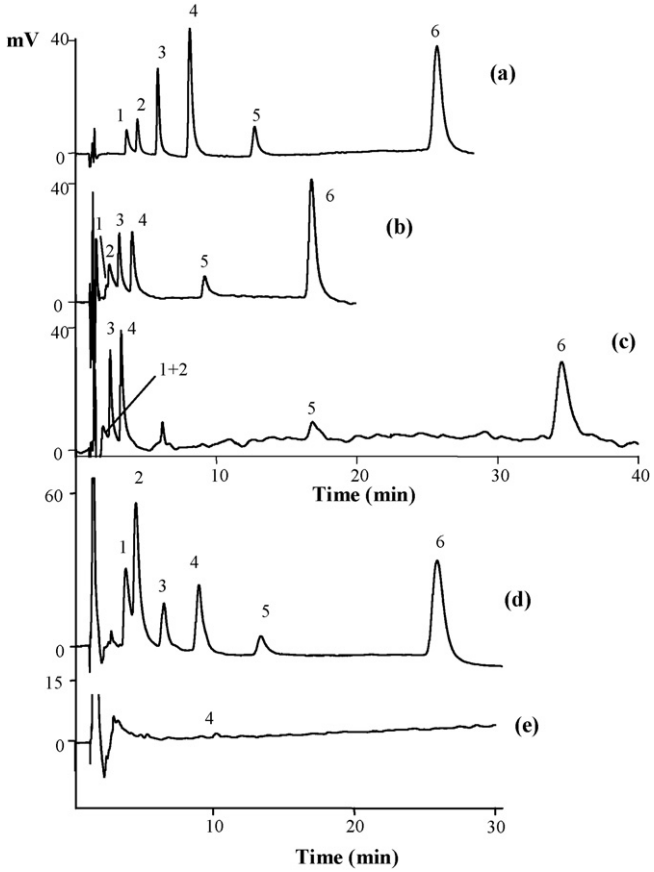

Fig. 4. Chromatograms obtained with the Nova-Pak column under the conditions: (a) 10 mM BMIm-BF_4 and 19% (v/v) of acetonitrile; (b) 10 mM HMIm-BF_4 and 20% (v/v) of acetonitrile; and (c) 10 mM MOIm-BF_4 and 15% (v/v) of acetonitrile, (d) spiked chicken infant food extracted according to the optimal conditions and (e) non-spiked chicken infant food extracted according to the optimal conditions. Concentrations of HAs in (a–c) as indicated in the caption of Table 1. Concentrations of HAs spiked in (d) as indicated in Section 2.

Table 3
Figures of merit of the chromatographic methods obtained for each IL under the optimum conditions: Nova-Pak column and 1 mM of IL concentration in the mobile phase.

HA	IL	Linearity range (μg mL^{-1})	(Slope ± SD) × 10^{-5}	*R*	RSD[a] (%)
	BMIm-BF_4 and 19% (v/v) of acetonitrile				
NH		0.05–2.42	19.8 ± 0.1	0.999	7.0 (1.45)
H		0.02–0.82	69 ± 1	0.998	6.2 (0.49)
Trp-P-2		0.02–0.74	31.4 ± 0.5	0.999	2.6 (0.44)
Trp-P-1		0.05–2.33	19.4 ± 0.5	0.998	6.9 (1.40)
AαC		0.06–3.22	5.0 ± 0.1	0.999	5.8 (1.93)
MeαAC		0.02–0.97	95 ± 1	0.999	2.2 (0.58)
	HMIm-BF_4 and 20% (v/v) of acetonitrile				
NH		0.12–2.42	19.3 ± 0.1	0.986	7.0 (1.45)
H		0.05–0.82	48.0 ± 0.2	0.995	7.0 (0.49)
Trp-P-2		0.04–0.74	185.0 ± 0.4	0.998	7.9 (0.44)
Trp-P-1		0.12–3.22	103.0 ± 0.1	0.999	5.6 (1.40)
AαC		0.16–3.22	27.3 ± 0.2	0.986	8.0 (1.93)
MeαAC		0.05–0.97	723 ± 2	0.998	8.3 (0.58)
	MOIm- BF_4 and 15% (v/v) of acetonitrile				
NH + H		0.16–2.23	1.5 ± 0.1	0.991	8.3 (1.94)
Trp-P-2		0.12–2.33	21.9 ± 0.3	0.999	2.8 (0.44)
Trp-P-1		0.16–3.22	12 ± 2	0.965	8.0 (1.40)
AαC		0.05–0.97	27.1 ± 0.1	0.992	7.6 (1.93)
MeαAC		0.17–3.23	778 ± 1	0.999	7.6 (0.58)

[a] Run-to-run ($n = 5$) on day-to-day ($n = 3$) samples analyzed. Values in parenthesis are the concentration values used (μg mL^{-1}).

An important improvement was obtained in the detection limits. Table 4 lists the detection limits obtained when using the ILs under the optimal conditions. They were calculated as three times the signal to noise ratio. Table 4 also includes a comparison with the LODs obtained in a previous work using HPLC–ECD with ammonium acetate as mobile phase additive [25] and those obtained

Table 4
Detection limits of the chromatographic methods under the optimum conditions.

HA	LOD (ng injected)				
	BMIm-BF_4[a]	HMIm-BF_4[a]	MOIm-BF_4[a]	[25][b]	[30][a]
NH	0.122	0.070	0.580	2.68	0.025
H	0.124	0.019		1.13	0.025
Trp-P-2	0.010	0.058	0.014	0.41	0.005
Trp-P-1	0.026	0.280	0.052	0.16	0.054
AαC	0.026	0.720	0.188	1.62	0.022
MeAαC	0.002	0.190	0.520	2.14	0.033
NH	0.122	0.070	0.580	2.68	0.025

[a] Calculated as three times the signal to noise ratio.
[b] Calculated as described by Cuadros et al. [35].

by other authors [30]. The lowest detection limits were obtained with BMIm-BF_4. LODs were lower when using ILs than when using ammonium acetate and, with some exceptions, were comparable to those obtained by other authors.

As a general trend, ILs as mobile phase additives improved the calibration curves linearity and the detection limits for all the studied amines compared with ammonium acetate [25]. This effect was especially remarkable when using BMIm-BF_4 as additive.

3.5. Optimization of the extraction method and application to meat-based infant foods

The significant performance of ILs as mobile phase additives in HPLC–ECD for several HAs encouraged us to develop an analytical application. The extraction of HAs from food products was usually carried out using a method described by Gross and other authors [24,36,37]. This method is mainly characterized for presenting several SPE steps, due to the complexity of the food matrices. The present application intends to utilize only one SPE step, considering that a focused microwave-assisted extraction step [25] in conjunction with a freezing step is previously conducted [25,27]. Hence, the proposed second clean-up and preconcentration step was a solid-phase extraction procedure.

The percentage of methanol in the extractant phase was optimized in order to ensure a good solubilization of the samples when applying microwaves, altogether with a high retention of amines in the SPE cartridge. A percentage of 20% (v/v) of methanol in the extractant phase (sodium hydroxide) was selected as a compromise solution.

The pH is another important parameter that must be controlled before loading the SPE cartridges. Extractant solutions with sodium hydroxide concentration of 0.05 M are good enough to ensure a good sample solubilization by microwaves [25]. However, such low concentration values do not ensure a good retention of the amines on the SPE cartridges. At the same time, high sodium hydroxide concentrations can plug the cartridges. Some authors have recommend using high pH extractant solutions followed by a dilution of the sample extracts with ammonium acetate to reach a pH value of 8, before loading the SPE cartridges [37]. Therefore, it was decided to use a high hydroxide concentration as extractant solution (0.8 M), and then to dilute the obtained supernatant with ammonium acetate to reach a pH value of 8. In addition, SPE cartridges were previously conditioned with 500 μL of ammonium acetate. A washing step of the loaded samples was also introduced to eliminate sample matrix interferences, ensuring that no losses of HAs were taking place. Consequently, cartridges were washed with 5 mL of Milli-Q water before the sample elution.

A careful selection of the SPE elution solvent was also carried out. Gross and some other authors make use of the mixture methanol:ammonia (9:1) as the elution solvent [36,37]. However, the injection of such mixture generated a noisy baseline in our optimized chromatographic system. Several mixtures BMIm-BF_4:acetonitrile, with IL concentrations ranging from 1 to 25 mM, were tested to ensure both good elution and chromatographic compatibility. The optimum mixture was formed by 10 mM BMIm-BF_4:acetonitrile (1:1), with an optimum elution volume of 1 mL. It should be highlighted that ILs solutions are used, for first time, as eluting agents in SPE.

The whole optimized method was applied to the determination of HAs in two kinds of meat-based infant foods: veal and chicken. It has been described that the macro-constituents of meat samples, mainly the lipids, are responsible of the low extraction efficiencies usually obtained when determining HAs in meat extracts [38]. This problem has relatively been overcome by developing tedious cleaning procedures involving several SPE steps [36,37]. Table 5 shows the obtained extraction efficiencies as well as the method precision when analyzing meat-based infant foods with the proposed extraction method and HPLC–ECD. It should be highlighted that the obtained recoveries were comparable to the ones obtained with similar matrices [36–39]. Furthermore, the proposed extraction method required less clean-up procedures than the ones usually described in the literature, decreasing therefore the overall analytical time. Average recoveries of 69 and 59% were obtained for spiked veal and chicken infant foods, respectively. Higher recoveries were generally obtained with veal infant foods, except for AαC. Lowest recoveries were always obtained with NH in both kinds of samples. The obtained precision, expressed as relative standard deviation, varied from 3.6% for AαC to 20.5% for Trp-P-1 in the veal infant foods; and from 2.5% for H to 12.2% for NH in the chicken infant foods. Fig. 4 shows representative chromatograms of spiked (Fig. 4d) and non-spiked (Fig. 4e) chicken infant food samples subjected to the whole extraction optimized procedure.

Table 5
Extraction efficiency of the proposed extraction method when working with spiked samples.

HA	Recovery ± SD[a] veal infant foods	Recovery ± SD[a] chicken infant foods
NH	48 ± 2	41 ± 5
H	70 ± 3	47 ± 1
Trp-P-2	66 ± 6	61 ± 4
Trp-P-1	79 ± 16	55 ± 4
AαC	69 ± 2	89 ± 7
MeAαC	81 ± 5	60 ± 5

[a] $n = 5$.

The obtained detection limits for the overall method were 9.15 ng g^{-1} for NH, 9.30 ng g^{-1} for H, 0.780 ng g^{-1} for Trp-P-2, 1.95 ng g^{-1} for Trp-P-2, 1.95 ng g^{-1} for AαC, and 0.165 ng g^{-1} for MeAαC. Similar detection limits have been reported for lyophilized meat extract [40] and infant food samples [39]. Trp-P-1 was the only amine detected in the studied infant foods, but it could not be quantified.

4. Conclusions

It has been shown that ILs significantly decrease the retention factors and peak-widths of a group of HAs in HPLC–ECD, especially when compared with the common mobile phase additive ammonium acetate. An important improvement was also observed in the background currents of the ECD, a lower noise about 300% improvement was obtained with ILs. A comparison between the studied C18 stationary phases reflected that ILs produced best improvements in the less modified silica stationary phase with moderate silanol activity.

The significant performance of ILs as mobile phase additives in HPLC–ECD encouraged us to develop an analytical application for the HAs. The chromatographic conditions were optimized to carry out the application with meat-based infant foods. Furthermore, an extraction method based on a focused-microwave-assisted extraction followed by a SPE procedure was completely optimized, with important reductions in the overall extraction time. Finally, both the optimized extraction and chromatographic method were successfully applied to the determination of heterocyclic amines in meat-based infant food samples, with detection limits in the nanogram per gram region.

Acknowledgements

A. Martín-Calero thanks the Consejería de Industria del Gobierno de Canarias for her contract, reference ID-TF-07/074. This work was supported by the project CTQ2007-67084/BQU and CTQ2008-06253/BQU financed by Ministerio de Educación y Ciencia (Spain).

References

[1] L.R. Snyder, J.J. Kirkland, J.L. Glajch, Practical HPLC Method Development, 2nd edn., Wiley, New York, 1997.
[2] S.D. Rogers, J.G. Dorsey, J. Chromatogr. A 892 (2000) 57.
[3] C. Stella, S. Rudaz, J.-Y. Gauvrit, P. Lanteri, A. Huteau, A. Tchapla, J.-L. Veuthy, J. Pharm. Biomed. Anal. 43 (2007) 89.
[4] F. Gritti, C. Perdu, G. Guiochon, J. Chromatogr. A 1180 (2008) 73.
[5] J.J. Gilroy, J.W. Dolan, L.R. Snyder, J. Chromatogr. A 1000 (2003) 757.
[6] L. He, W. Zhang, L. Zhao, X. Liu, S. Jiang, J. Chromatogr. A 1007 (2003) 39.
[7] R. Kaliszan, M.P. Marszall, M.J. Markuszewski, T. Baczek, J. Pernak, J. Chromator. A 1030 (2004) 263.
[8] M.P. Marszall, T. Baczek, R. Kaliszan, J. Sep. Sci. 29 (2006) 1138.
[9] Y. Polyakova, Y.M. Koo, K.H. Row, Biotechnol. Bioprocess. Eng. 11 (2006) 1.
[10] M.J. Ruiz-Ángel, S. Cardá-Broch, A. Berthod, J. Chromatogr. A 1119 (2006) 202.
[11] M.P. Marszall, R. Kaliszan, Crit. Rev. Anal. Chem. 37 (2007) 127.
[12] M.P. Marszall, T. Baczek, R. Kaliszan, Anal. Chim. Acta 547 (2005) 172.
[13] A. Berthod, M.J. Ruiz-Ángel, S. Huget, Anal. Chem. 77 (2005) 4071.
[14] X. Han, D.W. Armstrong, Acc. Chem. Res. 40 (2007) 1079.
[15] J. Liu, G. Jiang, Y. Chi, Y. Cai, Q. Zhou, J.-T. Hu, Anal. Chem. 75 (2003) 5870.
[16] A. Berthod, S. Cardá-Broch, Anal. Bioanal. Chem. 380 (2004) 168.
[17] J.L. Anderson, D.W. Armstrong, Anal. Chem. 77 (2005) 6453.
[18] V. Pino, J.L. Anderson, J.H. Ayala, V. González, A.M. Afonso, J. Chromatogr. A 1182 (2008) 145.
[19] Q. Wang, G.A. Baker, S.N. Baker, L.A. Colón, Analyst 131 (2006) 1000.
[20] M. Nagao, T. Ushijima, N. Watanabe, E. Okochi, M. Ochiai, H. Nakagama, T. Sugimura, Environ. Mol. Mutagen. 39 (2002) 158.
[21] M. Sanz-Alaejos, V. González, A.M. Afonso, Food Addit. Contam. 25 (2008) 2.
[22] R.J. Turesky, Toxicol. Lett. 168 (2007) 219.
[23] M. Sanz-Alaejos, J.H. Ayala, V. González, A.M. Afonso, J. Chromatogr. B 862 (2008) 15.
[24] M.T. Galcerán, P. País, L. Puignou, J. Chromatogr. A 655 (1993) 101.
[25] A. Martín-Calero, V. Pino, J.H. Ayala, V. González, A.M. Afonso, J. Liq. Chromatogr. Relat. Technol. 30 (2007) 27.
[26] E. Barceló-Barrachina, E. Moyano, L. Puignou, M.T. Galcerán, J. Chromatogr. B 802 (2004) 45.
[27] J. Seo, H.-Y. Kim, B.C. Chung, J. Hong, J. Chromatogr. A 1067 (2005) 303.
[28] L. Cárdenes, A. Martín-Calero, J.H. Ayala, V. González, A.M. Afonso, Anal. Lett. 39 (2006) 405.
[29] A. Martín-Calero, J.H. Ayala, V. González, A.M. Afonso, Anal. Chim. Acta 582 (2007) 259.
[30] E. Bermudo, V. Ruiz-Calero, L. Puignou, M.T. Galcerán, Anal. Chim. Acta 536 (2005) 83.
[31] V.R. Meyer (Ed.), Practical High-Performance Liquid Chromatography, John Wiley & Sons, Chichester, England, 1994.
[32] E. Soczewinski, C.A. Wachtmeister, J. Chromatogr. 7 (1962) 311.
[33] J. Flieger, J. Chromatogr. A 1175 (2007) 207.
[34] B.K. Lavine, J.P. Ritter, S. Peterson, J. Chromatogr. A 946 (2002) 83.
[35] L. Cuadros-Rodríguez, A.M. García-Campaña, C. Jiménez-Linares, M. Román-Ceba, Anal. Lett. 26 (1993) 1243.
[36] G.A. Gross, A. Grüter, J. Chromatogr. 592 (1992) 271.
[37] F. Toribio, L. Puignou, M.T. Galcerán, J. Chromatogr. A 836 (1999) 223.
[38] F. Toribio, R. Busquets, L. Puignou, M.T. Galcerán, Food Chem. Toxicol. 45 (2007) 667.
[39] F. Calbiani, M. Careri, L. Elviri, A. Mangia, I. Zagnoni, Food Addit. Contam. 24 (2007) 833.
[40] F. Toribio, E. Moyano, L. Puignou, M.T. Galcerán, J. Chromatogr. A 948 (2002) 267.

Talanta 79 (2009) 752–761

Contents lists available at ScienceDirect

Talanta

journal homepage: www.elsevier.com/locate/talanta

Chromatographic retention prediction and octanol–water partition coefficient determination of monobasic weak acidic compounds in ion-suppression reversed-phase liquid chromatography using acids as ion-suppressors

Xin Ming, Shu-ying Han, Zheng-chun Qi, Dong Sheng, Hong-zhen Lian*

Key Laboratory of Analytical Chemistry for Life Science (Ministry of Education of China), School of Chemistry & Chemical Engineering and Center of Materials Analysis, Nanjing University, 22 Hankou Road, Nanjing 210093, China

ARTICLE INFO

Article history:
Received 11 December 2008
Received in revised form 25 April 2009
Accepted 29 April 2009
Available online 15 May 2009

Keywords:
Reversed-phase liquid chromatography
Retention behavior
Prediction
Ion-suppressor
Octanol–water partition coefficient (K_{ow})
Apparent octanol–water partition coefficient (K''_{ow})
Monocarboxylic acid
Monohydrating phenol

ABSTRACT

Although simple acids, replacing buffers, have been widely applied to suppress the ionization of weakly ionizable acidic analytes in reversed-phase liquid chromatography (RPLC), none of the previously reported works focused on the systematic studies about the retention behavior of the acidic solutes in this ion-suppression RPLC mode. The subject of this paper was therefore to investigate the retention behavior of monobasic weak acidic compounds using acetic, perchloric and phosphoric acids as the ion-suppressors. The apparent octanol–water partition coefficient (K''_{ow}) was proposed to calibrate the octanol–water partition coefficient (K_{ow}) of these weak acidic compounds, which resulted in a better linear correlation with log k_w, the logarithm of the hypothetical retention factor corresponding to neat aqueous fraction of hydroorganic mobile phase. This log K''_{ow} – log k_w linear correlation was successfully validated by the results of monocarboxylic acids and monohydrating phenols, and moreover by the results under diverse experimental conditions for the same solutes. This straightforward relationship not only can be used to effectively predict the retention values of weak acidic solutes combined with Snyder–Soczewinski equation, but also can offer a promising medium for directly measuring K_{ow} data of these compounds via Collander equation. In addition, the influence of the different ion-suppressors on the retention of weak acidic compounds was also compared in this RPLC mode.

1. Introduction

Organic modifiers and water are the most common mobile phase components for reversed-phase liquid chromatography (RPLC). For the RPLC separation of weakly ionizable compounds, conventionally, acids, bases or buffers are added in the aqueous mobile phase according to nature of analytes. The functions of these additives are suppressing dissolution of ionizable solutes, covering active and polar sites of stationary phase surface, and/or buffering mobile phase to adjust chromatographic retention on lipophilic stationary phase, to amend peak shape, and to improve resolution of ionizable solutes [1–4].

Actually, most environmental and biomedical molecules are ionizable more or less. The theories and practices on separation of weakly ionizable solutes in RPLC using buffers as ion-suppressors have been extensively studied. However, most buffers used as ion-suppressors in RPLC are prone to isolating from mobile phase and clogging in the connecting tube of chromatographic instrumentation, especially micro- or nano-scale LC tubing, owing to the low solubility in organic modifiers such as methanol and acetonitrile, and therefore a time-consuming redevelopment of the separation is often required. On the other hand, liquid chromatography–mass spectrometry (LC–MS) has become a popular technique that can provide excellent specificity instead of LC with UV–vis detection. At the same time, many buffer constituents such as metal salts and phosphates are nonvolatile, causing fouling and subsequent failure of ionization sources [2,5,6]. The incompatibility of many buffers with mass spectrometry limits their applicability in LC–MS. Then postcolumn removal of nonvolatile buffer components has been developed recently in hybrid LC–MS for separation and analysis of weakly ionizable compounds [2]. Though this technique is a potential solution, the more convenient practice is still to substitute simple acids or bases as mobile phase additives for nonvolatile buffers. The primary purpose of this paper is to investigate the RPLC retention behavior of weakly ionizable monobasic acidic compounds using acetic, perchloric and phosphoric acids as ion-suppressors.

It is well known that retention prediction before experimental separation is a subject of fundamental studies to allow fast optimization of chromatographic conditions, to improve peak

* Corresponding author. Tel.: +86 25 83686075; fax: +86 25 83325180.
E-mail address: hzlian@nju.edu.cn (H.-z. Lian).

0039-9140/$ – see front matter © 2009 Elsevier B.V. All rights reserved.
doi:10.1016/j.talanta.2009.04.069

resolution and to decrease analysis time. There are some useful systematic approaches to aid selectivity optimization, such as chemometrics, computer-assisted optimization, and quantitative structure–retention relationships (QSRR). Among these above-mentioned methods, however, only QSRR relates chromatographic retention to molecular structure of solutes [7,8].

Nowadays, the influence of chromatographic variables such as mobile phase type and composition on the retention of neutral molecules has been well understood [9,10]. For weakly ionizable compounds, there have been some reports describing their RPLC retention behaviors [11–13]. Roses and Bosch's group has systematically and deeply studied the retention of weakly ionizable compounds on RPLC which was summarized in a review [14]. Recently, they deduced a general equation for prediction of the retention of weak acids and bases as a function of mobile phase pH and column temperature based on buffer solutions and organic modifiers as the eluents [15]. They also established a model that relates the chromatographic hydrophobicity index (CHI) of ionzable solutes to mobile phase pH as well [16]. However, all of above scientists paid their primary attention on buffers as ion-suppressors. This is mainly because the study about buffer solutions was thought easy to perform due to the constant pH and ion strength during chromatographic process. Another probable reason is that there were not contemporary stationary phases capable of enduring extremely acidic or alkaline mobile phases. On the other hand, these retention prediction models generally include sets of rigorous equations, respectively, composed of odd parameters that are often difficult to obtain, having the prediction a little bit discommodious and therefore unpractical.

The octanol–water partition coefficient (K_{ow} or P_{ow}) expressing compound hydrophobicity has been widely accepted as providing a good indication of the distribution of analytes into biological membranes. This has made it one of the most commonly reported physical properties of drugs, pesticides and other chemicals [17,18]. To measure K_{ow} by RPLC, in the past, there was significant interest in correlating the logarithm of K_{ow} with the logarithm of retention factor k of the solute under a specific chromatographic condition [19–21]. As many commercial software products can be employed to compute the K_{ow} value with acceptable accuracy, the linear relationship between log K_{ow} and log k has become useful for the prediction of RPLC retention [22]. It was further suggested that log k_w, the logarithm of the retention factor obtained by extrapolating to neat aqueous fraction of binary mobile phase, gives a more accurate correlation with log K_{ow} [23]. However, in general ion-suppression RPLC mode with pure acids as the additives, eluents were not acidic enough to absolutely suppress the ionization of the analytes for protecting stationary phase in practical operation. Actually, k reflected the average behavior of all existing species of a solute including the molecule and its ions [11]. Thus, it is inappropriate to ignore the hydrophobicity difference between the molecule and its ions [24]. The K_{ow} value of a solute, only revealing the lipophilicity of the unionized species, lost their predictive capability for explaining the chromatographic behavior of ionizable ones. In our previous paper [25], apparent octanol–water partition distribution coefficient (K''_{ow}) reduced from experimental octanol–water partition coefficient (K'_{ow}, that is, octanol–water distribution coefficient D_{ow}) [24] was put forward to calibrate K_{ow} values of weakly ionizable solutes, and the introduction of K''_{ow} was primarily considered to cause a better correlation with log k_w than K_{ow}.

In this paper, an in-depth experimental study was made in order to investigate retention behavior of weakly ionizable monobasic acidic compounds using monocarboxylic acids (derivatives of benzoic acid) and monohydrating phenols (derivatives of phenol) as the model compounds in RPLC employing acetic, perchloric and phosphoric acids as ion-suppressors, respectively. The K_{ow} of these weakly ionizable monobasic acidic compounds was calibrated to corresponding K''_{ow} to obtain good linear relationship between log K''_{ow} and log k_w. This correlation was further validated by the experiments under different column parameters in different HPLC instrumentation. This log K''_{ow} – log k_w linear relationship can be applied to immediately predict the retention behavior of weakly ionizable acidic solutes combined with Snyder–Soczewinski equation in this ion-suppression RPLC with simple acids as the additives. This correlation also offered a reliable protocol for verifying the K_{ow} values reported or software-computed, and even for forecasting unknown K_{ow} values for weak acidic compounds.

2. Theory

In liquid chromatography, general Snyder–Soczewinski equation relating k to volume fraction of organic modifier in binary aqueous mobile phase, C_B, has the form [9]:

$$\log\ k = \log\ k_w - SC_B \tag{1}$$

where S, the regression coefficient of C_B, is a constant for a given solute–eluent combination.

The linear relationship between log K_{ow} and log k_w, known as Collander equation, has been illustrated experimentally and theoretically [19]

$$\log\ K_{ow} = m\ \log\ k_w + n \tag{2}$$

This correlation concerned by most works was limited to neutral solutes when the mobile phase was usually near neutral [10,21,26]. In that situation, the k_w value was certainly the retention factor of neutral species of the analyte. It was reasonable to compare log k_w with log K_{ow} for unionizable solutes, but not just so for the substituted benzoic acids and phenols studied in this ion-suppression RPLC.

On one hand, K_{ow} or P_{ow} of a solute employed in most studies refers to hydrophobicity of the neutral form of the solute, which is completely different from that of its ionic forms ($K_{ow}{}^{+\,or\,-}$ values) [27]. The hydrophobicity of the tested weakly acidic compound should be expressed by K''_{ow} (or D_{ow}) [24] that takes into account the amount of compound in its molecular and ionic states combining K_{ow} and $K_{ow}{}^{+\,or\,-}$ values. The K''_{ow} of a monobasic acidic solute is described by

$$K'_{ow} = \frac{[\mathrm{HA}]_o + [\mathrm{A}^-]_o}{[\mathrm{HA}]_w + [\mathrm{A}^-]_w} \tag{3}$$

The subscripts o and w refer to the octanol (or oil) and the aqueous phase, respectively. Using the expression of dissociation constant K_a, the K''_{ow} can be trivially formulated as

$$K'_{ow} = \frac{K_{ow} + K^-_{ow}(K_a/[\mathrm{H}^+])}{1 + (K_a/[\mathrm{H}^+])} \tag{4}$$

in which, K^-_{ow} is octanol–water partition coefficient of the A^- anionic form. Usually K^-_{ow} is thought to be very small when compared to K_{ow} of its neutral form. The approximation of K'_{ow} was expressed by K''_{ow} [25].

$$K''_{ow} = \frac{[\mathrm{HA}]_o}{[\mathrm{HA}]_w + [\mathrm{A}^-]_w} = \frac{K_{ow}}{1 + K_a/[\mathrm{H}^+]} \tag{5}$$

On the other hand, the k of an acidic solute at a certain mobile phase pH was given as a weighted average of the retention factors of all neutral and ionic species of the solute [11]. Although it has been reported that when the pH of mobile phase was adjusted to 3 pH units lower than pK_a of the solute [26], the neutral species of an acidic solute played dominant role of the weighted average of k and the contribution of all ionic species to overall retention of the solute could be neglected, the actual pH value of the mobile phase could

not be too low in order to protect the stationary phase. Therefore, for a tested acidic compound, k had the form as follows:

$$k = k_0 x_0 + k_1 x_1 \quad (6)$$

where k_0 and k_1 are retention factors of undissociated and dissociated acids or phenols, respectively, and x_0 and x_1 are the mole fractions of the corresponding species.

Thus, K''_{ow} involving the contribution of all ionic species to the total hydrophobicity of the analyte should linearly correlate with k_w theoretically in this RPLC mode based on Eq. (2) for neutral solutes. And it is obvious that the use of K''_{ow} should produce a better correlation with k_w, compared with the relationship between K_{ow} and k_w.

3. Experimental

3.1. Apparatus

The HPLC system used was a Varian 5060 liquid chromatograph (Walnut Creek, CA, USA), a Rheodyne 7725i injector valve equipped with a 10-μL loop (Cotati, CA, USA), and a Waters 486 tunable UV absorbance detector (Milford, MA, USA). Data acquisition and processing were performed on a JS-3050 chromatographic working station (Johnsson Separation Science and Technology Corporation, Dalian, China). All validation experiments were carried out on a Waters Alliance 2695 Separations Module equipped with a vacuum degasser, a quaternary pump and an auto-sampler, and a 996 UV–vis photodiode-array detector (PDA) (Waters). The separation was controlled and the chromatograms were recorded by a Waters Empower chromatography manager system. All experimental retention times (t_R) were the average of at least twice injection determination at 1.0 mL/min mobile phase flow rate with the injection volume of 10 μL, and the detection wavelength was set at 254 nm. The column temperature was maintained at 30 °C, except in the column temperature validation experiment controlled at 40 °C.

The pH values of mobile phases were measured with SevenMulti electrochemical analytical meter (Metter-Toledo Instruments Co., Ltd., Schwerzenbach, CH). The pH measurements were calibrated with usual aqueous standard reference buffers (pH 4.01 and 7.00 at 25 °C), and adopted in $^{W}_{W}$pH scale, i.e. the pH of aqueous fraction before mixing with organic modifiers [14].

The experiments were mainly carried out on Kromasil C_{18} column (150 mm × 4.6 mm ID, Hanbon Sci. & Tech. Co. Ltd., Huai'an, China). Gemini C_{18} columns (150 mm × 4.6 mm ID and 250 mm × 4.6 mm ID) used for validation experiments were purchased from Phenomenex (Torrance, CA, USA). The particle size of all above columns was 5 μm. In addition, Kromasil C_{18} column (150 mm × 4.6 mm ID, Hanbon) with particle size of 7 μm was used for validation experiment.

3.2. Chemicals and reagents

Water was Robust pure water (Guangdong Robust Food and Beverage Co. Ltd., Guangzhou, China). HPLC-grade methanol and acetonitrile were purchased from Hanbon and Caledon Laboratories Co. Ltd. (Georgetown, ON, Canada), respectively. Acetic acid was of analytical-reagent grade (Sinopharm Group Chemical Reagent Co., Ltd., Shanghai, China). Perchloric acid (70–72%) was of guaranteed reagent (Tianjin Third Reagent Factory, Tianjin, China). Phosphoric acid (85%) was of analytical-reagent grade (Nanjing Chemical Reagent Co., Ltd., Nanjing, China). Table 1 lists the known log K_{ow} values determined by the shake-flask method [28] and pK_a of the model compounds to be investigated. The K_{ow} values by classical shake-flask method were adopted in order to assure the accuracy of experimental results. 2,4,6-Trinitrophenol, which determined log K_{ow} value by shake-flask method was available, was used but not included in Table 1. In addition, 2,4-dichlorobenzoic, 2-nitrobenzoic and 4-ethylbenzoic acids, only whose calculated log K_{ow} values were adopted because the determined log K_{ow} values by shake-flask method were unavailable at the time of investigation, were used for correctness inspection of the retention prediction and log K_{ow} checkout. All these derivatives of benzoic acid and phenol with the purity of 98% or greater were obtained from Aldrich (Milwaukee, WI, USA), E. Merck (Rahway, NJ, USA), Shanghai First Reagent Factory (Shanghai, China), Tianjin Second Reagent Factory (Tianjin, China), Nanjing Chemical Reagent Factory (Nanjing, China), Taixing Seventh Chemical Factory (Taizhou, China) and/or Shengming Fine Chemicals Co. Ltd. (Yangzhou, China). Their purities were checked by HPLC and then used without further purification. Stock solutions of each test compounds (ca. 1.0 mg/mL) were prepared in methanol and stored in refrigerator before injection.

3.3. Procedure

3.3.1. Acquisition of log k_w

Each benzoic acid derivative was eluted on Kromasil C_{18} (5 μm, 150 mm × 4.6 mm ID) column by the mobile phase composed of methanol and aqueous acid (acetic, perchloric or phosphoric acid) solution with different $^{W}_{W}$pH. The volume fraction of methanol in the binary mobile phase was run in the range of 0.8 and 0.1, and all compounds were analyzed under at least four different methanol–aqueous acid solution ratios. Then t_R for all the compounds were recorded at each ratio of methanol–aqueous acid solution along with the dead time t_0 of the chromatographic system. The t_0 for calculating the retention factor via $k = (t_R - t_0)/t_0$ was determined by using $NaNO_3$ as the unretained solute. Because k_w values of the solutes are usually too high to obtain by experi-

Table 1
log K_{ow} and pK_a values of monocarboxylic acids and monohydrating phenols studied as model compounds.

Compounds	log K_{ow}[a]	pK_a[b]	Compounds	log K_{ow}[a]	pK_a[b]
Benzoic acid	1.87[a1]	4.21[b1]	3-Cyanophenol	1.70[c1]	8.61[d1]
2-Methylbenzoic acid	2.18[a2]	3.98[b2]	3-Nitrophenol	2.00[c2]	8.36[d2]
3-Methylbenzoic acid	2.37[a3]	4.25[b3]	2-Nitrophenol	1.73[c3]	7.23[d3]
4-Methylbenzoic acid	2.36[a4]	4.37[b4]	2,4-Dimethylphenol	2.54[c4]	10.58[d4]
2-Chlorobenzoic acid	1.98[a5]	2.90[b5]	2,4-Dinitrophenol	1.54[c5]	4.00[d5]
3-Chlorobenzoic acid	2.68[a6]	3.84[b6]	4-Nitrosophenol	1.29[c6]	6.48[d6]
4-Chlorobenzoic acid	2.65[a7]	3.99[b7]	2,5-Dimethylphenol	2.33[c7]	10.41[d7]
3-Nitrobenzoic acid	1.83[a8]	3.46[b8]	2,5-Dichlorophenol	2.92[c8]	7.50[d8]
4-Nitrobenzoic acid	1.89[a9]	3.45[b9]	2-Phenylphenol	3.09[c9]	10.01[d9]
4-Methoxybenzoic acid	1.96[a10]	4.50[b10]			
4-Cyanobenzoic acid	1.56[a11]	3.51[b11]			

[a] a1, a5, a8, a9, c1–c3, c5, c9 from [29]; a2, a4 from [30]; a3, a6, a7, a10, a11 from [31]; c4 from [32]; c6 from [33]; c7 from [34]; c8 from [23]. Only values determined by the shake-flask method were used.

[b] b1–b10, d1, d2, d6 from [35]; d3, d5, d7–d9 from [36]; d4 from [37].

ment using neat aqueous fraction as the eluent, for each benzoic acid derivative, a plot of log k versus proportion of methanol in the mobile phase was drawn, and the log k_w of the analyte was subsequently obtained by extrapolation to neat aqueous eluent according to Eq. (1).

To compare the effect of different organic modifiers on the retention behavior of benzoic acids in this mode of ion-suppression chromatography, binary hydroorganic solvent systems using acetonitrile instead of methanol were experimented as aforementioned with acetic, perchloric or phosphoric acid as additive at only two $^{W}_{W}$pH values, respectively.

Acquisition of k_w of phenol derivatives was performed in the same procedure. Each of phenols was eluted by the mobile phases only composed of methanol and aqueous acetic or perchloric acid solution with different $^{W}_{W}$pH.

The K''_{ow} value of an analyte was calibrated from K_{ow} value according to Eq. (5). The relationships between log K''_{ow} and log k_w for benzoic acids and phenols were respectively established.

3.3.2. *Validation of* log K''_{ow} − log k_w *linearity of weak acidic analytes*

To demonstrate the better relationship between log K''_{ow} and log k_w than that between log K_{ow} and log k_w, a series of validation experimental data were gathered from the elution of 11 benzoic acid derivatives on different columns by using at least four volume ratios of methanol to aqueous acetic acid solution with $^{W}_{W}$pH of 3.50 as the mobile phase. First of all, the exactly same column (Kromasil C_{18}, 5 μm, 150 mm × 4.6 mm ID) used in the above experiment was transferred to Waters Alliance 2695 Separations Module to repeat this procedure under the same elution condition. Next, the column temperature was arisen to 40 °C on the Waters Alliance 2695 Separations Module, and the t_R of the solutes were recorded still under the same elution condition. After that, these benzoic acids were chromatographed on three other columns, i.e. Gemini C_{18} (5 μm, 150 mm × 4.6 mm ID), Gemini C_{18} (5 μm, 250 mm × 4.6 mm ID) and Kromasil C_{18} (7 μm, 150 mm × 4.6 mm ID), on Waters 2695 Separations Module under the same elution condition. Besides, another compound, 2,4-dichlorobenzoic acid, which is structurally similar to the model compounds, was eluted on Kromasil C_{18} column (5 μm, 150 mm × 4.6 mm ID) under the same elution condition to check up the reliability of the proposed log K''_{ow} − log k_w linear relationship for other arbitrary derivatives of benzoic acid.

3.3.3. *Investigation on suitability of* log K''_{ow} − log k_w *linearity for all weakly ionizable monobasic acidic compounds*

In order to investigate the suitability of log K''_{ow} − log k_w linear relationship for all weakly ionizable monobasic acidic compounds, a set of 11 benzoic acid derivatives and nine phenol derivatives were eluted by using methanol–aqueous acetic acid solution with $^{W}_{W}$pH of 3.50 as the mobile phase. The obtained data were processed as a whole for all benzoic acids and phenols according to the procedure described in Section 3.3.1, that is, the k_w values of all these compounds were extrapolated and their K''_{ow} values were calculated under pH 3.50, then the regression was taken between log K''_{ow} and log k_w of the 20 monobasic acidic compounds.

4. Results and discussion

4.1. *Relationship between* log K''_{ow} *and* log k_w *of weak acidic analytes*

4.1.1. *Calibration of* K_{ow} *of the model compounds*

The retention behaviors of the analytes were studied by extrapolating the log k with the corresponding C_B to get log k_w, in which either methanol or acetonitrile was employed as the organic modifier of aqueous mobile phase with different pH. The log k_w of benzoic acids and phenols on Kromasil C_{18} (5 μm, 150 mm × 4.6 mm ID) column in Varian 5060 HPLC system were obtained. At the same time, log K''_{ow} was calculated through K_{ow} and K_a of the analyte, and pH of the mobile phase, which was supposed as a constant during the change of C_B [25]. Then the relationship between log K''_{ow} and log k_w for a set of 11 benzoic acids and a set of nine phenols, as well as the relationships between log K_{ow} and log k_w of both groups (see Tables 2 and 3) was respectively obtained.

This experiment indicated that log K''_{ow} linearly correlated with log k_w in this ion-suppression RPLC mode using both methanol and acetonitrile as organic modifiers. From the values of the linear correlation coefficients (r) for benzoic acids presented in Table 2, it is clear that when the mobile phase pH was low, namely <3,

Table 2
The relationships between log K_{ow} and log k_w, and the relationships between log K''_{ow} and log k_w for 11 benzoic acids (r represents the regression correlation coefficient).

Mobile phases	$^{W}_{W}$pH	log $K_{ow}(y)$–log $k_w(x)$	log $K''_{ow}(y)$–log $k_w(x)$
Methanol–aqueous acetic acid solution	2.29	$y = 1.07x + 0.13$, $r = 0.977$	$y = 1.10x + 0.05$, $r = 0.981$
	2.68	$y = 1.00x + 0.00$, $r = 0.954$	$y = 1.08x - 0.21$, $r = 0.966$
	2.80	$y = 0.98x + 0.03$, $r = 0.948$	$y = 1.00x - 0.09$, $r = 0.961$
	3.50	$y = 0.84x + 0.40$, $r = 0.938$	$y = 1.13x - 0.42$, $r = 0.973$
	3.81	$y = 0.75x + 0.74$, $r = 0.853$	$y = 1.25x - 0.52$, $r = 0.975$
	4.07	$y = 0.73x + 0.81$, $r = 0.837$	$y = 1.34x - 0.76$, $r = 0.972$
Methanol–aqueous perchloric acid solution	2.28	$y = 1.17x - 0.51$, $r = 0.966$	$y = 1.20x - 0.58$, $r = 0.965$
	2.43	$y = 1.16x - 0.46$, $r = 0.980$	$y = 1.20x - 0.58$, $r = 0.979$
	2.69	$y = 1.14x - 0.40$, $r = 0.982$	$y = 1.21x - 0.60$, $r = 0.977$
	2.82	$y = 1.11x - 0.32$, $r = 0.980$	$y = 1.20x - 0.59$, $r = 0.977$
	3.50	$y = 0.94x + 0.09$, $r = 0.954$	$y = 1.24x - 0.77$, $r = 0.963$
	3.82	$y = 0.68x + 0.62$, $r = 0.861$	$y = 1.04x - 0.53$, $r = 0.908$
	4.07	$y = 0.61x + 0.78$, $r = 0.833$	$y = 1.02x - 0.60$, $r = 0.883$
Methanol–aqueous phosphoric acid solution	2.29	$y = 0.88x - 0.09$, $r = 0.974$	$y = 1.02x - 0.50$, $r = 0.966$
	4.07	$y = 0.62x + 0.75$, $r = 0.914$	$y = 1.14x - 1.06$, $r = 0.953$
Acetonitrile–aqueous acetic acid solution	2.29	$y = 1.40x - 0.29$, $r = 0.916$	$y = 1.90x - 1.22$, $r = 0.925$
	3.81	$y = 0.86x + 0.62$, $r = 0.899$	$y = 1.89x - 1.43$, $r = 0.954$
Acetonitrile–aqueous perchloric acid solution	2.29	$y = 1.25x - 0.14$, $r = 0.939$	$y = 1.28x - 0.22$, $r = 0.934$
	3.81	$y = 0.86x + 0.62$, $r = 0.940$	$y = 1.67x - 1.18$, $r = 0.966$
Acetonitrile–aqueous phosphoric acid solution	2.29	$y = 1.03x + 0.23$, $r = 0.949$	$y = 1.23x - 0.19$, $r = 0.967$
	4.07	$y = 0.92x + 0.65$, $r = 0.947$	$y = 1.84x - 1.37$, $r = 0.949$

Table 3
The relationships between log K_{ow} and log k_w, and the relationships between log K''_{ow} and log k_w for nine phenols (r represents the regression correlation coefficient).

Mobile phases	$^{W}_{W}$pH	log $K_{ow}(y)$–log $k_w(x)$	log $K''_{ow}(y)$–log $k_w(x)$
Methanol–aqueous acetic acid solution	2.20	$y = 0.99x + 0.26$, 0.919	$y = 0.99x + 0.26$, 0.918
	2.60	$y = 1.03x - 0.08$, 0.929	$y = 1.03x - 0.08$, 0.927
	2.80	$y = 0.97x + 0.08$, 0.924	$y = 0.97x - 0.04$, 0.921
	3.00	$y = 0.96x + 0.02$, 0.928	$y = 0.97x - 0.03$, 0.925
	3.20	$y = 0.95x + 0.01$, 0.930	$y = 0.96x - 0.01$, 0.925
	3.60	$y = 0.96x + 0.02$, 0.935	$y = 0.97x - 0.03$, 0.924
	4.00	$y = 0.95x + 0.11$, 0.942	$y = 1.00x - 0.03$, 0.931
Methanol–aqueous perchloric acid solution	2.20	$y = 0.84x + 0.15$, 0.931	$y = 0.85x + 0.13$, 0.928
	2.60	$y = 0.84x + 0.17$, 0.931	$y = 0.84x + 0.16$, 0.927
	2.80	$y = 0.82x + 0.21$, 0.937	$y = 0.82x + 0.20$, 0.932
	3.00	$y = 0.86x + 0.14$, 0.942	$y = 0.86x + 0.12$, 0.934
	3.20	$y = 0.86x + 0.16$, 0.934	$y = 0.86x + 0.14$, 0.923
	3.60	$y = 0.84x + 0.30$, 0.946	$y = 0.86x + 0.22$, 0.941
	4.00	$y = 0.83x + 0.36$, 0.941	$y = 0.88x + 0.20$, 0.935

the correlation between log K''_{ow} and log k_w approximated to that of log K_{ow} and log k_w; while along with the increase of the pH value, log K''_{ow} was more suitable for correlation than log K_{ow} with log k_w, especially using acetic acid as ion-suppressor. This phenomenon was reasonable because when pH of the mobile phase was low, the ion-suppressors in eluents almost completely suppress the dissociation of benzoic acids, and in consequence the solutes were predominantly in molecular state. The hydrophobicity of the solutes dovetailed into the definition of K_{ow}, referring to the unionized species, and K''_{ow} could not show the superiority to K_{ow} here. Whereas, when pH of mobile phase was increased, dissociation of benzoic acids was less suppressed by ion-suppressors in eluents and therefore much more ionized forms existed in the eluents. Using original K_{ow} for neutral solutes without any manipulation in this situation led to lack of some retention information of ionized benzoic acids, as a result, a poorer correlation between log K_{ow} and log k_w.

For phenols, however, the r values of log K''_{ow} – log k_w linearity were almost equal to those of log K_{ow} – log k_w in Table 3, that is, the linear correction between octanol–water partition coefficient and retention factor is not so remarkably increased by using K''_{ow} instead of K_{ow}. This could be explained by that, phenols normally have significantly greater pK_a values than benzoic acids, there are very fewer ionic species in weakly acidic mobile phase, and the eluents in the range of experimental pH were acidic enough to suppress dissociation of phenols, although not for benzoic acids. It is believed that when mobile phase pH is higher, the better linear relationship between log K''_{ow} and log k_w would be obtained than that between log K_{ow} and log k_w, which will be further investigated in the next step of our experiment. However, the peak shape of all phenols was obviously improved once the acid additives were added into hydroorganic eluent.

4.1.2. Linear relationship between log K''_{ow} and log k_w under different conditions

The verification results summarized in Table 4 indicated that an established log K''_{ow} – log k_w correlation can be generalized to different LC instrumentation systems, and to C_{18} columns of different brand and different parameter under different temperature. Obviously, the observed better linear relationship between log K''_{ow} and log k_w than that between log K_{ow} and log k_w especially at high mobile phase pH does not depend on the particular chromatographic condition but reflected a general feature of the weakly acidic compounds tested in this ion-suppression mode. Therefore, Eq. (2) should be transferred to the following general equation for weakly ionizable acidic solutes:

$$\log K''_{ow} = m \log k_w + n \quad (7)$$

4.1.3. Suitability of log K''_{ow} – log k_w linear correlation for all weakly ionizable monobasic acidic compounds

Phenols were chromatographed at the same time as benzoic acids on Kromasil C_{18} (5 μm, 150 mm × 4.6 mm ID) column in Waters Alliance HPLC system by methanol–aqueous acetic acid solution with $^{W}_{W}$pH of 3.50 for verification of log K''_{ow} – log k_w linear correlation. The r value of log K''_{ow} – log k_w relationship was also approximate to that of log K_{ow} – log k_w, shown in Table 4, which was in agreement with the results in Section 4.1.1. Moreover, log K''_{ow}, log K_{ow} and log k_w of benzoic acids and phenols were treated as a single set because they were eluted by the identical chromatographic condition in a run. The relationship

Table 4
The relationships between log K_{ow} and log k_w, and the relationships between log K''_{ow} and log k_w for benzoic acids and phenols eluted by methanol–aqueous acetic acid solution at $^{W}_{W}$pH of 3.50 (r represents the regression correlation coefficient).

Sample sets	Instrument	C_{18} columns			Column temperature (°C)	log $K_{ow}(y)$–log $k_w(x)$	log $K''_{ow}(y)$–log $k_w(x)$
		Brand	Dimension $L \times$ ID (mm)	Particle size (μm)			
11 Benzoic acid	Varian 5060[a]	Kromasil	150 × 4.6	5	30	$y = 0.84x + 0.40$, $r = 0.938$	$y = 1.13x - 0.42$, $r = 0.973$
	Waters 2695	Kromasil	150 × 4.6	5	30	$y = 0.76x + 0.61$, $r = 0.928$	$y = 1.03x - 0.13$, $r = 0.958$
	Waters 2695	Kromasil	150 × 4.6	5	40	$y = 0.79x + 0.58$, $r = 0.947$	$y = 1.07x - 0.18$, $r = 0.980$
	Waters 2695	Kromasil	150 × 4.6	7	30	$y = 0.92x + 0.19$, $r = 0.929$	$y = 1.29x - 0.79$, $r = 0.995$
	Waters 2695	Gemini	150 × 4.6	5	30	$y = 1.18x + 0.12$, $r = 0.848$	$y = 1.50x - 0.51$, $r = 0.900$
	Waters 2695	Gemini	250 × 4.6	5	30	$y = 0.93x + 0.45$, $r = 0.910$	$y = 1.31x - 0.44$, $r = 0.980$
Nine phenols	Waters 2695	Kromasil	150 × 4.6	5	30	$y = 0.83x + 0.37$, $r = 0.981$	$y = 0.85x + 0.31$, $r = 0.981$
20 phenols and benzoic acids	Waters 2695	Kromasil	150 × 4.6	5	30	$y = 0.80x + 0.49$, $r = 0.959$	$y = 0.91x + 0.14$, $r = 0.966$

[a] From Table 2.

between log K''_{ow} and log k_w of all of the 20 compounds was also much more linear than that between log K_{ow} and log k_w, and the r value was close to both for separately treated phenols and benzoic acids (Table 4). This outcome proved that the proposed better linear correlation between log K''_{ow} and log k_w (Eq. (7)) than that between log K_{ow} and log k_w for benzoic acids and phenols can be extrapolated to all weakly ionizable monobasic acidic analytes.

4.2. The important significance of log K''_{ow} − log k_w linear correlation

4.2.1. Retention prediction of weak acidic compounds in ion-suppression RPLC

The good linear correlation between log K''_{ow} and log k_w for weak acidic solutes has been established experimentally. An equivalent correlation between log K''_{ow} − log k_w and log K_{ow} − log k_w at lower pH, but an improved correlation of log K''_{ow} − log k_w at higher pH proved that log K''_{ow} is superior to nude log K_{ow} in prediction of monobasic acidic compounds in this ion-suppression RPLC.

The first step of our prediction method was to predict the k_w value of a monocarboxylic acid via Eq. (7) which was a general equation deduced from the 11 model benzoic acids under various elution conditions. K''_{ow} of the compound to be predicted at the experiment pH was calculated via Eq. (5). Each specific forms of Eq. (7) under the particular elution conditions listed in Table 2 were applied to estimate k_w of the solutes eluted under the relevant elution condition. Interestingly, the intercepts and slopes of all regressions with methanol as organic modifier were very close, which seems that values of the intercepts and slopes were approximately independent of the kind of ion-suppressors added and the pH of mobile phase, only determined by the employed column and organic modifier. We tried to establish a semiempirical equation (Eq. (8)) with respect to the correlation between log K''_{ow} and log k_w. The two constants of Eq. (8) ($m = 0.87$, $n = 0.45$) were from the averages of intercepts and slopes of the linear regressions of log K''_{ow} − log k_w by using different ion-suppressors at various pH (Table 2).

$$\log K''_{ow} = 1.15 \log k_w - 0.52, \text{ that is,}$$

$$\log k_w = 0.87 \log K''_{ow} + 0.45 \quad (8)$$

No semiempirical equation was given here for monocarboxylic acid eluted by acetonitrile as organic modifier because in this experiment only six regressions of straight lines were drawn for acetonitrile, and moreover, the values of the intercepts and slopes were very different, respectively (Table 2), the averages of them would cause large inaccuracy. This is likely because the dependences of log k of an analyte on concentration of acetonitrile in aqueous mobile phase are not strictly linear and may be expressed by quadratic equations. However, the correlation between log k and methanol concentration is linear in the wide range of the investigated organic modifier concentrations. Flieger [38] attributed this difference to the different adsorption mechanism on stationary phase between methanol and acetonitrile, that is, they form mono- and multi-molecular adsorbed layers, respectively.

Fig. 1 shows the consistency between the model-simulated and experimentally extrapolated log k_w of 11 benzoic acids using methanol and aqueous acetic or perchloric acid solution as the mobile phase at pH of 3.50. Also, the comparison between the results via the individual relationship equations between log K''_{ow} and log k_w (Eq. (7)) under a specific experimental condition (Table 2) and via the semiempirical equation (Eq. (8)) was given in Fig. 1. Good agreement between simulated and extrapolated log k_w values, no matter which equation was used, is an indication that k_w obtained by model prediction accords with that experimentally

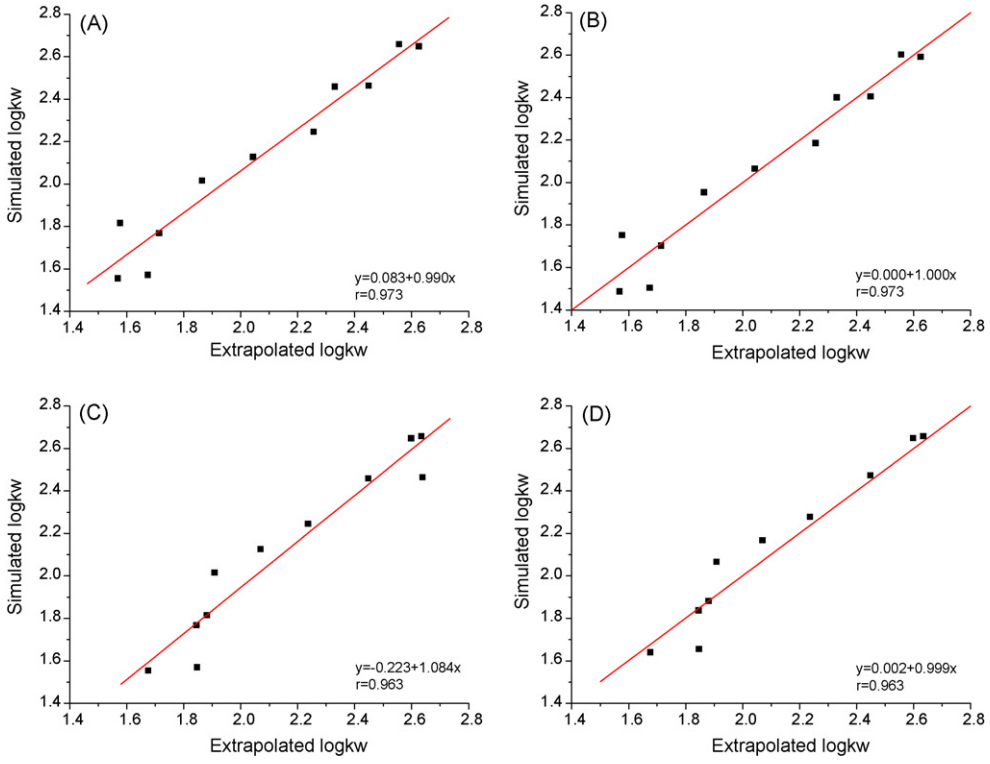

Fig. 1. Prediction of k_w of model compounds eluted by methanol–aqueous acetic (A and B) and perchloric (C and D) acid solution at $^{w}_{w}$pH of 3.50. (A and C) Simulated log k_w values were derived by the individual equation between log K''_{ow} and log k_w under each specific elution conditions (Eq. (7), Table 5); (B and D) simulated log k_w values were derived by the semiempirical equation (Eq. (8)). r corresponded to the correlation regression coefficient between logarithms of the model-simulated and experimentally extrapolated k_w values.

extrapolated via Eq. (1), permitting the further prediction of k of the analyte as following.

Generally, the t_R of a solute at arbitrary volume fraction of organic modifier in binary mobile phase can be predicted by Eq. (1) according to k_w model-simulated beforehand. For a given RPLC system composed of a given column and organic modifier, the coefficient S in Eq. (1) is often observed to be roughly constant, even for solutes of varying molecular size and structure. When the organic modifier is methanol or acetonitrile, the value of S is usually about 3 [9]. For RPLC of weakly ionizable acidic compounds using acids as the ion-suppressors, in fact, S values are slightly dependent on the ion-suppressors and pH of the mobile phase. It can been seen from Table 5, S values from the mobile phase using acetic acid as the additive (usually below 3) were significantly less than those from the mobile phase using perchloric acid as the additive (usually above 3). Moreover, the relative standard deviations (RSDs) of S measurement using acetic acid as the additive were larger than those using perchloric acid as the additive. This is because the retention of acidic solutes becomes weaker due to the organic modifier function of acetic acid. In addition, the concentration of acetic acid in mobile phase increases with the increase of aqueous fraction, resulting in retention reduction. Even now, the S values of the solutes in this present experiment varied from 2.64 to 3.37 without regard to the ion-suppressor used (the last column in Table 5), confirming that the usability of 3 as the value of parameter S in rough estimation of retention of solutes with unknown S. Thus the logarithm of k of the analytes at a specific volume fraction of methanol in the eluent can be predicted in our model through the above two steps.

The validation of this prediction model was carried out by three sections, which were comparisons of measured and predicted retention data of (1) all 11 model compounds using 40% (v/v) methanol and aqueous acetic acid solution at $^{W}_{W}$pH of 3.50 (Table 6); (2) 3-chlorobenzoic acid, a random solute chosen from the group of model compounds, using aqueous 40% (v/v) methanol solution with acetic or perchloric acid as ion-suppressor at different pH (Table 7); and (3) another substituted monobasic carboxylic acid, 2,4-dichlorobenzoic acid, using 40% (v/v) methanol and aqueous acetic acid solution at $^{W}_{W}$pH of 3.50 in validation experiment. The model-predicted data agreed with the experimentally measured ones on the whole except two data marked [a] and [b] in Table 7, and the reason for these exceptions will be described in the following Section 4.3. In addition, the deviations observed in Tables 6 and 7 presumedly came from the imprecise average rather than the rigorous S values adopted at different mobile phase pH. For 2,4-dichlorobenzoic acid (log K_{ow} 2.71 calculated by Broto's fragmentation method [39], pK_a 2.72 [36]), 3 was taken as the S value for their log k prediction. The measured log k of 2,4-dichlorobenzoic acid eluted by 40% (v/v) methanol and aqueous acetic acid solution at $^{W}_{W}$pH of 3.50 were 1.20, and the corresponding log k model-calculated were 1.01. In spite better correctness of S value is obtained from given mobile phase at given pH on given column, complete awareness of precise S values of every compounds is very difficult and therefore unpractical for retention prediction. In addition, another monohydrating phenol, 2,4,6-trinitrophenol (log K_{ow} 2.03 determined by shake-flask method [29], pK_a 0.33 [36]), was put into the group of benzoic acids and phenols studied for retention behavior prediction. The data point of 2,4,6-trinitrophenol seriously outlay the log K''_{ow} − log k_w straight line of either phenols or mixture of phenols and benzoic acids. This is because the pK_a value of 2,4,6-trinitrophenol (0.33) is so small that its acidity is even stronger than phosphoric acid, it does not belong to weak acids, and therefore its chromatographic retention behavior does not abide by the linear relationship between log K''_{ow} and log k_w for weakly ionizable compounds.

From these results, the reliability and practicability of this prediction method, proposed for the first time, can be deducted. And this protocol was characterized by training enough model solutes with accurate and reliable K_{ow} to determine the accurate parameters in Eq. (7) and considering the difference of the kind of ion-suppressor. The characteristic gave reasons for the error, which bear out the supposition, of the predicted retention time in this experiment. In future work, this prediction model would be consummated by chromatographing a great amount of solutes with experimental K_{ow} value available to get more precise slope and intercept of Eq. (7) in the light of the kind of ion suppressor used in order to obtain simulated retention time with less deviation from the experimental one.

4.2.2. Correction of known K_{ow} and estimation of unknown K_{ow} of weak acidic compounds

Retention prediction discussed above is one of the applications of the linear relationship between log K''_{ow} and log k_w. In addition, as a means of simplifying K_{ow} measurement, RPLC-determined retention factors have been commonly used as a predictive basis via well-known Collander relationship. Therefore, this new linear regression can be used for direct determination of K_{ow} values or revision of the unreliable reference K_{ow} data as well. The computed K_{ow}, by commercial software or quantitative structure method, only gives the value range in some accuracy. Considerable uncertainties existed in computed log K_{ow}, because these software editions only mechanically use fragmentation method. The software-computed K_{ow} values for all isomers of a compound are always the same, for example, 2-, 3- and 4-methylbenzoic acids have the absolutely same log K_{ow} value, 2.08 by Crippen's fragmentation [40] or 2.21 by Viswanadhan's fragmentation [41], but in fact they are totally not, the log K_{ow} value determined by shake-flask method of 2-, 3- and 4-methylbenzoic acids being 2.18, 2.37 and 2.36, respectively (see Table 1).

For this purpose, at least four retention times of a weakly acidic compound from different volume fractions of organic modifier in binary aqueous acidic mobile phase should be measured to obtain log k_w value of the solute based on Eq. (1). Then the prediction calculation was carried out as the following procedure: (1) log K''_{ow} is driven from log k_w according to Eq. (7) or (8), and (2) final K_{ow} is calculated from three parameters in Eq. (5) including pH value of the mobile phase, K''_{ow} and K_a values of the solute to be measured. The relationship between model-simulated and reference log K_{ow} values of 11 model benzoic acids was shown in Table 8. It can be more easily observed from Table 8 that these model-simulated K_{ow} values are very close to those obtained by classical shake-flask method, confirming the capability of this model for prediction of hydrophobicity of these compounds. The reason why K_{ow} values can be accurately determined is that the process is disrelated to S value, and that the organic modifier effect of acetic acid can be ignored at not too low mobile phase pH (e.g. 3.50). This reliable measurement was proposed because it is simpler, more convenient in practice than previous common chromatographic method to get K_{ow} of the ionizable compounds by using buffers as ion-suppressors.

Furthermore, two other compounds, 2-nitrobenzoic and 4-ethylbenzoic acids, having no experimentally obtained K_{ow} values available up to date, were studied in correction of K_{ow}. The software-computed log K_{ow} of them are 1.18 (Broto's fragmentation method [39]) and 2.61 (Viswanadhan's fragmentation method [41]), respectively. The pK_a values are 2.10 and 4.35, respectively [36]. They were eluted by methanol–water with acetic acid (pH 3.81 and 4.07) or perchloric acid (pH 2.82 and 3.50) as ion-suppressor, respectively. The log K_{ow} values of 2-nitrobenzoic and 4-ethylbenzoic acids from four measurements with different ion-suppressor at different pH were 1.76 and 2.74, respectively, with the RSDs of 6.6% and 1.0%. Considering the reliability of this measurement model, the deviation of 1.76 (the average of 1.88, 1.79, 1.60 and 1.76) from the computed value 1.18 indicated the uncertainty of the

Table 5
The S values of benzoic acids eluted by methanol–aqueous acetic and perchloric acid solution at different $^{W}_{W}$pH.

Compounds	HAc		$HClO_4$		HAc and $HClO_4$	
	Mean	RSD (%, $n=6$)	Mean	RSD (%, $n=7$)	Mean	RSD (%, $n=13$)
Benzoic acid	2.81	3.9	3.00	0.4	2.91	4.2
2-Methylbenzoic acid	3.08	10.9	3.08	9.2	3.08	9.6
3-Methylbenzoic acid	3.07	9.9	3.31	8.1	3.20	9.4
4-Methylbenzoic acid	3.13	6.2	3.57	6.4	3.37	9.1
2-Chlorobenzoic acid	2.55	16.3	2.99	4.7	2.79	13.0
3-Chlorobenzoic acid	3.07	10.3	3.39	2.1	3.24	8.3
4-Chlorobenzoic acid	2.94	9.3	3.49	0.5	3.23	10.4
3-Nitrobenzoic acid	2.44	16.3	3.02	2.5	2.75	14.5
4-Nitrobenzoic acid	2.27	15.7	2.97	3.1	2.64	16.5
4-Methoxybenzoic acid	3.07	4.9	3.49	2.2	3.30	7.5
4-Cyanobenzoic acid	2.52	9.7	3.22	1.6	2.89	13.7

software-computed log K_{ow} of 2-nitrobenzoic acid. So the K_{ow} of this compound should be corrected as 1.76, which almost was a constant with the variation of ion-suppressor and mobile phase pH, according to the experiment in this RPLC mode. On the other hand, the experimental value 2.74 (the average of 2.72, 2.78, 2.72 and 2.73) of 4-ethylbenzoic acid showed that this software-computed log K_{ow} of 2.61 has acceptable accuracy.

4.3. Influence of ion-suppressors on retention behavior of weak acidic compounds

In this ion-suppression RPLC mode, acetic, perchloric and phosphoric acids were employed as ion-suppressors. The function of acetic and perchloric acids has been extensively discussed in this group's previous work [25]. Perchloric or phosphoric acid in the mobile phase was mainly as ion-suppressor, while acetic acid was not only regarded as ion-suppressor (the ionized fraction) but also as the organic modifier (the unionized fraction) in the eluent. The k values of benzoic acids and phenols increased with the decrease of mobile phase pH adjusted by perchloric and phosphoric acids, while increased at first and subsequently decreased with the decrease of mobile phase pH adjusted by acetic acid. Fig. 2 displays the typical k—mobile phase pH correlation of 3-cyanophenol. Obviously, the role of organic modifier played by acetic acid molecule was more evident when methanol ratio and $^{W}_{W}$pH were both low.

Table 6
The comparison of measured and predicted retention data of 11 benzoic acids using 40% methanol and 60% acetic acid solution at $^{W}_{W}$pH of 3.50 as the mobile phase.

Compounds	Measured	Model-calculated[a]			
		By individual equation (Eq. (7), Table 2)		By semiempirical equation (Eq. (8))	
	$\log k_{Exp}$	$\log k_{Cal}$	$\lvert\Delta\rvert$[b]	$\log k_{Cal}$	$\lvert\Delta\rvert$[b]
Benzoic acid	0.75	0.79	0.04	0.85	0.10
2-Methylbenzoic acid	1.04	0.95	0.09	1.01	0.03
3-Methylbenzoic acid	1.16	1.12	0.04	1.18	0.02
4-Methylbenzoic acid	1.17	1.06	0.11	1.12	0.05
2-Chlorobenzoic acid	0.69	0.39	0.30	0.46	0.23
3-Chlorobenzoic acid	1.34	1.30	0.04	1.35	0.01
4-Chlorobenzoic acid	1.35	1.31	0.04	1.37	0.02
3-Nitrobenzoic acid	0.74	0.60	0.14	0.69	0.05
4-Nitrobenzoic acid	0.70	0.70	0.00	0.76	0.06
4-Methoxybenzoic acid	0.80	0.75	0.05	0.81	0.01
4-Cyanobenzoic acid	0.52	0.33	0.19	0.40	0.12

[a] The specific S values from Table 5 were used for model-calculation of $\log k_{Cal}$.
[b] $\Delta = \log k_{Cal} - \log k_{Exp}$.

Table 7
The comparison of measured and predicted retention data of 3-chlorobenzoic acid using 40% methanol and 60% aqueous acetic or perchloric acid solution at different $^{W}_{W}$pH.

Ion-suppressors	$^{W}_{W}$pH	Measured $\log k_{Exp}$	Model-calculated by semiempirical equation (Eq. (8))[a]	
			$\log k_{Cal}$	$\lvert\Delta\rvert$[b]
Acetic acid	2.29	1.05	1.48[a]	0.43
	2.68	1.19	1.47[b]	0.28
	2.80	1.24	1.27	0.03
	3.50	1.34	1.35	0.01
	3.81	1.22	1.24	0.02
	4.07	1.08	1.12	0.04
Perchloric acid	2.28	1.43	1.48	0.05
	2.43	1.42	1.48	0.06
	2.69	1.29	1.47	0.18
	2.82	1.38	1.46	0.08
	3.50	1.35	1.35	0.00
	3.82	1.21	1.24	0.03
	4.07	1.20	1.12	0.08

[a] The specific S values from Table 5 were used for model-calculation of $\log k_{Cal}$.
[b] $\Delta = \log k_{Cal} - \log k_{Exp}$.

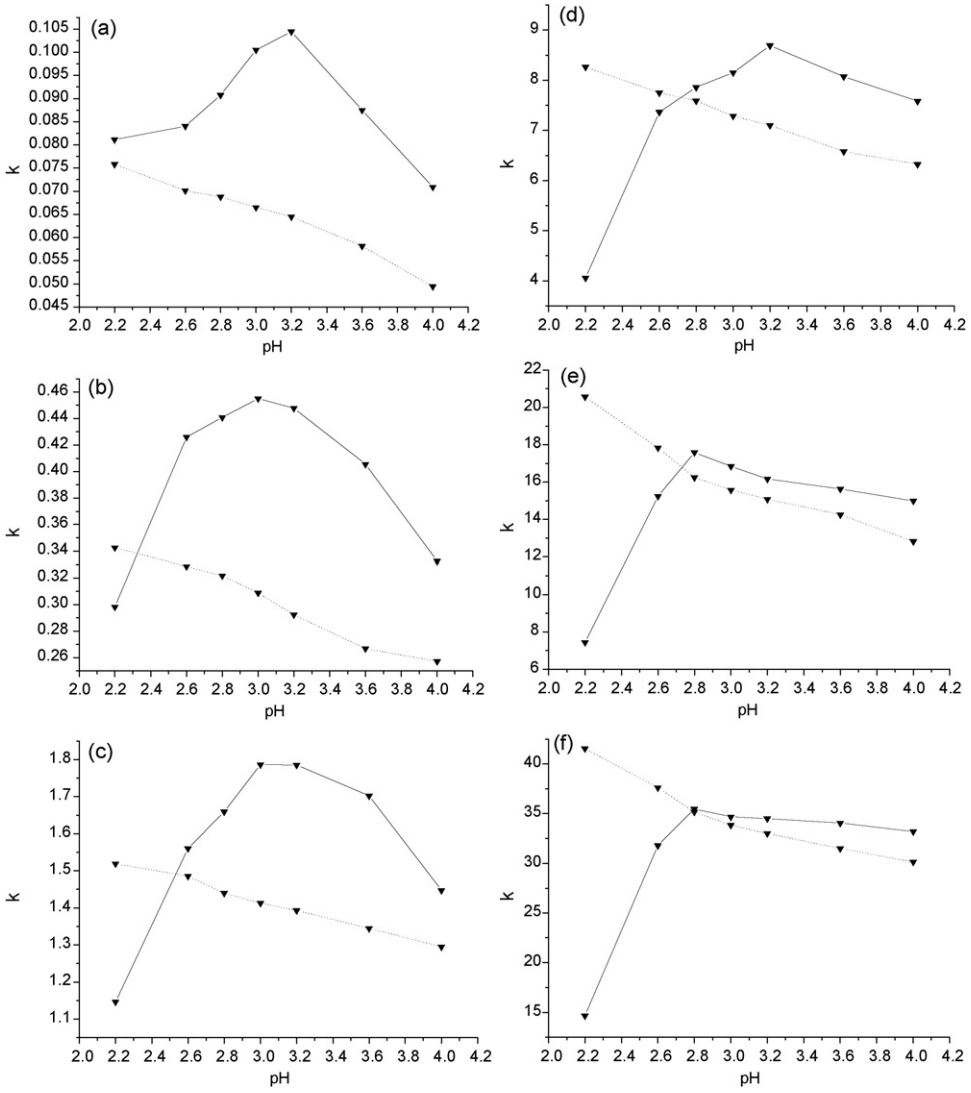

Fig. 2. Correlation between k and mobile phase pH for 3-cyanophenol eluted by methanol–aqueous acetic (solid line) and perchloric (dash line) acid solution with ${}^{W}_{W}$pH of 2.20, 2.60, 2.80, 3.00, 3.20, 3.60 and 4.00, respectively. Methanol contents (vol%) in the mobile phase were 80 (A), 60 (B), 40 (C), 20 (D), 10 (E) and 0 by extrapolation (F).

The deviation of experimental retention data from the predicted ones, marked as [a] and [b] in Table 7, with acetic acid as ion-suppressor at ${}^{W}_{W}$pH of 2.29 and 2.68 can be ascribed to this function of acetic acid as organic modifier. The concentration of acetic acid is as high as 1.52 mol/L, i.e. ca. 0.8 (vol%), when giving ${}^{W}_{W}$pH of 2.29. Such an amount of acetic acid molecules made the eluent more lipophilicity and largely occupied the stationary phase surface, which lead to the decrease of retention of analytes.

Table 8
The comparison of measured and reference log K_{ow} data of 11 benzoic acids using methanol–aqueous acetic acid solution at ${}^{W}_{W}$pH of 3.50 as the mobile phase.

Compounds	Reference[a]	Measured			
		Simulation of log K''_{ow} by individual equation (Eq. (7), Table 2)		Simulation of log K''_{ow} by semiempirical equation (Eq. (8))	
	log $K_{ow(Ref)}$	log $K_{ow(Exp)}$	$\lvert\Delta\rvert$[b]	log $K_{ow(Ref)}$	$\lvert\Delta\rvert$[b]
Benzoic acid	1.87	1.80	0.07	1.70	0.17
2-Methylbenzoic acid	2.18	2.34	0.16	2.19	0.01
3-Methylbenzoic acid	2.37	2.45	0.08	2.22	0.17
4-Methylbenzoic acid	2.36	2.39	0.03	2.34	0.02
2-Chlorobenzoic acid	1.98	2.25	0.27	2.10	0.12
3-Chlorobenzoic acid	2.68	2.63	0.05	2.65	0.03
4-Chlorobenzoic acid	2.65	2.65	0.00	2.53	0.12
3-Nitrobenzoic acid	1.83	1.84	0.01	1.77	0.06
4-Nitrobenzoic acid	1.89	1.79	0.10	1.62	0.27
4-Methoxybenzoic acid	1.96	1.88	0.08	1.86	0.10
4-Cyanobenzoic acid	1.56	1.89	0.33	1.58	0.02

[a] From Table 1.
[b] $\Delta = \log K_{ow(Exp)} - \log K_{ow(Ref)}$.

Moreover, the lower methanol content in the mobile phase and the higher acetic acid concentration in whole eluent, the stronger the organic modifier effect of acetic acid. When using perchloric acid as the ion-suppressor, however, the predicted k values were in good agreement with the experimental values regardless the methanol content and pH of the mobile phase (Table 7). Accordingly, the retention prediction and log K_{ow} measurement by this model had better avoid using acetic acid as ion-suppressor with mobile phase pH lower than 3.0 in order to ensure the reliability of results. If so, the concentration of acetic acid in whole mobile phase is not too high after all, the difference between k values using different acids as ion-suppressors is rather small, and furthermore, is close up along with the decrease of methanol content (Fig. 2). Deviation of retention predication originated mainly from the adoption of approximate average S value.

5. Conclusions

The retention behavior of a group of derivatives of benzoic acid and phenol in ion-suppression chromatography, using three simple acids instead of buffers as ion-suppressors, was systematically studied for the first time. The apparent octanol–water partition coefficient K''_{ow} was proposed to comprehensively express the hydrophobicity (octanol–water partition coefficient K_{ow}) of the solutes in different forms in this RPLC mode. The linear relationship between log K''_{ow} and log k_w has been established within the wide range of the ion-suppressor pH, described as Eqs. (7) and (8), and this correlation was better than that of log K_{ow} with log k_w. Then, this correction can allow the straightforward prediction of the retention of the solute to optimize of separations with satisfactory accuracy. Also, this correlation can provide a powerful method for determination of K_{ow} by the measurement of retention data of the weak acidic solutes, which could correct the reference K_{ow} values with the uncertainties and therefore could have the retention behavior for more ionizable compounds predictable. This relationship has been characterized by dealing with the experimental results of restricted sets of 11 benzoic acids and nine phenols using methanol and acetonitrile as the organic modifiers. With the possibility of the detection of numerous analytes as the model compounds and the inclusion and evaluation of the difference of ion-suppressors and other parameters in the future work, it is possible to obtain the more precise slope and intercept of this relationship to improve the prediction of retention and the determination of the hydrophobicity of the solutes. The dual role of acetic acid in this RPLC model as ion-suppressor and organic modifier was played when the pH is low, which is different from perchloric and phosphoric acids only as the ion-suppressors.

Acknowledgements

This work was supported by National Natural Science Fund of China (20575027), National Basic Research Program of China (973 program, No. 2009CB421601), National Science Funds for Creative Research Groups (20821063), and Analysis & Test Fund of Nanjing University. We are grateful to Prof. Wan-fang Lu, School of Chemistry & Chemical Engineering, Nanjing University, for her helpful and instructive comments.

References

[1] R.B. Cole (Ed.), Electrospray Ionization Mass Spectrometry, John Wiley and Sons, New York, 1997, p. 323.
[2] M.S. Gardner, R.D. Voyksner, C.A. Haney, Anal. Chem. 72 (2000) 4659.
[3] Q. Liu, W.S. Cai, X.G. Shao, Talanta 77 (2008) 679.
[4] K.B. Borges, E.F. Freire, I. Martins, M.E.P.B. de Siqueira, Talanta 78 (2009) 233.
[5] X.B. Luo, B. Chen, S.Z. Yao, Talanta 66 (2005) 103.
[6] A.R.B. de Quiros, M.A. Lage-Yusty, J. Lopez-Hernandez, Talanta 78 (2009) 643.
[7] A.M. Siouffi, R. Phan-Tan-Luu, J. Chromatogr. A 892 (2000) 75.
[8] T. Vasiljevic, A. Onjia, D. Cokesa, M. Lausevic, Talanta 64 (2004) 785.
[9] L.R. Snyder, J.W. Dolan, J.R. Gant, J. Chromatogr. 165 (1979) 3.
[10] N. Chen, Y. Zhang, P. Lu, Chin. J. Anal. Chem. 21 (1993) 384.
[11] C. Horvath, W. Melander, I. Molnar, Anal. Chem. 49 (1977) 142.
[12] R.M. Lopes Marques, P.J. Schoenmakers, J. Chromatogr. 592 (1992) 157.
[13] J.A. Lewis, D.C. Lommen, W.D. Raddatz, J.W. Dolan, L.R. Snyder, J. Chromatogr. 592 (1992) 183.
[14] X. Subirats, M. Roses, E. Bosch, Sep. Purif. Rev. 36 (2007) 231.
[15] L.G. Gagliardi, C.B. Castells, C. Rafols, M. Roses, E. Bosch, Anal. Chem. 78 (2006) 5858.
[16] E. Fuguet, C. Rafols, E. Bosch, M. Roses, J. Chromatogr. A 1173 (2007) 110.
[17] S. Dmitrienko, E.N. Myshak, L.N. Pyatkova, Talanta 49 (1999) 309.
[18] S. Griffin, S.G. Wyllie, J. Markham, J. Chromatogr. A 864 (1999) 221.
[19] T. Braumann, J. Chromatogr. 373 (1986) 191.
[20] H. Zou, Y. Zhang, M. Hong, P. Lu, J. Chromatogr. 625 (1992) 169.
[21] C. Helweg, T. Nielsen, P.E. Hansen, Chemosphere 34 (1997) 1673.
[22] C.H. Lochmuller, M. Hui, J. Chromatogr. Sci. 36 (1998) 11.
[23] W.E. Hammers, G.J. Meurs, C.L. de Ligny, J. Chromatogr. 247 (1982) 1.
[24] A. Berthod, S. Carda-Broch, M.C. Garcia-Alvarez-Coque, Anal. Chem. 71 (1999) 879.
[25] H.Z. Lian, W.H. Wang, D.N. Li, J. Sep. Sci. 28 (2005) 1179.
[26] Y. He, Y. Zhao, L. Wang, F. An, H. Mo, K. Yang, Y. Liu, G. Yu, X. Xu, Environ. Chem. 13 (1994) 195.
[27] M.J. Ruiz-Angel, S. Carda-Broch, M.C. Garcia-Alvarez-Coque, A. Berthod, J. Chromatogr. A 1063 (2005) 25.
[28] J. Sansgter, Octanol–Water Partition Coefficients: Fundamentals and Physical Chemistry, Wiley, Chichester, 1997.
[29] A. Leo, C. Hansch, D. Elkins, Chem. Rev. 71 (1971) 525.
[30] H. Tomida, Chem. Pharm. Bull. Jpn. 26 (1978) 2824.
[31] C. Hansch, J. Am. Chem. Soc. 86 (1964) 5175.
[32] J. Rogers, A. Wong, Int. J. Pharm. 6 (1980) 339.
[33] Ya.I. Korenman, A.T. Alymova, N.S. Kobeleva, Zh. Fiz. Khim. 55 (1981) 1242.
[34] Ya.I. Korenman, Zh. Prikl. Khim. 46 (1973) 380.
[35] J.A. Dean (Ed.), Lange's Handbook of Chemistry, 15th ed., McGraw-Hill, New York, 1999.
[36] J. Buckingnam (Ed.), Dictionary of Organic Compounds, 6th ed., Chapman & Hall, London, 1996.
[37] W.B. Yao, T. Xie, Y.M. Gao (Eds.), Handbook of Physical Chemistry, Shanghai Scientific & Technical Publishers, Shanghai, 1985.
[38] J. Flieger, J. Chromatogr. A 1175 (2007) 207.
[39] P. Broto, G. Moreau, C. Vandycke, Eur. J. Med. Chem. Chim. Theor. 19 (1984) 71.
[40] A.K. Ghose, G.M. Crippen, J. Chem. Inf. Comput. Sci 27 (1987) 21.
[41] V.N. Viswanadhan, A.K. Ghose, G.R. Revankar, R.K. Robins, J. Chem. Inf. Comput. Sci 29 (1989) 163.

Talanta 79 (2009) 627–632

Contents lists available at ScienceDirect

Talanta

journal homepage: www.elsevier.com/locate/talanta

Development of a rapid and automatic optosensor for the determination of cromolyn in biological samples

L. Molina-García, E.J. Llorent-Martínez, M.L. Fernández-de Córdova, A. Ruiz-Medina *

Department of Physical and Analytical Chemistry, Faculty of Experimental Sciences, University of Jaén, Campus las Lagunillas, E-23071 Jaén, Spain

ARTICLE INFO

Article history:
Received 20 October 2008
Received in revised form 15 April 2009
Accepted 21 April 2009
Available online 3 May 2009

Keywords:
Cromolyn
Sequential injection analysis
Optosensor
Urine
Pharmaceuticals

ABSTRACT

Disodium cromoglycate (SCG) is an anti-allergic drug, which is applied locally or inhaled. After administration, a very small portion of the drug is absorbed, being the most eliminated part unchanged in the urine and bile; therefore, its determination in urine is indicative of the dose absorbed. Here, the first spectroscopic method for the determination of SCG, making use of a sequential injection optosensor with terbium-sensitized luminescence detection, is described. The cationic resin Chelex-100 was used as solid support in the detection area. The measurements were made at 336/545 nm ($\lambda_{ex}/\lambda_{em}$) and the system was calibrated for two sample volumes, 150 and 800 μl, depending on the samples analyzed. A detection limit of 15 ng ml^{-1} and a RSD lower than 2% ($n = 10$) were observed using the highest sample volume. The proposed method does not use any organic solvent or surfactant, so being environmental friendly. The analyte was satisfactorily determined in pharmaceuticals and human urine, the latter being spiked at the concentrations found after the administration of the drug.

1. Introduction

Disodium cromoglycate (SGC), also known as cromolyn, is a potent and well-known anti-allergic agent almost free from side effects and highly soluble in water. It is effective for treating asthma and allergic rhinitis [1,2] and its action mechanisms have been described as the inhibition effect against the release of the chemical mediator like histamine and the slow-reacting substance of anaphylaxis from the human lung [3]. Only a very small portion of the drug (approximately 1–3%) is absorbed by the gastrointestinal tract after oral administration [2–4]; however, after inhalation, the drug is well absorbed by the respiratory epithelium into the systemic circulation and rapidly eliminated unchanged in approximately equal proportions in the urine and bile [5]. Therefore, the urinary excretion of the drug is the indicator of the dose absorbed by the body. The structure of the drug is as follows:

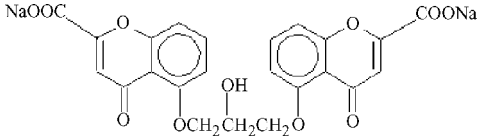

Although the determination of SCG has been performed using thin-layer chromatography with densitometry detection [6] or by means of a radioimmunoassay [7] or using cathodic stripping voltammetry [8], all the recent methods developed for the determination of SCG involve liquid chromatography [1–3,9,10]. Hence, there is a complete absence of easy-to-use spectroscopic methodologies for the determination of SCG not only in biological fluids, but also in pharmaceuticals. As a result, the development of a rapid, simple and automatic method for the routine determination of the drug in both matrices is an interesting option.

In this paper, the coupling of sequential injection analysis (SIA) and solid phase spectroscopy (SPS) employing terbium-sensitized luminescence as detection technique is reported for the determination of SCG. SIA methodology shows complete automation, rapidity and simplicity [11,12], while the introduction of SPS provides the required selectivity and sensitivity [13,14]. These last characteristics are enhanced when the solid support is employed in the same sensing zone, as it is shown in this paper.

Luminescence spectroscopy offers the possibility of more selective detection techniques, such as the use of lanthanide-sensitized luminescence. Lanthanide ions, such as europium and terbium, exhibit weak absorption coefficients and low fluorescence quantum yields. When chelated with organic ligands, such as SCG, the luminescence quantum yield is greatly enhanced; the excitation light is absorbed and collected by the organic ligand, which serves as an antenna chromophore, being this process followed by an energy transfer of the collected energy to the chelated lanthanide ion, which then emits line-like bands in the spectrum of the lanthanide ion [15,16].

Taking into account these characteristics, in this paper we propose the determination of SGC by means of the formation of a chelate with terbium (III). This is the first spectroscopic method

* Corresponding author. Tel.: +34 953 212759; fax: +34 953 212940.
E-mail address: anruiz@ujaen.es (A. Ruiz-Medina).

0039-9140/$ – see front matter © 2009 Elsevier B.V. All rights reserved.
doi:10.1016/j.talanta.2009.04.039

for the determination of this analyte not only in pharmaceuticals, but also in such a chelate matrix as human urine. The use of the solid support provides the rigidity required to enhance the luminescence intensity of the system, so avoiding the use of surfactants, commonly employed in liquid phase [15,17].

2. Experimental

2.1. Reagents and solutions

SGC, terbium (III) nitrate pentahydrate, sodium acetate and acetic acid were obtained from Sigma (Alcobendas, Madrid, Spain). Ethylenediaminetetraacetic acid sodium salt 2-hydrate (EDTA) was obtained from Panreac (Barcelona, Spain). All reagents were of analytical grade. SGC stock solution of 200 mg l^{-1} was prepared by dissolving the required weight in deionized water; it was kept in the dark under refrigeration at 4 °C and remained stable for at least 3 months. Terbium (III) and EDTA stock solutions of 0.1 and 0.05 M, respectively, were prepared in deionized water.

Required SGC and terbium (III) solutions were prepared daily with suitable dilution in deionized water.

Sephadex-SP C-25 in sodium form, 40–120 μm average particle size, Sephadex-QAE A-25, 40–120 μm average particle size and Sephadex-CM C-25, 40–120 μm average particle size (all from Sigma, Alcobendas, Madrid, Spain), C_{18} bonded phase silica gel beads (Waters, Milford, USA), 55–105 μm of average particle size and Chelex-100 in sodium form, 200–400 mesh (Fluka, Buchs, Switzerland) were tested as sensing supports.

2.2. Instrumentation

Luminescence measurements were performed with a Cary-Eclipse Luminescence Spectrometer (Varian Inc., Mulgrave, Australia), controlled by a computer equipped with a Cary-Eclipse (Varian) software package for data collection and treatment. The phosphorescence mode was used for all analytical measurements. The delay and gate times used were 0.1 and 3 ms, respectively. Instrument excitation and emission slit widths were set at 10 and 20 nm, respectively. The detector voltage was 600 or 650 V depending on the sample volume used.

The SIA system was composed of a Cavro XP 3000 (Cavro Scientific Instruments, Sunnyvale, CA, USA) pump equipped with a 5 ml syringe and a Valco (Valco Instruments Co. Inc., Houston, TX, USA) 10-port selection valve. PTFE tubing of 0.8 mm internal diameter was used in the manifold; the same tubing was also used for the 2 ml holding coil. The system was computer controlled using a home-written software program (Sagittarius version 3.0.25) based on MS Visual Basic 6.0 (Microsoft). The manifold used is shown in Fig. 1.

A Hellma flow cell 176.752-QS (25 μl of inner volume and a light path length of 1.5 mm) was used. The cell was filled with Chelex-100 solid support microbeads, and was blocked at the outlet with glass wool to prevent displacement of the resin particles.

The level of the resin packed in the flow cell had to be carefully established in order to ensure that the upper part of the resin was just in the light path, so obtaining the best sensitivity.

2.3. Preparation of real samples

2.3.1. Pharmaceutical drugs

The pharmaceutical drugs were chosen in several presentations: *eye drops*, *capsules* and *solutions*. The preparation was as follows: 0.5 ml of eye drops or solution was dissolved and diluted with deionized water in a 100 ml volumetric flask; in the case of capsules, ten of them were homogenized and sample solution was prepared by accurately weighing an appropriate amount of the powder and diluted with deionized water to 100 ml in a volumetric flask. In order to obtain a SCG concentration included in the linear dynamic range, working dilutions were prepared with deionized water before measuring.

2.3.2. Urine samples

Urine samples were obtained from healthy volunteers and required no further pre-treatment; only when turbidity was observed, a filtration step was required. The samples were spiked with a suitable SCG concentration, diluted with deionized water and directly inserted in the flow system.

2.4. General SIA procedure

In order to condition the solid support when the flow cell was filled for the first time, 800 μl of the carrier solution (0.05 M sodium acetate/acetic acid solution, pH 5.9) were aspirated into the syringe pump from a reservoir and passed through the sensing zone.

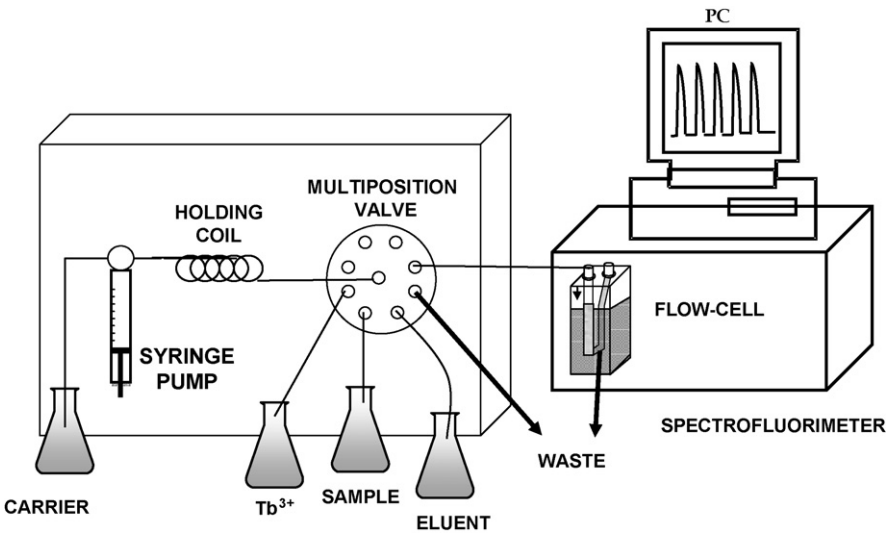

Fig. 1. Configuration of the proposed system.

2.4.1. Drug samples

Two 75 μl aliquots of sample solution and another two 75 μl aliquots of 6×10^{-3} M terbium (III) solution were sequentially aspirated, in double-sandwich mode, into the syringe pump, at a flow-rate of 5 ml min^{-1}. Next, 1 ml of carrier solution was aspirated too. Then, the mix was pumped towards the flow cell at a rate of 1.2 ml min^{-1}, passing previously through the holding coil. Once the signal from terbium (III)–SCG chelate was registered at 336/545 nm ($\lambda_{ex}/\lambda_{em}$), the solid support was regenerated by passing through it 1 ml of 0.05 M EDTA solution (eluent) and 1 ml of carrier solution.

Before a new injection was made, and in order to avoid samples contamination, the portion of tubing still filled with the previous sample was cleaned with 300 μl of the next sample and 500 μl of carrier solution, remaining the system ready for a new injection. This process was also performed at a flow-rate of 5 ml min^{-1}.

2.4.2. Urine samples

In this case, the procedure is the same that above described for drug samples, but the volumes of the aliquots of both sample and terbium (III) solutions injected in the system were 400 μl.

3. Results and discussion

3.1. Selection of the solid support

In lanthanide-sensitized luminescence, the efficiency of the energy transfer between the analyte (ligand) and the lanthanide ion is governed by the nature of the ion, the ligand, the ligand–ion bond and the solvent. The energy gap between the excited and ground-state levels of the lanthanide ion and the rigidity of the molecular structure also contribute to the enhancement of the luminescence intensity of the system. Therefore, a careful selection of the solid support used for the sorption of the terbium (III)–SGC chelate provides the required rigidity of the system, avoiding the use of surfactants.

As expected, the most suitable type of solid support for the retention of terbium (III)–SCG chelate should be of cationic nature due to its probable positive charge. However, solid supports of different nature were tested: three cationic exchangers (Sephadex-SP C-25, Sephadex-CM C-25 and Chelex-100); one anionic exchanger (Sephadex QAE A-25); and one non-ionic support, silica gel C_{18}.

Different procedures were tested for the formation of the chelate between terbium (III) and the analyte: (a) on-line: sequential aspiration of terbium (III) and sample solutions into the holding coil, or aspiration of both solutions in a sandwich mode, using a holding coil and (b) off-line: direct addition of terbium (III) solution to the sample solution.

The three described procedures were tested for each solid support tested. No signal was observed for the anionic and non-ionic solid supports. In the case of the cationic supports, the best analytical signal was obtained when using Chelex-100 (an enhancement close to 80% in the signal). Hence, this last one was chosen as the optimum solid support for the sensing zone.

Usually, the use of surfactants and enhancing reagents, such as trioctylphosphine oxide, is required in order to provide rigidity to the system and to complete the coordination sphere of Tb (III). However, the use of the solid support allows to obtain similar sensitivity and to avoid these additional compounds.

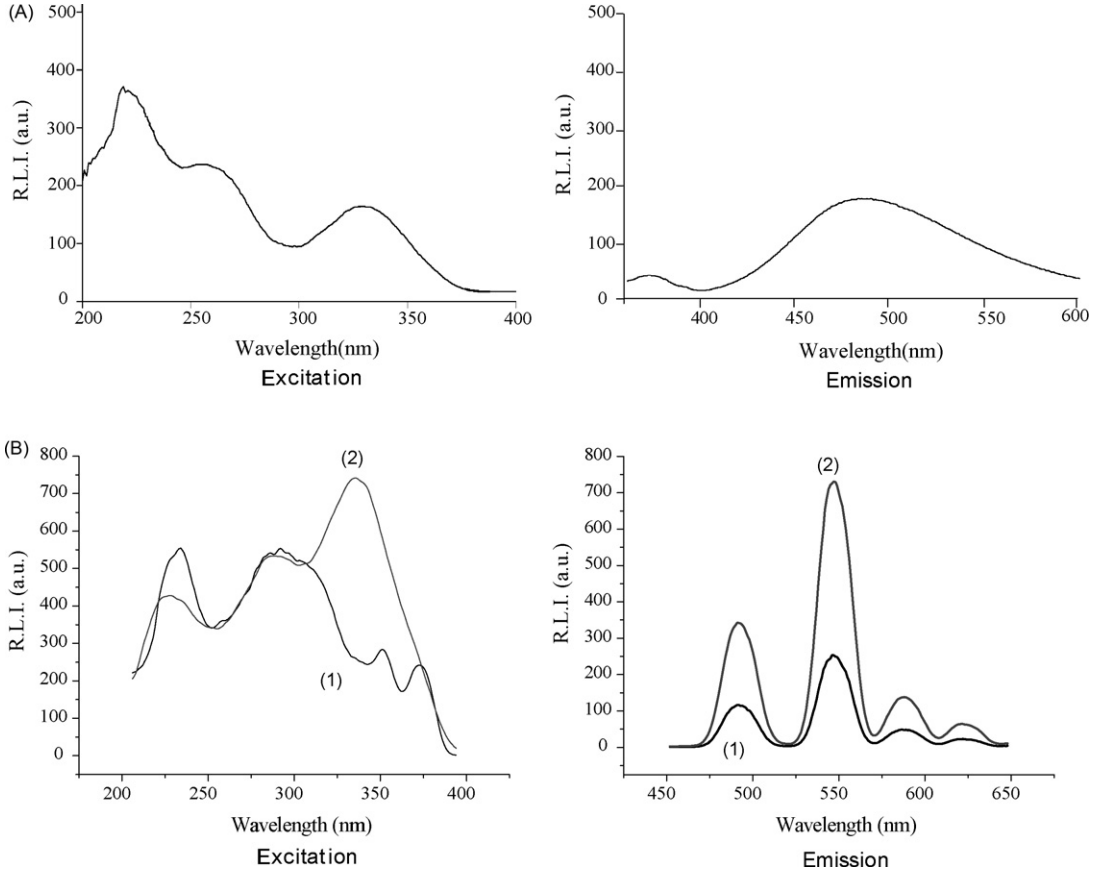

Fig. 2. (A) Fluorescence excitation and emission spectra of 5 mg l^{-1} SCG, in aqueous solution. (B) Delayed luminescence excitation and emission spectra, on the solid support, of: (1) 6×10^{-3} terbium (III) and (2) chelate between 6×10^{-3} terbium (III) and 1.2 mg l^{-1} SCG (800 μl sample volume).

3.2. Instrumental variables

As it has been previously stated, the excitation and emission wavelengths correspond to the analyte and terbium ion, respectively. To select the optimum wavelengths, the fluorescence spectra of SCG together with the delayed luminescence spectra of terbium (III) and terbium (III)–SCG chelate retained on the solid support, were recorded. These spectra are all shown in Fig. 2.

As shown in Fig. 2A, SCG presents two main excitation bands, at 230 and 336 nm, and one emission band at 485 nm. These excitation bands are also present in the excitation spectrum of the Tb (III)–SCG chelate, which is consistent with the energy transfer process from SCG to terbium (III) (Fig. 2B). Although the SCG fluorescence excitation band placed at 230 nm is more intense than the one at 336 nm (Fig. 2A) the net signal between the chelate and terbium (III) is higher when recording the spectrum at 336 nm (Fig. 2B); in addition, the solid support signal is also higher at 230 nm. Hence, 336 nm was selected as the optimum excitation wavelength.

On the other hand, three emission bands characteristic of terbium (III) can be observed around 490, 545 and 590 nm, corresponding to the $^5D_4 \rightarrow {}^7F_6$, $^5D_4 \rightarrow {}^7F_5$ and $^5D_4 \rightarrow {}^7F_4$ transitions, respectively [15]. These bands are the same for the terbium (III)–SGC chelate (Fig. 2B). The most intense band is that situated at 545 nm and, consequently, it was chosen for the measurement of the emission.

The excitation and emission slit widths were tested in the range 5–20 nm, observing that the increase of the slit widths provided a higher net signal (the chelate terbium (III)–SGC signal minus the terbium (III) signal). On the other hand, the influence of the photomultiplier tube voltage was also studied in the range 425–700 V. In both cases, the optimum values were selected as a compromise between the highest sensitivity and the lowest blank signal (the terbium (III) signal plus the chelate signal). They are shown in Table 1.

Finally, the delay and gate times (instrumental variables available when measuring in the phosphorescence mode) were also optimized. The net signal increased when increasing the gate time and decreased when increasing the delay time. The values selected for these variables were 3 and 0.1 ms, respectively.

3.3. Chemical variables

3.3.1. Selection of the carrier solution

The pH of the carrier solution was investigated in the range 2.0–8.0. pH values above 8.0 caused the hydrolysis of terbium (III) and its precipitation. The highest net signal was observed in the pH range 5.0–6.5. Two different buffer solutions, acetate and phosphate, were tested in this pH range at several concentrations (0.01–0.2 M). For both solutions, an increase in the concentration, and consequently in the ionic strength, caused decreasing analytical signals, due to the elution of the chelate terbium (III)–SGC from the solid support. Finally, a 0.05 M sodium acetate/acetic acid solution (pH 5.9) provided the best sensitivity and repeatability.

Table 1
Analytical parameters.

Parameter	Sample volume	
	150 μl	800 μl
Excitation/emission slits (nm/nm)	10/20	10/20
Photomultiplier tube voltage (V)	650	600
Blank signal	290	245
Linear dynamic range (mg l^{-1})	0.2–4	0.05–2
Detection limit (mg l^{-1})	0.06	0.015
Quantitation limit (mg l^{-1})	0.2	0.05
RSD (%) (n = 10)	1.8[a]	1.6[b]
Sampling frequency (h^{-1})	12	11

[a] SCG concentration, 1 mg l^{-1}.
[b] SCG concentration, 0.4 mg l^{-1}.

3.3.2. pH of sample solution

In the same way as previously described for the carrier solution, the pH of the sample solution was also studied. The maximum signal was obtained in the pH range 4.0–7.5. Higher or lower pH values caused a decrease in the signal due to a worse buffering capacity of the carrier. Therefore, it is not necessary to adjust the pH of the sample solution except in the cases in which this one is out of the optimum pH range. For this reason, before measuring the samples their pH was checked.

3.3.3. Terbium solution concentration

The concentration of the terbium (III) solution was also tested, as it was critical for the analytical signal. This study was performed for a SCG concentration within the high part of the linear dynamic range. Terbium (III) concentration was tested from 5×10^{-5} up to 8×10^{-3} M, observing that the signal increased up to a concentration 6×10^{-3} M and then remained constant. Hence, this value was selected as the optimum one.

3.3.4. Selection of the eluent

Although the carrier solution itself caused a slow elution of the terbium (III)–SGC chelate, an eluting solution had to be used to get a rapid regeneration of the solid support after the measurement. An EDTA solution was selected for this purpose. A ternary chelate, probably of anionic nature, between terbium (III), EDTA and SCG is formed and desorbed from the solid support. Different volumes and concentrations of EDTA solution were tested, finally choosing 1000 μl of 0.05 M EDTA solution for the complete regeneration of the sensing zone.

3.4. SIA variables

Before optimizing the SIA variables, the best procedure for the formation of the chelate between terbium ion and SCG had to be decided. Taking into account one of the main goals of this paper was to provide complete automation; different approaches were studied for making the formation of the chelate on-line instead of off-line. Although the reaction between terbium and SCG is produced instantaneously, the mixture between both solutions was not homogenous using just the holding coil. Therefore, two different strategies were employed: (a) sequential aspiration of terbium and SCG solutions into the holding coil and using a reactor placed before the flow-through cell; (b) aspirating several aliquots of terbium and sample solution sequentially into the holding coil.

The second strategy provided better results in terms of speed (10% higher) and sensitivity (15% higher) therefore it was the selected one. In addition, two different approaches were studied here: (a) sandwich mode: terbium–SCG–terbium; (b) aspirating two aliquots of each solution: terbium–SCG–terbium–SCG. This second mode provided the best sensitivity, as the mixture between both solutions was clearly favored. Hence, the "double-sandwich" mode was employed.

The effect of the SIA variables was also evaluated: volume of solutions (sample, carrier and eluting solution) and flow-rate.

3.4.1. Volume of solutions

When increasing the volume of the sample aspirated, the amount of chelate sorbed on the resin also increases; this increase makes the analytical response higher and, thus, the sensitivity is improved. However, the sampling frequency diminishes with the volume increase, making it necessary to adopt a compromise solution. The sample volume was varied from 100 up to 1200 μl, noticing that the analytical signal increased linearly only

up to 800 μl. Therefore, 150 and 800 μl were the volumes used for pharmaceuticals and urine samples, respectively. These volumes produced the required sensitivity, as long as obtaining a higher sampling frequency in the case of pharmaceuticals.

The volumes of carrier and EDTA solutions were also studied, obtaining as optimum values for the complete regeneration of the sensing zone 1 ml for each solution. In the case of terbium the same volumes of sample and terbium solutions were used depending on the applications, i.e., 150 or 800 μl for pharmaceuticals or urine samples, respectively.

3.4.2. Flow-rate

The flow-rate was investigated from 0.4 up to 1.8 ml min^{-1} (using an 1 mg l^{-1} SGC solution). By increasing it, the sampling frequency increased but the analytical signal decreased and the possibility of overpressures in the system has to be taken into account too. The signal was observed to decrease very slightly up to 1.2 ml min^{-1}; hence, this last one was the chosen flow-rate as a compromise between sensitivity and sample-throughput. The flow-rate employed for solutions' aspiration into the syringe pump and holding coil was 5 ml min^{-1}.

3.5. Figures of merit

Taking into account the optimized conditions, the analytical parameters of the system were studied for two different sample volumes, 150 and 800 μl (Table 1). The proposed methodology was able to produce analytical fits with good linearity in the range 0.2–4 and 0.05–2 mg l^{-1}. The data were fitted by standard least-squares calibration.

The repeatability was established for ten independent analyses of sample solutions, obtaining RSDs lower than 2% for both calibration volumes. The detection limit was estimated as the concentration of analyte which produced an analytical signal equal to three times the standard deviation of the background luminescence [18]. A detection limit as low as 0.015 mg l^{-1}, when using 800 μl sample volume, was obtained. The quantitation limit (K = 10) [19] and the sampling frequency were also evaluated. The solid support used allowed making at least 150 determinations before replacing it.

3.6. Interference study

Since the determination of SCG was carried out in both pharmaceuticals and human urine, the possible interference from different organic and inorganic species which can be found along with the analyte in these samples was tested. This study was performed by adding different amounts of the possible interfering species to a solution containing 400 ng ml^{-1} of SCG. A foreign species was considered not to interfere if it produced an error smaller than $\pm 2\sigma$ in the analytical signal, being σ the standard deviation. If any interference was observed, the ratio interfering species:analyte (w:w) was reduced progressively until this interference ceased.

In the case of pharmaceuticals, the excipients tested were lactose, saccharose, glucose and starch, obtaining tolerated interfering species/analyte ratios (w/w) higher than 1000. For biological fluids, the tolerated ratios were also above 1000 for Na^+, K^+, NH_4^+, Cl^-, I^-, and NO_3^-; above 400 for urea, Mg^{2+} SO_4^{2-} and PO_4^{3-}; above 80 for Ca^{2+}, CO_3^{2-} and uric acid; and 3 for Cu^{2+} and Fe^{3+}. In all cases, the tolerated ratios observed were higher than the ones normally found in real samples. Checking all these values, Cu^{2+} and Fe^{3+} are the species with higher interference effect. Nevertheless, their levels in urine are lower than the tolerated ratio, making it possible to determine SCG in this matrix with the proposed system. By comparing the tolerated ratios of Cu^{2+} and Fe^{3+} obtained in homogenous solution with the ratios observed in solid phase, we found that the use of the sensing zone enhanced the tolerance to these metals a hundredfold. For this reason, it would not be possible to perform the determination of SGC in homogenous solution without a previous elimination of both species.

It is worthy mentioning that this increase in the selectivity is mainly achieved by the use of the solid support, since it allows the discrimination between terbium (III)–SCG chelate and the possible interfering species in the sorption on the solid support.

Table 2
Determination and recovery study in pharmaceutical preparations.

Pharmaceutical	Added (mg ml^{-1})	Recovery (%)	RSD (%)[a]
Cusicrom fuerte (Ltd. Cusí)[b]	–	102	0.8
	20	104	2.1
	40	97	1.5
	60	103	1.2
Frenal Compositum (Ltd. Sigma-tau)[c]	–	103	1.5
	10 mg	103	2.2
	20 mg	101	1.8
	40 mg	97	1.6
Cusicrom fuerte (Ltd. Alcon)[d]	–	98	2.4
	25	97	2.2
	50	104	1.2
	75	99	0.7

[a] Means of three determinations.
[b] 40 mg ml^{-1}.
[c] 20 mg per capsule.
[d] 40 mg ml^{-1}.

3.7. Analytical applications

Following the procedure previously described, the proposed optosensor was applied to the determination of SCG in both pharmaceuticals and human urine.

Pharmaceutical samples, prepared as described under Section 2.3, were introduced by triplicate into the system. Three pharmaceuticals available in the Spanish Pharmacopoeia were analyzed: capsules (*Frenal compositum*), a solution (*Cusicrom fuerte*) and eye drops (*Cusicrom fuerte*). In all cases, the SCG amounts determined by the proposed method were in good agreement with those ones provided by the manufacturer. In order to evaluate the accuracy of the method, a recovery study was also performed by adding three different levels of SGC concentration to the tested pharmaceuticals. The results obtained are shown in Table 2, with recoveries ranging from 97 up to 104% and RSDs lower than 3% in all cases.

In the case of urine samples, since SGC was not detected in the samples coming from healthy volunteers, a recovery study was carried out. Four different samples were spiked with known amounts of SGC (ranging from 0.5 up to 12 μg ml^{-1}) and then, the required dilutions with deionized water were made. The spiked amounts of SCG in human urine were those providing the expected concentrations after administration of the pharmaceutical [2]. Satisfactory recoveries were obtained in all cases (Table 3) demonstrating the applicability of the proposed method.

3.8. Conclusions

For the first time, a spectroscopic method has been developed for the determination of SCG. By means of using sequential injection analysis, the proposed method presents a complete automation, making it suitable for routine determination of the analyte. In addition, the employment of the solid support in the flow-through cell, as long as a highly selective and sensitive determination technique, terbium-sensitized luminescence, makes it possible to determine

Table 3
Recovery study in urine.

Sample	Spiked ($\mu g\,ml^{-1}$)	Found ($\mu g\,ml^{-1}$)	Recovery (%) ±RSD[a]
Urine-1	1	1.02	102 ± 2
	2	2.10	105 ± 2
	4	3.90	98 ± 1
Urine-2	0.5	0.52	104 ± 3
	1	1.07	107 ± 2
	2	1.94	97 ± 2
Urine-3	5	5.15	103 ± 1
	10	9.60	96 ± 1
	12	12.50	104 ± 2
Urine-4	3	2.90	97 ± 1
	6	6.06	101 ± 2
	8	7.80	98 ± 1

[a] Means of three determinations.

SCG not only in pharmaceuticals, but also in human urine at the levels normally found in patients after the drug administration. The employment of the solid support provides also the required rigidity to the system, making the use of surfactants unnecessary and, therefore, allowing the development of environmental friendly methodologies. The recovery study performed in human urine demonstrates the accuracy and selectivity of the method, requiring no pre-treatment for the samples. These results allow the easy and rapid analysis of SCG using a non-costly analytical instrumentation.

Acknowledgment

The authors are grateful to the "Consejería de Innovación, Ciencia y Empresa (Junta de Andalucía)", Project P07-FQM-02673, for financial support.

References

[1] Z. John Lin, R. Abbas, L.M. Rusch, L. Shum, J. Chromatogr. B 788 (2003) 159.
[2] M. Lindström, J. Olof Svensson, L. Meurling, K. Svartengren, M. Anderson, M. Svartengren, Respir. Med. 98 (2004) 9.
[3] K. Mawatari, S. Mashiko, Y. Sate, Y. Usui, F. Ilinuma, M. Watanabe, Analyst 122 (1997) 715.
[4] G.G. Shapiro, P. Konig, Pharmacotherapy 5 (1985) 156.
[5] G.F. Moss, K.M. Jones, J.T. Ritchie, J.S. Cox, Toxicol. Appl. Pharmacol. 24 (1972) 525.
[6] V. Kocic-Pesic, D. Radulovic, D. Pecanac, L. Zivanovic, Farmaco 47 (1992) 1563.
[7] K. Brown, J.J. Gardner, W.J.S. Lockley, J.R. Preston, D.J. Wilkinson, Ann. Clin. Biochem. 20 (1983) 31.
[8] F.C. Pereira, A.G. Fogg, M.V.B. Zanoni, Talanta 60 (2003) 1023.
[9] O.A. Aswania, S.A. Corlett, H. Chrystyn, J. Chromatogr. B 690 (1997) 373.
[10] M.L. Ozoux, J. Girault, J.M. Malgouyat, O. Pasquier, J. Chromatogr. B 765 (2001) 179.
[11] J. Ruzicka, G.D. Marshall, Anal. Chim. Acta 237 (1990) 329.
[12] C. Frank, F. Schroeder, R. Ebinghaus, W. Ruck, Talanta 70 (2006) 513.
[13] A. Molina-Díaz, A. Ruiz-Medina, M.L. Fernández-de Córdova, J. Pharm. Biomed. Anal. 28 (2002) 399.
[14] A. Domínguez-Vidal, P. Ortega-Barrales, A. Molina-Díaz, Talanta 56 (2002) 1005.
[15] N. Arnaud, J. Georges, Analyst 124 (1999) 1075.
[16] E.J. Llorent-Martínez, P. Ortega-Barrales, A. Molina-Díaz, Anal. Biochem. 347 (2005) 330.
[17] N. Arnaud, J. Georges, Anal. Chim. Acta 476 (2003) 149.
[18] IUPAC, Spectrochim. Acta B 33 (1976) 241.
[19] D. MacDougall, W.B. Crummett, et al., Anal. Chem. 52 (1980) 2242.

Talanta 79 (2009) 975

Contents lists available at ScienceDirect

Talanta

journal homepage: www.elsevier.com/locate/talanta

Corrigendum

Corrigendum to "Fractionation analysis of oxyanion-forming metals and metalloids in leachates of cement-based materials using ion exchange solid phase extraction" [Talanta 78 (2009) 736–742]

Mesay Mulugeta[a], GretheWibetoe[a,*], Christian J. Engelsen[b], Walter Lund[a]

[a] *Department of Chemistry, University of Oslo, P.O. Box 1033, Blindern, N-0315 Oslo, >Norway*
[b] *SINTEF Building and Infrastructure, P.O. Box 124, Blindern, N-0314 Oslo, Norway*

The authors regret that Figs. 5 and 6 of their paper and the accompanying discussion give partly wrong information for the leachates pH-adjusted with HNO_3. In a continuing study relevant to this paper, the authors identified that NO_3^- from the addition of HNO_3, affected the retention of anionic analyte species more than expected based on the evaluation reported in the published paper. However, the author's continuing study indicated that the developed method can still be used for the outlined objective with some procedural adjustments. The authors also emphasize that the procedure presented in this paper is valid for leachates not treated with HNO_3. The effect of NO_3^- on the analytes' retention and the procedural adjustments will be described in the continuing study together with method applications on other leachate samples than those analysed in the published paper.

The authors would like to apologise for any inconvenience this may have caused to the readers of the paper.

DOI of original article: 10.1016/j.talanta.2008.12.036.
* Corresponding author. Tel.: +47 22855516; fax: +47 22855441.
E-mail address: grethe.wibetoe@kjemi.uio.no (GretheWibetoe).

0039-9140/$ – see front matter
doi:10.1016/j.talanta.2009.04.011

Talanta 79 (2009) 723–729

Contents lists available at ScienceDirect

Talanta

journal homepage: www.elsevier.com/locate/talanta

Inductively coupled plasma–optical emission spectrometry/mass spectrometry for the determination of Cu, Ni, Pb and Zn in seawater after ionic imprinted polymer based solid phase extraction

Jacobo Otero-Romaní [a], Antonio Moreda-Piñeiro [a], Pilar Bermejo-Barrera [a,*], Antonio Martin-Esteban [b]

[a] Department of Analytical Chemistry, Nutrition and Bromatology, Faculty of Chemistry, University of Santiago de Compostela, Avenida das Ciencias, s/n, 15782 Santiago de Compostela, Spain
[b] Department of Environment, National Institute for Agriculture and Food Research (INIA), Carretera de A Coruña, Km 7,5, 28040 Madrid, Spain

ARTICLE INFO

Article history:
Received 16 January 2009
Received in revised form 23 April 2009
Accepted 28 April 2009
Available online 9 May 2009

Keywords:
Ionic imprinted polymer
Copper
Nickel
Lead
Zinc
Seawater
Solid phase extraction
Inductively coupled plasma–optical emission spectrometry
Inductively coupled plasma–mass spectrometry

ABSTRACT

The capabilities of a synthesized ionic imprinted polymer (IIP), originally prepared for Ni recognition/pre-concentration from seawater, have been evaluated for other trace elements pre-concentration. The polymer has been synthesized by the precipitation polymerization technique using a ternary pre-polymerization complex formed by the template (Ni), the monomer (2-(diethylamino) ethyl methacrylate, DEM) and a non-vinylated chelating agent (8-hydroxyquinoline, 8-HQ). Since the complexing agent (8-HQ) is trapped into the polymeric matrix, but is not linked to the polymer chains, specific interactions between the functional groups (present in the monomer and the complexing agent) and other trace elements rather than Ni may occur.

Results have shown that the IIP offers imprinting properties for the template (Ni(II)) and also for Cu(II), Pb(II), Zn(II), As(V) and Cd(II), with analytical recoveries close to 100% for all elements except for As(V) and Cd(II) (around 70%), whereas the non-imprinted polymer (NIP) did not show affinity for any trace element. In addition, the polymer does not interact with alkaline or alkaline-earth metals, so Na, K, Mg and Ca from the seawater salt matrix could be effectively removed. Variables affecting the IIP-solid phase extraction (SPE) process (pH, load flow rate and concentration and volume of the eluting solution) were completely studied. Inductively coupled plasma–optical emission spectrometry (ICP-OES) and inductively coupled plasma–mass spectrometry (ICP-MS) have been used as multi-element detectors.

Acidified seawater samples must only be treated to fix an alkaline pH (8.5 ± 0.5) and passed through IIP-SPE cartridges. After seawater sample loading (250 mL), analytes were eluted with 2.5 mL of 2.0 M nitric acid, offering a pre-concentration factor of 100. Therefore, the limits of detection (LODs) of the method were 0.14, 0.15, 0.18 and 0.03 $\mu g\,L^{-1}$, for Ni, Cu, Pb and Zn, respectively, when using ICP-OES detection and 0.0022, 0.0065, 0.0040 and 0.009 $\mu g\,L^{-1}$, for Ni, Cu, Pb and Zn, respectively, for ICP-MS detection. Accuracy of the method was assessed by analyzing SLEW-3 (estuarine water), and TM-23.3 and TM-24 (lake water) certified reference materials.

1. Introduction

The protection of marine and continental waters against contamination has increased in recent years to allow adequate conditions for aquatic life and a responsible use of such natural resources. The European Union has therefore established several Directives on the quality of continental and marine waters and for marine ecosystems. These European Directives limit the levels of some trace elements such as Ag, As, Cd, Cr, Cu, Hg, Ni, Pb and Zn in seawater used for mollusk production [1]. Therefore, the development of fast and reliable analytical methods to assess trace elements in water is a current topic. This fact is especially important for seawater analysis because of the high salt content which is a source of spectral and matrix interferences [2,3] and because most of the target metals are present at very low levels [4].

Solid phase extraction (SPE) is, by far, one of the most used sample pre-treatments for complex matrices such as seawater, mainly because trace analyte pre-concentration and sample matrix (salts) removal are achieved at time [5]. Bonded silica sorbents are used in typical SPE procedures for organic compound pre-concentration and also for trace elements [6–8]. However, it has been reported that interfering compounds are often co-extracted with the target

* Corresponding author.
E-mail address: pilar.bermejo@usc.es (P. Bermejo-Barrera).

0039-9140/$ – see front matter © 2009 Elsevier B.V. All rights reserved.
doi:10.1016/j.talanta.2009.04.066

analytes and a matrix effect can be observed using these conventional sorbents [6]. Therefore, more selective systems for separation of trace elements are required and the development or synthesis of new sorbents has increased in recent years [9]. High selectivity can be expected from sorbents such as inmunosorbents (ISs) and molecularly imprinted polymers (MIPs) [10]. However, the main advantage of MIPs over ISs is the fast and less expensive synthesis and the high degree of molecular recognition. Synthesized sorbents in the presence of ions, instead of molecules, as templates generate ionic imprinted polymers (IIPs), which offer all the benefits derived from MIPs and a high capacity for recognizing ions.

Ionic imprinting polymerization is based on the preparation of a highly cross-linked polymer around an ion (the template) in the presence of a suitable monomer (vinylated reagent) or in the presence of a monomer and an auxiliary/complexing non-vinylated reagent [11,12]. As recently reviewed by Rao et al. [12], there are four different approaches for the synthesis of metal ion imprinted polymers, viz. (i) linear chain polymers carrying metal-binding groups being cross-linked with a bifunctional reagent; (ii) chemical immobilization by preparation of binary complexes of metal ions with ligands having vinyl groups, isolation and then polymerization with matrix-forming monomers; (iii) surface imprinting conducted on an aqueous–organic interface; (iv) trapping of non-vinylated chelating ligand via imprinting of binary/ternary mixed ligand complexes of metal ions with non-vinylated chelating agent and vinyl ligand. The first three approaches use vinylated reagents, which form complexes with the template (metal ion) and can polymerize through the vinyl groups. Therefore, the complexing ligand is chemically immobilized in the polymeric matrix. The main drawback of these approaches is the fact that complexing ligands showing vinyl groups are scarce and are not available, so the synthesis of these complexing monomers must be performed in the laboratory. Some examples of these complexing monomers are those based on amino acids such as methacryloylhistidine (MAH) [9,13], and N-methacryloly-(l)-cysteinemethylester (MAC) [14–16], or N-methacryloyl-L-glutamic acid (MAGA) [17], which have been widely used for recognizing Al [17], Cd [14,15], Cu [13], Fe [16] and Ni [9]. Other ligands such as (2Z)-N,N′-bis(2-aminoethylic)but-2-enediamide for Cd [18] and o-phenylenediamine for Se [19] have also been reported as bifunctional monomers.

The use of specially synthesized vinylated ligands can be avoided when using the trapping technique. In this case, a ternary monomer non-vinylated ligand–metal complex is formed; therefore, the number of useful ligands is large because most of the metal complexing agents are not vinylated reagents. After polymerization, the non-vinylated ligand is not chemically bonded to the polymer chains, but instead is trapped inside the polymeric matrix. By using the trapping approach, different non-vinylated reagents such dimethylglyoxime for recognizing palladium [20], diazoaminobenzene [21] for recognizing mercury, cetyltrimethyl ammonium bromide [22] for recognizing Cd and Zn, and derivatives of quinoline, mainly 5,7-dichloroquinoline-8-ol for lanthanides [23–26], Pd [27], U [28–30] and Co and Ni [31] have been successfully applied.

The aim of the current work has been the study of the capabilities of a synthesized ionic imprinted polymer, originally prepared for Ni recognition/pre-concentration from seawater, for other trace elements pre-concentration. The polymer has been synthesized by the precipitation polymerization technique using a ternary pre-polymerization complex formed by the template (Ni), the monomer (2-(diethylamino) ethyl methacrylate, DEM) and a non-vinylated chelating agent (8-hydroxyquinoline, 8-HQ). Inductively coupled plasma–optical emission spectrometry (ICP-OES) and inductively coupled plasma–mass spectrometry (ICP-MS) have been used as multi-element detectors.

2. Experimental

2.1. Instrumentation

Optima 3300 DV inductively coupled plasma atomic emission spectrometer (PerkinElmer, Norwalk, CT, USA) equipped with an autosampler AS 91 (PerkinElmer) and a Gem-Cone cross-flow nebulizer type (PerkinElmer) was used for multi-elemental determinations. 820-MS inductively coupled plasma quadrupole mass spectrometer (Varian, Mulgrave, Australia) equipped with an SPS3 autosampler (Varian) and a MicroMist nebulizer type (Varian). Temperature-controllable incubation camera (Stuart Scientific, Surrey, UK) equipped with a low-profile roller (Stovall, Greensboro, NC, USA) was used for the polymerization process. Vacuum manifold station (Waters, Milford, MA, USA) connected to a vacuum pump (Millipore Co., Bedford, MA, USA) was used for SPE. IIPs were packed into 5 mL syringes (Brand, Wertheim, Germany) between replacement Teflon frits (Supelco, Bellefonte, PA, USA). ORION 720A plus pH-meter with a glass–calomel electrode (ORION, Cambridge, UK) was used for pH measurements.

2.2. Reagents

Ultra-pure water of resistivity 18 MΩ cm obtained from a Milli-Q purification device (Millipore Co.) was used to prepare all the solutions. 70% nitric acid and analytical grade $NiCl_2{\cdot}6H_2O$ were purchased from Panreac (Barcelona, Spain). Single standard solutions (1000 mg L^{-1}) of Al, As, Cd, Co, Cr, Cu, Fe, Mn, Ni, Pb, Sn, Ti, V and Zn were from Merck (Darmstadt, Germany). Ammonia 25% (v/v), ammonium chloride, and 8-hydroxyquinoline were purchased from Merck. HPLC grade acetonitrile and toluene were obtained from Scharlab (Barcelona, Spain). 2-(diethylamino) ethyl methacrylate (DEM) used as monomer was from Sigma–Aldrich (Steinheim, Switzerland). Divinylbenzene-80 (DVB) from Sigma–Aldrich was treated in order to remove the polymerization inhibitor by passing a few milliliters of the reagent through a mini-column containing around 0.5 g of neutral alumina (Sigma–Aldrich). 2,2′-azobisisobutyronitrile (AIBN) was purchased from Fluka (Buchs, Switzerland). This reagent was purified by crystallization at −20 °C after dissolving the reagent in methanol (Merck) at 50–60 °C. After purification, this reagent was stored at 4 °C. Estuarine seawater (SLEW-3) certified reference material was obtained from the National Research Council of Canada. Lake water (TM-24 and TM-23.3) certified reference materials were purchased from the National Water Research Institute of Canada. All glass and plastic material was rigorously cleaned and kept into 10% (v/v) nitric acid for at least 48 h. The material was then rinsed three times with ultra-pure water before being used.

2.3. Seawater collection

Seawater samples (1 L) were collected from the Ría de Muros-Noia estuary (north-western Spain) in pre-cleaned high density polyethylene bottles. After collection, seawater samples were filtered through 0.45 μm polycarbonate membrane Nucleopore filters (Millipore) and then acidified at a pH lower than 2.0 by adding 1.0 mL of concentrated nitric acid in order to avoid metal adsorption onto the inner bottle walls. Acidified seawater samples were then stored at low temperature.

2.4. ICP-OES/MS measurements

Multi-element determinations (As, Cd, Cu, Ni, Pb and Zn) were performed by ICP-OES (axial configuration) using the operating conditions and emission wavelength lines given in Table 1. Determinations were performed by using aqueous standards in 2.0 M nitric

Table 1
Operating ICP-OES conditions.

General		
	Radiofrequency power/W	1300
	Sample uptake rate/mL min^{-1}	1.5
	Stabilization delay/s	45
	Number of replicates	4
	Integration time/s	5
	Nebulizer type	Cross-flow
	Axial view	
Gas flows/L min^{-1}		
	Plasma	15.0
	Auxiliary	0.5
	Nebulizer	0.8
Detection wavelengths/nm		
	Cu	327.393
	Ni	231.604
	Pb	224.688
	Zn	213.857

acid covering metal concentrations within the 0–0.25 mg L^{-1} range for As, Cd, Cu, Ni and Pb, and between 0 and 1.0 mg L^{-1} for Zn.

Similarly, As, Cd, Cu, Ni, Pb and Zn were measured by ICP-MS under operating conditions listed in Table 2. The use of H_2 in the collision cell at a flow rate of 80 mL min^{-1} gave the best sensitivity as well as minimised possible polyatomic interferences for the target elements [32]. This flow was optimized by monitoring the counts for a 2.0 M nitric acid eluate containing the target elements. Finally, determinations were performed by using aqueous standards in 2.0 M nitric acid with metal concentrations from 0 to 0.25 mg L^{-1} (As, Cd, Cu, Ni and Pb) and Zn concentrations from 0 to 1.0 mg L^{-1}.

Table 2
Operating ICP-MS conditions.

General		
	Radiofrequency power/W	1400
	Sample uptake rate/r.p.m.	3.0
	Stabilization delay/s	35
	Number of replicates	3
	Integration time/s	5
	Nebulizer type	MicroMist
Gas flows/L min^{-1}		
	Plasma	17.0
	Auxiliary	1.65
	Sheath	0.27
	Nebulizer	0.99
Torch alignment/mm		
	Sampling death	7.0
Ion optics/V		
	First extraction lens	−32
	Second extraction lens	−164
	Third extraction lens	−231
	Corner lens	−206
	Mirror lens right	25
	Mirror lens left	24
	Mirror lens bottom	27
	Entrance lens	3
	Fringe Bias	−4.9
	Entrance plate	−3.4
	Pole bias	0
CRI/mL min^{-1}		
	Skimmer gas source	H_2
	Sampler gas source	OFF
	Skimmer flow	80
	Sampler flow	0
Mass-to-ratio		
	Cu	63
	Ni	60
	Pb	208
	Zn	66

2.5. Synthesis of nickel ionic imprinted polymer particles

0.0334 g of $NiCl_2{\cdot}6H_2O$, 56.5 μL of DEM and 0.0817 g of 8-HQ were mixed in 12.5 mL of porogen (3:1 acetonitrile:toluene). This solution was stirred for 5 min and then filtrated. Finally, 500 μL of DVB (cross-linker) and 41.3 mg of AIBN (initiator) were added, the glass tubes purged with N_2 and immediately sealed just before thermal induction of the precipitation polymerization. The temperature was ramped from room temperature to 60 °C over 2 h, and then maintained at 60 °C for further 24 h. Always, a low stirring rate of 33 r.p.m. was used. The polymer was vacuum filtered, washed with acetonitrile and then oven-dried overnight at 40 °C. Finally, the polymer (around 300 mg) was packed into 5 mL cartridges between Teflon frits. It should be mentioned that the polymer was synthesized in the presence of a double amount of 8-HQ with respect to DEM. This gives a Ni/DEM/8-HQ molar ratio of 1/2/4. The mass of polymer obtained after polymerization was 0.300 g and the efficiency of the polymerization process, taking into account a theoretical amount of synthesized polymer of 0.5 g, was 60%. The template (Ni(II) ions) was removed from the polymer particles by extensive washing with 2.0 M nitric acid (5.0 mL aliquots). Negligible nickel (template) concentrations by ICP-MS in the washing/filtrate solutions were found after passing 50 mL of the washing solution. Blank polymer particles (non-imprinted polymer, NIP) were also prepared in the same way than IIP, but without the template. The NIP was then subjected to the same washing pretreatment as described above.

The synthesized materials (IIP and NIP) were characterized by scanning electron microscopy (SEM), energy dispersive X-ray fluorescence (EDXRF) and microanalysis (elemental H, C, N and O composition). This information is given elsewhere [35].

2.6. IIP-solid phase extraction

Multi-element aqueous standard solutions were prepared in 100 or 250 mL of 0.1 M/0.1 M NH_4Cl/NH_3 buffer solution at pH 8.5 ± 0.5. Similarly, 100 or 250 mL of acidified seawater samples were treated with volumes of a 5.0 M ammonia solution (with the 100–500 μL range), to readjust the pH to 8.5 ± 0.5. Then, the solutions were passed through cleaned and conditioned IIP cartridges at a flow rate of 3.0 mL min^{-1} by using a vacuum manifold station. The cartridges were then rinsed with 2.5 mL of the 0.1 M/0.1 M NH_4Cl/NH_3 buffer solution at pH 8.5 ± 0.5, and then, the retained ions were subsequently eluted with two 1.25 mL aliquots of 2.0 M nitric acid solution at a flow rate of 1.5 mL min^{-1}. A pre-concentration factor of 40 or 100 was achieved under these operating conditions. After elution, the IIPs were treated with 10 mL of Milli-Q water and then conditioned by passing 10 mL of the 0.1 M/0.1 M NH_4Cl/NH_3 buffer solution at the working pH (8.5).

Blanks of the procedure were also obtained by applying the SPE procedure above described. In this case, around 1 L of Milli-Q water was acidified by adding 1.0 mL of concentrated nitric acid (pH lower than 2), and then 100 mL aliquot samples were treated with the buffer solution to fix the pH 8.5 ± 0.5, and were subjected to the SPE procedure.

3. Results and discussion

3.1. Optimization of trace elements IIP-SPE from seawater

3.1.1. Effect of pH

A set of experiments was carried out by applying the preconcentration procedure (Section 2.6) to 100 mL aliquots of an aqueous solution containing the template, Ni(II), and other metals (Al, As, Cd, Co, Cr, Cu, Fe, Mn, Pb, Sn, Ti, V and Zn) at 50 μg L^{-1} each

one. The same experiments were carried out by using the NIP. The different pHs tested (from 4.0 to 9.0) were fixed by using 0.1 M/0.1 M NH_4Cl/NH_3 buffer solutions.

Three replicate SPE were performed at each pH and after ICP-OES detection, the polymeric material offered specific interactions for Ni and also for Cu(II), Pb(II), Zn(II), As(III) and Cd(II) since the analytical recoveries for the non-imprinted polymer are quite lower than when using the IIP for most of the tested pHs. Other trace elements were not specifically retained at any pH.

Fig. 1 shows the effect of the pH on the analytical recovery of Ni, Cu, Pb, Zn, As and Cd after IIP/NIP-SPE. It can be observed that Ni and Zn are only quantitatively retained in the IIP at pHs in-between 8.0 and 9.0, whereas Cu and Pb are quantitatively retained at all tested pHs. As and Cd show analytical recoveries near 70% at all pHs tested.

The fact that other ions in addition to the template (Ni(II)) interact with the specific cavities formed for nickel must be explained keeping in mind the presence of the non-vinylated agent (8-HQ). After polymerization, this agent is trapped into the polymeric matrix and the specific cavities formed for nickel during the polymerization are influenced by the presence of 8-HQ which can interact with other ions, although the shape and/or size of such ions was different to the template. The pre-concentrating capacities of the synthesized polymer for Ni(II), Cu(II), Pb(II) and Zn(II) are in agreement with other pre-concentration studies based on resins-immobilized 8-HQ, such as those reported by Howard et al. for silica-immobilized 8-HQ [33], and by Askun et al. for 8-HQ anchored poly(styrene-divinylbenzene) microbeads [34]. For both supports, the same divalent trace elements (Cu, Ni and Zn [33], and Pb, Cd, Ni and Co [34]) were selectively pre-concentrated. This selectivity must be related to a metal complexation with the immobilized 8-HQ because many elements are complexed with 8-HQ in solution [6]. Therefore, the "flexibility" of the imprinting cavities, attributed to 8-HQ, gives the possibility of using this IIP for the selective pre-concentration of a certain number of elements: Cu, Ni, Pb and Zn. From the previous studies (Fig. 1), a compromise pH of 8.5 ± 0.5 was chosen to achieve the highest analytical recovery for this group of elements.

3.1.2. Effect of the load flow rate

Different experiments were performed in order to find the optimum load flow rate for the sample solutions. Different aliquots from the same seawater sample were passed subsequently at 1.5, 3.0, 6.0 and 12 mL min^{-1}. The flow rates were fixed by using a vacuum manifold station. Results have shown the same As, Cd, Ni and Zn concentrations for all flow rates tested; however, Cu and Pb concentrations decrease for flow rates larger than 3 mL min^{-1}. In order to achieve the highest analytical recovery in the lowest period of time, a 3 mL min^{-1} load flow rate was chosen, and used for further experiments.

3.1.3. Effect of nitric acid volume/concentration for elution

Different experiments were performed in order to find the optimum nitric acid concentration/volume for the eluting solution. After sample loading and rinsing (Section 2.6), the retained analytes were eluted by passing volumes of 2.5 mL of nitric acid at concentrations of 1.0, 2.0, 3.0, 4.0 and 5.0 M at a flow rate of 1.5 mL min^{-1}. After measuring by ICP-OES against an aqueous calibration in 1.0, 2.0, 3.0, 4.0 or 5.0 M nitric acid, quantitative analytical recoveries were obtained for all cases; thus, an eluting solution of 2.0 M nitric acid was selected for further studies.

Regarding the volume of the eluting solution, volumes of 2.5 and 3.0 mL of a 2.0 M nitric acid solution were tested. Experiments in triplicate at a fixed flow rate of 1.5 mL min^{-1} have shown that an efficient metal elution is reached under both nitric acid volumes, although the elution process must be done in two steps. Therefore, analytes were eluted subsequently with two 1.5 mL aliquots (3.0 mL of the eluting solution) or 1.25 mL aliquots (2.5 mL of the eluting solution). In order to achieve the highest pre-concentration factor, an eluting volume of 2.5 mL was chosen (pre-concentration factor of 100 for a seawater sample volume of 250 mL).

3.2. Effect of major components from seawater

Different experiments were carried out to observe interactions between the polymeric material and the major metals present in seawater (Na^+, K^+, Ca^{2+}, Mg^{2+}, Cl^- and SO_4^{2-}). To check possible interaction of the major cations, a seawater sample was subjected eleven times to the proposed procedure and the concentrations of major ions were determined by ICP-OES. After pre-concentration (factor pre-concentration of 100), values around 30, 2, 10 and 5 mg L^{-1} were found for Na, K, Mg and Ca, respectively. These concentrations are very low taking into account the concentration of such elements in seawater (around 11490, 399, 1293 and 413 mg L^{-1}, for Na, K, Mg and Ca, respectively [4]).

To check possible retention of chloride and sulphate, a seawater sample was subjected eleven times to the proposed procedure (pre-concentration factor of 100) and the nitric acid eluates were measured by ICP-MS (m/z ratios of 32 and 35 for sulphur and chlorine, respectively). Negligible signals for both analytes were obtained, which means they are not retained in the polymeric matrices or that potential polyatomic interferences are avoided by using collision cell. Therefore, it can be concluded that salt matrix is efficiently removed while a selective pre-concentration of Ni, Cu, Pb and Zn is achieved.

3.3. Cross-reactivity

Different experiments were conducted in order to evaluate the cross-reactivity among nickel and other selected trace elements (Al, As, Cd, Cr, Cu, Mn, Pb, Sn, Ti, V, and Zn). 100 mL aliquots of an aqueous standard solution at pH of 8.5 ± 0.5 containing 50 μg L^{-1} of nickel and other trace metals were subjected three times to the optimized SPE procedures by using cartridges prepared with IIP and NIP materials. After elution and ICP-OES measurements, parameters such as extraction efficiency, distribution ratio (D) and selectivity coefficient ($S_{Ni/M}$), defined as shown in Table 3, were calculated. As it was expected, results (Table 3) show that the polymeric material (IIP) does not discriminate between Ni, Cu, Pb and Zn, as they remain linked to the polymer (percent extraction higher than 99%) and only detach after acidic elution. It can be concluded that the polymer offers imprinting properties for Ni (the template) and also for Cu, Pb and Zn whereas the NIP material did not show affinity for Ni, Cu, Pb or Zn (percent extraction within 10–27%), indicating that those specific cavities formed for nickel during the IIP polymerization are responsible of Ni, Cu, Pb and Zn retention. The IIP material is specific for Ni, Cu, Pb and Zn, and other transition metals (Cr, Sn, Ti, V, As, Cd, Mn and Al) are not retained.

3.4. Analytical performances for the IIP-SPE–ICP-OES/MS procedures

3.4.1. Calibration. Evaluation of matrix effect

Three different calibration graphs were performed: (1) external aqueous calibrations in 2.0 M nitric acid; (2) standard addition calibrations, obtained after spiking a pool of nitric acid eluates from different 100 mL aliquots from the same seawater sample with the target elements; and (3) standard addition calibrations prepared following the IIP-SPE pre-concentration procedure (100 mL seawater sample spiked with 1.0, 2.0 and 4.0 μg L^{-1} for As, Cd, Cu, Ni and Pb and 5, 10 and 20 μg L^{-1} for Zn, and subjected to the IIP-SPE procedure (Section 2.6)). External aqueous calibrations and standard

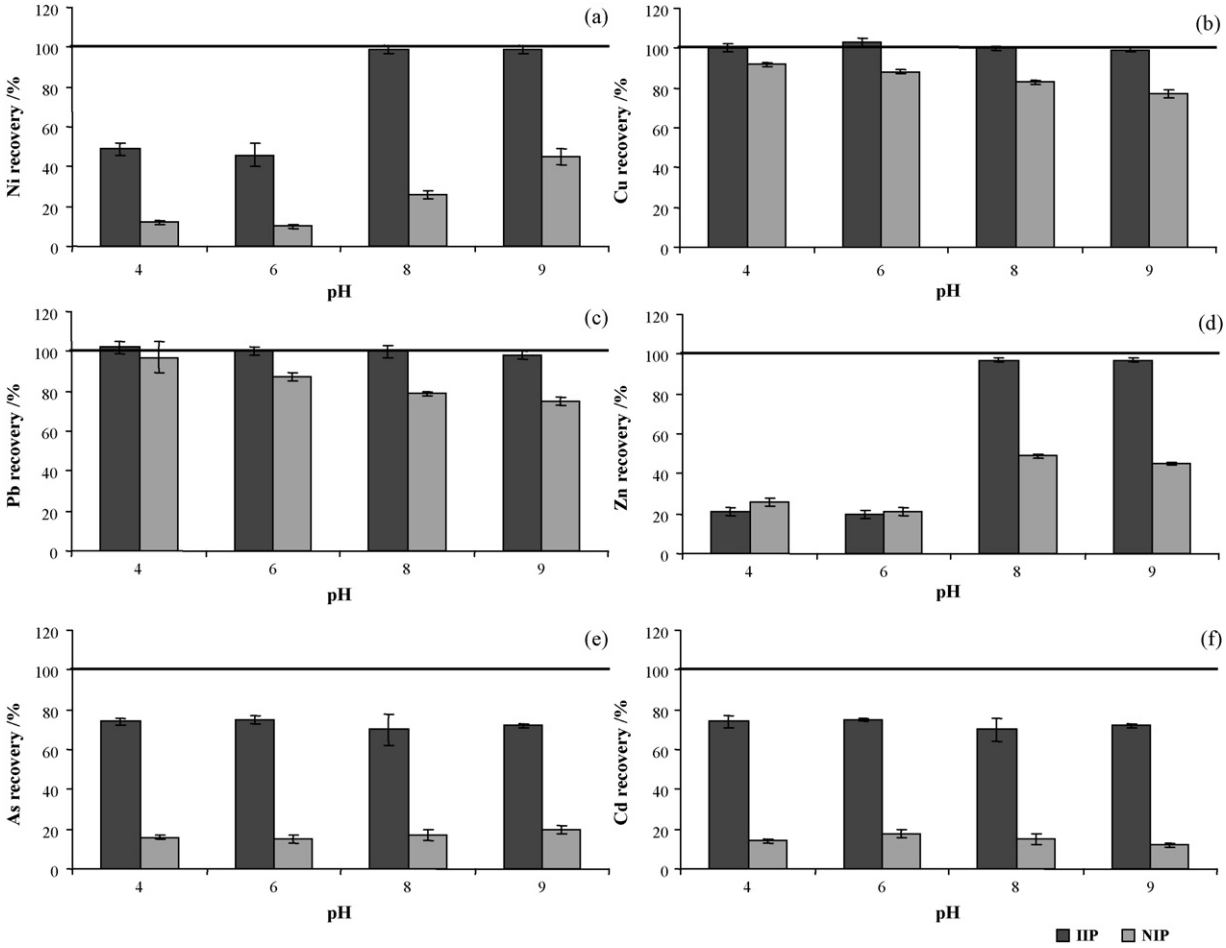

Fig. 1. Effect of pH on nickel (a), copper (b), lead (c), zinc (d), arsenic (e) and cadmium (f) analytical recovery after solid phase extraction with an ionic imprinted polymer (IIP) and a blank or non-imprinted polymer (NIP).

addition calibrations were tested covering metal concentrations between 0 and 0.25 mg L^{-1} (As, Cd, Cu, Ni and Pb) and between 0 and 1.0 mg L^{-1} (Zn).

For all cases, three different external aqueous calibrations, standard addition calibrations and "procedure" addition calibrations were performed on different days. The mean and the standard deviation of the slopes (ICP-OES and ICP-MS) are given in Table 4. After statistical comparison of the means by the multiple range test (95% confidence range), it has been obtained that slopes for external aqueous calibration in 2.0 M nitric acid and standard addition calibrations are statistically comparable for all elements when using either ICP-OES and ICP-MS. Therefore, it can be concluded that salt matrix is efficiently removed during the pre-concentration stage. This result agrees with the fact that there is no interaction between Na and K with the polymeric material [35]. In addition, slopes of the external aqueous calibration in 2.0 M nitric acid and the "procedure" addition calibrations are also statistically similar (95% confidence range), for those elements which were quantitatively retained by the polymer (Ni, Cu, Pb and Zn). The slopes for other elements (As and Cd), which show specific interactions but non-quantitative retention, were not statistically comparable. The same results have been obtained when comparing the standard addition calibrations and the standard addition calibration prepared following the IIP-SPE pre-concentration procedure. Therefore, an external aqueous calibration in 2.0 M nitric acid can be used to determine Ni, Cu, Pb and Zn in seawater after IIP-SPE, but a standard addition calibration prepared following the IIP-SPE pre-concentration procedure is needed for the quantitative determination of As and Cd in the nitric acid eluates after IIP-SPE.

The feasibility of external aqueous calibration offers a practical advantage so that tedious and time consuming standard addition techniques are not necessary. It should be mentioned that most of the reported pre-concentration methods require the establishment of a standard addition graph of the overall SPE and analytical determination procedure [8], so the synthesized polymer is advantageous for Ni, Cu, Pb and Zn pre-concentration/determination in seawater.

3.4.2. Sensitivity of the method

The limits of detection and quantification were calculated according to LOD = (3S.D.)/*m* and LOD = (10S.D.)/*m*, where S.D. is the standard deviation of eleven measurements of a procedural blank (acidified Milli-Q water treated as a sample) and *m* is the slope of the external 2.0 M nitric acid calibration graph. Values after a pre-concentration factor of 100 are listed in Table 5. Such LODs and LOQs are low enough to determine Ni, Cu, Pb and Zn levels in unpolluted seawater samples. These values are similar to those reported by other authors when using ICP-MS (0.01 μg L^{-1} for Ni using Amberlite XAD-4 immobilized butane-2,3-dione bis(N-pyridimoacetylhydrazone) [36], and from 0.0001 μg L^{-1} (Pb) to 0.001 μg L^{-1} (Ni) for Chelex 100 down-sized packed mini-columns [37]), ICP-OES (values from 0.02 to 1.13 μg L^{-1} for the use of C18 [6]) and ETAAS (0.10 μg L^{-1} for Ni using Amberlite XAD-4 [38] or Amberlite XAD-2 with Eriochorme blue black R as chelating agent [39]). Finally, other sorbent materials based on IIPs have offered LODs for

Table 3
Extraction (%), distribution ratios (D) and selectivity coefficients ($S_{Ni/M}$) for IIP and NIP.

Element	Extraction (%)[a]	Distribution ratio (D)[b]	Selectivity coefficient ($S_{Ni/M}$)[c]
Ionic imprinted polymer (IIP)			
Ni	99	99	–
Cu	99	99	1.0
Pb	99	99	1.0
Zn	99	99	1.0
Cr	80	4.0	25
Sn	78	3.5	28
Ti	80	4.0	25
V	21	0.3	372
As	72	2.6	38
Cd	71	2.4	40
Mn	16	0.2	520
Al	24	0.3	314
Non-ionic imprinted polymer (NIP)			
Ni	10	0.1	–
Cu	23	0.3	0.4
Pb	27	0.4	0.3
Zn	19	0.2	05
Cr	75	3.0	0.04
Sn	73	3.0	0.04
Ti	79	3.8	0.03
V	21	0.3	0.42
As	14	0.2	0.68
Cd	14	0.2	0.68
Mn	12	0.1	0.81
Al	21	0.3	0.42

A_1 = Amount of metal ion in aqueous solution at equilibrium; A_2 = Amount of metal ion enriched by IIP/NIP at equilibrium. A_T = Total amount of metal ion used in extraction. D_{Ni} = Distribution ratio for Ni; D_M = Distribution ratio for M (M = Cu, Pb, Zn, Cr, Sn, Ti, V, As, Cd, Mn and Al).

[a] $\% = (A_2/A_T) \times 100$.

[b] $D = (A_2/A_1)$.

[c] $S_{Ni/M} = D_{Ni}/D_M$.

Ni of 5.0 μg L^{-1} (FAAS detection) [31], 0.3 μg L^{-1} [9] or 0.18 μg L^{-1} [35] when using ETAAS, and 0.16 μg L^{-1} for ICP-OES measurements [40].

3.4.3. Repeatability and accuracy of the method

The repeatability of the overall procedure was assessed by analyzing a seawater sample eleven times. The IIP-SPE pre-concentration procedure implies a pre-concentration factor of 40 (100 mL of seawater sample). The percent relative standard deviation (RSD) values were 4, 7, 8 and 7% for Ni, Cu, Pb and Zn

Table 4
Means and standard deviations (mean ± S.D.) for aqueous calibration in 2.0 M nitric acid, standard addition and standard addition calibrations prepared following the IIP-SPE pre-concentration procedure (N = 3).

	Aqueous calibration	Standard addition	Standard addition calibration following the IIP-SPE
ICP-OES[a]			
Ni	6.8 ± 0.1	6.6 ± 0.1	6.6 ± 0.2
Cu	63 ± 2	62 ± 2	61 ± 1
Pb	3.1 ± 0.1	2.9 ± 0.1	2.9 ± 0.2
Zn	10 ± 0.2	10 ± 0.1	9.9 ± 0.1
As	6.5 ± 0.3	6.1 ± 0.2	3.7 ± 0.2
Cd	6.1 ± 0.1	6.0 ± 0.1	3.7 ± 0.2
ICP-MS[b]			
Ni	545 ± 35	530 ± 27	496 ± 27
Cu	1394 ± 85	1385 ± 71	1291 ± 111
Pb	74754 ± 587	71825 ± 1115	70078 ± 4192
Zn	9137 ± 255	9195 ± 366	9049 ± 709
As	364 ± 4	362 ± 14	63 ± 1
Cd	3544 ± 287	3467 ± 167	2225 ± 192

[a] L mg^{-1}.

[b] L μg^{-1}.

Table 5
LOD and LOQ of the methods.

	LOD/μg L^{-1}	LOQ/μg L^{-1}
ICP-OES		
Ni	0.14	0.47
Cu	0.15	0.50
Pb	0.18	0.60
Zn	0.03	0.11
ICP-MS		
Ni	0.0022	0.0073
Cu	0.0065	0.0217
Pb	0.0040	0.0133
Zn	0.009	0.031

determination by ICP-OES, while RSDs of 6% for Ni and 5% for Cu, Pb and Zn were achieved by using ICP-MS.

Analytical recovery was assessed for three concentration levels, after spiking different aliquots from the same seawater sample with 1.0, 2.0 and 4.0 μg L^{-1} of Ni, Cu, Pb, and with 5, 10 and 20 μg L^{-1} of Zn. Each concentration level (low, medium and high) was tested by triplicate; thus, analytical recoveries (Table 6) are given as mean ± S.D. for three independent measurements. It can be concluded that good analytical recovery (within the 95–105% range) are reached for all the target elements and concentration levels.

The analysis of estuarine water (SLEW-3) and lake water (TM-23.3 and TM-24) was performed to assess accuracy. Each CRM was subjected to the IIP-SPE procedure three times using a sample volume of 100 mL (pre-concentration factor of 40). Then, determinations were carried out by ICP-OES and ICP-MS. Results, listed in Table 7, reveal good agreement between concentrations found and the certified values for the three certified reference materials. This fact has been proved after applying a t-test (95% confidence range) for comparing the mean values.

3.4.4. Study of the lifetime of the Ni-IIP support

Three different Ni-IIP cartridges were tested in order to know the number of sequential solid phase extraction (loading/elution cycles) that can be performed without losses on pre-concentration efficiency. Experiments were carried out by treating estuarine seawater samples and aqueous standard solutions containing 1.0 μg L^{-1} of Ni, Cu and Pb, and 5.0 μg L^{-1} of Zn. After each five loading/elution cycles with estuarine seawater samples an aqueous standard solution was pre-concentrated and the analytical recovery calculated. Results have shown that Cu, Pb and Zn are not efficiently retained/elute after around twenty uses (analytical recoveries lower than 95%). However, quantitative analytical recoveries were obtained for Ni up to 40 SPE cycles. It must be said that the lifetime of the polymer is larger for the analyte template (Ni) than for other target elements (Cu, Pb and Zn). Therefore, the

Table 6
Analytical recovery of the methods (N = 3).

	Low[a]	Medium[b]	High[c]
ICP-OES			
Ni	105 ± 7	103 ± 3	102 ± 2
Cu	95 ± 3	98 ± 3	100 ± 2
Pb	93 ± 2	98 ± 1	104 ± 4
Zn	99 ± 3	99 ± 6	104 ± 5
ICP-MS			
Ni	103 ± 2	104 ± 1	100 ± 1
Cu	95 ± 5	103 ± 2	99 ± 1
Pb	95 ± 2	105 ± 1	101 ± 3
Zn	108 ± 2	109 ± 1	101 ± 2

[a] 1.0 μg L^{-1} for Ni, Cu and Pb; 5 μg L^{-1} for Zn.

[b] 2.0 μg L^{-1} for Ni, Cu and Pb; 10 μg L^{-1} for Zn.

[c] 4.0 μg L^{-1} for Ni, Cu and Pb; 20 μg L^{-1} for Zn.

Table 7
Analysis of certified reference materials. Each material was analyzed by triplicate.

	ICP-OES					
	SLEW-3		TM-23.3		TM-24	
	Certified/$\mu g\,L^{-1}$	Found/$\mu g\,L^{-1}$	Certified/$\mu g\,L^{-1}$	Found/$\mu g\,L^{-1}$	Certified/$\mu g\,L^{-1}$	Found/$\mu g\,L^{-1}$
Ni	1.2 ± 0.1	1.3 ± 0.1	5.4 ± 0.6	5.7 ± 0.3	3.5 ± 3.0	3.3 ± 0.3
Cu	1.6 ± 0.1	1.4 ± 0.1	9.1 ± 0.6	9.2 ± 1.0	8.0 ± 4.1	7.2 ± 0.5
Pb	0.009 ± 0.001	< LOD	3.2 ± 0.3	3.3 ± 0.6	7.3 ± 2.6	6.9 ± 1.8
Zn	0.20 ± 0.04	0.20 ± 0.02	–[a]		5.4 ± 2.3	5.1 ± 3.0

	ICP-MS			
	SLEW-3		TM-23.3	
	Certified/$\mu g\,L^{-1}$	Found/$\mu g\,L^{-1}$	Certified/$\mu g\,L^{-1}$	Found/$\mu g\,L^{-1}$
Ni	1.2 ± 0.1	1.3 ± 0.04	5.4 ± 0.6	5.8 ± 0.1
Cu	1.6 ± 0.1	1.6 ± 0.02	9.1 ± 0.6	9.6 ± 0.7
Pb	0.009 ± 0.001	<LOD	3.2 ± 0.3	3.5 ± 0.3
Zn	0.20 ± 0.04	0.19 ± 0.02	–[a]	

[a] Not given.

Ni-IIP cartridges can be used at least forty times without losing the efficiency of the adsorbent IIP for nickel determination; however, for a multi-element pre-concentration, the IIP can only be used twenty-five times.

4. Conclusions

Ion imprinted polymer particles synthesized from a ternary [Ni(II)-DEM-8-HQ] pre-polymer complex have shown imprinting properties for Ni and also for Cu, Pb and Zn. The synthesized polymeric material has not offered affinity for major elements in seawater samples, such as sodium and potassium, efficiently removing the salt matrix of seawater. Therefore, Ni, Cu, Pb and Zn can be measured against external aqueous calibrations in 2.0 M nitric acid. The synthesized IIP can be used at least twenty-five times without losing the adsorbent properties for the target analytes. In addition, the lifetime of the material can be increased up to 40 SPE cycles if only nickel is determined. Because the large life time of the polymer and the low cost of the synthesis, the Ni-IIP results cost effective when comparing to other adsorbents commonly used for SPE. The fast kinetics for adsorption/elution is other advantage. Volumes of 100 mL of seawater can be treated in 40 min. When using a vacuum manifold station and several samples are simultaneously treated, a sampling frequency of nine samples per hour is achieved. Finally, the IIP-SPE–ICP-OES/MS method has offered accurate results for the analysis of low salinity samples (lake water) and high salinity samples (estuarine water).

Acknowledgements

We wish to thank Verónica Piñeiro-Gómez from “Rede de Infraestructuras de Apoio á Investigación e ao Desenvolvemento Tecnolóxico” (RIAIDT) at the University of Santiago de Compostela for ICP-MS technical support. J. Otero–Romaní is grateful for the financial support provided by “Consellería de Innovación e Industria and Dirección Xeral de I+D+i – Xunta de Galicia” for a doctoral grant and for a scholarship to attendance INIA in Madrid (Spain).

References

[1] Directive of the Council of 10 November 1979 (79/923/CEE) Relative to Quality of Water for Keeping Molluscs, Off. J. Eur. Comm. (1979), No. L 281.
[2] J.L. Todolí, L. Gras, V. Hernandis, J. Mora, J. Anal. At. Spectrom. 17 (2002) 142.
[3] J. Nölte, ICP Emission Spectrometry. A Practical Guide, Wiley–VCH, Weinheim, 2003.
[4] Merian (Ed.), Metals and Their Compounds in the Environment, VCH, New York, 1991.
[5] N.J.K. Simpson (Ed.), Solid Phase Extraction, Principles, Techniques and Applications, Marcel Dekker, New York, 2000.
[6] J. Otero-Romaní, A. Moreda-Piñeiro, A. Bermejo-Barrera, P. Bermejo-Barrera, Anal. Chim. Acta 536 (2005) 213.
[7] G. Abbasse, B. Ouddane, J.C. Fischer, J. Anal. At. Spectrom. 17 (2002) 1354.
[8] C.D. Skinner, E.D. Salin, J. Anal. At. Spectrom. 18 (2003) 495.
[9] A. Ersöz, R. Say, A. Denizli, Anal. Chim. Acta 502 (2004) 91.
[10] A. Martin-Esteban, Fresenius J. Anal. Chem. 370 (2001) 795.
[11] T.P. Rao, S. Daniel, J.M. Gladis, Trends Anal. Chem. 23 (2004) 28–35.
[12] T.P. Rao, R. Kala, S. Daniel, Anal. Chim. Acta 578 (2006) 105.
[13] R. Say, E. Birlik, A. Ersöz, F. Yilmaz, T. Gedikbey, A. Denizli, Anal. Chim. Acta 480 (2003) 251.
[14] M. Andaç, R. Say, A. Denizli, J. Chromatogr. B 811 (2004) 119.
[15] S. Asir, L. Uzun, D. Tuerkmen, R. Say, A. Denizli, Sep. Sci. Technol. 40 (2005) 3167.
[16] O. Saatcilar, N. Satiroglu, R. Say, S. Bektas, A. Denizli, J. Appl. Polym. Sci. 101 (2006) 3520.
[17] M. Andaç, E. Oezyapi, S. Senel, R. Say, A. Denizli, Ind. Eng. Chem. Res. 45 (2006) 1780.
[18] Y. Zhai, Y. Liu, X. Chang, S. Chen, X. Huang, Anal. Chim. Acta 593 (2007) 123.
[19] M. Khajeh, Y. Yamini, E. Ghasemi, J. Fasihi, M. Shamsipur, Anal. Chim. Acta 581 (2007) 208.
[20] S. Daniel, J.M. Gladis, T.P. Rao, Anal. Chim. Acta 488 (2003) 173.
[21] Y. Liu, X. Chang, D. Yang, Y. Guo, S. Meng, Anal. Chim. Acta 538 (2005) 85.
[22] Y.K. Lu, X.P. Yan, Anal. Chem. 76 (2004) 453.
[23] V.M. Biju, J.M. Gladis, T.P. Rao, Anal. Chim. Acta 478 (2003) 43.
[24] R. Kala, V.M. Biju, T.P. Rao, Anal. Chim. Acta 549 (2005) 51.
[25] V.M. Biju, J.M. Gladis, T.P. Rao, Talanta 60 (2003) 747.
[26] R. Kala, T.P. Rao, Sep. Sci. Technol. 41 (2006) 233.
[27] S. Daniel, P.E.J. Babu, T.P. Rao, Talanta 65 (2005) 441.
[28] J.M. Gladis, T.P. Rao, Anal. Lett. 36 (2003) 2107.
[29] J.M. Gladis, T.P. Rao, Mikrochim. Acta 146 (2004) 251.
[30] P. Metilda, J.M. Gladis, T.P. Rao, Anal. Chim. Acta 512 (2004) 63.
[31] R.S. Praveen, S. Daniel, T.P. Rao, Talanta 66 (2005) 513.
[32] T.W. May, R.H. Wiedmeyer, At. Spectrosc. 19 (1998) 150.
[33] M. Howard, H.A. Jurbergs, J.A. Holcombe, J. Anal. At. Spectrom. 14 (1999) 1209.
[34] H. Askun, B. Gulbakan, O. Celikbicak, C. Uzun, O. Guven, B. Salih, J. Appl. Polym. Sci. 107 (2008) 2714.
[35] J. Otero-Romaní, A. Moreda-Piñeiro, P. Bermejo-Barrera, A. Martin-Esteban, Anal. Chim. Acta 630 (2008) 1.
[36] H. Yang, K. Huang, S. Jiang, C. Wu, C. Chou, Anal. Chim. Acta 382 (1993) 175.
[37] D. Rahmi, Y. Zhu, E. Fujimori, T. Umemura, H. Haraguchi, Talanta 72 (2007) 600.
[38] M. Soylak, L. Elci, J. Trace Microprobe Tech. 18 (2000) 397.
[39] E. Olbrycheszynska, K. Brajter, W. Matuszewski, M. Trojanowicz, M. Frenzel, Talanta 39 (1992) 779.
[40] N. Jiang, X. Chang, H. Zheng, Q. He, Z. Hu, Anal. Chim. Acta 577 (2006) 225.

Talanta 79 (2009) 911–915

Contents lists available at ScienceDirect

Talanta

journal homepage: www.elsevier.com/locate/talanta

Hollow fiber-based liquid-phase microextraction (HF-LPME) of ibuprofen followed by FIA-chemiluminescence determination using the acidic permanganate–sulfite system

María Ramos Payán, Miguel Ángel Bello López*, Rut Fernández-Torres, Mercedes Villar Navarro, Manuel Callejón Mochón

Department of Analytical Chemistry, Faculty of Chemistry, University of Seville, Seville-41012, Spain

ARTICLE INFO

Article history:
Received 4 February 2009
Received in revised form 6 May 2009
Accepted 13 May 2009
Available online 22 May 2009

Keywords:
Hollow fiber liquid-phase microextraction
HF-LPME
Chemiluminescence
Flow-injection analysis
Ibuprofen
Permanganate

ABSTRACT

Hollow fiber-based liquid-phase microextraction (HF-LPME) is a relatively new technique employed in analytical chemistry for sample pretreatment which offers more selectivity and sensitivity than any traditional extraction technique. This paper describes a three-phase HF-LPME method for ibuprofen using a polypropylene membrane supporting dihexyl ether followed by a chemiluminescence (CL) determination using the CL enhancement on the acidic permanganate–sulfite system in a FIA configuration which is the first time that both techniques have been combined for analytical purposes. The CL intensity (peak area) was proportional to the log of ibuprofen concentration in the donor phase over the range 0.1–20 μg mL^{-1}. The detection limit was 0.03 μg mL^{-1} of ibuprofen in the donor phase. The method was satisfactory reproducible and has been applied to the ibuprofen determination in pharmaceuticals and in real human urine samples.

1. Introduction

In the last years, there has been an increasing interest in developing new sample pretreatment approaches to determine all type of analytes in several matrices; this is of special importance in the analysis of biological and environmental samples. Liquid–liquid extraction (LLE) is a classical and common technique used for the preconcentration and cleanup prior to chromatographic or electrophoretic analysis that requires large organic solvent consumption. It is also tedious and analyte-loss is frequent due to multi-stage operations that cannot be neglected.

Some interest has been focused on the miniaturising of analytical LLE. The main idea behind this has been to facilitate automation, to speed up extractions, and to reduce the consumption of organic solvents. Liquid-phase microextraction (LPME), based on a droplet of water-immiscible organic solvent hanging at the end of a microsyringe needle (single drop microextraction, SDME) [1–2], is a simple, inexpensive, fast, effective and virtually solvent-free sample pretreatment technique. However, SDME is not very robust, and the droplets may be lost from the needle tip of the microsyringe during extraction. This is especially the case when samples are stirred vigorously to speed up the extraction process. More importantly, it requires careful and elaborate manual operations; however, the sensitivity and the precision of the SDME methods developed are relatively poor. This is why prolonged extraction time and faster stirring rates are not recommended.

Audunsson [3] introduced an alternative concept for LPME that was developed by Thordarson et al. [4] and for Pedersen-Bjergaard and Rasmussen [5] based on the use of single, low-cost, disposable, porous, hollow fibers made of polypropylene. In this concept, the analytes of interest are extracted from aqueous samples, through a thin layer of organic solvent (several microlitres) immobilized within the pores of a porous hollow fiber, and into an acceptor solution inside the lumen of the hollow fiber. In hollow fiber liquid-phase microextraction (HF-LPME), the organic phase is protected by the fiber, and it appears that the hollow fiber decelerates the process of organic solvent dissolution into the bulk solution. Another factor contributing to the improved sensitivity of LPME is that the surface area for the rod-like configuration of the two-phase HF-LPME system is larger than the spherical one adopted by the drop-based SDME method. The disposable nature of the hollow fiber totally eliminates the possibility of sample carryover and ensures reproducibility. In addition, the small pore size prevents large molecules and particles present in the donor solution from entering the accepting phase, and at the same time, most macromolecules do not enter the hollow fiber because they are not soluble

* Corresponding author. Tel.: +34 954557172; fax: +34 954557168.
E-mail address: mabello@us.es (M.Á.B. López).

0039-9140/$ – see front matter © 2009 Elsevier B.V. All rights reserved.
doi:10.1016/j.talanta.2009.05.018

in the organic phase present in the pores, thus yielding very clean extracts. HF-LPME has been widely applied to a variety of environmental and biological samples. Several reviews that focus on basic extraction principles, technical setup, recovery, enrichment, extraction speed, selectivity, applications and future trends in hollow fiber-based LPME have been reported. [6–9]

There are two modes used: two-phase HF-LPME and three-phase HF-LPME. In two-phase HF-LPME, the analytes are extracted by passive diffusion from the sample into the hydrophobic organic solvent supported by the fiber, and in three-phase HF-LPME the analytes were extracted through an organic solvent immobilized in the pores of fiber and further into a new aqueous phase in the lumen of fiber.

Compared with LLE and SPE, HF-LPME gives a comparable and satisfactory sensitivity and much better enrichment of analytes, and the consumption of solvent is significantly reduced by up to several hundred or several thousand times. The LPME technique is simple, fast, and inexpensive. Due to the small volume of the extracting solvent, the extracted samples do not require further concentration prior to analysis and thus total analysis time considerably decreases in comparison to traditional LLE procedure. Additional advantages of LPME also make the technique attractive. Since, LPME tolerates a wide pH range; it can be used in applications that would not be suitable for solid-phase extraction (SPE) or solid-phase microextraction (SPME). Sample carryover can be avoided because the hollow fibers are inexpensive enough to be single-used and disposed. In cases, where a large number of samples are prepared by SPE, an equivalent LPME preparation procedure could also be more economical. It has been proven that HF-LPME is very useful for extraction of drugs and metabolites from biological matrices and pollutants from environmental samples with simultaneous cleanup of the extracts [10–12].

On the other hand, in opposition with chromatographic or electrophoretic methods, analytical methods combining chemiluminescence (CL) with flow-injection techniques have the advantages of simplicity, rapidity, use of non-expensive instrumentation. CL methods have found extensive applications in many interesting areas, but their main disadvantages are usually related, in general, with their poor selectivity. So HF-LPME can be an excellent sample pretreatment alternative for FIA-CL methods and their application to analytes into complex matrices as environmental and biological samples.

In this work, the CL determination has been carried on the basis of the known CL system acidic permanganate–sulfite. Hidson and Barnettt [13] published in 2001 a wide review about the analytical applications of this CL system. Stauff and Jaeschke [14] studied the oxidation of sulfur dioxide with acidic potassium permanganate and proposed a mechanism to explain the CL reaction which involves the sulfite oxidation to produce an excited molecule of sulfur dioxide, which emits radiation in the range of 300–550 nm [15]. The energy of the excited molecule can be transferred to a fluorescent molecule added into the system [16] in order to obtain a higher quantum efficiency which can allow its sensitive determination. Another way to enhance the CL emission is the use of non-fluorescent compounds but which are capable of amplifying the emission (sensitizers) through several mechanisms [17–19].

We have verified that the presence of ibuprofen ((*R*,*S*)-2-(4-isobutylphenyl)-propionic acid) (Fig. 1), a non-steroidal anti-inflammatory drug widely used, enhances the CL of the system acidic potassium permanganate/sodium sulfite. On this basis, a flow-injection method was developed for the determination of ibuprofen which has been directly applied to its rapid determination in pharmaceuticals. This method cannot be directly applied to the ibuprofen determination in human urine due to the high CL of the sample blanks, but the use of a previous HF-LPME overcomes this selectivity problem and allowed an adequate procedure for the ibuprofen determination in urine.

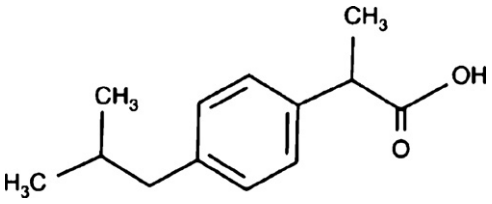

Fig. 1. Chemical structure for ibuprofen.

Ibuprofen has a pK_a value of 4.30 so a three-phase HF-LPME has been developed using a acid donor phase and a basic solution as acceptor phase which was directly injected into the FIA system.

All the HF-LPME and FIA parameters have been optimized in order to propose a rapid and simply determination of ibuprofen which is the first analytical procedure proposed that combines both techniques. The method has been applied to the determination of ibuprofen in human urine.

2. Experimental

2.1. Chemicals and materials

All chemicals were of analytical-reagent grade or better. All solutions and dilutions were prepared with ultrapure water (Milli-Q, Milipore, Bedford, MA). Ibuprofen, dihexyl ether and 1-octanol were purchased from Fluka–Sigma–Aldrich (Madrid, Spain) and the rest of products were obtained from Merck (Darmstadt, Germany). Working solution of 1.5×10^{-4} M $KMnO_4$ in 5×10^{-2} M H_3PO_4 was prepared daily by diluting the 3×10^{-3} M $KMnO_4$ stock solution. The solution of 1.5×10^{-3} M Na_2SO_3 was prepared daily. Working solutions of ibuprofen were prepared by adequate dilutions from a 200 μg mL^{-1} ibuprofen stock solution. Q3/2 Accurel KM polypropylene hollow fiber (600 μm i.d., 200 μm wall thickness and 0.2 μm pore size) was purchased from Membrana (Wuppertal, Germany). Human urine samples were collected from healthy volunteers.

2.2. Equipment

The FIA system used in this work is shown in Fig. 2. To deliver flow streams, a peristaltic pump Minipuls 3 from Gilson (Gilson, Inc., Middleton, WI, USA) was used. Polytetrafluoroethylene (PTFE) tubing (0.8 mm i.d.) was used to connect all components in the flow system. 100 or 20 μl loops were placed in the injection valve. The CL signal was measured by a ChemLab Chemiluminescence Detector model CL2 (Camspec, Cambridge, UK) where the carrier streams were mixed through a Y-shaped element previously to the 60 μl/5 mm path length glass flow cell. CL data were acquired with a personal computer using Clarity Lite software (DataApex Ltd., Prague, The Czech Republic).

Sample stirring were performed on an ANS-00/1 magnetic stirrer from Science Basic Solutions (Rubí, Barcelona, Spain).

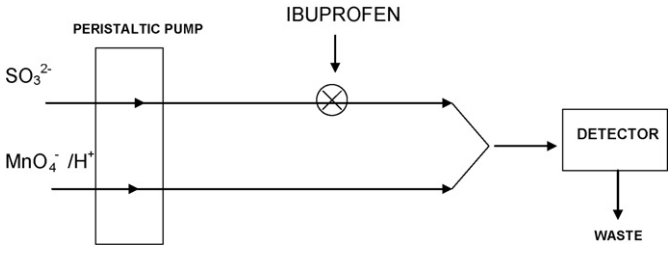

Fig. 2. Schematic diagram of the FIA system used for the ibuprofen determination.

A HPLC equipment (Merck-Hitachi) consisted of a L-7100 pump, a Rheodyne (Cotati, CA, USA) model 7725i injection valve with a 20-μl sample loop, a Lichrospher® 100 RP-18 column (125 mm × 4 mm i.d., 5 μm) (Merck, Darmstadt, Germany), and a model L-7455 diode array detector controlled by a Merck-Hitachi D-7000 interface equipped with a HPLC System Manager® software was used to realize chromatographic determinations.

2.3. FIA analysis procedure

By keeping the six-way valve in washing position, acidic permanganate and sulfite solutions were continuously pumped into the manifold at a flow rate of 1.5 mL min^{-1}. Ibuprofen solutions were injected into the sulfite stream from the valve loop. The content of ibuprofen was determined from the calibration plot of CL emission intensity versus log of ibuprofen concentration.

2.4. Supported liquid membrane preparation and extraction procedure

Hollow fibers were cut into 27 cm pieces, washed with acetone in ultrasonic bath and dried. The fiber was soaked in the membrane phase (dihexyl ether) during 5 s to impregnate pores of the support, and rinsed with water on the outside by placing into an ultrasonic bath for 30 s in order to remove the excess of organic solvent. The lumen of the prepared fiber piece was filled with 50 μL of acceptor phase (pH 10 aqueous solution) using a HPLC syringe. Both open ends of the fiber were closed by means of hot soldering tool and adhesive tape. During extraction, the membrane portion that contains the acceptor phase (Fig. 3) was immersed in the 50 mL sample solution (pH 2) contained in a 50 mL glass beaker. The sample was stirred for 15 min by means of a magnetic stirrer at 300 rpm. After extraction, the fiber was taken out, one of the ends was cut and the acceptor phase was extract using a HPLC syringe and injected into the FIA system through the 20 μL loop.

2.5. Preparation of real samples

Pharmaceuticals were dispersed into pH 8 aqueous solutions. The non-soluble fraction was removed by filtration or centrifugation, and the samples were diluted with water. Suitable aliquots were taken and diluted with water for their measurements.

Spiked and real urine samples were simply diluted 1:10 with HCl pH 2 aqueous solution and submitted to HF-LPME procedure.

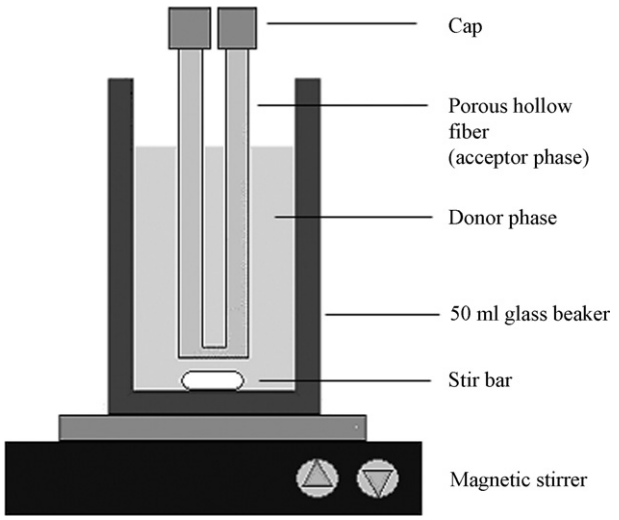

Fig. 3. Schematic diagram of the HF-LPME procedure.

3. Results and discussion

3.1. Optimization of experimental variables for FIA-CL

The CL that results from the acidic permanganate and sulfite reaction has a low intensity. When ibuprofen was added into the system, the CL increases which indicates that it is a sensitive enhancer of the CL of this reaction. The sensitizing effect of ibuprofen is also related to the acid, permanganate and sulfite concentrations. Thus, several tests were performed to choose the best experimental conditions in order to obtain maximum CL signals.

Variable concentrations of HCl, HNO_3, H_2SO_4 and H_3PO_4 were tested, and the results obtained indicated that the strongest CL occur if H_3PO_4 is used; so, it was chosen to obtain acid pH; H_2SO_4 produced slightly lower CL intensity than H_3PO_4. CL intensity increases with the H_3PO_4 concentration reaching a maximum value between 2.5×10^{-2} and 6.5×10^{-2} mol L^{-1} when 5.0×10^{-5} M permanganate and 5.0×10^{-4} M sulfite at a flow rate of 1.0 mL min^{-1} were used. A H_3PO_4 concentration of 5×10^{-2} M was chosen as the optimum acidic medium for the sulfite/permanganate/ibuprofen reaction.

The effect of permanganate concentration was checked in the range 1×10^{-5} to 3.0×10^{-3} mol L^{-1} keeping a H_3PO_4 concentration of 5×10^{-2} M, sulfite concentration of 5.0×10^{-4} M and flow rate of 1.0 mL × min^{-1} were also kept constant. The CL increases with the permanganate concentration reaching a maximum value from 6×10^{-5} M to 2×10^{-4} M; higher permanganate concentrations resulted in a decrease of the emission intensity, which could be due to a permanganate absorption [19,20]. A permanganate concentration of 1.5×10^{-4} M was chosen as optimum.

When the effect of sulfite concentration was checked at previously chosen H_3PO_4 and permanganate concentrations at a flow rate of 1.0 mL min^{-1}, maximum CL was obtained when sulfite concentration was between 8×10^{-4} and 1.75×10^{-3} mol L^{-1}, the decrease at higher sulfite concentrations can be due to the resulting sulfite/permanganate relation. A 1.5×10^{-3} M Na_2SO_3 solution was chosen as optimum.

The effect of the flow rate was tested keeping the H_3PO_4, permanganate and sulfite concentrations at the chosen values; the CL signal increases up to 1.3 mL min^{-1} and remains stable from this value up to 4.5 mL min^{-1}. A flow rate of 1.5 mL min^{-1} was selected as the optimum in order to minimize reagents consumption.

3.2. Linearity, sensitivity and precision

The chemiluminescence intensity (peak area) using the optimized conditions previously described was proportional to the log of concentration of ibuprofen over the range 2–100 μg mL^{-1}. The detection limit calculated as three times the standard deviation of the background signal (3σ) was 0.5 μg mL^{-1} of ibuprofen. The relative standard deviation for 15 repetitive determinations of 30 μg mL^{-1} ibuprofen (intraday repeatability) was 0.8%. The interday repeatability ($n = 3$; 5 days) was 1.6%.

3.3. Kinetic characteristics of CL reaction

The CL reaction between permanganate, sulfite and ibuprofen occurs immediately after the mixing and is very fast. It is a flash-type emission and is apparently controlled by the mixing speed. The possible mechanism of this CL reaction has been previously established [21].

3.4. Determination of ibuprofen in pharmaceuticals

The proposed FIA-CL method was applied to the analysis of several pharmaceuticals: Gelofeno® (tablets) (Lab. Gelos, S.L.),

Table 1
Ibuprofen determination in several pharmaceuticals by the FIA-CL proposed procedure and compared with content labeled and obtained by another HPLC method.

Pharmaceutical	Label content (mg)	Proposed method[a]	HPLC method[a]
Gelofeno®	200	195 ± 3	198 ± 3
	400	399 ± 1	402 ± 2
	600	597 ± 4	595 ± 4
Neobrufen®	600	592 ± 6	601 ± 2
Ibuprofeno Cinfa®	600	600 ± 2	597 ± 3

[a] Average ± standard deviation (n = 5).

Neobrufen® (effervescet powder) (Aboot Laboratories) and Ibuprofeno Cinfa® (tablets) (Lab. Cinfa). Results obtained were compared with labeled contents and those from an HPLC method [19]. Table 1 shows the results obtained. As can be seen, good agreement between labeled, HPLC and FIA-CL contents was obtained.

3.5. Optimization of experimental conditions for HF-LPME extraction

First, several tests with donor phases pH 1–2 and acceptor phases pH 10–11 were carried out in order to choose the more adequate liquid supported on the polypropilene membrane; dihexyl ether and 1-octanol were checked, and the best results were obtained with dihexyl ether, so this was the liquid support selected.

Based on the pK_a value for ibuprofen (4.30), donor HCl aqueous solutions within 1–4 pH range were tested using 50 mL of aqueous ibuprofen of 5.0 mg L^{-1} extracted at 300 rpm during 30 min and 50 μL of aqueous pH 10 NaOH solution was used as acceptor phase; ibuprofen extraction decreases a pH value higher than 2.5. pH 2 aqueous solutions were selected as donor phase and then NaOH aqueous solutions with pH values between 8 and 12 were tested as acceptor phase; maximum ibuprofen extraction was carried out with acceptor phases with pH higher than 9.5; accordingly, pH 10 solutions were selected as acceptor phase.

Using the selected donor and acceptor phases, the influence of the stirring time was checked; as can be seen in Fig. 4 maximum extraction was obtained for values higher than 10 min, so a stirring time of 15 min at 300 rpm was selected as optimum value.

3.6. Linearity, sensitivity and precision for HF-LPME extraction

Using the selected HF-LPME conditions, several aqueous pH 2 solutions with different ibuprofen concentrations were submitted to the liquid microextraction procedure and analyzed according to the described experimental procedure. The CL intensity (peak area) was proportional to the log of ibuprofen concentration in the donor phase over the range 0.1–20 μg mL^{-1}. The detection limit calculated as three times the standard deviation of the background signal (3σ) was 0.03 μg mL^{-1} of ibuprofen. The relative standard deviations for

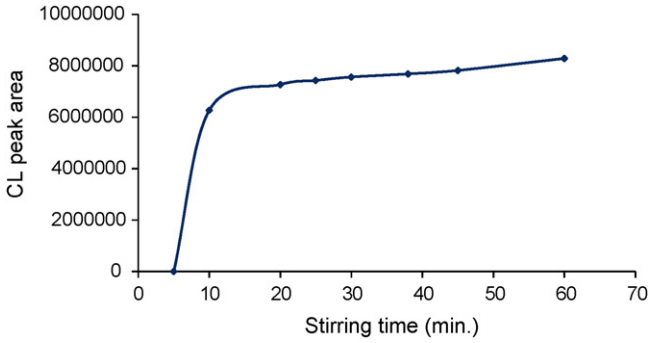

Fig. 4. Influence of the stirring time (300 rpm) on the HF-LPME.

Table 2
Ibuprofen recoveries using HF-LPME/FIA-CL from spiked human urine samples.

Spiked concentration (μg mL^{-1})	Measured concentration (μg mL^{-1})[a]
5.0	4.97 ± 0.06
10.0	9.84 ± 0.19
15.0	15.05 ± 0.12

[a] Average ± standard deviation (n = 5).

Table 3
Ibuprofen contents after the oral administration of a 600 mg dose for the analyzed real urine samples using HF-LPME/FIA-CL proposed method and compared with another HPLC method.

Time (min)	Proposed method (μg mL^{-1})[a]	HPLC method (μg mL^{-1})[a]
30	1.23 ± 0.12	1.30 ± 0.07
60	2.65 ± 0.16	2.59 ± 0.10
90	6.31 ± 0.09	6.40 ± 0.08
120	18.93 ± 0.10	19.05 ± 0.07
150	22.35 ± 0.06	22.28 ± 0.11
180	12.38 ± 0.14	12.40 ± 0.09
210	3.07 ± 0.14	3.12 ± 0.09

[a] Average ± standard deviation (n = 5).

15 repetitive determinations of 1 and 10 μg mL^{-1} ibuprofen (intraday repeatability) were 1.2% and 0.8%, respectively. The interday repeatabilities (n = 3; 5 days) were 1.8% and 1.1% for those concentration values.

3.7. Human urine analysis using HF-LPME extraction

Direct analysis of ibuprofen in urine samples using the FIA-CL proposed method is not possible due to matrix interference that produces very high CL signal for blank samples; so, the proposed HF-LPME procedure was applied for this purpose.

Recovery assays were performed using spiked human urine samples from volunteers to obtain ibuprofen concentrations of 5, 10 and 15 μg mL^{-1} which were submitted to the HF-LPME extraction and FIA-CL determination procedure described in the experimental section. The results obtained are shown in Table 2, with good agreement between spiked and measured quantities.

Human real urine samples from a volunteer were collected at intervals of 30 min after the administration of a 600 mg oral dose of ibuprofen. Table 3 shows the concentration values obtained by the HF-LPME/FIA-CL proposed procedure and by an HPLC method [22]. As can be seen, a good agreement between both analytical methods is evident.

4. Conclusions

This study presents a rapid hollow fiber-based liquid-phase microextraction (HF-LPME) method for ibuprofen combined with the chemiluminescence determination using its sensitizing effect on the acidic permanganate/sulfite reaction into a FIA configuration. The applicability of the method for urine samples has been demonstrated. The simplicity of the extraction process and analysis procedure, including the use of aqueous solutions only, makes the developed method as an attractive alternative to other methods. The FIA-CL method has been also successfully applied to the determination of ibuprofen in pharmaceuticals.

References

[1] H.G. Liu, P.K. Dasgupta, Anal. Chem. 68 (1996) 1817.
[2] M.A. Jeannot, F. Cantwell, Anal. Chem. 68 (1996) 2236.
[3] G. Audunsson, Anal. Chem. 58 (1986) 2714.
[4] E. Thordarson, S. Pálmarsdóttir, L. Mathiasson, A. Jönsson, Anal. Chem. 68 (1996) 2559.

[5] S. Pedersen-Bjergaard, K.E. Rasmussen, Anal. Chem. 71 (1999) 2650.
[6] E. Psillakis, N. Kalogerakis, Trends Anal. Chem. 22 (2003) 565.
[7] K.E. Rasmussen, S. Pedersen-Bjergaard, Trends Anal. Chem. 23 (2004) 1.
[8] S. Pedersen-Bjergaard, K.E. Rasmussen, J. Chromatogr. B 817 (2005) 3.
[9] S. Pedersen-Bjergaard, K.E. Rasmussen, J. Chromatogr. A 1184 (2008) 132.
[10] S. Zorita, L. Martensson, L. Mathiasson, J. Sep. Sci. 30 (2007) 2513.
[11] S. Zorita, T. Barri, L. Mathiasson, J. Chromatogr. A 1157 (2007) 30.
[12] S. Zorita, P. Hallgren, L. Mathiasson, J. Chromatogr. A 1192 (2008) 1.
[13] B.J. Hindson, N.W. Barnett, Anal. Chim. Acta 445 (2001) 1.
[14] J. Stauff, W. Jaeschke, Z. Naturforsch. 33B (1978) 293.
[15] I.M. Psarellis, N.T. Deftereos, E.G. Sarantonis, A.C. Calokerinos, Anal. Chim. Acta 294 (1994) 27.
[16] Y. Zhuang, S.C. Zhang, J.S. Yu, Anal. Bioanal. Chem. 375 (2003) 281.
[17] S.S. Al-Tamrah, A. Townshend, A.R. Wheatley, Analyst 112 (1987) 883.
[18] Y. Zhuang, H. Song, J. Pharm. Biomed. Anal. 44 (2007) 824.
[19] A. Campiglio, Analyst 123 (1998) 1053.
[20] J.L. López-Paz, A. Townshend, Anal. Commun. 33 (1996) 31.
[21] L. Yinhuan, L. Jiuru, Luminescence 22 (2007) 326.
[22] R. Cueva-Mestanza, M.E. Torres-Padron, Z. Sosa-Ferrera, J.J. Santana-Rodriguez, Biomed. Chromatogr. 22 (2008) 1115.

Talanta 79 (2009) 787–795

Contents lists available at ScienceDirect

Talanta

journal homepage: www.elsevier.com/locate/talanta

Immunomagnetic separation and rapid detection of bacteria using bioluminescence and microfluidics

Jingmin Qiu[a], Yun Zhou[b], Hui Chen[b], Jin-Ming Lin[a,b,*]

[a] State key Laboratory of Environmental Chemistry and Ecotoxicology, Research Center for Eco-Environmental Sciences, Chinese Academy of Science, P.O. Box 2871, Beijing 100085, China
[b] The Key Laboratory of Bioorganic Phosphorus Chemistry & Chemical Biology, Department of Chemistry, Tsinghua University, Beijing 100084, China

ARTICLE INFO

Article history:
Received 17 March 2009
Received in revised form 30 April 2009
Accepted 4 May 2009
Available online 12 May 2009

Keywords:
Immunomagnetic bead
Bacteria
Salmonella
Staphylococcus aureus
Bioluminescence
Microfluidics

ABSTRACT

This paper describes an immunomagnetic separation of target bacterial cells from others by using magnetic bead. The surface of bead was coated with antibodies which can capture specific organism. The binding efficiency of immunomagnetic bead (IMB) capturing target bacterial cells was higher than 98% when the concentrations of target and interferent bacterial cells were at the same level. The concentration of bacteria was determined indirectly by detecting adenosine 5′-triphosphate (ATP) employing bioluminescence (BL) reaction of firefly luciferin–ATP. Benzalkonium chloride (BAC) was used as an ATP extractant from living bacterial cells. We found that BAC could enhance the light emission when the concentration of BAC was less than 5.3×10^{-2}% (w/v) and the BL intensity reached its maximum at the concentration of BAC was 2.7×10^{-2}%, which was 10-fold stronger than that without BAC. Based on the principle of the IMB, a microfluidic chip combined with immunofluorescence assay for separating and detecting bacteria simultaneously was also developed. The IMBs were magnetically fixed in the beadbeds of chip channels with a 3-mm diameter of NdFeB permanent magnet. The target bacterial cells can be captured magnetically and observed by a fluorescent microscope.

1. Introduction

Rapid detection of bacteria is necessary for the safety of food products, the veracity of clinical diagnostics, the future progress of gene engineering, the prohibition of threat of possible biological warfare, etc. [1,2]. Previously, the microbiological methods, containing replication bacterial cells to 10^9 cell/mL, specific identification on selective media and biochemical tests, provided us a traditional way to detect bacteria, which usually cost several days [3]. So a truly rapid and sensitive monitoring system for detecting and identifying bacteria is in great demand. Adenosine 5′-triphosphate (ATP) is present in all living cells and the amount of it per cell remains fairly constant ($\sim 10^{-18}$ mol/cell) [4]. Therefore, an assay of ATP is responsible for the concentration of bacterial cells. Firefly bioluminescence (BL) is routinely used for the detection of ATP due to the number of photons (BL intensity) is directly proportional to the concentration of ATP [5–7], which can be measured at femtomole levels using the luciferin–ATP reaction [8].

In the assay of intracellular ATP from bacterial cells, ATP extractants are used for releasing ATP from living bacterial cells. Plenty of choices in ATP extractant are available, such as trichloroacetic acid (TCA), Triton X-100, ethanol, and benzalkonium chloride (BAC). Among ATP extractant, BAC is widely used because it can extract ATP from more living cells especially bacteria [9]. Previously, it is reported that BAC inhibits the activity of luciferase besides releasing ATP in the BL reaction; the way to eliminate the inhibitory effect is to dilute the extracts containing intracellular ATP and BAC, thus resulting in lowing of sensitivity for determining ATP. Another method to eliminate the inhibitory effect, which does not induce a decrease in determining ATP, is to use liposome, composed of phosphatidylcholine and cholesterol, the function of which in BL reaction is achieved by associating with BAC before BAC inhibiting luciferase [10–12]. However, there are some disadvantages by introducing liposome: the procedure is too complex; it costs too much time in synthesizing satisfied liposome for the BL reaction; the improved degree in sensitivity by the liposome is limited. So it is necessary to establish a more convenient method to improve the sensitivity in the BL reaction. According to experiments, we found that when the concentration of BAC was less than some value, BAC itself could enhance the BL intensity, which means that it does not need other reagents to improve the sensitivity in the BL reaction.

The immunomagnetic bead composed of magnetic particle core inside and polymer group conjugated by antibodies on the sur-

* Corresponding author at: Department of Chemistry, Tsinghua University, Qinghua Yuan, Haidian, Beijing 100084, China. Tel.: +86 10 62792343; fax: +86 10 62792343.
E-mail address: jmlin@mail.tsinghua.edu.cn (J.-M. Lin).

0039-9140/$ – see front matter © 2009 Elsevier B.V. All rights reserved.
doi:10.1016/j.talanta.2009.05.003

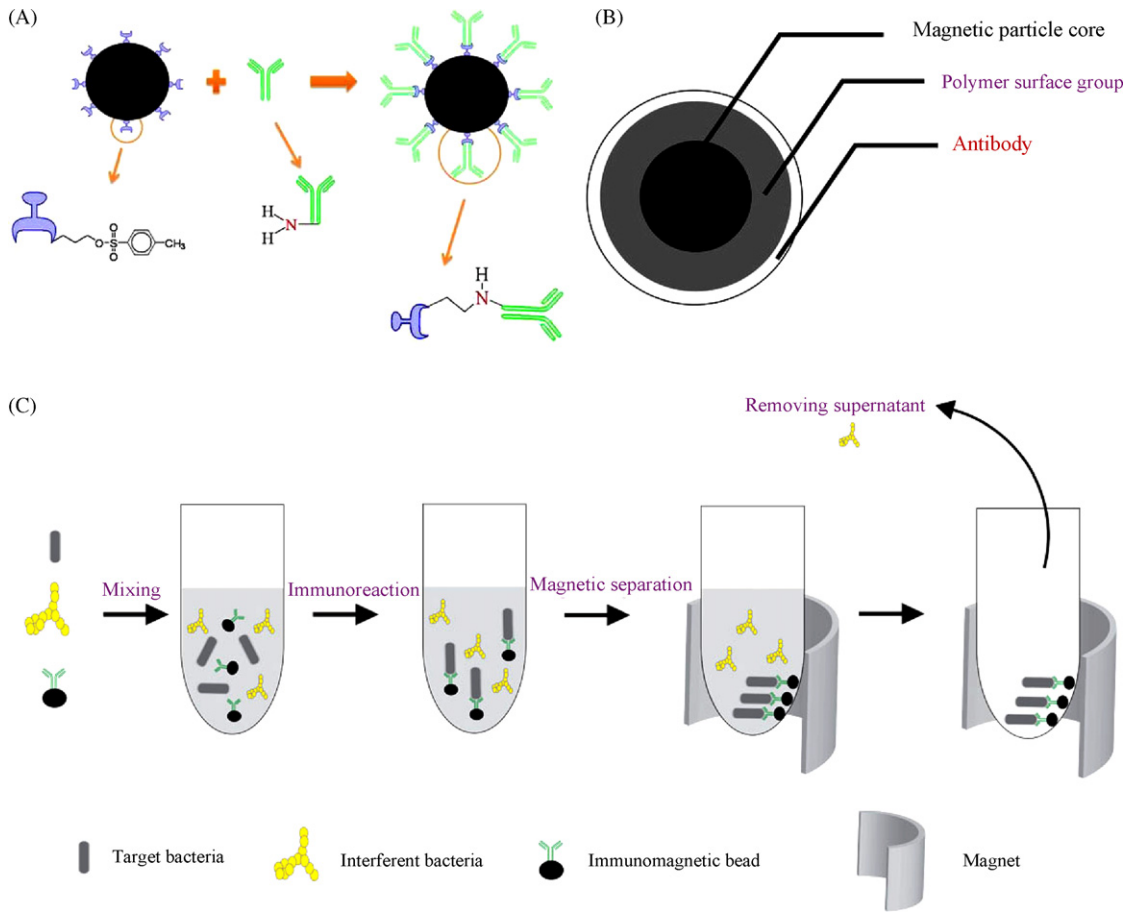

Fig. 1. The illustration of IMB used in experiments. (A) The schematic mechanism of synthesizing IMB anti-*S.aureus*. (B) The structure of IMB. (C) Schematic illustration of the immunomagnetic separation process for separating *Salmonella* in a tube of the bioluminescence method. Scale bar = 10 μm.

face, are designed for immunomagnetic separation (IMS) [13]. Typically, the beads are 1–5 μm spheres containing γ-Fe_2O_4, $MeFe_2O_4$ (Me = Co, Mn, Ni), and Fe_3O_4 to make them superparamagnetic in the presence of magnetic field. The antibody coated on the surface of the IMB could capture the target organism when they are close to IMB. So IMS is a rapid, specific, efficient and technically simple method that can be used for separation of target organism directly from non-target organism and other particles without any need for centrifugation or filtration [14–16].

Microfluidic systems, an attractive platform for rapid few cells functional analysis, appear to offer a powerful means to automate and miniaturize sample preparation for bioassays [17–19]. On-chip assays using micron-sized fluidic channels have demonstrated the ability to perform rapid and sensitive biological assays. In addition, the small dimensions of microdevices allow for the creation of portable analytic devices. Magnetic bead-beds within a microfluidic device was proposed for capturing cells in order to obtain a more controllable and compact magnetic bed, which can improve the capture efficiency. Furdui [20] reported a similar approach, in which the detection results were obtained by the PCR step. However, the PCR step is time consuming and off-line. So we developed an on-chip immunofluorescence assay for bacteria analyzing using microfluidic chip combined with the bacterial cells capture of IMB. Before introducing into microchip, bacterial cells were firstly mixed with the FITC-labeled antibodies, which supported an easily way to detect by charge coupled devices (CCD) in the microscope. Separation is achieved by bacteria—FITC-labeled antibodies complex captured by bead-beds in the chamber of microchannel [21], and detection is obtained by observing the fluorescent phenomena from the bead-beds.

In this paper, the optimum conditions on separating and detecting bacterial cells based on bioluminescence and microfluidics were studied. *Salmonella* (CGMCC 1.1552) and *Staphylococcus aureus* (*S. aureus*, CGMCC 1.363) were used as the test target bacteria, which were chosen to form a model system due to the ready availability of immunoassay reagents and they are the typical ones of gram positive and negative bacteria. Results from this analyte can be generalized and extended to other bacterial species by changing IMB and antibodies.

2. Experimental

2.1. Chemical and reagents

Salmonella (CGMCC 1.1552) and *Staphylococcus aureus* (*S. aureus*, CGMCC 1.363) are from China General Microbiological Culture Collection Center (Beijing, China). The magnetic beads were purchased from Invitrogen Dyanl (Oslo, Norway) and its diameter is 2.8 μm in average. Luciferase from firefly (*Photinuspyralis*) and D-luciferin were obtained from Promega (Madison, USA). Benzalkonium chloride (BAC, Predominantly $C_{12}H_{25}N(CH_3)_2C_7H_7Cl$, also contains C_{12} and C_{16} homologues) was purchased from Sigma–Aldrich Co. (USA). Adenosine 5′-triphosphate disodium salt (ATP) and magnesium chloride were obtained from Amresco (Ohio, USA). EDTA, dithiothreitol, bovine serum albumin (BSA), D-glucose, and 2-[4-(2-hydroxyethyl)-1-piperazinyl] ethanesulfonic acid (Hepes) were obtained from Genview (Texas, USA). Yeast extract and tryp-

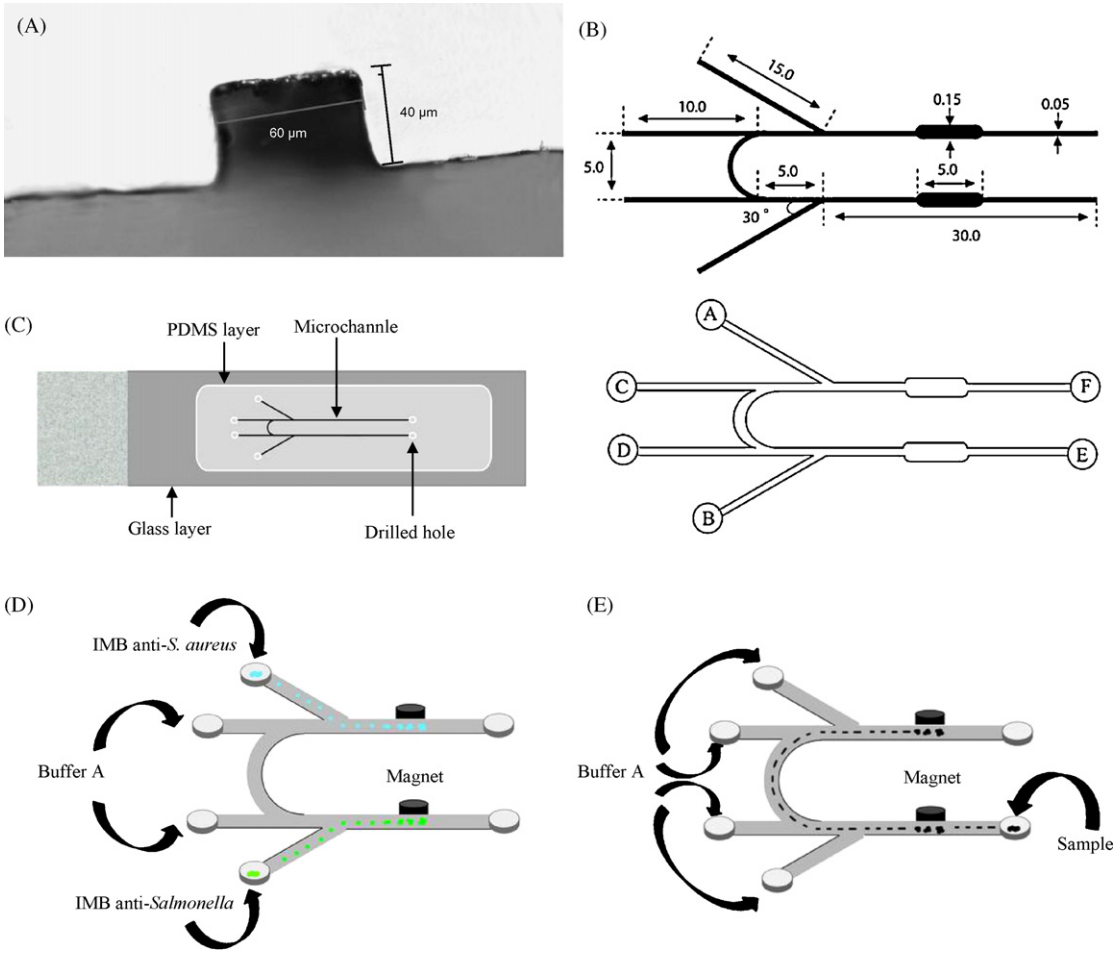

Fig. 2. The schematic of the microfluidic device. (A) The depth and width of the microchip. (B) Layout of the U-type microchip used for separation and detection of bacteria. Dimensions (in mm) correspond to the photomask features. Reservoirs A–B, C–D and E represent the inlets of IMB, buffer solutions and bacterial sample, respectively, and F is the outlet. (C) The appearance of the PDMS/glass microfluidic chip. (D) IMB is pumped to the channel for capture with a magnet. (E) The sample (bacteria and FITC-labeled antibodies) is introduced from reservoir E. Beads show as blue and green streaks, sample as dark staff.

tone were purchased from Oxoid Ltd. (Basingstoke, Hampshire, England). Sodium chloride was obtained from Beihua Fine Chemicals Co., Ltd. (Beijing, China). Beef extract was purchased from Shuangxuan Microorganism Culture Factory (Beijing, China). IMB anti-*Salmonella* was obtained from Invitrogen Dynal (Oslo, Norway). FITC-labeled anti-*Salmonella* antibody, FITC-labeled anti-*S. aureus* antibody and anti-*S. aureus* antibody were purchased from Abcam (Cambridge, UK).

A 10.0 mM solution of ATP was daily prepared by dissolving the compound with the "buffer A" (25 mM Hepes and 2.0 mM EDTA, pH 7.6). Working solution was prepared by serial dilution with the "buffer A". A 1.0% (w/v) solution of BAC was prepared by dissolving the compound with the "buffer A", and stored at 4 °C. A luciferase solution was prepared by dissolving 50 mg of luciferase in 10 mL of "buffer L" (25 mM Hepes, 2.0 mM EDTA, 20 mM magnesium chloride, 1.2 mg/mL BSA, and 2.0 mM dithiothreitol, pH 7.6); a luciferin solution was prepared by dissolving 5 mg luciferin in 5 mL with the "buffer L". The luciferase and luciferin solution were stored in portions of 200 μL and 100 μL at −20 °C, respectively. When used, the two portions were mixed and 4.8 mL "buffer L" was added into the mixture. Other reagents were commercially available as analytical reagent or laboratory grade materials. All solutions were prepared with ultrapure deionized water from a UV ultrapure water system (EASYpure® II, Barnstead International, USA).

The multilite luminometer containing the equipment of chemiluminescence and UV detection was obtained from Biotech (Synergy 4, Vorment, USA). The microscope (DMI 4000) and the fluorescent source (CTR 4000) were purchased from Leica (Wetzlar, Germany).

2.2. Preparation of bacteria samples

The target organism was *Salmonella*; the interferent bacterial cell was *S. aureus*. They were grown 3–5 h at 37 °C in BPY culture (10 g/L tryptone, 5 g/L beef extract, 5 g/L yeast extract, 5 g/L D-glucose, and 5 g/L sodium chloride). The culture was grown to midlog phase (OD_{600} = ~0.6). Optical density at 600 nm (OD_{600}) was measured with the multilite luminometer in a 96-well plate. The bacterial cells were collected by centrifugation at 10,000 rpm for 5 min at 4 °C by a centrifuge (centrifuge 5804 R, Eppendorf, USA). The pellet was suspended in 1.0 mL of the "buffer A" solution. Working cell suspensions were prepared by serially diluting with the "buffer A" solution. All bacteria suspensions were stored on a crushed ice bath until the extraction of ATP from bacterial cells.

For microfluidics, FITC-labeled anti-*Salmonella* antibody and FITC-labeled anti-*S. aureus* antibody were diluted with "buffer A" solution to reach the final dilutions of 1:40 and 1:10, respectively. The number of working bacterial cells in the process of serially diluting was 3, which meant the bacterial cells in the experiment had been diluted by 1000-fold. Then, the antibody and cells were mixed and shaken up for 5 min on a crash ice bath according to the relationship of antibody–antigen.

2.3. Bioluminescence detection

The BL experimental procedure consisted in pipetting a 100-μL portion of the ATP (standard samples or intracellular extracts) solution into a well of 96-well plate in the multilite luminometer. Then a 50-μL of portion of luciferase–luciferin mixture solution was injected into the well. Light output was integrated for 10 s, following a 2 s' delay (shaking), with readings presented as relative light units (RLU). Bacterial numbers in sample dilutions were determined as colony forming units (CFU) from triplicate plate counts.

For intracellular ATP assays, a 100-μL portion of bacteria suspension was mixed with some portion of 1.0% BAC solution in a 2-mL plastic cuvette to extract ATP from bacterial cells. After incubating on a crashed ice bath for approximately 5 min, the extract was diluted with some portion of "buffer A" solution to make the final volume of mixture become 1.0 mL. The 100-μL aliquot of the diluted extract was added into a well of 96-well plate, and then 50-μL portion of luciferase–luciferin mixture solution was injected into the well, light output was measured after 2 s' shake in the multilite luminometer.

2.4. Immunomagnetic separation

IMB anti-*S. aureus* (Fig. 1A) was synthesized as the instructions of "Dynabeads® M-280 Tosylactivated"; the process was shown in Fig. 1A. Assays employing IMB anti-*Salmonella* (Fig. 1C) for separating *Salmonella* as showed in Fig. 1C were performed by taking 100-μL portion of bacterial dilutions in a 2-mL tube and adding 50-μL washed IMB anti-*Salmonella* dilution solution. These were mixed at room temperature using a Dynal MPC-1 sample mixer (Invitrogen Dynal AS, Oslo, Norway) for 10 min before being immobilized using a Dynal MPC magnet (Invitrogen Dynal AS, Oslo, Norway) for 2 min. The immobilized beads were then washed with a 150-μL portion of "buffer A" and re-suspended in 1 mL portion of "buffer A" after adding a 40-μL portion of 1.0% BAC solution for bioluminescence assay.

2.5. Chip fabrication

Polydimethylsiloxane (PDMS)/glass microfluidic chip (Fig. 2C) was fabricated using the standard soft lithography method [22–25]. The microscale channels were designed using the Adobe Illustrator software and then printed out on a transparency by a high resolution puncher as shown in Fig. 2. The transparency was then used as the photomask in photolithography for the fabrication of a master on a silicon wafer. We used negative photoresist SU-8 2050 (MicroChem, Newton, MA, USA). PDMS (Silicone elastomer, Dow Corning, Midland Michigan, USA) prepolymer mixture consisting of monomer and curing agent with the mass ratio of 10:1 was poured on the SU-8/silicon wafer master and then cured at the temperature of 60 °C for 0.5 h. The peeled PDMS stamp (about 5 mm thick) with structures of the microchannels at the surface was then drilled six inlet and outlet holes. A glass slide (7105, Sail Brand, Jiangsu, China) was pre-cleaned in (H_2O:NH_4OH (27%):H_2O_2 (30%) = 5:1:1, volumetric ratio) solution with stirring at around 70 °C for 1 h and then rinsed with pure water and dried. The PDMS chip and the glass slide were oxidized using a Plasma Cleaner (PDC-32G, Harrick, USA) in atmosphere for 1.5 min and then immediately put into contact to form the PDMS/glass microchip. The depth and width (Fig. 2A) of microchip were 40 μm and 60 μm, respectively.

For magnetic bead-beds, IMB for *Salmonella* and for *S. aureus* was introduced into microchannels from A and B inlet using a 250-μL syringe (gastight #1725, Hamilton, Switzerland) by a pump (PHD 2000, Harvard, USA) for 10 min at 0.10 μL/min, respectively, and

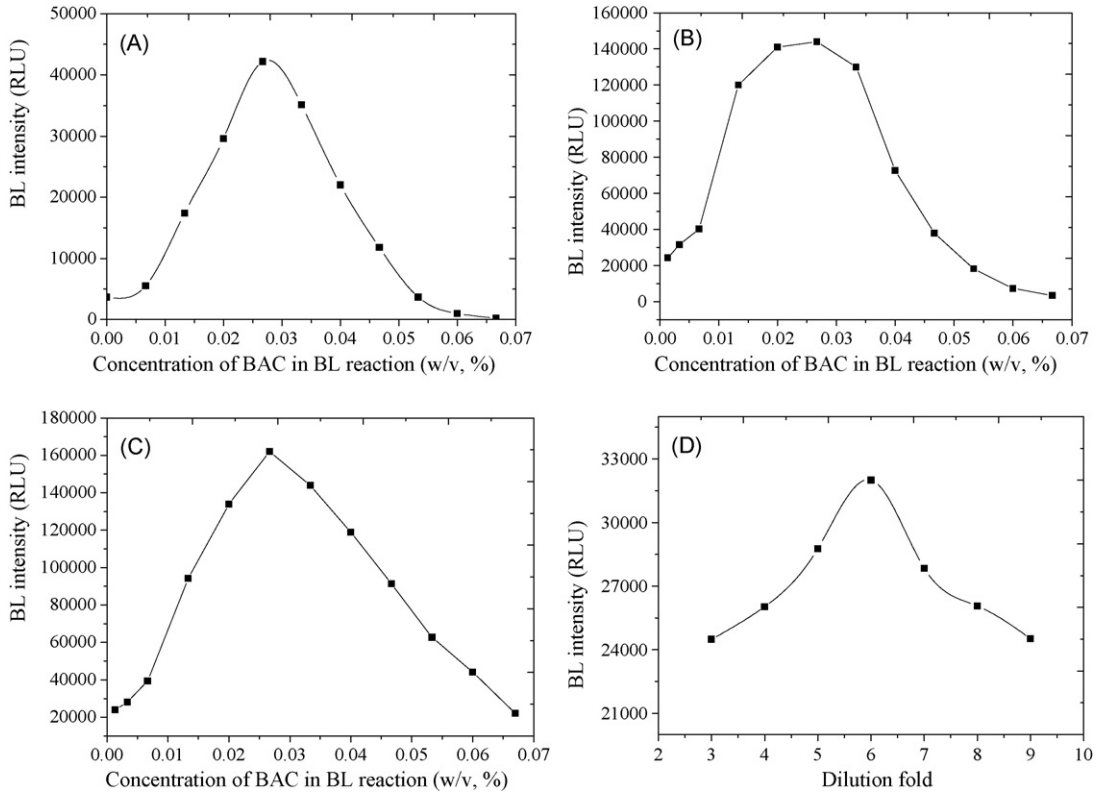

Fig. 3. The optimized conditions on separating bacteria using bioluminescence. Effect of BAC concentrations on BL response curves. (A) The standard ATP, [ATP] = $\sim 10^{-10}$ M. (B) *Salmonella*, the cell number is $\sim 10^5$ CFU/mL. (C) *S. aureus*, the cell number is $\sim 10^5$ CFU/mL. (D) Effect of dilution fold of IMB on BL intensity. Cell numbers: 10^5 CFU/mL, [BAC] = 2.7×10^{-2}%.

captured magnetically with a 3 mm diameter NdFeB permanent magnet (Yingke Hongye Technical Corp., Beijing, China), as shown in Fig. 2D.

2.6. Chip operating procedure

Bead-beds were prepared as described, as shown in Fig. 2E, then the sample 1 (*Salmonella*, FITC-labeled anti-*Salmonella* antibodies) was firstly pumped through the chip from E inlet using a 100-μL syringe (gastight #1710, Hamilton, Switzerland) for 20 min at 0.10 μL/min, simultaneously other inlets except F were pumped "buffer A" at 0.05 μL/min in order to keep the sample flowing circularly in the U-type microchannel. Next, sample 2 (*S. aureus*, FITC-labeled anti-*S. aureus* antibodies) was introduced. The results were obtained by using the fluorescent microscope equipped with a digital camera under I3 filter set (470–490 nm).

3. Results and discussion

3.1. Effect of BAC on the BL reaction

To investigate the effect of BAC on the BL reaction, light emission was observed in standard ATP and intracellular ATP from *Salmonella* and *S. aureus* cells, respectively. The concentration of BAC was in the range of 6.7×10^{-3} to 6.7×10^{-2}% in both mixtures. The results, as shown in Fig. 3, indicated the BL intensity and the amount of light emission were remarkably enhanced with the concentration of BAC increasing until 2.7×10^{-2}%, after that the BL intensity decreased rapidly. Besides that, the BL intensity was stronger than that without BAC until the concentration of BAC was up to 5.3×10^{-2}%. At the maximum point, the BL intensity was improved by a factor of 10 times compared to that without BAC. The mechanism of firefly bioluminescence decomposition can be deduced as follows [26].

Firefly luciferin reacts with ATP under the catalysis of luciferase and Mg^{2+}, yielding adenylluciferin, a mid-product (reaction (1)), which will be oxidation by O_2 according to nucleophilic acyl substitution, making CO_2 is left and yielding oxyluciferin (reaction (2)), which is in the excited state (marked as *) and unstable. Next oxyluciferin* decays to the ground state, accompanied with light as the energy of emission from the reaction as the form of photons (reaction (3)):

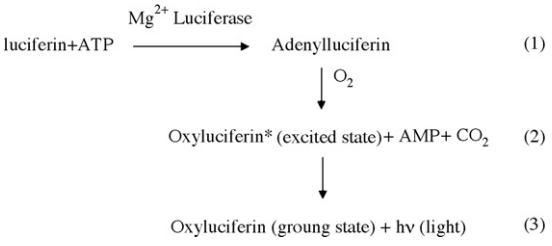

The reaction (1) is the rate-determining step (RDS) of the three reactions. So the above observations can be interpreted as follows. BAC, one of the cationic surfactants, the polar head of which can attract the anionic groups of luciferin and ATP, leads to accelerate the reaction (1) due to improve the combination of ATP and luciferin. Besides, BAC can inhibit the activity of luciferase. Therefore, before the concentration of BAC was up to 5.3×10^{-2}%, the improvement from BAC could counteract its inhibitory effect, thus resulting the enhancement of BL intensity with increasing concentration of BAC. On the contrary, after the concentration of BAC was more than 5.3×10^{-2}%, the inhibitory effect was dominant in the BL reaction, inducing the decrease of BL intensity.

The investigation in intracellular ATP from bacterial cells was shown in Fig. 3B (*Salmonella*) and Fig. 3C (*S. aureus*), which were examined by adding different volume of 1.0% BAC solution in a 100-μL of bacteria dilution. The volume of 1.0% BAC was in the range of 10–100 μL, and the concentration of BAC in releasing ATP and BL reaction was shown in Table 1. Bacterial cell number of both is ~10^5 CFU/mL. The trend of both curves in Fig. 3B and C was as similar to Fig. 3A, which suggests: firstly, the reason for the enhancement and decrease of the BL intensity is from BAC instead of ATP; secondly, the activity of intracellular ATP and standard ATP was same in the BL reaction; finally, the efficiency of BAC releasing ATP is high. The BL intensity reached maximum when the concentration of BAC was 2.7×10^{-2}% in both Fig. 3A and B, which means the optimum concentration of BAC is 2.7×10^{-2}% in this method of detecting bacteria.

Table 1
The BAC concentrations in releasing ATP and BL reaction.

Portion of adding BAC (μL)	Concentration of BAC in releasing ATP (w/v)	Concentration of BAC in BL reaction (w/v)
100 (1.0%)	0.50%	0.07%
90 (1.0%)	0.47%	0.06%
80 (1.0%)	0.44%	0.05%
70 (1.0%)	0.41%	0.05%
60 (1.0%)	0.38%	0.04%
50 (1.0%)	0.33%	0.03%
40 (1.0%)	0.29%	0.03%
30 (1.0%)	0.23%	0.02%
20 (1.0%)	0.17%	0.01%
100 (0.1%)	0.05%	0.01%
50 (0.1%)	0.03%	0.00%
20 (0.1%)	0.02%	0.00%

3.2. Measurement of ATP in bacterial extracts

The calibration curve for standard ATP and intracellular ATP shown in Fig. 4 was prepared under the optimum concentration of BAC. The detection limit for ATP and bacteria was defined as the concentration of ATP and cell numbers that produced the BL intensity equal to 3-fold of the blank intensity counted in the mixture containing no ATP or bacterial extracts. The detection limit of standard ATP in this method is 10^{-17} M and the linear range is 10^{-17}–10^{-14} M. Correlation coefficient for linear regression analysis is indicative of small errors and excellent linear reliability ($r^2 > 0.996$). In applications, as shown in Fig. 4B and C, the detection limit of both bacteria is 10 CFU/mL and the linear range is 10^1–10^4 CFU/mL, which is better than previous reports. So using this method we can detect bacterial cells even when they are in very low concentration.

3.3. Immunomagnetic separation

The efficiency of IMB capturing target bacterial cells is examined by condition of dilution fold and selectivity, and the results were shown in Fig. 3D and Table 2, respectively. The concentration of bacterial cells (*Salmonella*) is ~10^5 CFU/mL, and incubation time is approximately 10 min. Then the IMB capturing bacteria was removed by employing magnetic field. Next BAC was added in the washed bacteria–IMB complex suspension solution on a crashed ice bath to release ATP. Finally, luciferin–luciferase solution was injected in the extracts and detection began after shaking. The results, in Fig. 3D, show the BL intensity increased and reached maximum when dilution fold was 6, after which BL intensity decreased with the dilution fold increasing. The reason for the increase in BL intensity is maybe due to the beads density decreases gradually with the dilution fold increasing, which results in the capacity of beads blocking releasing ATP is weaker than before. Later, that there are relatively fewer beads to capture bacteria with the dilution fold continuous increasing may well explain the decrease of BL inten-

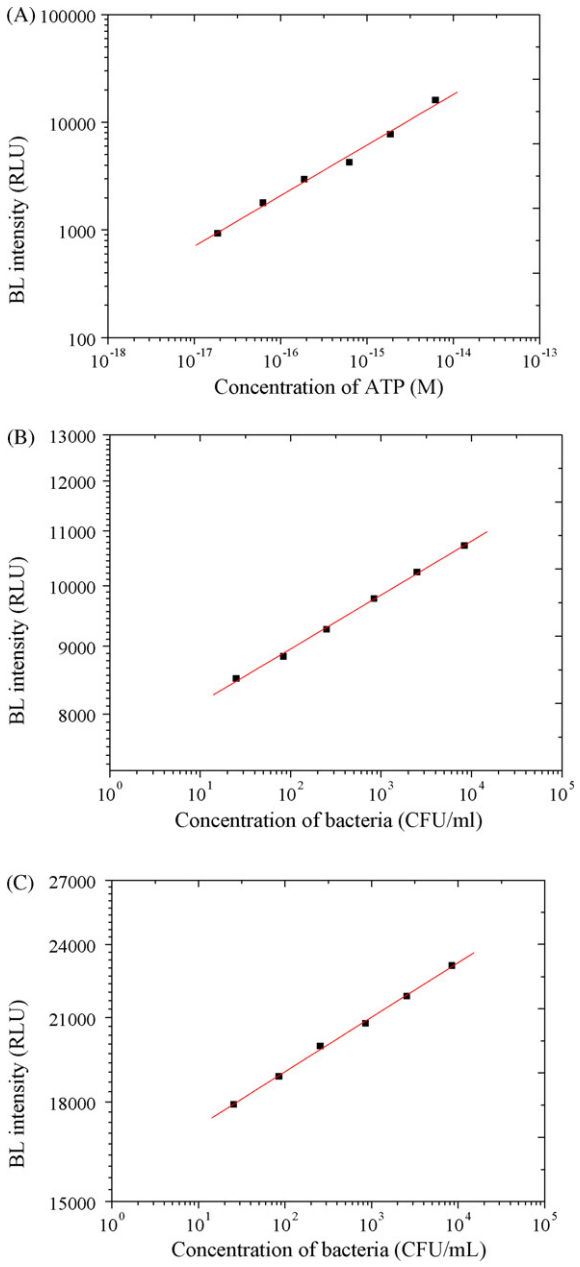

Fig. 4. The results of detecting bacteria using bioluminescence. Linear range of standard and intracellular ATP concentrations. [BAC] = 2.7×10^{-2}%. (A) Standard ATP's, $r^2 = 0.996$. (B) *Salmonella*'s, $r^2 = 0.999$. (C) *S. aureus*', $r^2 = 0.999$.

sity. So the optimum dilution fold of IMB is 6 in immunomagnetic separation.

The selectivity of the IMB was examined by using the *S. aureus* as an interferent for the *Salmonella* target cells. The colonies produced by the two species onto BPY agar could be easily identified and separately counted (*S. aureus*, yellow; *Salmonella*, white). The results in Table 2 indicate no significant non-specific binding of *S. aureus*. However, the binding efficiency of the *Salmonella* was reduced in the presence of higher concentration of *S. aureus*. The experiments showed that, although not so much *S. aureus* cells were captured by the beads, there could have been non-specific binding of cell-free material, which appeared to interact with the antibodies on the beads with the effect of reducing the number of binding sites available to capture the *Salmonella* cells. Therefore, the selectivity of IMB in immunomagnetic separation is acceptable.

3.4. Microfluidic chip method

In order to make good use of IMB, magnetically captured bead-bed was designed in a microfluidic chip (see Fig. 2). Initial formation of the bead-bed is an important step in preparing the device for sample capture. Bead capture was maximized through the use of an asymmetric magnetic field, achieved by placing a magnet on only one side of the chip. In the U-type microchip, the chamber (the part of the channel expanding outwards) provided a place to form bead-beds, shown in Fig. 5A and B, illustrating the magnetic beads were almost totally captured by the outside magnet and there was no bead in the microchannel.

Fig. 5C–H showed that there was no affinity between IMB and FITC-labeled antibodies and IMB alone could not be observed by the fluorescent microscope.

Fig. 6C and D demonstrated that when sample 1 (*Salmonella* and FITC-labeled anti-*Salmonella* antibodies) was introduced through the microchannel, only the bead-beds composed of the IMB anti-*Salmonella* were observed, so did the bead-beds composed of IMB anti-*S. aureus* when sample 2 was introduced, shown in Fig. 6A and B. So it is suggested that the two kinds of bacterial cells were separated and detected simultaneously by using the U-type microchip.

3.5. Primary application for detecting bacterial cells

The optimized conditions for the separation and detection of target bacteria from interferent and others are described in Sections 2.2–2.4. To demonstrate the utility of this method, target bacterial cells (*Salmonella*) were measured with and without interferent bacterial cells (*S. aureus*). One sample only contained target bacterial cells and the other also contained interferent bacterial cells. Initially, the number of bacterial cells in the two samples was very low, then the bacterial cells in the two samples replicated at the same condition until the culture was grown to midlog phase (OD_{600} = ~0.6) in 3–5 h. The two samples were separated by using IMB and extracted ATP by BAC. Finally, whether or not the original sample contained the target bacterial cells could be judged by comparing the BL signals in the reaction of the extracts and luciferase–luciferin solution, because the signal from the sample in the presence of target bacterial cells must be stronger than that without target bacterial cells. The results showed that the BL intensity with target bacterial cells was at least 100 times higher than that in the presence of interferent bacterial cells alone.

Table 2
Specific capture of *Salmonella* onto immunomagnetic bead from a mixed culture containing an excess of *S. aureus* cells.

Salmonella (CFU/mL) in suspension	*S. aureus* (CFU/mL) in suspension	*S. aureus*:*Salmonella* ratio	*Salmonella* (CFU/mL) on beads	*S. aureus* (CFU/mL) on beads
2.0×10^3	2.1×10^3	1.1:1	2.0×10^3 (98.5%)	1.3×10^0 (0.06%)
1.7×10^3	1.9×10^4	10.7:1	1.4×10^3 (76.4%)	2.1×10^1 (0.11%)

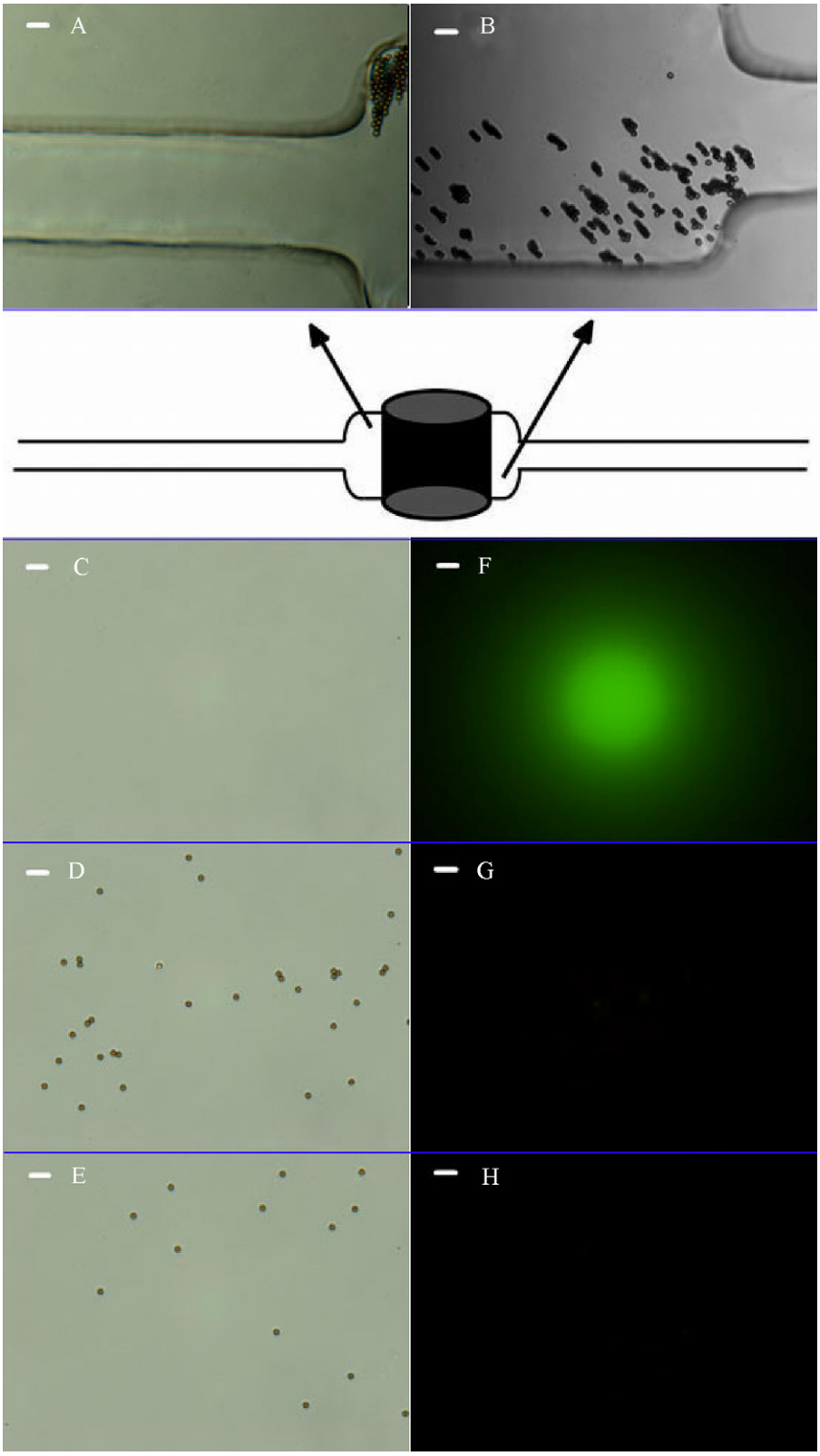

Fig. 5. The images of bead-beds and fluorescent microphotograph of IMB and FITC-labeled antibodies. (A) The left of the chamber placing bead-beds, showed there was no bead in the microchannel. (B) The right of the chamber, just close to the shadow cast by the magnet above. (C) The normal FITC-labeled antibodies. (D) The normal magnetic beads. (E) The normal magnetic beads after mixed with FITC-labeled antibodies. (F) The FITC-labeled antibodies exposed in the fluorescence. (G) The magnetic beads exposed in the fluorescence. (H) The magnetic beads after mixed with FITC-labeled antibodies exposed in the fluorescence. Scale bar = 10 μm.

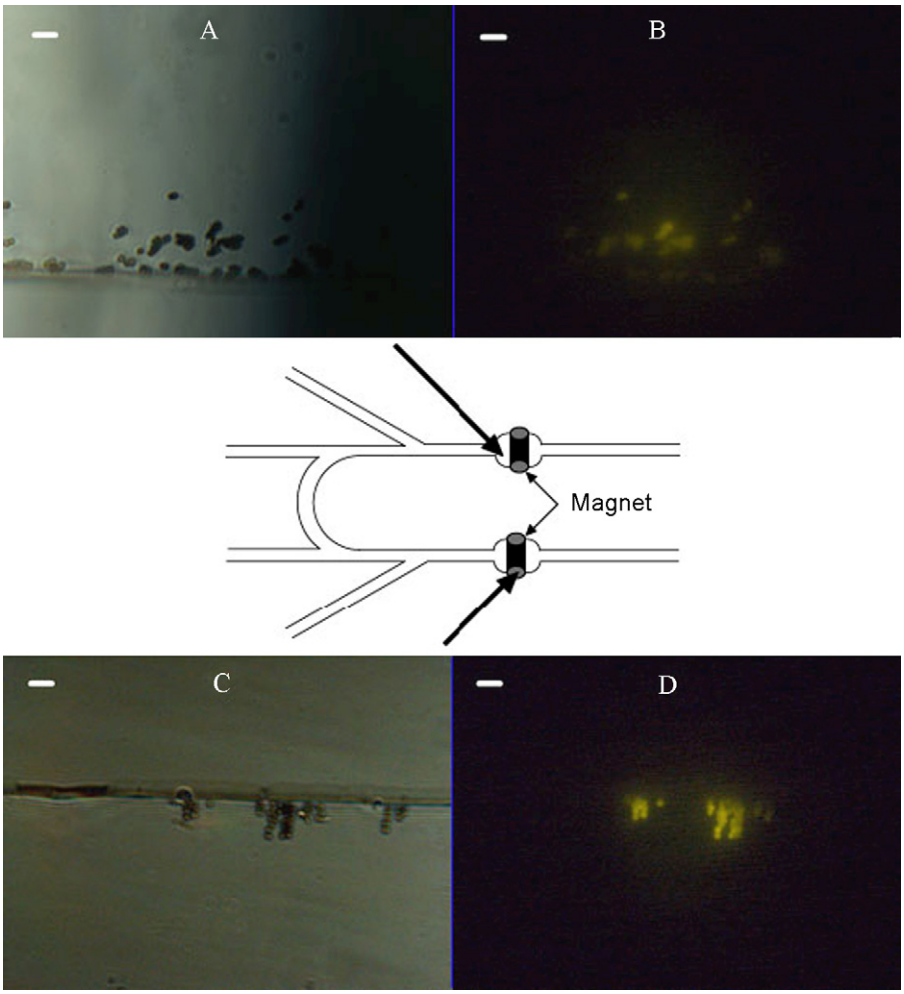

Fig. 6. The results of separation and detection of bacteria using the microfluidic chip. (A) Normal bead-beds composed of IMB anti-*S. aureus*, in the right of the shadow cast by the magnet above. (B) Bead-beds composed of IMB anti-*Salmonella* was exposed in the fluorescence, showing the bead-beds captured *S. aureus*. (C) Normal bead-beds composed of IMB anti-*Salmonella*, under the shadow cast by the magnet above. (D) Bead-beds composed of IMB anti-*Salmonella* was exposed in the fluorescence, showing the bead-beds captured *Salmonella*. Scale bar = 10 μm.

4. Conclusions

We found that except for the inhibitory effect on luciferase, BAC can not only release ATP from bacterial cells, but also enhance the BL intensity at some range of concentration. In addition, high efficiency in separating bacterial cells can be achieved by employing immunomagnetic bead. As a result, a highly sensitive and rapid immune bioluminescence method was established for separating and detecting bacteria, which was applied to *Salmonella* in the presence of *S. aureus* as interferent. Furthermore, a U-type PDMS/glass microchip was developed to separate and detect bacteria simultaneously.

Acknowledgements

This work was supported by National Natural Science Foundation of China (No. 90813015), National Key Technology R&D Program (2006BAK02A13) and National Basic Research Program of China (973 Program, No. 2007CB714507).

References

[1] M. Magliulo, P. Simoni, M. Guardigli, E. Michelini, M. Luciani, R. Lelli, A. Roda, J. Agric. Food Chem. 55 (2007) 4933.
[2] M. Zourob, S. Mohr, B.J.T. Brown, P.R. Fielden, M.B. McDonnellc, N.J. Goddard, Lab Chip 5 (2005) 1360.
[3] D.J. Squirrell, R.L. Price, M.J. Murphy, Anal. Chim. Acta 457 (2002) 109.
[4] Y. Mine, J. Agric. Food Chem. 45 (1997) 3723.
[5] X.-L. Su, Y. Li, Anal. Chem. 76 (7) (2004) 1824.
[6] F.C. Han, J. Luo, H.F. Zhang, D.C. He, X.J. Yan, World J. Microbiol. Biotechnol. 23 (2007) 1041.
[7] H. Xu, G.-L. Zhang, F.-B. Zhang, Chem. Ind. Eng. (China) 20 (2003) 27.
[8] N. Hattor, T. Sakakibara, N. Kajiyama, T. Igarashi, M. Maeda, S. Murakami, Anal. Biochem. 319 (2003) 287.
[9] T. Kiesslich, C.B. Oberdanner, B. Krammer, K. Plaetzer, J. Biochem. Biophys. Methods 57 (2003) 247.
[10] E.N. Efremenko, R.E. Azizov, A.A. Raeva, V.M. Abbasov, S.D. Varfolomeyev, Int. Biodeter. Biodegr. 56 (2005) 94.
[11] K. Fromell, G. Hulting, A. Ilichev, A. Larsson, K.D. Caldwell, Anal. Chem. 79 (2007) 8601.
[12] B.R. Branchini, T.L. Southworth, M.H. Murtiashaw, R.A. Magyar, S.A. Gonzalez, M.C. Ruggiero, J.G. Stroh, Biochemistry 43 (2004) 7255.
[13] N. Nakata, A. Oshoda, H. Tani, T. Kamidate, Anal. Sci. 19 (2003) 1183.
[14] R.H. Liu, J. Yang, R. Lenigk, J. Bonanno, P. Grodzinski, Anal. Chem. 76 (2004) 1824.
[15] T. Chen, J.-D. Lei, A.-J. Tong, Luminescence 20 (2005) 256.
[16] T. Taguchi, A. Arakaki, H. Takeyama, S. Haraguchi, M. Yoshino, M. Kaneko, Y. Ishimori, T. Matsunaga1, Biotechnol. Bioeng. 96 (2007) 272.
[17] B. Liu, M. Ozaki, H. Hisamoto, Q. Luo, Y. Utsumi, T. Hattori, S. Terabe, Anal. Chem. 77 (2005) 573.
[18] A. Sin, S.K. Murthy, A. Revzin, R.G. Tompkins, M. Toner, Biotechnol. Bioeng. 91 (2005) 816.
[19] D.C. Duffy, J.C. McDonald, O.J.A. Schueller, G.M. Whitesides, Anal. Chem. 70 (1998) 4974.
[20] V.I. Furdui, D.J. Harrison, Lab Chip 4 (2004) 614.
[21] M. Mujika, S. Arana, E. Castano, M. Tijero, R. Vilares, J.M. Ruano-López, A. Cruz, L. Sainz, J. Berganza, Biosens. Bioelectron. 24 (2009) 1253.

[22] N. Bao, B. Jagadeesan, A.K. Bhunia, Y. Yao, C. Lua, J. Chromatogr. A 1181 (2008) 153.
[23] T. Kamidate, T. Kinkou, H. Watanabe, Anal. Biochem. 244 (1997) 62.
[24] T. Kamidate, K. Yanashita, H. Tani, A. Ishida, M. Notani, Anal. Chem. 78 (2006) 337.
[25] T. Kamidate, S. Niwa, N. Nakata, Anal. Chim. Acta 424 (2000) 169.
[26] B.R. Branchini, M.H. Murtiashaw, R.A. Magyar, N.C. Portier, M.C. Ruggiero, J.G. Stroh, J. Am. Chem. Soc. 124 (2002) 2112.

Talanta 79 (2009) 669–675

Contents lists available at ScienceDirect

Talanta

journal homepage: www.elsevier.com/locate/talanta

Selective separation and determination of primidone in pharmaceutical and human serum samples using molecular imprinted polymer-electrospray ionization ion mobility spectrometry (MIP-ESI-IMS)

B. Rezaei, M.T. Jafari*, R. Khademi

Department of Chemistry, Isfahan University of Technology, Isfahan 84156-83111, Iran

ARTICLE INFO

Article history:
Received 5 April 2009
Received in revised form 21 April 2009
Accepted 21 April 2009
Available online 3 May 2009

Keywords:
Molecular imprinted polymer
Electrospray ionization
Ion mobility spectrometry
Primidone

ABSTRACT

Application of electrospray ionization ion mobility spectrometry (ESI-IMS) as the detection technique for separation method based on molecular imprinted polymer (MIP) was investigated and evaluated. The method is exhaustively validated, including sensitivity, selectivity, recovery, reproducibility, and column capacity. The linear dynamic range of 0.02–2.00 μg mL^{-1} was obtained for primidone analysis with ESI-IMS. The recovery of drug analyzed was calculated to be above 90% and the relative standard deviation (RSD), was below 3% for all experiments. Various real samples were analyzed with the coupled techniques, and the results obtained revealed the efficient clean-up of the samples using MIP separation before the analysis by ESI-IMS as a detection technique.

1. Introduction

Primidone (5-ethyl-5-phenyl-hexahydropyrimidine-4,6-dione) is an anticonvulsant of the pyrimidinedione class. It is used mainly to treat complex partial, simple partials, generalized tonic–clonic seizures, myoclonic, and akinetic seizures. Since 1980s it has been a valuable alternative to propranolol in the treatment of essential tremor. Unlike other anticonvulsants such as carbamazepine and valproic acid, primidone is rarely used in the treatment of bipolar disorder or any other psychiatric problem. Primidone has been occasionally used to treat long QT syndrome, cerebral palsy, and athetosis [1].

Several methods have been reported for determination of primidone which include colorimetry [2], spectrophotometry [3], polarography [4], thin layer chromatography (TLC) [5], gas chromatography [6], and high performance liquid chromatography (HPLC) [7]. Most commonly, HPLC and spectrophotometric methods are used for analysis of this compound. However, HPLC method requires a long run time involving gradient elution using expensive solvents. The spectrophotometric methods suffer from a number of disadvantages, such as narrow range of determination, requiring heating or extraction, long time for the reaction to complete, using non-aqueous systems, stability of the colored product formed, etc. [8].

Molecularly imprinted polymers (MIPs) are extensively cross-linked polymers containing specific recognition sites with a predetermined selectivity for analytes of interest. The molecular imprinting technique is a powerful method for preparing artificial recognition sites with predetermined selectivity for a wide range of target molecules. The procedure for synthesizing an MIP is based on the polymerization of a functional monomer and a cross-linking agent in the presence of a template. When the imprinted molecule is removed, the imprinted polymer with a high affinity for the template molecule is obtained. This affinity is due to the shape and the arrangement of the functional groups of the monomer units [9]. The MIPs are used as antibody-like materials for high selectivity and sensitivity, chemical inertness, long-term stability, availability in large quantities and insolubility in water and most organic solvents [10,11]. Several reviews have been published in recent years, demonstrating the significance of this approach to develop selective sample pretreatment methods [12–15]. Hence, MIP is a well-developed tool in the analytical field and has been extensively used to recognize the wide range of different chemical templates such as proteins [12], drugs [13,14], pesticides [16,17], and bacteria [18] in relatively complex matrices. Consequently, the imprinted polymers have become increasingly attractive in many fields of chemistry and biology, particularly as an affinity material for sensors [19,20], binding assays [21], artificial antibodies [22,23], adsorbents for solid-phase extraction [24,25], and chromatographic stationary phases [26,27]. A variety of methods such as radio-ligand displacement, chromophore- and fluorophore-labelled template analogues, electroactive analogues

* Corresponding author. Tel.: +98 311 391 2351; fax: +98 311 391 2350.
E-mail address: jafari@cc.iut.ac.ir (M.T. Jafari).

0039-9140/$ – see front matter © 2009 Elsevier B.V. All rights reserved.
doi:10.1016/j.talanta.2009.04.046

displacement, chemiluminescent detection, utilizing the quartz crystal microbalance devices (QCM), surface plasmon resonance spectroscopy (SPR), and electrochemical techniques have been used as detection techniques for MIPs [15]. However, a lot of these methods are time consuming, expensive, and quite laborious.

Ion mobility spectrometry (IMS) has been developed as an instrumental analytical technique for detecting and identifying organic compounds based upon the mobility of gas phase ions in a weak electric field. IMS equipment is robust and easy to miniaturize for field operation and provides a very fast, sensitive, inexpensive tool for the efficient analysis and characterization of various chemical compounds [28]. This method plays an important role in practical applications such as industrial and environmental monitoring and, drug and explosives detection [29]. O'Donnell et al. [30] have newly published a review on pharmaceutical applications of ion mobility spectrometry.

Ionization source is one of the key parts of the instrument and ^{63}Ni is a common ionization source for IMS. Other methods such as corona discharge, surface ionization, photo-ionization, and electrospray ionization (ESI) can be used as an ionization source for IMS. Recently [31], we have also shown that the corona discharge IMS can be another alternative technique for determination of antibiotic compounds after separation by solid-phase extraction (SPE). The results obtained reveal the capability of the SPE-IMS system for analysis of these compounds in a complex matrix of chicken meat. Electrospray ionization method converts sample molecules from liquid to gas phase ions. This nonradioactive ionization source has become attractive as a method for IMS determination of biomolecules [28]. This method may also be used for detection of inorganic compounds such as uranyl acetate in water [32]. The main advantages of ESI are possibility of direct introduction of liquid samples into IMS, retaining molecular information due to the soft ionization processes, and formation of multiply charged ions in some instances [28].

The objective of this work is to investigate the capability of the ESI-IMS as the detection system for MIP separation technique (MIP-ESI-IMS) and to analyze primidone (as an antiepileptic drug) in the complex matrices such as pharmaceutical and human serum samples. The results validate the capability of the ESI-IMS for the analysis of the compound after separation by MIP.

2. Experimental

2.1. Chemicals

The standard drugs of primidone, theophylline, and allopurinol were purchased from Sigma–Aldrich. Methacrylic acid (MAA), ethylene glycol dimethacrylate (EDMA), and 2,2′-azobis (2-isobutyronitrile) (AIBN) were purchased from Merck. The solvents, including dimethylformamide (DMF), acetone, HPLC-grade methanol, and acetic acid, were also purchased from Merck. Water was 18-MΩ deionized, prepared by Barnstead Ultrapure Water Systems.

2.2. Ion mobility spectrometry

The electrospray ionization ion mobility spectrometer (ESI-IMS) used for this research was designed and constructed at Isfahan University of Technology and has been described previously [33]. In brief, the main parts of the instrument are: the IMS cell, the electrospray needle, two high voltage power supplies, a pulse generator, an analogue to digital converter and a computer. In this work, the IMS cell of the system was constructed from 16 aluminum rings, which were separated from each others by thin PTFE rings. The IMS cell length was divided into three regions, the electrospray region (3 cm), the desolvation region (4 cm), and the drift region (11 cm in length). The drift and desolvation rings have the inner diameter of 4 and 2.1 cm, respectively. The aluminum rings are connected by a series of resistors to form the electric field gradient. The electrospray needle (P/N 7768-01, Hamilton, Reno, NV, USA) inserted into a Teflon tube to eliminate the corona discharge problem and it is fixed at one end of the cell. The Bradbury–Nielsen shutter grid is made of two series of parallel wires biased to a potential, creating an orthogonal field relative to the drift field, to block ion passage to the drift tube. The grid potential is removed for a short period of time by the pulse generator, to admit an ion pulse to the drift region. Generally, this period of time was selected 200 μs. Preheated nitrogen was employed as the drift and the desolvation gases with flow rates of 500 and 900 mL min^{-1}, respectively. The default Faraday plate detector configuration consisted of a 21-mm-diameter stainless steel plate positioned ∼1.0 mm behind the aperture grid. The high-speed A/D module (12-bit dynamic range) was used to measure the spectrometer output and to convert the analogue signal to a digital one. All mobility data were collected by data acquisition software and each IMS spectrum was the average of 50 individual spectra. Table 1 summarizes the operating conditions under which the IMS spectra were taken.

Table 1
Typical operating conditions during the experimental runs.

Operating parameters	Setting
Needle voltage	11.40 kV
Target electrode voltage	9.00 kV
Liquid flow rate	6 μL min^{-1}
Drift field	600 V cm^{-1}
Desolvation field	600 V cm^{-1}
Drift gas flow (N_2)	500 mL min^{-1}
Desolvation gas flow (N_2)	900 mL min^{-1}
Drift tube length	11 cm
Shutter grid pulse	0.3 ms
Number of IMS averages	50
Scan time	20 ms
Number of points per ion mobility spectrum	500

2.3. Molecular imprinted polymer

Molecular imprinted polymer was synthesized using primidone as a model template and MAA as a complementary functional monomer. MAA is the best functional monomer to establish selective hydrogen bonding interactions with the functional groups of primidone. EDMA was also used as a cross-linker which is able to provide sufficient rigidity of the cross-linked polymer. This is necessary for formation and functioning of the template specific binding sites [34,35].

In this work, non-covalent method with primidone was employed in the molecularly imprinted polymer synthesis. Thus, primidone (0.8 mmol), functional monomer (MAA, 3.9 mmol), cross-linker (EDMA, 19.5 mmol) and initiating agent (AIBN, 0.3 mmol) were dissolved in porogen (DMF, 8.5 mL). The molar ratio of template/monomer/cross-linker was 1:5:25. The solution was transferred into a glass tube and deoxygenated with N_2 stream for 10 min, sealed under nitrogen and then left to polymerize in an oil bath at 60 °C for 24 h. After polymerization, the glass tube was broken, and the polymer was mechanically grounded in a mortar. A steel sieve was employed to select particles with sizes ≤200 μm and a Soxhlet extraction system was also used to remove the analyte from the polymer. Afterward, the prepared MIP particles, kept at the room temperature overnight, were used through the SPE procedure. The preparation steps for MIP are shown in Fig. 1. As a reference, non-imprinted polymer (NIP) was also prepared in the same way but without the addition of the template (primidone). To evaluate the imprinting effect and the non-specific absorptions, the selectivity of NIP and MIP was also compared.

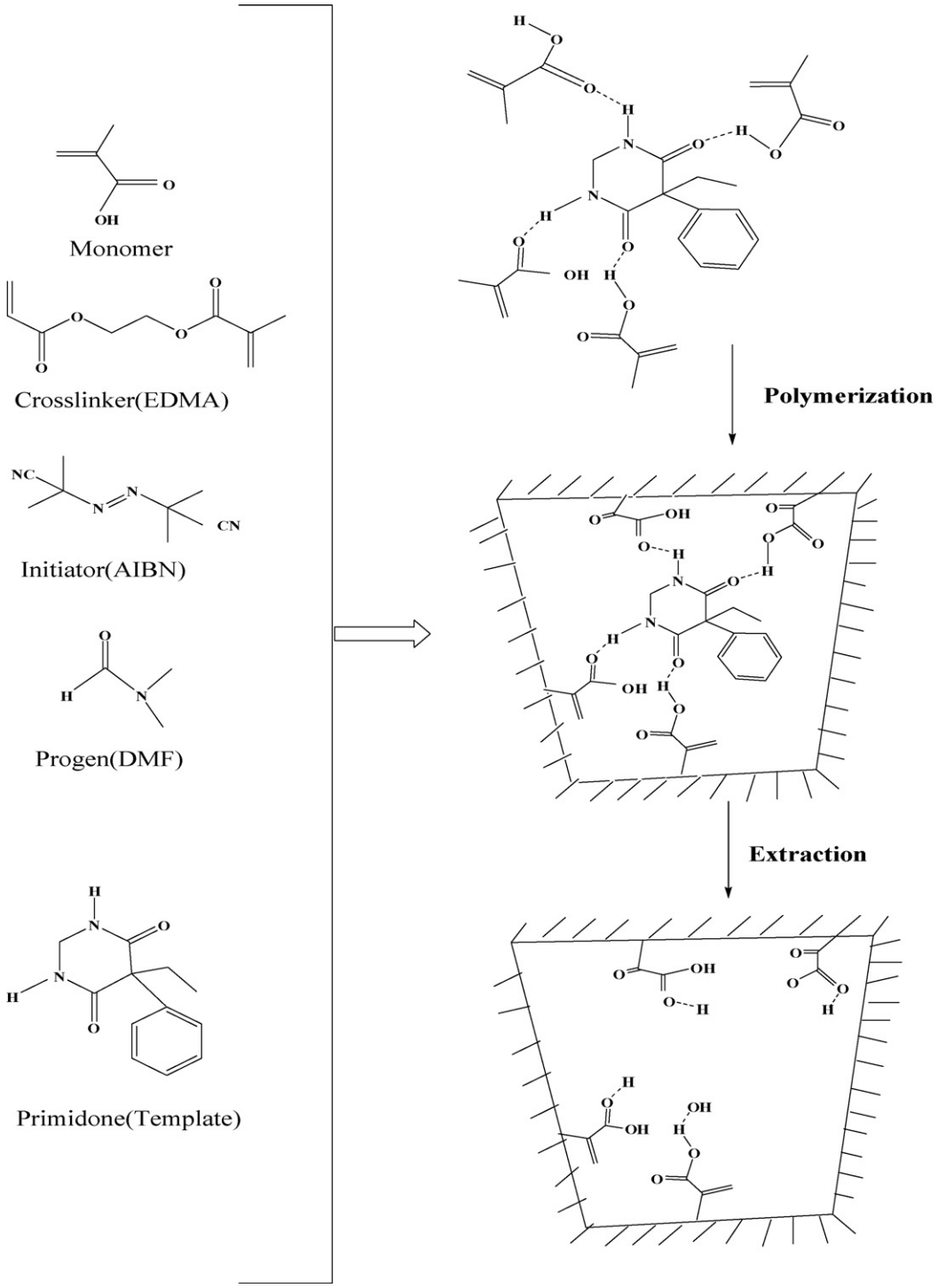

Fig. 1. Diagrammatic representation of hypothetical imprinted polymer formation using methacrylic acid (MAA) as the functional monomer and primidone as the template.

2.4. Extraction of primidone from the MIP

Removal of the primidone print molecule from the MIP particles was accomplished through a Soxhlet extraction. A sample of the primidone-imprinted polymer (2.0 g) was placed inside the extraction thimble. The extraction solvent (100 mL) was a mixture of methanol and acetic acid (5:5). Heat was applied to the solvent flask, at a rate that caused filling and eventual emptying of the extraction chamber. The extraction was continued for 24 h to produce the anti-primidone polymer particles. Quantification of the extracted primidone was accomplished by using UV spectrophotometer (Jasco, V-570) at 248 nm. Soxhlet extraction was not performed on the non-imprinted polymer particles.

2.5. Preparation of columns

The polymer particles were dispensed into a stainless steel column measuring 5 cm in length and 0.4-cm i.d. until the column bed was fully packed. A 10-μm frit was used in the end of column fitting to ensure no loss of the MIP. Methanol (2 mL) was run through the column to ensure uniform particle packing. The column was capped and connected to a 10-mL gastight syringe (Hamilton, Reno,

NV, USA) via a PTFE tube. Sample solution was delivered into the column by a programmable syringe pump (New Era Pump System Inc., USA). The preparation of a non-imprinted polymer column was achieved in a similar manner.

2.6. Pharmaceutical and serum sample analysis

The pharmaceutical samples were selected from primidone tablet with two different brands (Sobhan Pharm. Co. and AstraZeneca Co.). Ten primidone tablets of each brand were accurately weighed in order to find the average weight of each tablet. Then, the tablets were finely powdered using a mortar. An equivalent quantity of the powder containing a known amount of the active material was weighed and sonicated for 15 min, filtered into a volumetric flask and completed to the mark with methanol:water (90:10) to make a stock solution of primidone. Working solutions were prepared by successive dilution of the stock solutions for determination of primidone.

A 0.5-mL human serum sample was spiked with primidone (in water) to provide a working concentration of 0.44, 0.88, and 1.3 $\mu g\,mL^{-1}$. The serum sample was placed into a glass vial containing 4.0 mL of methanol, vortexed for 10 s, and centrifuged at 4000 rpm for 20 min. A 1.0-mL aliquot of the methanol layer was placed into the another glass vial and 3.0 mL methanol was added and centrifuged again at 4000 rpm for 10 min. One milliliter of the supernatant was diluted to 10 mL, and 2.0 mL of the aliquot was injected onto the anti-primidone column. After the solution had passed through the MIP column, it was washed by 2 mL of methanol:water, 3:7 with the flow rate of 0.1 mL min^{-1}. This solution washed out undesirable materials, which were chemically similar to the analyte or the analyte molecules adsorbed to non-specific binding point of MIP. Finally, the analyte was eluted with 2 mL of methanol:acetic acid (5:5). The flow rate was 0.1 mL min^{-1} in this step. The eluate was evaporated to dryness at ambient temperature under a stream of nitrogen and the residue was dissolved in 2 mL of methanol:water 90:10. After sonication for 5 min, this solution was directly delivered into the electrospray needle of the IMS.

3. Results and discussion

3.1. Ion mobility spectrum

The ion mobility spectrum of primidone compared with background spectrum is shown in Fig. 2. These spectra were obtained in the optimized IMS conditions given in Table 1. The primidone ion mobility spectrum shows two ion peaks (P_1 and P_2) with the reduced mobility values of 1.45 and 1.37 $cm^2\,V^{-1}\,s^{-1}$, respectively. Since there is not any report on reduced mobility for the product ions originating from primidone in the literature, the chemical formula of the ions, could not be characterized. In fact, the coupling of IMS to a mass spectrometer (MS) is needed for characterization of the chemical formula of the product ions.

3.2. Calibration curve and analytical parameters

In this work, a series of standards in the range 0.01–20 $\mu g\,mL^{-1}$ of primidone was prepared in methanol:water (90:10) and used to determine the analytical parameters of the instrument. When the standard solution of primidone was sprayed, the P_1 and P_2 peaks were appeared after a short time. When a stable electrospray was achieved, the sum area of the two ion peaks was calculated and considered as the response of ESI-IMS for each concentration of the compound. Ten ion mobility spectra were acquired to obtain the averaged data points. The response of ESI-IMS was plotted against the concentration of this compound (Fig. 3) and

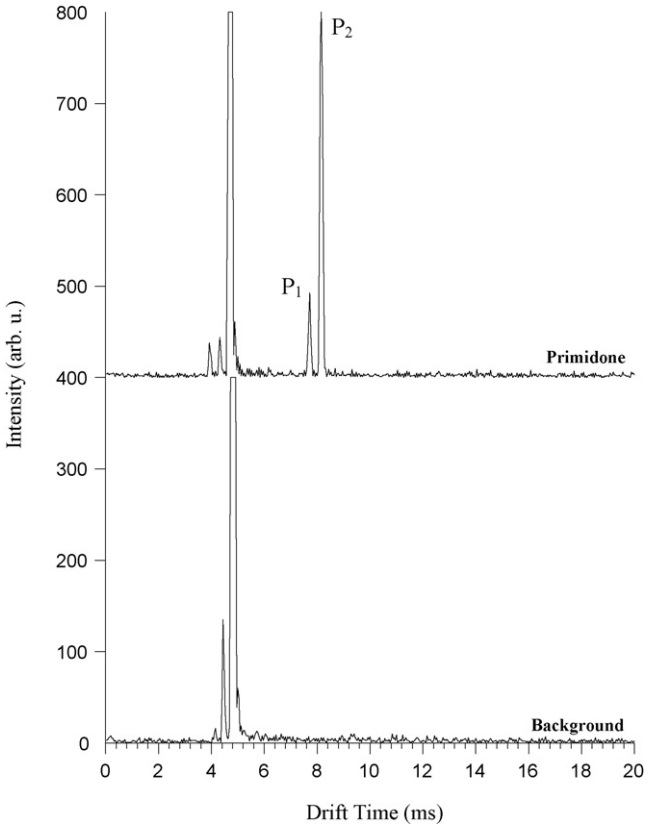

Fig. 2. The ion mobility spectrum of the primidone drug compared with the background spectrum.

calibration curve equation was developed by least-squares method. The analytical parameters of the proposed ESI-IMS method for the determination of primidone are summarized in Table 2. According to the data, good linearity was observed for primidone in the ranges 0.02–2.00 $\mu g\,mL^{-1}$. The linear dynamic range is about 2 orders of magnitude which is typical for electrospray ionization source and for most IMS systems. Using the standard definition of S/N = 3, the detection limit of 0.0051 $\mu g\,mL^{-1}$ was determined for this compound. The correlation coefficient was greater than 0.99 for the compound. The quantitative results obtained in this work

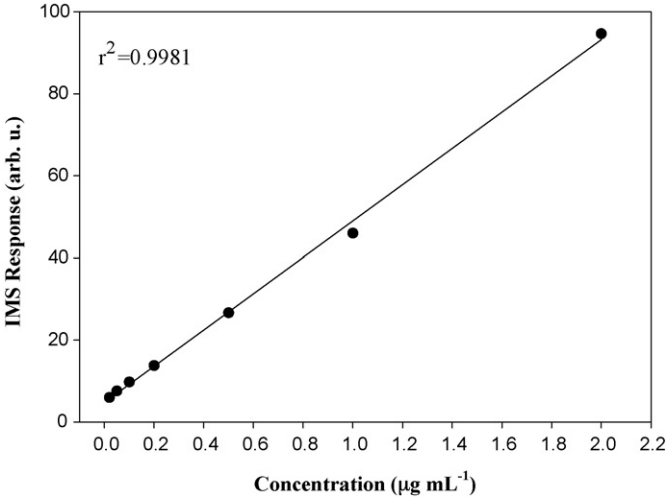

Fig. 3. Plots of IMS response against the concentration of primidone, the plot shows the linear dynamic range of 0.02–2.00 $\mu g\,mL^{-1}$.

Table 2
Analytical parameters for determination of primidone using ESI-IMS.

Parameter	Value
Linear range ($\mu g\,mL^{-1}$)	0.02–2.00
Correlation coefficient	0.9981
Limit of detection, LOD ($\mu g\,L^{-1}$)	5.1
Relative standard deviation, % RSD ($n = 4$, 1.0 $\mu g\,mL^{-1}$)	2.40

are promising for development of this method as analytical tools for detection of primidone in liquid samples.

3.3. Effect of solvent ratio and extraction time

In this work, target molecules present in MIPs were removed by Soxhlet extraction with successive volumes of appropriate solvent until the extract monitoring by IMS showed undetectable levels of primidone. Therefore, it is necessary to obtain the best solvent ratio (methanol–acetic acid) for the extraction of primidone from the polymer. The Soxhlet extraction with various ratios of methanol:acetic acid (9:1, 7:3, and 5:5) in different times, from 2 to 12 h, was followed by UV determination to obtain the optimum rebinding conditions. Fig. 4 shows that the best ratio of eluting solvent was 5:5, but because of bleeding primidone from MIPs, the extraction time of 24 h was selected for complete extraction of primidone.

3.4. Effect of pH of test solution

The effect of pH of test solution on the performance of MIP was studied by varying the pH in the range of 3–9 in steps of 1. The obtained results were shown in Fig. 5. As this figure shows, when the pH was increased from 3 to 9, no considerable deviation was observed in the adsorption of the analyte on the MIP sorbent. This figure shows the recoveries were changed in the range of 91.6–94.3%, when the pH was varied from 3 to 9. Therefore, the pH of the test solution was adjusted to ~7 for all of the experiments.

3.5. Effect of flow rate

The selective binding of primidone to the imprinted polymer had to be optimized in order to circumvent a decreased sensitivity of the MIP technique. In this technique, the selectivity can be enhanced by accessibility to the binding sites inside the porous polymer particles

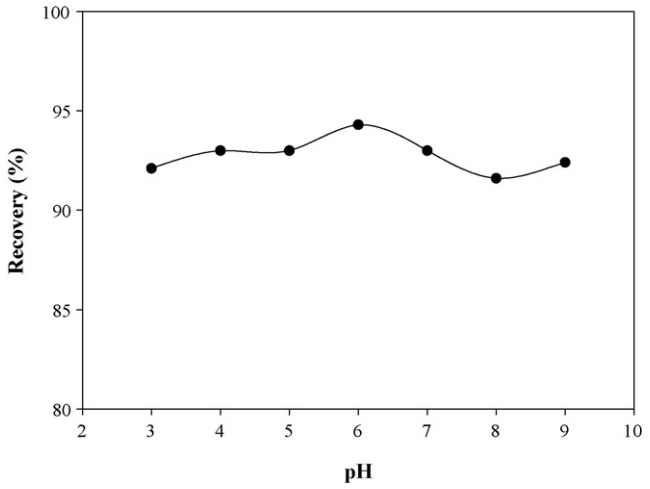

Fig. 5. The effect of eluent pH on the recovery percentage of extracted primidone.

which are affected by molecular diffusion [36]. Since the sample flow velocity dictated the time available for diffusion, analyte selectivity of MIP was evaluated by varying the flow rate over a range of 0.05–1.00 mL min^{-1}. Standard solution of 100.0 mg L^{-1} primidone was injected into the column, followed by adsorption of the bound analyte. The recoveries were calculated and plotted against the flow rate, Fig. 6. According to this figure, primidone displayed a trend of increased binding efficiency with decreasing flow rate, which provided more time for the diffusion of primidone molecules to the strong and selective binding sites inside the MIP particles. At the low flow rate of 0.05 mL min^{-1}, which was most favorable to the selective binding of primidone, in addition to time consuming, non-specific binding of other interferences still occurred and their elimination was essential before primidone could be determined accurately.

3.6. Performance of the MIP

In this work, parameters such as selectivity, reproducibility, and retention capacity (sorption capacity) were studied for investigation of MIP performance. The main problem associated with SPE columns packed with ordinary stationary phases is low selectivity of the retention mechanism. MIPs capable of producing materials

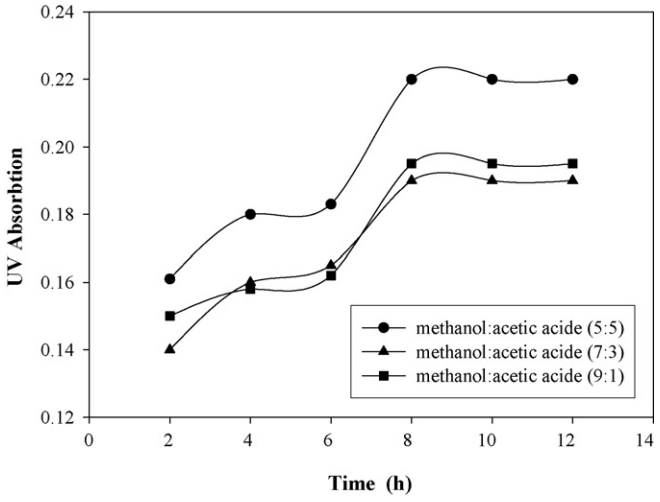

Fig. 4. The plots of the extracted primidone using Soxhlet extraction versus the extraction time onto the different ratios of methanol:acetic acid (■) 9:1, (▲) 7:3, and (●) 5:5.

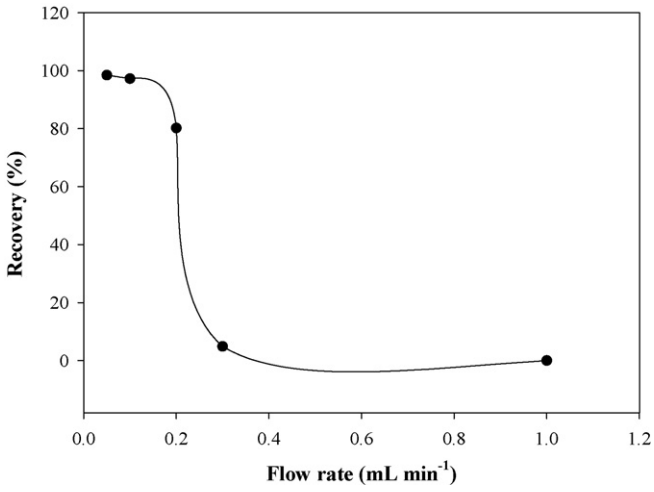

Fig. 6. Recoveries obtained for primidone regarding to the amount of drug present in the solution after loading of 100.0 mg L^{-1} primidone (2.0 mL) versus the flow rate of mobile phase.

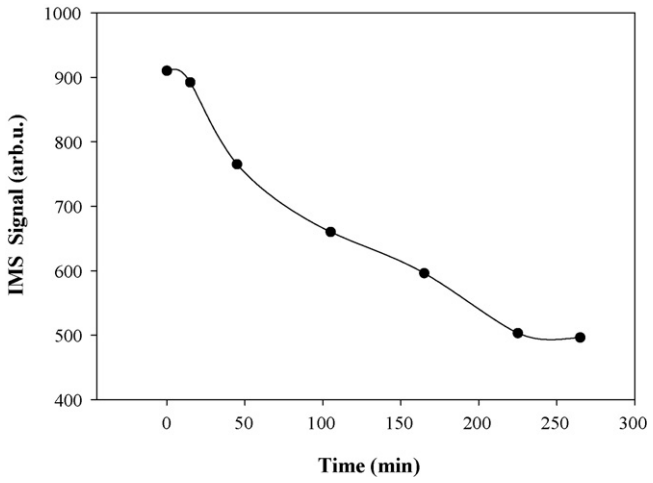

Fig. 7. The relationship between the ESI-IMS response of adsorbed primidone and adsorption time, when 0.08 g of imprinted polymer was added to 100 mL of the drug solution (10.0 μg mL^{-1}).

with "antibody-like" selectivity are extensively cross-linked polymers containing specific recognition sites with a predetermined selectivity for analytes of interest. The chemical and physical robustness of the MIP, in combination with the polymer's stability, selectivity and sensitivity, has been proven to be a good sorbent for molecularly imprinted solid-phase extraction (MISPE) applications. The selectivity of MIPs for target compound and related analogues was evaluated by determining the extraction efficiency of several compounds such as theophylline and allopurinol. In this regard, the sample solution (100 μg mL^{-1}) of each compound was prepared and passed through the MIP column. Washing, elution and other processes for sample preparation were carried out according to those for primidone which were mentioned previously. Ion mobility spectra of the respective solution were obtained with no theophylline, and allopurinol ion peaks revealing that the MIP polymer did not adsorb a significant amount of selected interference material. Therefore, it can be assumed that proposed MIP polymer is not selective about interferences and this leads to less matrix effects on instrumental analysis of primidone. In this work, the MIP polymer which had been used several times (n = 5) for the analysis of the primidone samples, was used for the extraction of a sample with the 0.5 μg mL^{-1} concentration. The obtained results indicate the recovery percentage of about 93%, pointing out that there is an acceptable reproducibility for using the synthesized MIP.

Another critical step in any MIP-based protocol is the determination of retention capacity, as it allows the high extraction efficiency to be revealed. For determination of retention capacity in this work, 0.08 g of imprinted polymer was added to 100 mL of the analyte standard solution (10.0 μg mL^{-1}), and the IMS signal of the supernatant was explored at different times. Fig. 7 shows the response of the IMS versus the elapsed time. According to this figure, the signal is maximum at the initial time (t = 0) and decays exponentially as the time increases. The IMS signal reaches to the constant value after about 250 min. The retention capacity was calculated to be 6.9 mg g^{-1} in this work.

3.7. Real sample analysis

To demonstrate the applicability of the coupled MIP-IMS system for the analysis of real sample, two categories of real sample including pharmaceutical samples and spiked plasma of human blood were analyzed. In this regard, the primidone drug of the samples was extracted according to the procedure described in Section 2.6. For plasma protein precipitation, where the sample is mixed

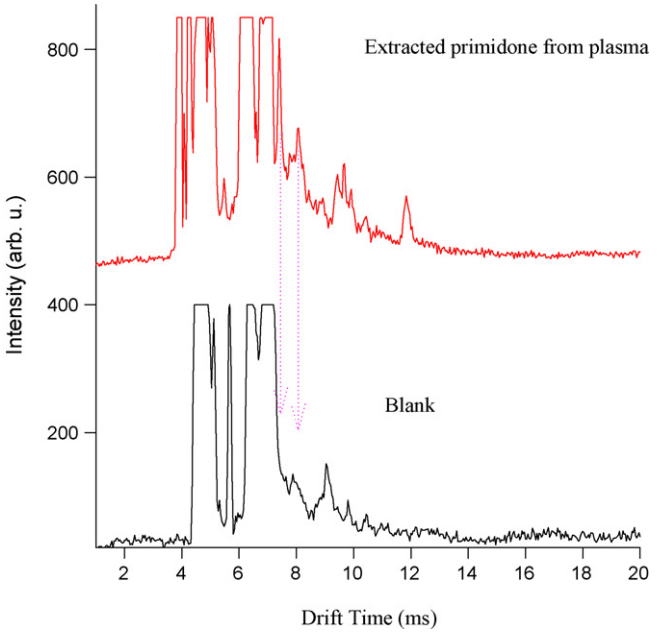

Fig. 8. The ion mobility spectrum of primidone extracted from plasma sample (1.3 μg mL^{-1}) compared with the blank spectrum.

with an organic solvent, using acetonitrile or methanol is often the method of choice when detection is by a sensitive and specific method such as MIP-IMS so that the dilution of the sample is not a limiting factor. Previous studies [37,38] have indicated that the methanol yields a better precipitation efficiency of plasma protein, and three times methanol of the plasma volume can precipitate the plasma proteins completely. In this work, methanol was used for protein precipitation of plasma samples. However, during the extraction of plasma samples with MIP, a column blockage problem arose. To overcome this problem, two protein precipitation steps were separately accomplished before the MIP separation (Section 2.6).

The ion mobility spectrum of primidone extracted from spiked plasma sample using MIP sorbent is shown in Fig. 8. According to this figure, it is clearly observed that the major interferences of plasma matrix could be eliminated by MIP system. Ion mobility analysis of real samples was carried out by the previously mentioned method (Section 3.2) and the results are shown in Table 3. Based on these results, the extraction recoveries of the analytes from the real samples were satisfactory and consequently, the proposed coupled system of MIP-IMS can be easily employed for the analysis of primidone in pharmaceutical and blood samples.

Table 3
Recovery percentages of primidone for spiked samples (n = 4 and 3 for tablet and blood samples, respectively).

Sample	Primidone added (μg mL^{-1})	Average of primidone found (μg mL^{-1})	Recovery percentage
Tablet 1[a]	–	0.66	–
	0.50	1.06	109.4 ± 8.0
	1.00	1.75	95.0 ± 1.4
Tablet 2[b]	–	0.55	–
	0.50	1.10	98.0 ± 3.0
	1.00	1.84	87.0 ± 3.0
Blood	0.44	0.45	108.0 ± 8.7
	0.88	0.90	102.8 ± 2.1
	1.30	1.19	91.3 ± 6.8

[a] From AstraZeneca Co.
[b] From Sobhan Pharm. Co.

4. Conclusions

The research conducted in this work is expanding the MIP as a powerful technique for selective separation of primidone and followed for detection with electrospray ionization ion mobility spectrometry (ESI-IMS) as a very sensitive analytical tool. Electrospray ionization ion mobility spectrometry has many desirable characteristics to be integrated with MIP separations. The results obtained in this research showed that ESI-IMS is extremely compatible with these separations and the MIP-ESI-IMS system has great capability for providing highly selective analysis of trace chemical and biochemical compounds. Based on the obtained results, manual introduction of samples to the ESI-IMS is useful for showing potential of this detection technique. However, it is required an online feeding of the MIP column eluate into the ESI-IMS detector is necessary. This work is being expanded to the analysis of various compounds such as drugs and pesticides in complex biological and environmental extracts.

Acknowledgment

We wish to express our gratitude to the Center of Excellence for Sensors, Isfahan University of Technology (IUT), Iran for the financial support.

References

[1] http://en.wikipedia.org/wiki/Primidone.
[2] J.W. Huisman, Clin. Chim. Acta 13 (1966) 323.
[3] M. Contin, M. Balboni, E. Callegati, C. Candela, F. Albani, R. Riva, A. Baruzzi, J. Chromatogr. B 828 (2005) 113.
[4] M. Romer, L.G. Donaruma, P. Zuman, Anal. Chim. Acta 88 (1977) 261.
[5] C.M. Davis, D.C. Fenimore, J. Chromatogr.: Biomed. Sci. Appl. 222 (1981) 265.
[6] H. Nau, D. Jesdinsky, W. Wittfoht, J. Chromatogr.: Biomed. Sci. Appl. 182 (1980) 71.
[7] V. Ferranti, C. Chabenat, S. Ménager, O. Lafont, J. Chromatogr. B 718 (1998) 199.
[8] T. Saffaj, M. Charrouf, A. Abourriche, Y. Aboud, A. Bennamara, M. Berrada, Dyes Pigments 70 (2006) 259.
[9] Y. Tan, L. Nie, S. Yao, Analyst 126 (2001) 664.
[10] L.Q. Lin, J. Zhang, Q. Fu, L.C. He, Y.C. Li, Anal. Chim. Acta 561 (2006) 178.
[11] J.O. Mahony, K. Nolan, M.R. Smyth, B. Mizaikoff, Anal. Chim. Acta 534 (2006) 31.
[12] A. Bossi, F. Bonini, A.P.F. Turner, S.A. Piletsky, Biosens. Bioelectron. 22 (2007) 1131.
[13] D.A. Spivak, Adv. Drug Deliv. Rev. 57 (2005) 1779.
[14] C.A. Lorenzo, A. Concheiro, J. Chromatogr. B 804 (2004) 231.
[15] C. Alexander, H.S. Andersson, L.I. Andersson, R.J. Ansell, N. Kirsch, I.A. Nicholls, J. O'Mahony, M.J. Whitcombe, J. Mol. Recognit. 19 (2006) 106.
[16] C. Baggiani, F. Trotta, G. Giraudi, C. Giovannoli, A. Vanni, Anal. Commun. 36 (1999) 263.
[17] I. Ferrer, F. Lanza, A. Tolokan, V. Horvath, B. Sellergren, G. Horvai, D. Barcelo, Anal. Chem. 72 (2000) 3934.
[18] A. Aherne, C. Alexander, M.J. Payne, N. Pérez, E.N. Vulfson, J. Am. Chem. Soc. 118 (1996) 8771.
[19] F.L. Dickert, P. Lieberzeit, M. Tortschanoff, Sens. Actuators B 65 (2000) 186.
[20] K. Hirayama, Y. Sakai, K. Kameoka, K. Noda, R. Naganawa, Sens. Actuators B 86 (2002) 20.
[21] I. Chianella, M. Lotierzo, S.A. Piletsky, Anal. Chem. 74 (2002) 1288.
[22] N. Lavignac, C.J. Allender, K.R. Brain, Anal. Chim. Acta 510 (2004) 139.
[23] L. Ye, K. Mosbach, React. Funct. Polym. 48 (2001) 149.
[24] A. Molinelli, R. Weiss, B. Mizaikoff, J. Agric. Food Chem. 50 (2002) 1804.
[25] R. Weiss, A. Molinelli, M. Jakusch, B. Mizaikoff, Bioseparation 10 (2001) 379.
[26] C.C. Hwang, W.C. Lee, J. Chromatogr. B 765 (2001) 45.
[27] S. Peter, L. Schweitz, S. Nilsson, Electrophoresis 24 (2003) 3892.
[28] G.A. Eiceman, Z. Karpas, Ion Mobility Spectrometry, 2nd ed., CRC Press, Boca Raton, 2005.
[29] G.A. Eiceman, Trends Anal. Chem. 21 (2002) 259.
[30] R.M. O'Donnell, X. Sun, P.B. Harrington, Trends Anal. Chem. 27 (2008) 44.
[31] M.T. Jafari, T. Khayamian, V. Shaer, N. Zarei, Anal. Chim. Acta 581 (2007) 147.
[32] H.M. Dion, L.K. Ackerman, H.H. Hill, Talanta 57 (2002) 1161.
[33] M.T. Jafari, Talanta 77 (2009) 1632.
[34] T.A. Sergeyeva, S.A. Piletsky, O.O. Brovko, E.A. Slinchenko, L.M. Sergeeva, T.L. Panasyuk, A.V. El'skaya, Analyst 124 (1999) 331.
[35] T.A. Sergeyeva, S.A. Piletsky, O.O. Brovko, E.A. Slinchenko, L.M. Sergeeva, A.V. El'skaya, Anal. Chim. Acta 392 (1999) 105.
[36] W.M. Mullett, E.P.C. Lai, J. Pharm. Biomed. Anal. 21 (1999) 835.
[37] W. Kang, J.H. Jeong, E. Ma, K. Kwon, J. Pharm. Biomed. Anal. 44 (2007) 1178.
[38] Y. Xu, J. Huang, F. Liu, S. Gao, Q. Guo, J. Chromatogr. B 852 (2007) 101.

Talanta 79 (2009) 947–952

Contents lists available at ScienceDirect

Talanta

journal homepage: www.elsevier.com/locate/talanta

Microwave assisted extraction of iodine and bromine from edible seaweed for inductively coupled plasma-mass spectrometry determination

Vanessa Romarís-Hortas, Antonio Moreda-Piñeiro, Pilar Bermejo-Barrera*

Department of Analytical Chemistry, Nutrition and Bromatology, Faculty of Chemistry, University of Santiago de Compostela, Avenida das Ciencias, s/n, 15782 – Santiago de Compostela, Spain

ARTICLE INFO

Article history:
Received 15 January 2009
Received in revised form 15 May 2009
Accepted 20 May 2009
Available online 27 May 2009

Keywords:
Microwave assisted extraction
Tetramethylammonium hydroxide
Iodine
Bromine
Edible seaweed
Inductively coupled plasma-mass spectrometry

ABSTRACT

The feasibility of microwave energy to assist the solubilisation of edible seaweed samples by tetramethylammonium hydroxide (TMAH) has been investigated to extract iodine and bromine. Inductively coupled plasma-mass spectrometry (ICP-MS) has been used as a multi-element detector. Variables affecting the microwave assisted extraction/solubilisation (temperature, TMAH volume, ramp time and hold time) were firstly screened by applying a fractional factorial design ($2^{5-1}+2$), resolution V and 2 centre points. When extracting both halogens, results showed statistical significance (confidence interval of 95%) for TMAH volume and temperature, and also for the two order interaction between both variables. Therefore, these two variables were finally optimized by a 2^2 + star orthogonal central composite design with 5 centre points and 2 replicates, and optimum values of 200 °C and 10 mL for temperature and TMAH volume, respectively, were found. The extraction time (ramp and hold times) was found statistically non-significant, and values of 10 and 5 min were chosen for the ramp time and the hold time, respectively. This means a fast microwave heating cycle. Repeatability of the over-all procedure has been found to be 6% for both elements, while iodine and bromine concentrations of 24.6 and 19.9 ng g^{-1}, respectively, were established for the limit of detection. Accuracy of the method was assessed by analyzing the NIES-09 (Sargasso, *Sargassum fulvellum*) certified reference material (CRM) and the iodine and bromine concentrations found have been in good agreement with the indicative values for this CRM. Finally, the method was applied to several edible dried and canned seaweed samples.

1. Introduction

The ability of seaweed to concentrate inorganic species from seawater has been well recognized and thus, seaweed is considered as a natural source of essential elements [1]. Although these marine products have largely consumed in Asian countries since ancient times, the current interest on health food in western countries has led to an increase on the presence of seaweed in western markets and also to the development of seaweed-based industries in Europe. This last fact has conducted to such industries to seek data on the concentrations of both essential and toxic elements before commercialization of the products. Most of the required information consists of the detection and/or determination of heavy metals, mainly arsenic, mercury, cadmium, lead and tin; and also bioactive compounds [2]. Among the different bioactive compounds present in seaweed, iodine is an important micronutrient element with a well recognized bioactivity on the synthesis of thyroid hormones (thyroxine, T4; and triiodothyronine, T3) [3]. Although lack of iodine leads to iodine deficiency disorder excessive iodine dietary intake can result in serious pathological problems. Therefore, recommended iodine intakes have been established by several international organizations [4–7]. Concerning bromine, this element is not currently considered to be essential for health, although it has been reported certain therapeutic uses of bromine as an anti-epileptic agent in some paediatric cases [8]. Nowadays, the widespread production and use of brominated flame retardants (BFRs) have increased the interest on bromine compounds contamination [9] and the bromine determination as a first screening to assess BFRs in biological and environmental materials.

Because seaweed is a complex matrix, drastic operating conditions are needed for extracting trace compounds. However, sample pre-treatments based on the use of acids, commonly used for the multi-element determinations, can led to lack of accuracy for both iodine and bromine, because the generation and lost of volatile species (Br_2, I_2, HI or HBr) [10–12]. In addition, it has also been reported that the signal of iodine is less stable in acidic media than in alkaline media for inductively coupled plasma-optical emission spectrometry/mass spectrometry (ICP-OES/MS) [10,13,14]. Therefore, although some recent applications of acid digestion procedures to assess iodine can be found in the literature [15–17], most

* Corresponding author.
E-mail address: pilar.bermejo@usc.es (P. Bermejo-Barrera).

0039-9140/$ – see front matter © 2009 Elsevier B.V. All rights reserved.
doi:10.1016/j.talanta.2009.05.036

of the current sample pre-treatment methods for assessing iodine use alkaline reagents such as ammonia and, mainly, tetramethylammonium hydroxide (TMAH) [10,13,14,18–21]. In general, a total dissolution of the sample matrix is not reached when using TMAH as a reagent and therefore, TMAH-based methods are commonly referred as extraction or leaching procedures [11,13]. The extraction of iodine by the action of TMAH has been performed under mild conditions using drying ovens at temperatures around 90 °C [10,14,19]. Under these conditions, the extraction is performed for several hours. Microwave energy has been used for speeding up the extraction process, some times by means of domestic microwave ovens [18,21], and another times with focused microwave ovens in which the test tubes with the sample and the alkaline reagent are put into open vessels containing water [17,20]. A temperature of 90 °C is also used as an extracting temperature in these two last methods. The use of drastic conditions, using TMAH and microwave energy in high pressure reactors are not reported for leaching iodine and bromine simultaneously from complex matrices such as seaweed, which are expected to lead to shorter extraction times and high extraction efficiencies.

Concerning the detection techniques used to analyze these halogens, catalytic spectrophotometry, mainly based on the Sandell–Kolthoff reaction, offers good sensitivity and cost-effectiveness, and it is the procedure of choice for standard and official methods to assess iodine in foodstuff [22]. However, the main drawback of these methodologies is associated to the fact that iodine must be present as iodide so that the catalysed reaction occurs. This implies that all iodine forms must be as iodide in the final solution, and distillation and or reduction of iodine species steps after samples solubilisation and just before iodide determination are needed [18,21]. This leads to time consuming sample pre-treatments. On the other hand, analytical determinations based on ICP-OES/MS technologies are not influenced by the element form, measurements in the sample extracts can directly be performed and different elements can be measured at the same time. ICP-OES has been used to assess both elements [8,14,15] although it is not a very sensitive technique for halogens. When coping with TMAH extracts, the direct aspiration of solubilised samples leads to a non-stable plasma and bad repeatability of measurements. To increase sensitivity and avoid direct sample nebulization, some authors have developed methods based on the use of (I_2) vapour generation as a sampling technique coupled to ICP-OES [23,24]. These methodologies also offer as drawbacks bad repeatability and memory effects, moreover all the halogen forms must be converted into any species susceptible to form volatile molecules. All these limitations are avoided when using ICP-MS, which offers higher sensitivity. Therefore, the aim of the current work has been the development of a fast and reliable microwave assisted extraction (MAE) method using a modern laboratory microwave oven and TMAH under drastic conditions. ICP-MS has been used for the simultaneous and fast determination of total iodine and total bromine in the TMAH extracts from seaweed samples.

2. Experimental

2.1. Instrumentation

Iodine and bromine measurements were performed with an 820-MS inductively coupled plasma-mass spectrometer (Varian, Mulgrave, Australia) equipped with SPS3 autosampler (Varian) and a Micromist Low Flow nebulizer type (Varian) coupled to a computer controlled Peltier-cooled spray chamber and a low noise double off-axis quadrupole. An Ethos Plus microwave lab-station (Milestone, Sorisole, Italy) with 100 mL closed Teflon vessels with Teflon covers, HTC adapter plate and HTC safety springs (Milestone) were used for extracting iodine and bromine from seaweed samples. A centrifuge Centromix (Selecta, Barcelona, Spain) was used to separate solid and liquid phases. LYPH–LOCK® 6 L freeze dry system, model 77530 (Labconco Corporation, Kansas City, PO, USA) was used for freeze drying canned seaweed (seaweed in brines). A vibrating ball mill (Retsch, Haan, Germany), equipped with zircon cups (15 mL) and zircon balls (7 mm diameter), was used to pulverize dried seaweeds. An oven model 207 from Selecta was used to dried seaweed samples at low temperature. Sieves with nylon mesh (CISA, Barcelona, Spain) were used for sieving.

2.2. Reagents and standard solutions

Ultrapure water, 18 MΩ cm resistivity, obtained from a Milli-Q purification device (Millipore Co., Bedford, MA, USA) was used throughout this work. The alkaline extraction/solubilisation was performed with tetramethylammonium hydroxide 25% (v/v) in water (Merck, Darmstadt, Germany). Standard stock solutions of 1000 mg L^{-1} of iodide and bromide were prepared from 99.5% potassium iodide (Merck) and 99.0% potassium bromide (Probus, Barcelona, Spain), respectively. Tellurium chloride and yttrium nitrate standard solutions, 1000 mg L^{-1}, were from SCP Science (Montreal, Canada). The certified reference material was NIES-09 (Sargasso, *Sargassum fulvellum*) from the National Institute for Environmental Studies (Ibaraki, Japan).

2.3. Edible seaweed samples

Seaweed samples were supplied from a local manufacturer. These products have been harvested in the Galician coast (northwestern Spain) and include six main Atlantic seaweeds: *Porphyra* (Nori) and *Palmaria* (Dulse), as red seaweed, *Undaria pinnatifida* (Wakame), *Himanthalia elongata* (Sea spaghetti) and *Laminaria ochroleuca* (Kombu), as brown seaweed and *Ulva Rigida* (Sea Lettuce), as green seaweed. Dried seaweeds, approximately 100 g, were put into an oven for one day at a low temperature of 40° C to remove water traces. Leaves were cut into small pieces and then pulverized with a vibrating ball mill for 20 min in order to obtain particle sizes smaller than 300 μm [10,18]. The particle size was established after sieving (250 μm). Canned seaweed (Sea spaghetti and Furbelows – *Saccorhiza polyschides*) in brines, approximately 25 g wet weight, was lyophilized at −40 °C for two weeks and afterwards were milled following the process explained before. Dried powdered samples were stored in polyethylene bottles.

2.4. Microwave alkaline digestion

MAE procedure consisted of weighing 0.25 g of powdered seaweed into microwave Teflon vessels, and adding 10 mL of ultrapure water and 10 mL of TMAH. Vessels were then capped and subjected to microwave irradiation (Table 1). After cooling down, sample extracts were centrifuged for 10 min at 3000 rpm and the supernatant was transferred into 50 mL flasks. The solid residue

Table 1
Microwave assisted extraction program.

	Power (W)	Initial temperature (°C)	Final temperature (°C)	Ramp time (min)	Hold time (min)
1	1000	20 (room temperature)	200	10	0
2	1000	200	200	0	5

Table 2
Operating ICP-MS conditions.

General		
	Radiofrequency power (W)	1380
	Peristaltic pump speed (mL min^{-1})	0.45
	Stabilization delay (s)	35
	Number of replicates	3
	Nebulizer type	MicroMist
Gas flows (L min^{-1})	Nebulizer	0.98
	Plasma	17.0
	Auxiliary	1.65
	Sheath	0.27
	Skimmer cone	Nickel
	Sampler cone	Nickel
Torch alignment (mm)		
	Sampling death	7.0
Ion optics (V)		
	First extraction lens	−32
	Second extraction lens	−164
	Third extraction lens	−231
	Corner lens	−206
	Mirror lens right	25
	Mirror lens left	24
	Mirror lens bottom	27
	Entrance lens	3
	Fringe bias	−4.9
	Entrance plate	−3.4
	Pole bias	0
CRI (mL min^{-1})		
	Skimmer gas source	H_2
	Sampler gas source	OFF
	Skimmer flow	80
	Sampler flow	0
Mass-to-charge ratio		
	Br	79
	I	127

was rinsed with a small volume of water and after centrifugation the water rinses were combined with the above mentioned supernatant. Finally, extracts were filtered through 0.45 μm filters (Millipore) before ICP-MS measurements.

2.5. ICP-MS measurement

Iodine and bromine determination were performed by ICP-MS following the operation conditions listed in Table 2. TMAH extracts were conveniently diluted before ICP-MS measurement and the dilution was varied from 1:1 to 1:20. Preliminary studies were conducted for selecting the calibration type (standard addition and internal standard calibrations) and for minimising the isobaric interferences when measuring ^{127}I and ^{79}Br. Tellurium at a concentration of 2 mg L^{-1}, was selected for iodine determinations, while yttrium at 2 μg L^{-1} was chosen as an internal standard for bromine determinations. Similarly, the use of H_2 in the collision cell at a flow rate of 80 mL min^{-1} gave the best sensitivity and linear ranges for iodine and bromine determinations [17]. Calibrations have covered iodide and bromide concentrations between 0 and 1000 μg L^{-1}.

3. Results and discussion

3.1. Assignment of experiments and screening design

Some variables inherent to the MAE procedure; such as microwave power output, number of reactors and total volume (water + TMAH), as well as the sample mass, were conveniently fixed. The total volume inside the vessels was fixed to 15 mL. Regarding to the seaweed sample, all experiments were performed with a fixed seaweed mass of 0.25 g. Seaweed samples were pulverized and particle size was fixed within the 50–250 μm range (double sieving), according to Fecher et al [10], in order to guarantee a quantitative iodine releasing.

Variables affecting the MAE; such as temperature, ramp time and hold time, TMAH volume and a fifth variable (*dummy factor*) [25], have been screened by a $2^{5-1}+2$ fractional factorial design of resolution V with 2 centre points which results in fully randomized 18 runs. The low and high levels defining the experimental domain of these variables, the planned trials and the results of the response variables are summarized in Tables S1 and S2 in the supplementary material.

The extraction temperature has been programmed in two steps. The first one leads an increase on the temperature from room temperature to the extraction temperature. The time needed to reach the extraction temperature has been called *ramp time* (t_{ramp}). The second stage consists of a microwave heating at the extraction temperature. The time of heating at the extraction temperature has been called *hold time* (t_{hold}).

After performing the experiments, the iodine and bromine concentrations were measured against standard addition graphs. The analysis of variance (ANOVA) technique at a 95.0% confidence level, used to estimate the variable effects, can be visualised as standardized main effect Pareto charts (Fig. 1), where a minimum t value is given, considering as significant variables those that offer standardized effects higher than $\pm t$.

As shown, graphs illustrate that the most statistically significant variable is the TMAH volume for the extraction of both elements, followed by the extraction temperature with a t value quite close to the critical t value. After discarding the statistically non-significant variables, it is noticeable the presence of a statistically significant two order interaction between the variables TMAH volume and extraction temperature, as shown in Fig. 2. This means that extraction temperature is also a statistically significant variable and it must simultaneously be studied with the TMAH volume.

3.2. Optimization of variables affecting MAE of iodine and bromine from seaweed

Since ramp and hold times have been found as statistically non-significant factors, both were fixed at convenience values; 10 and 5 min for ramp time and hold time, respectively. To optimize those statistically significant variables (TMAH volume and extraction temperature) an orthogonal 2^2 + star central composite design (CCD) with 5 centre points and 2 replicates, resulting in 26 fully randomized runs, was used. Since TMAH was found to be the most statistically significant variable (positive effect), the experimental field definition for this variable was extended to larger values (low value 5 mL and high value 15 mL). Similarly, the experimental domain for the extraction temperature was also extended to the 125–190 °C range. Since some experiments are going to be prepared with large TMAH volumes, the total volume was fixed at 20 mL. Table S3 in the supplementary material lists the experimental runs from the CCD as well as the iodine and bromine concentrations measured against standard addition graphs; while, Fig. 3 shows the response surfaces for target analytes. It can be seen that higher iodine and bromine concentrations are obtained for high temperatures; while the effect of TMAH volume on iodine extraction is less important when performing the MAE at high temperatures. Concerning bromine, the effect of TMAH volume leads to maximum responses for intermediate volumes and also at high temperatures. Therefore, in order to get the best conditions for the simultaneous extraction of both elements a compromise TMAH volume of 10 mL (TMAH concentration of 12.5% (m/v)) was chosen. The selected temperature was 200 °C, which is the highest temperature studied in these experiments. Temperatures higher than this value could not

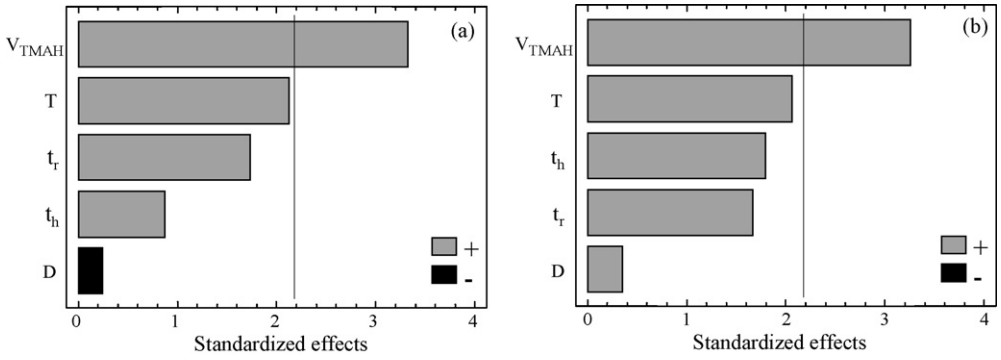

Fig. 1. Standardized main effect Pareto chart after $2^{5-1}+2$ fractional factorial design for iodine (a) and bromine (b).

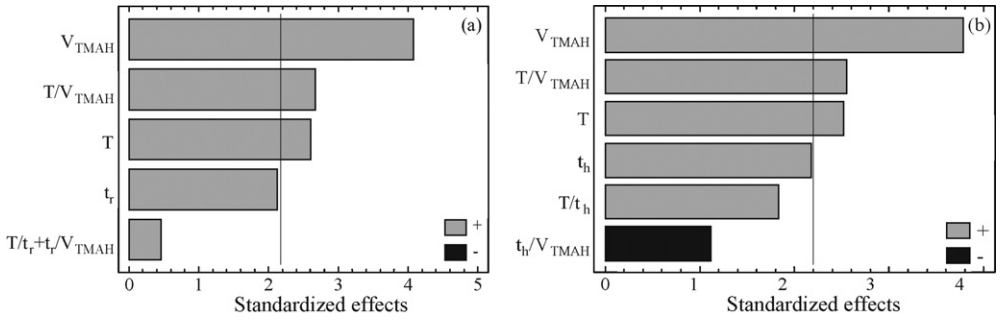

Fig. 2. Standardized two order interaction effect Pareto chart after $2^{5-1}+2$ fractional factorial design for iodine (a) and bromine (b).

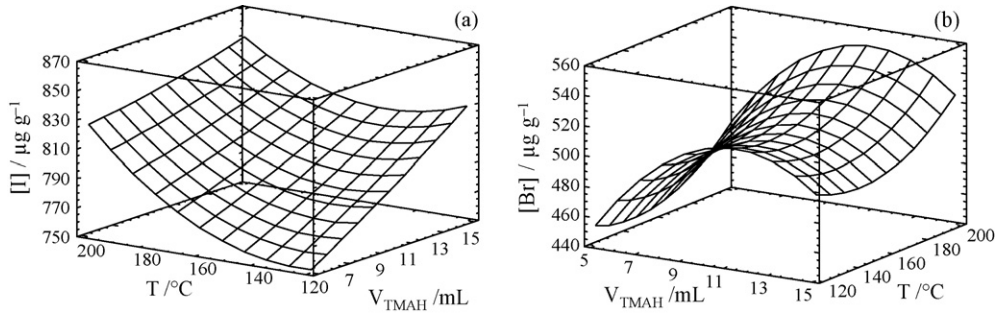

Fig. 3. Estimated response surfaces after 2^2 + star central composite design for iodine (a) and bromine (b).

be used because sample carbonization inside the vessels occurs. MAE operating conditions are summarized in Table 1.

3.3. Robustness of the method

The optimization of the MAE procedure was completed with a robustness study. The optimized MAE method (Table 1) was applied to different sample masses from the same seaweed, ranging from 0.1 to 0.5 g. As can be seen in Fig. 4, the measured iodine and bromine concentrations are similar from MAE experiments prepared with different sample masses. Therefore, the MAE method can be applied to large sample masses to improve sensitivity without lack of analyte recovery.

In addition, as it has been proved that the MAE procedure works when using small amounts of sample (until 0.1 g), a study of the effect of the extracting volume on the iodine and bromine recovery was carried out for small amounts of sample. The experiment consisted of performing MAE with 0.1 g of sample and using two

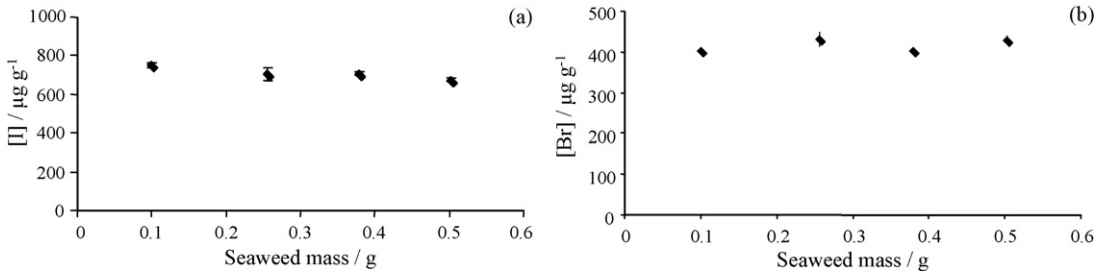

Fig. 4. Effect of the seaweed sample mass on the extracted iodine (a) and bromine (b) concentrations.

different TMAH volumes; the optimum TMAH volume, 10 mL; and 5 mL. After ICP-MS measurements, iodine and bromine concentrations for three replicates were 736 ± 34 and $416 \pm 28\ \mu g\,g^{-1}$ for iodine and bromine, respectively, when using a TMAH volume of 5 mL; while the concentrations were 753 ± 55 and $401 \pm 22\ \mu g\,g^{-1}$ for iodine and bromine, respectively, for the use of 10 mL. Therefore, the MAE method can be applied to small amounts of sample and for such cases, the TMAH volume can also be small without losing of extraction efficiency.

3.4. Analytical performances

Throughout the current work, linearity of the method has been proved until $1000\ \mu g\,L^{-1}$, obtaining R^2 values higher than 0.9996 when determining iodine and bromine. Matrix effect was observed and the application of the standard addition technique was found to give accurate results. The existence of matrix effect for iodine and bromine determinations was statistically tested (95% confidence interval) after applying the *F*-test to compare the variances and the *t*-test to compare the mean slopes of seven aqueous calibration and standard addition graphs.

The limit of detection (LOD) and the limit of quantification (LOQ) were calculated attending the following criterion:

$$\frac{3\text{S.D.}}{m}$$

$$\frac{10\text{S.D.}}{m}$$

where S.D. is the standard deviation of 10 replicates of a blank and *m* is the slope of the standard addition graph. For iodine, the instrumental LOD and LOQ were 0.12 and $0.41\ \mu g\,L^{-1}$ while for bromine 0.10 and $0.33\ \mu g\,L^{-1}$ were found. Keeping in mind the dilution and dried seaweed masses, LODs were 25 and $20\ ng\,g^{-1}$ for iodine and bromine, respectively. Similarly, the LOQ was $82\ ng\,g^{-1}$ for iodine and $66\ ng\,g^{-1}$ for bromine.

The repeatability of the over-all procedure (MAE–ICP-MS) was assessed by preparing (MAE) a seaweed sample twelve times and by measuring (ICP-MS) the concentration of iodine and bromine once in each extract. R.S.D. values of 5.8% and 6.3% were obtained for iodine and bromine, respectively, when using 0.25 g samples.

Accuracy of the method was studied by analyzing the CRM NIES-09. This material offers indicative values of 520 and $270\ \mu g\,g^{-1}$ for iodine and bromine, respectively. The CRM was subjected to the optimized MAE procedure five times, and each alkaline extract was analyzed by triplicate, resulting in 15 measurements. Results, expressed as mean ± S.D. were $525 \pm 59.5\ \mu g\,g^{-1}$ for iodine and $274 \pm 17.1\ \mu g\,g^{-1}$ for bromine in NIES-09. After applying a *t*-test for statistical comparisons, it was found that no significant statistical difference exists in any case and accuracy of the current method was proved.

3.5. Application

The optimized MAE–ICP-MS method has been applied to thirty-five edible dried seaweed samples and one canned seaweed sample. Dried seaweed included seven Nori samples and four Dulse samples (red seaweed); eight Kombu, seven Sea spaghetti and five Wakame samples (brown seaweed); and four Sea lettuce samples (green seaweed). Each sample was subjected to the optimized MAE procedure three times and each extract was measured three times by ICP-MS. Iodine and bromine concentration ranges in dried seaweed are summarized in Table 3, where it can be seen that the highest bromine ($849–1424\ \mu g\,g^{-1}$) and, especially iodine ($3703–7088\ \mu g\,g^{-1}$), concentrations can be found in Kombu samples. In general, iodine contents are lower in green seaweed (Sea lettuce) and red seaweed (Dulse and Nori) than in brown seaweed (Wakame, Sea spaghetti, and Kombu). Finally, canned seaweed sample gave an iodine concentration of $70 \pm 3\ \mu g\,g^{-1}$ and bromine concentration of $359 \pm 24\ \mu g\,g^{-1}$.

Table 3
Iodine and bromine concentration ranges in edible seaweed harvested in Galicia (north-western Spain).

	Iodine concentration range ($\mu g\,g^{-1}$)	Bromine concentration range ($\mu g\,g^{-1}$)
Sea lettuce[a]	66–137	466–529
Dulse[a]	77–128	279–451
Nori[b]	35–102	59–116
Sea spaghetti[b]	63–266	353–475
Kombu[c]	3703–7088	849–1424
Wakame[d]	63–326	139–750

[a] Four samples.
[b] Seven samples.
[c] Eight samples.
[d] Five samples.

4. Conclusions

A quantitative iodine and bromine extraction from seaweed was achieved by MAE using TMAH at a high extraction temperature. The MAE was found to be a fast sample pre-treatment and represents an advantage over conventional TMAH-based methods which need several hours to complete the extraction. The method was also found to be robust and quantitative iodine and bromine extraction can be obtained under several sample masses and TMAH volume combinations, which allow the use of larger amounts of sample to assess low analyte concentrations. The use of this sample treatment in combination with ICP-MS determination results in a fast and reliable methodology for routinely assessing iodine and bromine in seaweed. After analyzing different seaweed types harvested in the Galician coast, it can be concluded that Kombu samples, belonging to the brown seaweed type, content by far the highest iodine and bromine levels. In addition, bromine concentrations are higher than iodine concentrations in most of the seaweed analyzed, except for Kombu types, which offer higher iodine levels, and for Nori samples (red seaweed types), which show similar iodine and bromine contents.

Acknowledgements

The authors wish to thank the Ministerio de Ciencia y Tecnología (Project number AGL2006-11034) and Xunta de Galicia (Grupo de Referencia Competitiva 2007/000047-0) for financial support. We are also grateful to the seaweed-based industry ALGAMAR in Redondela (Pontenvedra), Spain, for supplying dried and canned seaweed samples. We wish also to thank Dr. Verónica Piñeiro-Gómez (Rede de Infraestructuras de Apoio á Investigación e ao Desenvolvemento Tecnolóxico, RIAIDT, at the University of Santiago de Compostela) for ICP-MS technical support. Vanessa Romarís-Hortas thanks Xunta de Galicia for a Terceiro Ciclo pre-doctoral grant and to Ministerio de Ciencia e Innovación for a FPU pre-doctoral grant.

Appendix A. Supplementary data

Supplementary data associated with this article can be found, in the online version, at doi:10.1016/j.talanta.2009.05.036.

References

[1] V.J. Chapman, D.J. Chapman, Sea Vegetables (Algae as Food for Man), Chapman & Hall, London, 1980.

[2] C.S. Kumar, P. Ganesan, P.V. Suresh, N. Bhaskar, J. Food Sci. Technol. 45 (2008) 1.
[3] M. Haldimann, A. Alt, A. Blanc, K. Blondeau, J. Food Comp. Anal. 18 (2005) 461.
[4] Recommended Dietary Allowances, National Research Council—Food and Nutrition Board, National Academy Press, Washington, 1989.
[5] Nordic Nutrition Recommendation 1996, Scand. J. Nutr./Noeringsforskning 40 (1996) 161.
[6] Recommended Nutrient Intakes for Canadians, Health and Welfare Canada—Department of Supply and Services, Ottawa, 1983.
[7] Dietary Reference Values for Food, Energy and Nutrients for the UK: Report on Health and Social Subjects No. 41, Department of Health, UK, 1991.
[8] T.D.B. Lyon, P.A. Robin, W.S. Watson, D. Littlejohn, J. Anal. Atom. Spectrom. 20 (2005) 757.
[9] A. Covaci, S. Voorspoels, L. Ramos, H. Neels, R. Blust, J. Chromatogr. A 1153 (2007) 147.
[10] P.A. Fecher, I. Goldmann, A. Nagengast, J. Anal. Atom. Spectrom. 13 (1998) 977.
[11] H.M. Kingston, L.B. Jassie, Introduction to Microwave Sample Preparation: Theory and Practice, ACS Professional Reference Book, Washington, DC, 1998.
[12] F. di Narda, R. Toniolo, S. Susmel, A. Pizzariello, G. Bontempelli, Talanta 60 (2003) 653.
[13] G. Knapp, B. Maichin, P. Fecher, S. Hasse, P. Schramel, Fresenius J. Anal. Chem. 362 (1998) 508.
[14] E. Niedobová, J. Machát, V. Kanický, V. Otruba, Microchem. J. 150 (2005) 103.
[15] J. Naozuka, M.A. Mesquita Silva da Veiga, P.V. Oliveira, E. de Oliveira, J. Anal. Atom. Spectrom. 18 (2003) 917.
[16] M. Shah, R.G. Wuilloud, S.S. Kannamkumarath, J.A. Caruso, J. Anal. Atom. Spectrom. 20 (2005) 176.
[17] K.-E. Wang, S.-J. Jiang, Anal. Sci. 24 (2008) 509.
[18] D. Gamallo-Lorenzo, M.C. Barciela-Alonso, A. Moreda-Piñeiro, A. Bermejo-Barrera, P. Bermejo-Barrera, Anal. Chim. Acta 542 (2005) 287.
[19] K. Tagami, S. Uchida, I. Hirai, H. Tsukada, H. Takeda, Anal. Chim. Acta 570 (2006) 88.
[20] J.-H. Chen, K.-E. Wang, S.-J. Jiang, Electrophoresis 28 (2007) 4227.
[21] A. Moreda-Piñeiro, A. Bermejo-Barrera, P. Bermejo-Barrera, Bot. Mar. 50 (2007) 65.
[22] N. Choengchan, K. Lukkanakul, N. Ratanawinmarnwong, W. Waiyawat, P. Wilairat, D. Nacapricha, Anal. Chim. Acta 499 (2003) 115.
[23] E. Niedobová, J. Machát, V. Otruba, V. Kanicky, J. Anal. Atom. Spectrom. 20 (2005) 945.
[24] E.A. Vtorushina, A.I. Saprykin, G. Knapp, J. Anal. Chem. 63 (2008) 643.
[25] W.P. Gardiner, G. Gettinby, Experimental Design Techniques in Statistical Practice: A Practical Software-based Approach, Horwood Publishing Limited, West Sussex, 1998.

Talanta 79 (2009) 810–817

Contents lists available at ScienceDirect

Talanta

journal homepage: www.elsevier.com/locate/talanta

The development and inter-laboratory verification of LC–MS libraries for organic chemicals of environmental concern☆

Charlita Rosal[a], Don Betowski[a], Joe Romano[b], Joshua Neukom[c], Dennis Wesolowski[c], Lawrence Zintek[c,*]

[a] US EPA Office of Research and Development/National Exposure Research Laboratory-Environmental Sciences Division, Las Vegas, NV 89119, United States
[b] Waters Corporation, Milford, MA 01757, United States
[c] US EPA Region 5 Chicago Regional Laboratory, Chicago, IL 60605, United States

ARTICLE INFO

Article history:
Received 7 January 2009
Received in revised form 4 May 2009
Accepted 6 May 2009
Available online 15 May 2009

Keywords:
Liquid chromatography–mass spectrometry
Library
Verification
Transferability
Drinking water

ABSTRACT

The development, verification, and comparison study between LC–MS libraries for two manufacturers' instruments and a verified protocol are discussed. Compounds in the libraries are among those considered by the U.S. EPA Office of Water as threats to drinking water including pesticides, drugs of abuse, and pharmaceuticals. The LC–MS library protocol was verified through an inter-laboratory study that involved Federal, State, and private laboratories. The results demonstrated that the libraries are transferable between the same manufacturer's product line, and have applicability between manufacturers. Although ion abundance ratios within mass spectra were shown to be different between the manufacturers' instruments, the NIST search engine match probability was at 96% or greater for 64 out of 67 compounds evaluated.

Published by Elsevier B.V.

1. Introduction

Gas chromatography coupled with mass spectrometry (GC–MS) is one of the best techniques for identifying unknown compounds in environmental samples. A major reason for its utility is the searchable libraries of mass spectra that have been compiled using electron impact ionization. These libraries are essentially instrument independent, so whichever brand of GC–MS is used, a compound can theoretically be tentatively identified, if it is included in the mass spectral libraries. This is made possible by the use of standard 70-eV electron impact ionization using a standardized tuning procedure as described elsewhere [1]. Libraries of mass spectra, such as the NIST [2] library, have automatic searching routines which list the top possibilities.

The more recently introduced liquid chromatography–mass spectrometry (LC–MS) has advantages over GC–MS for organic compounds that are thermally labile, polar, or non-volatile. Derivatization of polar analytes and solvent extraction of drinking water are not required prior to analysis, both of which greatly increase the analysis time. Water samples can be analyzed directly after filtration through a syringe-driven disposable filter to remove debris that can clog the LC injector, tubing, or column.

Additionally, highly-polar or low-volatility organic compounds do not traverse GC columns or do so over such a long time that discrete gas chromatographic peaks may not be observed. Thermally unstable compounds are often degraded in the GC inlet or later in a hot GC column. HPLC separations are generally accomplished at room temperature, so thermal stability of the analyte is usually not an issue. Eluting analytes are then ionized to produce spectra via electrospray ionization (ESI), atmospheric pressure chemical ionization (APCI), or atmospheric pressure photoionization (APPI).

However, LC–MS has not had the benefit of searchable libraries that contain reproducible spectra for several reasons. First, the pressure in the LC–MS ion source (no greater than 1 atm) is higher relative to GC–MS because of the need to convert liquid to gas in the interface between the HPLC and the MS. Ions created at atmospheric pressure undergo ion-molecule collisions which alter the ion distribution depending on their residence time in the source and other factors. On the other hand, electron impact (EI) ionization that is typical of GC–MS systems operates at low gas pressure, which prevents ion-molecule collisions regardless of the ion source

☆ Notice: The U.S. Environmental Protection Agency (EPA) through its Office of Research and Development (ORD), collaborated in the research described here with EPA Region 5 Chicago Regional Laboratory and Waters Corporation. This manuscript has been subjected to the EPA's peer and administrative review and has been approved for publication. Mention of trade names or commercial products does not constitute endorsement or recommendation by EPA for use.

* Corresponding author. Tel.: +1 312 886 2925; fax: +1 312 886 2591.
E-mail address: zintek.lawrence@epa.gov (L. Zintek).

0039-9140/$ – see front matter. Published by Elsevier B.V.
doi:10.1016/j.talanta.2009.05.004

design. The fragmentation process is reproducible due to standard tuning criteria and the use of a standard 70 eV. There are many treatises written on the mechanisms that produce ions in EI ionization [3].

In atmospheric ionization sources (ESI, APCI, or APPI), multiple ion-molecule collisions remove energy from precursor ions, which then lack sufficient internal energy to fragment. This "soft ionization" generally provides mass spectra lacking product ions. A product ion due to loss of a water or carbon dioxide molecule can appear from some compounds. In addition to the precursor ion, adduct ions are often observed depending on the ionization environment due to the use of solvents and modifiers to optimize chromatography and sensitivity. These simple spectra, while they are indicative of the molecular weight, do not present the diagnostic power of the EI ionization spectra with its rich fragmentation pattern. A spectrum with a precursor ion and a few adduct ions is certainly not unique to a certain compound. Therefore, a library of such spectra would provide little discrimination among analytes.

To provide multiple product ions from analytes, the energy of collisions must be increased sufficiently to break bonds within the precursor ion. Single MS-stage instruments can use in-source collision-induced dissociation (CID), but the presence of various solvent, additive, and contaminant molecules can cause variation in the product ion spectra, and not all ions observed may originate from the analyte. Instruments, such as triple quadrupole mass spectrometers and ion traps, can focus the ion of interest and energize this species to effect further fragmentation free of extraneous ions. Both the ion trap and triple quadrupole mass spectrometers generate fragmentation by applying a voltage or energy to the ionized species and simultaneously add a collision gas to cause reactive collisions resulting in diagnostic ions. These product ions are related to the structure of the protonated or deprotonated molecule and could thus be used for diagnostic purposes. In principle, compilation of mass spectral libraries for each type of ionization and for both ion trap and triple quadrupole instruments should be feasible.

To provide reproducible product ion spectra for a library, voltage and collision gas pressures must be reproducible for individual instruments and for similar instruments that use the library. These requirements were not met by early ion traps and triple quadrupole mass spectrometers, and compilation of mass spectral libraries was not practical. However, an attempt was made to standardize conditions in triple quadrupole mass spectrometers. By using the kinetics of a well-defined reaction, Martinez [4] attempted to standardize conditions to generate reproducible spectra. Martinez's method was not valid for ion traps and little support was forthcoming from the analytical community for this attempt to standardize spectra. Consequently, the mass spectral library idea floundered.

Also desirable would be HPLC mass spectral libraries for single-stage quadrupole instruments, which are the workhorses for environmental analyses. Unfortunately, these instruments are not effective at generating product ions. An attempt was made to add a repeller to the ion sources of single quadrupole systems that could break apart protonated molecules [5], which were effective at generating product ions. However, this was not reproducible from instrument to instrument.

There have been direct efforts to generate EI ionization spectra under LC conditions. The particle beam LC–MS interface [6] removed most of the solvent in the interface before solvated ions entered the ion source and struck heated surfaces. The desolvated molecules were then ionized by 70-eV electrons to provide EI-searchable mass spectra. This worked well for certain compounds [7], but was not universally adopted because of problems with thermal degradation and low volatility of compounds.

Another effort is the recent work by Granot and Amirav [8] to generate LC–MS spectra with EI ionization in supersonic molecular beams. This method shows some promise, but it is too early to predict its commercial application. Cappiello and Palma [9] interfaced a nanoscale LC to a direct electron ionization system to examine small to medium molecular weight molecules of different polarities. This technique shows some promise for those compounds that might have matrix problems when introduced through API interfaces.

Only recently have the electronics of mass spectrometers become stable enough that reproducible voltages and pressures provide reproducible CID spectra, at least on a single instrument. This stability is important in the collision region of a triple quadrupole mass spectrometer or the source region of a single quadrupole mass spectrometer through CID.

Therefore, it should be possible to collect spectra from an individual mass spectrometer and expect that these spectra will form a standardized library that the user can search during subsequent analyses. In fact, there should be two such libraries. The first would be generated from triple stage quadrupoles (LC–MS/MS), in which a single ion is focused, presumably the protonated molecule, in the first quadrupole and then sent into the second quadrupole or the collision cell, which contains an inert gas, such as argon, where the ion would undergo energetic collisions to produce product ions, which would be scanned in the third quadrupole and then detected. The other library from LC–MS spectra would be produced by some kind of device (repeller, cone, etc.) in the ion source that is effective at generating product ions. There would be no discrimination of the ions, so every ion in the source at the time of fragmentation would add to this spectrum. The first library described above would be "purer" than the latter because of the fact that interference ions could be present in the source as the voltages were applied to fragment the ion of interest.

Some attempts to compile searchable LC–MS and LC–MS/MS libraries with modern instruments have shown promise [10–15] while others encountered difficulties that precluded their use [16]. Encouraged by the success of Gergov et al. [11] in developing libraries for drugs, we attempted to create LC–MS and LC–MS/MS libraries for chemicals that could cause harm and disrupt distribution in a drinking water system. The ability to quickly and accurately identify a large number of organic compounds has become an important goal in this effort. LC–MS library technology is not only potentially useful for drinking water but also to identify or characterize agents that could be used in a terrorist incident, to monitor food safety, and to screen product quality.

LC–MS and LC–MS/MS libraries have been compiled for identification of chemicals that might pose a threat to drinking water. The Chicago Regional Laboratory (CRL) of the U.S. Environmental Protection Agency initially developed these libraries based on compounds that were potential threats to our nation's water supply. To validate the library protocol [17], other laboratories were recruited to verify that they could identify the chemicals in drinking water by comparing library mass spectra of standards with mass spectra from simulated unknowns obtained using the same solvents, methods, and instrument make as used by the CRL. In addition, the US EPA Office of Research and Development-Las Vegas Laboratory was recruited to test the library protocol with an instrument from a different manufacturer to determine if the library might have more general application.

2. Experimental

2.1. Instrumentation

The LC–MS Library System Protocol was developed using a Waters Corporation Quattro Premier™ triple quad (Milford, MA) with the ZSpray™ dual orthogonal sampling interface with Waters MassLynx™ 4.0 software. Other models used by the other labs

during the validation were ZQ™ single quad and Quattro Micro™ triple quad. However, to test the applicability of the protocol across different makes, a Thermo Electron Corporation Finnigan TSQ Quantum Ultra AM™ triple quadrupole mass spectrometer (San Jose, CA) was tested in this study. MS and MS/MS library-searchable spectra were generated for comparison with the CRL libraries.

2.2. Library development

The first list of target compounds included in the library project was supplied by the Water Security Division of the US EPA Office of Water. These compounds of concern are toxic substances and are readily available. The target list was divided into two groups, base/neutral and acidic compounds. The first library protocol addressed the base/neutral compounds.

Most of the compounds in Table 1 were obtained as neat standards, generously provided by the US EPA Office of Pesticide Programs (OPP) National Pesticide Standards Repository. The others were purchased from Aldrich Chemical Company (Milwaukee, WI), Cambridge Isotope Laboratories (Andover, MA), and Cerilliant (Round Rock, TX). The standards were diluted using a 50:50 water:acetonitrile mixture to an approximate concentration of 400 ppm (parts per million).

To acquire library mass spectra, the CRL infused standard solutions into a 'T' junction where they combined with mobile phase (5 mM ammonium bicarbonate in 50:50 water:acetonitrile, pH 10) before entering the mass spectrometer. Infusion was used to obtain optimal cone and collision energies for a compound to produce substantial fragmentation while maintaining at least 10% abundance of the precursor ion. After these settings were obtained, LC–MS analysis (25 ng of material on column) was undertaken to acquire retention time data and to verify that the cone and collision energies during infusion provided similar fragmentation when the standard eluted from the column. The amount of material injected was used to make sure that the concentration levels provided enough ion statistics to provide quality spectra for identification with different library searching techniques.

For MS scanning (single quadrupole), the electrospray source conditions were as follows: capillary voltage: 3.5 kV; extractor: 2 V; RF lens voltage: 0.2 V; source temperature: 120 °C; desolvation temperature: 300 °C; desolvation gas flow: 500 L h^{-1}; cone gas flow: 50 L h^{-1}. The analyzer section was maintained as follows: entrance: 50 V; exit: 50 V; collision: 2 V; multiplier: 650 V. These were the optimal settings used at the CRL, but optimal settings may vary slightly from instrument to instrument. The optimal cone voltage was different for each compound; these values were tabulated (for MS and MS/MS) and are listed in Table 1 together with collision energies for each compound.

For MS/MS scanning (triple quadrupole), the electrospray source conditions were the same as for the MS scanning mode. The analyzer settings for the MS/MS scanning mode were as follows: entrance: −1 V; exit: 2 V; collision: variable (see Table 1); multiplier: 650 V.

The solvent gradient under which MS and MS/MS data were recorded was as follows: 95:5 (H_2O:100 mM NH_4HCO_3, pH 10) at time = 0; hold for 2 min; 95:5 (acetonitrile:100 mM NH_4HCO_3) at time = 20.0 min; hold for 2 min; back to original conditions at time = 30.0 min. The flow rate was 0.3 mL min^{-1}. The column temperature was 30 °C and the sample compartment was held at 15 °C.

The diagnostic precursor and product ions with relative abundances exceeding 5% are listed in Table 1. They represent spectra taken both under source CID (MS) and MS/MS conditions using the collision cell.

The instruments were tuned and calibrated according to the procedures given by the manufacturer. The initial protocol followed by the volunteer labs is given in the following sections.

2.3. Tentative identification of an unknown

2.3.1. LC conditions and settings

The LC conditions were set to screen water samples and were not optimized for chromatographic separation. The Waters Alliance® 2695 HPLC with an XBridge™ C18, 2.1 mm × 150-mm column packed with 3.5-μm diameter particles, was used during the study. Any column capable of performing at high pH with adequate separation of these analytes may be used. The library protocol was not based on retention time of the analytes but on matching of spectra. The injection volume was 100 μL of a filtered water sample if possible. The elution gradient and other conditions were described earlier.

2.3.2. MS method file conditions and settings

To acquire MS and MS/MS spectra, the mass spectrometer was tuned using the conditions specified earlier (see Section 2.2). The MS method file, made up of one or more individual MS scanning functions, was created to detect compounds of interest at specific retention times and cone voltage settings. For example, a cone voltage of 35 V is the optimal value for aldicarb sulfone, buprofezin, carbofuran, and three other compounds in Table 1 to acquire product ion mass spectra most similar to those in the library, while a cone voltage of 75 V is optimal for 2-aminobenzimidazole, cyprodinil, and thiabendazole. The combination of several such MS scanning functions, each with a different cone voltage, is best suited to screen for multiple compounds in a sample. This screening approach is used to maximize the number of compounds screened simultaneously.

To ensure mass spectra were acquired for water samples at the optimal or nearly optimal cone voltage for each compound in the library, the cone voltage was cycled through six values: 15, 30, 45, 60, 75, and 90 V during acquisition. A 0.3-s scan was acquired for each voltage separated by a 0.1-s interscan delay. The total cycle time was 2.4 s and HPLC chromatographic peak widths were typically 20–40 s.

With in-source CID, co-eluting compounds can yield composite mass spectra containing product ions from multiple precursor ions, and good library matches are not likely. MS/MS is then necessary to isolate individual precursor ions before product ions are produced by CID to provide clean product ion spectra. Library-matchable product-ion spectra are then provided by the enhanced sensitivity and selectivity of MS/MS. For each unknown, MS/MS scanning methods require user input of the optimal cone voltage, collision energy, and precursor ion m/z such as shown in Table 1 into a menu.

Similar retention times for a tentatively identified compound and the standard provide an orthogonal measure to strengthen tentative identifications made using the library.

3. Results and discussion

3.1. Library searching

After full scan spectra at various voltages have been recorded for each compound, these spectra were searched against the MS library as described by the Masslynx™ or NIST library search manual. When >70% probability scores were obtained or when the operator thought a match was possible, the cone voltages from the library were compared with those for the acquired product ion spectra, and a tentative identification was made when they were consistent. The evidence for a somewhat doubtful, tentative identification of a compound could be enhanced by acquiring product ion spectra at the optimal cone voltage (and collision energy for MS/MS) for the compound from Table 1 to provide the strongest mass spectral evidence for the tentative identification. If the product ion spectrum is a match in the MS/MS library

Table 1
Library compounds.

Compound	CAS number	Nominal mass (g/mol)	Cone MS[a] (V)	Cone MS/MS (V)	Collision MS/MS (eV)	Precursor > MS/MS product ions (m/z units)
2-Aminobenzimidazole	934-32-7	133	75	48	32	134 > 92, 80
3-Hydroxy carbofuran	16655-82-6	237	40	30	9	220 > 163, 135
Acetamipirid	135410-20-7	222	46	25	14	223 > 126
Acetochlor	34256-82-1	269	32	28	11	270 > 224, 148
Acibenzolar-s-methyl[b]	135158-54-2	210	60	37	23	211 > 168, 136, 91
Aconitine	302-27-2	645	88	60	43	646 > 586, 105
Alachlor	15972-60-8	269	34	22	13	270 > 238, 162
Alanine[b]	56-41-7	89	32	19	12	90 > 44
Aldicarb	116-06-3	190	15	10	4	208 > 191, 116
Aldicarb sulfone	1646-88-4	222	35	25	8	223 > 166, 148, 76
Aldicarb sulfoxide	1646-87-3	206	25	20	5	207 > 132, 89
Allethrin	584-79-2	302	34	20	9	303 > 151, 135
Ametryn	834-12-8	227	58	35	20	228 > 186, 96
Amitraz	33089-61-1	293	34	22	11	294 > 253, 163
ANTU	86-88-4	202	46	27	15	203 > 186, 144
Atrazine	1912-24-9	215	55	38	19	216 > 174, 96, 79
Atropine	51-55-8	289	58	40	23	290 > 124, 93
Azinphos-methyl	86-50-0	317	25	18	6	318 > 261, 160
Azoxystrobin	131860-33-8	403	35	25	11	404 > 372
Bentazon[b]	25057-89-0	240	−55	−35	−24	239 > 197, 132
Bromoxynil[c]	1689-84-5	275	−53			276 > 79, 81, 185, 274, 123
Buprofezin	69327-76-0	305	35	22	13	306 > 201, 116
Butylate	2008-41-5	217	49	24	16	218 > 190, 162, 156, 100, 89
Carbaryl	63-25-2	201	25	20	5	202 > 145
Carbendazim	10605-21-7	191	40	30	15	192 > 160
Carbofuran	1563-66-2	221	35	25	11	222 > 165, 123
Chloramben[b]	133-90-4	205	−31	−20	−8	204 > 160
Chlorimuron-ethyl	90982-32-4	414	42	28	13	415 > 369, 213, 186
Chlorobenzilate[b,c]	510-15-6	324	−22			323 > 295, 249
Chlorsulfuron	64902-72-3	357	38	29	13	358 > 167, 141
Clethodim	99129-21-2	359	42	23	14	360 > 268, 164
Clodinafop-propargyl[c]	105512-06-9	349	46			350 > 266, 268, 91, 238, 269
Clomazone	81777-89-1	239	46	26	14	240 > 125, 128
Colchicine	64-86-8	399	72	41	29	400 > 358, 310
Cotinine	486-56-6	176	54	35	20	177 > 146, 98, 80
Coumarin[b]	91-64-5	146	55	35	20	147 > 103, 91
Cyanazine	21725-46-2	240	55	36	21	241 > 214, 104, 96
Cyclanilide	113136-77-9	273	−38	−24	−13	272 > 228, 192, 160
Cycloheximide	66-81-9	281	45	30	16	282 > 264, 246
Cyprodinil	121552-61-2	225	75	48	28	226 > 210, 108, 93
Cyromazine	66215-27-8	166	58	34	21	167 > 125, 85
Daminozide	1596-84-5	160	32	20	11	161 > 143, 115, 101
DDVP[b]	62-73-7	220	44	32	15	221 > 145, 127, 109
Desethyl atrazine	19988-24-0	169	48	32	16	170 > 128, 86
Desisopropyl atrazine	1007-28-9	173	57	32	22	174 > 132, 104, 96
Diazinon	333-41-5	304	50	30	18	305 > 169, 153
Dicrotophos	141-66-2	237	35	25	9	238 > 193, 112
Digitoxin	71-63-6	764.4	31	22	9	783 > 748, 636
Digoxin[b]	20830-75-5	780.4	33	22	10	782 > 652, 97
Diphacinone	82-66-6	340	45	30	14	341 > 323, 263, 235
Diuron	330-54-1	232	40	30	14	233 > 72
Dodine[b]	2439-10-3	287	67	40	23	228 > 186, 85, 71
Emetine, HCl[b]	483-18-1	480	140	55	37	481 > 436, 246, 165
EPTC	759-94-4	189	40	22	12	190 > 162, 128, 89, 86
Ethiofencarb	56729-20-5	225	25	18	7	226 > 169, 164, 107
Ethion[b]	563-12-2	384	30	20	8	385 > 215, 199
Ethoprophos	13194-48-4	242	42	27	13	243 > 215, 173, 131
Fenitrothion[b,c]	122-14-5	277		32	17	278 > 246, 125
Fensulfothion	115-90-2	308	50	35	18	309 > 281, 253, 157
Fenthion[b]	55-38-9	278	55	30	16	279 > 247, 169
Formothion	2540-82-1	257	34	25	14	279 > 116, 88, 118, 231, 145
Heroin	561-27-3	369	97	44	36	370 > 328, 165
Hexazinone	51235-04-2	252	38	28	13	253 > 171, 85
Imazalil	35554-44-0	296	55	35	21	297 > 255, 159, 109
Imazamethabenz-methyl	81405-85-8	288	52	33	19	289 > 257, 229, 86
Imazaquin	81335-37-7	311	60	36	24	312 > 270, 267, 252, 199, 86
Imazethapyr	81335-77-5	289	58	35	23	290 > 248, 245, 230, 177, 86
Imidacloprid	13826-41-3	255	40	29	14	256 > 209, 175, 84
Isofenphos	25311-71-1	345	18	10	4	346 > 287, 245
Isoxaflutole	141112-29-0	359	41	30	11	360 > 251
Kresoxim-methyl	143390-89-0	313	30	20	7	314 > 282, 267, 206, 116
LAMPA	40158-98-3	323	60	34	25	324 > 281, 223
LSD	50-37-3	323	59	34	24	324 > 281, 223
Malathion	121-75-5	330	30	22	8	331 > 285, 127
Mesotrione	104206-82-8	339	−29	−16	−8	338 > 291

Table 1 (*Continued*)

Compound	CAS number	Nominal mass (g/mol)	Cone MS[a] (V)	Cone MS/MS (V)	Collision MS/MS (eV)	Precursor > MS/MS product ions (*m/z* units)
Metalaxyl	57837-19-1	279	40	28	13	280 > 248, 220, 192
Methamidophos	10265-92-6	141	50	35	18	143 > 125, 113, 95
Methiocarb	2032-65-7	225	30	22	8	226 > 169, 121
Methomyl	16752-77-5	162	22	16	6	163 > 122, 106, 88
Methoprene	40596-69-8	310	22	15	6	311 > 279, 237, 219, 191
Metolachlor	51218-45-2	283	36	22	12	284 > 252
Metsulfuron-methyl	74223-64-6	381	35	23	11	382 > 167, 141
Mevinphos	7786-34-7	224	27	20	7	225 > 193, 127, 99
Molinate	2212-67-1	187	37	26	13	188 > 126, 98, 83
Monocrotophos	6923-22-4	223	30	21	8	224 > 193, 98
Naled[b]	300-76-5	378	24	23	8	379 > 127
Napropamide	15299-99-7	271	45	28	14	272 > 199, 171, 129, 74
Naptalam	132-66-1	291	−38	−23	−12	290 > 246
Nicotine	54-11-5	162	50	35	18	163 > 132, 130, 117, 106
Oxamyl	23135-22-0	219	20	14	6	237 > 220, 90, 72
Permethrin[b]	52645-53-1	390	32	24	8	408 > 355, 183
Phorate[b]	298-02-2	260	20	18	6	261 > 75
Phosalone[b]	2310-17-0	367	36	25	9	368 > 322, 182
Phosmet[b]	732-11-6	317	30	20	7	318 > 160
Pirimicarb	23103-98-2	238	42	28	14	239 > 182, 72
Pirimiphos-methyl	29232-93-7	305	60	42	24	306 > 164, 136, 108, 95
Prometon	1610-18-0	225	56	35	20	226 > 184, 142
Prometryn	7287-19-6	241	56	36	21	242 > 200, 158
Propachlor	1918-16-7	211	41	26	14	212 > 170, 152
Propamocarb	24579-73-5	188	39	26	14	189 > 144, 102
Propoxur	114-26-1	209	28	20	7	210 > 168, 153, 111
Prosulfuron	94125-34-5	419	45	30	15	420 > 167, 141
Pyridaben	96489-71-3	364	34	25	11	365 > 309, 147
Pyridaphenthion	119-12-0	340	50	37	18	341 > 313, 205, 189
Quinine	56-54-2	324	73	38	28	325 > 160, 81
Resmethrin[b]	10453-86-8	338	42	25	15	339 > 321, 293, 171, 143, 121, 91
Sethoxydim	74051-80-2	327	45	25	15	328 > 282, 220, 180, 178
Simazine	122-34-9	201	55	40	20	202 > 174, 132, 124, 104, 96
Simetryn	1014-70-6	213	60	40	21	214 > 186, 144, 124, 96
Spiroxamine	118134-30-8	297	51	32	17	298 > 144, 100
Strychnine	57-24-9	334	95	66	44	335 > 184, 156, 144, 129
Tebuconazole	107534-96-3	307	53	34	20	308 > 165, 151, 125
Tebufenpyrad	119168-77-3	333	70	48	26	334 > 171, 145, 117
Temephos	3383-96-8	466	62	35	22	467 > 419, 405, 357, 249, 155, 125
Terbumeton	33693-04-8	225	45	33	16	226 > 170, 114
Terbuthylazine	5915-41-3	229	45	31	14	230 > 174
Thiabendazole	148-79-8	201	75	44	29	202 > 175, 131, 92
Thiamethoxam	153719-23-4	291	33	20	10	292, 246, 211, 210, 132
Thifensufuron-methyl	79277-27-3	387	38	26	11	388 > 167, 141
Thiram	137-26-8	240	21	12	7	241 > 196, 120, 88
Tralkoxydim	87820-88-0	329	44	25	15	330 > 284, 164, 138, 122
Triadimefon	43121-43-3	293	45	28	16	294 > 225, 197
Tri-allate[b]	2303-17-5	303	41	26	15	304 > 262, 143, 128, 86
Triasulfuron	82097-50-5	401	42	28	15	402 > 219, 167, 141
Trichlorfon[b]	52-68-6	256	39	26	12	257 > 221, 127
Trifloxystrobin[b]	141517-21-7	408	40	24	13	409 > 206, 186, 116
Trinexapac-ethyl	95266-40-3	252	39	25	13	253 > 207, 185, 69
Triticonazole	131983-72-7	317	36	25	12	318 > 70
Warfarin	81-81-2	308	42	25	13	309 > 251, 163

[a] For full scan (single quadrupole) MS analysis, the collision energy was maintained at 2 eV and the collision gas (argon) remained off.

[b] These compounds have not been verified in interlaboratory studies.

[c] Those compounds in this table that *only* have MS settings are in the MS library *only*; and those compounds that *only* have MS/MS settings are *only* in the MS/MS library.

there is a high probability that the unknown has been identified.

3.2. Inter-laboratory verification of protocol and libraries

Thirteen solutions containing a total of 129 organic compounds included in the CRL libraries were prepared and distributed by CRL to the six participating laboratories. Each unknown sample contained between 9 and 11 analytes. Each participating lab received 6 or 7 unknown solutions that they were required to characterize. The unknown solutions were mixed considering retention time so the compounds would not co-elute. The samples were allotted so that a total of three laboratories received each individual chemical. The concentration of each analyte was 20 times (at a minimum) the noise level found at CRL. The laboratories did not know what compounds were contained in the solutions they received. Each laboratory was required to identify the constituents in the solutions they received using LC–MS Library System Protocol Version 1.2 created by CRL [17].

Identification of an analyte was required by at least two out of three laboratories that received it for the library spectra to be considered verified. Any less than two correct identifications would require further work on the spectra in the library or consultation with the participating labs depending on possible reasons for the misidentification. Compounds that were not correctly identified would be listed as not verified in the library until they were satisfactorily identified in blind samples by at least two out of three laboratories.

Table 2
Results of inter-laboratory verification.

Legend reason codes	Definitions		
A	Found by participating lab		
B	Found at CRL, oversight by participating lab		
C	Found at CRL, masked by high background noise level		
D	Not found at CRL, participating lab did not follow protocol		
F	Not found at CRL, background noise level high		
Compound	Lab result one reason	Lab result two reason	Lab result three reason
Acibenzolar-s-methyl	C	F	A
Bentazon	A (not confirmed by MS/MS)	A	C
Chloramben	C	F	C
Chlorobenzilate	B	A	F
Coumarin	B	A	F
DDVP	F	A	F
Digoxin	B	C	A
Dodine	F	A	F
Emetin, HCl	A	F	B
Ethion	C	A	F
Fenthion	F	F	C
Naled	C	F	A
Permethrin	A	B	F
Phorate	F	F	A
Phosmet	A	B	F
Trifloxystrobin	A	D	B
Alanine	F	C	C
Fenitrothion	F	F	F
Phosalone	C	C	F
Resmethrin	F	F	F
Tri-allate	C	F	F
Trichlorfon	F	F	F

The results using Waters instrumentation verified 107 out of 129 compounds contained in the library as shown in Table 1. The compounds with the letter "b" were not verified through the inter-laboratory process. The reasons are discussed here and tabulated in Table 2.

LAMPA, which is iso-LSD, has the same mass spectrum as LSD and cannot be distinguished by this protocol. LAMPA is not psychoactive, but like LSD, it is classified as a Schedule I drug under the Controlled Substance Act of 1970. Because LSD is prepared from ergot alkaloids with isomeric configuration at the C-8 position, both LSD and LAMPA are present in most illicit drug preparations. An LC–MS library cannot distinguish between LSD and LAMPA since they are sterioisomers. Therefore, if LAMPA or LSD is identified in a sample, it was verified to be reported as LAMPA/LSD.

Dicrotophos, used as a spiking compound, degraded to monocrotophos and was identified by two participating labs as monocrotophos in the sample.

Fenitrothion was identified by MS/MS only. The compound provided insufficient ion abundance in MS full scans to be tentatively identified in the MS single quadrupole portion of the protocol.

Bromoxynil, chlorobenzilate, clodinafop-propargyl, and formothion were tentatively identified by MS only. No MS/MS spectra are in the library for these compounds due to poor MS/MS sensitivity.

The reasons the 22 compounds were not verified, after CRL reviewed all the data received from the participating labs, are provided in Table 2. Contributing factors may be poor sensitivity due to poor chromatography or matrix interferences caused by elevated chromatograph baselines. It is also believed that some compounds may have decomposed in the water samples before being analyzed by the participating labs. Bentazon was found by two labs, but one lab was not able to confirm its presence by MS/MS. There were no false positives reported by the participating laboratories.

3.3. Library protocol modifications and library searching for the Thermo Finnigan instrument

A Thermo Finnigan instrument was used to compile similar LC–MS and LC–MS/MS libraries. The instrument was tuned according to the manufacturer's specifications and for maximum sensitivity before spectral acquisition. Other than this initial optimization process, similar procedures as noted above were followed to develop a standardized library that could be compared with the Waters/CRL libraries. Infusing each compound into the ESI source allowed for maximizing the signal by tuning the gas flows and voltages, while observing the $[M+H]^+$ or $[M-H]^-$ ion. As with the Waters instrument, each standard was infused into a 'T' junction, where it combined with the mobile phase before entering the mass spectrometer. The electrospray source conditions for both MS and MS/MS scanning were as follows: spray voltage, 4000 V; sheath gas pressure, 40 units; auxiliary gas pressure, 10 units; and capillary temperature, 250 °C. During this process, source CID voltages (for LC–MS spectra) and collision energies (for LC–MS/MS spectra) were manipulated for each compound to generate fragmentation while maintaining at least 10% abundance of the precursor ion. Once these settings were obtained, LC–MS analysis of 25 ng of material on-column was performed to acquire retention time data and to verify that similar product ion spectra were obtained with the source CID voltages and collision energies used during infusion. The collision gas (argon) was kept at 1.5 mTorr and the collision energy was increased to reduce the precursor ion to 10% of the resulting base peak.

A subset of the 129 unknown compounds sent to the US EPA Office of Research and Development Laboratory in Las Vegas was analyzed for independent confirmation on instrumentation from a manufacturer other than that used in the inter-laboratory study. MS spectra were acquired with a Thermo Finnigan TSQ Quantum Ultra AM^{TM} triple quadrupole mass spectrometer at collision energies of 10, 20, 30, 40, 50, 60, and 76 V (maximum). Each spectrum at each voltage was examined to determine the highest probability match and the instrument provided excellent matches with the Waters/CRL LC–MS library.

The 67-compound subset of the unknown standards was then tested against this library. The probability indicated the confidence that the unknown spectrum matched that particular compound's spectrum in the CRL library. The matches demonstrated that the LC–MS libraries are transferable between the Waters and Thermo Finnigan instruments even though the ion ratios within spectra were often different between the instruments. Even so, the NIST search engine probability match factor was high and correctly identified the simulated unknowns as shown in Table 3. The MS cone/source CID voltages were compared between the voltage under which the Waters/CRL library was developed and the voltage that resulted in the greatest match factor using the Thermo Finnigan NIST search and are presented in Table 3.

Based on the NIST searching algorithm the probabilities of finding each simulated unknown in the Waters/CRL library was 96% or greater except for metsulfuron-methyl, monocrotophos, and phosmet, which had probabilites of 83, 94, and 90%, respectively. Examples of these searches are given in Fig. 1 for propachlor and Fig. 2 for metsulfuron-methyl.

As can be seen, the algorithm ranks the occurrence of ions greater than the ion abundance. Since each spectrum is searched against the whole library, one can see from the search results in Fig. 1 that for propachlor, there is very little probability that the compound is anything other than propachlor; the next highest probability is 0.98% for terbumeton. The search results for metsulfuron-methyl are more tentative as the forward and reverse search results are poor, but the probability that the compound is metsulfuron-methyl is still at 83% with the next highest proba-

Table 3
LC–MS library match probability of spectra acquired by the Thermo Finnigan instrument against the Waters/CRL LC–MS library.

Compound	MS cone/source CID (V)		NIST probability
	Waters/CRL library	Thermo Finnigan	
2-Aminobenzimidazole	75	60	97
3-Hydroxy carbofuran	40	50	99
Acetamipirid	46	40	99
Acetochlor	32	50	99
Alachlor	34	50	98
Aldicarb	15	20	99
Ametryn	58	60	99
Amitraz	34	40	97
Atropine	58	60	96
Azinphos-methyl	25	40	99
Azoxystrobin	35	50	99
Buprofezin	35	40	99
Carbaryl	25	40	99
Carbofuran	35	40	99
Clodinafop-propargyl	46	50	98
Clomazone	46	60	99
Colchicine	72	76	97
Cyanazine	55	76	98
Cycloheximide	45	60	99
Cyprodinil	75	60	99
Diazinon	50	40	99
Dicrotophos	35	40	99
Ethiofencarb	25	40	99
Ethoprophos	42	40	99
Fensulfothion	50	76	98
Hexazinone	38	60	98
Imazalil	55	50	98
Imazamethabenz-methyl	52	60	99
Imidacloprid	40	50	99
Isofenphos	18	20	99
Kresoxim-methyl	30	20	99
Malathion	30	30	98
Methiocarb	30	30	99
Methomyl	22	40	99
Metolachlor	36	40	99
Metsulfuron-methyl	35	30	83
Mevinphos	27	30	98
Monocrotophos	30	40	94
Naled	24	30	98
Napropamide	45	60	99
Nicotine	50	40	98
Oxamyl	20	30	97
Phosmet	30	30	90
Pirimicarb	42	40	98
Pirimiphos-methyl	60	60	99
Prometon	56	60	99
Prometryn	56	60	99
Propachlor	41	50	99
Propamocarb	39	30	99
Propoxur	28	50	99
Prosulfuron	45	76	99
Pyridaben	34	40	99
Pyridaphenthion	50	60	98
Quinine	73	60	96
Sethoxydim	45	40	97
Simetryn	60	50	99
Spiroxamine	51	50	99
Tebuconazole	53	50	98
Tebufenpyrad	70	76	98
Temephos	62	60	99
Terbumeton	45	40	99
Thiamethoxam	33	50	99
Triadimefon	45	30	98
Triasulfuron	42	50	98
Trichlorfon	39	30	97
Trifloxystrobin	40	40	99
Warfarin	42	30	99

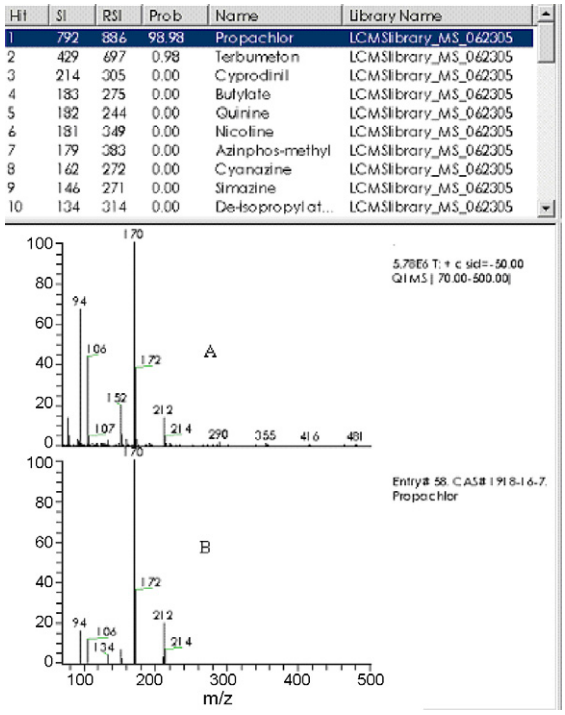

Fig. 1. LC–MS library search of propachlor acquired on a Thermo Finnigan instrument (A) compared to the library spectrum generated from a Waters instrument (B).

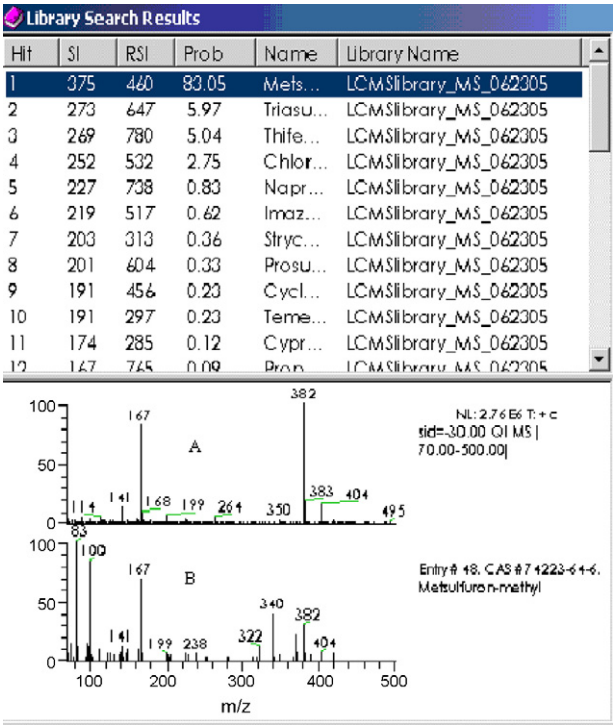

Fig. 2. LC–MS library search of metsulfuron-methyl acquired on a Thermo Finnigan instrument (A) compared to the library spectrum generated from a Waters instrument (B).

bility at 6%. On further review the Waters/CRL LC–MS library for metsulfuron-methyl most likely had interferences, which were not filtered out with the source CID LC–MS arrangement. Review of the Waters/CRL LC–MS/MS library (products of *m*/*z* 382) showed that ions at *m*/*z* 83, 100, and 340 were all absent; consequently, these ions were attributed to co-eluting impurities with the metsulfuron-methyl.

4. Conclusion

The Waters/CRL LC–MS library protocol was verified through an inter-laboratory study that involved Federal, State, and private laboratories. The results demonstrated that the libraries are transferable between the same manufacturer's product line, and have applicability between manufacturers. The ion ratios within a mass spectrum were different between two manufacturers' instruments, but the same product ions were usually observed. Despite the ion ratio differences, the NIST search engine match probability was 96% or greater for all of the compounds except for three. This work will be extended for the analysis of real world samples and the development of more sensitive MS/MS methods to enable low level analysis of select analytes. Through a cooperative research and development agreement (CRADA) between Waters Corporation and the US EPA Region 5 CRL, the libraries and protocol can be obtained from U.S. EPA Region 5 CRL free of charge.

Acknowledgements

We would like to thank the following participants in the inter-laboratory validation: Jeff Hardy, Indiana State Chemist; Julia Jiang, Minnesota Department of Public Health; Patricia Schermerhorn, Diane Rains, and Paul Golden, US EPA Office of Pesticide Programs; and Harold Johnson, Gordon Kearney, and Aisling O'Connor, Waters Corporation. We would like to especially thank the US EPA Office of Pesticide Programs (OPP) National Pesticide Standards Repository for providing many of the standards and the US EPA Office of Water/Water Security Division and Office of Research and Development/National Homeland Security Research Center for financial support.

References

[1] EPA Method 624 Appendix A 40 CFR Part 136, US EPA, Washington, DC, 2008.
[2] NIST Standard Reference Database 1A, NIST/EPA/NIH Mass Spectral Library with Search Program: (Data Version: NIST 05, Software Version 2.0d), NIST, 2005.
[3] F.W. McLafferty, Interpretation of Mass Spectra, University Science Books, Mill Valley, 1980.
[4] R.I. Martinez, Journal of the American Society for Mass Spectrometry 1 (1990) 272.
[5] J. Yinon, T.L. Jones, L.D. Betowski, Rapid Communications in Mass Spectrometry 3 (1989) 38.
[6] R.C. Willoughby, R.F. Browner, Analytical Chemistry 56 (1984) 2626.
[7] L.D. Betowski, C.M. Pace, M.R. Roby, Journal of the American Society for Mass Spectrometry 3 (1992) 823.
[8] O. Granot, A. Amirav, International Journal of Mass Spectrometry 244 (2005) 15.
[9] A. Cappiello, P. Palma, Advances in LC–MS Instrumentation, Elsevier Science & Technology Books, 2007.
[10] S. Dresen, J. Kempf, W. Weinmann, Forensic Science International 161 (2006) 86.
[11] M. Gergov, W. Weinmann, J. Meriluoto, J. Uusitalo, I. Ojanperä, Rapid Communications in Mass Spectrometry 18 (2004) 1039.
[12] P. Marquet, F. Saint-Marcoux, T.N. Gamble, J.C.Y. Leblanc, Journal of Chromatography B 789 (2003) 9.
[13] P. Marquet, N. Venisse, L.É.G. Lachâtre, Analusis 28 (2000) 925.
[14] A. Schreiber, J. Efer, W. Engewald, Journal of Chromatography A 869 (2000) 411.
[15] W. Weinmann, A. Wiedemann, B. Eppinger, M. Renz, M. Svoboda, Journal of the American Society for Mass Spectrometry 10 (1999) 1028.
[16] M.J. Bogusz, R.-D. Maier, K.D. Kruger, K.S. Webb, J. Romeril, M.L. Miller, Journal of Chromatography A 844 (1999) 409.
[17] L. Zintek, J. Neukom, LC–MS-Library System Protocol Version 1. 2, US EPA, Region 5 Chicago Regional Laboratory, Chicago, 2006.

Talanta 79 (2009) 871–876

Contents lists available at ScienceDirect

Talanta

journal homepage: www.elsevier.com/locate/talanta

Comparison of extraction methods for volatile compounds of Muscat grape juice

E. Sánchez-Palomo[a], M.E. Alañón[a], M.C. Díaz-Maroto[a,b,*], M.A. González-Viñas[a], M.S. Pérez-Coello[a]

[a] Área de Tecnología de los Alimentos, Facultad de Ciencias Químicas, Campus Universitario, s/n, Universidad de Castilla-La Mancha, 13071 Ciudad Real, Spain
[b] IRICA (Instituto Regional de Investigación Científica Aplicada) Universidad de Castilla-La Mancha, Campus Universitario, s/n, 13071 Ciudad Real, Spain

ARTICLE INFO

Article history:
Received 4 February 2009
Received in revised form 4 May 2009
Accepted 13 May 2009
Available online 22 May 2009

Keywords:
Gas chromatography–mass spectrometry
Extraction techniques
Volatile compounds
Muscat grape juice

ABSTRACT

Typical flavour of Muscat d'Alexandrie wines is mainly due to volatile compounds coming from grapes of this variety. Therefore, the choice of grapes is crucial to obtain musts with a great aromatic potential, which will contribute to the final aroma of wines derived from those musts. In this study, three sampling techniques, liquid–liquid extraction (LLE), solid phase extraction (SPE) and simultaneous distillation-extraction (SDE), were compared for the analysis of volatile compounds in Muscat grape juice. Results showed that although the three techniques can be recommended for the quantitative analysis of volatile compounds from musts, LLE and SPE are better sample preparation techniques than SDE, mainly for determination of polar compounds such as acids or alcohols.

1. Introduction

Aroma is one of the major factors that determine the nature and quality of wines. The volatile compounds derived from grapes are the main responsible for the varietal aroma of wines and they are influenced by numerous factors such as the grape variety, culture practices, soil type, climate, etc. [1,2]. These varietal aromas are very important in the enjoyment and appreciation of wine and hence in its economic valuation. Therefore, the choice of grapes is crucial to obtain musts with a great aromatic potential which will have a strong influence on the quality of wines.

However, the volatile compounds responsible for the varietal aroma are present in only trace amounts, which means that to carry on their identification and quantification, an effective method of enrichment is required prior to their analysis by gas chromatography–mass spectrometry (GC–MS).

Different extraction methods have been established for this purpose. Classical liquid–liquid extraction based on organic solvent extraction is certainly one of the most frequently reported methods in the literature for the isolation of volatile compounds in musts [3–7]. An advantage of this method is that all volatile compounds (low, medium and high volatility) can be analysed in one extraction step. Nevertheless, because LLE requires large amounts of high purity solvents, this technique is relatively tedious and time-consuming. Furthermore, extracts have to be concentrated. This step can bring about the loss of certain compounds as well as artefact formation and eventual interferences resulting from solvent impurities in chromatographic analysis [3–5]. However, in the last few years, numerous efforts have been made to diminished these disadvantages of LLE method, in particular with the introduction of liquid–liquid microextraction (LLEM) technique which has already been applied to volatiles analysis in grapes [8,9]. Other extraction technique which has been successfully applied to must aroma components is solid-phase extraction (SPE) [10–14]. This technique based on adsorbent materials where analytes are bound to active sites on a surface, allows the determination of a wide range of volatile compounds, requires smaller quantities of solvents and shorter time of analyses but is relatively tedious. SPE has been successfully used to study the evolution of aromatic compounds of grapes during ripening [15] and to determine the potential aroma in several varieties of Spanish grapes [16].

The simultaneous steam distillation-solvent extraction technique (SDE), proposed by Godefroot et al. [17], has been applied to grape juice in order to extract the volatile aroma components [6,18,19].

Several authors have found some limitations of the SDE technique like the low recovery of the most volatile compounds and the loss and thermal degradation of certain compounds [19–21]. Nevertheless, SDE technique achieves generally higher recoveries of volatile compounds than other isolation techniques such as headspace [22] or stir bar sorptive extraction (SBSE) [19].

Headspace techniques have also been used with the purpose of carrying out the isolation of volatile compounds from musts by means of purge and trap [6,23] or by means of SPME [24,25]. These techniques are less sensitive for the isolation of low volatile

* Corresponding author at: IRICA (Instituto Regional de Investigación Científica Aplicada) Universidad de Castilla-La Mancha, Campus Universitario, s/n, 13071 Ciudad Real, Spain. Tel.: +34 926 295300x3423; fax: +34 926 295318.
E-mail address: MariaConsuelo.Diaz@uclm.es (M.C. Díaz-Maroto).

0039-9140/$ – see front matter © 2009 Elsevier B.V. All rights reserved.
doi:10.1016/j.talanta.2009.05.019

Table 1
Calibration curves and performance characteristics obtained by LLE ($n = 5$).

Compounds	Linearity range (mg/L)	Slope	Intercept	LOL (%)	r^2	Detection limit (μg/L)	Quantification limit (μg/L)	RSD (%)
(*E*)-2-Hexenal	0.01–0.40	0.43	0.00	97.89	0.998	0.02	0.09	2.0
1-Hexanol	0.20–6.00	0.68	0.00	98.43	0.998	0.01	0.06	5.2
(*E*)-3-Hexen-1-ol	0.01–0.33	0.78	0.00	97.83	0.999	0.01	0.05	0.5
(*Z*)-3-Hexen-1-ol	0.01–0.33	0.75	0.00	98.74	0.998	0.01	0.07	1.6
(*E*)-2-Hexen-1-ol	0.10–3.03	0.57	0.00	97.52	0.997	0.01	0.06	3.9
(*Z*)-Linalool oxide furan	0.01–0.35	0.64	0.00	98.95	0.999	0.02	0.10	8.2
(*E*)-Linalool oxide furan	0.01–0.35	0.42	0.00	98.72	0.998	0.01	0.05	7.9
Benzaldehyde	0.01–0.45	0.82	0.00	98.27	0.997	0.01	0.04	2.6
Linalool	0.05–1.56	0.89	0.00	98.35	0.997	0.01	0.04	5.8
α-Terpineol	0.01–0.33	1.05	0.00	98.97	0.999	0.01	0.04	4.7
β-Citronellol	0.02–0.46	1.11	0.00	98.35	0.995	0.01	0.04	3.2
Nerol	0.02–0.66	0.88	0.00	99.29	0.999	0.01	0.04	6.2
Geraniol	0.02–0.57	0.72	0.00	99.35	0.999	0.01	0.05	4.1
Benzyl alcohol	0.05–1.43	1.28	-0.02	98.30	0.997	0.01	0.03	6.4
Phenylethyl alcohol	0.06–1.69	1.11	0.00	98.33	0.997	0.01	0.04	2.7

compounds and the results obtained are difficult to relate to the real concentration of compounds in the matrix. Stir bar sorptive extraction (SBSE) is one of the latest techniques developed. It has been applied to volatile constituents of musts by several authors [19,26–28]. Although it has been demonstrated that relative recoveries and reproducibility are generally lower for the SBSE technique in the analysis of volatile grape juice, it seems to be a more sensitive technique than SDE [19].

In order to select the best extraction technique for studying the volatile composition of musts, three different classical extraction techniques, LLE, SPE and SDE were evaluated for qualitative and quantitative determination of volatile components of a Muscat grape juice.

2. Experimental

2.1. Reagents and standards

The chemical standards were supplied by Aldrich (Gillingham, U.K.), Fluka (Buchs, Switzerland) and Sigma (St. Louis, MO). LiChrolut EN resins, prepacked in 500 mg cartridges (6 mL total volume) or in bulk, were obtained from Merck (Darmstadt, Germany). Dichloromethane and methanol, GC-quality, was obtained from Scharlau (Barcelona, Spain); absolute ethanol glucose and fructose were from Panreac, (Barcelona, Spain). Pure water was obtained from a Milli-Q purification system (Millipore, U.S.A.).

2.2. Must samples

Commercial Muscat d'Alexandrie grape samples were purchased from a local store. Grapes were gently pressed manually (under nitrogen atmosphere), with a rapid skin separation and with the addition of SO_2 (80 mg/L).

2.3. Isolation and concentration techniques

2.3.1. Liquid–liquid extraction

200 mL of sample was extracted continuously with 100 mL of n-pentane-dichloromethane (60/40, v/v) in downwards displacement extractors for 12 h using 4-nonanol as internal standard. The extract was then concentrated in a water bath using a 50 cm Vigreux column to a volume of 1 mL and then under stream of nitrogenous to a volume of 200 μL.

2.3.2. Solid phase extraction

Volatile compounds were extracted using the method developed by Günata et al. [11]. One hundred millilitres (100 mL) were fractionated on preconditioned polypropylene-divinylbenzene cartridges (Lichrolut EN (40–120 μm), Merck, 0.5 g of phase) using 4-nonanol as internal standard with subsequent elution with 10 mL of dichloromethane. Extracts were concentrated under nitrogenous stream to a volume of 200 μL.

2.3.3. Simultaneous distillation-extraction

Enrichment of the sample was achieved using a micro scale simultaneous distillation extraction apparatus (Chrompack Middelburg, The Netherlands) in the high-density solvent configuration. 70 mL volume of sample was used for analysis, using 4-nonanol as internal standard and 2 mL of dichloromethane as extractive solvent. The sample temperature was maintained at 110 °C with a silicon bath at pressure atmospheric and the temperature of cold finger was −3 °C. The extraction was considered to be

Table 2
Calibration curves and performance characteristic obtained by SPE ($n = 5$).

Compounds	Linearity range (mg/L)	Slope	Intercept	LOL (%)	r^2	Detection limit (μg/L)	Quantification limit (μg/L)	RSD (%)
(*E*)-2-Hexenal	0.01–0.40	0.41	0.01	98.44	0.996	0.04	0.07	5.6
1-Hexanol	0.20–6.00	0.55	0.11	98.90	0.998	0.04	0.05	6.4
(*E*)-3-Hexen-1-ol	0.01–0.33	0.52	0.01	97.91	0.992	0.04	0.06	6.2
(*Z*)-3-Hexen-1-ol	0.01–0.33	0.62	0.00	98.37	0.997	0.03	0.05	6.1
(*E*)-2-Hexen-1-ol	0.10–3.03	0.59	−0.09	98.98	0.998	0.03	0.05	7.2
(*Z*)-Linalool oxide furan	0.01–0.35	0.50	0.00	97.78	0.993	0.04	0.06	3.5
(*E*)-Linalool oxide furan	0.01–0.35	0.50	0.00	98.03	0.996	0.04	0.06	7.0
Benzaldehyde	0.01–0.45	0.89	0.00	97.99	0.996	0.02	0.03	6.9
Linalool	0.05–1.56	0.98	0.00	98.18	0.996	0.02	0.03	9.5
α-Terpineol	0.01–0.33	1.14	0.00	97.74	0.995	0.02	0.03	3.7
β-Citronellol	0.02–0.46	1.27	−0.04	98.88	0.995	0.02	0.02	2.5
Nerol	0.02–0.66	1.03	0.00	97.71	0.981	0.02	0.03	5.9
Geraniol	0.02–0.57	0.98	−0.02	97.97	0.993	0.02	0.03	8.6
Benzyl alcohol	0.05–1.43	1.09	0.00	98.19	0.997	0.02	0.03	7.4
Phenylethyl alcohol	0.06–1.69	1.30	−0.06	99.14	0.985	0.02	0.03	2.0

Table 3
Calibration curves and performance characteristic obtained by SDE ($n = 5$).

Compounds	Linearity range (mg/L)	Slope	Intercept	LOL (%)	r^2	Detection limit (μg/L)	Quantification limit (μg/L)	RSD (%)
(*E*)-2-Hexenal	0.01–0.40	0.50	0.01	99.17	0.999	0.03	0.04	5.4
1-Hexanol	0.20–6.00	0.54	0.00	99.03	0.999	0.03	0.03	2.6
(*E*)-3-Hexen-1-ol	0.01–0.33	0.81	0.00	99.33	0.999	0.02	0.02	5.1
(*Z*)-3-Hexen-1-ol	0.01–0.33	0.51	0.00	99.03	0.999	0.03	0.03	3.7
(*E*)-2-Hexen-1-ol	0.10–3.03	0.48	0.00	99.35	0.999	0.03	0.04	2.2
(*Z*)-Linalool oxide furan	0.01–0.35	0.44	0.00	99.28	0.999	0.04	0.04	7.5
(*E*)-Linalool oxide furan	0.01–0.35	0.42	0.01	99.52	0.999	0.04	0.04	0.8
Benzaldehyde	0.01–0.45	0.77	0.02	98.34	0.997	0.02	0.02	7.3
Linalool	0.05–1.56	0.86	0.00	98.91	0.999	0.02	0.02	6.9
α-Terpineol	0.01–0.33	1.18	0.00	98.57	0.998	0.01	0.01	6.2
β-Citronellol	0.02–0.46	1.10	0.02	98.16	0.995	0.01	0.02	2.3
Nerol	0.02–0.66	0.65	0.02	99.45	0.999	0.07	0.20	10.2
Geraniol	0.02–0.57	0.59	0.00	99.16	0.997	0.03	0.03	5.6
Benzyl alcohol	0.05–1.43	0.20	−0.02	99.44	0.998	0.08	0.08	4.0
Phenylethyl alcohol	0.06–1.69	0.40	0.00	96.17	0.998	0.05	0.05	5.0

complete in 2 h. Extracts were then concentrated under nitrogenous stream to a volume of 200 μL.

2.4. Synthetic must solutions

Calibration curves were obtained using LLE, SPE and SDE, and subsequent injection onto the GC-system, in duplicate, of synthetic must solutions (100 g of glucose and 100 g of fructose in 1 L of Milli-Q water, pH adjusted to 3.5 with tartaric acid), containing defined amounts of the compounds of interest, at six increasing concentrations included in the ranges in which each compounds are normally found in grape musts [1,2]. The ranges of concentrations of defined amounts of compounds are shown in Tables 1–3.

2.5. GC–MS analysis

An Agilent gas chromatograph model 6890 N coupled to a mass selective detector model 5973 *inert* was used. An amount of 1 μL of extract was injected in splitless mode on a BP-21 capillary column (50 m × 0.32 mm i.d.; 0.32 μm film thickness). Oven temperature program was: 70 °C (5 min)–1 °C/min–95 °C (10 min)–2 °C/min–190 °C (40 min). Injector and transfer line temperatures were 250 °C and 280 °C, respectively. Mass detector conditions were: electronic impact (EI) mode at 70 eV; source temperature: 178 °C; scanning rate: 1 scan/s; mass acquisition range: 40–450 amu. As carrier gas was used helium under a flow rate of 0.7 mL/min.

Peak identifications were based on comparison of their mass fragmentation with those of pure standards and/or with those reported by commercial libraries such as Wiley A and NBS75K. The quantitative analysis of positively identified compounds was performed by total ion current using the calibration curves proposed for each method.

2.6. Statistical analysis

The Student–Newman–Keuls test was applied to discriminate among the chemical data. Statistical processing was carried out by using the SPSS 14.0 for Windows statistical package.

3. Results and discussion

3.1. Calibration curves and performance characteristics

To study the linear character and the performance characteristics of the three extraction methods tested (LLE, SPE and SDE), six solutions containing defined amounts of synthetic volatile compounds normally found in grape musts (Tables 1–3) were prepared in synthetic must. The volatile compounds selected together with the ranges of linearity and performance parameters of calibration curves of each method are summarized in Tables 1–3. Each compound was added in the concentration range expected in grape musts.

Linear range covered the volatile compound concentrations expected in the samples since good regression coefficients (r^2) were

Table 4
Regression analysis of LLE compared with SPE and SDE.

Compounds	LLE-SPE					LLE-SDE				
	r^2	Slope	Confidence limits for the slope	Intercept	Confidence limits for the intercept	r^2	Slope	Confidence limits for the slope	Intercept	Confidence limits for the intercept
(*E*)-2-Hexenal	0.998	0.978	0.946–1.011	0.013	−0.006–0.032	0.997	0.973	0.935–1.015	0.002	−0.005–0.009
1-Hexanol	0.997	0.997	0.938–1.017	0.142	0.036–0.248*	0.995	0.962	0.912–1.012	0.095	−0.039–0.228
(*E*)-3-Hexen-1-ol	0.992	1.030	0.962–1.097	0.004	−0.006–0.014	0.995	1.024	0.970–1.077	−0.005	−0.013–0.003
(*Z*)-3-Hexen-1-ol	0.998	0.994	0.961–1.026	0.0002	−0.004–0.004	0.998	0.994	0.962–1.026	0.0002	−0.004–0.004
(*E*)-2-Hexen-1-ol	0.992	1.009	0.944–1.075	0.009	−0.078–0.097	0.992	1.015	0.949–1.082	−0.026	−0.115–0.060
(*Z*)-Linalool oxide furan	0.992	0.983	0.922–1.048	0.002	−0.008–0.012	0.999	0.975	0.972–1.034	−0.001	−0.021–0.005
(*E*)-Linalool oxide furan	0.991	1.022	0.951–1.093	0.011	−0.001–0.022	0.999	1.007	0.982–1.038	−0.001	−0.005–0.005
Benzaldehyde	0.993	0.975	0.902–1.048	−0.007	−0.022–0.008	0.990	0.999	0.927–1.071	−0.004	−0.019–0.010
Linalool	0.994	1.015	0.956–1.074	−0.019	−0.059–0.022	0.994	0.989	0.934–1.045	0.004	−0.034–0.043
α-Terpineol	0.997	1.035	0.998–1.073	0.077	0.0131–0.002*	0.999	1.016	0.988–1.043	−0.003	−0.008–0.0002
β-Citronellol	0.999	0.987	0.962–1.012	−0.003	−0.008–0.002	0.998	0.988	0.956–1.020	0.019	0.012–0.025*
Nerol	0.997	1.022	0.983–1.061	−0.008	−0.020–0.003	0.999	1.029	1.013–1.045*	0.001	−0.003–0.006
Geraniol	0.999	0.993	0.971–1.015	0.001	−0.005–0.006	0.999	1.020	0.998–1.042	0.001	−0.005–0.006
Benzyl alcohol	0.997	1.015	0.976–1.055	0.007	−0.017–0.031	0.999	0.990	0.970–1.009	−0.012	−0.020–1.20*
Phenylethyl alcohol	0.998	1.023	0.991–1.051	0.015	−0.009–0.039	0.994	0.996	0.932–1.048	0.003	−0.041–0.046

* Significant differences.

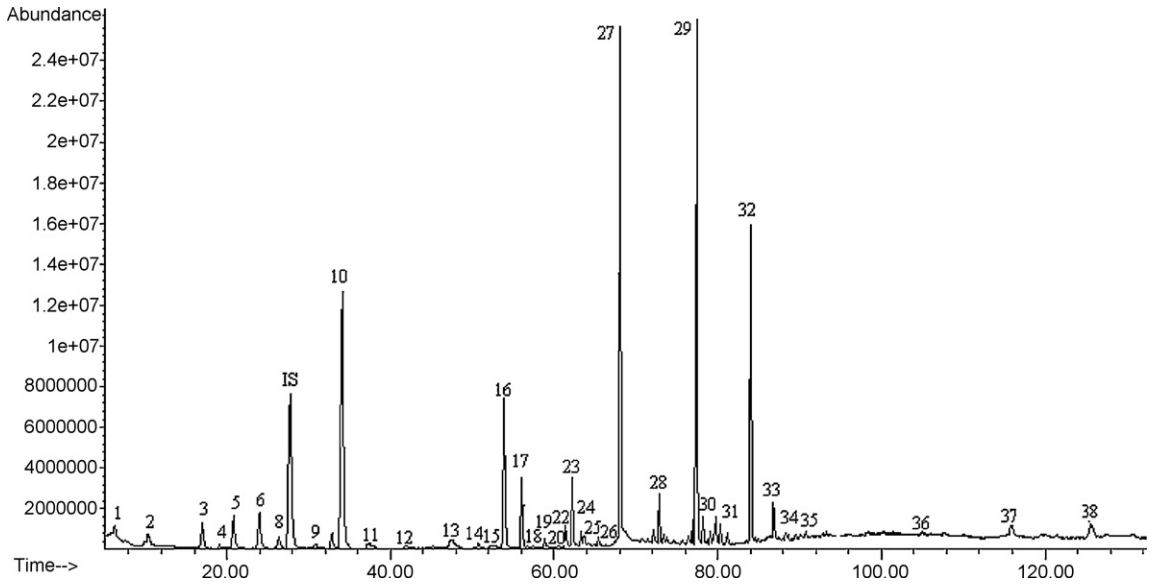

Fig. 1. Total ion chromatogram from must grapes of Muscat obtained by SPE. Time scale in minutes. For peak identification see Table 5.

obtained for all methods in all cases. These results were also corroborated by the term "limit of linearity", the concentration at which the calibration curve departs from linearity" (LOL) which displayed in all cases values superior to 95% (Tables 1–3). This parameter is obtained by the following equation in which RSD_b is the relative standard deviation of the slope expressed as a percentage.

$$LOL(\%) = 100 - RSD_b$$

Detection limit (calculated as three times the standard deviation of the noise of the baseline) and the quantification limit (calculated as ten times the standard deviation of the noise of the baseline) obtained by interpolation of calibrated curves of each compound analyzed in the three extraction techniques were in all cases inferior to the minimum concentration found in musts [1,2].

The low detection and quantification limits observed, revealed that the three techniques have a high sensitivity and they are suitable for the quantitative analysis. In general, the detection limits of volatile compounds extracted by LLE were lower than those detected in SDE and SPE techniques. Meanwhile, the quantification limits of certain compounds such as linalyl oxides and (*E*)-2-hexanal extracted by LLE and SPE were slightly higher than those of the rest of the compounds. The quantification limits of nerol, benzyl alcohol and phenylethyl alcohol calculated for the SDE were also slightly higher probably due to the lower volatility of these compounds [29].

To study the reproducibility of the three extraction methods, five analyses of the same synthetic must solution containing defined amounts of volatile components were carried out. Tables 1–3 show, respectively, the relative standard deviation (RSD) obtained for each compound with the three extraction techniques evaluated. The reproducibility of the three methods were satisfactory since RSDs for all compounds studied ranged from 0.5 to 10.2%.

In order to compare the three extraction methods tested, a regression analysis were made between data obtained for each point of the calibrated curve with each compounds analyzed by means of LLE and SPE, as well as by means of LLE and SDE. Table 4 shows the coefficient of determination (r^2), slopes and intercepts calculated. In no cases were ideal results obtained (intercept equal to zero and slope equal to one), which is the reason why the confidence limits for both were calculated ($\alpha = 0.05$). In order to carry out these operations, the standard deviation of the slope and intercept were calculated determining the statistical $S_{y/x}$ previously.

If the value 1 is included in the confidence interval belonging to the slope, it can be considered that slope is not significantly different from 1. Similarly, if the value 0 is included in the confidence interval belonging to the intercept, it is possible to assume that intercept is not significantly different from 0. Results obtained when comparing the SPE with the LLE showed that results calculated from both methods are not significantly different except for 1-hexanol and α-terpineol. These two compounds presented concentrations slightly superior when the LLE is used. Comparing LLE with the SDE, only two compounds, β-citronellol and nerol, displayed significant differences between results obtained by both methods.

3.2. Analysis of volatile compounds in musts of Muscat grapes

Although the validation and comparison of the three extraction techniques studied were made with synthetic must solutions, natural must is a complex matrix in which other components exist and could influence on the recovery of volatile compounds responsible for the aroma. The effect of the matrix must be considered when an extraction technique is used with quantitative purposes. Therefore, the three extraction methods were applied to real samples of Muscat must.

Gas chromatographic analysis of the extracts obtained by means of LLE, SPE and SDE made it possible to identify 38 volatile components of Muscat grape juice by their mass spectral data. The quantification process only was applied to the compounds included in the calibration set by means of the calibration curves obtained previously. The total ion chromatogram of the extract obtained by SPE is showed in Fig. 1. Table 5 shows the detected compounds in the three extracts.

The qualitative composition of the three organic extract obtained was similar, characterizing the volatile profile of must derived from Muscat grapes, a very aromatic variety. Among the compounds identified were aldehydes and alcohols of six carbon atoms like hexanal or 1-hexanol, compounds give rise to the herbaceous aromas of the grapes and musts [30]. The majority of compounds detected are monoterpenes (linalool, terpineol, nerol, geraniol) and poly-oxygenated terpenes. This group of terpenes has a great sensorial relevance since they are responsible for the floral and fruit aromas of this variety of grape [30].

An important group of benzoid compounds was also found. Among them, the most remarkable benzoid compounds from the

Table 5
Volatile compounds identified in Muscat grape must by LLE, SPE and SDE.

Compounds	KI[a]	m/z[b]	LLE	SPE	SDE
(1) Hexanal	1080	41/44/56	+	+	+
(2) (*E*)-2-Hexenal	1225	55/69/83	+	+	+
(3) 1-Hexanol	1354	56/43/41/55	+	+	+
(4) (*Z*)-3-Hexen-1-ol	1371	41/67/55/82	+	+	+
(5) (*E*)-2-Hexen-1-ol	1410	57/82/41	+	+	+
(6) (*Z*)-linalol oxyde furan	1432	153/152/135	+	+	+
(7) 2-Furancarboxaldehyde	1448	97/96/98	–	–	+
(8) (*E*)-linalool oxyde furan	1459	153/152	+	+	+
(9) Benzaldehyde	1529	77/105/106	+	+	+
(10) Linalool	1554	71/93	+	+	+
(11) Diethyl malonate	1576	115/133/88	+	+	-
(12) Ho-trienol	1623	71/82/43	+	+	+
(13) α-terpineol	1720	59/93/121/136	+	+	+
(14) 2(5H)-Furanone, 3-methyl-	1743	41/69/98	+	+	+
(15) p-mentha-1(7). 2-dien-8-ol (isomer I)	1743	94/79/59	+	+	+
(16) (*Z*)-linalol oxyde pyran	1768	68/94	+	+	+
(17) (*E*)-linalool oxyde pyran	1791	68/94/155	+	+	+
(18) β-citronellol	1798	69/81/123	+	+	+
(19) p-mentha-1(7). 2-dien-8-ol (isomer II)	1802	59/79/94	+	+	+
(20) Nerol	1812	69/93	+	+	+
(21) β-Damascenone	1820	69/121/190	–	–	+
(22) Hexanoic acid	1841	60/73/87	+	+	+
(23) Geraniol	1861	69/93/123	+	+	+
(24) Benzyl Alcohol	1864	79/108/107	+	+	+
(25) 2(5H)-Furanone, 5-methyl-	1892	69/98/41	+	+	-
(26) Phenylethyl alcohol	1902	91/92/65	+	+	+
(27) 2,6-dimethyl-3,7-octadiene-2,6-diol	1953	82/71/43	+	+	+
(28) 3,7-dimethyl-1-octen-3,7-diol	1967	71/59/121	+	+	–
(29) 2,6-dimethyl-1,7-octadiene-3,6-diol	1983	67/43/71	+	+	–
(30) Nonanoic acid	2202	60/73/129	+	+	–
(31) Benzoic acid, 4-ethoxy, ethyl ester	2243	121/138/166	+	+	+
(32) (*Z*)-8-Hydroxylinalool	2310	71/121/137	+	+	–
(33) Geranic acid	2329	69/100/123	+	+	+
(34) Benzoic acid	2457	77/105/122	+	+	+
(35) Dodecanoic acid	2517	60/73/157	+	+	–
(36) Tetradecanoic acid	–	73/60/43	+	+	–
(37) Methylvanillil eter	–	137/168/122	+	+	–
(38) Hexadecanoic acid	–	43/60/73	+	+	–

[a] Kovat's index calculated on a BP-21 capillary column.
[b] Characteristic ions in the mass spectrum.

sensorial point of view are benzaldehyde, phenylethyl alcohol and bencylalcohol [31].

The most noticeable differences found in the qualitative profile of must were the occurrence of 2-furancarboxaldehyde and β-damascenone which only were identified in the extracts obtained by SDE technique. The presence of 2-furancarboxaldehyde can be attributable to sugar thermal degradation produced during the sample heating, fact that is in a good agreement with the comments of others authors [19,29]. Whereas, the occurrence of β-damascenone can be explained by the release of its glycosides precursors by acid hydrolysis during the sample heating.

Despite this fact, SDE is a very convenient isolation technique to carry out a characterization of volatile profile of musts since, with a good calibration in a good model system, the occurrence of these artefacts should not be a problem. However, these products might be co-eluted with target compounds and upset the identification and quantification process.

On the other hand, high polar compounds like acids (geranoic, benzoic, dodecanoic, tetradecanoic and hexadecanoic acid) and alcohols (2,6-dimethyl-3,7-octadiene-2,6-diol, 3,7-dimethyl-1-octen-3,7-diol, 2,6-dimethyl-1,7-octadiene-3,6-diol and hydroxylinalool) were not detected by SDE (Table 5). This fact can be attributed to a poor extraction due to their high affinity for the aqueous phase and consequently their low water/solvent partition coefficients or because their low volatility [29]. Nevertheless, these compounds are minor components of musts and the majority of them do not play an important sensorial role.

Table 6 shows quantitative results obtained using the calibration curves calculated previously. In general, results obtained by the three techniques were quite similar, although small differences were found in some compounds. The must contained significant quantities of C_6 alcohols, mainly (*E*)-2-hexen-1-ol and 1-hexanol

Table 6
Volatile compounds concentration (μg/L) and relative standard deviations in the three organic extracts of Muscat must.

Compounds	LLE		SPE		SDE	
	Mean*	RSD (%)	Mean*	RSD (%)	Mean*	RSD (%)
(*E*)-2-Hexenal	7.73[a]	1.68	10.5[b]	2.49	9.60[b]	0.72
1-Hexanol	123[a]	0.93	123[a]	2.66	95.6[b]	1.34
(*E*)-3-Hexen-1-ol	n.d.	–	n.d.	–	n.d.	–
(*Z*)-3-Hexen-1-ol	16.0[a]	1.54	10.9[b]	0.30	11.3[b]	1.81
(*E*)-2-Hexen-1-ol	148[a]	3.76	118[b]	0.34	124[b]	1.75
(*Z*)-Linalool oxide furan	163[a]	1.97	145[b]	0.12	148[b]	1.07
(*E*)-Linalool oxide furan	64.9[a]	3.21	60.3[a]	1.00	68.6[a]	0.96
Benzaldehyde	7.44[a]	0.02	8.31[b]	2.44	8.38[b]	2.15
Linalool	639[a]	2.24	693[a]	1.93	629[a]	0.70
α-Terpineol	8.25[a]	1.64	5.04[a]	3.62	7.04[a]	4.17
β-Citronellol	2.04[a]	1.68	3.24[b]	5.76	3.13[b]	0.50
Nerol	8.82[a]	2.56	5.87[b]	2.02	3.17[c]	5.04
Geraniol	91.2[a]	3.94	82.6[a]	0.51	90.4[a]	2.60
Benzyl alcohol	8.11[a,b]	0.57	8.53[a]	5.57	7.73[b]	2.46
Phenylethyl alcohol	6.34[a]	2.52	6.46[a]	0.31	5.04[b]	2.16

n.d.: not detected.
* According to the result of the Student–Newman–Keuls test, mean values in the same row with different superscript (a, b, c) are significantly different ($p < 0.05$).

whose concentrations extracted were slightly higher when the LLE technique is used.

The concentrations of almost monoterpenes and polyoxigenated terpenes were independent of the extraction technique used, except in the case of β-citronellol, nerol and (*Z*)-linalool oxide furan whose concentrations were slightly superior in the extracts obtained by LLE.

The benzene derivates (benzaldehyde, benzyl alcohol and phenylethyl alcohol) are known to be characteristic compounds in grape must and SDE seems not to extract them efficiently.

4. Conclusions

Results show that the three extraction methods studied can be used for the qualitative and quantitative determination of volatile compounds from musts. Nevertheless, when wishing to choose one of these isolation techniques, it would be convenient to consider other factors such as the amount of solvent required or the time consumption.

Despite the fact that extracts obtained by means of SPE and LLE displayed a similar qualitative composition. LLE seems to extract slightly higher concentration of compounds from must in comparison with the other techniques tested. However, SPE required smaller amount of solvent and sample and shorter extractions times.

On the other hand, extraction procedure by means of SDE was the fastest and it used minor amount of sample and solvent, obtaining good quantitative results for the more relevant shift aroma to compounds of aroma must. However, it should be taken into account the difficulty of SDE in extracting compounds with low volatility and the possible appearance of artefacts formed during sample heating such as furancarboxaldehyde (product of Maillard reaction) and the liberation of volatile compounds from their glycosylated forms by acid hydrolysis such as β-damascenone.

References

[1] C. Flanzy, Enología Fundamentos Científicos y Tecnológicos, AMV Ed.-Mundi Prensa, Madrid, España, 2000.
[2] P. Ribereau-Gayon, Y. Glories, A. Maujean, D. Dubourdieu, Handbook of Enology, Vol. 2, Wiley, UK, 2000.
[3] P.J. Hardy, J. Agric. Food Chem. 17 (1969) 656.
[4] P. Schreier, F. Drawert, A. Junder, J. Agric. Food Chem. 24 (1976) 331.
[5] P. Schreier, F. Drawert, F. Winkler, J. Agric. Food Chem. 27 (1979) 365.
[6] G.P. Blanch, G. Reglero, M. Herraiz, J. Chromatogr. Sci. 29 (1991) 11.
[7] M.E.O. Mamede, G.M. Pastore, Food Chem. 96 (2006) 586.
[8] J. Cacho, J. Melendez, V. Ferreira, V. Mikrochim. Acta 108 (1992) 61.
[9] C. Aubert, S. Baumann, H. Arguel, J. Agric. Food Chem. 53 (2005) 8881.
[10] P.J. Williams, C.R. Strauss, B. Wilson, R.A. Massy-Westropp, J. Chromatogr. 235 (1982) 471.
[11] Y.Z. Gunata, C.L. Bayonove, R.L. Baumes, R.E. Cordonnier, J. Chromatogr. 331 (1985) 83.
[12] S.G. Viorin, R.L. Baumes, Z.Y. Gunata, M.S. Bitteur, C.L. Bayonove, C. Tapiero, J. Chromatogr. 590 (1992) 313.
[13] S.G. Voirin, R.L. Baumes, J.C. Sapis, C.L. Bayonove, J. Chromatogr. 595 (1992) 269.
[14] R. di Stefano, Bull. OIV 64 (1991) 219.
[15] L. Carballeira Lois, S. Cortés Diéguez, M.L. Gil de la Peña, E. Fernández Gómez, Chromatographia 53 (2001) 350.
[16] E. López-Tamames, N. Carro-Marioño, Y.Z. Gunata, C. Sapis, R. Baumes, C. Bayonove, J. Agric. Food Chem. 45 (1997) 1729.
[17] M. Godefroot, P. Sandra, M. Verzele, J. Chromatogr. 203 (1981) 325.
[18] A.J. Núñez, J.M.H. Bemelmans, H. Maarse, Chromatographia 18 (1984) 153.
[19] D.J. Caven-Quantrill, A.J. Buglass, J. Chromatogr. A 1117 (2006) 121.
[20] P. Frakas, J. Sadecka, M. Kovac, B. Siegmund, E. Leitner, W. Pfannhauser, Food Chem. 60 (4) (1997) 617.
[21] A. Chaintreau, Flavour Fragrance J. 16 (2001) 136.
[22] P. Dirinck, F. Van Opstaele, F. Vandendriessche, Food Chem. 59 (4) (1997) 511.
[23] L. Rosillo, M.R. Salinas, J. Garijo, G.L. Alonso, J. Chromatogr. A 847 (1999) 155.
[24] A. Rapp, H. Hastrich, L. Engel, Vitis 15 (1976) 29.
[25] E. Sánchez-Palomo, M.C. Díaz-Maroto, M.S. Pérez-Coello, Talanta 66 (2005) 1152.
[26] M.R. Salinas, A. Zalacain, F. Pardo, G.L. Alonso, J. Agric. Food Chem. 52 (2004) 4821.
[27] D.J. Caven-Quantrill, A.J. Buglass, Flavour Fragrance J. 22 (2007) 206.
[28] D.J. Caven-Quantrill, Alan J. Buglass, Flavour Fragrance J. 23 (2008) 239.
[29] L. Castro-Vázquez, M.S. Pérez-Coello, M.D. Cabezudo, G.I.T. Lab. J. 5 (2002) 228.
[30] H. Guth, J. Agric. Food Chem. 45 (1997) 3027.
[31] E. Sánchez-Palomo, M.A. González-Viñas, M.C. Díaz-Maroto, A. Soriano-Pérez, M.S. Pérez-Coello, Food Chem. 103 (2) (2007) 631.

Talanta 79 (2009) 706–711

Contents lists available at ScienceDirect

Talanta

journal homepage: www.elsevier.com/locate/talanta

Analytical speciation of mercury in fish tissues by reversed phase liquid chromatography–inductively coupled plasma mass spectrometry with Bi^{3+} as internal standard

María Maldonado Santoyo, Julio Alberto Landero Figueroa, Kazimierz Wrobel, Katarzyna Wrobel *

Department of Chemistry, University of Guanajuato, L. de Retana 5, 36000 Guanajuato, Mexico

ARTICLE INFO

Article history:
Received 3 March 2009
Received in revised form 24 April 2009
Accepted 27 April 2009
Available online 3 May 2009

Keywords:
Mercury speciation
Extraction
Internal standard
HPLC–ICP-MS

ABSTRACT

In this work, the quantification of two mercury species (Hg^{2+} and CH_3Hg^+) in fish tissues has been revisited. The originality of our approach relies on the use of Bi^{3+} as internal standard (IS) and on the modification of typical extraction conditions. The IS (125 μl, 1000 μg l^{-1} Bi^{3+}) was added to the aliquot of fresh fish tissue (400–500 mg). A high-speed blender and ultrasound-assisted homogenization/extraction was carried out in the presence of perchloric acid (1.5 ml, 0.6 mol l^{-1}), L-cysteine (500 μl, 0.75 mol l^{-1}) and 500 μl toluene:methanol (1:1). Perchloric acid was used for protein denaturation and precipitation, toluene helped to destroy lipid structures potentially sequestering CH_3Hg^+, L-cysteine was used to form water-soluble complexes with Bi^{3+}, Hg^{2+} and CH_3Hg^+. The excess of perchloric acid was eliminated by addition of potassium hydroxide (pH 5 with acetic acid). The obtained extract, was diluted with the mobile phase (1:1) and introduced (20 μl) to the reversed phase HPLC–ICP-MS system. The separation was achieved by isocratic elution (2.5 mmol l^{-1} cysteine, 12.5 mmol l^{-1} $(NH_4)_2HPO_4$, 0.05% triethylamine, pH 7.0:methanol (96:4)) at a flow rate 0.6 ml min^{-1}. Column effluent was on-line introduced to ICP-MS for specific detection of ^{202}Hg, ^{200}Hg and ^{209}Bi. Analytical signal was defined as the ratio between $^{202}Hg/^{209}Bi$ peak areas. The detection limits evaluated for Hg^{2+} and CH_3Hg^+ were 0.8 and 0.7 μg l^{-1}. Recovery of the procedure, calculated as the sum of species concentrations found in the sample with respect to total ICP-MS-determined Hg was 91.9% for king mackerel muscle and 89.5% for red snapper liver. In the standard addition experiments, the recovery results were 98.9% for Hg^{2+} and 100.6% for CH_3Hg^+. It should be stressed that the use of Bi^{3+} as IS enabled to improve analytical performance by compensating for incomplete extraction and for imprecision of sample handling during relatively non-rigorous protocol.

1. Introduction

Inorganic mercury (Hg^{2+}) and methylmercury (CH_3Hg^+) are the primary species of this element found in marine organisms and fish consumption is the main source of methylmercury for humans. Once the related environmental and toxicological risks had been recognized, different governmental agencies established acceptable mercury concentrations in food-related products [1]. In particular, U.S. Food and Drug Administration (FDA) has a regulatory action level of CH_3Hg^+ in fish at 1 mg kg^{-1} wet mass (wm) [2]. Accordingly, there is a strong demand for robust analytical procedures providing reliable data on both, total mercury and its chemical species in these complex biological matrices.

In the actual state-of-the-art in speciation analysis, a preference can be noted for using liquid chromatography separation coupled to element specific detector [3–6]. In particular, the hyphenation of high performance liquid chromatography (HPLC) with inductively coupled plasma mass spectrometry (ICP-MS) offers the following advantages: (i) no need for derivatization of mercury species, (ii) different mechanisms of separation available and separation accomplished at room temperature, (iii) easy coupling between HPLC and ICP-MS, (iv) exceptional features of ICP-MS in terms of interference-free and sensitive detection as well as its capability for isotopic analysis [7–9].

While separation/quantification part of analytical protocol is not problematic nowadays, the quantitative extraction of inorganic and organic mercury without affecting natural distribution of species is still a challenge. Several procedures have been studied under acidic or alkaline conditions and the addition of complexing agents such as L-cysteine, 2-mercaptoethanol, thiourea, ammonium pyrrolidine dithiocarbamate, sodium diethyldithiocarbamate or dithizone has been considered [8–12]. More recently, ultrasound- and microwave-assisted extractions have gained strength, since they offer enhanced sample throughput and require lower amounts of the reagents [4,7,8,12,13]. However it has often been commented that the accuracy of final results is compromised by possible losses

* Corresponding author. Tel.: +52 473 7327555; fax: +52 473 7326252.
E-mail address: katarzyn@quijote.ugto.mx (K. Wrobel).

0039-9140/$ – see front matter © 2009 Elsevier B.V. All rights reserved.
doi:10.1016/j.talanta.2009.04.057

of volatile species during digestion at high temperature and elevated pressure, species inter-conversion, or sample contamination [14,15]. Different strategies have been explored to overcome the above limitations, including the use of mild extraction conditions [10,11,16] or the addition of a mercury species as internal standard (Hg^{2+}, ethylmercury or methylpropylmercury) [17–19]. It should be stressed however that the method of internal standard has been explored exclusively in gas chromatography separations. On the other hand, speciated isotope dilution mass spectrometry (SIDMS) has been recommended as a definitive quantification technique and also a diagnostic tool, which enables to evaluate/correct for species transformations and non-quantitative recovery [15,20–22]. Even though SIDMS for mercury speciation has been accepted as a standardized US EPA method (method 6800) [4,23], uncertainties due to measured isotope amount ratios and those associated with the natural isotopic abundance of Hg [24], as well as the availability of stable isotope enriched standards and high cost of the analysis are still the limiting factors.

Worth mentioning is that, for easier sample handling and for analytical reliability purposes, the quantification results are usually referred to the mass of dried or freeze-dried sample [12]. However, the regulatory levels are always expressed as the concentration levels in wet mass in order to facilitate the evaluation of edible portions [1]. In this work, the novel procedure is proposed for mercury speciation in fresh fish tissues, in which bismuth ion is added to the sample as internal standard thus correcting for imprecisions committed during the entire procedure. The extraction conditions reported previously have been modified and the requirement for rigorous protocol has been eliminated. The proposed procedure may be useful for fast quantitative evaluation of mercury species in fish samples providing data that could be directly compared to the values established by different governmental regulations (as Hg concentration in wet mass).

2. Experimental

2.1. Instrumentation

An Agilent series 1200 liquid chromatographic system was used and the column effluent was introduced to inductively coupled plasma-mass spectrometry system via the short-length Teflon tubing.

A model 7500ce ICP-MS (Agilent Technologies, Tokyo, Japan) was used with a Meinhard nebulizer for total mercury determination and with a MiraMist Teflon® nebulizer for speciation analysis. A Peltier-cooled chamber was operated at 2 °C. Tuning procedure was performed daily using diluted Agilent solution (Li, Y, Tl, Ce, 1 μg l^{-1} each). The chromatographic and ICP-MS instrumental operating conditions are given in Table 1.

A high-speed blender Ultra-Turrax® T25 was used for sample homogenization.

2.2. Reagents and samples

All chemicals were of analytical reagent grade. Deionized water (18.2 MΩ cm, Labconco, USA), HPLC-grade methanol and analytical reagent-grade toluene (Fisher Scientific, Pittsburgh, USA) were used throughout.

The standard solutions of mercury species (1000 mg l^{-1} Hg) were prepared by dissolving mercury chloride in 1% nitric acid and methylmercury iodide in methanol (Sigma reagents) and were kept in amber glass vials, at 4 °C. Stock solution of the internal standard was prepared by dissolving bismuth nitrate (Sigma) in 1% nitric acid (1000 mg l^{-1} Bi). Working solutions were prepared daily by appropriate dilution.

Table 1
HPLC–ICP-MS instrument operating conditions.

ICP-MS—total mercury determination	
Forward power	1500 W
Nebulizer gas flow	0.9 ml min^{-1}
Make-up gas	0.12 ml min^{-1}
Sample introduction	Meinhard nebulizer
Sample and skimmer cones	Nickel
Sample depth	10 mm
Channels monitored	^{202}Hg, ^{200}Hg, ^{209}Bi
Acquisition mode	Spectrum analysis
Dwell time	100 ms
HPLC–ICP-MS—speciation analysis	
Column	Gemini C18 (150 mm × 3 mm, 5 μm)
Mobile phase	2.5 mmol l^{-1} L-cysteine, 12.5 mmol l^{-1} $(NH_4)_2HPO_4$, 0.05% triethylamine, pH 7.0:methanol (96:4)
Temperature	Ambient
Flow	0.6 ml min^{-1}
Injection volume	20 μl
Forward power	1500 W
Nebulizer gas flow	0.9 ml min^{-1}
Make-up gas	0.12 ml min^{-1}
Sample introduction	MiraMist Teflón® nebulizer
Sample and skimmer cones	Nickel
Sample depth	10 mm
Channels monitored	^{202}Hg, ^{200}Hg, ^{209}Bi
Acquisition mode	Time-resolved analysis
Dwell time	60 ms

The following Sigma reagents were used: nitric acid, perchloric acid, phosphoric acid, acetic acid, ammonium phosphate dibasic, L-cysteine, triethylamine, potassium hydroxide, hydride peroxide.

The king mackerel and red snapper fishes were self-caught in Gulf of Mexico, Tabasco, Mexico.

2.3. Determination of total mercury

The digestion procedure reported elsewhere was slightly modified [12]. In brief, five aliquots of fresh tissue (0.4–0.5 g) were precisely weighed in 8 ml digestion vials, 100 μl of IS solution (1000 μg l^{-1} Bi), 3 ml of nitric acid (1:1) were added and the vials were closed. The samples were heated in a water bath (60 °C during 12 h), cooled down, 1 ml of hydrogen peroxide was added and the samples were again heated (60 °C, 1 h). Afterwards, the samples were cooled down, diluted to 20 ml with deionized water, centrifuged (10,000 × *g*, 10 min) and the supernatants introduced to ICP-MS. Alternatively, a portion of fresh tissue (10 g) was dried (40 °C, 48 h) [12] and homogenized. Five aliquots (0.2 g) were precisely weighed and total mercury was determined as described above. Moisture content was derived from the mass of fresh and dried samples (five replicates of 1 g fresh tissue, these samples were not used for mercury analysis). External calibration solutions contained 0, 0.2, 1.0, 5.0, 10, 25 μg l^{-1} Hg (inorganic mercury standard) and 5.0 μg l^{-1} Bi.

2.4. Analytical speciation procedure

Five aliquots of fresh tissue (0.4–0.5 g) were precisely weighed in 15 ml Falcon tubes, 125 μl of IS (1000 μg l^{-1} Bi) was added and the polythron homogenization was carried out in the presence of perchloric acid (1.5 ml, 0.6 mol l^{-1}), L-cysteine (500 μl, 0.75 mol l^{-1}) and 500 μl toluene:methanol (1:1) (0.5–2 min). The mixtures were sonicated (room temperature, 1 h), centrifuged (10,000 × *g*, 10 min) and 1000 μl of supernatant withdrawn. The excess of perchloric acid was precipitated with 70 μl of potassium hydroxide, 9 mol l^{-1} and 10 μl of acetic acid was added to adjust pH 5. Then, the samples were again centrifuged (10,000 × *g*, 10 min); the supernatant

diluted 1:1 with the mobile phase and introduced to the HPLC–ICP-MS system (Table 1). The dried tissues (0.2 g) were analyzed using this same procedure. External calibration was performed with a series of standard solutions containing Hg^{2+} and CH_3Hg^+ (0, 5.0, 10, 25, 50 μg l^{-1} Hg each) and IS (10 μg l^{-1} Bi). For recovery experiments, one mercury species (Hg^{2+} or CH_3Hg^+) was added to the fresh tissue (100 μg kg^{-1}, 200 μg kg^{-1} Hg) together with IS. These same concentrations were used for the method of standard addition, however in this case both mercury species (Hg^{2+} and CH_3Hg^+) were added to the sample. Blank was always run in parallel.

3. Results and discussion

The intent of this work was to develop relatively non-rigorous and reliable procedure for the determination of Hg^{2+} and CH_3Hg^+ in fish tissues. To do so, the use of bismuth ion as an internal standard (IS) had been proposed and the extraction conditions have been studied. To the best of our knowledge, this is the first application of IS to analytical speciation of mercury based on liquid chromatography separation.

3.1. Bismuth ion as internal standard

The aliquot of bismuth nitrate was added to the fresh tissue in order to compensate for possible imprecisions committed during the entire procedure. Bismuth was selected because of its similar affinity to sulfhydryl group as compared to mercury species [25–27]. In particular, it was anticipated that bismuth would match the behavior of inorganic mercury during extraction and HPLC separation. The concentration levels of Hg^{2+} in marine organisms are significantly lower than those of methylmercury and the majority of available reference materials are certified for total mercury and/or CH_3Hg^+, but not for Hg^{2+}. The use of Bi^{3+} should improve relatively poor reliability of the results for Hg^{2+} that had been observed in different studies and attributed to low concentrations, noncertified values and high uncertainties of the analytical results [8,9,11]. Furthermore, ^{209}Bi is one of the high mass IS recommended in the US EPA method 6020A and also in other applications [28]. With regard to the general requirements, ^{209}Bi is close to Hg isotopes in mass, however its ionization potential (7.3 eV) is lower than that for mercury (10.4 eV) [29]. Platinum had been proposed as the better match for mercury [28], but it was not used in this study, due to lower affinity of metal ion to thiols. Finally, it was experimentally verified that natural concentration levels of Bi in fish tissues were below the detection limit (<0.05 μg l^{-1} in the sample digest).

3.2. Liquid chromatography separation with ICP-MS detection

Several liquid chromatographic conditions have been reported for the separation of organic and inorganic mercury species [7–9,26,30–32]. In particular, Percy et al. studied separation of inorganic mercury and methylmercury considering their different coordination chemistry towards thiols [26]. Since in the present work L-cysteine is used for the extraction of Bi^{3+}, Hg^{2+} and CH_3Hg^+ from fish tissues, the mobile phase composition was adopted from the above study and the final conditions are given in Table 1. In Fig. 1, a chromatogram obtained under the finally selected conditions is presented. It can be observed that bismuth and inorganic mercury species presented almost identical chromatographic behavior, which confirms the formation of L-cysteine complexes and, hence the feasibility of Bi^{3+} as IS in HPLC–ICP-MS speciation of mercury. Total separation time (3 min) was comparable to the results reported by other authors [8,26]. The external calibration was

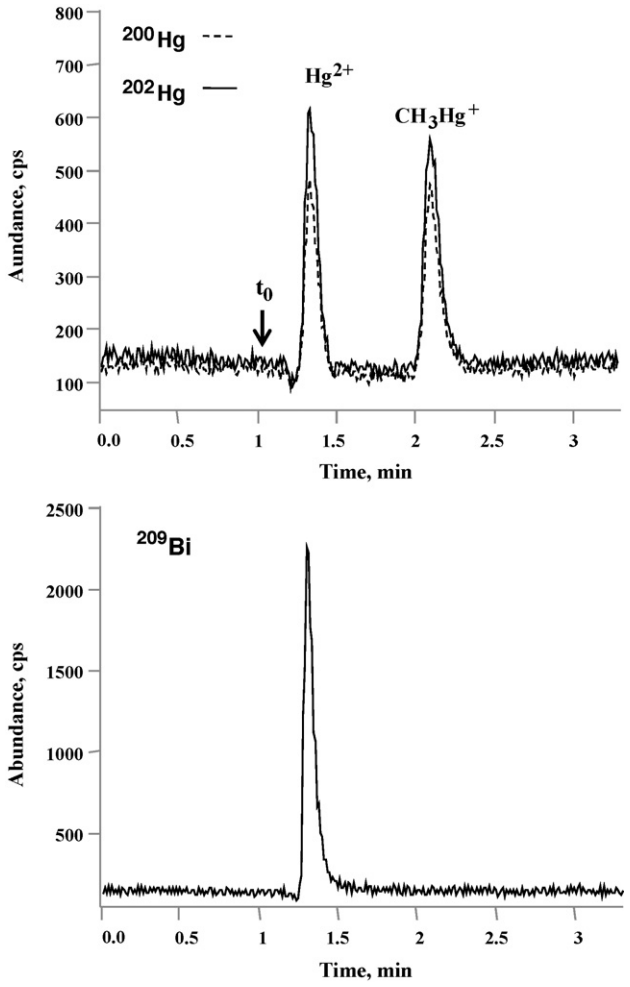

Fig. 1. High performance liquid chromatography–inductively coupled plasma mass spectrometry chromatogram of standard solution containing Hg^{2+}, CH_3Hg^+ (10 μg l^{-1} Hg) and Bi^{3+} (10 μg l^{-1} Bi).

accomplished and the analytical figures of merit for the two mercurial species are presented in Table 2. As can be observed, using the method of IS, better linearity, enhanced precision and slightly lower detection limits were obtained.

3.3. Extraction procedure

The experimental conditions proposed in this work for mercury extraction from fish tissues involve the use of perchloric acid,

Table 2
Analytical figures of merit evaluated for the speciation procedure proposed.

Parameter	Hg^{2+}		CH_3Hg^+	
	With IS	Without IS	With IS	Without IS
Retention time, min	1.31 ± 0.02		2.06 ± 0.03	
Retention factor	0.25		0.96	
Calibration range, μg l^{-1} Hg	0–50		0–50	
Signal mode	Peak area		Peak area	
Analytical signal	$^{202}Hg/^{209}Bi$	^{202}Hg	$^{202}Hg/^{209}Bi$	^{202}Hg
R^2	0.9986	0.9896	0.9999	0.9998
Std. error for slope, %	5.1	5.5	3.4	4.2
Std. error for intercept, %	7.0	7.8	5.8	7.7
DL, μg l^{-1}	0.8	0.9	0.7	0.9
CV, % (10 μg l^{-1} Hg, n = 5)	3.6	5.4	3.3	5.1
CV, % (50 μg l^{-1} Hg, n = 5)	2.8	5.9	3.0	4.8

DL: detection limit calculated as three standard deviations of the baseline noise versus calibration slope.

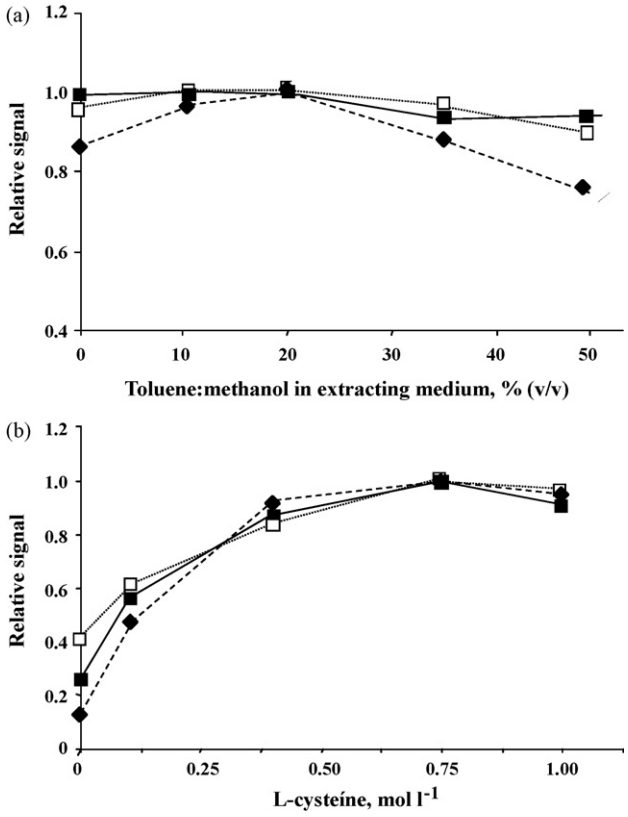

Fig. 2. Effect of toluene:methanol (1:1) percentage (a) and L-cysteine concentration (b) in the extracting medium on the relative analytical signals of inorganic mercury (–■–), methylmercury (–♦–) and bismuth (. . .□. . .), obtained by HPLC–ICP-MS. Chromatographic and detection conditions given in Section 2.

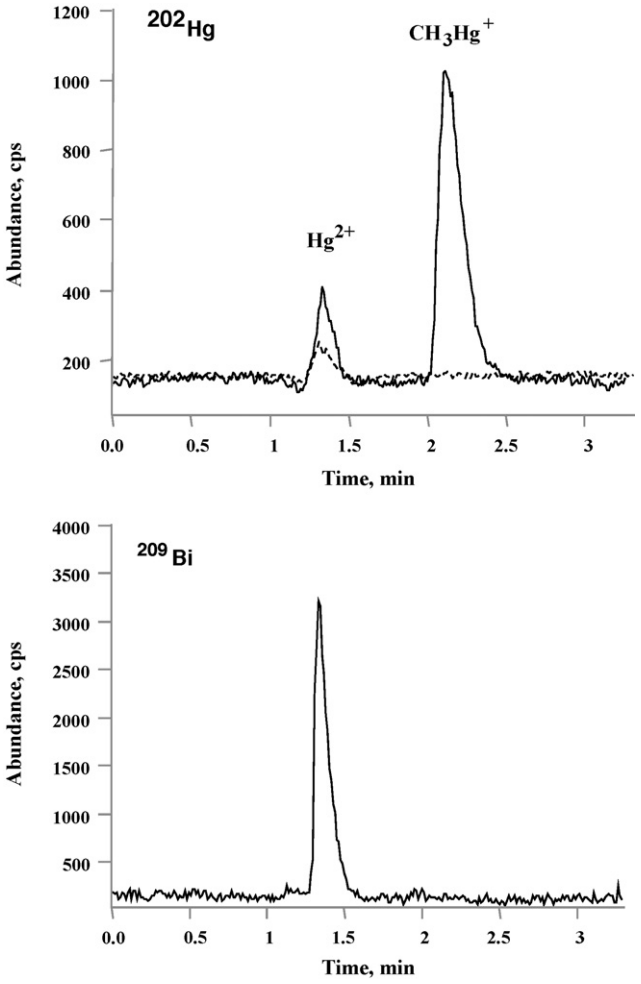

Fig. 3. HPLC–ICP-MS chromatogram of (┈) king mackerel tissue extract and (—) blank.

L-cysteine, toluene:methanol mixture, IS, homogenization/extraction aided by a high-speed blender and sonication. The original approach relies on the use of perchloric acid (final concentration 0.4 mol l^{-1}) for denaturation and precipitation of proteins [33]. The excess of acid was eliminated by precipitation of potassium perchlorate (addition of potassium hydroxide). Final pH 5 was adjusted with acetic acid and the precipitate was removed by centrifugation. On the other hand, the use of L-cysteine, toluene and methanol was adopted from earlier studies. In particular, toluene helped to destroy lipid structures potentially sequestering CH_3Hg^+ [10], L-cysteine was employed to form water-soluble complexes with Bi^{3+}, Hg^{2+} and CH_3Hg^+ [5,8,25,26]. The effects of L-cysteine concentration and toluene:methanol percentage were studied in fresh muscle tissue of king mackerel. In Fig. 2, relative analytical signals obtained for Hg^{2+}, CH_3Hg^+ and Bi^{3+} are presented as the function of percentage of toluene:methanol (1:1) in the extraction medium and molar concentration of L-cysteine. These results were obtained using final extraction, chromatographic and ICP-MS conditions, while changing one variable (see Section 2.4). It can be observed that the highest relative responses for the two mercury species and for bismuth were obtained for 0.75 mol l^{-1} L-cysteine and for 20% (v/v) of toluene:methanol in the extracting medium. Finally, it was experimentally verified that, blender parameters (time 0.5–2 min) and sonication time (40–80 min) had no significant effect on Hg^{2+} and CH_3Hg^+ results obtained in fresh tissue using IS method. A chromatogram of the respective tissue extract is presented in Fig. 3 together with a blank chromatogram. The retention times of Hg^{2+}, CH_3Hg^+ and Bi^{3+} corresponded to those obtained in the analysis of standard solution.

3.4. Analysis of fish tissues

The proposed procedure was evaluated using two types of fish tissue. In the first approach, total mercury was determined in fresh and dried samples, using the internal standard method, as described in Section 2. The results obtained for king mackerel muscle were 227.1 ± 9.3 μg kg^{-1} wm, 958.4 ± 35.4 μg kg^{-1} dm and those obtained for red snapper liver were 126.2 ± 10.8 μg kg^{-1} wm, 450.3 ± 30.9 μg kg^{-1} dm, respectively. The moisture content was 76.8 ± 0.4% in the muscle and 73.1 ± 0.5% in the liver material. Accordingly, no statistically significant differences were found between the results obtained in dried and fresh material (ANOVA, $p < 0.05$). Furthermore, these results were within the concentration range of total mercury reported in FDA monitoring program (1999–2004): 230–1670 μg kg^{-1} wm for king mackerel from Gulf of Mexico and from the levels below the detection limit up to 1366 μg kg^{-1} wm for snapper [34].

In further development, the speciation analysis in fresh tissues was carried out. For quantification, the peak area for ^{202}Hg (without IS), or the ratio between peak areas $^{202}Hg/^{209}Bi$ (with IS) were used. The results obtained by external calibration and by the method of standard addition are presented in Table 3. With the use of IS, a good agreement can be observed between the results obtained by external calibration and by the method of standard addition. If the IS had not been considered, the precision was clearly poorer (standard deviation values obtained for five sample replicates) and the

Table 3
Quantitative results obtained for mercury species in two different fish tissues, μg kg^{-1} wet mass (wm).

Internal standard	Hg^{2+}		CH_3Hg^+	
	Ext. calibration	Std. addition	Ext. calibration	Std. addition
King mackerel muscle, 227.1 ± 9.3 μg kg^{-1} wm				
With IS	28.4 ± 1.3	27.5 ± 2.2	178.9 ± 3.5	181.2 ± 4.7
Without IS	13.1 ± 2.5	26.8 ± 3.6	113.8 ± 4.3	176.6 ± 5.6
Red snapper liver, 126.2 ± 10.8 μg kg^{-1} wm				
With IS	35.7 ± 1.4	36.3 ± 2.6	75.7 ± 5.0	76.5 ± 5.5
Without IS	30.8 ± 2.6	35.9 ± 4.1	54.8 ± 6.2	77.2 ± 7.2

Table 4
Recovery results obtained in the analysis of the king mackerel muscle.

Species determined	Species concentration ± SD, μg kg^{-1} (n = 3)				Recovery, %	
	Species added		Found		With IS	Without IS
	Hg^{2+}	CH_3Hg^+	With IS	Without IS		
Hg^{2+}	0	0	27.5 ± 2.2	26.8 ± 3.6	–	–
	100	0	126.4 ± 6.7	100.6 ± 7.1	98.9	73.8
CH_3Hg^+	0	0	181.2 ± 4.7	176.6 ± 5.6	–	–
	0	200	382.4 ± 28.2	338.6 ± 33.1	100.6	81.0
Bi^{3+}	250	–	–	188.7 ± 12.1	–	75.5

results obtained by external calibration were significantly lower with respect to those from the method of standard addition. The procedure recovery was evaluated as a ratio between the sum of Hg^{2+} and CH_3Hg^+ concentrations obtained in speciation analysis (standard addition with IS) and total Hg determined by ICP-MS. The recovery values were 91.9% and 89.5% for king mackerel muscle and for red snapper liver, respectively. Speciation analysis was repeated using dried fish tissues and quantification of mercury species was accomplished by the method of standard addition with IS. The concentrations of Hg^{2+} and CH_3Hg^+ found in mackerel muscle were 133.9 ± 8.7 μg kg^{-1} dm and 703.7 ± 45.1 μg kg^{-1} dm and, in snapper liver 154.2 ± 11.2 μg kg^{-1} dm and 231.3 ± 16.0 μg kg^{-1} dm, respectively. Using dried material, the procedure recovery was 87.4% for muscle and 85.6% for liver. These results indicate that the extraction from fresh tissue was more efficient as compared to the dried material. The relative distribution of CH_3Hg^+ in the dried muscle was slightly lower with respect to the fresh tissue; 83.0% versus 86.8% (total Hg eluted from the column considered as 100%). Similar tendency was observed in the results obtained for snapper liver; methylmercury accounted for 60.0% while analyzing dried material and in the fresh tissue it accounted for 67.8% of Hg eluted from the column.

Table 5
Comparison of different extraction and HPLC–ICP-MS procedures for mercury speciation in fish tissues.

Analytical procedure		DL, μg l^{-1}(Hg)		Species recovery, %		Ref
Extraction	HPLC	CH_3Hg^+	Hg^{2+}	CH_3Hg^+	Hg^{2+}	
2-Mercaptoethanol in 2% MeOH, MW: 65 °C, 5 min	C18, 150 mm × 1 mm, 5 μm; 2-mercaptoethanol 0.2%, MeOH 2%, EDTA 1 mg/L, pH 2.8; separation time: 17 min	0.2	0.2	95 ± 5	96 ± 8	[7]
2-Mercaptoethanol 0.1%, KCl 0.15%, HCl 0.1%, shaking: room temp., 12 h	C18, 150 mm × 3.9 mm, 5 μm; 2-mercaptoethanol 0.1%, MeOH 5%, CH_3COONH_4 60 mM, pH 2.8; separation time: 13 min	0.2	0.2	Complete recovery of total Hg in reference materials		[16]
25% TMAH; MW: 40 W, 4 min; neutralization with CH_3COOH	C18, 150 mm × 3.2 mm, 3 μm; 2-mercaptoethanol 0.01%, MeOH:H_2O (1:1); sep. time: 4 min	0.5[a]	–	83–100	–	[9]
25% KOH or TMAH in MeOH, water bath 70 °C, 30 min, sonication 30 min, adjustment to pH 4	C18, 150 mm × 4.6 mm, 2 μm; 50 mM pyridine, 0.5% L-cysteine, 5% MeOH, pH 3; separation time: 4 min	0.78	0.46	99 ± 4	–	[8]
5 M HCl, 0.25 M NaCl MW: 60 °C, 10 min	C18, 150 mm × 4.6 mm, 2 μm; 50 mM pyridine, 0.5% L-cysteine, 5% MeOH, pH 3; separation time: 4 min	0.78	0.46	100%	–	[4]
5 M HCl; sonication: room temp., 30 min; cloud point extraction of DDTC mercurial chelates	C18, 150 mm × 4.6 mm, 5 μm; MeOH:acetonitrile:H_2O (35:40:25); separation time: 14 min	0.013	0.006	82–115% in water samples, in fish not reported		[11]
Procedure proposed in this study		0.7	0.8	100.6	98.9	

MW: microwave assisted extraction.
[a] Detection limit as μg/g (Hg).

The concentration and relative distribution of mercury species in different organs would depend on the environmental conditions, food regimes, age and size of the fish. In spite of important discrepancies among different studies, our results seem to be consistent with previous data reporting about 80% of CH_3Hg^+ with respect to total Hg in muscle [35] and relatively lower percentage of this species in liver than in muscle [36,37].

The spike recoveries for individual species were determined in fresh tissues enriched by adding the appropriate amount of Hg^{2+} or CH_3Hg^+ standard. Bismuth recovery was also examined. The results obtained are presented in Table 4. For quantification performed without IS, the recoveries of mercury species were 73.8% for Hg^{2+} and 81.0% for CH_3Hg^+, similar to the recovery value evaluated for internal standard (75.5%). However, taking the analytical signal as a ratio $^{202}Hg/^{209}Bi$, the recoveries for the two mercurial species were close to 100%. These results confirm the feasibility of Bi^{3+} as IS in the extraction and HPLC–ICP-MS determination of mercury species in fish tissues.

Finally, in Table 5 the proposed procedure is compared with respect to several methods reported previously. As can be observed, the chromatographic separation time, limits of detection and species recoveries obtained in this work are similar to those obtained under other extraction and separation conditions. The important advantage of the procedure devised in this study is non-rigorous protocol that can be applied directly to fresh fish tissues. In this protocol, only the amount of sample and of IS added must be accurately and precisely measured.

4. Conclusions

In this work, bismuth inorganic ion was proposed as internal standard for the quantification of Hg^{2+} and CH_3Hg^+ in fish. A high-speed blender and ultrasound-assisted homogenization/extraction was carried out in fresh tissues, in the presence of IS, perchloric acid, L-cysteine and toluene:methanol (1:1). Speciation analysis was performed by reversed phase liquid chromatography separation of respective L-cysteine complexes with on-line ICP-MS detection of Hg and Bi. Due to similar polarity and size of inorganic mercury and bismuth complexes both, their extraction and chromatographic behavior were almost identical, complying with the general requirements for IS. Furthermore, ICP-MS multielemental features enabled to quantify Hg and Bi co-eluting from the chromatographic column. Quite importantly, the recovery of the procedure was better while using fresh tissues than dried material. In summary, the feasibility of Bi^{3+} as IS relies on the compensation for incomplete extraction of mercury species and the enhanced precision of the results obtained using relatively non-rigorous protocol. The proposed procedure could be of interest for fast evaluation of mercury species in fish samples, providing data that can be directly compared to the values established by different governmental regulations (as Hg concentration in wet mass).

Acknowledgments

The financial support from CONACYT (Mexico), project 49405 and from CONCYTEG (Mexico), project 23681 is gratefully acknowledged.

References

[1] J. Burger, M. Gochfeld, Environ. Res. 99 (2005) 403.
[2] www.cfsan.fda.gov/~comm/haccp4.htlm, Fish and fisheries products hazards and controls guidance, U.S. Food and Drug Administration, Center for Food Safety and Applied Nutrition, 2001.
[3] T. Hasegawa, M. Asano, K. Takatani, H. Matsuura, T. Umemura, H. Haraguchi, Talanta 68 (2005) 465.
[4] L. Hinojosa Reyes, G.M. Rahman, G.M. Mizanur, H.M.S. Kingston, Anal. Chim. Acta 631 (2009) 121.
[5] P. Houserova, D. Matejicek, V. Kuban, J. Pavlickova, J. Komarek, J. Sep. Sci. 29 (2006) 248.
[6] Y. Li, X.-P. Yan, L.-M. Dong, S.-W. Wang, Y. Jiang, D.-Q. Jiang, J. Anal. Atom. Spectrom. 20 (2005) 467.
[7] L.F. Chang, S.J. Jiang, A.C. Sahayam, J. Chromatogr. A 1176 (2007) 143.
[8] L.H. Reyes, G.M. Mizanur Rahman, T. Fahrenholz, H.M. Skip Kingston, Anal. Bioanal. Chem. 390 (2008) 2123.
[9] D.S. Vidler, R.O. Jenkins, J.F. Hall, C.F. Harrington, Appl. Organomet. Chem. 21 (2007) 303.
[10] A.M. Carro, M.C. Mejuto, J. Chromatogr. A 882 (2000) 283.
[11] J. Chen, H. Chen, J. Xianzhong, C. Haiting, Talanta 77 (2009) 1381.
[12] A.I. Cabanero Ortiz, Y. Madrid Albarran, C. Camara Rica, J. Anal. Atom. Spectrom. 17 (2002) 1595.
[13] M.V. Balarama Krishna, D. Manjusha Rajint, D. Karunasagar, J. Arunachalam, Talanta 67 (2005) 70.
[14] A.V. Hirner, Anal. Bioanal. Chem. 385 (2006) 555.
[15] M. Leermakers, W. Baeyens, P. Quevauviller, M. Horvat, Trends Anal. Chem. 24 (2005) 383.
[16] M. Wang, W. Feng, J. Shi, F. Zhang, B. Wang, M. Zhu, B. Li, Y. Zhao, Z. Chai, Talanta 71 (2007) 2034.
[17] D. Yan, L. Yang, Q. Wang, Anal. Chem. 80 (2008) 6104.
[18] A. Prieto, O. Zuloaga, A. Usobiaga, N. Etxebarria, L.A. Fernandez, C. Marcic, A. de Diego, J. Chromatogr. A 1185 (2008) 130.
[19] R. Garcia Fernandez, M. Montes Bayon, J.I. Garcia Alonso, A. Sanz-Medel, J. Mass Spectrom. 35 (2000) 639.
[20] M. Monperrus, E. Tessier, S. Veschambre, D. Amouroux, O. Donard, Anal. Bioanal. Chem. 381 (2005) 854.
[21] E. Bjoern, T. Larsson, L. Lambertsson, U. Skyllberg, W. Frech, Ambio 36 (2007) 443.
[22] K. Inagaki, T. Kuroiwa, T. Narukawa, T. Yarita, A. Takatsu, K. Okamoto, K. Chiba, Anal. Bioanal. Chem. 391 (2008) 2047.
[23] G.M. Rahman Miznaur, T. Fahrenholz, H.M.S. Kingston, J. Anal. Atom. Spectrom. 24 (2009) 83.
[24] R. Clough, S.T. Belt, E.H. Evans, B. Fairman, T. Catterick, J. Anal. Atom. Spectrom. 18 (2003) 1039.
[25] D. Chaleil, F. Lefevre, P. Allain, G.J. Martin, J. Inorg. Biochem. 15 (1981) 213.
[26] A.J. Percy, M. Korbas, G.N. George, J. Gailer, J. Chromatogr. A 1156 (2007) 331.
[27] E.M. Krupp, B.F. Milne, A. Mestrot, A.A. Meharg, J. Feldmann, Anal. Bioanal. Chem. 390 (2008) 1753.
[28] S.M. Wilbur, E. Soffey, Agilent ICP-MS J. 17 (2003) 2.
[29] J.J. Thompson, R.S. Houk, Appl. Spectrosc. 41 (1987) 801.
[30] R. Rai, W. Maher, F. Kirkowa, J. Anal. Atom. Spectrom. 12 (2002) 1560.
[31] S.C. Hight, J. Cheng, Anal. Chim. Acta 567 (2006) 160.
[32] B. Vallant, R. Kadnar, W. Goessler, J. Anal. Atom. Spectrom. 22 (2007) 322.
[33] K. Wrobel, K. Wrobel, J.A. Caruso, J. Anal. Atom. Spectrom. 17 (2002) 1048.
[34] www.cfsan.fda.gov/~frf/seamehg2.html (consulted 20.02.09).
[35] R. Maury-Brachet, G. Durrieu, D. Yannick, A. Boudou, Sci. Tot. Environ. 368 (2006) 262.
[36] A.P. Baeta, H.A. Kehring, O. Malm, I. Moreira, WIT Trans. Biomed. Health 10 (2006) 183.
[37] P. Marsalek, Z. Svobodova, T. Randak, J. Svehla, Acta Vet. BRNO 74 (2005) 427.

Talanta 79 (2009) 796–803

Contents lists available at ScienceDirect

Talanta

journal homepage: www.elsevier.com/locate/talanta

Validation of an environmental friendly segmented flow method for the determination of phenol index in waters as alternative to the conventional one

Ana R. Sousa*, Maria A. Trancoso

LAACQ (Laboratório de Análises Ambientais e Controlo de Qualidade), INETI, Estrada do Paço do Lumiar, Edif. E, 1° Andar, 1649-038 Lisbon, Portugal

ARTICLE INFO

Article history:
Received 28 November 2008
Received in revised form 29 April 2009
Accepted 5 May 2009
Available online 19 May 2009

Keywords:
Environmental preservation
Segmented flow analysis (SFA)
Phenol index
Water analysis
Validation/quality assurance

ABSTRACT

Phenolic compounds are a sort of common pollutants in water. Phenol index becomes an expedite indicator for the evaluation of the contamination level of water samples, in spite of the knowledge of the individual phenol and its derivatives are also important.

In this work, an environmental friendly method for the determination of phenols, using a segmented flow system based on the conventional method's reactions without the liquid–liquid extraction step, was validated.

Three linear dynamic ranges using C_6H_5OH: 1–10 $\mu g\,l^{-1}$, 10–200 $\mu g\,l^{-1}$ and 0.2–2.5 $mg\,l^{-1}$, with a coefficient of variation lower than 2%, were obtained. Several method's performance parameters were determined: limits of detection, limits of quantification, precision through duplicate analysis and trueness using the reference materials purchased from LGC Promochem, RTC no. QCI-043-2 Lot:P1. Measurement uncertainty was evaluated using an interlaboratory approach based on proficiency testing data. Relative combined uncertainty for phenols in water samples, $u_c^{rel}(\gamma_{sample})$, of 0.054 were obtained, in according to those imposed by the Portuguese Legislation: target $u_c^{rel}(\gamma_{sample}) = 0.58$ for 1 $\mu g\,l^{-1}$ of phenol (surface waters) and target $u_c^{rel}(\gamma_{sample}) = 0.06$ for 500 $\mu g\,l^{-1}$ of phenol (wastewaters).

A high efficiency reduction and elimination of reagents and wastes, reduction of analysis time and exposition of the analyst were also obtained.

1. Introduction

Phenolic compounds are organic pollutants, which occur frequently in natural and wastewaters. They can have industrial origin from different activities such as production of synthetic plastics, paints, drugs, polymers, pesticides, detergents, deodorants, paper and cellulose [1,2]. These compounds appear in a list of dangerous substances of the Environmental Protection Agency (EPA) due to their toxicity, bioaccumulation, persistency in the environment and carcinogenic properties [3]. They affect taste and the odour of drinking water and fish. Numerous phenolic compounds show toxic effects in animals and plants since they easily penetrate into skin and cellular membrane [1].

Several analytical procedures have been proposed for detection of individual phenolic compounds either chromatographic methods or spectrophotometric ones [4,5]. Although the knowledge of individual phenolic compounds is very important, the fast and simple attainment of the results obtained are equally important in the environmental monitoring point of view. Therefore, analytical methods that give direct information about the total phenol compound contents are very suitable once that reduction of time and costs occurs.

The reference method for the determination of phenols stipulated by the Portuguese Legislation (DL no. 236/98) [6] is based on the reaction between phenols and 4-aminoantipyrine to form antipyrine dyes. This methodology involves a distillation step followed by a liquid–liquid extraction using enormous quantities of sulfuric acid and chloroform with a great environmental impact. On the other hand it is a time-consuming procedure, requires high manual labour and a lot of laboratory glassware.

The development of flow techniques capable of being implemented in routine laboratories has brought a new element to the analytical chemistry, allowing the measurements to be carried out faster, reducing both analysis time and consumption of reagents, production of less wastes and minimum intervention of the analyst, constituting an advantageous alternative to the traditional method.

Segmented flow analysis was one of the first techniques widely imposed in the laboratories requiring a large volume of analysis. Samples are sequentially aspirated and, between them, air bubbles are located which separate the flow established, including also a

* Corresponding author. Tel.: +351 21 0924755; fax: +351 21 7162641.
E-mail address: rita.sousa@ineti.pt (A.R. Sousa).

0039-9140/$ – see front matter © 2009 Elsevier B.V. All rights reserved.
doi:10.1016/j.talanta.2009.05.009

washing cycle. The air bubbles are eliminated before reaching the detector flow cell.

In this work, a validation and quality assurance program was developed for implementation of a segmented flow system used to determine phenols, as alternative to the conventional method, fulfilling the requirements of the DL no. 236/98 for natural and wastewaters. This program includes the control of: (i) the calibration function characteristics namely test of the variances homogeneity, for the working range boundaries, and Mandel's test, for linearity; (ii) limit of detection (LOD) and limit of quantification (LOQ); (iii) stability of calibration functions; (iv) interferences; (v) precision through duplicate analysis; (vi) trueness using reference materials. The uncertainty measurement was estimated using an interlaboratory approach.

The procedure was based on the oxidative coupling of phenols with 4-aminoantipyrine (4-AAP) in alkaline medium as described by Eq. (1) [2]. Notice that phenol, *ortho*-, *meta*- and *para*-substituted phenols could be detected under proper pH conditions, but *para*-substituted by aryl, alkyl, nitro, benzoyl compounds do not react efficiently or do not react at all with 4-AAP [2]. The products of the reaction are generally red compounds having absorbance of 505 nm [7,8]:

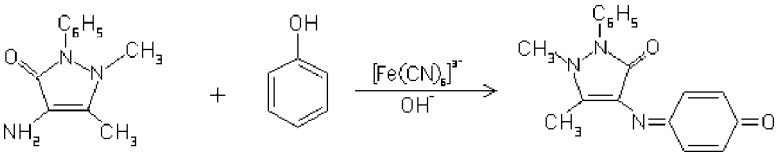

(1)

When reporting phenols content using C_6H_5OH for calibration, the results represent the minimum amount of phenolic compounds in the real sample. For that, in this work we decided to use the term phenol index in spite of phenols.

2. Experimental

2.1. Reagents and solutions

All chemicals were of analytical-reagent grade and obtained from Merck, Darmstadt, Germany, unless stated otherwise. All solutions were prepared with grade-II water [9] obtained from a Millipore Milli-Q system (Millipore, Bedford, MA). All solutions were stored in glass bottle. All reagents were stored in plastic or glass bottles washed with water several times.

A stock 1.0 g l^{-1} phenol calibration standard solution (CS), was prepared by dissolving 0.201 g of C_6H_5OH (purity: 99.75% (w/w)) in water using a 200 ml volumetric flask [7]. A stock 1.0 g l^{-1} phenol quality control standard solution (QCS) was prepared, as described for CS, but using phenol reagent from an independent lot. Both solutions were stored at 2–6 °C in the absence of light.

Either calibration standard solutions (CSS) or quality control standard solutions (QCS) were prepared through successive dilution from CS and QC solutions, respectively.

The 4-aminoantipyrine (4-AAP) solution was prepared by dissolution of 0.065 g of 4-aminoantipyrine and 0.5 ml of Brij 35 (30% (v/v)), supplied by SKALAR Analytical B.V., Breda, Netherlands, in 100 ml of water. This solution (colour reagent solution) was daily prepared.

A 1.5 mol l^{-1} phosphoric acid solution was prepared by dilution of 10 ml of H_3PO_4 (85% (v/v)) into a 100 ml volumetric flask, in water (distillation reagent solution).

The oxidizing reagent solution prepared by dissolving a 0.20 g amount of potassium hexacyanoferrate (III), 0.30 g of boric acid and 0.50 g of potassium chloride in around 50 ml of water. The pH of this solution was adjusted to 10.3 ± 0.2 by addition of a 1 mol l^{-1} KOH solution and then transferred to a 100 ml volumetric flask and diluted with water. This solution was daily prepared.

Buffer solutions were used with pH of 4.01 ± 0.02, 7.00 ± 0.02 and 10.00 ± 0.05.

A 100 g l^{-1} copper (II) sulphate solution was prepared by dissolution of 156.44 g of $CuSO_4{\cdot}5H_2O$ in water. The solution was transferred to a 1000 ml volumetric flask and diluted to volume with water. This solution was used to preserve samples that could not be analyzed within 4 h of collection (1 ml of 100 g l^{-1} copper (II) sulphate solution per 100 ml of sample).

Aqueous individual solutions, to be used on the ruggedness tests, of 1 g l^{-1} sodium dichloroisocyanurate (0.32 g l^{-1} in chloride), 1.2 g l^{-1} sodium sulphite solution (1 g l^{-1} in SO_3^{2-}), 2.2 g l^{-1} sodium sulphide solution (0.91 g l^{-1} in S^{2-}), 5.4 g l^{-1} a sulphanilamide (1 g l^{-1} in NH_2^-), 2.4 g l^{-1} of oil and grease and 1.0 g l^{-1} of a purified humic acid (Sigma–Aldrich, Steinheim, Germany) were prepared. Notice that the oil and grease solution was prepared weighting two drops of a mixture, in volume, containing 37.5% of *n*-hexadecane, 37.5% of isooctane and 25.0% of benzene and diluted to 50 ml with water [10].

Solutions containing approximately 1 mg l^{-1} of phenol, *o*-cresol, *m*-cresol, *p*-cresol, 2,6-dimethylphenol, 4-*tert*-butylphenol, *m*-chlorophenol, 2,4-dichlorophenol, 2,6-dichlorophenol, 2,4,6-trichlorophenol and pentachlorophenol were employed for evaluation of the relative response of the method to different phenols.

2.2. Apparatus

A Model/type SAN Plus SA 5000 segmented flow system from SKALAR Analytical B.V., Breda, Netherlands, was used. This system was composed by an autosampler Model/type SA 1052 for 120 samples, chemistry unit with pump rising valves and chemistry modules, a photometer detector Model/type SA 6250, a personal computer which can control the sampler by a interface Model/type SA 8502 and a software program for data acquisition and instrumental control, *FlowAccess*®. All tubing was made of PTFE (polytetrafluoroethylene). In Fig. 1 shows the segmented flow injection manifold used [7,11].

An Orion model 420 A (Orion Research, Inc., USA) pH meter with an Orion combined electrode calibrated with buffer solutions was used to carry out the pH measurements.

All weights were done using a calibrated Mettler Toledo AT 200 analytical balance, with 200 mg capacity and 0.1 mg readability.

2.3. Reference materials

Reference materials were purchased from LGC Promochem, RTC no. QCI-043-2 Lot:P1 (Middlesex, UK) with a phenol concentration of 5.01 ± 1.51 mg l^{-1} in water.

2.4. Sample pre-treatment: preservation of phenol compounds

Phenolic compounds in water are subject to both biochemical and chemical oxidation. Therefore, unless the samples are analyzed in a period of 4 h after collection, there must be preserved as soon as collected using the following procedure: (i) samples are filtered to avoid the risk of transport tubes clogging; (ii) the filtered samples are acidified at pH < 2 with a 1.5 mol l^{-1} of phosphoric acid solution and (iii) 1 ml of 100 g l^{-1} $CuSO_4$ solution was added to each 100 ml

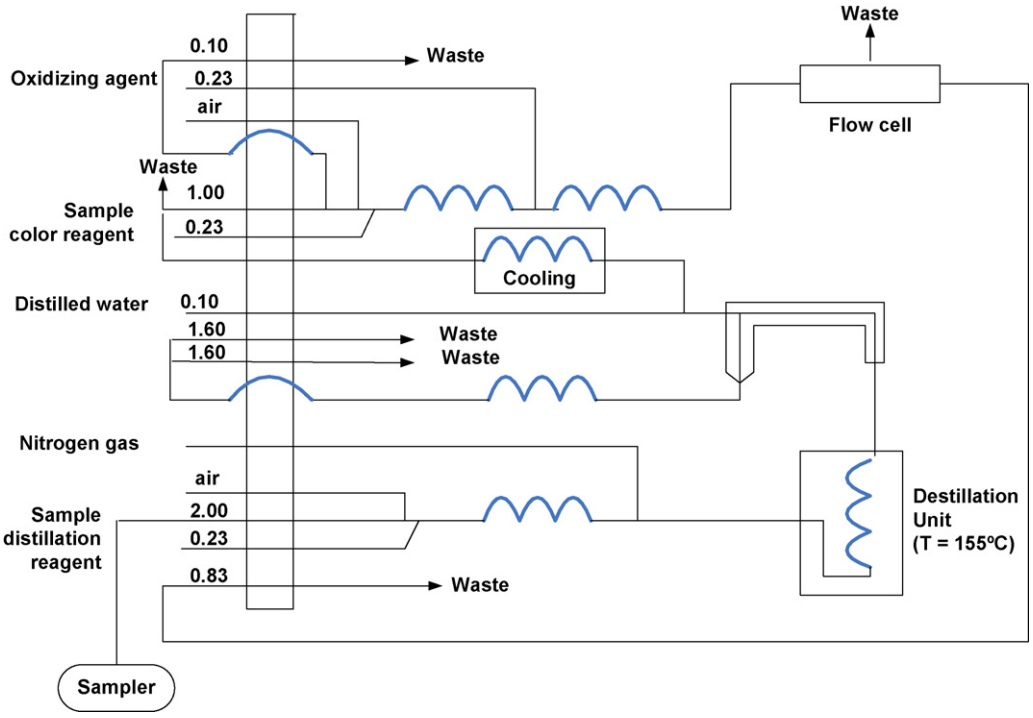

Fig. 1. Segmented flow injection manifold adapted from [7].

of sample. The samples are then stored in plastic flasks, in the dark and in a refrigerator at a temperature 2–6 °C of until 1 month.

2.5. Instrumental conditions and working sequence

Before to switch the equipment the waste facilities available were checked, the pump deck were greased, the tubes to the autosampler system were connected in according to the calibration curve selected. After that, all pump decks were closed and the phenol cell was placed inside the photometer. Switch on the equipment following the sequence: chemistry unit, computer waiting until the desktop is displayed, interface, the pump in standby position, the autosampler and nitrogen gas supply (0.9–1.0 bar). After this the reactor control unit (temperature of 155 °C) and photometers (phenol filter wavelength (λ) of 505 nm and a correction filter with λ = 720 nm) were switched on. After system stabilization (around 30 min) flowing water, all the operational conditions (e.g. selecting the working range, standards, QC, samples, washing times) used to the determination of phenol index were set in the software system (*FlowAccess*®). The sample was fed into a stream, mixed with the distillation reagent solution and distilled at 155 °C, inline, with a pH < 2. This distillation step reduces, significantly, the interferences. The distillate, containing steam volatile phenolic compounds, was mixed with segmented flowing solutions either colour reagent and oxidizing reagent solution. Phenolic compounds in the distillate were oxidized by hexacyanoferrate (III) and combined with 4-aminoantipyrine forming a yellow condensation product, which absorbs at 505 nm [8].

2.6. Ruggedness test

The ruggedness of the proposed method has been evaluated using a Youden Ruggedness test, to either small-uncontrolled fluctuations or the presence of some species with no interfering effect, following the procedure presented by Feinberg and Ducauze [12]. The Youden test is based on the realization of a number of tests in the same sample matrix, in the presence of several possible interference species. In the experiments, two levels were considered for each factor, symbolized by + and −. The first level, + sign, means the presence of the species represented by the factors A–E and the − sign means the opposite.

Six experimental factors (A) 0.32 mg l^{-1} of chloride, (B) 1 mg l^{-1} of sulphite, (C) 0.91 mg l^{-1} of sulphide, (D) 1 mg l^{-1} of amines, (E) 12 mg l^{-1} of oils and grease and (F) 1 mg l^{-1} of humic acid were selected.

This statistic method was applied for spiking tap water and natural waters, both with a spiked phenol concentration at 2 μg l^{-1} and 20 μg l^{-1}. Eight solutions which constituted eight different combinations for the six factors were prepared and analyzed for each sample matrix and two replicate measurements were performed for each solution. The recovery was then calculated for each analysis.

The variance of each factor (i) was given by Eq. (2):

$$\sigma_i^2 = \left(\frac{2}{N}\right)[T^2(X_{i+}) + T^2(X_{i-})] - \left(\frac{T^2(X)}{N}\right) \quad (2)$$

where i takes the values 1 to p, being p the number of factors ($p = 6$, in this work) and test values, $T(X_{i+})$ and $T(X_{i-})$, are the sum of the results obtained at the levels + and −, respectively, for the factor i. The sum embraced n combinations (eight experiments) and r repetitions (two replicate measurements in this work) and $N = rm$ ($N = 16$). The ratio $F_i = \sigma_i^2/\sigma_R^2$ was compared with $F_{(1,(N-p-1),0.95)}$ from the literature [12]. The residual variance, σ_R^2, was determined by the following equation:

$$\sigma_R^2 = \frac{(N-1)\sigma_T^2 - \sum_{i=1}^{p}\sigma_i^2}{(N-p-1)} \quad (3)$$

The total variance, σ_T^2, was calculated by Eq. (4), in witch x_i represents each recovery [12]:

$$\sigma_T^2 = \left[\sum_{i=1}^{n} x_i^2 - \frac{T^2(X)}{N}\right](N-1) \quad (4)$$

Table 1
Characteristics of calibration functions.

$[C_6H_5OH]$ ($\mu g\,l^{-1}$)	$y=(a\pm s_a)+(b\pm s_b)x$	r	TV	PG	LOD ($\mu g\,l^{-1}$)	V_{x_0}
1–10	$y=(-1.7\pm0.3)+(3.19\pm0.04)x$	0.9993	2.7	−3.8	0.6	0.02
10–200	$y=(-0.8\pm2.0)+(3.30\pm0.02)x$	0.9998	5.1	−6.4	2	0.01
$(0.2–2.5)\times10^3$	$y=(45\pm48)+(3.16\pm0.03)x$	0.9995	5.0	8.3	65	0.02

y, peak height; a, intercept; s_a, standard deviation of the intercept; b, slope; s_b, standard deviation of the slope; x, concentration of phenol ($\mu g\,l^{-1}$); r, correlation coefficient; TV, testing value for homogeneity of variances [14]; PG, testing value for linearity evaluation (Eq. (6)); LOD, limit of detection (Eq. (7)); V_{x_0}, coefficient of variation [16].

3. Results and discussion

The performance criteria included on the validation program applied to determination of phenol index in waters and wastewaters samples using a segmented flow system were working range and linearity, limit of detection (LOD) and limit of quantification (LOQ), specificity, precision and trueness. Measurement uncertainty of the results was estimated based on accuracy concept [13]. The measurand is the mass concentration of phenols ($\mu g\,l^{-1}$) that react with the 4-AAP. In this work, the phenol index, in waters and wastewater samples, expressed in C_6H_5OH, was calculated by Eq. (5):

$$\gamma_{sample} = \gamma_{cal}.F_{dil} \quad (5)$$

where γ_{cal} ($mg\,l^{-1}$) is the mass concentration of C_6H_5OH measured and F_{dil} the ratio dilution of the samples.

3.1. Calibration functions

In order to warrant the homogeneity of variances required by the least square regression and fulfilling the DL no. 236/98 [6] three working ranges have been selected (Table 1). Admissible maximum values (AMV), in according to Attach I and XVIII of the DL no. 236/98 [6], for surface water and wastewaters to discharge in the environment, are 1 and 500 $\mu g\,l^{-1}$, respectively. In Table 1 the regression equations and characteristics of the calibration functions are shown. The homogeneity of variances was verified by F-test [14,15]. In all situations no significant difference between the variances were obtained since the testing values (TV) are lower than the critical value of F ($F_{9;9;0.99}=5.35$). The linearity was evaluated by Mandel's test [15]. As can be seen from Table 1, the linear functions provide the best fittings since test values PG given by Eq. (6) were lower than critical F values ($F_{1;7;0.99}=12.25$):

$$PG = \frac{(N-2)s_{y_1}^2 - (N-3)s_{y_2}^2}{s_{y_2}^2} \quad \text{with the degree of freedom } f = 1 \quad (6)$$

where s_{y_1} and s_{y_2} are the residual standard deviation of the linear and second order calibration function, respectively, and N is the number of points. High precision was also obtained since the coefficient of variation, V_{x_0} of the regression lines were lower than 0.03 [16].

The limit of detection (LOD) was calculated in according to IUPAC recommendations [17] using the s_{y_1} value for estimation of the blank standard deviation and the intercept of calibration line in spite of the blank peak height value, as recommended by Miller and Miller [18]. In this conditions the LOD values for phenol concentrations are given by Eq. (7), where b is the slope of the calibration lines and considering $K=3$. As can be seen from Table 1, the proposed method discriminates phenol compounds with levels higher than 0.6 $\mu g\,l^{-1}$ (LOD), fulfilling the LOD values required by DL no. 236/98 for surface waters (LOD = 1 $\mu g\,l^{-1}$) and wastewaters discharged on the environment (LOD = 500 $\mu g\,l^{-1}$) [6]:

$$LOD = \frac{K \times s_{y_1}}{b} \quad (7)$$

Table 2
Phenol recoveries ($\bar{R}_m$) for several phenols using the proposed method and literature values.

Compound	$\bar{R}_m \pm s$	
	Presented method	Literature [2,5]
Phenol	1.0 ± 0.01	1.00
o-Cresol	0.62 ± 0.02	0.84–0.85
m-Cresol	0.57 ± 0.01	0.70–0.86
p-Cresol	0	0–0.03
2,6-Dimethylphenol	0.14 ± 0.01	0.56–0.66
4-*tert*-Butylphenol	0	n.a.
m-Chlorophenol	0.46 ± 0.01	n.a.
2,4-Dichlorophenol	0.15 ± 0.02	n.a.
2,6-Dichlorophenol	0.24 ± 0.03	n.a.
2,4,6-Trichlorophenol	0	n.a.
Pentachlorophenol	0	n.a.

s, standard deviation; n.a., not available.

In routine analysis, a quality control program was implemented in order to warrant the performance of the calibration functions. After stabilization (around 15–30 min) the contaminations were evaluated using the blank reagent (wash) that corresponds to the instrumental zero. The analysis can be started when the wash value is inside the interval 500 ± 20 D.U. The sensibility was monitoring with the tracer (the highest concentration standard solution), that must be lower than 10%. The intercept value of the calibration curve should be inside the interval 0 ± 3 D.U. in according to the warning limits of individual control charts, except for the highest linear range [19]. Although correlation coefficient, r, does not prove linearity in routine, $r\geq0.999$ was used as an indicator of linearity (Table 1).

3.2. Interferences evaluation

Table 2 shows the recoveries of some phenol compounds, commonly present in waters, and compare them with others previously reported. Phenol compounds with *para*-substituted groups (*p*-cresol, 4-*tert*-butylphenol, 2,4,6-trichlorophenol and pentachlorophenol) do not react with 4-AAP [2,4,5]. Phenol recoveries lower than 1.0 was obtained, with exception for C_6H_5OH, in agreement with the literature [2,5].

Although the methods for determination of phenols based on the oxidative coupling with 4-AAP gives lower concentration of phenols, the knowledge of a phenol index in water is very important when monitoring pollutants in environment [2].

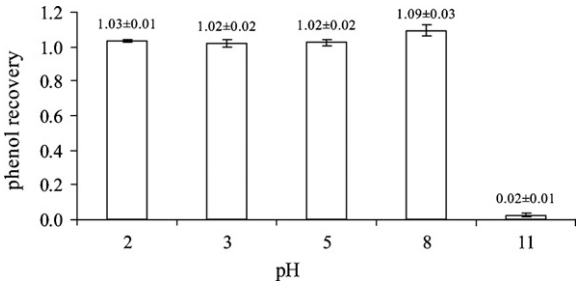

Fig. 2. Influence of samples initial pH on the phenol recovery.

Table 3
Ruggedness tests for interferences evaluation of Cl^-, SO_3^{2-}, S^{2-}, NH_2^- oils and grease and humic acid using recoveries of samples fortified with 2 μg l^{-1} of C_6H_5OH.

	Experiment								σ_i^2	$F_i = \sigma_i^2/\sigma_R^2$
	1	2	3	4	5	6	7	8		
Spiked tap water										
Factor										
A	+	+	+	+	–	–	–	–	3.20	1.60
B	+	+	–	–	+	+	–	–	5.63	2.81
C	+	–	+	–	+	–	+	–	2.38	1.19
D	+	+	–	–	–	–	+	+	8.12	4.05
E	+	–	+	–	–	+	–	+	1.41	0.70
F	+	–	–	+	+	–	–	+	2.83	1.41
Phenol recovery results (replicate measurements)										
1	1.51	1.09	2.34	5.47	1.68	1.86	1.44	1.62		
2	1.48	1.07	2.32	5.47	1.67	2.05	1.63	1.61		
Sum	2.99	2.16	4.65	10.94	3.36	3.91	3.08	3.24	$\sigma_T^2 = 1.81$	$F_{(1,9,0.95)} = 5.12$
Spiked surface water										
Factor										
A	+	+	+	+	–	–	–	–	0.70	0.68
B	+	+	–	–	+	+	–	–	0.69	0.67
C	+	–	+	–	+	–	+	–	2.90	2.81
D	+	+	–	–	–	–	+	+	1.67	1.62
E	+	–	+	–	–	+	–	+	4.27	4.12
F	+	–	–	+	+	–	–	+	2.68	2.59
Phenol recovery results (replicate measurements)										
1	1.74	1.29	4.14	0.81	1.55	1.93	1.52	1.50		
2	1.72	1.28	4.33	1.00	1.54	1.92	1.51	1.49		
Sum	3.46	2.57	8.46	1.81	3.09	3.85	3.02	2.99	$\sigma_T^2 = 0.97$	$F_{(1,9,0.95)} = 5.12$

A, Cl^-; B, SO_3^{2-}; C, S^{2-}; D, NH_2^-; E, oils and grease; F, humic acid; sign (+), presence of interfering compound; sign (–), absence of interfering compound; σ_i^2, variance of each factor (Eq. (2)); σ_R^2, residual variance (Eq. (3)); σ_T^2, total variance (Eq. (4)); $F_{(f_1,f_2,1-\alpha)}$, tabled value of the *F*-distribution (Fisher–Snedecor) with f_1 and f_2 degrees of freedom and a confidence level of $(1-\alpha)$.

Table 4
Ruggedness tests for interferences evaluation of Cl^-, SO_3^{2-}, S^{2-}, NH_2^-, oils and grease and humic acid using recoveries of samples fortified with 20 μg l^{-1} of C_6H_5OH.

	Experiment								σ_i^2	$F_i = \sigma_i^2/\sigma_R^2$
	1	2	3	4	5	6	7	8		
Spiked tap water										
Factor										
A	+	+	+	+	–	–	–	–	0.01	0.04
B	+	+	–	–	+	+	–	–	0.12	0.43
C	+	–	+	–	+	–	+	–	0.78	2.86
D	+	+	–	–	–	–	+	+	0.58	2.12
E	+	–	+	–	–	+	–	+	1.16	4.24
F	+	–	–	+	+	–	–	+	0.69	2.50
Phenol recovery results (replicate measurements)										
1	1.08	0.83	2.35	0.64	1.21	1.37	1.07	1.10		
2	1.08	0.86	2.41	0.66	1.20	1.39	1.08	1.08		
Sum	2.16	1.69	4.76	1.30	1.41	2.76	2.15	2.18	$\sigma_T^2 = 0.25$	$F_{(1,9,0.95)} = 5.12$
Spiked surface water										
Factor										
A	+	+	+	+	–	–	–	–	1.47	1.25
B	+	+	–	–	+	+	–	–	1.60	1.36
C	+	–	+	–	+	–	+	–	2.02	1.72
D	+	+	–	–	–	–	+	+	2.29	1.95
E	+	–	+	–	–	+	–	+	2.44	2.07
F	+	–	–	+	+	–	–	+	3.96	3.37
Phenol recovery results (replicate measurements)										
1	0.99	1.21	4.09	0.88	1.07	1.43	1.22	1.02		
2	0.97	1.20	4.09	0.88	1.07	1.40	1.22	1.02		
Sum	1.96	2.42	8.18	1.75	2.15	2.83	2.44	2.04	$\sigma_T^2 = 1.06$	$F_{(1,9,0.95)} = 5.12$

A, Cl^-; B, SO_3^{2-}; C, S^{2-}; D, NH_2^-; E, oils and grease; F, humic acid; sign (+), presence of interfering compound; sign (–) absence of interfering compound; σ_i^2, variance of each factor (Eq. (2)); σ_R^2, residual variance (Eq. (3)); σ_T^2, total variance (Eq. (4)); $F_{(f_1,f_2,1-\alpha)}$, tabled value of the *F*-distribution (Fisher–Snedecor) with f_1 and f_2 degrees of freedom and a confidence level of $(1-\alpha)$.

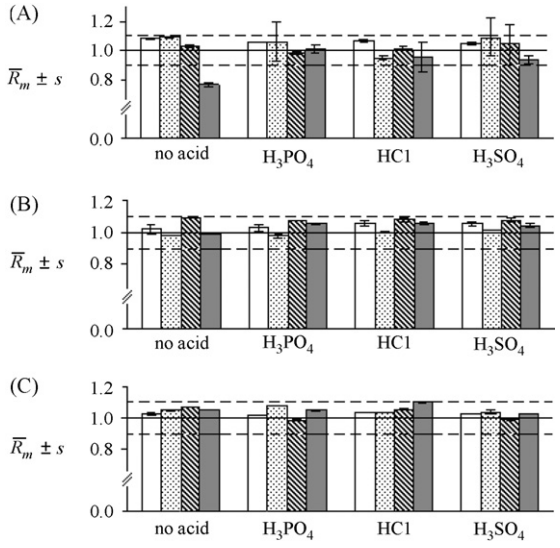

Fig. 3. Influence of different acids used in sample preservation; *s*, standard deviation. □ Blank; ⬚ tap water; ▨ surface water; ■ wastewater. (A) Water samples fortified with 2 μg l^{-1} of C_6H_5OH; (B) water samples fortified with 20 μg l^{-1} of C_6H_5OH; (C) water samples fortified with 1000 μg l^{-1} of C_6H_5OH.

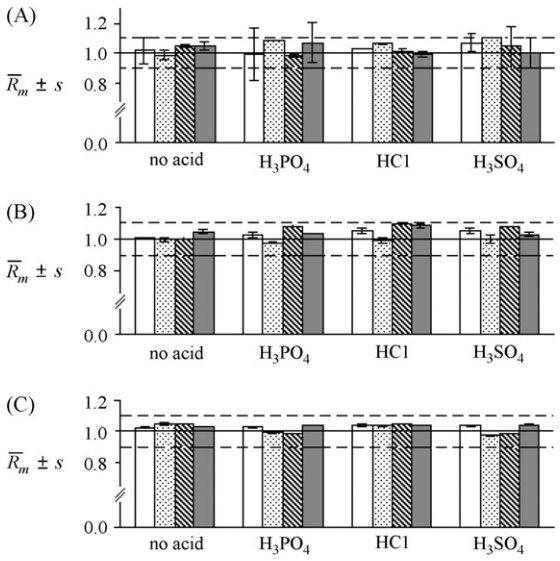

Fig. 4. Influence of $CuSO_4$ used in sample preservation; *s*, standard deviation. □ Blank; ⬚ tap water; ▨ surface water; ■ wastewater. (A) Water samples fortified with 2 μg l^{-1} of C_6H_5OH; (B) water samples fortified with 20 μg l^{-1} of C_6H_5OH; (C) water samples fortified with 1000 μg l^{-1} of C_6H_5OH.

The distillation step, used to isolate phenol, was carried out on acid pH. Recoveries of 1 mg l^{-1} C_6H_5OH standard solutions at pH from 2 to 11 were assessed since the water sample can have different origins. As can be seen in Fig. 2, recoveries close to 1.0 ± 0.1 were obtained whenever pH ≤ 8. Therefore, the initial pH of samples has to be lower than 8. The acidification needed to preserve the phenol compounds did not influence the phenol recovery. It is possible to use different acids: H_3PO_4 [20], HCl [7] and H_2SO_4 [7,10].

Fig. 3 shows the phenol recoveries, $\bar{R}_m$, obtained from tap water, surface water and wastewater spiked with 2, 20 and 1000 μg l^{-1} of C_6H_5OH and preserved with above reported acids. $\bar{R}_m$ values are close to 1.0 ± 0.1 showing that the mentioned acids could be used.

The ISO 6439:1990 [20] indicates that copper (II) sulphate addition inhibits the biological degradation. This reagent eliminates the compound interferences that may originate H_2S in acid solutions [20]. In Fig. 4 phenol recoveries for tap, surface water and wastewater spiked with 2 μg l^{-1}, 20 μg l^{-1} and 1 mg l^{-1} of C_6H_5OH in the presence of copper (II) sulphate in different experimental conditions (presence and absence of H_3PO_4, HCl and H_2SO_4). All recovery values obtained were 0.9–1.1 when acidified solutions were used. In this work, phenol compounds in the samples were preserved by addition of H_3PO_4 and $CuSO_4$.

Others interferences on the phenol index determination by 4-AAP, namely chlorine [20], amines [20], sulphur compounds [10,20], oils and grease [10,20] and humic acid were evaluated using a ruggedness test. The factorial model (eight factors) was performed, using both spiked tap water and spiked surface water with C_6H_5OH (C_{spike} = 2 μg l^{-1} and C_{spike} = 20 μg l^{-1}) in the presence of 0.32 mg l^{-1} for chlorine, 1 mg l^{-1} for SO_3^{2-}, 0.91 mg l^{-1} for S^{2-}, 1 mg l^{-1} for NH_2^-, 12 mg l^{-1} for oils and grease and 1 mg l^{-1} of humic acid, as shown in Tables 3 and 4, respectively. Phenol index for each combination sample was analyzed and recoveries calculated. From Tables 3 and 4 no significant influence of either each combination or simultaneous presence of the five compounds on the phenol index results, since the calculated F_i values were always lower than the critical value of F ($F_{1,9,0.95}$ = 5.12).

3.3. Precision and trueness

The precision of the method was evaluated in within-laboratory reproducibility conditions from duplicate analysis [15]. The estimated standard deviation value of the process, *s*, was obtained by Eq. (8), where d_2 is a tabulated correction factor for the calculation of *s* from the average range (d_2 = 1,128 for duplicates); $\bar{R}$ is the average range calculated $\bar{R} = R/n$; the range, *R*, is the difference between duplicate pairs $R = (x_2 - x_1)$ and *n* is the number of subgroups [18]:

$$s = \frac{\bar{R}}{d_2} \quad (8)$$

Relative standard deviations, *RSD*, are shown in Table 5 for dynamic ranges with lower phenol concentration. *RSD* values decrease with the increasing of the phenol concentration. *RSD* values of 0.07 close to the AMV (1 μg l^{-1}) were obtained, fulfilling the requirements for precision established by DL no. 236/98 [6] for surface water (±0.30). Assuming a triangular distribution [21], the target relative uncertainty for precision of 0.17 was obtained.

No sufficient data in the highest concentration range were available for R-charts establishment. Relative range, R^{rel}, lower than 0.10

Table 5
Precision estimated from replicate analysis and trueness from reference material.

$[C_6H_5OH]$ (μg l^{-1})	Precision				Trueness			
	$\bar{x}$	*N*	$\bar{R}$	*RSD*	$\gamma_{RM} \pm U_{RM}$ (mg l^{-1})	$\bar{\gamma}_{lab}$ (mg l^{-1})	$R_m \pm s$	*z*-Score
1–10	5.0	12	0.38	0.07		5.29	1.06 ± 0.02	0.36
10–200	58	15	0.75	0.01	5.01 ± 1.51	5.12	1.02 ± 0.01	0.15
(0.2–2.5) × 10^3	–	–	–	0.029[a]		5.29	1.06 ± 0.06	0.37

$\bar{x}$, mean mass concentration; *N*, number of assays; $\bar{R}$, mean range; *RSD*, residual standard deviation ($RSD = s/\bar{x}$ and $s = \bar{R}/d_2$, with d_2 = 1.128 [15]); γ_{RM}, mass concentration of the reference material (RM); U_{RM}, expanded uncertainty of RM; $\bar{\gamma}_{lab}$, mean mass concentration for RM analysis; $\bar{R}_m$, phenol recoveries; *s*, standard deviation.

[a] Standard uncertainty from duplicate acceptance criteria assuming a triangular distribution.

Table 6
Wastewater proficiency test (PT) for phenol.

$\bar{\gamma}_{PT}$ (mg l^{-1})	s_{robust} (mg l^{-1})	$u(\bar{\gamma}_{lab})$ (mg l^{-1})	n	$\bar{\gamma}_{lab}$ (mg l^{-1})	z-Score	RMS_{bias}	$u^{rel}_{trueness}$	$u^{rel}(\bar{\gamma}_{PT})$	$u^{rel}_c(\gamma_{sample})$
1.16	0.27	0.062	5	1.18	0.11	0.02	0.05	0.04	0.054
1.02	0.15	0.024	8	1.03	0.09				

$\bar{\gamma}_{PT}$, mass concentration of the assigned value; s_{robust}, standard uncertainty; $u(\bar{\gamma}_{PT})$, standard uncertainty associated with $\bar{\gamma}_{PT}$; n, number of assays; $\bar{\gamma}_{lab}$,- mass concentration of the laboratory result; RM analysis; RMS_{bias}, root mean of the bias; $u^{rel}_{trueness}$, relative standard uncertainty associated with trueness; $u^{rel}(\bar{\gamma}_{PT})$, mean relative standard uncertainty of the assigned value; $u^{rel}_c(\gamma_{sample})$, relative combined uncertainty.

($RSD \leq 0.03$ assuming a triangular distribution) was considered as our own quality criterion. Our acceptance criteria are half of the ones required by DL no. 236/98 [6] for residual water.

The trueness evaluation was estimated by a reference material (RM) RTC no. QCI-043-2 using the overall procedure. The reference solution was diluted in order to bracket the three working range. From Table 5, the performance of the method can be considered satisfactory because the z-score parameter is lower than 2 [22]. The method was also considered unbiased whenever the phenol recoveries were from 0.9 to 1.1. Although the research described in this work was validated using either reference materials or proficiency test (PT) data, additional validation was performed through spiked tap water, surface water and wastewaters. RM recoveries inside the interval of 1.0 ± 0.1 were also obtained for all ranges as imposed by DL no. 236/98 for wastewaters [6]. For surface water, trueness limits of ±0.5 were required for the DL no. 236/98 at the AMV (1 μg l^{-1}), being our recovery values markedly inferiors.

3.4. Uncertainty measurement

In this work uncertainty were estimated using an interlaboratory approach based on proficiency testing (PT) data [23] which include all uncertainty contributions. Evaluation of laboratory performance was previously done through z-score parameter (since this approach requires no significant bias). As can be seen from Table 6 the performance of the laboratory was classified as satisfactory since $|z| \leq 2$ [22].

The relative combined uncertainty, $u^{rel}_c(\gamma_{sample})$ was calculated using Eq. (9), that associates the relative standard uncertainty of precision, RSD, estimated in within-laboratory reproducibility (Table 5), and the relative standard uncertainty associated with trueness, $u^{rel}_{trueness}$:

$$u^{rel}_c(\gamma_{sample}) = \sqrt{(u^{rel}_{trueness})^2 + RSD^2} \quad (9)$$

The $u^{rel}_{trueness}$ component was estimated from the proficiency testing data in according to Eq. (10) (Table 6) combining the laboratory bias given by the root mean of the bias, RMS_{bias} (Eq. (11)) and the mean relative uncertainty of the assigned value, $u^{rel}(\bar{\gamma}_{PT})$:

$$u^{rel}_{trueness} = \sqrt{(RMS_{bias})^2 + [u^{rel}(\bar{\gamma}_{PT})]^2} \quad (10)$$

$$RMS_{bias} = \sqrt{\frac{\sum_{i=1}^{n}(\bar{\gamma}_{lab} - \bar{\gamma}_{PT})^2}{n}} \quad (11)$$

where $\bar{\gamma}_{lab}$ is the laboratory result and $\bar{\gamma}_{PT}$ is the PT assigned value.

From Table 6, $RMS_{bias} = 0.02$ calculated over the last 2 years, $u^{rel}(\bar{\gamma}_{PT}) = 0.04$ and $u^{rel}_{trueness} = 0.05$, was obtained. Target $u^{rel}_{trueness} = 0.35$ for 1 μg l^{-1} of phenol (AMV of surface waters) and target $u^{rel}_{trueness} = 0.06$ for 500 μg l^{-1} of phenol (AMV of surface waters) are imposed by trueness limits in DL no. 236/98 [6]. A relative combined uncertainty for γ_{sample}, $u^{rel}_c(\gamma_{sample})$, of 0.054 was estimated.

The measurand is within the interval provided by the expanded uncertainty. This uncertainty was calculated multiplying the $u^{rel}_c(\gamma_{sample})$ by a coverage factor of 2 for a confidence level of 0.95.

Table 7
Consumption of reagents and sample per assay in the two different procedures for the determination of phenol index.

	Presented method	ISO 6439:1990
4-AAP (mg)	0.18	40
$K_3[Fe(CN)_6]$ (mg)	0.54	160
H_3PO_4 (ml)	0.27	5
$CHCl_3$ (ml)	–	140
Sample (ml)	2.3	500
NaCl (g)	–	150
NaOH (g)	–	1

Table 8
Concentration of phenol index in several wastewater samples obtained by the conventional method and the methodology validated in this work.

Concentration of phenol index in samples (mg l^{-1})	
ISO 6439 [20]	Validated method
1.17[a] (z-score = 0.95)	1.02[a] (z-score = 0.09)
1.10[a] (z-score = 0.30)	1.16[a] (z-score = 0.00)
<0.05 (LOQ)	0.004
<0.05 (LOQ)	0.003
<0.05 (LOQ)	0.018
<0.05 (LOQ)	0.018
<0.05 (LOQ)	0.002
<0.05 (LOQ)	0.002

[a] Samples of proficiency testing performance of laboratory satisfactory (z-score) ≤ 1.0.

4. Conclusions

Concerning sample and reagent consumptions, the studied method only require a total volume of both sample and reagents of 3.14 ml per overall procedure (Table 7), in spite of 1000 ml to the conventional method [20]. The analysis time was also reduced to approximately 5 min (1 h per sample in the conventional method). Associated to these characteristics with the reduction of organic solvent exposition and the increasing of laboratory productivity it can be concluded that the validated procedure is a sustainable and environmentally friendly alternative to the reference method.

The procedure limit of detection (0.6 μg l^{-1}) and the metrological precision and trueness characteristics of the method make this validated method suitable for the determination of phenol index in natural waters and wastewaters since the requirements of the DL no. 236/98 are fulfilled.

This method could be applicable to the screening of phenols in waters and wastewaters and is an excellent alternative for the conventional one as shown in Table 8 for different waters.

References

[1] F. Lanças, I. Olivares, P. Alves, J. Environ. Sci. Health, Part B 42 (2007) 491.
[2] F. Rocha, K. Lupetti, O. Fatibello-Filho, Talanta 62 (2004) 463.
[3] EPA, USA EPA List of Drinking Water Contaminants & MCLs, 2004, http://www.epa.gov/safewater/mcl.html (accessed November 2008).
[4] I. Nukatsuka, S. Nakamura, K. Watanabe, K. Ohzeki, Anal. Sci. 16 (2000) 269.
[5] W. Frenzel, J. Oleksy-Frenzel, Anal. Chim. Acta 261 (1992) 253.

[6] Decreto-Lei no. 236/98, Diário da República Portuguesa, Lisboa, 1998, 176 Série I-A: 3675.
[7] SKALAR Methods, Analysis: Phenol Index, Catnr. I497-001 issue 081004/MH/99231275, SKALAR Analytical B.V., Breda, Netherlands, 2004.
[8] ISO (International Organization for Standardization), ISO 14402, Water Quality—Determination of Phenol Index by Flow Analysis (FIA and CFA), 1st ed., ISO, Geneva, Switzerland, 1999.
[9] ISO (International Organization for Standardization), ISO 3696, Water for Analytical Laboratory Use—Specification and Test Methods, ISO, Geneva, Switzerland, 1987.
[10] APHA-AWWA-WEF, Standard Methods for the Examination of Water and Wastewater, 21th ed., American Public Health Association, American Water Works Association, Water Environmental Federation, Method 5530, Washington, DC, 2005.
[11] SANplus, Analyser. SKALAR Analytical B.V., Breda, Netherlands, 2004.
[12] M. Feinberg, C. Ducauze, Analusis 8 (1980) 185.
[13] VIM (International Vocabulary of Metrology), Basic and General Concepts and Associated Terms, 3rd ed., BIPM, IEC, IFCC, ILAC, ISO, IUPAC, IUPAP and OIML, 2008.
[14] ISO (International Organization for Standardization), ISO 8466-1, Water Quality—Calibration and Evaluation of Analytical Methods and Estimation of Performance Characteristics. Part 1. Statistical Evaluation of the Linear Calibration Function, ISO, Geneva, CH, Switzerland, 1990.
[15] W. Funk, V. Dammann, G. Donnevert, Quality Assurance in Analytical Chemistry, VCH, Weinheim/New York/Basel/Cambridge/Tokyo, 1995.
[16] R. Kellner, J. Mermet, M. Otto, H. Widmer, Analytical Chemistry, Wiley-VCH, Weinheim/New York/Chichester/Brisbane/Singapore/Toronto, 1998.
[17] IUPAC (International Union of Pure and Applied Chemistry), Spectrochim. Acta, Part B 33 (1978) 241.
[18] J. Miller, J. Miller, Statistics and Chemometrics for Analytical Chemistry, 5th ed., Pearson Education Limited, 2005.
[19] ISO (International Organization for Standardization), ISO 8248, Shewhart Control Charts, ISO, Geneva, CH, Switzerland, 1991.
[20] ISO (International Organization for Standardization), ISO 6439, Water Quality – Determination of Phenol Index – 4-Aminoantipyrine Spectrometric Methods After Distillation, 2nd ed., ISO, Geneva, Switzerland, 1990.
[21] GUM (Guide to the Expression of Uncertainty in Measurement), 1st ed., BIPM, IEC, IFCC, IUPAC, IUPAP, IOML, ISO, 1993.
[22] Eurolab 2007 (The European Federation of National Associations of Measurement, Testing and Analytical Laboratories), Measurement Uncertainty Revisited: Alternative Approaches to Uncertainty Evaluation, Technical Report No. 1/2007, http://www.eurolab.org (accessed November 2008).
[23] B. Magnusson, T. Näykki, H. Hovind, M. Krysell, Handbook for Calculation of Measurement Uncertainty in Environmental Laboratories, 2nd ed., Nordtest Report TR 537, Nordest, Espoo, Finland, 2004.

Talanta 79 (2009) 676–680

Contents lists available at ScienceDirect

Talanta

journal homepage: www.elsevier.com/locate/talanta

Determination of naproxen in human urine by high-performance liquid chromatography with direct electrogenerated chemiluminescence detection

Yonghua Sun, Zhujun Zhang*, Zhijun Xi, Zuolong Shi

College of Chemistry and Materials Science, Shaanxi Normal University, Key Laboratory of Analytical Chemistry for Life Science of Shaanxi Province, Xi'an 710062, China

ARTICLE INFO

Article history:
Received 19 February 2009
Received in revised form 21 April 2009
Accepted 23 April 2009
Available online 3 May 2009

Keywords:
Electrogenerated chemiluminescence
Liquid chromatography
Dual-electrode system
Naproxen

ABSTRACT

A simple and sensitive liquid chromatographic method coupled with electrogenerated chemiluminescence (ECL) was described for the separation and quantification of naproxen in human urine. The method was based on the ECL of naproxen in basic $NaNO_3$ solution with a dual-electrode system. Factors affected the ECL emission were investigated. Under the optimal conditions, the ECL intensity has a linear relationship with the concentration of naproxen in the range of 4.0×10^{-8} g mL^{-1} to 2.0×10^{-6} g mL^{-1} and the detection limit was 1.6×10^{-8} g mL^{-1} (S/N = 3). Application of the method to the analyses of naproxen in human urine proved feasible.

1. Introduction

Naproxen (6-methoxy-a-methyl-2-naphthalene acetic acid, Fig. 1), a non-steroidal anti-inflammatory drug (NSAID) derived of propionic acid, is widely used to moderate pain relief in the treatment of many diseases [1]. Recently, it has been approved for over-the-counter use in the United States. NSAIDs, including naproxen are commonly employed to reduce ongoing inflammation, pain and fever, since they are able to block [2] the cyclooxygenase (Cox) enzymes (Cox-1 and Cox-2), that both produce prostaglandins; these classes of compounds have several important functions, as the promotion of inflammation, pain and fever. However, prostaglandins produced by the Cox-1 enzyme, are also able to protect the stomach, support platelets and blood clotting. Thus, NSAIDs can cause ulcers in the stomach and promote bleeding after an injury or surgery. Moreover, they are associated with other serious side effects, i.e. kidney failure, and with a number of minor side effects, such as nausea vomiting, diarrhoea, constipation, decreased appetite, rash, dizziness, headache and drowsiness. When anti-inflammatory treatments become chronic, as in the case rheumatoid arthritis, the patients are exposed to the drugs for prolonged time periods. The potential misuse and involuntary intake of naproxen as residues in food could pose a health risk in people, for example allergy, severe gastrointestinal lesion, changes in renal function and nephrotoxicity [3–5].

In view of the above considerations, the development of a simple and sensitive method for the determination of naproxen in biological fluids could be very useful for toxicological and pharmaceutical purposes. Several methods dealing with naproxen determination in pharmaceutical preparation or biological fluids have been reported, including chemiluminescence [6,7], spectrofluorometry [8,9], differential pulse voltammetry [10], gas chromatography mass spectrometry [11], electrophoresis [12] and high-performance liquid chromatography (HPLC) with varied detection [13,14]. Although these methods have been successfully applied to analysis of naproxen in various matrices, some of these methods lack sensitivity and suffer from tedious procedure, time consuming or high cost.

ECL has become an important and valuable detection method in analytical chemistry in recent years. ECL is a means of converting electrical energy into radiative energy. It involves the production of reactive intermediates from stable precursors at the surface of an electrode. These intermediates then react under a variety of conditions to form excited states that emit light [15]. ECL allows the detection of analytes at low concentrations over a wide linear range. This is partly due to the electrochemical excitation during ECL reactions. The absence of an excitation light source produces a low background signal. This allows a highly sensitive detection without expensive instrumentation. The electrochemical initiation of the ECL reaction also introduces great temporal control over the reaction [16]. The majority of analytical applications of ECL now appearing in the literature are concerned with the indirect ECL of $Ru(bpy)_3^{2+}$ [17,18] and luminol [19,20]. In contrast with the indirect ECL, direct ECL does not need luminescence additives, such as $Ru(bpy)_3^{2+}$ or luminol. However, organic molecules having struc-

* Corresponding author. Tel.: +86 029 85308748.
E-mail address: zzj18@hotmail.com (Z. Zhang).

0039-9140/$ – see front matter © 2009 Elsevier B.V. All rights reserved.
doi:10.1016/j.talanta.2009.04.048

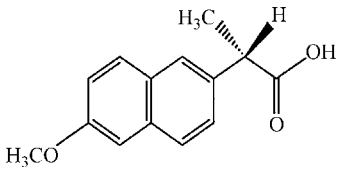

Fig. 1. The structure of naproxen.

tural character capable of direct ECL have been explored relatively infrequently when compared to the indirect ECL of $Ru(bpy)_3^{2+}$ and luminol. In our previous work, a sensitive direct ECL method has been developed and used to post-column determination of ofloxacin in human serum [21].

In our present work, a new ECL method was developed to determinate naproxen. It was based on the ECL of naproxen in basic $NaNO_3$ solution. Factors affected the ECL emission of naproxen were investigated and a simple mechanism was proposed. Under the optimal conditions, the method has been used for determination of naproxen in human urine.

2. Experimental

2.1. Apparatus and reagents

The experimental setup for HPLC–ECL is shown in Fig. 2(a). The analyses were carried out using a LC-6A (Shimadzu, Tokyo, Japan) liquid chromatography equipped with a Rheodyne 7725i syringe loading sample injector valve (Cotati, CA, USA) and a Agilent Zorbax SB-C_{18} column (I.D.: 250 mm × 4.6 mm, particle size: 5 μm, pore size: 80 Å, Agilent, USA). A dual-electrode electrochemical flow-cell (Fig. 2b) was used for the ECL experiments. The constant current was supplied by a JH2C galvanostat (Shanghai Electric Instrument Plant, Shanghai, China). The flow-cell contained a coiled Pt wire working electrode (∅ 0.2 mm) and a stainless steel counter electrode attached to the flow-cell outlet and positioned close to and directly opposite the Pt working electrode. The flow-cell was placed close to the window of the photomultiplier tube. Data collection and processing were performed using an IFFL-D Flow Injection Chemiluminescence Analyzer (Xi'an Remax Electronic Science-Tech Co. Ltd., Xi'an, China). Electrochemical data was obtained using Pt wires as the working electrode and counter electrode, and an Ag/AgCl electrode was used as the reference electrode. The Fluorescence spectra were recorded using a F-4600 fluorescence spectrophotometer (Hitachi, Tokyo, Japan).

Naproxen was obtained from the Institute of Pharmaceutical and Biomaterial Authentication of China (Beijing, China). Acetonitrile was of HPLC grade (Tianjin Kermel Chemical Reagent Co., Ltd., Tianjin, China). All the other reagents were of analytical reagent grade unless specified otherwise. Deionized and doubly distilled water was used throughout.

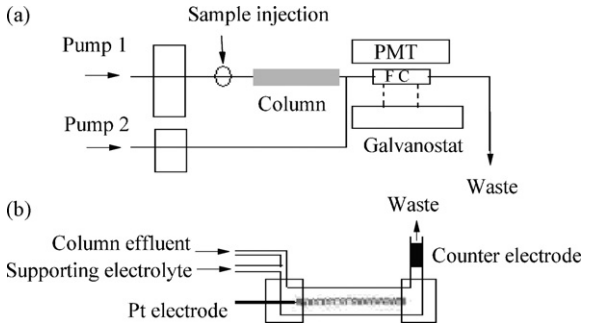

Fig. 2. Schematic diagram of the HPLC–ECL system (a) and side view of the FC (b). FC, flow-cell; PMT, photomultiplier tube.

2.2. Standard solutions

Stock solutions of naproxen (2.0 mg mL^{-1}) in acetonitrile were prepared and kept in the freezer at −4 °C. The diluted solutions were prepared, just before use, by accurate dilution with the mobile phase.

2.3. Preparation of urine samples

Urine samples were collected from healthy donors. The samples were prepared according to the reference with minor modification [22]. Aqueous standard solutions of naproxen were added into 1.0 mL of urine samples and centrifuged at 5000 rpm for 5 min; finally, 20 μL of the resulting mixture was injected.

2.4. Procedure

The mobile phase was pumped through the column at a flow rate of 1.0 mL min^{-1}. The column effluent was mixed with the supporting electrolyte (2.5 mL min^{-1}) at a mixing-tee and then flowed into the flow-cell. Until stable baseline was achieved, 20 μL standard solution or sample solution was injected into the mobile phase. The quantitative determination was based on the net ECL intensity $I = I_S - I_0$, where I_S is the ECL intensity in the presence of naproxen and I_0 is the intensity of blank signal.

3. Results and discussion

3.1. Optimization of the ECL system

In our preliminary investigations, it was found that the electrooxidation of naproxen in basic $NaNO_3$ solution was accompanied with ECL emission. Further experiments compared the ECL intensity of naproxen (1.0×10^{-7} g mL^{-1}) in different supporting electrolyte (1.0 mol L^{-1}) including KCl, $NaNO_3$, $LiNO_3$, $NaClO_4$, Na_2SO_4 and tetraethyl ammonium bromide (0.3 mol L^{-1}). The results showed that the ECL intensity of naproxen was varied. The ECL performance of naproxen in basic $NaNO_3$ solution was similar with that in basic $LiNO_3$ solution; in KCl, Na_2SO_4, $NaClO_4$ and tetraethyl ammonium bromide solution, no ECL emission was observed; in our present work, $NaNO_3$ was selected as the supporting electrolyte for further investigation.

The $NaNO_3$ concentration and the current intensity had a very important effect on ECL intensity of naproxen. As shown in Fig. 3, the ECL intensity increased with the increase of current intensity

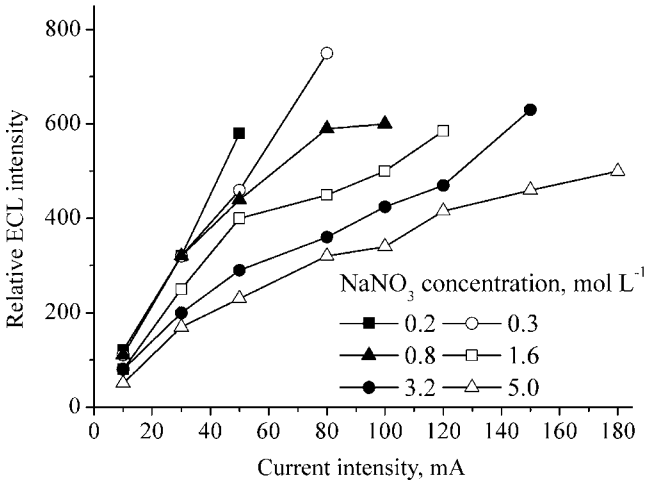

Fig. 3. Effects of $NaNO_3$ concentration and current intensity on the ECL intensity of naproxen. mA: milliampere.

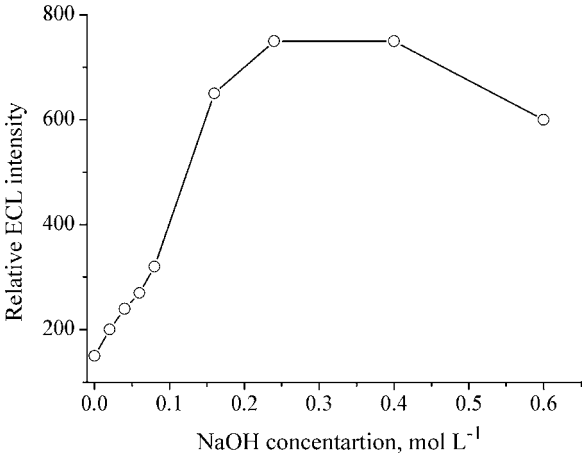

Fig. 4. Effect of NaOH concentration on the ECL of naproxen.

at each level of the $NaNO_3$ concentration, but at each level of the current intensity, the ECL intensity decreased with the increase of $NaNO_3$ concentration from 0.2 mol L^{-1} to 5.0 mol L^{-1}. To obtain the maximum ECL intensity, a 80 mA current and a 0.3 mol L^{-1} $NaNO_3$ solution were selected for subsequent studies.The ECL emission of naproxen in neutral and acid $NaNO_3$ solution was very weak, but strong in basic $NaNO_3$ solution. The alkalinity of the supporting electrolyte was investigated by adding various concentrations of NaOH into the supporting electrolyte. The results (Fig. 4) showed that the ECL intensity increased with the increase of the NaOH concentration from 0 mol L^{-1} to 0.24 mol L^{-1} and then decreased with the increase of the NaOH concentration from 0.24 mol L^{-1} to 0.6 mol L^{-1}.

Acetonitrile or methanol was the generally used organic mobile phase in reversed-phase high-performance liquid chromatography, and in most cases it has important effect in post-column CL or ECL detection. The ECL emission of naproxen in the medium of acetonitrile/water and methanol/water were compared. As shown in Fig. 5, the ECL intensity in acetonitrile/water was higher than that in methanol/water. In the medium of acetonitrile/water, the ECL intensity increased with the increase of the ratio of acetonitrile/water from 10% to 80%, while in the medium of methanol/water, the ECL intensity decreased with the increase of the ratio of methanol/water. Thus, it could be seen that the ECL reaction of naproxen is well compatible with a mobile phase of acetonitrile/water.

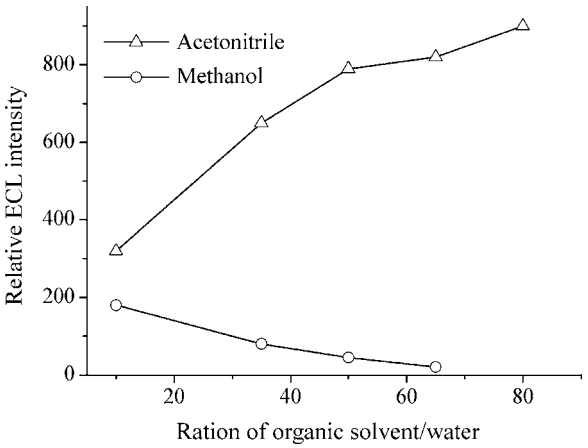

Fig. 5. ECL emission of naproxen in acetonitrile and methanol.

Table 1
Detection of naproxen by HPLC with different detector.

Method	LOD (ng mL^{-1})	Linear range (ng mL^{-1})	Reference
MECC–LIF	70	100–2000	[11]
SPE–HPLC–UV	30	200–20000	[13]
SPE-HPLC-FL standard urine	0.3 24 (LOQ)	8–96	[14]
This method	16	40–2000	

MECC: micellar electrokinetic capillary chromatography; LIF: laser-induced fluorescence; SPE: solid-phase extraction; LOQ: limits of quantification.

The flow rate of the supporting electrolyte has also been investigated. Although maximum ECL intensity was obtained at 1.0 mL min^{-1}, a higher flow rate of 2.5 mL min^{-1} (the maximum flow rate of the pump) was applied due to higher signal-to-noise ratio could be obtained under higher flow rate.

3.2. Method performance

Under the optimum conditions as those described above, the calibration graph of ECL intensity versus naproxen concentration was linear in the range of 4.0×10^{-8} g mL^{-1} to 2.0×10^{-6} g mL^{-1}; the regression equation was $I = 1077.1C + 12.05$ (C: naproxen concentration, 10^{-6} g mL^{-1}) with a correlation coefficient of 0.993. The limit of detection (LOD) was 1.6×10^{-8} g mL^{-1} (S/N = 3). As compared in Table 1, the present method has a wider linear range, lower or comparative detection limit than some of the previously reported HPLC methods.

3.3. Sample analysis

For separation and detection of naproxen in urine sample, the mobile phase was a mixture of acetonitrile/water (65/35, v/v, adjusted the pH to 5.0 with phosphoric acid). HPLC separation of naproxen in urine sample was performed isocratically at a flow rate of 1.0 mL min^{-1} and the eluate from the column was continuously monitored by ECL. Fig. 6 shows typical chromatograms of a 1.0×10^{-6} g mL^{-1} standard naproxen solution (a) and a human urine sample spiked with 6.4×10^{-7} g mL^{-1} naproxen (b).

Following the procedure described in Section 2.4, the proposed method was applied to the analysis of naproxen in human urine. The validation of the proposed method and a recovery test were carried out on spiked samples of human urine. The intra-day precision was tested with 9 repeated injections of each sample solution spiked with naproxen. The inter-day precision of the proposed method was studied by analyzing the same spiked samples, injected three times every day for each sample

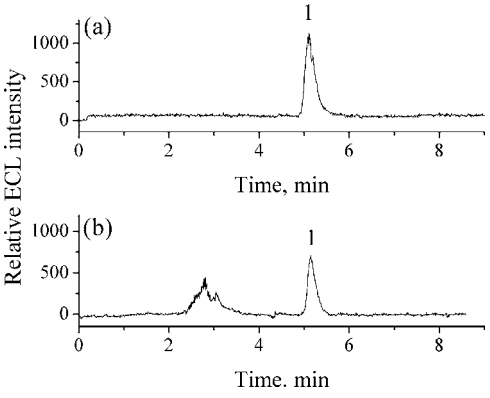

Fig. 6. Typical chromatograms of a standard (1.0×10^{-6} g mL^{-1}) (a) and a urine sample spiked with 6.4×10^{-7} g mL^{-1} naproxen (b). Mobile phase, ACN–water (65:35, v/v, pH 5.0).

Table 2
Determination of naproxen in human urine.

Detected (ng mL^{-1})	Added (ng mL^{-1})	Found (ng mL^{-1}) (recovery, %)[a]	Precision (RSD)	
			Intra-day (%)[b]	Inter-day (%)[c]
1				
39.6	20.0	59.1 ± 2.5 (98)	4.3	5.8
	40.0	78.1 ± 3.7 (96)	4.7	6.1
	60.0	100.5 ± 5.0 (101)	5.0	5.3
2				
81.2	20.0	100.7 ± 3.9 (98)	3.9	4.9
	40.0	119.5 ± 4.4 (96)	3.7	5.7
	60.0	138.5 ± 4.6 (95)	3.3	5.3

RSD: relative standard deviation.
[a] Mean of three determinations.
[b] Nine repeated injections of each sample solution.
[c] Three repeated injections of each sample solution on three consecutive days.

solution, on three consecutive days. The results were showed in Table 2.

3.4. Possible ECL mechanism

The electrochemical behavior and the corresponding ECL–potential relationship of the blank solution and naproxen solution were investigated. Fig. 7 shows the cyclic voltammograms and the corresponding ECL–potential curves of a solution in the absence and in the presence of 1.0×10^{-4} g mL^{-1} naproxen.

For a solution without addition of naproxen (Fig. 7a, lines 1 and 3), the oxidation of water occurred around at about 1.5 V, and no obvious ECL signal was observed in its corresponding ECL–potential curves (Fig. 7b, lines 1 and 3). For a solution in the presence of 1.0×10^{-4} g mL^{-1} naproxen, the oxidation peak of water around 1.5 V decreased (Fig. 7a, lines 2 and 4). Companied with the oxidation of water, weak ECL signal was observed around 1.5 V in its corresponding ECL–potential curves (Fig. 7b, line 4), and stronger ECL emission was observed when the potential was more positive than 2.5 V (Fig. 7b, line 2). Further experiments showed that the ECL intensity from the counter electrode was 25 times higher than that from the working electrode. Namely, the ECL emission was mainly from the electrode on which the reduction reaction occurred.

In order to identify the light emitter, fluorescence spectra were measured. The excitation spectrum of naproxen has two peak around 263 nm and 332 nm (Fig. 8, line 1), and the maximum emission spectrum was around 352 nm (Fig. 8, line 2). The fluorescence intensity of naproxen decreased after 10 min electrolysis (Fig. 8, lines 3 and 4) and no new spectrum was observed. The ECL spectrum was also recorded. The maximum wavelength was around 438 nm, which was largely different form the fluorescence emission spectrum of naproxen. The results indicated that naproxen was consumed in the electrochemical reaction and new unstable intermediate was produced. Considering that nitrate could be reduced electrochemically [23,24], it seemed reasonable to suppose that naproxen was electrochemically oxidized to produce an unstable intermediate. This unstable intermediate further reacted at the counter electrode with the reduction product of nitrate to generate the ECL emission. However, the detailed mechanism is still unclear and a deeper investigation of these reactions is needed.

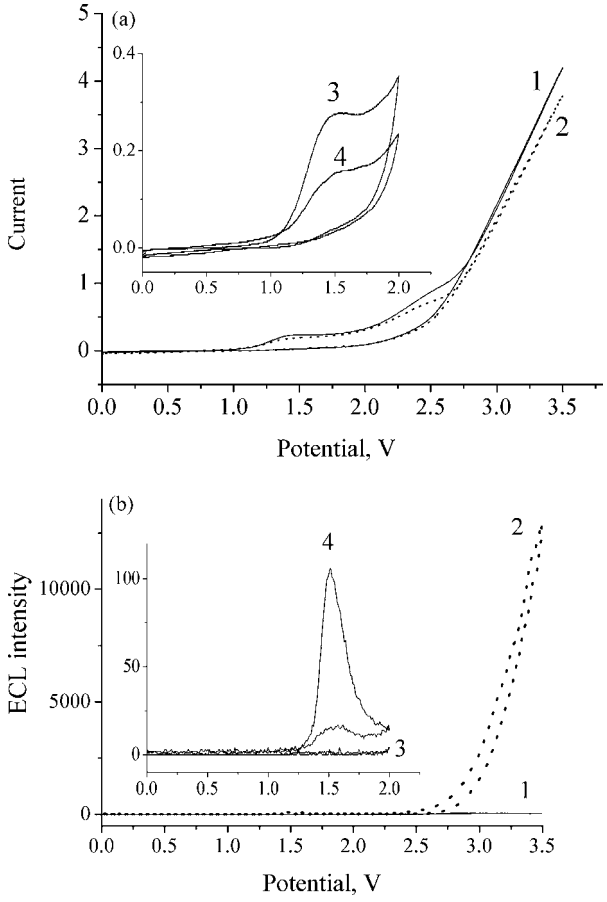

Fig. 7. Cyclic voltammograms (a) and corresponding ECL–potential curves (b). 1, 3: solutions in the absence of naproxen. 2, 4: 1.0×10^{-4} mol L^{-1} naproxen. Supporting electrolyte: 0.3 mol L^{-1} $NaNO_3$ and 0.24 mol L^{-1} NaOH. Scan rate: 100 mV/s.

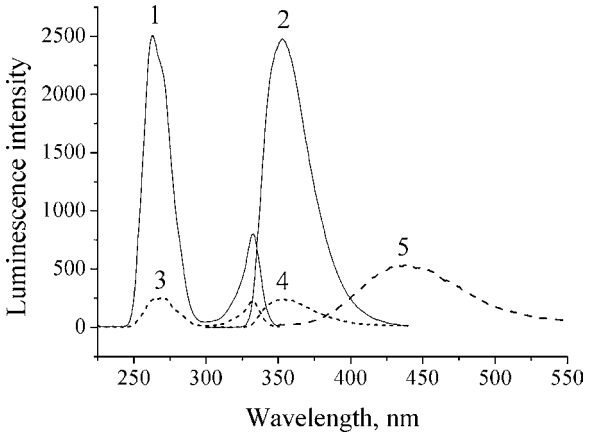

Fig. 8. Fluorescence spectra and ECL spectrum. 1, 2: excitation and emission spectrum of 1.0×10^{-4} g mL^{-1} naproxen; 3, 4: excitation and emission spectrum of 1.0×10^{-4} g mL^{-1} naproxen after 10 min electrolysis; 5: ECL spectrum.

4. Conclusions

In this paper, a new and simple direct ECL method was developed for determination of naproxen in human urine. The ECL reaction was well compatible with the mobile phase of HPLC. The proposed method allowed for the sensitive determination of naproxen in human urine samples, and offered wider linear range, lower detection limit. Compared with the indirect ECL of $Ru(bpy)_3^{2+}$ or luminol, present method was more simple and convenient to operate.

Acknowledgement

This study was supported by the Natural Science Foundation of China (No. 30470886).

References

[1] C.S. Boynton, C.F. Dick, G.H. Mayer, J. Clin. Pharmacol. 28 (1988) 512.
[2] M. Osiri, L.W. Moreland, Arthritis Care Res. 12 (1999) 35.
[3] G. Singh, G. Triadafilupoulos, J. Rheumatol. 26 (1999) 18.
[4] I.F. Fries, New Engl. J. Med. 341 (1999) 1397.
[5] L. Kovacevic, J. Bernstein, R.P. Valentini, A. Imam, N. Gupta, T.K. Mattoo, Pediatr. Nephrol. 18 (2003) 826.
[6] X.L. Cheng, L.X. Zhao, M.L. Liu, J.M. Lin, Anal. Chim. Acta 558 (2006) 296.
[7] Y.H. Li, J.R. Lu, Anal. Chim. Acta 577 (2006) 107.
[8] E.P. Zisiou, P.C.A.G. Pinto, M.L.M.F.S. Saraiva, C. Siquet, J.L.F.C. Lima, Talanta 68 (2005) 226.
[9] G.A. Ibañez, G.M. Escandar, J. Pharm. Biomed. Anal. 37 (2005) 149.
[10] N. Adhouma, L. Monser, M. Toumi, K. Boujlel, Anal. Chim. Acta 495 (2003) 69.
[11] Á. Sebők, A. Vasanits-Zsigrai, G. Palkó, G. Záray, I. Molnár-Perl, Talanta 76 (2008) 642.
[12] C. Albrecht, W. Thormann, J. Chromatogr. A 802 (1998) 115.
[13] A. Aresta, F. Palmisano, C.G. Zambonin, J. Pharm. Biomed. Anal. 39 (2005) 643.
[14] E. Mikami, T. Goto, T. Ohno, H. Matsumoto, M. Nishida, J. Pharm. Biomed. Anal. 23 (2000) 917.
[15] M.M. Richter, Chem. Rev. 104 (2004) 3003.
[16] K.A. Fähnrich, M. Pravda, G.G. Guilbault, Talanta 54 (2001) 531.
[17] R. Pyati, M.M. Richter, Annu. Rep. Prog. Chem. Sect. C 103 (2007) 12.
[18] J.P. Choi, A.J. Bard, Anal. Chim. Acta 541 (2005) 141.
[19] A. Wróblewska, O.V. Reshetnyak, E.P. Koval'chuk, R.I. Pasichnyuk, J. Blaźejowski, J. Electroanal. Chem. 580 (2005) 41.
[20] A.W. Knight, Trends Anal. Chem. 18 (1999) 47.
[21] Y.H. Sun, Z.J. Zhang, Z.J. Xi, Anal. Chim. Acta 623 (2008) 96.
[22] U.G. Sidelmann, I. Bjørnsdottir, J.P. Shockcor, S.H. Hansen, J.C. Lindon, J.K. Nicholson, J. Pharm. Biomed. Anal. 24 (2001) 569.
[23] A.J. Bard, R. Parsons, J. Jordan (Eds.), Standard Potentials in Aqueous Solutions, Marcel Dekker, New York, 1985.
[24] O. Brylev, M. Sarrazin, L. RouéL, D. Bélanger, Electrochim. Acta 52 (2007) 6237.

Talanta 79 (2009) 926–934

Contents lists available at ScienceDirect

Talanta

journal homepage: www.elsevier.com/locate/talanta

Determination of tetracyclines in food samples by molecularly imprinted monolithic column coupling with high performance liquid chromatography

Xiangli Sun[a], Xiwen He[a], Yukui Zhang[a,b], Langxing Chen[a,*]

[a] Department of Chemistry, Nankai University, Tianjin 300071, PR China
[b] Dalian Institute of Chemical Physics, Chinese Academy of Sciences, Dalian 116011, PR China

ARTICLE INFO

Article history:
Received 5 January 2009
Received in revised form 15 May 2009
Accepted 19 May 2009
Available online 27 May 2009

Keywords:
Molecularly imprinted solid phase extraction (MISPE)
In situ polymerization
Molecularly imprinted monolithic column
Tetracyclines
Determination

ABSTRACT

A novel solid phase extraction (SPE) method for determination of tetracyclines (TCs) in milk and honey samples by molecularly imprinted monolithic column was developed. Using tetracycline (TC) as the template, methacrylic acid (MAA) as the functional monomer, ethylene glycol dimethacrylate (EGDMA) as the cross-linker, methanol as the solvent, cyclohexanol and dodecanol as the mixed porogenic solvents, a TC imprinted monolithic column was prepared by in situ molecular imprinting technique for the first time, and the optimal synthesis conditions and the selectivity of TC imprinted monolithic column were investigated. The interfering substances in food samples and TCs can be separated successfully on imprinted column. Molecularly imprinted solid phase extraction (MISPE) coupling with C18 column was used to determinate the TCs in milk and honey. The recoveries of this method for six tetracyclines antibiotics such as tetracycline (TC), oxytetracycline (OTC), minocycline (MINO), chlortetracycline (CTC), metacycline (MTC) and doxycycline (DTC) were investigated, and high recoveries of 73.3–90.6% from milk samples and 62.6–82.3% from honey samples were obtained. A method for determination of TCs at low concentration level in milk and honey samples was successfully developed by using the monolithic column as the precolumn for solid phase extraction of six TCs compounds.

1. Introduction

Food contamination owing to chemicals from natural or man-made sources poses severe risks to human health. Thus, there is a constant requirement for good analytical protocols based on efficient analytical processes (sensitive, selective, fast and inexpensive) by legislation, health authorities and companies operating in the food market. Usually, the complexity of food matrices and contaminants presented in food at low concentration (ng to $\mu g\,g^{-1}$) levels require analysis perform only after some clean-up and preconcentration steps [1], and thus there is a considerable interest in developing new selective and sensitive methods for extracting and isolating components from complex food matrices. For this purpose, the solid phase extraction (SPE) technique is the most widely used for sample pre-treatment method due to factors such as convenience, cost, timing saving and simplicity. However, the common solid phase extraction materials show a lack of selectivity except immunoadsorbents which are very selective but expensive and not suitable for harsh environments. As economical, rapid and selective clean-up methods are needed, the application of SPE procedures involving molecularly imprinted polymers (MIPs), called MISPE, offering the advanced specificity in comparison with traditional SPE adsorbents, has received increasing attention over the past decade as an attractive alternative for the analysis of complex samples [1–6] where analyte selectivity in the presence of very complex samples represents the main problem.

MIPs are tailor-made materials that can exhibit high affinity and selectivity towards a given target or group of target molecules. MIPs are synthesized by polymerization of functional monomers and a cross-linker around a template. Extraction of the template leaves behind recognition sites of functional and shape complementarity to the template. [7,8] Due to their high selectivity, physiochemical stability and applicability in harsh chemical media, MIP has been used in fields where a certain degree of selectivity is required such as separation media [9], mimicking antibody [10], chemical and biochemical sensing [11]. Traditionally, MIPs have been synthesized in bulk polymerization followed by a grinding and sieving process to acquire the desired particle size for chromatographic purposes. This time-consuming process commonly yields irregular particles in shape and size, which limits the chromatographic efficiency. To overcome these disadvantages, the MIP monolithic columns are prepared by in situ polymerization directly inside chromatographic columns [12–16]. This strategy enables us to avoid the tedious grinding and sieving procedures as well as the prob-

* Corresponding author. Tel.: +86 22 23505091; fax: +86 22 23502458.
E-mail addresses: xianglisun@mail.nankai.edu.cn (X. Sun), xiwenhe@nankai.edu.cn (X. He), ykzhang@dicp.ac.cn (Y. Zhang), lxchen@nankai.edu.cn (L. Chen).

0039-9140/$ – see front matter © 2009 Elsevier B.V. All rights reserved.
doi:10.1016/j.talanta.2009.05.033

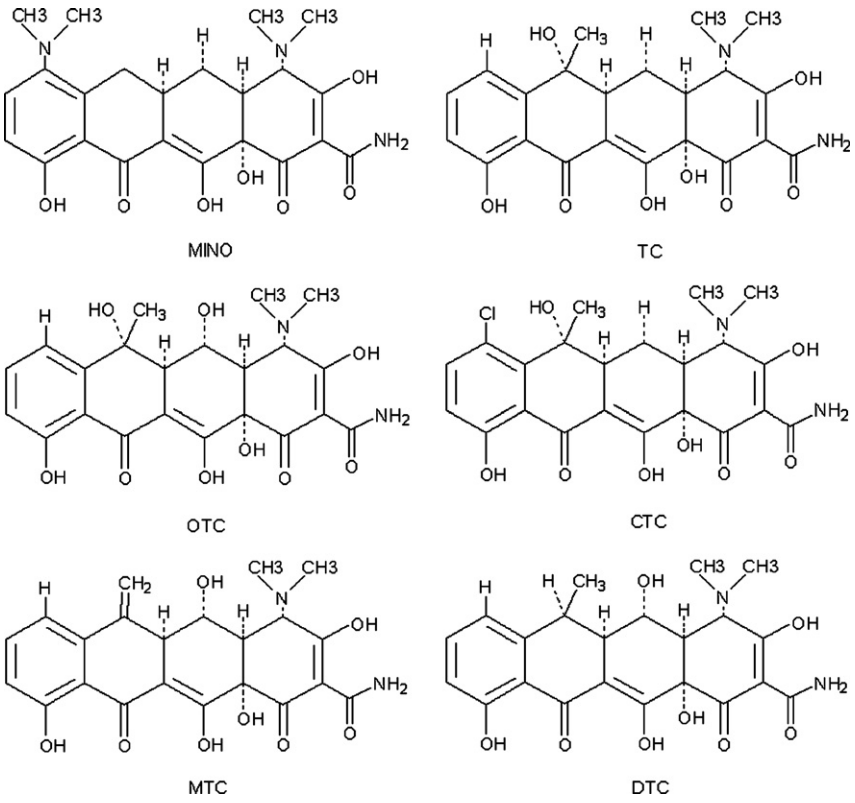

Fig. 1. Chemical structures of the tetracyclines used in this study.

lems of costly particle loss and particle inhomogeneity and easily obtained a MIP column with good resolution and low backpressure at high flow rate. Compared with conventional particle columns, the monolithic column has attracted significant interest because of their ease of preparation, high reproducibility and rapid mass transport. Furthermore, the preparation of this type of MIP is more cost-efficient, because it requires much smaller amount of template molecules.

Tetracyclines (TCs) (Fig. 1) are broad-spectrum antibiotics, which have been commonly used in veterinary medicine for the purpose of prevention and treatment of disease. However, the widespread use of them could lead to TCs residues in animal-producing foods. Many countries have defined the maximum residue limits for the TCs in various foods, for example, European Union (EU) has set the maximum residue limits (MRLs) for tetracycline, oxytetracycline and chlortetracycline as 0.3 mg kg^{-1} in liver, and 0.1 mg kg^{-1} in milk or muscle tissues [17]. The US Food and Drug Administration (FDA) has set the MRLs for the sum of tetracycline, chlortetracycline, and oxytetracycline residues as 2 mg kg^{-1} in muscle, 6 mg kg^{-1} in liver, and 0.4 mg kg^{-1} in milk [18]. Due to the widespread use of TCs in the animal industry, there are several comprehensive review articles on the analysis of TCs in biological, food and soil matrices [19–22]. Currently, a few reports on the imprinting of antibiotics TCs in preparing biological and food samples have appeared [23–28]. In the study performed by Cai and Gupta [23], the MIP with TC template synthesized in bulk was used to evaluate the mechanism of recognition and TC binding. Trotta et al. [24] and Suedee et al. [25] described the application of molecularly imprinted membrane to the discrimination of TC. Xiong et al. [26] used MISPE method combined with flow-injection chemiluminescence (FI-CL) for the determination of residual TC in fish samples. Caro et al. [27] described for the first time the application of a MIP imprinted with tetracycline antibiotics to the direct extraction of TC and OTC from tissue sample extracts. Hu et al. [28] prepared and evaluated the solid phase microextraction fiber based on molecularly imprinted polymers for trace analysis of tetracyclines in complicated samples. But there is no work about the synthesis of the TC molecularly imprinted monolithic column and its application to real sample analysis.

In this work, using tetracycline (TC) as the template, methacrylic acid (MAA) as the functional monomer, ethylene glycol dimethacrylate (EGDMA) as the cross-linker, methanol as the solvent, cyclohexanol and dodecanol as the mixed porogenic solvents, a TC imprinted monolithic column was prepared by in situ molecular imprinting technique for the first time, and the optimal synthesis conditions and the selectivity of TC imprinted monolithic column were investigated. The interfering substances in food samples and TCs can be separated successfully on imprinted column. Further, a MISPE–HPLC procedure has been employed for determination of TCs by using the MIPs monolith as precolumn coupling the HPLC with C18 column. The results indicated that the method can be applied to the simultaneous multi-residue analysis of six TCs in the spiked milk and honey samples.

2. Experimental

2.1. Materials

TC and oxytetracycline (OTC) were purchased from Sigma (Steinheim, Germany), and minocycline (MINO), chlortetracycline (CTC), metacycline (MTC) and doxycycline (DTC) were purchased from National Institute for the Control of Pharmaceutical and Biological Products (Beijing, China). Sulfadiazine (SMD) was purchased from Sigma (Steinheim, Germany). EGDMA was purchased from Guangzhou Shuangjian Trade Ltd. (Guangzhou, China). MAA and 2,2′-azobisisobutyronitrile (AIBN) were purchased from Tianjin Chemical Reagent Company (Tianjin, China). Methanol and acetonitrile were purchased from Tianjin Concord Technology Co. Ltd.

(Tianjin, China). EGDMA was distilled and AIBN was recrystallized before use. Methanol and acetonitrile were HPLC grade. Other reagents were analytical grade.

2.2. Instrumentation

Analyses were performed on a Shimadzu LC-20A HPLC system (Shimadzu, Kyoto, Japan), consisting of two LC-20AD pumps, a diode array detector (SPD-M20A). The data were collected and analyzed using the LC solution software. The separation was performed on a Shimadzu VP-ODS column (5 μm particle size, 150 mm × 4.6 mm). The morphology of monolithic stationary phase was studied by a FEI QUANTA 200 scanning electron microscope (SEM). For the determination of the pore size distribution of the monolith, a Quantachrome N_2 Absorption–Desorption Analysis (Nova 2000e, America) was used.

2.3. Preparation and modification of TC imprinted monolithic columns

TC imprinted monolithic columns were prepared by in situ thermal polymerization method in a polar solvent for the first time. The template molecule TC (0.1 mmol), functional monomer MAA (0.8 mmol) were dissolved in a mixture of methanol (20 mmol) and the porogenic solvents (cyclohexanol and dodecanol), which has been indicated in Table 1. The mixture was surged ultrasonically for 30 min and swirled for 6 h, then cross-linker EGDMA and initiator AIBN (20 mg) were added into mixture solution. The solution was purged with N_2 for 15 min before pouring the polymerization mixture into the stainless steel column (100 mm × 4.6 mm I.D.) sealed with a dead nut at the bottom. The column was then sealed at the top and polymerization was thermally initiated at 60 °C in a water bath and allowed to continue for 12 h at this temperature. After the polymerization ended, the seal was removed, the column was connected to an HPLC pump and washed exhaustively with methanol to remove the template molecule, porogenic solvents and unreacted monomers. Final, washing with acetonitrile/acetic acid (94:6, v/v) ensured the removal of the template. The non-imprinted blank monolithic column was prepared in the same way in absence of the template in the reaction solution.

The TC MIP_1–MIP_{11} as imprinted monolithic column under different experimental condition combinations (template/monomer/cross-linker/porogenic solvent) used in the present study are summarized in Table 1.

2.4. HPLC conditions of the monolithic stationary phases

The retention factors (k') and the separation factor (α) were measured by injecting 100 μL of SMD (50 mg L^{-1}) and TC (50 mg L^{-1}) acetonitrile solutions separately onto each column. The mobile phases of MIP_1–MIP_9 were acetonitrile/acetic acid (98:2, v/v) at a flow rate of 0.5 mL min^{-1}, but the mobile phases of MIP_{10} and MIP_{11} were acetonitrile/acetic acid (96:4, v/v) at a flow rate of 0.3 mL min^{-1} and acetonitrile/acetic acid (90:10, v/v) at a flow rate of 0.1 mL min^{-1}, respectively. The detection wavelength was set at 270 nm (there is superposition in the UV absorbance of TC and SMD). Acetone was used as the unretained tracer to measure the void volume. All the procedures were carried out at the room temperature.

The retention factors (k') was determined by equation $k' = (t_R - t_0)/t_0$, where t_R and t_0 are the retention times of the solute and the void marker, respectively. The separation factor (α) was determined by $\alpha = k'_{TC}/k'_{SMD}$, where k'_{TC} and k'_{SMD} are the retention factors of TC and SMD, respectively.

2.5. Preparation and procedure for determination of food-based samples

Milk and honey were selected for the spiked sample analysis. A 10 mL volume of milk sample was added into a 50 mL polypropylene tube, and TCs mixed standard solutions, 40 mL 5% $HClO_4$ solution were also added. The mixed sample was shaken for 6 h. After the mixture was centrifuged for 10 min at 4000 rpm, the supernatant was filtered through a 0.22 μm filter. The filtrate was concentrated to 20 mL and stored in 4 °C for further work. The spiking concentrations for each TCs were set with four levels of 0.10, 0.50, 1.0 and 5.0 mg L^{-1}, respectively.

A 5 mL volume of honey sample was added into a 50 mL polypropylene tube, and TCs mixed standard solutions, 40 mL 5% $HClO_4$ solution were also added. The mixed sample was shaken for 6 h. After the mixture was centrifuged for 10 min at 4000 rpm, the supernatant was filtered through a 0.22 μm filter. The filtrate was concentrated to 15 mL and stored in 4 °C for further work. The spiking concentrations for each TCs were set with four levels of 0.10, 0.50, 1.0 and 5.0 mg L^{-1}, respectively.

The obtained sample solutions were passed through the TC imprinted or non-imprinted monolithic column in a stainless steel column (100 mm × 4.6 mm I.D.), using the mobile phase of methanol/acetonitrile (20:80, v/v) at a flow rate of 0.5 mL min^{-1}. Wavelength was set at 350 nm and 100 μL sample solution was injected every 4 min. After 20 injections, the monolithic column was eluted with acetonitrile/acetic acid (95:5, v/v) at a flow rate of 1.0 mL min^{-1}. The elutes were collected and evaporated under a stream of nitrogen and concentrated to required volume depending on the final TCs concentration. After the imprinted monolithic column as the purification process, 100 μL extracted food solution was injected into HPLC with C18 column. The analyses of sample were performed on Shimadzu LC-20A HPLC system under the gradient condition: acetonitrile/NaH_2PO_4 (pH = 3.00, 0.01 mol L^{-1}) (9:91, v/v) from 0 to 10 min, acetonitrile/NaH_2PO_4 (12:88, v/v) from 10 to 18 min, acetonitrile/NaH_2PO_4 (18:82, v/v) from 18 to 40 min; the flow rate was 2.0 mL min^{-1} and the detection wave-

Table 1
The optimization for preparation of TC imprinted monolithic stationary phases.

Polymer	Template (mmol)	Monomer (mmol)	EDMA (mmol)	AIBN (mg)	Methanol (mmol)	Cyclohexanol (g)	Dodecanol (g)
MIP_1	0.1	0.8	3.5	20	20	0.50	0.60
MIP_2	0.1	0.8	4.0	20	20	–	1.10
MIP_3	0.1	0.8	4.0	20	20	0.20	0.90
MIP_4	0.1	0.8	4.0	20	20	0.40	0.70
MIP_5	0.1	0.8	4.0	20	20	0.50	0.60
MIP_6	0.1	0.8	4.0	20	20	0.60	0.50
MIP_7	0.1	0.8	4.0	20	20	0.70	0.40
MIP_8	0.1	0.8	4.0	20	20	1.10	–
MIP_9	0.1	0.8	4.5	20	20	0.50	0.60
MIP_{10}	0.1	0.8	5.0	20	20	0.50	0.60
MIP_{11}	0.1	0.8	6.0	20	20	0.50	0.60

length was set at 350 nm (the maximal absorbance wavelength of TCs).

3. Results and discussion

3.1. Optimization of preparation conditions affecting the performance of molecularly imprinted monolithic stationary phases

The template TC has both hydrogen-bond donor and acceptor sites, the carboxylic group of MAA can form strong hydrogen bonds with hydroxyl and amide groups of TC (Fig. 2), so the TC imprinted monolithic column was prepared in chromatographic column based on non-covalent molecular imprinting technique. When attempting to fabricate monoliths with not only good imprinted efficiency but also optimized pore size distribution for a specific application, a number of factors have to be taken into account. These factors include the mol ratio of template and monomer, composition of pore forming solvent mixture and the content of cross-linker. Firstly, an appropriate mol ratio of template and monomer is considered to be very important [29]. In this work, the mol ratio of template and monomer was chosen 1:8 according to the former work [27]. We investigated the effect of solvent, porogen and cross-link degree to the retention factors k' and the separation factors α. The results were shown in Table 2.

The selection of the solvents is crucial for the preparation of the molecularly imprinted monolithic stationary phase, at least three requirements are met on the selection of the right solvent mixture. First, template molecule, initiator, monomer and cross-linker have to be soluble in the porogenic solvents. Second, the solvents should produce large pores, in order to assure good flow-through properties of the resulting polymers. Finally, the porogenic solvents should be of relatively low polarity, in order to reduce the interferences during complex formation between the imprint molecule and the monomer. It is thought that the polar-protic nature of the porogens used is very important to obtain high selectivity MIPs [30]. Porogenic solvents, i.e. cyclohexanol and dodecanol, toluene and dodecanol, toluene and isooctane, which have frequently been used in the preparation of monolithic stationary phases, were tested for their dissoluble capabilities. These investigations revealed that the template molecular could not be dissolved in it, so we had to add another solvent which can dissolve template molecule, initiator, monomer and cross-linker. We investigated the solvents such as methanol, acetonitrile, acetone, toluene and dimethylsulfoxide (DMSO) and found only the high polar solvent of methanol and the low polar porogenic solvents of cyclohexanol and dodecanol could fulfil all three requirements. The porogenic solvents methanol, cyclohexanol and dodecanol are used to prepare the TC imprinted monoliths in this work.

As shown in Table 2, the mass ratio of cyclohexanol and dodecanol also affects the separation performance through the changes in separation factor (α) and backpressure of the monolithic stationary phases. When the cross-link degree was 83.3% and the total

Table 2
Effect of polymerization conditions on separation performance of TC imprinted monolithic column.

Polymer	T:M:C[a] (mol ratio)	Cross-link degree[b]	C:D[c] (mass ratio)	k'	a
MIP_1	1:8:35	81.4%	5:6	0.60	4.50
MIP_2	1:8:40	83.3%	0:11	0.30	1.00
MIP_3	1:8:40	83.3%	2:9	1.17	2.62
MIP_4	1:8:40	83.3%	4:7	1.31	3.43
MIP_5	1:8:40	83.3%	5:6	2.82	8.00
MIP_6	1:8:40	83.3%	6:5	1.25	4.09
MIP_7	1:8:40	83.3%	7:4	0.56	1.45
MIP_8	1:8:40	83.3%	11:0	0.29	1.00
MIP_9	1:8:45	84.9%	5:6	1.36	8.64
MIP_{10}	1:8:50	86.2%	5:6	4.91	15.9
MIP_{11}	1:8:60	88.2%	5:6	3.00	17.6

[a] T:M:C where T stands for template, M stands for monomer and C stands for cross-linker.
[b] Cross-link degree stands for cross-linker content in monomer content mixture.
[c] C:D where C stands for cyclohexanol and D stands for dodecanol.

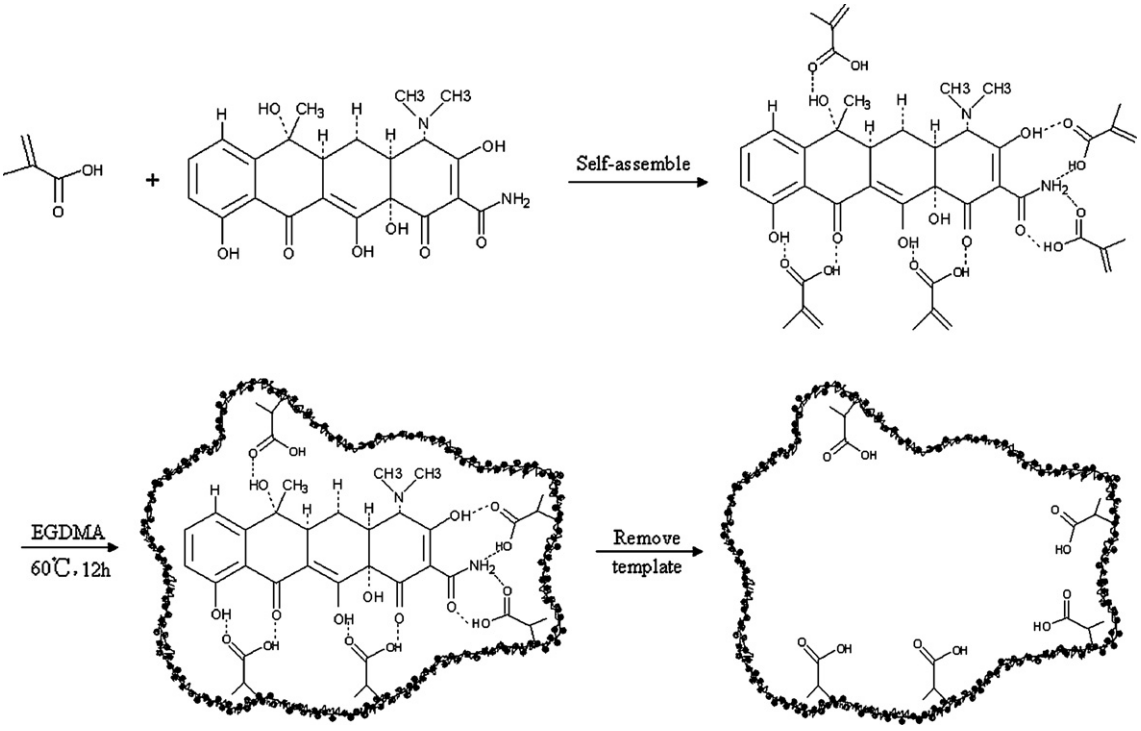

Fig. 2. Scheme of the synthesis route for TC MIPs.

quantity of porogenic solvents was 1.1 g, with the mass ratio of cyclohexanol and dodecanol changing in the range from 0:11 to 11:0, the separation factor α increased firstly and diminished subsequently, meanwhile the backpressure increased all along. When the mass ratio of cyclohexanol and dodecanol is increased from 0:11 (MIP_2) to 5:6 (MIP_5), the separation factor α increased from 1.00 to 8.00 and k' increased from 0.30 to 2.82. However, with the mass ratio increasing from 5:6 (MIP_5) to 7:4 (MIP_7), α and k' decreased from 8.00 to 1.45 and 2.82 to 0.56, respectively. When the mass ratio reached 5:6 (MIP_5) in the porogenic mixture, the resulting TC imprinted monolith had the highest separation factor ($\alpha = 8.00$). This behaviour is attributed to a balance between the requirements of low flow resistance and high separation factor (α). Finally, a sufficient solubility of the template molecule, a high separation factor ($\alpha = 8.00$) and appropriate backpressure of the column (4.0 MPa at 1.0 mL min^{-1} acetonitrile) were obtained under the optimal mass ratio 5:6 of cyclohexanol and dodecanol and used in TC imprinted monoliths preparation.

The amount of cross-linker plays a large role in the pore size distribution of the monoliths. It has been reported previously that the amount of cross-linker should be high enough not only to maintain the stability of the recognition sites and the recognition cavities in the polymerization, but also to have some extent of the flexibility make the template enter the cavities easily [7]. As shown in Table 2, the cross-link degrees of MIP_1, MIP_5, MIP_9–MIP_{11} were higher than 80%, and controlled at 81.4%, 83.3%, 84.9%, 86.2% and 88.2%, respectively. The backpressures of MIP monoliths were increased with increase of the cross-link degree. For example, when 1.0 mL min^{-1} acetonitrile was used as mobile phase, the backpressures of MIP_1, MIP_5, MIP_9 were 2.1, 4.0 and 10.6 MPa, respectively. Due to higher cross-link degree decreased the average pore size within the monolith, the backpressures of MIP_{10} and MIP_{11} were both larger than

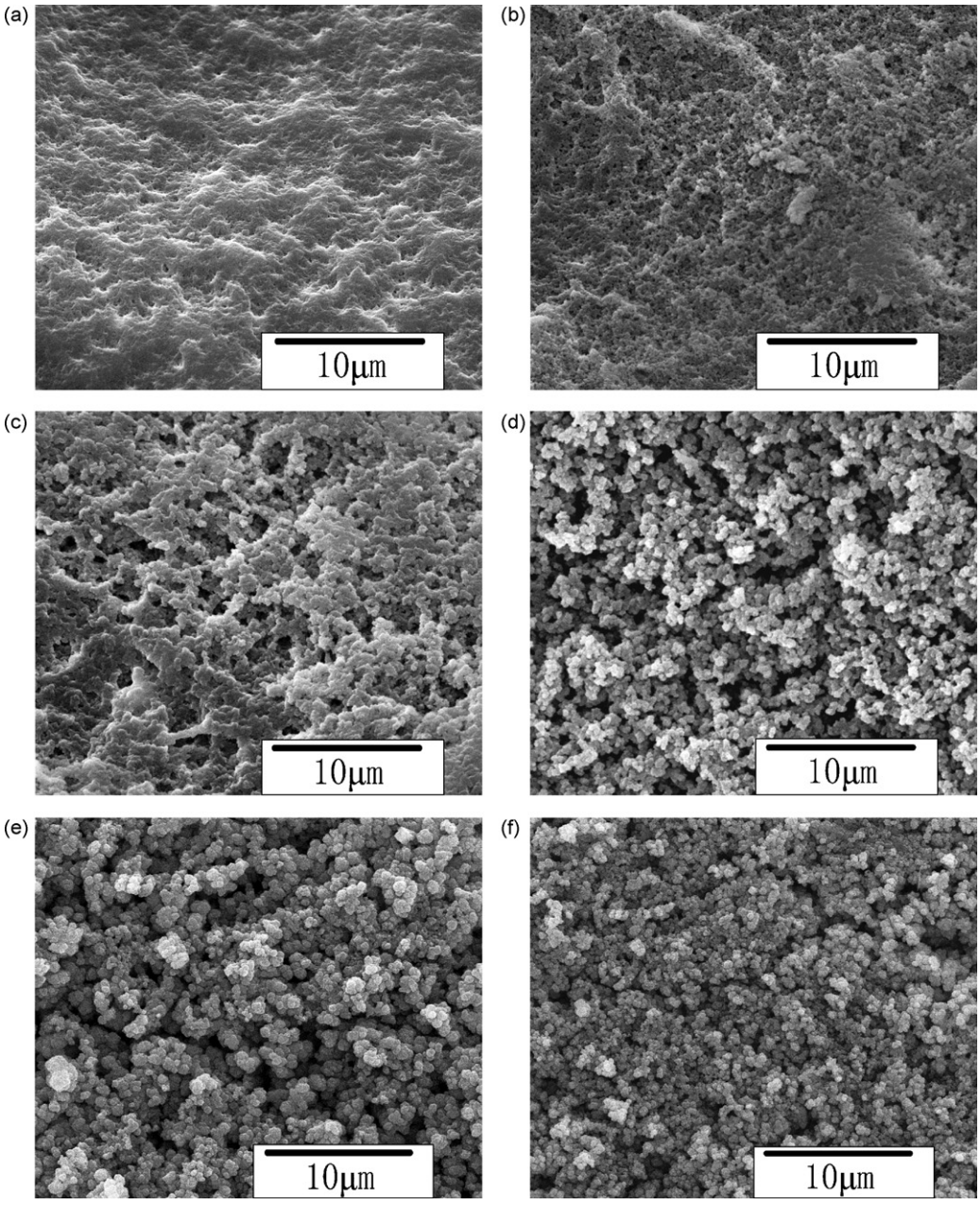

Fig. 3. Scanning electron microscope (SEM) images of TC imprinted monolithic columns MIP_{11} (a), MIP_{10} (b), MIP_9 (c), MIP_1 (d), MIP_5 (e) and non-imprinted monolithic column NIP_5 (f).

20.0 MPa, and only 0.3 and 0.1 mL min^{-1} acetonitrile were permitted to flow through MIP_{10} and MIP_{11}, respectively. The retention factors (k') of template and separation factors (α) of MIP_5, MIP_9 to MIP_{11} prepared under the optimal mass ratio 5:6 of cyclohexanol and dodecanol were larger than that of MIP_1. Under the same mobile phase, the separation factors of MIP_5 and MIP_9 were nearly same, but the backpressure of MIP_9 (10.6 MPa) was 2.5 times as that of MIP_5. Considering the requirements of low flow resistance and high separation factor (α), the cross-link degree of 83.3% was chosen for the best matrix of MIP monolith.

The SEM images of the molecularly imprinted monolithic stationary phases (MIP_1, MIP_5, MIP_9–MIP_{11}) prepared in the presence of the template molecule TC and NIP_5 (the non-imprinted blank monolithic column corresponding to MIP_5) are shown in Fig. 3. It can be seen that with increasing the cross-link degree, the pore diameter of monolithic stationary phases diminished clearly with increasing the cross-link degree and in comparing with NIP_5 the well-proportioned flow-through pores were embedded in the network skeleton of MIP_5. The result of the pore size distribution based on N_2 absorption–desorption analysis indicated that the average pore diameter is 25 nm.

3.2. Efficiency of the molecularly imprinted monolithic column

To evaluate the imprinting efficiency of the MIP monolith and to identify the influence of mobile composition on the retention time of TCs, HPLC analyses were performed. 200 mg L^{-1} six TCs acetonitrile solutions were analyzed at a flow rate of 0.5 mL min^{-1} under the mobile phase containing acetonitrile/acetic acid (97:3, v/v). The chromatograms of six TCs obtained on TC imprinted column showed the broadening and tailing phenomenon on the peaks of TCs. In comparison with TC imprinted column, almost no peak discrimination between TCs and acetone was observed on the non-imprinted blank column, which suggested that the recognition sites in the molecularly imprinted monolith originated from the molecular imprinting process because the imprinted recognition cavities in the MIP have complementary space and scheduled multiple interaction points, such as hydrogen bonding, to the TCs molecules. Furthermore, the retention times of six tetracyclines (TC, MINO, OTC, CTC, MTC and DTC) were identical due to their similar structures, which was shown in Fig. 4a.

The recognition of analytes in organic mobile phase is most likely due to the hydrogen bonding between template and polymer. A mobile phase containing polar substance acetic acid was used to weaken the binding of template to the MIP and to release it from the imprinting cavity of the stationary phase more quickly. The retention factors of the six TCs on the monolithic column (MIP_5) were investigated when the mobile phase change from pure acetonitrile to binary mixtures of acetonitrile and acetic acid. When the concentration of acetic acid in the mobile phase was lower than 0.2%, almost no peaks of TCs were detected, and the result indicated that TCs were held on the imprinted column. In detail, the effects of concentration of acetic acid in the range of 0.2–5% on the retention factors of the six TCs were studied, which were shown in Fig. 4b. As the concentration of acetic acid increased gradually, the retention factors of six TCs on the MIP decreased. The reason is that in organic media, the specific recognition of the MIPs monolith was acquired through the hydrogen bond interaction between the TCs molecule and the polymer. When amount of acetic acid in the mobile phase increased from 0.2 to 5%, the strong polar molecule would compete against TCs for forming hydrogen bond with the carboxyl group on the recognition sites of MIP monolith, which resulted in the retention factors of TCs decreasing greatly. In order to enhance the column efficiency of MIP, gradient elution was also used to shorten the elution times as well as improve the peak shapes of analytes (Fig. 5a).

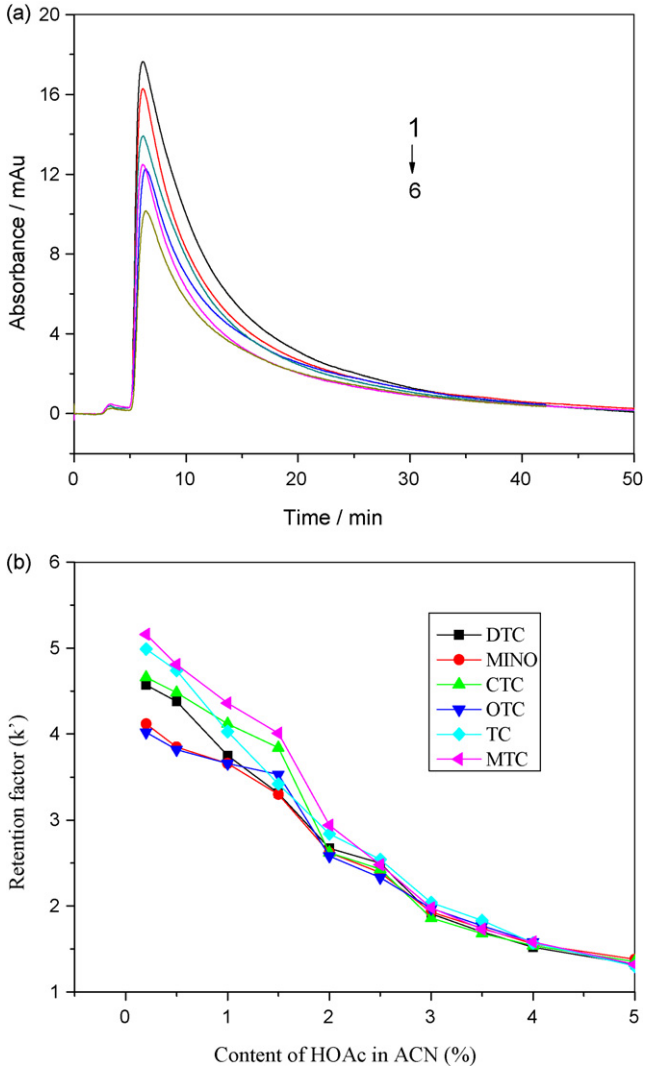

Fig. 4. Chromatograms of 200 mg L^{-1} six TCs acetonitrile solution on TC imprinted monolithic column (a). Mobile phase: acetonitrile/acetic acid (97:3, v/v) at a flow rate of 0.5 mL min^{-1}; detection wavelength: 350 nm. Peak designation: OTC (1); DTC (2); MINO (3); TC (4); CTC (5); MTC (6). Effect of the content of acetic acid in acetonitrile mobile phase on the retention factors of six TCs (b).

In order to evaluate the dynamic binding capacities of TCs on imprinted monolithic column, breakthrough curves of six TCs on imprinted monolith were investigated. As shown in Fig. 5b, the dynamic binding capacities of six compounds at 10% breakthrough were similar, while the phenomenon proved that the special molecular imprinting process made the TC imprinted column have similar binding capacities to six TCs.

Because of the food matrix complexity, an exhaustive pre-treatment of the sample is always required. The use of a selective sorbent such as a MIP can be very useful to obtained cleaner chromatographs. In this work, as the tool of sample pre-treatment, the interfering substances in milk or honey samples and TCs can be separated successfully on the TC imprinted monolithic column. The mobile phase containing polar substance acetic acid and gradient elution conditions were optimized. The chromatograms of separation of the interfering substances in milk or honey and TCs were obtained under the following condition: methanol/acetonitrile (20:80, v/v) from 0 to 4 min at a flow rate of 0.5 mL min^{-1}, then acetonitrile/acetic acid (95:5, v/v) from 4 to 40 min at a flow rate of 1.0 mL min^{-1}, which was shown in Fig. 6. The chromatogram on

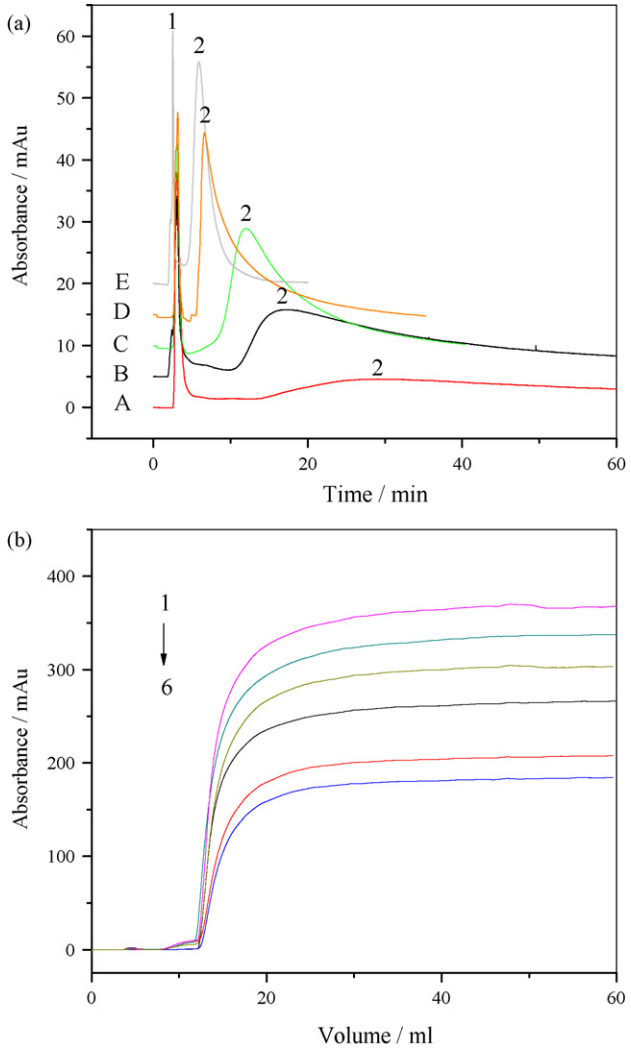

Fig. 5. Chromatograms of SMD and TCs on TC imprinted monolithic column using different gradient conditions (a). Gradient conditions: from 0 to 4 min acetonitrile at a flow rate of 0.5 mL min^{-1}, after 4 min acetonitrile/acetic acid (99:1, v/v) at a flow rate of 0.5 mL min^{-1} (A); acetonitrile/acetic acid (95:5, v/v) at a flow rate of 0.5 mL min^{-1} (B), 1.0 mL min^{-1} (C), 1.5 mL min^{-1} (D) and 2.0 mL min^{-1} (E). Samples: 100 μL of 50 mg L^{-1} SMD and six TCs acetonitrile solutions; detection wavelength: 270 nm. Peak designation: SMD (1); TCs (2). Breakthrough curves of the six TCs on TC imprinted monolithic column at a flow rate of 0.5 mL min^{-1} (b). 10 mg L^{-1} of six TCs acetonitrile solutions were employed for breakthrough analysis. OTC (1); DTC (2); MINO (3); TC (4); CTC (5); MTC (6).

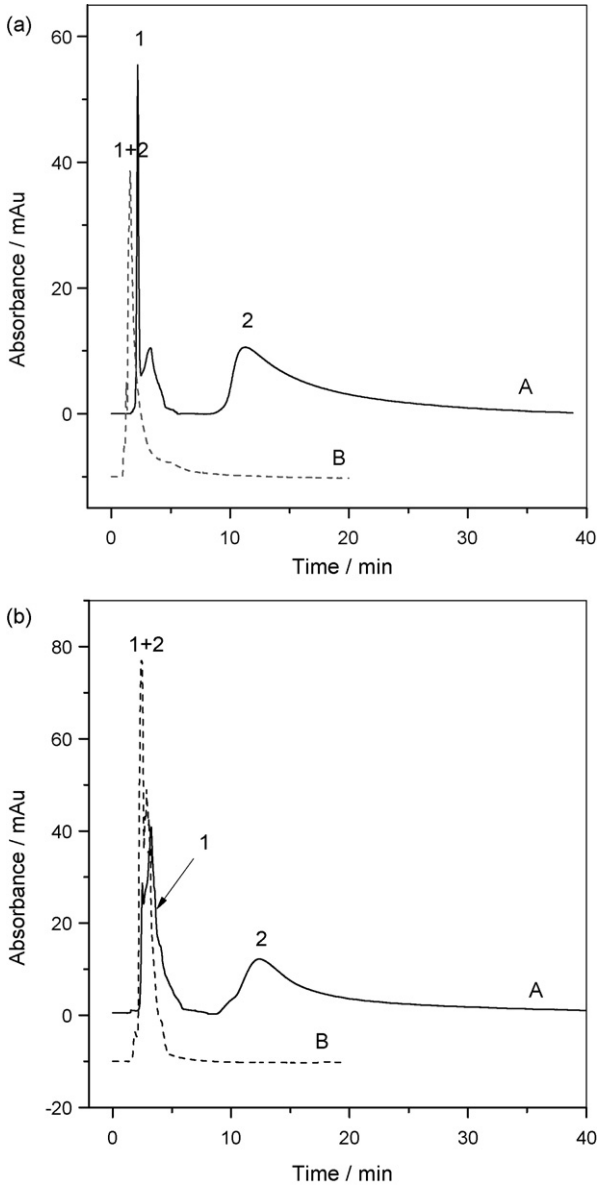

Fig. 6. Chromatograms of the interfering substances and TCs in milk (a) and in honey (b) were obtained by TC imprinted (A) and non-imprinted (B) monolithic column, respectively. Gradient condition: methanol/acetonitrile (20:80, v/v) from 0 to 4 min at a flow rate of 0.5 mL min^{-1}, then acetonitrile/acetic acid (95:5, v/v) from 4 to 40 min at a flow rate of 1.0 mL min^{-1}. Samples: 100 μL 5% $HClO_4$ extracted milk or honey solutions spiked with 30 mg L^{-1} (MINO, TC, OTC, CTC, MTC, DTC); detection wavelength: 350 nm. Peak designation: interfering substances (1); TCs (2).

the non-imprinted blank column was compared with that of MIP column under the same chromatographic condition. It can be seen that the interfering substances in milk or honey and TCs can be separated completely on imprinted column, but not be separated on non-imprinted column.

These results indicated that when spiked food sample solutions were passed through the imprinted monolithic column using the mobile phase without acetic acid, the TCs in samples were adsorbed on the imprinted column while the interfering substances were eluted following the mobile phase in a short time. Using continuous injection every 4 min, the TCs of every injection were selectively adsorbed on the imprinted column, then eluted with acetonitrile/acetic acid (95:5, v/v). The purpose of selective extraction for TCs in food samples can be obtained by collecting elutes. The simple MISPE method was employed as pre-treatment of the sample in this work.

3.3. Determination of TCs in milk and honey

The applicability of the imprinted monolithic column as the pre-column for solid phase extraction of six TCs compounds coupling with C18 column on determination of trace TCs in milk and honey was evaluated. 0.01 mol L^{-1} NaH_2PO_4 solution containing acetonitrile was selected as the mobile phase in this work, the influences of mobile composition on the retentions of six TCs were investigated and the separation conditions of six TCs were optimized.

The effects of pure 0.01 mol L^{-1} NaH_2PO_4 solution containing different concentrations of acetonitrile in the range of 5–40% (v/v) on the retentions of six TCs were investigated. The retention times of six TCs decreased by increasing the concentration of acetonitrile in the mobile phase. The effect of the pH value of 0.01 mol L^{-1} NaH_2PO_4 solution on retention times and resolution factors in the

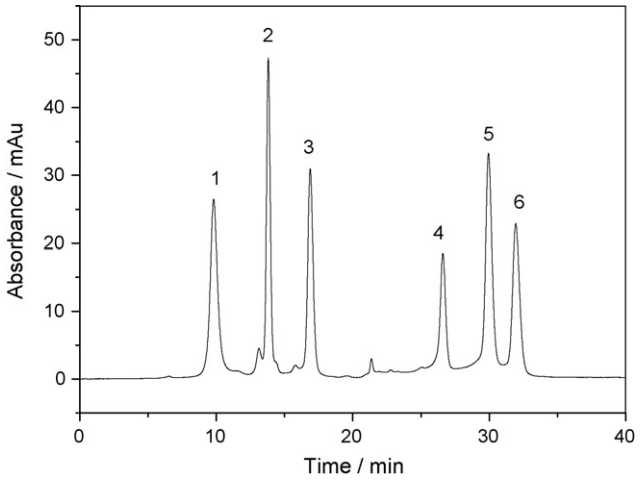

Fig. 7. Chromatogram of the six TCs on C18 analytical column. Samples: 100 μL of 10 mg L^{-1} (MINO, OTC, TC, CTC, MTC and DTC) mixture solutions; detection wavelength: 350 nm. Peak designation: MINO (1); OTC (2); TC (3); CTC (4); MTC (5); DTC (6).

range of pH 2.00–4.50 (the low pH was needed for keeping TCs stable) was also investigated. The results showed that the pH value of the mobile phase did not greatly affect the retentions of TCs, and pH 3.00 was selected in the HPLC analyses. Furthermore, the gradient elution was also used to shorten the analytical time. The typical chromatogram of separation of the six TCs was shown in Fig. 7 using the gradient condition as follow: acetonitrile/NaH_2PO_4 (pH = 3.00, 0.01 mol L^{-1}) (9:91, v/v) from 0 to 10 min, acetonitrile/NaH_2PO_4 (12:88, v/v) from 10 to 18 min, acetonitrile/NaH_2PO_4 (18:82, v/v) from 18 to 40 min; the flow rate was 2.0 mL min^{-1}.

The calibration curves were drawn for quantitative determination of six TCs. The linear equation, linear range and detection limit were shown in Table 3. The linearity for six TCs was determined by injecting of 100 μL standard solutions of these compounds. The calibration curves showed a range of linearity between 0.050 and 10 mg L^{-1} for six TCs. The higher linear regression coefficients ($r > 0.9996$) were obtained for all tested analytes. The detection limits (S/N = 3) of the MINO, OTC, TC, CTC, MTC and DTC are 16.7, 10.2, 16.1, 18.8, 15.0 and 17.3 μg L^{-1}, respectively.

The determination of TCs in milk and honey samples was investigated using TC monolithic column coupling the C18 analytical column. The chromatograms of spiking food samples before and after treated by MISPE in comparison with NISPE are shown in Fig. 8. It can be seen there are many peaks of the interfering substances in food samples and the peaks of six TCs are unclear for 5% $HClO_4$ extracted sample solution due to matrix complexity (chromatogram D in Fig. 8). After treated by MISPE, the significant interference from food components is eliminate, thus quantification of the six TCs can be successfully achieved. It can be seen from Fig. 8, the sensitivities of six TCs in spiked milk and honey sample were greatly enhanced with MIP monolithic column-HPLC (chromatogram A in Fig. 8). The MISPE possessed extraction efficiency much higher than that of the NISPE for six TCs (chromatogram B in Fig. 8). The spiking concentration for each TCs was set with four levels of 0.10, 0.50, 1.0 and 5.0 mg L^{-1} using standard addition method and the recoveries of six TCs in the food samples were shown in Table 4, The recoveries of six TCs in the spiked milk and honey samples were 73.3–90.6%, 62.6–82.3%, respectively. The results indicated that the TC imprinted monolithic column could be applied for selective determination of trace TCs in compli-

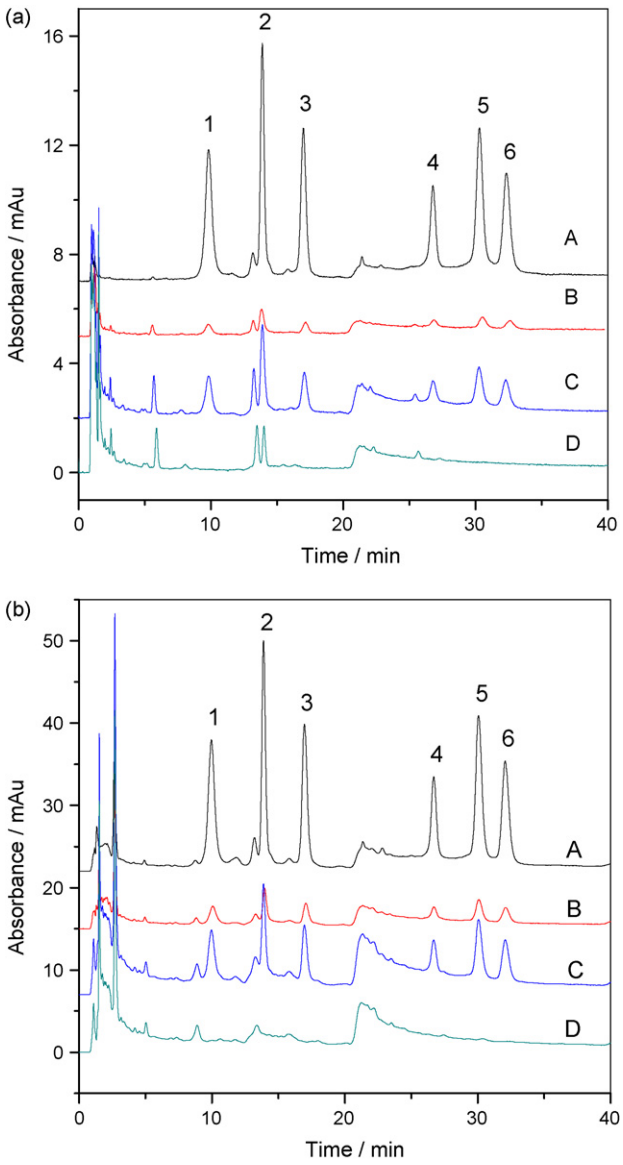

Fig. 8. Chromatograms of six TCs in spiked sample solutions with TC imprinted and non-imprinted monolithic column by injection volume of 100 μL. 1.0 mg L^{-1} and 2.0 mg L^{-1} TCs was spiked for milk (a) and honey (b) sample, respectively. Spiked sample solution extracted with imprinted column (A) and non-imprinted column (B), TCs spiked sample solution (C) and 5% $HClO_4$ extracted sample solution (D). Peak designation: MINO (1); OTC (2); TC (3); CTC (4); MTC (5); DTC (6).

Table 3
Regression analysis of calibration curves and detection limits of six tetracyclines.

Tetracyclines	Regression equation	r	Linear range (mg L^{-1})	Detection limit (μg L^{-1})
MINO	$Y = -6.46 \times 10^3 + 1.06 \times 10^5 X$	0.9999	0.050–10	16.7
OTC	$Y = 1.09 \times 10^3 + 1.29 \times 10^5 X$	0.9998	0.050–10	10.2
TC	$Y = -6.48 \times 10^3 + 1.06 \times 10^5 X$	0.9998	0.050–10	16.1
CTC	$Y = -8.61 \times 10^3 + 8.73 \times 10^4 X$	0.9997	0.050–10	18.8
MTC	$Y = -1.22 \times 10^4 + 1.32 \times 10^5 X$	0.9997	0.050–10	15.0
DTC	$Y = -8.40 \times 10^3 + 9.03 \times 10^4 X$	0.9996	0.050–10	17.3

Table 4
Recoveries of six TCs for spiked milk and honey samples ($n = 5$).

Compounds	Milk								Honey							
	0.10 mg L^{-1}		0.50 mg L^{-}		1.0 mg L^{-1}		5.0 mg L^{-1}		0.10 mg L^{-1}		0.50 mg L^{-}		1.0 mg L^{-}		5.0 mg L^{-1}	
	Recovery	RSD	Recovery	RSD	Recovery	RSD	Recovery	RSD	Recovery	RSD	Recovery	RSD	Recovery	RSD	Recovery	RSD
MINO	75.5	7.1	78.8	4.6	80.4	5.7	81.7	3.6	62.6	8.7	66.5	6.9	72.4	5.8	76.1	6.3
OTC	76.2	6.5	77.8	5.3	82.6	3.5	83.2	2.5	64.8	9.3	68.3	7.4	74.1	6.1	78.8	5.4
TC	73.3	5.4	84.5	6.2	90.5	4.3	89.0	3.8	71.2	6.7	74.6	6.1	80.1	4.6	82.3	4.5
CTC	73.7	8.9	77.3	7.1	84.7	5.1	83.8	3.5	69.2	9.5	71.1	7.6	76.5	6.3	79.6	5.2
MTC	75.8	8.1	81.6	7.4	89.9	6.8	90.6	5.2	68.7	8.3	70.4	7.1	79.3	6.8	78.2	5.8
DTC	74.4	6.4	80.9	6.8	84.9	5.3	84.8	4.1	69.4	8.1	71.4	6.2	79.8	5.3	76.5	5.1

cated samples. Furthermore, the characteristics of the TC imprinted monolithic column are stable when used near two years (used approximately 200 times).

4. Conclusions

In this work, the TC imprinted monolithic column was directly prepared in a stainless steel column by in situ polymerization for the first time using MAA and EGDMA as the monomer and cross-linker, respectively. The obtained monolithic column showed good flow-through property and selectivity for six TCs. Thus, a method for quantitative determination of TCs in milk and honey samples was successfully developed by using the monolithic column as the precolumn for solid phase extraction of six TCs compounds, such as MINO, TC, OTC, CTC, MTC and DTC. While a commercial C18 column was adopted as the analytical column to couple with MIP-precolumn, the effective analysis of the TCs at low concentration level in the real samples as complex as milk and honey can be achieved.

Acknowledgements

The authors gratefully appreciate the financial support by Hi-Tech Research and Development Program of China (863 Program, Nos. 2007AA10Z432 and 2006AA10Z438), the National Natural Science Foundation of China (grant numbers: 20675040 and 20875050), National Basic Research Program of China (No. 2007CB914100) and the Natural Science Foundation of Tianjin (grant number: 07JCYBJC00500).

References

[1] C. Baggiani, L. Anfossi, C. Giovannoli, Anal. Chim. Acta 591 (2007) 29.
[2] T.H. Jiang, L.X. Zhao, B.L. Chu, Q.Z. Feng, W. Yan, J.M. Lin, Talanta 78 (2009) 442.
[3] F. Puoci, M. Curcio, G. Cirillo, F. Iemma, U.G. Spizzirri, N. Picci, Food Chem. 106 (2008) 836.
[4] B. Boyd, H. Björk, J. Billing, O. Shimelis, S. Axelsson, M. Leonora, E. Yilmaz, J. Chromatogr. A 1174 (2007) 63.
[5] F.G. Tamayo, E. Turiel, A. Martín-Esteban, J. Chromatogr. A 1152 (2007) 32.
[6] B. Sellergren, F. Lanza, in: B. Sellergren (Ed.), Molecularly Imprinted Polymers: Man-made Mimics of Antibodies and their Applications in Analytical Chemistry, Elsevier Science, Amsterdam, Netherlands, 2001, pp. 355–375.
[7] G. Wulff, Angew. Chem. Int. Ed. 34 (1995) 1812.
[8] K. Haupt, A. Dzgoev, K. Mosbach, Anal. Chem. 70 (1998) 628.
[9] H. Zhang, L. Ye, K. Mosbach, J. Mol. Recognit. 19 (2006) 248.
[10] G. Wulff, Chem. Rev. 102 (2002) 1.
[11] K. Haupt, K. Mosbach, Chem. Rev. 100 (2000) 2495.
[12] J. Matsui, T. Kato, T. Takeuchi, M. Suzuki, K. Yokoyama, E. Tamiya, I. Karube, Anal. Chem. 65 (1993) 2223.
[13] J.J. Ou, L.H. Hu, L.G. Hu, X. Li, H.F. Zou, Talanta 69 (2006) 1001.
[14] H.W. Sun, F.X. Qiao, G.Y. Liu, J. Chromatogr. A 1134 (2006) 194.
[15] P. Pruim, M. Öhman, Y.L. Huo, P.J. Schoenmakers, W.T. Kok, J. Chromatogr. A 1208 (2008) 109.
[16] X.L. Dong, R.A. Wu, J. Dong, M.H. Wu, Y. Zhu, H.F. Zou, J. Chromatogr. B 875 (2008) 317.
[17] Commission Regulation No. 2377/90, Off. J. Eur. Commun. (18 August 1990) No. L224.
[18] U.S. Code of Federal Regulations, Title 21, Part 556, Sections 150, 500, and 720, US Government Printing Office, Washington DC, 2003 (Chapter 1).
[19] S. O'Connor, D.S. Aga, Trends Anal. Chem. 26 (2007) 456.
[20] H. Oka, Y. Ito, H. Matsumoto, J. Chromatogr. A 882 (2000) 109.
[21] C.R. Anderson, H.S. Rupp, W.H. Wu, J. Chromatogr. A 1075 (2005) 23.
[22] F.J. Schenck, P.S. Callery, J. Chromatogr. A 812 (1998) 99.
[23] W.S. Cai, R.B. Gupta, Sep. Purif. Technol. 35 (2004) 215.
[24] F. Trotta, C. Baggiani, M.P. Luda, E. Drioli, T. Massari, J. Membr. Sci. 254 (2005) 13.
[25] R. Suedee, T. Srichana, T. Chuchome, U. Kongmark, J. Chromatogr. B 811 (2004) 191.
[26] Y. Xiong, H.J. Zhou, Z.J. Zhang, D.Y. He, C. He, Analyst 131 (2006) 829.
[27] E. Caro, R.M. Marcé, P.A.G. Cormack, D.C. Sherrington, F. Borrull, Anal. Chim. Acta 552 (2005) 81.
[28] X.G. Hu, J.L. Pan, Y.L. Hu, Y. Huo, G.K. Li, J. Chromatogr. A. 1188 (2008) 97.
[29] S.L. Moullec, A. Bégos, V. Pichon, B. Bellier, J. Chromatogr. B 850 (2007) 24.
[30] X.D. Huang, H.F. Zou, X.M. Chen, Q.Z. Luo, L. Kong, J. Chromatogr. A 984 (2003) 273.

Talanta 79 (2009) 562–569

Contents lists available at ScienceDirect

Talanta

journal homepage: www.elsevier.com/locate/talanta

Type I collagen-mediated synthesis of noble metallic nanoparticles networks and the applications in Surface-Enhanced Raman Scattering and electrochemistry

Yujing Sun[a,b], Lanlan Sun[a,b], Baohua Zhang[a,b], Fugang Xu[a,b], Zhelin Liu[a,b], Cunlan Guo[a,b], Yue Zhang[a,b], Zhuang Li[a,*]

[a] State Key Laboratory of Electroanalytical Chemistry, Changchun Institute of Applied Chemistry, Chinese Academy of Science, Changchun 130022, Jilin, People's Republic of China
[b] Graduate School of the Chinese Academy of Sciences, Beijing 100039, People's Republic of China

ARTICLE INFO

Article history:
Received 9 January 2009
Received in revised form 9 April 2009
Accepted 12 April 2009
Available online 22 April 2009

Keywords:
Type I collagen
Template
Noble metallic nanoparticles
Networks
SERS
Electrocatalysis

ABSTRACT

In this paper, we demonstrated an effective enviromentally friendly synthesis route to prepare noble metallic (Au, Ag, Pt and Pd) nanoparticles (NPs) networks mediated by type I collagen in the absence of any seeds or surfactants. In the reactions, type I collagen served as stabilizing agent and assembly template for the synthesized metallic NPs. The hydrophobic interaction between collagen and mica interface as well as the hydrogen bonds between inter- and intra-collagen molecules play important roles in the formation of collagen–metallic NPs networks. The noble metallic NPs networks have many advantages in the applications of Surface-Enhanced Raman Scattering (SERS) and electrochemistry detection. Typically, the as-prepared Ag NPs networks reveal great Raman enhancement activity for 4-ATP, and can even be used to detect low concentration of DNA base, adenine, without any label step. Furthermore, the cyclic voltammograms showed Pt NPs networks have good electrocatalytic ability for the reduction of O_2.

1. Introduction

Materials composed of multi-dimensional ensembles of nanoparticles (NPs) are becoming more and more important in material science and analytical science fields. Porous network nanostructures have attracted much attention due to their enhanced optical, catalytic, SERS and magnetic properties. For example, three-dimensional (3D), highly ordered porous gold and Ag films greatly enhanced SERS signals [1,2]. Ionic liquids-stabilized Pt NPs 2D networks showed good electrocatalytic ability to O_2 [3]. Fe nanostructured magnetic networks revealed enhancement in the coercivity [4]. On the other hand, noble metallic NPs are unique supports for the study of biomolecules because of the size compatibility, chemical inertness and high dispersibility in aqueous solutions. It is necessary to investigate the synthesis and assembly of noble metallic NPs to form network-like nanostructures and the applications in analytical sciences.

There are two conventional strategies that can be used to fabricate the network-like nanostructures. The first strategy is the non-template synthesis. This strategy requires comparatively exotic processing technologies such as electron-beam lithography [5] or nanosphere lithography [6], sputtering technology [4], laser ablation technology [7]. So it was limited by the relatively high cost of fabrication and low surface area of the metal structure. The other strategy is the template synthesis, which is an elegant chemical approach for the fabrication of nanostructures, in particular for the preparation of diverse network-like nanomaterials.

Commonly used sacrificial template silica or polymer microspheres and porous anodic aluminum oxide (AAO) are called hard templates [1,8,9]. This kind of templates has several advantages, such as long-range periodic structures and ordered metal nanostructures with adjustable pore size. However, the defects also obviously exist. The diversity of template material is limited, the preparative process is complex due to the requirement of building blocks with superior quality and advanced features, and it is difficult to control the infiltration of the desired composite metals into the interstitial voids. The other kind of building blocks is called soft templates, such as biomacromolecules, polymers, ionic liquids, micelle systems, and so on. Among that, biomolecules as templates to synthesize network-like nanostructures have attracted increasing attention due to their easily assembly, controllable dimensions, large surface area, low cost and environmentally benign. Various biomolecules were used to synthesize and assemble porous or fibrous inorganic materials with unique pore or surface structures, like DNA [10–12], proteins or peptides [13,14], viruses [15,16] as well as carbohydrates [17].

In this work, for the first time we reported the preparation of 2D Au, Ag, Pt, and Pd NPs networks using type I collagen molecules

* Corresponding author. Tel.: +86 431 5262057; fax: +86 431 5262057.
E-mail address: zligroup@yahoo.com.cn (Z. Li).

0039-9140/$ – see front matter © 2009 Elsevier B.V. All rights reserved.
doi:10.1016/j.talanta.2009.04.027

as a medium without adding seeds or surfactants. Firstly, type I collagen is an abundant structural protein in the extracellular matrix (ECM) of animals, could satisfy the "green synthesis" requirement. Secondly, this method is quite facile, rapid and inexpensive. The reported DNA network template methods cost higher because they need oligonucleotides with special bases sequence and took longer time than collagen-mediated method [11,12]. Type I collagen–nanohydroxyapatite biocomposite scaffolds can prepare by electrostatic cospinning, but this method required precision instrument [13]. We have reported some research about the type I collagen assembled Ag NPs films [18,19]. Here, this article is intended to make a more effective wet-chemical route to synthesis four noble metallic NPs networks. These prepared noble metallic nanostructures have potential applications in SERS detection and electrochemistry. Typically, the as-prepared Ag NPs networks including lots of nanoscale pores and NPs aggregations effectively enhance the SERS signals, and can detect low concentration of DNA bases without any labeling step. The Pt NPs networks consist of many small Pt NPs, have large surface area to volume and show good electrocatalytic activity for O_2 reduction.

2. Experimental section

2.1. Chemicals and materials

Type I collagen from calf skin (cell culture tested, acid soluble) and 4-aminothiophenol (4-ATP) were supplied by Sigma–Aldrich (U.S.A.). Acetic acid (CH_3COOH, A.R.), $HAuCl_4$, H_2PtCl_6 and $PdCl_2$ were obtained from Beijing Chemical Co. (Beijing, China). $AgNO_3$ (A.R.) and sodium borohydride (A.R.) were bought from Shanghai Sangon Biological Engineering Technology & Services CO., Ltd. (Shanghai, China). 100 ng/μL type I collagen was obtained by dissolving 1 mg collagen in 100 mL 0.2 M acetic acid. 56.4 mM H_2PdCl_4 solution was obtained by the following steps, 1 g $PdCl_2$ was dissolved in 36 mL of 0.2 M aqueous HCl solution and then diluted to a 100 mL volume with ultrapure water. All of these chemicals and materials were used without further purification. Quartz wafers were cleaned by being immersed in a slightly boiling piranha solution (7:3 mixture of 98% H_2SO_4 and 30% H_2O_2) for 40 min and then rinsed with copious amounts of water. The water used in the whole experiment was ultrapure water (18 MΩ cm) from Milli-Q system.

2.2. Synthesis

1 mL type I collagen (100 ng/μL) was added into 10 mL of $HAuCl_4$ (1.0 mM and 0.5 mM, respectively), and vigorously stirred for 10 min. After that, 10 mM $NaBH_4$ solution was added dropwise slowly under strongly stirring, until the color of colloid was unchanged. The final Au colloid was wine red. H_2PtCl_6 (0.5 mM), H_2PdCl_4 (0.5 mM) and $AgNO_3$ (0.5 mM) were used to prepare colloids by the same experimental steps.

2.2.1. Control experiment

10 mM $NaBH_4$ solution was added into 10 mL 0.5 mM $HAuCl_4$ dropwise slowly under strongly stirring until the color was unchanged, without adding collagen solution. 30 μL of each colloid was dropped onto the Si wafers immediately and dried in the air.

2.2.2. Comparison experiment

For comparison, the citric-capped Ag NPs were prepared as the typical method reported by Lee and Meisel [20]. In brief, 9 mg $AgNO_3$ was dissolved in 50 mL H_2O and brought to boiling, a solution of 1% sodium citrate (1 mL) was added rapidly. The solution was kept on boiling for approximately 1 h. A SERS substrate was prepared by dropping 30 μL of Ag colloid onto freshly cleaved mica.

2.3. Instruments

UV–vis absorbance spectra were measured with a CARY 50 Conc UV–vis spectrometer (Varian, U.S.A.). The scanning electron microscopy (SEM) images and energy-dispersive spectroscopy (EDS) were produced by an XL30ESEM FEG field emission scanning electron microscopy (SEM, FEI Company with 20 KV operating voltage). TEM measurement was made on a JEOL 2000 transmission electron microscope operated at an accelerating voltage of 200 kV. Fourier transform infrared (FT-IR) spectra were obtained on a Bruker IFS66 V spectrometer equipped with a DGTS detector, recording with a resolution of 4 cm^{-1}. The X-ray photoelectron spectra (XPS) were performed on an ESCLAB MK II instrument using Mg as the exciting source. The charging calibration was performed by referring the C 1s to the binding energy at 284.6 eV. The operating pressure in the analysis chamber was below 10^{-9} torr with an analyzer pass energy of 50 eV. The SERS spectra were collected by a Renishaw 2000 model confocal microscopy Raman Spectrometer with an air-cooled charge coupled device (CCD) and a holographic notch filter (Renishaw Ltd., Gloucestershire, U.K.). And the excitation line was 514.5 nm produced by Ar ion laser. Cyclic voltammetry was performed with CHI 660A electrochemical workstation (CH Instrument Co., U.S.A.) in a conventional three-electrode electrochemical cell with the Pt nanostructure modified ITO as working electrode, a platinum foil as counter electrode, and KCl-saturated Ag/AgCl as reference electrode. The Pt NPs network modified ITO electrode was prepared by placing a drop of colloidal solution on an ITO surface and dried in the air.

3. Results and discussion

3.1. Preparation and characterization of the type I collagen-mediated Au nanostructures

3.1.1. The effect of $HAuCl_4$ concentration on the formation of collagen-mediated Au nanostructures

UV–vis absorption spectra have been proved to be very sensitive to the formation of Au and Ag NPs. Fig. 1 shows the UV–vis absorption spectra of type I collagen solution, $HAuCl_4$ solution, the mixture of collagen and $HAuCl_4$ solution, and the obtained Au col-

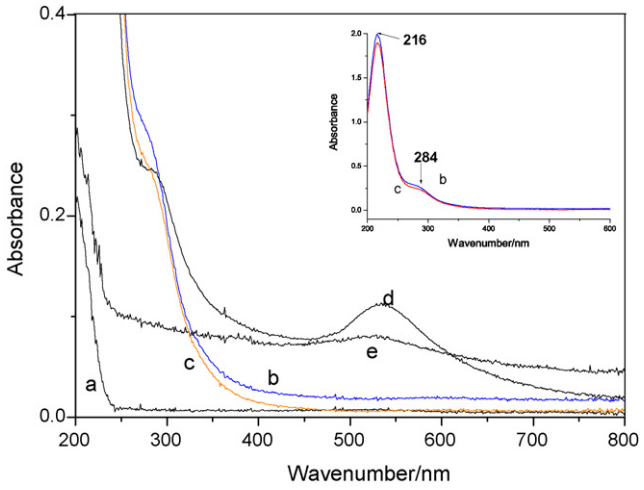

Fig. 1. UV–vis absorbance spectral monitored (a) type I collagen solution, (b) $HAuCl_4$ solution, (c) the mixture of collagen and $HAuCl_4$ solution, (d) the prepared Au colloids by 1.0 mM, and (e) 0.5 mM $HAuCl_4$.

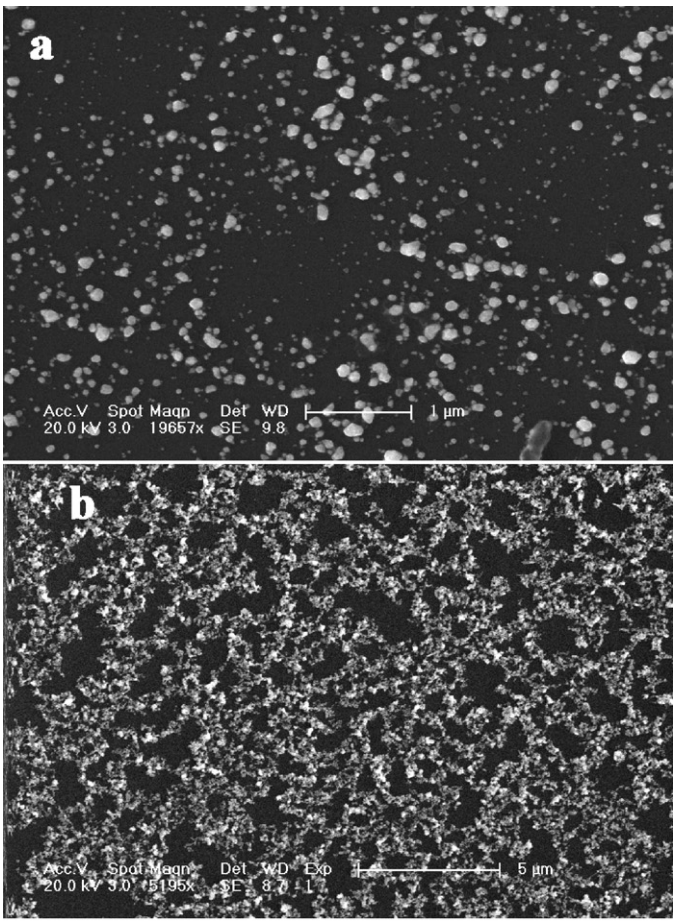

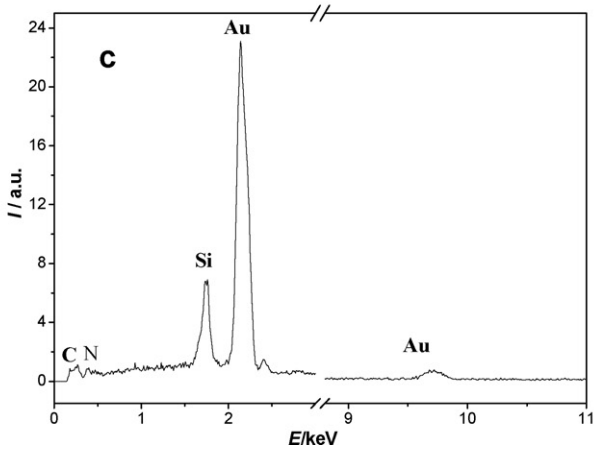

Fig. 2. FE-SEM images of Au nanostructures, corresponding to Fig. 1d (A), and Fig. 1e (B), (c) the EDX analysis of B.

loids from different ratios of the mixture. Type I collagen has no obvious adsorption in the measured band range (curve a). Two peaks at 216 and 284 nm exhibit the present of $AuCl_4^-$ ions in aqueous $HAuCl_4$ and in the mixture of collagen and $HAuCl_4$ solution (curve b and c in the inset image) [21]. When the collagen concentration was 1.0 mM, and the $AuCl_4^-$/collagen mixed solution was reduced by $NaBH_4$, the peak at 284 nm fell down, meanwhile the peak at around 533 nm occurred, which indicated the formation of Au NPs in the mixed solution (curve d) [20] and the corresponding SEM image was shown in Fig. 2A. It can be seen that inhomogeneous Au NPs appear on the substrate. When the collagen concentration was 0.5 mM, the UV–vis absorption peak occurred at 525 nm

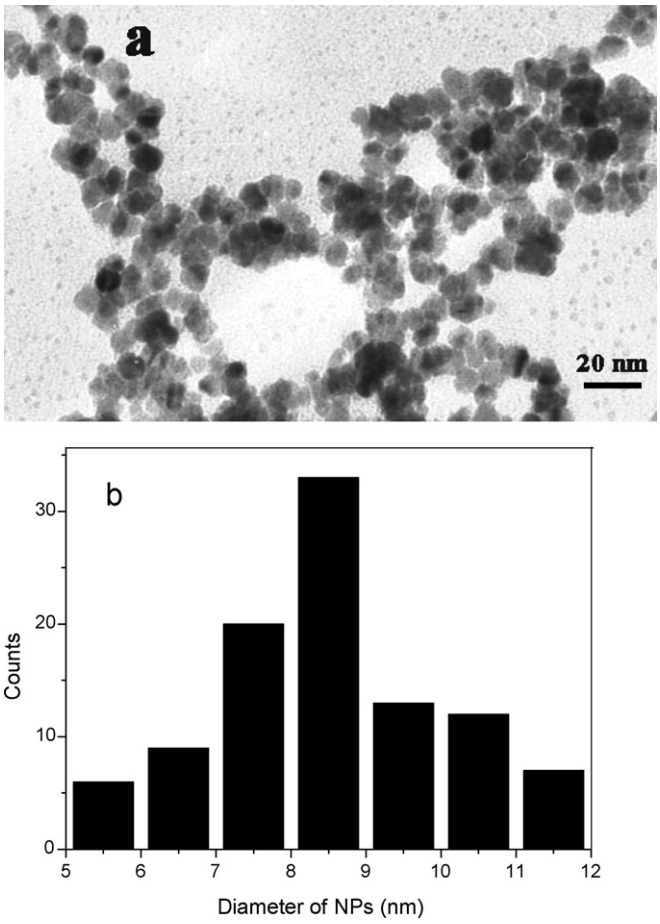

Fig. 3. TEM image corresponding to Fig. 2A (A) and the diameter histogram of the Au NPs (B).

(curve e) with a large peak width at half height and a long tail. The flat absorption profile is the characteristic of the network-like Au nanostructures proved by Pei et al. [22] and Wang and co-workers [7]. Fig. 2B gives the corresponding SEM image, Au NPs assembled into networks and the networks were uniformly covered on the surface. The good agreement between SEM and UV–vis characterizations confirmed the formation of network-like structures of Au NPs. The chemical composition of the networks in Fig. 2B was determined by elemental analysis, and the SEM-EDS was shown in Fig. 2C. The Si signal is from the substrate of Si wafer, the strong peak indicates the existence of Au NPs, and the C, N, O signals come from collagen molecules, which presumably imply the formation of collagen–Au NPs composites.

The collagen–Au NPs composites were measured by TEM in order to observe the Au NPs networks structure. Fig. 3A presents the TEM image corresponding to the sample in Fig. 2B, and it can be further identified that the whole networks actually is the aggregates of NPs and the NPs connect each other to form the network-like nanostructures. Fig. 3B shows the histogram for the diameter of measured Au NPs shown in Fig. 3A, and a statistical analysis shows the diameter is about 8.3 ± 1.5 nm. The size of nanospheres on the networks was obviously smaller and more uniform than that in Fig. 2A. Previous studies revealed that the concentration of the capping agents have strong influence to the size and shape of metal NPs [22,23]. It is hypothesized that at low collagen concentration, growing Au NPs nuclei were adsorbed onto the energetically favorable sites of collagen molecules, which caused the assembly of Au NPs along the collagen chains. At relative high concentration, the specificity was lost when both specific and non-specific adsorptions of colla-

gen occurred. The more uniform coverage of collagen on the nuclei hided the intrinsic differences between sites, resulting in isotropic growth of the nuclei into spherical particles.

3.1.2. *The influence of type I collagen molecules to the formation of Au NPs networks*

A control experiment was done to understand the function of type I collagen molecules in the formation of Au NPs network. 0.5 mM $HAuCl_4$ solution was directly reduced by $NaBH_4$ solution, without adding collagen solution. The as-prepared colloids were unstable, and precipitation was formed rapidly in a few minutes. The colloids were immediately dropped onto a silicon wafer for SEM characterization, and the SEM image exhibits there are many small coagulated particles, and small and large particles coexisted (the SEM image was not shown). In the absence of collagen, uniform NPs network cannot form. We suggest that collagen molecules served as suitable templates to assemble Au NPs.

To further know the interaction between collagen molecules with Au NPs, FT-IR and XPS measurements were applied to study the Au NPs networks. Fig. 4a and b show the FT-IR spectrum of free collagen and collagen-templated Au NPs networks, respectively. The characteristic peaks of amide I band at 1650 cm^{-1} and the amide II band at 1538 cm^{-1} are present in pure collagen (curve a), owing to the abundant glycine, praline, and hydroxyproline in type I collagen molecules [19,24], while some slight shifts are observed in curve b. These changes were caused by the connection of the collagen molecules and Au NPs, according to the results reported by Bhattacharya et al., who proved that amines bind with Au NPs through electrostatic/covalent interaction [25].

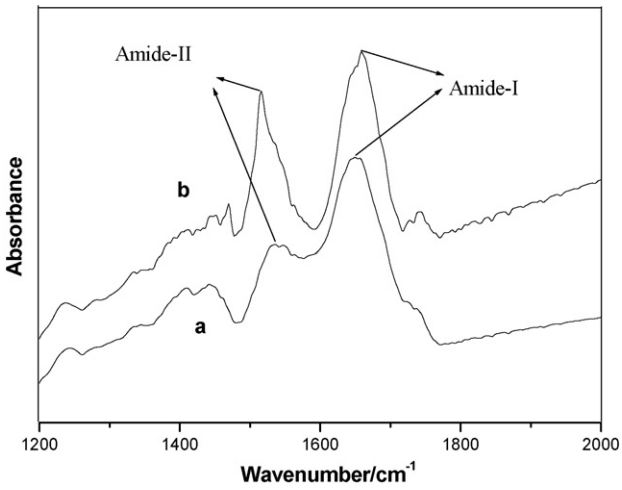

Fig. 4. FT-IR spectra of type I collagen (curve a) and type I collagen–Au NPs networks (curve b).

XPS is proved to be a powerful tool for surface analysis that provides diverse information regarding the structure and chemical state of the type I collagen–Au NPs complex [26]. High-resolution XPS spectra presented in Fig. 5 reveal the existence of (A) Au 4f, (B) C 1s and (C) N 1s spectral regions. Fig. 5A shows the Au $4f_{7/2}$ and $4f_{5/2}$ peaks occur at 83.4 eV and 87.0 eV, respectively. These values were very comparable to those of pure Au [27]. The narrow widths of the bands indicate that the Au component is situated in a simi-

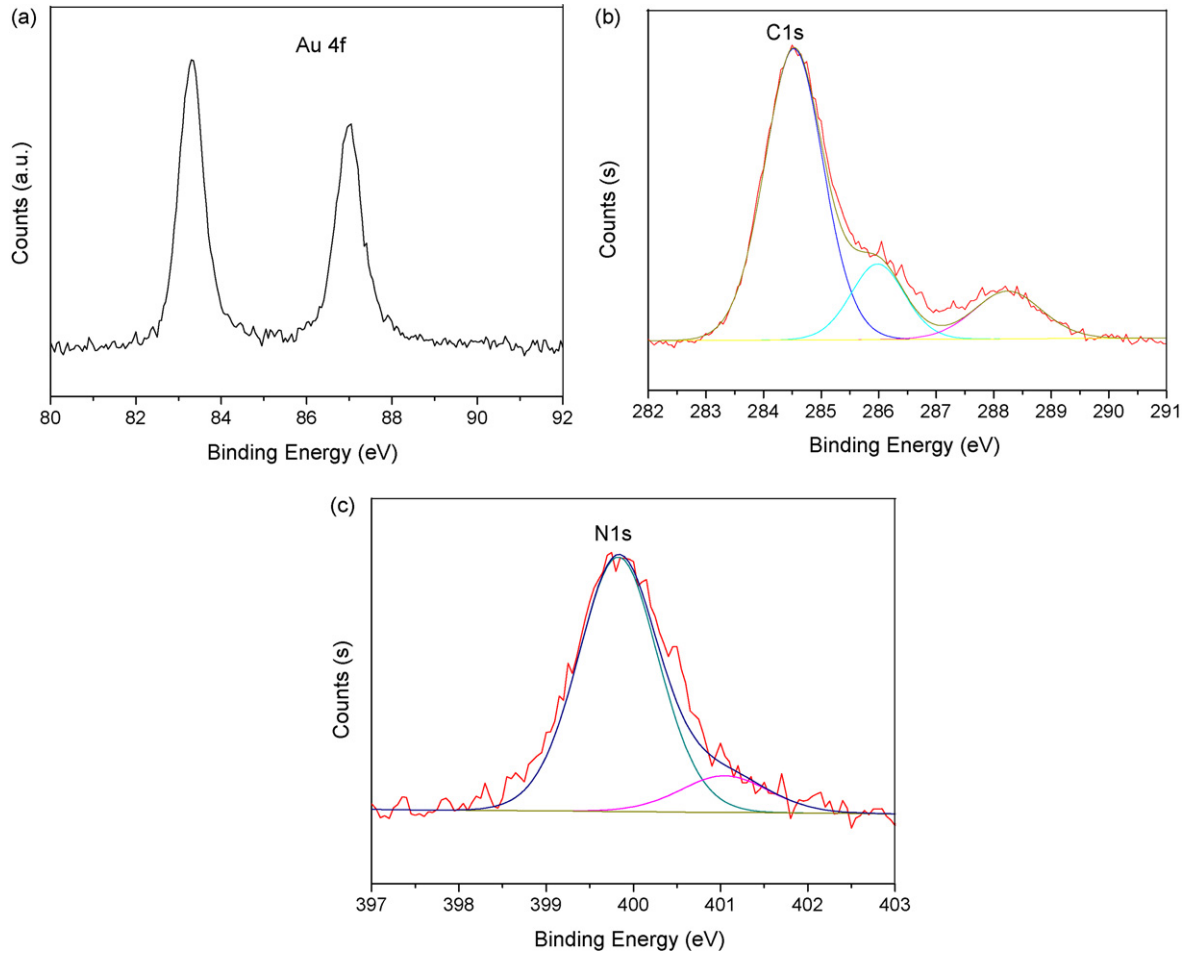

Fig. 5. High-resolution XPS spectra of the fabricated type I collagen–Au NPs networks: (A) Au 4f, (B) N 1s and (C) C 1s. (B and C) were given after spectra fitting.

lar condition throughout the resulting protein–Au nanostructures [28]. Fig. 5B shows the C 1s region resulting from type I collagen–Au NPs networks, where three major peaks were observed at 284.5, 286.0 and 288.2 eV, corresponding to the existence of C–C, C–N and N–C=O of collagen molecules [29,30]. N 1s positioned at two peaks, 399.8 and 401.1 eV, as shown in Fig. 5C. We assigned the main peak at 399.8 eV to the nitrogen atoms of the collagen molecules, which revealed the interactions between the amino groups and the Au NPs. The minor peak at 401.1 eV suggests the presence of N as charged species, indicating electrostatic interaction between collagen and Au NPs. The NH group on the molecule chains combines with H^+ to form NH_2^+, which makes the collagen molecules positively charged [31].

The XPS, IR, UV–vis, and SEM images confirmed our hypothesis that when collagen molecules were introduced into reaction solution as a template, an initial connection between the gold salt and the protein molecular chains took place and the collagen provided the special platforms for the assembly of prepared Au NPs to form the network-like nanostructures. The excellent assembly property of collagen has been confirmed in many literatures [29,32,33]. Based on the discussion above, we suggest that Au NPs assembled along the collagen molecules in suitable condition. After the Au colloids were dropped onto silicon wafer, the solvent evaporated slowly, and the hydrophobic interaction of peptide residues on collagen chains play a pivotal role, furthermore the inter- and intra-molecule hydrogen bonds reinforce and the collagen molecules self-assemble to widely linked networks [29,32,33]. It should be noted that the details of the interaction between collagen–Au composites and substrate requires further investigation.

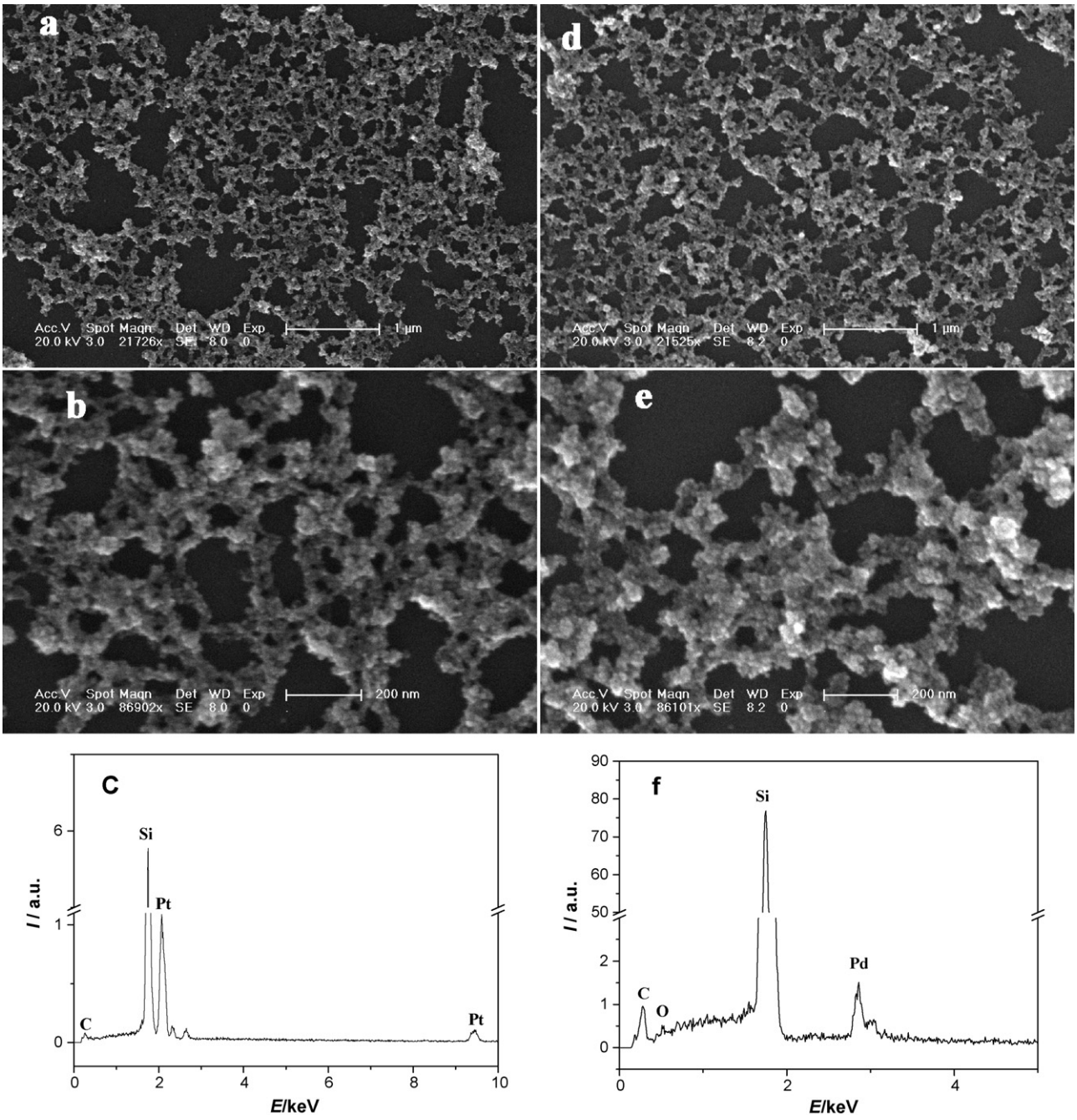

Fig. 6. FE-SEM images of Pt NPs networks (A and B), Pd NPs networks (D and E), and the corresponding EDS spectra (C and F), respectively.

3.2. Preparation and characterization of the type I collagen-mediated Pt, Pd and Ag nanostructures

Based on the analysis above, we suppose that type I collagen molecules can be applied as an effective template to synthesize noble metallic nanostructures including Pt, Pd, Ag. Fig. 6A–E present the morphologies of Pt, Pd nanostructures prepared by the same strategy as that for Au NPs networks. It can be clearly observed that both of them formed comparatively uniform metal NPs networks. Ag colloids were prepared by the same experimental method, and the morphologies of as-prepared Ag nanostructures were shown in Fig. 7. Fig. 7A exhibits the Ag nanostructures, and the magnified image was shown in Fig. 7B, it can be observed that the networks consist of 20–40 nm nanospheres and their aggregations. Obviously, the diameter of Ag nanospheres was larger than that of the Au, Pt, Pd nanospheres on networks (around 10 nm).

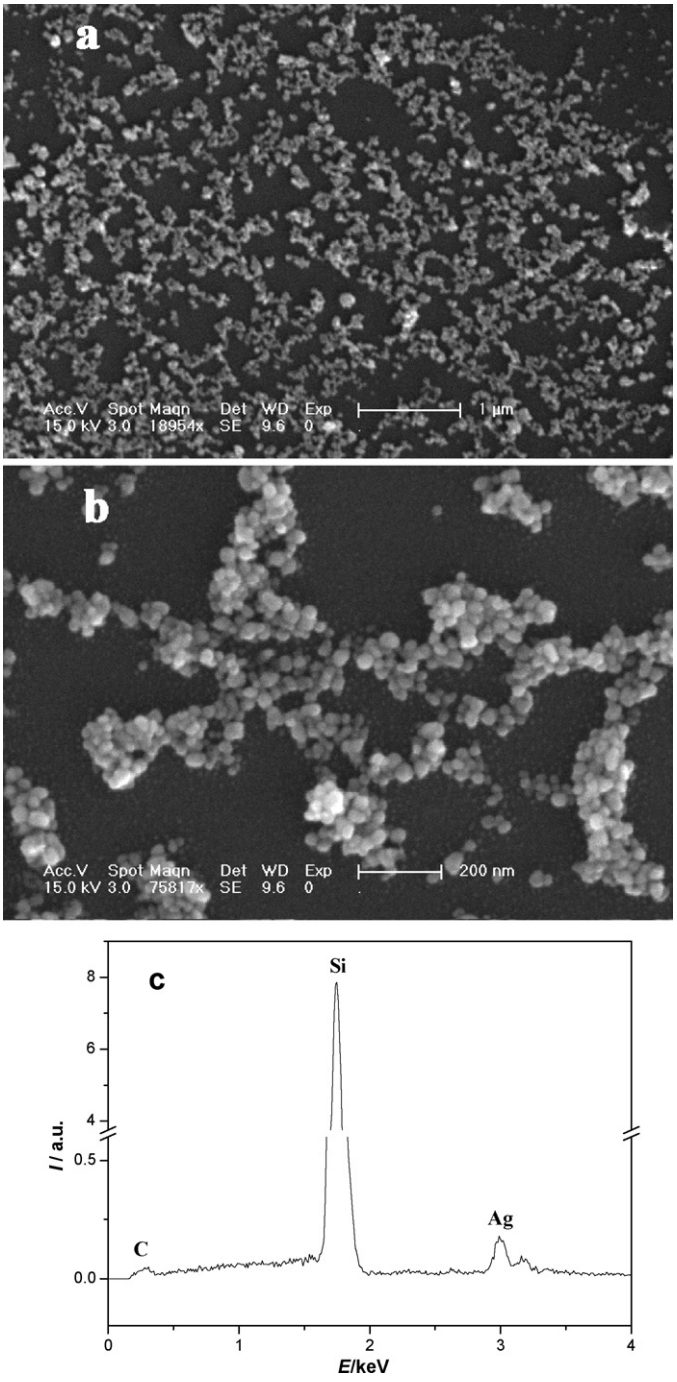

Fig. 7. FE-SEM images of (A) Ag NPs networks, (B) the magnified image of (A), and the EDS analysis (C).

EDS show the corresponding peaks of Pt, Pd and Ag (Fig. 6C, F and Fig. 7C), demonstrating that the main components of these three nanostructures are metallic Pt, Pd and Ag, respectively. The low-intensity peak of C proved the existence of the template collagen molecules.

The difference between morphologies of Ag NPs networks and other three metal NPs networks are ascribed to the effect of different noble metallic ions used at present study. The pH values of the mixture of the negatively charged metallic ions ($AuCl_4^-$, $PtCl_6^{2-}$, and $PdCl_4^{2-}$) and collagen solutions were all around 3.0, and that of Ag^+ and collagen solution was 3.2. As well known, type I collagen is a polyelectrolyte, whose isoelectric point is 7.6. Collagen molecules are positively charged and show good assemble properties in acidic solution [18,19,33]. To the negatively metal ions (take $AuCl_4^-$ as an example), the initial association of the positively charged protein with negatively charged $AuCl_4^-$ occurs because of electrostatic interactions. Subsequently, Au NPs on the collagen chains were reduced in situ, a covalent interaction between the gold and collagen takes place due to the presence of amines in the glycine, proline and hydroxyproline residues in type I collagen [25,34]. But the positively charged collagen molecules cannot adsorb Ag^+. After the addition of BH_4^-, negatively charged Ag NPs were produced in solution firstly, and then adsorbed onto collagen molecules by the electrostatic interaction. The "freely" Ag NPs produced in solution were larger and more inhomogeneous than the Au NPs formed in situ on the collagen chains.

3.3. The applications of type I collagen-templated Ag and Pt NPs networks in SERS and electocatalysis

Noble metal NPs have been widely applied in optics and catalysis due to their inherent properties such as SPR and high density. We choose type I collagen-templated Ag NPs networks and Pt NPs networks as representative examples for researching the basic applications in SERS and electrocatalysis.

3.3.1. SERS spectra of 4-ATP on the type I collagen-templated Ag NPs networks

Herein, 4-ATP was selected as a probe molecule because it can form a self-assembled monolayer on metal surface and most of its distinct Raman bands have been assigned in literatures [35,36]. Fig. 8a and b illustrate the SERS spectrum of 10^{-7} M 4-ATP on the substrates of citrate-capped Ag NPs and collagen-templated Ag NPs networks, respectively. It is obvious that collagen–Ag NPs networks show better enhancement ability than citrate-capped Ag NPs film. For instance, the intensity of the peak at 1078 cm^{-1} in curve b are approximate four times as that in curve a. The main peaks at 1577, 1434, 1390 and 1143 cm^{-1} belong to the b_2 vibration mode, which suggest that the enhancement via charge-transfer resonance mechanism is significant [18,35–37]. Two other main peaks, 1184 and 1078 cm^{-1}, are ascribed to the a1 vibration mode, which imply that electromagnetic mechanism is also important [18,35–37].

3.3.2. SERS spectra of adenine on the type I collagen-templated Ag NPs networks

One of the potential applications for SERS in the biophysical/biochemical and biomedical fields is the rapid detection, quantification, and characterization of DNA and DNA fragments [38,39]. Compared with the fluorescence technique currently used for DNA analysis, SERS does not require any labeling step because it is a technique of vibrational spectroscopy that shows detailed fingerprint information of DNA bases. To explore the capability of the as-prepared collagen–Ag NPs networks for the detection of DNA

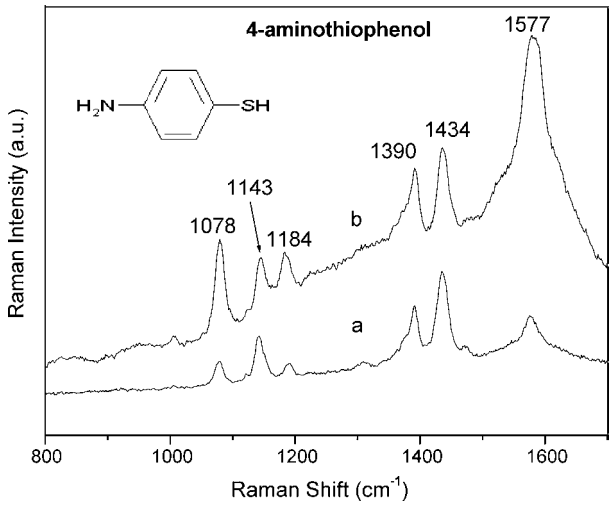

Fig. 8. SERS spectra of 10^{-6} M 4-ATP on prepared collagen–Ag NPs networks (curve b) and on citrate-capped Ag NPs film (curve a).

base, adenine was chosen as the probe molecule. Fig. 9 displays the SERS spectra of 10^{-4} M adenine on Ag NPs networks and citrate-capped Ag NPs films. Two distinct Raman bands are observed at 730 and 1328 cm^{-1}, assigned to the purine ring breathing mode and the CN stretching mode, respectively [38,39]. In contrast, the citrate-capped Ag NPs represent extremely weak SERS enhancement (curve a). The SERS signal intensity at 730 cm^{-1} from Ag NPs networks is approximately as five times as that obtained on normal Ag NPs films, indicating that type I collagen-templated Ag NPs networks is highly suitable for SERS detections.

SERS is known to be a very local phenomenon generally arising at the junction of adjacent Ag NPs and rough surfaces [40,41] The obtained high SERS enhancement of 4-ATP and adenine on collagen-templated Ag NPs networks is possibly attributed to two main reasons. One factor is the formation of many nanoscale pores on uniform Ag NPs networks. Berlin et al. and Sailor et al. have obtained high SERS enhancements on their respectively prepared silver-coated silicon nanopores substrates [2,42]. Another successful research also get high SERS signals on ordered macroporous Au/Ag bimetallic nanostructures by Lu et al. [8]. The second factor is the formation of Ag NPs aggregations on collagen molecule

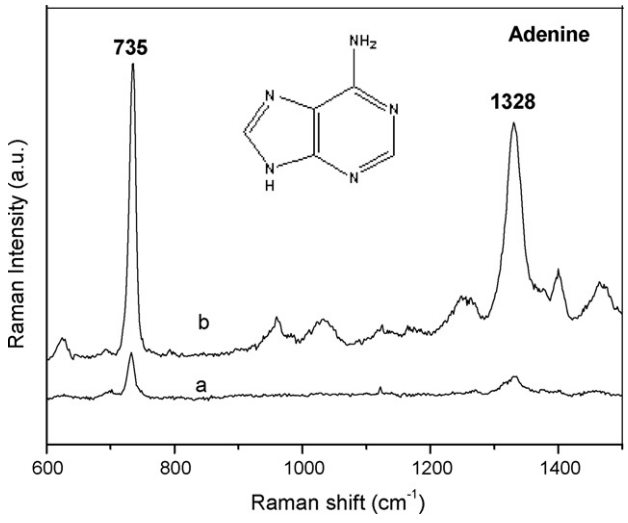

Fig. 9. SERS spectra of 10^{-4} M adenine on collagen–Ag NPs networks (curve b) and on citrate-capped Ag NPs film (curve a).

chains, as shown in Fig. 7B. Indeed, the electric enhancement might occur at the junction of two or more colloids [43].

3.3.3. *Electrocatalytic property of O_2 on the type I collagen-templated Pt NPs networks*

Regarding the use of Pt as the most efficient catalyst for O_2 reduction, we investigated the electrocatalytic activity of the collagen-templated Pt NPs networks modified electrode for dioxygen reduction in detail. Fig. 10A gives the representative cyclic voltammograms (CVs) of the bare ITO (curve a) and Pt NPs network modified ITO (curve b) in 0.1 M H_2SO_4 saturated by ultrahigh-purity nitrogen at a scan rate of 50 mV s^{-1} from −0.2 V to 1.5 V. It can be observed that the CV of Pt NPs networks modified ITO electrode (curve b) is similar to that of a polycrystalline Pt electrode, indicating that the hydrogen adsorption/desorption peaks and the formation and removal of platinum surface oxide peaks [44,45]. No current peak appears at bare ITO electrode in this region. Fig. 9b shows the CVs for O_2 reduction at these two electrodes in N_2-saturated (curves a and c), and in air-saturated (curves b and d). These electrodes only give small background current in N_2-saturated 0.1 M H_2SO_4 (curves a and c). Compared to the bare ITO (curve b), a remarkable cathodic peak appears at 0.33 V (curve d) of CV obtained at Pt NPs network modified ITO electrode, which is attributed to the catalytic reduction of O_2 [3,44,45]. The good electrocatalytic ability can be ascribed to the high surface area of

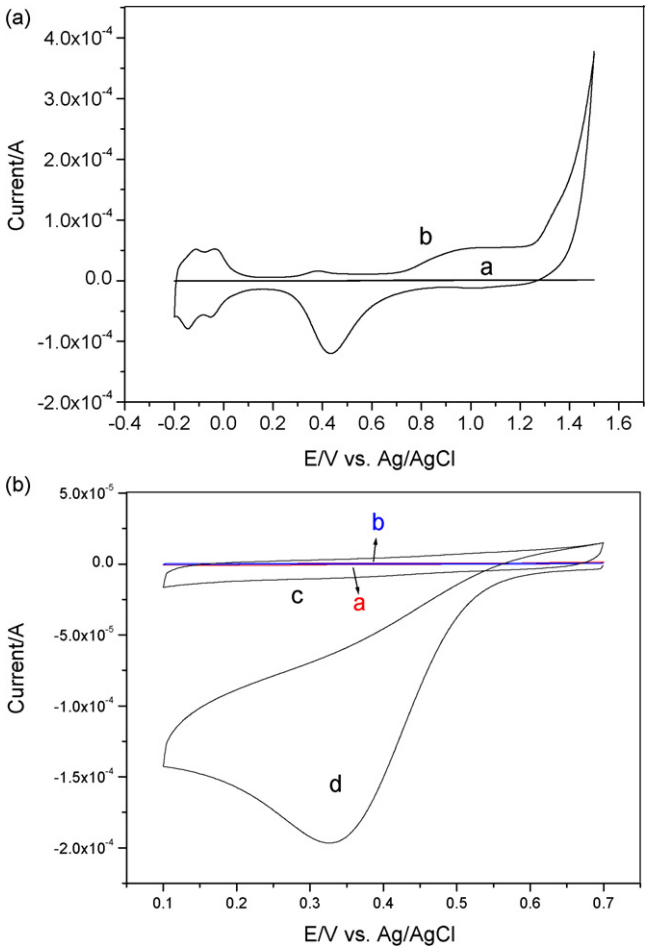

Fig. 10. Cyclic voltammograms of (a) the bare ITO (curve a) and Pt NPs network modified ITO (curve b) in N_2-saturated 0.1 M H_2SO_4, and (b) these two electrodes in N_2-saturated (curve a (red) and c), and in air-saturated (curve b (blue) and d) 0.1 M H_2SO_4. Scan rate: 50 mV s^{-1}. (For interpretation of the references to color in this figure legend, the reader is referred to the web version of the article.)

the collagen-templated Pt NPs networks. From Fig. 6A, it is can be observed that a great deal of small Pt NPs assemble to networks, and these small NPs supply high surface area to volume and high surface activity, both of them are in favor of good catalytic activity.

4. Conclusion

In summary, we demonstrated an effective and environmentally friendly template method to prepare 2D network nanostructures including Au, Ag, Pt and Pd NPs. The major advantage of the synthesis route is that type I collagen, an ordinary and excellent biocompatible protein molecule, can work as stabilizing agent and assembled template. The hydrophobic action and hydrogen bonds play important roles in the formation of collagen–Au NPs networks. As the representative collagen-templated noble nanomaterials, the Ag NPs networks can be used as a SERS substrate with high sensitivity and the Pt NPs networks show good electrocatalytic ability for O_2 reduction. It is also expected that these collagen-templated 2D porous noble metal nanostructures can find wider applications in biosensors, SPR, and so on.

Acknowledgments

This work was supported by the National Natural Science Foundation of China (20775077) and Chinese Academy of Sciences (KJCX2-YW-H11).

References

[1] P.M. Tessier, O.D. Velev, A.T. Kalambur, J.F. Rabolt, A.M. Lenhoff, E.W. Kaler, J. Am. Chem. Soc. 122 (2000) 9554.
[2] S. Chan, S. Kwon, T.-W. Koo, L.P. Lee, A.A. Berlin, Adv. Mater. 15 (2003) 1595.
[3] H. Chen, S. Dong, Langmuir 23 (2007) 12503.
[4] J.A. Barnard, H. Fujiwara, V.R. Inturi, J.D. Jarratt, T.W. Scharf, J.L. Weston, Appl. Phys. Lett. 69 (1996) 2758.
[5] N. Félidj, J. Aubard, G. Lévi, J.R. Krenn, M. Salerno, G. Schider, B. Lamprecht, A. Leitner, F.R. Aussenegg, Phys. Rev. B 65 (2002) 075419.
[6] A.D. McFarland, M.A. Young, J.A. Dieringer, R.P. Van Duyne, J. Phys. Chem. B 109 (2005) 11279.
[7] C.D. Chen, Y.T. Yeh, C.R.C. Wang, J. Phys. Chem. Solids 62 (2001) 1587.
[8] L. Lu, A. Eychmüller, Acc. Chem. Res. 41 (2008) 244.
[9] H. Masuda, K. Fukuda, Science 268 (1995) 1466.
[10] W.E. Ford, O. Harnack, A. Yasuda, J.M. Wessels, Adv. Mater. 13 (2001) 1793.
[11] I. Willner, F. Patolsky, J. Wasserman, Angew. Chem. Int. Ed. 40 (2001) 1861.
[12] Y. Maeda, H. Tabata, T. Kawai, Appl. Phys. Lett. 79 (2001) 1181.
[13] V. Thomas, D.R. Dean, M.V. Jose, B. Mathew, S. Chowdhury, Y.K. Vohra, Biomacromolecules 8 (2007) 631.
[14] G. Wei, J. Reichert, K.D. Jandt, Chem. Commun. (2008) 3903.
[15] W. Shenton, D. Pum, U.B. Sleytr, M. Stephen, Nature 389 (1997) 585.
[16] E. Dujardin, C. Peet, G. Stubbs, J.N. Culver, S. Mann, Nano Lett. 3 (2003) 413.
[17] S. Polarz, B. Smarsly, J.H. Schattka, Chem. Mater. 14 (2002) 2940.
[18] Y. Sun, G. Wei, Y. Song, L. Wang, L. Sun, C. Guo, Tao. Yang, Z. Li, Nanotechnology 19 (2008) 115604.
[19] Y. Sun, L. Wang, L. Sun, C. Guo, T. Yang, Z. Liu, F. Xu, Z. Li, J. Chem. Phys. 128 (2008) 074704.
[20] P.C. Lee, D. Meisel, J. Phys. Chem. 86 (1982) 3391.
[21] K. Torigoe, K. Esumi, Langmuir 8 (1992) 59.
[22] L. Pei, K. Mori, M. Adachi, Langmuir 20 (2004) 7837.
[23] Y.N. Tan, J.Y. Lee, D.I.C. Wang, J. Phys. Chem. C 112 (2008) 5463.
[24] X. Liao, M. Zhang, B. Shi, Ind. Eng. Chem. Res. 43 (2004) 2222.
[25] R. Bhattacharya, C. Patra, S. Wang, L. Lu, M. Yaszemski, D. Mukhopadhyay, P. Mukherjee, Adv. Funct. Mater. 16 (2006) 395.
[26] L. Shang, Y. Wang, L. Huang, S. Dong, Langmuir 23 (2007) 7738.
[27] S. Johnson, S. Evans, R. Brydson, Langmuir 14 (1998) 6639.
[28] Y. Zhou, R. Ma, Y. Ebina, K. Takada, T. Sasaki, Chem. Mater. 18 (2006) 1235.
[29] C.C. Dupont-Gillain, B. Nysten, P.G. Rouxhet, Polym. Int. 48 (1999) 271.
[30] R. Petoral Jr., K. Uvdal, J. Phys. Chem. B 107 (2003) 13396.
[31] J. Sharma, N. Chaki, A. Mandale, R. Pasricha, K. Vijayamohanan, J. Colloid Interface Sci. 272 (2004) 145.
[32] M. Mertig, U. Thiele, J. Bradt, G. Leibiger, W. Pompe, H. Wendrock, Surf. Interface Anal. 25 (1997) 514.
[33] X. He, J. Cai, T. Zhao, X. Wang, Z. Liang, Biotechnology (Chinese) 14 (2004) 35.
[34] N. Dai, X.J. Wang, F.A. Etzkorn, J. Am. Chem. Soc. 130 (2008) 5396.
[35] E. Hao, G.C. Schatz, J. Chem. Phys. 120 (2004) 357.
[36] M. Osawa, M. Naoki, Y. Katsumasa, U. Isamu, J. Phys. Chem. 98 (1994) 12702.
[37] Y. Wang, H. Chen, S. Dong, E. Wang, J. Chem. Phys. 124 (2006) 074709.
[38] K. Kneipp, H. Kneipp, I. Itzkan, R. Dasari, M. Feld, Chem. Rev. 99 (1999) 2957.
[39] L. Lu, K. Ai, Y. Ozaki, Langmuir 24 (2008) 1058.
[40] A.M. Michaels, J. Jiang, L. Brus, J. Phys. Chem. B 104 (2000) 11965.
[41] J. Jiang, K. Bosnick, M. Maillard, L. Brus, J. Phys. Chem. B 107 (2003) 9964.
[42] H. Lin, J. Mock, D. Smith, T. Gao, M.J. Sailor, J. Phys. Chem. B 108 (2004) 11654.
[43] M.D. Musick, C.D. Keating, L. Andrew Lyon, S.L. Botsko, D.J. Peña, W.D. Holliway, T.M. McEvoy, J.N. Richardson, M.J. Natan, Chem. Mater. 12 (2000) 2869.
[44] M. Huang, Y. Shao, X. Sun, H. Chen, B. Liu, S. Dong, Langmuir 21 (2005) 323.
[45] H. Chen, Y. Wang, S. Dong, Inorg. Chem. 46 (2007) 10587.

Talanta 79 (2009) 856–862

Contents lists available at ScienceDirect

Talanta

journal homepage: www.elsevier.com/locate/talanta

Combined on-line transmission FTIR measurements and BTEM analysis for the kinetic study of a consecutive reaction in aqueous–organic phase medium

Martin Tjahjono*, Chong Huiheng, Effendi Widjaja, Kanicha Sa-ei, Marc Garland

*Institute of Chemical and Engineering Sciences, Agency for Science, Technology and Research (A*STAR), 1 Pesek Road, Jurong Island, Singapore 627833, Singapore*

ARTICLE INFO

Article history:
Received 6 March 2009
Received in revised form 11 May 2009
Accepted 11 May 2009
Available online 20 May 2009

Keywords:
On-line reaction monitoring
Multivariate analysis
Solvent effect
Spectral deconvolution

ABSTRACT

Combined on-line transmission FTIR spectroscopy and band-target entropy minimization (BTEM) analysis were employed in order to monitor and analyze the kinetics of the alkaline hydrolysis reaction of diethyl phthalate (DEP) in aqueous–ethanol solvent mixture. This reaction is irreversible and involves two consecutive steps with the formation of the observable mono-ion intermediate species. The pure component mid-FTIR spectra of the reactive species involved in this reaction, namely DEP, mono-ion intermediate and di-ion product were successfully reconstructed using BTEM. Their corresponding concentrations were also calculated and subsequently employed to derive the kinetic rate parameters. The effect of temperature and the solvent mixture compositions on these two consecutive reaction steps were also discussed. The temperature variation study showed that both reaction rate coefficients increased with temperature. Both rate coefficients were also affected by the solvent mixture compositions and reached minimum values at certain water–ethanol solvent composition (circa 60% (v/v)). This study shows the utility of combined on-line transmission FTIR spectroscopy and chemometric techniques for the present, rather complex, consecutive organic reaction. Moreover, the present type of approach could facilitate better understanding of a wide variety of organic reactions that are performed in aqueous and mixed aqueous–organic solvents.

1. Introduction

A wide variety of complex organic reactions can be successfully carried out in water and mixed aqueous–organic solvents [1–5]. These include, but are not restricted to, alkylations, carbonylations, metathesis, hydroformylation, etc. Mixed aqueous–organic solvents are particularly attractive due to inherent solvation advantages since they generally increase the solubility of hydrophobic reactants. Due to the increasing interest in greener chemical processes, the use of water as a solvent in organic synthesis is attracting considerable attention [6,7]. Many processes which target the degradation of environmental pollutants also utilize water as the reaction medium, i.e., wet oxidation, photochemistry, etc. In summary, water and mixed aqueous–organic solvent systems play an important role in chemical processing.

A variety of difficulties are frequently encountered when trying to monitor and analyze aqueous reactions. This situation is particularly acute for in situ spectroscopic investigations. For example, UV–vis does not readily lend itself to the needed level of molecular specificity [8], particularly when complex chemo- and regio-selective reactions are occurring. NMR, which has the needed molecular specificity, generally lacks the needed sensitivity to detect minor species and side reactions. In addition, on-line NMR has the additional difficulty associated with the continuous need to re-shim the field in order to maintain good spectral measurements over a wide range of concentrations [9]. Therefore vibrational techniques have received considerable interest, since at least in principle, they afford reasonably good molecular specificity, but are at the same time, rather robust spectroscopic techniques.

Three vibrational techniques, namely, Raman [10–13], attenuated total reflectance (ATR) [14–16] and transmission FTIR [17,18] have been used for investigating aqueous systems. Raman spectroscopy is convenient since water is a poor scatterer. Consequently, signals arising from the other solutes are more easily detected. The disadvantage is that minor constituents may not be detected since the Raman effect is generally small, i.e., circa 1 in 10^6 to 10^8 photons [19]. ATR has been widely used, since it is suitable for characterization of liquids which have strong absorptivities, i.e., water, however, the spectra produced by ATR–FTIR possess some peak shifts and intensity differences [20]. Moreover, interpretation and quantitative analysis are hindered due to the non-linear optical effects associated with the absorption–reflection nature of this method [21]. Transmission FTIR is a relatively less utilized method of analysis. This is largely due to the strong absorptivity of

* Corresponding author. Tel.: +65 6796 3960; fax: +65 6316 6185.
E-mail address: martin_tjahjono@ices.a-star.edu.sg (M. Tjahjono).

0039-9140/$ – see front matter © 2009 Elsevier B.V. All rights reserved.
doi:10.1016/j.talanta.2009.05.014

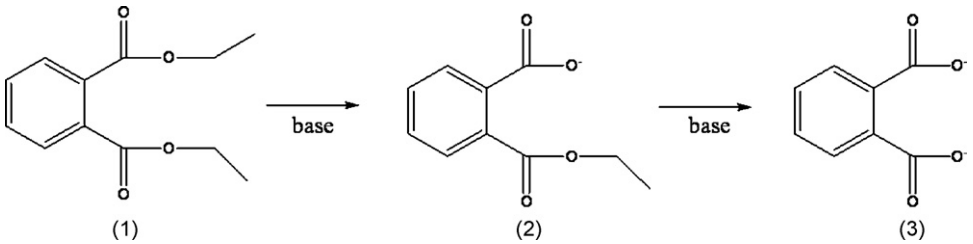

Scheme 1. The alkaline hydrolysis consecutive transformation of diethyl phthalate (1) to mono-ion intermediate (2) and di-ion product (3).

water over most of the mid-infrared range. This in turn necessitates the use of very thin path-lengths, i.e., ~50 μm or less. However, in contrast to ATR, spectra obtained from transmission FTIR are more readily interpreted and often more suitable for quantitative analysis.

The present contribution focuses on on-line transmission FTIR and its combination with an advanced chemometric technique, band-target entropy minimization (BTEM), in order to monitor and analyze the kinetics of a consecutive organic reaction performed in aqueous–organic phase. More specifically, a rather complex consecutive reaction system, namely alkaline hydrolysis reaction of diethyl phthalate (DEP) in water–ethanol solvent mixture is investigated. DEP has been widely used in many industrial areas (i.e., cosmetic, paper, ink, paint industries, etc.) and as other phthalates, it is considered toxic and hazardous to human health [22]. The hydrolysis of DEP is a potentially important degradation pathway from an environmental perspective [23]. The reaction mechanism for this reaction has been proposed to involve two consecutive reaction steps, with the formation of the observable mono-ion intermediate as shown in Scheme 1 [24–26]. A series of experiments were conducted at various reaction conditions (i.e., different temperatures, concentrations of DEP, and solvent mixture compositions) in order to investigate their effects on these two consecutive reaction steps.

The present contribution demonstrates the usefulness of the present approach for this reaction, and suggests a wider utility of combined transmission FTIR measurements and chemometrics techniques for analyzing complex aqueous phase chemistry.

2. Experimental aspects

2.1. Materials

Diethyl phthalate (Alfa Aesar, 99%) and NaOH pellets (Merck, pro analysi, >99%) were used without further purification. 2-Ethoxycarbonyl benzoic acid or monoethyl phthalate, MEP was prepared from phthalic anhydride (Sigma–Aldrich, ACS reagent, >99%) and purified according to an existing procedure [27] using toluene for extraction. Both ^{1}H and ^{13}C NMR spectra of the MEP were measured in $CDCl_3$ on a Bruker Advance 400 MHz. Chemical shift values of ^{1}H NMR spectra were recorded in parts per million (δ) from an internal standard of residual chloroform (7.26 ppm). Chemical shift values of ^{13}C NMR spectra were recorded in ppm from the central peak of $CDCl_3$ (77.0 ppm). The chemical shifts of the ^{13}C NMR spectra are consistent with the literature [28]. ^{1}H NMR (400 MHz, $CDCl_3$) δ 9.17 (br s, 1H), 7.91–7.93 (m, 1H), 7.70–7.72 (m, 1H), 7.55–7.63 (m, 2H), 4.40 (q, J = 7.2 Hz, 2H), 1.38 (t, J = 7.2 Hz, 3H); ^{13}C NMR (125 MHz, $CDCl_3$) δ 172.3, 168.1, 133.5, 132.2, 130.8, 130.0, 129.8, 128.8, 62.0, 13.9.

Solvent mixtures were prepared by mixing ethanol (VMR International Ltd., HPLC grade, 99.7–100%, v/v) with de-ionized ultra-pure water (Young Lin Instrument, Aquamax™ – Basic 321 Water Purification System). The reactions were carried out in water–ethanol solvent mixtures since DEP has low solubility in water (0.1 g/100 g at 20 °C [29], 896 ± 20 mg/L at 25 °C [23]).

2.2. Equipment

The experimental setup consisted of a 50 mL glass jacketed reactor equipped with a magnetic stirrer, a Teflon membrane pump (Cole-Parmer), and a flow-through IR transmission cell. The temperature of the reactor was kept isothermal using a temperature bath circulator (Polyscience 9105, with temperature stability ±0.05 K). The liquid solution was pumped in a closed-loop from the reactor through the pump to the infrared flow-through cell and recycled back to the reactor.

Mid-infrared spectra were collected using a mid-infrared VERTEX 70 FT-IR Bruker spectrometer. The CaF_2 single crystal windows used (Korth Monokristalle, Kiel, Germany) had dimensions of diameter 20 mm by thickness 2 mm. Two sets of Viton gaskets provided sealing and Teflon spacers (thickness of 25 μm) were used between the windows. Purified air system (Specken-Drumag, Germany) was used to purge the spectrometer.

2.3. Experimental procedures

The reaction was carried out in alkaline water–ethanol solvent mixtures (the total amount of solvent was 50 mL). In this regard, pure water, ethanol, and sodium hydroxide were added sequentially into the reactor with stirring rate of circa 400 rpm. At each

Table 1
Summary of the experimental runs performed in this study.

Exp run	T (°C)	% (v/v) EtOH–H_2O	NaOH (g)	DEP (g)
Reproducibility				
1	20	50	0.7919	0.2850
2	20	50	0.8153	0.2760
3	20	50	0.8093	0.2794
Mass variations of reactant (DEP)[a]				
4	20	50	0.7853	0.1683
5	20	50	0.7950	0.4178
Temperature variations[b]				
6	25	50	0.8032	0.2784
7	30	50	0.7943	0.2792
8	35	50	0.8070	0.2763
9	40	50	0.8072	0.2808
Solvent mixture variations[c]				
10	20	40	0.7954	0.2807
11	20	60	0.8175	0.2766
12	20	70	0.8052	0.2780
13	20	80	0.8076	0.2795

[a] Exp runs 1 and 4–5 are used to study the effect of DEP concentration (Section 4.3).
[b] Exp runs 1 and 6–9 are used to study the effect of temperature (Section 4.4).
[c] Exp runs 1 and 10–13 are used to study the effect of solvent mixtures (Section 4.5).

step, the liquid was thoroughly mixed and circulated through the infrared cell in order to measure the infrared spectra of pure water, water + ethanol, and water + ethanol + sodium hydroxide, respectively. The homogeneity of the solutions was confirmed by the stability of the infrared spectral measurements.

Next, DEP was added into the reactor using a gas-tight syringe. The amount of DEP used in the reaction was determined by measuring the masses of the syringe before and after the injection using a balance (GR-200, A&D, Japan) with a precision of $\pm 10^{-4}$ g. The reaction started immediately upon introduction of DEP into the reactor. The infrared spectra of the solution (in the range 1000–4000 cm^{-1} and with resolution of 2 cm^{-1}) were taken automatically every 60 s to monitor the reactions. Co-added scans of 16 spectra were measured in order to ensure good signal-to-noise ratio.

A total of 13 experimental runs involving DEP were conducted at various reaction conditions (i.e., different temperatures, amount of DEP, and solvent mixture composition). Replicates of the experimental runs were also performed in order to confirm the reproducibility of the kinetic measurements. All experimental runs performed with DEP are summarized in Table 1. An experimental reaction temperature of 293 K was chosen in order to evaluate solvent mixture effects and reproducibility since the reaction rates at this temperature are relatively slow and thus conveniently followed by on-line FTIR. The solvent mixture composition at 50% (v/v) was chosen in order to study the temperature effects since this mixture composition provides both good solubility of DEP as well as fast dissolution of the sodium hydroxide.

One experimental run was similarly performed using MEP (instead of DEP) as a reactant. MEP was instantaneously deprotonated and became the mono-ion intermediate once it was introduced into the alkaline water–ethanol media. This run was carried out in order to confirm the irreversibility of the reaction.

3. Numerical aspects

The numerical analyses for the present kinetic study can be partitioned into three main steps: (1) spectroscopic data processing and deconvolution of the pure component spectra (2) determination of concentrations and (3) evaluation of the kinetic rate parameters. These three steps are described in detail in the following sections.

3.1. Spectroscopic data processing and deconvolution of the pure component spectra

The infrared spectra of water, water + ethanol, and water + ethanol + sodium hydroxide were measured sequentially before the reaction started (see experimental Section 2.3). The optimal subtraction procedures [30] were subsequently performed in order to obtain the pure component spectra of water, ethanol, and sodium hydroxide. Additionally, the infrared spectrum of the background (moisture) was determined directly from a separate measurement of the empty chamber.

Singular value decomposition and thereafter BTEM analysis [31–33] were performed on the raw reaction spectra to obtain the normalized pure component spectra of the reactive species (i.e., reactant, intermediate and product), without recourse to any a priori information or libraries. Only 10–15 significant transposed right singular vectors (obtained from SVD) were used in order to reconstruct the pure component spectra of these reactive species.

In order to perform further quantitative analysis, the raw reaction spectra were subsequently treated in order to subtract [30] the spectral contributions from the background (moisture), solvents (water and ethanol) and sodium hydroxide in water–ethanol mixtures as well as to correct the slight baseline shifts using a constant baseline correction [34]. These pre-processed spectra were subsequently noted as $\mathbf{A}_{k\times\nu}$ and used to obtain the concentrations of the reactive species.

3.2. Determination of concentrations

Infrared absorbance spectra generally obey the empirical Lambert–Beer–Bouguer law (Eq. (1)), where absorbance spectra $\mathbf{A}_{k\times\nu}$ can be related to the concentration $\mathbf{C}_{k\times s}$ of the s species present, the normalized pure component absorptivities $\hat{\mathbf{a}}_{s\times\nu}$ (obtained from BTEM analysis) and the scaling elements $\mathbf{d}_{s\times s}$, which combine the contribution from path length and molar absorptivities of each species. The subscripts k and ν denote the number of spectra in one experimental run and the number of data channels associated with the spectroscopic wavenumber range, respectively. In the present implementation, $\mathbf{A}_{k\times\nu}$ is the pre-processed absorbance which now only contains the contributions from the reactant, mono-ion intermediate, and di-ion product (i.e., $s = 3$),

$$\mathbf{A}_{k\times\nu} = \mathbf{C}_{k\times s}\mathbf{d}_{s\times s}\hat{\mathbf{a}}_{s\times\nu} \tag{1}$$

Concentrations for these three observable species can be estimated from Eq. (2), where $[\hat{\mathbf{a}}_{s\times\nu}]^{+}$ is the pseudo-inverse matrix of $\hat{\mathbf{a}}_{s\times\nu}$. In order to determine these concentrations, the proper scaling elements $\mathbf{d}_{s\times s}$ must be first evaluated.

$$\mathbf{C}_{k\times s} = \mathbf{A}_{k\times\nu}[\hat{\mathbf{a}}_{s\times\nu}]^{+}(\mathbf{d}_{s\times s})^{-1} \tag{2}$$

Since the three reactive species, namely reactant DEP (1), mono-ion intermediate (2), and di-ion product (3) contain the same chemical group (i.e., $C_6H_4(COO^-)_2$) and since the reaction was carried out in a closed system, the total concentrations of the chemical group $C_6H_4(COO^-)_2$ at any reaction time are conserved and should be equal to the initial concentration of DEP used in each run, $C_1^{\mathbf{o}}$ (Eq. (3)). It should be noted that Eq (3) implicitly assumes that the volume changes due to reactions in this dilute concentration range are negligible.

$$\text{Minimize}\,\mathbf{G} = \sum_{k}\left(C_{k1}^{\mathbf{o}} - \sum_{s=1,2,3}\mathbf{C}_{ks}\right)^2 \quad \text{w.r.t.}\,\mathbf{d}_{3\times 3} \tag{3}$$

Using a least square minimization procedure (Eq. (3)), the scaling elements $\mathbf{d}_{3\times 3}$ could be evaluated. All calculations described in Sections 3.1 and 3.2 were performed in MATLAB (v. R2007b) with in-house written algorithms.

3.3. Determining the kinetic model parameters

Since the sodium hydroxide is provided in ~10-fold excess (compared to the reactant DEP), the kinetic model corresponding to the reaction in Scheme 1 can be written as two irreversible pseudo-first order consecutive reactions. The associated ordinary differential equations (ODEs) for the concentrations of DEP (1), intermediate mono-ion (2), and product di-ion (3) versus time are shown in Eqs. (4)–(6).

$$\frac{dC_1}{dt} = -k_1' C_1 \tag{4}$$

$$\frac{dC_2}{dt} = k_1' C_1 - k_2' C_2 \tag{5}$$

$$\frac{dC_3}{dt} = k_2' C_2 \tag{6}$$

The analytical solutions for the above kinetic models can be accordingly derived and are shown in Eqs. (7)–(9) for the concentrations

of the reactant DEP (1), intermediate mono-ion (2), and product di-ion (3), respectively.

$$C_1 = C_1^{o} \ \exp(-k'_1 t) \tag{7}$$

$$C_2 = \frac{k'_1 C_1^{o}}{k'_2 - k'_1}[\exp(-k'_1 t) - \exp(-k'_2 t)] \tag{8}$$

$$C_3 = C_1^{o}\left\{1 - \frac{1}{k'_2 - k'_1}[k'_2 \ \exp(-k'_1 t) - k'_1 \ \exp(-k'_2 t)]\right\} \tag{9}$$

The corresponding pseudo-first order rate coefficients k'_1 and k'_2 were evaluated by minimizing the differences between the concentrations of the three components obtained from analytical calculation and from the spectroscopic measurements. These calculations were performed using a spreadsheet software (Microsoft Excel 2003).

4. Results and discussion

4.1. Infrared spectroscopic analysis

The typical infrared spectra of the alkaline hydrolysis reaction of DEP in water–ethanol solvent mixtures in the wavenumber range of 1200–1500 cm^{-1} are shown in Fig. 1(a). In order to highlight the spectral changes due to the contributions of DEP, mono-ion intermediate and di-ion product, the spectral contributions from the background (moisture) and other components (water, ethanol and sodium hydroxide) are subtracted from the reaction spectra in Fig. 1(a). The resulted spectra are shown in Fig. 1(b). It should be noted that the spectral contribution of ethanol, which is also a product from these reactions, has been subtracted in this step.

BTEM [31–33] analyses were employed in order to deconvolute the pure component spectra of the reactant DEP, the intermediate mono-ion and the product di-ion species. As frequently practiced, datasets from different runs were first combined. Subsequently, three peaks at 1301 cm^{-1}, 1396 cm^{-1}, and 1403 cm^{-1} were chosen as targets. These bands correspond to the reactant, intermediate and the product species, respectively. The reconstructed pure component spectra of the reactant DEP, intermediate and product are shown in Fig. 2(i)–(iii), respectively. The reconstructed pure component spectra show the anticipated major bands from the anti-symmetric stretching vibration of C–O–C at circa 1300 cm^{-1} (seen in DEP and intermediate), as well as the symmetric stretch of carboxylate at circa 1400 cm^{-1} (seen in the intermediate and product). Minor signals are due to various vibrational modes of CH_2 and CH_3 (i.e., at circa 1250–1490 cm^{-1}) and C–C stretch of the benzene ring (circa 1445–1500 cm^{-1}). The reconstructed pure component spectra of DEP and di-ion product obtained from this study are in good agreement with those reported in Reference [35,36], respectively.

The pure component spectra of water, ethanol and 'sodium hydroxide' could be obtained in a relatively simple way by using subtraction procedures [30]. It should be noted that the 'sodium hydroxide spectrum' should represent the spectrum of sodium hydroxide as well as its interaction with ethanol and water. The typical spectra of water, ethanol and 'sodium hydroxide' are provided in Fig. 3, respectively. Whereas water does not show any localized signals in the region 1200–1500 cm^{-1}, ethanol shows various vibrational modes of CH_2 and CH_3 (i.e., at 1300–1490 cm^{-1}) as well as the deformation of OH (circa 1264 and 1422 cm^{-1}). The 'sodium hydroxide' estimate shows the deformation of OH (circa 1260 cm^{-1}) as well as the characteristic vibrations of ethanolate at 1385 and 1457 cm^{-1} formed from the reaction of ethanol with sodium hydroxide [37]. It should be mentioned that the pure component spectra of water, ethanol and 'sodium hydroxide' could vary slightly between experimental runs especially when different temperatures and solvent compositions were used. It is therefore neccesary to obtain these spectral estimates from each individual experimental run.

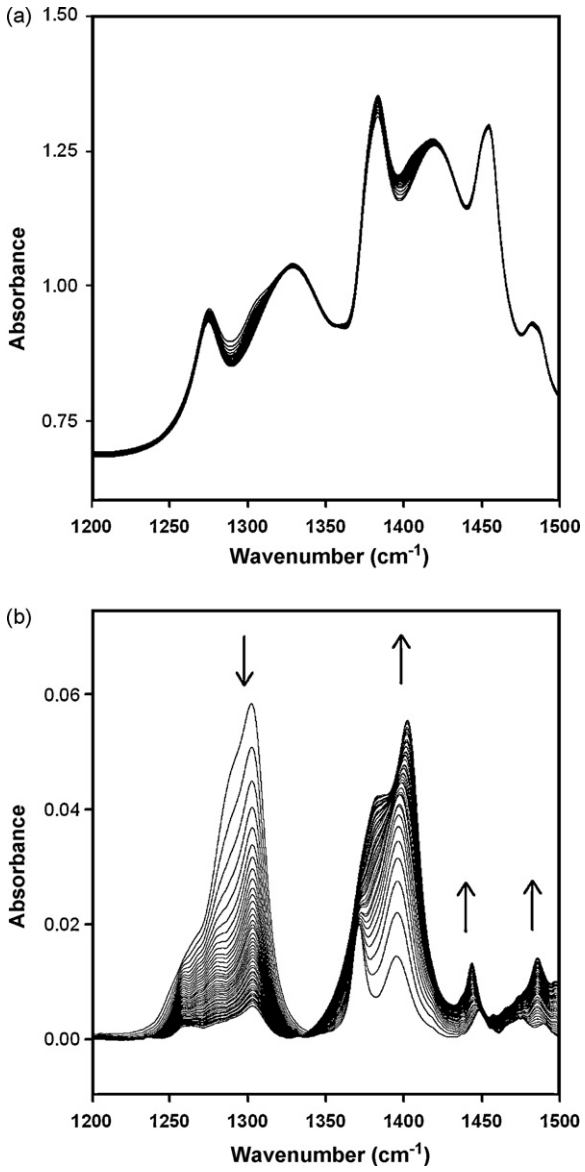

Fig. 1. Infrared reaction spectra of the alkaline hydrolysis reaction of DEP in ethanol–water (50:50, % (v/v)) solvent mixture and at $T = 20\,^{\circ}C$ (Exp run 1) (a) before and (b) after moisture and water–ethanol–NaOH spectral subtractions.

Finally, having obtained the pure component spectra for each constituent it is now possible to determine the associated signal intensities. In particular, the three minor constituents, namely reactant DEP, intermediate and product are responsible for only circa 0.054%, 0.310%, and 0.664% of the total integrated signal intensity, respectively. In other words, the signal in Fig. 1(b) associated with the three aromatic compounds present in the system corresponds to only circa 1% of the raw experimental spectroscopic data (Fig. 1(a)).

4.2. Kinetic analysis

In the present kinetic investigation, only concentrations of the DEP, mono-ion intermediate and di-ion product were used for the kinetic analysis. Using the methodology described in Section 3, the

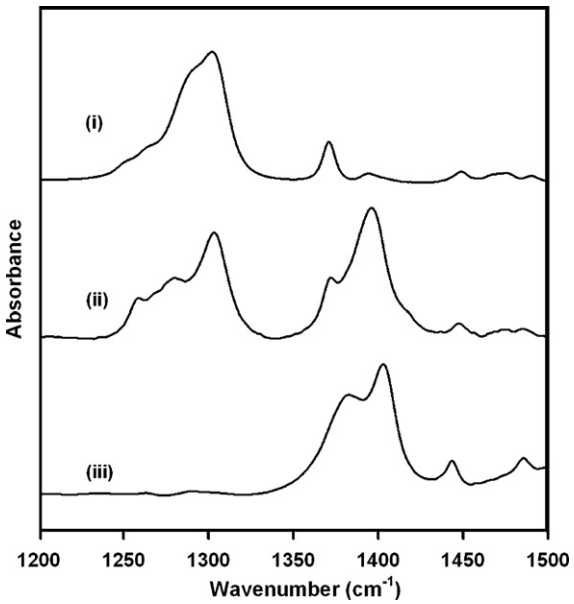

Fig. 2. The pure component spectra of (i) reactant DEP, (ii) mono-ion intermediate, and (iii) di-ion product, obtained using BTEM.

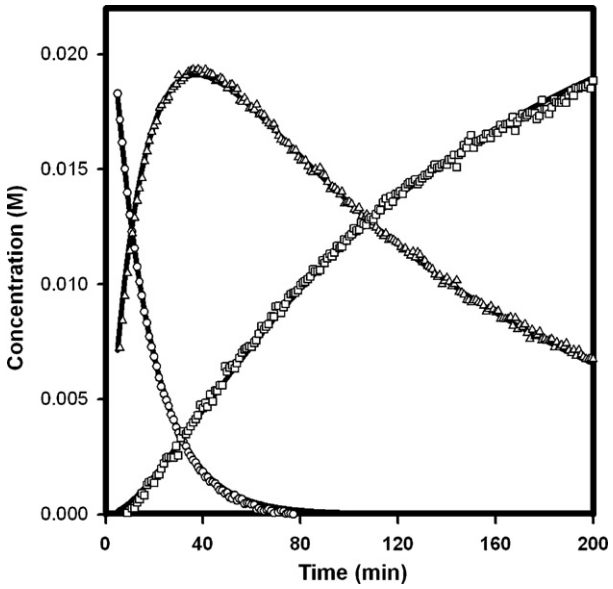

Fig. 4. Concentration profiles of reactant DEP (○), mono-ion intermediate (△) and di-ion product (□) from Exp run 1. Solid lines represent the corresponding concentrations obtained from the kinetic models (Eqs. (7)–(9)).

concentration profiles for the reactant, intermediate and product could be calculated. The results taken from Exp run 1 are shown in Fig. 4.

The concentrations obtained from the kinetic models in Eqs. (7)–(9) were subsequently compared to the concentration profiles obtained from the spectroscopy measurements. A least square minimization procedure was performed in order to determine the two corresponding pseudo-first order rate coefficients, k'_1 and k'_2. The calculated concentrations are consistent with the concentration profiles obtained from the spectroscopic measurements (see Fig. 4). This result indicates that the proposed model (Eqs. (4)–(6)) satisfactorily describes the kinetics of the present consecutive hydrolysis reaction.

Subsequently, a similar procedure of analysis was repeated to evaluate the kinetic parameters from other experimental runs listed in Table 1. The determined pseudo-first order rate coefficients, k'_1 and k'_2 are summarized in Table 2.

To facilitate further analysis at different solvent compositions and temperatures, the pseudo-first order rate coefficients should be transformed to second order rate coefficients. Since the addition of sodium hydroxide to the ethanol–water mixtures gives rise, nearly instantaneously, to an equilibrium involving ethanolate ion (Eq. (10)) [38–40], the concentration of hydroxide ion between experimental runs should vary depending on the temperature as well as the solvent composition used. Indeed, the formation of the ethanolate ion is experimentally confirmed by the present spectroscopy measurements (see Fig. 3(iii)).

$$EtOH + OH^- \rightleftharpoons EtO^- + H_2O \quad (10)$$

In order to facilitate the reaction rate comparison, the concentrations for the hydroxyl ion in each experimental run should be calculated by considering the equilibrium process in Eq. (10).

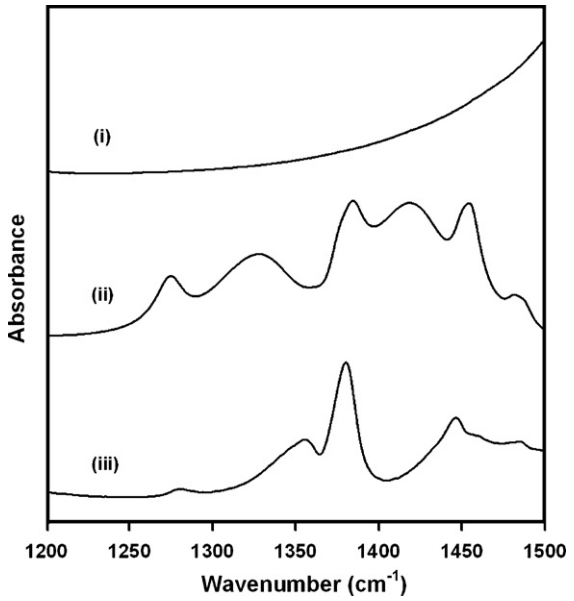

Fig. 3. The pure component spectra of (i) water, (ii) ethanol, and (iii) 'NaOH' in ethanol–water mixtures, obtained using a subtraction procedure.

Table 2
Summary of the pseodo-first order rate coefficients (k'_1 and k'_2) as well as the second order rate coefficients (k_1 and k_2) for the two consecutive steps.

Exp run	$k'_1 \times 10^3$ (s^{-1})	$k'_2 \times 10^4$ (s^{-1})	$k_1 \times 10^3$ ($L\,mol^{-1}\,s^{-1}$)	$k_2 \times 10^4$ ($L\,mol^{-1}\,s^{-1}$)
Reproducibility				
1	1.1	1.2	3.4	3.8
2	1.1	1.3	3.4	4.1
3	1.1	1.3	3.4	4.2
Average	1.1	1.3	3.4	4.0
Mass variations of reactant (DEP)				
4	1.1	1.3	3.5	4.1
5	1.1	1.2	3.3	3.9
Temperature variations				
6	1.3	1.7	4.0	5.0
7	1.8	2.0	5.2	5.9
8	2.7	3.1	7.7	9.0
9	3.6	3.9	10.4	11.4
Solvent mixture variations				
10	1.29	1.09	3.77	3.15
11	0.92	1.08	3.03	3.53
12	0.95	1.48	3.58	5.60
13	1.07	1.69	5.03	7.95

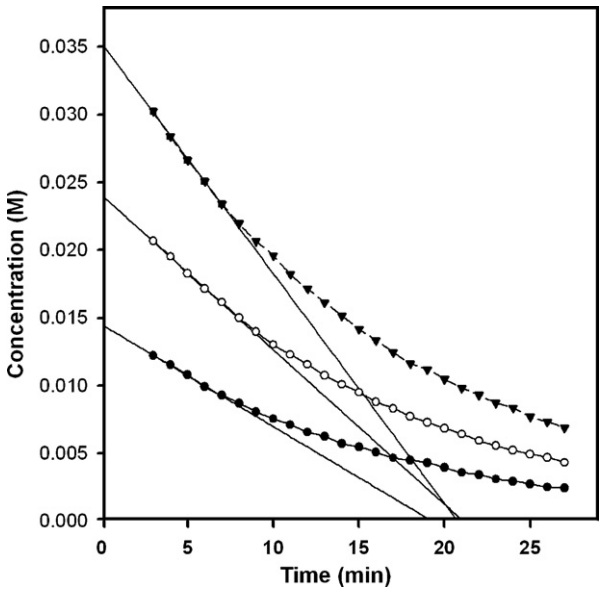

Fig. 5. Effect of the initial concentration of the reactant DEP on the rate of reaction. Exp run 1 (○), Exp run 4 (●), and Exp run 5 (▼). The initial rates are represented by the solid lines.

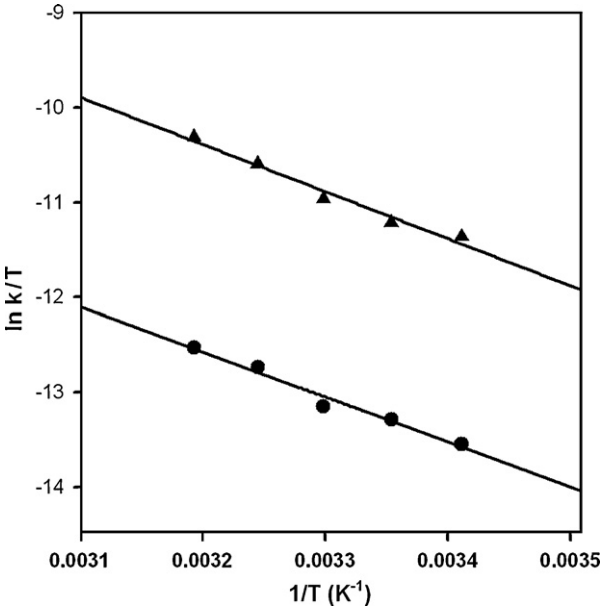

Fig. 6. Effect of temperature on the second order rate coefficients k_1 (▲) and k_2 (●), for 50% (v/v) ethanol–water solvent mixtures.

The equilibrium constant for Eq. (10) at several temperatures have been reported [38–40] and these values were utilized to calculate the hydroxyl ion concentration in solution. Since the variation of hydroxyl ion concentrations during the course of reaction is small (initial NaOH is in ~10 fold excess relative to DEP), the hydroxyl ion concentrations were treated as constants in each run. The obtained hydroxyl ion concentrations were subsequently used to transform the pseudo-first order rate coefficients k'_1 and k'_2 to second order rate coefficients k_1 and k_2 as follows.

$$k_1 = \frac{k'_1}{[OH^-]} \quad (11)$$

$$k_2 = \frac{k'_2}{[OH^-]} \quad (12)$$

The estimated second order rate coefficients k_1 and k_2 for various experimental runs are reported in Table 2.

In all cases, the second order rate coefficient k_1 is greater than k_2. The smaller reaction rate coefficient in the second consecutive step might be due to the electrostatic repulsion between the mono-anion intermediate and the hydroxide ion, which is not the case in the first reaction step between the DEP and hydroxyl ion.

Table 2 also shows that good reproducibility in the estimated rate coefficients can be achieved from the replicate measurements. In fact, the Exp run 1 was performed weeks before Exp runs 2 and 3. This demonstrates the robustness of the present experimental setup as well as the consistency of the on-line spectroscopy measurements.

4.3. Effect of the initial DEP concentration

The initial concentration of reactant DEP was varied according to Table 1 and the time-dependent concentrations of DEP are shown in Fig. 5.

A higher rate of reaction is observed from those experiments performed at higher initial concentrations of DEP as shown by the slope of the solid lines in Fig. 5. Analysis of the data shows that the kinetic rate coefficients (k_1 and k_2) obtained from these three experimental runs (Table 2) are very similar. This is reasonable since these experimental runs were carried out at the same reaction temperature and with the same solvent mixture ratios. In addition, the similar kinetic rate coefficients confirm that the model (Eqs. (4)–(6)) is accurate.

4.4. Effect of temperature

The effect of temperature on the second order rate coefficients k_1 and k_2 is shown in Fig. 6. Both rate coefficients are consistently increasing with temperature. The plot of $\ln k/T$ versus $1/T$ results in straight lines. The corresponding slopes and intercepts of the Eyring representation provided values of the enthalpy of activations ($\Delta^{\ddagger}H$) and the entropy of activation ($\Delta^{\ddagger}S$). The determined activation parameters for the first and second reaction were $\Delta^{\ddagger}H = 41.4$ and 39.6 kJ mol^{-1} and $\Delta^{\ddagger}S = -151.4$ and -175.5 J mol^{-1} K^{-1}, respectively. Both the sign and the magnitude of the entropies of activation for the two reactions are consistent with the associative nature of the elementary steps involved.

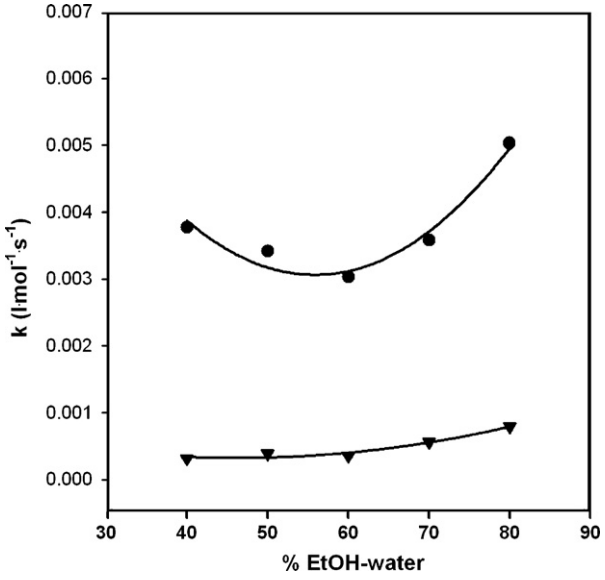

Fig. 7. Effect of solvent mixture on the second order rate coefficients k_1 (●) and k_2 (▼), at temperature 20 °C.

4.5. Effect of solvent mixtures

The effect of different solvent mixtures on the kinetic rate coefficients is shown in Fig. 7. These rate coefficients show minima at certain water–ethanol solvent compositions (circa 60% (v/v)). These solvent mixture effects on the reaction are similar to those observed in previous studies [41–44]. As noted by Blandamer and Burgess [45], addition of an organic co-solvent (i.e., ethanol) would appear to destabilize the OH^- ion, and this will, in part, contribute to a decrease in $\delta\Delta^{\ddagger}G$ (the change in the free energy of activation with change in solvent) and thus an increase in rate coefficient. In contrast, the rate of reaction involving a hydrophobic ion/molecule will tend to decrease with the addition of the co-solvent ethanol since ethanol can stabilize such ion/molecule. Since both OH^- and hydrophobic ions/molecules are present in the present systems, extrema in the values of k_1 and k_2 are expected. Since DEP is considered more hydrophobic than the mono-ion intermediate, a more pronounced curvature is observed in the values of k_1.

5. Conclusions

In the present study, it has been demonstrated that combined on-line transmission FTIR spectroscopy and chemometric techniques can facilitate the analysis of a rather complex, consecutive organic reaction carried out in mixed aqueous–organic solvent. The transmission infrared measurements in the mid-IR (particularly 1200–1500 cm^{-1}) resulted in high quality spectra of the organic vibrations (particularly, various CH_2 and CH_3 modes, as well as C–O–C and O–C–O). In addition, due to the transmission nature of the measurements, quantitative results (pure component spectra, concentrations and rates) were readily obtained. The various chemometric analyses, but particularly BTEM, permitted rather straightforward processing of the spectroscopic measurements. As a consequence, it was possible to determine the kinetics of the two individual organic reactions taking place. The present approach, of using high quality transmission FTIR spectroscopy together with chemometric techniques, is not restricted to the present reaction alone, but appears to be applicable to a wide variety of complex organic syntheses conducted in mixed aqueous–organic solvents. Due to (a) the increasing number of complex organic syntheses conducted in mixed aqueous–organic solvents, (b) the limited number of robust on-line analytical options available and (c) the experimental ease of using transmission FTIR techniques under non-ambient conditions, the present approach should be useful in a variety of experimental situations.

Acknowledgements

This work was supported by Agency for Science, Technology and Research (A*STAR), Singapore. The authors would like to thank Prof B.G. Cox for a valuable discussion.

References

[1] C.J. Li, T.H. Chan, Comprehensive Organic Reactions in Aqueous Media, second ed., John Wiley & Sons, Hoboken, NJ, 2007.
[2] P. Knochel (Ed.), Modern Solvent in Organic Synthesis, Topics in Current Chemistry, vol. 206, Springer, Berlin, 1999.
[3] D.J. Adams, P.J. Dyson, S.J. Tavener, Chemistry in Alternative Reaction Media, Chichester, West Sussex, England; Hoboken, N.J., J. Wiley, 2004.
[4] B. Cornils, W.A. Herrmann, Aqueous-phase Organometallic Catalysis: Concepts and Applications, second ed., Wiley-VCH, Weinheim, 1998.
[5] F. Joó, Aqueous Organometallic Catalysis, Kluwer Academic Publishers, Dordrecht, Boston, 2001.
[6] J.B.F.N. Engberts, in: P. Tundo, A. Perosa, F. Zecchini (Eds.), Methods and Reagents for Green Chemistry: An Introduction, Wiley-Interscience, Hoboken, NJ, 2007.
[7] R.A. Sheldon, I. Arends, F.V. Rantwuk, Green Chemistry and Catalysis, Wiley-VCH, Weinheim, 2007 (Chapter 1).
[8] C. Zhang, Fundamentals of Environmental Sampling and Analysis, John Wiley, Hoboken, NJ, 2007 (Chapter 8).
[9] T.D.W. Claridge, High-Resolution NMR Techniques in Organic Chemistry, first ed., Pergamon, Amsterdam, New York, 1999.
[10] Y. Jiang, M. Garland, K.J. Carpenter, P.S. Suresh, E. Widjaja, J. Polym. Sci., Part A: Polym. Chem. 45 (2007) 5697–5704.
[11] O. Elizalde, M. Azpeitia, M.M. Reis, J.M. Asua, J.R. Leiza, Ind. Eng. Chem. Res 44 (2005) 7200–7207.
[12] E. Venardou, E. Garcia-Verdugo, S.J. Barlowa, Y.E. Gorbaty, M. Poliakoff, Vib. Spectrosc. 35 (2004) 103–109.
[13] T.L. Williams, T.W. Collette, in: I.R. Lewis, H.G.M. Edwards (Eds.), Handbook of Raman Spectroscopy: From the Research Laboratory to the Process Line, Marcel Dekker, New York, 2001.
[14] S.C. Kang, Y.J. Choi, H.Z. Kim, J.B. Kyong, D.K. Kim, Macromol. Res. 12 (2004) 107–111.
[15] Z. Zhang, G.E. Ewing, Spectrochim. Acta, Part A 58 (2002) 2105–2113.
[16] R. Nomen, J. Sempere, K. Avilés, Chem. Eng. Sci. 56 (2001) 6577–6588.
[17] R. Pacheco, A. Karmali, M.L.M. Serralheiro, P.I. Haris, Anal. Biochem. 346 (2005) 49–58.
[18] R.P. Sperline, Langmuir 13 (1997) 3715–3726.
[19] R.A. Meyers (Ed.), Encyclopedia of Analytical Chemistry: Applications, Theory, and Instrumentation, Wiley, Chichester, New York, 2000, p. 13113.
[20] M. Hancer, R.P. Sperline, J.D. Miller, Appl. Spectrosc. 54 (2000) 138–143.
[21] K. Yamamoto, H. Ishida, Vib. Spectrosc. 8 (1994) 1–36.
[22] S.V. Mohan, S. Shailaja, M.R. Krishna, P.N. Sarma, J. Hazard. Mater. 146 (2007) 278–282.
[23] N.L. Wolfe, W.C. Steen, L.A. Burns, Chemosphere 9 (1980) 403–408.
[24] N. Venkatasubramanian, G.V. Rao, Tetrahedron Lett. 52 (1967) 5275–5280.
[25] G.V. Rao, N. Venkatasubramanian, Aust. J. Chem. 24 (1971) 201–203.
[26] Y. Chen, J. Li, Y.T. Li, X.-C. Zeng, J. Therm. Anal. Cal. 63 (2001) 483–491.
[27] J.F. Goggans, J.E. Copenhaver, J. Am. Chem. Soc. 61 (1939) 2909–2910.
[28] C.-S. Giam, T.E. Goodwin, T.K. Yano, J. Chem. Soc. Perkin Trans. 2 (1978) 831–833.
[29] L. Fishbein, P.W. Albro, J. Chromatogr. 70 (1972) 365–412.
[30] L. Chen, M. Garland, Appl. Spectrosc. 56 (2002) 1422–1428.
[31] E. Widjaja, C.Z. Li, M. Garland, Organometallics 21 (2002) 1991–1997.
[32] W. Chew, E. Widjaja, M. Garland, Organometallics 21 (2002) 1982–1990.
[33] E. Widjaja, C.Z. Li, W. Chew, M. Garland, Anal. Chem. 75 (2003) 4499–4507.
[34] K.R. Beebe, R.J. Pell, M.B. Seasholtz, Chemometrics: A Practical Guide, Wiley, New York, 1988 (Chapter 3).
[35] H. Nishikiori, J. Shindoh, N. Takahashi, T. Takagi, N. Tanaka, T. Fujii, Appl. Clay Sci. 43 (2009) 160–163.
[36] J.S. Loring, M. Karlsson, W.R. Fawcett, W.H. Casey, Spectrochim. Acta Part A 57 (2001) 1635–1642.
[37] K. Chandran, R. Nithya, K. Sankaran, A. Gopalan, V. Ganesan, Bull. Mater. Sci. 29 (2006) 173–179.
[38] F.F. Caldin, G. Long, J. Chem. Soc. (1954) 3737–3742.
[39] J. Murto, Ann. Acad. Sci. Fenn. Ser. A2 117 (1962) 1–84.
[40] V.B. Sunderland, D.W. Watts, Int. J. Pharm. 27 (1985) 1–15.
[41] W.J. Svirbely, A.D. Kuchta, J. Phys. Chem. 65 (1961) 1333–1337.
[42] W.J. Svirbely, F.A. Kundell, J. Am. Chem. Soc. 89 (1967) 5354–5359.
[43] M.N. Khan, J. Phys. Org. Chem. 7 (1994) 412–419.
[44] I.-H. Um, G.-J. Lee, H.-W. Yoon, S.-S. Kwon, Tetrahedon Lett. 33 (1992) 2023–2026.
[45] M.J. Blandamer, J. Burgess, Chem. Soc. Rev. 4 (1975) 55–75.

Talanta 79 (2009) 665–668

Contents lists available at ScienceDirect

Talanta

journal homepage: www.elsevier.com/locate/talanta

Chaotic parameters and their role in quantifying noise in the output signals from UV, TGA and DSC apparatus

José S. Torrecilla*, Ester Rojo, Juan C. Domínguez, Francisco Rodríguez

Department of Chemical Engineering, Faculty of Chemistry, University Complutense of Madrid, Avda. Complutense s/n, 28040 Madrid, Spain

ARTICLE INFO

Article history:
Received 4 February 2009
Received in revised form 15 April 2009
Accepted 21 April 2009
Available online 3 May 2009

Keywords:
Fractal dimension
Liapunov exponent
UV
TGA
DSC
1-Ethyl-3-methylimidazolium ethylsulfate

ABSTRACT

Two fractal dimensions and the Liapunov exponent (LE) have been applied to detect noisy output signals from UV spectrophotometer (UV), thermogravimetric analyzer (TGA) and differential scanning calorimeter (DSC) apparatus of 1-ethyl-3-methylimidazolium ethylsulfate ionic liquid ([emim][$EtSO_4$]). The data collected from these three pieces of equipment were classified before calculating LE, regularization (RD) and box dimensions (BD). The RD and LE are able individually to detect and quantify noisy output signals with a mean error value less than 5% in all cases tested. Given that the LE can be calculated using a really simple method, this chaotic parameter has been selected as the most suitable to detect noise of signals from these apparatus.

1. Introduction

In recent years, ionic liquids (ILs) have continued to attract the interest of researchers. ILs are chemicals composed of an organic cation and an inorganic or organic anion. Due to the nature of ions, ILs exhibit mixed inorganic and organic characters [1]. Recently, due to their unique properties, ILs have attracted increasing attention as replacements for conventional organic solvents in many fields, *viz.* catalysis, extraction processes, electrochemistry, etc. [1,2].

To model and/or control any chemical process, the measurement of IL concentration and the knowledge of their physicochemical properties are required. Due to the lack of knowledge of these topics, softwares which predicts or estimates their properties are being used in the design, modelization and/or control of chemical processes [3–5]. Recently, these measurements have been carried out by the interpolation in physicochemical properties, proton nuclear magnetic resonance (^{1}H NMR) spectroscopy [6], gas chromatograph (GC) [7], UV spectroscopy [4,5], etc. As is known, the presence of noise in this measurement can affect reliable quantification of IL. In relation to the properties of ILs, nearly all physicochemical properties of chemicals are taken from analytical equipment, and these measurements must be carried out with accuracy. As is known, the achievement of this goal depends on the variable measured (melting temperature, heat capacity, composition, etc.), the stability of instrumental response against time, the robustness of its calibration model, etc. All of these can be affected by the presence of noise in the measured property. The measurement process is made difficult and masks the true values of the properties. Given that tiny perturbations might generate an essential change in the state of non-linear systems, when the signal-to-noise ratio (SNR) is low, reliable detection is necessary. Because of this, the models of the processes based on statistical methods such as neural networks [8–10], genetic algorithms [11], fuzzy methods [12], chaotic methods [13], etc. have been applied to check and/or filter noisy signals.

The number of bibliographic references where the chaotic parameters are successfully applied to fault diagnosis is as yet scarce. In the chemistry field, to the best of our knowledge, the application of these parameters to detect noisy output signal without using their specific models is not found in the literature. Because of this, Liapunov exponent and fractal dimension calculated using regularization and box methods have been applied here to detect noisy output signals from UV spectrophotometer (UV), thermogravimetric analyzer (TGA) and differential scanning calorimeter (DSC).

2. Materials and methods

Detailed descriptions of the ionic liquid used, UV spectrophotometer, TGA, DSC apparatus and the chaotic parameters used are shown here.

* Corresponding author. Tel.: +34 91 394 42 40; fax: +34 91 394 42 43.
E-mail address: jstorre@quim.ucm.es (J.S. Torrecilla).

0039-9140/$ – see front matter © 2009 Elsevier B.V. All rights reserved.
doi:10.1016/j.talanta.2009.04.043

Table 1
Operating conditions of TGA and DSC experiments.

Operating conditions	TGA	DSC
IL used	[emim][$EtSO_4$]	[emim][$EtSO_4$]
Temperature range (K)	303.15–1173.15	133.15–303.15
Initial weight range of sample (mg)	7–16	9–21
N_2 flow (mL min^{-1})	50	50
Heating rate (K min^{-1})	10	10

2.1. Reagents, solutions and instrumentation

In this work, 1-ethyl-3-methylimidazolium ethylsulfate ionic liquid ([emim][$EtSO_4$], ≥95% purity, from Sigma–Aldrich Chemie GmbH, chloride content <30 ppm) was used. All stock solutions were prepared using an AG 245 Mettler Toledo analytical balance (precision 0.01 mg). A Varian Cary 1E UV–vis spectrophotometer was employed for absorbance measurements using quartz cells with a path length of 1 cm [5].

The weight loss during the sample decomposition was measured by a Mettler Toledo TGA/SDTA851e Thermogravimetric Analyser, using a nitrogen atmosphere. Given the specific chemical to be measured, the TGA experiment mainly depends on its initial weight, temperature, heating rate, and inert gas flow (nitrogen, argon, etc.). Due to the high hygroscopic nature of [emim][$EtSO_4$] IL, all experiments were carried out in a vacuum atmosphere glove box under dry nitrogen. The experimental conditions of every experiment carried out to design, optimize and test the linear models (*vide infra*) are shown in Table 1. The TGA equipment is able to measure the sample weight loss as a function of temperature or heating time with an accuracy of ±1 μg. The sample temperature is measured to an accuracy of ±0.1 K. More details about TGA experiments can be found in the literature [14].

The measurements of the heat flow associated with material transitions as a function of temperature were carried out on a Mettler Toledo DSC821^e. The differential scanning calorimeter equipment was calibrated according to the temperature range used and the manufacturer's instructions [15]. The temperature measurements were carried out with an accuracy of ±0.1 K. The experimental conditions of every experiment carried out to design, optimize and test the linear models are shown in Table 1. In every experiment, stainless steel pans with a volume of 120 μL and a purge flow of 50 mL min^{-1} of dry nitrogen were used. The temperature range is between 133.15 and 303.15 K, whereas the heating/cooling rate is fixed at 10 K min^{-1} [14].

2.2. Chaotic parameters used

Fractal dimension, in general, is a number that quantitatively describes how an object fills its space. In plane geometry, objects are solid and continuous and given that they have no holes, they have integer dimensions. Fractals are rough and often discontinuous, and so, they present non-integer dimensions. From a fractal geometry point of view, the fractal dimension is a measure of complexity that is used to describe the irregular nature of lines, curves, planes or volumes. In this work, the regularization dimension (RD) and the box dimension (BD) using a plain box method have been computed by Fraclab version 2.0 (Toolbox of Matlab version 7.01.24704, R14) [16]. Considering the original signal as fractal, its graph will have an infinite length. Taking into account RD and that all regularized versions have a finite length, the RD measures the speed at which this convergence to the infinite takes place [16]. To calculate BD, the software works exactly in the same way as when computing the regularization dimension except that in this case different box sizes are tested. In almost all cases, on numerical samples, the estimation of fractal dimension by the box method is less accurate than the calculation by the regularization method. All necessary parameters values to calculate RD and BD were selected by default configuration settings of the software used [16].

Table 2
Quantity of [emim][$EtSO_4$] in design and validation processes.

Operating conditions	TGA (mg)	DSC (mg)	UV (ppm)
Design process	7.3142	9.7000	608
First validation process	7.3142	9.7000	608
Second validation process	15.7741	20.8120	10

Liapunov exponents (LEs) characterize the dynamics of a complex process and quantify the average growth of infinitesimally small errors in initial points. LE values characterize the rate of separation of infinitesimally close trajectories. This can be used to measure the sensitivity of a system's behavior to initial conditions [17]. The LE parameter has been calculated following Eq. (1).

$$\mathrm{LE} = \frac{1}{\Delta t_m} \sum_{k=1}^{m} \log_2 \frac{L(t_k)}{L(t_{k-1})} \quad (1)$$

where Δt_m and $L(t_k)$ are the prediction time interval and the distance between the developed points in the phase space, respectively. This parameter is one of the most sensitive to determine chaotic dynamic. Depending on the sign of the maximal LE (MLE), different types of attractors (dynamical systems evolve after a long time) can be found. MLE < 0 represent stable fixed, MLE = 0 or MLE = ∞ imply stable limit cycle or noise respectively and 0 < MLE < ∞ implies chaos which mean that neighboring points of trajectories in the phase space diverge [18–20].

3. Results and discussion

The diagnosis of output signals from UV, TGA and DSC apparatus have been tested here. The test procedure applied consists of five stages: (i) from each piece of equipment, at least ten different profiles have been measured (absorbance, weight loss and rate of heat flow to simple profiles); (ii) ten percentages between 0.10 and 5.41% of a random noise is added to the output signal previously measured; (iii) using these noisy profiles, the LE, BD and RD parameters are calculated; (iv) linear models have been defined; (v) statistical tools are applied to verify the linear models by two types of validation samples. Given that a high correlation coefficient value does not guarantee that any linear regression fits well the data, in every case correlation coefficient and standard deviation have been calculated [21].

3.1. Noisy signals

Taking into account that the noise test of every piece of equipment has been successfully carried out, every output signal is free of noise. The experimental conditions and the sample weight are shown in Tables 1 and 2. Once the output signals of the apparatus have been measured, in order to reach a low signal-to-noise ratio, random data between −1 and 1 have been added to them. To tune the SNR, ten different percentages (0.1, 0.69, 1.28, 1.87, 2.46, 3.05, 3.64, 4.23, 4.82 and 5.41%) of random data have been added to the original signal (free of noise). The total profile and a detail of an enlargement area of the output signal of the TGA, DSC and UV apparatus with 0.1% of noise is shown in Fig. 1. As can be seen the 0.1% noise added is hardly detectable.

3.2. Chaotic parameters

Given that all Liapunov exponents are non-integer and positive, Table 3, these describe some different strange attractors; whose

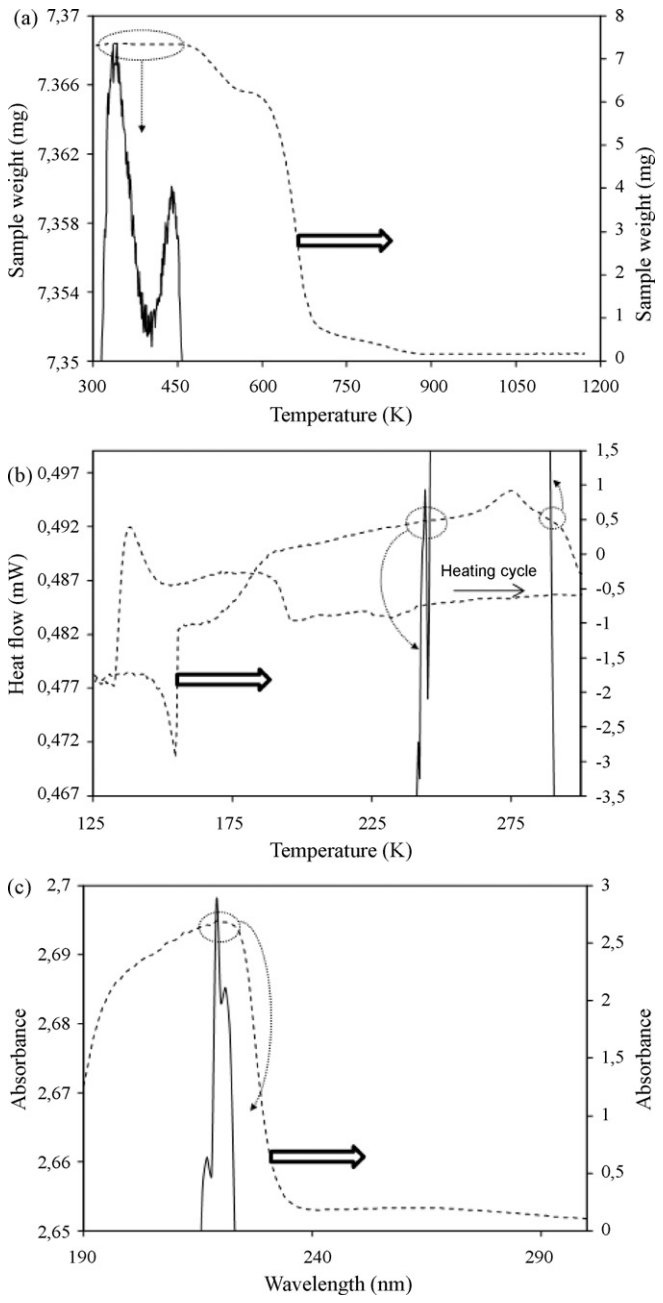

Fig. 1. Output signals with 0.1% of noise: (a) TGA; (b) DSC; (c) UV spectrophotometer (— total profile; ⬭ area of profile enlarged; — enlarged of ⬭).

trajectories appear to skip around randomly. This is probably due to the addition of random noise to the output signals. The LE values calculated using the output signals from the UV spectrophotometer are closer to zero than those from the other apparatus and therefore the trajectories can be explained using other type of attractor. In all cases, LE values are close to 0 and slightly decrease linearly (correlation coefficient, $R^2 > 0.980$) with the added noise percentage except in the DSC case. In this case, the final LE values are a consequence of two different trends, i.e. the variation of LE values with the added noise is made of a slightly increase and decrease depending on the cooling and the heating cycles of the DSC measurements, respectively (see Fig. 1b). And as consequence of this, the final LE values shown a really slightly increase with the added noise. In Table 4 are shown the linear models and their statistical results. In addition, the LE range of values is less than 8×10^{-3} per percentage unit of noise.

Given that RD and BD parameters define the output signals tortuosity and taking into account that the RD and BD values of the added random data (to make the noisy signals) are respectively 2.26 and 1.77, their values increase linearly ($R^2 > 0.973$ and $R^2 > 0.936$, respectively) with the percentage of noise added, Table 3. Their lineal models and statistical results are shown in Table 4.

3.3. Validation processes

Two validation processes have been used. In the first, another sample using the same quantity of [emim][$EtSO_4$] and similar experimental conditions as those used in the linear models design have been used. And finally, in the second, other quantities of [emim][$EtSO_4$] and the aforementioned experimental conditions have been used to calculate new profiles.

In the first validation process, once the profiles of all apparatus have been measured following the experimental conditions shown in Tables 1 and 2, five percentages (1, 2, 3, 4 and 5%) of noise have been added to the output signal of the equipment studied. Then, the chaotic parameters have been calculated. And finally, interpolating these LE, RD and BD values in the models shown in Table 4, every noise percentage added initially has been estimated, Table 5. In the light of these results, a linear relationship between LE and RD parameters and the noise added can be assumed. In this sense, although the relationship between RB and the noise is apparently linear, this statement is not clear enough in all tested cases. Probably due to the fact that if the box method is used to calculate the fractal dimension, the prediction is less accuracy (*vide supra*).

In the second validation process, the noise percentage added is similar to first validation process and the quantity of sample is different from the samples used at the design stage, Table 2. As is expected, the statistical results are the worst (in all cases $R^2 < 0.78$

Table 3
Chaotic parameters.

Noise (%)	TGA			DSC			UV		
	LE	RD	BD	LE	RD	BD	LE	RD	BD
0	0.1617	1.0043	0.8848	0.05416	1.3020	0.9251	2.614×10^{-4}	1.6646	0.9964
0.1	0.1613	1.0048	0.8839	0.05417	1.3069	0.9250	2.611×10^{-4}	1.6698	0.9860
0.69	0.1578	1.007	0.8956	0.05418	1.3080	0.9311	2.585×10^{-4}	1.7358	1.0268
1.28	0.1530	1.0097	0.9139	0.05420	1.3104	0.9424	2.554×10^{-4}	1.8181	1.0608
1.87	0.1476	1.0112	0.9287	0.05422	1.3138	0.9554	2.518×10^{-4}	1.8895	1.0984
2.46	0.1422	1.0143	0.9385	0.05423	1.3179	0.9623	2.477×10^{-4}	1.9487	1.1203
3.05	0.1369	1.0162	0.9540	0.05425	1.3226	0.9724	2.431×10^{-4}	1.9974	1.1342
3.64	0.1320	1.0197	0.9637	0.05426	1.3277	0.9777	2.380×10^{-4}	2.0387	1.1457
4.23	0.1275	1.0202	0.9685	0.05427	1.3330	0.9852	2.324×10^{-4}	2.0746	1.1612
4.82	0.1232	1.0226	0.9724	0.05428	1.3385	0.9894	2.263×10^{-4}	2.1057	1.1716
5.41	0.1193	1.0250	0.9772	0.05429	1.3441	0.9945	2.197×10^{-4}	2.134	1.1754
Range	0.0424	0.0207	0.0924	1.3×10^{-4}	0.0420	0.0694	4.170×10^{-5}	0.4694	0.1790

Table 4
Linear models* and statistical results calculated during the design process (correlation coefficient R^2 and standard deviation, σ).

	LE				RD				BD			
	a	*b*	R^2	σ	*a*	*b*	R^2	σ	*a*	*b*	R^2	σ
TGA	−122.7	19.9	0.998	0.07	261.1	−262.3	0.995	0.08	54.0	−47.9	0.965	0.20
DSC	4.2×10^4	2.3×10^3	0.988	0.12	137.2	−178.7	0.980	0.20	73.2	−67.7	0.984	0.16
UV	-1.3×10^5	35.0	0.980	0.16	11.1	−18.7	0.973	0.19	27.9	−28.1	0.936	0.31

*Noise (%) = $a \times$ [chaotic parameter] + b.

Table 5
Estimation values of noise added in the first validation process.

Noise (%)	TGA			DSC			UV		
	LE	RD	BD	LE	RD	BD	LE	RD	BD
1	0.97	0.87	0.80	1.05	1.05	1.05	0.93	0.93	0.70
2	1.99	2.21	1.70	2.11	2.21	2.13	1.82	1.72	1.69
3	3.04	3.23	3.30	3.11	3.23	2.15	2.91	2.71	3.33
4	3.99	4.15	4.21	3.98	4.16	4.24	3.90	4.18	4.25
5	4.98	4.81	4.76	4.91	4.81	4.90	5.14	5.24	4.70

and standard deviation, $\sigma < 3$). This is due to the fact that in all cases tested, the output signals depend on the quantity of IL used, and as the chaotic parameters calculated quantify the main characteristic of their profiles, the linear relation between chaotic parameters and noise has changed. From these results, when the intention is to detect noise using the method described here, the concentration value of the sample must be constant. The presence of noise in an output signal can be easily detected using LE or RD parameters. Given that LE values can be more easily calculated, Eq. (1), this chaotic parameter is the most suitable to detect and quantify the noise in noisy output signals.

4. Conclusions

In this work, the random noise of noisy output signals has been detected and quantified by the application of three chaotic parameters, *viz.* Liapunov exponent, regularization and box dimensions. To make the noisy signals used, random data between −1 and 1 have been added to different percentages on different output signals free of noise from a UV spectrophotometer, a thermogravimetric analyzer and a differential scanning calorimeter. Given that their correlation coefficient values reached in the design and in the first validation process ($R^2 > 0.980$, in most cases), linear relations between the LE or RD parameters and the quantity of random noise added can be assumed. Taking into account as a criterion the simplicity of the mathematical procedure to calculate these parameters, LE is the most suitable parameter for the required purpose.

In the chemistry field, thanks to these novel mathematical relations, detection and quantification of noisy signals can be achieved. In addition, the mathematical method developed and applied is very simple.

Acknowledgement

José S. Torrecilla is supported by a Ramón y Cajal research contract from the “Ministerio de Ciencia e Innovación” in Spain.

References

[1] W. Nelson, Green Solvents for Chemistry: Perspectives and Practice, Oxford University press, New York, 2003.
[2] E.F. Borra, O. Seddiki, R. Angel, D. Eisenstein, P. Hickson, K.R. Seddon, S.P. Worden, Nature 447 (2007) 979.
[3] J. Palomar, V.R. Ferro, J.S. Torrecilla, F. Rodríguez, Ind. Eng. Chem. Res. 46 (2007) 6041.
[4] J.S. Torrecilla, E. Rojo, J. García, F. Rodríguez, Ind. Eng. Chem. Res. 47 (2008) 4025.
[5] J.S. Torrecilla, A. Fernández, J. García, F. Rodríguez, Ind. Eng. Chem. Res. 46 (2007) 3787.
[6] A. Arce, O. Rodriguez, A. Soto, Chem. Eng. Sci. 61 (2006) 6929.
[7] G.W. Meindersma, A.J.G. Podt, A.B.S. De Haan, Fluid Phase Equilib. 247 (2006) 158.
[8] J.S. Torrecilla, A. Fernández, J. García, F. Rodríguez, Sens. Actuators B: Chem. 133 (2008) 426.
[9] J.M. Aragón, M.C. Palancar, Comput. Ind. Eng. 21 (1997) 631.
[10] R. Javadpour, G.M. Knapp, Comput. Ind. Eng. 45 (2003) 323.
[11] Y. He, D. Guo, F. Chu, Math. Comput. Simul. 57 (2001) 95.
[12] X. Liu, L. Ma, J. Mathew, Mech. Syst. Signal Proc. 23 (2009) 690.
[13] W. Wei, L. Qiang, Z. Guojie, Measurement 41 (2008) 904.
[14] A. Fernández, J.S. Torrecilla, J. García, F. Rodríguez, J. Chem. Eng. Data 52 (2007) 1979.
[15] J. Schawe, R. Riesen, J. Widmann, M. Schbnell, K. Vogel, U.U. Jorimann, Low temperature calibration, in: UserCom (Information for Users of METTLER TOLEDO Thermal Analysis Systems), vol. 9, METTLER TOLEDO, Schwerzenbach, Switzerland, 1999, pp. 1–4.
[16] J.L. Véhel, http://complex.futurs.inria.fr/FracLab/manual.html. 2009.
[17] P.G. Drazin, Nonlinear Systems, Cambridge University Press, Cambridge, United Kingdom, 1992.
[18] H.L. Swinney, J.P. Gollub, Physica D 18 (1986) 448.
[19] A. Wolf, J.B. Swift, H.L. Swinney, J.A. Vastano, Physica D 16 (1985) 285.
[20] H. Kant, T. Schreiber, Nonlinear Timer Series Analysis, Cambridge University Press, Cambridge, 2005.
[21] R.D. Chirico, M. Frenkel, V.V. Diky, K.N. Marsh, R.C. Wilhoit, J. Chem. Eng. Data 48 (2003) 1344.

Talanta 79 (2009) 557–561

Contents lists available at ScienceDirect

Talanta

journal homepage: www.elsevier.com/locate/talanta

Review

Simultaneously fluorescence detecting thrombin and lysozyme based on magnetic nanoparticle condensation

Liqing Wang, Lanying Li, Ying Xu, Guifang Cheng*, Pingang He, Yuzhi Fang*

Department of Chemistry, East China Normal University, Shanghai 200062, China

ARTICLE INFO

Article history:
Received 24 March 2009
Received in revised form 19 May 2009
Accepted 21 May 2009
Available online 27 May 2009

Keywords:
Aptamer
Thrombin
Lysozyme
Fluorescence detection
Magnetic nanoparticle

ABSTRACT

In this protocol, a fluorescent aptasensor based on magnetic separation for simultaneous detection thrombin and lysozyme was proposed. Firstly, one of the anti-thrombin aptamer and the anti-lysozyme aptamer were individually immobilized onto magnetic nanoparticles, acting as the protein captor. The other anti-thrombin aptamer was labeled with rhodamine B and the anti-lysozyme aptamer was labeled with fluorescein, employing as the protein report. By applying the sandwich detection strategy, the fluorescence response at 515 nm and 578 nm were respectively corresponding to lysozyme and thrombin with high selectivity and sensitivities. The fluorescence intensity was individually linear with the concentration of thrombin and lysozyme in the range of 0.13–4 nM and 0.56–12.3 nM, and the detection limits were 0.06 nM of thrombin and 0.2 nM of lysozyme, respectively. The preliminary study on simultaneous detection of thrombin and lysozyme in real plasma samples was also performed. It shows that the proposed approach has the good character for simultaneous multiple protein detection.

Contents

1. Introduction

Development of convenient, specific, sensitive high-throughput assays for proteins recognition and detection remains an extremely important goal. Among the development of aptamer-based analytical methods, fluorescent methodology is one of the most main techniques to transduce aptamer recognition events to detectable signals [1]. Fluorophore-labeled aptamers can be used to signal aptamer recognition events by monitoring the changes of fluorescence intensity, anisotropy [2] or fluorescence energy transfer [3]. Traditionally, monitoring fluorescence intensity, the target proteins have to be labeled with fluorescence molecule. As the uniform labeling of proteins is difficult, large numbers of target proteins

* Corresponding authors. Tel.: +86 21 62233508/62233510; fax: +86 21 62233508.
E-mail addresses: gfcheng@chem.ecnu.edu.cn (G. Cheng), yzfang@chem.ecnu.edu.cn (Y. Fang).

0039-9140/$ – see front matter © 2009 Elsevier B.V. All rights reserved.
doi:10.1016/j.talanta.2009.05.034

were impossible to be labeled and most of them were detected by competitive immunoassay which is time-consuming and shortened linear dynamic ranges. Currently, there are a lot of assays monitoring the changes of fluorescence intensity or anisotropy such as molecular beacon [4–6]. The imperfection of most fluorescent projects is that the high background depresses the selectivity and sensitivity although the improvement has been endeavored by many works [7]. Considering the demerits of present aptamer-based fluorescence methods, there is an obvious need to develop more sensitive fluorescent methods to signal aptamer recognition events. Usually, there are many components of proteins in real biological sample. Just detecting one kind of protein cannot meet the requirement of the proteome analysis. Simultaneous detection of different kind of proteins is necessary for proteome analysis and clinic diagnosis.

Herein, we describe a simple, general and sensitive aptamer-based fluorescent approach for simultaneously detecting thrombin and lysozyme. Thrombin is the last endoprotease that naturally functions as a blood clotting factor to convert fibrinogen to fibrin. Lysozyme is a part of the innate immune system and it functions by attacking bacteria peptidoglycans and hydrolyzes the glycosidic bond. Both of thrombin and lysozyme are the most important enzymes in physiology and pathology. Wang and his co-workers applied a competitive assay for simultaneously detecting thrombin and lysozyme by QDs-tagged proteins [8]. In this paper, the detection strategy is based on magnetic nanoparticles to concentrate and separate the target proteins bound with fluorophore-labeled aptamers. Magnetic nanoparticles have been utilized to separate and concentrate biomolecules for magically enhancing the sensitivity in many studies including electrochemical biosensors [9], immunomagnetic electrochemi-luminescence biosensors [10]. However, few applications of magnetic microspheres in fluorescent-based biosensors have been reported due to their heterogeneity in aquatic solution limiting its application in quantitative fluorescence analysis [11]. When magnetic nanoparticles are wrapped by water-soluble polymer, they become excellently homogeneous in aquatic medium [12,13]. In the strategy as illustrated in Fig. 1, we utilize around 50 nm magnetic nanoparticles (MNPs). The target proteins, such as thrombin and lysozyme, firstly were individually captured by anti-thrombin aptamers and anti-lysozyme aptamer which were immobilized onto the MNPs. And then, another anti-thrombin aptamer labeled with rhodamine B and anti-lysozyme aptamer labeled with fluorescein were respectively bound to their target proteins to transduce the aptamer recognition event to detectable fluorescence. Rhodamine B signals at 578 nm was corresponding to thrombin and fluorescein at 515 nm was assign to lysozyme. Nearly no interference exists between fluorescence signals of rhodamine B and fluorescein in simultaneous detection. The other coexistence proteins and unbounded report aptamers are easily washed out in the presence of under magnetic field. Hence, the magnetic utilization not only eliminates non-specific absorption of coexistence proteins and depresses fluorescent background, but also concentrates trace target proteins resulting in the enhanced fluorescence signals as well. Therefore, the approach selectivity and sensitivity has been improved.

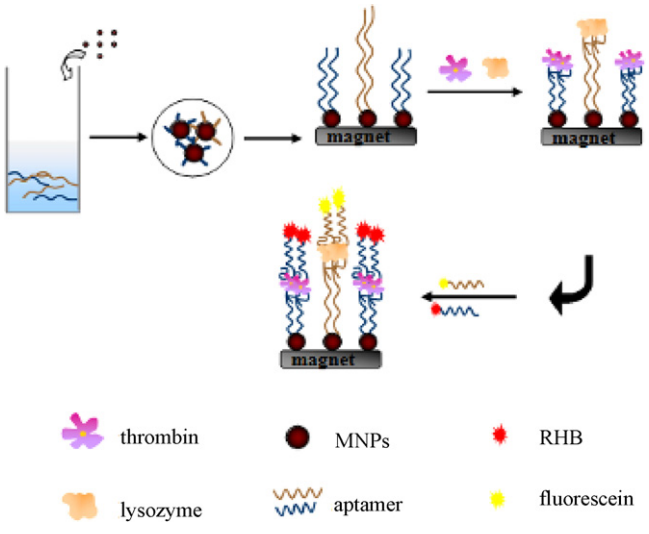

Fig. 1. Schematic representation of fluorescent detection for target proteins in sandwich-type system.

2. Experiments

2.1. Materials

Purified thrombin, lysozyme, bovine serum albumin (BSA) were purchased from Dingguo Biological Technology Corporation of Beijing. 19 bp anti-thrombin DNA aptamer, H_2N-ATAGGTTGGTGTGGGTTGG-3′ (aptamer I), 34 bp anti-thrombin DNA aptamer, H_2N-CTATCAGTCCGTGGTAGGGCAGGTTGGGGTGACT-3′ (aptamer II), 42 bp anti-lysozyme aptamer H_2N-ATCTACGAATTCATCAGGGCTAAAGAGTGCAGAGTTACTTAG-3′ (aptamer III) were custom synthesized from Shenergy Biocolor Biological Science & Technology Company, Shanghai. Rhodamine B, fluorescein, acetylacetone and all other inorganic chemicals were bought from Guoyao Chemicals Company (Jiangsu, China). N-hydroxysuccinimide (NHS) and N-(3-dimethylamnopropyl)-N-ethylcarbodiimide hydrochloride (EDC) were purchased from Sigma. Hyperfiltration membrane (7000 MWCO) was brought from Dingguo Biological Technology Corporation (Beijing, China). Purified water used for all sample preparations was obtained from Aquapro system (specific resistance is 18 MΩ). Unless specified, the buffers used in the following detection were PBS buffer (2.00 mM Na_2HPO_4, pH 7.3) and the physiological buffer (pH 7.3) was made up of 2.00 mM tris–HCl buffer with 1.0 mM $MgCl_2$, 1.0 mM $CaCl_2$, 0.14 M NaCl, 5.0 mM KCl.

2.2. Instrumentation

HZQ-C swing bed machine (Donglian Electronic Technology Ltd., China) and a super thermostatic bath 501 (Shanghai Laboratory Apparatus Factory, China) were used for facilitating the incubation of MNP–aptamer, fluorephore–aptamer and its corresponding protein. Fluorescence signal was collected in a 1 cm cell on a Fl-4500 fluorescence spectrophotometer (Hitachi, Japan).

2.3. Preparation of the carboxyl group modified magnetic nanoparticles

The magnetic nanoparticles used in the experiments with carboxyl group modification was prepared by mixing 2 ml of Fe_3O_4 (about 100 mg) alcohol suspended solution, which had been prepared according to Ref. [14], with 60 ml of alcohol solution containing 7 g of polyethylene glycol (PEG) and 10 ml of water, and then the mixture was dispersed by supersonic for about 20 min. 20 ml of styrene (St), 2 ml of acroleic acid, 0.2 ml of divinylbenzene and 1 g of benzoyl hydroperoxide were successively added into the mixture solution. After stirred at a velocity of 300–400 r min^{-1} for 10 min, the temperature gradually raised to 70 °C and keeping at 300 r min^{-1} stirring for 9 h until a brownish-yellow particles were obtained. The particles were washed with ethanol for several times and kept in PBS (pH 7.3) at 4 °C for the following use. The average

diameter of the carboxyl modified magnetic nanoparticles (MNPs) is about 50 nm.

2.4. Preparation of the aptamer functioned MNPs and fluorephore labeled aptamers

The aptamer (I or III) immobilized on MNPs was prepared by mixing 100 μl of MNPs (50 mg/ml) suspension with 4.3 mg of NHS. After treated with ultrasonic for 30 min, 2 O.D. of aptamer (I or III) (about 66 μg) and 4.6 mg of EDC were added into above suspension and the mixture was diluted by 500 μl of tris–HCl buffer (pH 7.3) and gently stirred at room temperature for 8 h. The aptamer functioned MNPs was washed with tris–HCl buffer for several times. It was re-suspended in 500 μl of tris–HCl buffer (pH 7.3) and stored at 4 °C, which can keep stable for months. The content of aptamer immobilized onto MNPs was measured by UV–vis absorbance of aptamer at 260 nm. The MNPs–aptamer and the MNP–aptamer III was equally mixed before protein detection.

Aptamer labeling with fluorescent dye such as rhodamine B or fluorescein was prepared by mixing 500 μl of 1.0×10^{-3} mol/L fluorescent dye with 4.3 mg of NHS and stirred for 30 min to activate the carboxyl groups on fluorephore. Then, 2 O.D. of aptamer (II or III) and 5 mg of EDC were added and stirred at room temperature for 8 h. The resulting fluorephore–aptamer were dialyzed with a dialyzer (MWCO 7000) to remove the unbound fluorescent dye, and then stored at 4 °C.

2.5. Incubation of thrombin and lysozyme with the MNP–aptamer and the fluorephore–aptamer and fluorescence detection

MNP–aptamer (I) and MNP–aptamer (III) mixture, target proteins (thrombin and lysozyme) and the fluorephore labeled aptamer were mixed together and incubated in tris–HCl buffer at 37 °C for 30 min. After being washed with tris–HCl buffer for five times to eliminate coexisting proteins and unbounded report aptamers, the MNPs–aptamer/protein/aptamer sandwich was re-suspended in 800 μl of tris–HCl buffer for fluorescence detection. The emission at 515 nm of fluorescein with its excitation at 480 nm and emission at 578 nm of rhodamine B with its excitation at 540 nm were collected for lysozyme and thrombin detection, respectively.

3. Results and discussion

3.1. Characteristic of the MNPs

The granularity of MNPs was determined by transmission electron microscope (TEM), which showed that obtained particles are spherical and well proportioned with the average diameter at about 50 nm (Fig. 2). The carboxyl content on the surface of MNPs was measured by conductance titration with a standard NaOH solution and the result is 0.49 mmol/g. Considering the diameter of the MNPs it can be estimated that there was about 1.7×10^{-19} mol carboxyl on the surface of one nanoparticle.

The IR spectrophotometric experiment was carried out to analyze the MNPs before and after aptamer modification (Fig. 3). Compared with IR spectrum of carboxyl modified MNPs, IR spectrum of aptamer functioned MNPs exhibited difference, i.e. the peak (1782 cm^{-1}) of the stretch vibration of C=O on carboxyl became sharp, strong and shifted to 1752 cm^{-1} indicating the carboxyl has changed. The peaks of stretch vibration of $-CH_2-O-P$ (1095 cm^{-1} and 1123 cm^{-1}) represented the existence of oligonucleotide on the MNP surface. Thus, it can be concluded that the capture aptamer was successfully immobilized onto MNPs through amidation reaction between amino functioned aptamer and carboxyl modified MNPs.

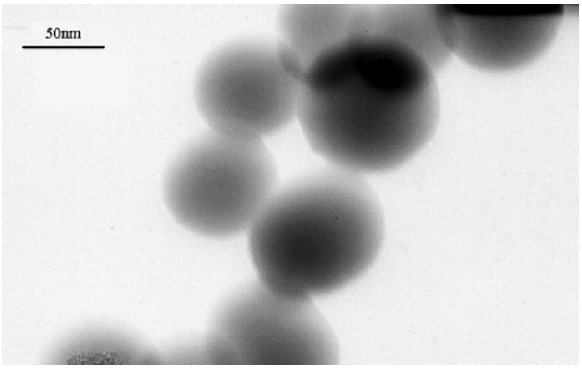

Fig. 2. TEM image of carboxyl modified MNPs.

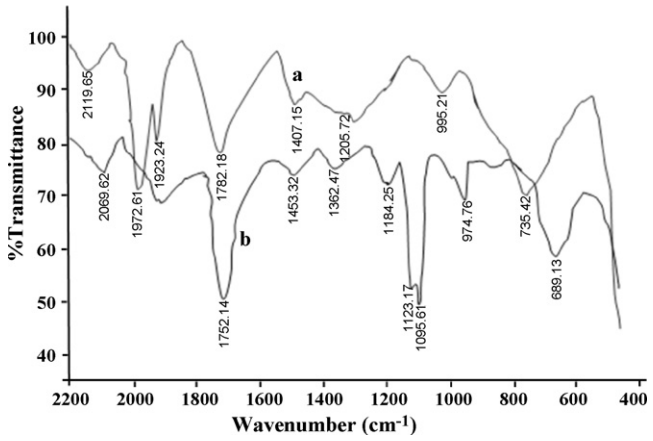

Fig. 3. IR spectrum of carboxyl modified MNPs (a) and aptamer (I) functioned MNPs (b).

3.2. The fluorescence detection of the MNP–aptamer/protein/fluorephore–aptamer system formation

The formation of the MNP–aptamer/protein/fluorephore–aptamer system was investigated by fluorescence measurement. As shown in Fig. 4, the fluorescence spectra excited at 480 nm and 540 nm

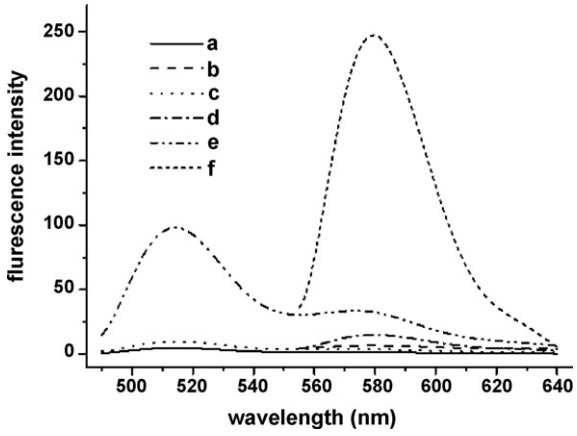

Fig. 4. Fluorescence spectra of the MNPs–aptamer (I) and MNPs–aptamer (III) mixture suspension excited at 480 nm (a) and at 540 nm (b); the MNPs–aptamer mixture suspension incubated with aptamer (II)–rhodamine B and aptamer (III)–fluorescein without lysozyme and thrombin excited at 480 nm (c) and at 540 nm (d); the mixture suspension incubated with lysozyme and thrombin in the presence of aptamer (II)-rhodamine B and aptamer (III)–fluorescein excited at 480 nm (e) and at 540 nm (f) ($c_{MNP-aptamer(I)}$ = 9.5 nM, $c_{rhodamine\ B-aptamer(II)}$ = 9.0 nM, $c_{MNP-aptamer(III)}$ = 9.1 nM, $c_{fluorescein-aptamer(III)}$ = 9.4 nM, $c_{thrombin}$ = 2.5 nM, $c_{lysozyme}$ = 2.5 nM).

of the mixture suspension of MNP–aptamer (I) and MNP–aptamer (III) (curves a and b) and that of the MNP–aptamer mixture suspension incubated with aptamer (II)–rhodamine B and aptamer (III)–fluorescein (curves c and d) were very low, which indicated the absorption of free fluorephore–aptamer onto the MNP–aptamers was very low, and thus, the influence of non-specific absorption of fluorephore–aptamer on the target protein detection could be neglected. When 2.5 nM of thrombin and 2.5 nM of lysozyme were added into the mixture suspension of MNP–aptamer and fluorephore–aptamer, the fluorescence responses both at 515 nm and 578 nm were significantly enhanced (curves e and f) and nearly no interference on the fluorescence detection of thrombin and lysozyme had been found.

3.3. Optimization of the target proteins incubation with their corresponding aptamers

It has been reported that the physiological buffers such as tris–HCl and PBS could maintain the bioactivity of target protein [15]. A small amount of $Mg^{2+}$and Ca^{2+} were necessary for aptamer and protein combination, because they could stabilize the G-quarter structure of the aptamer to bind with the target protein [16]. Considering Ca^{2+} and Mg^{2+} would be precipitated by the phosphate anion, tris–HCl buffer was selected as the incubation buffer. The incubation temperature was investigated from 20 °C to 65 °C and the larger fluorescence response was achieved in the range of 30–45 °C when the incubation time was lasted out for 30 min. Thus, the optimization of incubation was carried out in 0.02 M tris–HCl solution with both 1.0 mM $Mg^{2+}$and Ca^{2+} for 30 min at 37 °C to form a stable MNP–aptamer/target protein/fluorephore–aptamer structure.

3.4. Detecting target protein

The simultaneous specific detection of thrombin and lysozyme based on MNP–aptamer and fluorephore–aptamer system was tested by two different experiments. Firstly, MNP-random sequence of olignucleotides and fluorephore-random sequence of olignucleotides were respectively instead of MNP–aptamer and fluorephore–aptamer to act as target protein captor and reporter. Secondly, MNP–aptamers and fluorephore–aptamers incubated with different target proteins, such as thrombin, lysozyme, thrombin and lysozyme mixture, thrombin, lysozyme and coexistence protein (BSA) mixture. As shown in Fig. 5, the MNP-random sequence and the fluorephore-random sequence resulted in the fluorescence signals (columns a and b) as low as the background which is the response of MNP–aptamer and fluorephore–aptamer mixture (column c). The fluorescence responses at 515 nm and 578 nm was increased while in the presence of the target proteins of lysozyme (columns e and f) and thrombin (columns d and f). Column g obtained in the presence of BSA was only slightly higher than the column d and column f obtained without BSA. All the results revealed that the target protein cannot bind to the random sequence of olignucleotide whatever it acted as the captor or the reporter, and coexistence protein such as BSA had no evident effect on thrombin and lysozyme detection though BSA was performed in 1000-fold excess of thrombin and lysozyme. The fluorescence signal produced only attributed to the target proteins existence such as thrombin and lysozyme. Additionally, as it can be found that the fluorescent response of thrombin was much larger than that of lysozyme, it may ascribe to that thrombin has two distinct epitopes to respectively bind with aptamer I and II while lysozyme only has one. Both of the capture and the report aptamers of thrombin respectively bound with their corresponding epitopes without interference. However, in the lysozyme detection system, both of the capture and the report aptamers of lysozyme were competitively combined with the only one distinct epitope. Therefore, when one of the aptamers (the captor or the reporter) bound to the distinct epitope of lysozyme, the other aptamer (the reporter or the captor) had to bind to another lower affinity site of lysozyme. In this sense, sandwich device is more suitable for detection of the target with two or more distinct epitopes than that with only one distinct epitope. Additionally, the high fluorescence efficiency of rhodamine B also enhanced its fluorescence signal of thrombin.

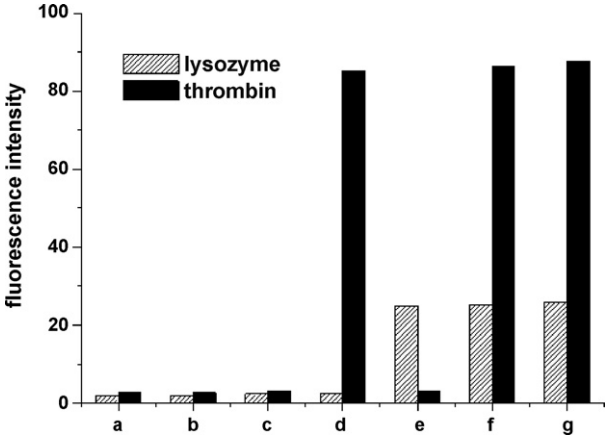

Fig. 5. Specific combination of the aptamers and the target proteins, the MNP-random sequence of olignucleotides/thrombin + lysozyme/fluorephore–aptamers (a), the MNP–aptamers/thrombin + lysozyme/fluorephore-random sequence of olignucleotides (b), the MNP–aptamers/fluorephore–aptamers without thrombin and lysozyme (c), the MNP–aptamers/thrombin/fluorephore–aptamers (d), the MNP–aptamers/lysozyme/fluorephore–aptamers (e), the MNP–aptamers/thrombin + lysozyme/fluorephore–aptamers (f), and the MNP–aptamers/thrombin + lysozyme + BSA/fluorephore–aptamers (g), ($c_{\text{MNP–aptamer(I)}}$ = 9.5 nM, $c_{\text{rhodamine B aptamer(II)}}$ = 9.0 nM, $c_{\text{MNP–aptamer(III)}}$ = 9.1 nM, $c_{\text{fluorescein–aptamer(III)}}$ = 9.4 nM, c_{thrombin} = 0.91 nM, c_{lysozyme} = 0.92 nM and c_{BSA} = 0.95 μM).

3.5. Simultaneously detecting thrombin and lysozyme

The procedure of thrombin and lysozyme detection was based on the specific combination of the target protein and their corresponding aptamer as shown in Section 2.4. Different amount of thrombin and lysozyme were incubated with the definite amount of MNP–aptamer (I), MNP–aptamer (III), rhodamine B–aptamer (II) and fluorescein–aptamer (III) mixture, and then the fluorescent measurement was carried out after the process of incubation and washing. Increasing the quantity of thrombin from 0.13 nM to 4.0 nM and that of lysozyme from 0.56 nM to 12.3 nM, the fluorescent intensity at 578 nm (ex 540 nm) and 515 nm (ex 480 nm) was linear with the concentration of the individual target protein (Fig. 6). The equation of the resulting calibration plot for thrombin and lysozyme are $I = 98.1c_{\text{thrombin}}$ (nM) − 4.04 with correlation coefficient 0.996 and P 0.015, and $I = 30.9c_{\text{lysozyme}}$ (nM)-4.58 with correlation coefficient 0.998 and P 0.012, respectively. The detection limit of thrombin and lysozyme were estimated as 0.06 nM and 0.2 nM by using 3σ (where σ is the standard deviation of a blank solution, $n = 10$). The reproducibility and stability of fluorescent signal of this assay were tested by measuring five thrombin and lysozyme concentrations in five independent measurements. The coefficients of variation were small at each protein concentration (Table 1).

3.6. Detection of thrombin in human plasma samples

To test whether the assay could be applied for simultaneous detection of thrombin and lysozyme in real biological samples, experiments were carried out in human plasma samples. As thrombin is present in its native precursor form, i.e. prothrombin in

Table 1
The reproducibility of thrombin and lysozyme detection.

$c_{protein}$ (nM)	Thrombin			Lysozyme		
	Fluorescence (578 nm)	Average	RSD %	Fluorescence (515 nm)	Average	RSD %
0.56	53.0, 49.8, 52.7, 53.9, 51.3	52.1	3.1	17.0, 15.0, 16.5, 13.0, 13.9	15.7	11.6
0.89	86.5, 84.3, 85.8, 85.0, 87.7	85.9	1.6	27.7, 25.9, 24.0, 26.4, 24.4	25.7	4.8
1.12	97.9, 99.1, 97.0, 97.2, 100.1	98.3	1.2	30.8, 29.4, 29.2, 32.0, 31.7	30.5	4.2
1.34	120.3, 121.9, 122.7, 124.5, 123.5	122.6	1.3	36.1, 34.5, 36.5, 34.1, 38.1	35.9	4.5
2.69	251.6, 252.3, 252.0, 252.9, 254.4	252.6	0.43	76.1, 73.9, 74.0, 75.3, 77.5	75.3	2.0

Table 2
The detection results of thrombin and lysozyme in the human plasma samples.

Sample	Thrombin						Lysozyme					
	Found in diluted plasma (nM)	RSD[a] (%)	Added amount (nM)	Found amount (nM)	Recovery %	Amount in plasma (μM)	Found in diluted plasma (nM)	RSD[a] (%)	Added amount (nM)	Found amount (nM)	Recovery %	Amount in plasma (μM)
1	1.48	0.89	1.40	2.77	92.1		9.35	0.53	2.4	11.6	93.8	
2	1.56	0.76	1.40	3.02	104.3	0.477	9.56	0.31	2.4	12.0	101.7	2.82
3	1.70	1.12	1.40	3.18	105.7		9.23	0.77	2.4	11.5	94.6	

[a] The results listed in the table were obtained from four independent experiments.

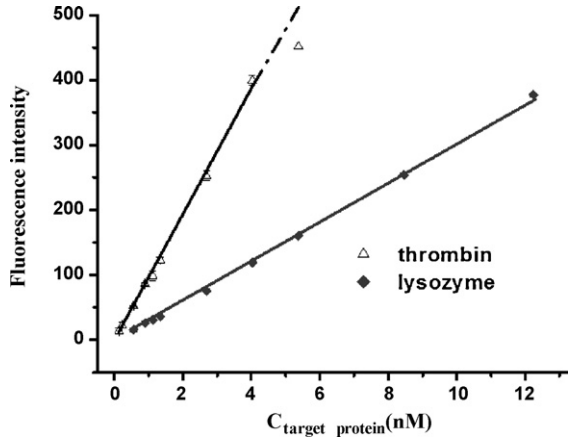

Fig. 6. The calibration plot of fluorescence response vs. the concentration of thrombin and lysozyme ($c_{MNP-aptamer(I)}$ = 12 nM, $c_{MNP-aptamer(III)}$ = 12 nM, $c_{rhodamine\ B-aptamer(II)}$ = 13 nM, and $c_{fluorescein-aptamer(III)}$ = 13 nM).

plasma, a pretreatment was done by adding 10 μl of 0.25% pancrease enzyme and 900 μl of 5.3×10^{-3} mol/L fish DNA into 100 μl plasma, which to activate the prothrombin into thrombin and also protect the aptamers from degradation. After 300-times dilution, a definite amount of the diluted plasma was detected according to the procedure described in Section 2.4. Three different plasma samples were detected and the amount of thrombin and lysozyme found in plasma with recovery were shown in Table 2. The amount of thrombin and lysozyme in human plasma were calculated at 0.477 μM and 2.82 μM, respectively.

4. Conclusions

In this work, we demonstrate the simultaneous detection of thrombin and lysozyme based on aptamer for specific combination and MNP for efficient separation. The assay has been performed in real sample and some satisfied results were obtained. Considering the design of this assay described here is not limited to some specific proteins; it would be generally applicable to a large number of proteins and result in an enhanced specificity and increased affinity. Development of magnetic nanoparticles for separation brought about the low detection limit of the target proteins, meeting with the requirement for simultaneously detection of specific proteins in biological sample, which would also find wide applications in research of medical diagnosis and pharmacology.

Acknowledgments

Financial support from the National Science Foundation of China (NSFC, Grants nos. 20775027 and 20675031) is gratefully acknowledged.

References

[1] H. Urata, K. Nomura, S.I. Wada, M. Akagi, Biochem. Biophys. Res. Commun. 360 (2007) 459–463.
[2] M.N.D.M. Kolpashchikov, J. Am. Chem. Soc. 126 (2004) 9266–9270.
[3] H. Ozaki, A. Nishihira, M. Wakabayashi, M. Kuwahara, H. Sawai, Bioorg. Med. Chem. Lett. 16 (2006) 4381–4384.
[4] R. Yamamoto, T. Baba, P.K. Kumar, Genes Cells 5 (2000) 389–396.
[5] M.N. Stojanovic, P. De Prada, D.W. Landry, J. Am. Chem. Soc. 123 (2001) 4928–4931.
[6] X. Fang, A. Sen, M. Vicens, W. Tan, Chem. Biochem. 4 (2003) 829–834.
[7] N. Hamaguchi, A. Ellington, M. Stanton, Anal. Biochem. 294 (2001) 126–131.
[8] J.A. Hansen, J. Wang, A. Kawde, Y. Xiang, K.V. Gothelf, G. Collins, J. Am. Chem. Soc. 128 (2006) 2228–2229.
[9] G.F. Cheng, J. Zhao, Y.H. Tu, P.G. He, Y.Z. Fang, Anal. Chim. Acta 533 (2005) 11–16.
[10] M. Mujika, S. Arana, E. Castano, M. Tijero, R. Vilares, J.M. Ruano-Lopez, A. Cruz, L. Sainz, J. Berganza, Biosens. Bioelectron. 24 (2009) 1253–1258.
[11] M. Careria, L. Elviri, J.B. Lagosa, A. Mangiaa, F. Speronia, M. Terenghia, J. Chromogr. A 1206 (2008) 89–94.
[12] E. Matijevic, Chem. Mater. 5 (1993) 412.
[13] X. Younan, B. Gates, Y. Yin, Y. Lu, Adv. Mater. 12 (2000) 693.
[14] M. Ma, Y. Zang, W. Yu, H.Y. Shen, H.Q. Zhang, N. Gu, Colloids Surf. A: Physicochem. Eng. 212 (2003) 219–222.
[15] H.A. Ho, M. Leclerc, J. Am. Chem. Soc. 126 (2004) 1384–1387.
[16] C. Kneuer, M. Sameti, U. Bakowsdy, T. Schiestel, H. Schirra, H. Schmidt, C.M. Lehr, Bioconjug. Chem. 11 (2000) 923–926.

Talanta 79 (2009) 739–745

Contents lists available at ScienceDirect

Talanta

journal homepage: www.elsevier.com/locate/talanta

Preparation and characterization of monolithic column by grafting pH-responsive polymer

Xiaoyi Wei[a,b], Li Qi[a,*], Gengliang Yang[c], Fuyi Wang[a]

[a] Beijing National Laboratory for Molecular Sciences, Laboratory of Analytical Chemistry for Life Science, Institute of Chemistry, Chinese Academy of Sciences, No. 2 North First Street, Zhongguancun, Beijing 100190, China
[b] Graduate School, Chinese Academy of Sciences, Beijing 100049, China
[c] College of Pharmacy, Hebei University, Baoding 071002, China

ARTICLE INFO

Article history:
Received 4 January 2009
Received in revised form 27 April 2009
Accepted 29 April 2009
Available online 7 May 2009

Keywords:
Monolithic column
Graft
Methacrylic acid
pH-responsive polymer

ABSTRACT

A novel modified monolithic column with pH-responsive polymer chains was prepared by grafting methacrylic acid onto the poly(glycidyl methacrylate-*co*-ethylene dimethacrylate) monolith. The grafting polymerization was achieved in an in situ manner which was performed by pumping methacrylic acid directly through an acidic hydrolysis monolithic column using potassium peroxydisulfate initiated free-radical polymerization. The grafted monolithic column was demonstrated to be the pH-responsive to the pore structure and the chromatographic characterization. The permeability of the column and the retention factors of five benzene homologues decreased due to the conformational changes of the polymer chains when the pH of mobile phase increased from 4.5 to 7.5. Furthermore, the modified monolithic column was used as the pH-responsive stationary phase and exhibited an excellent separation of four basic proteins.

1. Introduction

Polymer-based monolithic columns developed in the early 1990s [1] are widely used as efficient stationary phases for all types of chromatographic separations [2]. The major advantages of polymer monoliths exhibit high porosity, low resistance to hydraulic flow, fast mass transfer, and the simplicity of the in situ preparation process from liquid precursors. All of these features combine to enable excellent separations to be achieved at a high flow rate [3]. However, one of the drawbacks of monolithic materials with large pores is a limited surface area of pore walls and as result of a limited amount of functional groups available on the pore wall surface [4,5].

The introduction of functional groups onto the surface of porous chromatographic support via grafting polymerization of vinyl monomers originally containing functional groups is a versatile approach for the preparation of materials with controlled incorporation of functional groups [6]. On the one hand, polymer chains grafted onto a substrate are designated as polymer brushes or tentacles, and they would provide multiple functionalities emanating from each individual surface site and dramatically increase the surface group density [7]. For example, Frechet and co-workers [8] have demonstrated that Ce(IV) initiated grafting poly(2-acrylamido-2-methylpropanesulfonic acid) onto the internal surface of porous monolith could afford an excellent separation medium for biopolymers, and an increase in the dynamic binding capacity. On the other hand, grafting functional monomers from the monoliths can also provide some special properties. Svec and co-workers [9] involved a kind of thermal-responsive material poly(N-isopropylacrylamide) onto the monolithic column, and the prepared monolith could present the different ability in response to external temperature.

Recently, another intelligent material which can respond to environmental stimulin, such as the pH stimulus-responsive polymers, have attracted significant interest since they undergo large conformational changes when being exposed to different pH environments [10]. The polymer brushes can swell or shrink at different pH environment, and can receive much attention in the field of controlled drug delivery [10,11] or bioconjugates [12]. Feng and co-workers [13] prepared a kind of pH-responsive grafted silica containing acrylic acid (AAc) and butyl acrylate (BA), and involved it to be a pH-responsive stationary phase at different HPLC mode. So far to our best knowledge, the preparation of in situ grafting the pH-responsive polymer onto the polymer monolithic column and the characterization for chromatographic separation have not yet been explored.

In this study, we introduced a method to graft methacrylic acid (MAA) onto the internal surface of hydrolyzed poly-(glycidyl ethacrylate-*co*-ethylene dimethacrylate) [p(GMA-EDMA)]

* Corresponding author. Tel.: +86 10 82627290; fax: +86 10 62559373.
E-mail address: qili@iccas.ac.cn (L. Qi).

0039-9140/$ – see front matter © 2009 Elsevier B.V. All rights reserved.
doi:10.1016/j.talanta.2009.04.062

monolith with potassium peroxydisulfate ($K_2S_2O_8$) initiated in an in situ polymerization. The resultant polymer chains were investigated as a pH-responsive stationary phase for HPLC mode. Furthermore, we used this kind of modified monolithic column for the fast separation of proteins.

2. Experimental

2.1. Chemicals and materials

Glycidyl methacrylate (GMA), ethylene glycol dimethacrylate (EDMA) and methacrylic acid (MAA) were purchased from Acros (NJ, USA), which were all distilled under vacuum prior to use. 2,2′-Azobisisobutyronitrile (AIBN) was produced by Shanghai Chemical Plant (Shanghai, China) and refined before use. 1-Dodecanol and cyclohexanol were from Fuchen Chemical Plant (Tianjin, China). Potassium peroxydisulfate ($K_2S_2O_8$) was provided by Beihua Fine Chemical Co., Ltd. (Beijing, China). Lysozyme (Lys), α-chymotrypsinogen A (α-Chy A), cytochrome *C* (Cyt *C*) and human immunoglobulin G (IgG) were all obtained from Xinjingke Biotechnology Co., Ltd. (Beijing, China). Other reagents were all of analytical reagent grade. Water was prepared from a triple distilled water system and solutions were filtered through a 0.45 μm membrane before use.

2.2. Preparation of the grafted monolithic column

Preparation of this general monolithic column was described in detail elsewhere [14]. Briefly, a poly(GMA-*co*-EDMA) polymerization mixture with 0.50 mL GMA, 0.50 mL EDMA, 0.25 mL dodecanol, 1.75 mL cyclohexanol and 30 mg AIBN was prepared and homogenized in an ultrasonic bath for 10 min, and then purged with nitrogen for 5 min before being drawn by the stainless-steel tube (50.0 mm × 4.6 mm i.d.), which was sealed at both ends. After the polymerization was allowed to proceed at 60 °C for 24 h, the column was flushed with methanol to remove the porogen and other soluble compounds present in the polymer rod.

In situ grafting polymerization of methacrylic acid onto the surface of the prepared monolith was carried out in two sequential steps: firstly, the epoxy groups on the surface of poly(GMA-EDMA) monolithic column were hydrolyzed to hydroxyl groups for 4 h at 60 °C using 0.25 M sulfuric acid at a flow rate of 0.1 mL min^{-1}. After that, the grafting solution with 6.0 mL MAA in 40 mL aqueous solution containing 20 mg $K_2S_2O_8$ was delivered to the column at a flow rate of 0.1 mL min^{-1}. The polymerization reaction was allowed to proceed for 4 h at 60 °C. After completion of the reaction, the column was washed with at least 100 mL of distilled water in order to remove excess monomer and ungrafted homopolymer remaining inside the monolith. Finally, the grafted monolithic column was obtained.

2.3. Instrumentation

A scanning electron microscope (SEM, model S-4300, Hitachi, Japan) was used to examine the microscopic morphology of the monoliths after sputter coating gold to the dried monolith samples. Fourier transform infrared spectroscopy (FT-IR) information of the monoliths before and after grafting was obtained by using a FT-IR spectrophotometer (Tensor-27, Bruker, Germany). The pore size distribution of the monolithic materials was determined using an autopore III 9220 mercury intrusion porosimeter (V3.04, Micromeritics, USA). Chromatographic investigations were carried out with a Shimadzu LC-20A HPLC system (Shimadzu, Japan) consisting of a binary LC-20AT HPLC pump and an SPD-20A UV–vis detector. Data processing was performed with an HW-2000 chromatography workstation (Nanjing Qianpu Software, China).

2.4. Characterization of the grafted monolith

2.4.1. Scanning electron microscope

The surface morphological studies of monoliths before and after grafting were investigated by SEM. Furthermore, the structures of the grafted monolith at different pH were also measured under SEM [15]. The two monolith pieces were suspended separately in buffer solutions of pH 4.5 and 7.5 for 12 h and then dried at 60 °C overnight. The dried samples were sputter coated with gold particles under reduced pressure conditions and observed under SEM.

2.4.2. Hydrodynamic properties

The flow hydrodynamic behavior of the monoliths was described by the pressure drop of monolithic column at different flow rates using methanol as mobile phase [16]. The hydraulic permeability of the monolith was calculated using the hydrodynamic data from the Darcy's law [17]:

$$\frac{\Delta P}{L} = \frac{u\mu}{B_0} \quad (1)$$

where ΔP stands for back pressure (Pa), L for column length (m), u for superficial velocity (m s^{-1}), μ for mobile-phase viscosity (Pa s), and B_0 for hydraulic permeability (m^2). The value of B_0 can be used as an index for evaluating the quality of monoliths, helping improve the monolithic preparation.

2.4.3. Column efficiency of monoliths

The plate theory was used to investigate the homogeneity and efficiency of the monoliths [16]. The plate heights for monolithic columns were calculated by the chromatographic runs performed in an isocratic mode by using lysozyme as the analyte, and 20 mM sodium phosphate buffer (pH 7.0) plus 0.5 M NaCl as the mobile phase [18]. In a column with a length of L, the theoretical plate number (N) was calculated by the flowing equation:

$$N = 5.54\left(\frac{t_R}{t_W}\right)^2 \quad (2)$$

where t_R and t_W were the retention times and the peak width at half height, respectively. The plate height (h) was calculated according to Eq. (3):

$$h = \frac{L}{N} \quad (3)$$

2.5. Chromatographic conditions

The chromatographic properties of the grafted monolithic column were evaluated in an isocratic operation using a mixture of acetonitrile and 20 mM phosphate buffer at pH 4.5 and 7.5 (30/70, v/v) as an eluent at a flow rate of 1.0 mL min^{-1}. A series of benzene, methyl, ethyl, propyl benzene homologues and naphthalene were injected through the 20 μL loop and detected at 254 nm. Besides, the controlled experiment was carried out by the non-grafted monolith.

The modified monolithic column for separation proteins was firstly equilibrated with 20 mM phosphate buffer at pH 7.0, and then a 10 μL aliquot of a mixture of protein probes (0.5 mg mL^{-1} each of IgG, α-Chy A, Cyt *C*, and Lys) was injected. The elution was accomplished by a step salt concentration gradient ranging from the starting buffer A (20 mM phosphate buffer at pH 7.0) to a final buffer B composition of 0.5 M NaCl in buffer A. The gradient procedure was set up as follows: 0–2.0 min, from 100% A to 12% B; 2.0–5.0 min, 12% B; 5.0–6.0 min, 12% B to 18% B; 6.0–9.0 min, 18% B; 9.0–12.0 min, 100% B; at last 12.0–14.0 min, 100% B. The flow rate

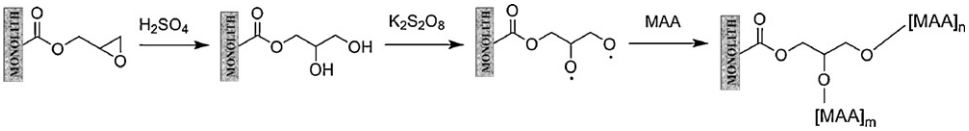

Fig. 1. The schematic representation of the grafting reaction of methacrylic acid onto the surface of poly(GMA-*co*-EDMA) monolith.

was 1.0 mL min^{-1}, and the detection was by UV spectrophotometry at 280 nm.

3. Results and discussion

3.1. In situ grafting polymerization

To obtain monoliths carrying the active functionality as pendant groups for the next modification in the porous polymer matrix, a poly(GMA-EDMA) monolithic column was synthesized according to Section 2.2. Due to the active epoxy groups on the surface of the monolithic column, two sequent steps were prepared for grafting in the in situ manner. In the first step, the monolith was hydrolyzed by acid to obtain many active hydroxyl groups. Then, the grafting polymerization of methacrylic acid onto the monolith was achieved by free-radical polymerization in the presence of initiator. In this system, grafting polymerization was initiated by the decomposition of the inorganic agents ($K_2S_2O_8$), and the generation of the primary radicals in turn abstract hydrogen atoms from the hydroxyl groups on the backbone to generate secondary radicals, facilitating the reaction active sites for the MAA monomer polymerization [19,20]. The schematic representation of grafting reaction is presented in Fig. 1. This new modified polymerization was achieved by grafting MAA onto the surface of the polymer monolithic column using a redox initiation system. In addition, in this kind of "in situ grafting from" technique in the polymerization, the monomers were initiated by the radicals directly generated from the thermal-decomposition of initiators on the matrix surface, avoiding the complicated polymerization procedures and the space hindrance of the polymer chains. As a result, the polymerization proceeds mainly on the matrix surface, and would lead to higher polymer grafting density [13].

Several factors might influence the grafting polymerization, such as the monolithic properties, the monomer concentration, the grafting reaction temperature, the reaction time, as well as the flow rate through the column, thus, the suitable preparation conditions were needed to be investigated in detail. Finally, we found experimentally that the satisfied grafting preparation could be obtained 15% (v/v) MAA monomer in aqueous solutions flowing through the column at 0.1 mL min^{-1} during 60 °C for 4 h in the grafting polymerization. If larger amounts of monomer concentration (25%, v/v) or longer reaction time (8 h) was involved, however, the grafted brushes would result in a plugged column after the polymerization reaction, and poor permeability of the monolith would be found.

3.2. Characterization of grafted monolith

FT-IR spectroscopy, SEM and mercury intrusion porosimetry were carried out to characterize the grafted monolithic column.

The presence of polymethacrylic acid (pMAA) on the surface was confirmed by FT-IR spectroscopy (Fig. 2A). Compared with the spectrum of the non-grafted monolith, a characteristic absorption at 3300–3500 cm^{-1} and 1636.80 cm^{-1} was observed in the spectrum of the modified monolith, which was assigned to the characteristic stretching vibrations of OH and C=O in the carboxyl group of polymer chains pMAA [21]. The appearance of these peaks evidenced the successful grafting of polymer chains onto the surface of the prepared monolith.

Fig. 3A and B shows the different surface morphology of the monolith before and after grafting with the same magnification. As shown in Fig. 3B, the globular structure was clearly expanded upon grafting polymer chains along the surface of the pores with a decreasing of the macropores, and the surface was rough compared with the bare counterpart one (Fig. 3A). Then the pore size distribution curves of non-grafted and grafted monolith are investigated. As displayed in Fig. 2B, it has been found that most macropores had a diameter around 1.2 μm for the non-grafted monolith. The pore size distribution of the grafted one became narrow with the peak at about 0.72 μm. And the average pore diameter further decreased from 163 nm to 115 nm after modification. Although the polymer chains on the surface occupied partial void pores, resulting in 6.8% both the porosity and pore volume reduced, the specific surface area of grafted monolith (57.1 $m^2\ g^{-1}$) was larger than the bulk monolith (44.3 $m^2\ g^{-1}$).

With the above optimized conditions, the grafted monolithic column was prepared. The experimental results of hydraulic flow resistance before and after the grafting polymerization were investigated. Fig. 4A indicates that there is a linear relationship between pressure drop and flow velocity as both columns, and illustrates that the material even after grafting is still rigid and not prone to swelling. According to Eq. (1), the permeability of the non-grafted monolith was calculated by 5.1×10^{-14} m^2, while it was only 9.9×10^{-15} m^2 for the grafted one, a fivefold decrease indicating

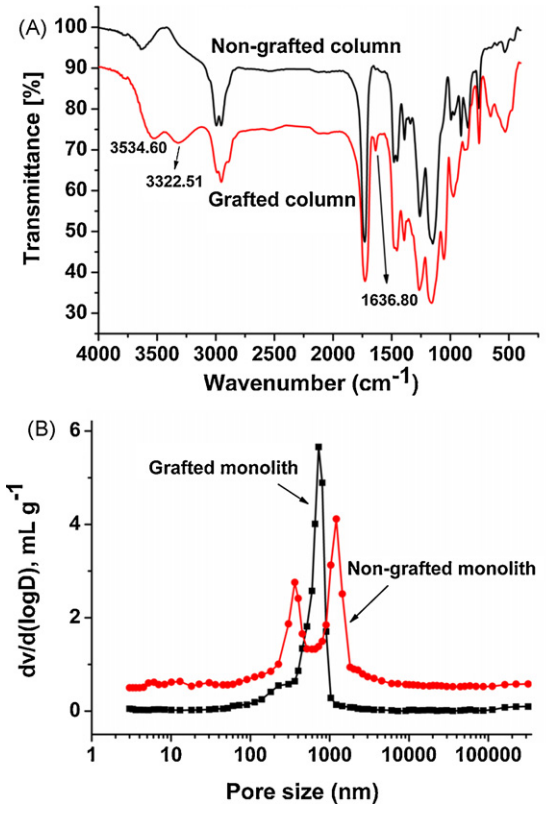

Fig. 2. (A) FT-IR spectra of non-grafted and grafted monoliths and (B) the pore size distribution curves of non-grafted and grafted monolith.

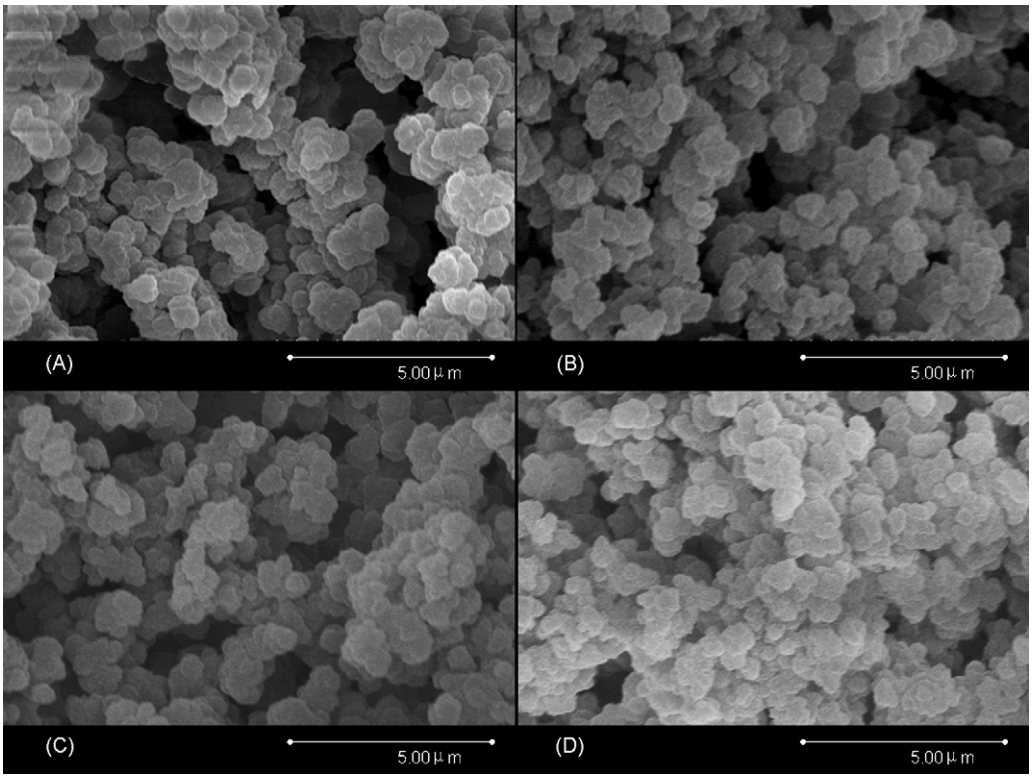

Fig. 3. Scanning electron micrographs of the monoliths. (A) The original monolith; (B) grafted monolith using a solution of 15% MAA solution for 4 h at 60 °C; (C) grafted monolith at pH 4.5; (D) grafted monolith at pH 7.5.

that the flow resistances within the monolith were increased after the grafting polymerization. The reason could be easily explained that the grafted polymer chains or brushes on the surface took up partial void spaces within pores, which must decrease the effective cross-areas of fluid-flow channels and consequently increase the liquid flow resistance. The conclusion was accordance with the decrease of the macropores and pore volume described above. Although the permeability was a little lower, the monolithic column was as well suitable for the chromatographic separation even at the flow rate of 2.0 mL min^{-1}.

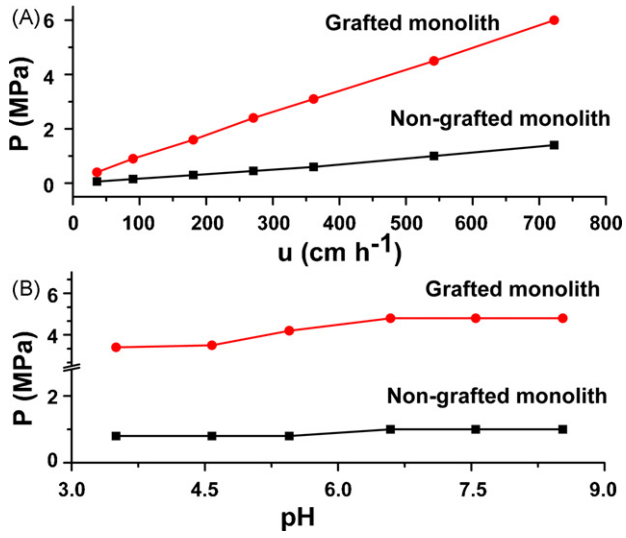

Fig. 4. The drop pressures of grafted and non-grafted monolith at different flow velocity (A) and different pH (B).

3.3. Characterization of pH-responsive polymer

It is well known that polymer chains pMAA can undergo a marked pH-induced conformational transition in solution [22,10], exhibiting a gradual globule-to-extended conformational transition at different pH. At a low pH or close to its pK_a (reported to be 4.65–5.35 at different high molecular weights [10]), pMAA chains are charge neutral and adopt a compact form, due to hydrophobic interactions, which results in the aggregation of a thin shrunken polymer layer. However, at a relatively high pH, the polymer chains expanded as a random coil, due to ionization of functional groups and consequently coalesce with each other. Taking advantage of such special conformational transition, the pMAA-grafted onto the monolith was expected to present a pH-responsive function, swelling and shrinking by the change of pH in the aqueous medium to effect on the architecture of the pores and the chromatographic characterization.

Fig. 4B shows the drop pressures of the grafted and non-grafted monolith at different pH range from 3.5 to 8.5 with the flow rate of 1.0 mL min^{-1}. The grafted stationary phase showed a higher pressure at a high pH (7.5) than at a low pH (4.5). However, the drop pressures for non-grafted column in response to pH were almost consistent. The obvious differences could be explained by a pH-responsive conformational change of the pMAA polymer chains. On the one hand, when pH was below 4.5, the polymer chains were wrapped on the surface because of hydrogen bonding between carboxylic acid groups of MAA, presenting lower resistance, larger permeability for the mobile phase. On the other hand, with the pH increased, the carboxylic acid groups on the pMAA were completely dissociated, causing a large charge density inside the brush. They reflected stronger repellent electrostatic interactions, and led to the adjacent tentacles to be as far away from each other as possible, so they extended and produced high resistance for the mobile phase. The same conclusion was also confirmed by SEM studies. At

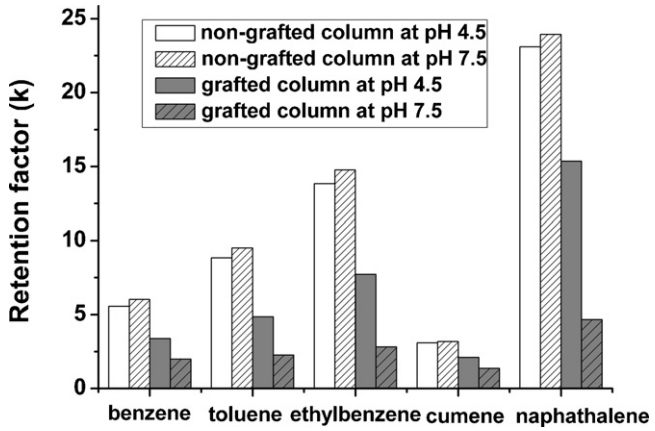

Fig. 5. The effects of pH on the five benzene homologues on grafted monolithic column and non-grafted monolithic column.

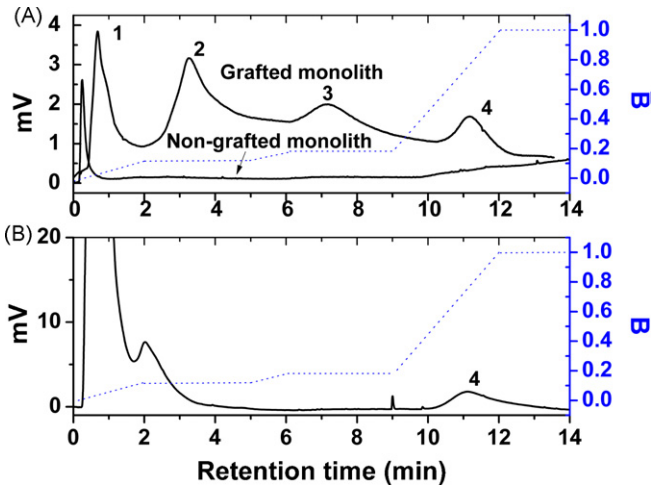

Fig. 7. Chromatograms of separation the protein mixtures on the grafted column. (a) A mixture of IgG, α-Chy, Cyt *C* and Lys. (b) A diluted solution of chicken egg white. Mobile phase, buffer (A): 20 mM PBS, pH 7.0, buffer (B): buffer A containing 0.5 M NaCl, pH 7.0; gradient: 0–2.0 min, from 100% A to 12% B; 2.0–5.0 min, 12% B; 5.0–6.0 min, 12% B to 18% B; 6.0–9.0 min, 18% B; 9.0–12.0 min, 100% B; at last 12.0–14.0 min, 100% B; the flow rate was 1.0 mL min^{-1}; detection was 280 nm.

pH 7.5 (Fig. 3D), the stretch of polymer chains and the increase in thickness of the globules might plug the pores in the column, with lower porosity instead, while the compact chains could maintain their original appearance at pH 4.5 (Fig. 3C).

Furthermore, five benzene homologues (benzene, toluene, ethylbenzene, cumene, and naphthalene) were chosen as modal analytes to investigate the properties of pH-responsive stationary phase. To describe the retention of the neutral molecules on the grafted monolithic column, here we defined the retention factor (k) by using the following equation:

$$k = \frac{t_R - t_o}{t_o} \quad (4)$$

where t_R and t_o are the retention time of the compounds and sodium nitrite, respectively. As shown in Fig. 5, the retention factors of five analytes on the grafted monolith under both pH 4.5 and pH 7.5 were a little lower than ones on the non-grafted column. It suggested that the surface of the stationary phase became a little hydrophilicity due to grafting the polar functional carboxylic groups of polymer chains [23]. As a result, the interaction between the analytes and the stationary phase was reduced and the retention factors decreased. In addition, when the pH of mobile phase increased from 4.5 to 7.5, the retention factors of the analytes on the grafted monolithic column decreased dramatically, meanwhile, the opposite result was obtained on the non-grafted column. This result might be due to the different confirmations of the stationary phase induced under two pH conditions. Fig. 6 shows the schematic illustration of the retention mechanism between the pH-responsive stationary phase and the analytes at different pH. When pH of the mobile phase was 4.5, the pMAA chains were charged neutral and exhibited a strong hydrophobic interaction with the small molecules by reversed-phase liquid chromatographic (RPLC) mode, and thus, more elution volume was needed and the retention factors of the analytes were high. However, at a high pH (pH 7.5), the grafted chains turned to form a highly repulse ionization polymer structure, and a relatively hydrophilic surface was obtained [24], resulting in a weak interaction with the hydrophobic analytes, and a decrease in the retention factors.

Therefore, the experimental results exhibited that the grafted stationary phase could show pH-responsive hydrophilic–hydrophobic surface property alterations to the small analytes. Besides, it could be demonstrated that introduction of functional groups via a graft polymerization represented a new approach to the control of the surface chemistry of porous polymer monoliths and opened new avenues to the preparation of monolith with tailoring surface chemistries [25].

3.4. Separation of proteins

As it has been discussed above, the modified stationary phase could exhibit the hydrophobic–hydrophilic conformation to effect on the retention factors of the small analytes after grafting the pH-responsive polymer pMAA. Furthermore, we presume that this kind of conformation alteration might also work on the separation of the biomolecules, such as proteins. Thus, a protein mixture including human immunoglobulin G (IgG, p*I* 7.0), α-chymotrypsinogen A (α-Chy A, p*I* 9.5), cytochrome *C* (Cyt *C*, p*I* 10.6), and lysozyme (Lys, p*I* 11.0) was tested on the pH-responsive monolithic column. An almost complete separation was achieved using a step gradient elution with increasing sodium chloride concentration in Fig. 7A. The four proteins were found to be eluted in the order predicted from their p*I* values [26]. Proteins with more basic isoelectric pH values might bind tighter to the column and be eluted later than proteins with less ones. For the control experiment, the non-grafted mono-

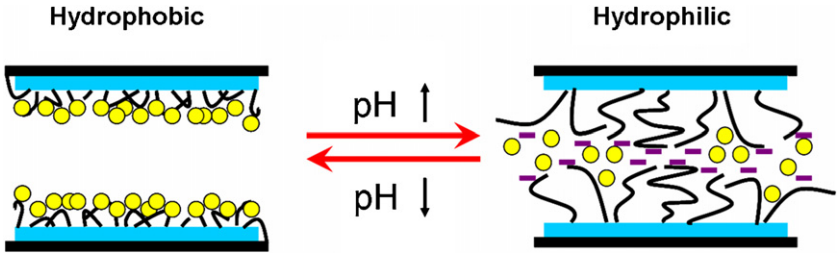

Fig. 6. The schematic illustration of the retention mechanism between the pH-responsive stationary phase and the analytes at different pH.

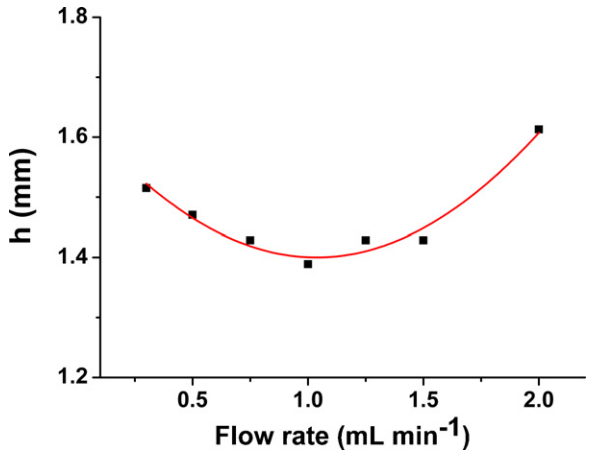

Fig. 8. Effects of pH values on the retention time of four proteins. Mobile phase: buffer (A), 20 mM PBS, at pH from 3.0 to 7.0, buffer (B), buffer A containing 0.5 M NaCl. Other conditions were similar with Fig. 7.

lithic column was also carried out to separate four proteins. The chromatograms were quite different from the ones in the grafted column, due to none of grafting functionalities on the surface of the monolith.

The column efficiencies of the grafted monoliths were investigated as described in Section 2.4.3. As shown in Fig. 8, a Van Deemter curve was determined for the grafted monolithic column. The optimum theoretical flow rate was 1.0 mL min^{-1} with the lowest plate height values of 1.4 mm.

3.4.1. Effects of pH on the protein elution

In order to explain the pH-responsive of the monolith on the proteins, the effects of different pH range from 3.0 to 8.0 in mobile phase on the grafted monolith are shown in Fig. 9. It could be found that the retention time of the proteins at low pH were a little longer than at the high pH. Such results could also be attributed to the pH-responsive property of the stationary phase. However, the pH-sensitive effects on the retention time of the proteins were less obvious than the ones of the benzene homologues described above, it might be due to the complex structure of the proteins and the mutual interactions between the stationary phase and the proteins (such as the ion-exchange interaction).

Nevertheless, it could be confirmed that the surface chemistry of the monolithic column had presented a nature of pH-responsive

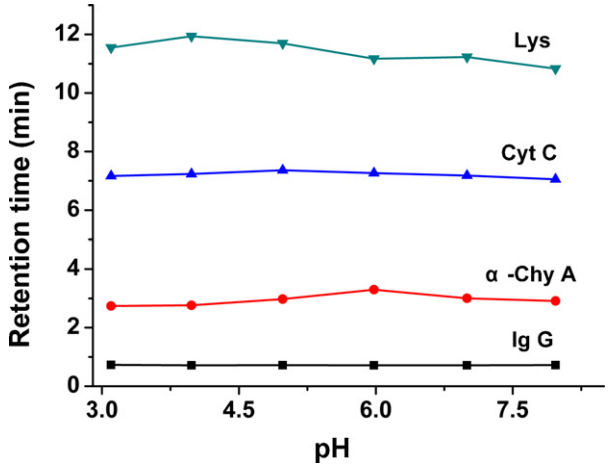

Fig. 9. Dependence of column efficiency on mobile-phase flow rate for the grafted monolithic column under isocratic elution with 20 mM phosphate buffer (pH 7.0) in 0.5 M NaCl.

Table 1
Proteins mass recovery on the grafted monolithic column.

	IgG	α-Chy A	Cyt *C*	Lys
Recovery (%)	98.8	95.4	96.3	94.7

not only on the hydrophobic small molecules, but also on the biomolecules after grafting pMAA. Therefore, introduction of functional groups via a graft polymerization can open a new avenue to the preparation of monolith with special properties.

3.4.2. Protein recovery

The protein recovery experiments with the modified column were performed with a protein concentration of 0.5 mg mL^{-1} at a gradient elution described in Section 2.5. The protein recovery was calculated as the percentage of the peak area of protein leaving the column with respect to the peak area of the same amount of protein injected into the HPLC system with a connector [18]. The mass recoveries of four proteins obtained from the modified column were listed in Table 1. It displayed that all mass recoveries were greater than 94.0%. The relative standard deviations (RSD) of recoveries for four proteins in three parallel tests were all less than 10.0%. As a high mass recovery of proteins by using the grafted column was obtained in this study, it could be indicated that there was almost no specific adsorption between proteins and the stationary phase.

3.4.3. Effects of organic solvent on the protein elution

Iso-propanol (IPA) was usually used as an additive in the mobile phase to detect any hydrophobic adsorption between the solutes and the prepared material [26]. After adding 1.0% (v/v) or 3.0% (v/v) IPA into the mobile phase, the retention time of four proteins decreased only by less than 2.0% compared with the absence of any organic solvent in the mobile phase. This fact indicated that the grafted monolith was more hydrophilic and showed little hydrophobic interaction between proteins and stationary phase.

3.4.4. Reproducibility and stability

The reproducibility of the prepared monolithic column was assessed through the RSD of the retention time of four proteins. Three monolithic columns were prepared with the same graft polymerization composition, as described in Section 2.2. The column-to-column (n = 3) reproducibilities of the four proteins measurements were 2.2, 2.2, 1.7, 1.2%, respectively. While, the run-to-run reproducibility (n = 5) of four proteins measurements gave RSD values for retention time of 0.24, 0.74, 0.79, 0.31%, respectively. Even after 10 months, the grafted column was again used for proteins separation, with no significant difference in retention times (RSD < 5.0%). This clearly confirmed that the preparation method of this kind of grafted monolith was universally applicable, and the robustness of the columns since their performance did not appear to deteriorate either with time or number of injections [27].

3.5. Application

Since lysozyme was the only basic protein in the highly abundant proteins of chicken egg white (CEW) [28], the prepared method was applied for the purification of the Lys from CEW by the grafted monolith. The chicken egg white was obtained from fresh egg and dissolved in phosphate buffer (pH 7.0), then, the solution was diluted with buffer at 1:4 (v/v). After centrifuged at 6000 rpm for 15 min, the sample was filtered through 0.45 μm membranes and stored at 0 °C prior to use. The effective separation of CEW proteins was shown in Fig. 7B. Quantitative analysis of Lys samples was accomplished over the range of 0.2–4.0 mg mL^{-1} using the protocol. By interpolating the peak area on the calibration curve, the content of the Lys in CEW samples was obtained as 1.37 mg mL^{-1}.

4. Conclusion

In this study, a modified monolithic column grafted by the polymer chains pMAA onto the p(GMA-*co*-EDMA) monolith was prepared and the chromatographic characterization was also measured. At a low pH, the carboxyl groups of the macromolecule chains of the pMAA can be a neutral contract form. However, as the environmental pH increases, the polymer chains charge negatively and expand, exhibiting a relatively hydrophilic surface on the monolithic column. As a result, the permeability of the grafted monolith and the retention factors of five benzene homologues were investigated and presented both a reduce direction when pH increased from pH 4.5 to 7.5. It was concluded that the surface characterization of the grafted monolithic column was related to the environmental pH. Meanwhile, this kind of pH-responsive stationary phase was also successfully used to separate four basic proteins using a salt gradient.

Acknowledgements

We gratefully acknowledge the financial support from NSFC (No. 20875091 and No. 20675084), Ministry of Science and Technology of China (No. 2007CB714504) and Chinese Academy of Science (Bai Ren Project).

References

[1] T.B. Tennikova, B.G. Belenkii, F. Svec, J. Liq. Chromatogr. 13 (1990) 63.
[2] E.G. Vlakh, T.B. Tennikova, J. Sep. Sci. 30 (2007) 2801.
[3] F. Svec, L. Geiser, LC GC N. Am. 24 (2006) 22.
[4] A. Hanora, I. Savina, F.M. Plieva, V.A. Izumrudov, B. Mattiasson, I.Y. Galaev, J. Biotechnol. 123 (2006) 343.
[5] J.A. Tripp, F. Svec, J.M.J. Frechet, J. Comb. Chem. 3 (2001) 216.
[6] I.N. Savina, I.Y. Galaev, B. Mattiasson, J. Chromatogr. A 1092 (2005) 199.
[7] F. Svec, J. Sep. Sci. 27 (2004) 747.
[8] C. Viklund, F. Svec, J.M.J. Frechet, K. Irgum, Biotechnol. Prog. 13 (1997) 597.
[9] E.C. Peters, F. Svec, J.M.J. Frechet, Adv. Mater. 9 (1997) 630.
[10] J.B. Qu, L.Y. Chu, M. Yang, R. Xie, L. Hu, W.M. Chen, Adv. Funct. Mater. 16 (2006) 1865.
[11] A. Tuesca, K. Nakamura, M. Morishita, J. Joseph, N. Peppas, A. Lowman, J. Pharm. Sci. 97 (2008) 2607.
[12] J.M. Saunders, T. Tong, C.L. Maitre, T.J. Freemont, B.R. Saunders, Soft Matter 3 (2007) 486.
[13] Q. Ma, M. Chen, H.R. Yin, Z.G. Shi, Y.Q. Feng, J. Chromatogr. A 1212 (2008) 61.
[14] F. Svec, J.M.J. Frechet, J. Chromatogr. A 702 (1995) 89.
[15] A. Kumar, S.S. Lahiri, H. Singh, Int. J. Pharm. 323 (2006) 117.
[16] K.F. Du, D. Yang, Y. Sun, J. Chromatogr. A 1163 (2007) 212.
[17] C. Martin, J. Coyne, G. Carta, J. Chromatogr. A 1069 (2005) 43.
[18] E. Unsal, B. Elmas, B. Caglayan, M. Tuncel, S. Patir, A. Tuncel, Anal. Chem. 78 (2006) 5868.
[19] M.I.H. Mondal, Y. Uraki, M. Ubukata, K. Itoyama, Cellulose 15 (2008) 581.
[20] G. Bayramoglu, H. Erdogan, M.Y. Arica, J. Appl. Polym. Sci. 108 (2008) 456.
[21] M. Ignatova, S. Voccia, B. Gilbert, N. Markova, D. Cossement, R. Gouttebaron, R. Jerome, C. Jerome, Langmuir 22 (2006) 255.
[22] M. Kaholek, W.K. Lee, J.X. Feng, B. LaMattina, D.J. Dyer, S. Zauscher, Chem. Mater. 18 (2006) 3660.
[23] C. Viklund, A. Nordstro, K. Irgum, F. Svec, J.M.J. Frechet, Macromolecules 34 (2001) 4361.
[24] D. Fournier, R. Hoogenboom, H.M.L. Thijs, R.M. Paulus, U.S. Schubert, Macromolecules 40 (2007) 915.
[25] I.N. Savina, I.Y. Galaev, B. Mattiasson, J. Mol. Recognit. 19 (2006) 313.
[26] Y.M. Wei, X.D. Huang, R.X. Liu, Y.H. Shen, X.D. Geng, J. Sep. Sci. 29 (2006) 5.
[27] Z.J. Jiang, N.W. Smith, P.D. Ferguson, M.R. Taylor, J. Sep. Sci. 31 (2008) 2774.
[28] M.Y. Arica, M. Yilmaz, E. Yalcın, G. Bayramoglu, J. Chromatogr. B 805 (2004) 315.

Talanta 79 (2009) 971–974

Contents lists available at ScienceDirect

Talanta

journal homepage: www.elsevier.com/locate/talanta

Short communication

Study on homogeneous competitive immune reaction by fluorescence correlation spectroscopy: Using synthetic peptide as antigen

Chao Xie, Chaoqing Dong, Jicun Ren*

College of Chemistry & Chemical Engineering, State Key Laboratory of Metal Matrix Composites, Shanghai Jiaotong University, 800 Dongchuan Road, Shanghai, 200240, PR China

ARTICLE INFO

Article history:
Received 25 February 2009
Received in revised form 11 May 2009
Accepted 11 May 2009
Available online 20 May 2009

Keywords:
Fluorescence correlation spectroscopy
Homogeneous immunoassay
Synthetic peptides
CA125

ABSTRACT

In this paper, fluorescence correlation spectroscopy (FCS) is used for investigation of homogeneous immune reaction using synthetic peptide as antigen. The binding process of CA125 peptide antigen and its antibody was systematically investigated. The dissociation constant and dissociation rate for antigen–antibody complex were determined, which were $k_{diss} = 0.94 \pm 0.05$ nM and $k_{off} = 0.00215 \pm 0.0001$ s^{-1}, respectively. Under optimal conditions, the detection limit of the competitive immunoassay was 4×10^{-10} M (S/N = 3). The good recoveries were obtained with human serum samples. Our preliminary results demonstrated that the homogeneous competitive immunoassay based on FCS is simple, rapid, sensitive and small sample and reagent requirement, and this method maybe possess great potential applications in clinical diagnosis, food and environmental analyses and biological and biomedical studies.

1. Introduction

Immunoassay is currently one of very widely used analytical technologies in clinical diagnosis [1,2], food [3] and environmental analyses [4,5] and biological [6,7] and biomedical studies [8,9]. Conventional heterogeneous immunoassays always require multiple separation and washing steps [10,11]. Generally, homogeneous assays are attractive detection formats because they are amenable to automation, reduce the risk of contamination and eliminate time-consuming washing steps [12]. To date, several analytical methods have been used in homogeneous immunoassays, such as fluorescence polarization [13,14], fluorescence resonance energy transfer [15,16], bioluminescence resonance energy transfer (BRET) [17,18], surface plasmon resonance [19,20], and chemiluminescence [15,21]. However, most of the homogeneous immunoassays are generally less sensitive than their heterogeneous counterparts due to their high background noise.

Fluorescence correlation spectroscopy (FCS) [22–24] appears to be an attractive choice for homogeneous immunoassays [25–27] due to their certain advantages, such as high sensitivity, extremely small sample requirement, and short measuring times, etc. Unfortunately, to distinguish the two components in FCS analysis, their diffusion coefficients must differ by a factor of at least 1.6, which corresponds to a molecular weight ratio of 4 (1.6^3, according to the Stokes–Einstein relation) [28,29]. Here we devised a new homogeneous immunoassay strategy using synthetic peptides as antigen to overcome the above limitation, since synthetic peptides have lower molecule weight (<5 kDa) than that of native antigen (>200 kDa) [30,31].

In this work, the binding process of CA125 peptide antigen and its antibody was systematically investigated. The dissociation constant and dissociation rate for antigen–antibody complex were determined. Furthermore, we evaluated the sensitivity, specificity, reversibility and recovery of this competitive immunoassay.

2. Experimental

2.1. FCS instrumentation

FCS measurements were carried on a home-built FCS system [32]. In brief, an inverted fluorescence microscope (IX71, Olympus, Japan) was applied as the optical system. The 532 nm YVO4 laser was reflected by a dichroic mirror (550DRLP, Omega Optical, USA), and then focused into a sample solution by a water immersion objective (UplanApo, 60× NA1.2, Olympus, Japan). The about 30 μL sample was placed on a coverslip. The fluorescence emission was filtered by a band-pass filter (605DF50, Omega Optical, USA), and then was collected after passing the 35 μm pinhole by avalanche photodiodes (SPCM-AQR14, PerkinElmer EG&G, Canada). The yielded signals were tracked and correlated by a real time correlator (ALV-5000/EPP, ALV-GmbH, Germany). The measuring time per sample was 30 s.

* Corresponding author. Tel.: +86 21 54746001; fax: +86 21 54741297.
E-mail address: jicunren@sjtu.edu.cn (J. Ren).

0039-9140/$ – see front matter © 2009 Elsevier B.V. All rights reserved.
doi:10.1016/j.talanta.2009.05.013

2.2. Reagents

High-purity rabbit anti-CA125 and non-labeled CA125 antigen were purchased from Beijing Biosynthesis Biotechnology CO., Ltd (Beijing). The synthesis and fluorescent labeling of CA125 peptide antigen were conducted by GL Biochem (Shanghai) Ltd. The TMR-labeled CA125 peptide antigen sequence is TMR-AHX-DPKSPGVDREQLY. The purity of the dye-labeled antigen was proven to be more than 95.15% by HPLC, and the identification was preformed by mass spectrometry (MW = 2029.26). CA125 antibody concentration was calculated based on its molecular mass of 200 kDa. All samples were diluted with 100 mM PBS buffer (pH 7.4) containing 1 mg/mL BSA unless otherwise indicated.

2.3. Data analyses

All FCS data were analyzed with the standard equation for particles diffusing in a three-dimensional Gaussian volume element and nonlinearly fitted with the Origin 6.0 software package based on the Levenberg–Marquardt algorithm. This fit is based on the two-component model as following [28]:

$$G(\tau) = \frac{1}{N}\left[1 - T + T\exp\left(\frac{-\tau}{\tau_T}\right)\right]\left[\frac{1-Y}{(1+(\tau/\tau_{free}))\sqrt{1+(\omega_0^2/Z_0^2)(\tau/\tau_{free})}} + \frac{Y}{(1+(\tau/\tau_{bound}))\sqrt{1+(\omega_0^2/Z_0^2)(\tau/\tau_{bound})}}\right] \quad (1)$$

where N is the total average number of fluorescent molecules in the excitation detection volume, ω_0 is the beam waist radius and $2Z_0$ is the beam height, T is the average fraction of fluorescent molecules in the triplet state with relaxation time τ_T, Y denotes the bound ratio of antibody to antigen, if $Y = 0$, the Eq. (1) denotes the single-component model. τ_{free} and τ_{bound} are the characteristic diffusion times of the free TMR-labeled antigen and the binding complex. The average numbers of TMR-labeled antigen and the binding complex can be calculated by $N_{free} = N \times (1 - Y)$, $N_{bound} = N \times Y$, respectively. Binding data were analyzed with the simple binding model based on a stoichiometry of one antigen molecule per each antibody.

$$\text{antigen}* + \text{antibody} \Leftrightarrow \text{antigen}* - \text{antibody}$$

$$K_{ass} = \frac{[\text{antigen}* - \text{antibody}]}{[\text{antigen}*][\text{antibody}]} = \frac{1}{k_{diss}}$$

$$\text{With } Y = \frac{[\text{antigen}* - \text{antibody}]}{[\text{antigen}*] + [\text{antigen}* - \text{antibody}]}$$

$$\text{Then } Y = \frac{[\text{antibody}]}{k_{diss} + [\text{antibody}]} \quad (2)$$

where k_{diss} is the dissociation constant, [antibody] is the concentration of free antibody in mixture solution. Eq. (2) can be applied to calculate k_{diss}, but it must be multiplied by a scaling factor (m). Additionally, to match the parameter's range, a constant (C) must be added into Eq. (2), considering the observed parameter having a nonzero value for the unbound state [22,33]:

$$Y = \frac{m[\text{antibody}]}{k_{diss} + [\text{antibody}]} + C \quad (3)$$

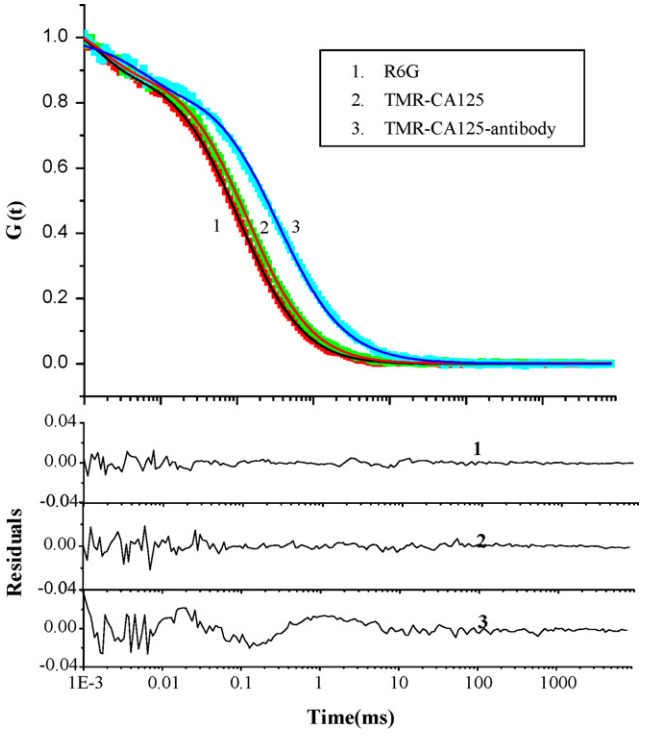

Fig. 1. Normalized fluorescence correlation curves of R6G, TMR-labeled CA125 peptide antigen, and antigen–antibody complex. Fits were performed with the structure factor determined using 1 nM R6G solution. The diffusion times of R6G, TMR-labeled CA125 peptide antigen, and antigen–antibody complex are 90 ± 4 μs, 150 ± 4 μs and 434 ± 10 μs, respectively. The residuals of three fit correlation curves are shown as "1", "2" and "3" standing for fit residuals of R6G, TMR-labeled CA125 peptide antigen, and antigen–antibody complex, respectively.

3. Results and discussion

3.1. Analysis of diffusion behaviors

Typical FCS curves of Rhodamine 6G, TMR-labeled CA125 antigen and immune complex and corresponding fit residuals are shown in Fig. 1. In experiments, the excitation volume was determined with a 1 nM Rhodamine 6G solution as standard substance. The obtained ω_0 and Z_0 were 0.34 ± 0.01 μm and 1.64 ± 0.04 μm, respectively, and thus the detection volume of 1.05 ± 0.05 fL was obtained based on the formula $V = \pi^{\frac{3}{2}}\omega_0^2 Z_0$ [27,34]. The value of ω_0 and Z_0 would be kept constant in the following fittings. The diffusion coefficient and diffusion time of free TMR-labeled CA125 antigen and the immune complex were determined as $D = (1.93 \pm 0.05) \times 10^{-10}$ m^2 s^{-1}, $\tau_{free} = 150 \pm 4$ μs and $D = (0.6 \pm 0.01) \times 10^{-10}$ m^2 s^{-1}, $\tau_{bound} = 434 \pm 10$ μs, respectively. Every sample measurement repeated 10 times and the sampling time was 30 s. This result shows that FCS can be used to distinguish the two components reliably, since there is significant difference between the diffusion coefficient of CA125 antigen and antibody–antigen complex. Furthermore, we observed a neglectable change in fluorescence intensity of free antigen (22 ± 1 kHz per molecular) and bound complex (23 ± 1 kHz per molecular). This data illustrated that the stoichiometry of this immune reaction was 1:1. Thus, FCS can be used to investigate the immune reaction conveniently.

3.2. Analysis of immune reaction

The affinity of this interaction was investigated by titration of TMR-labeled antigen with antibody. In the measurements, various concentrations of antibodies (from 0 nM to 160 nM) were titrated to a fixed concentration (1 nM) TMR-labeled CA125 antigen solution. Fig. 2(a) shows an example of the normalized correlation curves. We could see that curves shifted to the

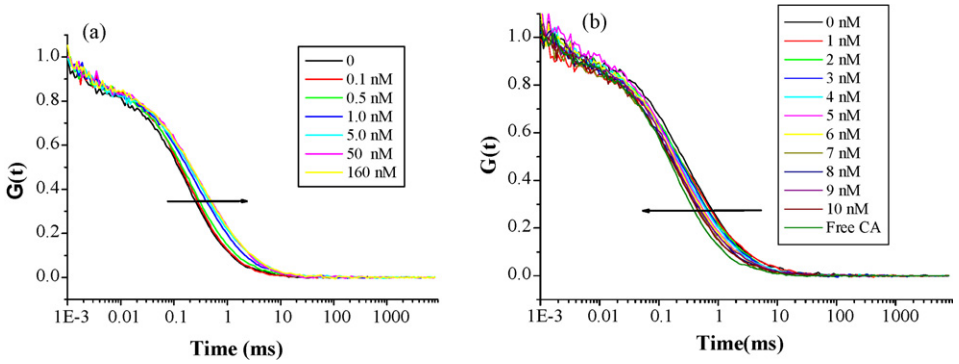

Fig. 2. (a) Normalized fluorescence correlation curves of TMR-CA125 and immune complex. Antibodies (concentration increased from 0 nM to 160 nM) were titrated into TMR-labeled CA125 antigen solution kept at a fixed concentration (1 nM). The arrow indicated the shift of curves with the increase of antibody concentration. (b) Unlabeled CA125 antigen (0–10 nM) were added into the mixture which composed of TMR-peptide (1 nM) and antibody (40 nM) prepared in advance. The arrow showed the shift of curves with the increase of unlabeled CA125 antigen, indicating the decreasing the fraction of the immune complex.

right with the increase of antibody concentration, indicating the increase of the fraction of the immune complex during the titration.

To evaluate the reversibility of this immunoassay, the unlabeled CA125 antigen was used to displace the TMR-peptide from the immune complex. A mixture of TMR-peptide (1 nM) and antibody (40 nM) was prepared in advance, and in this case the labeled antigen was completely bound to the antibody. Displacement experiments were carried out by adding unlabeled CA125 antigen into the mixture. As shown in Fig. 2(b), with an increase of unlabeled antigen, the increase of TMR-antigen concentration results in the shift of correlation curves to the left, indicating a decrease in the fraction of the immune complex. Our results document that this immune reaction possesses good specificity and reversibility, and can be used in competitive immunoassay.

3.3. Determine of dissociation constant

The dissociation constant k_{diss} of this interaction was obtained by titration experiment and fitting the data according to Eq. (3). The titration curve was shown in Fig. 3. The fraction of the immune complex (Y) was a function of the antibody concentration, and was obtained by two-component fits according to Eq. (1). The solid line represented a fit with Eq. (3), and the dissociation constant k_{diss} was 0.94 ± 0.05 nM. This data illustrated that the antibody used in this study had a good affinity to CA125 peptide antigen.

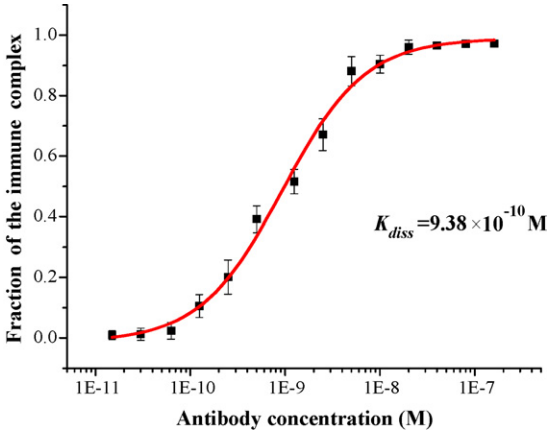

Fig. 3. Titration curve obtained from FCS measurements. The faction of the immune complex was potted as function of antibody concentration. The curve was fitted according to Eq. (3), and the k_{diss} was 0.94 ± 0.05 nM.

3.4. Determine of dissociation rate

FCS can be used for real time and on-line observation of the immune reaction process. Herein, the dissociation rate (off-rate) was determined by using competitive displacement of the labeled antigen with unlabeled antigen in immune complex. Initially, the TMR-labeled CA125 antigen (1 nM) was mixed with antibody (40 nM), incubated for 30 min at room temperature, and then a 200-fold molar excess of the unlabeled CA125 antigen was added to replace the labeled antigen. Autocorrelation curves were collected every 10 s for the first 500 s, and then the collection interval was increased to 2 min. The data were shown in Fig. 4 and fit by using a single-exponential rate model: $Y = \exp(-k_{off} \times t) + C$ [23,35], where Y is the bound ratio of antibody to antigen, k_{off} is the dissociation rates, and C is a constant. The result obtained was $k_{off} = 0.00215 \pm 0.0001\ s^{-1}$. According to this value and the reaction dissociation constant obtained above, the rate constant of the forward reaction between antigen and antibody was calculated to be $k_{on} = 2.28 \pm 0.05 \times 10^6\ M^{-1}\ s^{-1}$. The data illustrated that the reaction rate in this immune system was very fast. And the reaction is well suitable for developing a rapid homogeneous competitive immunoassay by FCS technique.

3.5. Sensitivity, detection limit and reproducibility

Under the optimized conditions, competitive immunoassay was performed by adding unlabeled CA125 antigen (concentration from

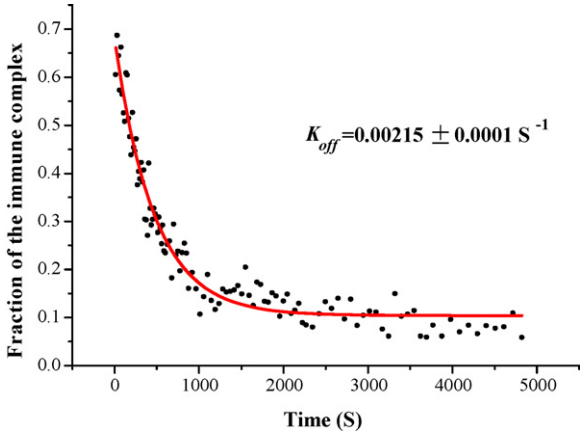

Fig. 4. Dissociation kinetic curve of the antigen and antibody complex. The TMR-labeled CA125 antigen (1 nM) was premixed with antibody (40 nM) and then incubated for 30 min at room temperature. Then, a 200-fold molar excess of the unlabeled CA125 antigen was added to replace the labeled antigen. The data were fitted using a single-exponential rate model. The off-rate is $0.00215 \pm 0.0001\ s^{-1}$.

2×10^{-10} M to 2×10^{-8} M) into the immune complex solution. The immune complex was obtained by mixed the TMR-labeled CA125 peptide (1 nM) and antibody (40 nM) and incubated for 30 min at room temperature. Then we calculated the fraction (%) of the labeled antigen and the immune complex according to two-component model of Eq. (1). The calibration curve of the antigen was obtained by plotting the fraction of free TMR-labeled antigen against the antigen concentration (the calibration equation: $Y = 0.136 \times X + 0.03$). The detection limit for antigen was 4×10^{-10} M (S/N = 3). The linearity of the calibration curve ranged from 4×10^{-10} to 6×10^{-9} M ($R > 0.99$). The relative standard deviations (RSDs) for intra- and inter-assay were less than 5% ($n = 10$) and 20% ($n = 3$), respectively.

3.6. Recovery experiments with human serum samples

The applicability of the present method was tested with human serum samples. Two serum samples from healthy volunteers were first diluted 100 times with buffer in order to decrease the viscosity of serum samples, and then a given antigen was added into the serum sample solution. FCS was used to measure the fraction of the TMR-antigen in samples. The measured recoveries were 81% and 92% respectively, and the result was acceptable for the concentration in the middle of the linear range. Since healthy human serum samples are extremely low in CA125 content, we cannot directly detect the CA125 concentration in serum samples at present. The future work is to develop the suitable pretreatment technique of serum samples, and apply FCS for assay of real samples in clinical diagnosis and food safety field.

4. Conclusion

In this paper, we systematically investigated the homogeneous competitive immune reaction using short synthetic peptide as antigen on the basis of fluorescence correlation spectroscopy technique. The reaction of the CA125 peptide antigen and its antibody was chosen as a mode of the reaction. FCS can be conveniently used to differentiate the antigen and immune complex in the homogeneous immune reaction due to smaller molecule weight of CA125 peptide antigen. The dissociation constants and dissociation rates of the immune reaction were determined, and the sensitivity, specificity and reversibility of this competitive immunoassay were also investigated. In competitive immunoassay, the satisfactory recovery was obtained with human serum samples. Our preliminary results demonstrate that FCS is a simple and efficient tool for investigation of immune reaction using synthetic peptide as antigen. Furthermore, our data also illustrate that the FCS based homogeneous competitive immunoassay using synthetic peptide as antigen is rapid, sensitive and small sample and reagent requirements. This method possesses great potential applications in clinical diagnosis, food and environmental analyses and biological and bio-medicine studies.

Acknowledgments

This work was financially supported by the National Natural Science Foundation of China (No.20675052, 20727005), National High-Tech R&D Program (2006AA03Z324).

References

[1] Z. Lin, X. Wang, Z.J. Li, S.Q. Ren, G.N. Chen, X.T. Ying, J.M. Lin, Talanta 75 (2008) 965.
[2] P. Su, X.X. Zhang, Y.C. Wang, W.B. Chang, Talanta 60 (2003) 969.
[3] J.A. Gabaldon, A. Maquieira, R. Puchades, Talanta 71 (2007) 1001.
[4] G. Fillmann, G.M. Watson, E. Francioni, J.W. Readman, M.H. Depledge, Mar. Environ. 54 (2002) 823.
[5] M.A. Gonzalez-Martinez, R. Puchades, A. Maquieira, Anal. Chem. 73 (2001) 4326.
[6] C.M. Niemeyer, M. Adler, R. Wacker, Nat. Protoc. 2 (2007) 1918.
[7] J.H. Wang, W.H. Huang, Y.M. Liu, J.K. Cheng, J. Yang, Anal. Chem. 76 (2004) 5393.
[8] Z.F. Fu, H. Liu, H.X. Ju, Anal. Chem. 78 (2006) 6999.
[9] H.X. Chen, X.X. Zhang, Electrophoresis 29 (2008) 3406.
[10] K. Aurich, S. Nagel, G. Glockl, W. Weitschies, Anal. Chem. 79 (2007) 580.
[11] B. Du, Z. Li, Y. Cheng, Talanta 75 (2008) 959.
[12] X. Liu, Q. Dai, L. Austin, J. Coutts, G. Knowles, J.H. Zou, H. Chen, Q. Huo, J. Am. Chem. Soc. 130 (2008) 2780.
[13] D.S. Smith, S.A. Eremin, Anal. Bioanal. Chem. 391 (2008) 1499.
[14] G.I. Hatzidakis, A.M. Tsatsakis, E.K. Krambovitis, A. Spyros, S.A. Eremin, Anal. Chem. 74 (2002) 2513.
[15] K. Kuningas, T. Ukonaho, H. Pakkila, T. Rantanen, J. Rosenberg, T. Lovgren, T. Soukka, Anal. Chem. 78 (2006) 4690.
[16] G. Wang, J. Yuan, X. Hai, K. Matsumoto, Talanta 70 (2006) 133.
[17] R. Arai, H. Nakagawa, K. Tsumoto, W. Mahoney, I. Kumagai, H. Ueda, T. Nagamune, Anal. Biochem. 289 (2001) 77.
[18] Y. Yamakawa, H. Ueda, A. Kitayama, T. Nagamune, J. Biosci. Bioeng. 93 (2002) 537.
[19] I. Coille, G. Gauglitz, J. Hoebeke, Anal. Bioanal. Chem. 372 (2002) 293.
[20] I.H. El-Sayed, X. Huang, M.A. El-Sayed, Nano Lett. 5 (2005) 829.
[21] Y. Zhou, Y.H. Zhang, C.W. Lau, J.Z. Lu, Anal. Chem. 78 (2006) 5920.
[22] S.Y. Tetin, K.M. Swift, E.D. Matayoshi, Anal. Biochem. 307 (2002) 84.
[23] C.Q. Dong, P.D. Zhang, R. Bi, J.C. Ren, Talanta 71 (2007) 1192.
[24] P. Sengupta, K. Garai, J. Balaji, N. Periasamy, S. Maiti, Biophys. J. 84 (2003) 1977.
[25] F. Fujii, M. Horiuchi, M. Ueno, H. Sakata, I. Nagao, M. Tamura, M. Kinjo, Anal. Biochem. 370 (2007) 131.
[26] O.A. Mayboroda, A. van Remoortere, H.J. Tanke, C.H. Hokke, A.M. Deelder, J. Biotechnol. 107 (2004) 185.
[27] Z. Foldes-Papp, U. Demel, G.P. Tilz, J. Immunol. Methods 260 (2002) 117.
[28] P. Schwille, F.J. Meyer-Almes, R. Rigler, Biophys. J. 72 (1997) 1878.
[29] K. Bacia, S.A. Kim, P. Schwille, Nat. Methods 3 (2006) 83.
[30] K. Kessenbrock, R. Raijmakers, M.J. Fritzler, M. Mahler, Curr. Med. Chem. 14 (2007) 2831.
[31] E. Gimenez, C. de Bolos, V. Belalcazar, D. Andreu, E. Borras, B.G. De la Torre, J. Barbosa, J. Segura, J.A. Pascual, Anal. Bioanal. Chem. 388 (2007) 1531.
[32] P.D. Zhang, L. Li, C.Q. Dong, H.F. Qian, J.C. Ren, Anal. Chim. Acta 546 (2005) 46.
[33] S.Y. Tetin, T.L. Hazlett, Methods 20 (2000) 341.
[34] M. Rarbach, U. Kettling, A. Koltermann, M. Eigen, Methods 24 (2001) 104.
[35] J. Schuler, J. Frank, U. Trier, M. Schafer-Korting, W. Saenger, Biochemistry 38 (1999) 8402.

Talanta 79 (2009) 730–733

Contents lists available at ScienceDirect

Talanta

journal homepage: www.elsevier.com/locate/talanta

A novel tris(2,2′-bipyridine)ruthenium(II)/tripropylamine cathodic electrochemiluminescence in acetonitrile for the indirect determination of hydrogen peroxide

Baiqing Yuan[a], Hongwei Du[b], Tianyan You[a,*]

[a] State Key Laboratory of Electroanalytical Chemistry, Changchun Institute of Applied Chemistry, Chinese Academy of Sciences, 5625 Renmin Street, Changchun, Jilin 130022, PR China
[b] Pediatric Endocrinology and Metabolism Department, the First Hospital of Jilin University, Changchun, Jilin 130021, PR China

ARTICLE INFO

Article history:
Received 8 December 2008
Received in revised form 25 April 2009
Accepted 29 April 2009
Available online 7 May 2009

Keywords:
Acetonitrile
Cathodic electrochemiluminescence
Hydrogen peroxide
Inhibition
Tripropylamine
Tris(2,2′-bipyridine)ruthenium(II)

ABSTRACT

A novel tris(2,2′-bipyridine)ruthenium(II) ($Ru(bpy)_3^{2+}$) cathodic electrochemiluminescence (ECL) was generated at −0.78 V at the Pt electrode in acetonitrile (ACN), which suggested that the cathodic ECL differed from conventional cathodic ECL. It was found that tripropylamine (TPrA) could enhance this cathodic ECL and the linear range (log–log plot) was 0.2 μM–0.2 mM. In addition, hydrogen peroxide (H_2O_2) could inhibit the cathodic ECL and was indirectly detected with the linear range of 27–540 μM. The RSD ($n = 12$) of the ECL intensity in the presence of 135 μM H_2O_2 was 0.87%. This method was also demonstrated for the fast determination of H_2O_2 in disinfectant sample and satisfactory results were obtained.

1. Introduction

Tris(2,2′-bipyridine)ruthenium(II) ($Ru(bpy)_3^{2+}$) electrochemiluminescence (ECL) has been a powerful tool in analytical chemistry because of its high sensitivity, wide linear range, simplicity, and good stability [1]. There are two detection modes for the different analytes including enhanced ECL detection (direct detection) and inhibition ECL detection (indirect detection). Concerning the direct detection mode, oxalate ($C_2O_4^{2-}$) [2,3] and nitrogen-containing compounds [4–8] can be directly detected by the oxidative-reduction type ECL. In addition, hydrogen peroxide (H_2O_2) [9] and peroxydisulfate ($S_2O_8^{2-}$) [10] can be directly determined by the reductive-oxidation type ECL. Regarding the indirect detection mode, some inorganic compounds [11] and organic acids [12,13] can be indirectly detected based on their inhibition of $Ru(bpy)_3^{2+}$/tripropylamine (TPrA) or $Ru(bpy)_3^{2+}/C_2O_4^{2-}$ ECL system.

In general, the two ECL detection modes are usually carried out in aqueous solution. However, the applied potential is either much more positive (>1.05 V vs. SCE) or negative (<−1.25 V vs. SCE), and thus the influence of water is inevitable. Concerning anodic ECL, oxygen evolution occurs easily, resulting in decreased ECL intensity. In addition, the most often used Pt electrode needs reactivation [14]. Regarding cathodic ECL, some particular electrodes such as oxide-covered tantalum electrode [15] or bismuth electrode [16] were used because of the very negative potential of $Ru(bpy)_3^{2+}$ reduction, where hydrogen evolution occurs at conventional metal electrode.

In order to eliminate the influence of water, ECL could be generated in organic solution such as acetonitrile (ACN). Bard's group [17] first demonstrated the $Ru(bpy)_3^{2+}/S_2O_8^{2-}$ cathodic ECL in ACN. Here, a novel $Ru(bpy)_3^{2+}$ cathodic ECL was demonstrated at the Pt electrode at −0.78 V in ACN. It was found that $S_2O_8^{2-}$ could not enhance this cathodic ECL, while TPrA could, which indicated that the cathodic ECL differed from the conventional cathodic ECL. In addition, H_2O_2 could inhibit this cathodic ECL. There are a lot of reports about the detection of H_2O_2 by direct ECL detection [18–22]. The first sensing application of quantum dot ECL was demonstrated to detect H_2O_2 by Ju's group [18]. Cui et al. [22] presented a H_2O_2 sensor based on the ECL of luminol-reduced gold nanoparticles. However, among these ECL detection methods, few reports were used to detect H_2O_2 in real sample. In our study, H_2O_2 was simply and indirectly detected based on its inhibition of the cathodic ECL with good reproducibility. In addition, this method was applied for the fast determination of H_2O_2 in disinfectant sample.

* Corresponding author. Fax: +86 431 85262850.
E-mail address: youty@ciac.jl.cn (T. You).

0039-9140/$ – see front matter © 2009 Elsevier B.V. All rights reserved.
doi:10.1016/j.talanta.2009.04.064

2. Experimental

2.1. Chemicals and solutions

Tris(2,2′-bipyridine)ruthenium(II) dichloride hexahydrate ($Ru(bpy)_3Cl_2 \cdot 6H_2O$) and tripropylamine (TPrA) were purchased from Aldrich (Milwaukee, WI, USA) and used without further purification. Tetrabutylammonium perchlorate (TBAP, electrochemical grade) was obtained from Fluka (Milwaukee, WI, USA). Acetonitrile (ACN), acetic acid (HAc), sodium acetate (NaAc), and aqueous hydrogen peroxide (H_2O_2) (30%) were purchased from Beijing Chemical Factory. H_2O_2 disinfectant sample (2.5–3.5%) was obtained from Hebei Jianjing medical and chemical factory. All the reagents and chemicals were of analytical reagent grade. ACN-based media containing 40 mM TBAP, 1 M HAc, and 20 mM NaAc was used as buffer solution. All solutions were prepared with ACN.

2.2. Instrumentation

Cyclic voltammograms were performed with a CH Instrument model 800 voltammetric analyzer (Austin, TX, USA) using a 500 μm Pt disc working electrode (or a 3 mm GC electrode), a platinum coil counter electrode (CE), and a Ag pseudo-reference electrode in a poly(dimethylsiloxane) (PDMS) detection cell sealed by a modified plastic sample vial with three holes for the three electrode, respectively. The corresponding ECL signals were measured with a photomultiplier tube (PMT, Xi'an Remex Electronic Science Tech Co., Ltd., Xi'an, China) installed under the PDMS detection cell. Unless mentioned otherwise, the Pt electrode was used as the working electrode and all potentials were referenced to Ag pseudo-reference electrode. According to the literature [9], the CE was isolated by a porous ceramic tip and a glass capillary filled with ACN-based media containing 40 mM TBAP, 1 M HAc, and 20 mM NaAc. It needed to be emphasized that cathodic ECL was generated when CE was not isolated (called exposed CE), otherwise there was no cathodic ECL.

3. Results and discussion

3.1. Cathodic ECL in ACN

One of the most attractive features of $Ru(bpy)_3^{2+}$ ECL in ACN is that there is no influence of water on the ECL intensity. However, $Ru(bpy)_3(ClO_4)_2$ was often used instead of $Ru(bpy)_3Cl_2$ in ACN because Cl^- was easily oxidized preceding the oxidation of $Ru(bpy)_3^{2+}$ and its oxidation influenced the ECL intensity [23,24]. Moreover, the preparation of $Ru(bpy)_3(ClO_4)_2$ needed recrystallization and dryness [25–28]. We reported a strong $Ru(bpy)_3Cl_2$/TPrA anodic ECL system in ACN by inhibiting the oxidation of Cl^- using acetate buffer without $Ru(bpy)_3(ClO_4)_2$ [29]. Not only was the influence of water eliminated, but also the Pt electrode reactivation, necessary for aqueous ECL system, was not needed. In addition, a cathodic ECL was observed at −0.78 V.

Fig. 1 shows the cyclic voltammograms (Fig. 1A) and their corresponding ECL curves (Fig. 1B) of 2 mM $Ru(bpy)_3^{2+}$ in ACN with exposed (solid line) and isolated (dotted line) CE. From Fig. 1A, we can see that there was no obvious change in the cyclic voltammograms whether the CE was isolated or not. With the potential scanned negatively, a broad reductive peak could be observed between 0.4 and −0.65 V, which was attributed to the reduction of oxygen (no peak when saturated with N_2, not shown). When it was more negative than −0.65 V, there was an increasing reductive current and a corresponding cathodic ECL was observed at about −0.78 V with exposed CE (Fig. 1B, solid line). According to the literature [24], $Ru(bpy)_3^{2+}$ was reduced at about −1.33 V

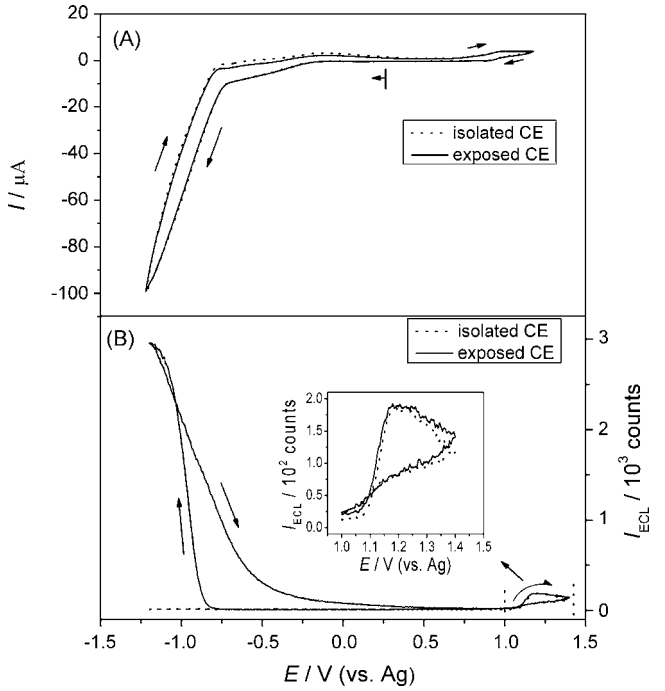

Fig. 1. Cyclic voltammograms (A) and their corresponding ECL curves (B) of 2 mM $Ru(bpy)_3^{2+}$ in ACN with exposed (solid line) and isolated CE (dotted line). Buffer solution, 40 mM TBAP + 1 M HAc + 20 mM NaAc in ACN; scan rate, 0.1 V/s; PMT voltage, 600 V.

vs. Ag pseudo-reference electrode in ACN, which suggested that $Ru(bpy)_3^+$ could not be generated. In addition, the cathodic ECL could not be enhanced by $S_2O_8^{2-}$, proving that $Ru(bpy)_3^+$ was not generated. Therefore, this cathodic ECL is different from conventional cathodic ECL. When the potential was scanned positively, $Ru(bpy)_3^{2+}$ started to oxidize at about 1.0 V and reached the maximum oxidization peak around 1.18 V, and a corresponding anodic ECL similar to the conventional anodic ECL in aqueous solution could be observed.

Dong's group [30] reported a novel cathodic ECL at a glassy carbon electrode (GC) at −0.4 V (vs. Ag/AgCl) in aqueous solution, which was caused by the reduction of oxygen. Choi and Bard [9] also investigated this cathodic ECL and they considered that the counter electrode reaction was another important factor for the cathodic ECL besides the reduction of oxygen.

When the CE was isolated by a porous ceramic tip, the cathodic ECL disappeared but the anodic ECL had no change in our study (Fig. 1B, dotted line). Therefore, the CE reaction also contributed to the cathodic ECL. In addition, the cathodic ECL did not disappeared but increased after the solution was saturated with N_2, which suggested oxygen did not contributed to the cathodic ECL. Here, oxygen only quenched the ECL, which accords with the literature [24]. The ECL behaviour of $Ru(bpy)_3^{2+}$ at GC electrode was also investigated in ACN (supporting information, Figure SI-1) and the result showed that oxygen was easily reduced and a cathodic ECL was generated. In addition, both the reduction of oxygen and CE reaction were dispensable to generate the cathodic ECL at the GC electrode.

It was noted that homoconjugation, heteroconjugation, and ion-pair often take place in ACN, which might be another reason to generate the cathodic ECL [29,31–33]. When only TBAP was used as supporting electrolyte, the cathodic ECL was not generated, and there was still not cathodic ECL while HAc was added. The adding of NaAc was indispensable to produce the cathodic ECL. However, the mechanism was not clear.

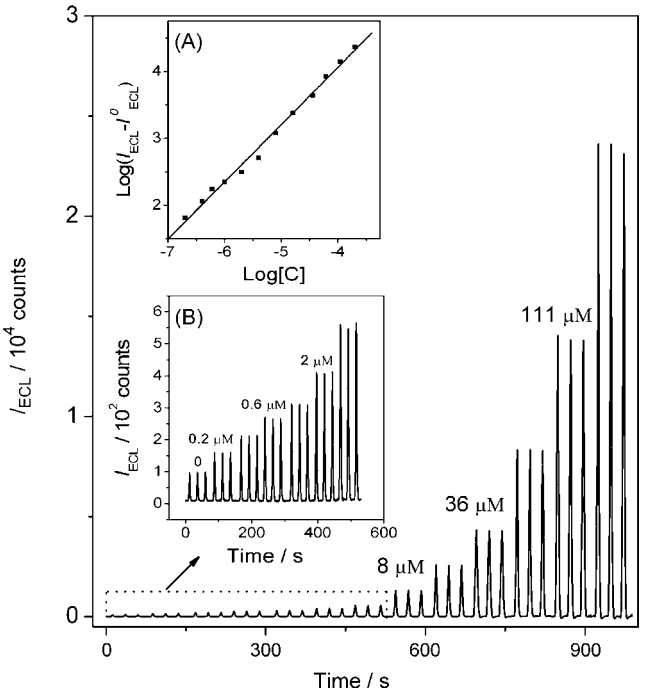

Fig. 2. ECL curves for the determination of TPrA. Scan range, 0.25–0.85 V. Other conditions are the same as in Fig. 1. Inset: (A) log–log plot of the increase in ECL intensity vs. the TPrA concentration and (B) ECL curves at low TPrA concentration.

3.2. Enhanced cathodic ECL by TPrA

The ECL intensity vs. potential for 2 mM $Ru(bpy)_3^{2+}$ in the presence and absence of 8 μM TPrA was investigated (Figure SI-2). The ECL intensity increased sharply when TPrA was added and the maximum ECL intensity appeared at about −1.05 V. It was noted that the ECL intensity was very high (3000 counts) even when PMT was biased at low voltages (600 V). Therefore, in order to obtain wide linear range, −0.85 V was selected as the detection potential. The ECL curves for the determination of TPrA are presented in Fig. 2. When the concentration of TPrA was larger than 0.2 mM, the ECL intensity went beyond the maximum range of the luminescence detector, which limited the linear range. The linear range (log–log plot) was 0.2 μM–0.2 mM with a correlation coefficient of 0.9963, which was compatible to that obtained by the cathodic ECL in aqueous solution [30]. In contrast, no cathodic ECL was observed even in the presence of 1 mM TPrA when the CE was isolated.

3.3. The indirect determination of H_2O_2 by cathodic ECL

It was reported that H_2O_2 could inhibit the anodic ECL in aqueous solution [34,35]. However, in organic solution, H_2O_2 could not inhibit the anodic ECL but the cathodic ECL in our study (Fig. 3). Fig. 4 shows the ECL curves for 2 μM $Ru(bpy)_3^{2+}$/10 mM TPrA in the presence (solid line) and absence (dotted line) of 135 μM H_2O_2. Without H_2O_2, ECL intensity occurred at about −0.78 V and the maximum ECL peak was observed around −0.92 V. After H_2O_2 was added, the ECL intensity decreased to 1/3. H_2O_2 standard solution was prepared from aqueous H_2O_2. To confirm whether water affected on the ECL intensity, the experiments were conducted. We found that there was no obvious influence on the ECL intensity and reproducibility in the presence of 1% water (v/v). Thus, a simple indirect detection of H_2O_2 was established based on its inhibition of $Ru(bpy)_3^{2+}$/TPrA cathodic ECL. The effect of the TPrA concentration on the decreased ECL intensity in the presence of 135 μM H_2O_2 was investigated (Fig. 5). With higher [TPrA], the decreased

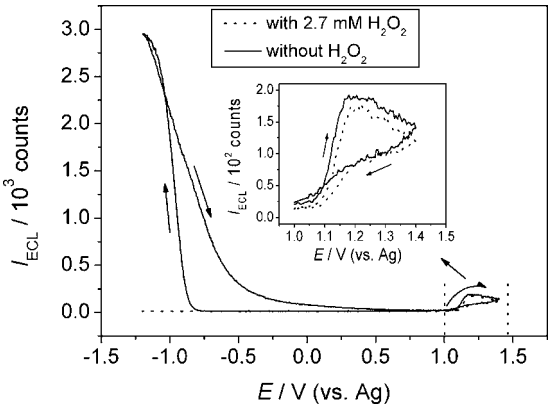

Fig. 3. ECL curves for 2 mM $Ru(bpy)_3^{2+}$ at the Pt electrode in the presence (dotted line) and absence (solid line) of 2.7 mM H_2O_2. Conditions are the same as in Fig. 1.

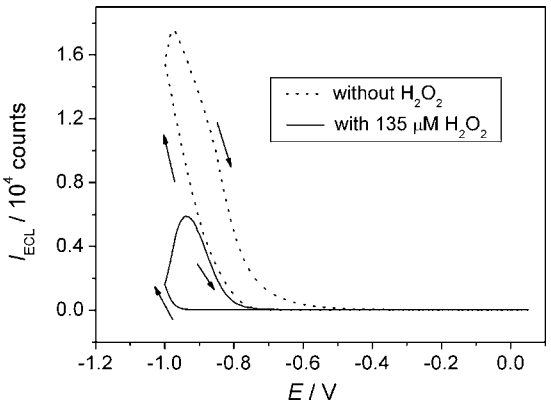

Fig. 4. ECL curves for 2 μM $Ru(bpy)_3^{2+}$/10 mM TPrA in the presence and absence of 135 μM H_2O_2. PMT voltage, 900 V; buffer solution, 40 mM TBAP + 1 M HAc + 20 mM NaAc in ACN.

ECL intensity increased until 10 mM. When it was beyond 10 mM, the decreased ECL intensity decreased. Therefore, 10 mM TPrA was selected as the optimum concentration.

The reproducibility of 2 μM $Ru(bpy)_3^{2+}$/10 mM TPrA cathodic ECL system in the presence and absence of 135 μM H_2O_2 was also investigate. The RSDs (n = 12) of the ECL intensity were 0.39 and 0.87% respectively, which suggested that the proposed method was feasible for the indirect determination of H_2O_2.

By this method, the detection limit of H_2O_2 was 27 μM, which is lower than that obtained by $Ru(bpy)_3^{2+}/C_2O_4^{2-}$ system in aqueous

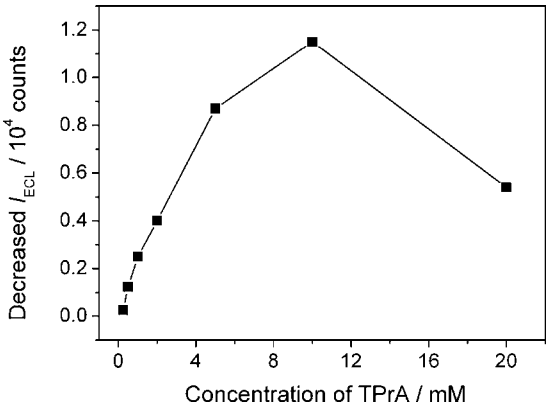

Fig. 5. Effect of the TPrA concentration on the decreased ECL intensity of 2 μM $Ru(bpy)_3^{2+}$ in the presence of 135 μM H_2O_2. PMT voltage, 900 V; buffer solution, 40 mM TBAP + 1 M HAc + 20 mM NaAc in ACN.

solution (2 mM) [34] and that obtained by a screen printed tubular microband electrode [36], and is comparable to that obtained by an imaging electrochemiluminescent sensor array (10 μM) [37], but is higher than that obtained by $Ru(bpy)_3^{2+}$/TPrA indirect ECL coupled with flow injection (0.1 μM) [35]. The linear range was 27–540 μM with a correlation coefficient of 0.9986. This method was successfully applied for the determination of H_2O_2 in disinfectant sample. The disinfectant sample was diluted in the detection solution (1:9217) and then detected. It was found that the content of H_2O_2 was in the range of 2.1–3.4%, which was in accord with the value labeled (2.5–3.5%). The recovery was in the range of 93–104%.

4. Conclusions

A novel cathodic ECL in ACN was presented, by which TPrA was directly detected with a wide linear range. It was found that H_2O_2 could inhibit the cathodic ECL but not the anodic ECL. H_2O_2 could be simply detected based on its inhibition with good reproducibility. This proposed method was also successfully used for the fast determination of H_2O_2 in disinfectant sample with satisfactory results.

Acknowledgements

The authors are grateful to the National Science Foundation of China (nos. 20605020 and 20875085), Chinese Academy of Sciences (no. KJCX2-YW-H11), and Foundation of Distinguished Young Scholars of Jilin Province (no. 20060112) for their financial support.

Appendix A. Supplementary data

Supplementary data associated with this article can be found, in the online version, at doi:10.1016/j.talanta.2009.04.064.

References

[1] X.Q. Liu, L.H. Shi, W.X. Niu, H.J. Li, G.B. Xu, Angew. Chem. Int. Ed. 45 (2006) 1.
[2] I. Rubinstein, A.J. Bard, J. Am. Chem. Soc. 103 (1981) 512.
[3] H.N. Choi, S.H. Cho, W.Y. Lee, Anal. Chem. 75 (2003) 4250.
[4] J.B. Noffsinger, N.D. Danielson, Anal. Chem. 59 (1987) 865.
[5] S.N. Brune, D.R. Bobbitt, Anal. Chem. 64 (1992) 166.
[6] T.M. Downey, T.A. Nieman, Anal. Chem. 64 (1992) 261.
[7] W.Y. Lee, T.A. Nieman, Anal. Chem. 67 (1995) 1789.
[8] L. Dennany, R.J. Forster, J.F. Rusling, J. Am. Chem. Soc. 125 (2003) 5213.
[9] J.P. Choi, A.J. Bard, Anal. Chim. Acta 541 (2005) 143.
[10] H.S. White, A.J. Bard, J. Am. Chem. Soc. 104 (1982) 6895.
[11] Y.W. Chi, Y.Q. Dong, G.N. Chen, Anal. Chem. 79 (2007) 4521.
[12] J. McCall, C. Alexander, M.M. Richter, Anal. Chem. 71 (1999) 2523.
[13] H. Cui, F. Li, M.J. Shi, Y.Q. Pang, X.Q. Lin, Electroanalysis 17 (2005) 590.
[14] Y.B. Zu, A.J. Bard, Anal. Chem. 72 (2000) 3223.
[15] F. Gaillard, Y.E. Sung, A.J. Bard, J. Phys. Chem. B 103 (1999) 667.
[16] L.Z. Hu, H.J. Li, S.Y. Zhu, L.S. Fan, L.H. Shi, X.Q. Liu, G.B. Xu, Chem. Commun. 40 (2007) 4146.
[17] H.S. White, A.J. Bard, J. Am. Chem. Soc. 104 (1982) 6891.
[18] G. Zou, H.X. Ju, Anal. Chem. 76 (2004) 6871.
[19] S.N. Ding, J.J. Xu, H.Y. Chen, Chem. Commun. 34 (2006) 3631.
[20] H. Jing, H.X. Ju, Anal. Chem. 79 (2007) 6690.
[21] G.F. Jie, B. Liu, J.J. Miao, J.J. Zhu, Talanta 71 (2007) 1476.
[22] H. Cui, W. Wang, C.F. Duan, Y.P. Dong, J.Z. Guo, Chem. Eur. J. 13 (2007) 6975.
[23] N.E. Tokel-Takvoryan, A.J. Bard, J. Am. Chem. Soc. 94 (1972) 2862.
[24] N.E. Tokel-Takvoryan, A.J. Bard, J. Am. Chem. Soc. 95 (1973) 6582.
[25] W.L. Wallace, A.J. Bard, J. Phys. Chem. 83 (1979) 1350.
[26] R.S. Glass, L.R. Faulkne, J. Phys. Chem. 85 (1981) 1160.
[27] A.J. Bard, F.R. Fan, Acc. Chem. Res. 29 (1996) 572.
[28] F.R. Fan, D. Cliffel, A.J. Bard, Anal. Chem. 70 (1998) 2941.
[29] B.Q. Yuan, J.S. Huang, J.Y. Sun, T.Y. You, Electrophoresis 30 (2009) 479.
[30] W.D. Cao, G.B. Xu, Z.L. Zhang, S.J. Dong, Chem. Commun. 14 (2002) 1540.
[31] S.P. Porras, E. Kenndler, J. Chromatogr. A 1037 (2004) 455.
[32] S.P. Porras, M. Jussila, Electrophoresis 28 (2007) 3590.
[33] I.M. Kolthoff, M.K. Chantooni, J. Am. Chem. Soc. 97 (1975) 1376.
[34] F. Jameison, R.I. Sanchez, L.W. Dong, J.K. Leland, D. Yost, M.T. Martin, Anal. Chem. 68 (1996) 1298.
[35] C.Y. Wang, H.J. Huang, Anal. Chim. Acta 498 (2003) 61.
[36] F.J. Rawsona, W.M. Purcell, J. Xu, D.C. Cowell, P.R. Fielden, N. Biddle, J.P. Hart, Electrochim. Acta 52 (2007) 7248.
[37] A. Chovin, P. Garrigue, N. Sojic, Electrochim. Acta 49 (2004) 3751.

Talanta 79 (2009) 700–705

Contents lists available at ScienceDirect

Talanta

journal homepage: www.elsevier.com/locate/talanta

Facile detection of proteins on a solid-phase membrane by direct binding of dextran-based luminol–biotin chemiluminescent polymer

Huan Zhang[a], Takayuki Shibata[a], Tomasz Krawczyk[a], Tsutomu Kabashima[a], Jianzhong Lu[b], Myung K. Lee[c], Masaaki Kai[a,d,*]

[a] Faculty of Pharmaceutical Sciences, Graduate School of Biomedical Sciences, Nagasaki University, 1-14, Bunkyo-Machi, Nagasaki 852-8521, Japan
[b] School of Pharmacy, Fudan University, Shanghai 200032, China
[c] College of Pharmacy, Chungbuk National University, San4 8, Kaeshin-Dong, Heungduk-Gu, Cheongju 361-763, South Korea
[d] Global COE Program, Nagasaki University, Japan

ARTICLE INFO

Article history:
Received 12 January 2009
Received in revised form 26 April 2009
Accepted 27 April 2009
Available online 3 May 2009

Keywords:
Protein detection
Microchip
Chemiluminescence
Luminol-containing macromolecule

ABSTRACT

Facile and non-radioactive methods are desired for the sensitive detection and quantification of various proteins. Herein we describe a novel chemiluminescence (CL)-detection method of particular proteins based on direct binding of a dextran–luminol–biotin (DLB) CL polymer to the proteins on a poly(vinylidene difluoride) membrane. Among 32 kinds of the proteins screened, several proteins such as drug-metabolizing enzymes, cytochrome p450 (CYP)1A2, CYP2E1, and CYP3A4 had the ability to bind directly to the DLB polymer. The binding site in the polymer was owing to the framework of the modified dextran, which underwent oxidation and reduction procedures. This interaction might be the comprehensive effect of both electrostatic interaction and steric complementarities. CL intensity of the proteins detected by the polymer could be further enlarged by the mediation of avidin. The proposed CL-imaging method possesses potential as a rapid, facile, inexpensive and selective detection of the proteins.

1. Introduction

Enzyme-linked immunosorbent assay (ELISA) on 96-wells plastic plate or membrane matrix has been widely used in immunoassay with respect to its specificity and sensitivity. Antibody is indispensable in ELISA; it is routinely utilized as an analytical reagent for specific recognition and binding with an antigen. However, the preparation of a specific antibody to an antigen is expensive, time consuming and laborious, and the antibodies are sensitive to temperature because of irreversible denaturation. Artificial antibody-like receptors, such as aptamer and molecular imprinting polymer (MIP) could be the solution to such problems. Aptamer is a short DNA or RNA oligonucleotide that provides specific binding to a target protein. Fifteen years since their discovery, however, aptamers have been obtained only for limited number of proteins because the production of the aptamers is difficult [1,2]. MIPs are the synthetic compounds that might be substituted for antibodies in immunoassay; however, the hydrophobic nature and highly cross-linked structure of the polymer limit the access of the large protein molecules to the binding sites of MIPs [3–5].

The possibility of use of peroxidase or metal enzymes has been recently reported for the sensitive chemiluminescence (CL) detection of particular proteins in the ELISA system. It utilizes the fact that the native enzymes such as horse radish peroxidase could catalyze the CL reaction between luminol and hydrogen peroxide [6,7]. In this technique, for example, the electrophoresis should be conducted with the usage of non-denatured gel and running at low temperature to keep the proteins active; otherwise CL signal cannot be seen. CL-imaging methods offer many advantages for high-throughput evaluation, high sensitivity, simple instrumentation, and exclusion of the usage of radioisotopes [8,9]. We reported a CL immunoassay for the sensitive detection of a CYP3A4 protein utilizing two antibodies and a dextran–luminol–biotin (DLB) polymer [10]. However, our recent experiments have indicated that the DLB polymer directly bound to some proteins on a membrane in the absence of blocking agents of the framework of the DLB polymer and dextran.

In this study, therefore we developed a novel CL-imaging method for particular proteins such as CYP proteins on a PVDF membrane (Fig. 1). The advantage of this method is to permit facile, rapid, inexpensive and sensitive detection for those proteins on a solid-phase membrane, because the DLB polymer as a signal probe indicated the possibility of the direct binding to

* Corresponding author at: Faculty of Pharmaceutical Sciences, Graduate School of Biomedical Sciences, Nagasaki University, 1-14, Bunkyo-Machi, Nagasaki 852-8521, Japan. Tel.: +81 95 819 2438; fax: +81 95 819 2438.
E-mail address: ms-kai@nagasaki-u.ac.jp (M. Kai).

0039-9140/$ – see front matter © 2009 Elsevier B.V. All rights reserved.
doi:10.1016/j.talanta.2009.04.056

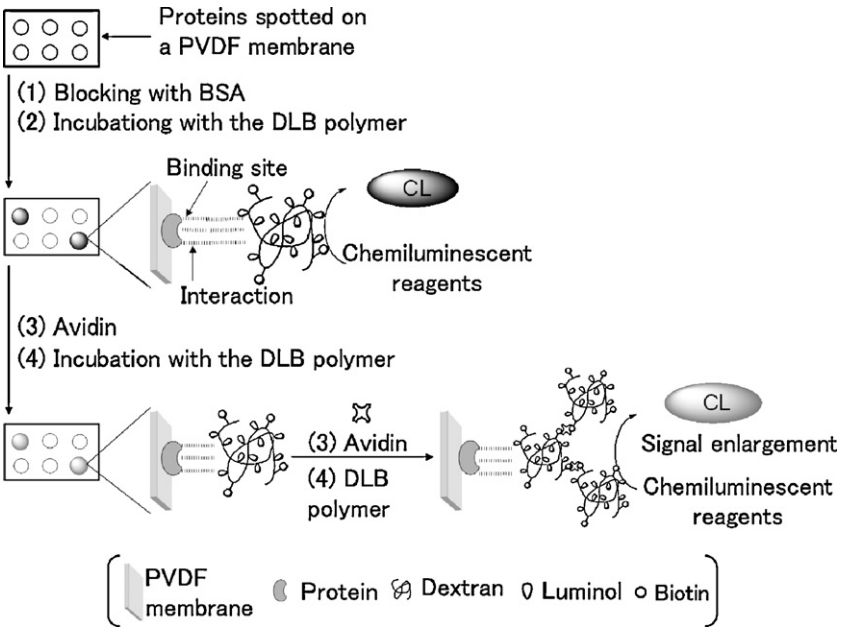

Fig. 1. CL detection of a protein on a PVDF membrane by the DLB polymer.

the target proteins. Many proteins exist in blood plasma, such as complement proteins, proteins for blood coagulation, adhesion proteins, lipoproteins, protease inhibitors, immunoglobulin, hormones, enzymes, disease-related markers, and so on [11]. We screened 32 kinds of commercially available proteins to be detected by the DLB polymer. Among them, lysozyme, fibroblast growth factor 5 (FGF5), cytochrome c, β-nerve growth factor (β-NGF), CYP1A2, CYP2E1, CYP3A4, prolactin and concanavalin A exhibited relatively strong interactions with the polymer. Furthermore, several experiments were conducted to clarify the mechanism of the interaction between the DLB polymer and the proteins.

2. Experimental

2.1. Reagents and chemicals

Dextran T500 (average MW 5×10^5 Da) was purchased from Pharmacia Fine Chemicals (Sweden). Sodium periodate and avidin were purchased from Wako (Japan). 6-Hydrazidohexyl-D-biotinamide was purchased from Dojindo (Japan). Luminol and sodium borohydride were purchased from Nacalai Tesque (Japan) and used without further purification. Nylon membranes and poly(vinylidene difluoride) (PVDF) membranes (0.45 μm pore size) were supplied by Millipore (Billerica, MA, USA). Tetra-n-butylammonium hydroxide (TBA) was supplied by Sigma–Aldrich (St. Louis, MO, USA). Adrenocorticotropin hormone (40 residues, human) and a peptide fragment (21 residues) of CYP3A4 (human) were purchased from AnaSpec (San Jose, CA, USA). Growth hormone (human recombinant) and parathyroid hormone (human recombinant) were purchased from Atgen (Korea). Mouse β-nerve growth factor (β-NGF) was supplied by Austral Biologicals (San Ramon, CA, USA). A peptide fragment (12 residues) of CYP1A2 (human) was supplied by Biomol (USA). Ceruloplasm (human plasma), concanavalin A (canavalia ensiformis), cytochrome c (equine heart), fibrinogen (human plasma), follicle-stimulating hormone (human pituitary), peanut lectin (arachis hypogaea), luteinizing hormone (human pituitary), serum amyloid A (human serum), superoxide dismutase (human recombinant), thrombin (bovine), thyroglobulin (human thyroid), transferring, β_2-microglobulin (human), and haptoglobin were purchased from Calbiochem (Germany). Bovine serum albumin (BSA) was purchased from Nacalai Tesque (Japan). Hemoglobin (human) was purchased from Nutritional Biochemicals (USA). CYP1A2 (human recombinant), CYP2E1 (human recombinant), CYP3A4 (human recombinant), monoclonal anti-CYP1A2 antibody (mouse anti-human), and polyclonal anti-CYP1A2 antibody (rabbit anti-human) were supplied by Oxford Biochemical Research (USA). Fibroblast growth factor 5 (FGF5, human recombinant) and prolactin (mouse recombinant) were supplied by R & D Systems (USA). Bovine serum albumin (BSA), lysozyme (chicken egg white), myoglobin (equine skeletal muscle), α-amylase (*aspergillus oryae*), and β-lactoglobulin (bovine milk) were purchased from Sigma (St. Louis, MO, USA).

2.2. Synthesis of a DLB polymer and its related compounds (Fig. 2)

Dextran T500 (400 mg) with ca. 500 kDa in average molecular weight was dissolved in water (40 mL) followed by precipitating with methanol. The precipitate was filtered, re-dissolved in water (60 mL), and then sodium periodate (317 mg) was added. The reaction mixture was stirred at room temperature until the 310 nm UV-absorption band corresponding to sodium periodate disappeared. Then, the reaction mixture was poured into methanol (300 mL), the precipitate of partially oxidized dextran (ox-Dex) was filtered off and used in the next step.

To the oxidized dextran was added dimethyl sulfoxide (DMSO) (40–80 mL) and the mixture heated at 100 °C to dissolve the oxidized dextran completely. 6-Hydrazidohexyl-D-biotinamide (30 mg) was then added to the solution and allowed to stir at room temperature for 3 h. Glacial acetic acid (16 mL) and luminol (240 mg) were subsequently added into the reaction mixture and left stirring at 60 °C overnight. The mixture was poured into methanol (400 mL). Methanol was removed from the precipitate by careful decantation, and then another 500 mL of methanol was added to the precipitate. After stirring for 30 min, a yellowish powder (DLB polymer) of the conjugates was collected by filtration. In the case of the synthesis of the dextran-based compound containing only luminol (DL), the addition of 6-hydrazidohexyl-D-biotinamide was omitted.

The modified dextran polymer was dissolved in ethyleneglycol (20–60 mL). Excess of sodium borohydride (870 mg) was added

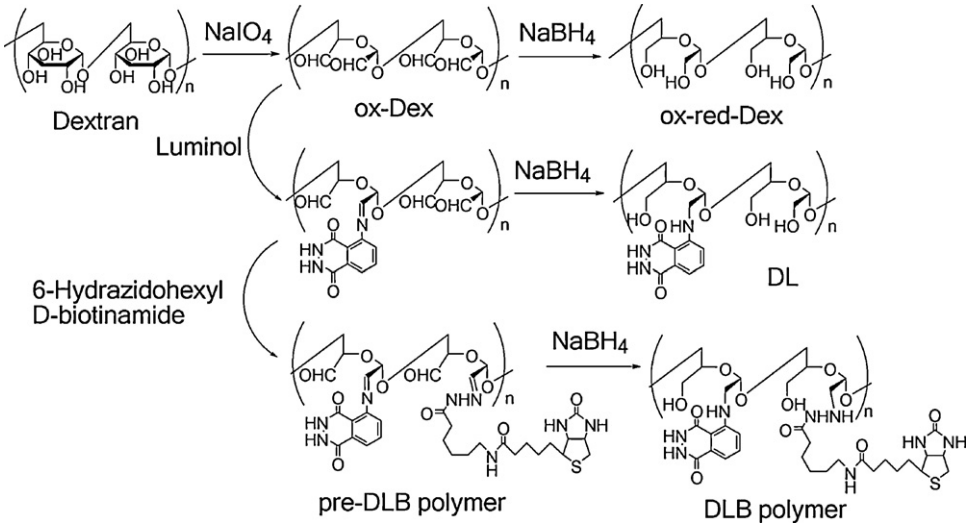

Fig. 2. Synthetic pathway of dextran-based polymers.

into the ice-cooled reaction mixture and the mixture was left stirring at room temperature for 4 h. Then reaction was continued at 4 °C overnight without stirring. The desired polymer was reprecipitated by acetone (200 mL), washed three times with methanol (300 mL) to remove the unreacted biotin and luminol. The precipitate was then dried *in vacuo* overnight. Three dextran-related compounds were obtained: oxidized and reduced dextran (ox-red-Dex) as a white powder (150–200 mg), DL as a pale yellow powder (250–300 mg) and DLB polymer as a pale yellow powder (150–200 mg).

2.3. CL detection of DLB polymer on a nylon membrane

Aqueous solution of DLB polymer was spotted on a nylon membrane and dried *in vacuo* for 10 min. The membrane was then washed with methanol (2.0 mL) at 37 °C for 5 min, and dried again *in vacuo* for 10 min. The membrane was immersed for 10 s in a mixture consisting of 700 μL of acetonitrile, 300 μL of 0.5 M TBA and 50 μL of 30% hydrogen peroxide for the CL reaction. The CL-imaging detection was conducted by a CCD camera (Light capture AE-6971/2 device, ATTO, Japan) for 2.0 min of exposure time.

2.4. Binding constant of DLB polymer to avidin

A PVDF membrane was dotted with 3.0 μL of 100% ethanol followed by spotting of avidin (0.5 nM) in water. The membrane was dried *in vacuo* at 37 °C for 10 min. The PVDF membrane was incubated with different concentrations of DLB polymer (0.05–0.15 mg mL^{-1}) in 2.0 mL of 25 mM Tris buffer (pH 7.2) at 37 °C for 30 min. The membrane was washed twice at 37 °C with 4.0 mL of 10 mM phosphate buffer saline (PBS) containing 0.15% (w/v) Triton X-100. After the consecutive washing of the membrane with 2.0 mL of 75% (v/v) methanol, the membrane was dried *in vacuo* at 37 °C for 10 min. The CL reaction and imaging detection were performed as described above. Using Scatchard plot method, the binding constant *K* of the polymer to avidin and the binding molar ratio of avidin to the polymer was calculated.

2.5. Detection of proteins on a PVDF membrane by DLB polymer

A PVDF membrane was spotted by ethanol (3.0 μL) followed by spotting of various proteins in 25 mM Tris buffer (pH 7.2). The membrane was dried *in vacuo* at 37 °C for 30 min. The membrane was blocked with 3.0 mL of 3% BSA in 10 mM PBS (pH 7.2), followed by washing with 3.0 mL of the PBS. The membrane was incubated in a mixture (2.0 mL) of 2.0 mg DLB polymer and 4.0 mg BSA in 25 mM Tris buffer (pH 7.2) at 37 °C for 30 min. After the reaction, the membrane was washed three times with 5.0 mL of 10 mM PBS containing 1% Triton X-100, followed by washing the membrane with 2.0 mL of 75% methanol. The membrane was dried *in vacuo* at 37 °C for 20 min. The CL reaction and imaging detection were performed as described above.

3. Results and discussion

Prior to the investigation of the direct binding of our DLB polymer to proteins, we successively synthesized a series of dextran-related compounds (Fig. 2). The synthetic route to the DLB polymer was consisted of 4 steps: partial oxidation of dextran for oxidized dextran (ox-Dex), coupling between ox-Dex and luminol for ox-Dex containing luminol (DL), biotinylation of DL without reduction for ox-Dex containing luminol and biotin (pre-DLB polymer), and reduction of pre-DLB polymer for the DLB polymer. In order to evaluate the protein-binding mechanism of the DLB polymer, ox-red-Dex was synthesized by reduction of ox-Dex without luminol and biotin.

According to the elemental analysis data, the atomic composition of the synthesized DLB polymer and its molecular weight can be deduced. The atomic composition of the synthesized DLB polymer was 43% C, 5.8% H, 4.4% N, and 0.17% S, and its molecular weight was found to be approximately 6.3×10^5 Da. These data indicate that this polymer contained approximately 560 and 34 molecules of luminol and biotin, respectively in a dextranT500 molecule (3100 glucose units). The aqueous solution of the DLB probe gave approximately 300 times higher CL intensity at the same amount (1.0 fmol) of free luminol. It was found that the increased introduction of luminol gives more intense CL for the probe.

The CL intensity from the DLB polymer was measured by using different amounts of the polymer immobilized on a nylon membrane. The DLB polymer could be visualized by means of CL detection. The CL intensity was proportional to the amount of the polymer [$y = 0.1583x - 0.243$, $r^2 = 0.9965$, where y = CL intensity ($\times 10^6$), x = amount of the DLB polymer (ng) and r^2 = correlation coefficient]. Therefore, a large number of luminol molecules were chemically introduced into the polymer and the bound luminol did not lose from the polymer during the assay treatment. Next we investigated the binding ability of the polymer to avidin. It was shown that the CL intensity increased with the increased amounts

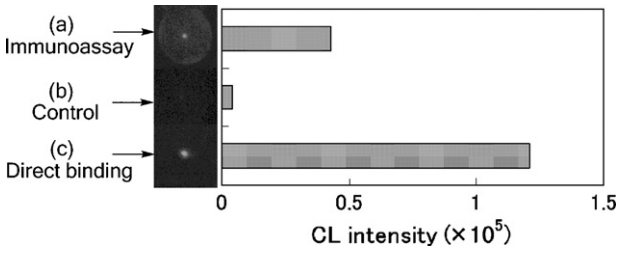

Fig. 3. CL detections of CYP3A4 by immunoassay using anti-CYP3A4 antibody, biotin-containing anti-IgG antibody, and by direct binding of DLB polymer. CYP3A4 (200 ng) spotted on a PVDF membrane was incubated at 37 °C for 2 h (a) with the first and second antibodies, or (b) without the antibodies in 10 mM PBS for control. After washing, the protein was detected by CL reaction after the incubation at 37 °C for 30 min with a mixture [DLB polymer (4 mg), streptavidin (4 mg), BSA (6 mg), dextran (6 mg) and ox-red-Dex (20 mg) in 2 mL of 10 mM PBS] for immunoassay, and (c) for the direct binding of DLB polymer, the membrane was incubated with a mixture [DLB polymer (4 mg) and BSA (6 mg) in 2 mL of 10 mM PBS], and after washing, the protein was detected by CL reaction.

of the polymer. The result indicates that biotin moieties in the polymer can bind to avidin. By using Scatchard plot method, the binding constant and the binding molar ratio of avidin to DLB polymer were about $5.1 \times 10^6\ M^{-1}$ and 60, respectively.

The DLB polymer was originally used for the detection of CYP3A4 by binding to biotin-containing anti-IgG antibody (second antibody) that bound to anti-CYP3A4 antibody (first antibody) binding to CYP3A4 in immunoassay. When CYP3A4 blotted on a PVDF membrane was treated with a mixture of streptavidin, BSA, dextran, ox-red-Dex, the antibodies and the DLB polymer, the detection of CYP3A4 could be achieved in the presence of the antibodies (Fig. 3a). On the other hand, negligible light was emitted from the protein in the absence of the antibodies (Fig. 3b). Although the polymer could be applicable to immunoassay for the sensitive and specific detection of a target protein [10], in the absence of blocking substances such as ox-red-Dex and dextran, CL emission from CYP3A4 was observed when the membrane was incubated with a mixture of the DLB polymer and BSA (Fig. 3c). This result indicated that the DLB polymer has a binding site in the molecule.

The above findings encouraged us to apply the DLB polymer to detect directly various proteins on a PVDF membrane, which included CYP proteins, carbohydrate-binding proteins, hormones, and plasma proteins (Table 1). The data indicated that CYP1A2 had the highest affinity to the polymer. CYP2E1, CYP3A4, lysozyme, FGF5, cytochrome c, β-NGF, and prolactin showed the strong CL. Hemoglobin, serum amyloid A and concanavalin A exhibited moderate binding affinity, while no signal was observed with the other proteins and peptides. Therefore, these bindings of the polymer to the proteins are not due to the molecular size of the proteins. It seems that the polymer might bind to particular proteins with relatively high isoelectronic point (p*I*), since there were several proteins with high p*I* values showing no affinity to the polymer, and concanavalin A even with a low p*I* value of 5 slightly bound to the polymer. No specific reason of the preference of the polymer to proteins can be clarified at this stage. However, interesting results were obtained from two shorter fragments of CYP1A2 (12 residues) and CYP3A4 (21 residues). No CL signals from these fragments were observed, even though the fragments have higher p*I* values. The results indicated that a specific region of the polymer participates in the protein binding.

It should be noted that the DLB polymer did not bind to the immunoglobulin proteins such as monoclonal and polyclonal anti-CYP1A2 antibodies, as shown in Table 1. By utilizing this characteristic, the development of a new detection method specific for the CYP proteins will be possible, in which several CYP proteins are individually recognized and captured by each anti-CYP antibody immobilized separately on a solid-phase membrane, following the direct detection of the CYP proteins on the membrane by the DLB polymer.

Table 1
The list of the proteins used in this study and their corresponding CL intensities.

Protein (100 ng)	MW ($\times 10^3$ Da)	p*I*	CL intensity %[a]
Lysozyme	14[b]	11.0[b]	30
Fragment (12 residues) of CYP1A2	1.3	10.0[c]	0
Fragment (21 residues) of CYP3A4	2.6	9.7[c]	0
FGF5	27	9.4[c]	88
Cytochrome c	13	9.4[b]	17
β-NGF	27[b]	9.3[b]	35
CYP1A2	58	9.2[c]	100
Luteinizing hormone	29	8.8[b]	0
CYP2E1	53	8.3[c]	57
CYP3A4	66	8.3[c]	23
Adrenocorticotropin hormone (40 residues)	4.5	8.1[c]	0
Parathyroid hormone	9.6	8.1[b]	0
Myoglobin	18[b]	8.1[b]	0
Hemoglobin	65[b]	6.9[b]	7
Monoclonal anti-CYP1A2 antibody	150[b]	6.5[b]	0
Peanut lectin	110	6.5[b]	0
Prolactin	23	6.1[b]	37
Serum amyloid A	12	5.9[c]	8
Fibrinogen	341	5.6[b]	0
Follicle-stimulating hormone	36	5.6[b]	0
Polyclonal anti-CYP1A2 antibody	150[b]	5.5[b]	0
α-Amylase	45[b]	5.5[b]	0
Thrombin	34	5.5[b]	0
β_2-Microglobulin	12	5.5[b]	0
Transferrin	80	5.3[b]	0
β-Lactoglobulin	18[b]	5.1[b]	0
Concanavalin A	104	5.0[b]	13
Growth hormone	20	5.0[b]	0
BSA	66	4.8[b]	0
Superoxide dismutase	32	4.8[b]	0
Thyroglobulin	660	4.5[b]	0
Ceruloplasm	134	4.4[b]	0
Haptoglobin	86	4.2[b]	0

Other MW and p*I* that were not labeled were obtained from the product description of the company.

[a] CL intensity obtained from CYP1A2 was taken as a reference (100%).

[b] MW and p*I* were obtained from a laboratory book.

[c] p*I* was calculated from the amino acid sequence by the computer software on internet.

We investigated the interaction between cytochrome c (cyt c) and the DLB polymer by using gel filtration liquid chromatography (GFLC). Cyt c has its maximum absorption at 408 nm, while the DLB polymer has no absorption at 408 nm (Fig. 4a and b). On the other hand, the DLB polymer showed two fluorescence (FL) peaks at the retention times of 13.5 min and 20.5 min. These FL peaks were identified as the luminol moiety in the macromolecular polymer (13.5 min) and free luminol at 20.5 min. However, the small amount of free luminol (approximately 1%, w/w) did not interfere with the detection of a target protein on a membrane, because it could be sufficiently removed from the membrane by washing with PBS containing 1% Triton X-100 and 75% methanol.

When the DLB polymer was mixed with cyt c before injection to GFLC, a new broad peak was detected at the retention time of 12.5 min with both the detections of absorbance at 408 nm and FL (Fig. 4c), indicating the formation of a complex between cyt c and the DLB polymer. In order to confirm the binding site of the DLB polymer to the protein, we synthesized two compounds similar to the DLB polymer; one was DL that does not contain biotin, and the other one was ox-red-Dex in which the dextran was oxidized and reduced without biotin and luminol. These frameworks of the DLB polymer were used to evaluate their binding abilities to cyt c. Fig. 4d shows that DL could bind to cyt c, indicating that the biotin moiety in the polymer was not the binding site for the protein. From Fig. 4e, it is clear that ox-red-Dex had the ability to bind to cyt c, suggesting

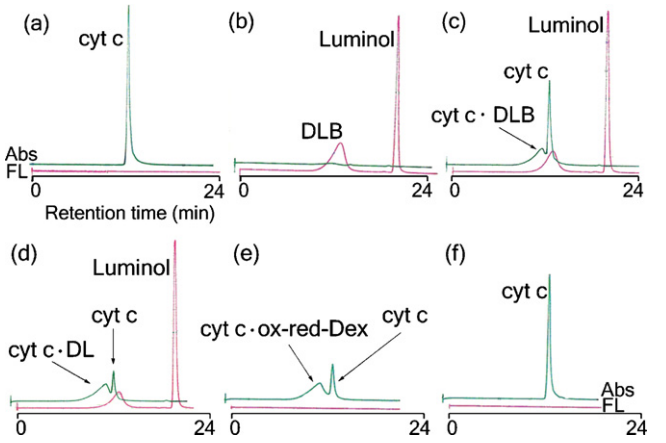

Fig. 4. GFLC identification of the interaction between the DLB polymer and cytochrome c. Samples: (a) 1 mg mL^{-1} cytochrome c (cyt c); (b) 1 mg mL^{-1} DLB polymer (DLB); (c) a mixture of 1 mg mL^{-1} DLB and 1 mg mL^{-1} cyt c at 37 °C for 1 h; (d) a mixture of 1 mg mL^{-1} DL and 1 mg mL^{-1} cyt c at 37 °C for 1 h; (e) a mixture of 1 mg mL^{-1} ox-red-Dex and 1 mg mL^{-1} cyt c at 37 °C for 1 h; (f) a mixture of 1 mg mL^{-1} pristine dextran and 1 mg mL^{-1} cyt c at 37 °C for 1 h. GFLC conditions: injection volume, 10 μL; column, TSK gel T2000SW; eluent, 20 mM PBS (pH 7.2); flow rate, 1.0 mL/min; absorbance detection (Abs), λ_{ab} = 408 nm; FL detection, $\lambda_{excitation}$ = 254 nm and $\lambda_{emission}$ = 370–430 nm.

that the luminol moiety in the polymer did not bind to the protein. As shown in Fig. 4f, the pristine dextran did not bind to the protein. These results lead to the conclusion that the framework produced by oxidization and reduction of dextran has the ability to interact with the protein.

The protein binding of a series of dextran-related compounds was further evaluated employing CYP2E1 spotted on a PVDF membrane. Fig. 5a indicates that CL intensity obtained from the conjugate of DLB or DL polymer with CYP2E1 was nearly the same. The results confirm that biotin and luminol moieties in the polymer had no influence on the interaction with CYP2E1.

We synthesized pre-DLB polymer having many free aldehyde groups in the framework. The pre-DLB polymer gave only less than half of the CL intensity obtained with the DLB polymer for the detection of CYP2E1 (Fig. 5a). In addition, the background signal was increased with the pre-DLB polymer. Therefore, this pre-DLB polymer was not used for the detection. We thought first that there would be aldehyde groups in the DLB polymer left unreacted, since the reaction of the aldehyde group in the polymer with NH_2 group in the protein might result in non-specific binding of the polymer to any proteins. However, the DLB polymer definitely showed the preference to the particular proteins (Table 1).

We additionally investigated to clarify the mechanism of their interaction. We considered that the binding force might be an electrostatic one. We measured the zeta potential of the DLB polymer on a Malvern zetasizer. The average zeta potential of the polymer was about −27.32 mV (n = 3) in the experimental condition of 25 mM Tris buffer at pH 7.2. The pI values of CYP1A2, FGF5, CYP2E1, β-NGF, lysozyme, CYP3A4, and cytochrome c were 9.2, 9.4, 8.3, 9.3, 11, 8.3, and 9.4, respectively. In the experimental pH region, these proteins should have positive charges. The DLB polymer was allowed to react with CYP2E1 in various concentrations of the binding buffer, Tris buffer at pH 7.2 (Fig. 5b). Higher concentration of the buffer resulted in lower binding ability of the DLB polymer to the protein. Fig. 5c shows that pH of the binding buffer affected the interaction between the polymer and the protein. We noticed that the binding between the DLB polymer and CYP2E1 is stronger at a neutral pH. Therefore, the binding of the polymer would be one of results of an electrostatic interaction between negative charges of the polymer and positive charges of the protein. However, as shown in

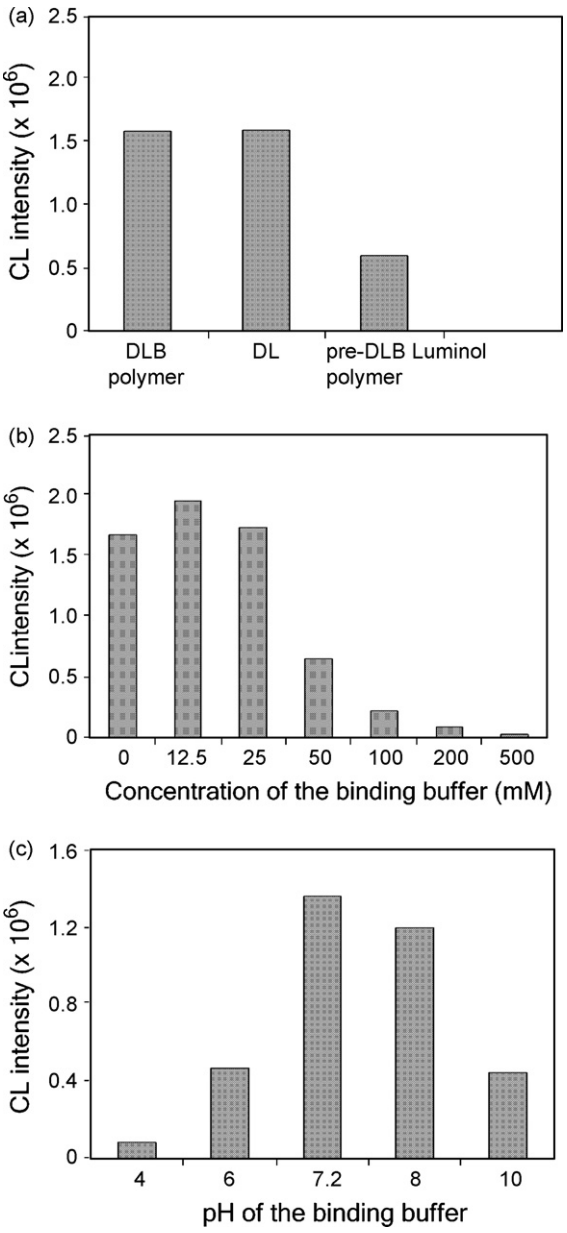

Fig. 5. (a) Direct detection of CYP2E1 with a series of dextran–luminol-related compounds. CYP2E1 protein (200 ng) spotted on a PVDF membrane, and the membrane was incubated with the DLB polymer, DL, pre-DLB polymer or free luminol in 2.0 mL of 25 mM Tris buffer (pH 7.2) at 37 °C for 30 min. (b) The influence of the concentration of the binding buffer. CYP2E1 protein (200 ng) was spotted on a PVDF membrane, and the membrane was incubated with the DLB polymer in different concentrations of Tris buffer of pH 7.2 at 37 °C for 30 min. (c) The influence of pH of the binding buffer. CYP2E1 protein (200 ng) was spotted on a PVDF membrane, and the membrane was incubated with the DLB polymer in different pHs of 25 mM Tris buffer at 37 °C for 30 min.

Table 1, some proteins such as luteinizing hormone (pI 8.8), adrenocorticotropin hormone (40 residues, pI 8.1), parathyroid hormone (pI 8.1) and myoglobin (pI 8.1), did not bind to the polymer, even that they had positive charges at the neutral condition. In addition, other proteins such as concanavalin A (pI 5), serum amyloid A (pI 5.9), prolactin (pI 6.1), and hemoglobin (pI 6.9) interacted with the polymer, despite they have negative charges in the binding buffer. Concanavalin A was a carbohydrate-binding protein, and thus it might be absorbed on the polysaccharide groups in the polymer. Although peanut lectin (pI 6.5) was also carbohydrate-binding proteins, the protein did not interact with the polymer. Therefore, the binding between the polymer and the particular proteins might be

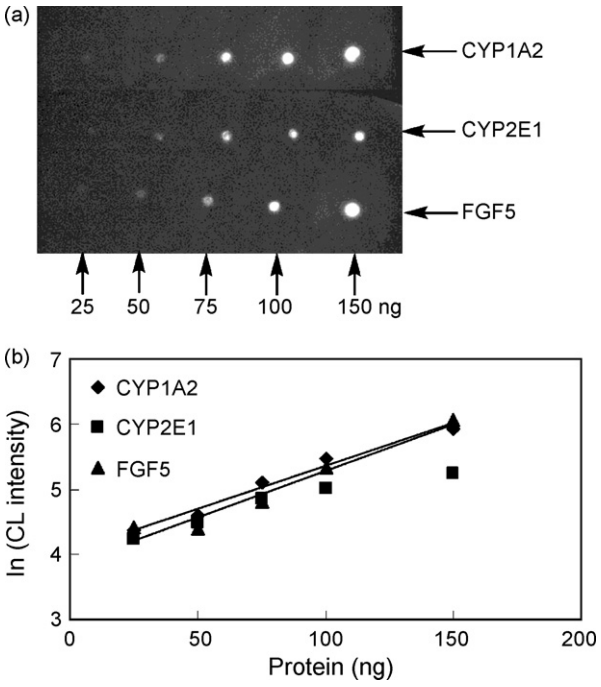

Fig. 6. (a) CL imaging and (b) calibration curves of proteins on a PVDF membrane. CYP1A2, CYP2E1 and FGF5 (25–150 ng each) were spotted on a PVDF membrane, and the membrane was detected by the DLB polymer.

caused by not only the electrostatic interaction but also another interaction.

Another hypothesis was the steric complementarity that played an important role in the interaction between the DLB polymer and the proteins. Since the framework of the polymer has a linear long chain structure, its chain having many hydroxyl groups after oxidation and reduction of dextran might be able to form a special anchoring site or a binding domain, which led to the specific binding of the DLB polymer to the particular proteins. The structural complementarity might be the other binding force between the DLB polymer and the proteins.

The efficiency of the DLB polymer on the binding to the proteins was investigated by the CL detection of different amounts of a protein absorbed onto a PVDF membrane. As shown in Fig. 6, the proteins of CYP1A2, CYP2E1 and FGF5 were detected and visualized by the DLB polymer. The logarithm of CL intensity was proportional to the amounts of the protein spotted on the membrane [$y = 0.0131x + 4.0504$, $r^2 = 0.9773$ for CYP1A2; $y = 0.0142x + 3.8593$, $r^2 = 0.949$ for FGF5; $y = 0.0081x + 4.121$, $r^2 = 0.9366$ for CYP2E1; whereas y = ln (CL intensity), x = amount of protein (ng) and r^2 = correlation coefficient].

The DLB polymer contains numerous biotin moieties which can bind specifically to avidin protein. Therefore, after the binding of the polymer to the proteins, the addition of avidin followed by further addition of the polymer might lead to the formation of a polymer–avidin assembly, which would result in the enlargement of the CL intensity, as shown in Fig. 1. The efficiency of the assembly was investigated with different amounts of CYP2E1 spotted on a PVDF membrane (Fig. 7). When the membrane spotted with CYP2E1 was treated with avidin and the DLB polymer, the CL signal was increased with the increasing amounts of avidin. These results indicate that avidin was unambiguously involved in the polymeric polymer assembly. Therefore, the enhancement of the CL signal was successfully achieved by the addition of avidin into the polymer solution.

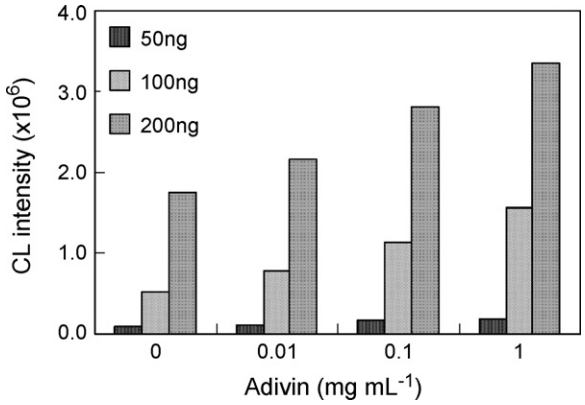

Fig. 7. The effect of avidin concentration on the enhancement of CL signal from CYP2E1 bound to the DLB polymer. CYP2E1 protein (50 ng, 100 ng or 200 ng) was spotted on a PVDF membrane. After the binding reaction with the DLB polymer, the membrane was additionally incubated with avidin (0.01–1 mg mL^{-1}) at 37 °C for 10 min in order to form the avidin–DLB polymer assembly.

4. Conclusions

The proposed CL-imaging method provided the facile detection for several proteins such as CYP1A2, CYP2E1 and CYP3A4 on a PVDF membrane by using the DLB polymer. This polymer exhibited sufficient solubility in water, strong CL signal and high ability to bind to avidin. After screening various proteins, we found that the CYPs, lysozyme, FGF5, cytochrome c, β-NGF, and prolactin strongly bound to the DLB polymer. CL intensity from each protein bound to the polymer was logarithmically proportional to the amounts of each protein absorbed onto the membrane. By the mediation of avidin, the DLB polymer gave enlarged CL signal. The results in this study suggest that the binding ability of the polymer to the proteins was due to its framework, and neither luminol nor biotin moieties in the polymer, and might be caused by the comprehensive function of both electrostatic and steric complementarities.

Acknowledgements

This work was supported by grants-in-aid for Scientific Research from the Ministry of Health, Labor, and Welfare of Japan, and partly from the Ministry of Education, Culture, Sports, Science and Technology of Japan and the Global Center of Excellence Program at Nagasaki University.

References

[1] S.D. Jayasena, Clin. Chem. 45 (1999) 1628.
[2] C.R. Ireson, L.R. Kelland, Mol. Cancer Ther. 5 (2006) 2957.
[3] I. Surugiu, L. Ye, E. Yilmaz, A. Dzgoev, B. Danielsson, K. Mosbach, K. Haupt, Analyst 125 (2000) 13.
[4] K. Haupt, Anal. Chem. 75 (2003) 377.
[5] J. Svitel, I. Surugiu, A. Dzgoev, K. Ramanathan, B. Danielsson, J. Mater. Sci. Mater. Med. 12 (2001) 1075.
[6] H. Chen, H. Zhao, L. Huang, W.R. Baeyens, J.R. Delanghe, D. He, J. Ouyang, Electrophoresis 26 (2005) 4260.
[7] Q. Tao, Z. Wang, H. Zhao, W.R. Baeyens, J.R. Delanghe, L. Huang, J. Ouyang, D. He, X. Zhang, Proteomics 7 (2007) 3481.
[8] A. Roda, M. Guarigli, E. Michelini, M. Mirasoli, P. Pasini, Anal. Chem. 75 (2003) 463A.
[9] A.M. Powe, K.A. Fletcher, N.N. St Luce, M. Lowry, S. Neal, M.E. McCarroll, P.B. Oldham, L.B. McGown, I.M. Warner, Anal. Chem. 76 (2004) 4614.
[10] H. Zhang, C. Smanmoo, T. Kabashima, J. Lu, M. Kai, Angew. Chem. Int. Ed. Engl. 46 (2007) 8226.
[11] T. Satoh, K. Nishiyama, M. Nagahata, A. Teramoto, K. Abe, Polym. Adv. Technol. 15 (2004) 720.

Talanta 79 (2009) 836–844

Contents lists available at ScienceDirect

Talanta

journal homepage: www.elsevier.com/locate/talanta

Metabonomics study of atherosclerosis rats by ultra fast liquid chromatography coupled with ion trap-time of flight mass spectrometry

Fengxia Zhang[a,b,1], Zhenhua Jia[c,1], Peng Gao[b], Hongwei Kong[b], Xiang Li[b], Jing Chen[b], Qin Yang[b], Peiyuan Yin[b], Jiangshan Wang[b], Xin Lu[b], Famei Li[a], Yiling Wu[c,*], Guowang Xu[a,b,**]

[a] Department of Analytical Chemistry, School of Pharmacy, Shenyang Pharmaceutical University, Shenyang 110016, China
[b] CAS Key laboratory of Separation Science for Analytical Chemistry, Dalian Institute of Chemical Physics, Chinese Academy of Sciences, Dalian 116023, China
[c] The Integration of Traditional and Western Medical Research Academy of Hebei Province, Shijiazhuang 050035, China

ARTICLE INFO

Article history:
Received 16 November 2008
Received in revised form 8 May 2009
Accepted 8 May 2009
Available online 19 May 2009

Keywords:
Atherosclerosis
Metabonomics
UFLC/MS-IT-TOF
Plasma
Urine
Rats

ABSTRACT

An ultra fast liquid chromatography coupled with IT-TOF mass spectrometry (UFLC/MS-IT-TOF) metabonomic approach was employed to study the plasma and urine metabolic profiling of atherosclerosis rats. Acquired data were subjected to principal component analysis (PCA) for differentiating the atherosclerosis and the control groups. Potential biomarkers were screened by using S-plot and were identified by the accurate mass and MS^n fragments information obtained from UFLC/MS-IT-TOF analysis. 12 metabolites in rat plasma and 8 metabolites in urine were identified as potential biomarkers. Concentrations of leucine, phenylalanine, tryptophan, acetylcarnitine, butyrylcarnitine, propionylcarnitine and spermine in plasma and 3-O-methyl-dopa, ethyl N2-acetyl-L-argininate, leucylproline, glucuronate, t6A N(6)-(N-threonylcarbonyl)-adenosine and methyl-hippuric acid in urine decreased in atherosclerosis rats. Ursodeoxycholic acid, chenodeoxycholic acid, LPC (C16:0), LPC (C18:0) and LPC (C18:1) in plasma and hippuric acid in urine were in higher levels in atherosclerosis rats. The alterated metabolites demonstrated abnormal metabolism of phenylalanine, tryptophan, bile acids and amino acids. This research proved that metabonomics is a promising tool for disease research.

1. Introduction

Atherosclerosis, a kind of diet-related metabolic disorder, is a multifactorial disease. It is characterized by the injury to vessel wall caused by lipid accumulation, chronic inflammation, cell death, and thrombosis, which usually results in heart disease and stroke [1]. Heart events are a leading cause of morbidity and mortality in industrialized countries [2,3]. It was reported that atherosclerosis is associated with increased oxidative stress [4–7]. High fat diet, as one of the risk factors, increases oxidative stress in rats and humans [5,8]. Fardet et al. found that hyperlipidic diets led to a significant increase of oxidative stress in liver and aorta of rats [9]. Kleemann et al. reported that high cholesterol diets not only adjusted metabolic and transport processes but also induced pro-inflammatory gene expression in ApoE*3 Leiden transgenic mice, and found some new regulators that control both lipid metabolism and inflammation [10]. Metabonomics, as an important platform of systems biology, has been defined as "the quantitative measurement of the dynamic multiparametric metabolic response of living organism to pathophysiological stimulation or genetic modification" [11,12]. It has been extensively applied to many fields, such as understanding the biochemical basis of diseases, drug toxicity and the diagnosis and treatment of diseases according to the global metabolic profiles in biological fluids (serum, plasma, urine) and tissues combined with multivariate analysis [13–22]. High-field proton nuclear magnetic resonance (NMR) spectroscopy has been widely applied for its nondestructive advantages of direct analysis of biological samples with simple or no sample preparation procedures [23–27]. In recent years, mass spectrometry (MS)-based techniques have been frequently used in metabonomics research. High-performance liquid chromatography (HPLC) coupled with MS is a powerful tool for the metabolic profiles of biological samples [14,17,20–22,28–32]. Metabonomics approaches have been used for observing the subtle metabolic changes under some disease or specific diet conditions and provided informative data for elucidating biochemical basis of diseases [14,9,33–35].

Ultra fast liquid chromatography coupled with IT-TOF mass spectrometry (UFLC/MS-IT-TOF) has an ability to gain high throughput metabolic profiling of biological samples due to the LC system

* Corresponding author at: The Integration of Traditional and Western Medical Research Academy of Hebei Province, No. 238 Tianshan Street, Hi-tech Development Zone of Shijiazhuang, Hebei Province, Shijiazhuang 050035, China.
** Corresponding author at: CAS Key laboratory of Separation Science for Analytical Chemistry, Dalian Institute of Chemical Physics, Chinese Academy of Sciences, 457 Zhongshan Road, Dalian 116023, China. Fax: +86 411 84379559.
E-mail address: xugw@dicp.ac.cn (G. Xu).
[1] The two authors contributed equally to this work.

0039-9140/$ – see front matter © 2009 Elsevier B.V. All rights reserved.
doi:10.1016/j.talanta.2009.05.010

using a column with stationary phase of 2.2 μm particles. Because the separation efficiency is improved compared to traditional LC systems, UFLC/MS-IT-TOF, to a great potential, facilitates the following identification of metabolites by accurate mass and MS^n analysis (n = 1–10) [36]. In this article, atherosclerosis model rats were established by treating the male Wistar rats with high fat diets [9,10,37–40]. Corresponding plasma and urine samples were collected from the disease and control rats for the metabonomic analysis by using UFLC/MS-IT-TOF. Principal component analysis (PCA) was performed for investigating the metabolic changes of atherosclerosis, and the potential biomarkers were identified accordingly.

2. Materials and methods

2.1. Chemicals

Acetonitrile of HPLC grade was purchased from Tedia (OH. USA), and formic acid of HPLC grade was obtained from Sigma–Aldrich (St. Louis, MO, USA). Distilled water was purified using a Milli-Q system (Millipore, Bedford, MA, USA). Cholesterol was purchased from Dingguo Biotechnology Company (Beijing, China) and sodium cholate was supplied by AoBo Star Biotechnology Company (Beijing, China). Propylthiouracil was obtained from Fosun Pharmaceutical Zhaohui Biotechnology Company (Shanghai, China) and vitamin D_3 was purchased from BASF Vitamin Limited Company. Methionine was obtained from Sigma–Aldrich and serum homocysteine detection kit was supplied by Jiuqiang Biotechnology Company (Beijing, China).

2.2. Animals and sample collection

Eighteen male Wistar rats weighing 180–200 g were freely accessible to common food and water in the first week. After that they were separated randomly into two groups (n = 9/group). The case group was first administrated with vitamin D_3 with a total amount of 700 000 unit/kg for 3 days. Then, the rats were fed with methionine for two weeks. At the beginning of the third week, high fat diets and methionine were supplied simultaneously for these rats. The high fat diets consist of 4% cholesterol (weight/weight, w/w), 1% sodium cholate, 0.5% propylthiouracil, 10% lards (w/w) and 84.5% basic diet (w/w). The control rats were fed with the common diet during the whole experimental period. Rats were firstly reared 5 per cage during the model development period, and then transferred into metabolic cages (1 per cage) for collecting the 24 h urine samples. When urine samples were collected, rats were only freely accessible to water. All the samples were stored at −80 °C. Rats were anesthetized with 10% chloral hydrate, and blood samples containing EDTA anticoagulant were obtained by carotid artery cannula. Blood was centrifuged at 3000 rpm for 10 min and the supernatant was collected and stored at −80 °C before analysis.

2.3. Sample preparation

Prior to analysis, the plasma samples were thawed at room temperature. Acetonitrile (800 μL) was added to plasma (200 μL) and vortex-mixed vigorously for 30 s. The mixture was settled at 4 °C for 10 min, and then centrifuged at 15 000 × g for 10 min at 4 °C. The supernatant (900 μL) was pipetted out and lyophilized.

All urine samples were thawed totally, and then centrifuged at 13 000 × g for 10 min to remove solid materials. Every 100 μL supernatant was taken for each sample, diluted with 300 μL of distilled water and vortex-mixed for 30 s. The solution was then filtered through a 0.22 μm nylon filter film to eliminate particulate matter.

2.4. Chromatographic separation

The LC system employed was an ultra fast liquid chromatography (UFLC) system (Shimadzu, Kyoto, Japan) equipped with a tunable UV detector (set at 254 nm) for the plasma analysis. The column was a 50 mm × 2.0 mm (2.2 μm) Shimpack XR ODS column (Shimadzu, Kyoto, Japan). The mobile phases were water with 0.1% formic acid (phase A) and acetonitrile with 0.1% formic acid (phase B). A linear gradient elution of 2–98% B was applied from 0 to 35 min at a total flow rate of 0.3 mL/min. The column temperature was maintained at 35 °C. The lyophilized plasma samples were dissolved in 180 μL of distilled water/acetonitrile (1:4). Every 4 μL sample solution was injected for each run.

Urine samples were analyzed with the same LC systems with 10 μL injection volume using the columns mentioned above. Sample glass vials were maintained at 4 °C. The column temperature was set at 35 °C. The column was eluted under gradient conditions at a total flow rate of 0.3 mL/min. The mobile phase A consisted of 0.1% aqueous formic acid, and phase B was acetonitrile. The mobile phase was linearly increased from 2% to 35% B over 25 min, and then increased to 98% B over the next 2 min. After that, phase B returned to 2% in 0.1 min, and then the column was equilibrated with 2% phase B for another 7 min until the next run.

2.5. Mass spectrometry

ESI-IT-TOFMS was performed on a novel hybrid ion-trap time-of-flight mass spectrometer (Shimadzu, Kyoto, Japan) equipped with an ESI source in positive ion mode. Interface voltage was 4.5 kV for positive mode and −3.5 kV for negative mode. The flow rate of the nebulizing gas was 1.5 L/min, and the drying gas (N_2) pressure was 0.2 MPa. Curved Desorption Line (CDL) and heat block temperature were both 200 °C. Detector voltage of the TOF analyzer was 1.60 kV. Ultra-high purity argon was used as the collision gas and ion cooling gas. The flight tube temperature was 40 °C, ion trap pressure was 1.6×10^{-2} Pa and ion accumulated time was 20 ms. The scan range was from 100 to 1000 m/z. Data were collected for 35 min (25 min for urine samples) using LCMS solution software (Shimadzu, Kyoto, Japan).

2.6. Data analysis

The raw data were processed by the Phenomenome Profiler M Series version 2.5 (AM+, Canada). Briefly, the raw data were converted to the Profiler data format, and then were subjected to peak picking. The peak picking parameters were as follows: data smooth option was of smoothing points 3 with times of smoothing of 2 for each scan. The noise calculation was supported by the cutoff of 0.1% base peak. That is to say, if the peak intensity is less than one-thousandth of the base peak, the peak will not be picked. Picked peaks were aligned using Profiler's clustering algorithm according to the retention time (t_r) and m/z of each ion. Subsequently, a matrix for multivariate data analyses was generated by the software using a mass clustering window of 0.005 Da and the retention time clustering window of 0.2 min. In the matrix, the retention time, m/z and respective ion intensities were included. If certain ion intensity was less than the noise value in corresponding sample, zero was assigned to it. The individual ion fragment intensity was normalized to the sum of all the peak intensities in the relative chromatogram. These data were handled according to the "80% rule" [18,41,42], only the variables with values above zero presenting in at least 80% of each group were kept for the following analysis. The normalized data were processed by PCA utilizing SIMCA-P 11.0 (Umetrics AB, Umeå, Sweden) after pareto-scaled procedure, which can reduce the influence of noise and artifacts on the model established [43].

Table 1
Determination of the total cholesterol, low-density lipoprotein and homocysteine in the plasma of atherosclerosis and control rats.

	Control group	Atherosclerosis group
Total cholesterol (mmol/L)	1.40 ± 0.35	4.29 ± 0.82*
Low-density lipoprotein (mmol/L)	0.23 ± 0.07	0.74 ± 0.12*
Homocysteine (μmol/L)	9.90 ± 0.61	14.32 ± 2.66*

* $P < 0.01$ (compared with control group).

3. Results and discussion

3.1. Pathological characteristics of atherosclerosis rats

Table 1 shows that plasma total cholesterol, low-density lipoprotein and homocysteine concentrations significantly increased ($P < 0.01$) in atherosclerosis rats. The results of hematoxylin–eosin (HE) staining and Masson staining (Fig. 1A and B, respectively) were characterized by partial loss of endothelial cells, thickness of endomembrane, hyperplasy and disordered arrangement of vascular smooth muscle cells (VSMCs), proliferation of collagen fiber, local tubal wall's entering the lumina and hyperplasy of fiber in aortas of atherosclerosis rats. All those results showed that the rat models exhibited the typical pathological features of earlier period of atherosclerosis.

3.2. Metabonomic analysis based on the urine and plasma metabolic profiling

Metabonomic study based on the UFLC/MS-IT-TOF analysis was applied to understand the metabolic profiling of atherosclerosis and to identify the potential biomarkers revealing the occurrence of the disease.

3.2.1. Urine and plasma metabolic profiling analysis in atherosclerosis rats

Rat plasma and urine metabolites were profiled by UFLC/MS-IT-TOF. Fig. 2 shows the typical base peak chromatograms (BPCs) of the plasma and urine from the atherosclerosis and control rats, respectively. The distinct plasma and urine metabolic profiles implied that metabolic changes had taken place in the rats suffering from atherosclerosis.

Because sample analysis would last for several days, the retention time shift, the m/z accuracy deviation and other drifts of the instrument stability were unavoidable. Metabonomics asks for method robustness, so standard samples were analyzed for determining inter-day and intra-day precision of the analysis. The relative standard deviations of retention times, m/z and ion fragment peak areas were calculated (Table 2). For intra-day precision, the relative standard deviations of retention times and ion peak areas were from 0.044% to 1.2% and from 0.77% to 2.9%, respectively; those of m/z were from 2.12E-05% to 9.97E-05%. For inter-day precision in 3 days, the relative standard deviations of retention times and ion peak areas were from 0.071% to 1.3% and from 1.1% to 9.1%, respectively; those of m/z were from 1.17E-05% to 8.27E-05%. The results indicated that the method showed good repeatability for plasma and urine analysis.

After peak alignment, about 2300 peaks of ions (ESI^+ mode) in rat plasma and about 3000 peaks of ions (ESI^+ mode) in rat urine were extracted by Phenomenome Profiler M applying the method mentioned above. After normalization, the plasma and urine data were imported to SIMCA-P, respectively.

PCA, partial least-squares to latent structures discriminant analysis (PLS-DA), and orthogonal partial least-squares to latent structures (OPLS) are the efficient and robust methods for gaining the model of information-abundant biological data [17,18,43,44]. PCA is an unsupervised multivariate data analysis method and it gives the comprehensive view of the clustering trend for the multidimensional data. In order to gain an overview of the rat urine and plasma metabolic profiling, here, PCA was used in the subsequent UFLC/MS-IT-TOF data analysis. The parameter R^2X showed that the established model was capable of differentiating the atherosclerosis rats from controls according to either plasma or urine profiling data. Fig. 3A and C shows the PCA score plot of the atherosclerosis rats and controls based on the plasma and urine metabolic profiles, respectively. In the plasma PCA score plot, the atherosclerosis and control groups were separated clearly. The three components explained 65.2% of the total variances. A good separation was also seen between the atherosclerosis rats and the controls in the PCA score plot of urinary metabolites by the first two components, which explained 59.3% of all variances. The results from the unsupervised analysis of PCA showed the significant metabolic changes occurring in the atherosclerosis rats.

3.2.2. Identification of potential biomarkers

There are many methods for biomarker discovery in metabonomics, for example, from the loading plot in the PCA model. The combination of loading plot and the corresponding loading plot

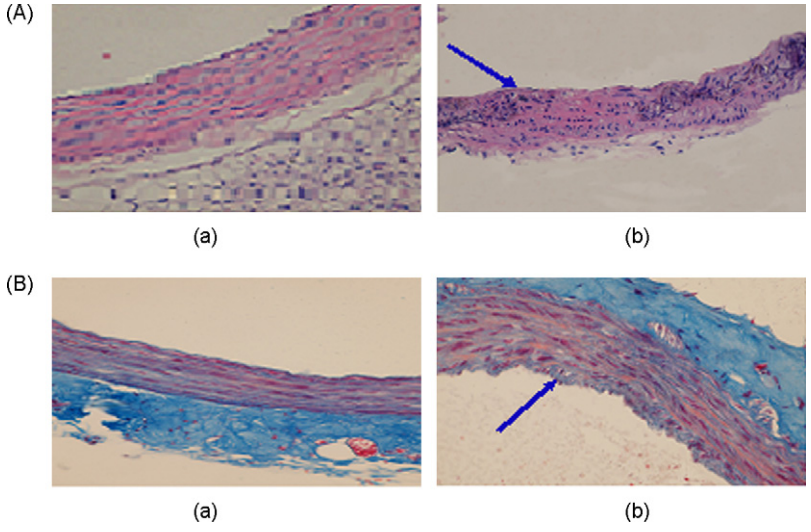

Fig. 1. HE staining (A) and Masson staining (B) of aortas in control and atherosclerosis rats (400×). Arrows highlight the lesions sites. (a) Control and (b) atherosclerosis.

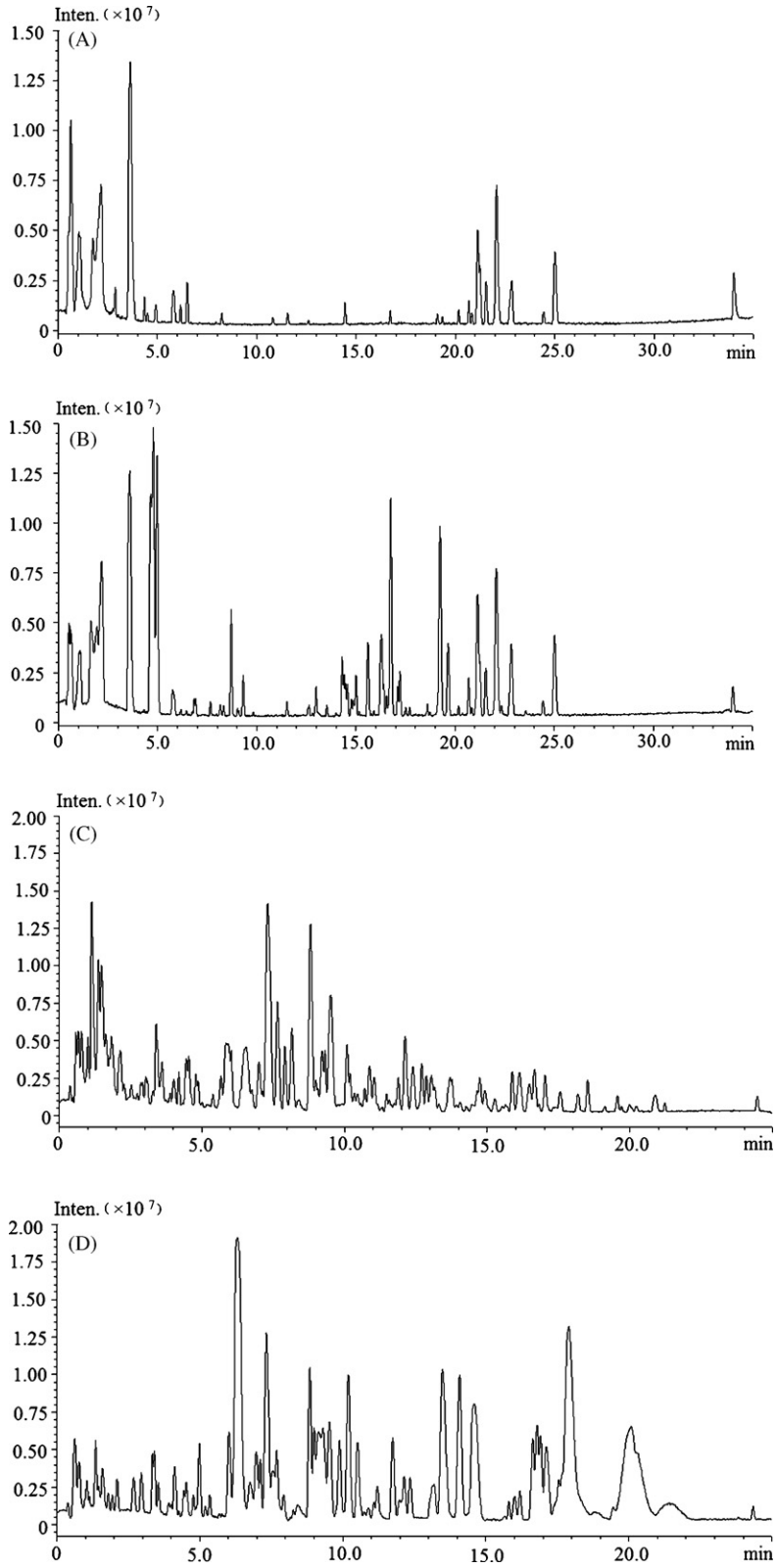

Fig. 2. Typical base peak chromatograms (BPC) obtained from plasma and urine in atherosclerosis rats and controls (ESI^+mode). (A) Plasma of the control rats; (B) plasma of the atherosclerosis rats; (C) urine of the control rats; (D) urine of the atherosclerosis rats.

with jack-knifed confidence intervals to exclude some metabolites with great confidence intervals is another method for the biomarker discovery. The potential biomarkers can also be selected from the variable importance for projection (VIP) plot which concludes the contribution of an ion for the model (e.g. PLS-DA, OPLS and PLS and so on) [18,43]. S-plot is a tool for visualization and interpretation of multivariate classification models. It images both the covariance and correlation between the metabolites and the modeled class

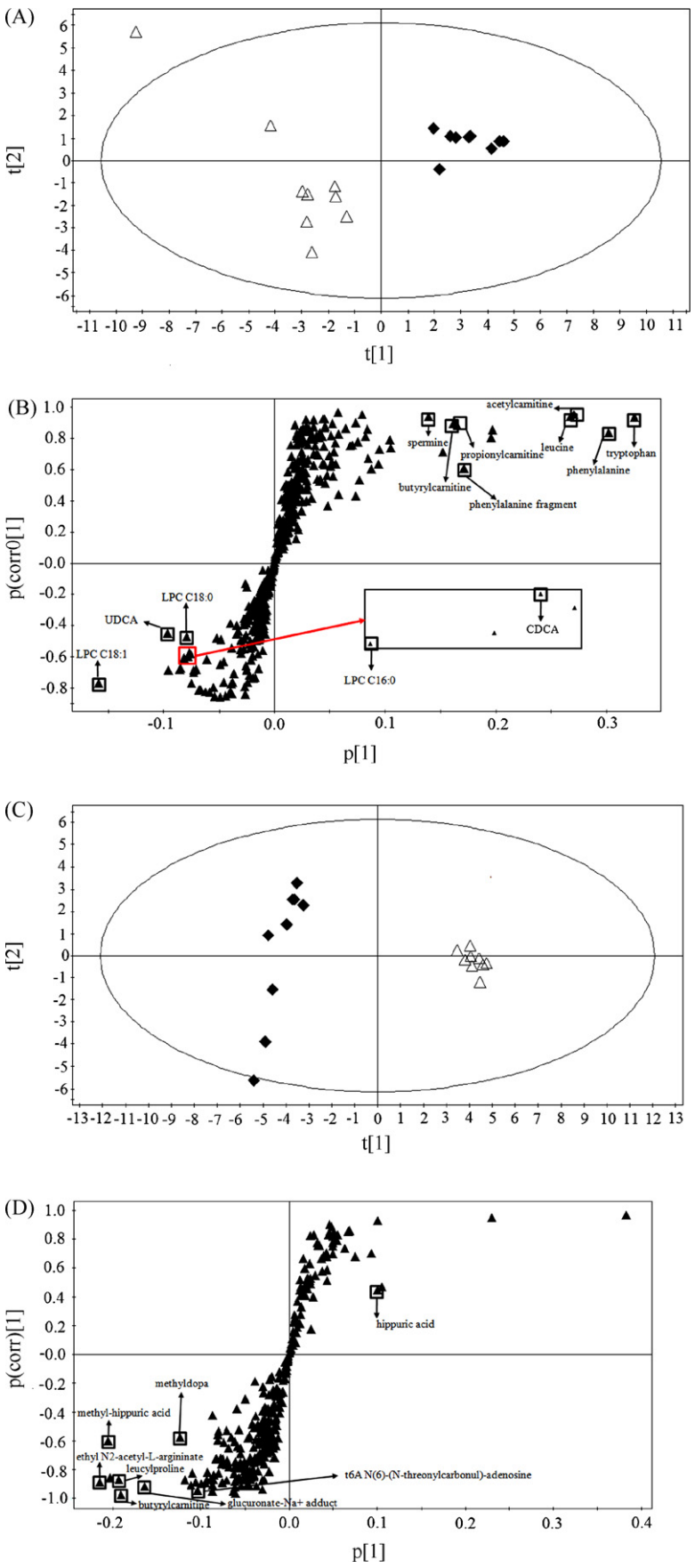

Fig. 3. (A) PCA score plot based on the plasma metabolic profiling of the atherosclerosis (Δ) and control (♦) rats; (B) S-plot based on plasma profiling; (C) PCA score plot based on the urinary metabolic profiling of the atherosclerosis (Δ) and control (♦) rats; (D) S-plot based on urine profiling. The potential biomarkers validated by authentic standards and literatures in the S-plot figures are marked with square.

Table 2
Intra-day and inter-day precisions of the analytical method.

Name	Intra-day precision (n = 8)			Inter-day precision (n = 12 in 3 days)		
	t_r (RSD, %)	m/z (RSD, %)	Area (RSD, %)	t_r (RSD, %)	m/z (RSD, %)	Area (RSD, %)
Phenylalanine	1.2	3.12E-05	2.7	1.3	5.64E-05	2.2
Tryptophan	0.51	5.68E-05	1.7	0.41	1.07E-04	8.5
Hippuric acid	0.14	2.97E-05	1.6	0.45	3.99E-05	5.4
GUDCA	0.052	9.97E-05	2.9	0.23	1.17E-04	7.3
GCA	0.072	2.67E-05	0.77	0.27	5.65E-05	1.8
CA	0.31	6.68E-05	2.1	0.27	8.27E-05	2.8
UDCA	0.043	3.66E-05	2.4	0.078	6.18E-05	9.1
GCDCA	0.14	5.57E-05	1.2	0.30	7.11E-05	1.1
CDCA	0.044	2.12E-05	1.9	0.071	7.40E-05	5.4
DCA	0.063	4.95E-05	1.8	0.075	6.86E-05	3.8

GUDCA: glycoursodeoxycholic acid; GCA: glycocholic acid; CA: cholic acid; UDCA: ursodeoxycholic acid; GCDCA: glycochenodeoxycholic acid; CDCA: chenodeoxycholic acid; DCA: deoxycholic acid.

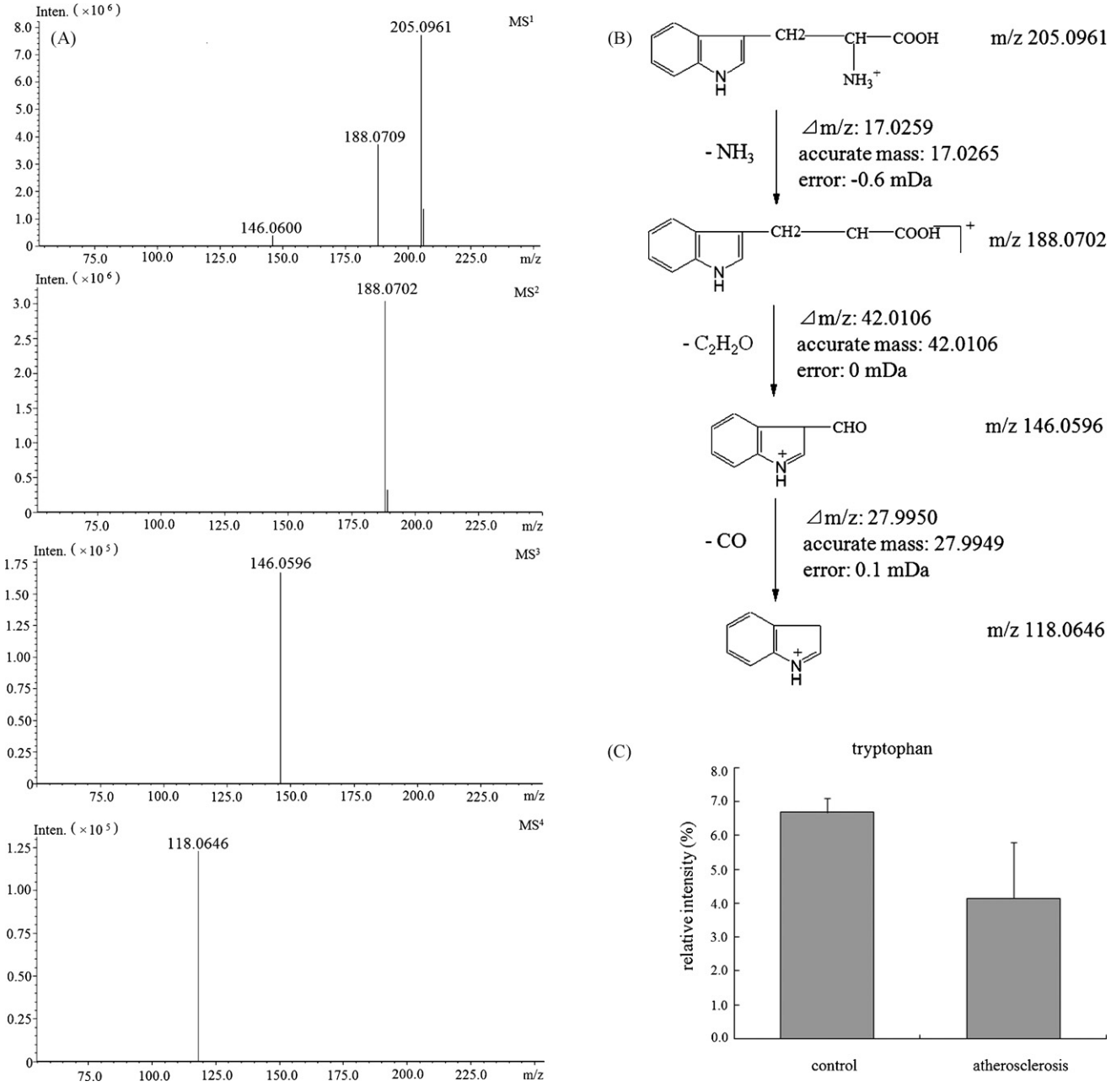

Fig. 4. (A) MS^1 to MS^4 spectra of the metabolite ion with m/z 205.0961 in the S-plot shown in Fig. 3B, the metabolite is identified as tryptophan; (B) putative fragmentation scheme of the theoretical fragmentation patterns of tryptophan in the ESI^+ mode; (C) comparison of tryptophan in the plasma in the control and atherosclerosis rats.

Table 3
Potential biomarkers selected showing difference between the atherosclerosis and control rats based on plasma metabolic profiling (ESI^+ mode).

Peak no.	m/z	t_r (min)	Identification result	Levels in atherosclerosis
1	204.0970	0.63	Acetylcarnitine[a]	↓
2	203.0520	0.70	Spermine[a]	↓
3	132.1028	1.1	Leucine[b]	↓
4	218.1389	1.2	Propionylcarnitine[a]	↓
5	294.1555	1.9	UN	↓
6	120.0820	2.2	Phenylalanine fragment[b]	↓
7	166.0867	2.2	Phenylalanine[b]	↓
8	232.1541	2.8	Butyrylcarnitine[a]	↓
9	205.0981	3.6	Tryptophan[b]	↓
10	346.9474	5.8	UN	↓
11	251.1025	6.5	UN	↓
12	357.2807	16.7	UDCA fragment[b]	↑
13	357.2800	19.6	CDCA fragment[b]	↑
14	496.3425	21.6	LPC C16:0[a]	↑
15	522.3591	22.8	LPC C18:1[a]	↑
16	524.3747	25.0	LPC C18:0[a]	↑

[a] Identified by the accurate mass and observed MS^n fragments which were acquired from UFLC/MS-IT-TOF analysis and literatures.
[b] Identified based on retention time and MS^n spectrum of an authentic standard. UN: unknown. LPC: lysophosphatidylcholines. The levels of potential biomarkers in atherosclerosis rats compared with controls were labeled with (↓) down-regulated and (↑) up-regulated.

designation for identification of statistically significant and biochemically interesting metabolites which can avert the increase of false positives (type I error) [43]. Fig. 3B and D shows the S-plots based on plasma and urine metabolic profiling data. The significant metabolites related to the group separation were selected as potential biomarkers from the S-plots. These plasma and urine metabolites had high correlations with atherosclerosis. They were of importance for classification.

Let us take m/z 205.0981 as an example to show the procedure of the biomarker identification. Firstly, the accurate mass of the ion was obtained from UFLC/MS-IT-TOF spectrum both in ESI^+ and ESI^- modes (data were not shown). $[M+H]^+$ ion and $[M-H]^-$ ion were found, therefore, we obtained the molecular weight (MW) of the metabolite ion after comparing the $[M+H]^+$ ion and $[M-H]^-$ ion. Secondly, we applied the Formula Predictor to predict the formula of the ion (applying the nitrogen rule). It gave three candidates. The first one had a high score, and the formula was $C_{11}H_{12}N_2O_2$. We also searched the online database, for example, METLIN database (http://metlin.scripps.edu) and human metabolite database (http://hmdb.ca) to identify the biomarkers by using accurate mass and MS^n information. The ion of m/z 205.0981 was searched by comparing the extract mass with those enrolled in the METLIN database. There were two candidate compounds for the m/z 205.0981 (mass difference lower than 5 mDa). One was tryptophan and the other was a kind of drug (it is excluded owing to exogenous substance). Subsequently, the MS^n analysis of m/z 205.0981 in plasma and standard tryptophan were performed by using UFLC/MS-IT-TOF in the same chromatographic and mass spectrometry conditions. The MS^1 to MS^4 spectra of m/z 205.0981 are shown in Fig. 4A. The retention time and MS^1 to MS^4 spectra of m/z 205.0981 were the same as those of tryptophan (the MS^1 to MS^4 spectra of tryptophan standard were not shown), therefore, the m/z 205.0981 was identified as tryptophan. A putative fragmentation scheme of the theoretical fragmentation pattern of tryptophan is shown in Fig. 4B. Fig. 4C presents the change of tryptophan in plasma of different rats. Compared to the control group, tryptophan concentration was down-regulated in plasma of atherosclerosis rats. The other biomarkers were identified with the same strategy as used for tryptophan when commercial standards were available. Some metabolites were identified by using MS^n analysis and/or comparing the extract mass and MS^n fragments as described in the literature [14,18,22,35,45–47] when standard was not available. Tables 3 and 4 display the identification results of potential biomarkers showing concentration difference between the atherosclerosis and control rats based on plasma and urine metabolic profiling (ESI^+ mode). 16 endogenous metabolites in plasma and 15 endogenous metabolites in urine were selected as potential biomarkers, and 12 metabolites in plasma and 8 endoge-

Table 4
Potential biomarkers of the atherosclerosis rats based on urine metabolic profiling (ESI^+ mode).

Peak no.	m/z	t_r (min)	Identification result	Levels in atherosclerosis
1	212.1027	0.76	3-O-methyl-dopa[a]	↓
2	158.1174	0.78	UN	↑
3	245.1568	1.0	Ethyl N2-acetyl-L-arginate[a]	↓
4	233.1121	1.0	UN	↓
5	229.1529	1.3	Leucylproline[a]	↓
6	153.0661	1.5	N-methyl-2-pyridone-5-carboxamide[b]	↓
7	217.1173	1.6	Glucuronate–Na^+ adduct[a]	↓
8	232.1273	1.9	Butyrylcarnitine[a]	↓
9	180.0676	6.0	Hippuric acid[c]	↑
10	172.0974	7.1	(3-Methylcrotonyl)glycine methyl ester[b]	↓
11	413.1416	7.2	t6A N(6)-(N-threonylcarbonyl)-adenosine[a]	↓
12	194.0814	7.4	Methyl-hippuric acid[a]	↓
13	276.1264	7.9	UN	↓
14	300.1000	10.2	UN	↑
15	255.0644	16.7	UN	↑

[a] Identified by the accurate mass and observed MS^n fragments which were acquired from UFLC/MS-IT-TOF analysis and literatures.
[b] Identified in the METLIN database, but have not been confirmed with standard. UN: unknown. The levels of potential biomarkers in atherosclerosis rats compared with controls were labeled with (↓) down-regulated and (↑) up-regulated.
[c] Identified based on retention time and MS^n spectrum of an authentic standard.

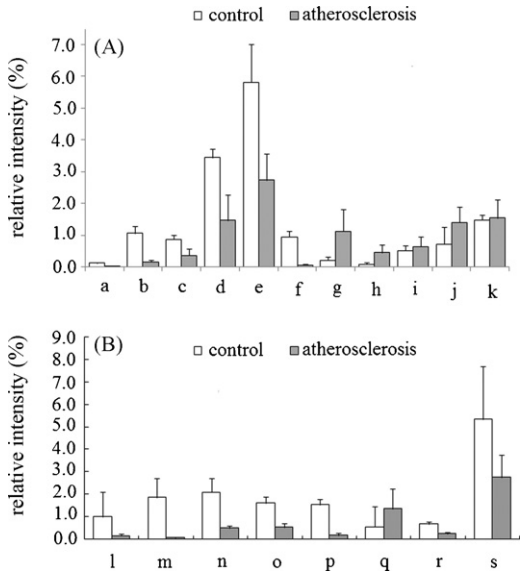

Fig. 5. Comparison of the relative intensity of putative potential biomarkers in the plasma (A) and urine (B) in the control and atherosclerosis rats. Identification—a: acetylcarnitine, b: propionylcarnitine, c: spermine, d: leucine, e: phenylalanine, f: butyrylcarnitine, g: UDCA, h: CDCA, I: LPC C16:0, j: LPC C18:1, k: LPC C18:0, l: 3-O-methyl-dopa, m: ethyl N2-acetyl-L-argininate, n: leucylproline, o: glucuronate–Na+ adduct, p: butyrylcarnitine, q: hippuric acid, r: t6A N(6)-(N-threonylcarbonyl)-adenosine, s: methyl-hippuric acid.

nous metabolites in urine were verified by authentic standards and literatures.

3.2.3. Study of metabolic changes in atherosclerosis rats

To investigate the change of the potential biomarkers in the body fluids of atherosclerosis rats, we compared the relative intensity of putative potential biomarkers in plasma (Fig. 5A) and urine (Fig. 5B) in the control and atherosclerosis rats. The results showed that butyrylcarnitine decreased both in plasma and in urine in atherosclerosis rats. In the plasma of atherosclerosis rats, concentrations of leucine, phenylalanine, tryptophan, acetylcarnitine, propionylcarnitine and spermine were all down-regulated, but ursodeoxycholic acid (UDCA), chenodeoxycholic acid (CDCA), LPC C16:0, LPC C18:0 and LPC C18:1 were up-regulated. 3-O-methyl-dopa, ethyl N2-acetyl-L-argininate, leucylproline, glucuronate–Na+ adduct, t6A N(6)-(N-threonylcarbonyl)-adenosine and methyl-hippuric acid had a decrease in the urine of atherosclerosis rats. Hippuric acid increased in the urine of rats compared with the control group.

These metabolites mentioned above might play important roles in the metabolic changes of atherosclerosis. UDCA and CDCA are two bile acids, are principally synthesized in the liver from cholesterol, they play a key role in dietary lipid absorption and cholesterol homeostasis [48,49]. The concentration increase of UDCA and CDCA in plasma of atherosclerosis rats disturbed energy homeostasis and glucose metabolism, inhibited cholesterol metabolism [48].

Lysophosphatidylcholine (LPC) plays a significant role in the process of inflammation, cell proliferation and tumor cell invasiveness [50,51]. According to our research, LPC was up-regulated in atherosclerosis rats. The result was consistent with the report in the literature [52]. Inflammation was a key part in the pathogenesis of atherosclerosis, and lipoprotein-associated phospholipase A2 (Lp-PLA2, one of the active production is LPC) has been recognized as a novel marker that takes part in the vascular inflammation. Enhanced expression of Lp-PLA2 and increasing of LPC were observed in symptomatic carotid atherosclerotic plaques in humans [52–54], LPC plays key roles in the progress of atherosclerosis and inflammatory diseases [55].

Phenylalanine and tryptophan are two essential amino acids which cannot be synthesized in vivo and can be obtained only from the daily foods, they are the precursors of tyrosine and serotonin, respectively. Based on our study, homocysteine increased remarkably, and phenylalanine, tryptophan and leucine were all down-regulated prominently in atherosclerosis rats.

There are still some biomarkers not identified, and the specific relationship between biomarkers and the occurrence of atherosclerosis remains to be investigated by advanced methods and combinations with other data (proteomics, transcriptomics and genomics) in the future.

4. Conclusions

In this study, a sensitive and precise metabonomic method, based on UFLC/MS-IT-TOF, was applied to investigate the metabolic changes of atherosclerosis. 20 endogenous metabolites were identified in plasma and urine of atherosclerosis rats by using metabonomic method combined with multivariate data analysis. The results showed abnormal metabolism of bile acids, LPCs, amino acids in atherosclerosis rats. This research also demonstrated that UFLC/MS-IT-TOF-based metabonomic approach was a promising tool to find and identify potential biomarkers. If it can be combined with genomics, transcriptomics and proteomics study, metabonomics will give a better and further understanding of biochemical essence of diseases.

Acknowledgements

This study has been supported by the National Basic Research Program of China (Nos. 2005CB523301 and 2006CB503902), ICST (No. 2006DFB32460) and National Key Project of Scientific and Technical Supporting Programs (No. 2006BAK02A12) from State Ministry of Science & Technology of China, the National Natural Science Foundation of China (Nos. 20675082 and 90709004), and the Knowledge Innovation Program of the Chinese Academy of Sciences (K2006A12–K2006A14).

References

[1] E. Braunwald, N. Engl. J. Med. 337 (1997) 1360–1369.
[2] A.J. Lusis, Nature 407 (2000) 233–241.
[3] C.J. Murray, A.D. Lopez, Lancet 349 (1997) 1436–1442.
[4] F. Bonomini, S. Tengattini, A. Fabiano, R. Bianchi, Histol. Histopathol. 23 (2008) 381–390.
[5] W. Tsai, Y. Li, C. Lin, T. Chao, J. Chen, Clin. Sci. 106 (2004) 315–319.
[6] R.W. Alexander, Trans. Am. Clin. Climatol. Assoc. 109 (1998) 129–145.
[7] R. Olinski, D. Gackowski, M. Foksinski, R. Rozalski, K. Roszkowski, P. Jaruga, Free Radic. Biol. Med. 33 (2002) 192–200.
[8] H. Gaenzer, W. Sturm, G. Neumayr, R. Kirchmair, C. Ebenbichler, A. Ritsch, B. Föger, G. Weiss, J.R. Patsch, Cardiovasc. Res. 52 (2001) 509–516.
[9] A. Fardet, R. Llorach, J.F. Martin, C. Besson, B. Lyan, E.P. Guillot, A. Scalbert, J. Proteome Res. 7 (2008) 2388–2398.
[10] R. Kleemann, L. Verschuren, M.J. van Erk, Y. Nikolsky, N.H.P. Cnubben, E.R. Verheij, A.K. Smilde, H.F.J. Hendriks, S. Zadelaar, G.J. Smith, V. Kaznacheev, T. Nikolskaya, A. Melnikov, E. Hurtcamejo, J. van der Greef, B. van Ommen, T. Kooistra, Genome Biol. 8 (2007) R200.
[11] J.K. Nicholson, J.C. Lindon, E. Holmes, Xenobiotica 29 (1999) 1181–1189.
[12] J. van der Greef, P. Stroobant, R. Van der Heiden, Curr. Opin. Chem. Biol. 8 (2004) 559–565.
[13] D.R. Ekman, H.C. Keun, C.D. Eads, C.M. Furnish, J.C. Rockett, D.J. Dix, Metabolomics 2 (2006) 63–73.
[14] P. Yin, P. Mohemaiti, J. Chen, X. Zhao, X. Lu, A. Yimiti, H. Upur, G. Xu, J. Chromatogr. B (2008) 322–327.
[15] L.K. Schnackenberg, R.D. Beger, Y.P. Dragan, Metabolome Analyses: Strategies for Systems Biology, Springer Perss, New York, 2005, Chapter 10. pp. 159–171.
[16] E. Holmes, O. Cloarec, J.K. Nicholson, J. Proteome Res. 5 (2006) 1313–1320.
[17] M. Kellert, S. Wagner, U. Lutz, W.K. Lutz, Chem. Res. Toxicol. 21 (2008) 761–768.
[18] Y. Wang, J. Wang, M. Yao, X. Zhao, J. Fritsche, P. Schmitt-Kopplin, Z. Cai, D. Wan, X. Lu, S. Yang, J. Gu, H.U. Häring, E.D. Schleicher, R. Lehmann, G. Xu, Anal. Chem. 80 (2008) 4680–4686.

[19] J. Chen, X. Zhao, J. Fritsche, P. Yin, P. Schmitt-Kopplin, W. Wang, X. Lu, H.U. Haring, E.D. Schleicher, R. Lehmann, G. Xu, Anal. Chem. 80 (2008) 1280–1289.
[20] L. Jia, C. Wang, H. Kong, J. Yang, F. Li, G. Xu, J. Pharm. Biomed. Anal. 43 (2007) 646–654.
[21] L. Jia, C. Wang, H. Kong, Z. Cai, G. Xu, Metabolomics 2 (2006) 95–104.
[22] J. Yang, X. Zhao, X. Liu, C. Wang, P. Gao, J. Wang, L. Li, J. Gu, S. Yang, G. Xu, J. Proteome Res. 5 (2006) 554–561.
[23] N.G. Psihogios, I.F. Gazi, M.S. Elisaf, K.I. Seferiadis, E.T. Bairaktari, NMR Biomed. 21 (2008) 195–207.
[24] E.M. Lenz, R.E. Williams, J. Sidaway, J. Pharm. Biomed. Anal. 44 (2007) 845–852.
[25] A.W. Nicholls, J.K. Nicholson, J.N. Haselden, C.J. Waterfield, Biomarkers 5 (2000) 410.
[26] J.K. Nicholson, I.D. Wilson, Nat. Rev. Drug Discov. 2 (2003) 668–676.
[27] N. Jiang, X. Yan, W. Zhou, Q. Zhang, H. Chen, Y. Zhang, X. Zhang, J. Proteome Res. 7 (2007) 3678–3686.
[28] S. Inagaki, T. Noda, J.Z. Min, T. Toyo'oka, J. Chromatogr. A 1176 (2007) 94–99.
[29] L. Jia, J. Chen, P. Yin, X. Lu, G. Xu, Metabolomics 4 (2008) 183–189.
[30] T.B. Murdoch, H. Fu, S. MacFarlane, B.C. Sydora, R.N. Fedorak, C.M. Slupsky, Anal. Chem. 80 (2008) 5524–5531.
[31] R.D. Beger, R.D. Holland, J. Sun, L.K. Schnackenberg, P.C. Moore, C.L. Dent, P. Devarajan, D. Portilla, Pediatr. Nephrol. 23 (2008) 977–984.
[32] S. La, H.H. Yoo, D.H. Kim, Res. Toxicol. 18 (2005) 1887–1896.
[33] A. Scalbert, D. Milenkovic, R. Llorach, C. Manach, C. Leroux, Energy and Protein Metabolism and Nutrition, issue 124, Wageningen Academic Publishers, Netherlands, 2007, pp. 259–276.
[34] M.J. Gibney, M. Walsh, L. Brennan, H.M. Roche, B. German, B. van Ommen, Am. J. Clin. Nutr. 82 (2005) 497–503.
[35] P. Yin, X. Zhao, Q. Li, J. Wang, J. Li, G. Wang, J. Proteome Res. 5 (2005) 2135–2143.
[36] N. Yoshinaga, T. Aboshi, C. Ishikawa, M. Fukui, M. Shimoda, R. Nishida, C.G. Lait, J.H. Tumlinson, N.J. Mori, Chem. Ecol. 33 (2007) 1376–1381.
[37] L. Wang, M. Zhang, Y. Ji, W. Dong, Acta Lab Anim. Sci. Sin. 10 (2002) 113–115.
[38] D. Matthias, C.H. Becker, R. Riezler, P.H. Kindling, Atherosclerosis 122 (1996) 201–216.
[39] J. Buján, J.M. Bellón, C. Sabater, J. Francisca, G.H. Natalio, D. Belén, J. Eduardo, Atherosclerosis 122 (1996) 141–152.
[40] J. Yang, Y. Guo, Z. Wu, S. Hei, Y. Song, T. Hu, Chin. J. Cardiol. Med. 9 (2004) 353–356.
[41] M.P. Hodson, G.J. Dear, A.D. Roberts, C.L. Haylock, R.J. Ball, R.S. Plumb, C.L. Stumpf, J.L. Griffin, J.N. Haselden, Anal. Biochem. 362 (2007) 182–192.
[42] S. Bijlsma, L. Bobeldijk, E.R. Verheij, R. Ramaker, S. Kochhar, I.A. Macdonald, B. van Ommen, A.K. Smilde, Anal. Chem. 78 (2006) 567–574.
[43] S. Wiklund, E. Johansson, L. Sjöström, E.J. Mellerowicz, U. Edlund, J.P. Shockcor, J. Gottfries, T. Moritz, J. Trygg, Anal. Chem. 80 (2008) 115–122.
[44] U. Lutz, R.W. Lutz, K. Lutz, Anal. Chem. 78 (2006) 4564–4571.
[45] D.J. Crockford, J.C. Lindon, O. Cloarec, R.S. Plumb, S.J. Bruce, S. Zirah, P. Rainville, C.L. Stumpf, K. Johnson, E. Holmes, J.K. Nicholson, Anal. Chem. 78 (2006) 4398–4408.
[46] C. Wang, S. Xie, J. Yang, Q. Yang, G. Xu, Anal. Chim. Acta 525 (2004) 1–10.
[47] X. Zhao, W. Wang, J. Wang, J. Yang, G. Xu, J. Sep. Sci. 29 (2006) 2444–2451.
[48] S.M. Houten, M. Watanabe, J. Auwerx, EMBO J. 25 (2006) 1419–1425.
[49] M. Watanabe, S.M. Houten, C. Mataki, M.A. Christoffolete, B.W. Kim, H. Sato, N. Messaddeq, J.W. Harney, O. Ezaki, T. Kodama, K. Schoonjans, A.C. Bianco, J. Auwerx, Nature 439 (2006) 484–489.
[50] K.E. Olofsson, L. Andersson, J. Nilsson, H. Björkbacka, Biochem. Biophys. Res. Commun. 370 (2008) 348–352.
[51] Z. Zhao, Y. Xiao, P. Elson, H. Tan, S.J. Plummer, M. Berk, P.P. Aung, I.C. Lavery, J.P. Achkar, L. Li, G. Casey, Y. Xu, Clin. Oncol. 25 (2007) 2696–2701.
[52] S. Lavi, J.P. McConnell, C.S. Rihal, A. Prasad, V. Mathew, L.O. Lerman, A. Lerman, Circulation 115 (2007) 2715–2721.
[53] N. Aiyar, J. Disa, Z. Ao, H. Ju, S. Nerurkar, R.N. Willette, C.H. Macphee, D.G. Johns, S.A. Douglas, Mol. Cell. Biochem. 295 (2007) 113–120.
[54] D. Mannheim, J. Herrmann, D. Versari, M. Gossl, F.B. Meyer, J.P. McConnell, L.O. Lerman, A. Lerman, Stroke 39 (2008) 1448–1455.
[55] T. Matsumoto, T. Kobayashi, K. Kamata, Curr. Med. Chem. 14 (2007) 3209–3220.

Talanta 79 (2009) 953–958

Contents lists available at ScienceDirect

Talanta

journal homepage: www.elsevier.com/locate/talanta

Mg^{2+}/Na^{+}-doped rutile TiO_2 nanofiber mats for high-speed and anti-fogged humidity sensors

Hongnan Zhang[a], Zhenyu Li[a], Li Liu[b], Ce Wang[a,*], Yen Wei[a,c,**], Alan G. MacDiarmid[a]

[a] The Alan G. MacDiarmid Institute, Jilin University, Changchun, 130012, PR China
[b] College of Physics, Jilin University, Changchun, 130012, PR China
[c] Department of Chemistry, Drexel University, Philadelphia, PA, 19104, USA

ARTICLE INFO

Article history:
Received 19 January 2009
Received in revised form 18 May 2009
Accepted 21 May 2009
Available online 27 May 2009

Keywords:
Electrospinning
Humidity sensor
Rutile TiO_2 nanofibers
High-speed
Anti-fogged

ABSTRACT

Mg^{2+} and Na^{+} doped rutile TiO_2 nanofibers have been prepared through in situ electrospinning technique and calcination with poly(vinyl pyrrolidone) (PVP) nanofibers as sacrificed template. The as-prepared composite nanofibers are spin-coated onto a ceramic substrate with three pairs of carbon interdigital electrodes to measure its humidity sensing behaviors. The product exhibits high-speed response (2 s) and recovery (1 s) for detecting moisture. Additionally, under UV irradiation, a water contact angle (θ) of nearly 0° has been observed based on the product, providing our humidity sensor with the anti-fogged properties.

1. Introduction

The past several decades have witnessed the huge progress on the fabrication of humidity sensors for their practical applications in air-quality control, environmental monitoring, healthcare, defense and security, etc. [1,2]. Recently, taking the advantages of large surface area, high surface to volume ratio, and special physical and chemical properties of one-dimensional (1D) metallic oxide nanostructures, the synthesis of sensitive humidity sensors based on 1D metallic oxide nanostructures is of current interest [3–7]. Hitherto, many sensitive and stable humidity sensors have been reported. For example, Fu and Wang reported the fast humidity sensors based on pure CeO_2 nanowires [3]. Zhang and Wang studied the humidity sensing performances based on Ba-doped CeO_2 nanowires [4]. Mathur and coworkers used the individual tin oxide nanowires to detect the water vapor in different gaseous environments [5]. Wang and co-workers investigated the humidity sensing properties based on a single SnO_2 nanowire [6]. Our group presented the highly sensitive and stable humidity nanosensors based on LiCl doped TiO_2 electrospun nanofibers [7]. Although huge and significant progresses on humidity sensors have been obtained, high-speed humidity sensor with both response time and recovery time less than 2 s, during the whole relative humidity measurement, has still not be obtained yet. Additionally, no papers on anti-fogged and high-speed humidity sensors have been reported.

TiO_2, as an important metallic oxide, has been widely investigated in the fields of environmental cleaning [8] and protection [9], sensors [10], anti-fogged mirror [11], and solar cells [12]. Recently, rutile TiO_2 (1 1 0) has also been proven to be active sites for water dissociation [13]. Those outstanding properties make rutile TiO_2 a good candidate in synthesizing humidity sensors. Mg^{2+} and Na^{+} are often used in humidity sensors to facilitate the ionic conduction during the humidity sensing measurement [14,15]. In this paper, 1D rutile TiO_2 nanofiber, Mg^{2+}, and Na^{+} are combined, for the first time, to form a novel type high-speed and anti-fogged humidity sensor via electrospinning and calcination. The response time and recovery time, during the whole relative humidity (RH: 11–95%), are 2 s and 1 s, respectively. Most importanly, under UV irradiation, a water contact angle (θ) of nearly 0° has been observed based on the product, endowing our humidity sensor with the anti-fogged properties.

2. Experimental

2.1. Chemical

$MgCl_2$ (>95%), tetrabutyl titanate (>95%), ethanol (>95%) and acetic acid (>95%) were of analytical grade and purchased

* Corresponding author. Tel.: +86 431 85618292; fax: +86 431 85198292.
** Corresponding author at: The Alan G. MacDiarmid Institute, Jilin University, Changchun, 130012, PR China. Tel.: +86 431 85618292/+1 215 895 2650; fax: +86 431 85198292/+1 215 895 1265.
E-mail addresses: cwang@jlu.edu.cn (C. Wang), weiyen@drexel.edu (Y. Wei).

0039-9140/$ – see front matter © 2009 Elsevier B.V. All rights reserved.
doi:10.1016/j.talanta.2009.05.035

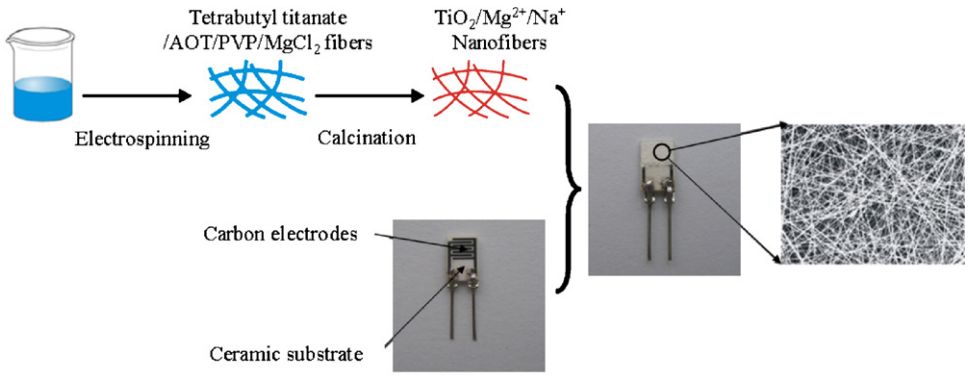

Fig. 1. Schematic diagrams of the steps to fabricate Mg^{2+}/Na^{+}-doped TiO_2 nanofiber mats for humidity measurement via electrospinning and calcination.

from Tianjin Chemical Company. Poly(vinyl pyrrolidone) (Mw: 1,300,000) and dioctyl sulfosuccinate sodium (AOT: $C_{20}H_{37}OSNa$) were purchased from Aldrich.

2.2. The whole procedures for humidity sensor

In a typical procedure, 1.5 g of tetrabutyl titanate was mixed with 3 mL of acetic and 3 mL of ethanol in glovebox under vigorous stirring for 10 min. Subsequently, this solution was added to 7.5 mL of ethanol containing 0.45 g of poly(vinyl pyrrolidone) (PVP), 0.02 g of dioctyl sulfosuccinate sodium (AOT: $C_{20}H_{37}OSNa$) and a suitable amount of $MgCl_2$ under vigorous stirring for 30 min. The mixture was loaded into a glass syringe and connected to high-voltage power supply for electrospinning, 12 kV was provided between the cathode (a flat aluminum foil) and anode (syringe) at a distance of 20 cm. Then, calcination (600 °C in air for 3 h) has been used to remove PVP and to convert both tetrabutyl titanate into rutile TiO_2 nanofibers and AOT into Na^{+} according to previous reported method [16].

Consequently, the as-prepared Mg^{2+}/Na^{+} doped TiO_2 nanofibers were mixed in a weight ratio of 100:5 and were ground with deionized water to form a dilute paste. The paste was screen-printed onto a ceramic substrate (7 mm × 5 mm, 0.5 mm in thick) with three pairs of carbon interdigital electrodes (electrodes width and distance: 0.15 mm) to form a film with the thickness about 10 μm, and then the film was dried at 60 °C in air for 5 h. Finally, the humidity sensor was fabricated after aging at 95% RH with a voltage of 1 V, 100 Hz for 24 h. The characteristic curves of humidity sensitivity were measured on a ZL5 intelligent LCR test meter (Made in Shanghai, China) at room temperature. The voltage applied in our studies was AC 1 V. The controlled humidity environments were achieved using supersaturating aqueous solutions of different salts of LiCl, $MgCl_2$, $Mg(NO_3)_2$, NaCl, KCl and KNO_3 in a closed glass vessel at room temperature, which yielded 11%, 33%, 54%, 75%, 85% and 95% RH, respectively. This method was established by Wang [17,18]. The procedures for the preparation of the new sensors are illustrated in Fig. 1.

2.3. Measurements

The X-ray powder diffraction (XRD) data were collected on an X'Pert MPD Philips diffractometer (Cu Kα X-radiation at 40 kV and 50 mA). Scanning electron microscopy (SEM) images were recorded on a SHIMADZU SSX-550 (Japan) instrument. The humidity measured machine was ZL5 intelligent LCR test meter made in Shanghai China. Water CA was measured with an OCA20 (Dataphysics, Germany) at ambient temperature.

3. Results and discussion

3.1. Materials characterization

Fig. 2a shows the SEM image of the TiO_2 nanofibers containing 5.56 wt.% Mg^{2+} and 0.22 wt.% Na^{+}, indicating a large scale of composite nanofibers with the average diameter of 200 nm can be obtained via our method. In XRD pattern, as shown in Fig. 2b, (1 1 0), (1 0 1), (2 0 0), (1 1 1), (2 1 0), (2 1 1), (2 2 0), (0 0 2), (3 1 0), (3 0 1) and (1 1 2) peaks at 2θ = 27. 35°, 36.0°, 39.15°, 41.2°, 44°, 54.25°, 56.55°, 62.75°, 63.9°, 68.95°, and 69.8° can be clearly detected correspond-

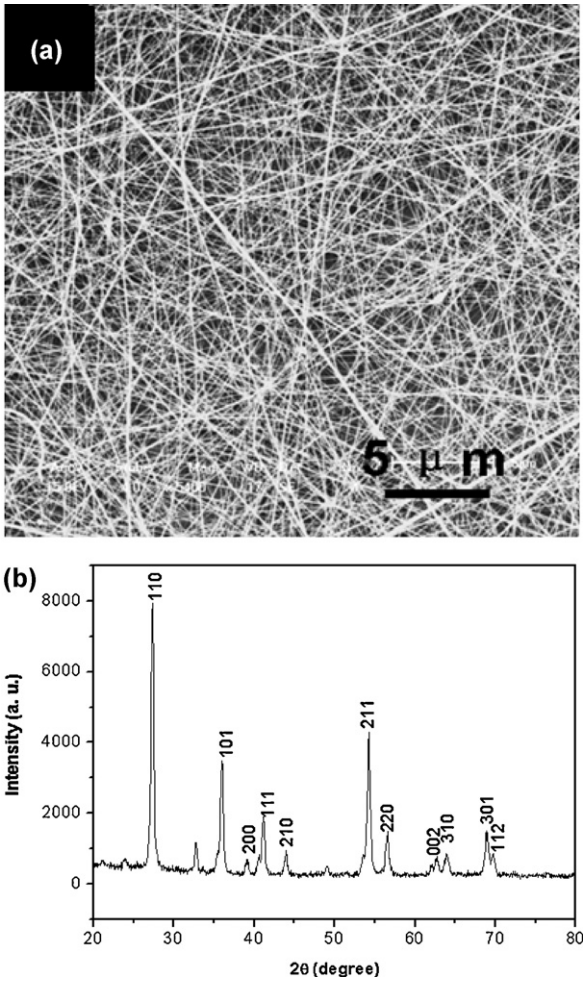

Fig. 2. (a) SEM image and (b) XRD pattern of the as-prepared product.

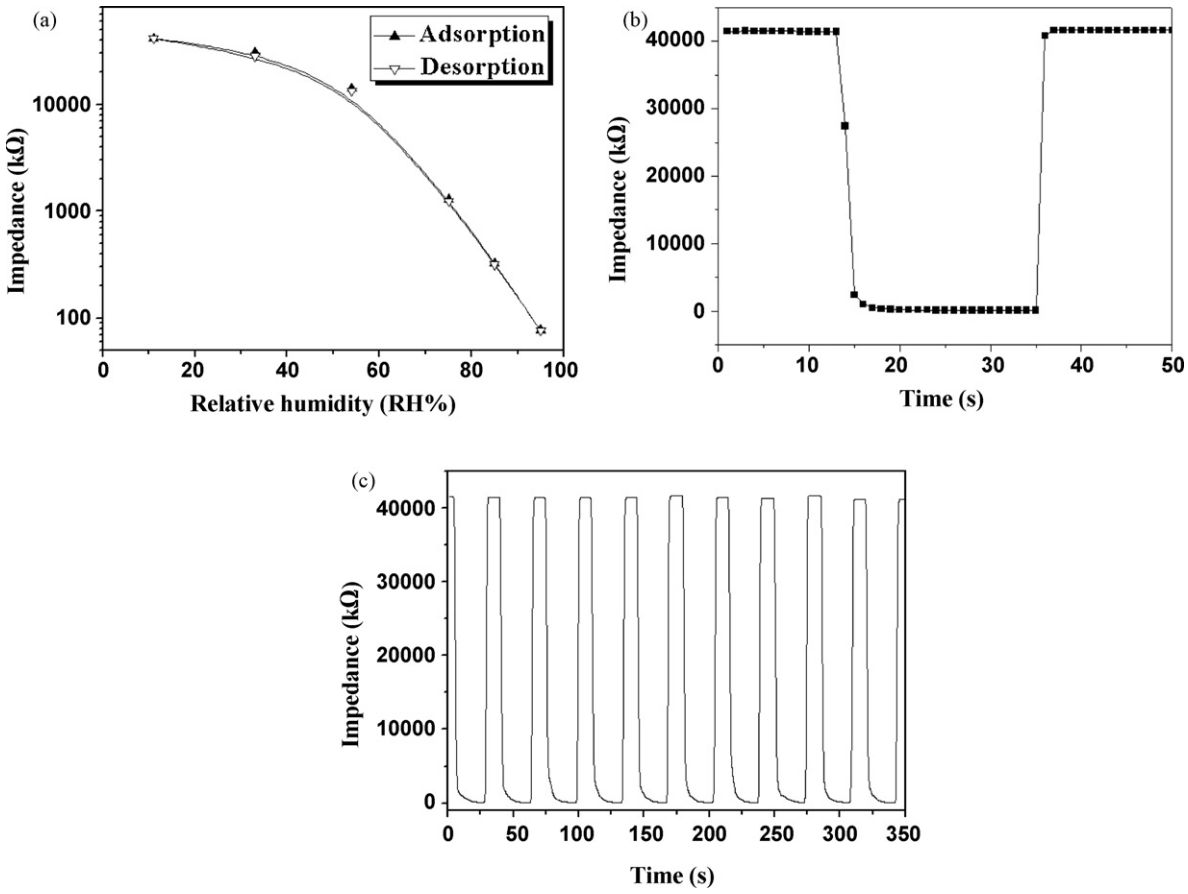

Fig. 3. (a) Humidity hysteresis of the product, (b) and (c) are response and recovery behaviors of the product for one circle and ten circles, respectively.

ing to the rutile TiO_2 phase, confirming those TiO_2 nanofibers are rutile.

3.2. Humidity sensing properties

3.2.1. Humidity sensing properties based on Mg^{2+} and Na^{+} doped rutile TiO_2 nanofiber mats

It has been proven that at high frequencies, the dielectric phenomenon did not appear owing to the adsorbed water molecules could not be polarized [19]. Therefore, the operation AC voltage and frequency are kept at 1 V and 100 Hz, respectively, in the following experiments. Fig. 3a shows the humidity hysteresis characteristic of the as-prepared humidity sensor. A good linearity with impedance varying about 3 orders of magnitude (10^7–10^5 Ω) can be observed. In addition, the lines for adsorption and desorption processes, during the whole humidity sensing measurement, are perfectly inosculated, which *surpassed* all the previous humidity sensors reported before. Fig. 3b shows the typical response and recovery characteristic curves for one cycle with the RH changing from 11% to 95%, confirming the response time and recovery time are 2 s and 1 s, respectively. In comparison to those results reported before, the response and recovery behaviors of our product have been further improved owing to the rutile TiO_2 (1 1 0) can act as active sites for water dissociation. From the curves for 10 cycles, as shown in Fig. 3c, the highest and lowest impedance values varied little, confirming the good reproducibility of our product.

3.2.2. Relative humidity of real world samples measured by as-prepared nanofiber mats

To evaluate the usefulness of as-prepared sensor in actual environment, the detection of the real world samples was carried out. In this study, we tested the RH of actual air at different times within three continuous days, of which the first two are sunny and rainy on the last. Here the commercial hygrometer ZDR-20 (Hangzhou Zeda Instruments Co., Ltd) is used as a reference of theoretical value and our experiment results are list in Table 1. All these data show that whether on sunny or rainy days the RH we got has excellent inosculation with the data displayed on ZDR-20. After calculation, we know that the relative error between them is far less than 10%, which suggests that our sensor has rather high exactitude apart from good sensitivity. However, our experimental response time is only 2 s, which is much faster than that (≥5 s) of the hygrometer when they are exposed to the real world samples at the same time, confirming the practical use based on our product.

3.2.3. Affections of TiO_2 crystal structure on the humidity sensing properties

From the XRD patterns, as shown in Fig. 4a, we can clearly see that when the sintering temperature is 500 °C, the crystal structure

Table 1
Relative humidity of real world samples measured by as-prepared sensor and ZDR-20 hygrometer.

Samples		As-prepared sensor		ZDR-20
		Impedance (kΩ)	RH (%)	RH (%)
Day 1	8:00 a.m.	21,634	42.2	42.0
	3:30 p.m.	35,818	21.8	23.2
Day 2	8:00 a.m.	17,014	49.1	49.6
	3:30 p.m.	32,390	29.2	30.1
Day 3	Rainy	3,474	66.4	65.9

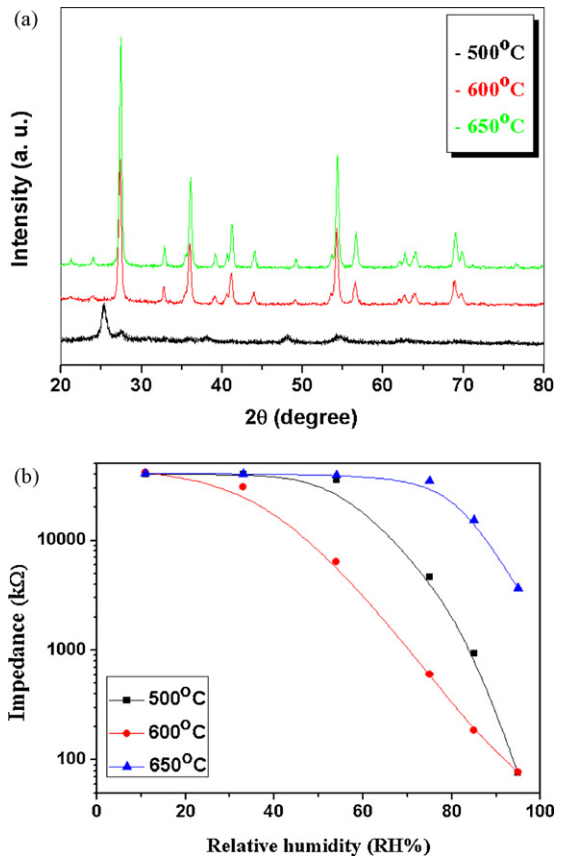

Fig. 4. (a) XRD patterns and (b) dependence of impedance on the RH for the products calcinated at different temperatures.

of TiO_2 is anatase. When the sintering temperatures are more than 600 °C, the crystal structure of TiO_2 is rutile. Fig. 4b shows the affection of the TiO_2 crystal structures on the linearity characteristics, confirming the linearity of rutile structure (600 °C) is better than that of the anatase structure (500 °C). However, when the sintering temperature is 650 °C, the linearity became poor for the ionic conduction can not be formed during the whole humidity sensing measurement, implying the formation of $MgTiO_3$, and Na_2TiO_3 at high temperature.

3.3. Basic humidity sensing principles

The analysis of complex impedance plots is useful for studying the sensing behavior of humidity sensors [20]. The complex impedance plots of the product at different RH are shown in Fig. 5a–f in the frequency range from 40 Hz to 100 kHz. At low RH (11%, 33%, and 54%), a semicircle due to the film impedance is observed. The semicircle indicates a "non-Debye" behavior, and many investigations have explained that it is due to a kind of polarization and can be modeled by an equivalent circuit of parallel resistor and capacitor [21]. With increasing the RH (75%, 85% and 95%), a line appears in the low frequency range and the semicircle becomes small. The higher the RH is, the longer the line and the smaller the semicircle is. The line represents Warburg impedance, and is due to the diffusion of the electroactive species at the electrodes [22]. The equivalent circuits of such complex impedance plots are shown in Fig. 5g and h. Here R_f represents the resistance of the product, which decreases as RH increases. C_f is the capacitance of the film and Z_i the impedance at the electrode/sensing film interface. According to Fig. 5, $R_f \ll Z_i$ at low RH, and the impedance change of the sensor is mostly determined by R_f. At high RH, the magnitudes of R_f and Z_i are the same and the impedance change of the sensor is determined by both R_f and Z_i.

3.4. Anti-fogged properties and the UV irradiation effect on the humidity sensing characteristics

For several decades, scientists have proven that TiO_2 is a photosensitive material and UV light can change the surface structure of TiO_2 [23]. When the TiO_2 structures are irradiated with UV light, the photogenerated hole reacts with lattice oxygen to form surface oxygen vacancies that allow water molecules to coordinate kinetically resulting the wettability of the TiO_2 surface changing from hydrophilic to hydrophobic, vice versa. Fig. 6a shows the change of the water contact angle (CA) of the composite nanofiber mat under the UV irradiation (obtained from two 1000 W high-pressure Hg lamp (λ = 310–380 nm) for 10 min), indicating a super-hydrophilic surface with the water contact angle ($0 \pm 1°$) can been obtain. When the product was placed in dark for 20 days, the surface structure of the as-prepared product recovered. Those results endow our product with the applications in anti-fogged and self-cleaning exterior tiles [24]. Fig. 6b shows the effect of UV irradiation on the humidity sensing characteristics of the sensor. After the prod-

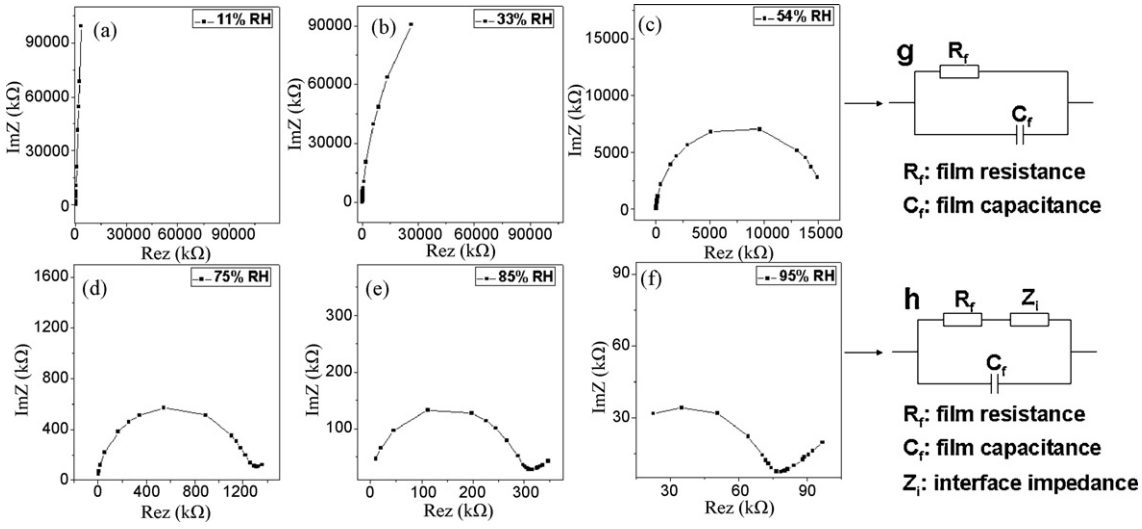

Fig. 5. Complex impedance plots of the product at different relative humidities: (a) 11%; (b) 33%; (c) 54%; (d) 75%; (e) 85% and (f) 95% and equivalent circuits of the product (g and h).

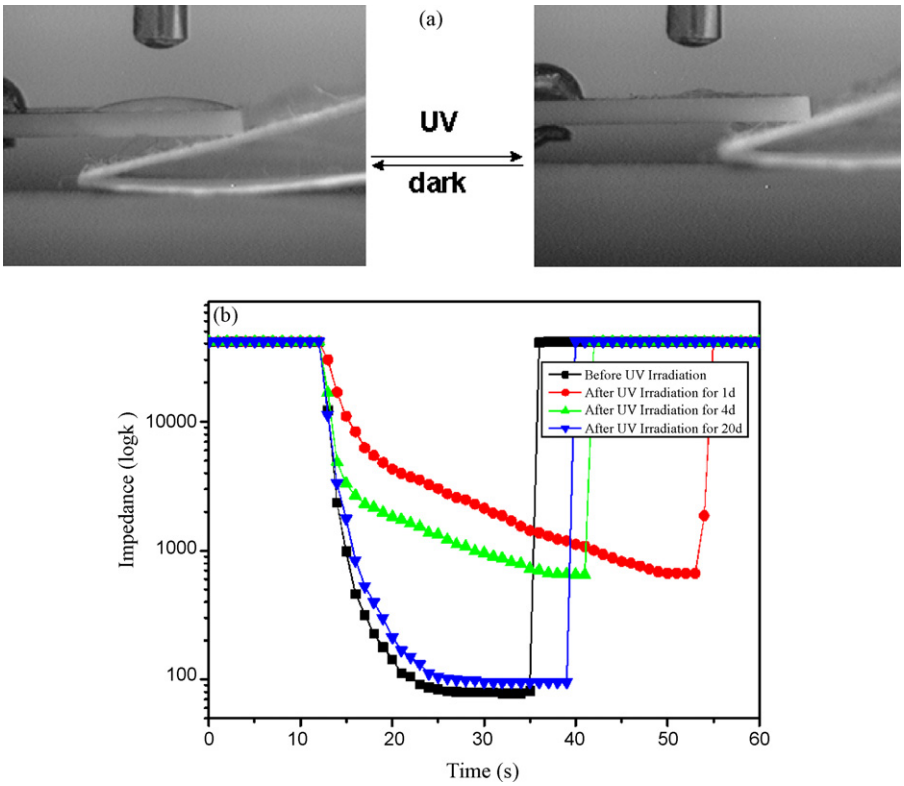

Fig. 6. (a) Photographs of the change of water contact angle (CA) of the product when it was irradiated with UV light. (b) Response and recovery behaviors before and after UV irradiation (impedance (log kΩ) vs. time (s)).

uct was placed in dark for 1 day, the impedance ($10^6\ \Omega$) of the sensor at high RH is greater than that ($10^5\ \Omega$) of the product without UV irradiation. However, when the product was put in dark for 20 days, the response and recovery behavior (impedance $10^5\ \Omega$) returned to similar values as the sensor before UV irradiation.

This phenomenon could be attributed to that the amounts of surface oxygen vacancies on the TiO_2 nanofibers increased under the UV irradiation, which increased the concentration of the chemisorbed oxygen species (O_2^-, O^-, O^{2-}) on the surface of TiO_2 nanofibers [23]. At the same time, Mg^{2+} and Na^+ temporarily reacted with O^{2-} to form metastable MgO and Na_2O under the UV irradiation, leading to poor ionic conduction at the high RH. When the sensor was placed in dark, the amounts of the photogenerated holes on TiO_2 substrate started to reduce, reducing the concentration of the chemisorbed oxygen species (O_2^-, O^-, and O^{2-}) on the surface of TiO_2 nanofibers, which caused those metastable MgO and Na_2O are converted to Mg^{2+} and Na^+ and O^{2-}, making the humidity performance come back. The whole changes of the Mg^{2+}/Na^+-doped TiO_2 nanofiber under the UV light and in dark have been illustrated in Fig. 7.

In order to prove that Mg^{2+} ions and Na^+ ions, located on the surface of the TiO_2 nanofibers, temporarily reacted with O^{2-} to form metastable MgO and Na_2O under the UV irradiation, causing the ionic conduction cannot be formed under the high RH. We investigated the affection of UV irradiation on the impedance of pure rutile TiO_2 nanofiber mat located on the working electrodes (as shown in Fig. 8). From the curve, it can be clearly seen that the ionic conduction of the UV irradiated nanofiber mat are easily formed than that of the nanofiber mat without UV irradiation for the impedance of the former is lower than that of the latter. This result can directly prove that the formation of metastable MgO and Na_2O under the UV irradiation owing to the impedance of the UV irradiated product cannot be lowered under the high RH.

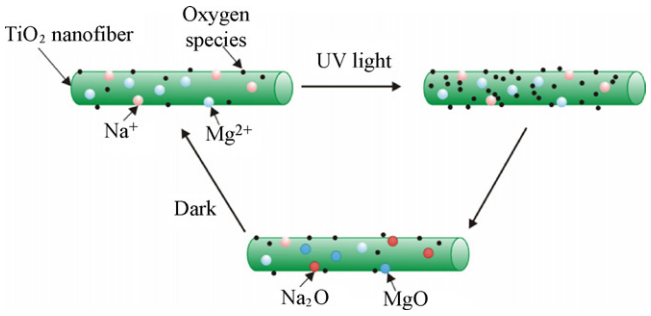

Fig. 7. Schematic diagrams of the changes of the Mg^{2+}/Na^+-doped TiO_2 nanofiber under the UV light and in dark.

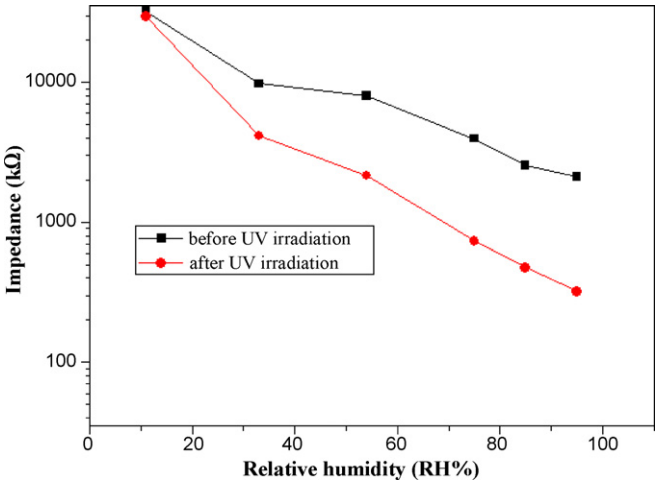

Fig. 8. The affection of UV irradiation on the impedance of pure rutile TiO_2 nanofiber mat located on the working electrodes.

4. Conclusion

In summary, we present a simple, effective, and low-cost route for fabrication of Mg^{2+}/Na^{+} doped rutile TiO_2 nanofiber mats. High-speed response time (2 s) and recovery time (1 s), good reproducibility, and anti-fogged properties can be achieved based on our product, those outstanding properties make our product a good candidiate in fabricating practical humidity sensor.

Acknowledgements

We acknowledge finacial support from in part by the National 863 Project (No. 2007AA03Z324), National 973 Project (No. 2007CD936203), and NSFC grants (Nos. 20674027 and 50873045).

References

[1] S. Zampolli, I. Elmi, J. Sturmann, S. Nicoletti, L. Dori, G.C. Cardinali, Sens. Actuators B 105 (2005) 400.
[2] C.S. Lao, Q. Kuang, Z.L. Wang, M.-C. Park, Y. Deng, Appl. Phys. Lett. 90 (2007) 262107.
[3] X.Q. Fu, C. Wang, H.C. Yu, Y.G. Wang, T.H. Wang, Nanotechnology 18 (2007) 145503.
[4] Z. Zhang, C. Hu, Y. Xiong, R. Yang, Z.L. Wang, Nanotechnology 18 (2007) 465504.
[5] F. H-Ramirez, S. Barth, A. Tarancon, O. Casals, E. Pellicer, J. Rodriguez, A. Rodriguez, J.R. Morante, S. Mathur, Nanotechnology 18 (2007) 424016.
[6] Q. Kuang, C.S. Lao, Z.L. Wang, Z.X. Xie, L.S. Zheng, J. Am. Chem. Soc. 129 (2007) 6070.
[7] Z. Li, H. Zhang, W. Zheng, W. Wang, H. Huang, C. Wang, A.G. MacDiarmid, Y. Wei, J. Am. Chem. Soc. 130 (2008) 5036.
[8] P. Novotna, J. Zita, J. Krysa, V. Kalousek, J. Rathousky, Appl. Catal. B 79 (2008) 179.
[9] M. Crisan, A. Braileanu, M. Raileanu, M. Zaharescu, D. Crisan, N. Dragan, M. Anastasescu, A. Ianculescu, I. Nitoi, V.E. Marinescu, S.M. Hodorogea, J. Non-Cryst. Solids 354 (2008) 705.
[10] P.I. Gouma, M.J. Mills, K.H. Sandhage, J. Am. Ceram. Soc. 83 (2000) 1007.
[11] R. Wang, K. Hashimoto, A. Fujishima, M. Chikuni, E. Kojima, A. Kitamura, M. Shimohigoshi, T. Watanabe, Nature 388 (1997) 431.
[12] J.R. Jennings, A. Ghicov, L.M. Peter, P. Schmuki, A.B. Walker, J. Am. Chem. Soc. 130 (2008) 13364.
[13] S.C. Li, Z. Zhang, D. Sheppard, B.D. Kay, J.M. White, Y. Du, I. Lyubinetsky, G. Henkelman, Z. Dohnálek, J. Am. Chem. Soc. 130 (2008) 9080.
[14] C.H. Lin, C.H. Chen, Sens. Actuators B 129 (2008) 531.
[15] J.P. Lukaszewicz, Sens. Actuators B 60 (1999) 184.
[16] D. Li, Y. Xia, Nano Lett. 3 (2003) 555.
[17] P. Feng, X.Y. Xue, Y.G. Liu, T.H. Wang, Appl. Phys. Lett. 89 (2006) 243514.
[18] Y.X. Liang, Y.J. Chen, T.H. Wang, Appl. Phys. Lett. 85 (2004) 666.
[19] V. Bondarenka, S. Grebinskij, S. Mickevičius, V. Volkov, G. Zacharova, Sens. Actuators B 28 (1995) 227.
[20] Y. Sadaoka, M. Matsuguchi, Y. Sakai, S. Mitsui, J. Mater. Sci. 23 (1998) 2666.
[21] E. Traversa, G. Gnappi, A. Montenero, G. Gusmano, Sens. Actuators B 31 (1996) 59.
[22] C.D. Feng, S.L. Sun, H. Wang, C.U. Segre, J.R. Stetter, Sens. Actuators B 40 (1997) 217.
[23] X. Feng, J. Zhai, L. Jiang, Angew. Chem. Int. Ed. 44 (2005) 5115.
[24] A. Fujishima, K. Hashimoto, T. Watanabe, TiO_2 Photocatalysis Fundamentals and Applications, BKC Inc., Tokyo, Japan, 1999.

Talanta 79 (2009) 780–786

Contents lists available at ScienceDirect

Talanta

journal homepage: www.elsevier.com/locate/talanta

Direct electrochemistry and electrocatalysis of hemoglobin immobilized in a magnetic nanoparticles-chitosan film

Na Zheng, Xia Zhou, Weiying Yang, Xiangjun Li*, Zhuobin Yuan

College of Chemistry and Chemical Engineering, Graduate University of Chinese Academy of Sciences, Beijing 100049, China

ARTICLE INFO

Article history:
Received 4 March 2009
Received in revised form 27 April 2009
Accepted 4 May 2009
Available online 12 May 2009

Keywords:
Fe_3O_4 nanoparticles
Direct electrochemistry
Electrocatalysis
Hemoglobin
Hydrogen peroxide

ABSTRACT

Magnetic nanoparticles (Fe_3O_4) were synthesized by a chemical coprecipitation method. X-ray diffraction (XRD) and transmission electron microscope (TEM) were used to confirm the crystallite structure and the particle's radius. The Fe_3O_4 nanoparticles and chitosan (CS) were mixed to form a matrix in which haemoglobin (Hb) can be immobilized for the fabrication of H_2O_2 biosensor. The Fe_3O_4–CS–Hb film exhibited a pair of well-defined and quasi-reversible cyclic voltammetric peaks due to the redox of Hb–heme Fe (III)/Fe (II) in a pH 7.0 phosphate buffer. The formal potential of Hb–heme Fe(III)/Fe(II) couple varied linearly with the increase of pH in the range of 4.0–10.0 with a slope of 46.5 mV pH^{-1}, indicating that electron transfer was accompanied with single proton transportation in the electrochemical reaction. The surface coverage of Hb immobilized on Fe_3O_4–CS film glassy carbon electrode was about 1.13×10^{-10} mol cm^{-2}. The heterogeneous electron transfer rate constant (k_s) was 1.04 s^{-1}, indicating great facilitation of the electron transfer between Hb and magnetic nanoparticles-chitosan modified electrode. The modified electrode showed excellent electrocatalytic activity toward oxygen and hydrogen peroxide reduction. The apparent Michaelis–Menten constant K_M^{app} for H_2O_2 was estimated to be 38.1 μmol L^{-1}.

1. Introduction

Direct electrochemistry of redox proteins or enzymes has been the research focus for many years in views of the good model for mechanistic studies of their electron transfer activity in biological systems and serves as a foundation for fabricating electrochemical biosensors and bioreactors without using chemical mediators [1,2]. Unfortunately, because of the deep bury of the electroactive prosthetic groups, the adsorptive denaturation of proteins onto electrodes and the unfavorable orientations at electrodes, the proteins or enzymes exhibit a rather slow rate of heterogeneous electron transfer at conventional electrodes, although their electron transfer is quite fast in biological systems [3]. Generally, modification of the electrodes' surfaces by deposition of various films, including self-assembled monolayers (SAMs) [4], electropolymerization [5], layer by layer assembly [6], covalent-bonded immobilization [7] is an effective way to enhance the rate of electron transfer and obtain direct electrochemistry of redox enzymes or proteins. Successful examples have included cast films of proteins with insoluble surfactants [8], hydrogel polymers [9], biopolymers [10], clay [11], etc.

Recently, nanoparticles have attracted increasing attention because the nanoparticles could adsorb redox enzymes and proteins without loss of their biological activity. In addition, the electron transfer activity and biocatalytic activity of enzymes increased when they were adsorbed on nanomaterials [12]. Many metal oxide nanoparticles such as copper oxide [13], zinc oxide [14], titanium oxide [15], zirconium oxide [16] are used successfully for immobilization and direct electrochemistry of enzymes and proteins. Fe_3O_4 nanoparticles have been used to immobilize enzymes [17,18], because of their good biocompatibility, strong superparamagnetic property, low toxicity and easy preparation [19–21], especially, magnetite is found to exist in the human brain, the particles of this materials are generally smaller than 200 nm, and, in most cases, are on the order of a few tens of nanometers [22,23]. So, it is meaningful to study the bioactivity and biocatalysis of enzymes and proteins when they are entrapped in the Fe_3O_4 nanoparticles.

Hemoglobin (Hb), an important redox respiratory protein in red cells, has a molecular weight of approximately 64,500. It contains the porphyrin complex of iron (II) or hemin (III) as a prosthetic group and has four electroactive heme redox centers in its respective four polypeptide chains. It is reported that hemoglobin can be used as a substitute of horseradish peroxidase (HRP) to catalyze the reduction of peroxide hydrogen [24], and it is also an ideal model protein for studying the electron transfer of heme molecules.

However, when nanoparticles such as Fe_3O_4 are used to immobilized proteins and enzymes, the tendency to aggregation of nanoparticles limits their further applications, so it is necessary to disperse Fe_3O_4 in a suitable matrix to prevent aggregation. Chitosan

* Corresponding author. Tel.: +86 010 88256336; fax: +86 010 88256336.
E-mail address: lixiangj@gucas.ac.cn (X. Li).

0039-9140/$ – see front matter © 2009 Elsevier B.V. All rights reserved.
doi:10.1016/j.talanta.2009.05.002

(CS) is a kind of natural polysaccharide, which is derived from chitin, has good biocompatibility, biodegradability, low toxicity, haemostatic potential, good film forming character and anti-infectional activity [25]. Due to its desirable properties, chitosan has been widely used for electrochemical biosensing platforms combined with metal nanoparticles [26], carbon nanotubes [27] and ionic liquids [28]. Moreover, the CS can facilitate the immobilization of enzymes like Hb because it contains primary amino groups which provide a hydrophilic environment compatible with the biomolecules [29]. The isoelectric point of CS is around pH 8.5 [30]. So CS has positive charges in solutions [31]. With the isoelectric point at 5.9 [32], Fe_3O_4 nanoparticles have negative surface charges at pH 8.0. In this research, Fe_3O_4–CS composites were constructed by electrostatic interactions between positively charged CS particles and negatively charged Fe_3O_4.

In this paper, we studied the direct electron transfer and electrocatalysis of Hb in the Fe_3O_4–CS interfaces. The Hb embedded in the Fe_3O_4–CS was characterized by the UV–vis and FTIR spectroscopy to indicate that the secondary structure of Hb was not destroyed and retained its biological activity. The electrode modified with Fe_3O_4–CS–Hb film had high stability and displayed significant biological activities. The electrocatalytic reduction of oxygen and hydrogen peroxide in this electrode has been observed, showing the possible potential application of the film as the third generation biosensor of hydrogen peroxide.

2. Experimental

2.1. Chemicals and materials

Bovine hemoglobin (Hb, MW 64,500) purchased from Sigma Chemical Co. was used without further purification. Hydrogen peroxide (H_2O_2, 30%) was obtained from Beijing Chemical Works (Beijing, China). Chitosan (molar weight $\sim 1 \times 10^6$, 75–85% deacetylation) was supplied by Sigma (St. Louis, MO, USA). Other chemicals were of analytical reagent grade. Phosphate buffer solutions (PBS) were prepared by 0.1 M KH_2PO_4 and 0.1 M K_2HPO_4, and the pH was adjusted with 0.1 M H_3PO_4 or 0.1 M NaOH. All aqueous solutions were prepared in doubly distilled water.

2.2. Synthesis of Fe_3O_4 nanoparticles

Fe_3O_4 nanoparticles were self-synthesized according to the literature [33]. In a typical process, deionizated water was placed in a 3-neck round-bottom flask and deoxygenated by bubbling N_2 for 30 min. Then certain concentrated ferrous chloride hexa-hydrate ($FeCl_3 \cdot 6H_2O$) and ferric chloride tetra-hydrate ($FeCl_2 \cdot 4H_2O$) aqueous solutions were added. Later certain concentrated ammonium hydroxide (NH_4OH) in the long-stem funnel was added with vigorous stirring until the pH of the mixture reached above 10 and the reaction continued for 30 min in a constant temperature water bath. The product was washed several times with deionizated and deoxygenated water, then dried in vacuum at 60 °C for 12 h. Finally Fe_3O_4 nanoparticles were obtained.

2.3. Apparatus and electrochemical measurements

The structure and morphology of Fe_3O_4 nanoparticles were characterized by a X-ray diffractometer (XRD, MSAL XD-2 powder X-ray diffractometer using Cu Kα radiation of wavelength 1.5406 Å at 30 kV and 30 mA) and transmission electron microscopy (TEM, H800, Hitachi Instrument Co., Japan). The image of the modified electrode was characterized by scanning electron microscopy (SEM, KYKY-2800 microscope, KYKY Technology Development Ltd., China) at an accelerating voltage of 20 keV. X-ray photoelectron spectroscopy data were obtained with an ESCALab220i-XL electron spectrometer from VG Scientific using 300W Al Kα radiation. The UV–vis absorption spectroscopy study was carried out using a UV–vis 2550 Spectrophotometer (Shimadzu, Kyoto, Japan). FTIR spectra were recorded with Nicolet 360v FTIR spectrophotometer (Nicolet Instrumental, USA).

The electrochemical measurements were carried out using a computer-controlled electrochemical analyzer (CHI 660A, CH Instruments, Austin, TX, USA) with a three-electrode cell. The Fe_3O_4–CS–Hb/GCE was used as the working electrode, a platinum wire as the counter electrode, and a saturated calomel electrode (SCE) as the reference electrode. All potentials were quoted with respect to SCE. Phosphate buffer (0.1 M pH 7.0) was used as the supporting electrolyte. All experimental solutions were thoroughly deoxygenated by bubbling high-purity nitrogen and maintained under nitrogen atmosphere during measurements. All electrochemical measurements were performed at ambient temperature 18 ± 2 °C.

2.4. Preparation of the Fe_3O_4–CS–Hb/GCE

Prior to coating, glassy carbon electrode (GCE, diameter 3.0 mm) was polished before each experiment with 1.0, 0.30 and 0.05 μm α-alumina powder and sonicated in 1:1 nitric acid, ethanol, doubly distilled water in turn, and then dried at room temperature. The Fe_3O_4–CS–Hb/GCE was prepared as follows. The aqueous dispersion of Fe_3O_4 nanoparticles was prepared by vigorous stirring for about 8 h in pH 8.0 buffer. The suspension was stirred for 30 min just before preparing the films. Then CS (dissolved in acetic acid solution), which is served as a dispersant to prevent Fe_3O_4 nanoparticles aggregation, was added into aqueous. Later Hb solution was added to the suspension and stirred for 30 min. The Hb molecules were absorbed on the surface of CS during mixing. Then, 3 μL of the resulting mixture was pipetted onto the surface of GCE. A small plastic bottle was fitted tightly above the electrode surface to serve as a closed evaporation chamber, to make sure the solvent evaporated slowly and more uniform film formed. The film was dried at 4 °C overnight in air and the Fe_3O_4–CS–Hb/GCE was obtained. If it was not used immediately, the electrode was stored at 4 °C in a refrigerator. In the above procedure, if Fe_3O_4 nanoparticles were absent, the electrode obtained was the Hb–CS/GCE.

3. Results and discussion

3.1. Structural and morphology characterization of Fe_3O_4 nanoparticles

The structure of the as-obtained product was firstly characterized by X-ray diffraction (XRD) (Fig. 1). The strong diffraction peaks at 2θ angles of 30°, 35°, 42° and 62.5° may correspond to the crystal plane of (2 2 0), (3 1 1), (4 0 0) and (4 4 0) of the cubic phase. All peaks were consistent with that reported previously [33]. According to Scherrer formula, the average diameter of prepared Fe_3O_4 is about 8.8 nm.

TEM was used to view the size of Fe_3O_4 particles in aqueous dispersions (Fig. 2A), showing that the average particle size of Fe_3O_4 was 40 nm. This size was larger than the size of 8.8 nm obtained by XRD, indicating some extent of aggregation of the particles.

3.2. Characterization of modified film by SEM

In order to investigate the formation of the modified film, SEM image of Fe_3O_4–CS film on ITO glass was given in Fig. 2B. It shows that Fe_3O_4 nanoparticles are well dispersed, which could confirm

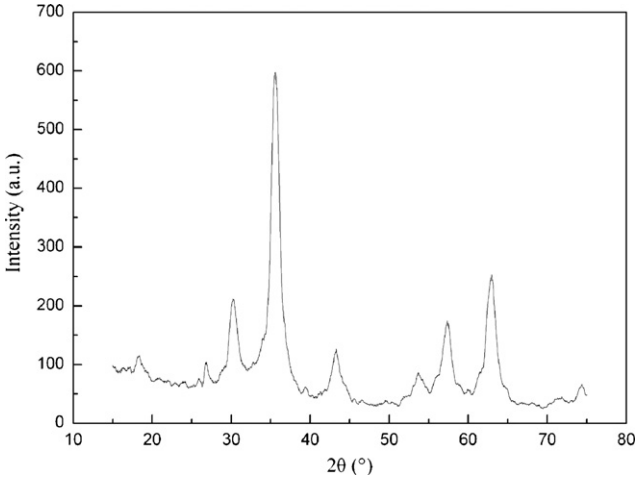

Fig. 1. XRD patterns taken from the Fe_3O_4 samples prepared.

that Fe_3O_4 nanoparticles have been successfully entrapped in the chitosan film.

3.3. Conformational studies of Hb

In order to confirm the existence of Hb on the surface of Fe_3O_4–CS composite, XPS experiment was carried out. Fig. 3A shows the XPS spectrum of Hb immobilized on the surface of Fe_3O_4–CS composite in the N1s regions. It can be observed that the characteristic peak of N1s of N was at 399.9 eV (Fig. 3A). Since N is from Hb, the result indicated the existence of Hb on the surface of Fe_3O_4–CS composite.

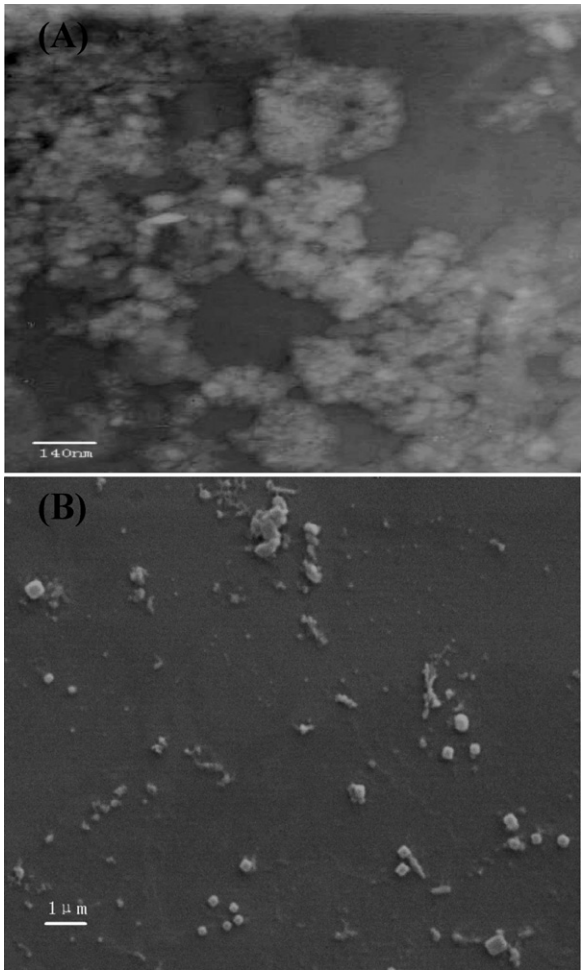

Fig. 2. (A) TEM image of Fe_3O_4 nanoparticles in aqueous dispersions. Scale bar: 140 nm. (B) SEM image of Fe_3O_4–CS film.

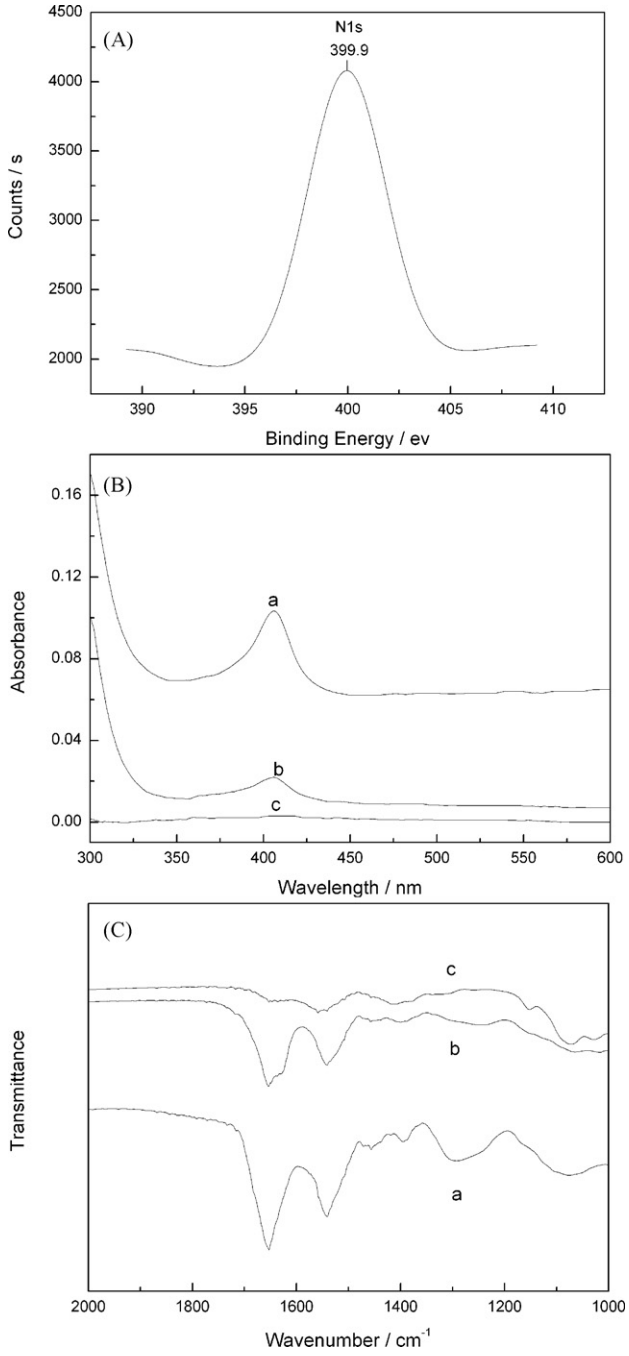

Fig. 3. (A) The XPS spectrum of Hb immobilized on the surface of Fe_3O_4–CS composite in N1s region. (B) UV–vis spectra of Hb (a), Fe_3O_4–CS–Hb (b) and Fe_3O_4–CS composite (c). (C) FTIR spectra of Hb (a), Fe_3O_4–CS–Hb (b) and Fe_3O_4–CS composite (c).

UV–vis spectroscopy is a conventional tool for monitoring the possible change of the Soret absorption band in the heme group region. The band shift may provide the information of possible denaturation of heme protein, particularly conformational change [34]. Fig. 3B shows the UV–vis spectra of Hb (Fig. 3B(a)), Fe_3O_4–CS–Hb (Fig. 3B(b)) and Fe_3O_4–CS composite (Fig. 3B(c)) in pH 7.0 PBS, respectively. The Soret band of Fe_3O_4–CS–Hb appeared

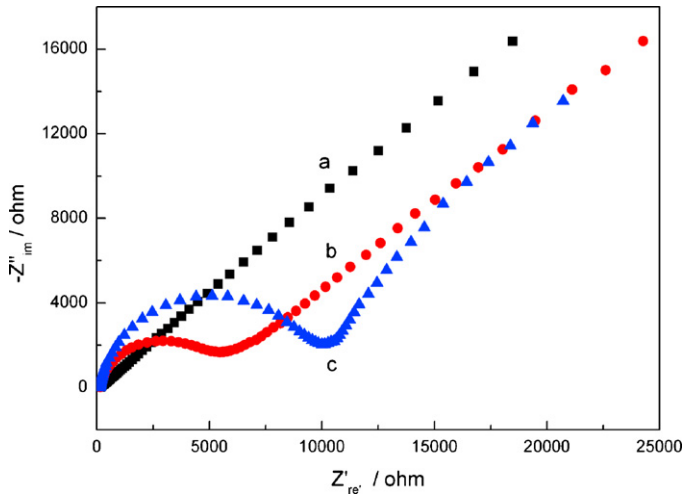

Fig. 4. EIS of: bare GCE (a); Fe_3O_4/GCE (b) and Fe_3O_4–CS–Hb/GCE (c) in 0.1 mol L^{-1} KCl containing 1 mmol L^{-1} $K_3[Fe(CN)_6]$.

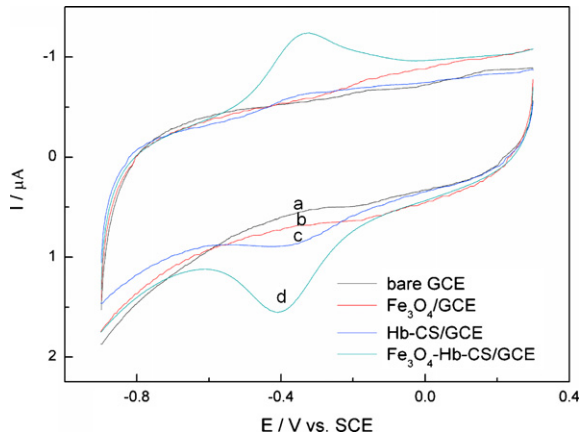

Fig. 5. Cyclic voltammograms of bare GCE (a), Fe_3O_4/GCE (b), Hb–CS/GCE (c), Fe_3O_4–CS–Hb/GCE (d) in 0.1 M pH 7.0 PBS. Scan rate: 200 mV s^{-1}.

at 405 nm (Fig. 3B(b)), the same as that of native Hb in phosphate buffer (Fig. 3B(a)), indicating that the secondary structure of Hb immobilized on the surface of Fe_3O_4–CS was not destroyed and Hb retained its biological activity.

The immobilization of Hb on the surface of Fe_3O_4–CS did not alter the structure of Hb. This conclusion can also be verified by the FTIR spectra. Fig. 3C(a) is the FTIR spectrum of Hb. The amide I band of Hb, which was caused by C=O stretcthing vibrations of peptide linkages, appeared at 1653 cm^{-1}. The signal at 1541 cm^{-1} indicated the characteristic of amide II, which resulted from a combination of N–H in plane bending and C–N stretching vibrations of the peptide groups. The characteristic amide I and II bands of proteins provide detailed information on the secondary structure of polypeptide chain [35]. Fig. 3C(b) is the FTIR spectrum of Fe_3O_4–CS–Hb. The amide I (1654 cm^{-1}) and II (1541 cm^{-1}) bands appeared essentially the same positions as those of free Hb, suggesting an unchanged secondary structure for the intercalated Hb.

In electrochemical impedance spectroscopy (EIS), the impedance change of the electrode surface can characterize the stepwise-assemble process of the surface-modified electrode. In EIS, the semicircle part at higher frequencies corresponds to the electron-transfer limited process; its diameter is equal to the electron transfer resistance, R_{et}, which controls the electron transfer kinetics of the redox probe at the electrode interface. At bare GCE, an almost straight line could be observed (Fig. 4a), showing a diffuse limiting step of the electrochemical processes. After dripping Fe_3O_4 nanoparticles on the surface of the electrode, an obvious interfacial R_{et} was observed (Fig. 4b). This may be ascribed to the film's weak conductivity. When Hb–CS was assembled onto the Fe_3O_4 membrane, the R_{et} increased obviously (Fig. 4c), which proved the successful assemble of Hb–CS.

3.4. Direct electrochemistry of Fe_3O_4–CS–Hb/GCE

Fig. 5 shows the cyclic voltammograms of bare GCE (a), Fe_3O_4/GCE (b), Hb–CS/GCE (c) and Fe_3O_4–CS–Hb/GCE (d) in deaerated 0.1 M pH 7.0 PBS at a scan rate of 200 mV s^{-1}. No redox peaks were observed in the cyclic voltammogram of the bare GCE and Fe_3O_4/GC electrode (Fig. 5a and b), indicating that Fe_3O_4 was non-electroactive. When the electrode was modified with Hb–CS, the redox peaks of Hb could be observed (Fig. 5c), but the current was much less than Fe_3O_4–CS–Hb/GCE, suggesting that the direct electron thansfer was difficult between Hb and the electrode. A pair of well-defined and nearly symmetrical redox peaks was observed at the Fe_3O_4–CS–Hb/GCE (Fig. 5d), indicating that Fe_3O_4 nanoparticles in the film could increase the adsorption ability for Hb and favor the orientation of Hb. It was no doubt that the pair peaks arose from Hb entrapped in the composite film. The anodic peak potential (E_{pa}) and cathodic peak potential (E_{pc}) were located at −0.324 and −0.412 V, respectively. Its formal potential (defined as the average of E_{pa} and E_{pc}), $E^{0\prime}$ was −0.368 V vs. SCE, a characteristic of the Hb–heme Fe(III)/Fe(II) redox couple. Thus, this also suggested that Hb immobilized on Fe_3O_4–CS did not denature. The separation of peak potentials ($\Delta E_p = E_{pa} - E_{pc}$) was 88 mV at a scan rate of 200 mV s^{-1}, and almost unchanged with the increase of v. So Fe_3O_4–CS film provided a better microenvironment for Hb to undergo a facile electron transfer reaction. The results implied that the electron transfer rate between Hb and GCE was relative fast. Moreover, the ratio of the cathodic current to the anodic current was close to one. These electrochemical parameters suggested that Hb underwent a quasi-reversible redox process at Fe_3O_4–CS–Hb/GCE, which can also attributed to the synergistic promotion action of Fe_3O_4 and CS.

According to Faraday laws, $\Gamma^* = Q/nFA$, where Q is the charge involved in the reaction, n is the number of electron transferred, F is the Faraday constant and A is the effective area of the GCE, the surface concentration of electroactive Hb (Γ^*) was calculated to be 1.13×10^{-10} mol cm^{-2} for Fe_3O_4–CS–Hb/GCE. The value was larger than the theoretical monolayer coverage of Hb (1.89×10^{-11} mol cm^{-2}) [36] on the basis of the crystallographic dimensional structure of Hb and assuming that the biomolecule adopts an orientation with the long axis parallel to the electrode surface [37]. The bigger surface coverage can be ascribed to the expanded interspace to hold more Hb molecules, indicating that intercalated Hb in the composited film participated in the electron transfer process. Therefore, the present Fe_3O_4 nanoparticles is a promising material for increasing the functional density of Hb, allowing the electric communication with the underlying GCE. According to the Laviron equation [38],

$$I_p = \frac{n^2F^2Av\Gamma}{4RT} = \frac{nFQv}{4RT}$$

the number n of electrons involved in the direct electron transfer reaction of Hb was calculated to be $n = 0.90$, indicating that the redox reaction of the adsorbed Hb on the Fe_3O_4 modified electrode was a single electron transfer reaction.

The typical cyclic voltammograms of Fe_3O_4–CS–Hb/GCE in pH 7.0 PBS at different scan rates are shown in Fig. 6. The electrode modified with the Fe_3O_4–CS–Hb composite displayed well-defined peaks and showed almost equal height of reduction and oxidation peaks at the same scan rate. With the increase of the scan rate,

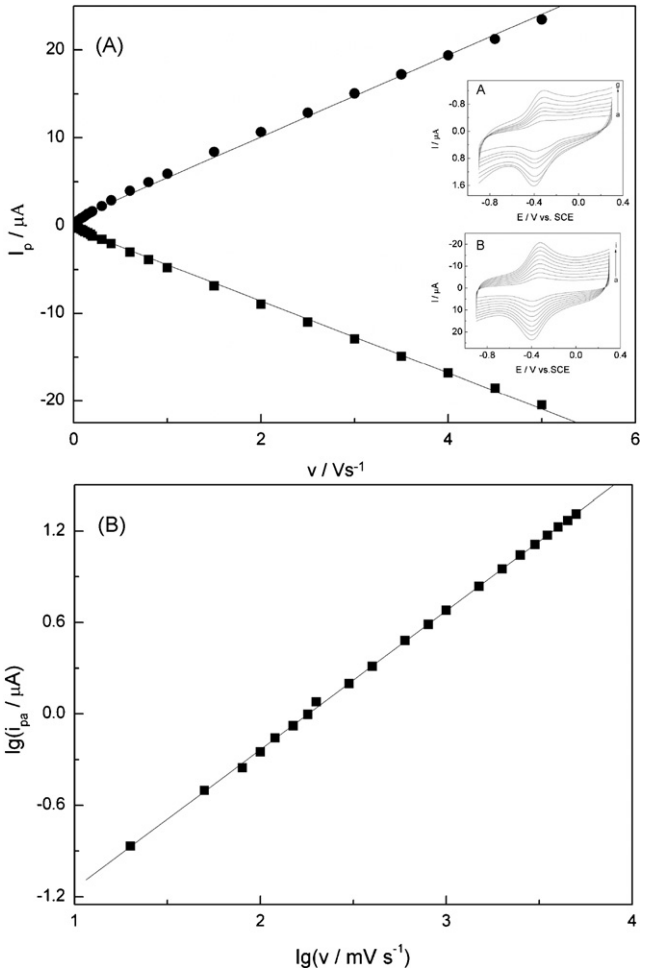

Fig. 6. (A) Plots of peak current vs. scan rate from Fig. 9 inset A, B. Inset A: Cyclic voltammograms of Fe_3O_4–CS–Hb/GCE in 0.1 M pH 7.0 PBS at the low scan rate of (a) 50, (b) 80, (c) 100, (d) 120, (e) 150, (f) 180, (g) 200 mV s^{-1}. Inset B: Cyclic voltammograms of Fe_3O_4–CS–Hb/GCE in 0.1 M pH 7.0 PBS at the high scan rate of (a) 1000, (b) 1500, (c) 2000, (d) 2500, (e) 3000, (f) 3500, (g) 4000, (h) 4500, (i) 5000 mV s^{-1}. (B) Plot of logarithm of I_{pa} vs. logarithm of v.

the cathodic and anodic peak currents increased simultaneously in Fig. 6(A). Furthermore, integration of reduction peaks at different scan rates gave nearly constant charge (Q) values which indicated a surface-controlled process, in which nearly all electroactive proteins in the films are reduced on the forward cathodic scan, with full conversion of the reduced proteins back to their oxidized forms on the reversed anodic scan. The slope obtained by linear regression of log I_{pa} vs. log v was 0.91 for Hb (Fig. 6(B)), which corresponded to the characteristic of a thin-layer electrochemical behavior. The potential separation between anodic and cathodic peaks (ΔE_p) was larger than the theoretical value of 0 mV for a surface process, which was probably attributed to the long distance between the heme of Hb and the electrode surface for the deep-buried electroactive centers in polypeptides.

The electron transfer rate constant k_s can be estimated with equation $k_s = mnFv/RT$ when the peak-to-peak separation is less than 200 mV [38], where m is a parameter related to the peak-to-peak separation. The k_s value was calculated to be 1.04 s^{-1} at the scan rate of 150 mV s^{-1}, which was larger than that of Hb immobilized on Au–colloid–cysteamine-modified gold electrode (0.49 s^{-1}) [39], Hb modified CNT powder microelectrodes electrodes (0.062 s^{-1}) [40]. Thus, Fe_3O_4 can provide a microenvironment for Hb to undergo a facile electron transfer reaction.

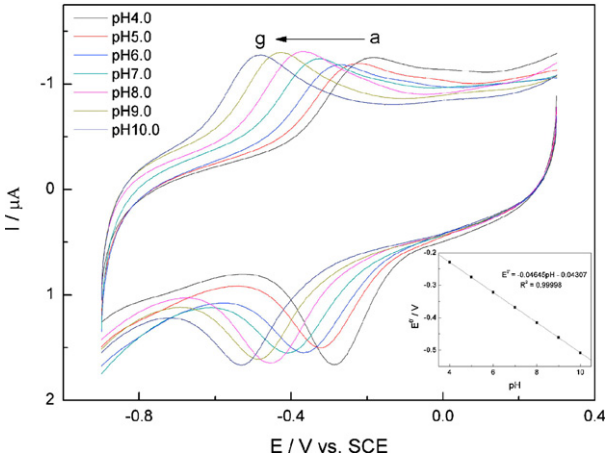

Fig. 7. Cyclic voltammograms of the Fe_3O_4–CS–Hb/GCE in 0.1 M pH7.0 PBS at pH: (a) 4.0, (b) 5.0, (c) 6.0, (d) 7.0, (e) 8.0, (f) 9.0 and (g) 10.0. Scan rate: 200 mV s^{-1}. Inset: the plot $E^{0\prime}$ of Hb vs. pH of the solution.

3.5. Effect of solution pH on peak potential of Hb at Fe_3O_4–CS–Hb/GCE

In most cases, the solution pH is essential to the electrochemical behaviors of proteins. Generally, the $E^{0\prime}$ of the redox couple depends on the solution pH which indicates the participation of proton in the redox process. The cyclic voltammograms of Fe_3O_4–CS–Hb/GCE at different pH solutions were measured at a scan rate of 200 mV s^{-1} (Fig. 7). A pair of stable and well-defined redox peaks were obtained. An increase of solution pH caused a negative shift in both cathodic and anodic peak potentials for Hb, indicating that proton was involved in the electrode reaction of Hb. $E^{0\prime}$ shifted linearly to the negative direction with a slope −46.5 mV pH^{-1} by increasing pH, which was a bit smaller than the theoretical value −57.6 mV pH^{-1} at 18 °C for a reversible one proton coupled single-electron transfer [41]. This may be owing to the effect of the protonation states of trans ligands to the heme iron and amino acids around the heme or to the protonation of water molecules coordinated to the center [42] that may exist in different states under different pH values. Thus, the electron-transfer between Hb and the electrode can be presented by

$$\text{HbhemeFe(III)} + \text{H}^+ + \text{e}^- \leftrightarrow \text{HbhemeFe(II)}$$

3.6. Electrocatalysis of Hb in Fe_3O_4–CS film

It is well known that proteins and enzymes containing the heme group, such as horseradish peroxidase, cytochrome c, hemoglobin and myoglobin, have the ability to reduce O_2 and H_2O_2 electrocatalytically. In order to estimate the electrochemical catalytic activity of Fe_3O_4–CS–Hb/GCE for the reduction of O_2 and H_2O_2, the cyclic voltammetry has been performed.

When the solution was deoxygenated thoroughly, a pair of well-defined redox peaks can be obtained with almost the equal height of the reduction and oxide peaks (Fig. 8A(b)). However, when Fe_3O_4–CS–Hb/GCE was dipped in a pH 7.0 PBS without deaerating O_2, only a significant reduction peak at about −0.32 V was observed while oxidation peak of Hb Fe(II) disappeared (Fig. 8A(d)), suggesting that Hb Fe (II) reacted with oxygen. For Fe_3O_4/GC, the reduction peak of oxygen was observed at about −0.81 V (Fig. 8A(c)), far more negative than the catalytic peak potential. Therefore, the over-potential required for reduction of O_2 was lowered by about 0.5 V by Fe_3O_4–CS–Hb film. Catalytic efficiency (defined as the ratio of reduction peak current in the presence (I_c) and absence (I_d) of oxygen, I_c/I_d) decreased with increasing the scan rate for

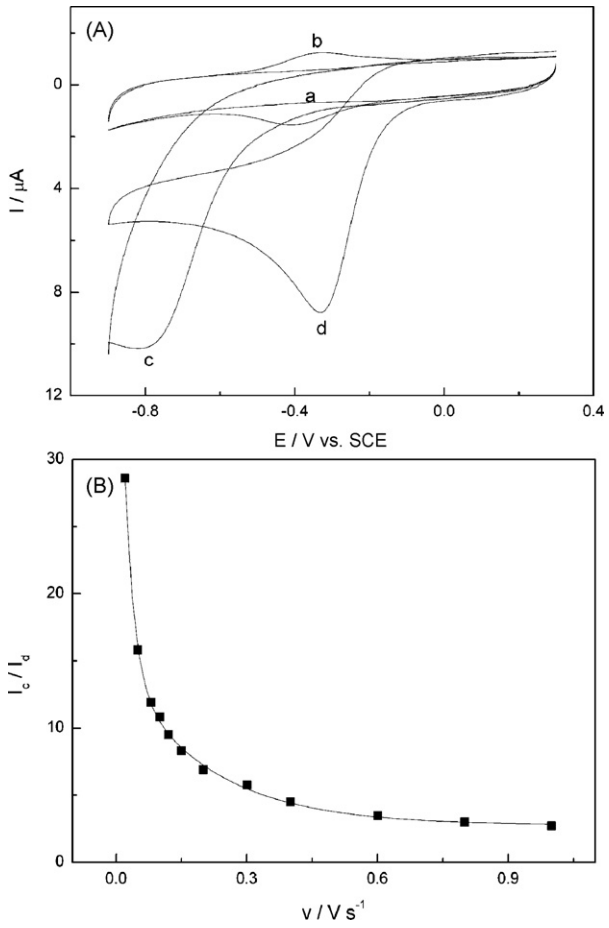

Fig. 8. (A) Cyclic voltammograms in 0.1 M pH 7.0 PBS at 200 mV s^{-1} for Fe_3O_4/GCE (a), Fe_3O_4–CS–Hb/GCE (b) without oxygen present, Fe_3O_4/GCE (c), Fe_3O_4–CS–Hb/GCE (d) with oxygen present. (B) Influence of scan rate on catalytic efficiency, I_c/I_d, for Fe_3O_4–CS–Hb film in pH 7.0 PBS buffer, where I_c is the CV reduction peak current in buffers with air and I_d is the CV reduction peak current in buffers without oxygen.

Fe_3O_4–CS–Hb/GC electrode (Fig. 8B), also a characteristic of electrochemical catalytic reduction of oxygen by the heme proteins [43].

Fe_3O_4–CS–Hb/GCE also showed good catalytic activity toward hydrogen peroxide. When H_2O_2 was added to a pH 7.0 PBS, compared with the system without H_2O_2, the voltammograms of Fe_3O_4–CS–Hb/GCE showed a significant increase in the reduction peak at −0.41 V with the decreasement of the oxidation peak (Fig. 9). Moreover, the reduction peak increased gradually with the gradually addition of H_2O_2. The direct reduction of H_2O_2 at Fe_3O_4/GCE was hardly observed in the studied potential window (Fig. 9a), indicating the catalytic current resulted from the immobilized Hb. The mechanisms can be expressed as follows [44]:

$$Hb(Fe^{3+}) + H_2O_2 \rightarrow CompoundI(Fe^{4+}{=}O) + H_2O$$

$$CompoundI(Fe^{4+}{=}O) + e + H^+ \rightarrow CompoundII$$

$$CompoundII + e + H^+ \rightarrow Hb(Fe^{3+}) + H_2O$$

The current response was linear to the concentration of H_2O_2 in the range from 5 to 90 μmol L^{-1}. The regression equation is I (μA) = 1.59 + 0.026c (μmol L^{-1}) with a coefficient of 0.999. The sensitivity was 0.026 μA μM^{-1} and the detection limit was 5.0×10^{-7} mol L^{-1} based on S/N = 3, which was lower than that of 60 μM for a nickel oxide nanoparticles based H_2O_2 biosensor [12].

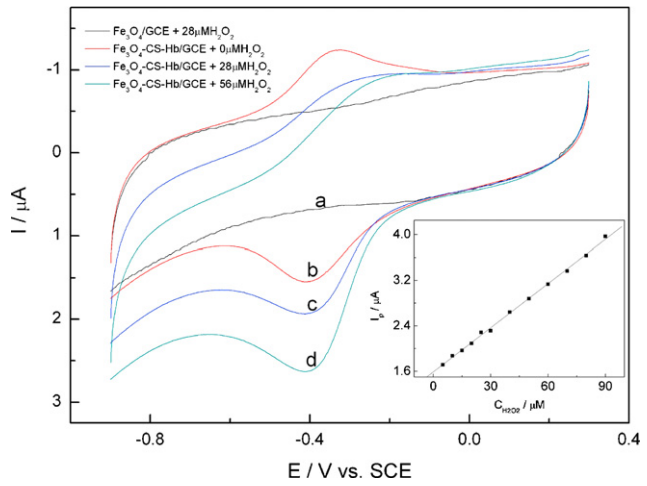

Fig. 9. Cyclic voltammograms of Fe_3O_4/GCE with 28 μM H_2O_2 (a), Fe_3O_4–CS–Hb/GCE without H_2O_2 (b) and with different H_2O_2 concentrations in 0.1 M pH 7.0 PBS at 200 mV s^{-1}: 28 μM (c) and 56 μM(d). Inset: Plot of catalytic peak current vs. the concentration of H_2O_2. Scan rate: 200 mV s^{-1}.

The electrocatalytic current (i_{cat}) linearly increased with increasing the concentration of H_2O_2 in the beginning and thereafter began to level off (Fig. 9 Inset), indicating that the relationship between i_{cat} and the concentration of H_2O_2 showed a Michaelis–Menten response. The apparent Michaelis–Menten constant (K_M^{app}), which can provide an indication of the enzyme–substrate kinetics, can be calculated according to Lineweaver–Burk equation [45]:

$$\frac{1}{I_{ss}} = \frac{1}{I_{max}} + \frac{K_M^{app}}{I_{max}C}$$

where I_{ss} is the steady-state current after the addition of substrate, C is the bulk concentration of substrate and I_{max} is the maximum current under saturated substrate solution. K_M^{app} can be obtained by the analysis of slope and intercept of the plot of the reciprocals of the steadystate current vs. H_2O_2 concentration. The Michaelis–Menten constant of the system (K_M^{app}) in this work can be calculated to be 38.1 μmol L^{-1} (calculated from the linear range in Fig. 9 Inset), implying that the Fe_3O_4–CS–Hb/GCE exhibited a higher affinity for hydrogen peroxide. As is well known the smaller K_M^{app} shows the higher catalytic ability. The value of K_M^{app} for Hb in this work was smaller than 1.4 mmol L^{-1}, the value obtained when Hb was adsorbed onto chitosan stabilized gold nanoparticles modified electrode [24], and also smaller than 83.3 μmol L^{-1} for a graphite electrode modified with a *N*,*N*-dimethylformamide film [46], which indicated that Hb entrapped in composite Fe_3O_4–CS–Hb film had good affinity to H_2O_2 and higher enzymatic activity toward H_2O_2 reduction.

3.7. *Stability and reproducibility of Fe_3O_4–CS–Hb/GCE*

We studied the storage stability of the sensor by storing it at 4 °C when not in use and measured intermittently. Eight days later the response of the composite electrode still retained its activity 92% of its initial value.

The reproducibility of the current response for the Fe_3O_4–CS–Hb/GCE was examined at a H_2O_2 concentration of 20 μM and the relative standard deviation was 2.5% for 10 independent determinations.

3.8. H_2O_2 determination in real sample

We investigated the concentration of H_2O_2 in eyedrops as real sample by means of the as-prepared H_2O_2 biosensor. The sample was diluted with pH 7.0 PBS to 30 μM. The concentration of H_2O_2 was calculated to be 29.86 μM by standard addition method. The recovery rate was calculated to be 99.5%. The result indicated that this method can be directly used to determine H_2O_2 in real samples. The phenomenon might be ascribed to the high selectivity of the biosensor.

4. Conclusions

Magnetic nanoparticles (Fe_3O_4) were successfully synthesized by a chemical coprecipitation method. It demonstrated that magnetic nanoparticles is an attractive material to immobilize Hb to achieve its direct electrochemistry on GCE. Redox peak currents increased linearly with the increase of scan rate, indicating a surface-controlled electrode process. The results indicated that Fe_3O_4–CS film was an attractive matrix to provide a favorable microenvironment for redox proteins and enzymes to undergo a facile electron transfer reaction and Hb entrapped in composite Fe_3O_4–CS–Hb film had good affinity to H_2O_2 and higher enzymatic activity toward H_2O_2 reduction. Thus it was expected to have widely potential applications in direct electrochemistry, biosensors and biocatalysis.

Acknowledgments

This work was supported by the National Natural Science Foundation of China (20775088) and the Foundation of State Key Laboratory of Environmental Chemistry and Ecotoxicology, Research Center for Eco-Environmental Sciences, Chinese Academy of Sciences (KF2008-06).

References

[1] J.F. Rusling, Acc. Chem. Res. 31 (1998) 363.
[2] F.A. Armstrong, G.S. Wilson, Electrochim. Acta 45 (2000) 2623.
[3] A. Heller, Acc. Chem. Res. 23 (1990) 128.
[4] S.F. Hou, K.S. Yang, H.Q. Fang, H.Y. Chen, Talanta 47 (1998) 561.
[5] L.N. Wu, M. McIntosh, X.J. Zhang, H.X. Ju, Talanta 74 (2007) 387.
[6] L.Z. Yang, H.Y. Liu, N.F. Hu, Electrochem. Commun. 9 (2007) 1057.
[7] D. Du, X. Huang, J. Cai, A.D. Zhang, J.W. Ding, S.Z. Chen, Anal. Bioanal. Chem. 387 (2007) 1059.
[8] J. Yang, N. Hu, Bioelectrochem. Bioenergy 48 (1999) 117.
[9] L. Shen, R. Huang, N.F. Hu, Talanta 56 (2002) 1131.
[10] H. Liu, N. Hu, Anal. Chim. Acta 481 (2003) 91.
[11] Y. Zhou, N. Hu, Y. Zeng, J.F. Rusling, Langmuir 18 (2002) 211.
[12] A. Salimi, E. Sharifi, A. Noorbakhsh, S. Soltanian, Electrochem. Commun. 8 (2006) 1499.
[13] G.L. Luque, M.C. Rodríguez, G.A. Rivas, Talanta 66 (2005) 467.
[14] Y.L. Liu, Y.H. Yang, H.F. Yang, Z.M. Liu, G.L. Shen, R.Q. Yu, J. Inorg. Biochem. 99 (2005) 2046.
[15] E. Topoglidis, C.J. Campbell, A.E.G. Cass, J.R. Durrani, Electroanalysis 18 (2006) 882.
[16] G. Zhao, J.J. Feng, J.J. Xu, H.Y. Chen, Electrochem. Commun. 7 (2005) 724.
[17] D.H. Chen, M.H. Liao, J. Mol, Catal. B Enzym. 16 (2002) 283.
[18] D. Cao, P. He, N. Hu, Analyst 128 (2003) 1268.
[19] P.A. Dresco, V.S. Zaitsev, R.J. Gambino, B. Chu, Langmuir 15 (1999) (1945).
[20] R.V. Mehta, R.V. Upadhyay, S.W. Charles, C.N. Ramchand, Biotechnol. Tech. 11 (1997) 493.
[21] M. Koneracka, P. Kopcansky, M. Antalik, M. Timko, C.N. Ramchand, D. Lobo, R.V. Mehta, R.V. Upadhyay, J. Magn. Magn. Mater. 201 (1999) 427.
[22] J. Dobson, FEBS Lett. 496 (2001) 1.
[23] P.P. Schultheiss-Grassi, R. Wessiken, J. Dobson, Biochim. Biophys. Acta 1426 (1999) 212.
[24] J.J. Feng, G. Zhao, J.J. Xu, H.Y. Chen, Anal. Biochem. 342 (2005) 280.
[25] E. Renbutsu, M. Hirose, Y. Omura, F. Nakatsubo, Y. Okamura, Y. Okamoto, H. Saimoto, Y. Shigemasa, S. Minami, Biomacromolecules 65 (2005) 2385.
[26] X.L. Luo, J.J. Xu, Y. Du, Anal. Biochem. 334 (2004) 284.
[27] Y. Zhou, H. Yang, H.Y. Chen, Talanta 76 (2008) 419.
[28] X.B. Lu, J.Q. Hu, X. Yao, Z.P. Wang, J.H. Li, Biomacromolecules 7 (2006) 975.
[29] H. Okuma, E. Watanabe, Biosens. Bioelectron. 17 (2002) 367.
[30] S.H. Baek, B. Kim, K.D. Suh, Colloids Surf. A: Physicochem. Eng. Aspects 316 (2008) 292.
[31] S. Ogawa, E.A. Decker, D.J. McClements, J. Agric. Food Chem. 52 (2004) 3595.
[32] G.D. Mendenhall, Y. Geng, J. Hwang, J. Colloid Interface Sci. 184 (1996) 519.
[33] J.J. Huang, Z.S. Xu, C.F. Yi, J. Hubei Univ. Nat. Sci. 291 (2007) 50.
[34] Z.H. Chi, S.A. Asher, Biochemistry 37 (1998) 2865.
[35] J.K. Kauppinen, D.J. Moffate, H.H. Mantsch, D.G. Lameron, Appl. Spectrosc. 35 (1981) 271.
[36] C.C. Silva, H.H.B. Rocha, F.N.A. Freire, M.R.P. Santos, K.D.A. Saboia, J.C. Goes, A.S.B. Sombra, Mater. Chem. Phys. 92 (2005) 260.
[37] E. Laviron, J. Electroanal. Chem. 101 (1979) 19.
[38] E. Laviron, J. Electroanal. Chem 100 (1979) 263.
[39] H.Y. Gu, A.M. Yu, H.Y. Chen, J. Electroanal. Chem. 516 (2001) 119.
[40] Y.D. Zhao, Y.H. Bi, W.D. Zhang, Q.M. Luo, Talanta 65 (2005) 489.
[41] A.M. Bond, Modern Polarographic Methods in Analytical Chemistry, Dekker, New York, 1980, p. 29.
[42] I. Yamazaki, T. Araiso, Y. Hayashi, H. Yamada, R. Makino, Adv. Biophys. 11 (1978) 249.
[43] C.P. Andrieux, C. Blocman, J.M. Fumas-Bouchiant, F.M. Halla, J.M. Saveant, J. Electroanal. Chem. 113 (1980) 19.
[44] H.Y. Xiao, H.X. Lu, H.Y. Chen, Anal. Biochem. 278 (2000) 22.
[45] J. Li, S.N. Tan, H. Ge, Anal. Chim. Acta 335 (1996) 137.
[46] Y.X. Xu, F. Wang, X.X. Chen, S.S. Hu, Talanta 70 (2006) 651.

Talanta 79 (2009) 893–899

Contents lists available at ScienceDirect

Talanta

journal homepage: www.elsevier.com/locate/talanta

Indirect chemiluminescence-based detection of mefenamic acid in pharmaceutical formulations by flow injection analysis and effect of gold nanocatalysts

Evangelos G. Zisimopoulos, George Z. Tsogas, Dimosthenis L. Giokas, Nikolaos I. Kapakoglou, Athanasios G. Vlessidis*

Laboratory of Analytical Chemistry, Department of Chemistry, University of Ioannina, 45110-Ioannina, Greece

ARTICLE INFO

Article history:
Received 4 March 2009
Received in revised form 7 May 2009
Accepted 13 May 2009
Available online 22 May 2009

Keywords:
Mefenamic acid
Chemiluminescence
Luminol
Pyrogallol
Gold nanoparticles
Periodate

ABSTRACT

A highly sensitive flow injection-chemiluminescence detection (FI-CL) method based on periodate oxidation of two popular luminescent compounds for the determination of mefenamic acid (MFA) is presented. The method is an indirect CL detection method based on the CL emission generated during the oxidation of Pyrogallol (Pg) or Luminol (Lu) with the excess of periodate that remains after oxidation of MFA within the time period of 15 min. The MFA calibration curves obtained with either luminescent compounds were linear over a wide concentration range, depending on the system employed, offering detection limits in the range of low to ultra-low $\mu g\,L^{-1}$ levels. Gold nanoparticles (Au-NPs) were also assessed as means for enhancing the CL signal. Pg-periodate was not affected by the presence of gold nanocatalysts as opposed to Lu-periodate CL signal which exhibited a significant increase in the presence of citrate synthesized Au-NPs. The reproducibility of the method, expressed by the relative standard deviation (R.S.D.), was very satisfactory and always below 5% as evidenced by repeated measurements ($n \geq 10$) of standard solutions at two concentration levels (2 and 20 $\mu g\,L^{-1}$).

1. Introduction

Mefenamic acid (MFA), *N*-(2,3-xylyl)anthranilic acid is a non-steroidal anti-inflammatory drug (NSAID) used as potent analgesic and anti-inflammatory agent in the treatment of osteoarthritis, rheumatoid arthritis and other painful musculosketal illnesses [1]. Due to its widespread use, extensive literature regarding its determination in pharmaceutical formulations and biological fluids has been published involving the use of various techniques like titrimetric analysis [2], proton nuclear magnetic resonance (PNMR) [3], atomic absorption spectrometry [4], spectrophotometry [5,6], fluorimetry [7,8] and liquid chromatography (LC) [9,10].

Although a growing number of publications employing chemiluminescence (CL) as a detection approach in pharmaceutical and clinical analysis have been presented [11–16], to the best of our knowledge, only one study has been devoted to the determination of MFA with this technique [17]. In these study, the determination is based on direct CL emission produced from the electronic excitation (oxidation) of MFA in the presence of $Ru(bipy)_3^{3+}$ and acidic cerium(IV) sulphate, affording good analytical characteristics and enabling the determination of MFA at concentrations as low as 50 $\mu g\,L^{-1}$. However, CL detection using appropriate luminescent compounds like luminol, pyrogallol, lucigenin, peroxyoxalate etc, has been shown, in several occasions, to provide a considerable improvement in the analytical features of a CL method, especially with regards to the detection limits, owing to the high signals emitted during the oxidation of these highly luminescent compounds [16,18–21]. To exploit these features the selected oxidant must be able to oxidize the target analyte thus provide an estimate of its concentration based on the CL signal emitted from the excitation of the selected luminescent compound from the remaining amount of oxidant.

Over the last years, a new approach to enhance the analytical detection limits of CL reactions based on the catalytic effect of metal nanoparticles has received considerable attention. Especially when combined with luminescent species that produce an intense light signal upon their oxidation, like luminol, a significant enhancement in the CL signal can be attained which can be exploited towards the trace determination of various analytes [22–24]. In essence, the enhancement of CL emission is based on the interaction of catalyst nanoparticle surface with the reactants or the intermediates of the CL reactions between the luminescent compound and the oxidant which facilitates the radical generation and electron-transfer processes taking place on the surface of the gold nanoparticles.

* Corresponding author. Tel.: +30 26510 98401; fax: +30 26510 98781.
E-mail address: avlessid@cc.uoi.gr (A.G. Vlessidis).

0039-9140/$ – see front matter © 2009 Elsevier B.V. All rights reserved.
doi:10.1016/j.talanta.2009.05.024

Since surface-mediated reactions occur size [22–25] and the surface modification of the metal nanoparticles [25] are crucial in the observed signal. However, citrate capped nanoparticles are usually exploited in luminol-oxidant solutions [22,23] which renders the reactivity with other luminescent compounds and other nanoparticle synthetic procedures an issue that merits further investigation.

Motivated by the lack of published work on the CL determination of MFA, an indirect determination approach was developed based on the CL emission generated during the on-line oxidation of two popular luminescence compounds, namely luminol and pyrogallol, with the excess of periodate that remains after off-line oxidation of MFA. The results show a considerable improvement in the detection limits as compared to direct CL generated from MFA oxidation. The optimum experimental conditions for the analytical determination of MFA were investigated and the influence of colloidal dispersions of nano-sized gold particles, synthesized with various procedures was assessed. The results suggest that the influence of gold nanocatalysts as means for enhancing the analytical signal depend both on the synthetic procedure adopted for the preparation of gold colloids as well as on the luminescent compound employed for the generation of the CL emission signal. Under the optimum experimental conditions, the method was successfully applied to the determination of MFA in commercial pharmaceutical formulations.

2. Experimental

2.1. Reagents and materials

All reagents were of analytical grade unless otherwise stated. Mefenamic acid (MFA) (Sigma, St. Louis, USA), Pyrogallol (Pg) (Merck, Darmstadt, Germany), hydroxylamine-hydrochloride (Hx) (Merck) and Luminol (Lu) (Merck) were used as purchased without any further purification. Buffer solutions of KH_2PO_4–NaOH (Sigma) (pH 8.00) were prepared by dissolving a tenth of the formula weight of the corresponding salts in water and diluting to 900 mL, adjusting to the desired pH by the addition of 1 M NaOH titrisol solution (Merck) and making up to 1 L with distilled water. Oxidant stock solutions of potassium periodate (KIO_4) (Fluka Chemie AG, Switzerland), were prepared by dissolving 2.3000 g in buffer solution and further diluting to 1.0 L. Gold (III) chloride trihydrate ($HAuCl_4{\cdot}3H_2O$, 99.9%) (Sigma), tri-sodium citrate (>99.0%) (DBH Poole, Dorset, UK), sodium borohydride ($NaBH_4$, >96%) (Fluka), ascorbic acid (Merck) and cetyltrimethyammonium bromide (CTAB) (Merck) used for the synthesis of gold nanoparticles were employed as purchased.

Stock solution of 100 mg L^{-1} MFA, was prepared by dissolving the appropriate amount in HPLC grade ethanol (Merck) and stored in the refrigerator at 4 °C, protected from the light. Working solutions of MFA were prepared by appropriate dilution in water:ethanol (2:1). Working solutions of 2.5×10^{-3} M KIO_4 were prepared by appropriate dilution in the buffer medium (pH 8). Working solutions of Lu (1×10^{-3} M) and Pg (0.5×10^{-3} M) were prepared daily by dissolving appropriate amounts in 0.1 M NaOH and distilled water, respectively.

2.2. Apparatus

A F.I.A. manifold equipped with a flow-cell CL-detector was used throughout the study (Fig. 1a). The reagents were pumped through with the aid of a peristaltic pump (Gilson, Minipuls 3). The red sensitive photomultiplier (Thorn, EMI 9865 B) combined with power supply at 1400 kV was used for detecting the emission of light. A conventional recorder (Linear 1200), was used for recording the CL-signals. A pH meter (WTW 552 Model) equipped with a glass electrode, was employed to measure the pH values of the buffer solutions.

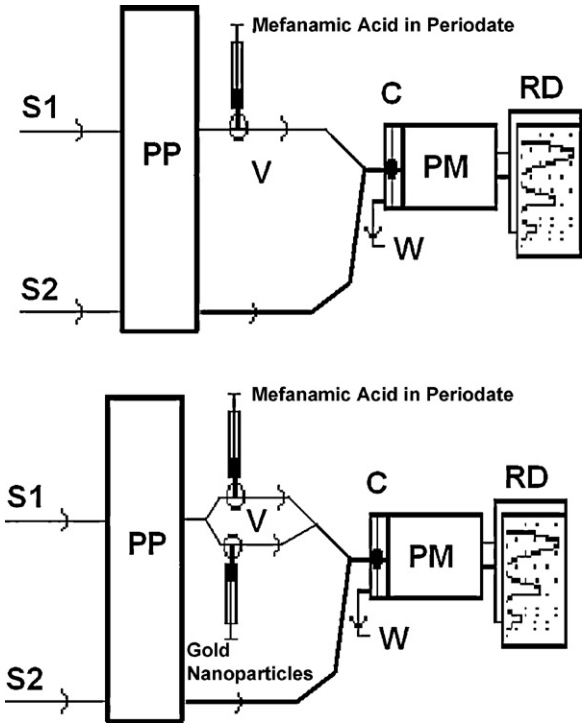

Fig. 1. Schematic diagram of the FI-apparatus employed for the measurements. S1: carrier stream (buffer solution), S2: chemiluminescence reagent (Pg or Lu), PP: peristaltic pump, V: injection valve, C: CL flow-through cell, W: cell wastes, PM: photomultiplier, RD: recorder.

In order to incorporate GNPs in the flow injection-CL manifold, the carrier stream was split into two streams; in the first stream the MFA oxidized solution was injected through a 100 μL loop while in the second gold nanoparticle solution was injected through a 500 μL loop. Both loops were opened simultaneously with the aid of an automated switch controller and they were merged with CL-reagent stream just in front of the CL-cell (Fig. 1b).

2.3. Synthesis of gold nanoparticles

Gold nanoparticles (Au-NPs) of ca. 4 nm were prepared following the procedure of Jana et al. (2001) [26]. Briefly, $HAuCl_4{\cdot}3H_2O$ (1.0×10^{-2} M, 0.5 mL) and tri-sodium citrate (0.01 M, 0.5 mL) were added to doubly distilled water (18.5 mL) and stirred for 5 min followed by the addition of $NaBH_4$ (0.1 M, 0.5 mL).

Colloids of larger diameter were synthesized following two different procedures. In the first, 16 nm diameter gold colloids were prepared by the citrate reduction method by boiling a 50 mL solution of $HAuCl_4$ (10^{-2}%, w/w). Subsequently, 1 mL of 1% trisodium citrate was added rapidly under vigorous stirring and the solution was maintained at the boiling point for 15 min. The heating source was removed and the colloid was cooled at room temperature [27].

In the second procedure, gold nanoparticles of diameters 5–18 nm (±10–15% standard deviation) were prepared from 4 nm gold particle seeds using the seeding growth approach [26,28]. Briefly, a growth solution consisting of 200 mL of a 0.1 M solution of the surfactant, cetyltrimethylammonium bromide (CTAB) in water, and 5 mL of a 1×10^{-2} M $HAuCl_4$ solution was prepared. Three Erlenmeyer flasks (25 mL) were taken and labelled A, B, and C. In each flask, 9 mL of the growth solution was placed and 50 mL of a 0.1 M ascorbic acid solution in water was added. To flask A, 2.5 mL of the ca. 4 nm gold seeds were added, and the solution was stirred for 10 min, resulting in 5.5 ± 0.6 nm gold nanoparticles. To flask B, 2.5 mL of the particles in flask A were added to the contents

of the flask, and stirring took place for 10 min. The nanoparticles prepared in this manner were 8.0 ± 0.8 nm in diameter. To flask C, 1.0 mL of the solution from flask B was added, and the solution was stirred vigorously for 10 min, resulting in ca. 18 nm particles (17.0 ± 2.5 nm).

2.4. Samples and sample pre-treatment

Commercial pharmaceutical formulations (syrup, capsules and suppository) were purchased from local pharmacies and stored according to the instructions of the manufacturer. Before analysis the samples were diluted to 200 mL of HPLC grade ethanol, mixed and left to stand for 10 min protected from light at room temperature. The mixture was centrifuged at 4000 rpm for 10 min and 10 mL from the supernatant ethanolic extract containing MFA were withdrawn with the aid of a Pasteur pipette. Additional dilution, which was necessary to bring MFA concentration within the measuring range of the established calibration curves, was performed in water: ethanol (2:1) mixture.

2.5. Analytical procedure

An 1.0 mL aliquot of the diluted sample containing MFA was mixed with 9.0 mL of 2.5×10^{-3} M potassium periodate solution into a small vial and the mixture was left to react at room temperature for 15 min with periodic mixing. The MFA oxidized solution was injected into the carrier stream (buffer solution) through a 100 μL sampling valve merged with CL-reagent stream (Pg or Lu) just in front of the CL-cell (Fig. 1). The generated CL-emission was detected by a red sensitive photomultiplier tube. The recorded CL-signal, was attributed to the oxidation of Pg (or Lu) from the excess of periodate that remains after the oxidation of MFA in the initial solution.

3. Results and discussion

3.1. Effect of CL-reagent concentration

Preliminary attempts to optimize CL reagents concentration showed that the CL emission of Pg-IO_4^- was very weak compared to that of Lu-IO_4^-. To overcome this drawback hydroxylamine (Hx) was added to the Pg-IO_4^- system leading to the formation of the condensation product Pg–Hx, which acts as a sensitizer in the oxidation of Pg with IO_4^- [29]. Evidently, a considerable signal increase was observed with maximum at 1 mM Hx while at higher concentration no further gains are attained (inset graph Fig. 2).

The effect of Pg and Lu concentration on the CL emission signal was then investigated in the range of 0.25–3.0 mM. The results depicted in Fig. 2 show that the signal soars up to 0.5 mM for Pg and 1.0 mM for Lu and gradually levels off at higher concentrations due to the inner filter effect [30].

3.2. Effect of pH value

CL-emission is sensitive to changes in pH as determined by the effective pH-range of the oxidant and by the nature of CL-reagent [6]. The influence of pH on the CL emission of both systems was investigated and the results are gathered in Fig. 3. For the Pg-IO_4^- system a continuous increase in the pH range of 2.0–8.0 was observed, reaching a maximum at pH 8.0 while for Lu-IO_4^- system the optimum pH is observed at strongly alkaline conditions (pH ≈ 12.5). These results are in concurrence with previous findings [29,30] suggesting that no other pH-depended reactions occur due to the presence of MFA and its oxidation by-products in the sample mixture. Not surprisingly, the pH dependence of the CL signal in the Pg-IO_4^--Hx system follows the same pattern as Pg-IO_4^- since the effect of Hx is attributed to the decrease in the inner filter effect with the increase in Hx due to dilution of the quenching CL species [29].

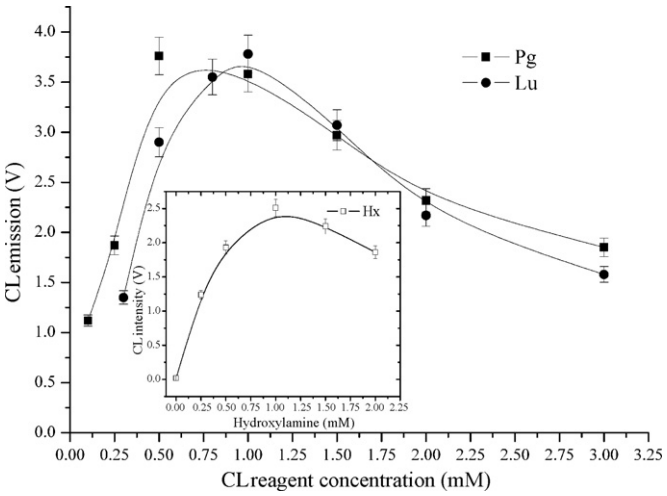

Fig. 2. Effect of pyrogallol and luminol concentration on the CL signal. [IO_4^-] = 2.0 mM, flow rate = 1.5 mL min^{-1}, pH 8.0 for Pg-IO_4^- (pH 12.5 for Lu-IO_4^-), [Hx] = 1 mM (in Pg only), PMT voltage = 1400 kV.

3.3. Effect of periodate concentration

The concentration of oxidant plays a predominant role in the generation of the CL signal and determines not only the signal intensity but also the reaction kinetics in the CL cell. Fig. 4 depicts the influence of increasing periodate concentration on the CL signal of Pg and Lu. In the Pg-IO_4^- system, signal increases with periodate concentration up to 3.0 mM, above which it exceeds the dynamic measuring range of the detector. On the other hand, although Lu signal exhibits a similar pattern it reaches a plateau above 2.5 mM IO_4^-. Based on these observations and in order to reduce the uncertainty of measurements when working at the upper limit of the measuring range of the detector, the value of 2.5 mM IO_4^- was selected as optimum and used throughout the remaining work.

3.4. Effect of reaction time

The incubation time of MFA with the oxidant (IO_4^-) at room temperature, before entering the F.I.A. layout, was a critical parameter in

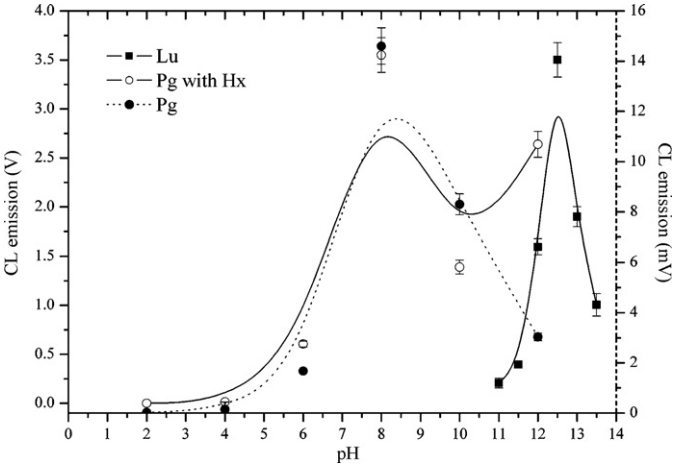

Fig. 3. CL signal intensity as a function of pH. [IO_4^-] = 2.0 × 10^{-3} M, [Pg] = 0.5 mM (incl. 1 mM Hx), [Lu] = 1 mM, flow rate = 1.5 mL min^{-1}, PMT voltage = 1400 kV. Dot line corresponds to right *Y*-axis.

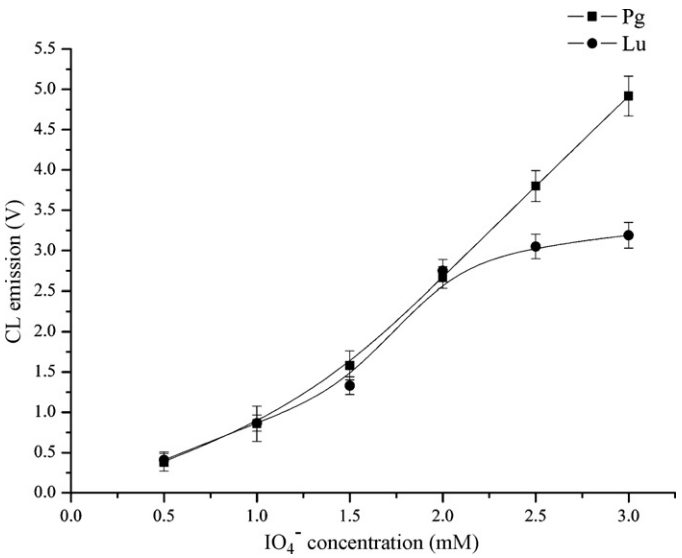

Fig. 4. CL intensity *vs.* oxidant (periodate) concentration. [Pg] = 0.5 mM (incl. 1 mM Hx), [Lu] = 1 mM, pH 8.0 for Pg-IO_4^- (pH 12.5 for Lu-IO_4^-), flow rate = 1.5 mL min^{-1}, PMT voltage = 1400 kV.

the determination of MFA with both CL reagents since it determines the CL emission according to the excess of periodate. The optimum reaction time was assessed in the range of 1–60 min. The kinetic profile of Fig. 5 shows that MFA oxidation consumes periodate and reaches a plateau at 7 min which is maintained up to 15 min. At longer incubation times the signal slightly increases, suggesting the formation of by-products that enhance the CL signal. However, the reproducibility of the measurements is deteriorated indicating that these reactions proceed very slowly and are not completed within a time span of 60 min which increases CL signal variability. Considering the fact that no significant gains are attained at incubation times longer than 15 min, this value was selected for the remaining work in order to ensure the reproducibility of the measurements and abridge the experimental analysis time.

3.5. Effect of flow rate

In FIA/CL-detection systems flow rate is a crucial parameter that determines the CL-reaction time. Therefore flow rate must be regulated in such a way, that the CL reaction is completed before the excited product enters the flow cell, thus having no loss of the emitted light and generate the maximum signal. The results of Fig. 6 show that the Pg-IO_4^- system yields its maximum signal 1.70 mL min^{-1}, while the Lu-IO_4^- exhibits a stable response.

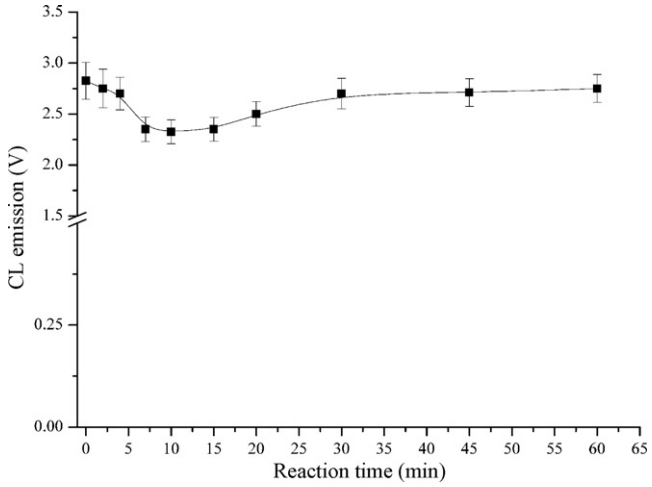

Fig. 5. Kinetic profile of MFA oxidation with periodate. [MFA] = 20 μg L^{-1}, [Pg] = 0.5 mM (incl. 1 mM Hx), pH 8.0, flow rate = 1.5 mL min^{-1}, PMT voltage = 1400 kV.

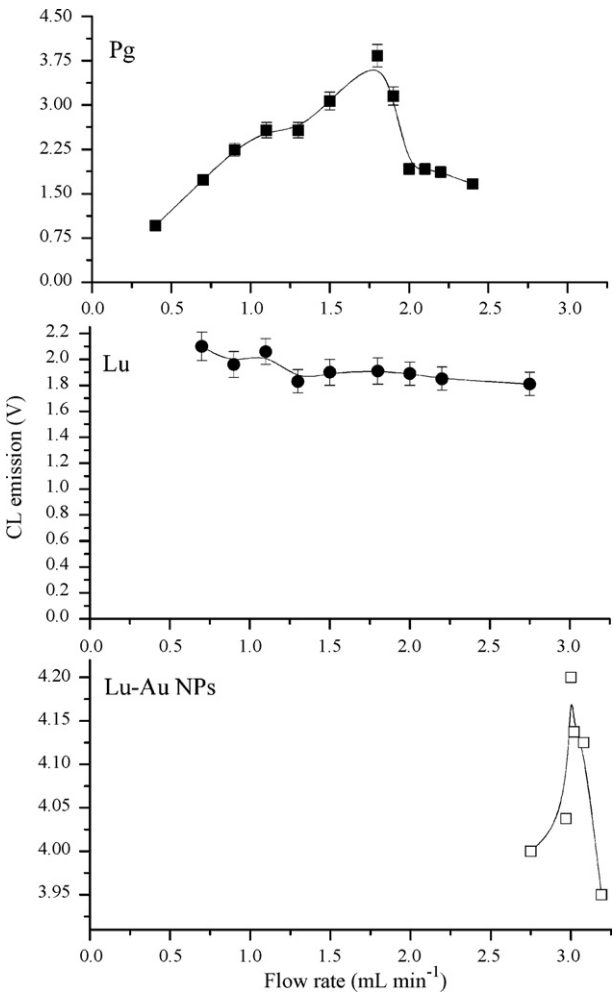

Fig. 6. Effect of flow rate on the CL signal. [Pg] = 0.5 mM (incl. 1 mM Hx), [Lu] = 1 mM, pH 8.0 for Pg-IO_4^- (pH 12.5 for Lu-IO_4^-), PMT voltage = 1400 kV.

3.6. Effect of sample volume

The variation of CL intensity with the injected sample volume was studied in the range of 50–500 μL. The results showed that higher CL intensity was obtained by increasing sample volumes up to about 100 μL. Further increase in sample volume had no significant effect on CL intensity. Thus, a 100 μL sample loop was selected for subsequent experiments.

3.7. Effect of the photomultiplier (PMT) voltage

A relatively high sensitivity with low noise level was obtained using a PMT voltage in the range of 1300–1400 kV. The value of 1400 kV was selected as the optimal one to obtain maximum sensitivity, with the minimum background noise.

3.8. Effect of gold nanoparticles

Gold nanoparticles (Au-NPs) were assessed as means for catalyzing the chemiluminescence reactions thus increase the intensity

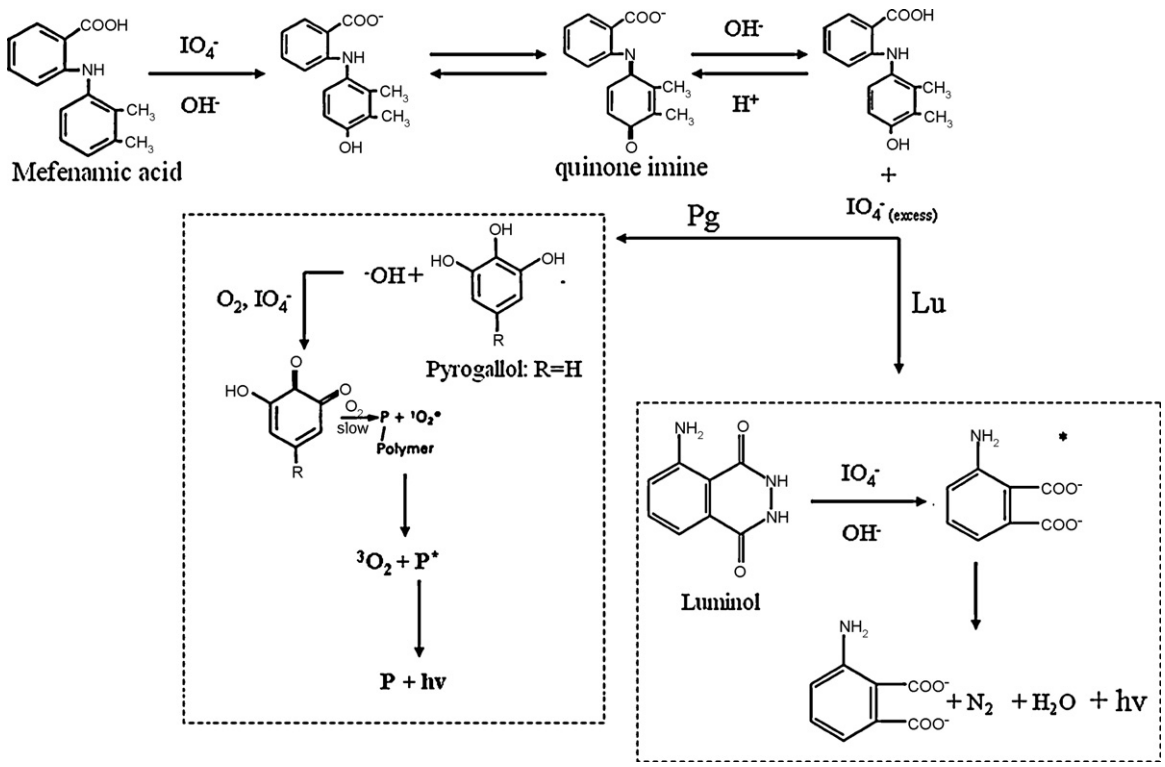

Fig. 7. Proposed reaction pathways involved in the determination of MFA with periodate and Pyrogallol (Pg) or Luminol (Lu) chemiluminescence.

of the CL-signal. Colloidal Au-NPs with diameters of 4–18 nm synthesized according to different procedures in order to assess the influence of the synthetic procedure on the CL response.

Au-NPs synthesized either with the CTAB seeding growth approach or with the citrate reduction method did not have any effect on the analytical signal of Pg-IO_4^- irrespectively of nanoparticle size and concentration. On the other hand, the CL-emission of the Lu-IO_4^- system strongly depended on the synthetic procedure. Au-NPs synthesized with the CTAB seeding growth approach deteriorated the analytical signal and completely quenched any CL emission at higher nanoparticle concentration. This behavior is contradictory to the catalytic effect of Au NPs [22–24] and it was attributed to the excess of CTAB in the Au-NP solution mixture. Experiments with increasing CTAB concentration (in the absence of Au-NPs) verified the validity of this assumption and completely quenched the CL signal at concentrations up to the critical micellar concentration (c.m.c. = approx. 1 mM). This is attributed to the formation of ion-association complexes between the excited 3-aminophthalate dianion and the cationic surfactant [31]. However, the concentration of CTAB from the synthetic procedure was significantly higher (0.1 M). In aqueous solutions, concentrations higher than the c.m.c. enhance the analytical signal because the excited species, 3-aminophthalate ions, could be concentrated in the Stern zone of the CTAB micelle and thus cause an enhancement in CL intensity [31]. However, most of the CTAB was located on the Au-NPs surface which probably masked their catalytic effect on the Lu-IO_4^- signal while free CTAB could form ion pairs with 3-aminophthalate dianion thus quench the CL signal. This phenomenon is more evident at nanoparticles of smaller size. Approximately half amount of 8 nm Au-NPs was adequate to completely quench the CL signal compared to 16 nm size nanoparticles.

On the other hand, a completely different response was observed when Au-NPs synthesized with the citrate reduction method were employed. In concurrence with previous studies, a significant enhancement in the CL signal was observed. The experimental parameters in the presence of citrate synthesized Au-NPs were re-assessed involving nanoparticle size and concentration, volume injected into the carrier stream and flow rate. The results revealed that optimum CL signals were observed by injecting 500 μL from a 2-fold diluted solution containing 4 nm sized Au-NPs. More concentrated solutions increased the CL signal above 5 V which was the upper measuring range of the detector while lower injection volumes or larger nanoparticles produced weaker signals. Interestingly, the optimum signal was observed at a flow rate of 3.00 mL min^{-1} suggesting an increase in the reaction kinetics (Fig. 6c). Therefore, it can be concluded that the enhancement effect of Au-NPs is due to their catalytic action and not because of their involvement in the chemical reactions.

3.9. Reaction mechanisms

The reaction mechanisms involved in the proposed method are summarized in Fig. 7. Periodate react with MFA towards the formation of a quinine imine structure which is stable at the alkaline conditions applied [32,33]. The excess of periodate remaining after its consumption by MFA react either with luminol or prygallol according to the reaction pathways depicted in Fig. 7 [29,34,35].

3.10. Analytical parameters

Under the optimum experimental conditions, the analytical features of each method were calculated and the results are summarized in Table 1. The detection limits, calculated as $LOD_{(3\sigma)}$ where $3\sigma = [(3 \times \text{noise})/\text{slope}]$ were significantly low especially when compared to previous methods employing direct oxidation of MFA and measurement of the emitted CL signal. [17]; this is favourable when high dilution of samples is necessary to eliminate matrix effects. The reproducibility of the measurements, estimated by the relative standard deviation of multiple measurements, was very satisfactory and always below 5%.

Table 1
Analytical features of the method for the determination of mefenamic acid.

	Pg-IO_4	Lu-IO_4	Lu-IO_4-Au NPs
Calibration curve	CL (mV) = 3.24(±0.017) − 0.024(±6 × 10^{-4}) × C_{MFA}	CL (mV) = 2.20(±0.047) − 0.213(±0.017) × C_{MFA}	CL (mV) = 3.43(±0.01) − 0.183(±0.004) × C_{MFA}
Linearity (R^2)	0.9988	0.9981	0.9979
LOD (μg L^{-1})	2.10	0.67	0.16
LOQ (10S/N)	7.00	2.23	0.53
R.S.D. (%)	2.22 (n = 10, C = 20 μg L^{-1})	3.78 (n = 10, C = 20 μg L^{-1})	4.06 (n = 15, C = 2 μg L^{-1})

Table 2
Determination of mefenamic acid in real samples.

Sample	Method	Measured (±SD)[a] (μg L^{-1})	Expected (μg L^{-1})[b]	%Recovery (±SD)
Syrup	Pg-IO_4	19.77 ± 0.07	20.0	98.8 ± 0.5
	Lu-IO_4	19.56 ± 0.08	20.0	97.8 ± 0.4
	Lu-IO_4-Au NPs	19.46 ± 0.28	20.0	97.3 ± 1.3
Capsules	Pg-IO_4	19.65 ± 0.10	20.0	98.2 ± 0.4
	Lu-IO_4	19.36 ± 0.08	20.0	96.8 ± 0.4
	Lu-IO_4-Au NPs	19.71 ± 0.09	20.0	98.5 ± 0.5
Suppository	Pg-IO_4	20.19 ± 0.13	20.0	100.9 ± 0.5
	Lu-IO_4	20.36 ± 0.28	20.0	101.8 ± 0.8
	Lu-IO_4-Au NPs	20.81 ± 0.32	20.0	104.5 ± 1.0

[a] Average of five measurements ± standard deviation.
[b] Expected value based on dilutions.

3.11. Interferences

The effect of various foreign species on the determination of MFA was investigated considering the tolerance limit of a foreign species as the concentration that causes a relative error greater than ±5% in the recovery of 20 μg L^{-1} MFA. No interference was observed for 100-fold excess of K^+, Na^+, Ca^{2+}, Mg^{2+}, Al^{3+}, $SO_3{}^-$, $NO_3{}^-$, $MoO_4{}^{2-}$, ascorbic acid, urea, glucose, fructose, lactose, sucrose, starch and citric acid and 50-fold excess of $SO_4{}^{2-}$, Cu^{2+} and Fe^{3+}. However, $NO_2{}^-$ and Cr^{3+} were found to interfere with the analysis when present at concentrations higher than 5 times the concentration of MFA due to the fact that these species may be oxidized to $NO_3{}^-$ and $CrO_4{}^{2-}$ respectively. However, $NO_2{}^-$ and Cr^{3+} are unlike to co-exist in commercial mixtures of MFA. Since the recorded CL-signal stems from the excess of periodate that remains after the oxidation of MFA in the initial solution, higher tolerance ratio's can be attained by regulating the relative excess of periodate in the MFA oxidation mixture.

3.12. Application in real samples

The determination of MFA with the aid of indirect CL detection was pursued in various pharmaceutical formulations. The data gathered in Table 2 show satisfactory agreement between measured and expected values in various samples. The presence of excipients in syrup and capsules pose as no threat to the determination of MFA although some of the excipients contained in suppository samples seem to induce positive interferences. However, the magnitude of these interferences was not statistically significant at the 95% probability level as evidenced by Student t-test analysis among the three methods and the expected values.

4. Conclusions

In this work, an indirect CL detection method based on the CL emission generated during the oxidation of pyrogallol or luminol with the excess of periodate that remains after oxidation of mefenamic acid is presented. The results suggest that indirect CL offers a considerable improvement in the sensitivity of the analysis of mefenamic acid with very good reproducibility. The effect of gold nanocatalysts as means for enhancing the analytical signal was found to depend on the synthetic procedure adopted for the preparation of gold colloids when the CL signal was emitted from Lu oxidation but was indifferent to the mechanism of Pg oxidation. Under the optimum experimental conditions, the determination of MFA with three different indirect CL methods was demonstrated with very satisfactory results and detection limits in the range of low to ultra-low μg L^{-1} levels. This is advantageous for pharmaceutical and clinical analysis because it enables high dilution of the sample in order to minimize potential matrix effects.

References

[1] Martindale, in: J.E.F. Reynolds (Ed.), The Extra Pharmacopoeia, 31st Edition, The Pharmaceutical Press, London, 1996.
[2] F.A. Aly, F. Belal, Pharmazie 49 (1994) 454.
[3] O.A. Mansour, M.F. Metwally, S.M. Sakr, M.I. Al-Ashmawi, Spectrosc. Lett. 23 (1990) 801.
[4] H. Salem, A.A. Kheir, Anal. Lett. 28 (1995) 1833.
[5] M.H. Abdel-Hay, M.A. Korany, M.M. Bedair, A.A. Gazy, Anal. Lett. 23 (1990) 281.
[6] C.S.P. Sastry, A.S.R.P. Tipirneni, M.V. Suryanarayana, Microchem. J. 39 (1989) 277.
[7] T. Perez-Ruiz, C. Martinez-Lozano, V. Tomás, J. Carpena, Talanta 47 (1998) 537.
[8] S.M. Sabry, Anal. Chim. Acta 367 (1998) 41.
[9] I.N. Papadoyannis, A.C. Zotou, V.F. Samanidou, J. Liquid Chromatogr. 15 (1992) 1923.
[10] A.K. Singh, Y. Jang, U. Mishra, K. Granley, J. Chromatogr. Biomed. Appl. 106 (1991) 351.
[11] A.C. Calokerinos, N.T. Deftereos, W.R.G. Baeyens, J. Pharm. Biomed. Anal. 13 (1995) 1063.
[12] K. Dai, A.G. Vlessidis, N.P. Evmiridis, Talanta 59 (2003) 55.
[13] G.Z. Tsogas, D.V. Stergiou, A.G. Vlessidis, N.P. Evmiridis, Anal. Chim. Acta 541 (2005) 151.
[14] B. Gomez-Taylor, M. Palomeque, J.V. Garcıa Mateo, J. Martınez Calatayud, J. Pharm. Biomed. Anal. 41 (2006) 347.
[15] D.L. Giokas, A.G. Vlessidis, N.P. Evmiridis, Anal. Chim. Acta 589 (2007) 59.
[16] K. Mervartova, M. Polasek, J.M. Calatayud, J. Pharm. Biomed. Anal. 45 (2007) 367.
[17] F.A. Aly, S.A. Al-Tamimi, A.A. Alwarthan, Anal. Chim. Acta 416 (2000) 87.
[18] M. Tsunoda, K. Imai, Anal. Chim. Acta 541 (2005) 13.
[19] L. Gámiz-Gracia, A.M. Garcıïa-Campaña, J.J. Soto-Chinchilla, J.F. Huertas-Pérez, A. González-Casado, TrAC Trends Anal. Chem. 24 (2005) 927.
[20] C. Lu, G. Song, J.M. Lin, TrAC Trends Anal. Chem. 25 (2006) 985.
[21] M. Sarahmetolu, R.A. Wheatley, C. Çakc, I. Kanzk, A. Townshend, Anal. Lett. 36 (2003) 749.
[22] Z.F. Zhang, H. Cui, C.Z. Lai, L.J. Liu, Anal. Chem. 77 (2005) 3324.
[23] H. Cui, Z.F. Zhang, M.J. Shi, J. Phys. Chem. B 109 (2005) 3099.
[24] P. Bertoncello, R.J. Forster, Biosens. Bioelectron. (2008), doi:10.1016/j.bios.2009.02.013.
[25] S.L. Xu, H. Cui, Luminescence 22 (2007) 77.
[26] N.R. Jana, L. Gearheart, C.J. Murphy, Langmuir 17 (2001) 6782.
[27] S. Li, X. Li, J. Xu, X. Wei, Talanta 75 (2008) 32.

[28] S.O. Obare, R.E. Hollowell, C.J. Murphy, Langmuir 18 (2002) 10407.
[29] N.P. Evmiridis, Analyst 112 (1987) 825.
[30] N.P. Evmiridis, N.K. Thanasoulias, A.G. Vlessidis, Talanta 46 (1998) 179.
[31] A. Safavi, M.A. Karimi, Anal. Chim. Acta 468 (2002) 53.
[32] M.S. Mahrous, M.M. Abdel-khalek, M.E. Abdel-Hamid, Talanta 32 (1985) 651.
[33] S. García, C. Sánchez-Pedreno, I. Albero, C. García, Mikrochim. Acta 136 (2001) 67.
[34] N.P. Evmiridis, A.G. Vlessidis, C.N. Thanasoulias, Bioinorg. Chem. Appl. 2007 (2007) 1 (article ID: 92595).
[35] B. Li, X. Zhang, C. Zhang, Anal. Chim. Acta 575 (2006) 212.